Editors

Leonard R. MacGillivray • Charles M. Lukehart

Metal-Organic Framework Materials

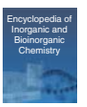
Encyclopedia of Inorganic and Bioinorganic Chemistry

Visit the online Encyclopedia of Inorganic and Bioinorganic Chemistry at **www.wileyonlinelibrary.com/ref/eibc**

WILEY

METAL-ORGANIC FRAMEWORK MATERIALS

EIBC Books



Application of Physical Methods to Inorganic and Bioinorganic Chemistry
Edited by Robert A. Scott and Charles M. Lukehart
ISBN 978-0-470-03217-6

Nanomaterials: Inorganic and Bioinorganic Perspectives
Edited by Charles M. Lukehart and Robert A. Scott
ISBN 978-0-470-51644-7

Computational Inorganic and Bioinorganic Chemistry
Edited by Edward I. Solomon, R. Bruce King and Robert A. Scott
ISBN 978-0-470-69997-3

Radionuclides in the Environment
Edited by David A. Atwood
ISBN 978-0-470-71434-8

Energy Production and Storage: Inorganic Chemical Strategies for a Warming World
Edited by Robert H. Crabtree
ISBN 978-0-470-74986-9

The Rare Earth Elements: Fundamentals and Applications
Edited by David A. Atwood
ISBN 978-1-119-95097-4

Metals in Cells
Edited by Valeria Culotta and Robert A. Scott
ISBN 978-1-119-95323-4

Metal-Organic Framework Materials
Edited by Leonard R. MacGillivray and Charles M. Lukehart
ISBN 978-1-119-95289-3

Forthcoming

The Lightest Metals: Science and Technology from Lithium to Calcium
Edited by Timothy P. Hanusa
ISBN 978-1-11870328-1

Sustainable Inorganic Chemistry
Edited by David A. Atwood
ISBN 978-1-11870342-7

Encyclopedia of Inorganic and Bioinorganic Chemistry

The Encyclopedia of Inorganic and Bioinorganic Chemistry (EIBC) was created as an online reference in 2012 by merging the Encyclopedia of Inorganic Chemistry and the Handbook of Metalloproteins. The resulting combination proves to be the defining reference work in the field of inorganic and bioinorganic chemistry. The online edition is regularly updated and expanded. For information see:

www.wileyonlinelibrary.com/ref/eibc

METAL-ORGANIC FRAMEWORK MATERIALS

Editors

Leonard R. MacGillivray

University of Iowa, Iowa City, IA, USA

Charles M. Lukehart

Vanderbilt University, Nashville, TN, USA

WILEY

This edition first published 2014
© 2014 John Wiley & Sons Ltd

Registered office

John Wiley & Sons Ltd, The Atrium, Southern Gate, Chichester, West Sussex,
PO19 8SQ, United Kingdom

For details of our global editorial offices, for customer services and for information about how to apply for permission to reuse the copyright material in this book please see our website at www.wiley.com.

The right of the authors to be identified as the authors of this work has been asserted in accordance with the Copyright, Designs and Patents Act 1988.

All rights reserved. No part of this publication may be reproduced, stored in a retrieval system, or transmitted, in any form or by any means, electronic, mechanical, photocopying, recording or otherwise, except as permitted by the UK Copyright, Designs and Patents Act 1988, without the prior permission of the publisher.

Wiley also publishes its books in a variety of electronic formats. Some content that appears in print may not be available in electronic books.

Designations used by companies to distinguish their products are often claimed as trademarks. All brand names and product names used in this book are trade names, service marks, trademarks or registered trademarks of their respective owners. The publisher is not associated with any product or vendor mentioned in this book. This publication is designed to provide accurate and authoritative information in regard to the subject matter covered. It is sold on the understanding that the publisher is not engaged in rendering professional services. If professional advice or other expert assistance is required, the services of a competent professional should be sought.

Library of Congress Cataloging-in-Publication Data

Metal-organic framework materials / editors, Leonard R. MacGillivray, Charles M. Lukehart.
pages cm
Includes bibliographical references and index.
ISBN 978-1-119-95289-3 (cloth)
1. Nanocomposites (Materials) 2. Organometallic compounds. 3. Metallic composites. 4. Polymeric composites. I. MacGillivray, Leonard R., editor. II. Lukehart, Charles M., 1946- editor.
TA418.9.N35M5245 2014
620.1'18–dc23

2014027085

A catalogue record for this book is available from the British Library.

ISBN-13: 978-1-119-95289-3

Set in 10/12pt TimesNewRomanMTStd by Laserwords (Private) Limited, Chennai, India
Printed and bound in Singapore by Markono Print Media Pte Ltd.

Encyclopedia of Inorganic and Bioinorganic Chemistry

Editorial Board

Editor-in-Chief

Robert A. Scott
University of Georgia, Athens, GA, USA

Section Editors

David A. Atwood
University of Kentucky, Lexington, KY, USA

Timothy P. Hanusa
Vanderbilt University, Nashville, TN, USA

Charles M. Lukehart
Vanderbilt University, Nashville, TN, USA

Albrecht Messerschmidt
Max-Planck-Institute für Biochemie, Martinsried, Germany

Robert A. Scott
University of Georgia, Athens, GA, USA

Editors-in-Chief Emeritus & Senior Advisors

Robert H. Crabtree
Yale University, New Haven, CT, USA

R. Bruce King
University of Georgia, Athens, GA, USA

International Advisory Board

Michael Bruce
Adelaide, Australia

Tristram Chivers
Calgary, Canada

Valeria Culotta
MD, USA

Mirek Cygler
Saskatchewan, Canada

Marcetta Darensbourg
TX, USA

Michel Ephritikhine
Gif-sur-Yvette, France

Robert Huber
Martinsried, Germany

Susumu Kitagawa
Kyoto, Japan

Leonard R. MacGillivray
IA, USA

Thomas Poulos
CA, USA

David Schubert
CO, USA

Edward I. Solomon
CA, USA

Katherine Thompson
Vancouver, Canada

T. Don Tilley
CA, USA

Karl E. Wieghardt
Mülheim an der Ruhr, Germany

Vivian Yam
Hong Kong

Contents

Contributors XI

Series Preface XV

Volume Preface XVII

PART 1: DESIGN AND SYNTHESIS **1**

Porous Coordination Polymer Nanoparticles and Macrostructures **3**
Julien Reboul and Susumu Kitagawa

Nanoscale Metal-Organic Frameworks **19**
Kyriakos C. Stylianou, Inhar Imaz and Daniel Maspoch

Mesoporous Metal-Organic Frameworks **39**
Yao Chen and Shengqian Ma

Porphyrinic Metal-Organic Frameworks **67**
Chao Zou, Min Zhao and Chuan-De Wu

Fluorinated Metal-Organic Frameworks (FMOFs): Concept, Construction, and Properties **85**
Pradip Pachfule and Rahul Banerjee

Synthesis and Structures of Aluminum-Based Metal-Organic Frameworks **99**
Norbert Stock

Polyrotaxane Metal-Organic Frameworks **115**
Stephen J. Loeb and V. Nicholas Vukotic

Photoreactive Metal-Organic Frameworks **135**
Anjana Chanthapally and Jagadese J. Vittal

Edible Metal-Organic Frameworks **159**
Ross Stewart Forgan

Mechanochemical Approaches to Metal-Organic Frameworks **173**
Tomislav Friščić

PART 2: POST-MODIFICATION **193**

Postsynthetic Modification of Metal-Organic Frameworks **195**
Andrew D. Burrows

PART 3: PROPERTIES AND APPLICATIONS **219**

Functional Magnetic Materials Based on Metal Formate Frameworks **221**
Ran Shang, Sa Chen, Zhe-Ming Wang and Song Gao

Metal-Organic Frameworks from Single-Molecule Magnets **245**
Athanassios D. Katsenis, Euan K. Brechin and Giannis S. Papaefstathiou

Open Metal Sites in Metal-Organic-Frameworks **259**
Yabing He and Banglin Chen

Gas Storage in Metal-Organic Frameworks **283**
Muwei Zhang, Hao Li, Zachary Perry and Hong-Cai Zhou

Metal-Organic Frameworks for Removal of Harmful Gases **303**
Jian Liu, B. Peter McGrail, Denis M. Strachan, Jun Liu, Jian Tian and Praveen K. Thallapally

Adsorption of Hydrocarbons and Alcohols in Metal-Organic Framework Materials **321**
Debasis Banerjee, Benjamin J. Deibert, Hao Wang and Jing Li

Metal Uptake in Metal-Organic Frameworks **343**
Michaele J. Hardie

Photoreactive Properties Hosted in Metal-Organic Frameworks **363**
Victoria J. Richards, Thomas J. Reade, Michael W. George and Neil R. Champness

Semiconducting Metal-Organic Frameworks **373**
Zhengtao Xu

Patterning Techniques for Metal-Organic Frameworks **387**
Paolo Falcaro and Mark J. Styles

Metal-Organic Frameworks in Mixed-Matrix Membranes **403**
Harold B. Tanh Jeazet and Christoph Janiak

Electrochemical Properties of Metal-Organic Frameworks **419**
Frédéric Jaouen and Adina Morozan

Applications of Metal-Organic Frameworks to Analytical Chemistry **443**
Na Chang, Cheng-Xiong Yang and Xiu-Ping Yan

Recent Solid-State NMR Studies of Quadrupolar Nuclei in Metal-Organic Frameworks **457**
Yining Huang, Jun Xu, Farhana Gul-E-Noor and Peng He

PART 4: NETS **471**

Single-Crystal to Single-Crystal Transformations in Metal-Organic Frameworks **473**
Subhadip Neogi, Susan Sen and Parimal K. Bharadwaj

Interpenetration and Entanglement in Coordination Polymers **523**
Stuart R. Batten

Index 539

Contributors

Debasis Banerjee *Rutgers University, Piscataway, NJ, USA*
- Adsorption of Hydrocarbons and Alcohols in Metal-Organic Framework Materials

Rahul Banerjee *CSIR-National Chemical Laboratory, Pune, India*
- Fluorinated Metal-Organic Frameworks (FMOFs): Concept, Construction, and Properties

Stuart R. Batten *Monash University, Melbourne, VIC, Australia* and *King Abdulaziz University, Jeddah, Saudi Arabia*
- Interpenetration and Entanglement in Coordination Polymers

Parimal K. Bharadwaj *Indian Institute of Technology Kanpur, Uttar Pradesh, India*
- Single-Crystal to Single-Crystal Transformations in Metal-Organic Frameworks

Euan K. Brechin *The University of Edinburgh, Edinburgh, UK*
- Metal-Organic Frameworks from Single-Molecule Magnets

Andrew D. Burrows *University of Bath, Bath, UK*
- Postsynthetic Modification of Metal-Organic Frameworks

Neil R. Champness *University of Nottingham, Nottingham, UK*
- Photoreactive Properties Hosted in Metal-Organic Frameworks

Na Chang *Tianjin Polytechnic University, Tianjin, PR China*
- Applications of Metal-Organic Frameworks to Analytical Chemistry

Anjana Chanthapally *National University of Singapore, Singapore*
- Photoreactive Metal-Organic Frameworks

Banglin Chen *University of Texas at San Antonio, San Antonio, TX, USA*
- Open Metal Sites in Metal-Organic-Frameworks

Sa Chen *Peking University, Beijing, PR China*
- Functional Magnetic Materials Based on Metal Formate Frameworks

Yao Chen *University of South Florida, Tampa, FL, USA*
- Mesoporous Metal-Organic Frameworks

Benjamin J. Deibert *Rutgers University, Piscataway, NJ, USA*
- Adsorption of Hydrocarbons and Alcohols in Metal-Organic Framework Materials

Paolo Falcaro *Commonwealth Scientific and Industrial Research Organization (CSIRO), Clayton South, VIC, Australia*
- Patterning Techniques for Metal-Organic Frameworks

Ross Stewart Forgan *University of Glasgow, Glasgow, UK*
- Edible Metal-Organic Frameworks

Tomislav Friščić *McGill University, Montreal, QC, Canada*
- Mechanochemical Approaches to Metal-Organic Frameworks

Song Gao *Peking University, Beijing, PR China*
- Functional Magnetic Materials Based on Metal Formate Frameworks

Michael W. George *University of Nottingham, Nottingham, UK*
- Photoreactive Properties Hosted in Metal-Organic Frameworks

Farhana Gul-E-Noor *The University of Western Ontario, London, ON, Canada*
- Recent Solid-State NMR Studies of Quadrupolar Nuclei in Metal-Organic Frameworks

Michaele J. Hardie *University of Leeds, Leeds, UK*
- Metal Uptake in Metal-Organic Frameworks

Peng He *The University of Western Ontario, London, ON, Canada*
- Recent Solid-State NMR Studies of Quadrupolar Nuclei in Metal-Organic Frameworks

Yabing He *Zhejiang Normal University, Jinhua, PR China*
- Open Metal Sites in Metal-Organic-Frameworks

Yining Huang *The University of Western Ontario, London, ON, Canada*
- Recent Solid-State NMR Studies of Quadrupolar Nuclei in Metal-Organic Frameworks

Inhar Imaz *ICN2 – Institut Catala de Nanociencia i Nanotecnologia, Barcelona, Spain*
- Nanoscale Metal-Organic Frameworks

Christoph Janiak *Heinrich-Heine-Universität, Düsseldorf, Germany*
- Metal-Organic Frameworks in Mixed-Matrix Membranes

Frédéric Jaouen *Université Montpellier II, Montpellier, France*
- Electrochemical Properties of Metal-Organic Frameworks

Athanassios D. Katsenis *National and Kapodistrian University of Athens, Athens, Greece*
- Metal-Organic Frameworks from Single-Molecule Magnets

Susumu Kitagawa *Kyoto University, Kyoto, Japan*
- Porous Coordination Polymer Nanoparticles and Macrostructures

Hao Li *Texas A&M University, College Station, TX, USA*
- Gas Storage in Metal-Organic Frameworks

Jing Li *Rutgers University, Piscataway, NJ, USA*
- Adsorption of Hydrocarbons and Alcohols in Metal-Organic Framework Materials

Jian Liu *Pacific Northwest National Laboratory, Richland, WA, USA*
- Metal-Organic Frameworks for Removal of Harmful Gases

Jun Liu *Pacific Northwest National Laboratory, Richland, WA, USA*
- Metal-Organic Frameworks for Removal of Harmful Gases

Stephen J. Loeb *University of Windsor, Windsor, ON, Canada*
- Polyrotaxane Metal-Organic Frameworks

Shengqian Ma *University of South Florida, Tampa, FL, USA*
- Mesoporous Metal-Organic Frameworks

Daniel Maspoch *ICN2 – Institut Catala de Nanociencia i Nanotecnologia, Barcelona, Spain* and *Institució Catalana de Recerca i Estudis Avançats (ICREA), Barcelona, Spain*
- Nanoscale Metal-Organic Frameworks

Adina Morozan *Université Montpellier II, Montpellier, France*
- Electrochemical Properties of Metal-Organic Frameworks

Subhadip Neogi *Indian Institute of Technology Kanpur, Uttar Pradesh, India*
- Single-Crystal to Single-Crystal Transformations in Metal-Organic Frameworks

V. Nicholas Vukotic *University of Windsor, Windsor, ON, Canada*
- Polyrotaxane Metal-Organic Frameworks

Pradip Pachfule *CSIR-National Chemical Laboratory, Pune, India*
- Fluorinated Metal-Organic Frameworks (FMOFs): Concept, Construction, and Properties

Giannis S. Papaefstathiou *National and Kapodistrian University of Athens, Athens, Greece*
- Metal-Organic Frameworks from Single-Molecule Magnets

Zachary Perry *Texas A&M University, College Station, TX, USA*
- Gas Storage in Metal-Organic Frameworks

B. Peter McGrail *Pacific Northwest National Laboratory, Richland, WA, USA*
- Metal-Organic Frameworks for Removal of Harmful Gases

Thomas J. Reade *University of Nottingham, Nottingham, UK*
- Photoreactive Properties Hosted in Metal-Organic Frameworks

Julien Reboul *Kyoto University, Kyoto, Japan*
- Porous Coordination Polymer Nanoparticles and Macrostructures

Victoria J. Richards *University of Nottingham, Nottingham, UK*
- Photoreactive Properties Hosted in Metal-Organic Frameworks

Susan Sen *Indian Institute of Technology Kanpur, Uttar Pradesh, India*
- Single-Crystal to Single-Crystal Transformations in Metal-Organic Frameworks

Ran Shang *Peking University, Beijing, PR China*
- Functional Magnetic Materials Based on Metal Formate Frameworks

Norbert Stock *Christian-Albrechts-Universität zu Kiel, Kiel, Germany*
- Synthesis and Structures of Aluminum-Based Metal-Organic Frameworks

Denis M. Strachan *Pacific Northwest National Laboratory, Richland, WA, USA*
- Metal-Organic Frameworks for Removal of Harmful Gases

Mark J. Styles *Commonwealth Scientific and Industrial Research Organization (CSIRO), Clayton South, VIC, Australia*
- Patterning Techniques for Metal-Organic Frameworks

Kyriakos C. Stylianou *ICN2 – Institut Catala de Nanociencia i Nanotecnologia, Barcelona, Spain*
- Nanoscale Metal-Organic Frameworks

Harold B. Tanh Jeazet *Heinrich-Heine-Universität, Düsseldorf, Germany*
- Metal-Organic Frameworks in Mixed-Matrix Membranes

Praveen K. Thallapally *Pacific Northwest National Laboratory, Richland, WA, USA*
- Metal-Organic Frameworks for Removal of Harmful Gases

Jian Tian *Texas A&M University, College Station, TX, USA*
- Metal-Organic Frameworks for Removal of Harmful Gases

Jagadese J. Vittal *National University of Singapore, Singapore*
- Photoreactive Metal-Organic Frameworks

Hao Wang *Rutgers University, Piscataway, NJ, USA*
- Adsorption of Hydrocarbons and Alcohols in Metal-Organic Framework Materials

Zhe-Ming Wang *Peking University, Beijing, PR China*
- Functional Magnetic Materials Based on Metal Formate Frameworks

Chuan-De Wu *Zhejiang University, Hangzhou, PR China*
- Porphyrinic Metal-Organic Frameworks

Jun Xu *The University of Western Ontario, London, ON, Canada*
- Recent Solid-State NMR Studies of Quadrupolar Nuclei in Metal-Organic Frameworks

Zhengtao Xu *City University of Hong Kong, Hong Kong, PR China*
- Semiconducting Metal-Organic Frameworks

Xiu-Ping Yan *Nankai University, Tianjin, PR China*
- Applications of Metal-Organic Frameworks to Analytical Chemistry

Cheng-Xiong Yang *Nankai University, Tianjin, PR China*
- Applications of Metal-Organic Frameworks to Analytical Chemistry

Muwei Zhang *Texas A&M University, College Station, TX, USA*
- Gas Storage in Metal-Organic Frameworks

Min Zhao *Zhejiang University, Hangzhou, PR China*
- Porphyrinic Metal-Organic Frameworks

Hong-Cai Zhou *Texas A&M University, College Station, TX, USA*
- Gas Storage in Metal-Organic Frameworks

Chao Zou *Zhejiang University, Hangzhou, PR China*
- Porphyrinic Metal-Organic Frameworks

Series Preface

The success of the *Encyclopedia of Inorganic Chemistry* (EIC), pioneered by Bruce King, the founding Editor in Chief, led to the 2012 integration of articles from the *Handbook of Metalloproteins* to create the newly launched *Encyclopedia of Inorganic and Bioinorganic Chemistry* (EIBC). This has been accompanied by a significant expansion of our Editorial Advisory Board with international representation in all areas of inorganic chemistry. It was under Bruce's successor, Bob Crabtree, that it was recognized that not everyone would necessarily need access to the full extent of EIBC. All EIBC articles are online and are searchable, but we still recognized value in more concise thematic volumes targeted to a specific area of interest. This idea encouraged us to produce a series of EIC (now EIBC) Books, focusing on topics of current interest. These will continue to appear on an approximately annual basis and will feature the leading scholars in their fields, often being guest coedited by one of these leaders. Like the Encyclopedia, we hope that EIBC Books continue to provide both the starting research student and the confirmed research worker a critical distillation of the leading concepts and provide a structured entry into the fields covered.

The EIBC Books are referred to as *spin-on* books, recognizing that all the articles in these thematic volumes are destined to become part of the online content of EIBC, usually forming a new category of articles in the EIBC topical structure. We find that this provides multiple routes to find the latest summaries of current research.

I fully recognize that this latest transformation of EIBC is built on the efforts of my predecessors, Bruce King and Bob Crabtree, my fellow editors, as well as the Wiley personnel, and, most particularly, the numerous authors of EIBC articles. It is the dedication and commitment of all these people that are responsible for the creation and production of this series and the "parent" EIBC.

Robert A. Scott
University of Georgia
Department of Chemistry

October 2014

Volume Preface

The field of metal-organic frameworks (MOFs) has experienced explosive growth in the past decade. The process of mixing readily available metal precursors with organic linkers has captured the imagination of chemists and materials scientists worldwide to an extent that discussions on uses of MOFs for energy storage, catalysis, and separations, as well as integrations into technologies such as fuel cells and electronics, have become commonplace. At the core of the explosion are uses of fundamental principles that define our understanding of inorganic chemistry and, more specifically, coordination chemistry. A main thesis that drives the design and formation of a MOF is that the linking of components will be sustained by coordination bonds and that the linkages will be propagated in space to reflect coordination geometries and requirements of metals. A critical backdrop is the field of solid-state chemistry that provides primary assessments and insights into the structure and properties of MOFs where concepts of crystal engineering help to drive new directions in design, synthesis, and improvement. Organic synthesis plays a vital role in not only the formation of molecules that link metals but also equipping a MOF with function that can be tailored. Moreover, it has been synergism between these highly fundamental disciplines that, collectively, have enabled the field of MOFs to grow and flourish to the exciting and highly interdisciplinary status that the field enjoys today.

Metal-Organic Framework Materials covers topics describing recent advances made by top researchers in MOFs including nanoparticles and nanoscale frameworks, mesoporous frameworks, photoreactive frameworks, polyrotaxane frameworks, and even edible frameworks, as well as functionalized frameworks based on porphyrins, fluorine, and aluminum. In addition, the volume features aspects on mechanochemical synthesis and post-synthetic modification, which provide discussions on new vistas on the "before" and "after" of framework design and construction.

Metal-Organic Framework Materials also gives up-to-date descriptions of the many properties and applications evolving from MOFs. Magnetic properties are highlighted as related to formates and single-molecule magnets while host–guest properties are discussed in terms of uptake and sequestering of gases, hydrocarbons, alcohols, and metals, as well as uses of open metal sites and photoreactive components in host design. Applications of MOFs to semiconductors, materials for patterning, integrations in mixed-matrix membranes, uses in electrochemical materials, and uses in analytical chemistry are also presented. Investigations that stem from solid-state chemistry based on characterizing MOFs using solid-state NMR analyses as well as studying single-crystal reactions of MOFs and understanding interpenetration and entanglement help us further understand the fundamentals of the field.

While the rapid and accelerating development of MOFs will prohibit a comprehensive treatment of the status of the field, we believe that *Metal-Organic Framework Materials* provides readers a timely update on established and fresh areas for investigation. The reader will develop firsthand accounts of opportunities related to fundamentals and applications of MOFs, as well as an emerging role of MOFs in defining a new materials space that stems from the general and main topic of inorganic chemistry.

Leonard R. MacGillivray
University of Iowa
Iowa City, IA, USA

Charles M. Lukehart
Vanderbilt University
Nashville, TN, USA

October 2014

Periodic Table of the Elements

Group →	1	2	3	4	5	6	7	8	9	10	11	12	13	14	15	16	17	18
Period → 1	1 H 1.0079																	2 He 4.0026
2	3 Li 6.941	4 Be 9.0122											5 B 10.811	6 C 12.0107	7 N 14.0067	8 O 15.9994	9 F 18.9984	10 Ne 20.179
3	11 Na 22.9898	12 Mg 24.305											13 Al 26.9815	14 Si 28.0855	15 P 30.9738	16 S 32.066	17 Cl 35.453	18 Ar 39.948
4	19 K 39.0983	20 Ca 40.078	21 Sc 44.9559	22 Ti 47.867	23 V 50.9415	24 Cr 51.996	25 Mn 54.9380	26 Fe 55.845	27 Co 58.933	28 Ni 58.693	29 Cu 63.546	30 Zn 65.409	31 Ga 69.723	32 Ge 72.64	33 As 74.9216	34 Se 78.96	35 Br 79.904	36 Kr 83.798
5	37 Rb 85.4678	38 Sr 87.62	39 Y 88.9059	40 Zr 91.224	41 Nb 92.9064	42 Mo 95.94	43 Tc 98.9062	44 Ru 101.07	45 Rh 102.9055	46 Pd 106.42	47 Ag 107.8682	48 Cd 112.41	49 In 114.818	50 Sn 118.710	51 Sb 121.760	52 Te 127.60	53 I 126.9045	54 Xe 131.29
6	55 Cs 132.9054	56 Ba 137.327	57-71 lanthanoids	72 Hf 178.49	73 Ta 180.9479	74 W 183.84	75 Re 186.207	76 Os 190.2	77 Ir 192.22	78 Pt 195.08	79 Au 196.9665	80 Hg 200.59	81 Tl 204.3833	82 Pb 207.2	83 Bi 208.9804	84 Po (209)	85 At (210)	86 Rn (222)
7	87 Fr (223)	88 Ra (226.0254)	89-103 actinoids	104 Rf (261.1088)	105 Db (262.1141)	106 Sg (266.1219)	107 Bh (264.12)	108 Hs (277)	109 Mt (268.1388)	110 Ds (271)	111 Rg (272)	112 Cn copernicium		114 Fl flerovium		116 Lv livermorium		

Atomic number → 3 (Li)
Atomic weight → 6.941 (Li)
Zintl border → (between 13 Al and 14 Si)

57 La lanthanum 138.9	58 Ce 140.12	59 Pr 140.9077	60 Nd 144.24	61 Pm (147)	62 Sm 150.36	63 Eu 151.96	64 Gd 157.25	65 Tb 158.9254	66 Dy 162.50	67 Ho 164.9304	68 Er 167.26	69 Tm 168.9342	70 Yb 173.04	71 Lu 174.967
89 Ac actinium 232.0381	90 Th 231.0359	91 Pa 238.0289	92 U 237.0482	93 Np (244)	94 Pu (243)	95 Am (247)	96 Cm (247)	97 Bk (251)	98 Cf (252)	99 Es (257)	100 Fm (260)	101 Md (259)	102 No (262)	103 Lr

Based on information from IUPAC, the International Union of Pure and Applied Chemistry (version dated 1st May 2013).
For updates to this table, see http://www.iupac.org/reports/periodic_table.

PART 1
Design and Synthesis

Porous Coordination Polymer Nanoparticles and Macrostructures

Julien Reboul and Susumu Kitagawa

Kyoto University, Kyoto, Japan

1	Introduction	3
2	Manipulation of the Size and Shape of PCP Crystals	4
3	PCP Crystal Assemblies and Macrostructures	11
4	Conclusion	16
5	Abbreviations and Acronyms	16
6	References	16

1 INTRODUCTION

The concept of "chemistry of organized matter" aims to extend the traditional length scales of synthetic chemistry through the assembly of nanostructured phases and the establishment of long-range organization.[1] Materials created by this approach possess properties that are either amplified versions of the properties of the smallest building blocks or emerged properties, not necessarily related to the building blocks.[1,2] Synthesized from the regular assembly of coordination complexes, porous coordination polymers (PCPs) are striking examples of such organized materials. Since the beginning of the development of PCPs in the early 1990s, PCPs were intensively studied due to scientific interest in the creation of nanometer-sized spaces and their enormous potential in applications such as gas storage, separation, photonics, and heterogeneous catalysis. Compared to other conventional porous solids such as zeolites and carbons, PCPs are of particular interest because they are synthesized under mild conditions and can be easily designed based on the appropriate choice or modification of the organic ligands and metal centers.

Beside the conventional research that aims at tuning PCP crystal characteristics at the molecular scale, recent research efforts focused on the extension of the level of design and organization of PCP crystals from the molecular to the nano- and macroscale.

Indeed, a special attention is currently given to the size- and shape-dependent properties of PCP crystals. Similarly to the case of zeolite nanocrystals, downsizing PCP crystals is expected to influence the sorption kinetics. The size decrease of porous materials also results in the decrease of the diffusion length within the bulk material toward the active sites, which is of high importance in catalysis and separation, especially in liquid-phase applications.[3] In addition to size-dependent properties related to their porosity, modulation of the size and shape of PCP crystals is expected to influence inherent properties of PCPs, such as their structural flexibility,[4] proton conduction[5] and charge transfer (ligand-to-metal or metal-to-ligand) abilities,[6] or luminosity (resulting from conjugated ligands).[7] Also, the preparation of stable and uniformly distributed suspensions of nanocrystals is a requisite for expanding the range of PCP applications. For instance, nanocrystalline and nontoxic PCPs are envisioned as drug delivery systems[8] and contrast agents.[9]

Regarding the construction of higher scale PCP-based materials, PCP crystals with well-defined shapes are of great interest as building units. A challenge today is to develop efficient strategies that allow the integration of PCPs into readily applicable devices that fully exploit the attributes of these materials. Thin films and patterned surfaces made of oriented and well-intergrown PCP crystals were shown to be promising for molecular separation[10,11] or sensing.[12–14] Three-dimensional PCP-based architectures possessing a multimodal porosity are useful to improve the molecular diffusion when used as separation systems and catalysts.[15,16]

Metal-Organic Framework Materials. Edited by Leonard R. MacGillivray and Charles M. Lukehart.
© 2014 John Wiley & Sons, Ltd. ISBN 978-1-119-95289-3

Owing to the highly reactive surfaces of PCPs (composed of partially coordinated organic ligands or uncoordinated metal centers), the possible modulation of the coordination equilibrium, and the large number of PCP framework available (implying a large range of possible synthesis conditions), many of the chemical and microfabrication methods established for the manipulation of both purely organic and inorganic compounds were applied for the synthesis of PCPs. As it will be illustrated later in this chapter, utilization of microwave treatment, microemulsion methods, or capping agents was successful for the control of the size and shape of PCP crystals. PCP crystal assemblies were obtained by employing Langmuir–Blodgett (LB) technology, hard or soft-templating approaches, and pseudomorphic replacement approaches.

This chapter attempts to give an overview of the most promising strategies applied so far for the synthesis of PCP nanocrystals and PCP-based macrostructures and composites. The second section of this chapter focuses on the control of the size and shape of PCP crystals. The third section describes the strategies employed for the synthesis of PCP-based polycrystalline macrostructures and composites.

2 MANIPULATION OF THE SIZE AND SHAPE OF PCP CRYSTALS

2.1 Microwave and Ultrasonication-assisted Synthesis

PCPs are generally synthesized in water or organic solvents at temperatures ranging from room temperature to approximately 250 °C (see ***Nanoscale Metal-Organic Frameworks***). Ovens or oil baths for which heat is transferred through conduction and convection are commonly used. Recently, microwave has been employed in order to reduce the energy consumption and the reaction time while increasing the yields.[17] Beside the advantage related to its energy efficiency, microwave heating was shown to have a significant impact on the size and morphology of the PCP crystals synthesized by this means.

In the microwave frequency range, polar molecules in the reaction mixture try to orientate with the electric field. When dipolar molecules try to reorientate with respect to an alternating electric field, they lose energy in the form of heat by molecular friction. Microwave heating therefore provides a rapid and uniform heating of solvents, reagents, intermediates, and products.[18] Application of this fast and homogeneous heating to the synthesis of PCPs provides uniform nucleation and growth conditions, leading to more uniform PCP crystals with smaller size than in the case of conventional heating processes.[19–21]

Examples of microwave synthesis resulting in the formation of PCP crystals with a narrow size distribution and comprised within the submicrometer regime are still scarce. Masel *et al*. produced nanocrystals of the cubic zinc carboxylate reticular $[Zn_4O(bdc)_3]$ (MOF-5 or IRMOF-1, where bdc = 1,4-benzenedicarboxylate), $[Zn_4O(Br\text{-}bdc)_3]$ (IRMOF2, where Br-bdc = 2-bromobenzenedicarboxylate), and $[Zn_4O(NH_2\text{-}bdc)_3]$ (IRMOF3, where NH_2-bdc = 2-amino-benzenedicarboxylate) at 150 W, in a few seconds and under relatively diluted concentrations.[22] Chang *et al*. reported the microwave synthesis of nanocrystals of the cubic chromium terephthalate $[Cr_3F(H_2O)_2O(bdc)_3{\cdot}nH_2O]$ (MIL-101) with a size range from 40 to 90 nm.[23] The authors clearly demonstrate the impact of irradiation time over the dimension of the crystals and the homogeneity of the sample. Small sizes were observed for materials prepared using short crystallization times (Figure 1). Nevertheless, physicochemical and textural properties of the crystals were similar to those of materials synthesized using the conventional hydrothermal method.

Ultrasonication is another alternative strategy to conventional heating processes that competes with microwave irradiation in terms of reduction of the crystallization time and crystal size.[24–26] Sonochemistry relies on the application of high-energy ultrasound to a reaction mixture. The rate acceleration in sonochemical irradiation stems from the formation and collapse of bubbles in solution, termed acoustic cavitation, which produces very high local temperatures (>5000 K) and pressures, resulting in extremely fast heating and cooling rates.[27] Development of sonochemical synthesis for the production of PCPs is still at an early stage. However, some recent reports already demonstrated the power of this means for the production of PCP nanocrystals with uniform sizes and shapes. Qiu *et al*. reported the synthesis of nanocrystals of a fluorescent PCP, $[Zn_3(btc)_2{\cdot}12H_2O]_n$ (with btc = benzene-1,3,5-tricarboxylate), with size ranging from 50 to 100 nm within 10 min. Interestingly, the size and the shape of the crystal were tunable by varying the reaction time.[28] Sonocrystallization of the zeolitic imidazolate frameworks $[Zn(PhIM)_2{\cdot}(H_2O)_3]$ (ZIF-7, where PhIM = benzylimidazole), $[Zn(MeIM)_2{\cdot}(DMF){\cdot}(H_2O)_3]$ (ZIF-8, where MeIM = 2-methylimidazole), $[Zn(PhIM)_2{\cdot}(DEF)_{0.9}]$ (ZIF-11), and $[Zn(Pur)_2{\cdot}(DMF)_{0.75}{\cdot}(H_2O)_{1.5}]$ (ZIF-20, where Pur = purine) led to the formation of uniform nanocrystals in shorter time than conventional solvothermal methods (6–9 h) and at lower temperatures (45–60 °C).[29]

2.2 Utilization of Ligand Deprotonating Agents

Addition of a base to deprotonate the organic linker was used as a strategy to regulate the early stage of crystallization. Li *et al*. prepared highly uniform suspensions of ZIF-7 nanocrystal suspensions by dissolving zinc nitrate and benzimidazolate (bim) into a polyethylene imine (PEI)-dimethylformamide (DMF)

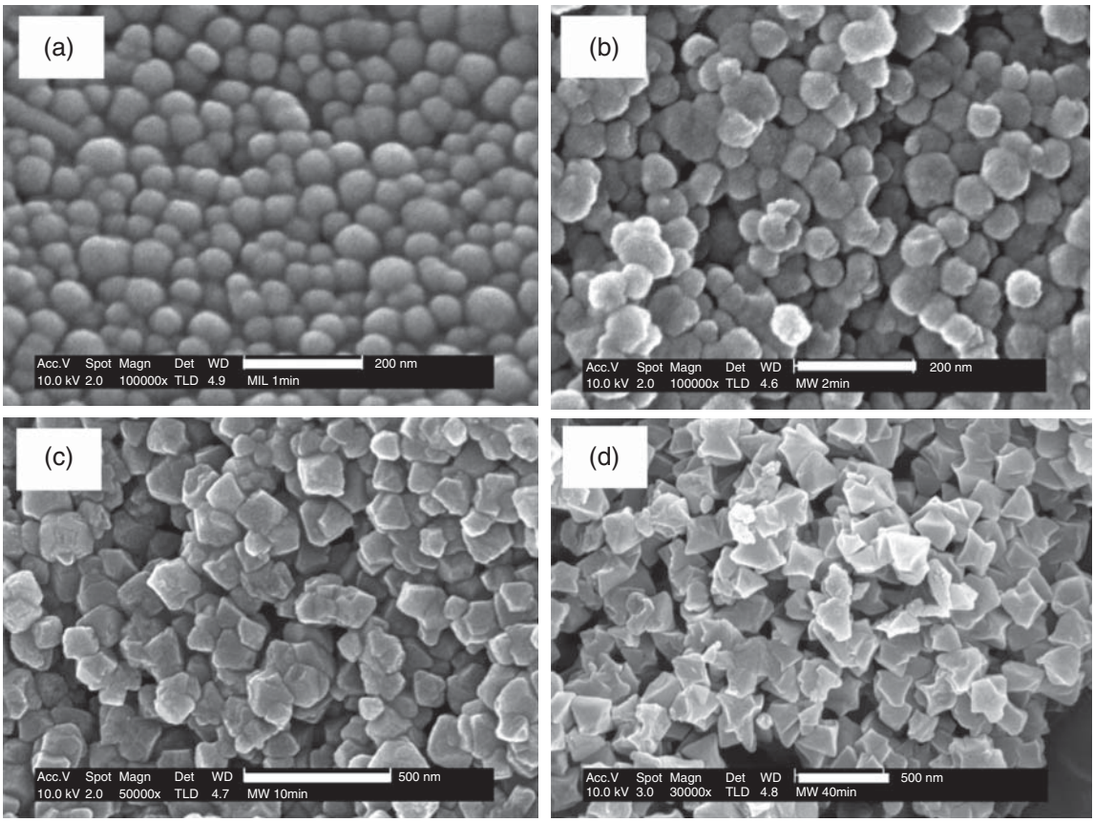


Figure 1 SEM images of MIL-101 prepared using microwave irradiation at 210 °C for various crystallization times: (a) 1, (b) 2, (c) 10, and (d) 40 min. White scale bars indicate (a,b) 200 nm and (c,d) 500 nm. (Adapted from Ref. 23. © WILEY-VCH Verlag GmbH & Co. KGaA, 2007.)

solution at room temperature (Figure 2). The authors could adjust the size of the nanocrystals from 40 to 140 nm by altering the molar ratio of PEI and the reaction duration. PEI has a high density of amino groups, it efficiently deprotonates bim and therefore permits a fast generation of a large number of ZIF-7 nuclei, which is a critical issue for the synthesis of nanoscale crystals.[30]

A similar strategy was followed by Xin *et al.* to produce Zn(ICA) (ZIF-90, where ICA = imidazole-2-carboxyaldehyde) with triethylamine (TEA) as the deprotonating agent at room temperature.[31] TEA was also employed to manipulate the particle size and shape of $[Cu_3(btc)_2]$[32] and a coordination polymer particle by mixing 4,40-dicarboxy-2,20-bipyridine (H_2dcbp) and $Cu(OAc)_2$ in mixed solvents of water at room temperature.[33]

2.3 Reverse Microemulsion

Reverse micelles or water-in-oil microemulsion systems are thermodynamically stable liquid dispersions containing surfactant aggregates with well-defined structures, typically characterized by a correlation length in the nanometer scale. Small water droplets in the microemulsion can be considered as nanoscopic reactors. They were used for the synthesis of a range of nanomaterials,[34] including organic polymers, semiconductors, and metal oxide and recently for the synthesis of nanoscale PCP crystals. Lin's group was the first to adapt the water-in-oil microemulsion-based methodology to the field of PCP for the production of $[Gd(bdc)_{1.5}\cdot(H_2O)]$ nanorods by stirring a microemulsion of $GdCl_3$ and bis(methylammonium)benzene-1,4-dicarboxylate in a 2:3 molar ratio in the cationic cetyltrimethylammonium bromide (CTAB)/isooctane/1-hexanol/water system for 2 h (Figure 3).[35,36] As the crystal formation takes place inside the droplet during the reverse microemulsion process, the morphologies and sizes of the colloidal particles are generally affected by the droplet structure and its ability to exchange the micellar-containing content.[37] Accordingly, the type of surfactant and the water-to-surfactant ratio (w) are critical parameters. For the same surfactant, Lin *et al.* demonstrated that the morphologies and sizes of the PCP

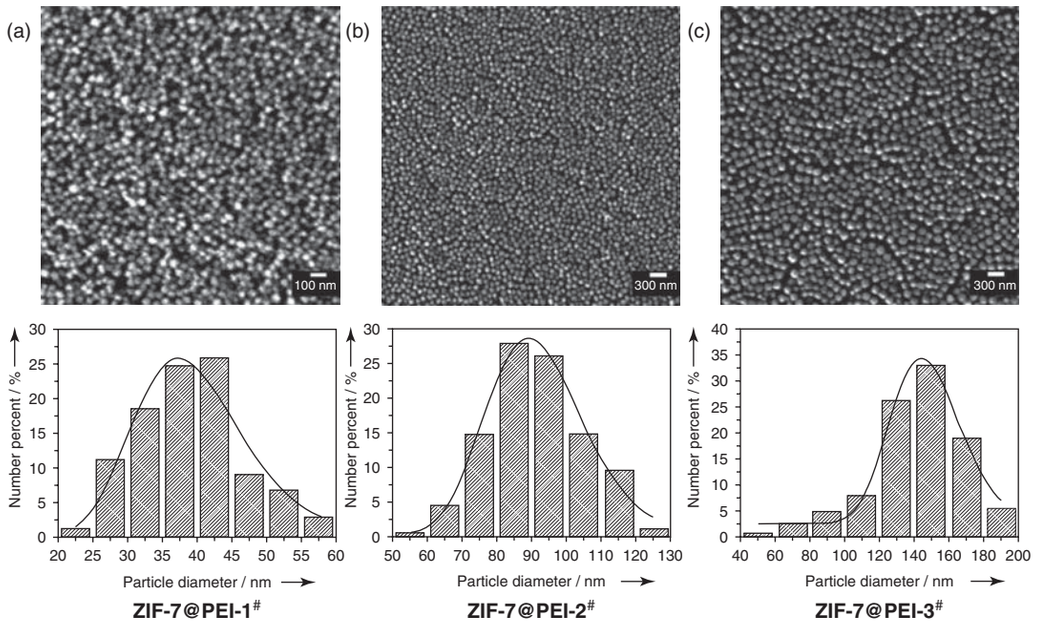


Figure 2 SEM images and size distributions of the ZIF-7 nanoparticles synthesized by adding various amount of a branched PEI (average Mw = 25 000): 0.140, 0.140, and 0.360 g for ZIF-7@PEI-1# (a), ZIF-7@PEI-2# (b), and ZIF-7@PEI-3# (c), respectively. (Adapted with permission from Ref. 30. © WILEY-VCH Verlag GmbH & Co. KGaA, 2010.)

nanorods were influenced by the *w* value of the microemulsion systems. Nanorods of 100–125 nm in length by 40 nm in diameter were obtained with $w = 5$. Significantly longer nanorods (1–2 μm in length and approximately 100 nm in diameter) were obtained with $w = 10$ under otherwise identical conditions. The authors also showed that a decrease in the concentration of reactants or a deviation of the metal-to-ligand molar ratio resulted in a decrease of the particle size.

Reverse emulsion in which water is replaced by a nonaqueous polar solvent such as ethylene glycol, acetonitrile, or DMF was obtained using the surfactant dioctyl sulfosuccinate sodium salt (also named Aerosol-OT, AOT).[38] Regarding PCP nanocrystal synthesis, utilization of such microemulsions was found to be of interest when PCP precursors are insoluble in water. Kitagawa *et al*. synthesized nanocrystals of a flexible PCP [Zn(ip)(bpy)] (CID-1, where ip = isophthalate and bpy = 4,4′-bipyridyl) in the nonaqueous system AOT/*n*-heptane/*N*,*N*-DMF.[39] Both the metal precursor ($Zn(NO_3)_2 \cdot 6H_2O$) and the ligands (H_2ip and bpy) being insoluble in water, a precursor solution was first prepared with DMF as solvent. A volume of AOT/*n*-heptane solution was then injected into the precursor solution and the microemulsion hence formed was sonicated for 10 min. Figure 4 illustrates the PCP nanocrystal formation and growth mechanism proposed by the authors. Briefly, the formation of the microemulsion under sonication is at the origin of the rapid apparition of a multitude of PCP nuclei within the DMF droplets. Merging of droplets during the process leads to the growth of the particles. As the particle size extends, their aggregation occurs, leading to the surface coordination of AOT. This surface coordination of AOT limits diffusion of metal ions and ligands to the crystal surface, which finally limits the particle growth and the reaction yield.

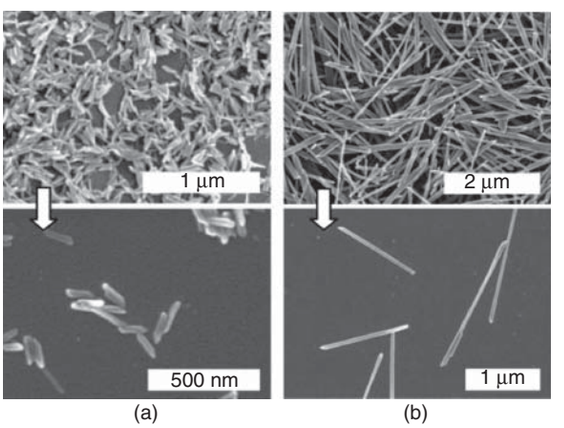


Figure 3 SEM images of $[Gd(bdc)_{1.5} \cdot (H_2O)_2]$ (1) nanorods synthesized with $w = 5$ (a) and $w = 10$ (b). (Adapted with permission from Ref. 35. Copyright (2006) American Chemical Society.)

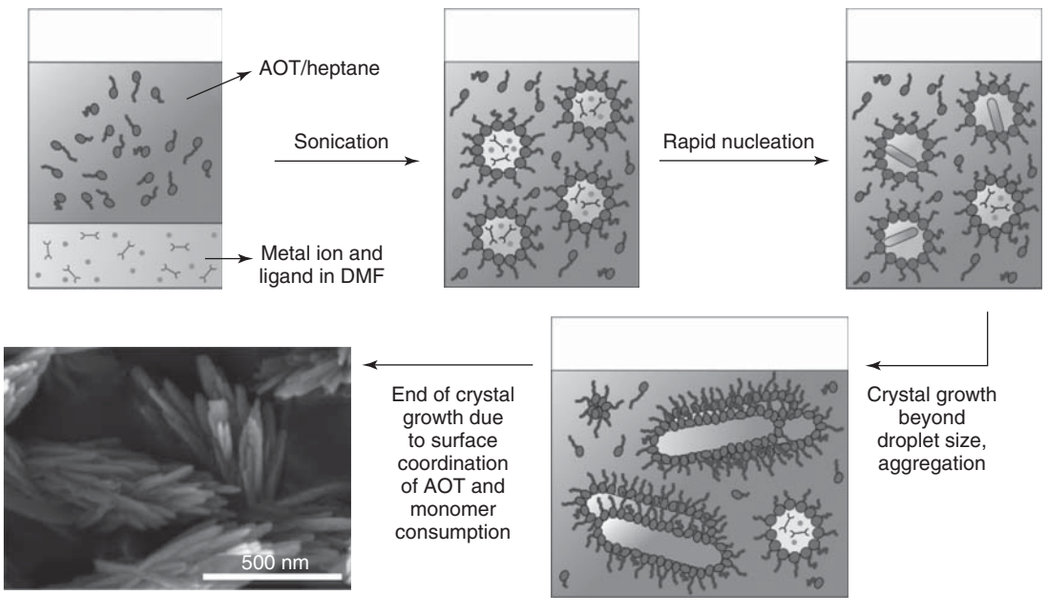


Figure 4 Model for PCP nanoparticle formation and growth through a nonaqueous reverse microemulsion process. (Reprinted by permission from Macmillan Publishers Ltd: Nature Chemistry, (Ref. 39), copyright (2010). http://www.nature.com/nchem/index.html.)

2.4 Utilization of Organic Additives

Modulation of the surface energy of crystals by the addition of various organic or inorganic additives is a well-known strategy for tuning their equilibrium morphology and size in a predictable way.[40]

The high interface energy of PCP crystals originates from the presence of partially uncoordinated organic linkers and unsaturated metal cations on their external surfaces. Ionic, dipolar, highly polarizable, or hydrophobic forces may thus exist on the crystal faces depending on the chemical nature of the organic ligands and of the pH of the medium. Consequently, saturation of the surface-dangling functions can be achieved with a wide variety of additives (via ionic or coordinative bonding, dipole–dipole, hydrogen bonding, van der Waals interactions, etc.). So far, control of the shape and size of PCP crystals was achieved using various polymers,[41] ionic surfactants,[42–45] and mixtures of polymers and surfactants.[46]

Coordination modulation approach consists in the utilization of monofunctional capping agents bearing the same functionality than the multifunctional ligands involved in the construction of the PCP frameworks. This strategy relies on the regulation of the coordination equilibrium at the crystal surface through the competition between the monofunctional and the multifunctional ligands for the complexation of the metal centers.[47]

Hermes *et al*. utilized *p*-perfluoromethylbenzenecarboxylate (pfmbc) as a modulator to block the growth of MOF-5.[48] A growth habit where a fast nucleation step precedes a slower step of particle growth was first verified by means of a time-resolved static light scattering (TLS) investigation without addition of the modulator. The addition of an excess of pfmbc to the reaction mixture after initiating the PCP growth stabilized the crystal extension around 100 nm, leading to the formation of highly stable colloidal suspensions at 25 °C. This result was in contrast to the uncapped case, for which the sedimentation occurs after a while. As observed by TLS, crystals grow in the shape of perfect cubes from the very beginning reflecting the 3D cubic framework of MOF-5. In the case of such isotropic crystal, where all the outer faces are similar, modulators most likely cover the entire crystal surface and induce the reduction of the overall crystal growth rate. In this system, the modulator quenches the crystal growth and prevents the aggregation of the nanocrystals.

Tsuruoka *et al*. extended the use of modulators to control the size and morphology of a crystal system based on an anisotropic framework.[47] The three-dimensional porous coordination framework $[Cu_2(ndc)_2(dabco)]$ (where ndc = 1,4-naphthalenedicarboxylate and dabco = 1,4-diazabicyclo[2.2.2]octane) has a tetragonal crystal system, in which the dicarboxylate layer ligands (ndc) link to the dicopper clusters to form two-dimensional square lattices, which are connected by amine pillar ligands (dabco) at the lattice points. The selective modulation of one of the coordination modes (ndc–copper) with acetic acid as the modulator resulted in the formation of nanocrystals with a square-rod morphology. The electron diffraction pattern of individual nanorods revealed a correlation between

the anisotropic crystal morphology and the tetragonal framework system; the major axis of the nanorod was coincident with the [001] direction of the framework. Therefore, the coordination mode of dabco–copper in the [001] direction is the more preferable interaction for crystal growth than the coordination mode of ndc–copper in the [100] direction. The ndc–copper interaction, which forms the two-dimensional layer, was impeded by the presence of acetic acid as the modulator because both ndc and acetate have the same carboxylate functionality. Therefore, the selective coordination modulation method enhanced the relative crystal growth in the [001] direction. Interestingly, transmission electron microscopy (TEM) time course analysis of this anisotropic crystal growth revealed an aggregation-mediated crystal growth mechanism where the modulator adsorbs onto specific faces of nanocrystals, thus coding for a subsequent aggregation process. Such oriented attachments are known to occur for the kinetically controlled regime in the presence of stabilizing additives.[49] Figure 5 illustrates the mechanism proposed by the authors for the formation of the $[Cu_2(ndc)_2(dabco)]$ nanorods. The growth process of nanocubes is a consequence of nanoparticle aggregation-mediated crystal growth. The selective coordination modulation on the (100) surfaces of the nanocubes induces the oriented attachment leading the growth of nanorods in the [001] direction.

Do *et al.* demonstrated the synthesis of $[Cu_2(ndc)_2(dabco)]$ with cubic and sheet-like morphologies by simultaneously modulating both copper–ndc and copper–dabco coordination modes.[50] In addition to the monocarboxylic acid that competes with ndc for the coordination of copper, the authors cunningly added amines containing a nitrogen atom with a lone pair capable of impeding the coordination between copper and dabco. As a result, both [100] and [001] directions of the crystal growth could be regulated to form nanocubes using both modulators, nanosheets using only the amine (pyridine), and nanorods using only the acetic acid.

A crucial consequence of the competitive interaction between the coordination mode used to construct the framework and the modulator–metal center is the reduction of the nucleation rate. This feature makes possible the formation of highly crystalline nanocrystals even under kinetically controlled regime where the fast nucleation would lead to poorly crystalline crystals in the absence of a modulator.

On the basis of these considerations, Diring *et al.* developed a strategy for the multiscale synthesis of PCP combining the coordination modulation method with the microwave-assisted synthesis, two apparently antagonistic conditions.[51] On one hand, microwave-assisted heating considerably accelerates nucleation and crystal growth processes, providing phase-pure materials with a homogeneous size distribution. On the other hand, a high concentration of monocarboxylic acid additive effectively slows down the reaction rate of carboxylate-based PCPs through the stabilization of the monomer precursors, thus allowing the formation of highly crystalline materials. The size of the cubic framework $[Cu_3(btc)_2]$ could be successfully tuned from 20-nm globular particles up to 2-μm cubic crystals through the modulation effect the *n*-dodecanoic acid as additive.

As summarized in Figure 6, increasing the concentration of monocarboxylic acid modulator unambiguously leads to the increased mean size of the resulting crystals (variation of *r* in Figure 6; *c* is the global concentration of reactants).

This tendency, which has already been observed with polymer additives,[52] is in opposition with conventional methods for tuning the crystal size, where higher concentrations of additives usually yield smaller crystals because of the efficient suppression of the framework extension. In this case, the monocarboxylic acid is expected to

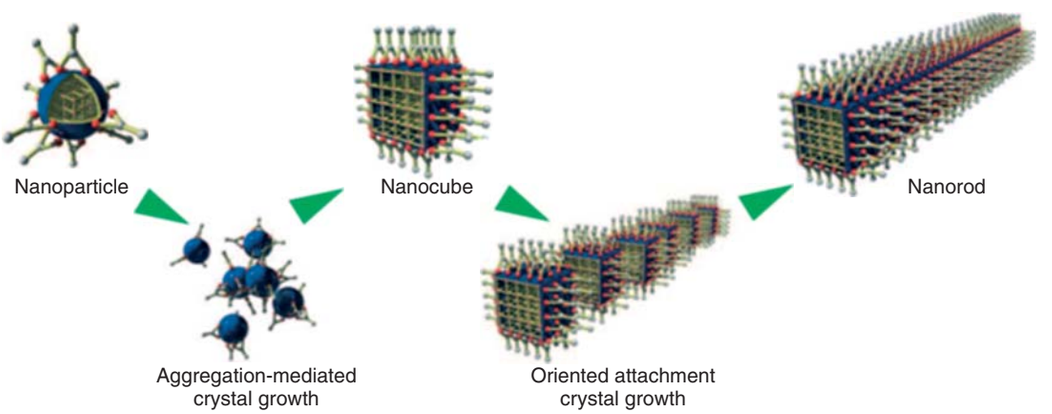


Figure 5 Proposed growth mechanism for $[Cu_2(ndc)_2(dabco)]$ nanorods. (Adapted with permission from Ref. 48. Copyright (2007) American Chemical Society.)

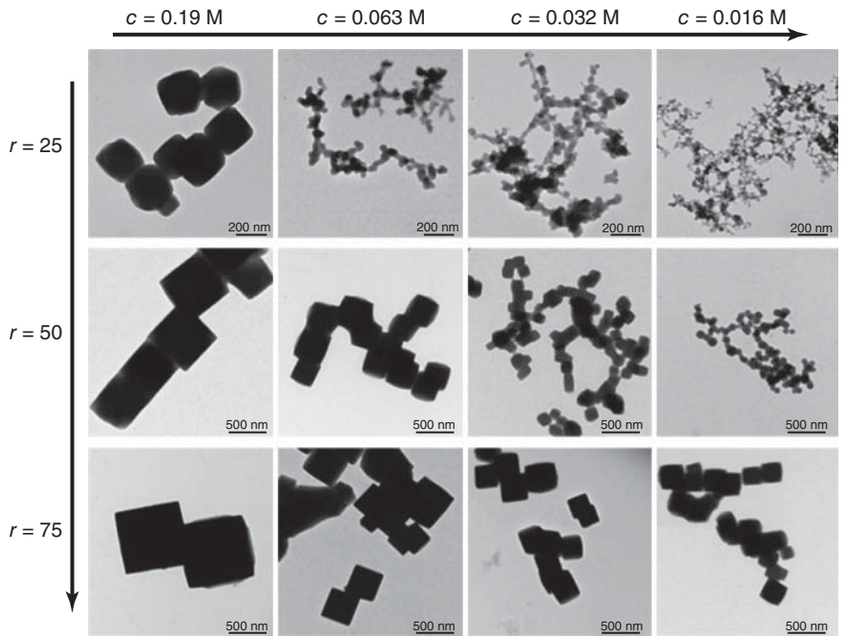


Figure 6 TEM images of samples obtained with various concentrations of dodecanoic acid and benzene-1,3,5-tricarboxylic acid. All samples were prepared under microwave irradiation (140 °C, 10 min). (Adapted with permission from Ref. 51. Copyright (2010) American Chemical Society.)

efficiently influence the nucleation process by creating a competitive situation for the complexation of copper(II) cations, thus decreasing the oversaturation of the precursor materials. Consequently, although the microwave-assisted heating is known to drastically increase the rates of the nucleation and crystal growth processes, high concentrations of additive, however, provide a slow nucleation (fewer nuclei) of the $[Cu_3(btc)_2]$ framework. A smaller number of crystals are indeed growing in line with the persistent nucleation during the heating process, leading to larger crystals with greater size polydispersity. With lower concentrations of the modulator, the nucleation occurs faster. A large number of nuclei are formed and they rapidly grow at the same time, while the available reagents are quickly depleted, affording smaller crystals with homogeneous size distribution. The correlation between the sorption properties and crystallinity of the nanoparticles indicated that the crystallinity of the obtained nanocrystals was comparable to that of bulk crystals obtained from optimized solvothermal methods. It is worth noting that although the excessive stabilization of the PCP precursor (at high modulator concentration) is inadequate for the formation of nanocrystals, it can be of interest for the synthesis of phase-pure sample containing PCP single crystals large enough for single-crystal experiment.[53]

Another example of the beneficial effect of the association of coordination modulation method with the microwave process was reported by Sakata *et al*. who controlled the crystal size and morphology of the zinc framework $[Zn_2(ndc)_2(dabco)]$.[54] Nanosized rod-shaped crystals were successfully synthesized under microwave condition with lauric acid as the modulator. Powder X-ray diffraction measurements and thermogravimetric analysis indicated that the nanocrystals maintain high crystallinity even after miniaturization into nanoscale. Interestingly, the conventional heating procedure using an oil bath with modulators did not give any nanosized crystals but rather resulted in the formation of micrometer-sized crystals. This is because the nucleation process was not accelerated enough to give the nanocrystals. Microwave heating was, therefore, essential to give rapid nucleation of the crystals. On the other hand, the microwave treatment without modulators gave no precipitation. This result indicates that nucleation of this framework system was too fast and that all starting materials were consumed to produce excessively small nuclei that remain in suspension. Here again, the complementary effect of the microwave treatment and coordination modulation method is critical for obtaining both nanosized and highly crystalline PCP crystals. By guaranteeing the production of a high amount of nuclei, microwave process makes the modulation strategy generalizable for the production of PCP nanocrystals with crystal systems for which the low nucleation rate would not permit the success of the coordination modulation under conventional heating.

Interestingly, microwave is not the only way to accelerate the crystal nucleation in the presence of a modulator. Ma *et al*. also succeeded in synthesizing nanosized crystals of MOF-5 and MOF-3 with appreciable crystallinity.[43] In this case, the appropriate tuning of the PCP nucleation rate was achieved by the combination of hexadecyltrimethylammonium bromide (CTAB), used to stabilize well-defined secondary building units, and the addition of an amine, used to trigger the rapid precipitation through the deprotonation of the organic ligands.

Microwave-assisted nucleation and crystal growth modulation of PCP crystals also enabled the control of the morphology of microscale crystals. Umemura *et al*. demonstrated the morphological transition of $[Cu_3(btc)_2]$, a rather complicated framework with twisted boracite topology (tbo) from octahedron to cuboctahedron-cube induced by an increase in the concentration of a monocarboxylic acid (lauric acid) as the modulator.[55] By suitably defining a coarse-grained standard unit of $[Cu_3(btc)_2]$ as its cuboctahedron main pore and determining its attachment energy on crystal surfaces, Monte Carlo coarse-grain modeling revealed the population and orientation of carboxylates and enabled to elucidate the important role of the modulator in determining the ⟨100⟩ and ⟨111⟩ growth throughout the crystal growth process. The authors proposed that the modulator acts as a growth-blocking agent specifically on the {100} faces because the growth of these faces involves a larger number of carboxylate compared to the growth of the {111} faces. Consequently, the increase of modulator concentration results in a change of crystal surface relative energies toward the stabilization of the {100} faces and therefore in the formation of cubes instead of octahedrons.

2.5 Size and Morphology Dependence of PCP Nanocrystal Sorption Properties

Beside the appropriate design of their chemical composition, the control of morphology and size of PCP crystals at the nanoscale provides an additional mean to modulate their physicochemical properties, in particular their sorption capacity. Recent studies showed that when PCP crystals are downsized to the nanometer scale and for peculiar morphologies, the external surface of the crystal starts to influence the sorption kinetics and sorption type. This phenomenon was explained by the decrease of the diffusion length toward the adsorption sites and by the enhanced accessibility of specific pore entrances.[56,57] Contribution of the size and shape of the crystals upon the sorption properties is an inherent feature of porous materials, which was exploited for facilitating their integration into catalysis, separation, or sensing systems.

Downsizing the crystals could also regulate PCP attributes arising from their unique hybrid nature, such as the flexibility of the hybrid framework. The reduction

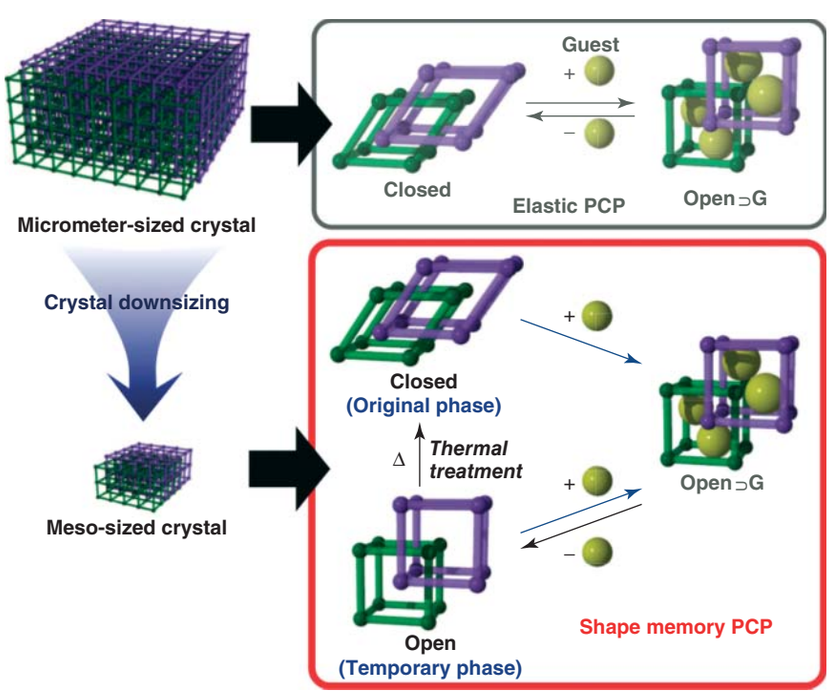


Figure 7 Schematic illustration of the induction of the shape-memory effect in porous frameworks through crystal downsizing, which suppresses the structural mobility. (Adapted from Ref. 58. Reprinted with permission from AAAS.)

of the crystal size by means of coordination modulation allowed Sakata *et al*. to suppress the structural mobility of the system [Cu_2(dicarboxylate)$_2$(amine)] composed of the twofold interpenetrated frameworks and therefore to isolate an unusual metastable open dried phase in addition to the two structures that contribute to the sorption process (i.e., a nonporous closed phase and a guest-included open phase). The closed phase was then recovered by thermal treatment.[58] These results suggest that framework flexibility could be controlled by crystal size. This shape memory effect applied to PCP is illustrated in Figure 7.

3 PCP CRYSTAL ASSEMBLIES AND MACROSTRUCTURES

3.1 Assemblies of Preformed PCP Crystals

Recent progresses in size and shape control of PCP crystals (illustrated in the previous section) made possible the use of PCP crystals as building blocks for the construction of superstructures (see ***Patterning Techniques for Metal-Organic Frameworks***). Sequential procedures, where the preparation of homogeneous suspensions of PCP crystals is followed by the application of chemical and physical microfabrication methods, were recently reported.

3.1.1 Crystal Suspensions Casted on Solid Platforms

Horcajada *et al*. [59] prepared smooth PCP films by the deposition of [$Fe_3OCl(muc)_3$] (where muc = muconate dicarboxylate) nanocrystals by a dip-coating method. Uniform nanocrystals were obtained by applying the coordination modulation method. Following a similar strategy, Guo *et al*. prepared luminescent thin films with controllable thickness by spin-coating of nanoscale [Ln(btc)(H_2O)] (where Ln = Dy^{3+}, Eu^{3+}, or Tb^{3+}).[60]

Yanai *et al*. recently demonstrated the first directional facet-to-facet attraction between ZIF-8 particles through simple capillary or van der Waals attraction, leading to well-defined clusters and hexagonal arrangements (Figure 8).[61] In this work, a spontaneous process associated with solvent evaporation triggered the formation of the assemblies.

3.1.2 Liquid–Air and Liquid–Liquid Interfacial Assembly

Tsotsalas *et al*. assembled PCP crystals of various composition and uniform morphologies (also synthesized through the action of monofunctional modulators) by an LB approach.[62] This method enabled the preparation of freestanding films composed of crystal monolayers. Noteworthy, the preferential crystal orientation observed after LB assembly depends on the crystal morphology.

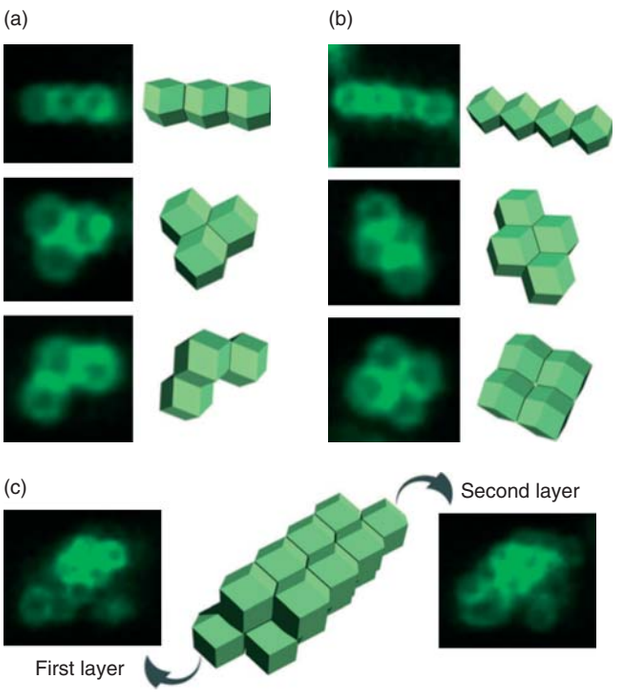


Figure 8 Confocal microscopy images of dye-modified particles and accompanying schematic illustrations. (a) Trimers were linear, triangular, and U-shaped. (b) Tetramers were linear, rhombic, and square. (c) Larger structures exhibited an fcc packing. (Adapted with permission from Ref. 61. © WILEY-VCH Verlag GmbH & Co. KGaA, 2012.)

Huo *et al*. also reported the assembly of PCP crystals at a liquid–liquid interface through the preparation of oil-in-water (o/w) Pickering emulsions stabilized by the assembly of preformed PCP nanocrystals at the o/w interface. The emulsions are formed by application of high shear forces to biphasic mixtures of dodecane and aqueous dispersions of PCP nanocrystals. Incorporation in the organic inner phase of monomers, cross-linkers, and an initiator enables the polymerization of the interior of the PCP vesicles (also named MOFsomes) to form capsular composite structures composed of PCP nanocrystals embedded within the surface of a polymer shell.[63] Pang *et al*. recently reported another example of PCP-based colloidosome formation where cubes of the framework [$Fe_3O(H_4ABTC)_{1.5}(H_2O)_3$]·($H_2O$)$_3$·($NO_3$) were employed as building units to stabilize emulsion droplets in a one-step emulsion-templating approach.[64] In this procedure, emulsified droplets were formed by vigorously stirring the PCP precursor mixture in the presence of polyoxyethylene (20) sorbitan trioleate (tween-85) and *tert*-butylamine. The authors proposed that tween-85 assists the formation of the emulsified droplets and cooperatively regulates the PCP crystal growth with the *tert*-butylamine. The hollow

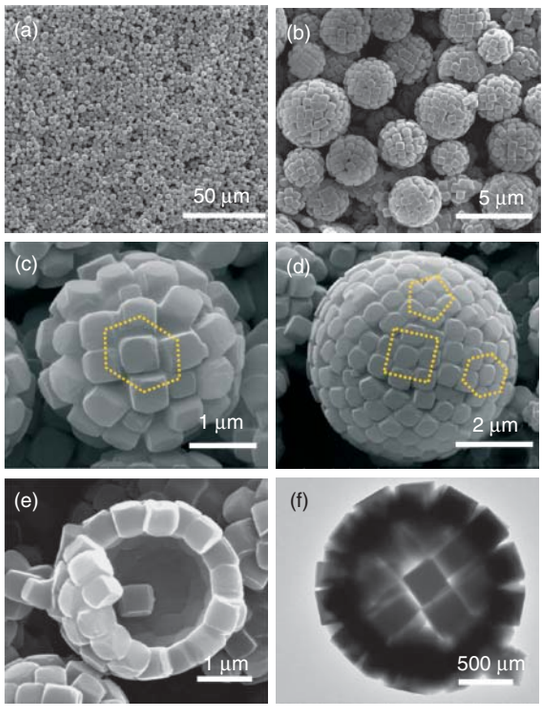


Figure 9 Colloidosomes composed of the PCP $[Fe_3O(H_4ABTC)_{1.5}(H_2O)_3]\cdot(H_2O)_3\cdot(NO_3)$. (a–e) SEM and (f) TEM images. (Adapted with permission from Ref. 64. Copyright (2013) American Chemical Society.)

superstructures are composed of a monolayer of PCP cubes nicely organized in polygonal domains (Figure 9).

3.1.3 Application of an External Electromagnetic Field

Yanai *et al*. assemble uniform 5-µm-sized PCP crystals into linear chains by means of the application of an external AC electric field.[65] Preferential facet-to-facet attachment was conducted by dipolar attractions between crystals. Modulation of the surface area and surface curvature by the use of polymers as capping agents made possible the selective attachment between facets. Noteworthy, the facet flatness allows the formation of locked assemblies after the removal of the external field. Falcaro *et al*. applied an external magnetic field to control the position of MOF-5 crystals with carbon-coated cobalt magnetic nanoparticles embedded in their framework.[66] Interestingly, the magnetic response of the composite crystals was strong enough to allow control of the position of isolated crystals or to induce the formation of interpenetrated PCP superstructures (obtained after a secondary growth process) in specific locations.

3.2 Positioning of the PCP Crystallization Site

3.2.1 Crystallization at a Solid–Liquid Interface

PCP crystallization from a substrate has been the most investigated strategy to synthesize PCP thin films and hierarchically porous materials so far. This method is traditionally accomplished by following two general procedures: the "secondary growth" process (or seeding approach) and the direct nucleation growth process achieved using solvothermal or microwave-assisted synthesis.

Secondary Growth Process This strategy is based on the decoupling of the PCP nucleation and growth steps. First, a seed layer is deposited on the surface of a substrate, which is subsequently immersed into a dilute solution containing the PCP precursors. The decoupling facilitates the control of the nucleation site location and their density. It also decreases the importance of the nature of the substrate, making the strategy applicable to a wide range of supports. Various strategies were proposed to prepare the seed layer on the support. Gascon *et al*. spin-coated on α-alumina porous supports a slurry composed of cross-linked one-dimensional Cu(II)-btc coordination polymers, priory obtained by the modification of the original $[Cu_3(btc)_2]$ recipe.[67] A dense coating of $[Cu_3(btc)_2]$ crystals with no preferred orientation was obtained after a second step under hydrothermal conditions in the presence of the PCP precursors.

Yoo *et al*. deposited MOF-5 seed crystals on the same α-alumina support using a microwave-induced thermal deposition. A thin layer of graphite was first deposited on the support. The seed deposition was then achieved under microwave treatment. In the precursor solution, the graphite layer was found to promote the rapid nucleation of MOF crystals on the substrate due to the intense and localized heat transfer resulting from the interaction of microwave radiations with the free electron of graphite. Solvothermal treatment in a growth precursor solution containing *N*-ethyldiisopropylamine resulted in the formation of continuous and oriented MOF-5 membranes.[68] Li *et al*. succeeded in manipulating the orientation of ZIF-7 films by spreading on the support nanocrystals with tailored size and aspect ratio.[30]

Direct Nucleation Growth Process This strategy relies on the promotion of the heterogeneous nucleation of PCP at a desired position by lowering the interface energy between the crystal being formed and the substrate. The selection of the support is a critical issue. Indeed, beyond the fact that the support acts as a backbone providing predetermined shape and mechanical stability to the final PCP structure, the surface of the support must provide the starting points for the crystallization event to occur.

Substrates with Preexistent Reactive Groups Exposed on the Surface The basic surface of Al_2O_3 substrates was shown to be suitable for promoting the nucleation of PCP framework such as $[Cu_3(btc)_2]$ containing acidic ligands. On the other hand, the acidic surface of SiO_2 substrates was suitable to facilitate the nucleation of PCP framework possessing both acidic and basic organic ligands such as $[Zn_2(bdc)_2(dabco)]$.[69,70] Interestingly, organic supports composed of polymers bearing chemical functions able to interact with the PCP framework components were successfully applied for the construction of multiporous PCP composites or membranes with enhanced mechanical properties.[71–73]

The highly reactive surface of a PCP crystal was also used as nucleation starting point for the heteroepitaxial growth of a PCP crystal with a different chemical composition. Furukawa *et al*. were the first to achieve both the single-crystal PCP core-shell heterostructures and the structural relationship between the shell and the core using X-ray diffraction analysis.[74] To guarantee the epitaxial growth to occur, core and shell crystals were both composed of isoreticular tetragonal frameworks $[M_2(dicarboxylate)_2(N\text{-ligand})]$ with similar unit cell parameters but consisting of different metal ions (Figure 10). A variation of the dicarboxylate ligands from the core to the shell allowed for the formation of other types of heterogeneous structures containing sequentially functionalized porous systems.[75,76] Sandwich-like structures[77] and membranes[78] with intriguing sorption and separation properties were also synthesized by this way.

Modification of the Substrate Surface In the case of substrates devoid of any suitable reactive groups, induction of the heterogeneous crystallization was accomplished by the deposition of nucleating zones on the surface. So far, different types of nucleating agents have been investigated.

Deposition of self-assembled monolayers possessing terminal functions able to mimic chemical functions involved in the PCP framework allowed for the nucleation and growth of membranes with a preferential crystallographic orientation through an epitaxial growth process.[79–81] Noteworthy, these nucleating entities were also used as templates for the formation of two-dimensional patterned crystal assemblies.[82,83]

Falcaro *et al*. precisely localized MOF-5 crystals using mineral microparticles as both nucleating seeds and carriers for embedding controlled functionality into PCP crystals.[84] The authors showed that nanostructured α-hopeite microparticles possess exceptional ability to nucleate PCP crystals. In a one-pot synthesis procedure, where a solution contains both precursors of the α-hopeite microparticles and of the MOF-5, the α-hopeite microparticles formed in the first few minutes of reaction act as nucleating agent on which the heterogeneous nucleation

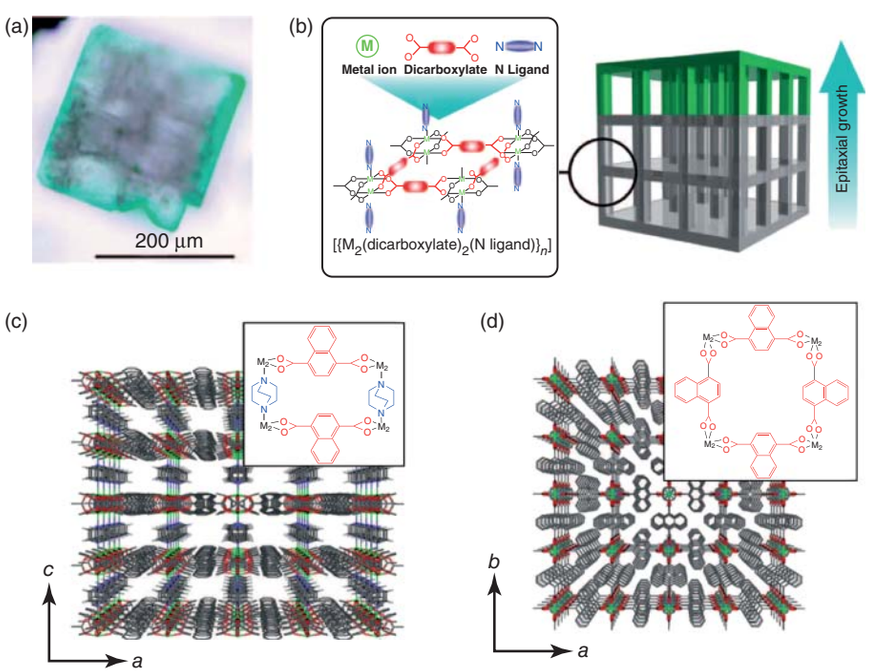


Figure 10 (a) Optical microscopic image of the sliced core–shell crystal. (b) Schematic illustration of the heterogeneous $[M_2(dicarboxylate)_2(N\text{-ligand})]$ frameworks. The crystal structure of $[Zn_2(ndc)_2(dabco)]$, the core crystal (gray), viewed along (c) the *b*-axis and (d) the *c*-axis. (Adapted with permission from Ref. 74. © WILEY-VCH Verlag GmbH & Co. KGaA, 2009.)

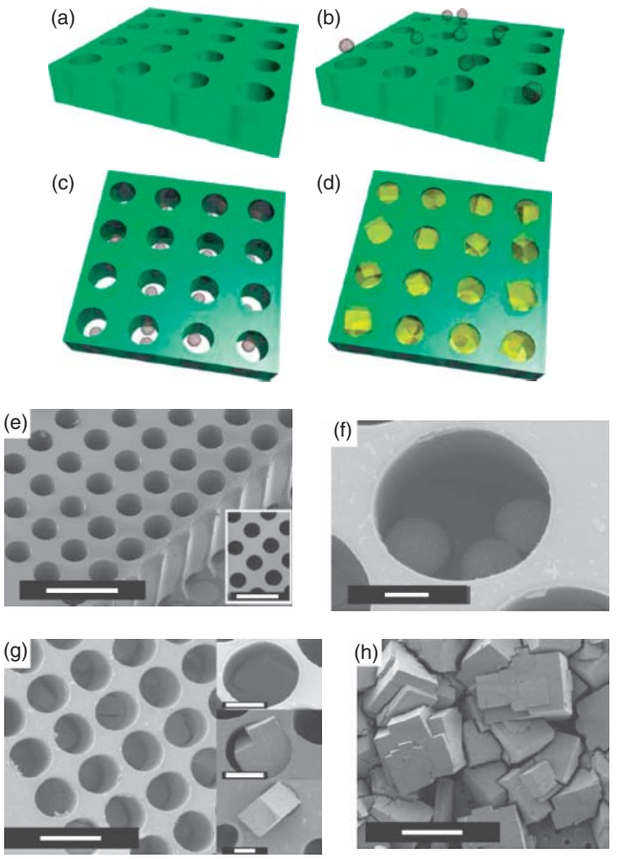


Figure 11 (a–d) Schematic illustration of the procedure used to control the MOF-5 crystal position. (a–c) Microparticles of α-hopeite are first deposited at predefined positions on a lithographed substrate. (d) The seeded substrate was then immersed into an MOF-5 precursor solution to induce the PCP growth from the α-hopeite microparticles. Scanning electron micrographs of (e) the lithographed substrate, (f) the α-hopeite inserted within the substrate hole, (g) the MOF-5 crystals within each substrate hole, and (h) the MOF-5 crystal film covering the substrate. (Reprinted by permission from Macmillan Publishers Ltd: Nature Communication, (Ref. 84), copyright (2011). http://www.nature.com/ncomms/index.html.)

of the PCP crystals occurs. Interestingly, this procedure reduces the MOF-5 synthesis time by 70% when compared with conventional method. The α-hopeite microparticles can be isolated before MOF-5 nucleate and subsequently deposited on a substrate, promoting the formation of dense PCP films or patterns (Figure 11).

Confinement of the PCP nucleation at a solid surface was also achieved by the deposition of the PCP precursors onto the surface before the induction of the PCP crystallization process. Schoedel *et al*. used a thin poly(ethylene oxide) gel layer deposited on a gold slide as a storage medium to confine a high concentration of metal ions near to a nucleating surface functionalized with self-assembled monolayers.[85] Very homogeneous PCP thin films were obtained in unique crystal orientation on COOH-functionalized SAMs after synthesis in the presence of the organic linker. Other groups reported the deposition of $[Cu_3(btc)_2]$ monodisperse crystals in patterns down to the single-crystallite level by the use of soft lithographic[86] and inkjet printing techniques.[87] These approaches required the preparation of stable precursor solutions free of particles and of controlled viscosity before the deposition. To this end, the kinetics of $[Cu_3(btc)_2]$ formation could be carefully controlled by adjusting the solvent composition.

3.2.2 *Crystallization at a Liquid–Liquid Interface*

Ameloot *et al*. took advantage of the difference in solubility characteristics of the organic and inorganic PCP precursors to prepare uniform thin $[Cu_3(btc)_2]$ layers through a self-completing growth mechanism.[88] In this strategy, PCP crystallization was confined at the interface between two immiscible solvents, each containing one of the two PCP precursors (Figure 12). On bringing the two solutions into contact, nucleation and growth of $[Cu_3(btc)_2]$ occur via a ligand exchange mechanism at the copper center. In aqueous solutions of copper acetate, the dominant structural unit is the acetate-bridged paddle-wheel-structured Cu(II) dimer $[Cu_2(CH_3COO)_4(H_2O)_2]$. At the interface between the aqueous and the organic solutions, exchange takes place between the carboxylate groups of the bridging acetate ligands and those of the btc ligands to form isostructural secondary building units, copper paddle-wheel-structured Cu(II) dimers $[Cu_2(btc)_4(H_2O)_2]$. The $[Cu_3(btc)_2]$ crystal lattice is formed by linking these building units together through the remaining carboxylate groups on the btc ligands.

3.2.3 *Pseudomorphic Replacement*

Pseudomorphic mineral replacement events consist in the transformation of a mineral phase, which is out of equilibrium into a more thermodynamically stable phase, involving dissolution and reprecipitation subprocesses.[89] This natural phenomenon is characterized by the preservation of the shape and dimensions of the replaced parent phase whenever the kinetics of its dissolution are coupled with the kinetics of nucleation and crystallization of the new phase. The initiation and spatiotemporal harmonization of these re-equilibration reactions rely on parameters that are controllable in the laboratory. Reboul *et al*. combined sol–gel process and pseudomorphic replacement to introduce organic elements into a preshaped dense metal oxide phase.[90] In the presence of an organic ligand solution and under microwave conditions, the dissolution of the metal oxide sacrificial phase provides the

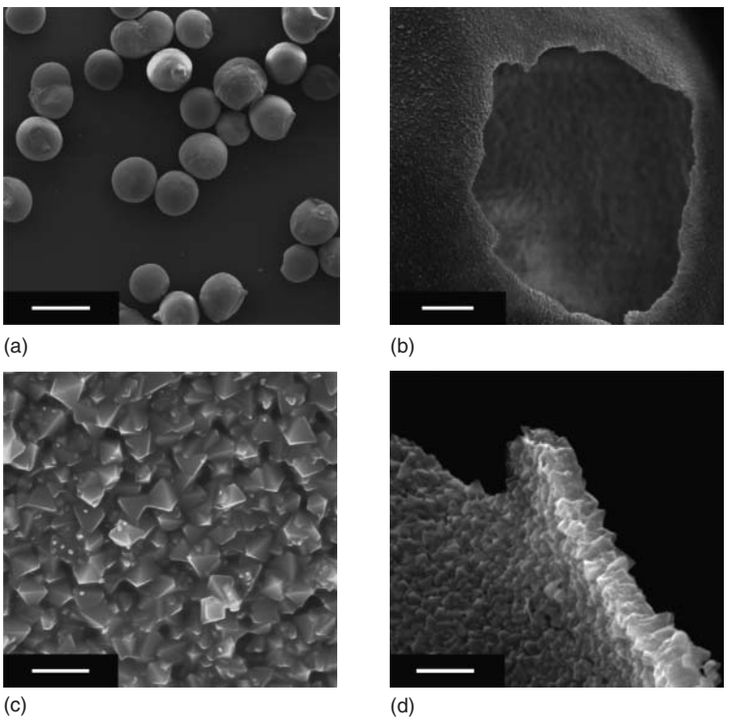


Figure 12 Scanning electron micrographs of hollow $[Cu_3(btc)_2]$ capsules synthesized through the crystallization of PCP crystals at the surface of metal-ion-containing aqueous droplets immersed in a ligand-containing organic solution. Scale bar: (a) 500, (b) 25, (c) 2, and (d) 2 μm. (Reprinted by permission from Macmillan Publishers Ltd: Nature Chemistry, (Ref. 88), copyright (2011). http://www.nature.com/nchem/index.html.)

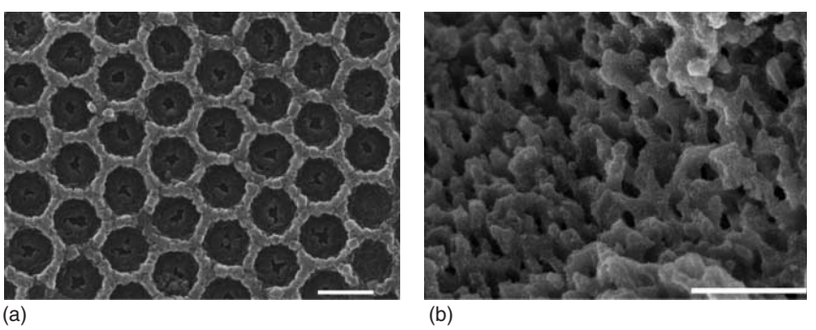


Figure 13 Scanning electron micrographs of [AlOH(ndc)] macrostructures obtained by the replication of (a) an alumina inverse opal two-dimensional pattern (scale bar = 1 μm) and (b) a macroporous alumina aerogel (scale bar = 10 μm). (Reprinted by permission from Macmillan Publishers Ltd: Nature Materials, (Ref. 90), copyright (2012). http://www.nature.com/nmat/index.html.)

metal cations required for the construction of the PCP framework. This process, named "coordination replication," led to the simultaneous formation of coordination complexes on the molecular scale and to the construction of a PCP architecture on the nano- and macroscale. Two and three-dimensional alumina inverse opal structures as well as multiporous macrostructured PCP architectures derived from alumina aerogels were synthesized by this method (Figure 13). By taking advantage of the unique characteristic of PCPs, whereby a suitable choice of both metal ions and organic ligands allows a tailored pore size, pore surface functionality, and framework flexibility, the authors constructed mesoscopic PCP architectures with different pore characteristics: highly hydrophobic in the case of [Al(OH)(ndc)], flexible upon hydration/dehydration in the case of [Al(OH)(bdc)], and mesoporous in the case

of $\{[Al_3O(OH)(H_2O)_2](btc)_2\}$. The potential use of this strategy for the preparation of materials with enhanced functionality compared to that of conventional powders was demonstrated. After coordination replication, the selection of both 1,4-naphthalenedicarboxylic acid as an organic ligand and a randomly structured alumina aerogel as the parent architecture led to the formation of a hierarchically porous system constructed from highly hydrophobic PCP crystals with efficient mass transport properties for water/ethanol vapor-phase separation.

Following the same strategy, Khaletskaya *et al*. synthesized well-dispersed core-shell composites made of an [AlOH(ndc)] crystal shell and individual gold nanorods as the core through the replication into PCP crystals of a thin alumina layer deposited on the surface of gold nanorods. In these composites, the photothermal conversion ability of the gold nanorods acts as an optical switch that enables to remotely release the guest molecules adsorbed within the PCP pores through an increase of molecular mobility. The potential of these materials as new light-induced molecular release systems was demonstrated by the release of anthracene (used as fluorescent probe molecule) under near-infrared irradiation.[91]

Potential of using the pseudomorphic replacement process in order to integrate PCPs with other functional materials was also demonstrated by Zhang *et al*. This group synthesized core-shell heterostructures composed of vertically standing arrays of ZnO nanorods coated with ZIF-8 crystals. These novel semiconductor@PCP composites are considered as promising new types of photoelectrochemical sensors with efficient molecule selectivity.[92]

4 CONCLUSION

Although PCP properties are commonly attributed to the PCP framework structures themselves, it is now well accepted that the control of PCP crystal size and morphology, as well as the control of their position, is a prerequisite in order to fully exploit their intrinsic performances. Because PCPs are crystalline materials, the driving force for their crystallization can be very strong and readily sustained. PCP crystals are therefore not so easily embedded within construction processes unless subject to kinetic regulation. On the other hand, the versatility of PCP synthesis conditions in terms of pH, temperature, and solvent makes their synthesis compatible with a wide range of physicochemical and mechanical microfabrication methods. It was, hence, possible to prepare uniform PCP nanocrystal suspensions or crystal assemblies in the form of membranes, pattern surfaces, hollow spheres, coatings, or multiporous architectures. At last, it is worth mentioning a recent promising approach for structuring PCP crystals, which consists in the application of organic *templates*.[93,94] In this strategy, the mild experimental conditions required for the synthesis of PCP allow the coexistence of the PCP precursors with the same supramolecular assemblies of surfactant molecules that are traditionally used for the synthesis of mesoporous metal oxide materials. The rational adjustment of the interactions between PCP precursors and surfactant molecules as well as the kinetics of surfactant assembly and PCP crystallization results in the cooperative assembly of surfactants and PCP growth units. Macro- or mesoporous PCP-based materials are recovered after the removal of the templates (see ***Mesoporous Metal-Organic Frameworks***).

5 ABBREVIATIONS AND ACRONYMS

AOT = Aerosol-OT; CTAB = cetyltrimethylammonium bromide; CTAB = combination of hexadecyltrimethylammonium bromide; DMF = dimethylformamide; LB = Langmuir–Blodgett; o/w = oil-in-water; PCP = porous coordination polymer; PEI = polyethylene imine; pfmbc = *p*-perfluoromethylbenzenecarboxylate; TEA = triethylamine; TEM = transmission electron microscopy; TLS = time-resolved static light scattering.

6 REFERENCES

1. H. Cölfen and S. Mann, *Angew. Chem. Int. Ed.*, 2003, **42**, 2350.
2. M. Antonietti and G. A. Ozin, *Chem. Eur. J.*, 2004, **10**, 28.
3. W. Song, R. E. Justice, C. A. Jones, V. H. Grassian, and S. C. Larsen, *Langmuir*, 2004, **20**, 4696.
4. S. Horike, S. Shimomura, and S. Kitagawa, *Nat. Chem.*, 2009, **1**, 695.
5. S. Bureekaew, S. Horike, M. Higuchi, M. Mizuno, T. Kawamura, D. Tanaka, N. Yanai, and S. Kitagawa, *Nat. Mater.*, 2009, **8**, 831.
6. S. Bordiga, C. Lamberti, G. Ricchiardi, L. Regli, F. Bonino, A. Damin, K.-P. Lillerud, M. Bjorgen, and A. Zecchina, *Chem. Commun.*, 2004, 2300.
7. M. D. Allendorf, C. A. Bauer, R. K. Bhakta, and R. J. T. Houk, *Chem. Soc. Rev.*, 2009, **38**, 1330.
8. P. Horcajada, R. Gref, T. Baati, P. K. Allan, G. Maurin, P. Couvreur, G. Férey, R. E. Morris, and C. Serre, *Chem. Rev.*, 2012, **112**, 1232.
9. J. Della Rocca, D. Liu, and W. Lin, *Acc. Chem. Res.*, 2011, **44**, 957.
10. H. Guo, G. Zhu, I. J. Hewitt, and S. Qiu, *J. Am. Chem. Soc.*, 2009, **131**, 1646.

11. H. Bux, F. Liang, L. Yanshuo, J. Cravillon, M. Wiebcke, and J. Caro, *J. Am. Chem. Soc.*, 2009, **131**, 16000.
12. X. Zou, G. Zhu, I. J. Hewitt, F. Sun, and S. Qiu, *Dalton Trans.*, 2009, 3009.
13. G. Lu and J. T. Hupp, *J. Am. Chem. Soc.*, 2010, **132**, 7832.
14. Y.-N. Wu, F. Li, W. Zhu, J. Cui, C.-A. Tao, C. Lin, P. M. Hannam, and G. Li, *Angew. Chem. Int. Ed.*, 2011, **50**, 12518.
15. R. Jin, Z. Bian, J. Li, M. Ding, and L. Gao, *Dalton Trans.*, 2013, **42**, 3936.
16. T. Hasell, H. Zhang, and A. I. Cooper, *Adv. Mater.*, 2012, **24**, 5732.
17. I. Bilecka and M. Niederberger, *Nanoscale*, 2010, **2**, 1358.
18. M. Tsuji, M. Hashimoto, Y. Nishizawa, M. Kubokawa, and T. Tsuji, *Chem. Eur. J.*, 2005, **11**, 440.
19. J.-S. Choi, W.-J. Son, J. Kim, and W.-S. Ahn, *Microporous Mesoporous Mater.*, 2008, **116**, 727.
20. E. Haque, N. A. Khan, J. H. Park, and S. H. Jhung, *Chem. Eur. J.*, 2010, **16**, 1046.
21. Y.-K. Seo, G. Hundal, I. T. Jang, Y. K. Hwang, C.-H. Jun, and J.-S. Chang, *Microporous Mesoporous Mater.*, 2009, **119**, 331.
22. Z. Ni and R. I. Masel, *J. Am. Chem. Soc.*, 2006, **128**, 12394.
23. S. H. Jhung, J.-H. Lee, J. W. Yoon, C. Serre, G. Férey, and J.-S. Chang, *Adv. Mater.*, 2007, **19**, 121.
24. W.-J. Son, J. Kim, J. Kim, and W.-S. Ahn, *Chem. Commun.*, 2008, 6336.
25. Z.-Q. Li, L.-G. Qiu, W. Wang, T. Xu, Y. Wu, and X. Jiang, *Inorg. Chem. Commun.*, 2008, **11**, 1375.
26. Z.-Q. Li, L.-G. Qiu, T. Xu, Y. Wu, W. Wang, Z.-Y. Wu, and X. Jiang, *Mater. Lett.*, 2009, **63**, 78.
27. K. S. Suslick, D. A. Hammerton, and R. E. Cline, *J. Am. Chem. Soc.*, 1986, **108**, 5641.
28. L.-G. Qiu, Z.-Q. Li, Y. Wu, W. Wang, T. Xu, and X. Jiang, *Chem. Commun.*, 2008, 3642.
29. B. Seoane, J. M. Zamaro, C. Tellez, and J. Coronas, *CrystEngComm*, 2012, **14**, 3103.
30. Y.-S. Li, H. Bux, A. Feldhoff, G.-L. Li, W.-S. Yang, and J. Caro, *Adv. Mater.*, 2010, **22**, 3322.
31. Z. Xin, X. Chen, Q. Wang, Q. Chen, and Q. Zhang, *Microporous Mesoporous Mater.*, 2013, **169**, 218.
32. F. Wang, H. Guo, Y. Chai, Y. Li, and C. Liu, *Microporous Mesoporous Mater.*, 2013, **173**, 181.
33. K. Wang, Z. Geng, Y. Yin, X. Ma, and Z. Wang, *CrystEngComm*, 2011, **13**, 5100.
34. M. A. López-Quintela, *Curr. Opin. Colloid Interface Sci.*, 2003, **8**, 137.
35. W. J. Rieter, K. M. L. Taylor, H. An, W. Lin, and W. Lin, *J. Am. Chem. Soc.*, 2006, **128**, 9024.
36. K. M. L. Taylor, A. Jin, and W. Lin, *Angew. Chem. Int. Ed.*, 2008, **47**, 7722.
37. C. Liu, B. Zou, A. J. Rondinone, Z. J. Zhang, and J. Phys, *Chem. B*, 2000, **104**, 1141.
38. R. E. Riter, J. R. Kimmel, E. P. Undiks, N. E. Levinger, and J. Phys, *Chem. B*, 1997, **101**, 8292.
39. D. Tanaka, A. Henke, K. Albrecht, M. Moeller, K. Nakagawa, S. Kitagawa, and J. Groll, *Nat. Chem.*, 2010, **2**, 410.
40. F. Jones and M. I. Ogden, *CrystEngComm*, 2010, **12**, 1016.
41. S. K. Nune, P. K. Thallapally, A. Dohnalkova, C. Wang, J. Liu, and G. J. Exarhos, *Chem. Commun.*, 2010, **46**, 4878.
42. Q. Liu, L.-N. Jin, and W.-Y. Sun, *Chem. Commun.*, 2012, **48**, 8814.
43. M. Ma, D. Zacher, X. Zhang, R. A. Fischer, and N. Metzler-Nolte, *Cryst. Growth Des.*, 2011, 11.
44. S.-B. Ding, W. Wang, L.-G. Qiu, Y.-P. Yuan, F.-M. Peng, X. Jiang, A.-J. Xie, Y.-H. Shen, and J.-F. Zhu, *Mater. Lett.*, 2011, **65**, 1385.
45. Y. Yuan, W. Wang, L. Qiu, F. Peng, X. Jiang, A. Xie, Y. Shen, X. Tian, and L. Zhang, *Mater. Chem. Phys.*, 2011, **131**, 358.
46. M. Pang, A. J. Cairns, Y. Liu, Y. Belmabkhout, H. C. Zeng, and M. Eddaoudi, *J. Am. Chem. Soc.*, 2012, **134**, 13176.
47. T. Tsuruoka, S. Furukawa, Y. Takashima, K. Yoshida, S. Isoda, and S. Kitagawa, *Angew. Chem. Int. Ed.*, 2009, **48**, 4739.
48. S. Hermes, T. Witte, T. Hikov, D. Zacher, S. Bahnmüller, G. Langstein, K. Huber, and R. A. Fischer, *J. Am. Chem. Soc.*, 2007, **129**, 5324.
49. H. Cölfen and M. Antonietti, *Angew. Chem. Int. Ed.*, 2005, **44**, 5576.
50. M.-H. Pham, G.-T. Vuong, F.-G. Fontaine, and T.-O. Do, *Cryst. Growth Des.*, 2012, **12**, 3091.
51. S. Diring, S. Furukawa, Y. Takashima, T. Tsuruoka, and S. Kitagawa, *Chem. Mater.*, 2010, **22**, 4531.
52. T. Uemura, Y. Hoshino, S. Kitagawa, K. Yoshida, and S. Isoda, *Chem. Mater.*, 2006, **18**, 992.
53. A. Schaate, P. Roy, A. Godt, J. Lippke, F. Waltz, M. Wiebcke, and P. Behrens, *Chem. Eur. J.*, 2011, **17**, 6643.
54. Y. Sakata, S. Furukawa, C. Kim, and S. Kitagawa, *Chem. Lett.*, 2012, **41**, 1436.
55. A. Umemura, S. Diring, S. Furukawa, H. Uehara, T. Tsuruoka, and S. Kitagawa, *J. Am. Chem. Soc.*, 2011, **133**, 15506.
56. H. Uehara, S. Diring, S. Furukawa, Z. Kalay, M. Tsotsalas, M. Nakahama, K. Hirai, M. Kondo, O. Sakata, and S. Kitagawa, *J. Am. Chem. Soc.*, 2011, **133**, 11932.
57. C. Y. Lee, Y.-S. Bae, N. C. Jeong, O. K. Farha, A. A. Sarjeant, C. L. Stern, P. Nickias, R. Q. Snurr, J. T. Hupp, and S. T. Nguyen, *J. Am. Chem. Soc.*, 2011, **133**, 5228.
58. Y. Sakata, S. Furukawa, M. Kondo, K. Hirai, N. Horike, Y. Takashima, H. Uehara, N. Louvain, M. Meilikhov, T. Tsuruoka, S. Isoda, W. Kosaka, O. Sakata, and S. Kitagawa, *Science*, 2013, **339**, 193.

59. P. Horcajada, C. Serre, D. Grosso, C. Boissière, S. Perruchas, C. Sanchez, and G. Férey, *Adv. Mater.*, 2009, **21**, 1931.
60. H. Guo, Y. Zhu, S. Qiu, J. A. Lercher, and H. Zhang, *Adv. Mater.*, 2010, **22**, 4190.
61. N. Yanai and S. Granick, *Angew. Chem. Int. Ed.*, 2012, **51**, 5638.
62. M. Tsotsalas, A. Umemura, F. Kim, Y. Sakata, J. Reboul, S. Kitagawa, and S. Furukawa, *J. Mater. Chem.*, 2012, **22**, 10159.
63. J. Huo, M. Marcello, A. Garai, and D. Bradshaw, *Adv. Mater.*, 2013, **25**, 2717.
64. M. Pang, A. J. Cairns, Y. Liu, Y. Belmabkhout, H. C. Zeng, and M. Eddaoudi, *J. Am. Chem. Soc.*, [Online early access], 2013. DOI: 10.1021/ja403994u. Published Online: July 3.
65. N. Yanai, M. Sindoro, J. Yan, and S. Granick, *J. Am. Chem. Soc.*, 2013, **135**, 34.
66. P. Falcaro, F. Normandin, M. Takahashi, P. Scopece, H. Amenitsch, S. Costacurta, C. M. Doherty, J. S. Laird, M. D. H. Lay, F. Lisi, A. J. Hill, and D. Buso, *Adv. Mater.*, 2011, **23**, 3901.
67. J. Gascon, S. Aguado, and F. Kapteijn, *Microporous Mesoporous Mater.*, 2008, **113**, 132.
68. Y. Yoo, Z. Lai, and H.-K. Jeong, *Microporous Mesoporous Mater.*, 2009, **123**, 100.
69. D. Zacher, A. Baunemann, S. Hermes, and R. A. Fischer, *J. Mater. Chem.*, 2007, **17**, 2785.
70. Y. Liu, Z. Ng, E. A. Khan, H.-K. Jeong, C.-B. Ching, and Z. Lai, *Microporous Mesoporous Mater.*, 2009, **118**, 296.
71. P. Küsgens, S. Siegle, and S. Kaskel, *Adv. Eng. Mater.*, 2009, **11**, 94.
72. L. D. O'Neill, H. Zhang, and D. Bradshaw, *J. Mater. Chem.*, 2010, **20**, 5720.
73. T. Ben, C. Lu, C. Pei, S. Xu, and S. Qiu, *Chem. Eur. J.*, 2012, **18**, 10250.
74. S. Furukawa, K. Hirai, K. Nakagawa, Y. Takashima, R. Matsuda, T. Tsuruoka, M. Kondo, R. Haruki, D. Tanaka, H. Sakamoto, S. Shimomura, O. Sakata, and S. Kitagawa, *Angew. Chem. Int. Ed.*, 2009, **48**, 1766.
75. K. Hirai, S. Furukawa, M. Kondo, H. Uehara, O. Sakata, and S. Kitagawa, *Angew. Chem. Int. Ed.*, 2011, **50**, 8057.
76. Y. Yoo and H.-K. Jeong, *Cryst. Growth Design*, 2010, **10**, 1283.
77. K. Hirai, K. Chen, T. Fukushima, S. Horike, M. Kondo, N. Louvain, C. Kim, Y. Sakata, M. Meilikhov, O. Sakata, S. Kitagawa, and S. Furukawa, *Dalton Trans.*, [Online early access], 2013. DOI: 10.1039/c3dt50679g. Published Online: April 08.
78. M. Meilikhov, S. Furukawa, K. Hirai, R. A. Fischer, and S. Kitagawa, *Angew. Chem. Int. Ed.*, 2013, **52**, 341.
79. F. Hinterholzinger, C. Scherb, T. Ahnfeldt, N. Stock, and T. Bein, *Phys. Chem. Chem. Phys.*, 2010, **12**, 4515.
80. H. Gliemann and C. Wöll, *Mater. Today*, 2012, **15**, 113.
81. E. Biemmi, C. Scherb, and T. Bein, *J. Am. Chem. Soc.*, 2007, **129**, 8054.
82. S. Hermes, F. Schröder, R. Chelmowski, C. Wöll, and R. A. Fischer, *J. Am. Chem. Soc.*, 2005, **127**, 13744.
83. O. Shekhah, H. Wang, S. Kowarik, F. Schreiber, M. Paulus, M. Tolan, C. Sternemann, F. Evers, D. Zacher, R. A. Fischer, and C. Wöll, *J. Am. Chem. Soc.*, 2007, **129**, 15118.
84. P. Falcaro, A. J. Hill, K. M. Nairn, J. Jasieniak, J. I. Mardel, T. J. Bastow, S. C. Mayo, M. Gimona, D. Gomez, H. J. Whitfield, R. Riccò, A. Patelli, B. Marmiroli, H. Amenitsch, T. Colson, L. Villanova, and D. Buso, *Nat. Commun.*, 2011, **2**, 237.
85. A. Schoedel, C. Scherb, and T. Bein, *Angew. Chem. Int. Ed.*, 2010, **49**, 7225.
86. R. Ameloot, E. Gobechiya, H. Uji-i, J. A. Martens, J. Hofkens, L. Alaerts, B. F. Sels, and D. E. De Vos, *Adv. Mater.*, 2010, **22**, 2685.
87. J.-L. Zhuang, D. Ar, X.-J. Yu, J.-X. Liu, and A. Terfort, *Adv. Mater.* [Online early access], 2013. DOI: 10.1002/adma.201301626. Published Online: June 28.
88. R. Ameloot, F. Vermoortele, W. Vanhove, M. B. J. Roeffaers, B. F. Sels, and D. E. De Vos, *Nat. Chem.*, 2011, **3**, 382.
89. A. Putnis, *Rev. Miner. Geochem.*, 2009, **70**, 87.
90. J. Reboul, S. Furukawa, N. Horike, M. Tsotsalas, K. Hirai, H. Uehara, M. Kondo, N. Louvain, O. Sakata, and S. Kitagawa, *Nat. Mater.*, 2012, **11**, 717.
91. K. Khaletskaya, J. Reboul, M. Meilikhov, M. Nakahama, S. Diring, M. Tsujimoto, S. Isoda, F. Kim, K. Kamei, R. A. Fischer, S. Kitagawa, and S. Furukawa, *J. Am. Chem. Soc.*, [online early access], 2013. DOI: 10.1021/ja403108x. Published online: May 14,.
92. W. Zhan, Q. Kuang, J.-Z. Zhou, X.-J. Kong, Z.-X. Xie, and L.-S. Zheng, *J. Am. Chem. Soc.*, 2013, **135**, 1926.
93. L.-B. Sun, J.-R. Li, J. Park, and H.-C. Zhou, *J. Am. Chem. Soc.*, 2012, **134**, 126.
94. Y. Zhao, J. Zhang, B. Han, J. Song, J. Li, and Q. Wang, *Angew. Chem. Int. Ed.*, 2011, **50**, 636.

Nanoscale Metal-Organic Frameworks

Kyriakos C. Stylianou and Inhar Imaz

ICN2 – Institut Catala de Nanociencia i Nanotecnologia, Barcelona, Spain

and

Daniel Maspoch

ICN2 – Institut Catala de Nanociencia i Nanotecnologia, Barcelona, Spain and Institució Catalana de Recerca i Estudis Avançats (ICREA), Barcelona, Spain

1	Introduction	19
2	MOF Nanochemistry: from 0D and 1D to 2D NanoMOFs	20
3	SURMOFs: NanoMOFs on Surfaces	23
4	Hybrid MOF Nanocomposites	25
5	MOF Superstructures	27
6	Properties and Applications	27
7	Conclusions and Perspectives	32
8	Related Articles	34
9	Abbreviations and Acronyms	34
10	References	34

1 INTRODUCTION

Metal-organic frameworks (MOFs) are a class of highly crystalline materials comprising ordered, extended one-dimensional (1D), two-dimensional (2D), and three-dimensional (3D) networks formed by metal ions or clusters connected to multifunctional organic ligands.[1] Over the last two decades, MOFs have garnered extensive attention due to their facile preparation, which generally involves diverse techniques (e.g., hydro-/solvo-thermal, microwave, mechanochemistry, and sonochemistry) commonly used for growing crystals of traditional and simple inorganic salts.[2] This methodological variety, together with the countless available combinations of metal coordination geometries and organic ligands, means that an infinite number of MOFs can now be synthesized.[3] The composition, size, shape, porosity, and properties of MOFs can be tailored, and they can be conferred with diverse functions, such as gate opening and flexible structural transformations[4–6]. Porous MOFs can exhibit high Brunner Emmet Teller (BET) surface areas (up to 7.000 $m^2\ g^{-1}$)[7] as well as tunable pore size and functionality, and they can host guest molecules within their cavities.[8] Therefore, porous MOFs offer great potential for storage of hazardous gases such as CO and CO_2, fuel applications with H_2 or CH_4,[8] catalysis,[9] sensing,[10] biomedicine[11], and gas–liquid separation (e.g., CO_2/CH_4 and xylene and alkane isomers).[12,13] The reader is referred to other chapters of this book as well as several other excellent reviews on the applications of MOFs, as this chapter comprehensively addresses the most recent advances in the synthesis and properties of nanoscale metal organic frameworks (nanoMOFs).[14]

Although MOFs show high promise for many of the aforementioned research areas, they do not always fulfill the relevant requirements for specific applications. For some applications MOFs must be miniaturized and the resulting miniaturized MOFs must be integrated onto surfaces. Miniaturization of MOFs down to the submicrometer regime (100–1000 nm), and further down, to the nanoscale (1–100 nm), is very important, as it bridges the gap between current MOF science and device-material

Metal-Organic Framework Materials. Edited by Leonard R. MacGillivray and Charles M. Lukehart.
© 2014 John Wiley & Sons, Ltd. ISBN 978-1-119-95289-3

fabrication in nanotechnology. NanoMOFs may exhibit different and/or enhanced properties and reactivity compared to the traditional bulk materials.[15] For example, Fajula *et al.*[16] demonstrated that increasing the textural porosity of the mesoporous organo-silicon compound MCM-41 and the particle external surfaces, reduces or even eliminates the mass transfer limits, thereby increasing the catalytic activity. Another characteristic example is that the internalization kinetics, the blood half-life and the distribution of the particles in the biosystem are all size dependent,[17] and there are many reports that smaller particles exhibit greater plasma circulation and are easily transported to the lymphatic system.[18] Motivated by these findings, MOF researchers are developing new nanofabrication methodologies, and adapting existing ones, for the controlled synthesis of nanoMOFs (zero dimension (0D), particle/crystals; 1D, wires, fibers and tubes; and 2D, layers); integration of nanoMOFs onto surfaces, to produce MOF thin films and membranes (or surface metal organic frameworks (*SURMOFs*)); and study of their properties.[15,19] Especially promising is the recent finding that nanoMOFs can be linked to nanomaterials from other classes, which is opening up avenues for designing MOF-based composites, and for controlling the growth and assembly of nanoMOFs into multifunctional MOF-based superstructures (Figure 1).

2 MOF NANOCHEMISTRY: FROM 0D AND 1D TO 2D NANOMOFs

2.1 0D and 1D NanoMOFs

The synthesis of 0D and 1D nanoMOF crystals chiefly depends on the spatial and/or temporal control of MOF crystal growth and nucleation. These processes can be partially controlled by adapting classical methodologies generally used to obtain bulk MOFs (e.g., solvothermal synthesis). This requires tuning of one or more of the reaction conditions, including the solvent (a poor solvent is often needed),[20] the MOF precursors, base (if needed), temperature and time, to promote nucleation and slow down the crystal growth. For instance, Horcajada *et al.*[21] reported that the careful selection of solvents, temperatures and reaction times was the key factor to synthesize nano-MIL-88A, nano-MIL-89, and nano-MIL-53 crystals smaller than 200 nm.

There are specific approaches for obtaining stable, highly dispersible nanoMOFs. These include using the aforementioned classical methodologies in combination with stabilizing agents that cap crystal growth. In some cases, sonication and microwave radiation are used to promote nucleation and reduce the crystal growth rate. Alternatively, nucleation, and crystal growth, can be spatially controlled by physically confining the MOF

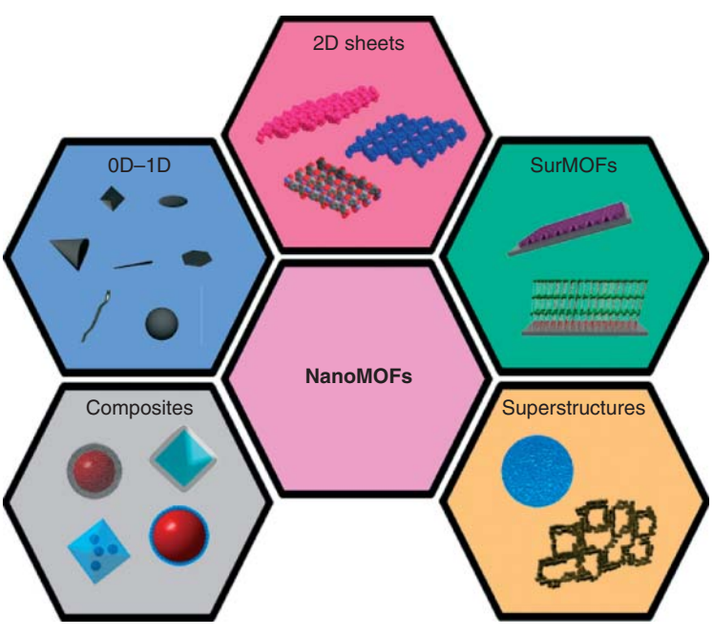


Figure 1 Representative illustration of the variety of nanoMOFs synthesized to date using different methodologies: *0D and 1D nanoMOF crystals* of diverse shape (e.g., spheres, cubes, octahedrons, fibers, and plates); *isolated 2D MOF nanosheets*, which are graphene-like nanomaterials; *nanoMOFs grown on surfaces (SURMOFs)*, including MOF thin-films and membranes; *MOF-based nanocomposites*, comprising MOFs combined with inorganic, organic or oxide nanoparticles; and *MOF superstructures*, assembled from MOFs and other components

reaction: for example, into droplets. Likewise, more advanced techniques, including the use of microfluidics and templates, are now enabling synthesis of an ever greater variety of nanoMOFs.

Among the most common approaches to inorganic nanoparticle synthesis is the use of stabilizing agents that cap particle growth and stabilize them to prevent them from aggregating. For example, gold nanoparticles are usually synthesized in the presence of weakly-bound coordinating ligands (e.g., citrate or tannic acid) or surfactants (e.g., PVP). Analogously, Guo *et al.*,[22] Tsuruoka *et al.*,[23] and Horcajada *et al.*[24] have controlled the growth of nanoMOFs by adding coordination modulators, such as monocarboxylic acids, which act as capping agents by forming coordination bonds with the metal center of the MOF. Such modulators include the monocarboxylate ligands dodecanoic acid and acetic acid. Selective use of these reagents at different concentrations has enabled control over the size of HKUST-1 crystals from 20 nm to 1 μm.[25] Also, Cravillon *et al.*[26] synthesized nano-ZIF-8 crystals (diameter: <20 nm) using an excess of sodium formate and *n*-butylamine. Both substances act as competitive modulating agents in the coordination equilibrium and the deprotonation equilibrium, respectively, during nucleation and growth. Apart from coordination modulators, excess reagents[27] or surfactants also can be used to control MOF crystal growth; this method also enables control over MOF shape and provides increased stability against agglomeration. For example, Ranft *et al.*[28] described a fast solvothermal synthesis strategy that has led to the isolation of sub-60-nm-sized nanoMOFs (nano-HKUST-1 and nano-IRMOF-3) under mild conditions and using a specific amount of polymer: PAA for the isolation of nanoHKUST-1, and a polymer–surfactant combination (PVP-CTAB) for nano-IRMOF-3. The adjustment of the type and amount of polymer or polymer–surfactant, reaction time and temperature was shown to be crucial parameters for fine tuning the particle size within a range from 30 to 300 nm.[28] Another example described by Nune *et al.*[29] showed that the preparation of hexagonal nano-ZIF-8 crystals (diameter: 57 ± 7 nm) could be achieved using the highly cationic surfactant poly(diallyldimethylammonium chloride).

Sonochemistry is a facile alternative method for synthesizing nanoMOFs: irradiation of the reagents with high intensity sonic or ultrasonic waves leads to acoustic cavitation, generating very high temperatures (5000 K) and pressures (>1000 atm). Crystals of nano-$[Zn_3(btc)_2 \cdot 12H_2O]$ have been prepared via ultrasonic irradiation treatment of zinc acetate and btc in 20% in water at room temperature and atmospheric pressure for 5 min.[30] Interestingly, the researchers were able to control the size of these crystals (50–900 nm) by simply modulating the reaction time.

Microwave chemistry is another attractive and conventional method for preparing nanoMOFs, as it enables short reaction times, fast kinetics of crystal nucleation and growth, and high yields (few or no side products).[21,31] Ni and Masel used microwave heating to produce sub-micrometer IRMOF-1, -2, and -3 crystals, achieving vastly shorter reaction times compared to other methods:[32] they exposed a DEF solution of the two building blocks (zinc(II) nitrate and the corresponding dicarboxylic acid organic ligand) at 150 W for only 25 s.

NanoMOF crystals can be also prepared using emulsions, most of which are suspensions of one liquid (in small droplets of diameter 50–1000 nm) in another liquid, and are stabilized. These dimensions can be exploited such that the droplets act as "nanoreactors" to confine the self-assembly, nucleation and growth of nanoMOFs. Briefly, this entails first dissolving the metal salt in water and the ligand in another solvent which is immiscible to water. A water-in-oil (or vice versa) emulsion is then prepared from a surfactant, and the collisions between droplets containing the precursors, or externally applied energy (e.g., heat, light, or microwave radiation) spontaneously induces their polymerization, thus delimiting their crystal growth inside the droplet. Mann *et al.* utilized this technique to synthesize Prussian blue cubic nanocrystals (diameter: 15 nm), one of the first examples of 0D nanoMOFs: they dissolved the Prussian blue precursors in water, used the resulting solution in a water-in-oil emulsion, and finally, exposed this emulsion to daylight.[33]

Rieter *et al.* and Taylor *et al*. utilized the size-limiting effects of oil-in-water microemulsions to synthesize 1D structures.[34–36] In this methodology, the size and shape of the micelles can be altered by adjusting the surfactant-to-water ratio, resulting in surfactant-stabilized water reservoirs in an organic phase that can be used as individual nanoreactors for the synthesis (Figure 2a). For example, this strategy was used to synthesize lanthanide-based nanoMOFs (Eu(III), Gd(III), or Tb(III) with bdc) in an emulsion of the cationic surfactant cetyltrimethylammonium bromide, isooctane, 1-hexanol, and water.[35] Variation of the surfactant-to-water ratio resulted in the formation of nanorods, whose sizes could be tuned from 100 to 125 nm in length and 40 nm in diameter, to 2 μm in length and 100 nm in diameter (Figures 2b and c). Importantly, the presence of the surfactant was found to be vital for enhancing the stability of the nanoMOFs against agglomeration.

Use of emulsions has enabled the design of more sophisticated nanoMOFs. Zhao *et al.*[37] recently reported an excellent example: they synthesized zinc(II) nitrate/H_2bdc nanospheres in an emulsion of the ionic liquid 1,1,3,3-tetramethylguanidinium acetate, supercritical CO_2 and the surfactant *N*-ethyl perfluorooctylsulfonamide (Figure 2d). They obtained highly uniform

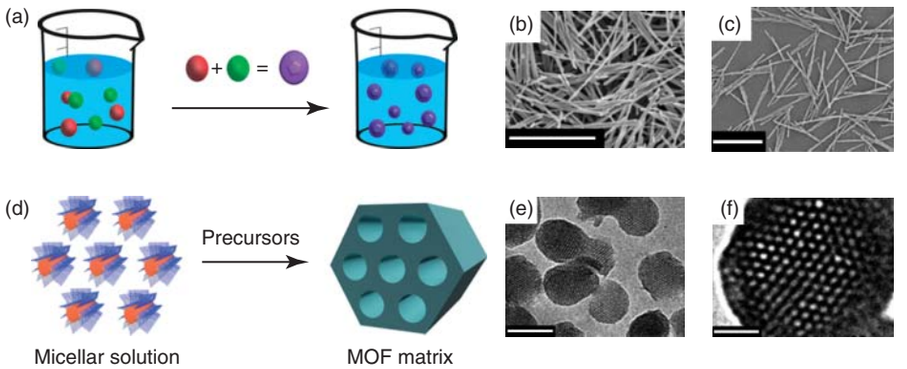


Figure 2 (a) Schematic representation of the emulsion methodology used for isolating 0D and 1D nanoMOFs. (b)–(c) Representative SEM images of nano-$[Gd(bdc)_{1.5}(H_2O)_2]$ rods prepared by stirring a microemulsion of $GdCl_3$ and bis(methylammonium)benzene-1,4-dicarboxylate in the cationic cetyltrimethylammonium bromide, and nano-$[Mn_3(btc)_2(H_2O)_6]$ rods synthesized at room temperature, respectively. Scale bars: 2 µm (b) and 4 µm (c). ((b) Reprinted with permission from Ref. 34. Copyright (2006) American Chemical Society.) ((c) Reprinted with permission from Ref. 36. Copyright (2008) American Chemical Society.) (d) Schematic representation of emulsion-template synthesis. (e)–(f) Representative TEM images of the mesoporous MOF spheres (diameter: 80 nm) showing the formation of highly ordered hexagonal pores. Scale bars: 80 nm (e) and 20 nm (f). ((e–f) Reproduced from Ref. 37. © Wiley-VCH Verlag GmbH & Co. KGaA, 2011.)

nanospheres (diameter: 80 nm) that incorporated well-ordered mesopores, in which the walls were composed of a microporous MOF. Although the structure of the pore walls could not be identified by comparison with known Zn(bdc)-type MOF structures, sorption measurements done on the nanoMOF crystals revealed well-pronounced mesoporosity along with moderate microporosity and a bimodal pore size distribution centered at 3.6 nm and 0.7 nm (Figures 2e–f).

Since the first examples of nanoMOFs synthesis were reported, more sophisticated methodologies have been developed that have given rise to unique shapes. For example, Puigmartí-Luis *et al.*[38] recently prepared long MOF-nanofibers by exploiting interfacial chemistry in a microfluidic environment. The reagent solutions (two aqueous solutions of copper(II) nitrate and aspartic acid in NaOH), were injected parallel into a microfluidic chip, creating a laminar flow of the reagents that enabled superior control of the interface of the two streams, where the Cu(II)-asp nanofibers formed within microseconds. Two examples of MOF nanotubes have been reported to date. Hou *et al.*[39] utilized alumina membranes as sacrificial templates for synthesizing Zr(IV)-phosphonate nanotubes. In their methodology, a film of a MOF is initially deposited on the template by deposition [e.g., via layer-by-layer (LbL) deposition]. Subsequent removal of the template via thermal or chemical techniques leaves behind a structure that mimics the size and shape of the template. In the second and more recent example, a self-sacrificing template strategy was used to prepare nano-$[Cd_2(btc)_2(H_2O)_2]$ tubes.[40] First, nano-$[Cd_2(btc)_2(H_2O)_2]$ rods were synthesized using a combination of ultrasonic synthesis and vapor diffusion, with triethylamine as deprotonating base agent. After the removal of the excess of triethylamine from the crude reaction under continuous ultrasonic irradiation, the nanorods then served as templates. A new MOF phase was then formed on the surface of each nanorod, which were simultaneously dissolved or chemically etched to form well-defined tubes (inner diameter: 50–150 nm; outer diameter: 100–300 nm). Interestingly, a similar chemical etching methodology was used to prepare hollow nano-Prussian blue cubes (dimensions: *ca.* 50 nm).[41]

2.2 2D NanoMOFs

The exotic mechanical, thermal, electronic, optical, and chemical properties of graphene have recently inspired the study of other graphene-like 2D materials.[42] Interestingly, 2D layered MOFs (MOF nanosheets) can potentially be a new source of these materials (Figure 3a). Although their development is in the early stages, the top-down (or deconstruction) method has been proposed as a promising strategy to fabricate them. This approach relies on the delamination or exfoliation of MOF nanosheets from bulk MOF crystals using ultrasonication irradiation or other methods. For instance, Li *et al.*[43] fabricated MOF nanosheets via delamination of bulk MOF-2 crystals. The delamination step was performed by dispersing dried MOF-2 crystals in acetone, and then subjecting them to ultrasonic radiation at room temperature (confirmed from the observation of the Tyndall effect) (Figure 3b). Sedimentation of the ultrasonicated suspension afforded a colloidal suspension of MOF-2 nanosheets. Figures 3c and d show representative scanning electron microscopy (SEM) and Atomic Force Microscopy images, respectively,

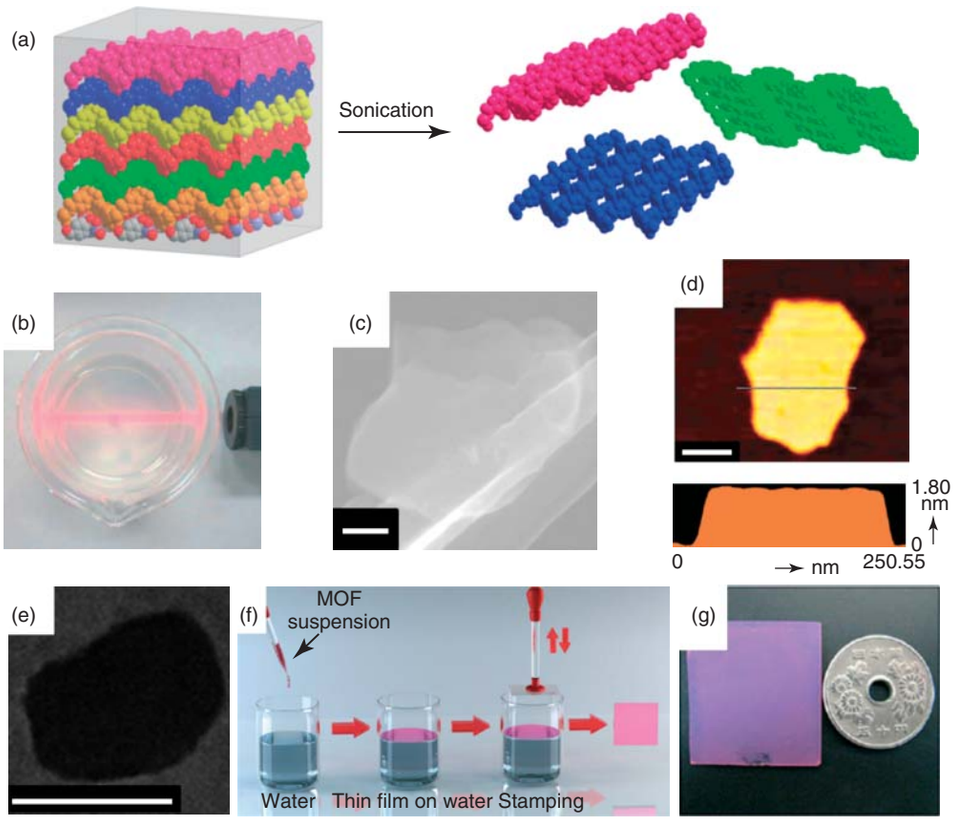


Figure 3 (a) Schematic illustration of the delamination process of a 2D bulk MOF (e.g., MOF-2) used for isolating MOF nanosheets. (b) Photograph of a colloidal suspension in acetone of MOF-2 nanosheets. The light beam was applied from the side to demonstrate the Tyndall effect. (c) Representative SEM image of MOF-2 nanosheets showing their morphology. Scale bar: 100 nm. (d) Depiction of an AFM image of a delaminated MOF-2 nanosheet (thickness: *ca.* 1.5 nm; lateral dimensions: 200–300 nm). Scale bar: 100 nm. ((b–d) Reproduced from Ref. 43 with permission of The Royal Society of Chemistry.) (e) Representative TEM image of a single Cu-TCPP nanosheet. Scale bar: 200 nm. (f) Illustration of the assembly of MOF Cu-TCPP nanosheets to form a thin film. (g) Photograph of the MOF thin film created after 15 deposition cycles on a quartz substrate. ((e–g) Reprinted with permission from Ref. 45. Copyright (2012) American Chemical Society.)

of the sheets. As observed in the images, the nanosheets had lateral dimensions of 100–1000 nm and a thickness of 0.7–6.0 nm (in agreement with the theoretical thickness of a single MOF-2 nanosheet: 0.7 nm). Similarly, Saines *et al.*[44] obtained several Mn(II), Co(II), and Zn(II)-DMS MOF nanosheets by exfoliating the corresponding bulk MOF crystals. In this case, the exfoliation was done via ultrasonication of an ethanolic colloidal suspension of the corresponding bulk MOF crystals. Importantly, some of the resulting nanosheets showed lateral dimensions close to 500 nm and unilamellar thicknesses around 1 nm. This approach has been also used by Xu *et al.*,[45] who exfoliated the 2D layered structure of Cu-TCPP by a modular assembly strategy. With this process, a "modularization" step was used for the synthesis of highly crystalline "modules" with a nanostructure that can be conveniently assembled into a thin film in the following "assembly" step. This method affords MOF thin films (Section 3), and it can be easily set up for different substrates at very high speed and with controllable thickness (Figures 3e–g).

3 SURMOFs: NANOMOFs ON SURFACES

The integration of nanoMOFs onto surfaces has attracted major interest over the last few years, as it enables facile incorporation of MOF properties (e.g., porosity, magnetism, and luminescence) into functional metallic, metal oxide, and organic substrates as well as into porous alumina and titania supports.[46–49] This method enables production of MOF thin films and membranes (or SURMOFs) with various compositions and controllable parameters (thickness; and pore size, functionalities, and orientation). Direct deposition is a straightforward way to form polycrystalline MOF films: it involves dip-coating

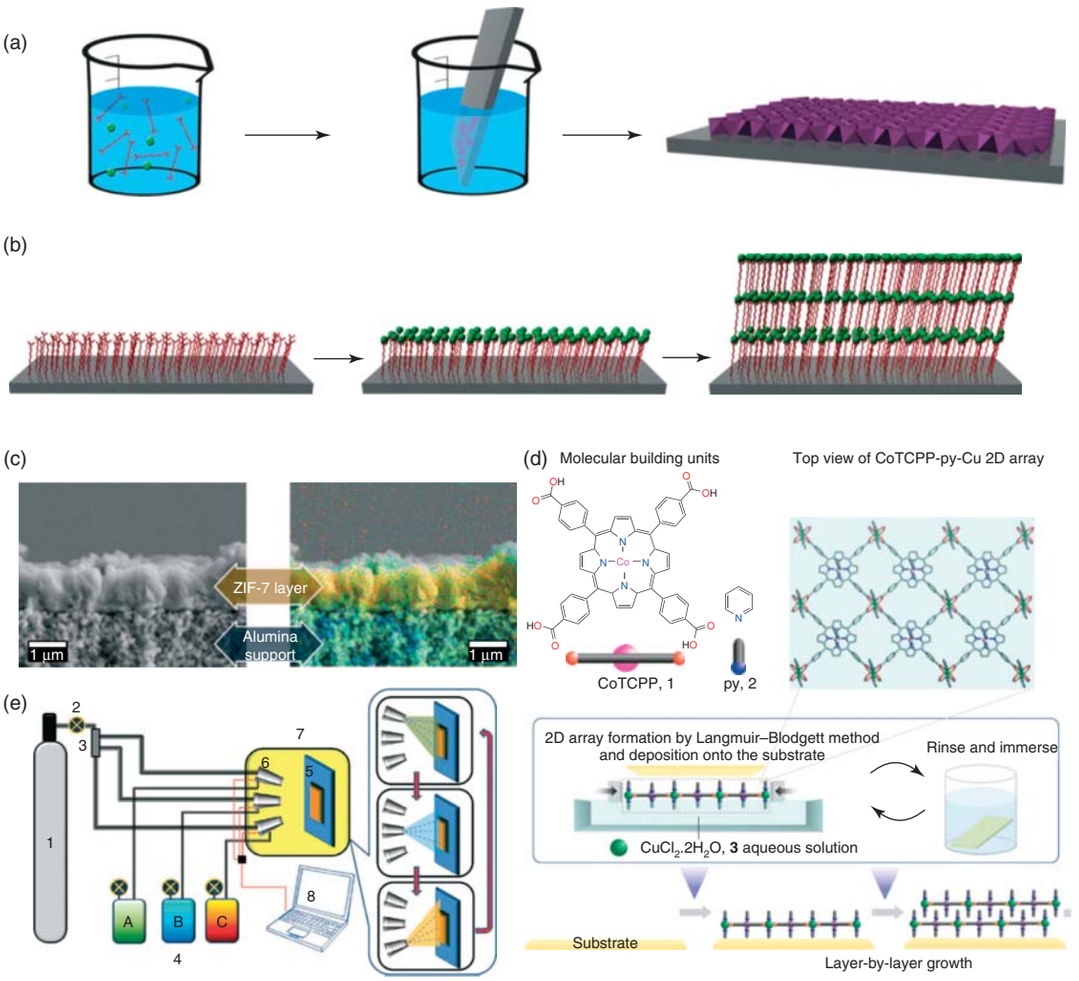


Figure 4 (a)–(b) Schematic illustration of direct deposition or in situ crystallization (a) and layer-by-layer (LbL) (b) approaches used for the construction of MOF thin films. (c) Cross section (left) and EDXS mapping of a ZIF-7 membrane made by direct deposition (orange: Zn; cyan: Al). (Reproduced from Ref. 53. © Wiley-VCH Verlag GmbH & Co. KGaA, 2010) (d) Schematic illustration of the Langmuir–Blodgett methodology using the 2D layered network of CoTCPP-py-Cu. The pre-formed 2D layered structure was deposited onto the substrate by the horizontal dipping method at room temperature. The substrate was then immersed into the pure solvent to remove excess starting materials or physisorbed components and dried. Iterative cycles of nanosheet deposition and rinsing/solvent immersion led to the sequential LbL growth of NAFS-1 thin films. (Reproduced from Ref. 62. © Nature Publishing Group, 2010.) (e) Illustration of the setup used for fabricating MOF thin films with the spray-coating method: (1) gas supply; (2) gas flow controller; (3) three-way valve gas distributor; (4) (A, B, C) solution storage containers; (5) sample holder; (6) dosing valves; (7) spray chamber; and (8) computer. (Reproduced from Ref. 61. © Wiley-VCH Verlag GmbH & Co. KGaA, 2011.)

the desired surfaces into a precursor solution,[50] a colloidal solution[51] or a suspension of seeds,[52] followed in some cases by the MOF crystal growth using conventional techniques (e.g., hydrothermal or microwave synthesis) (Figure 4a). An excellent example reported by Caro *et al.* was the growth of a ZIF-7 thin film on alumina supports. First, the supports were dipped into an aqueous polyethyleneimine dispersion of pre-synthesized nano-ZIF-7 crystals (dimensions: 30 nm).[53] Then, the seeded supports were vertically immersed into a solution of the ZIF-7 precursors, and subsequently microwave heated to 100 °C for 3 h to afford a large-scale, ordered polycrystalline ZIF-7 film (thicknesses: *ca.* 1 μm) (Figure 4c).

Surface composition can influence the formation of homogeneous MOF thin films. Reboul *et al.*[54] recently reported that a metal-dense Al(III) oxide surface provides Al(III) ions to spontaneously interact with the organic ligands bdc, btc, and ndc, to form thin films of [Al(OH)bdc], $[Al_3O(OH)(H_2O)_2(btc)_2]$, and [AlOH(ndc)], respectively. Likewise, surfaces can be modified to promote the nucleation and growth of MOF crystals. This is typically done in two ways: by introducing a self-assembled

monolayer (SAM) with a terminal functional group that can coordinate to metal ions;[55,56] or by oxidizing the metal surface to form metal ions that can coordinate to organic ligands.[57] These two types of treatment mimic the conditions of conventional MOF chemistry in which the organic ligands and the metal ions are used to build up the desired MOFs over large regions of surface, without defects. The treated surfaces can be then used as excellent chemical affinity templates: exposing them to the MOF precursor solutions under the optimum conditions affords denser, more stable MOF thin films with lesser defects.[50]

To date, several techniques have been used for growing nanoMOFs on pre-modified substrates. Polycrystalline MOF films are commonly created by submerging the pre-treated surfaces into the MOF precursor solution at room temperature, or under hydrothermal or microwave synthetic conditions. For example, Scherb *et al.*[58] demonstrated the formation of MIL-88b films by loading a COOH-terminated SAM with the desired MOF precursor solution at room temperature. Guo *et al*. prepared thin HKUST-1 film introducing a modified copper net together with the solutions of $Cu(NO_3)_2 \cdot 3H_2O$ and H_3btc dissolved in water/ethanol. The reactants and copper net were placed in a Teflon-lined autoclave to allow crystal growth at 120 °C for 3 days. After crystallization, an HKUST-1 membrane was obtained and washed several times with ethanol and dried at room temperature.[57]

To the best of our knowledge, there are currently only two methods for attaching a controlled number of unit cells of a MOF onto a surface to enable more precise control of the nanoscale thickness: liquid-phase epitaxy (LPE) and the Langmuir–Blodgett method. LPE is based on the stepwise LbL adsorption of components from the liquid phase onto a surface (Figure 4b). Typically, a SAM surface is alternatively immersed in the solution containing the metal ions and then in the solution of the organic ligands. Thus, the thickness of the MOF thin film can be controlled by the number of alternating cycles. For example, this methodology was used by Shekhah *et al.*[59] to fabricate (100) and (111) oriented HKUST-1 films on –COOH and –OH terminated SAMs, respectively, and non-interpenetrated MOF-508 films on 4,4′-bipyridil terminated SAMs.[60] LPE was also used by Arslan *et al.* for fabricating HKUST-1 thin films. However, in contrast to previous LPE procedures, the stock solutions of the reactants (copper(II) acetate and H_3btc) were deposited via spray-coating of surfaces modified with (Au) SAMs, which enabled markedly faster deposition and consequently, faster fabrication of polycrystalline HKUST-1 films (Figure 4e).[61] The Langmuir–Blodgett method relies on the formation and isolation of individual MOF layers, which are then sequentially transferred onto a substrate. Stacking of these layers by weak interactions leads to formation of the 3D MOF thin film. Makiura *et al*. reported the formation of the 2D layered [CoTCPP-py-Cu] network by spreading a chloroform/methanolic solution of the organic building blocks (Co(II)-TCPP and py) onto an aqueous solution of $CuCl_2$. The resulting MOF layers were then deposited onto an Si substrate, and stacked via sequential LbL growth. The π-stacking interactions between the pendant pyridine groups, which are coordinated axially to the paddlewheels, led to the generation of MOFs nanofilm on a solid surface (NAFS-1), the thickness of which could be controlled by controlling the number of stacked layers (Figure 4d).[62]

4 HYBRID MOF NANOCOMPOSITES

The advent of controlling the synthesis of MOFs at the nanoscale has inspired researchers to conceive of methods for combining nanoMOFs with other materials to obtain complex, hybrid nanocomposites that marry the best properties of each component—in some cases, enabling synergistic effects. Three major families of hybrid MOF nanocomposites have been described in the literature: inorganic-nanoparticle@MOF, organic-polymer@MOF, and oxide@MOF nanocomposites. These hybrid nanocomposites are prepared by using one component of the desired nanocomposites as a template to incorporate and/or grow, inside their porous structures or on their surfaces, the other component (or its precursors).

The most extensive family of MOF-based nanocomposites is the inorganic-nanoparticle@MOF composites, due to their potential applications in catalysis. These composites have been synthesized by first encapsulating the inorganic-nanoparticle precursors within the MOF cavities, and then synthesizing the nanoparticles inside these cavities.[63] The inorganic nanoparticle precursors are usually encapsulated via liquid impregnation, solvent-free gas-phase loading,[64] and by solid grinding of a volatile precursor in the presence of the activated MOF.[65] Examples include the embedding of Au nanoparticles in MOF-5, of Cu nanoparticles in MOF-5[64], and of Ag nanoparticles in HKUST-1, MOF-508, and MIL-68.[66]

Inorganic-nanoparticle@MOF composites can also be synthesized using the inorganic nanoparticles as templates. This strategy involves the functionalization of the surface of the inorganic nanoparticles with a surfactant, or a molecule containing functional groups such as carboxylic acid, hydroxyls, and pyridine moieties, that mimics those of the organic ligand used to construct the nanoMOFs. This enables coordination and consequently, the nanoMOF crystal growth, to be selectively done on the surface of the inorganic nanoparticles. This approach was followed by Lu *et al.* to incorporate different types of inorganic nanoparticles within nano-ZIF-8 crystals (Figure 5a). In a typical experiment, the inorganic nanoparticles were first synthesized and functionalized using PVP.

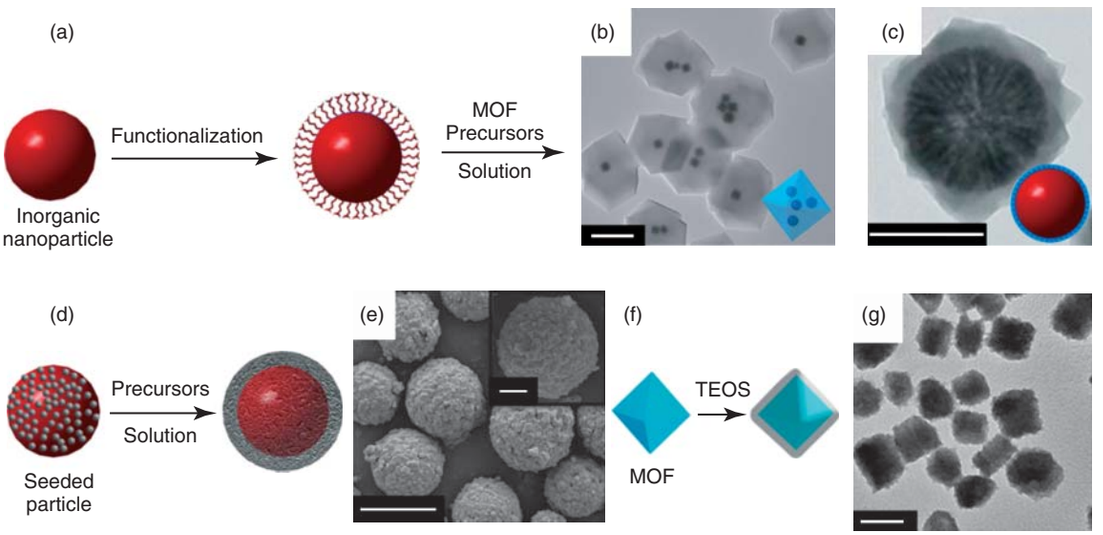


Figure 5 (a) Schematic representation of the preparation of functional composites using inorganic nanoparticles coated with molecules such as PVP or mercaptoacetic acid for the isolation of hybrid MOF nanocomposites. (b) Representative TEM image of nanoparticle@ZIF-8 composites that contain Ag cubes (average size: 160 nm). Scale bar: 500 nm. (Reproduced from Ref. 67. © Nature Publishing Group, 2012.) (c) Representative TEM image of an individual core/shell magnetic microsphere of Fe_3O_4@HKUST-1; the Fe_3O_4 nanoparticle is coated with nanoMOF crystals. Scale bar: 500 nm. (Reproduced from Ref. 68 with permission of The Royal Society of Chemistry. DOI: 10.1039/C2JM31167D) (d) Schematic illustration of a seeded particle template in which nanoMOFs can grow on top of them. (e) Representative SEM images of hybrid ZIF-8@mesoporous silica spheres. The mesoporous silica spheres of MSS act as the core and the template for the growth of ZIF-8 around them. Scale bar: 4 μm, inset: 1 μm. (Reproduced from Ref. 75 with permission of The Royal Society of Chemistry. DOI: 10.1039/C2CC34893D) (f) Schematic illustration of a nanoMOF crystal coated with a silica layer. (g) Representative TEM micrograph of PVP-functionalized nano-$Mn_3(btc)_2(H_2O)_6$ crystals coated with silica. Scale bar: 100 nm. (Reproduced from Ref. 76. © Elsevier, 2010.)

The functionalized nanoparticles were then mixed with zinc nitrate and 2-methylimidazole in methanol, and the resulting dispersion was kept at room temperate for 24 h without stirring. Under these conditions, the inorganic nanoparticles served as templates to selectively grow ZIF-8 on their surfaces, resulting in inorganic-nanoparticle@ZIF-8 nanocomposites in which the inorganic nanoparticles were embedded inside each nano-ZIF-8 crystal. Importantly, the authors demonstrated that this type of nanocomposites could be obtained with diverse inorganic nanoparticles, including Au, Pt, CdTe, Fe_3O_4, lanthanide-doped $NaYF_4$ and Ag nanoparticles (Figure 5b).[67] Ke *et al.* used this strategy to integrate Fe_3O_4 nanoparticles within HKUST-1 and MIL-100 crystals (Figure 5c). They synthesized core-shell Fe_3O_4@HKUST-1/MIL-100 nanocomposites using a step-by-step methodology, in which mercaptoacetic acid-functionalized Fe_3O_4 nanoparticles were dispersed alternatively in ethanol solutions of the corresponding metal salt and organic ligand precursors.[68]

Organic polymers are also excellent components for MOF hybrids, owing to their superb chemical properties, such as elasticity and conductivity. Uemura *et al.*,[69] who demonstrated the feasibility of synthesizing organic polymers (e.g., polypyrroles) inside the porous structures of bulk MOFs, did pioneering work on this area. More recently, Lee *et al.* used carboxylate-terminated polystyrene spheres as templates to prepare polystyrene@ZIF-8 core-shell composites. They prepared a thin, nanometer-sized layer of nano-ZIF-8 crystals around the polystyrene spheres by simply exposing the spheres twice to a methanolic solution of ZIF-8 precursors for 10 min at 70 °C.[54] The capability of nanoMOFs to stabilize Pickering emulsions[70] was also exploited by Huo *et al.*[71] to synthesize polystyrene@MOF nanocomposites in the form of hollow, microsized polystyrene capsules with nanoMOFs (nano-ZIF-8 and nano-MIL-101) integrated in the walls. These composites were created by first stabilizing oil-in-water Pickering emulsions with the nanoMOF crystals, followed by the controlled polymerization of the styrene and divinylbenzene contained in the oil phase. The combination of microporous nanoMOFs crystals with a hierarchically structured polymer membrane appears to be effective for the retention of encapsulated dye molecules. The same group also developed an approach combining the prototypical nano-ZIF-8 and nano-HKUST-1 crystals with cheap, abundant nontoxic gelatin hydrogels. The gelatin@ZIF-8 nanocomposites are readily dispersed in water forming colloidal solutions which are stable for several months.[72]

Finally, another interesting type of MOF hybrids results from combining MOFs with oxides, especially that of mesoporous SiO_2. The resulting hybrid nanomaterials can incorporate both mesoporosity and microporosity, and can be more stable or less toxic. For example, nanoMOF crystals have been grown inside the porous structures of COOH-functionalized mesostructured cellular silica foam, mesoporous MCM-41 and alumina structures.[54,73,74] Also, Sorribas *et al.*[75] prepared a uniform ZIF-8 layer (700 nm) around mesoporous silica spheres (diameter: 3 μm) (Figures 5d and e). They started by preparing a ZIF-8 seed layer on the surface of silica spheres. Owing to the attractive interactions between the terminal hydroxyl groups of the silica and the Zn(II) ions, this step simply required stirring the silica spheres in an aqueous solution of zinc nitrate and 2-methylimidazole for 5 min. The seeded microspheres were then mixed twice in a solution of the same ZIF-8 precursors. SiO_2@MOF nanocomposites can also be fabricated by enclosing the nanoMOF crystals within an SiO_2 shell. For example, nano-Tb(III)-*c,c,t*-(diamminedichlorodisuccinato)Pt(IV) crystals (diameter: 50 nm) and nano-Mn(bdc)$(H_2O)_2$ crystals (diameter: 100 nm) were coated with a silica shell (10 nm) that had previously been functionalized with PVP, and then treating the PVP-functionalized nanoMOFs with tetraethyl orthosilicate in a 4% (v/v) aqueous ammonia/ethanol mixture (Figures 5f–g).[76] Importantly, Huxford *et al.* demonstrated that such nanocomposites increase the stability of the nanoMOF, and facilitate their functionalization (e.g., with a fluorophore and a cell-targeting peptide).

5 MOF SUPERSTRUCTURES

Self-assembly of nanoMOF crystals into MOF superstructures could be employed to integrate MOFs into macroscale devices or to generate new functional materials. Consequently, this fledgling research area is poised to attract much interest in the near future. Unlike their corresponding nanoMOF counterparts or their corresponding bulk forms, these superstructures may exhibit new collective physiochemical properties, which in turn could extend their utility. To date, only a few well-defined MOF superstructures have been described, and most of them required use of sacrificial polymeric templates or interfacial synthesis, in which the spherical interface between two immiscible solvents, each containing one of the precursors, is used as the template. For example, the internal polystyrene of polystyrene@ZIF-8 nanocomposites (shown in Section 4) was used as a sacrificial template (dissolved in dimethylformamide (DMF)) to prepare hollow ZIF-8 superstructures.[77] Ameloot *et al.*[78] reported a process for the fabrication of larger, hollow MOF macrocapsules (diameter: *ca.* 500 μm) comprising nano-HKUST-1 crystals (Figure 6). Here, the HKUST-1 precursors (copper acetate in H_2O, and btc in octanol) were dissolved separately, and then each solution was delivered by syringe pump to a T-junction, where water droplets were generated by breaking-off in the co-flowing organic ligand solution. The nano-HKUST-1 crystals were then formed and assembled at the interface of the two solutions, leading to the formation of hollow HKUST-1 superstructures with defect-free walls (thickness: *ca.* 2 μm) (Figures 6b–d). In demonstrating the capacity of these superstructures to entrap guest species, the authors proposed their use as delivery systems, chemical sensors, or selective reactors containing molecular catalysts.

To avoid the use of emulsions and sacrificial hard templates, Carne-Sanchez *et al.*[79] have recently expanded the synthesis of hollow MOF superstructures at the liquid/air interface. They took advantage of the special conditions that rule crystallization during the drying of an atomized droplet to synthesize a wide range of MOFs (HKUST-1, NOTT-100, MIL-88A, MIL-88B, MOF-14, MOF-74 [M = Zn(II), Ni(II) and Mg(II)], UiO-66, ZIF-8, Cu(II) Prussian blue analogue (Cu-PB), MOF-5, and IRMOF-3) as hollow superstructures (Figures 6e–g).[79] The spray drying technique allows atomizing precursor solutions into aerosol droplets, which can be used as individual reactors to synthesize MOFs. In the hypothesized mechanism, the droplets suspended in a hot air stream start to evaporate and the reactants diffuse to the droplet shell where their concentration increases until a critical concentration is reached and crystallization of the MOF occurred. At this point, the mobility of the nanoMOF crystals reduced, and they packed within the shell of the droplet. Interestingly, the use of this approach allowed the combination of precipitation-crystallization of different species within the same single droplet. This capability opens up novel avenues for generating advanced encapsulation systems in which an active molecule or nanomaterial (e.g., dyes and magnetic iron oxide nanoparticles) can be entrapped within the MOF shell.[79]

6 PROPERTIES AND APPLICATIONS

The judicious choice of organic ligands and metal centers for the construction of porous MOFs[80], the recent developments in nanoscale MOF synthesis to obtain SURMOFs or hybrid MOF nanocomposites, and the growing area of MOF superstructures should greatly expand the utility of MOFs in new practical applications, including drug-delivery, medical imaging, sensor technology, functional membranes, and thin-films, as well as for traditional storage, separation, catalysis, and magnetic applications.[15,19,49]

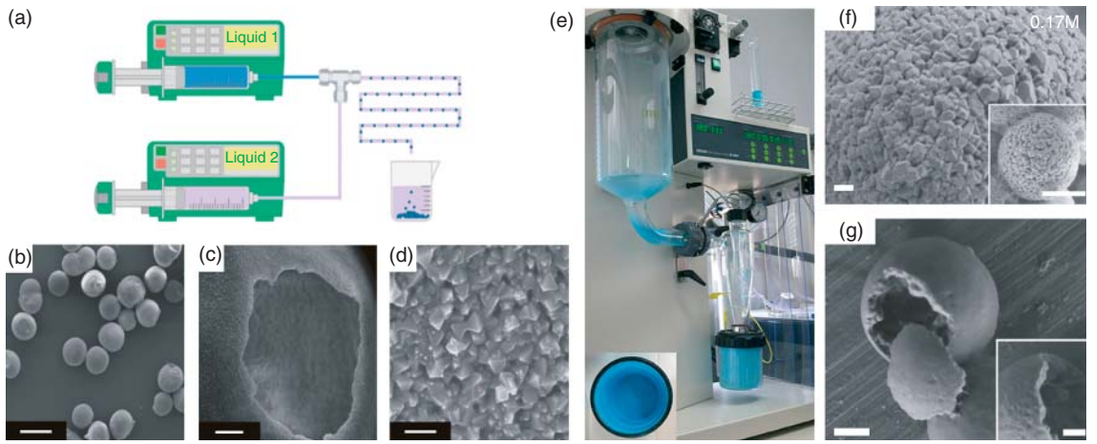


Figure 6 (a) Schematic illustration of the process used for preparing hollow MOF superstructures. First, the immiscible liquids are supplied by syringe pumps to a T-junction, where aqueous solution droplets (containing the metal ions) form inside the continuous organic phase (containing the organic ligand). The capsule shell (dark blue) is formed at the liquid–liquid interface while the droplets travel through hydrophobic tubing, before being collected in ethanol. (b) Representative SEM image of hollow HKUST-1 superstructures. Scale bar: 500 µm. (c) Representative SEM image of a single capsule crushed with a needle tip showing its hollow interior. Scale bar: 25 µm. (d) Detail of the wall of the defect-free capsule. Gaps between larger crystals are sealed by smaller, intergrown crystals. Scale bar: 2 µm. ((a–d) Reproduced from Ref. 78. © Nature Publishing Group, 2011.) (e) Image showing the spray-dryer apparatus after its use in synthesizing HKUST-1 superstructures, (f)–(g) FESEM images showing a single HKUST-1 superstructure and the assembly of nano-HKUST-1 crystals (scale bar: 500 nm, inset: 100 nm) and a mechanically broken hollow superstructure revealing its internal cavity and thickness of its wall (scale bar: 500 nm, inset: 200 nm). ((e–g) Reproduced from Ref. 79. © Nature Publishing Group, 2013.)

6.1 Gas Sorption and Separation

The porous nature of MOFs makes them promising candidates for gas sorption; thus, extensive research in this area has been done over the past 15 years.[8] Bulk MOFs exhibit diverse pore sizes and extremely high BET surface areas (up to 7000 $m^2 g^{-1}$),[7] and as such, can store many gases and absorb many functional molecules of different sizes (e.g., ferrocene[81] and myoglobin).[82] Although researchers have extensively explored these capabilities in bulk MOFs, chiefly driven by the great potential of these materials to soon replace fuel cells, very little work has been done on how the size and shape of nanoMOFs could influence the uptake or shape of the isotherm. For example, Tanaka *et al.*[83] compared bulk crystals and nanocrystals of the flexible [Zn(ip)(bipy)] for methanol uptake at 293 K and they have observed comparable performances in the two cases, but the shape of each isotherm was different and the kinetics for the nanoMOFs were dramatically higher. The same group also compared bulk crystals and nanocrystals of $[Cu_2(ndc)_2(dabco)]$, finding that the greater total uptake of CO_2 and of N_2 increased.[23] In another study, Cho *et al.*[84] showed that nanoMOF crystals constructed from In(III) and H_2bdc with different hexagonal shapes (rods, lumps, and disks) exhibited almost identical isotherm shapes and uptakes (H_2 and CO_2 uptakes of 140 and 333 $cm^3 g^{-1}$, respectively).

NanoMOFs crystals can also be assembled in such a way that the resulting MOF superstructures can show enhanced gas uptake performances: the microporosity characteristics derived from porous MOFs can be combined with the inherent mesoporosity of the superstructure. For example, Yue *et al.*[85] described a hierarchical Zn-MOF-74 material built up from the interconnection of nano-Zn-MOF-74 crystals. This novel material shows type-IV isotherms with hysteresis loops characteristic of large constricted mesopores in comparison to the typical type-I N_2 isotherm observed for the bulk microporous Zn-MOF-74.

Another field of interest is to create close-packed SURMOFs for use in membranes with high separation performance. Guo *et al.*[57] created nano-HKUST-1 membranes on an oxidized copper grid that showed a high permeation flux and excellent permeation selectivity for H_2 over CO_2, N_2, and CH_4. More recently, Caro *et al.* and Brown *et al.* prepared a series of improved nano-ZIF-8, nano-ZIF-7, nano-ZIF-90, and nano-ZIF-22 membranes that exhibited much better selectivities for H_2, by choosing nanoMOFs whose pore dimensions were close to the size of H_2.[50,86,87] They also formed nano-ZIF-90 membranes on polymeric hollow-fiber supports to fabricate high-surface-area membrane modules. The gas separation factors, permeances and selectivities of the polymeric-supported nano-ZIF-90 membrane indicated that it should be able to separate liquid alkanes (Figures 7a–f).[87]

The high separation capacity of MOFs is also being exploited for gas separation integrating nanoMOFs into gas chromatography columns. For instance, a capillary

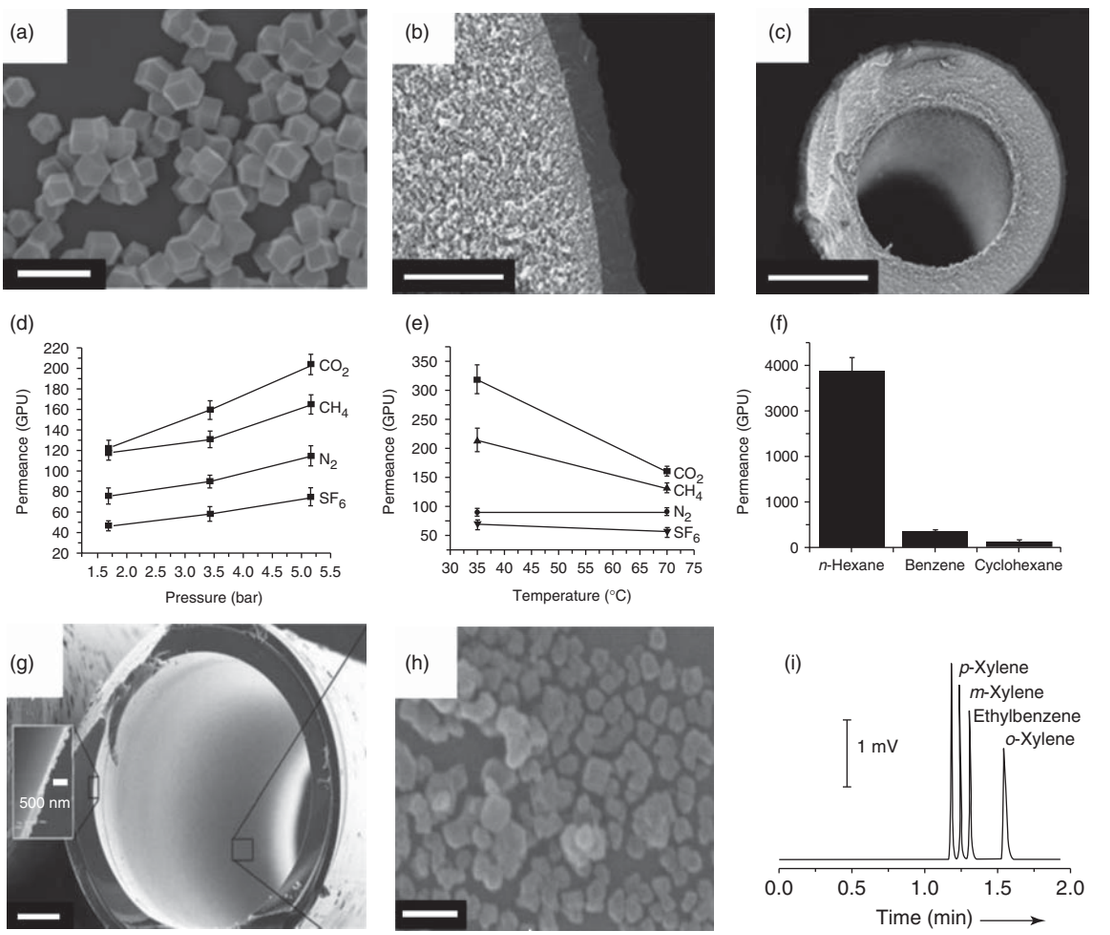


Figure 7 (a) Representative SEM image of nano-ZIF-90 crystals (average crystal: 400 nm). Scale bar: 1 μm. (b)–(c) Cross section SEM images showing the growth of nano-ZIF-90 membrane over the surface of a fiber. Scale bars for (b): 10 μm and (c): 100 μm. (d)–(f) Permeance values of gaseous CO_2, CH_4, H_2, and SF_6 at (d) 70 °C as a function of pressure and at (e) 50 psia as a function of temperature, and (f) Permeance values of hydrocarbons at 22 °C by pervaporation. ((a–f) Reproduced from Ref. 87. © Wiley-VCH Verlag GmbH & Co. KGaA, 2012) (g)–(h) Representative SEM images of the cross section of nano-MIL-101 coated capillary column (inset shows the thickness of the nano-MIL-101 coating) and nano-MIL-101 crystals deposited on the inner wall of the capillary column, respectively. Scale bars: 100 μm (g) and 500 nm (h). (i) Gas chromatography separation of xylene isomers and ethylene benzene on a nano-MIL-101 coated capillary column shown in (g) at 160 °C, showing N_2 flow rate. ((g–i) Reproduced from Ref. 89. © Wiley-VCH Verlag GmbH & Co. KGaA, 2010.)

coated with nano-MOF-5 crystals was tested for its efficacy in natural gas separation and benchmarked against a commercial Al_2O_3-based PLOT column.[88] Each column was run under its optimal operation conditions: albeit both columns separated all five components of natural gas (composition: 97.1% methane, 1.7% ethane, 0.7% propane, 0.2% isobutane, and 0.3% *n*-butane) with baseline resolution, the nano-MOF-5 column was 15% faster than the Al_2O_3 reference column. Similarly, Gu *et al.*[89] prepared a nano-MOF-based gas chromatography column by surface-coating a fused silica capillary column with nano-MIL-101 crystals. The resulting nanocomposite gas chromatography column had a 0.4 mm layer of nano-MIL-101 crystals on the inner wall, and after a carefully controlled conditioning program, enabled baseline separation of *o*-, *m*-, and *p*-xylenes from ethylbenzene at 160 °C within 1.6 min of sample injection (Figures 7g–i). Importantly, a total of only 1 mg of the nanoMOF was required to prepare the column, which is of significant importance given the elevated cost of some nanoMOFs over bulk zeolites and silica phases. This result makes nanoMOF-based capillary gas chromatography columns a realistic alternative to current columns. Other isomeric mixtures of substituted benzenes, and mixtures of *n*-alkanes, were also separated. Based on extensive control experiments, the researchers

attributed the observed selectivities to the polarity of nano-MIL-101 crystals combined with their unsaturated metal sites. Gu *et al.* also used the same dynamic coating method to prepare capillary columns of nano-ZIF-8 crystals for the separation of mixtures of linear and branched alkanes.[90] The small pore size (3.4 Å), sodalite cage structure and hydrophobic surface of nano-ZIF-8 crystals enabled effective separation of linear C6 and C8 alkanes from their corresponding branched isomers with baseline resolution.

6.2 Drug Delivery

MOFs exhibit many desired characteristics for their potential use as delivery platforms, including high surface areas and large pore sizes for encapsulation of drugs/active ingredients,[91,92] biodegradability, stability in water and physiologic media, and versatile functionality for post-synthetic grafting of drug molecules. Thus, an obvious application for nanoMOFs is as drug delivery agents.[21] In principle, there are two major strategies that one can use for nanoMOF-based delivery systems: (i) the drugs (or other active ingredient) is adsorbed inside the porous nanoMOFs, which can then be delivered by diffusion or degradation under specific conditions and at desired locations for subsequent local release of the cargo; or the drug (or other active ingredient) serves as one of the building blocks of the nanoMOFs (in which it is incorporated as one of the main organic ligands or post-synthetically attached), which can then be delivered while the nanoMOFs are degraded under certain conditions. An excellent example of the first type of potential nanoMOF drug delivery systems was reported by Horcajada *et al.*,[21] who showed the successful sorption of several antitumor or antiviral drugs, including busulfan, doxorubicin, azidothymidine triphosphate, and cidofovir, into nontoxic Fe(III)-based nanoMOFs (MIL-100, MIL-101, MIL-53, and MIL-88; size: 50–350 nm) crystals. Importantly, once all the adsorbed drugs had been incorporated into the porous structures, they could be released at different rates: doxorubicin and azidothymidine triphosphate adsorbed into nano-MIL-100 crystals were released after 3 and 5 days, respectively, whereas busulfan adsorbed into nano-MIL-53 crystals was released after 6 days.[93] Following the second approach, Taylor-Pashow *et al.*[94] synthesized nano-amino-MIL-101-Fe crystals (diameter: 200 nm) in which Bodipy, a fluorescent analog of the anticancer drug vinblastine, was grafted onto the nanoMOF through a covalent amine bond, with loading levels of up to 11% (w/w). Confocal microscopy of HT-29 cells that had been incubated with Bodipy-loaded nanocrystals revealed fluorescence inside the cells. Additionally, a Pt(IV)-based drug, *c,c,t*-$[PtCl_2(NH_3)_2(Oet)O_2CCH_2CH_2CO_2H]$ (ethoxysuccinato-cisplatin), was also grafted onto nano-amino-MIL-101 crystals, with an overall loading of 12.8% (w/w).[94]

6.3 Contrast Agents

NanoMOFs are also potential candidates for contrast agents in medical imaging applications because they can be constructed from paramagnetic metal ions such as Gd(III), Fe(III), and Mn(II). Among these, Gd(III) ions are extremely useful in magnetic resonance imaging (MRI), owing to their large magnetic moment and symmetric electronic ground state, both of which result from their seven unpaired orbital electrons. Chelates of the highly paramagnetic ion Gd(III) are extensively employed in the clinical setting; however, due to their low sensitivity, lack of selectivity, and low retention time, their efficacy is chiefly limited to areas of high accumulation. Among the strategies explored to overcome these problems is incorporation of Gd(III) ions or Gd(III)-chelates into nanostructures (e.g., liposomes, nanotubes, and inorganic nanoparticles)[95,96] to increase their circulation time and their relaxivity values. As an alternative class of nanostructure, nanoMOFs can store large amounts of Gd(III) ions within their frameworks. Lin *et al.* made an enormous contribution to this field by demonstrating the efficiency of nanoMOFs at modifying the relaxation times of the water protons in the surrounding medium when a magnetic field has been applied. They reported Gd(III)-based nanorods that showed exceptionally high longitudinal relaxivity (R_1) and transverse relaxivity (R_2) of 35.8 and 55.6 s^{-1}, respectively, per mM Gd(III) (Figures 8a–c),[34] whereas nanocrystals comprising Gd(III) metal ions connected through benzenehexacarboxylate had an impressive R_2 of 122.6 s^{-1} per mM Gd(III).[35]

Beyond the classically used Gd(III) ions, other metal ions such as Mn(II) and Fe(III) can also be used to increase contrast in MRI. For example, Taylor *et al.*[36] showed that nanorods of nano-$Mn(bdc)(H_2O)_2$ have an R_1 of 5.5 s^{-1} and an R_2 of 80.0 s^{-1} per mM Mn, whereas nanorods of nano-$Mn_3(btc)_2(H_2O)_6$ crystals exhibited an R_1 of 7.8 s^{-1} and an R_2 of 70.8 s^{-1} per mM Mn. Based on the R_1, the nano-$Mn_3(btc)_2(H_2O)_6$ crystals provided an efficient vehicle for the delivery of large doses of Mn(II) ions, which exhibited very high in vitro and in vivo R_1 values and afforded excellent MRI contrast enhancement. The surface of these nanoMOF crystals was also modified with a silica shell to enable covalent attachment of a cyclic RGD peptide and an organic fluorophore. The cell-targeting molecules on these nanoMOF crystals enhanced their delivery to cancer cells, thereby allowing for target-specific in vitro MRI. The MRI contrast enhancement was also demonstrated in vivo using a mouse model. Similar core/shell hybrid nanostructures have provided an ideal platform for targeted delivery of other imaging and therapeutic agents to diseased tissues (Figures 8d–g).[36] For example, Horcajada *et al.*[21] showed that nano-MIL-88A (comprising Fe(III) ions) exhibited a good R_1 of 50 s^{-1} per mM Fe(III), a sufficiently high value for in vivo use (Figures 8h and i). The researchers injected Wistar female

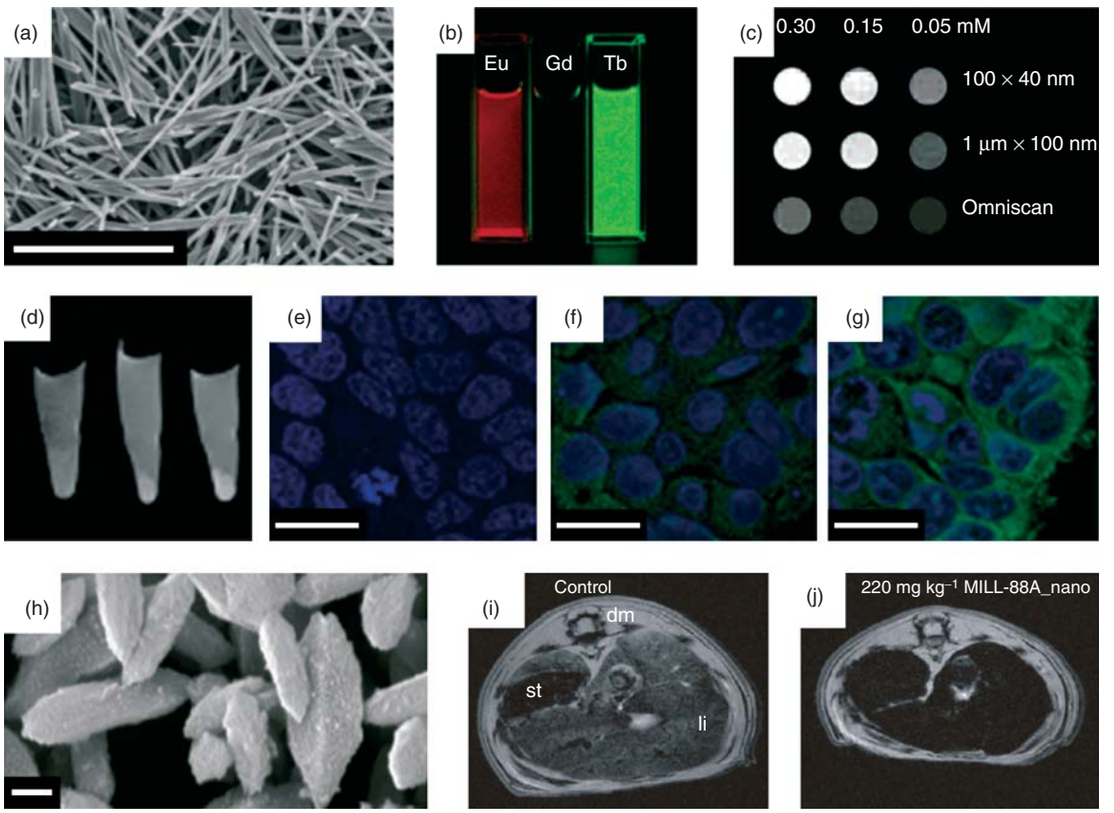


Figure 8 (a) Gd(III)-based rod-like nanocrystals synthesized using the emulsion methodology. (b) Luminescence images of ethanolic suspensions of Gd(III), and Gd(III)-based nanoMOFs, doped with 5 mol% Eu(III) and Tb(III). (c) *R*1-weighted Magnetic Resonance (MR) images of suspensions of nano-$Gd(bdc)_{1.5}(H_2O)_2$ crystals in water containing 0.1% xanthan gum. ((a–c) Reprinted with permission from Ref. 34. Copyright (2006) American Chemical Society.) (d) MR images of HT-29 cells incubated with nano-$Mn_3(btc)_2(H_2O)_6$ crystals, increasing concentrations from left to right. (e)–(g) Confocal images of HT-29 cells incubated with no nanocrystals (e), non-targeted Mn(II)-based nanoMOF (f), and cRGDfK-targeted Mn(II)-based nanoMOF (g). The cell nuclei were stained with DRAQ5 (blue) and nanocrystals were detected with rhodamine B (green). Scale bars: 20 μm. ((d–g) Reprinted with permission from Ref. 36. Copyright (2008) American Chemical Society.) (h) Representative SEM image of nano-MIL-88A crystals. Scale bar: 100 nm. (i)–(j) MR images acquired with gradient-echo or spin-echo sequence of control (untreated) rats and of rats injected with nano-MIL-88A crystals (dosing: 220 mg kg^{-1}) in their liver, respectively. ((h–j) Reproduced from Ref. 21. © Nature Publishing Group, 2010.)

rats with suspensions of nano-MIL-88A crystals (dosing: 22, 44, or 220 mg kg^{-1}) and after 30 min, imaged the animals with MRI. The gradient-echo and the spin-echo sequences showed that the organs were darker in treated animals than in untreated ones, confirming the temporary accumulation of nanocrystals in the liver (Figures 8i and j) and spleen.

Computed tomography (CT), another medical imaging technique, is based on X-ray attenuation by a specimen and can provide 3D images with excellent spatial resolution. Standard contrast agents for CT contain elements with a high *Z number* (e.g., iodine, barium, and bismuth), which can be incorporated in large amounts into nanoMOFs. As proof-of-concept, deKrafft *et al.*[97] fabricated nanoMOFs based on the associations of Zn(II) and Cu(II) ions with 2,3,5,6-tetraiodo-1,4-benzenedicarboxylic acid. Compared to commercial Iodoxanol, a clinically used iodinated contrast agent that contains 49% (w/w) iodine, their nano-$[Cu(I_4\text{-bdc})(H_2O)_2]\cdot 2H_2O$ and nano-$[Zn(I_4\text{-bdc})(EtOH)_2]\cdot 2EtOH$ crystals both contained 63% (w/w) iodine. Based on their results, the authors affirmed that these nanoMOFs should be capable of delivering high payloads of iodine, potentially representing a new class of CT contrast agents that do not suffer from the inherent drawbacks of small-molecule agents.

6.4 Catalysis

Nanocomposites comprising porous MOFs and catalytic inorganic nanoparticles exhibit promising catalytic performance.[98] Lu *et al.* showed that Pt@ZIF-8 nanocomposites catalyzed the oxidation of CO at 130 °C,

with a conversion of nearly 100% at 200 °C. The catalytic properties of Pt nanoparticles and the molecular sieving capability of the ZIF-8 matrix were combined and evaluated for liquid-phase hydrogenation with two substrates: *n*-hexene and *cis*-cyclooctene. Pt@ZIF-8 nanocomposites catalyzed the hydrogenation of the linear *n*-hexene molecule, albeit with a low conversion—presumably because of slow diffusion through the small pores (3.4 Å) of the nano-ZIF-8 crystals. Furthermore, the reusability of Pt@ZIF-8 nanocomposites as a catalyst for the hydrogenation of *n*-hexene was demonstrated by the observation of similar conversion efficiencies for consecutive runs (7.3%, 9.6%, and 7.1% for the first, second, and third runs, respectively). In contrast, no catalytic activity was observed for the sterically hindered substrate *cis*-cyclooctene, which is consistent with the small pore size of ZIF-8 (3.4 Å), but which also suggests the absence of Pt nanoparticles on the outer surface of the composite.[67]

6.5 Magnetism

Nano-Prussian blue crystals have shown fascinating superparamagnetic properties[99] for diverse potential applications, including as new photothermal ablation agents for cancer therapy.[100] Spin-crossover nanoMOFs are another class of attractive magnetic nanomaterials, as they enable thermal hysteresis to occur at room temperature and their spin configuration changes (from low to high) in function to external stimuli (e.g., heat or light). These spin changes usually imply a change in magnetic properties and therefore, are of great interest for electronic devices, switches, and memory devices. Coronado *et al.* made the first step in this area, demonstrating that nano-$[Fe(Htrz)_2(trz)(BF_4)]$ crystals (diameter: 10 nm) retain their spin-crossover properties.[101] Soon after, Boldog *et al.* compared the spin-crossover properties of bulk $[Fe(pz)Pt(CN)_4]$ crystals and related nanocrystals with dimension of $230 \times 230 \times 55$ nm and $61 \times 61 \times 21$ nm.[102] Interestingly, the spin-crossover of these nanocrystals remained constant, but their critical temperature decreased and the cooperativity of their spin crossover changed. This type of spin-crossover nanoMOFs have also been integrated onto surfaces to yield spin-crossover SURMOFs. In this context, Cobo *et al.* integrated similar nano-$[Fe(pz)[M(CN)_4]]$ crystals (M = Ni, Pd or Pt) on surfaces, leading to nanoscale films (thickness: *ca.* 150 nm) that displayed spin-crossover behavior with hysteresis at room temperature.[103]

6.6 Sensors

The interaction of guest molecules with the internal surface of porous nanoMOFs can induce dramatic changes in the physical properties of the nanoMOFs. This fact, combined with the high absorption capacities of nanoMOFs and the possibility to integrate them onto surfaces, makes them very attractive for creating novel sensors that are more sensitive and faster than current types. To date, several SURMOFs for gas (e.g., CO_2, ethanol, and methanol) sensing applications have been described.[104–107] For example, Bein *et al.* reported the selective growth of HKUST-1 thin films on functionalized quartz-crystal microbalance gold electrodes to obtain a device for evaluating mass variations: upon exposure to atmospheres with different relative humidities, the device detected water adsorption.[106] Kreno *et al.* compared a bare sensor to a nanoMOF-modified version that contained an Ag nanoparticle array coated with nano-HKUST-1 crystals: the modified sensor showed a 14-fold signal enhancement for CO_2 sensing.[104,105] These differences were attributed to the high capacity of the nano-HKUST-1 crystals to concentrate CO_2 within the MOF pores. Lu *et al.* built another very interesting selective surface sensor for chemical vapors and gases: a nano-ZIF-8-based Fabry–Pérot device based on the displacement of Fabry–Pérot interference peaks as a function of the exposure of the device to an analyte. They demonstrated that the nano-ZIF-8-based thin film can detect atmospheric ethanol.[107]

Another field of great interest is the design of fluorescent nanoMOF crystals for sensing of explosives. As a first approach, a significant selective quenching of the luminescence intensity of nano- $[Eu_2(bdc)_3(H_2O)_2]$ crystals in ethanol was observed in the presence of minute amounts of DNT and TNT explosives.[108] Similarly, fluorescent Cd(II)-based nanotubes have been developed for selective fluorescence quenching-based sensing of DNT and TNT explosives. Interestingly, the nanotubes exhibited a fluorescence quenching percentage of 72.5% within 10 s of being placed in DNT-saturated vapor, showing a detection limit as low as 18.1 ppb DNT.[40]

7 CONCLUSIONS AND PERSPECTIVES

Bulk MOFs are among the most attractive porous materials currently available, owing to their versatile architecture topologies, tunable pore sizes and functionalities, large surface areas, ability to selectively interact with atoms and molecules, capacity to encapsulate active species, and amenability for post-synthetic functional modification of their surfaces. At the nanoscale, nanoMOFs combine these unique properties with new, size-dependent properties which, if properly exploited, may expand the scope of these materials in numerous practical applications, including drug-delivery, medical imaging, sensing, and materials (functional membranes and thin-films), as well as more traditional storage, separation, and catalysis applications. Thus, since 2000, researchers have chiefly

focused on finding ways to prepare, isolate, and stabilize nanoMOFs, and to subsequently attach them to surfaces, by controlling their assembly and reactivity with other materials. This excellent but embryonic work is summarized in this Chapter, in which the first examples of isolated 0D, 1D, and 2D nanoMOFs, integrated MOFs on surfaces (SURMOFs), MOF-based nanocomposites and assembled MOF superstructures are described. These examples have shown promising applications in catalysis (using MOF-based nanocomposites) and in gas and liquid separation (using MOF-based membranes and incorporating 0D and 1D nanoMOFs in chromatographic columns). Gas storage, magnetic and sensing technologies derived from nanoMOFs are in the fledgling stages, as researchers aim to exploit the superior properties of nanoMOFs relative to their corresponding bulk forms. Inspired by inorganic nanoparticles, 0D and 1D nanoMOFs have also been proposed for biomedical applications—namely, as drug delivery systems and as contrast agents for medical imaging.

Despite the rather remarkable results obtained so far in the development of new methods for nanoMOFs synthesis and in the study of their properties and applications, the field of nanoMOFs remains in an embryonic stage; thus, much work remains to be done. For example, the use of nanoMOFs for biomedical applications requires not only the design of new nanoMOFs with interesting functionality but also method development to produce nanoMOF crystals of controlled size and shape in high quantities. Other research objectives include achieving greater stability and better dispersability in physiologic media, and avoiding their aggregation in these media; controlling the delivery of the active species; improving their functionalization with recognition species; and evaluating their toxicology and biodistribution, among many others. Importantly, most of these needs can be translated to other potential applications, which entail additional demands. For sensing, nanoMOF growth and surface integration must be improved (e.g., researchers must demonstrate integration of different nanoMOFs onto a single surface for simultaneous detection of distinct analytes). For catalysis, a better understanding of the size- and shape-dependence of molecular adsorption into nanoMOFs is needed, as are methods to grow nanoMOFs into beads or zeolites to improve their stability and catalytic activity. For separation, nanoMOFs should be integrated onto silica (silica@nanoMOF nanocomposites) to create HPLC-type columns, and a better understanding of the size- and shape-dependence of gas adsorption into nanoMOFs is also needed.

Achieving the aforementioned research objectives will demand a far better understanding of the existing methodologies to prepare nanoMOFs as well as the exploration of new synthetic routes. Thus, systematic studies of the methods outlined in this Chapter must be performed. These studies will help to answer many questions, such as: *What is the role of coordination modulators and surfactants in nanoMOFs? How they can be used to control the size, shape, stability, and dispersibility of nanoMOFs*? *Can microwave irradiation, ultrasonic irradiation, and use of emulsions be general methodologies for nanoMOFs synthesis? Can the exfoliation method be used to prepare large single MOF sheets? Can the assembly of nanoMOFs be controlled to create MOF superstructures with desired shapes?* The answers to these and many other questions will provide the basis for better controlling the synthesis of nanoMOFs and facilitate their exploitation for diverse applications.

Recently discovered techniques, such as the use of microfluidics to dictate the formation pathway of the assembled nanoMOFs by varying flow-rate conditions, the use of templates to guide the growth of nanoMOFs with desired sizes and shapes, and chemical etching to create hollow nanoMOF crystals, are expected to evolve strongly in the coming years, ultimately enabling better control of the synthesis of nanoMOFs. Also, new methodologies are likely to be developed. For example, MOF-on-MOF epitaxial growth can be explored to design new hybrid nanoMOF crystals with extremely high surface areas obtained by combining the porosity of different MOF components. Another clear example is the spray-drying method very recently reported by Carné *et al.*—which is a totally original, general, low-cost, rapid, and scalable way to fabricate large quantities of a wide variety of nanoMOF crystals. It is important to note here that this methodology enables assembly of the resulting nanoMOFs into hollow MOF superstructures which can encapsulate active species—from simple NaCl salt to Fe_3O_4 nanoparticles.[79]

Other important objectives that should be accomplished are shaping nanoMOFs into different forms and integrating them into different devices. In recent work different academic and industrial research groups have demonstrated that MOFs can be integrated into paper sheets,[109] textiles,[110] polymeric beads,[111] plastics, and gels,[112] for subsequent use in sensing and separation. NanoMOFs can also be integrated into specific locations of devices via lithographic methods. Carbonell *et al.*,[113,114] Ameloot *et al.*,[78] and Falcaro *et al.*[115] have recently reported the use of soft-nanolithography techniques, such as tip-based nanolithography or micro-contact printing, to grow nanoMOFs at desired locations on surfaces, with high precision over large areas.

In conclusion, the fledgling field of nanoMOFs is ripe with potential. We believe that the enormous progress made in the short time since their onset is generating great expectations for their use in conventional industrial processes (e.g., chromatographic separation, sensing, and medical diagnostics) within the next 5 to 10 years.

8 RELATED ARTICLES

Porous Coordination Polymer Nanoparticles and Macrostructures; Metal-Organic Frameworks in Mixed-Matrix Membranes; Patterning Techniques for Metal-Organic Frameworks;

9 ABBREVIATIONS AND ACRONYMS

asp = aspartic acid; bipy = bipyridine; CTAB = Cetyl trimethylammonium bromide; dabco = 1,4-diazabicyclo[2.2.2]octane; DEF = diethylformamide; DMF = dimethylformamide; DMS = 2,3-dimethylsuccinate; DNT = 2,4-dinitrotoluene; H_2ip = (isophthalic acid or 1,3-benzenedicarboxylic acid); H_2bdc = 1,4-benzenedicarboxylic acid; H_3btc = 1,3,5-benzene tricarboxylic acid; H_2ndc = naphthalene dicarboxylic acid; Htrz = 1,2,4-1*H*-triazole; MCM-41 = mesoporous organosilica; PVP = polyvinylpyrrolidone; PAA = poly(acrylic acid); py = pyridine; pz = pyrazine; TCPP = 5,10,15,20-tetrakis(4-carboxyphenyl)porphyrin; TNT = 2,4,6-trinitrotoluene; *SURMOF* = surface metal organic framework; BET = Brunner Emmet Teller; CT = Computed tomography; DMF = dimethylformamide; LbL = layer-by-layer; LPE = liquid-phase epitaxy; MOF = Metal-organic framework; MRI = magnetic resonance imaging; NAFS-1 = MOFs nanofilm on a solid surface; nanoMOF = nanoscale metal organic framework; SAM = self-assembled monolayer; SEM = scanning electron microscopy; 0D = zero dimension; 1D = one-dimensional; 2D = two-dimensional; 3D = three-dimensional.

MOFs: HKUST-1 = 3D network of formula [Cu_3(1,3,5-benzenetricarboxylate)$_2$], IRMOF-1, -2, -3 = 3D networks with general formula of [Zn_4O(dicarboxylate)$_3$] where dicarboxylates for IRMOF-1 (also referred as MOF-5) = 1,4-benzenedicarboxylic acid; IRMOF-2 = 2-bromo-1,4-benzene dicarboxylic acid and IRMOF-3 = 2-amino-1,4-benzene dicarboxylic acid, MIL-53 = 3D network of formula [M(OH)(1,4-benzenedicarboxylate)] where M = Al(III),Fe(III),Cr(III),V(III), MIL-68 = 3D network of formula [Fe(OH)(1,4-benzene dicarboxylate)]; MIL-88A = 3D network of formula [$Fe_3O(CH_3OH)_3$(1,4-benzene dicarboxylate)$_3$]; MIL-88B = 3D network of formula [Fe_3O(1,4-benzenedicarboxylate)$_3$]; MIL-89 = 3D network of formula [$Fe_6O_2Cl_2$(1,4-benzene dicarboxylate)$_6$]; MIL-100 = 3D network of formula [$M_3O(X)(H_2O)_2$(1,3,5-benzenetricarboxylate)$_2$] where: M = Al(III), Fe(III) and X = OH, F; MIL-101 = 3D network of formula [$Cr_3F(H_2O)_2O$(1,4-benzene dicarboxylate)$_3$]; MOF-2 = 2D network of formula [Zn_2(1,4-benzene dicarboxylate)$_2$]; MOF-5 = 3D network of formula [Zn_4O(1,4-benzene dicarboxylate)$_3$]; MOF-14 = 3D network of formula [Cu_3(1,3,5-benzene tribenzoate)2(H2O)3]; MOF-74 = 3D network of formula Zn_2(2,5-dihydroxy-1,4-benzenedicarboxylate); MOF-508 = 3D network of formula [Zn_4(1,4-benzene dicarboxylate)$_4$(bipyridine)$_2$]; NOTT-100 = 3D network of formula [Cu_2(biphenyl-3,3′,5,5′-tetracarboxylate)$(H_2O)_2$] UiO-66 = 3D network of formula $Zr_6O_4(OH)_4$(1,4-benzene dicarboxylate)$_6$; ZIF-7 = 3D network of formula [Zn(benzimidazole)$_2$]; ZIF-8 = 3D network of formula [Zn(2-methylimidazole)$_2$]; ZIF-22 = 3D network of formula [Zn(5-azabenzimidazole)$_2$]; ZIF-90 = 3D network of formula [Zn(2-carboxaldehyde imidazolate)$_2$].

10 REFERENCES

1. O. M. Yaghi, M. O'Keeffe, N. W. Ockwig, H. K. Chae, M. Eddaoudi, and J. Kim, *Nature*, 2003, **423**, 705.
2. S. T. Meek, J. A. Greathouse, and M. D. Allendorf, *Adv. Mater.*, 2011, **23**, 249.
3. D. J. Tranchemontagne, J. L. Mendoza-Cortes, M. O'Keeffe, and O. M. Yaghi, *Chem. Soc. Rev.*, 2009, **38**, 1257.
4. D. Tanaka, K. Nakagawa, M. Higuchi, S. Horike, Y. Kubota, T. C. Kobayashi, M. Takata, and S. Kitagawa, *Angew. Chem. Int. Ed.*, 2008, **120**, 3978.
5. J. Rabone, Y. F. Yue, S. Y. Chong, K. C. Stylianou, J. Bacsa, D. Bradshaw, G. R. Darling, N. G. Berry, Y. Z. Khimyak, A. Y. Ganin, P. Wiper, J. B. Claridge, and M. J. Rosseinsky, *Science*, 2010, **329**, 1053.
6. C. Serre, F. Millange, C. Thouvenot, M. Nogues, G. Marsolier, D. Louer, and G. Ferey, *J. Am. Chem. Soc.*, 2002, **124**, 13519.
7. O. K. Farha, I. Eryazici, N. C. Jeong, B. G. Hauser, C. E. Wilmer, A. A. Sarjeant, R. Q. Snurr, S. T. Nguyen, A. Ö. Yazaydın, and J. T. Hupp, *J. Am. Chem. Soc.*, 2012, **134**, 15016.
8. J.-R. Li, R. J. Kuppler, and H.-C. Zhou, *Chem. Soc. Rev.*, 2009, **38**, 1477.
9. J. Lee, O. K. Farha, J. Roberts, K. A. Scheidt, S. T. Nguyen, and J. T. Hupp, *Chem. Soc. Rev.*, 2009, **38**, 1450.
10. M. D. Allendorf, C. A. Bauer, R. K. Bhakta, and R. J. T. Houk, *Chem. Soc. Rev.*, 2009, **38**, 1330.
11. A. C. McKinlay, R. E. Morris, P. Horcajada, G. Ferey, R. Gref, P. Couvreur, and C. Serre, *Angew. Chem. Int. Ed.*, 2010, **49**, 6260.
12. S. Couck, J. F. M. Denayer, G. V. Baron, T. Remy, J. Gascon, and F. Kapteijn, *J. Am. Chem. Soc.*, 2009, **131**, 6326.
13. L. Alaerts, C. E. A. Kirschhock, M. Maes, M. A. van der Veen, V. Finsy, A. Depla, J. A. Martens, G. V. Baron, P. A. Jacobs, J. E. M. Denayer, and D. E. De Vos, *Angew. Chem. Int. Ed.*, 2007, **46**, 4293.

14. *MOF special issue, Chem. Soc. Rev.*, 2009, **38**, 1201 (19 articles).
15. A. Carne, C. Carbonell, I. Imaz, and D. Maspoch, *Chem. Soc. Rev.*, 2011, **40**, 291.
16. F. Fajula, A. Galarneau, and F. D. Renzo, *Microporous Mesoporous Mater.*, 2005, **82**, 227.
17. J. Wang, J. D. Byrne, M. E. Napier, and J. M. DeSimone, *Small*, 2011, **7**, 1919.
18. H. B. Na, I. C. Song, and T. Hyeon, *Adv. Mater.*, 2009, **21**, 2133.
19. D. Bradshaw, A. Garai, and J. Huo, *Chem. Soc. Rev.*, 2012, **41**, 2344.
20. S. Jung and M. Oh, *Angew. Chem. Int. Ed.*, 2008, **47**, 2049.
21. P. Horcajada, T. Chalati, C. Serre, B. Gillet, C. Sebrie, T. Baati, J. F. Eubank, D. Heurtaux, P. Clayette, C. Kreuz, J.-S. Chang, Y. K. Hwang, V. Marsaud, P.-N. Bories, L. Cynober, S. Gil, G. Ferey, P. Couvreur, and R. Gref, *Nat. Mater.*, 2010, **9**, 172.
22. H. Guo, Y. Zhu, S. Qiu, J. A. Lercher, and H. Zhang, *Adv. Mater.*, 2010, **22**, 4190.
23. T. Tsuruoka, S. Furukawa, Y. Takashima, K. Yoshida, S. Isoda, and S. Kitagawa, *Angew. Chem. Int. Ed.*, 2009, **48**, 4739.
24. P. Horcajada, C. Serre, D. Grosso, C. Boissière, S. Perruchas, C. Sanchez, and G. Férey, *Adv. Mater.*, 2009, **21**, 1931.
25. S. P. Diring, S. Furukawa, Y. Takashima, T. Tsuruoka, and S. Kitagawa, *Chem. Mater.*, 2010, **22**, 4531.
26. J. Cravillon, R. Nayuk, S. Springer, A. Feldhoff, K. Huber, and M. Wiebcke, *Chem. Mater.*, 2011, **23**, 2130.
27. J. Cravillon, C. A. Schröder, R. Nayuk, J. Gummel, K. Huber, and M. Wiebcke, *Angew. Chem. Int. Ed.*, 2011, **50**, 8067.
28. A. Ranft, S. B. Betzler, F. Haase, and B. V. Lotsch, *CrystEngComm*, 2013.
29. S. K. Nune, P. K. Thallapally, A. Dohnalkova, C. Wang, J. Liu, and G. J. Exarhos, *Chem. Commun.*, 2010, **46**, 4878.
30. L.-G. Qiu, Z.-Q. Li, Y. Wu, W. Wang, T. Xu, and X. Jiang, *Chem. Commun.*, 2008, 3642.
31. J. Klinowski, F. A. Almeida Paz, P. Silva, and J. Rocha, *Dalton Trans.*, 2011, **40**, 321.
32. Z. Ni and R. I. Masel, *J. Am. Chem. Soc.*, 2006, **128**, 12394.
33. S. Vaucher, M. Li, and S. Mann, *Angew. Chem. Int. Ed.*, 2000, **39**, 1793.
34. W. J. Rieter, K. M. L. Taylor, H. An, W. Lin, and W. Lin, *J. Am. Chem. Soc.*, 2006, **128**, 9024.
35. K. M. L. Taylor, A. Jin, and W. Lin, *Angew. Chem. Int. Ed.*, 2008, **47**, 7722.
36. K. M. L. Taylor, W. J. Rieter, and W. Lin, *J. Am. Chem. Soc.*, 2008, **130**, 14358.
37. Y. Zhao, J. Zhang, B. Han, J. Song, J. Li, and Q. Wang, *Angew. Chem. Int. Ed.*, 2011, **50**, 636.
38. J. Puigmartí-Luis, M. Rubio-Martínez, U. Hartfelder, I. Imaz, D. Maspoch, and P. S. Dittrich, *J. Am. Chem. Soc.*, 2011, **133**, 4216.
39. S. Hou, C. C. Harrell, L. Trofin, P. Kohli, and C. R. Martin, *J. Am. Chem. Soc.*, 2004, **126**, 5674.
40. R. Li, Y.-P. Yuan, L.-G. Qiu, W. Zhang, and J.-F. Zhu, *Small*, 2012, **8**, 225.
41. M. Hu, N. L. Torad, and Y. Yamauchi, *Eur. J. Inorg. Chem.*, 2012, **2012**, 4795.
42. A. K. Geim, *Science*, 2009, **324**, 1530.
43. P.-Z. Li, Y. Maeda, and Q. Xu, *Chem. Commun.*, 2011, **47**, 8436.
44. P. J. Saines, M. Steinmann, J.-C. Tan, H. H. M. Yeung, W. Li, P. T. Barton, and A. K. Cheetham, *Inorg. Chem.*, 2012, **51**, 11198.
45. G. Xu, T. Yamada, K. Otsubo, S. Sakaida, and H. Kitagawa, *J. Am. Chem. Soc.*, 2012, **134**, 16524.
46. D. Zacher, O. Shekhah, C. Woll, and R. A. Fischer, *Chem. Soc. Rev.*, 2009, **38**, 1418.
47. O. Shekhah, J. Liu, R. A. Fischer, and C. Woll, *Chem. Soc. Rev.*, 2011, **40**, 1081.
48. D. Zacher, R. Schmid, C. Wöll, and R. A. Fischer, *Angew. Chem. Int. Ed.*, 2011, **50**, 176.
49. A. Bétard and R. A. Fischer, *Chem. Rev.*, 2011, **112**, 1055.
50. A. Huang, W. Dou, and J. R. Caro, *J. Am. Chem. Soc.*, 2010, **132**, 15562.
51. A. Demessence, C. Boissiere, D. Grosso, P. Horcajada, C. Serre, G. Ferey, G. J. A. A. Soler-Illia, and C. Sanchez, *J. Mater. Chem.*, 2010, **20**, 7676.
52. H. Bux, A. Feldhoff, J. Cravillon, M. Wiebcke, Y.-S. Li, and J. Caro, *Chem. Mater.*, 2011, **23**, 2262.
53. Y.-S. Li, F.-Y. Liang, H. Bux, A. Feldhoff, W.-S. Yang, and J. Caro, *Angew. Chem. Int. Ed.*, 2010, **49**, 548.
54. J. Reboul, S. Furukawa, N. Horike, M. Tsotsalas, K. Hirai, H. Uehara, M. Kondo, N. Louvain, O. Sakata, and S. Kitagawa, *Nat. Mater.*, 2012, **11**, 717.
55. E. Biemmi, C. Scherb, and T. Bein, *J. Am. Chem. Soc.*, 2007, **129**, 8054.
56. D. Zacher, A. Baunemann, S. Hermes, and R. A. Fischer, *J. Mater. Chem.*, 2007, **17**, 2785.
57. H. Guo, G. Zhu, I. J. Hewitt, and S. Qiu, *J. Am. Chem. Soc.*, 2009, **131**, 1646.
58. C. Scherb, A. Schödel, and T. Bein, *Angew. Chem. Int. Ed.*, 2008, **47**, 5777.
59. O. Shekhah, H. Wang, D. Zacher, R. A. Fischer, and C. Wöll, *Angew. Chem. Int. Ed.*, 2009, **48**, 5038.
60. O. Shekhah, H. Wang, M. Paradinas, C. Ocal, B. Schupbach, A. Terfort, D. Zacher, R. A. Fischer, and C. Woll, *Nat. Mater.*, 2009, **8**, 481.
61. H. K. Arslan, O. Shekhah, J. Wohlgemuth, M. Franzreb, R. A. Fischer, and C. Wöll, *Adv. Funct. Mater.*, 2011, **21**, 4228.

62. R. Makiura, S. Motoyama, Y. Umemura, H. Yamanaka, O. Sakata, and H. Kitagawa, *Nat. Mater.*, 2010, **9**, 565.
63. M. Meilikhov, K. Yusenko, D. Esken, S. Turner, G. Van Tendeloo, and R. A. Fischer, *Eur. J. Inorg. Chem.*, 2010, **2010**, 3701.
64. S. Hermes, M. K. Schroter, R. Schmid, L. Khodeir, M. Muhler, A. Tissler, R. W. Fischer, and R. A. Fischer, *Angew. Chem. Int. Ed.*, 2005, **44**, 6237.
65. T. Ishida, M. Nagaoka, T. Akita, and M. Haruta, *Chem. Eur. J.*, 2008, **14**, 8456.
66. R. J. T. Houk, B. W. Jacobs, F. E. Gabaly, N. N. Chang, A. A. Talin, D. D. Graham, S. D. House, I. M. Robertson, and M. D. Allendorf, *Nano Lett.*, 2009, **9**, 3413.
67. G. Lu, S. Li, Z. Guo, O. K. Farha, B. G. Hauser, X. Qi, Y. Wang, X. Wang, S. Han, X. Liu, J. S. DuChene, H. Zhang, Q. Zhang, X. Chen, J. Ma, S. C. J. Loo, W. D. Wei, Y. Yang, J. T. Hupp, and F. Huo, *Nat. Chem.*, 2012, **4**, 310.
68. F. Ke, L.-G. Qiu, Y.-P. Yuan, X. Jiang, and J.-F. Zhu, *J. Mater. Chem.*, 2012, **22**, 9497.
69. T. Uemura, N. Yanai, and S. Kitagawa, *Chem. Soc. Rev.*, 2009, **38**, 1228.
70. B. Xiao, Q. Yuan, and R. A. Williams, *Chem. Commun.*, 2013, **49**, 8208.
71. J. Huo, M. Marcello, A. Garai, and D. Bradshaw, *Adv. Mater.*, 2013, **25**, 2717.
72. A. Garai, W. Shepherd, J. Huo, and D. Bradshaw, *J. Mater. Chem. B*, 2013, **1**, 3678.
73. Y.-K. Seo, J. W. Yoon, U. H. Lee, Y. K. Hwang, C.-H. Jun, and J.-S. Chang, *Microporous Mesoporous Mater.*, 2012, **155**, 75.
74. A. M. B. Furtado, J. Liu, Y. Wang, and M. D. LeVan, *J. Mater. Chem.*, 2011, **21**, 6698.
75. S. Sorribas, B. Zornoza, C. Tellez, and J. Coronas, *Chem. Commun.*, 2012, **48**, 9388.
76. R. C. Huxford, J. Della Rocca, and W. Lin, *Curr. Opin. Chem. Biol.*, 2010, **14**, 262.
77. H. J. Lee, W. Cho, and M. Oh, *Chem. Commun.*, 2012, **48**, 221.
78. R. Ameloot, F. Vermoortele, W. Vanhove, M. B. J. Roeffaers, B. F. Sels, and D. E. De Vos, *Nat. Chem.*, 2011, **3**, 382.
79. A. Carne-Sanchez, I. Imaz, M. Cano-Sarabia, and D. Maspoch, *Nat. Chem.*, 2013, **5**, 203.
80. S. Kitagawa, R. Kitaura, and S. Noro, *Angew. Chem. Int. Ed.*, 2004, **43**, 2334.
81. Y. K. Park, S. B. Choi, H. Kim, K. Kim, B. H. Won, K. Choi, J. S. Choi, W. S. Ahn, N. Won, S. Kim, D. H. Jung, S. H. Choi, G. H. Kim, S. S. Cha, Y. H. Jhon, J. K. Yang, and J. Kim, *Angew. Chem..Int. Ed.*, 2007, **46**, 8230.
82. Y. Chen, V. Lykourinou, T. Hoang, L.-J. Ming, and S. Ma, *Inorg. Chem.*, 2012, **51**, 9156.
83. D. Tanaka, A. Henke, K. Albrecht, M. Moeller, K. Nakagawa, S. Kitagawa, and J. Groll, *Nat. Chem.*, 2010, **2**, 410.
84. W. Cho, H. J. Lee, and M. Oh, *J. Am. Chem. Soc.*, 2008, **130**, 16943.
85. Y. Yue, Z.-A. Qiao, P. F. Fulvio, A. J. Binder, C. Tian, J. Chen, K. M. Nelson, X. Zhu, and S. Dai, *J. Am. Chem. Soc.*, 2013, **135**, 9572.
86. Y.-S. Li, H. Bux, A. Feldhoff, G.-L. Li, W.-S. Yang, and J. Caro, *Adv. Mater.*, 2010, **22**, 3322.
87. A. J. Brown, J. R. Johnson, M. E. Lydon, W. J. Koros, C. W. Jones, and S. Nair, *Angew. Chem. Int. Ed.*, 2012, **51**, 10615.
88. A. S. Münch, J. Seidel, A. Obst, E. Weber, and F. O. R. L. Mertens, *Chem. Eur. J.*, 2011, **17**, 10958.
89. Z.-Y. Gu and X.-P. Yan, *Angew. Chem. Int. Ed.*, 2010, **49**, 1477.
90. N. Chang, Z.-Y. Gu, and X.-P. Yan, *J. Am. Chem. Soc.*, 2010, **132**, 13645.
91. P. Horcajada, C. Serre, M. Vallet-Regi, M. Sebban, F. Taulelle, and G. Ferey, *Angew. Chem. Int. Ed.*, 2006, **45**, 5974.
92. P. S. Wheatley, A. R. Butler, M. S. Crane, S. Fox, B. Xiao, A. G. Rossi, I. L. Megson, and R. E. Morris, *J. Am. Chem. Soc.*, 2006, **128**, 502.
93. P. Horcajada, R. Gref, T. Baati, P. K. Allan, G. Maurin, P. Couvreur, G. Férey, R. E. Morris, and C. Serre, *Chem. Rev.*, 2011, **112**, 1232.
94. K. M. L. Taylor-Pashow, J. Della Rocca, Z. Xie, S. Tran, and W. Lin, *J. Am. Chem. Soc.*, 2009, **131**, 14261.
95. E. J. Werner, A. Datta, C. J. Jocher, and K. N. Raymond, *Angew. Chem. Int. Ed.*, 2008, **47**, 8568.
96. M.-S. Martina, J.-P. Fortin, C. Ménager, O. Clément, G. Barratt, C. Grabielle-Madelmont, F. Gazeau, V. Cabuil, and S. Lesieur, *J. Am. Chem. Soc.*, 2005, **127**, 10676.
97. K. E. deKrafft, Z. Xie, G. Cao, S. Tran, L. Ma, O. Z. Zhou, and W. Lin, *Angew. Chem. Int. Ed.*, 2009, **48**, 9901.
98. C.-H. Kuo, Y. Tang, L.-Y. Chou, B. T. Sneed, C. N. Brodsky, Z. Zhao, and C.-K. Tsung, *J. Am. Chem. Soc.*, 2012, **134**, 14345.
99. L. Catala, F. Volatron, D. Brinzei, and T. Mallah, *Inorg. Chem.*, 2009, **48**, 3360.
100. G. Fu, W. Liu, S. Feng, and X. Yue, *Chem. Commun.*, 2012, **48**, 11567.
101. E. Coronado, J. R. Galán-Mascarós, M. Monrabal-Capilla, J. García-Martínez, and P. Pardo-Ibáñez, *Adv. Mater.*, 2007, **19**, 1359.
102. I. Boldog, A. B. Gaspar, V. Martínez, P. Pardo-Ibañez, V. Ksenofontov, A. Bhattacharjee, P. Gütlich, and J. A. Real, *Angew. Chem. Int. Ed.*, 2008, **120**, 6533.
103. S. Cobo, G. Molnár, J. A. Real, and A. Bousseksou, *Angew. Chem. Int. Ed.*, 2006, **45**, 5786.

104. L. E. Kreno, J. T. Hupp, and R. P. Van Duyne, *Anal. Chem.*, 2010, **82**, 8042.

105. S. Achmann, G. Hagen, J. Kita, I. Malkowsky, C. Kiener, and R. Moos, *Sensors*, 2009, **9**, 1574.

106. E. Biemmi, A. Darga, N. Stock, and T. Bein, *Microporous Mesoporous Mater.*, 2008, **114**, 380.

107. G. Lu and J. T. Hupp, *J. Am. Chem. Soc.*, 2010, **132**, 7832.

108. H. Xu, F. Liu, Y. Cui, B. Chen, and G. Qian, *Chem. Commun.*, 2011, **47**, 3153.

109. U. Mueller, M. Schubert, F. Teich, H. Puetter, K. Schierle-Arndt, and J. Pastre, *J. Mater. Chem.*, 2006, **16**, 626.

110. A. Kumarsen, 'Coated textiles: principles and applications', CRC Press c/o Taylor & Francis Group, Boca Raton, 2008.

111. U. Mueller, L. Lobree, M. Hesse, O. Yaghi, M. Eddaoudi, US Patent Application, Pub. Number US/2003 0222023 A0222021, 2003.

112. Q. Wei and S. L. James, *Chem. Commun.*, 2005, 1555.

113. C. Carbonell, I. Imaz, and D. Maspoch, *J. Am. Chem. Soc.*, 2011, **133**, 2144.

114. C. Carbonell, K. C. Stylianou, J. Hernando, E. Evangelio, S. A. Barnett, S. Nettikadan, I. Imaz, and D. Maspoch, *Nat. Commun.*, 2013, 4.

115. P. Falcaro, A. J. Hill, K. M. Nairn, J. Jasieniak, J. I. Mardel, T. J. Bastow, S. C. Mayo, M. Gimona, D. Gomez, H. J. Whitfield, R. Riccò, A. Patelli, B. Marmiroli, H. Amenitsch, T. Colson, L. Villanova, and D. Buso, *Nat. Commun.*, 2011, **2**, 237.

Mesoporous Metal-Organic Frameworks

Yao Chen and Shengqian Ma

University of South Florida, Tampa, FL, USA

1	Introduction	39
2	Representative Structures and Examples	40
3	Strategies for the Design and Synthesis of MesoMOFs	46
4	Applications of Mesoporous MOFs	49
5	Conclusions	63
6	Acknowledgments	63
7	Related Articles	63
8	Abbreviations and Acronyms	63
9	References	64

1 INTRODUCTION

Metal–organic frameworks (MOFs), which are defined as the two-dimensional (2D) or three-dimensional (3D) coordination polymers composed of metal moieties and organic linkers, have attracted great attention over the past two decades. In particular, porous MOFs have emerged as a new generation of highly porous crystalline materials with potential applications in a variety of fields[1] such as gas separation and storage, heterogeneous catalysis, biocatalysis, sensors and biomedical applications. MOFs can be deliberately designed by pre-selecting the appropriate inorganic (metals or metal clusters) and organic (organic ligands) building blocks and/or by post-synthetic modifications (PSMs).[2] The unlimited choices of metals and organic building blocks give rise to enormous structural diversity, various metrics, and functionalities. According to the classification of IUPAC, the material with pore size <2 nm is microporous; pore size ranging from 2 to 50 nm is mesoporous; pore size >50 nm is defined as macroporous.[3] MOFs can exhibit cavities and/or open channels with a range of pore sizes from micro- to mesoporous. Compared to microporous MOFs, mesoporous metal–organic frameworks hereafter dubbed mesoMOFs,[4] allow for loading of cargos with large dimensions or fast diffusion of large active species, which dramatically broadens the applications of MOFs, and offer great opportunities for biocatalysis, sensing, and biomedical applications. In addition, mesoMOFs have demonstrated thus far the highest porosity and surface area which can facilitate the gas storage application, especially under high pressure. Traditional mesoporous materials, such as mesoporous silica, metal oxides, and activated carbon, are composed of either inorganic or organic compounds and suffer from intrinsic limitations. Specifically, the inorganic compounds exhibit a lack of structural flexibility, whereas the organic compounds are usually amorphous without crystalline structure. MesoMOFs combine inorganic and organic beneficial features within one system, and their structural versatility, together with amenability to be designed with specific functionality as well as extra-large surface areas, positions them in a unique place amongst traditional mesoporous materials.

MesoMOFs possess either channel- or cage-like meso-pores. The adsorption isotherms can be used to determine the size and shape of pores. Typically, mesoMOFs exhibit Type IV and Type V isotherms (Figure 1) featured with hysteresis loops (IUPAC classification).[5] However, Type I isotherm with secondary uptake platform is also observed in some mesoMOFs, especially those with the hierarchical structures possess both micro- and mesoporosity, such as MIL-100[6] and MIL-101.[7]

Compared with their micro- or meso-counterparts, mesoMOFs exhibit superior performance, especially in gas adsorption, catalysis, and biomedical applications.[8]

Metal-Organic Framework Materials. Edited by Leonard R. MacGillivray and Charles M. Lukehart.
© 2014 John Wiley & Sons, Ltd. ISBN 978-1-119-95289-3

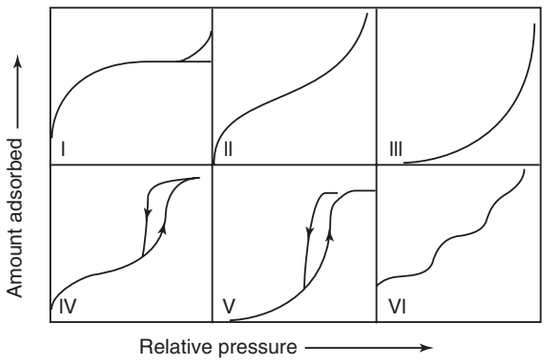


Figure 1 IUPAC classification of adsorption isotherms (Reproduced with permission from Ref. 4. © Taylor & Francis, 2010.)

However, up to now, only a small portion of the reported MOFs are mesoporous. In comparison to microporous MOFs, the applications of mesoMOFs have yet to be systemically and comprehensively developed.

2 REPRESENTATIVE STRUCTURES AND EXAMPLES

The pores of mesoMOFs refer not only to channels but also cavities (Table 1). In terms of the structures and pore shapes, mesoMOFs can be classified into two types, the channeled and caged mesoMOFs. Channeled mesoMOFs such as IRMOF-16[9] and BiO-MOF-100[10] possess 1D open meso-channels when viewing the structures along some specific directions. Caged mesoMOFs, such as MIL-100[6] and -101[7], possess polyhedral meso-cavities that are connected by micro- or meso-channels. The study of the structural features of mesoMOFs under different catalogs is fundamentally important for the understanding of principles for the mesoMOFs and thus facilitates the development of their properties and application.

2.1 Channeled MesoMOFs

2.1.1 MOF-5 Analog

In 2002, the first 3D mesoMOFs, IRMOF-16[9] (Figure 2) was reported by Yaghi's group. IRMOF-16 is

Table 1 The representative mesoMOFs and their structural features

MesoMOFs	Surface area ($m^2\ g^{-1}$)		Structure type	Pores size (Å)	Topology	Reference
	BET	Langmuir				
MIL100	—	3100	Cage	25 and 26	MTN	6
MIL101	4200	5900	Cage	29 and 34	MTN	7
IRMOF-16	1910	—	Channel	28.8	pcu	9
IRMOF-14	—	1936	Channel	24.5	pcu	9
IRMOF-16	—	1750	Channel	24.5	pcu	9
mesoMOF-1	726	—	Cage/channel	32 and 22.5 × 26.1	tbo	23
Bio-MOF-100	4300	—	Channel	28	LCS	10
MOF-74-XI	1760	—	Channel	98	bnn	14
MOF-545 (MMPF-6, or PCN-222)	2260	—	Channel	37	csq	11 55 56
NU-1000	2320	—	Channel	30	csq	12
JUC-48	629	—	Channel	21.1 × 24.9	etb	15
CYCU-3	2757	—	Channel	28.3 × 31.1	—	16
MOF-200	4530	10 400	Cage	18 × 28	qom	35
MOF-210	6240	10 400	Cage	26.9 × 48.3	toz	35
ZIF-95	1050	1240	Cage	25.1 × 14.3 30.1 × 20	poz	20
ZIF-100	595	780	Cage	35.6	moz	20
NOTT-112	3800	—	Cage	21	rht	18
NU-100 (PCN-610)	6143	—	Cage	27.4	rht	36
Tb-mesoMOF	1783	3855	Cage	39 and 47	MTN	21
UMCM-1	4160	6500	Channel	24 × 29	—	27
Bio-MOF-102	3222	—	Channel	26	LCS	28
Bio-MOF-103	2704	—	Channel	29	LCS	28
NU-111	5000	—	Cage	24	rht	37
DUT-9	—	—	Channel	22 and 23	—	33

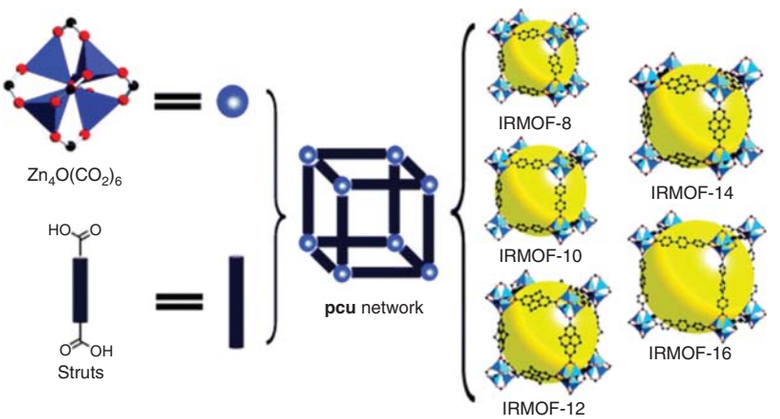


Figure 2 Illumination of the strategy to synthesize IRMOFs from $[Zn_4O(COO)_6]$ building blocks and dicarboxylates ligands (Reproduced from Ref. 8 with permission from The Royal Society of Chemistry. DOI: 10.1039/C1CS15196G.)

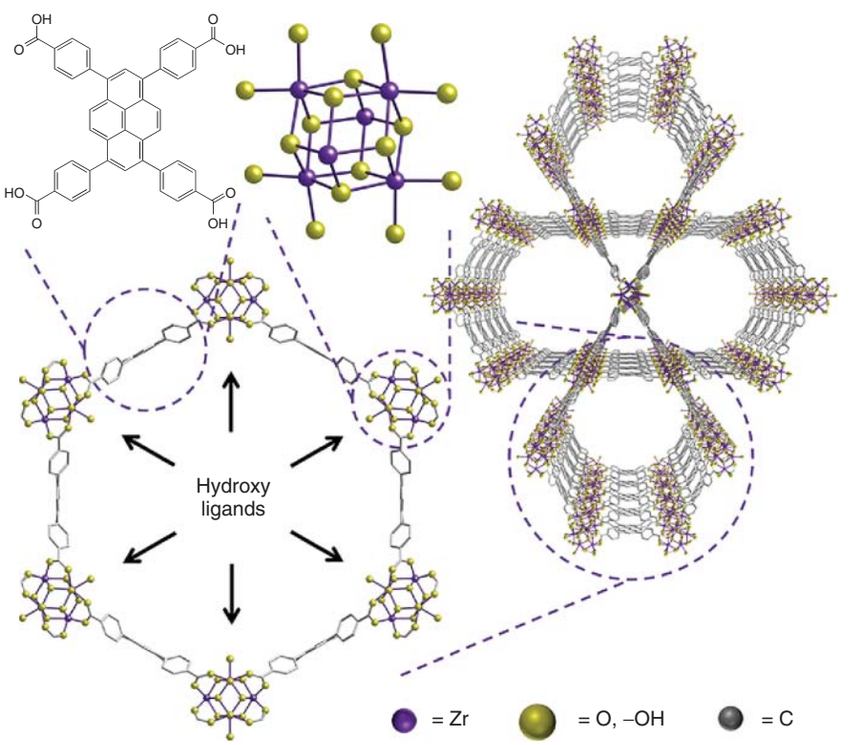


Figure 3 NU-1000 constructed from the $[Zr_6O_8(COO)_8(H_2O)_8]$ building blocks and rigid H_4TBAPy ligands (Reproduced with permission from Ref. 12. Copyright (2013) American Chemical Society.)

isoreticular to MOF-5, which is of a **pcu** net built from the $[Zn_4O(COO)_6]$ building blocks and triphenyl-4,4′-dicarboxylate (TPDC) ligands. IRMOF-16 possesses a fixed diameter of 28.8 Å and 91.1% free volume. In addition, the density of IRMOF-16 is as low as 0.21 g cm^{-3}.

2.1.2 MOF-545 Analog

In 2012, Yaghi, Zhou, and Ma groups coincidently reported the first mesoporous porphyrin-based MOFs, MOF-545[11] (or PCN-222,[54] MMPF-6[55]). MOF-545 can

be simplified into a **csq** net formed by the 8-connected $[Zr_6O_8(COO)_8(H_2O)_8]$ building blocks and 4-connected square planar tetrakis(4-carboxyphenyl)porphyrin (TCPP) ligands. In addition, MOF-545 can be viewed as a zirconium-carboxylate kagome-type layer in the *ab* plane further pillared by TCPP ligands. The 3D framework contains large hexagonal 1D channels of ~3.7 nm diameter along the *c* axis. MOF-545 possesses a high BET surface area up to 2260 $m^2 g^{-1}$.

Very recently, Hupp's group reported a MOF-545 analog, NU-1000,[12] by reaction of $ZrCl_4$ and 1,3,6,8-tetrakis(*p*-benzoicacid) pyrene (H_4TBAPy). NU-1000 is stable up to 500 °C and has high porosity of BET surface area up to 2320 $m^2 g^{-1}$. DFT analysis revealed both micropores of ~12 Å and mesopores of ~30 Å consistent with those observed in the structures (Figure 3).

2.1.3 *MOF-74 Analog*

In 2005, Yaghi's group firstly reported MOF-74 (Zn)[13], which was synthesized from dihydroxy-1,4-benzenedicarboxylic acid (H_2-DHBDC) and $Zn(NO_3)_2$. In MOF-74 (Figure 4), the infinite helical Zn-O-C rods are constructed from 6-coordinated Zn centers, hydroxyl groups, and carboxylates. The helical rods are further linked by phenyl units of DHBDC to produce **bnn** parallel rod packing and 1D hexagonal channels with coordinate zinc(II) ions decorating the edges of each channel. The 1D

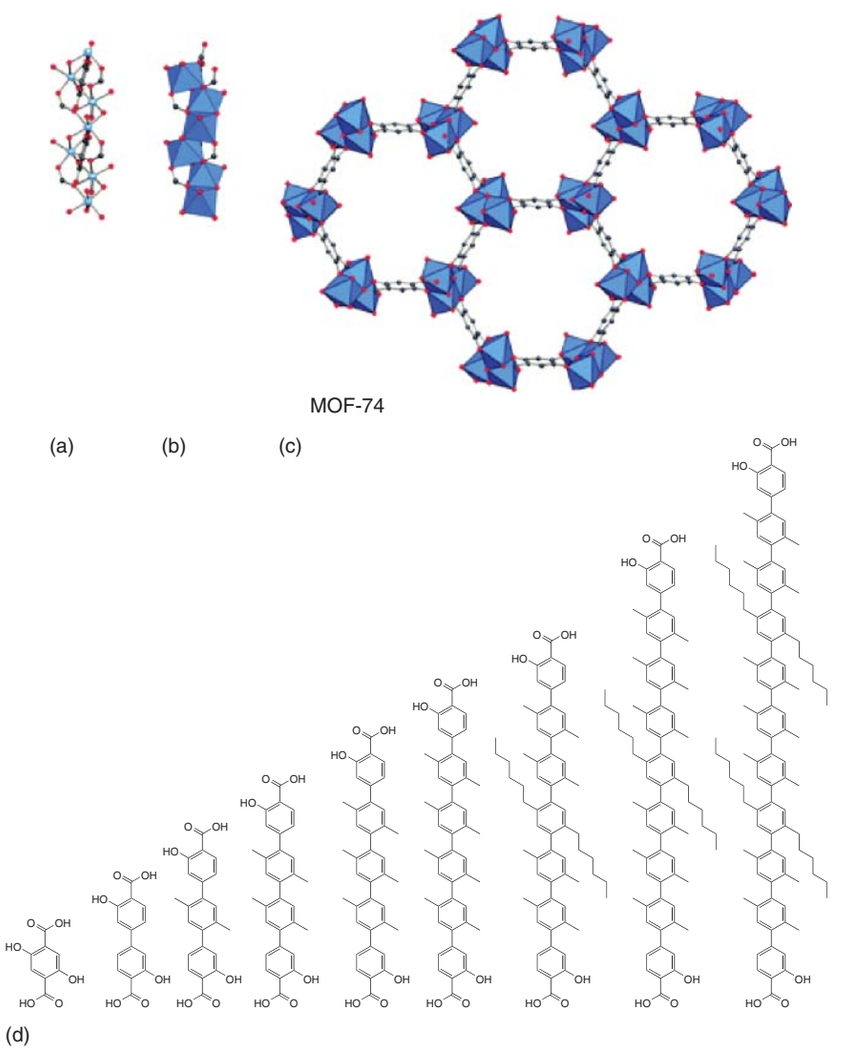


Figure 4 (a) SBU of MOF 74; (b) SBU with Zn shown as polyhedra of MOF 74; (c) view of crystalline framework with inorganic SBUs linked together via the benzene ring of 2,5-dihydroxybenzene-1,4-dicarboxylate; (d) ligands used for the formation of MOF 74 analogs (IRMOF-74-I to XI) (Reproduced with permission from Ref. 13. Copyright (2005) American Chemical Society.)

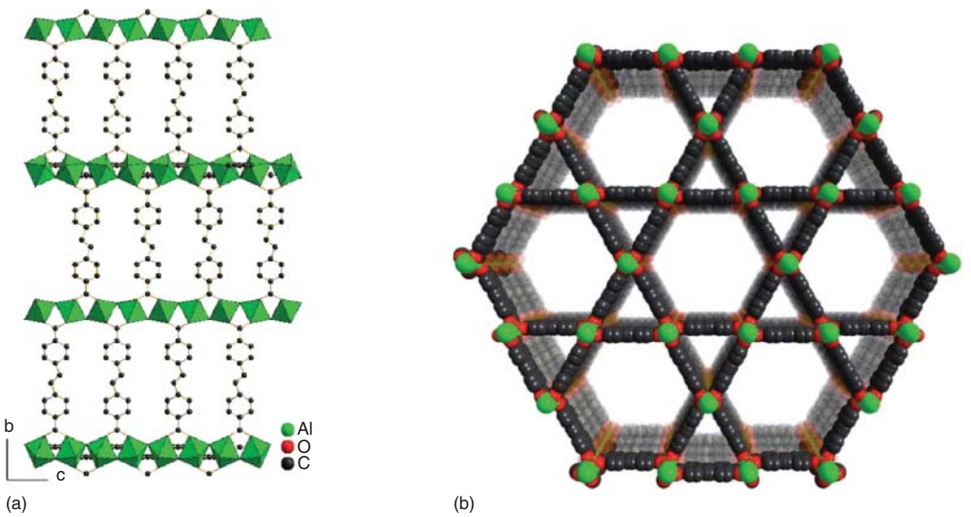


Figure 5 (a) The corner-shared 1D aluminum chains in CYCU-3; (b) the triangular channels and hexagonal channels in CYCU-3 (Reproduced from Ref. 16 with permission from The Royal Society of Chemistry. DOI: 10.1039/C2TA00030J.)

hexagonal channels have impenetrable walls based on the rod-shaped secondary building units (SBUs), which prohibit the formation of interpenetrated structure. Based on this idea, in 2012, Yaghi and coworkers extended the one phenyl rings to two, three, four, five, six, seven, nine, and eleven phenyl rings and succeeded to synthesize an isoreticular series of mesoporous MOF-74 structures (termed *IRMOF-74-I to XI*) with pore apertures ranging from 19 to 98 Å (Figure 4).[14] All these structures have non-interpenetrating structures and exhibit robust architectures confirmed by gas sorption data and thermal stability analysis. Up to now, MOF-74-XI retains the world record of pore size up to 98 Å and the lowest crystal density (guest-free) of 0.195 g cm^{-1} among reported MOFs.

2.1.4 Other Channeled MesoMOFs

With the exception of the mesoporous MOF-74 variants, there are also other examples with large 1D channels constructed from infinite rod-shaped building blocks. In 2007, Qiu and coworkers reported a mesoMOF, JUC-48, with 1D hexagonal channels of 24.5 × 27.9 Å.[15] JUC-48 was synthesized from Cd salts and biphenyl-4,4′-dicarboxylate (BPDC) in DMF by slow diffusion with triethylamine. Similar to MOF-74, the Cd centers are linked together by carboxylates to form 1D infinite chain, which are interconnected by BPDC ligands to generate a 3D non-interpenetrating structure.

In 2013, Lin and coworkers synthesized a MIL-68 analog, CYCU-3, from aluminum salts and 4,4′-stilbenedicarboxylic acid (H_2SDC).[16] Aluminum ions are 6-coordinated with carboxylate oxygens to form corner-shared 1D inorganic chains, which are further bridged by SDC ligands to form 3D frameworks with triangular channels and hexagonal channels (Figure 5). The hexagonal channels have cross-section sizes of approximately 28.3 × 31.1 Å (oxygen to oxygen) after removal of guest molecules. CYCU-3 demonstrated a BET surface area of 2757 m^2 g^{-1}. Pore size distribution analysis from N_2 sorption data revealed 16.0 and 27.4 Å pores consistent with those observed in the structure.

2.2 Caged MesoMOFs

2.2.1 rht-MesoMOFs

The **rht** net is a singular prototypical MOFs platform assembly by 24-connected and 3-connected vertices without self-interpenetration upon net expansion and decoration. In 2008, Eddaoudi and coworkers employed the supermolecular building blocks (SBBs) approach to synthesize the first rht-MOF reacted by 5-tetrazolylisophthalic acid and copper salts.[17] Since then, a number of mesoMOFs with **rht** nets have been reported by extending the C_3-symmetric rigid organic ligands. The **rht** net can be represented using three types of polyhedra by drawing straight lines between adjacent copper paddlewheels. The three types of polyhedra are fused to each other to form continuous channels. As shown in Figure 6, the smallest cage (B) is cuboctahedral formed from 24 isophthalate groups and 12 copper paddlewheels. Cage B incorporates both triangular and square windows. The second cage (C) is a truncated tetrahedron formed by 12 copper paddlewheels and 4 organic ligands and each vertex sharing one

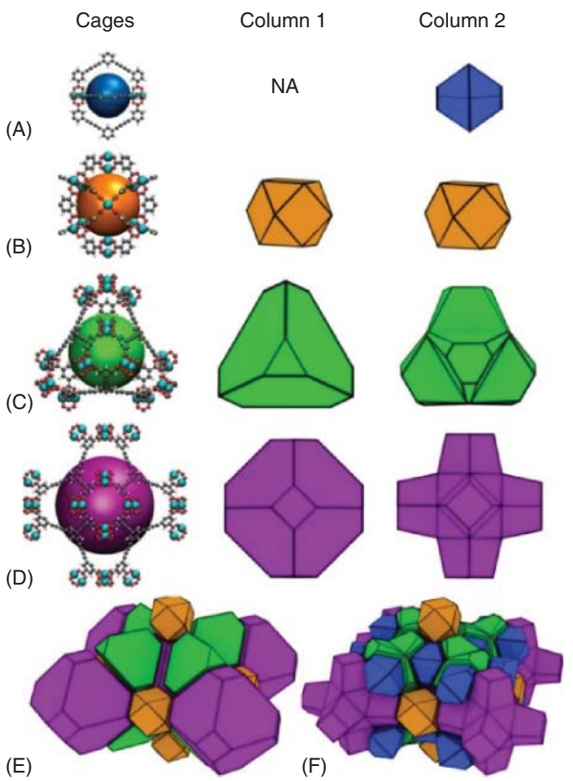


Figure 6 Illumination of the two approaches to simplify the rht-MOFs (Reproduced with permission from Ref. 19. Copyright (2012) American Chemical Society.)

triangle window with cage B. The largest cage (D) can be described as a truncated cuboctahedron formed by 24 copper paddlewheels and 8 organic ligands. The largest cage D can be mesoporous. For example, Schröder and coworkers reported that the cage D in NOTT-112 has a diameter up to 21 Å corresponding to the pore distribution analysis from Ar sorption data.[18] In 2012, Hupp and coworkers simplified the rht-MOFs into four fused cages by taking into account the curvature of the ligand as a linker between metal nodes (Figure 6). The existence of four cages was also proved by the pore size distributions analyzed from gas sorption data. [19]

2.2.2 *Zeolite-like MesoMOFs*

In 2008, Yaghi's group reported two novel zeolitic imidazolate frameworks (ZIFs), ZIF-95 and ZIF-100, synthesized from 5-chloro-benzimidazole and zinc salts.[20] ZIFs can mimic the widely studied SiO_2 zeolites because transition metals (Zn and Co) can replace the tetrahedral Si nodes and imidazolate can replace the oxygen linkers. ZIF-95 possesses a **poz** topology with four kinds of cages (A, B, C, and D). Among these cages, cages A and B have inner diameters of 25.1×14.3 Å and 30.1×20.0 Å, respectively. ZIF-100 exhibits a **moz** topology and consists of one unique cage of 35.6 Å inner diameter and 67.2 Å outer diameters. After activation, ZIF-95 and -100 exhibit Langmuir surface areas of 1240 and 780 $m^2\,g^{-1}$, respectively.

In 2004, a polyhedral-based MOFs, MIL-100, was reported by Ferey *et al.*[6] MIL-100 was synthesized from trimesic acid (H_3BTC), metallic Cr, HF in H_2O solution. Three Cr centers are linked by one μ_3-O and six carboxylates to form trimer building blocks, which are further connected by three BTC ligands to form SBBs with tetrahedron geometry (Figure 7 up). By treating these SBBs as 4-connected tetrahedral nodes, MIL-100 can be simplified into a zeolitic montmorillonite (**MTN**) net. There are two kinds of mesocages constructed by these SBBs via corner sharing mode. The small cage consists of 20 tetrahedron SBBs and has an internal diameter of ~25 Å. The larger cage is constructed by 28 tetrahedron SBBs and has an internal diameter of ~29 Å. It is noteworthy that although these cages are mesoporous, the cage windows are still within micro size range. In 2005, Ferey's group reported another mesoMOF, MIL-101,[7] synthesized from terephthalates (1,4-BDC), $Cr(NO_3)_3$ and fluorhydric acid in H_2O solution. Similar to MIL-100, the Cr trimer building blocks can construct tetrahedral SBBs, which can also build the **MTN** net (Figure 7 bottom). There are also two kinds of mesocages constructed by these SBBs via corner sharing mode. The small cage has an internal diameter of ~29 Å while the larger cage has an internal diameter of ~34 Å.

In 2007, Kim and coworkers reported a Tb-mesoMOF based on TATB ligands and Tb_4 moieties.[21] Similar to MIL-100, four Tb_4 moieties are linked by four TATB to form a tetrahedral SBB. These tetrahedral SBBs are further interconnected to form a 3D network with the **MTN** topology. There are two types of nanoscopic cages: (i) small cages that are of a 3.9-nm diameter surrounded by 20 SBBs and with 12 pentagonal windows; (ii) large cages that are of a 4.7-nm diameter defined by 28 SBBs and with 12 pentagonal and 4 hexagonal windows.

2.2.3 *Other Caged MesoMOFs*

The **tbo** net is another prototypical platform for MOFs. The most famous example is HKUST-1 synthesized from trimesic acid (H_3BTC) and copper salts. Yaghi and coworkers reported that using longer variants of BTC ligand such as 4,4′,4″-s-triazine-2,4,6-triyltribenzoate (TATB), 4,4′,4″-s-triazine-1,3,5-triyltriaminobenzenecarboxylic acid (H_3TATAB), 4,4′,4″-(1,3,4,6,7,9,9b-heptaazaphenalene-2,5,8-triyl)tribenzoate

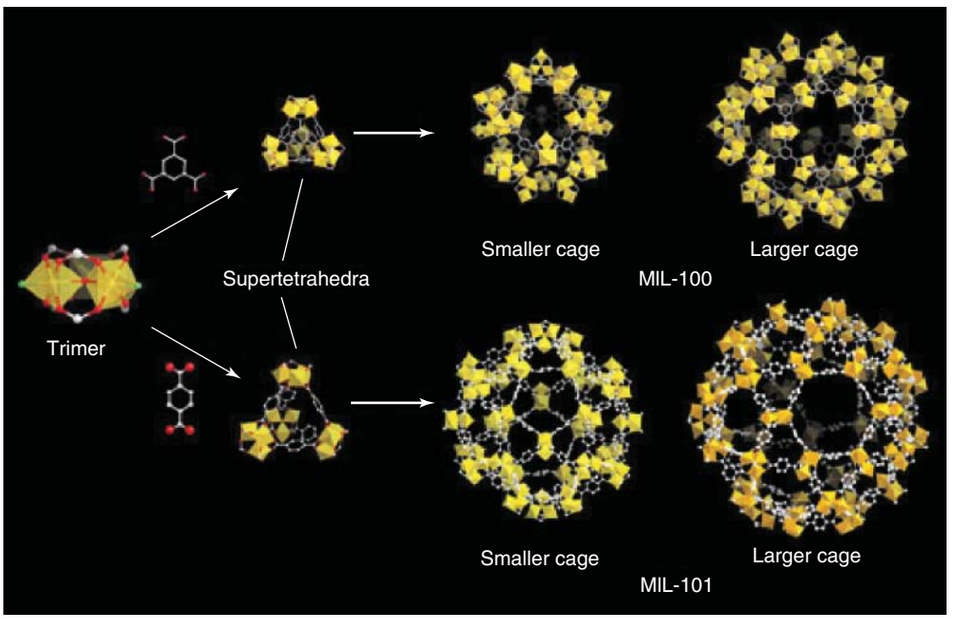


Figure 7 Illumination of the structures of cage-base MIL-100 and -101 (Reproduced with permission from Gérard Férey/University of Versailles' Lavoisier Institute. © Gérard Férey.)

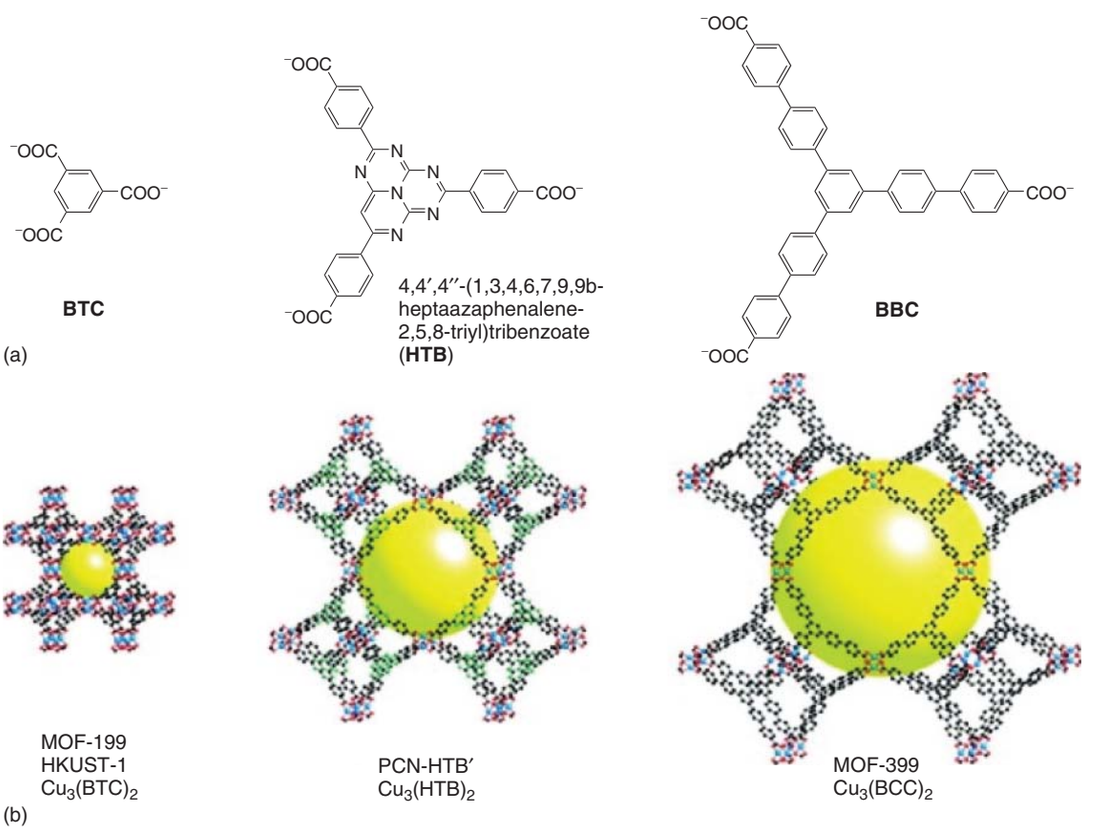


Figure 8 Molecular structures of organic linkers (a). Single crystal structures of HKUST-1, PCN-HTB′, and MOF-399 (b) (Reproduced with permission from Ref. 22. Copyright (2011) American Chemical Society.)

(HTB), and TATAB afforded tbo-MOFs with mesoporous cavities or channels (Figure 8).[22] In 2006, Zhou and coworkers reported mesoMOF-1 synthesized from H_3TATAB and $Cu(NO_3)_2$ in DMF.[23] MesoMOF-1 exhibits the protypical **tbo** net, which can be simplified into three polyhedral cages: small tetrahedral cage, middle octahemioctahedral cage, and largest rhombihexahedral cage. In mesoMOF-1, the large rhombihexahedral cage possess a diameter around 32 Å between the farthest copper paddlewheels. Normally, the long tricarboxylate ligands will prefer to form interpenetrating **tbo** nets. However, mesoMOF-1 is non-interpenetrating with large channels of 22.5 × 26.1 Å along all orthogonal directions. MesoMOF-1 exhibits the typical type IV N_2 sorption isotherm and demonstrated an interesting behavior of post-synthetic reaction with HX (X = F, Cl, Br) to enhance structure stability (300 °C compared with the pristine network 180 °C).

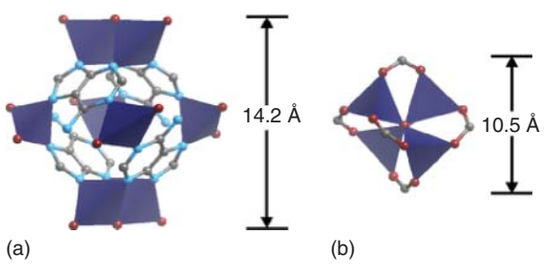


Figure 9 Structure and size of the zinc-adeninate building unit (ZABU) (a) compared with the structure and size of the basic zinc-carboxylate building unit (b) (Reproduced with permission from Macmillan Publishers Ltd: Nature Communications (Ref. 10), copyright (2012).)

3 STRATEGIES FOR THE DESIGN AND SYNTHESIS OF MESOMOFS

Currently, mesoMOFs are mainly synthesized by solvothermal method. Microwave-assisted strategy has also been reported for the fast synthesis of mesoMOFs.[24] Although this approach is not often used, it provides an opportunity for high speed MOFs synthesis with possible size and morphology control. In addition, three different strategies have been reported for the design of mesoMOFs: (i) synthesis of mesoMOFs by extended ligands and bulky SBUs; (ii) template-directed synthesis hierarchical mesoMOFs; and (iii) template-free synthesis hierarchical mesoMOFs.

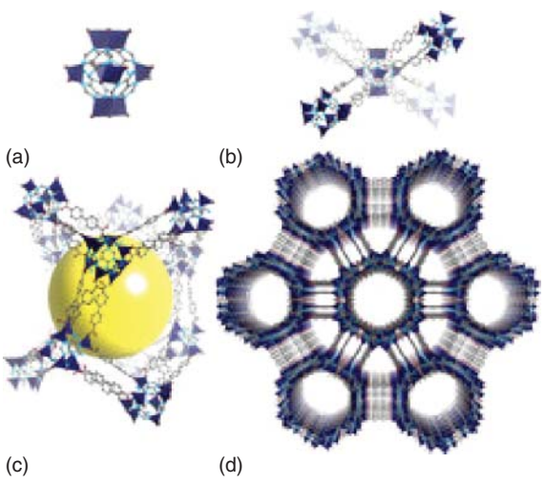


Figure 10 (a)–(d) Crystal structure of bio-MOF-100 (Reproduced with permission from Macmillan Publishers Ltd: Nature Communications (Ref. 10), copyright (2012).)

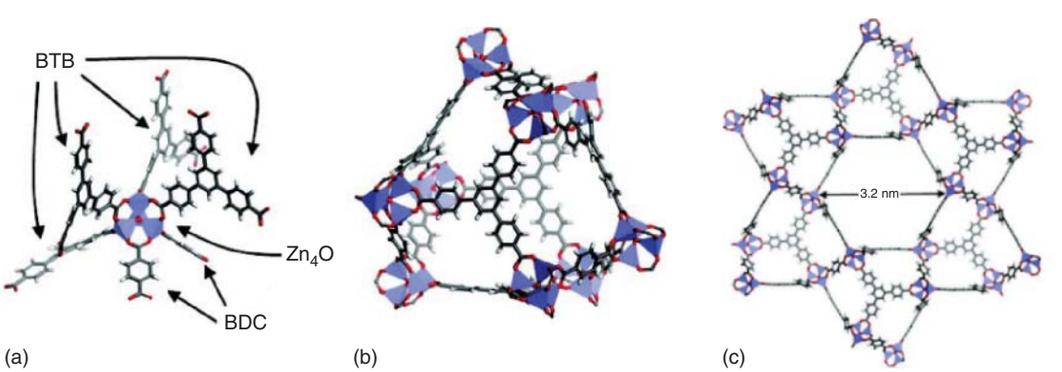


Figure 11 Structure of UMCM-1: (a) A Zn_4O cluster coordinated to two BDC linkers and four BTB linkers. Zn_4O clusters blue tetrahedra, C gray, H white, O red. (b) A microporous cage constructed of six BDC linkers, five BTB linkers, and nine Zn_4O clusters. (c) Structure of UMCM-1 viewed along the c axis illustrating the one-dimensional mesopore (Reproduced with permission from Ref 28. © Wiley-VCH Verlag GmbH & Co. KGaA, Weinheim, 2008.)

3.1 Synthesis of MesoMOFs by Extended Ligands and SBUs

In order to greatly broaden the utility of MOFs, extensive efforts have been devoted to the investigation of the strategies to enlarge the pore size of MOFs. One obvious approach is to use extended ligands or bulky secondary building blocks (SBUs) for the construction of mesoMOFs. This has been exemplified by the work of Yaghi's group in 2012.[14] They synthesized a series of isoreticular structures (IRMOF-74-1 to XI) of MOF-74 by extending the original MOF-74 linker from 1 phenylene ring to up to 11 rings (Figure 4). With the extended linkers, the pore apertures of these nine IRMOFs have been enlarged ranging from 14 to 98 Å. The extended ligand strategy usually requires multi-steps organic synthesis, and could be limited by the low stability or the interpenetration of the framework. Several strategies have been investigated for the control over interpenetration, such as utilization of oxalate as template,[25] temperature and concentration control,[26] liquid phase epitaxy,[27] and using sterically bulky groups or SBUs (see ***Interpenetration and Entanglement in Coordination Polymers***).[13]

One example for the bulky SBU strategy was reported by Rosi's and coworkers.[10] They synthesized a mesoMOF, Bio-MOF-100, by replacing the small 6-connected $[Zn_4O(COO)_6]$ octahedral building blocks with bulky zinc-adeninate 6-connected octahedral SBUs. Bio-MOF-100 with the lcs nets exhibits a high surface area of 4300 $m^2\ g^{-1}$, low crystal densities of 0.302 $g\ cm^{-1}$ and large pore volume of 4.3 $cm^3\ g^{-1}$ (Figures 9 and 10).

Mixed ligand strategy has also been reported to synthesis mesoporous MOFs. UMCM-1 reported by Matzger's group is based on two organic linkers, H_2BDC and 1,3,5-tris(4-carboxyphenyl)benzene (H_3BTB) (Figure 11).[28] Constituted by 1:1.33 ratio of 1,4-BDC:BTB, UMCM-1 features a hierarchical structure with both micro- and meso-pores. In UMCM-1, six 1,4-BDC and five BTB linkers are connected by nine $[Zn_4O(COO)_5]$ to form a microporous cage of 14 × 17 Å. Six such cages are connected to form a hexagonal meso-channel of 24 × 29 Å. UMCM-1 exhibits the typical type IV N_2 sorption isotherm and demonstrates a high Langmuir surface area of 6500 $m^2\ g^{-1}$.

Rosi and coworkers reported a stepwise ligand exchange strategy to prepare a series of reticular bio-MOF-100 analogs, among which Bio-MOF-102 and Bio-MOF-103 are mesoMOFs.[29] The exchange of ligands with longer dicarboxylate linkers was performed on single crystalline starting materials to synthesize mesoMOFs with larger cavities. Bio-MOFs-102 and -103 exhibit permanent mesoporosity with pore sizes of 2.6 and 2.9 nm and BET surface areas of 3222 and 2704 $m^2\ g^{-1}$, respectively (Figure 12).

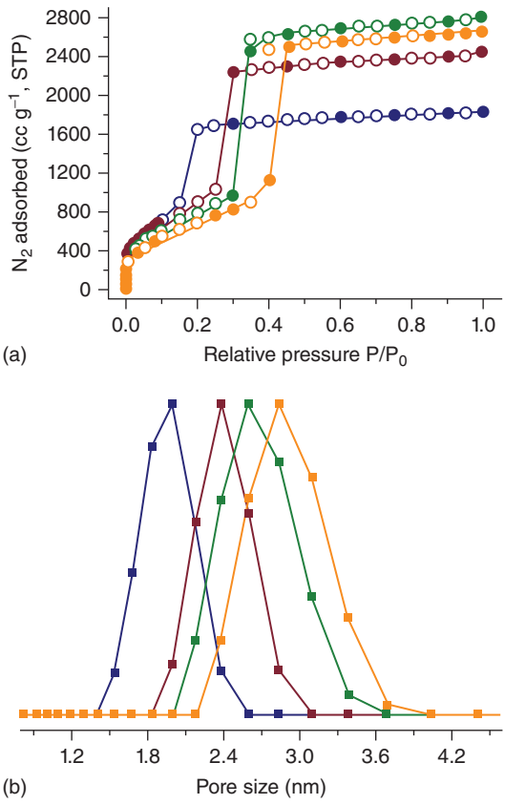
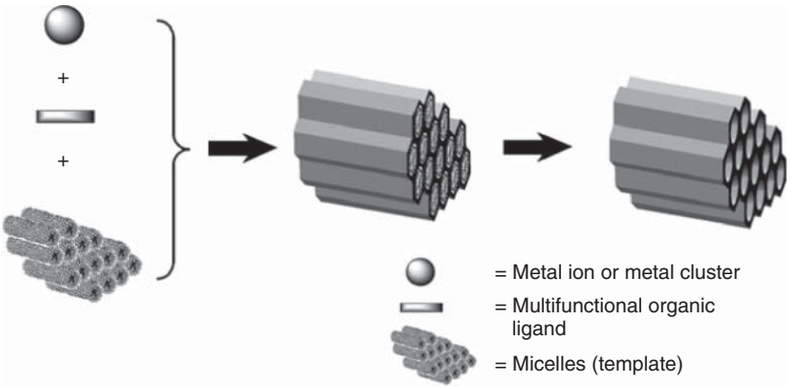


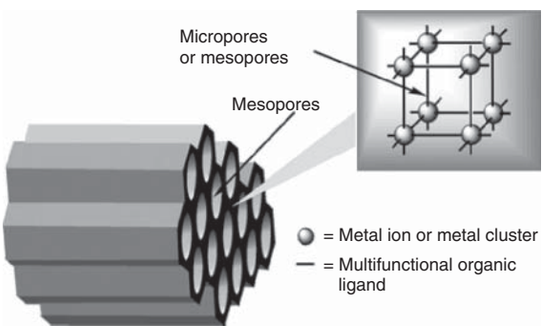
Figure 12 (a) N_2 adsorption isotherms of bio-MOF-101 (navy), bio-MOF-100 (red), bio-MOF-102 (green), bio-MOF-103 (orange) at 77 K. (b) Normalized pore size distribution (PSD) of bio-MOF-101 (navy), bio-MOF-100 (red), bio-MOF-102 (green), bio-MOF-103 (orange) calculated by quenched solid state functional theory (QSDFT) method (Reproduced with permission from Ref. 29. Copyright (2013) American Chemical Society.)

3.2 Template-Directed Synthesis of Hierarchical MesoMOFs

Another widely employed strategy to synthesize mesoMOFs is template-directed synthesis, which has long been used for efficient synthesis of mesoporous silica. In terms of this strategy, the structure-directing agent such as surfactants, block copolymers, and swelling agents, is used as the template to facilitate the formation of mesopores. The surfactant molecules first assemble into micelles and then serve as the template to direct the formation of porosity of the frameworks during the synthetic process. The porosity can be influenced and adjusted by synthetic conditions such as reactant concentration, pH, temperature, and the nature of surfactant. Usually, the as-synthesized MOFs are characteristic of hierarchical structures with both micro- and mesoporosity. In order to create permanent porosity, the template must be removed after synthesis.



Scheme 1 Mesostructured MOFs self-assembled from metal ions and multifunctional organic ligands in the presence of surfactant micelles as supramolecular templates (Reproduced with permission from Ref. 30. © Wiley-VCH Verlag GmbH & Co. KGaA, Weinheim, 2008.)



Scheme 2 Mesostructured MOFs in which mesopore walls are constructed from micro- or mesoporous MOFs assembled from metal ions and multifunctional organic ligands (Reproduced with permission from Ref. 30. © Wiley-VCH Verlag GmbH & Co. KGaA, Weinheim, 2008.)

The proper strategies for porosity activation are crucial for the retaining of mesoporosity and the prevention of collapse upon removal of guest molecules. Unfortunately, the template-directed strategy often suffers from the disintegration of the framework upon removal of the template molecules that are encapsulated in the crystal lattice.

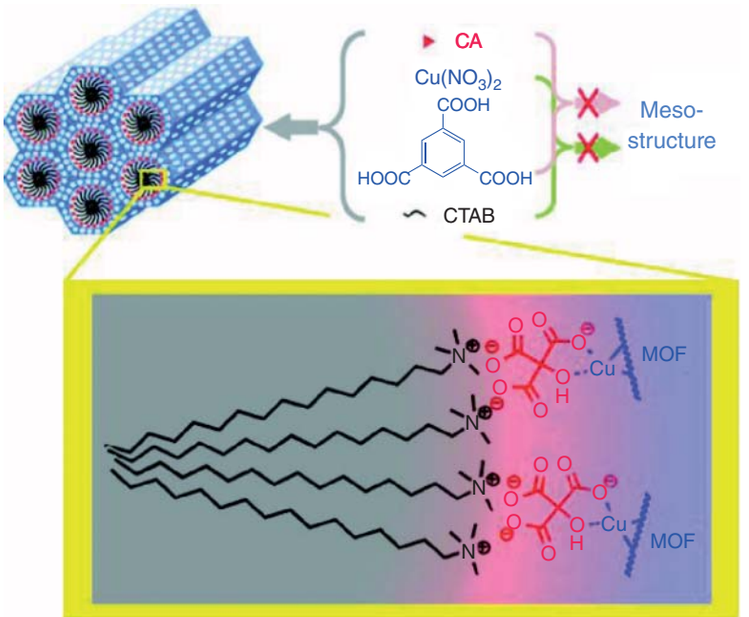
In 2008, Qiu *et al.*[30] first applied supramolecular template strategy for the design and construction of mesoMOFs using cetyltrimethylammonium bromide (CTAB) as the template and Cu^{2+} and 1,3,5-tricarboxylic acid (H_3BTC) as the building blocks (Scheme 1). The as-synthesized MOF exhibits hierarchical structure with adjustable interconnecting micropores and mesopores (Scheme 2). To further enlarge the size of the mesopores, H_3BTC was used as an auxiliary structure-directing agent to swell the surfactant micelles.

In 2012, Zhou's group reported a cooperative template system consist of CTAB as the template and citric acid (CA) as the chelating agent for the synthesis of a MOF with hierarchical structure.[31] In this system, CA acts as the chelating agent to bridge the template CTAB and the building blocks, Cu^{2+} and H_3BTC, during the formation of the MOF in which the walls of the mesopore are constructed by the surrounded micropores (Scheme 3).

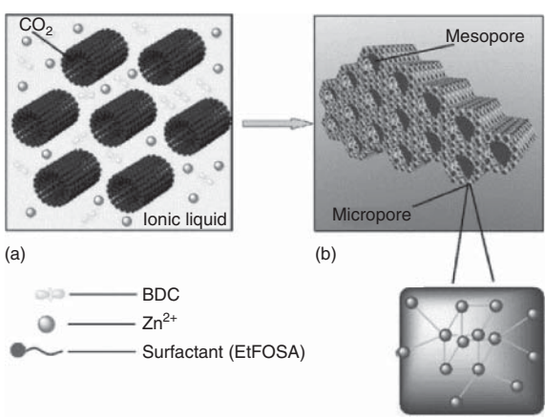
Super critical CO_2 and ionic liquid can also assist with the surfactant template to facilitate the formation of mesoMOFs. N-EtFOSA/IL/$SCCO_2$ (N-ethyl perfluorooctylsulfonamide, N-EtFOSA; ionic liquid, IL; supercritical CO_2, $SCCO_2$) system was reported by Zhao *et al.*[32] to synthesis mesoMOFs with long-range ordered mesopores. First, the surfactant (N-EtFOSA) assembles itself into micelles with the CO_2 molecules inside the core. The building blocks (Zn^{2+} ions and BDC) in the IL form a crystalline microporous framework and generate the microcavities in the micelles. Finally, after removal of the IL, CO_2, and the surfactant, the MOFs with both micro- and mesoporosity are constructed (Scheme 4).

3.3 Template-Free Synthesis of Hierarchical MesoMOFs

Very recently, Dai and coworkers reported a template-free synthesis of hierarchical mesoMOFs of Zn-MOF-74 of mesopores exceeding 15 nm by fast reaction of Zn salts and H_2-DHBDC at room temperature.[33] The surface morphology and porosity of the bimodal materials can be modified by etching the pore walls with various synthesis solvents for different reaction times. This template-free strategy broadens the preparation strategies of mesoMOFs, which was previously unattainable in the synthesis of mesoMOFs.



Scheme 3 Cooperative template-directed synthesis of MesoMOFs via self-assembly of metal ions and organic ligands (Reprinted with permission from Ref. 31. Copyright (2012) American Chemical Society.)



Scheme 4 Formation of the MOFs in the surfactant/ionic liquid/supercritical CO_2 system. (a) Formation of N-ethyl perfluorooctylsulfonamide (N-EtFOSA) cylindrical micelles and (b) MOFs with ordered mesopores and microporous structured walls (Reproduced with permission from Ref. 32. © Wiley-VCH Verlag GmbH & Co. KGaA, Weinheim, 2011.)

4 APPLICATIONS OF MESOPOROUS MOFs

4.1 Gas Sorption and Separation

As mesoMOFs possess the highest porosity (BET surface areas over 7000 $m^2\ g^{-1}$) among all porous materials, they are the promising candidates for gas (H_2, CH_4, and CO_2) storage especially under high pressure. Owing to the relative large pore sizes, most of the mesoMOFs (such as channeled mesoMOFs) are not favorable for gas separation application. However, some of the caged mesoMOFs are used for gas separation because their narrow windows can serve as the filter to separate gases of different sizes.

4.1.1 H_2 Storage

Hydrogen (H_2) is an environment friendly energy carrier and clean fuel. H_2 storage is significantly important for the development and viability of H_2-powered vehicles. The traditional H_2 storage approaches involve compressed H_2 gas tanks, liquid H_2 tank and cryogenic compressed H_2 and metal hydride. High-surface-area adsorbents for H_2 storage have attracted great attention recently. As mesoMOFs have the highest surface areas among all porous materials, mesoMOFs possess great advantage for H_2 storage under high pressure (see ***Gas Storage in Metal-Organic Frameworks***). The US Department of Energy (DOE) set the target of 5.5 wt% H_2 and 0.040 kg $H_2\ L^{-1}$ in 2015 and the ultimate targets of 7.5 wt% H_2 and 0.070 kg $H_2\ L^{-1}$. Actually, some mesoMOFs have already reached the DOE target numbers for H_2 storage despite low temperatures.

In 2010, Kaskel's group reported an Ni-based MOF, DUT-9, which has a high concentration of open nickel sites in $[NiO_2(btb)_2]$ clusters and high porosity.[34] The DUT-9 shows a maximum H_2 excess uptake of

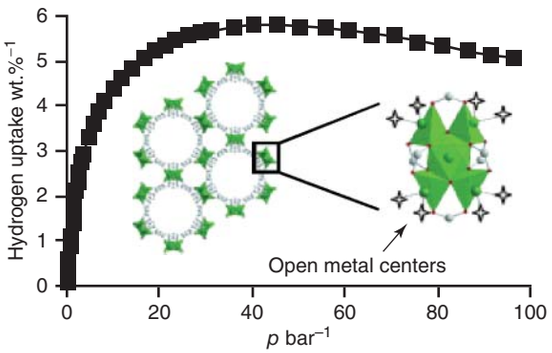


Figure 13 H_2 high-pressure excess adsorption isotherms at 77 K of DUT-9 (Reproduced with permission from Ref. 34. © Wiley-VCH Verlag GmbH & Co. KGaA, Weinheim, 2010.)

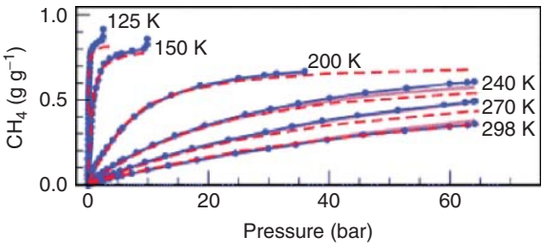


Figure 14 Total gravimetric gas uptake isotherms at various temperatures for CH_4 for NU-111 (Reproduced from Ref. 39 with permission from The Royal Society of Chemistry.)

5.85 wt% (52 mg g^{-1}) at 40 bar and 77 K by supercritical CO_2 drying (Figure 13).

In 2006, Férey and coworkers showed that MIL-101b(Cr) could adsorb 6.1 wt% H_2 at 8 MPa and 77 K, which can be ascribed to the high adsorption enthalpy (~10 kJ mol^{-1} at low uptake region) caused by open Cr sites.[35]

In 2010, Yaghi and coworkers reported a series of mesoMOFs based on the $[Zn_4O(COO)_6]$ building block.[36] Among these mesoMOFs, MOF-210 has high excess H_2 uptake of 86 mg g^{-1}, which is higher than the other $[Zn_4O(COO)_6]$ based MOFs such as MOF-5 and MOF-177.

The (3.24)-paddlewheel connected **rht** network is one well-studied MOFs platform. By extending the organic ligands, a number of rht-mesoMOFs have been reported. As the polyhedral based network and high concentration of open Cu sites can both benefit the H_2 uptake, rht-MOFs are excellent candidates for H_2 storage especially at high pressure and low temperature. In 2009, Schröder and coworkers reported NOTT-112 with **rth** net that exhibits high excess H_2 uptake, a maximum of 7.07 wt% between 35 and 40 bar. In 2010, Hupp's group reported another rht-mesoMOF, NU-100, which is a benchmark compound for H_2 storage with 99.5 mg g^{-1} at 56 bar. An isosteric heat of adsorption of ~6.1 kJ mol in low pressure uptake region was revealed by variable-temperature measurements, presumably because of the availability of open Cu sites in NU-100.[37]

4.1.2 CH_4 Storage

To replace the traditional fuels such as fossil and petrol (gasoline), clean fuels such as natural gases especially methane (CH_4) attract great attention because of both economic and environment considerations. There are two common methods for natural gas storage: (i) liquefaction at low temperature and (ii) compression to high pressure e.g., 200–300 bar at room temperature. Recently, the DOE has initiated a new CH_4 storage program with the following target: 0.5 g(CH_4) g^{-1}(sorbent) for gravimetric capacity and 263 cc (STP: 273.15 K, 1 atm)/cc. MesoMOFs have great potential for high-density CH_4 storage via physisorption. In 2010, Yaghi and coworkers reported three mesoMOFs, MOF-200, -205, and -210 with excess CH_4 uptake of 234, 258, and 264 m g^{-1} at 80 bar, which are among the highest values in MOFs. The calculated total uptakes are high (446, 394, and 476 mg g^{-1} for MOF-200, -205, and -210, respectively) because of the low density of activated samples.[36]

In 2013, Yildirim and coworkers tested the CH_4 uptake properties for a series of MOFs.[38] They found that the mesoMOF with high surface areas and pore volumes have good performance. For example, the rth-mesoMOF, NU-111, possesses a high surface are of 4932 m^2 g^{-1} and high pore volume of 2.09 cc g^{-1}. NU-111 exhibits equally high volumetric and gravimetric CH_4 uptake, both within around 75% of the new DOE targets at 300 K. The total gravimetric uptake of NU-111 reaches 0.35 g g^{-1} (205 cc cc^{-1}) representing the highest gravimetric CH_4 uptake recorded so far for a MOF (Figure 14).[39]

4.1.3 CO_2 Storage

The emission of greenhouse gases such as carbon dioxide (CO_2) and CH_4 is one of the major reasons for global warming. MOFs can serve as ideal platforms for CO_2 capture owing to their large surface area, pore volume, and the structural and chemical tunability. Owing to the high surface areas and large pore volumes, mesoMOFs demonstrate excellent performance for CO_2 storage at high pressure. Hupp and coworkers reported the rht-mesoMOF, NU-100 possessing very high CO_2 uptake of 2315 mg g^{-1} at 298 K and 40 bar. Yaghi and coworkers reported that MOF-210 demonstrated unprecedented CO_2 uptake of 2400 mg g^{-1} at 298 K and 60 bar.[37]

Chen and coworkers reported to incorporate a series of polyethyleneimine (PEI) into MIL-101 with different PEI loading.[40] The amine groups in PEI were

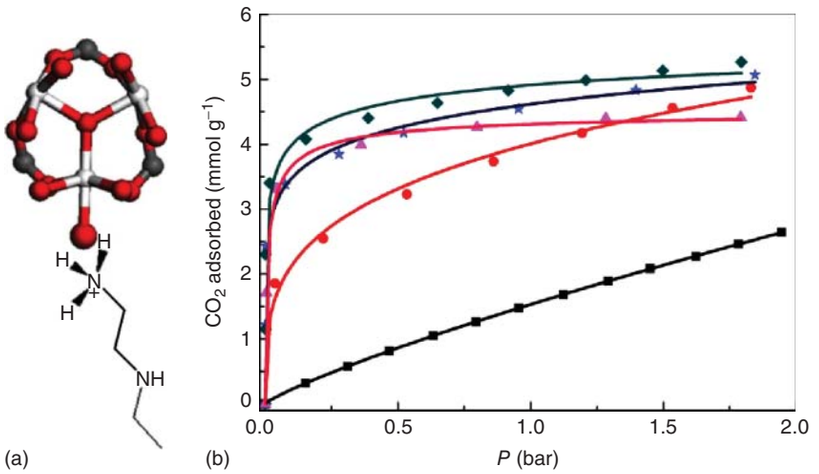


Figure 15 (a) PEI interact with Cr building blocks in MIL-101. (b) The CO_2 adsorption isotherms of the MIL-101 before and after loading PEI at 25 °C. Symbol: ■ MIL-101, ● PEI-MIL-101-50, ★ PEI-MIL-101-75, ◆ PEI-MIL-101-100, ▲ PEI-MIL-101-125 (Reprinted by permission from Macmillan Publishers Ltd: Scientific Reports (Ref. 40), copyright (2013).)

supposed to coordinate with the Cr centers in MIL-101. Although the surface areas and pore volumes of PEI-MIL-101 decreased, all the PEI-MIL-101 compounds exhibited dramatically enhanced CO_2 sorption (Figure 15). At 100 wt% PEI loading, the CO_2 adsorption capacity at 0.15 bar reached a very competitive value of 4.2 mmol g^{-1} at 25 °C, and, 3.4 mmol g^{-1} at 50 °C.

4.1.4 Gas Separation

Lots of works reported that ZIFs have a high affinity to CO_2 because of the large amount of nitrogen atoms. ZIF-98 and -100 possess mesosized cages but with very narrow pore windows of 3.65 and 3.35 Å, respectively. These aperture sizes are smaller than the kinetic diameter of CH_4 (3.8) and N_2 (3.64) but larger than the kinetic diameter of CO_2 (3.3 Å). So ZIF-98 and -100 show high affinity to CO_2 uptake but not N_2 and CH_4. The breakthrough experiments indicated that ZIF-95 and -100 possessed high selectivity for CO_2 versus CH_4, CO_2 versus CO, and CO_2 versus N_2 (50:50 v/v) of 4.3:1, 11.4:1, and 18.0:1, respectively for ZIF-95, and 5.9:1, 17.3:1, and 25:1, respectively, for ZIF-100.[20]

4.2 Heterogeneous Catalysis

The early heterogeneous catalysis study was simply based on metal powders, while highly dispersed catalytically active components with high-surface solid supports has quickly become the main stream. Compared to homogeneous system, heterogeneous catalysis possesses a number of beneficial features. One of the primary aims of applying a catalytically active component to a support is that the catalyst can be effectively recovered in straightforward manners, such as filtration, and such easy recovery and recycling is of paramount importance for large-scale industrial and commercial manufacturing process. Moreover, the support improves the dispersion of the catalyst and thus allows a more effective utilization of the catalytically active component. These features are of special importance with regard to expensive catalysts, such as enzymes and precious-metals. The facile separation of catalyst can minimize or eliminate catalyst contamination and thereby lead to a higher purity of the product, which will significantly reduce the cost of purification process. In addition, the solid support can often protect and stabilize the catalytically active components under storage and operational conditions, which can be achieved by suitable interactions between the active component and the support. In this context, heterogeneous catalysis is the trend for the industrial and commercial application of the catalyst.

Despite these advantages, there are several barriers to be overcome for heterogeneous catalysts. Generally, the diffusion of the reactant to the catalyst surface can often be the rate-limiting step in heterogeneous catalysis. The available surface area of the heterogeneous catalyst will potentially limit the number of available reaction sites, which will also affect the reaction rate. Therefore, materials with high porosity, large surface area, tunable pore size, and accessible structure are highly desirable for the construction of a proper microenvironment to increase the efficiency of heterogeneous catalysis. Porous materials with a broad range of pore sizes have been widely investigated as solid supports for heterogeneous catalysis,[41] such as microporous zeolite,

Table 2 Catalog of known catalytic mesoporous MOFs and summary of reactions catalyzed

mesoMOF	Substrate(s)	Reaction(s)	Reference
MIL-101	Benzaldehyde and ethyl cyanoacetate	Knoevenagel condensation	42
	Tetralin	Oxidation	43
	Alkenes	Oxidation	44
	Cyclohexane	Oxidation	45
	Epoxides and CO_2	Coupling reaction	46
MIL-101 Supported Polyoxometalates	Alkene and alcohol	Oxidation and epoxidation	47
	α-pinene	Oxidation	48
Pd/MIL-101	2-Haloanilines	Cycloaddition	49
	Indoles	C_2 Arylation	50
Pd/MIL-101(Cr)–NH_2	p-Chloropheno and aryl chlorides	Dehalogenation	51
Ni@MesMOF-1	Styrene or nitrobenzene	Reduction	52
PCN-100 and PCN-101	Benzaldehyde and 4-phenylbenzaldehyde	Knoevenagel condensation	53
CMOFs	Aldehydes	Asymmetric addition	54
MMPF-6(PCN222)	1,2,3-Trihydroxybenzene (THB) and ABTS	Oxidation	55 and 56
MP-11@Tb-mesoMOF	3,5-*di*-*tert*-butyl catechol	Oxidation	57
Mb@Tb-mesoMOF	THB and ABTS	Oxidation	58

THB, 1,2,3-trihydroxybenzene.

mesoporous metal oxide and silica, and macroporous polymers. MOFs possess some extraordinary properties that are perfectly appropriate for catalysis application, such as high surface area and porosity, structural versatility, and tunable pore size. Compared to microporous MOFs, the use of mesoporous MOFs as solid catalysts or the support is significantly interesting because their large pore sizes are favorable for the loading of large catalytically active components and the diffusion of substrates and products. Moreover, mesoMOFs can be tailored to create the proper environment around the catalytic active site, which provides the opportunity for chemo-, regio-, stereo- and/or enantioselectivity that cannot be expected from microporous MOFs. Table 2 shows the representative catalysis based on different catalogs of mesoMOFs.

The understanding of catalyst design and the insight into general parameters determining the catalytic activity, reactivity, and selectivity of a catalytic reaction has become the trend of the studies on heterogeneous catalysis. The rational design of heterogeneous catalyst should consider the essential attributes of activity, stability, selectivity, and recyclability. In terms of catalyst design, mesoMOFs provide an excellent platform for studying chemistry and physics of a catalytic process in a confined space. As the determination of crystal structures of MOFs is more accessible than other porous materials, the pore environments in mesoMOFs are much clearer than ever before. As shape, size, and chemical environments of the cages or channels of MOFs are well defined, it is possible to investigate and control their morphology, composition, size, and shape of catalytically active particles and the catalyst support, and even the interaction between the catalyst and the support. This will give rise to the improvements in catalytic performance and understanding of the basis of heterogeneous catalyst design.

However, although many remarkable and exciting developments have been achieved on MOFs-based catalysis over the past 20 years, heterogeneous catalysis based on mesoMOFs is still in an immature phase and much more territory remains to be explored.

Heterogeneous catalysis that represents one of the earliest applications proposed for MOFs[59] was demonstrated around 20 years ago.[60] However, along with the construction of the substantial foundation of the synthetic chemistry of MOFs, it is only recently that the catalytic studies of MOFs have been dramatically and extensively developed.

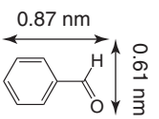
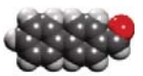
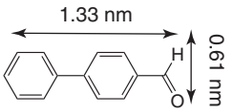
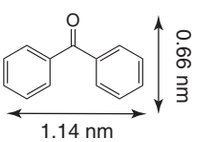
Generally, mesoporous MOFs can serve as the heterogeneous catalyst containing metal active sites or reactive functional groups, while they can also be utilized as the host matrices for the loading of guest active species or as nanoscopic reactors.

4.2.1 MesoMOFs as the Heterogeneous Catalyst

To design a mesoMOFs-based heterogeneous catalyst, several strategies can be used: (i) metal building blocks in mesoMOFs possess open metal sites as catalytic sites; (ii) mesoMOFs can be synthesized using ligands with reactive functional groups; and (iii) catalytic species can be grafted to mesoMOFs by PSM.

Zhou's group synthesized two isostructural mesoMOFs, PCN-100 and PCN-101 and demonstrated their size selective catalytic activity for Knoevenagel reaction of Butyl Cyanoacetate.[53] The two structures were constructed using $[Zn_4O(COO)_6]$ as SBUs and two extended ligands containing weakly basic amine groups, which are preferred by the catalysis of Knoevenagel reaction. PCN-100 and PCN-101 exhibit interesting size- and shape- selectivity towards substrates (Table 3).

Table 3 Knoevenagel condensation reaction of butyl cyanoacetate with substrates catalyzed by PCN-100 and -101 (Reprinted with permission from Ref. 53. Copyright (2010) American Chemical Society.)

Run	Substrate	Molecular size	Catalyst	Conversion (%)
a			PCN-100	93
			PCN-101	96
b			PCN-100	58
			PCN-101	65
c			PCN-100	0
			PCN-101	0

Although the heterogenization of chiral catalysis based on porous MOFs has been extensively studied by several groups,[61–63] only a few cases of chiral mesoMOFs catalysis have been reported. However, homochiral mesoMOFs exhibit impressive catalytic performance towards asymmetric and enantioselective catalysis.

In 2008, based on the robust *R*-BINOL-based tetracarboxylate ligand, Lin and coworkers designed two isostructural mesoMOFs, *R*-$[Cu_2L_{2a}(H_2O)_2]\cdot 12DEF\cdot 16H_2O$ and *R*-$[Cu_2L_{2a}(H_2O)_2]\cdot 16DMF\cdot 19H_2O$, which became the first example of chiral mesoMOFs.[64] Later on, based on these 4.4-connected networks, Lin and coworkers systematically designed a series of isoreticular chiral mesoMOFs with different channel sizes (CMOFs-2a–4b) (Figure 16).[54] After functionalization with $Ti(OiPr)_4$, the compounds exhibited excellent activities towards asymmetric addition of alkylzinc to aldehydes. In addition, by tuning the channel sizes of the chiral mesoMOFs, the enantioselectivities of these reactions can be adjusted.

Among catalytic mesoMOFs reported thus far, MIL-101 family has been mostly investigated. Crystallographically, MIL-101 possesses a rigid zeotype (MTN type) structure, consisting of two different quasi-spherical cages (2.9 and 3.4 nm), which are accessible through windows of about 1.2 and 1.6 nm (Figure 7).[7] With high surface area, high pore volumes, and good solvent/thermal stability (Cr-MIL-101 up to 300 °C), the MIL-101 family can serve as an excellent heterogeneous catalyst or solid support for various reactions, such as dehydrogenation, oxidation, and arylation.

In 2008, Férey and coworkers proposed an efficient strategy for the selective functionalization of the coordinatively unsaturated metal sites (CUS) in MIL-101, which opened the door for the catalytic studies of MIL-101 family.[42] The interior of MIL-101 was modified by chelated chromium (III) CUS with electron-rich functional groups (Figure 17). Using the grafting agents ED and DETA, they grafted thermally stable amine species in the surface to form the amine-grafted MIL-101, which demonstrated high catalytic activities in the Knoevenagel condensation model reaction.

Kim *et al.*[43] reported the selective oxidation of tetralin catalyzed by MIL-101 under various conditions. The influence of different factors was also investigated, such as a different oxidant, solvents, the substrate/oxidant ratio, and the amount of catalysts.

4.2.2 MesoMOFs as Solid Supports

Park *et al.*[52] embedded nickel nanoparticles into MesMOF-1 by a two-step strategy. The nickelocene was firstly sublimated into the evacuated MesMOF-1 at 85 °C for 1–3 hours, and then treated with H_2 at 95 °C for 5 hours (Figure 18). Three samples (1a,1b, and 1c) were obtained during different loading times (1, 2, and 3 hours), and the TGA analysis revealed enhanced encapsulation of metal nanoparticle along the increasing loading time. The as synthesized Ni@MesMOF-1 exhibit catalytic activity for the hydrogenolysis of nitrobenzene or hydrogenation of styrene.

MIL-101 can be utilized for selective catalysis either as the heterogeneous catalyst or the solid support. Kholdeeva's group investigated a series of MIL-101 supported polyoxometalate-based heterogeneous catalyst for selective liquid phase oxidation.[47]

Li *et al.*[49] and Huang *et al.*[50] both encapsulated palladium nanoparticles into the mesoporous cages of MIL-101 through the wetness impregnation method and

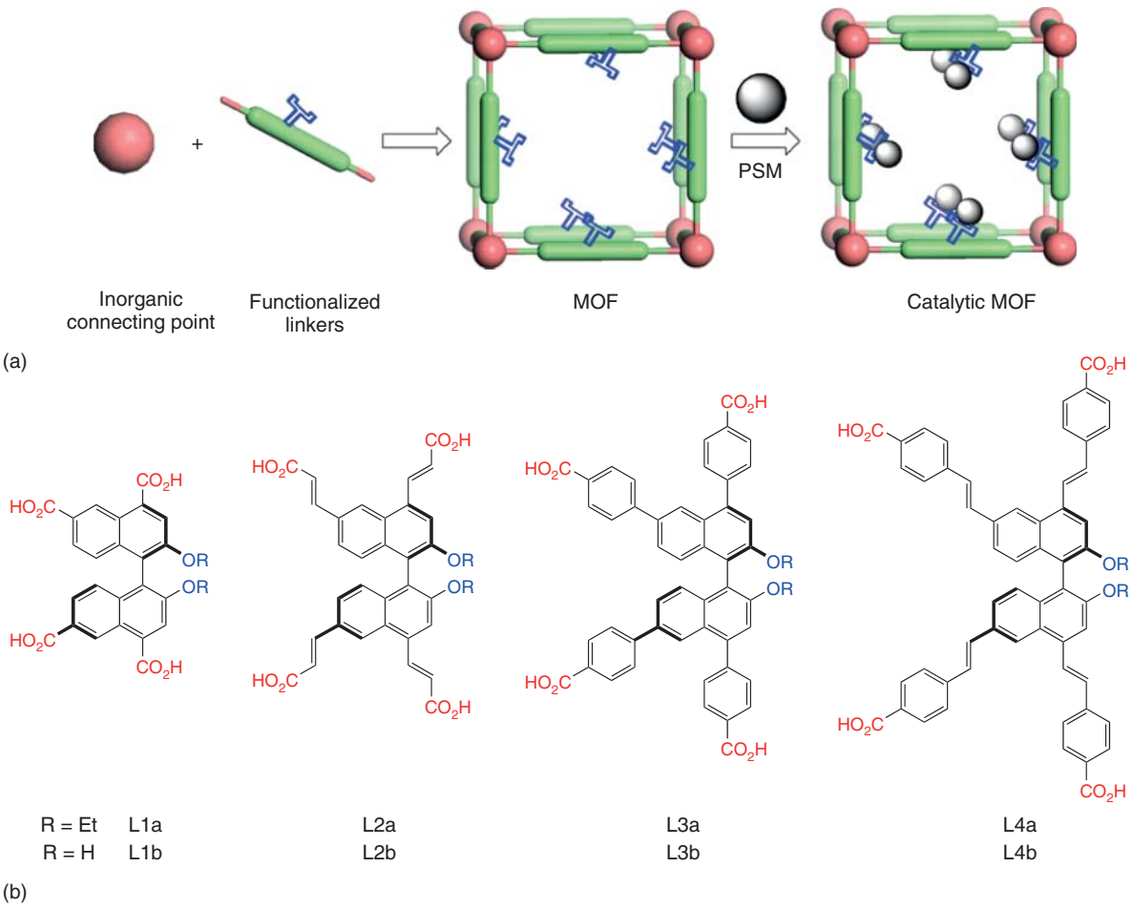


Figure 16 Schematic representation of a homochiral MOF and its postsynthetic modification (PSM) to give a catalytically active MOF. (a) The assembly of CMOFs and their PSM to give heterogenized asymmetric catalysts. (b) The chemical structures of the ligands used for this study. The L1a–L4a and L1b–L4b notations are used to described both the protonated (as in free ligands) and deprotonated forms (as in CMOFs) of (R)-tetracarboxylic acids. R = Et for CMOF-1a to -4a and R = H for CMOF-1b to -4b. The primary carboxylic acid groups highlighted in red are used to form CMOFs, whereas the secondary dihydroxy groups highlighted in blue react with $Ti(OiPr)_4$ on the PSM to form asymmetric catalysts (Reprinted by permission from Macmillan Publishers Ltd: Nature Chemistry (Ref. 54), copyright (2010).)

investigated their heterogeneous catalytic performance (Scheme 5). After their encapsulation into MIL-101 nanoscopic cages, the palladium nanoparticles exhibit superior catalytic activities and reusability towards both the domino synthesis of indole and the direct C_2 arylation of substituted indoles, which is probably due to the enhancement of surface hydrophobicity and the Lewis acid sites in the MIL-101 cages.

4.2.3 Biocatalysis

Because of the connection with reduced energy consumption, waste generation, and greenhouse gas emissions, biocatalysis has currently attracted a broad and increasing interest in areas as diverse as chemical, pharmaceutical, food, and energy production.[65] Biocatalysis not only possesses features such as high efficiency, high stereo-, chemo-, and regioselectivity, but is also environmental friendly.[66] However, the high cost, highly restricted reaction conditions, and the fragile nature of free enzymes handicaps their industrial applications. One of the biggest challenges in the industrial development of biocatalysis is to enhance the enzyme stability in organic solvents and to increase their endurance under harsh reaction conditions. The immobilization of the biocatalysts on solid supports provides a feasible and efficient solution to surmount these problems. Enzyme immobilization can improve the thermal and environmental stability and insolubilize the enzymes for recovery and recycling and, thus, eases the burden of biocatalyst cost. The solid support often broadens the applicable pH range of biocatalysts, and protects/stabilizes the enzyme from denaturing by organic solvents, high

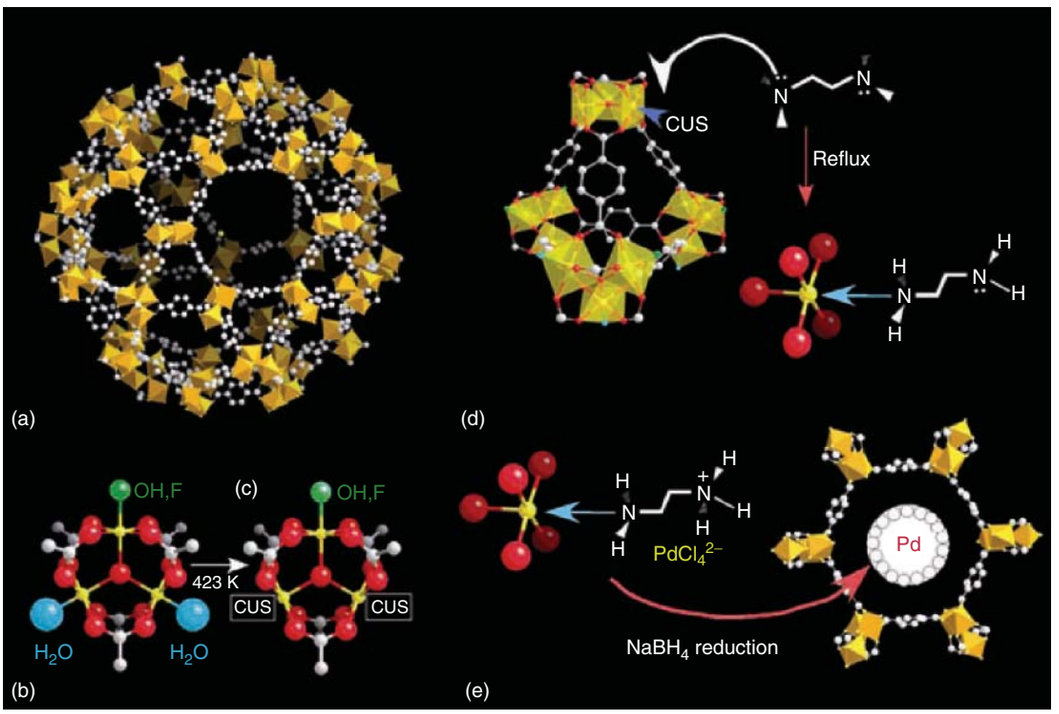


Figure 17 Site-selective functionalization of MIL-101 with unsaturated metal sites: (a) perspective view of the mesoporous cage of MIL-101 with hexagonal windows; (b), (c) evolution of coordinatively unsaturated sites from chromium trimers in mesoporous cages of MIL-101 after vacuum treatment at 423 K for 12 h; (d) surface functionalization of the dehydrated MIL-101 through selective grafting of amine molecules (i.e., ethylenediamine) onto coordinatively unsaturated sites; (e) selective encapsulation of noble metals in the amine-grafted MIL-101 via a three-step process. Chromium atoms/octahedra yellow, carbon atoms pale gray, oxygen atoms red (Reproduced with permission from Ref. 42. © Wiley-VCH Verlag GmbH & Co. KGaA, Weinheim, 2008.)

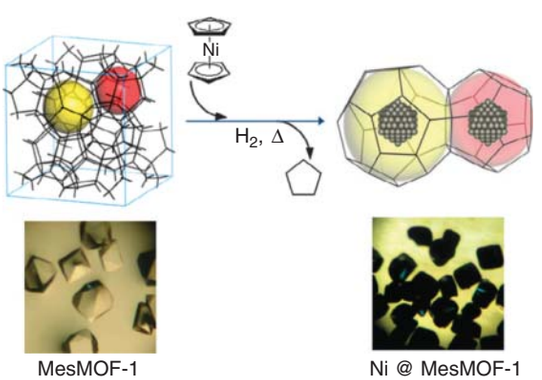
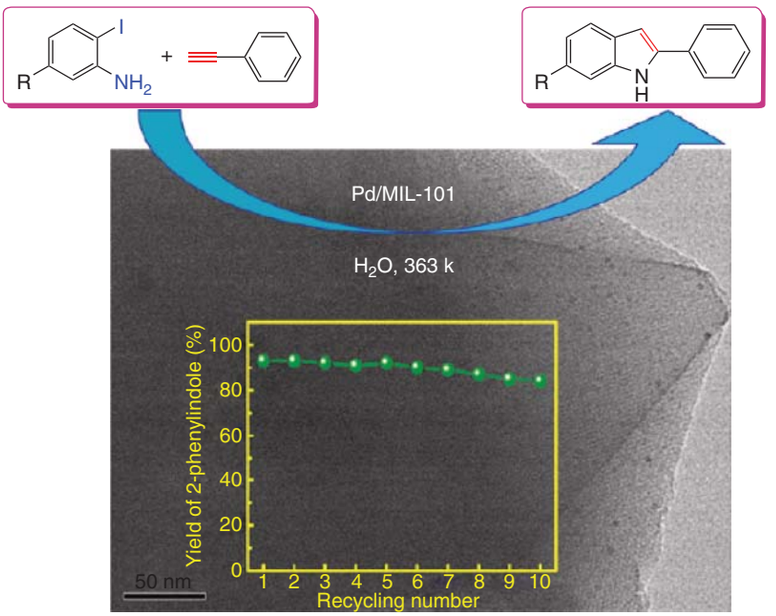


Figure 18 A two-step procedure for the preparation of Ni@MesMOF-1 is schematically shown with pictures for the crystals before and after Ni embedment (Reproduced from Ref. 52 with permission from The Royal Society of Chemistry.)

temperature, or autolysis. In addition, enzyme immobilization simplifies the overall design and performance control of the bioreactors. Therefore, the industrial or commercial applications of biocatalysts depend on the development of effective methods of immobilization.[67] Among the various types of immobilization methods, encapsulation exhibits advantages such as enhanced stability, controllable arrangement, and reduction of excessive denaturing.

An approach that continues to be more widely explored is the immobilization of enzymes in ordered mesoporous materials. Since Balkus and Díaz first published their work on the immobilization of proteins in ordered mesoporous materials in 1996,[68] extensive efforts have been devoted to developing suitable mesoporous matrixes and to optimize the immobilization conditions. In this context, mesoporous silica materials have been systematically and widely investigated, owing to the high surface areas with tunable, uniform pores. However, the leaching of immobilized catalysts from mesoporous silica leads to a great decrease of enzyme activity upon reuse, which is one of the biggest challenges for the further application of these materials. This leaching is probably due to the lack of specific interactions between the biomolecule and the mesoporous silica support.

MesoMOFs play an irreplaceable role in the development of heterogeneous biocatalysis because of their structural specificities: the high porosity and surface



Scheme 5 The palladium nanoparticles were encapsulated into MIL-101 and exhibit catalytic activity towards the domino synthesis of indole (Reprinted with permission from Ref. 49. Copyright (2011) American Chemical Society.)

area ensure the high loading and easy accessibility of catalytic active site; the nanoscale and tunable pore size provides the possibility of encapsulation of biomolecules; the relative large pores facilitate the ingress and diffusion of substrates and products. In particular, the large cage of mesoMOFs can be decorated with particular organic functional groups for specific interactions with biomolecules to prevent leaching, which makes them attractive to immobilize and stabilize proteins, vitamins, or drugs for biomedical or biocatalysis applications. Ion exchange and PSM (see ***Postsynthetic Modification of Metal-Organic Frameworks***) of mesoMOFs give rise to even broader applications. In addition, when an enzyme is encapsulated inside a confined space, the catalytic performance and behavior can be often distinguished from its free state. In terms of biocatalysis, many interesting phenomena have been observed during the heterogeneous catalytic process of immobilized enzyme.[69–71] Therefore, the studies on enzyme encapsulation by mesoporous solid supports are of fundamental importance for the understanding of the mechanisms and transport phenomena during the catalysis process. The well-defined pore structure makes mesoMOFs the perfect platforms for studies in this field. A rationally designed protocol for mesoMOF-based biocatalysis is usually composed of multiple steps: (i) synthesis of mesoMOFs with suitable pore size, structure and stability; (ii) selecting suitable enzymes with proper dimensions and interaction with mesoMOFs; (iii) encapsulation of enzymes into mesoMOFs with high loading and stability;

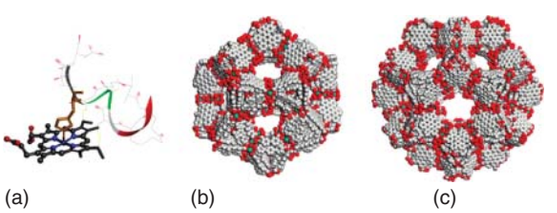


Figure 19 (a) Molecular structure of MP-11 (obtained from the solution structure of PDB 1OCD); (b) 3.9 nm-diameter cage, and (c) 4.7 nm-diameter cage in Tb-mesoMOF (Reprinted with permission from Ref. 57. Copyright (2011) American Chemical Society.)

(iv) selecting suitable test reaction and right substrates for the catalytic evaluation; (v) mechanistic studies.

As the pioneer in the research of biocatalysis application of mesoMOFs, in 2011, Ma's group successfully encapsulated Microperoxidase-11(MP-11), into Tb-mesoMOF.[57] The Tb-mesoMOF served as the host matrix because of its water stability and nanoscopic cages (3.9 and 4.7 nm in diameter) (Figure 19), and a loading of 19.1 μmol g^{-1} was achieved after ~50 h. The new system, MP-11@Tb-mesoMOF, demonstrated superior catalytic activity and recyclability in organic solvent (methanol), surpassing the mesoporous silica counterparts (Figure 20). This work became the first example of enzyme immobilization into a mesoporous MOF, and paved the way for

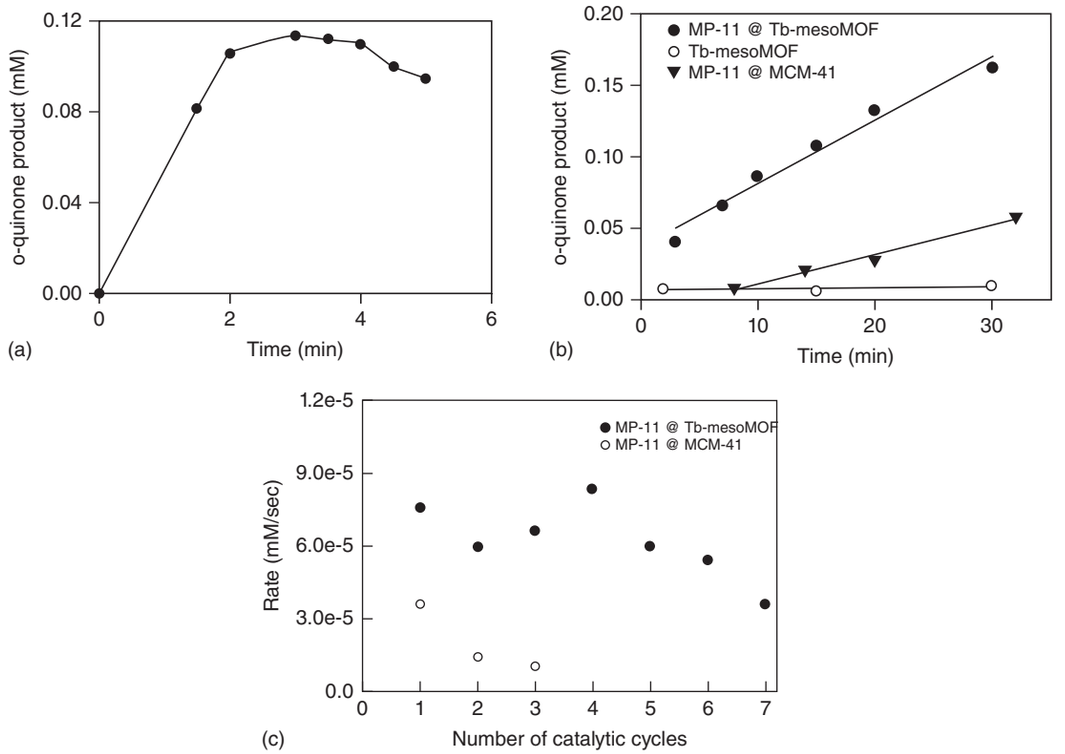


Figure 20 Kinetic traces for the oxidation of DTBC by (a) free MP-11in HEPES buffer (0.6 μM); (b) MP-11@Tb-mesoMOF (2.0 mg), Tb-mesoMOF (2.0 mg), and MP-11@MCM-41 (2.0 mg) in methanol with H_2O_2. (c) Reaction rates of MP-11@Tb-mesoMOF and MP-11@MCM-41 at different cycles (Reprinted with permission from Ref. 57. Copyright (2011) American Chemical Society.)

further studies of mesoMOFs as a new type of platforms for biocatalysis.

Compared to the homogeneous systems, heterogeneous biocatalysis can exhibit improved selectivity. When the solid support possesses hierarchical pores with large pores for protein ingress and small pores to allow diffusion of reactants and products, the immobilized enzyme may become a size-, or shape-selective catalyst, which is highly desirable in industry but not observed for the protein in homogeneous system.[72] Along the same line, Ma's group designed a size selective biocatalyst, Mb@Tb-mesoMOF, by the encapsulation of an oxygen binding protein, myoglobin (Mb), into a mesoMOF featuring hierarchical nanoscopic cages.[58] Tb-mesoMOF features type-IV sorption behavior with hierarchical pore sizes of 0.9, 3.0, and 4.1 nm as revealed by N_2 gas sorption studies at 77 K. After the encapsulation of Mb, Mb@Tb-mesoMOF demonstrated excellent peroxidative activity and reusability towards the oxidation of small substrate pyrogallol, in addition, an interesting size-selective catalytic performance was observed during the catalysis of pyrogallol (THB) and large substrate 2,2′-azinodi(3-ethylbenzothiazoline)-6-sulfonate (ABTS) (Table 4, Figure 21). It is notable that this size-selectivity is not exhibited by parent myoglobin in solution.

Table 4 Summary of catalysis results of THB and ABTS oxidation in the presence of 10 mM H_2O_2 in HEPES buffer (Reprinted with permission from Ref. 58. Copyright (2012) American Chemical Society.)

	Free Mb[(a)]	Mb@SBA-15	Mb@Tb-mesoMOF
Initial rate ($mM\ s^{-1}$) for THB reaction[(b)]	1.02×10^{-4}	8.96×10^{-5}	4.80×10^{-5}
Rate ($mM\ s^{-1}$) for THB reaction[(c)]	8.20×10^{-6}	6.10×10^{-6}	1.55×10^{-5}
Initial rate ($mM\ s^{-1}$) for ABTS reaction[(b)]	3.27×10^{-4}	2.00×10^{-4}	8.33×10^{-6}

[(a)] Diluted to 0.5 μM in HEPES buffer.
[(b)] Initial rate calculated in the first 4 min.
[(c)] Average rate over 1 h.

Liu *et al.*[73] proposed a simple approach for the construction of a trypsin–FITC@MOF bioreactor by a 30-min vortex-assisted host–guest interaction to immobilize the trypsin protease in mesoporous CYCU-4

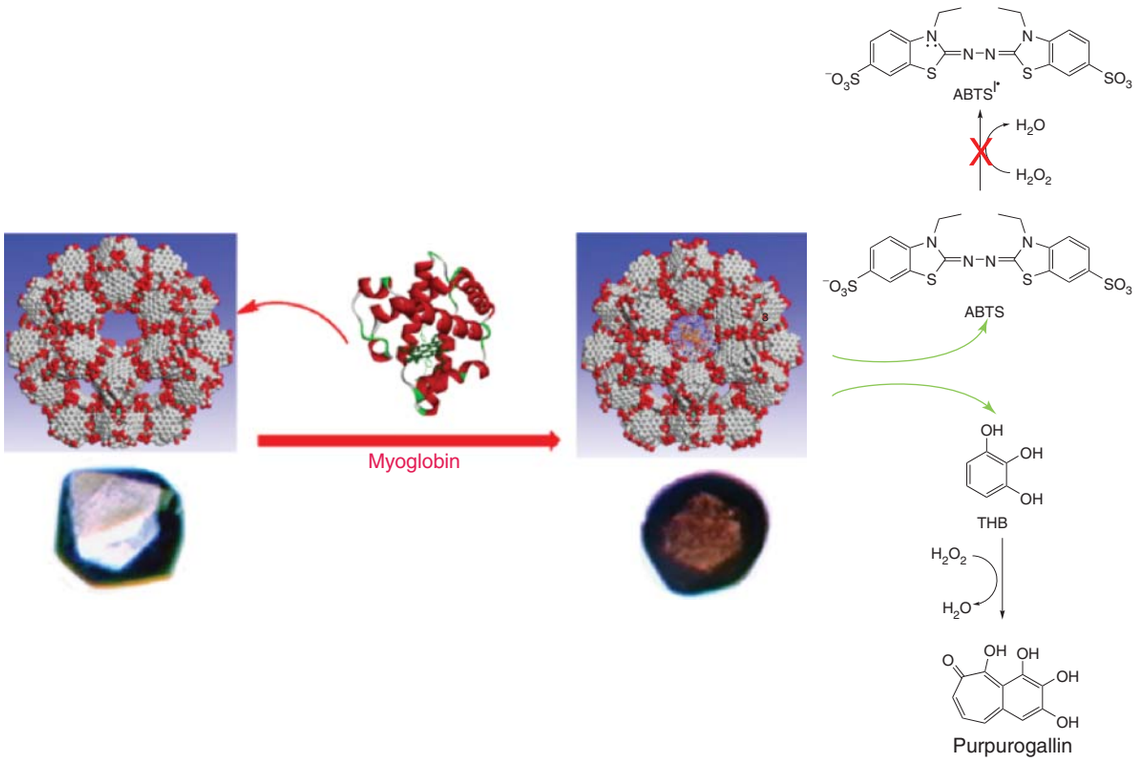


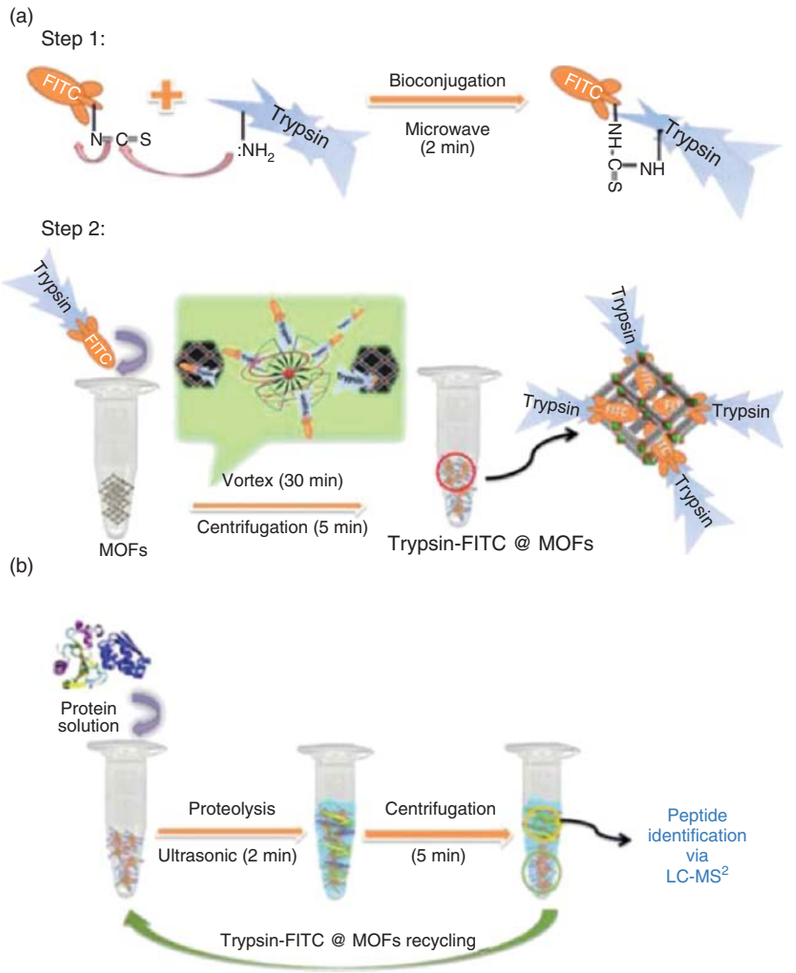
Figure 21 Myoglobin has been successfully immobilized into a mesoporous MOF with hierarchical pore sizes, which demonstrates interesting size-selective biocatalysis performance (Reprinted with permission from Ref. 58. Copyright (2012) American Chemical Society.)

MOF matrix (Scheme 6). To evaluate the synthetic efficiency of the biocatalyst, the fluorescence emission of trypsin–FITC solution was tracked before and after the immobilization for comparison. It was demonstrated that the trypsin–FITC@CYCU-4 can be efficiently formed within 15–60 min. The digestion reaction of the bulky bovine serum albumin (BSA) protein was conducted to evaluate the catalytic performance and reusability of the immobilized enzyme and analyzed by LC-MS.

Usually, in terms of encapsulation, when the dimensions of the entrapped catalysts are significantly larger than the pores or pore windows of the supporting material, traditional loading method such as impregnation will not be applied. Instead, either the active species will be assembled within the pores of the matrix ("ship-in-a-bottle" approach)[74] or the supporting matrix will be assembled around the catalyst ("bottle around ship" or "templated synthesis" approach). However, Ma's group demonstrated how a heme protein cytochrome c (Cyt c) (molecular dimension: of $\sim 2.6 \times 3.2 \times 3.3$ nm) can be encapsulated into the interior of Tb-mesoMOF (pore window: 1.3 and 1.7 nm) simply through incubation despite the larger molecular dimension of the protein relative to the access pore sizes.[75] Inspired by the protein translocation phenomena in nature, they proposed a protein transport mechanism upon encapsulation that contains the salient features of protein translocation into cellular organelles, which is distinguished from any existing mechanisms proposed for encapsulation of active species into porous supports. By tracking the encapsulation process through the steady state fluorescence spectra (Figure 22), the mechanistic studies suggest the Cyt c molecules must undergo a significant conformational change during translocation into the MOF interior through the relatively small nanopores (Scheme 7).

4.3 Drug Delivery

Over the past decade, the clinical prospect of nanoscale materials has become increasingly remarkable, particularly for the particle-mediated drug delivery. Nanotherapeutic formulations offer numerous advantages, including enhanced drug accumulation, reductions in systemic toxicity, and the ability to be surface-functionalized with passivating and targeting moieties.[76] There are several criteria for ideal drug delivery nanocarriers: (i) high efficiency of drug loading, (ii) controlled matrix degradation and drug release, and (iii) easy surface modification



Scheme 6 (a) Bioreactor fabrication and (b) protein digestion (Reproduced from Ref. 73 with permission from The Royal Society of Chemistry.)

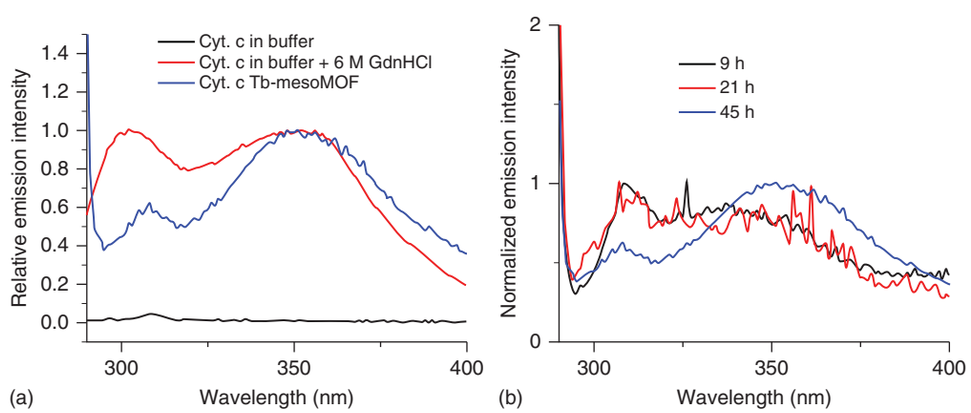
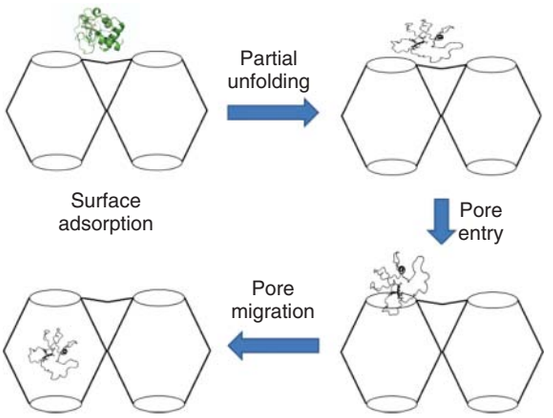


Figure 22 Fluorescence spectra of (a) Cyt c in HEPES buffer, Cyt c denatured by GdnHCl, and Cyt c@Tb-mesoMOF and of (b) Cyt c@Tb-mesoMOF after different incubation times (Reprinted with permission from Ref. 75. Copyright (2012) American Chemical Society.)



Scheme 7 Tentative mechanism for the translocation of Cyt c into the cavities of Tb-mesoMOF. This mechanism involves surface adsorption of the protein followed by partial unfolding. The partially unfolded protein partitions between the surface and exterior pores followed by migration into the large interior cavities (Reprinted with permission from Ref. 75. Copyright (2012) American Chemical Society.)

and functionalization for *in vivo* control and tracking. Moreover, hierarchical nanoparticles loaded with different active agents can form multifunctional drug delivery systems, which will make the association of therapeutics and diagnostics for personalized patient treatment a reality.[77] However, for traditional porous materials, such as the polymer matrix or silica, drug storage capacity and specific releasing capacity is greatly limited by the lack of structural versatility and interactions with the loaded active species. As an emerging material for drug delivery, mesoMOFs possess a number of advantages: high and regular porosity to ensure the high loading; tunable pore size for the entrapment of drugs with various dimensions; the remarkable structural flexibility and essentially limitless choice of organic building blocks provides the specific interactions with active species, which facilitate the controlled release. In addition, when MOFs are scaled down to nanoscale, nanoscale metal–organic frameworks (NMOFs) exhibit superior pharmacokinetic profiles and better control of the growth kinetics and nucleation of nanoparticles (see ***Nanoscale Metal-Organic Frameworks***).[78] However, to a large extent, this area remains relatively unexplored in mesoMOFs compared to other well-developed applications such as gas storage and heterogeneous catalysis. The application of mesoMOFs in drug delivery will critically depend on the modification and functionalization of their surfaces to engender stability, biocompatibility, and specific functionality (Figure 23).[79]

The first example of mesoMOFs-based drug delivery was reported by Férey and coworkers in 2006.[76] The model drug Ibuprofen was loaded into the rigid mesoMOFs, MIL-100 (Cr) and MIL-101(Cr), which exhibit a high drug loading capacity (up to 1.4 g drug g^{-1} solid). Compare to the MCM-41 silica counterpart, the mesoMOF system exhibits four times larger drug loading and longer releasing times under physiological conditions (3–6 days for mesoMOF and 2 days for MCM-41), which is probably due to the $\pi\cdots\pi$ and acid–base interactions between the frameworks and the guest drugs.

In 2010, Horcajada *et al.*[77] used iron (III) carboxylate NMOFs with engineered cores and surfaces as matrices for the adsorption and drug delivery of four challenging anticancer or antiviral drugs with different polarities, sizes and functional groups (busulfan, azidothymidine triphosphate, cidofovir, and doxorubicin) (Figure 24).

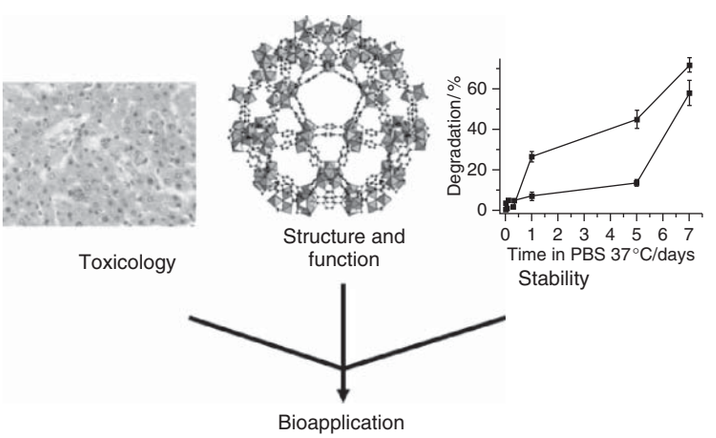


Figure 23 The structure and function of MOFs combined with acceptable toxicology and suitable biodegradation properties offer great promise for bio-applications (Reproduced with permission from Ref. 79. © Wiley-VCH Verlag GmbH & Co. KGaA, Weinheim, 2010.)

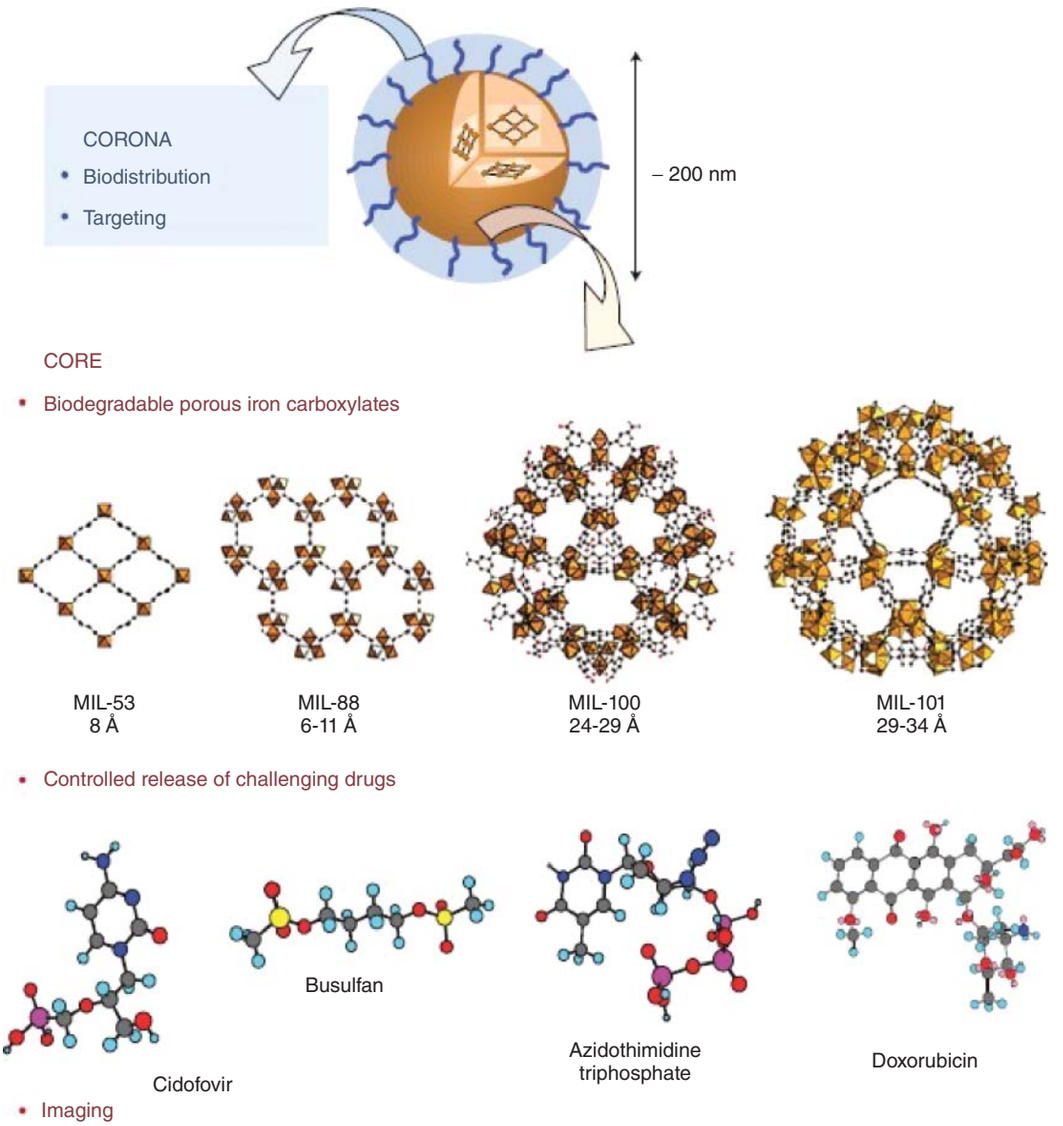


Figure 24 Scheme of engineered core–corona porous iron carboxylates for drug delivery (Reprinted by permission from Macmillan Publishers Ltd: Nature Chemistry (Ref. 77), copyright (2010).)

The drug loading and entrapment efficiency, degradability and cytotoxicity and kinetics of drug delivery were comprehensively investigated for the iron (III) carboxylate NMOFs-based drug delivery systems. In addition to high loading, remarkable entrapment efficiency and low cytotoxicity were observed as well. The comparison of the kinetics of drug delivery and the degradation profiles revealed that the drug delivery is mainly affected by the diffusion of the drug through the pores and/or drug-host interactions, not the degradation of MOF frameworks.

An alternative approach for the drug loading was proposed by Lin and coworkers in 2009.[80] After the modification of Fe-MIL-101 with amino groups, the active species, ethoxysuccinato-cisplatin (ESCP) prodrug and BODIPY dye, were allowed to covalently attach with Fe-MIL-101-NH_2 (MOFs 1a) through PSM to form the prodrug (Figure 25). This covalent interaction between the guests (drugs) and the matrix (MOFs framework) is usually stronger than the noncovalent loading, and the drug can be released through the decomposition of the host matrix. Therefore, it is critical to retain the functions and activities of agents after the decomposition of the host, which means that the active agents must be cleavable from the NMOFs under specific biological conditions.

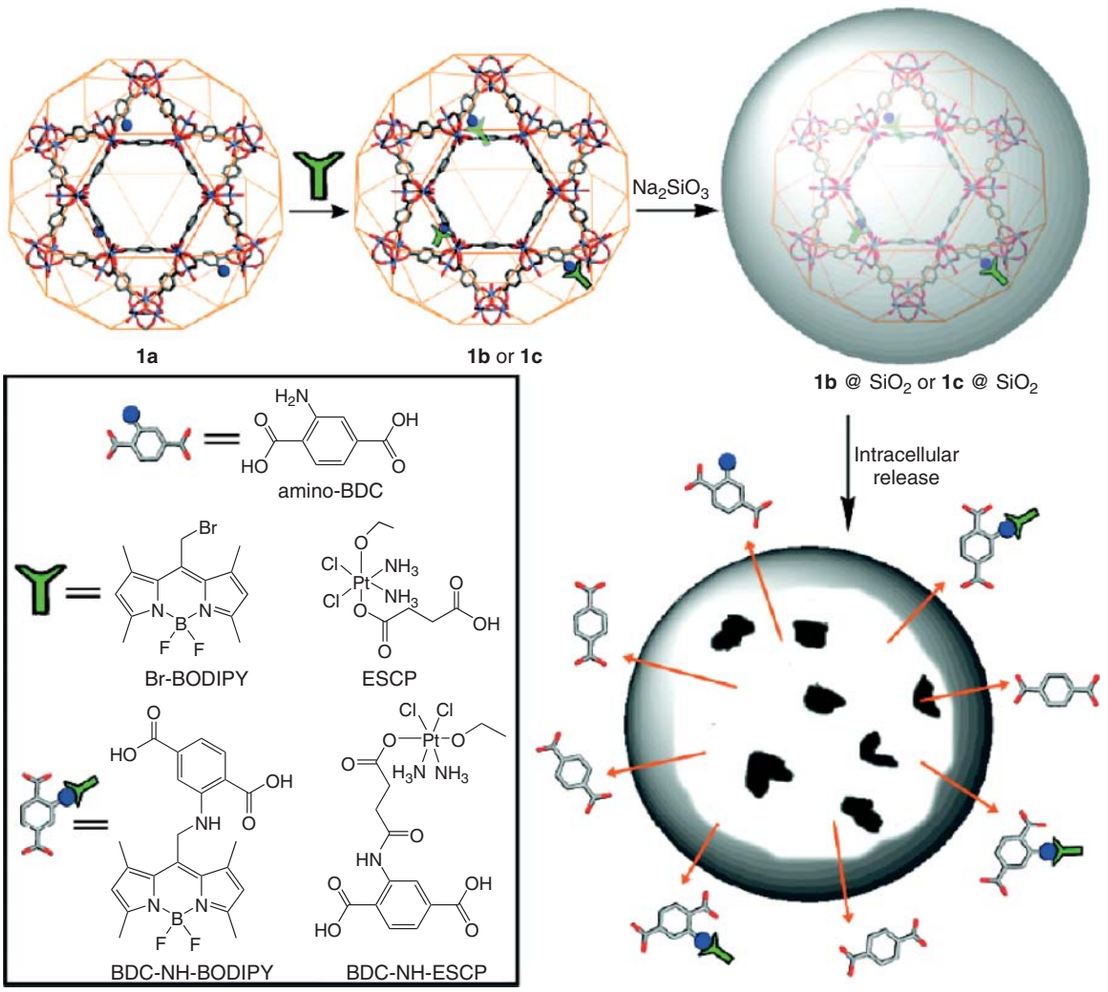


Figure 25 Schematics showing the covalent attachment incorporation and silica coating strategies (Reprinted with permission from Ref. 80. Copyright (2009) American Chemical Society.)

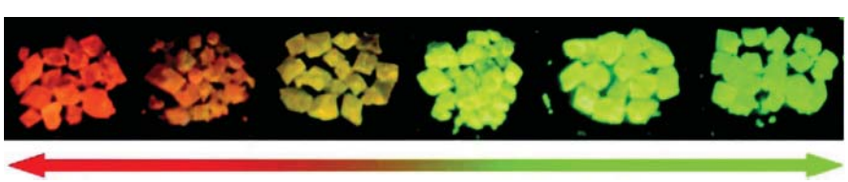


Figure 26 The Eu^{3+}/Tb^{3+}-doped samples illuminated with 365 nm laboratory UV light. The samples were prepared by doping 100 mg MOF with 2 mmol Ln^{3+} in 5 mL DMF. From left to right, Eu_1/Tb_0, $Eu_{0.8}/Tb_{0.2}$, $Eu_{0.7}/Tb_{0.3}$, $Eu_{0.6}/Tb_{0.4}$, $Eu_{0.3}/Tb_{0.7}$, and Eu_0/Tb_1 (Reproduced with permission from Ref. 86. © Wiley-VCH Verlag GmbH & Co. KGaA, Weinheim, 2011.)

4.4 Sensor

MOFs have shown potential in sensing various subjects, such as cations/anions, small molecules, gases/vapors.[81–83] Moreover, some special MOFs-based sensing such as pH, temperature, ionizing radiation, and explosives have also been reported.[84,85] However, compared with microporous MOFs, mesoMOFs have mostly remain unexplored for sensing applications. With the high, tunable, and regular porosity, mesoMOFs offer the opportunities to explore reversible and recyclable sensors for broad dimensions of sensing substrates. Indeed, the large or hierarchical pores of mesoMOFs permit the selective recognition and sensing of large substrates, and

allow for trapping molecules with large dimensions, such as some dye molecules, to assemble sensing devices or for fine-tuning the luminescence behavior. MesoMOFs can also interact with sensing substrates in different ways because of the existence of open metal sites and functional sites such as Lewis basic/acidic sites, which can enhance the sensitivity of the sensors.

In 2007, Fang *et al.*[15] synthesized JUC-48, a mesoMOF with 1D hexagonal nanotube-like channels (2.45 × 2.79 nm) and doped it into Rh6G dye solutions to afford JUC-48/Rh6G, which showed the strongest fluorescence emission peak at 563 nm at room temperature. Interestingly, the assembled JUC-48/Rh6G exhibited favorable temperature-dependent luminescent properties. When the temperature decreased from 298 to 77 K, the intensity of fluorescence signal was linearly enhanced with the emission peak remaining at 563 nm. These luminescent properties make JUC-48/Rh6G a promising candidate for temperature-sensing devices.

Lanthanide metal ions and related clusters possess unique luminescent and optical properties, and thus have been of intense interest over the decades. Lan *et al.*[86] encapsulated lanthanide(III) cation into a mesoMOF synthesized by the reaction of Zn_4O clusters and pre-designed tetratopic ligands. The mesoMOF was immersed into Eu^{3+} or Tb^{3+} solution with various concentration to load these lanthanide(III) cations with different ratios. After excitation at 365 nm using the laboratory UV light, the assembled samples demonstrated lanthanide sensitization by emitting their respective red and green colors (Figure 26). It is noteworthy that the high intensity of the signal enables the color to be visible by eye. These materials provide the potential for barcoded luminescent application.

5 CONCLUSIONS

Although tremendous progress has been achieved in the research field of mesoMOFs, the synthesis and application of MOFs are still dominated by microporous MOFs. However, along with further understanding of the basics and principles in the design of mesoMOFs and the development of crystal engineering and reticular chemistry, an increasing number of mesoMOFs with attractive properties are constructed through various strategies. With the enlarged pore size, mesoMOFs can remarkably expend the utilities of MOFs in a wide range of fields, and offer enormous opportunities for applications such as gas storage and separation, heterogeneous catalysis, biocatalysis, sensing, and drug delivery. In addition, with the extraordinary advantages of mesoMOFs, great progress and breakthroughs in developing them as multifunctional materials will be expected in the near future.

As with all of the emerging materials, there are also challenges and barriers to be overcome for further development of mesoMOFs, such as the improvement of activation strategies, the stability, and the mechanical strength. With the substantially increasing interest and continuous efforts towards mesoMOFs from both academia and industry, this class of prospective materials will remain at the forefront of the materials research and play important and irreplaceable roles in the development of porous materials and their future applications.

6 ACKNOWLEDGMENTS

The authors acknowledge the University of South Florida for financial support of this work.

7 RELATED ARTICLES

Porous Coordination Polymer Nanoparticles and Macrostructures; Metal-Organic Frameworks for Removal of Harmful Gases; Gas Storage in Metal-Organic Frameworks.

8 ABBREVIATIONS AND ACRONYMS

ABTS = 2,2′-azinodi(3-ethylbenzothiazoline)-6-sulfonate; BPDC = biphenyl-4,4′-dicarboxylate; BSA = bovine serum albumin; CA = citric acid; CH_4 = methane; CO_2 = carbon dioxide; CTAB = cetyltrimethylammonium bromide; CUS = coordinatively unsaturated metal sites; Cyt c = cytochrome c; DOE = Department of Energy; ESCP = ethoxysuccinato-cisplatin; H_2 = Hydrogen; H_3BTC = 1,3,5-tricarboxylic acid; H_3TATAB = 4,4′,4″-s-triazine-1,3,5-triyltrip-aminobenzenecarboxylic acid; HTB = 4,4′,4″-(1,3,4,6,7,9,9b-heptaazaphenalene-2,5,8-triyl)tribenzoate; IL = ionic liquid; Mb = myoglobin; mesoMOF = mesoporous metal–organic framework; MOF = Metal–organic framework; **MTN** = montmorillonite; N-EtFOSA = N-ethyl perfluorooctylsulfonamide; NMOF = nanoscale metal–organic framework; PEI = polyethyleneimine; PSM = post-synthetic modification; SBB = supermolecular building block; SBU = secondary building units; $SCCO_2$ = supercritical CO_2; SDC = 4,4′-stilbenedicarboxylic acid; TATB = 4,4′,4″-s-triazine-2,4,6-triyltribenzoate; TCPP = tetrakis(4-carboxyphenyl)porphyrin; TPDC = triphenyl-4,4′-dicarboxylate; ZIF = zeolitic imidazolate framework. 2D = two-dimensional; 3D = three-dimensional.

9 REFERENCES

1. L. R. MacGillivray, 'Metal-Organic Frameworks: Design and Application', John Wiley & Sons, Inc., Hoboken, 2010.
2. S. M. Cohen, *Chem. Rev.*, 2012, **3**, 126.
3. K. S. W. Sing, *Pure Appl. Chem.*, 1985, **57**, 603.
4. Q.-R. Fang, T. A. Makal, M. D. Young, and H.-C. Zhou, *Comments Inorg. Chem.*, 2010, **31**, 165.
5. S. Brunauer, L. S. Deming, W. E. Deming, and E. Teller, *J. Am. Chem. Soc.*, 1940, **62**, 1723.
6. G. Férey, C. Serre, C. Mellot-Draznieks, F. Millange, S. Surblé, J. Dutour, and I. Margiolaki, *Angew. Chem. Int. Ed.*, 2004, **43**, 6296.
7. G. Férey, C. Mellot-Draznieks, C. Serre, F. Millange, J. Dutour, S. Surble, and I. Margiolaki, *Science*, 2005, **309**, 2040.
8. W. Xuan, C. Zhu, Y. Liu, and Y. Cui, *Chem. Soc. Rev.*, 2012, **41**, 1677.
9. M. Eddaoudi, J. Kim, N. Rosi, D. Vodak, J. Wachter, M. O'Keeffe, and O. M. Yaghi, *Science*, 2002, **295**, 469.
10. J. An, O. K. Farha, J. T. Hupp, E. Pohl, J. I. Yeh, and N. L. Rosi, *Nat. Commun.*, 2012, **3**, 604.
11. W. Morris, B. Volosskiy, S. Demir, F. Gándara, P. L. McGrier, H. Furukawa, D. Cascio, J. F. Stoddart, and O. M. Yaghi, *Inorg. Chem.*, 2012, **51**, 6443.
12. J. E. Mondloch, W. Bury, D. Fairen-Jimenez, S. Kwon, E. J. DeMarco, M. H. Weston, A. Sarjeant, S. T. Nguyen, P. C. Stair, R. Q. Snurr, O. M. Farha, and J. T. Hupp, *J. Am. Chem. Soc.*, 2013. DOI: 10.1021/ja4050828.
13. N. L. Rosi, J. Kim, M. Eddaoudi, B. L. Chen, M. O'Keeffe, and O. M. Yaghi, *J. Am. Chem. Soc.*, 2005, **127**, 1504.
14. H. Deng, S. Grunder, K. E. Cordova, C. Valente, H. Furukawa, M. Hmadeh, F. Gándara, A. C. Whalley, Z. Liu, S. Asahina, H. Kazumori, M. O'Keeffe, O. Terasaki, J. F. Stoddart, and O. M. Yaghi, *Science*, 2012, **336**, 1018.
15. Q.-R. Fang, G.-S. Zhu, Z. Jin, Y.-Y. Ji, J.-W. Ye, M. Xue, H. Yang, Y. Wang, and S.-L. Qiu, *Angew. Chem. Int. Ed.*, 2007, **46**, 6638.
16. S.-H. Lo, C.-H. Chien, Y.-C. Lai, C.-C. Yang, J. J. Lee, D. S. Raja, and C.-H. Lin, *J. Mater. Chem. A*, 2013, **1**, 324.
17. F. Nouar, J. F. Eubank, T. Bousquet, L. Wojtas, M. J. Zaworotko, and M. Eddaoudi, *J. Am. Chem. Soc.*, 2008, **130**, 1833.
18. Y. Yan, X. Lin, S. Yang, A. J. Blake, A. Dailly, N. R. Champness, P. Hubberstey, and M. Schröder, *Chem. Commun.*, 2009, 1025.
19. O. K. Farha, C. E. Wilmer, I. Eryazici, B. G. Hauser, P. A. Parlla, K. O'Neill, A. A. Sarjeant, S. T. Nguyen, R. Q. Snurr, and J. T. Hupp, *J. Am. Chem. Soc.*, 2012, **134**, 9860.
20. B. Wang, A. P. Côté, H. Furukawa, M. O'Keeffe, and O. M. Yaghi, *Nature*, 2008, **453**, 207.
21. Y. K. Park, S. B. Choi, H. Kim, K. Kim, B.-H. Won, K. Choi, J.-S. Choi, W.-S. Ahn, N. Won, S. Kim, D. H. Jung, S.-H. Choi, G.-H. Kim, S.-S. Cha, Y. H. Jhon, J. K. Yang, and J. Kim, *Angew. Chem. Int. Ed.*, 2007, **46**, 8230.
22. H. Furukawa, J. Uribe-Romo, J. Kim, M. O'Keeffe, and O. M. Yaghi, *Inorg. Chem.*, 2011, **50**, 9147.
23. X.-S. Wang, S. Ma, D. Sun, S. Parkin, and H.-C. Zhou, *J. Am. Chem. Soc.*, 2006, **128**, 16474.
24. D.-Y. Hong, Y. K. Hwang, C. Serre, G. Férey, and J.-S. Chang, *Adv. Funct. Mater.*, 2009, **19**, 1537.
25. S. Ma, D. Sun, M. Ambrogio, J. A. Fillinger, S. Parkin, and H.-C. Zhou, *J. Am. Chem. Soc.*, 2007, **129**, 1858.
26. J. J. Zhang, L. Wojtas, R. W. Larsen, M. Eddaoudi, and M. J. Zaworotko, *J. Am. Chem. Soc.*, 2009, **131**, 17040.
27. O. Shekhah, H. Wang, M. Paradinas, C. Ocal, B. Schupbach, A. Terfort, D. Zacher, R. A. Fischer, and C. Woll, *Nat. Mater.*, 2009, **8**, 481.
28. K. Koh, A. G. Wong-Foy, and A. J. Matzger, *Angew. Chem. Int. Ed.*, 2008, **47**, 677.
29. T. Li, M. T. Kozlowski, E. A. Doud, M. N. Blakely, and N. L. Rosi, *J. Am. Chem. Soc.*, 2013. DOI: 10.1021/ja403810k.
30. L.-G. Qiu, T. Xu, Z.-Q. Li, W. Wang, Y. Wu, X. Jiang, X.-Y. Tian, and L.-D. Zhang, *Angew. Chem. Int. Ed.*, 2008, **47**, 9487.
31. L. B. Sun, J. R. Li, J. Park, and H. C. Zhou, *J. Am. Chem. Soc.*, 2012, **134**, 126.
32. Y. J. Zhao, J. L. Zhang, B. X. Han, J. L. Song, J. S. Li, and Q. A. Wang, *Angew. Chem. Int. Ed.*, 2011, **50**, 636.
33. Y. Yue, Z.-A. Qiao, P. F. Fulvio, A. J. Binder, C. Tian, J. Chen, K. M. Nelson, X. Zhu, S. Dai, and J. Am, *Chem. Soc.*, 2013. DOI: 10.1021/ja402694f.
34. K. Gedrich, I. Senkovska, N. Klein, U. Stoeck, A. Henschel, M. R. Lohe, I. A. Baburin, U. Mueller, and S. Kaskel, *Angew. Chem. Int. Ed.*, 2010, **49**, 8489.
35. M. Latroche, S. Surblé, C. Serre, C. Mellot-Draznieks, P. L. Llewellyn, J. Lee, J.-S. Chang, S. H. Jhung, and G. Férey, *Angew. Chem. Int. Ed.*, 2006, **45**, 8227.
36. H. Furukawa, N. Ko, Y. B. Go, N. Aratani, S. B. Choi, E. Choi, A. O. Yazaydin, R. Q. Snurr, M. O'Keeffe, J. Kim, and O. M. Yaghi, *Science*, 2010, **239**, 424.
37. O. K. Farha, O. Yazaydin, I. Eryazici, C. Malliakas, B. Hauser, M. G. Kanatzidis, S. T. Nguyen, R. Q. Snurr, and J. T. Hupp, *Nat. Chem.*, 2010, **2**, 944.
38. Y. Peng, V. Krungleviciute, I. Eryazici, J. T. Hupp, O. K. Farha, and T. Yildirim, *J. Am. Chem. Soc.*, 2013. DOI: 10.1021/ja4045289.
39. Y. Peng, G. Srinivas, C. E. Wilrner, I. Eryazici, R. Q. Snurr, J. T. Hupp, T. Yildirim, and O. K. Farha, *Chem. Commun.*, 2013, **49**, 2992.
40. Y. Lin, Q. Yan, C. Kong, and L. Chen, *Sci. Rep.*, 2013, **3**, 1859.

41. J. M. Thomas and W. J. Thomas, 'Principles and Practice of Heterogeneous Catalysis', VCH Verlagsgesellschaft mbH, Weinheim, 1997.
42. Y. K. Hwang, D.-Y. Hong, J.-S. Chang, S. H. Jhung, Y.-K. Seo, J. Kim, A. Vimont, M. Daturi, C. Serre, and G. Férey, *Angew. Chem. Int. Ed.*, 2008, **47**, 4144.
43. J. Kim, S. Bhattacharjee, K.-E. Jeong, S.-Y. Jeong, and W.-S. Ahn, *Chem. Commun.*, 2009, 3904.
44. N. V. Maksimchuk, K. A. Kovalenko, V. P. Fedin, and O. A. Kholdeeva, *Adv. Synth. Catal.*, 2010, **352**, 2943.
45. N. V. Maksimchuk, K. A. Kovalenko, V. P. Fedin, and O. A. Kholdeeva, *Chem. Commun.*, 2012, **48**, 6812.
46. N. V. Maksimchuk, O. V. Zalomaeva, I. Y. Skobelev, K. A. Kovalenko, V. P. Fedin, and O. A. Kholdeeva, *Proc. R. Soc. A*, 2012, **468**, 2017.
47. N. V. Maksimchuk, O. A. Kholdeeva, K. A. Kovalenko, and V. P. Fedin, *Israel J. Chem.*, 2011, **51**, 281.
48. O. A. Kholdeeva, N. V. Maksimchuk, and G. M. Maksimov, *Catal. Today*, 2010, **157**, 107.
49. H. Li, Z. Zhu, F. Zhang, S. Xie, H. Li, P. Li, and X. Zhou, *ACS Catal.*, 2011, **1**, 1604.
50. Y. Huang, Z. Lin, and R. Cao, *Chem. Eur. J.*, 2011, **17**, 12706.
51. Y. Huang, S. Liu, Z. Lin, W. Li, X. Li, and R. Cao, *J. Catal.*, 2012, **292**, 111.
52. Y. K. Park, S. B. Choi, H. J. Nam, D.-Y. Jung, H. C. Ahn, K. Choi, H. Furukawa, and J. Kim, *Chem. Commun.*, 2010, **46**, 3086.
53. Q.-R. Fang, D.-Q. Yuan, J. Sculley, J.-R. Li, Z.-B. Han, and H.-C. Zhou, *Inorg. Chem.*, 2010, **49**, 11637.
54. L. Ma, J. M. Falkowski, C. Abney, and W. Lin, *Nat. Chem.*, 2010, **2**, 838.
55. Y. Chen, T. Hoang, and S. Ma, *Inorg. Chem.*, 2012, **51**, 12600.
56. D. Feng, Z.-Y. Gu, J.-R. Li, H.-L. Jiang, Z. Wei, and H.-C. Zhou, *Angew. Chem. Int. Ed.*, 2012, **51**, 10307.
57. V. Lykourinou, Y. Chen, X.-S. Wang, L. Meng, T. Hoang, L.-J. Ming, R. L. Musselman, and S. Ma, *J. Am. Chem. Soc.*, 2011, **133**, 10382.
58. Y. Chen, V. Lykourinou, T. Hoang, L.-J. Ming, and S. Ma, *Inorg. Chem.*, 2012, **51**, 9156.
59. B. F. Hoskins and R. Robson, *J. Am. Chem. Soc.*, 1990, **112**, 1546.
60. M. Fujita, Y. J. Kwon, S. Washizu, and K. Ogura, *J. Am. Chem. Soc.*, 1994, **116**, 1151.
61. J. S. Seo, D. Whang, H. Lee, S. I. Jun, J. Oh, Y. J. Jeon, and K. Kim, *Nature*, 2000, **404**, 982.
62. L. Ma, C. Abney, and W. Lin, *Chem. Soc. Rev.*, 2009, **38**, 1248.
63. J. Lee, O. K. Farha, J. Roberts, K. A. Scheidt, and J. T. Hupp, *Chem. Soc. Rev.*, 2009, **38**, 1450.
64. L. Ma and W. Lin, *J. Am. Chem. Soc.*, 2008, **130**, 13834.
65. A. Schmid, J. S. Dordick, B. Hauer, A. Kiener, M. Wubbolts, and B. Wtholt, *Nature*, 2001, **409**, 258.
66. C. J. Reedy and B. R. Gibney, *Chem. Rev.*, 2004, **104**, 617.
67. D. N. Tran and K. J.Balkus Jr, *ACS Catal.*, 2011, **1**, 956.
68. F. J. Díaz and K. J.Balkus Jr, *J. Mol. Catal. B*, 1996, **2**, 115.
69. R. C. Rodrigues, C. Ortiz, À. Berenguer-Murcia, R. Torresd, and R. Fernàndez-Lafuente, *Chem. Soc. Rev.*, 2013, **42**, 6290.
70. C. H. Lei, Y. Shin, J. K. Magnuson, G. Fryxell, L. L. Lasure, D. C. Elliott, J. Liu, and E. J. Ackerman, *Nanotechnology*, 2006, **17**, 5531.
71. J. Liu, J. Peng, S. Shen, Q. Jin, C. Li, and Q. Yang, *Chem. Eur. J.*, 2013, **19**, 2711.
72. M. Hartmann, *Chem. Mater.*, 2005, **17**, 4577.
73. W.-L. Liu, S.-H. Lo, B. Singco, C.-C. Yang, H.-Y. Huang, and C.-H. Lin, *J. Mater. Chem. B*, 2013, **1**, 928.
74. A. Corma and H. Garcia, *Eur. J. Inorg. Chem.*, 2004, 1143.
75. Y. Chen, V. Lykourinou, C. Vetromile, T. Hoang, L.-J. Ming, R. Larsen, and S. Ma, *J. Am. Chem. Soc.*, 2012, **134**, 13188.
76. P. Horcajada, C. Serre, M. Vallet-Regí, M. Sebban, F. Taulelle, and G. Férey, *Angew. Chem. Int. Ed.*, 2006, **45**, 5974.
77. P. Horcajada, T. Chalati, C. Serre, B. Gillet, C. Sebrie, T. Baati, J. F. Eubank, D. Heurtaux, P. Clayette, C. Kreuz, J.-S. Chang, Y. K. Hwang, V. Marsaud, P.-N. Bories, L. Cynober, S. Gil, G. Férey, P. Couvreur, and R. Gref, *Nat. Mater.*, 2010, **9**, 172.
78. J. D. Rocca, D. Liu, and W. Lin, *Acc. Chem. Res.*, 2011, **44**, 957.
79. A. C. McKinlay, R. E. Morris, P. Horcajada, G. Férey, R. Gref, P. Couvreur, and C. Serre, *Angew. Chem. Int. Ed.*, 2010, **49**, 6260.
80. K. M. L. Taylor-Pashow, J. D. Rocca, Z. Xie, S. Tran, and W. Lin, *J. Am. Chem. Soc.*, 2009, **131**, 14261.
81. B. Chen, L. B. Wang, Y. Xiao, F. R. Fronczek, M. Xue, Y. J. Cui, and G. Qian, *Angew. Chem. Int. Ed.*, 2009, **48**, 500.
82. B. Chen, Y. Yang, F. Zapata, G. N. Lin, G. Qian, and E. B. Lobkovsky, *Adv. Mater.*, 2007, **19**, 1693.
83. B. V. Harbuzaru, A. Corma, F. Rey, P. Atienzar, J. L. Jordá, H. García, D. Ananias, L. D. Carlos, and J. Rocha, *Angew. Chem. Int. Ed.*, 2008, **47**, 1080.
84. H. Xu, F. Liu, Y. Cui, B. Chen, and G. Qian, *Chem. Commun.*, 2011, **47**, 3153.
85. B. V. Harbuzaru, A. Corma, F. Rey, J. L. Jordá, D. Ananias, L. D. Carlo, and J. Rocha, *Angew. Chem. Int. Ed.*, 2009, **48**, 6476.
86. Y. Q. Lan, H. L. Jiang, S. L. Li, and Q. Xu, *Adv. Mater.*, 2011, **23**, 5015.

Porphyrinic Metal-Organic Frameworks

Chao Zou, Min Zhao and Chuan-De Wu

Zhejiang University, Hangzhou, PR China

1	Introduction	67
2	Synthesis Strategies	67
3	Applications of Porphyrinic MOFs	76
4	Conclusions	81
5	Acknowledgments	82
6	Abbreviations and Acronyms	82
7	References	82

1 INTRODUCTION

Metal–organic frameworks (MOFs), emerged as a new class of porous functional materials, are self-assembled from organic linkers and inorganic joints of metal ions and/or metal-containing clusters.[1–6] Being developed at an extraordinary pace in the fields of inorganic chemistry, materials science, and related areas over the past two decades, MOF materials not only enrich the porous materials domain but have also been realized various applications in the fields of gas storage and separation,[1] sensing,[2] magnetics,[3] luminescence,[4] heterogeneous catalysis,[5] drug delivery,[6] and now even ubiquitous in the chemistry literature. In a short period of time, vast amounts of breakthroughs and discoveries have been achieved by crossover with correlated fields.

As an important class of essential functional molecules in biological processes, large quantities of porphyrins and their metalloderivatives have been synthesized to understand and mimic the functionalities in natural systems.[7] They have been realized as anticancer drugs,[8] biomimetic catalysts,[9] semiconductors,[10] superconductors,[11] electronic materials,[12] NMR image enhancement agents,[13] nonlinear optical materials,[14] and DNA-binding or cleavage agents.[15] Moreover, considering that porphyrins have the advances of high thermal and chemical stabilities, facile synthesis, and robust nature, there has been an explosive growth on design, synthesis, and applications of porous MOF materials containing porphyrin building blocks.

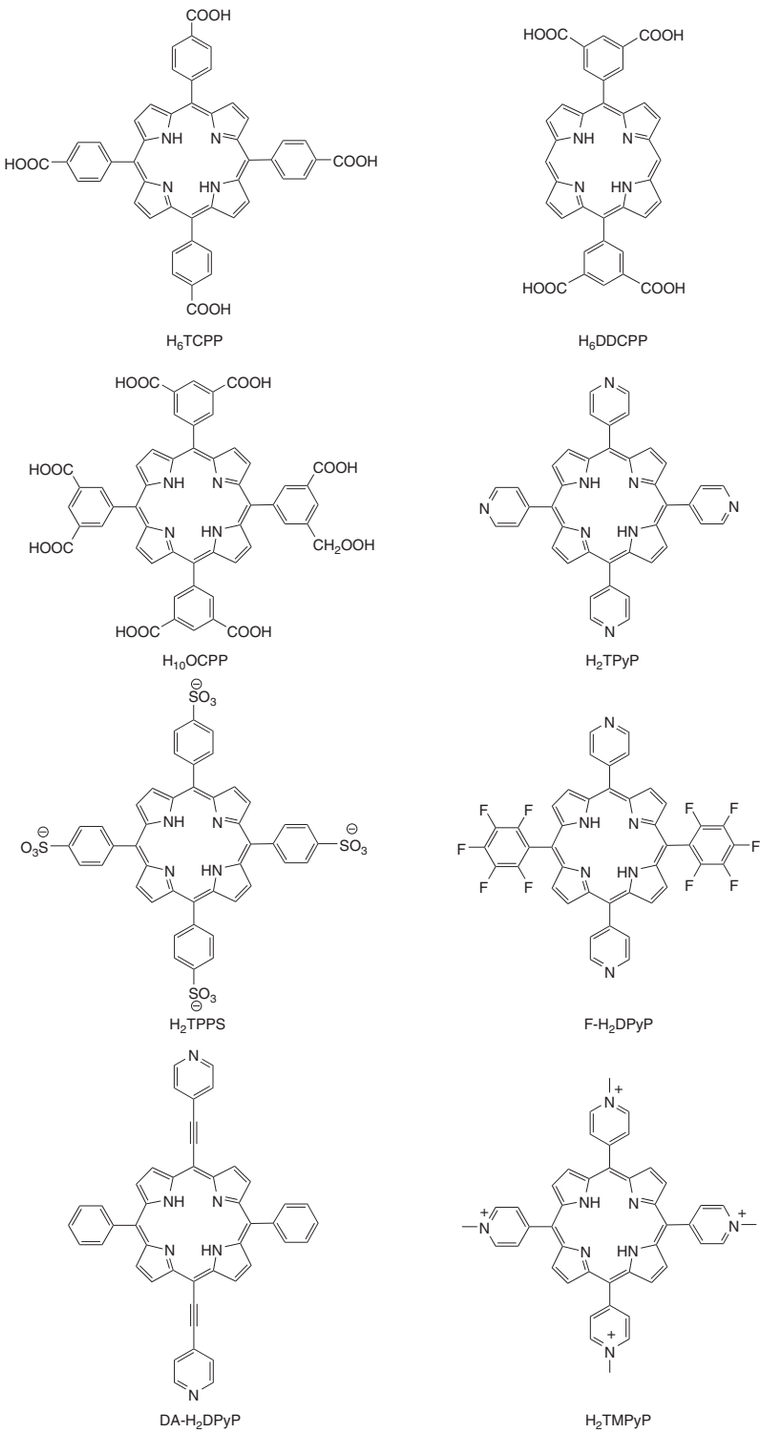
Porphyrinic MOFs are a special class of materials by incorporation of porphyrins as functional constituents of MOFs.[16–26] Considering that five related EIBC articles, such as ***Polyrotaxane Metal-Organic Frameworks***, ***Synthesis and Structures of Aluminum-Based Metal-Organic Frameworks***, ***Fluorinated Metal-Organic Frameworks (FMOFs): Concept, Construction, and Properties***, ***Functional Magnetic Materials Based on Metal Formate Frameworks***, and ***Metal-Organic Frameworks from Single-Molecule Magnets***, are relevant to the concepts and topics covered in this chapter, we will focus on the functional porphyrin-oriented work that involves recent progress on assembling novel porphyrinic network materials and developing in the applications of porphyrinic MOFs.

2 SYNTHESIS STRATEGIES

Although priori prediction of self-assembled coordination networks remains a challenge, it is feasible to organize porphyrinic MOFs by careful selection of organic and inorganic components with tailored properties by suitable strategies. As a kind of multidentate ligand, as shown in Scheme 1, porphyrins can coordinate with metal ions in multisites for the formation of varieties of structures. Among the reported methods, solvothermal reaction is frequently used in the synthesis of porphyrinic MOFs. Solvent, thermal ramping, temperature, and duration are the key factors to control over the coordination frameworks.

Ma and coworkers employed a supermolecular building block (SBB) strategy to construct a series of

Metal-Organic Framework Materials. Edited by Leonard R. MacGillivray and Charles M. Lukehart.
© 2014 John Wiley & Sons, Ltd. ISBN 978-1-119-95289-3



Scheme 1 Porphyrins and their abbreviations used for porphyrinic MOF constructions in this chapter

porous metal–metalloporphyrin frameworks (MMPFs). MMPF-1 was synthesized by solvothermal reaction of 5,15-bis(3,5-dicarboxyphenyl)porphine (H_6DDCPP) with copper nitrate (Figure 1).[27] MMPF-1 consists of nanoscopic rhombicuboctahedral cages with a high density of 16 open copper sites per cage. Each cage has three types of windows, square ($8.07 \times 8.07\ Å^2$), rectangular ($7.06 \times 7.18\ Å^2$), and triangular ($6.979 \times 6.979 \times 7.640\ Å^3$)

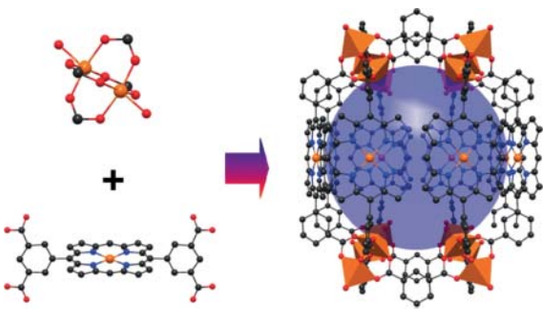


Figure 1 The cage unit in MMPF-1 built from DDCPP and paddle wheel $Cu_2(CO_2)_4$ secondary building units (SBUs)

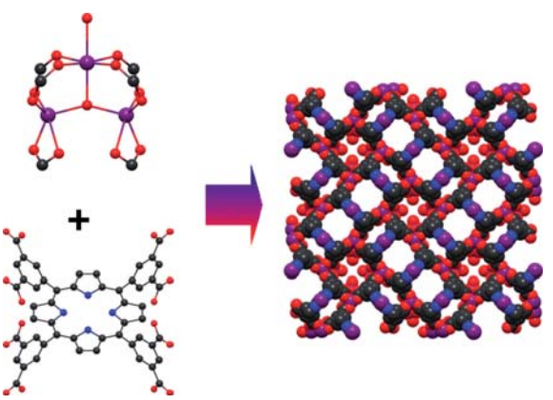


Figure 2 Self-assembly of OCPP ligands and cobalt trigonal prism SBUs to form MMPF-2 with three types of channels

windows. The rhombicuboctahedral cages in MMPF-1 are packed in the "ABAB" staking model to facilitate its selective gas adsorption of H_2 and O_2 over N_2, and CO_2 over CH_4.

They also used an octatopic porphyrin, tetrakis(3,5-dicarboxyphenyl)porphine (OCPP), to connect with various metal clusters, cobalt trigonal prisms of $Co_3(OH)(CO_2)_4$, triangular paddle wheel moieties of $Zn_2(CO_2)_3$ and $Cd(CO_2)_3$, to construct porous MMPFs, MMPF-2, MMPF-4, and MMPF-5.[28,29] In MMPF-2, as shown in Figure 2, OCPP bridges distorted cobalt trigonal prism $Co_3(OH)(CO_2)_4$ SBUs to generate a novel (6, 8, 8)-connected net.[28] MMPF-2 has two kinds of channels with dimensions of 10.046×10.099 Å^2 and 6.204×7.798 Å^2.

When OCPP is self-assembled with Zn or Cd ions, OCPP links up paddle wheel $M_2(CO_2)_3$ (M = Zn, Cd) moieties to promote formation of two porphyrinic MOFs, MMPF-4 and MMPF-5 (Figure 3).[29] The resulting augmented *pcu* topology networks, MMPF-4 (M = Zn) and MMPF-5 (M = Cd), contain two distinct polyhedral cages of cubicuboctahedron and octahemioctahedron. The cubicuboctahedral SBB composes of six Zn-OCPP moieties that are linked by eight $Zn_2(CO_2)_3$ SBUs with window dimensions of 7.831×8.048 Å^2 and internal diameter of 21.528 Å in MMPF-4. The octahemioctahedral SBB in MMPF-4 is enclosed by eight triangular $Zn_2(CO_2)_3$ paddle wheel molecular building blocks (MBBs) composed of six Zn-OCPP moieties that are linked by eight $Zn_2(CO_2)_3$ SBUs with window dimensions of 8.048×8.048 Å^2 and internal diameter of 11.189 Å.

Wu and coworkers preimplanted various metal ions in OCPP to construct porous porphyrinic MOFs with bimetal centers for catalytic application. The self-assembly of $MnCl_2$ or $CdCl_2$ with M-OCPP (M = Mn, Ni) results in three isostructural porous porphyrinic MOFs $[Mn_5Cl_2(MnCl\text{-}TDCPP)(DMF)_4(H_2O)_4]$ (ZJU-18), $[Mn_5Cl_2(Ni\text{-}TDCPP)(H_2O)_8]$ (ZJU-19), and $[Cd_5Cl_2(MnCl\text{-}TDCPP)(H_2O)_6]$ (ZJU-20).[30] In the crystal structures, the M-OCPP ($M = Mn^{III}Cl$ for ZJU-18 and ZJU-20, $M = Ni^{II}$ for ZJU-19) are linked by two kinds of binuclear $Mn^{II}{}_2(COO)_4Cl_2$ and trinuclear $Mn^{II}{}_3(COO)_4(\mu\text{-}H_2O)_2(H_2O)_6$ metal carboxylate SBUs to form a 3-periodic, binodal, edge-transitive net with reticular chemistry structure resource symbol *tbo* (Figure 4). The pore windows are of about 11.5 Å and pore cages about 21.3 Å in diameters in the three porphyrinic MOFs.

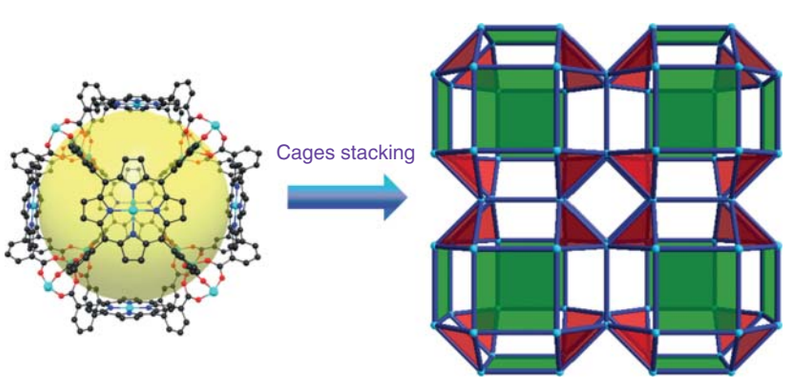


Figure 3 Construction of the augmented *pcu* network of MMPF-4 with two types of cavities by packing the cubicuboctahedral cages

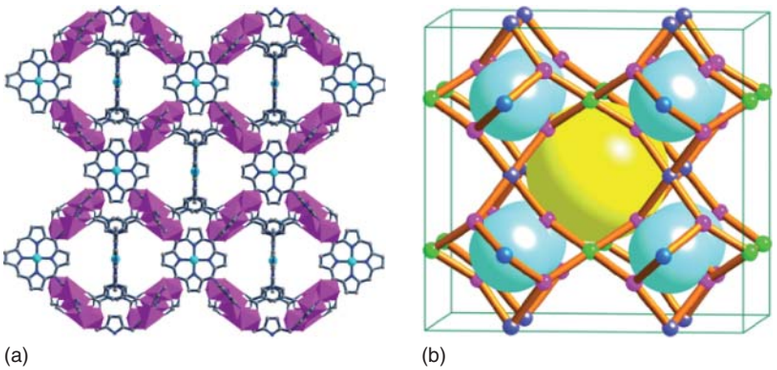


Figure 4 The crystal structure (a) and the *tbo* topology (b) of ZJU-18

To understand the porphyrin metal effect on the formation of porphyrinic MOFs, Wu and coworkers utilized a series of metal-tetracarboxylate porphyrin ligands (M-TCPP; M = H_2, Co^{II}, Ni^{II}, Cu^{II}, and $V^{IV}O$) and lead(II) ions to construct porphyrinic networks [$Pb_2(H_2TCPP)$], Pb_2(Co-TCPP)(H_2O)(DMF)], [Pb_2(Ni-TCPP)(DMF)(H_2O)], [Pb_2(Cu-TCPP)(DMF)(H_2O)], and [Pb_2(VO-TCPP)($H_2O)_2$].[31] Their structures based on Pb^{2+} ions and TCPP scaffolds differ in the framework topologies and conformations of porphyrin rings depending on the porphyrin metals (Figure 5). The different M-TCPP ligands manipulate the coordination networks via affecting the organization ways of the TCPP ligands and the coordination spheres of Pb^{2+} ions. Influenced by the porphyrin metals, Pb^{2+} ions in the polymeric chains are varied from triply (M = H_2), triply and doubly (M = Co^{II}, Ni^{II}, and Cu^{II}) to doubly (M = $V^{IV}O$) bridged by the carboxyl oxygen atoms in the five networks. On the other hand, the coordination driving force between TCPP and Pb nodes inversely affects the configurations of porphyrin rings. The combination of these two effects subsequently generates different networks, which complement the short output on the direction role of porphyrin metals in the construction of porphyrinic MOFs.

The Zhou and Yaghi groups independently employed M-TCPP (M = H_2, Fe, Mn, Co, Ni, Cu, and/or Zn) as bridging ligands and {Zr_6} metal clusters as connecting nodes to construct a series of highly stable three-dimensional (3D) hemelike MOFs, designated as PCN-222 (PCN = porous coordination network) or MOF-545.[32,33] The twisting connection between M-TCPP ligands and 8-branched {Zr_6} clusters, resulting in 3D coordination networks of *csq* topology, contains very large 1D open channels with diameters of up to 3.7 nm (Figure 6). The Yaghi group is also able to isolate another porphyrinic MOF [$Zr_6O_4(OH)_4(TCPPH_2)_3$] (MOF-525) of *ftw* topology based on TCPP ligands and {Zr_6} clusters.[33] MOF-525 consists of {$Zr_6O_4(OH)_4$} cuboctahedral units linked by porphyrin ligands in O_h symmetry (Figure 7).

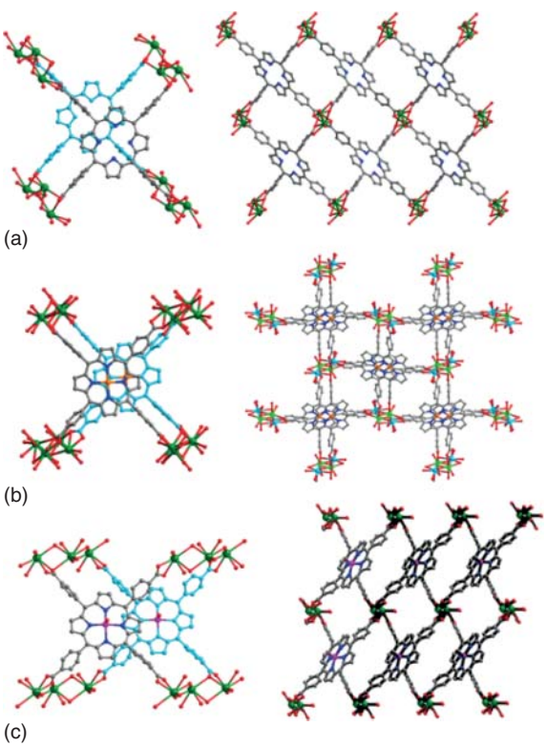


Figure 5 Stacking models of the porphyrin rings and the structures of (a) [$Pb_2(H_2TCPP)$]; (b) [Pb_2(M-TCPP)(DMF)(H_2O)] (M = Co^{II}, Ni^{II}, and Cu^{II}); and (c) [Pb_2(VO-TCPP)($H_2O)_2$]

Lang and coworkers utilized TPPS (5,10,15,20-tetrakis(4-sulfonatophenyl)porphyrin) and Pd-TPPS ligands to connect with lanthanide ions to build rare-earth layered hydroxides with intercalated tetrasulfonated porphyrins, $Ln_2(OH)_{4.7}(TPPS)_{0.33}$ (Ln = Eu^{3+}, Tb^3).[34] In the structure of $Eu_2(OH)_{4.7}(TPPS)_{0.33}$, the distorted octahedral oxometalate cluster $[Eu_6(\mu_6\text{-}O)(\mu_3\text{-}OH)_8(H_2O)_{14}]^{8+}$ SBUs are connected with six distorted porphyrin units (Figure 8). It is interesting that the original SBU loses

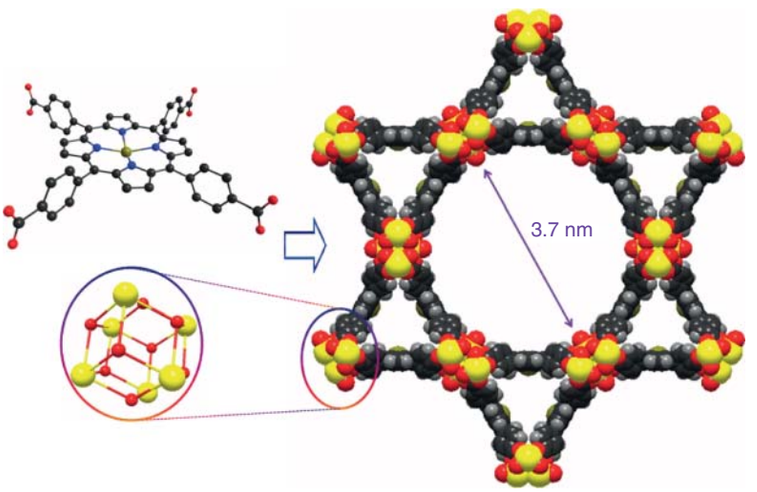


Figure 6 Self-assembly of highly stable 3D porphyrinic networks with large 1D opening channels by M-TCPP linking up $\{Zr_6\}$ clusters

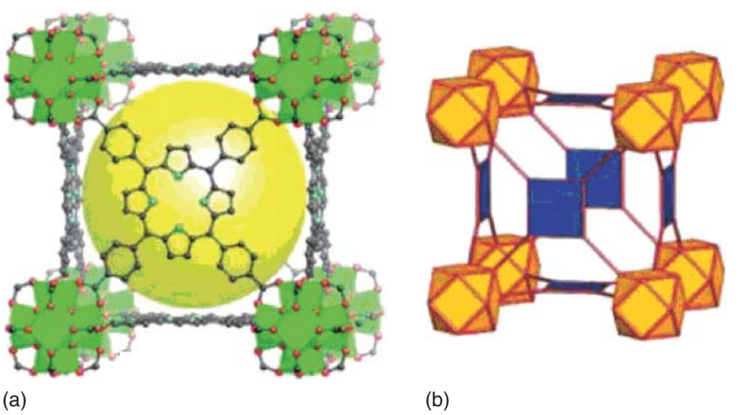


Figure 7 Crystal structure (a) and *ftw* topology net (b) of MOF-525

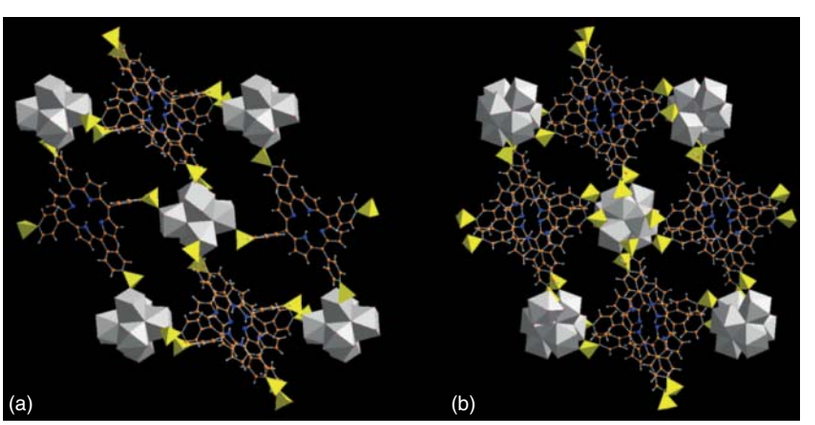
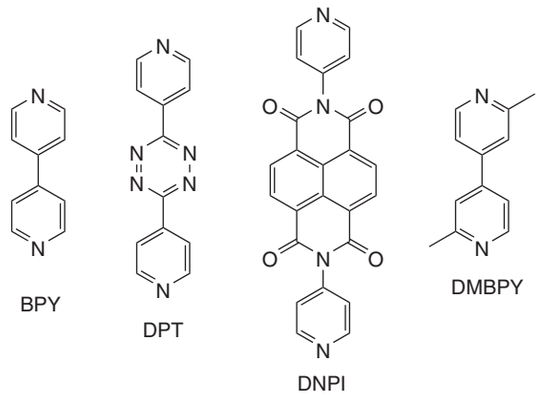


Figure 8 Polyhedral and ball-and-stick representations of the structures of MOF-Eu-TPPS (a) and its dehydrated product (b) as viewed along the *b* axis



Scheme 2 The ligands used in the synthesis of 3D pillared porphyrinic frameworks

both the coordinated water molecules and the central μ_6-O atom during activation. Such activation let the octahedral $[Eu_6(\mu_6\text{-}O)(\mu_3\text{-}OH)_8(H_2O)_{14}]^{8+}$ SBU transform into a trigonal antiprismatic $[Eu_6(\mu_3\text{-}OH)_8(H_2O)_2]^{10+}$ SBU in the resulting none porous material.

The Choe group constructed a series of porphyrinic MOFs based on porphyrin ligands M-TCPP and the secondary N-heteroaromatic ligands (Scheme 2).[25] The assembly of the biligand porphyrinic MOFs can be divided into two steps. At first, the carboxyl arms of TCPP are connected with metal centers to form paddle wheel $M_2(COO)_4$ (M = Zn, Co) SBUs for the construction of 2D layered networks (Figure 9). Secondly, the bidentate N-heteroaromatic ligands connect with the axial sites of $M_2(COO)_4$ (M = Zn, Co) SBUs into different 3D porphyrinic MOFs depending on the second bidentate N-heteroaromatic ligands.

In general, when a small pillar, such as triethylene diamine (DABCO), is employed, the 3D network is seldom interpenetrated. If the pillaring ligands are long enough, such as BPY, DNPI, and DPT, the porphyrinic MOFs will interpenetrate in multiple stacking arrangements. For examples, by selecting diverse metalloporphyrin linkers and BPY as pillars, three classes of stacking patterns were found in this set of materials, including AA, AB, and ABBA types.[35,36,38]

Because there are two kinds of metal sites of metalloporphyrins and paddle wheel $M_2(COO)_4$ metal clusters that are available to combine with pillaring ligands, the 2D porphyrin layers can be either homogeneously or heterogeneously pillared. Homogeneous pillaring means that two $M_2(COO)_4$ SBUs are connected by a dipyridyl pillar, whereas the heterogeneous pillaring connection occurs between $M_2(COO)_4$ cluster and TCPP linker.[36] If porphyrin metals do not have the ability to coordinate to pillaring ligands, such as Pd ions in TCPP, only homogeneous pillaring occurs between two porphyrin layers, as observed in PPF-5.[36]

Generally speaking, because pillaring ligands cannot distinguish paddle wheel metal and porphyrin metal sites, it is difficult to control the pillaring ways in porphyrinic MOFs, even homogeneous and heterogeneous pillaring can occur in a network, such as in PPF-4, $[Zn_2(ZnTCPP)(bpy)_{1.5}]$.[36] However, given the fact that porphyrin metals lie in the macrocycle plane, the structures of porphyrinic MOFs are very sensitive to the steric hindrance of pillaring ligands. The Choe group has simply methylated BPY to form DMBPY ligand, which enable the pillars to selectively coordinate to just paddle wheel metal sites rather than porphyrin core metals (Figure 10).[37] They hypothesized that the steric repulsion of the methyl group in DMBPY can lower the association constant of the pyridyl group to porphyrin metals, leading to prior combination with paddle wheel metal ions.

When much longer pillaring ligands, such as *N*,*N*′-di-(4-pyridyl)-1,4,5,8-naphthalenetetracarboxydiimide (DPNI) and 3,6-di-4-pyridyl-1,2,4,5-tetrazine (DPT), are used in the connection of 2D porphyrin layers, the

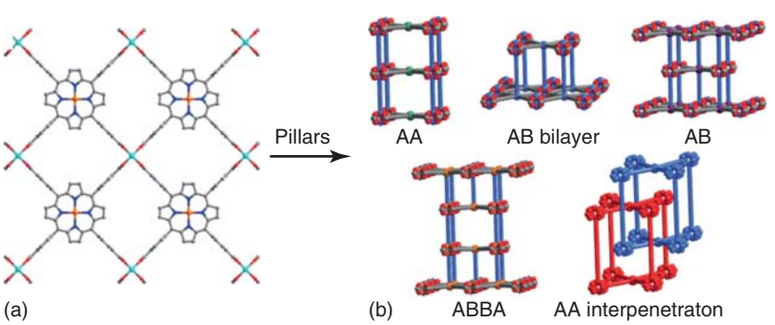


Figure 9 (a) The 2D porphyrin sheet formed from M-TCPP linking up paddle wheel $M_2(COO)_4$ SBUs; (b) The stacking patterns found in pillaring porphyrinic MOFs

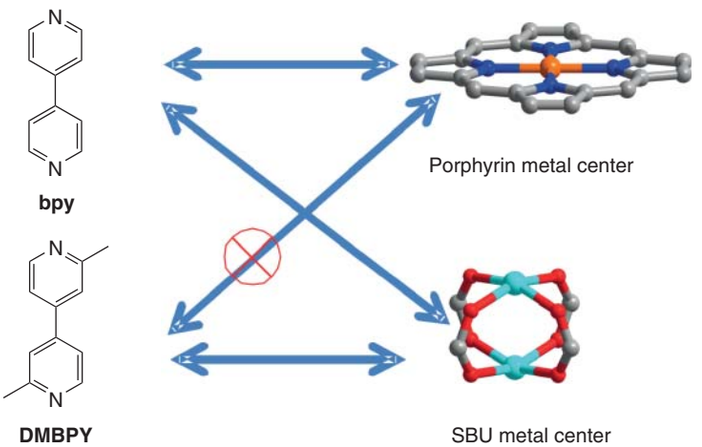


Figure 10 Schematic representation of the selective coordination ability of DMBPY and BPY between different metal centers

topologies of the resulting porphyrinic MOFs are varied form bilayer to interpenetrated networks.[38] It is interesting that the longer pillaring ligands in porphyrinic MOFs can be exchanged by shorter ligands with succeeded parent topological structures.[39] Owing to the porous nature of the porphyrinic MOFs PPF-18 and PPF-20, smaller dipyridyl linkers (BPY) can enter the interior pores by diffusion and subsequently replace the present longer pillaring DPNI units to form porphyrinic MOFs PPF-27 and PPF-4, respectively. Such replacement transformation strategy is valuable in stepwise control over the topologies of porphyrinic MOFs.

The Hupp group developed a series of dipyridyl porphyrins (F-H_2DPyP, DA-H_2DPyP) as pillars to connect with paddle wheel $M_2(COO)_4$ SBUs. Taking the free-base dipyridyl porphyrin and tetratopic carboxylate as building blocks, they synthesized the highly porous Zn(porphyrin)-based material F-ZnP and DA-ZnP.[40] The frameworks are constructed from sheets formed by the tetracarboxylate acid ligand (TCPB) with paddle wheel zinc nodes, pillared by dipyridyl porphyrin struts (Figure 11).

The Hupp group also used two kinds of porphyrin ligands, M^1-TCPP and F-M^2DPyP, as building blocks, to develop an extended family of porphyrinic MOFs that directly incorporate a series of metalloporphyrins (Figure 12).[41] The frameworks with two kinds of porphyrin metals formed by M^1-TCPP connecting with paddle wheel zinc nodes and pillared by dipyridyl F-M^2DPyP have large accessible channels and multiple active metal sites for catalytic application.

Polyoxometalates (POMs) are a unique class of discrete anionic metal–oxygen clusters, which attracted great interest because they can act as functional constituents in variety of solid materials. POMs have abundant oxygen donors on the cluster surfaces, which are effective inorganic ligands for the construction of organic–inorganic hybrid materials. However, the combination of POMs and porphyrins in hybrid materials is very difficult because of their adverse solubilities in either hydrophilic or hydrophobic solvents.

The Zubieta group employed hydrothermal synthesis method to synthesize POM-porphyrin-based hybrid materials by improving their solubility under hydrothermal conditions.[42] The hydrothermal treatment of MoO_3, $Cu(NO_3)_2$, TPyP in H_2O afforded a hybrid material of $[Cu(TPyP)Cu_2Mo_3O_{11}]$. Its 3D structure consists of 2D porphyrin networks that are linked by bimetallic oxide chains (Figure 13). When $FeCl_2$ was used instead of $Cu(NO_3)_2$ in the hydrothermal reaction, a hybrid material $[\{Fe(TPyP)\}_3Fe(Mo_6O_{19})_2]\cdot xH_2O$ was isolated as a 3D $[\{Fe(TPyP)\}_3Fe]_n^{4n+}$ host framework containing isolated $\{Mo_6O_{19}\}^{2-}$ guests in the cavities.

Recently, Wu and coworkers developed an effective synthetic strategy for the construction of POM-porphyrin hybrid materials under mild conditions.[43] They first reacted porphyrins with POMs to form zwitterion intermediates. The resulting zwitterions are soluble in either hydrophilic or hydrophobic solvents, which can overcome the discrepant solubilities of the two building components. On the basis of this strategy, they successfully constructed a 2D porphyrin-POM hybrid framework, $\{[Cd(MnTPyP)](PW_{12}O_{40})\}$, built from Cd-Mn-TPyP layers and interlayer inserted $[PW_{12}O_{40}]^{3-}$ anions.

Porphyrins can be encapsulated in the pores of coordination frameworks used as guests or templates in "one-pot" synthesis procedure. Such in situ formed framework materials are shaped in a "ship-in-a-bottle" configuration, which can stabilize the active metalloporphyrin sites in catalysis to mimic enzyme in organisms

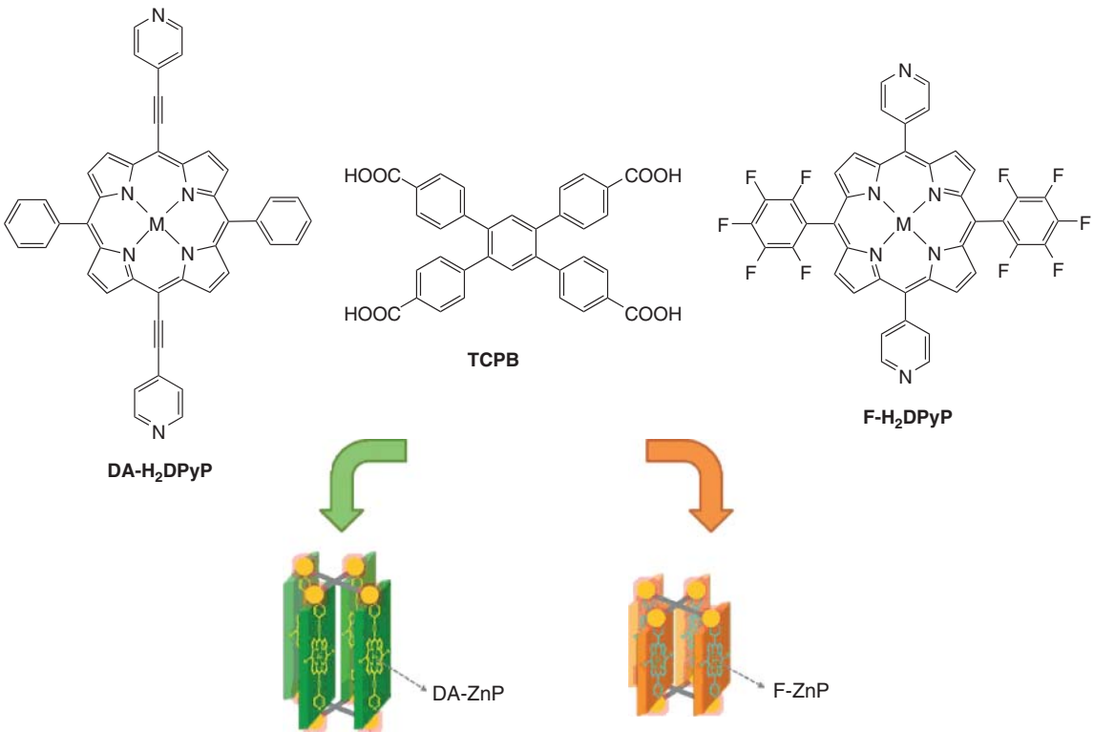


Figure 11 Schematic representation of porous F-MOF (F-ZnP) and DA-MOF (DA-ZnP), and their building ligands

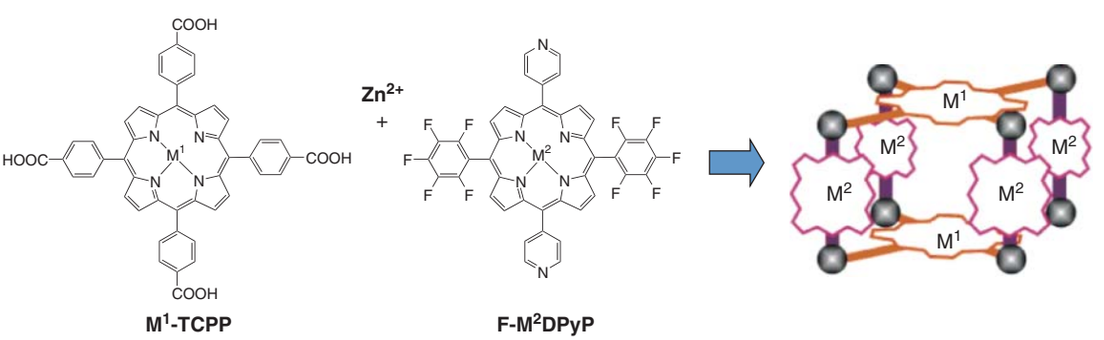


Figure 12 Schematic representation of the construction of porous porphyrinic MOFs with two kinds of metalloporphyrins [$M^1 = 2H$, Pd, Al(OH) or Fe(Cl), $M^2 = 2H$ or Mn(Cl)]

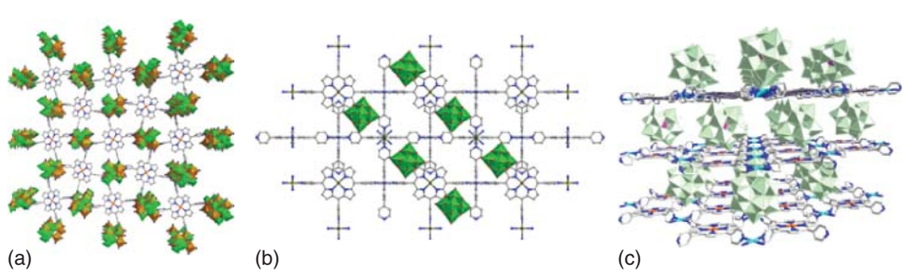
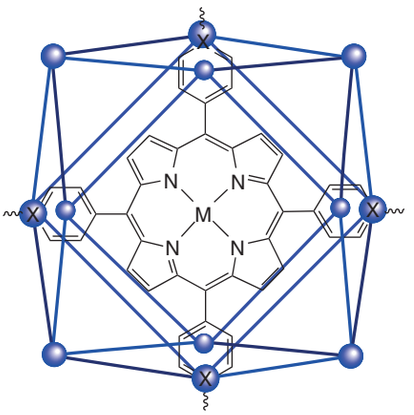


Figure 13 Crystal structures of POM-porphyrin hybrids: (a) $[Cu(TPyP)Cu_2Mo_3O_{11}]$, (b) $[\{Fe(TPyP)\}_3Fe(Mo_6O_{19})_2] \cdot xH_2O$ and (c) $\{[Cd(MnTPyP)](PW_{12}O_{40})\}$

(Scheme 3). Eddaoudi *et al.*[44] utilized an indium-imidazoledicarboxylate-based *rho*-ZMOF as a host and 5,10,15,20-tetrakis(1-methyl-4-pyridinio)porphyrins (H_2TMPyPs) as guests to generate a unique and tunable catalyst platform of H_2RTMPyP (Figure 14). The free-base porphyrins are readily available for metallation by various transition metal ions via postsynthesis. Anchoring and isolating catalytically active metalloporphyrins in the pores of MOFs can prevent their self-dimerization and degradation in oxidative catalysis.

Larsen *et al.*[45] used HKUST-1 as a host matrix to encapsulate catalytically active metalloporphyrins (either Fe^{3+}-tetrakis(4-sulphonatophenyl)porphyrin (Fe_4SP) or Mn_4SP) in "ship-in-a-bottle" manner by occupying one of the three nanoscale cages, named as MOMzyme-1 (Figure 15). The remaining cavities allow small molecules to access the active sites in catalysis, such as the channels in heme proteins.

The Zaworotko group used meso-tetra(N-methyl-4-pyridyl)porphyrin tetratosylate (TMPyP) as template to construct a series of metal–organic materials (MOMs) by reaction of benzene-1,3,5-tricarboxylate with transition metals (M = Fe, Mn, Co, Ni, Mg).[46] The resulting materials, porph@MOMs, as shown in Figure 16, by selectively



Scheme 3 Schematic presentation of "ship-in-a-bottle" porphyrin@MOFs

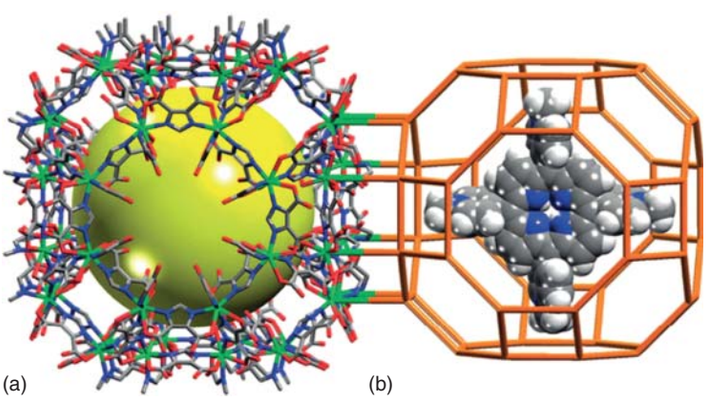


Figure 14 Crystal structure of *rho*-ZMOF (a) and schematic presentation of $[H_2TMPyP]^{4+}$ porphyrin enclosed in *rho*-ZMOF R-cage (b)

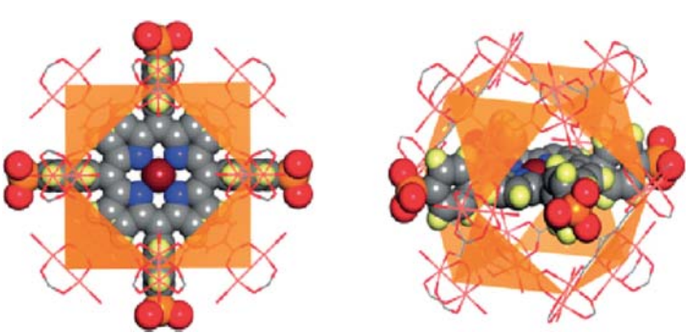


Figure 15 Diagram showing two equivalent orientations of Mn^{III}_4SP within the octahemioctahedral cage of HKUST-1 (Cu, Zn)

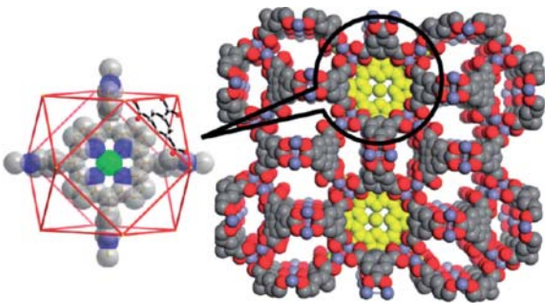


Figure 16 Illustration of porphyrin cations located in the octahemioctahedral cages

encapsulating divers metalloporphyrins in octahemioctahedral cages, can serve as the size-selective heterogeneous catalysts for oxidation of olefins.

The reaction of biphenyl-3,4′,5-tricarboxylic acid (H_3BPT) and $Cd(NO_3)_2$ with H_2TMPyP afforded Cd^{2+}-based porph@MOM P11 (Figure 17).[47] Porph@MOM P11 has a 3,6-connected *rtl* net, which is built from two 6-connected $[Cd_2(COO)_6]^{2-}$ MBBs. Cationic porphyrins are encapsulated in the micropores by occupying the alternating channels, whereas the remaining channels are occupied by solvent molecules. Porph@MOM P11 was proved to be a potential versatile platform with tunable functions for applications by undergoing metal ion exchange in a single-crystal to single-crystal manner.

3 APPLICATIONS OF PORPHYRINIC MOFs

As an emerging class of porous functional materials that consist of porphyrin building units, porphyrinic MOFs definitely comprehend the properties in their original application fields. The applications of porphyrinic MOFs include gas storage and separation, selective sorption of guest molecules, nanofilms, and light harvesting. Moreover, the well-known homogeneous biomimetic catalysis capabilities of metalloporphyrins make porphyrinic MOFs to emerge as efficient heterogeneous catalysts. The size- and/or shape-selective heterogeneous catalytic application is a logical target for researches on porphyrinic frameworks, which served as Lewis acid, oxidation, and photoactive catalysts.

3.1 Gas Storage and Separation

The Choe group revealed that PPF-1, Zn_2(ZnTCPP), a 2D porphyrin framework, assembled from Zn-TCPP and paddle wheel $Zn_2(COO)_4$ SBUs, has Langmuir surface area of 622.4 $m^2\,g^{-1}$.[48] The high-pressure H_2 adsorption experiment suggests that the hydrogen uptake of PPF-1 is of 2.0 wt% at 20 bar, which corresponds to 9.8 H_2 molecules adsorbed per formula unit.

Ma and coworkers studied the gas storage and separation abilities of MMPF-1.[27] MMPF-1 exhibits interesting selective adsorption of H_2 and O_2 over N_2, and CO_2 over CH_4. The interesting molecular sieving effect observed for MMPF-1 should be attributed to its small aperture sizes of ~3.5 Å, which exclude larger gas molecules of N_2 and CH_4, but allow the entry of smaller gas molecules of H_2, O_2, and CO_2.

MMPF-2, constructed from OCPP and cobalt trigonal prism SBUs, has BET surface area of 1410 $m^2\,g^{-1}$ as revealed by Ar adsorption experiment.[28] MMPF-2 can take up CO_2 33.4 wt% at 273 K and 19.8 wt% at 298 K under 760 torr pressure. The authors tentatively attribute the high CO_2 storage capabilities to the high density of open metal sites (~5 open cobalt sites per nm^{-3}) in MMPF-2, as open metal sites can increase the interactions between CO_2 and MOF materials.

MMPF-4 with a BET surface area of 958 $m^2\,g^{-1}$ has CO_2 storage capabilities of 24.4 wt% at 273 K and

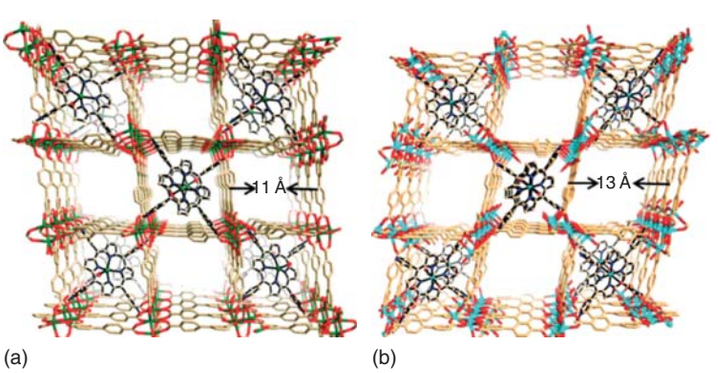


Figure 17 Crystal structures of (a) porph@MOM P11 and (b) porph@MOM P11-Cu as viewed down the *a* axis

13.2 wt% at 298 K.[29] Moreover, MMPF-4 has the selective uptake capacity of CO_2/N_2 (41:1) at 273 K and 1 bar. Such property renders MMPF-4 for potential separation of CO_2/N_2 in postcombustion flue-gas streams that are typically composed of 15% CO_2 and 85% N_2. MMPF-5 does not exhibit significant uptakes of Ar, N_2, and O_2 at either 77 or 87 K, but has a substantial CO_2 adsorption capacity of 67 $cm^3\ g^{-1}$ at 273 K because of the partial framework collapse after removal of the guest solvent molecules in the pores.[29]

Matsunaga *et al.*[49] report a series of isostructural porphyrinic metal carboxylate frameworks, $[Cu_2(MDDCPP)]$ ($M = Zn^{2+}$, Ni^{2+}, Pd^{2+}, $Mn^{3+}(NO_3)$ and $Ru^{2+}(CO)$), possessing an internal spherical cavity of about 20 Å in diameter. The internal cavity is surrounded by a total of 16 accessible metal sites from 8 metalloporphyrins and 8 paddle wheel $Cu_2(CO_2)_3$ SBUs. The multiple accessible metal sites let these porphyrinic MOFs take up hydrogen molecules of 0.81, 1.03, 0.55, 1.05, and 1.16 wt% at 77 K and 0.1 MPa for the analogs of Zn, Ni, Pd, Mn, and Ru in porphyrin, respectively. The order of H_2 uptakes is in good agreement with the almost linearly correlated order of BET surface area.

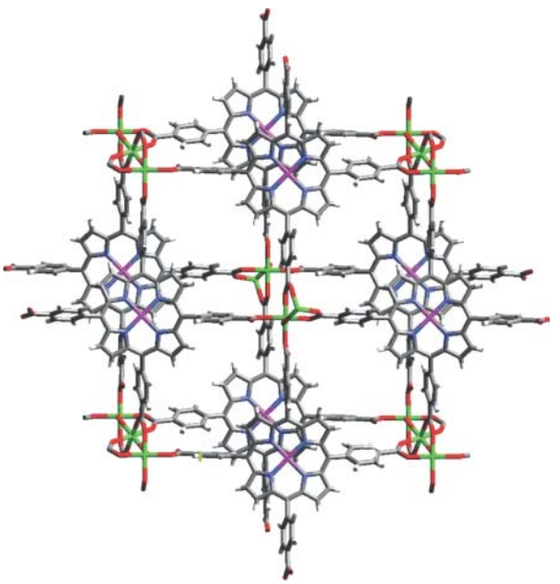


Figure 18 The crystal structure of PIZA-1

3.2 Selective Sorption of Guest Molecules

The porphyrinic framework PIZA-1, synthesized by the Suslick group, as shown in Figure 18, possesses a single and independent network with large bidirectional oval-shaped channels (9×7 Å^2) and another set of channels (14×7 Å^2).[50] The evacuated host framework, PIZA-1, has excellent size and shape selectivity to incorporate amines and alcohols. PIZA-1 has ultrahigh and rapid capacity for selective adsorption of water repeatedly, which cannot be matched by inorganic molecular sieves. Owing to the high hydrophobicity and strong coordinating ability, *n*-hexylamine was not substantially adsorbed by PIZA-1. However, nonpolar guests, such as *n*-hexane, can be sufficiently absorbed by successive washing of the solid with progressively higher concentrations of hexane in pyridine. The authors ascribed the phenomenon to the hydrophilic molecules that can maintain the porosity and let the hydrophobic guests enter the channels of PIZA-1.

3.3 Nanofilms by Layering Porphyrinic MOF Sheets

To facilitate the applications of MOFs in nanotechnological devices, such as sensors, catalysts, and electrodes, the highly ordered microporous MOFs were rationally fabricated as ultrathin films with well-ordered growth direction and film thickness, which opens an important way for their practical applications. As porphyrinic materials have the functions in various aspects, layering porphyrinic MOFs on suitable substrates for the formation of nanofilms has great prospects.

NAFS-1, consisting of metalloporphyrin building blocks, experienced the facile bottom-up fabrication at ambient conditions. The Kitagawa group has constructed the preferentially well-oriented MOF nanofilm on a solid surface (Figure 19).[51] Integration in a modular manner by a layer-by-layer (LbL) growth technique coupled with the Langmuir-Blodgett (LB) method, they could grow nanofilms of NAFS-1 with any desired thickness by repetitive process of successive sheet deposition and rinsing/solvent immersion. By employing free-base porphyrin MBBs and metal ion joints that retain the same in-plane molecular arrangement other than NAFS-1, they were able to fabricate highly crystalline MOF nanofilms (NAFS-2) under mild conditions on both gold and silicon surfaces.[52] The stacking topology can be fine-tuned by introduction of suitable additive, on the removal of the axially coordinated water, because the interlayer interactions in the nanofilms are weakly adhered to each other.

3.4 Light Harvesting and Energy Transfer

As part of the energy migration process, natural photosynthesis occurs through highly ordered porphyrinic pigments (chlorophylls). Hence, crystalline MOFs assembled from photoactive porphyrins might exhibit light-harvesting behavior that is similar to the natural photosynthesis system.

Hupp and coworkers have found that the molecular-exciton migrations in two Zn porphyrinic MOFs

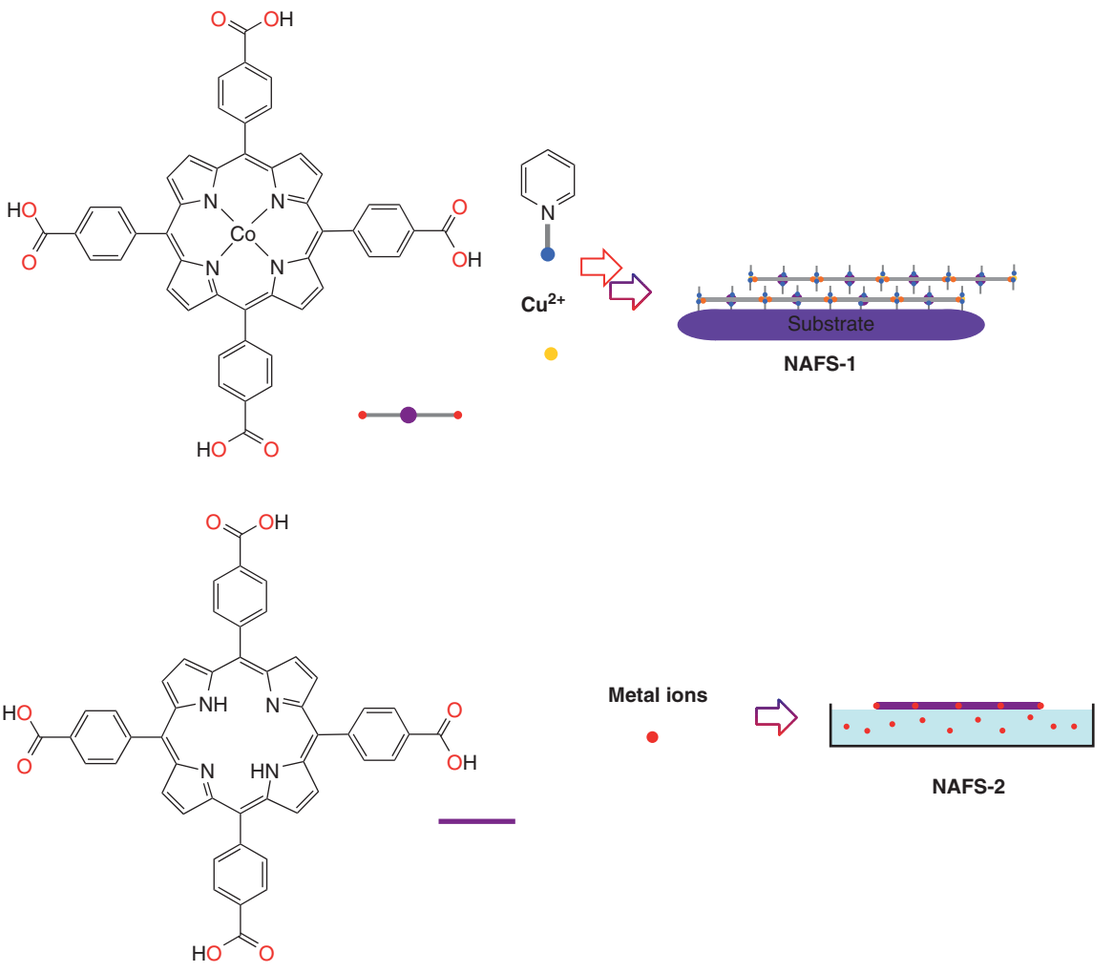


Figure 19 Schematic illustration of the assembly processes of NAFS-1 (a) and NAFS-2 (b)

(DA-MOF and F-MOF) are significantly anisotropic.[41] The translation is about a roughly 16-fold difference in the number of potential fluorophores visited by excitons in the two MOFs. The average numbers of chromophore-to-chromophore hops by singlet excitons are significantly affected by various factors, such as the symmetry, and the conjugation between organic groups. The difference results in greater dipolar coupling in DA-MOF and a larger overlap integral by engendering greater Q-band oscillator strength and better absorption/emission spectral overlap.

To break the coverage limitation of the absorption bands of porphyrinic MOFs in the visible spectral range for light-harvesting application, Hupp and coworkers used CdSe/ZnS core/shell quantum dots (QDs) to enhance light harvesting via energy transfer from QDs to porphyrinic MOFs.[53] The broad absorption band of the QDs in the visible region offers greater coverage of the solar spectrum by QD-MOF hybrid. Time-resolved emission studies showed that photoexcitation of the QDs is followed by energy transfer to the porphyrinic MOFs with efficiencies of more than 80%. This sensitization approach by a monolayer of QDs on the surface of the MOF can result in >50% increase in the number of photons harvested by a single monolayer MOF.

3.5 Heterogeneous Catalysis

Metalloporphyrins are widely and intensely investigated as models of enzymes such as catalase, peroxidases, and P450 cytochromes. The combination of metalloporphyrins as building blocks of porphyrinic MOFs renders them have the property to act as shape- and size-selective heterogeneous catalysts. To date, a number of porphyrinic MOFs were emerged as efficient catalysts in a range of reactions, especially in the oxidation of various

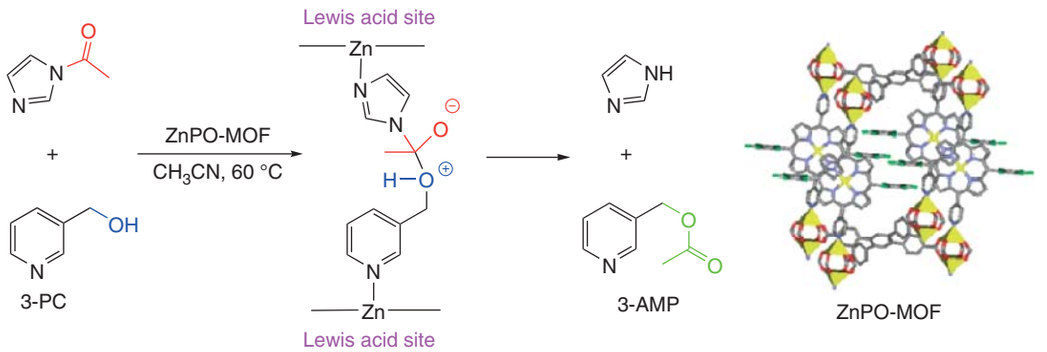


Figure 20 Schematic presentation of Lewis-acid-site-promoted catalysis in porous ZnPO-MOF

organic molecules, by mimicking the behaviors of P450 cytochromes in organisms.

3.5.1 *Lewis Acid Catalysis*

Assembly of zinc nitrate with F-H_2DPyP under solvothermal conditions afforded purple block crystals of ZnPO-MOF (Figure 20).[54] ZnPO-MOF has large 3D channels and high degree of porosity. The catalytic property of ZnPO-MOF was demonstrated by the acyl-transfer reaction between *N*-acetylimidazole (NAI) and 3-PC. The catalytic acyl-transfer reaction revealed ~2400-fold rate enhancement, contributed from Lewis acid activation and reactant preconcentration originated from large pores and fully reactant-accessible active sites in the porphyrinic MOF.

Wu and coworkers demonstrated that the porphyrinic MOF $[Zn_2(HCOO)(Fe^{III}(H_2O)$-TCPP)], constructed from paddle wheel $Zn_2(COO)_4$ SBUs, Fe^{III}-TCPP and formate ligands, is an efficient catalyst in the intermolecular aldol reaction of aldehydes and ketones (Figure 21).[55] The yields of aldol products are excellent (up to 99%). The catalytic efficiency is superior to its homogeneous constituents, such as FeCl-Me_4TCPP, $Zn(NO_3)_2$, and $FeCl_3$.

3.5.2 *Oxidation Catalysis*

Suslick *et al.*[16] found that the porphyrinic MOF, PIZA-3, is capable to heterogeneously oxidize a range of linear and cyclic alkanes and epoxidize cyclic alkenes. The oxidation performance is moderate, which is similar to the homogeneous or heterogeneous Mn^{III}-porphyrin catalysts. Since PIZA-3 did not have shape-selective property in the reaction, the authors concluded that the catalysis occurred on the exterior surface instead of inside the pores. Their hypothesis was proved by subsequent control experiment. They added the bases that are too peripherally bulky to

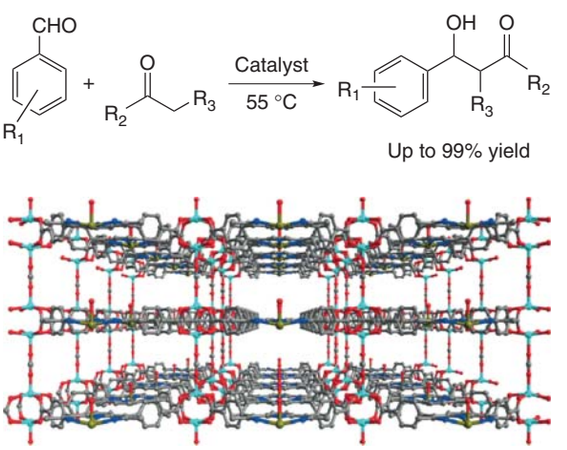


Figure 21 Aldol reaction of aldehydes with ketones catalyzed by $[Zn_2(HCOO)(Fe^{III}(H_2O)$-TCPP)]

access the pores (e.g., 3,5-di-bromo-pyridine or 1-phenylimidazole), but capable of coordinating to the surface porphyrin Mn sites, which substantially slowed down the catalysis rate.

It is a critical aspect to obtain porphyrinic frameworks that have both permanent porosity and internally accessible active sites for catalytic application. The Hupp group reports an extended family of porphyrinic MOFs that directly incorporate divers metal ions of Al^{3+}, Zn^{2+}, Pd^{2+}, Mn^{3+}, and Fe^{3+} in porphyrins.[42] The active sites in the large channels of these robust porphyrinic materials (RPMs) are readily accessible to substrate molecules. As an illustrative example, the manganese-containing RPM is catalytically competent for oxidation of styrene and cyclohexane. **ZnMn-RPM** is much superior to the homogeneous counterpart 5,10,15,20-tetrakis(pentafluorophenyl)porphyrin-MnCl (TPFPP(MnCl)) in term of the catalytic activity and stability.

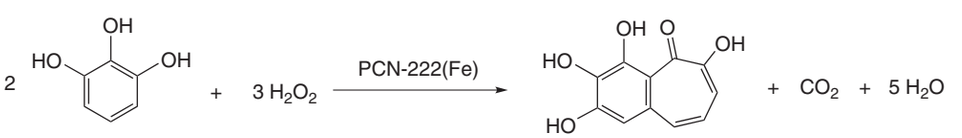
Wu and coworkers synthesized a porous Pd-MOF, assembled from Pd^{II}-porphyrins and cadmium(II) connecting nodes.[56] Pd-MOF incorporated porphyrin palladiums in the pores, underwent interesting single-crystal to single-crystal transformations from the solvent inclusion to solvent free to solvent inclusion frameworks, which conferred its high framework stability. The framework-immobilized solid showed significant styrene oxidation activity (100% conversion) for the selective formation of acetophenone (91% selectivity).

The POM-Mn^{III}-porphyrin based hybrid material {[Cd(MnTPyP)]($PW_{12}O_{40}$)}, consisting of catalytically active Mn^{III}-TPyP species and interlayered POMs, can efficiently oxidize alkylbenzene with tertbutylhydroperoxide (TBHP) oxidant.[44] {[Cd(MnTPyP)]($PW_{12}O_{40}$)} oxidized ethylbenzene to form one product of acetophenone (92.7% yield), which is superior to those of its precursors, such as Mn^{III}Cl-TPyP (73.6% yield of acetophenone) and $[PW_{12}O_{40}]^{3-}$ (not active). {[Cd(MnTPyP)]($PW_{12}O_{40}$)} also presents excellent size selectivity in the oxidation of a series of alkylbenzene.

To compare the catalytic efficiency of either metal nodes and/or porphyrin metals in porous porphyrinic frameworks, Wu and coworkers studied the catalytic activities of three isostructural porphyrinic MOFs ZJU-18, -19, and -20 in the oxidation of alkylbenzene.[30] ZJU-18 exhibits high efficiency in selective oxidation of alkylbenzene, in which 99% yield was realized for the transformation of ethylbenzene to acetophenone. The catalytic activity is much higher than that of ZJU-19 with active metal nodes only and that of ZJU-20 with active metalloporphyrin only. ZJU-18 is much superior to the molecular Mn^{III}Cl-Me_8OCPP counterpart in terms of catalytic activities (>99% for ZJU-18 vs 16% for Mn^{III}Cl-Me_8OCPP) and stabilities (sustained 15 cycles vs deactivated at the third cycle).

Zhou and coworkers demonstrate that a highly stable, mesoporous PCN-222(Fe) meets the prerequisites for biomimetic catalytic application (Scheme 4).[32] PCN-222(Fe) shows good peroxidase-mimic catalytic activity in the oxidation of pyrogallol, 3,3,5,5-tetramethylbenzidine, and o-phenylenediamine. The excellent catalytic performance of PCN-222(Fe) is attributed to the stable 3D structure with large open channels of 3.7 nm in diameter to increase the diffusion rate of substrates.

Wu and coworkers evaluated solid-surface-promoted heterogeneous catalytic property of porphyrinic



Scheme 4 Oxidation reaction of pyrogallol catalyzed by PCN-222(Fe)

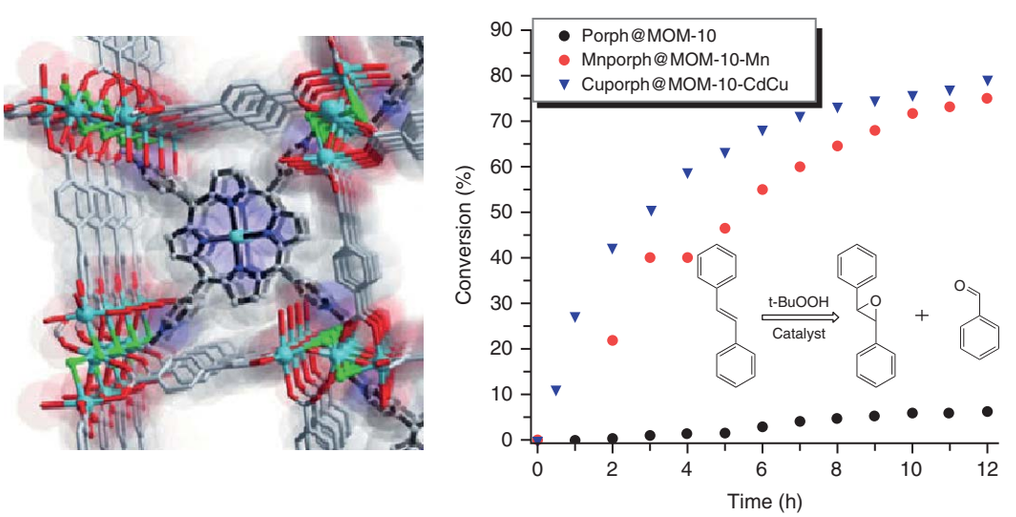


Figure 22 Comparison of the catalytic activities of porph@MOM-10, Mnporph@MOM-10-Mn, and Cuporph@MOM-10-CdCu in epoxidation of trans-stilbene

frameworks $[M_2(HCOO)_2(Mn^{III}\text{-TCPP})]$ (M = Zn or Cd) in selective epoxidation of olefins.[56] $[Zn_2(HCOO)_2(Mn^{III}\text{-TCPP})]$ is highly active for the epoxidization of a number of olefins with different sizes and dimensions. $[Zn_2(HCOO)_2(Mn^{III}\text{-TCPP})]$ can even activate the inert cyclohexane molecules at room temperature with 20.6% substrate conversion. Considering that the catalytic sites are inaccessible to substrate molecules, the authors designed a series of control experiments to confirm that the catalysis occurred on the solid surfaces, such as the particle and substrate size effect in catalysis.

Eddaoudi and coworkers developed a strategy for heterogenerization of porphyrin catalysts by impregnating free-base porphyrins into the pores of MOFs, and the catalytic function was realized by subsequent metalation with active metal ions of Mn, Cu, Zn, and Co via postsynthesis.[44] They proved that the H_2RTMPyP platform was efficient in heterogeneous cyclohexane oxidation. Mn-RTMPyP oxidized cyclohexane to cyclohexanol/cyclohexanone in 91.5% yield with turnover number of 23.5, based on the amount of oxidant consumption, which is noticeably higher than other systems of supported metalloporphyrins on zeolites or mesoporous silicates.

Zaworotko and coworkers proved that porph@MOM-10 is a versatile platform to serve as the parent of a series of porph@MOMs by exchanging with various metal ions.[57] The Mn-exchanged porph@MOM, Mnporph@MOM-10-Mn, efficiently epoxidized trans-stilbene into stilbene oxide and benzaldehyde (56% and 21% yields, respectively) with TBHP as the oxidant (Figure 22). Its catalytic efficiency is comparable to the activity of homogeneous Mn^{III}-TMPyP. The postmodified Cuporph@MOM-11-CdCu afforded 61% and 19% yields of stilbene oxide and benzaldehyde, respectively.

Zaworotko and coworkers also studied the epoxidation property of porph@MOM-4, containing "ship-in-a-bottle" encapsulated metalloporphyrins.[47] Porph@MOM-4 efficiently oxidizes ~85% styrene substrate into 30% styrene oxide and 57% benzaldehyde, whereas the homogeneous catalyst Fe^{III}-TMPyP only let ~35% conversion under the same conditions. To prove porph@MOM-4 has size selectivity, they studied the oxidation efficiency of larger-sized substrates such as trans-stilbene and triphenylethylene. Accompanying the increase in substrate size, there was a decrease in conversion. These results are consistent with the pore windows ($\sim 9 \times 9$ Å^2) of porph@MOM-4 that can select small substrate to enter the cages.

3.5.3 *Photocatalysis*

The Wu group utilized a photoactive tin(IV)-porphyrin (Sn^{IV}TPyP) as building blocks to construct a novel 3D porous porphyrinic MOF Sn-MOF.[58] In the crystal structure, tin(IV)-porphyrin struts link up Zn ions to form lamellar networks that are further connected by

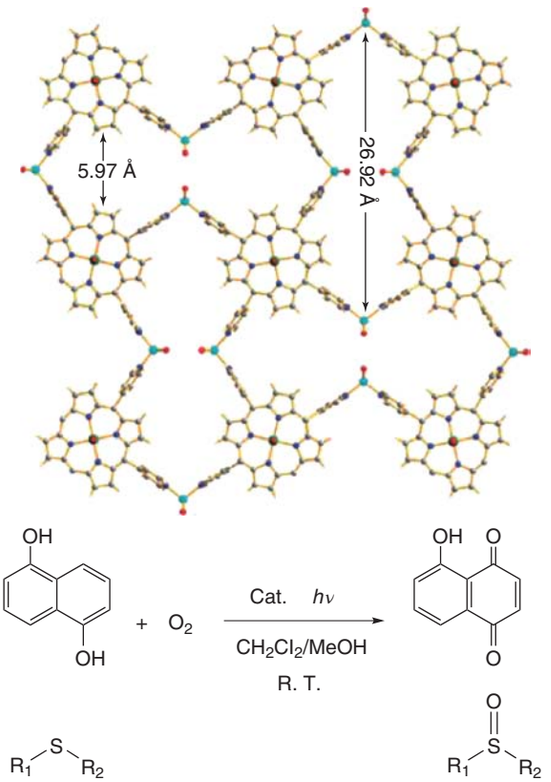


Figure 23 The structure of Sn-MOF and its application in photooxidation of phenol and sulfides

formates to coordinate to the Sn^{IV} centers (Figure 23). Sn-MOF presents remarkable photocatalytic activities in the oxygenation of phenol and sulfides under viable light irradiation, resulting in almost quantitative conversions with remarkable selectivity (>99%) in heterogeneous phases. When the homogeneous counterpart $Sn^{IV}(OH)_2$TPyP was used as a catalyst under identical conditions, the conversion of phenol is 98%, whereas TPyP and $Zn(NO_3)_2$ only generated trace amounts of the products. Moreover, the recovered $Sn^{IV}(OH)_2$TPyP is inactive after three cycles due to its self-oxidation, whereas Sn-MOF is recycled for six runs without loss of its catalytic activities because $Sn^{IV}(OH)_2$TPyP moieties are well-separated in the pores. This work demonstrates that immobilization of photoactive sites in the channel walls of porous porphyrinic MOFs can achieve outstanding photocatalytic performances in heterogeneous phases.

4 CONCLUSIONS

Metalloporphyrins are a kind of functional molecules that have robust structures, which are an ideal

class of building blocks for the construction of crystalline coordination networks. Controlled by the coordination driving force between porphyrin struts and metal nodes as well as their coordination geometries, a variety of porphyrinic MOFs have emerged as functional materials. Many porphyrinic MOFs are thermally robust and permanently porous on removal of solvent molecules. Primary researches on the properties and applications of porphyrinic MOFs revealed that they are the very promising materials for practical applications. The application fields of porphyrinic MOFs are varied from hydrogen storage, selective adsorption, nanofilm, to heterogeneous catalysis. It is remarkable that porous porphyrinic MOFs present interesting shape and size selectivity in various catalytic reactions, besides their superior high catalytic activities and stabilities. Being a class of crucial functional materials, porphyrinic MOFs will definitely receive more and more attention, which is ongoing in an explosive growth.

5 ACKNOWLEDGMENTS

Funding support from the NSF of China (Grant No. 21073158), Zhejiang Provincial Natural Science Foundation of China (Grant No. Z4100038), and the Fundamental Research Funds for the Central Universities (Grant No. 2013FZA3006) made the writing of this chapter possible.

6 ABBREVIATIONS AND ACRONYMS

DPNI = *N*,*N*′-di-(4-pyridyl)-1,4,5,8-naphthalene-tetracarboxydiimide; DPT = 3,6-di-4-pyridyl-1,2,4,5-tetrazine; H_2TMPyPs = 5,10,15,20-tetrakis(1-methyl-4-pyridinio)porphyrins; H_3BPT = biphenyl-3,4′,5-tricarboxylic acid; LB = Langmuir-Blodgett; LbL = layer-by-layer; MBB = molecular building block; MMPF = metal–metalloporphyrin framework; MOF = Metal–organic framework; NAI = *N*-acetylimidazole; PCN = porous coordination network; POM = Polyoxometalate; QD = quantum dot; RPM = robust porphyrinic material; SBB = supermolecular building block; TBHP = tertbutylhydroperoxide; TCPB = tetracarboxylate acid ligand; 3D = three-dimensional.

7 REFERENCES

1. J.-R. Li, R. J. Kuppler, and H.-C. Zhou, *Chem. Soc. Rev.*, 2009, **38**, 1477.
2. L. E. Kreno, K. Leong, O. K. Farha, M. Allendorf, R. P. Van Duyne, and J. T. Hupp, *Chem. Rev.*, 2011, **112**, 1105.
3. E. Coronado and G. Minguez Espallargas, *Chem. Soc. Rev.*, 2013, **42**, 1525.
4. M. D. Allendorf, C. A. Bauer, R. K. Bhakta, and R. J. T. Houk, *Chem. Soc. Rev.*, 2009, **38**, 1330.
5. J. Lee, O. K. Farha, J. Roberts, K. A. Scheidt, S. T. Nguyen, and J. T. Hupp, *Chem. Soc. Rev.*, 2009, **38**, 1450.
6. S. T. Meek, J. A. Greathouse, and M. D. Allendorf, *Adv. Mater.*, 2011, **23**, 249.
7. J. A. Shelnutt, X.-Z. Song, J.-G. Ma, S.-L. Jia, W. Jentzen, and C. J. Medforth, *Chem. Soc. Rev.*, 1998, **27**, 31.
8. M. C. Nielsen and T. Ulven, *Curr. Med. Chem.*, 2010, **17**, 3438.
9. D. Mansuy, *Coord. Chem. Rev.*, 1993, **125**, 129.
10. Z. Liu, A. A. Yasseri, J. S. Lindsey, and D. F. Bocian, *Science*, 2003, **302**, 1543.
11. I. Carmeli, A. Lewin, E. Flekser, I. Diamant, Q. Zhang, J. Shen, M. Gozin, S. Richter, and Y. Dagan, *Angew. Chem. Int. Ed.*, 2012, **51**, 7162.
12. J. Jiang, K. Kasuga, and D. P. Arnold, in 'Supramolecular Photosensitive and Electroactive Materials', ed H. S. Nalwa, Academic Press, San Diego, 2001, p.113.
13. M. Kobayashi, H. Tajiri, T. Hayashi, M. Kuroki, and I. Sakata, *Cancer Lett.*, 1999, **137**, 83.
14. S. Bella, C. Dragonetti, M. Pizzotti, D. Roberto, F. Tessore, and R. Ugo, in 'Molecular Organometallic Materials for Optics', eds. H. Bozec and V. Guerchais, Springer, Berlin, 2010, p. 1.
15. R. F. Barth, J. A. Coderre, M. G. H. Vicente, and T. E. Blue, *Clin. Cancer Res.*, 2005, **11**, 3987.
16. K. S. Suslick, P. Bhyrappa, J. H. Chou, M. E. Kosal, S. Nakagaki, D. W. Smithenry, and S. R. Wilson, *Acc. Chem. Res.*, 2005, **38**, 283.
17. K. S. Suslick, N. A. Rakow, M. E. Kosal, and J.-H. Chou, *J. Porphyr. Phthalocya.*, 2000, **4**, 407.
18. I. Goldberg, *Chem. Commun.*, 2005, **2005**, 1243.
19. I. Goldberg, *CrystEngComm.*, 2008, **10**, 637.
20. C. Zou and C.-D. Wu, *Dalton Trans.*, 2012, **41**, 3879.
21. S. J. Garibay, J. R. Stork, and S. M. Cohen, in 'Progress in Inorganic Chemistry', John Wiley & Sons, Inc., 2009, p. 335.
22. Y. Kobuke, *Eur. J. Inorg. Chem.*, 2006, **2006**, 2333.
23. A. Satake and Y. Kobuke, *Org. Biomol. Chem.*, 2007, **5**, 1679.
24. E. Iengo, E. Zangrando, and E. Alessio, *Eur. J. Inorg. Chem.*, 2003, **2003**, 2371.
25. L. DeVries and W. Choe, *J. Chem. Crystallogr.*, 2009, **39**, 229.
26. S. J. Lee and J. T. Hupp, *Coord. Chem. Rev.*, 2006, **250**, 1710.

27. X.-S. Wang, L. Meng, Q. Cheng, C. Kim, L. Wojtas, M. Chrzanowski, Y.-S. Chen, X. P. Zhang, and S. Ma, *J. Am. Chem. Soc.*, 2011, **133**, 16322.
28. X.-S. Wang, M. Chrzanowski, C. Kim, W.-Y. Gao, L. Wojtas, Y.-S. Chen, X. P. Zhang, and S. Ma, *Chem. Commun.*, 2012, **48**, 7173.
29. X.-S. Wang, M. Chrzanowski, W.-Y. Gao, L. Wojtas, Y.-S. Chen, M. J. Zaworotko, and S. Ma, *Chem. Sci.*, 2012, **3**, 2823.
30. X.-L. Yang, M.-H. Xie, C. Zou, Y. He, B. Chen, M. O'Keeffe, and C.-D. Wu, *J. Am. Chem. Soc.*, 2012, **134**, 10638.
31. C. Zou, M.-H. Xie, G.-Q. Kong, and C.-D. Wu, *CrystEngComm*, 2012, **14**, 4850.
32. D. Feng, Z.-Y. Gu, J.-R. Li, H.-L. Jiang, Z. Wei, and H.-C. Zhou, *Angew. Chem. Int. Ed.*, 2012, **51**, 10307.
33. W. Morris, B. Volosskiy, S. Demir, F. Gándara, P. L. McGrier, H. Furukawa, D. Cascio, J. F. Stoddart, and O. M. Yaghi, *Inorg. Chem.*, 2012, **51**, 6443.
34. J. Demel, P. Kubát, F. Millange, J. Marrot, I. Císařová, and K. Lang, *Inorg. Chem.*, 2013, **52**, 2779.
35. P. M. Barron, H.-T. Son, C. Hu, and W. Choe, *Cryst. Growth Des.*, 2009, **9**, 1960.
36. E.-Y. Choi, P. M. Barron, R. W. Novotny, H.-T. Son, C. Hu, and W. Choe, *Inorg. Chem.*, 2008, **48**, 426.
37. P. M. Barron, C. A. Wray, C. Hu, Z. Guo, and W. Choe, *Inorg. Chem.*, 2010, **49**, 10217.
38. H. Chung, P. M. Barron, R. W. Novotny, H.-T. Son, C. Hu, and W. Choe, *Cryst. Growth Des.*, 2009, **9**, 3327.
39. B. J. Burnett and W. Choe, *CrystEngComm*, 2012, **14**, 6129.
40. H.-J. Son, S. Jin, S. Patwardhan, S. J. Wezenberg, N. C. Jeong, M. So, C. E. Wilmer, A. A. Sarjeant, G. C. Schatz, R. Q. Snurr, O. K. Farha, G. P. Wiederrecht, and J. T. Hupp, *J. Am. Chem. Soc.*, 2012, **135**, 862.
41. O. K. Farha, A. M. Shultz, A. A. Sarjeant, S. T. Nguyen, and J. T. Hupp, *J. Am. Chem. Soc.*, 2011, **133**, 5652.
42. D. Hagrman, P. J. Hagrman, and J. Zubieta, *Angew. Chem. Int. Ed.*, 1999, **38**, 3165.
43. C. Zou, Z. Zhang, X. Xu, Q. Gong, J. Li, and C.-D. Wu, *J. Am. Chem. Soc.*, 2011, **134**, 87.
44. M. H. Alkordi, Y. Liu, R. W. Larsen, J. F. Eubank, and M. Eddaoudi, *J. Am. Chem. Soc.*, 2008, **130**, 12639.
45. R. W. Larsen, L. Wojtas, J. Perman, R. L. Musselman, M. J. Zaworotko, and C. M. Vetromile, *J. Am. Chem. Soc.*, 2011, **133**, 10356.
46. Z. Zhang, L. Zhang, L. Wojtas, M. Eddaoudi, and M. J. Zaworotko, *J. Am. Chem. Soc.*, 2012, **134**, 928.
47. Z. Zhang, L. Wojtas, M. Eddaoudi, and M. J. Zaworotko, *J. Am. Chem. Soc.*, 2013, **135**, 5982.
48. E.-Y. Choi, C. A. Wray, C. Hu, and W. Choe, *CrystEngComm*, 2009, **11**, 553.
49. S. Matsunaga, N. Endo, and W. Mori, *Eur. J. Inorg. Chem.*, 2012, **2012**, 4885.
50. M. E. Kosal, J.-H. Chou, S. R. Wilson, and K. S. Suslick, *Nat. Mater.*, 2002, **1**, 118.
51. R. Makiura, S. Motoyama, Y. Umemura, H. Yamanaka, O. Sakata, and H. Kitagawa, *Nat. Mater.*, 2010, **9**, 565.
52. S. Motoyama, R. Makiura, O. Sakata, and H. Kitagawa, *J. Am. Chem. Soc.*, 2011, **133**, 5640.
53. S. Jin, H.-J. Son, O. K. Farha, G. P. Wiederrecht, and J. T. Hupp, *J. Am. Chem. Soc.*, 2013, **135**, 955.
54. A. M. Shultz, O. K. Farha, J. T. Hupp, and S. T. Nguyen, *J. Am. Chem. Soc.*, 2009, **131**, 4204.
55. C. Zou, T. Zhang, M.-H. Xie, L. Yan, G.-Q. Kong, X.-L. Yang, A. Ma, and C.-D. Wu, *Inorg. Chem.*, 2013, **52**, 3620.
56. M.-H. Xie, X.-L. Yang, and C.-D. Wu, *Chem. Commun.*, 2011, **47**, 5521.
57. Z. Zhang, L. Zhang, L. Wojtas, P. Nugent, M. Eddaoudi, and M. J. Zaworotko, *J. Am. Chem. Soc.*, 2012, **134**, 924.
58. M.-H. Xie, X.-L. Yang, C. Zou, and C.-D. Wu, *Inorg. Chem.*, 2011, **50**, 5318.

Fluorinated Metal-Organic Frameworks (FMOFs): Concept, Construction, and Properties

Pradip Pachfule and Rahul Banerjee

CSIR-National Chemical Laboratory, Pune, India

1	Introduction	85
2	Summary	96
3	Abbreviations and Acronyms	96
4	References	96

1 INTRODUCTION

The substitution of fluorine into the organic/inorganic backbone of porous materials had been a major research topic because of its applications in various fields.[1–4] Relatively, the small size of fluorine coupled with the short C–F bond length have made C–F substitution attractive for the replacement of a number of functional groups, including C–OH, C–H, and C=O, for tuning the properties of compounds leading to various applications.[5] The most attractive feature associated with these compounds is their aqueous stability acquired through the hydrophobic nature of fluorine.[6,7] As a result, there has been a significant research attention toward the synthesis of fluorinated zeolites,[8–10] metal phosphates,[11–13] and metal-organic frameworks (MOFs).[14–17] It is to be believed that fluorine not only plays a vital role as a mineralizing agent but also favors the formation of well-crystalline phases.[18] In these fluorine-containing materials, because of smaller size of fluorine atoms (or fluoride anions), fluorine atoms can be easily accommodated within the small cavities of the three-dimensional (3D) framework.[19] Also, the trapped or coordinated fluorine atoms into the framework structures serve as stabilizing agents. In short, besides the properties such as mineralizer or structure directing agent, fluorine can give rise to 3D topologies with extra-large pores through coordination or intercalation or getting accommodated into the pores.

Fluorinated materials such as zeolites, metal phosphates, and MOFs[20] have been exploited for several applications such as water repellent and corrosion protecting surfaces.[21] Moreover, the same materials have been used for the oil spill cleanup via selective adsorption of oil and hydrocarbon over water.[22–24] Furthermore, fluorinated metal-organic frameworks (FMOFs) with porous architecture showed its applications for the selective adsorption of hydrocarbons such as methane, compared to its nonfluorinated analog.[25,26] An enhanced hydrogen adsorption enthalpy achieved for the fluorine-intercalated, carbonous compounds has been validated in the literature (Figure 1).[27] In these materials, the strong interaction of the semi-ionic C–F bonds with interacting H_2 molecules was the driving force for increased adsorption enthalpy, which leads to the higher adsorption at low pressure and elevated temperature.[14] Along this line, a report of fluorinated MOF by Omary and co-workers represented a new class of porous materials with superior volumetric gas uptake.[15] The fluorine-aligned channels present in the MOF framework have shown the unique hysteretic adsorption of H_2 into the first perfluorinated metal-organic framework (FMOF-1), which shows a promising way for filling up H_2 at high pressure but stored at lower pressure. Subsequently, Cheetham and co-workers highlighted the improved H_2 adsorption enthalpy (up to $8\,KJ\,mol^{-1}$) in the partially fluorinated MOFs, wherein fluorine-lined pores enhance the interaction with adsorbed H_2 molecules.[28,29] But, in contrary to aforementioned results, recent communications explain the decrease in overall H_2 uptake in partially fluorinated MOFs because of the decrease in pore size compared to its nonfluorinated counterparts, due to higher Van der Waals radii of fluorine (1.47 Å) than hydrogen (1.20 Å) present on ligands.[30] In one of our recent reports, we could enlighten the effect of fluorine insertion on the gas adsorption properties in partially fluorinated MOFs experimentally and using

Metal-Organic Framework Materials. Edited by Leonard R. MacGillivray and Charles M. Lukehart.
© 2014 John Wiley & Sons, Ltd. ISBN 978-1-119-95289-3

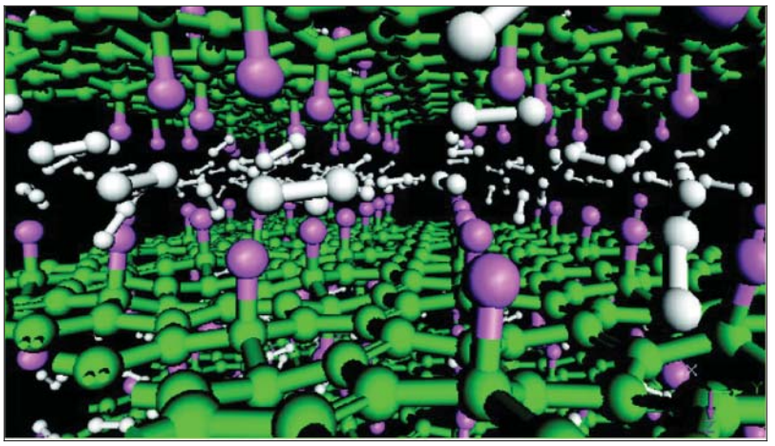


Figure 1 Fully optimized structures of the partially fluorinated graphite intercalation compounds with optimized H_2 molecules (Adapted with permission from Ref. 27. Copyright (2009) American Chemical Society.)

molecular simulations.[31,32] From these results, it is clear that as fluorine atoms in partially fluorinated MOFs are weakly interacting with gas molecules, other factors, such as pore size, curvature, and open metal sites, can also play a crucial role in the high gas uptakes within these FMOFs.

Although there are several reports for the synthesis and adsorption studies in FMOFs, depending on the structural arrangements, FMOFs can be divided into three parts: (i) anion-induced fluorination in MOFs; (ii) MOFs constructed by fluorinated ligands; and (iii) fluorination in MOFs via plasma-enhanced chemical vapor deposition (PECVD).

1.1 Anion-Induced Fluorination in MOFs

As the coordination of bi-pyridine ligands with metal centers forms a relatively flexible framework based on the binding of neutral pyridyl groups of ligands, it is believed to be an ideal connector between the transition metals for the formation of 3D frameworks. The 3D networks composed of pyridine ligands usually accompanies the porous structures with high surface area, periodic pore structure, large pore volume, and good gas storage properties.[30] Two potential binding sites of pyridine-based ligands that are arranged in a divergent (exo) manner and a rigid structure help to predict the network geometries.[33] However, from the literature survey, it is clear that the 3D networks with only bipyridine ligands are relatively rare because of the precipitate or gel formation in the presence of metal salts. It is to be believed that fluorine plays a dual role as a mineralizing agent, which favors the formation of well-crystalline phases during reaction.[18] Therefore, in order to overcome these issues regarding reactivity of bipyridine-based ligands, the attempts for the crystallization have been made by addition of fluorinated inorganic compounds such as SiF_6, PF_6, BF_4, GeF_6, PF_6, ZrF_6, and SbF_6. After the very first report about the synthesis of $[Zn(4,4'\text{-bpy})_2(SiF_6)]_n \cdot x\text{DMF}$, a single framework of octahedral coordination polymer with large square channel (11.4 Å), the opportunities for the synthesis of FMOFs with exposed fluorine atoms into the pores have picked up attention.[34] The structural arrangements of these kinds of MOFs represent square grid channels formed by the coordination of μ_2-SiF_6 molecule and 4,4′-bipyridine (bpy), wherein the existence of C–H···F hydrogen bonds between α-C–H hydrogen atoms and fluorine atoms of the SiF_6 ions has been observed (Figure 2). By utilizing the advantage of formation of large channels, various MOFs have been synthesized for a large number of applications. The counter anion, SiF_6, has been replaced by coordinating anions such as GeF_6, PF_6, ZrF_6, SbF_6, and BF_4, which binds to the metal centers through μ_1, μ_2, μ_3, or μ_4 modes of attachment through –F atoms. Similarly, the replacement of linear coordination ligand bpy was presented by other pyridine-based ligands such as pyrazine, 1,2-di(pyridin-4-yl)ethane, 4,4′-bipyridine-1,1′-dioxide, 4,4′-dipyridylacetylene, 1,4-di(pyridin-4-yl)benzene, and *N*-(Pyidin-4-yl) isoniconamide. Ward and co-workers reported three new MOFs by a potentially general route using a new multinucleating ligand, 2,6-bis[(3-(pyridin-2-yl)-1H-pyrazol-1-yl)methyl] pyridine, in the presence of chelating anions BF_4, SiF_6, PF_6, and Cu^{+2} as a metal center.[26] In these regards, Hosseini, Zaworotko, Uemura, and others showed the porosity tuning by modulation of the coordinating linear ligands.[34–38] Also, in the similar efforts by various groups, the several isostructural MOFs have been avenged by varying the metal nodes such as Zn, Cu, Cd, and Co.[39–41]

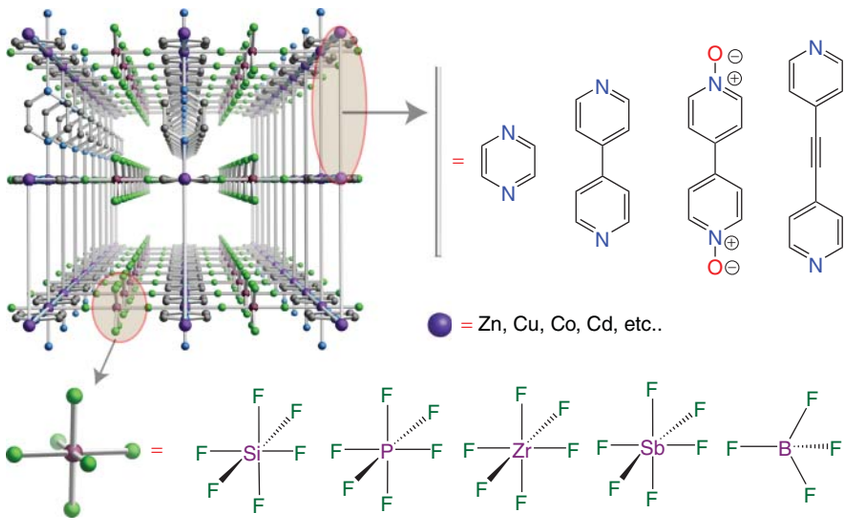


Figure 2 Representative scheme of partial fluorination achieved in MOFs via incorporation of coordinating anions such as SiF_6, PF_6, ZrF_6, SbF_6, and BF_4 through μ_1, μ_2, μ_3, or μ_4 modes of attachment through –F atoms (Hydrogen atoms and solvent molecules are omitted for clarity.)

In the same line, Jia *et al.*[42] deliberated the synthesis and characterization of Cu-based MOFs with coordinating PF_6, BF_4, ZrF_5, and SbF_6, where 4,4′-bipyridine-*N*,*N*′-dioxide (instead of bpy) has been used as a coordinating ligand. Formation of porous, chiral, and partially FMOFs using enantiomerically pure organic tectons with different lengths as well as infinite inorganic pillar based on $ZnSiF_6$ as a periodic rod-type construction unit with imposed distance between consecutive square planar nodes has been studied exclusively.[35,36] The first example of synthesis and crystal structure of two closely related copper (I) hexafluorosilicate π-complexes with 1-allylbenzotriazole having direct Cu^+–SiF_6^{2-} bond has been reported by Goreshnik *et al.* in 2011,[43] where the effect of small change in acidity of the reaction mixture on the coordination behavior of SiF_6 and Cu metal centers has been studied. In a very recent report, Nugent *et al.* showcased a control over pore size and functionality in a series of MOFs with coordinately saturated metal centers and periodically arrayed SiF_6^{2-} anions.[44] The demonstration of the reticular chemistry approach to control the pore size, which affords porous materials with exceptional selectivity, recyclability, and moisture stability for several industrially relevant CO_2 separation applications, has been explained on the basis of increased interactions between adsorbed gas molecules and pore functionalities (–F) present on the pore walls.[45]

In another type of anion-induced fluorination, $–F^-$ anions are incorporated (coordinated to the metal centers) into MOF structure by means of inorganic acids. Recently, Férey and co-workers and other research groups focused on the hydrothermal/solvothermal synthesis of aromatic poly-carboxylates with different trivalent metals such as rare-earth elements, 3D transition metals (V, Cr, Fe, etc.), and p block elements (Al, Ga, In, etc.) using solvothermal and hydrothermal routes.[46,47] Several partially fluorinated MOFs, namely, MIL-53, MIL-88, MIL-103, MIL-100, MIL-101, MIL-61, MIL-68, MIL-69, MIL-59, MIL-88 and so on, have been synthesized by hydrothermal/solvothermal treatment by reacting different metal salts and, carboxylic acids in various organic solvents. Most of structures among this MIL series exhibit infinite trans-connected chains of metal octahedra $MO_4(OH)_2$ or μ_3-oxo-bridged trinuclear octahedra $MO_5(H_2O)$ (M = V, Cr, Al, etc.) linked to each other through the carboxylate ligands (MIL-53, MIL-61, MIL-68, MIL-69, etc.), which exhibit breathing effects on different gas adsorption.

Although there are several reports on the synthesis of MOFs (especially MIL series) using aromatic poly-carboxylates with different trivalent metals such as V, Cr, Fe, Al, Ga, and In, the major problem remains in their poor crystallinity or amorphous by-products formation. In order to promote the crystal growth, addition of fluorine as a mineralizing agent (in the form of HF) was carried out. By using this crystallization method, the synthesis of MIL-53 with incorporated Cr/Al or the Cr-carboxylates MIL-100 and MIL-101 was achieved successfully.[48–50] The fluorine used in these synthesis protocols not only helps the crystallization but also satisfies the valences of the metal ions. In particular, MIL-100 has a cationic inorganic network formed by the coordination of chromium to the 1,3,5-benzene tricarboxylic acid, balanced by a negative default charge, which corresponds to one fluorine

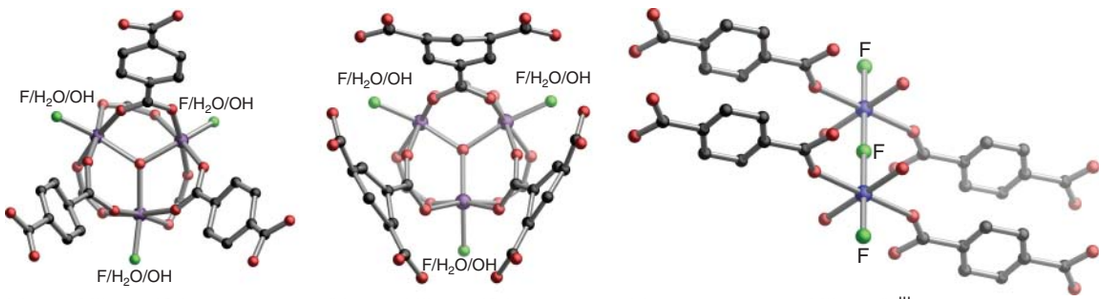


Figure 3 Representative examples of anion-induced partial fluorination in MOFs achieved via –F ions by the addition of hydrofluoric acid during MOF synthesis. (a) MIL-101 (Cr), (b) MIL-100 (Cr), and (c) MIL-71 (V^{III}) (Hydrogen atoms and solvent molecules are omitted for clarity.)

atom per three chromium atoms of the trinuclear units (Figure 3).[51] As estimated from the chemical and structural analyses, fluorine is involved in the terminal bond of the trimeric chromium species and partly substitutes the terminal water molecule attached to chromium. Similar structural arrangement of trimeric chromium species has been observed in the case of MIL-101 except the replacement of 1,3,5-benzene tricarboxylic acid by 1,4-benzene dicarboxylic acid. Although exact location and amount of fluorine were not clear in the MILs, the probable amount and position of fluorine in these MOFs were furnished by FT-IR spectra, chemical analysis, and quantification of carbon monoxide adsorption experiments. After successful synthesis of several Cr-based MIL frameworks, vanadium and 1,4-benzene dicarboxylic acid-based MIL-71 was synthesized. In MIL-71, coordinated fluorine was clearly identified and from the crystal structure it was clear that fluorine participates to the octahedral coordination sphere of vanadium (III) as shown in Figure 3.[52] The structure is formed because of corner-shared $VO_2(OH)_2F_2$ octahedra forming layers pillared by the terephthalate ligands.

1.2 MOFs Constructed by Fluorinated Ligands

Insertion of functionalized links associated with groups such as –F, $–NH_2$, –OH, and –COOH has proven to have good impact on enhancing the H_2 and CO_2 gas adsorption properties in MOFs.[53–55] Computational studies proved that the choice of both ligand and metal center plays an important role in gas–framework interactions. Inspired by the unusual stability, extraordinary functional properties (e.g., high electronegativity, smaller atomic size, and high effective nuclear charge), and numerous applications of fluorous molecules, researchers have devoted efforts to explore the synthesis and functional properties of fluorine-containing MOFs, wherein few or all the hydrogen atoms are substituted by fluorine atoms in ligands. One would assume that FMOFs, with fluorine-lined channels/pores, are expected to have enhanced thermal and chemical stability as well as catalytic activity, higher gas affinity, and so on (Figure 4).

After the very first report on the synthesis of partially fluorinated MOF by Li and co-workers using 4,4′-(hexafluoroisopropylidene)-bis(benzoic acid) as a coordinating ligand, the extraordinary gas adsorption properties made researchers excited to explore new MOF synthesis with fluorine-lined channels/pores (Figure 5a).[14] This report highlights the more optimal designs of MOFs, which retains a small pore size but have larger total pore volumes with protruding fluorine atoms into the pores. Subsequently, a successful report on FMOF-1 by the reaction of sodium salt of the perfluorinated ligand 3,5-bis(trifluoromethyl)-1,2,4-triazolate with silver nitrate in methanol has been made.[15] FMOF-1 corresponds to a class of 3D porous material with periodic fluorine-lined, semirectangular shaped, hollow tubes (~12 × 7 Å), with superior volumetric gas uptake. Furthermore, same group have productively isolated another fluorine containing MOF (FMOF-2), after performing the annealing followed by recrystallization of FMOF-1.[56] Based on crystal structures, FMOF-2 showed enlarged cages and channels with two times adsorption of toluene compared to FMOF-1.

The literature survey suggests that the perfluorinated aromatic linkers, 4,4′-(hexafluoroisopropylidene)bis-(benzoic acid) [H_2hfipbb/H_2hfbba], and 4,4′-(hexafluoroisopropylidene) diphthalic acid [H_2hfipdpt/H_2hfpdpt] are utilized widely for MOF synthesis. The probable reasons for using such ligands could be due to (i) a twisted conformation leading to a possible helical architecture leading to chirality; (ii) a different degree of deprotonation under different reaction conditions, which might result in variable coordination modes in the products; and (iii) a long and bent molecular structure of this primary building unit that might lead to the formation of microporous coordination frameworks with channels suitable for gas and solvent

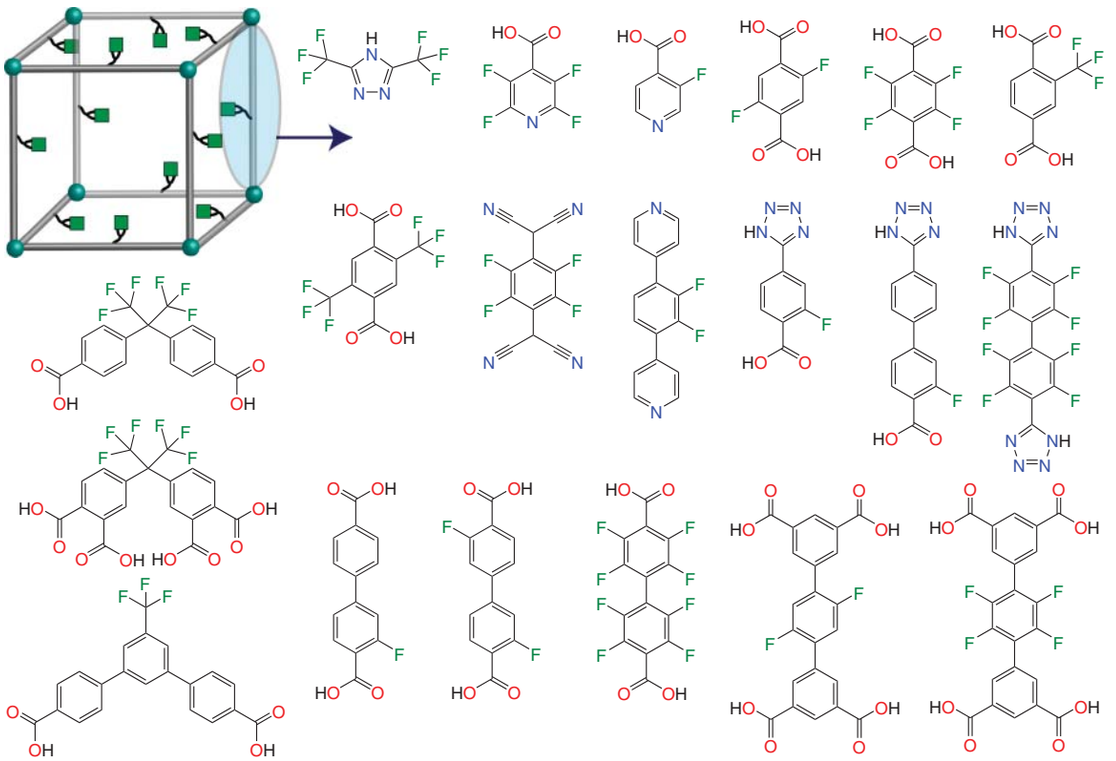


Figure 4 Ligands used for the synthesis of the partially or fully fluorinated MOFs with the coordination in the midst of suitable metal centers

adsorption/separation (Figure 5). The partially fluorinated MOFs synthesized using H_2hfbba and H_2hfpdpt as ligands showed promising results toward gas adsorption, separation, hydrocarbon separations, catalysis, sensors, and so on. Although there are several partially fluorinated MOFs reported using individual H_2hfbba/H_2hfpdpt as ligands, utilization of other N-containing co-ligands such as bipyridine, phenanthroline, pyridine, picolines, and imidazolyl-based ligands for MOF synthesis has also been tried vastly.[57–60] Owing to the bent structure of both the ligands, most of the structures with or without co-ligands fall into the same type of porous architectures as shown in Figure 5. Effect of solvent, temperature, co-ligands, and change in metal centers on the resulting MOF architecture obtained from H_2hfbba/H_2hfpdpt ligands had been studied in detail. In most of the structures, owing to the geometry of the ligand, its central atom being a sp^3 carbon, channels are square shaped with the fluorine atoms pointing inside/outside of them and with sufficient dimensions for the gas or hydrocarbon adsorption.

Utilizing μ_2, μ_3, or μ_4 coordination modes of 2,3,5,6-tetrafluoro-1,4-benzenedicarboxylic acid (tfbda), several partially or fully perfluorinated MOFs have been synthesized with or without addition of co-ligands. Various groups reported a large number of perfluorinated MOFs using tfbda as a ligand.[61–70] In the same line, the effect of fluorination on the gas adsorption properties of the pillared square grid nets based on paddle-wheel motifs containing terephthalate-based carboxylate linker and 1,4-diazabicyclo[2.2.2]octane as ligands has been studied.[30] Similarly, a partially fluorinated MOF, containing zinc, 1,2,4-triazolate, and tfbda, which displays a high physisorptive hydrogen adsorption enthalpy of 8 kJ mol^{-1}, as a result of fluorine atoms exposed to the pore surface, has been made.[28] The momentous difference between the carboxylate torsion angles aroused from fluorinated and nonfluorinated ligands, which leads to the formation of clearly different structures for the two groups of materials, has been studied in detail.[72] The use of perfluorinated ligands tends to increase the dimensionality; hence, it is very difficult to obtain isostructural phases from the same fluorinated and nonfluorinated ligand analogs.

Partially fluorinated MOFs, such as Zn(bpe)(tftpa) and Zn(bpe)(tftpa) · cyclohexanone [bpe = 1,2-bis(4-pyridyl)ethane], have been synthesized and its H_2 storage properties are reported.[29] The use of templating organic molecules to effectively block the interpenetration has been successfully demonstrated. Recently, an explanation on the basis of fluorinated and nonfluorinated MOFs and how linker modifications control the swelling property of

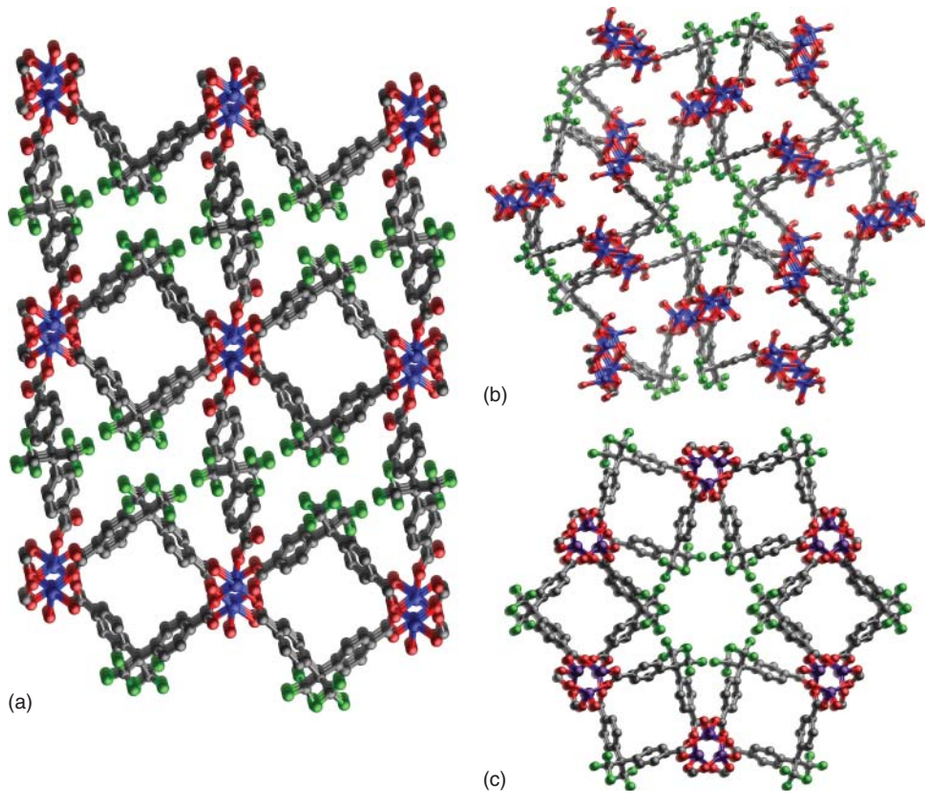


Figure 5 Partially fluorinated MOFs having different kinds of pores formed using bent 4,4′-(hexafluoroisopropylidene)bis-(benzoic acid) and 4,4′-(hexafluoroisopropylidene) diphthalic acid by coordination with suitable metal centers. (a) [Cu-(hfipbb)(H_2hfipbb)$_{0.5}$] MOF with optimal pore size for gas adsorption.[14] (b) [$Cd_2L(H_2O)]_2 \cdot 5H_2O$ MOF having ukv topology for high sorption selectivity and affinity for CO_2.[71] (c) [Zn-(hfipbb)$_2$] MOF having 3D-channeled structure with two kinds of very different parallel tunnels for hydrocarbon adsorption[101](Hydrogen atoms and solvent molecules are omitted for clarity.)

highly flexible iron(III) dicarboxylates MIL-88 has also been presented.[73] By using fluorinated and nonfluorinated tetracarboxylates, high capacity H_2 adsorption in Cu(II)-based tetracarboxylate framework materials was analyzed successfully.[74] Also, the role of pore size, ligand functionalization, and exposed metal sites on the gas adsorption have been studied in detail. In the similar report, a series of di-isophthalate ligand-based fluorinated and nonfluorinated MOFs with functionalized pore surfaces was synthesized.[75] A flexible porous coordination polymer was synthesized using soft secondary building units, which can undergo multiple reversible metal–ligand bond breaking.[76] Two MOFs having twofold interpenetrated structures, using terephthalic acid and 2,3-difluoro-1,4-bis(4-pyridyl)benzene, show dynamic structural transformations upon the removal and rebinding of guest molecules. Recently, three new superhydrophobic perfluorinated MOFs using 2,2′,3,3′,5,5′,6,6′-octafluoro-[1,1′-biphenyl]-4,4′-dicarbonitrile ligands and its derived carboxylate as well as tetrazolate-based MOFs have been reported.[77]

Although it was reported that the synthesis of isostructural phases from same fluorinated and nonfluorinated ligand is very difficult,[72] successful isolation of two pairs of isostructural fluorinated and nonfluorinated MOFs has been achieved using isonicotinic acid and 3-fluoroisonicotinic acid.[32] The synthesis of two pairs of Co (II)-based MOFs was executed using isonicotinic acid and its fluorinated analog 3-fluoro-isonicotinic acid ligands in the presence of different solvents. Similarly, using another set of ligands, 4-(1H-tetrazole-5-yl)benzoic acid and its fluorinated analog 2-fluoro-4-(1H-tetrazole-5-yl)benzoic acid, a pair of isostructural MOFs has been isolated in the presence of Cu(I) as a metal center.[31] We could study the effect of partial fluorination on the structure and gas adsorption properties of the resulting MOFs.

1.3 Plasma-Enhanced Chemical Vapor Deposition

As many MOFs are highly susceptible toward toxic chemicals, they are prone to decomposition by the moisture present in these gases. Owing to active interaction of

these MOFs with adsorbing moisture or other chemically active species, these materials further get degraded or lose their crystallinity. Although MOF-5 and HKUST-1 possesses high porosity, large surface area, and high gas uptake capacity, the degradation of these MOFs happens very quickly. So, there is a necessity to stabilize these structures as one could use these materials for applications at the industrial level.[78,79] Logically, the stabilization of these MOFs with hydrophobic materials will help to improve the inertness of these frameworks toward the moisture and other chemically active molecules/gases. Although few strategies such as placing hydrophobic groups on MOF linkers and surfactant-assisted drying has been employed to improve the stabilities of these MOFs, these methods may change the inherent nature and chemistry of the resultant MOFs.[80] Hence, there has always been a search for a method that will not induce the changes in the basic MOF structure, but still enhance the stability.

In this regard, Decoste *et al*.[81] proposed an alternative method for postsynthetic modification of Cu-BTC by a PECVD of perfluorohexane. The presynthesized and solvent-removed Cu-BTC crystals were converted to Cu-BTC plasma by using a PECVD method with a perfluorohexane precursor in a plasma reactor. The presence of CF_3 groups on the surface of the pores also adds to the hydrophobicity of the material, which actually causes the material to float in liquid water avoiding the entry of these molecules to destruct the whole MOF framework. The treatment of Cu-BTC with plasma perfluorohexane enhances not only the stability of Cu-BTC against degradation by water but also the ammonia adsorption capacities (Figure 6).

In this final section of this report, we would like to draw a structure property relationship in the FMOF series. Now, looking through the applications of the FMOFs, many of them has been exploited for gas adsorption, storage, gas/hydrocarbon separation, and so on. In this regard, depending on the end applications of these MOFs, they are divided into two parts: (i) FMOFs for gas adsorption and separation and (ii) FMOFs for hydrocarbon uptake.

1.4 Fluorinated MOFs for Gas Adsorption and Separation

Functionalization in MOFs, achieved via functionalized links, has played a vital role to achieve new applications such as catalysis, gas storage, separation, sensors, and biomedicine. In particular, the functionalization of MOFs achieved via insertion of organic links with functional groups such as –F, $–NH_2$, –OH, and –COOH on the organic spacer has also been proven to have a good impact on enhancing the H_2 and CO_2 gas adsorption properties. Literature reports showed that amino-functionalized MOFs can perform better for selective and reversible CO_2 adsorption.[82–85] Porous MOFs with exposed fluorine

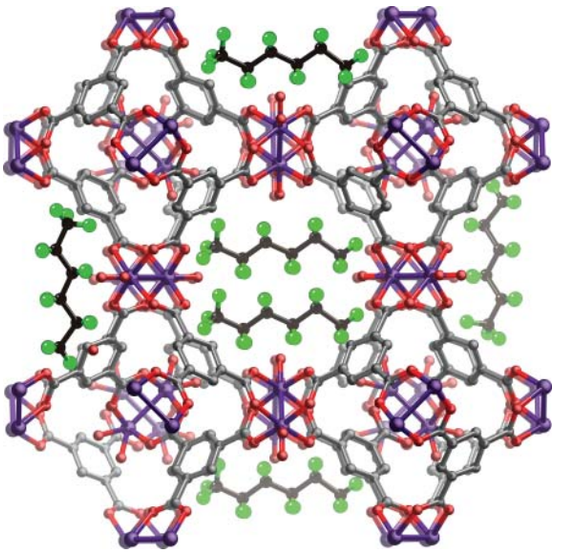


Figure 6 Representative image Cu-BTC MOF after PECVD via perfluorohexane[81] (Hydrogen atoms are omitted for clarity.)

atoms (FMOFs) show "high" physisorptive H_2 adsorption enthalpy resulting in the enhancement of the H_2 adsorption properties.[15,28] But, there has been reports of explicit comparison with nonfluorinated analogs that impart a "disadvantage" of fluorination toward H_2 adsorption.[30] However, by studying the systematic comparison between isostructural fluorinated and nonfluorinated MOFs, we could showcase that the enhancement of H_2 adsorption due to fluorination in MOFs is not an universal phenomenon, but it is rather system specific and can differ from system to system.[31,32] As a result, at this moment, it is very difficult to draw any conclusion regarding the impact of fluorination on H_2 and CO_2 adsorption, as there are very few systematic comparative studies of gas storage in iso-structural fluorinated and nonfluorinated MOFs.

The very first report on synthesis, structure, and room-temperature H_2 adsorption of a novel [Cu-(hfipbb)(H_2hfipbb)$_{0.5}$] fluorine-containing MOFs showed the probable application of FMOFs for gas adsorption (Figure 10a).[14] The superior performance showed by FMOF compared to as-received single-walled carbon nanotubes (SWNTs) and purified SWNTs emphasized the integrity of these MOFs for gas uptake. A promising hydrogen storage capacity of 1.6 wt% at 48 atm and room temperature (RT) showed by [Cu-(hfipbb)(H_2hfipbb)$_{0.5}$] inspired the researchers for the synthesis of other FMOFs with porous architectures containing exposed fluorine atoms into the pores. Furthermore, reports of synthesis and gas adsorption properties of perfluorinated MOFs and the utilization of FMOFs for hysteretic sorption of H_2 showcased a promising way for H_2 to be filled at high pressures but stored at lower pressures (Figure 7a).[15] The volumetric

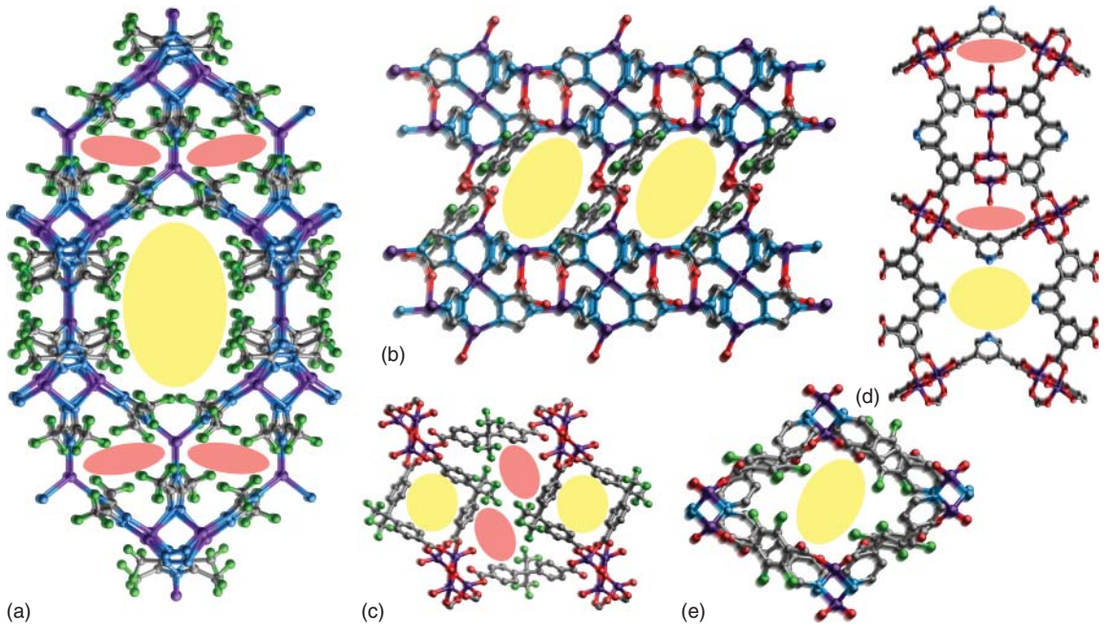


Figure 7 Representative literature-reported perfluorinated MOFs used for gas adsorption or separation. (a) Fully fluorinated FMOF-1 synthesized from perfluorinated ligand 3,5-bis(trifluoromethyl)-1,2,4-triazolate.[15] (b) Partially fluorinated Zn_5(1,2,4-triazolate)$_6$(tetra fluoroterephthalate)$_2(H_2O)_2 \cdot 4H_2O$ MOF synthesized from tfbda and 1,2,4-triazolate.[28] (c) Partially fluorinated FMOF-2 synthesized from 4,4′-(hexafluoroisopropylidene)-bis(benzoic acid).[25] (d) Representative structure of a series of Cu-based [1,1′:3′,1″-ter- phenyl]-3,3″,5,5″-tetracarboxylic acid functionalized MOFs.[75] (e) Partially fluorinated Zn(bpe)(tftpa) · cyclohexanone MOF synthesized from 2,3,5,6-tetrafluoro-1,4-benzenedicarboxylic acid and 1,2-bis(4-pyridyl)ethane[29] (Hydrogen atoms and solvent molecules are omitted for clarity.)

adsorption capacity of FMOF-1 for hydrogen at 77 K and 64 bar is as high as 41 kg m^{-3}, which can be attributed to the increased interactions between fluorine-lined porous channels and adsorbing H_2 molecules giving rise to the high physisorptive hydrogen adsorption enthalpy.

The utilization of small pores for the high hydrogen uptake with elevated adsorption affinity was successfully demonstrated with a partially fluorinated porous coordination polymer Zn_5(1,2,4-triazolate)$_6$(tetrafluoroterephthalate)$_2(H_2O)_2 \cdot 4H_2O$. This porous coordination polymer (PCP) exhibited high physisorptive hydrogen adsorption enthalpy (8 kJ mol^{-1}) because of the interaction of fluorine atoms exposed to the pore surface with H_2 and small pore size comparable to the hydrogen's molecular diameter (Figure 7b).[28] Similarly, a partially fluorinated MOF, Zn(bpe)(tftpa) · cyclohexanone, with fluorine atoms exposed to the pore surface, adsorbs 1.04 wt% H_2 at 77 K and 1 atm with an adsorption enthalpy of 6.2 kJ mol^{-1}, which signifies a trivial enhancement in the binding strength because of the presence of fluorine atoms (Figure 7e). The gas-induced expansion and contraction of a FMOF named "FMOF-2" for highly selective CO_2, H_2S, and SO_2 adsorption showed breathing behavior toward selected gas molecules (Figure 7c).[25] The same MOF has been further used in the temperature-dependent Kr/Xe selective adsorption.[86] An estimated Kr/Xe selectivity at 0.1 bar and 203 K shown by FMOFCu was attributed to the micro-tubes packed along the (101) direction connected through small bottleneck windows in FMOFCu. The effect of fluorination has been further explained in four iso-structural MOFs with various functionalized pore surfaces (–H, –N, $–CH_3$, and $–CF_3$), where MOFs were synthesized from a series of di-isophthalate ligands.[75] Among this series of MOFs, the MOF possessing free $–CF_3$ (PCN-308) groups in its framework showed highest H_2 uptake of 2.67 wt% at 77 K and 1 bar and CO_2 uptake of 15.4 wt% at 297 K and 1 bar. Despite being holding lower surface area, PCN-308 showed higher heat of adsorption for H_2 and CO_2 than that of its nonfluorinated versions. In a recent report, Santra *et al.*[87] showed an adsorption of 0.74 wt% of H_2 at 77 K/1 atm pressure and 2.78 wt% of H_2 at 77 K/41 bar pressure with isosteric heat of H_2 adsorption (Qst) value of ~7.9 kJ mol^{-1} at low coverage. In the partially fluorinated 3D MOF, $\{[Zn_4O(bfbpdc)_3(bpy)_{0.5}(H_2O)] \cdot (3DMF)\ (H_2O)\}_n$ (bpy = 4,4′-bipyridine and bfbpdc = 2,2′-bistrifluoromethyl-biphenyl-4,4′-dicarboxylate) enhancement in gas adsorption was assigned to the presence of the exposed metal site and fluorine atoms in the pore surface of the framework.

Although aforementioned results showed advantages of fluorine functionalization for high H_2/CO_2 uptake with increased heat of adsorption, one relevant

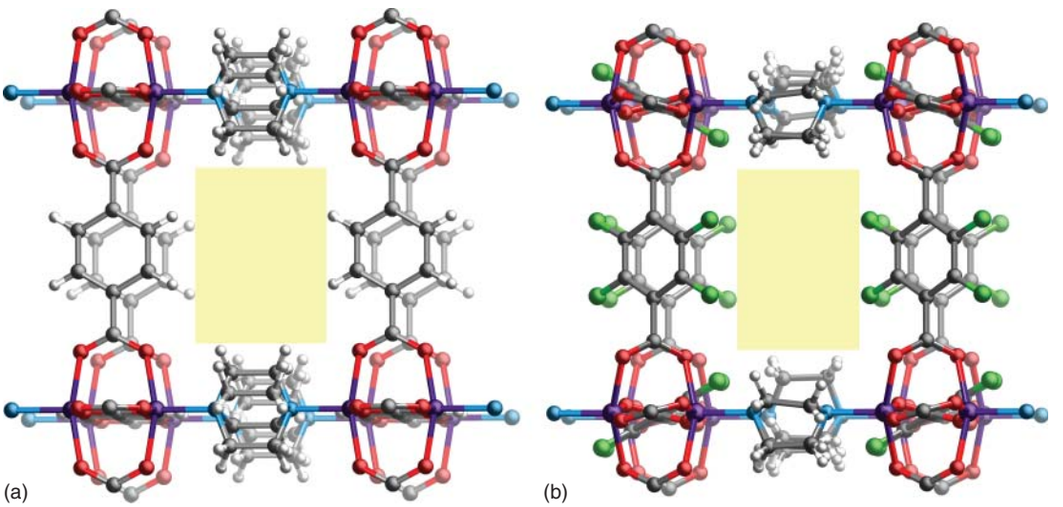


Figure 8 (a, b) Comparative structure of the Zn-containing 1,4-benzenedicarboxylic acid/tfbda and 1,4-diazabicyclo[2.2.2]octane-based MOFs[30]

report demonstrated the disadvantages of fluorine functionalization toward the incremental gas adsorption.[30] In this context, the author mentioned that "from the gas-sorption point of view, fluorinated MOF has a disadvantage compared to its non-fluorinated analogue not because of the slightly reduced pore size, but because of its higher framework density originating from the fluorine atoms. The densities for fluorinated and nonfluorinated MOFs based on crystallographic analysis are 1.034 and 0.826 g cm^{-3}, respectively." As shown in Figure 8, owing to the increased atomic size of fluorine over hydrogen, the overall pore size decreases comparatively. The decreased free space for gas adsorption further results into the overall decrease in the gas adsorption capacities. Also from the gas adsorption point of view, partially fluorinated tetrafluoroterephthalate-based MOF (density = 1.034 g cm^{-3}) has disadvantage compared to nonfluorinated terephthalate-based MOF (density = 0.826 g cm^{-3}), not because of the slightly reduced pore size, but because of its higher framework density originating from the fluorine atoms. Hence, it was evident that the fluorine functionalization was not fruitful leading toward the increase in gas uptake capacity.

In order to assess the effect of fluorine insertion on the gas adsorption properties of the MOFs, we had synthesized two isostructural MOFs with and without exposed

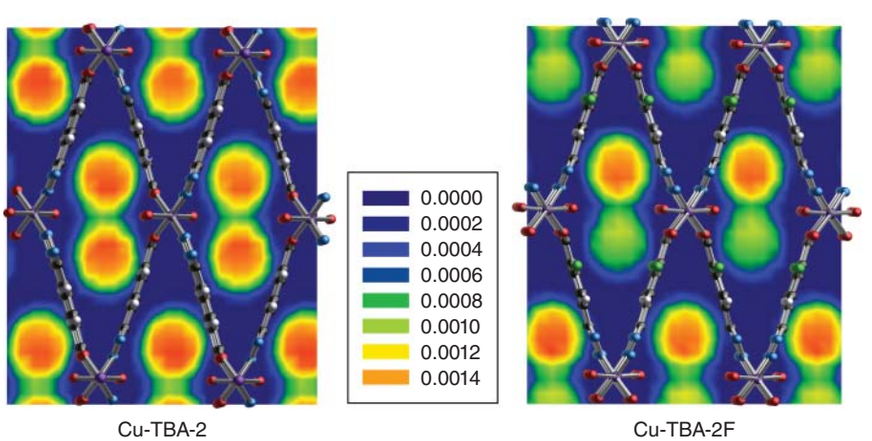


Figure 9 Effect of partial fluorination on the gas adsorption properties of a isostructural Cu-containing 4-(1H-tetrazole-5-yl)benzoic acid/2-fluoro-4-(1H-tetrazole-5-yl)benzoic acid-based MOFs determined by H_2 adsorption density contours in Cu-TBA-2 and -2F at 1 kPa (Reprinted with permission from Ref. 31. Copyright (2011) American Chemical Society.)

Table 1 Hydrogen uptake data of selective literature reported FMOFs

Name of MOF	BET surface area ($m^2\ g^{-1}$)	H_2 storage (wt%)	Qst ($KJ\ mol^{-1}$)	Reference
[Cu(hfipbb)(H_2hfipbb)$_{0.5}$]	—	0.23 (1 atm)	—	14
[Ag_2 (Ag_4-Tz_6)]	810	2.33 (64 bar)	—	15
Zn_5(1,2,4-triazolate)$_6$ (tetrafluoroterephthalate)$_2$(H_2O)$_2$ · $4H_2O$	100[a]	0.43 (1 atm)	8.0	28
Zn(bpe)(tftpa) · cyclohexanone	512	1.04 (1 atm)	6.2	29
[Zn_2(tfbdc)$_2$ (dabco)]	1070	1.78 (1 atm)	—	30
Cu_2(2-F-4-TBA)$_2$(DMF)$_2$	—	0.67 (1 atm)	—	31
[Co_3(FINA)$_4$(O)(C_2H_5OH)$_2$] · H_2O	547	1.97 (1 atm)	—	32
[Co(FINA)$_2$] · H_2O	152	0.82 (1 atm)	—	32
{[Zn(SiF_6)-(pyz)$_2$] · 2MeOH}$_n$	133	0.65 (1 atm) 1.09 (100 bar)	8.2	38
[Cu(N-(pyridin-4-yl)isonicotinamide)$_2$ (SiF_6)](EtOH)$_2$(H_2O)$_{12}$, UTSA-48a	285	0.59 (1 atm)	—	45
[Cu_2($C_{22}O_8H_8F_2$)(H_2O)$_2$] · 2DMF · $C_4O_2H_8$ · $4H_2O$, NOTT-105	2387	2.52 (1 atm) 5.4 (20 bar)	5.5	74
[Cu_2(H_4FTPTA) $2H_2O$], PCN-308 (–CF_3)	1418	2.67 (1 atm)	6.48	75
{[Zn_4O(bfbpdc)$_3$ (bpy)$_{0.5}$(H_2O)] · (3DMF) (H_2O)}$_n$	1450	0.74 (1 atm) 2.78 (41atm)	7.9	87
[Cu(SiF_6)(4,4′-bpy)$_2$]	713	1.21 (1 atm) 2.36 (18 bar)	—	88
[Co_2(hfbba)$_2$(3-mepy)$_2$] · (DMF)$_3$, Co-HFMOF-D	—	0.78 (1 atm)	—	89
Co(hfbba)(3-mepy)(H_2O), Co-HFMOF-W	—	0.67 (1 atm)	—	89
Mn(hfbba)(3-mepy)(H_2O)], Mn-HFMOF-W	—	0.72 (1 atm)	—	89
[Cu_2(hfbba)$_2$(3-mepy)$_2$] · (DMF)$_2$(3-mepy), F-MOF-4	—	0.58 (1 atm)	—	90
[Cu(bpy)$_2$(OTf)$_2$]$_n$-2D	630	0.63 (1 atm)	3.8	91
[Cu(bpy)$_2$(OTf)$_2$]$_n$-3D	—	0.8 (1 atm)	3.4	91
Co_3(hfbba)$_6$(phen)$_2$, FMOF-6	20	0.9 (1 atm)	—	92
[Zn_2(hfipbb)$_2$(bpdab)] · 2DMF	201	0.87 (20 bar)	—	93
[Cd_2(hfipbb)$_2$(DMF)$_2$] · 2DMF	125	0.57 (20 bar)	—	93
$Fe_3O(F_4BDC)_3(H_2O)_3$ · $(DMF)_{3.5}$	635	0.9 (1 atm)	—	61
$Cr^{III}_3OF\ x(OH)1-x(H_2O)_2$ · {1,3,5-BTC}$_2$ · nH_2O, MIL-100(Cr)	2700	3.3 (25 bar)	−5.6	94
$Cr_3F(H_2O)_2O$(1,4-BDC)$_3$ · nH_2O, MIL-101(Cr)	5500	6.1 (60 bar)	−9.3	94
$Cr^{III}_3O(H_2O)_2F${2,6-NDC}$_{1.5}$ · $6H_2O$, MIL-102(Cr)	42	1.0 (35 bar)	5.99	94

[a]Surface area is determined by Langmuir surface area method.
hfipbb/hfbba, 4,4′-(hexafluoroisopropylidene)bis-(benzoic acid); Tz, 3,5-bis(trifluorom- ethyl)-1,2,4-triazolate; tftpa/F_4BDC, tetra-fluoroterephthalate; 2-F-4-TBA, 2-fluoro-4-(1H-tetrazole-5-yl)benzoic acid; FINA, 3-fluoroisonicotinic acid; pyz, pyrazine; $C_{22}O_8H_8F_2$, 2′,5′-difluoro-[1,1′:4′,1′′-terphenyl]-3,3′′,5,5′′-tetracarboxylic acid; H4FTPTA, 5′-(trifluoromethyl)-[1,1′:3′,1′′-terphenyl]-3,3′′,5,5′′-tetracarboxylic acid; bfbpdc, 2,2′-Bis-trifuoromethyl-biphenyl-4,4′-dicarboxylic acid; bpy/4,4′-bpy, 4,4′-bipyridine; 3-mepy, 3-methyl pyridine; OTf, trifuoromethanesulfonate; bpdab, 1,4-bis(4-pyridyl)-2,3-diaza-1,3-butadiene; 1,3,5-BTC, 1,3,5-benzenetricarboxylic acid; 1,4-BDC,1,4-benezenedicarboxylic acid; 2,6-NDC, 2,6-naphthalenedicarboxylic acid.

fluorine atoms into the pores.[31] The partially fluorinated MOF, Cu-TBA-2F having protruding fluorine atoms into the pores, shows lower H_2/CO_2 adsorption compared to its nonfluorinated analog Cu-TBA-2. The experimental and theoretical observation shows the similar results like aforementioned case validated by Kim and co-workers. The steric hindrance developed and higher atomic size of protruding fluorine atoms in Cu-TBA-2 F results in the lower adsorption for H_2 and CO_2 (Figure 9). The similar results were further validated by us using two pairs of isostructural isonicotinic acid-based partially fluorinated and nonfluorinated MOFs. The increased H_2 uptake achieved obtained in perfluorinated MOFs Co-FINA-1 and Co-FINA-2 over their nonfluorinated counterparts Co-INA-1 and Co-INA-2 suggested the system-specific behavior of these FMOFs toward the H_2 adsorption (Table 1).[32]

1.5 Fluorinated MOFs for Gas Hydrocarbon Sorption or Separation

The separation of a mixture of hydrocarbons is a commercially important process as it has a wide range of applications in the chemical and polymer industries.[95] Existing methods for separation of hydrocarbons from mixtures including fractional distillation used to separate a gaseous mixture based on the difference in the boiling points of the constituents requires high-energy costs

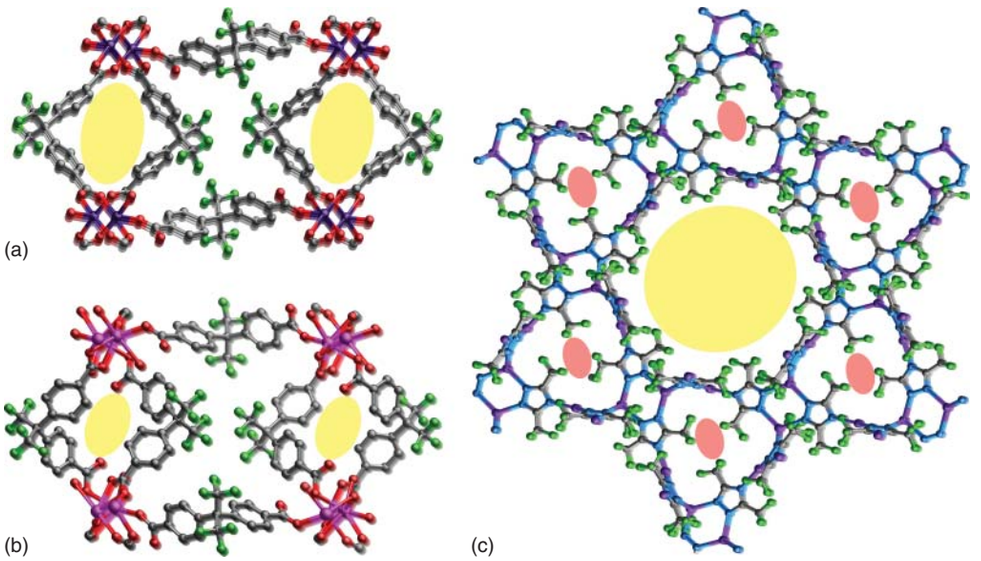


Figure 10 Representative examples of literature-reported perfluorinated MOFs used for hydrocarbon sorption or separation. (a) Partially fluorinated [Cu(hfipbb)(H_2hfipbb)$_{0.5}$] synthesized from 4,4′-(hexafluoroisopropylidene)-bis(benzoic acid).[102] (b) Partially fluorinated alkaline-earth polymer framework (AEPF)-1 synthesized from 4,4′-(hexafluoroisopropylidene)-bis(benzoic acid).[103] (c) Fully fluorinated FMOF-2 synthesized from perfluorinated ligand 3,5-bis(trifluoromethyl)-1,2,4-triazolate[56] (Hydrogen atoms and solvent molecules are omitted for clarity.)

because of their requirement of low temperatures and high pressure. In order to achieve energy-effective separation techniques for hydrocarbons, the exploitation of porous materials such as zeolites, hydrophobic polymers, carbon containing materials, and alumina compounds has been tried widely.[96,97] Particularly, the applications of modified Y zeolites (AgY and CeY) prepared using ion-exchange methods for hydrocarbons removal is well studied in the literature.[98] The adsorption breakthrough and on-site solvent-washing experiments, as well as computer simulation performed for the various Y zeolites showcased the adsorption and desorption behavior of typical sulfur (thiophene) and hydrocarbon (heptane) molecules. Similarly, hydrophobic and organophilic crystalline molecular sieve, a new polymorph of SiO_2 named "Silicalite", has been utilized for the selective adsorption of organic molecules over water.[99] The adsorption of the benzene, toluene, dichloromethane, 1,1-dichloro-1-fluoroethane, and so on has been successfully demonstrated using hydrophobic Y-Type zeolite.[100] Therefore, from the literature reports, it is clear that in order to achieve the adsorption and/or separation of the hydrocarbons in porous materials, hydrophobicity plays a crucial role. Owing to the versatility and high pore volume, the crystalline MOFs provide a cost-effective alternative way to separate C1–C3 and higher hydrocarbons at higher temperatures.[97] In response to the above observations, in order to achieve the hydrophobicity in MOFs, incorporation of hydrophobic groups or atoms such as methyl, ethyl, *n*-propyl, $-CF_3$, and –F has been performed. The hydrophobicity induced into the FMOFs either via anions, such as SiF_6, PF_6, ZrF_6, SbF_6, and BF_4, or via perfluorinated carboxylate, triazolate, and tetrazolate organic ligands is studied in the literature. Hydrophobicity in these MOFs facilitates the stability of porous compounds in the presence of water helps for the separation/adsorption of hydrocarbons (Figure 10).

The development of Teflon like channeled nanoporous MOF having a chiral and uni-nodal 4-connected net for hydrocarbon sorption has been reported in 2005 (Figure 5c).[101] Subsequently, a 3D [Cu(hfipbb)(H_2hfipbb)$_{0.5}$] MOF, with fluorine-lined micro-channels, showed strong interactions with hydrocarbons, which in turn had large values for the heat of adsorption.[102] As these channels are hydrophobic, they allow the separation of nonpolar molecules from water. The shape and size-selective [Cu(hfipbb)(H_2hfipbb)$_{0.5}$] MOF showed an efficient method of separating normal C4 from higher normal alkanes and olefins. Similarly, in a Ca-based MOF named AEPF-1 based on the organic linker 4,4′-(hexafluoroisopropylidene)bis(benzoic acid), reversible structural change upon removal or addition of guest-solvent molecules has been showcased.[103] The perfluorinated spongy and hydrophobic AEPF-1 shows selective adsorption of various organic compounds such as toluene, benzene, isopropyl alcohol, 1-butanol, acetone, and acetonitrile based on their size, shape, and polarity.

Furthermore, highly fluorous MOFs (FMOFs) with superior adsorption and hydrophobic properties

toward oil spill cleanup and hydrocarbon storage have been reported in 2011 by Omary and co-workers.[56] The Ag-containing 3,5-bis(trifluoromethyl)-1,2,4-triazolate-based, fully perfluorinated MOFs with highly hydrophobic channels have been employed for hydrocarbon adsorption. The hydrophobic FMOFs with remarkable air and water stability exhibit a high affinity to C6–C8 hydrocarbons of oil components. The FMOFs (FMOF-1 and FMOF-2) can selectively adsorb C6–C8 hydrocarbons in preference to water, through a combination of hydrophobicity and capillary action. In another report, the separation of C3/C4 hydrocarbon mixtures by adsorption using a mesoporous MIL-100(Fe) was recorded.[104] The fluorine-containing MIL-100(Fe) shows preferential isobutane adsorption over propane and propylene in a wide range of temperature (323–523 K) and pressure (0–300 kPa). Temperature-dependent propane, isobutene, and propylene adsorption at low pressures is demonstrated depending on the interaction of adsorbate with Fe(II) sites.

2 SUMMARY

In summary, depending on the source of fluorine, FMOFs can be divided into three types as anion-induced fluorination, ligand pursued fluorination, and PECVD. The FMOFs synthesized using aforementioned fluorine sources possesses the higher stability toward aqueous or other acidic/basic conditions compared to that of its nonfluorinated analogs. It is to be noted that fluorine not only plays a vital role as a mineralizing agent but also favors the formation of well-crystalline phases during MOF synthesis. The fluorine-induced hydrophobicity into the FMOFs undeniably brings advantages for the adsorption or separation of hydrocarbons. Similarly, the selective adsorption of CO_2, CH_4, and H_2S in FMOFs over other gases has been demonstrated successfully using perfluorinated MOFs. Although there are few literature precedents available for the enhanced H_2 uptake due to fluorine insertion into MOFs with increased H_2 adsorption enthalpy, enhancement in H_2 uptake by FMOFs is not a universal phenomenon, but rather it is system specific and can differ from system to system. Nevertheless, thorough research work is necessary on H_2 adsorption on iso-structural fluorinated/nonfluorinated MOFs before we can conclusively indicate a positive/negative effect of fluorination on enhancement of H_2 adsorption in MOFs. From these results, it is clear that as fluorine atoms in FMOFs are weakly interacting with gas molecules, other factors, such as pore size, curvature, and open metal sites, can also play crucial roles in the high gas uptakes in these FMOFs. The capacities of CO_2 and H_2 adsorption are basically related to the textural properties as well as the functional groups of the MOFs.

3 ABBREVIATIONS AND ACRONYMS

bfbpdc = 2,2′-bistrifluoromethyl-biphenyl-4,4′-dicarboxylate; bpe = 1,2-bis(4-pyridyl)ethane; bpy = 4,4′-bipyridine; FMOF = fluorinated metal-organic framework; FMOF-1 = first perfluorinated metal-organic framework; MOF = metal-organic framework; tfbda = 2,3,5,6-tetrafluoro-1,4-benzenedicarboxylic acid; 3D = three-dimensional.

4 REFERENCES

1. G. S. Newth, ‘Inorganic Chemistry’, Longmans, Green, and Company, New York, 1903.
2. W. M. Latimer and J. H. Hildebrand, ‘Reference Book of Inorganic Chemistry’, New York, The Macmillan Company, 1938.
3. S. Purser, P. R. Moore, S. Swallow, and V. Gouverneur, *Chem. Soc. Rev.*, 2008, **37**, 320.
4. S. T. Purrington, B. S. Kagen, and T. B. Patrick, *Chem. Rev.*, 1986, **86**, 997.
5. J. Burdeniuc, B. Jedicka, and R. H. Crabtree, *Chem. Ber.*, 1997, **130**, 145.
6. E. Clot, O. Eisenstein, N. Jasim, S. A. Macgregor, J. E. McGrady, and R. N. Perutz, *Acc. Chem. Res.*, 2011, **44**, 333.
7. R. J. Hunadi and K. Baum, *Synthesis*, 1982, **39**, 454.
8. C. A. Fyfe, D. H. Brouwer, A. R. Lewis, and J.-M. Chezeau, *J. Am. Chem. Soc.*, 2011, **123**, 6882.
9. L. A. Villaescusa, I. Bull, P. S. Wheatley, P. Lightfoot, and R. E. Morris, *J. Mater. Chem.*, 2003, **13**, 1978.
10. P. A. Barrett, M. A. Camblor, A. Corma, R. H. Jones, and L. A. Villaescusa, *J. Phys. Chem. B*, 1998, **102**, 4145.
11. R. E. Morris, A. Burton, L. M. Bull, and S. I. Zones, *Chem. Mater.*, 2004, **16**, 2844.
12. S. Oliver, A. Kuperman, A. Lough, and G. A. Ozin, *J. Mater. Chem.*, 1997, **7**, 807.
13. S. Girard, A. Tuel, C. Mellot-Draznieks, and G. Férey, *Angew. Chem. Int. Ed.*, 2002, **41**, 972.
14. L. Pan, M. B. Sander, X. Huang, J. Li, M. Smith, E. Bittner, B. Bockrath, and J. K. Johnson, *J. Am. Chem. Soc.*, 2004, **126**, 1308.
15. C. Yang, X. Wang, and M. A. Omary, *J. Am. Chem. Soc.*, 2007, **129**, 15454.
16. R. A. Fischer and C. Woll, *Angew. Chem. Int. Ed.*, 2008, **47**, 8164.
17. S. Biswas, T. Remy, S. Couck, D. Denysenko, G. Rampelberg, J. F. M. Denayer, D. Volkmer, C. Detavernierd, and P. V. Der Voort, *Phys. Chem. Chem. Phys.*, 2013, **15**, 3552.
18. T. Loiseau and G. Férey, *J. Fluorine Chem.*, 2007, **128**, 413.

19. M. Estermann, L. B. McCusker, C. Baerlocher, A. Merrouche, and H. Kessler, *Nature*, 1991, **352**, 320.
20. J. C. Biffinger, H. W. Kim, and S. G. DiMagno, *ChemBioChem*, 2004, **5**, 622.
21. M. Maes, L. Alaerts, F. Vermoortele, R. Ameloot, S. Couck, V. Finsy, J. F. M. Denayer, and D. E. De Vos, *J. Am. Chem. Soc.*, 2010, **132**, 2284.
22. H. Koller, A. Wölker, L. A. Villaescusa, M. J. Díaz-Cabañas, S. Valencia, and M. A. Camblor, *J. Am. Chem. Soc.*, 1999, **121**, 3368.
23. L. A. Villaescusa, P. A. Barrett, and M. A. Camblor, *Angew. Chem. Int. Ed.*, 1999, **38**, 1997.
24. P. A. Barrett, T. Boix, M. Puche, D. H. Olson, E. Jordan, H. Kollere, and M. A. Camblor, *Chem. Commun.*, 2003, 2114.
25. C. A. Fernandez, P. K. Thallapally, R. K. Motkuri, S. K. Nune, J. C. Sumrak, J. Tian, and J. Liu, *Cryst. Growth Des.*, 2010, **10**, 1037.
26. S.-I. Noro, S. Kitagawa, M. Kondo, and K. Seki, *Angew. Chem. Int. Ed.*, 2000, **39**, 2081.
27. H. Cheng, X. Sha, L. Chen, A. C. Cooper, M. Foo, G. C. Lau, W. H. Bailey, and G. P. Pez, *J. Am. Chem. Soc.*, 2009, **131**, 17732.
28. Z. Hulvey, E. H. L. Falcao, J. Eckerta, and A. K. Cheetham, *J. Mater. Chem.*, 2009, **19**, 4307.
29. Z. Hulvey, D. A. Sava, J. Eckert, and A. K. Cheetham, *Inorg. Chem.*, 2011, **50**, 403.
30. H. Chun, D. N. Dybtsev, H. Kim, and K. Kim, *Chem. Eur. J.*, 2005, **11**, 3521.
31. P. Pachfule, Y. Chen, S. C. Sahoo, J. Jiang, and R. Banerjee, *Chem. Mater.*, 2011, **23**, 2908.
32. P. Pachfule, Y. Chen, J. Jiang, and R. Banerjee, *Chem. Eur. J.*, 2012, **18**, 688.
33. C. Janiak and J. K. Vieth, *New J. Chem.*, 2010, **34**, 2366.
34. S. Subramanian and M. Zaworotko, *Angew. Chem. Int. Ed.*, 1995, **34**, 2127.
35. M.-J. Lin, A. Jouaiti, D. Pocic, N. Kyritsakas, J.-M. Planeix, and M. W. Hosseini, *Chem. Commun.*, 2010, **46**, 112.
36. M.-J. Lin, A. Jouaiti, N. Kyritsakas, and M. W. Hosseini, *CrystEngComm*, 2009, **11**, 189.
37. S. D. Burd, S. Ma, J. A. Perman, B. J. Sikora, R. Q. Snurr, P. K. Thallapally, J. Tian, L. Wojtas, and M. J. Zaworotko, *J. Am. Chem. Soc.*, 2012, **134**, 3663.
38. K. Uemura, A. Maeda, T. K. Maji, P. Kanoo, and H. Kita, *Eur. J. Inorg. Chem.*, 2009, **16**, 2329.
39. B. F. Abrahams, S. R. Batten, H. Hamit, B. F. Hoskins, and R. Robson, *Chem. Commun.*, 1996, 1313.
40. S.-I. Noro, R. Kitaura, M. Kondo, S. Kitagawa, T. Ishii, H. Matsuzaka, and M. Yamashita, *J. Am. Chem. Soc.*, 2002, **124**, 2568.
41. J. S. Fleming, K. L. V. Mann, S. M. Couchman, J. C. Jeffery, J. A. McCleverty, and M. D. Ward, *J. Chem. Soc. Dalton Trans.*, 1998, 2047.
42. J. Jia, A. J. Blake, N. R. Champness, P. Hubberstey, C. Wilson, and M. Schroder, *Inorg. Chem.*, 2008, **47**, 8652.
43. E. A. Goreshnik, Y. I. Slyvka, and M. G. Mys'kiv, *Inorg. Chim. Acta*, 2011, **377**, 177.
44. P. Nugent, Y. Belmabkhout, S. D. Burd, A. J. Cairns, R. Luebke, K. Forrest, T. Pham, S. Ma, B. Space, L. Wojtas, M. Eddaoudi, and M. J. Zaworotko, *Nature*, 2013, **495**, 80.
45. S. Xiong, Y. He, R. Krishna, B. Chen, and Z. Wang, *Cryst. Growth Des.*, 2013, **13**, 2670.
46. G. Férey, *Chem. Soc. Rev.*, 2008, **37**, 191.
47. G. Férey and C. Serre, *Chem. Soc. Rev.*, 2009, **38**, 1380.
48. K. Barthelet, J. Marrot, D. Riou, and G. Férey, *Angew. Chem. Int. Ed.*, 2002, **41**, 281.
49. G. Férey, C. Serre, C. Mellot-Draznieks, F. Millange, S. Surble, J. Dutour, and I. Margiolaki, *Angew. Chem. Int. Ed.*, 2004, **43**, 6296.
50. G. Férey, C. Mellot-Draznieks, C. Serre, F. Millange, J. Dutour, S. Surble, and I. Margiolaki, *Science*, 2005, **309**, 2040.
51. A. Vimont, J.-M. Goupil, J.-C. Lavalley, M. Daturi, S. Surble, C. Serre, F. Millange, G. Férey, and N. Audebrand, *J. Am. Chem. Soc.*, 2006, **128**, 3218.
52. K. Barthelet, K. Adil, F. Millange, C. Serre, D. Riou, and G. Férey, *J. Mater. Chem.*, 2003, **13**, 2208.
53. K. Sumida, D. L. Rogow, J. A. Mason, T. M. McDonald, E. D. Bloch, Z. R. Herm, T.-H. Bae, and J. R. Long, *Chem. Rev.*, 2012, **112**, 724.
54. J. Liu, P. K. Thallapally, B. P. McGrail, D. R. Brown, and J. Liu, *Chem. Soc. Rev.*, 2012, **41**, 2308.
55. A. Torrisi, R. G. Bell, and C. Mellot-Draznieks, *Cryst. Growth Des.*, 2010, **10**, 2839.
56. C. Yang, U. Kaipa, Q. Z. Mather, X. Wang, V. Nesterov, A. F. Venero, and M. A. Omary, *J. Am. Chem. Soc.*, 2011, **133**, 18094.
57. A. E. Platero-Prats, V. A. de la Peña-O'Shea, D. M. Proserpio, N. Snejko, E. Gutiérrez-Puebla, and Á. Monge, *J. Am. Chem. Soc.*, 2012, **134**, 4762.
58. J.-S. Hu, L. Qin, M.-D. Zhang, X.-Q. Yao, Y.-Z. Li, Z.-J. Guo, H.-G. Zheng, and Z.-L. Xue, *Chem. Commun.*, 2012, **48**, 681.
59. C.-C. Ji, L. Qin, Y.-Z. Li, Z.-J. Guo, and H.-G. Zheng, *Cryst. Growth Des.*, 2011, **11**, 480.
60. P. Pachfule, C. Dey, T. Panda, and R. Banerjee, *CrystEngComm*, 2010, **12**, 1600.
61. J. H. Yoon, S. B. Choi, Y. J. Oh, M. J. Seo, Y. H. Jhon, T.-B. Lee, D. Kim, S. H. Choi, and J. Kim, *Catal. Today*, 2007, **120**, 324.
62. F. A. Cotton, J. P. Donahue, C. Lin, and C. A. Murillo, *Inorg. Chem.*, 2001, **40**, 1234.

63. B. E. Bursten, M. H. Chisholm, R. J. H. Clark, S. Firth, C. M. Hadad, P. J. Wilson, P. M. Woodward, and J. M. Zaleski, *J. Am. Chem. Soc.*, 2002, **124**, 12244.
64. E. A. Mikhalyova, S. V. Kolotilov, M. Zeller, L. K. Thompson, A. W. Addison, V. V. Pavlishchuk, and A. D. Hunter, *Dalton Trans.*, 2011, **40**, 10989.
65. M. H. Chisholm, P. J. Wilson, and P. M. Woodward, *Chem. Commun.*, 2002, 566.
66. C. Seidel, C. Lorbeer, J. Cybińska, A.-V. Mudring, and U. Ruschewitz, *Inorg. Chem.*, 2012, **51**, 4679.
67. C. M. MacNeill, C. S. Day, A. Marts, A. Lachgar, and R. E. Noftle, *Inorg. Chim. Acta*, 2011, **365**, 196.
68. S.-C. Chen, Z.-H. Zhang, Q. Chen, H.-B. Gao, Q. Liu, M.-Y. He, and M. Du, *Inorg. Chem. Commun.*, 2009, **12**, 835.
69. R. Kitaura, F. Iwahori, R. Matsuda, S. Kitagawa, Y. Kubota, M. Takata, and T. C. Kobayashi, *Inorg. Chem.*, 2004, **43**, 6522.
70. B. Chen, Y. Yang, F. Zapata, G. Qian, Y. Luo, J. Zhang, and E. B. Lobkovsky, *Inorg. Chem.*, 2006, **45**, 8882.
71. L. Hou, W.-J. Shi, Y.-Y. Wang, Y. Guo, C. Jin, and Q.-Z. Shi, *Chem. Commun.*, 2011, **47**, 5464.
72. Z. Hulvey, J. D. Furman, S. A. Turner, M. Tang, and A. K. Cheetham, *Cryst. Growth Des.*, 2010, **10**, 2041.
73. P. Horcajada, F. Salles, S. Wuttke, T. Devic, D. Heurtaux, G. Maurin, A. Vimont, M. Daturi, O. David, E. Magnier, N. Stock, Y. Filinchuk, D. Popov, C. Riekel, G. Férey, and C. Serre, *J. Am. Chem. Soc.*, 2011, **133**, 17839.
74. X. Lin, I. Telepeni, A. J. Blake, A. Dailly, C. M. Brown, J. M. Simmons, M. Zoppi, G. S. Walker, K. M. Thomas, T. J. Mays, P. Hubberstey, N. R. Champness, and M. Schröder, *J. Am. Chem. Soc.*, 2009, **131**, 2159.
75. Y. Liu, J.-R. Li, W. M. Verdegaal, T.-F. Liu, and H.-C. Zhou, *Chem. Eur. J.*, 2013, **19**, 5637.
76. J. Seo, C. Bonneau, R. Matsuda, M. Takata, and S. Kitagawa, *J. Am. Chem. Soc.*, 2011, **133**, 9005.
77. T.-H. Chen, I. Popov, O. Zenasni, O. Daugulis, and O. Š. Miljanić, *Chem. Commun.*, 2013, **49**, 6846.
78. S. J. Yang and C. R. Park, *Adv. Mater.*, 2012, **24**, 4010.
79. Y. Cheng, A. Kondo, H. Noguchi, H. Kajiro, K. Urita, T. Ohba, K. Kaneko, and H. Kanoh, *Langmuir*, 2009, **25**, 4510.
80. J. Yang, A. Grzech, F. M. Mulder, and T. J. Dingemans, *Chem. Commun.*, 2011, **47**, 5244.
81. J. B. Decoste, G. W. Peterson, M. W. Smith, C. A. Stone, and C. R. Willis, *J. Am. Chem. Soc.*, 2012, **134**, 1486.
82. D. Britt, H. Furukawa, B. Wang, T. G. Glover, and O. M. Yaghi, *Proc. Natl. Acad. Sci. U. S. A.*, 2006, **103**, 10186.
83. J. An, R. P. Fiorella, S. J. Geib, and N. L. Rosi, *J. Am. Chem. Soc.*, 2009, **131**, 8401.
84. R. Vaidhyanathan, S. S. Iremonger, K. W. Dawson, and G. K. H. Shimizu, *Chem. Commun.*, 2009, 5230.
85. T. Panda, P. Pachfule, Y. Chen, J. Jiang, and R. Banerjee, *Chem. Commun.*, 2011, **47**, 2011.
86. C. A. Fernandez, J. Liu, P. K. Thallapally, and D. M. Strachan, *J. Am. Chem. Soc.*, 2012, **134**, 9046.
87. A. Santra, I. Senkovska, S. Kaskel, and P. K. Bharadwaj, *Inorg. Chem.*, 2013, **52**, 7358.
88. Q. Yu, J. Yang, Q. Zhao, J. Dong, and J. Li, *J. Coord. Chem.*, 2012, **65**, 1645.
89. P. Pachfule, R. Das, P. Poddar, and R. Banerjee, *Inorg. Chem.*, 2011, **50**, 3855.
90. P. Pachfule, R. Das, P. Poddar, and R. Banerjee, *Cryst. Growth Des.*, 2011, **11**, 1215.
91. A. Kondo, H. Kajiro, H. Noguchi, L. Carlucci, D. M. Proserpio, G. Ciani, K. Kato, M. Takata, H. Seki, M. Sakamoto, Y. Hattori, F. Okino, K. Maeda, T. Ohba, K. Kaneko, and H. Kanoh, *J. Am. Chem. Soc.*, 2011, **133**, 10512.
92. P. Pachfule, C. Dey, T. Panda, K. Vanka, and R. Banerjee, *Cryst. Growth Des.*, 2010, **10**, 1351.
93. W. Yang, X. Lin, A. J. Blake, C. Wilson, P. Hubberstey, N. R. Champness, and M. Schroder, *Inorg. Chem.*, 2009, **48**, 11067.
94. M. Latroche, S. Surblé, C. Serre, C. Mellot-Draznieks, P. L. Llewellyn, J.-H. Lee, J.-S. Chang, S. H. Jhung, and G. Férey, *Angew. Chem. Int. Ed.*, 2006, **45**, 8227.
95. S. I. Semenova, *J. Membr. Sci.*, 2004, **231**, 189.
96. B. Smit and T. L. M. Maesen, *Nature*, 1995, **374**, 42.
97. H. Wu, Q. Gong, D. H. Olson, and J. Li, *Chem. Rev.*, 2012, **112**, 836.
98. L. Lin, Y. Zhang, H. Zhang, and F. Lu, *J. Colloid Interface Sci.*, 2011, **360**, 753.
99. E. M. Flanigen, J. M. Bennett, R. W. Grose, J. P. Cohen, R. L. Patton, R. M. Kirchner, and J. V. Smith, *Nature*, 1978, **271**, 512.
100. J.-H. Yun and D.-K. Choi, *AIChE J*, 1998, **44**, 1344.
101. A. Monge, N. Snejko, E. Gutierrez-Puebla, M. Medina, C. Cascales, C. Ruiz-Valero, M. Iglesias, and B. Gomez-Lor, *Chem. Commun.*, 2005, 1291.
102. L. Pan, D. H. Olson, L. R. Ciemnolonski, R. Heddy, and J. Li, *Angew. Chem. Int. Ed.*, 2006, **45**, 616.
103. A. E. Platero-Prats, V. A. de la Pena-O'Shea, N. Snejko, A. Monge, and E. Gutierrez-Puebla, *Chem. Eur. J.*, 2010, **16**, 11632.
104. M. G. Plaza, A. M. Ribeiro, A. Ferreira, J. C. Santos, Y. K. Hwang, Y.-K. Seo, U.-H. Lee, J.-S. Chang, J. M. Loureiro, and A. E. Rodrigues, *Microporous Mesoporous Mater.*, 2012, **153**, 178.

Synthesis and Structures of Aluminum-Based Metal-Organic Frameworks

Norbert Stock

Christian-Albrechts-Universität zu Kiel, Kiel, Germany

1	Introduction	99
2	Summary of Al-Based MOFs	100
3	Synthesis of Al-MOFs	100
4	Structures of Al-Based MOFs	108
5	Conclusion	110
6	Related Articles	111
7	Abbreviations and Acronyms	111
8	References	111

1 INTRODUCTION

Metal–organic frameworks (MOFs) containing light and environmentally benign metals have attracted researchers from industry and academia since they are believed to be well suited for applications especially in the field of gas storage. Aluminum is one element of choice for the synthesis of such MOFs since it leads to stable and highly porous materials that can also be formed in water as a green solvent.[1–3] The potential application of the Al-based MOFs is well documented in various patents[4–25] mainly issued by the pioneers of this field—BASF and the groups of Ferey and Loiseau—and press releases have been issued announcing large scale testing and their solvent-free synthesis.[26]

Owing to the oxophilicity of Al^{3+} ions all Al-MOFs contain Al–O bonds. In contrast to the large number of microporous zeolites in which the aluminum ion in the framework is exclusively tetrahedrally surrounded, only octahedrally coordinated Al atoms have been observed in Al-MOFs until now. The majority of the limited number of reported Al-MOFs is based on polycarboxylic linker molecules although a few examples of porous aluminum phosphonates have been described in the literature.[27–29] The stability and the small number of Al-based MOFs stems from the same factors: the high charge (+3) of the metal ion and the small ionic radius (r(CN = 6): 0.675 Å). Hence dissolution of these MOFs in water is often kinetically hindered and at the same time they are almost exclusively obtained as microcrystalline products. The latter fact has impeded the structure elucidation and the determination of structure property relationship and hence the intensive investigation of this class of compounds.

The small scale synthesis of Al-MOFs—up to a few hundred milligrams—has been reported to be feasible in a wide range of reaction temperatures varying from room temperature to 220 °C. Conventional heating as well as microwave-assisted (MW) heating and electrochemical synthesis conditions have been employed.[30] High-throughput methods allow a systematic and efficient approach for the discovery of new and the synthesis optimization of known MOFs, and specifically have proven to be very helpful in the discovery and optimization of Al-based compounds.[31] In situ crystallization studies employing powder X-ray diffraction (PXRD) and nuclear magnetic resonance (NMR) spectroscopy helped to shed light on the formation of these compounds.

Owing to their favorable properties the synthesis of some of the Al-MOFs has been scaled to a multi-kilogram scale, reported examples are Al-MIL53 (Basolite A100) and an aluminum fumarate (Basolite A520).[2] Al-MIL-53 is also the most intensively and best studied Al-MOF since it (i) can be readily synthesized in water, (ii) can be modified with different functional groups by direct synthesis and post-synthetic modification (PSM), (iii) is chemically and thermally stable, (iv) exhibits a strong framework flexibility, and (v) was the first Al-MOF that was available in larger quantities. Accordingly many gas and liquid sorption and

Metal-Organic Framework Materials. Edited by Leonard R. MacGillivray and Charles M. Lukehart.
© 2014 John Wiley & Sons, Ltd. ISBN 978-1-119-95289-3

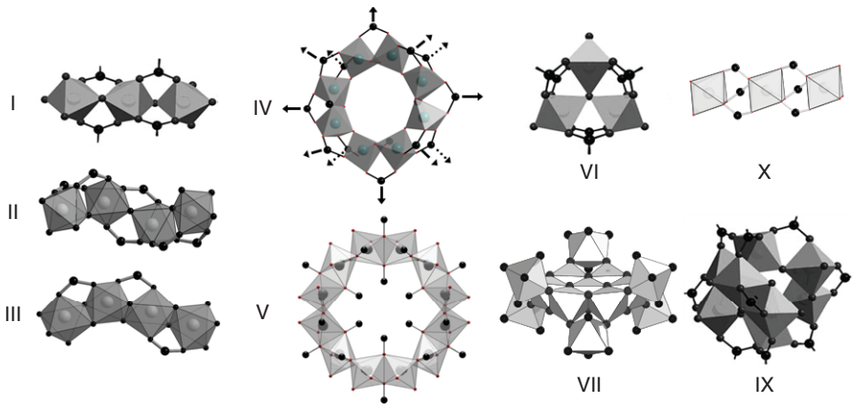


Figure 1 Inorganic building units observed in Al-MOFs. Numbering scheme corresponds to the building units listed in Table 1 (building unit VIII not shown). Units I, II, III, VII, and X are only sections of the 1D building units

separation studies have been performed for MIL-53 and its derivatives.[32–49] Amino-functionalized Al-MOFs have attracted particular interest (MIL-53-NH_2 and CAU-1-NH_2) since they exhibit beneficial properties in the adsorption of CO_2.[40,44,45,50,51] Al-based MOFs that are stable upon adsorption of H_2S, an adsorptive that usually leads to the decomposition of MOFs, are known[41,46,52] and some of the MOFs have been obtained as thin layers for possible sensor applications,[22,51,53] and as membranes[50,54–62] for separation processes.

In the following paragraphs a summary of known Al-MOFs (Section 2), their synthesis (Section 3) and their crystal structure (Section 4) are presented in detail.

2 SUMMARY OF Al-BASED MOFs

Although various patents on Al-MOFs have been issued only few of the described compounds have been characterized in detail. This is mainly due to the fact, that most of the compounds are only obtained as microcrystalline products, which in turn complicates the crystal structure determination. The majority of Al-based MOFs have been reported by groups from the Université de Versailles, France (MIL-type materials, MIL = Matériaux de l'Institut Lavoisier) and the Christian-Albrechts Universität (CAU-type materials) over the last decade. During the last 2 years the interest in using aluminum as a metal ion has increased and therefore new materials have been recently reported from other groups as well (Table 1).

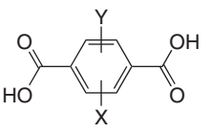
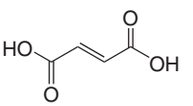
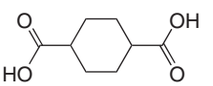
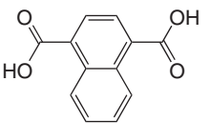
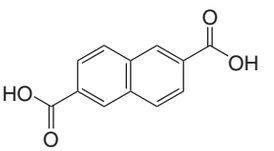
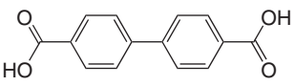
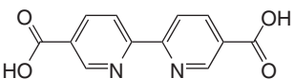
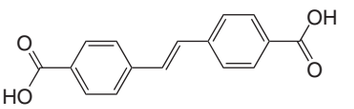
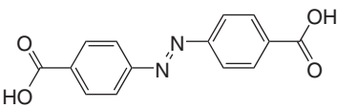
Noteworthy, until now only relatively few types of linker molecules have been reported to lead to crystalline Al-MOFs (Table 1). Terephthalic acid and its derivatives have been shown to lead to a surprising variety of framework structures. The studies demonstrate that the solvent employed plays a crucial role on the inorganic building unit observed in the final product. Table 1 summarizes various aspects of Al-MOFs: (i) the abbreviation of the Al-MOF and the method of structure determination/assignment, (ii) the chemical formula including functional groups attached to the linker and the abbreviation used in the chemical formula, (iii) the structural formula of the linker, and (iv) the inorganic building unit observed in the crystal structure and the solvents employed in the syntheses. These inorganic building units are also depicted in Figure 1.

3 SYNTHESIS OF Al-MOFs

Solvothermal syntheses are known to be often very sensible to small changes in the compositional as well as process parameters. The latter include reactor material and size, heating method, heating/cooling rate, reaction temperature and time, while chemical parameters cover the chemical composition of the starting mixture, e.g., molar ratio of the starting materials, pH, solvents/solvent mixtures, overall concentration or the cation source. The following sections cover studies where some of these parameters were systematically investigated. In addition PSM and post-synthetic exchange (PSE) reactions as well as modification reactions that occur during the solvothermal process or the activation procedure are described.

One of the most important parameter that has a strong influence on the product formation is the solvent in which the reactions are carried out. The first syntheses of Al-MOFs were exclusively carried out in water as the solvent using autoclaves at high temperatures (up to 220 °C) and employing long reaction times. This approach was mainly used for the synthesis of the MIL-type materials (Table 1, Figures 1 and 2). The first Al-MOF described

Table 1 List of directly synthesized functionalized and non-functionalized Al-MOFs and the organic linker molecules employed

Name and method of structure determination	Chemical formula of the MOF, abbreviation of the linker molecules and functional groups incorporated	Structural formula of the linker	Inorganic building unit and solvent used[(a)]	Reference
Ditopic linker				
MIL-53-X/Y (PDC, PD)	[Al(OH)(BDC-X/Y)] H_2BDC-X/Y X/Y = H, CH_3, F, Cl, Br, NH_2, NO_2, OH, SH, COOH		I, W, D, W/D	37,63–68
Basolite-520 (PDC)	[Al(OH)(O_2-C_2H_2-CO_2)]		I, W	3
CAU-13 (PD)	[Al(OH)(*trans*-1,4-CDC)] *trans*-1,4-H_2CDC		I, W/D	69
Al-PCP (PD)	[Al(OH)(1,4-NDC)] 1,4-H_2NDC		I, W	70
MIL-69 (PD) DUT-4 (PD) CAU-3-NDC (PD)	[Al(OH)(2,6-NDC)] [Al(OH)(2,6-NDC)] [$Al_2(OCH_3)_4$(2,6-NDC)] 2,6-H_2NDC		I, W I, D V, M	71 72 73
DUT-5 (PD)	[Al(OH)(2,6-BPDC)] 4,4′-H_2BPDC		I, D	72
MOF-253 (PDC)	[Al(OH)(2,6-BPyDC)] 4,4′-H_2BPyDC		I, D	74
CYCU-3 (PD)	[Al(OH)(4,4′-SDC)] 4,4′-H_2SDC		I, D	75
MIL-130 (PDC)	[Al(OH)(4,4′-ADC)] 4,4′-H_2ADC		I, D	4

(*continued overleaf*)

Table 1 (*Continued*)

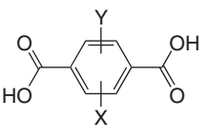
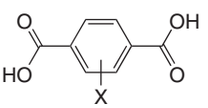
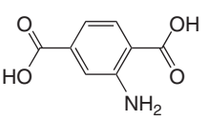
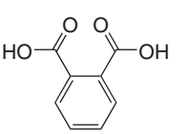
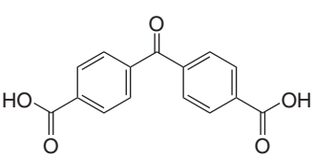
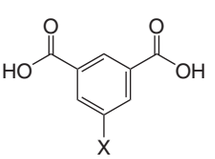
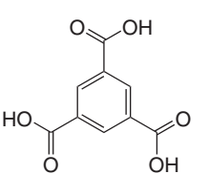
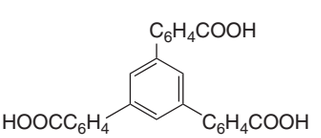
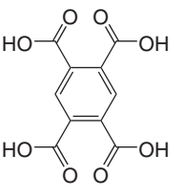
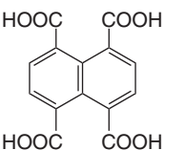
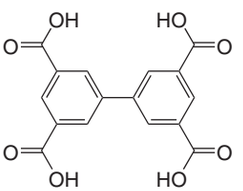
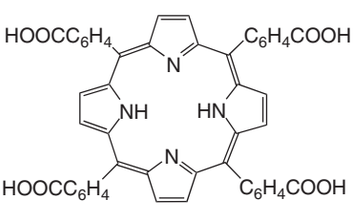
Name and method of structure determination	Chemical formula of the MOF, abbreviation of the linker molecules and functional groups incorporated	Structural formula of the linker	Inorganic building unit and solvent used[(a)]	Reference
CAU-1 (PD, PDC)	$[Al_4(OH)_2(OCH_3)_4(BDC\text{-}X)_3]$ $H_2BDC\text{-}X$ X/Y = H, NH_2, $NHCH_3$, NHCHO, OH, SH		IV, M	76–78
CAU-3 (PD)	$[Al_2(OCH_3)_4(BDC\text{-}X)]$ $H_2BDC\text{-}X$ X = H, NH_2		V, M	73
MIL-101-NH_2 (PDC)	$[Al_3O(H_2O)_2(OH)(BDC\text{-}NH_2)_3]$		VI, D	76,79
CAU-6 (PDC)	$[Al_{13}(OH)_{27}(H_2O)_6(BDC\text{-}NH_2)_3Cl_6(C_3H_7OH)_6]$ 1,4-$H_2BDC\text{-}NH_2$		VII, IP	80
CAU-15 (PD)	$[Al_2(OH)_4(1,2\text{-}BDC)]$ 1,2-H_2BDC		III, W/D	
CAU-8 (SD)	[Al(OH)(4,4′-BPhDC)] 4,4′-H_2BPhDC		I, W/D	81
CAU-10-X (PD, PCD)	[Al(OH)(1,3-BDC-X)] 1,3-H_2BDC-Y X = H, CH_3, Br, NH_2, NO_2, OH, OCH_3		II, W/D	82,83
Tritopic linker molecules				
MIL-96 (SD) MIL-100 (MD) MIL-110 (MD)	$[Al_{12}O(OH)_{18}(H_2O)_3(BTC)_6]$ $[Al_3O(H_2O)_2(OH)(BTC)_2]$ $[Al_8(OH)_{12}(BTC)_3]$ H_3BTC		VI, VIII, W VI, W IX, W	84 85 86
CAU-4 (PDC)	[Al(BTB)] H_3BTB		X, D	87

Table 1 (*Continued*)

Name and method of structure determination	Chemical formula of the MOF, abbreviation of the linker molecules and functional groups incorporated	Structural formula of the linker	Inorganic building unit and solvent used[(a)]	Reference
Tetratopic linker molecules				
MIL-118A (MD)	$[Al_2(OH)_2(H_2O)_2(BTEC)]$		I, W	88
MIL-118B (PD)	$[Al_2(OH)_2(BTEC)]$		I, T	88
MIL-120 (MD)	$[Al_4(OH)_8(BTEC)]$			89,90
MIL-121 (PD)	$[Al(OH)(H_2BTEC)]$		III, W, W/D	91
	1,2,4,5-H_4BTEC		I, W	
MIL-122 (PD)	$[Al_2(OH)_2(1,4,5,8\text{-NDC})]$		I, W	92
	1,4,5,8-H_4NDC			
NOTT-300 (PD)	$[Al_2(OH)_2(BPTC)]$		II, W	93
	3,3′,5,5′-H_4BPTC			
Al-PMOF (PD)	$[Al_2(OH)_2(H_2TCPP)]$		I, W	94
	H_6TCPP			

All structures with the exception of CAU-15 exhibit a 3D connectivity.
Solvent: W, water; D, DMF; M, methanol; IP, isopropanol; W/D, mixture of DMF and water; T, thermal treatment.
X-ray structure determination: MD, micro-diffraction on single crystals; SD, single-crystal diffraction; PD, powder diffraction (refinement); PDC, powder diffraction comparison of PXRD patterns.
[(a)]I: *trans* corner-sharing AlO_6 polyhedra; II: *cis* corner-sharing AlO_6 polyhedra; III: *cis* and *trans* edge-sharing AlO_6 polyhedra; IV: octameric ring of corner- and edge-sharing AlO_6 polyhedra, $\{Al_8(OH)_4(OCH_3)_8\}^{12+}$; V: dodecameric ring of edge-sharing AlO_6 polyhedra, $\{Al_{12}(OCH_3)_{24}\}^{12+}$; VI: trimeric building unit, $\{Al_3(\mu_3\text{-}O)(H_2O)_2(OH)\}^{6+}$; VII: condensation of the $[Al_{13}(OH)_{24}(H_2O)_{24}]^{15+}$ ions leads to columns of the composition $[Al_{13}(OH)_{27}(H_2O)_{18}]^{12+}$; VIII: *cis* and *trans* corner-sharing AlO_6 polyhedra; IX: octameric cluster composed of three bioctahedral edge-shared units capped by two threefold, corner-sharing AlO_6 polyhedra; X: non-interconnected AlO_6 polyhedra.

in 2003 by Ferey *et al*. with terephthalic acid as the linker molecule was Al-MIL-53, and in subsequent investigations by the same group larger or tri- and tetratopic linkers such as 2,6-naphthalenedicarboxylic acid and 1,3,5-benzenetricarboxylic acid were used. This led to the discovery of MIL-69, -96, -100, -110, -118, -120, -121, and -122. The first porous Al-MOF that was not reported by the Ferey group is Al-PCP, which contains 1,4-NDC^{2-} ions as linker molecules.[70] The successful use of organic solvents was first demonstrated in 2009 for the synthesis of DUT-4, -5 (DUT = Dresden University of Technology) and for CAU-1 and it had a number of consequences. The most important is the discovery of the unique inorganic building units ($\{Al_8(OH)_4(OCH_3)_8\}^{12+}$ and $\{Al_{12}(OCH_3)_{24}\}^{12+}$) in CAU-1 and -3. These new building units in combination with the common organic linker molecules (H_2BDC and its

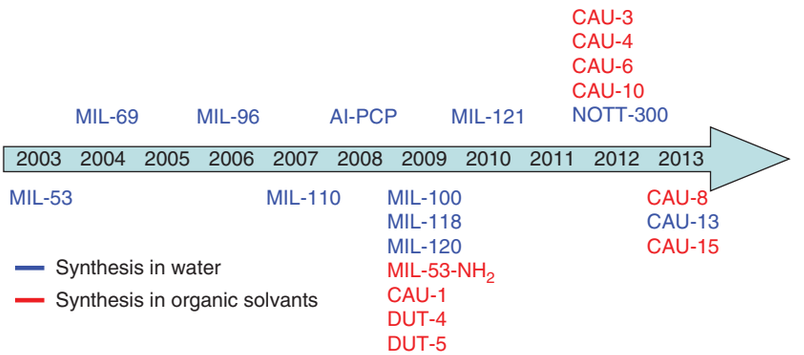


Figure 2 Timeline depicting the year of the first report of the new Al-MOFs. Compounds synthesized in water are shown in black, the ones obtained from organic solvents are shown in red

derivatives) led to new framework structures.[73,76] In addition, the solvent can have a strong influence on the porosity of the final MOF. In the case of the isoreticular compounds with the composition [Al(OH)(2,6-NDC)]·x solvent, i.e., MIL-69[71] and DUT-4,[72] the use of water as a solvent leads to a non-porous structure (MIL-69) while the use of DMF results in the formation of an open-framework.

Other important factors are the pH of the reaction mixture, as systematically demonstrated, for example, in the synthesis of the two MIL series MIL-96, -100, -110[95] and MIL-118, -120, -121.[91] The compounds can only be obtained as phase pure products when the pH of the starting mixture is precisely adjusted to the correct values. An example for the influence of the Al^{3+} salt is found in the synthesis of CAU-1 and Al-MIL-53-X derivatives. While the use of $Al(NO_3)_3 \cdot xH_2O$ results in the formation of MIL-53-NH_2, CAU-1 is only formed under identical reaction conditions when $AlCl_3 \cdot 6H_2O$ is used.[76] Optimized reaction conditions for differently functionalized Al-MIL-53 materials were shown to necessitate the use of different Al^{3+} salts.[64]

In most of the syntheses conventional electric (CE) heating was employed. Only few materials were synthesized at elevated temperatures under ambient pressure using round bottom flasks[96] and only one compound (Basolite520) was obtained from water under ambient conditions.[3] The synthesis of the latter Al-MOF was accomplished in high yields and a very high space-time-yield of $>3600\,kg\,m^{-3}\,day^{-1}$.[6] In contrast MW heating has been used in only a few studies, e.g., the synthesis of MIL-53,[97] MIL-53-COOH,[65,90] MIL-53-F,[66] MIL-96,[90,98] MIL-100,[98,99] MIL-110,[98] MIL-120,[90] as well as CAU-1 derivatives.[77,78,100] In some of these studies, MW heating was demonstrated to show how it led to substantially shorter induction and crystallization times in comparison to conventional heating.[77,97,100]

For the synthesis of Al-based MOFs most groups have employed standard solvothermal reaction systems with Teflon lined autoclaves, but high-throughput methods including 24 or 48 multiclaves have also been used in the Stock group.[31] The smaller reaction volumes ($V_{max} \sim 2\,mL$ or $300\,\mu L$, respectively) as compared to the standard autoclaves ($V_{max} \sim 20\,mL$) allows reducing the amounts of reagents, and owing to the large number of possible experiments, a systematic investigation of the reaction systems is possible (Table 2). This permits establishing reaction trends as well as structural trends. Recently the versatility of HT methods was demonstrated for the investigation of Al-MOFs taking the requirements of an industrial process into account and employing MW-assisted heating.[90]

Table 2 Reported high-throughput investigations of Al-MOFs and parameters that were of main importance

CAU-1-NH_2	Influence of solvents and reactant ratios, methanol as a solvent	76
CAU-3	Influence of the addition of base and the overall concentration	73
CAU-4	Influence of solvents and reactant ratios, DMF as a solvent	87
CAU-8	Influence of Al^{3+} salt, reactant and H_2O/DMF ratios, absolute concentration, reaction time and temperature and pH	81
CAU-10	Influence of Al^{3+} salt as well as reactant and H_2O/DMF ratios	82
CAU-13	Influence of mixed linker molar ratio	69
MIL-53-NH_2	Influence of solvents and Al^{3+} salt	76
MIL-53-COOH	MW-assisted heating, influence of reactant and H_2O/DMF ratios	90
MIL-96	MW-assisted heating, influence of reactant and H_2O/DMF ratios	90
MIL-101-NH_2	Influence of solvents for Al-MOFs; DMF as solvent	76
MIL-120	MW-assisted heating, influence of reactant and H_2O/DMF ratios	90
MIL-121	Influence of starting pH on selective formation of MIL-118, -120, -121	91

As an example, the detailed HT investigation of the chemical system $Al(NO_3)_3 \cdot 9H_2O/H_4BTEC/H_2O/NaOH$ is described in the following section, which led to the synthesis of three Al-MOFs. In this work the influence of the starting pH and the overall concentration on the phase formation was studied. The HT-methods enabled the authors to establish reaction conditions for the selective formation of the three compounds (MIL-118, -120 and -121), and based on the data synthesis-structure correlations could be established. Thus, low pH favors the formation of corner-sharing AlO_6 polyhedra as found in MIL-118 and -121, while higher pH values lead to edge-sharing AlO_6 polyhedra as observed in MIL-120. The increase of the starting pH leads to a higher degree of deprotonation of H_4BTEC and thus for MIL-121, -118, and -120 four, six, and eight carboxyl O atoms are connected to Al^{3+} ions, respectively (Figure 3).

PSM reactions of MOFs have been intensively studied during the last few years and various review articles have been reported on this topic. Owing to their thermal and chemical stability, the amino functionalized MOFs MIL-53-NH_2, and CAU-1-NH_2 were extensively used as starting materials to carry out linker modification reactions. These range from the formation of amides[67] and azides[11,23–25] to isocyanates and isothiocyanates.[101] For MIL-53 and MIL-53-OH the modification with 1,1′-ferrocenediyl-dimethylsilane[32] and the exchange of H^+ with Li^+ were reported.[42] Metal complexation within a MOF using free binding sites on the linker molecule has also been demonstrated. The compound MOF-253 contains non-coordinating 2,2′-bipyridine units and was employed to bind Pd^{2+} and Cu^{2+} ions.[74] The porphyrin-based MOF Al-PMOF, contains free-base porphyrin rings that can be metallated.[94] As a proof of concept the introduction of Zn^{2+} ions was demonstrated.

A very new reaction route for the synthesis of MOFs is the so-called postsynthetic ligand and metal ion exchange (PSE) processes.[102] Al-MIL-53-NH_2 and Al-MIL-53-Br were used in this study and ligand exchange reactions were demonstrated to take place under mild reaction conditions. In another experiment the incubation of Al-MIL-53-Br led to a mixed metal MOF Al/Fe-MIL-53-Br.

Another kind of PSM reaction has been reported during the activation of as synthesized Al-MOFs. Since they are mostly highly stable often severe treatment conditions are used. Nevertheless, these can result in an irreversible structural transformation as shown

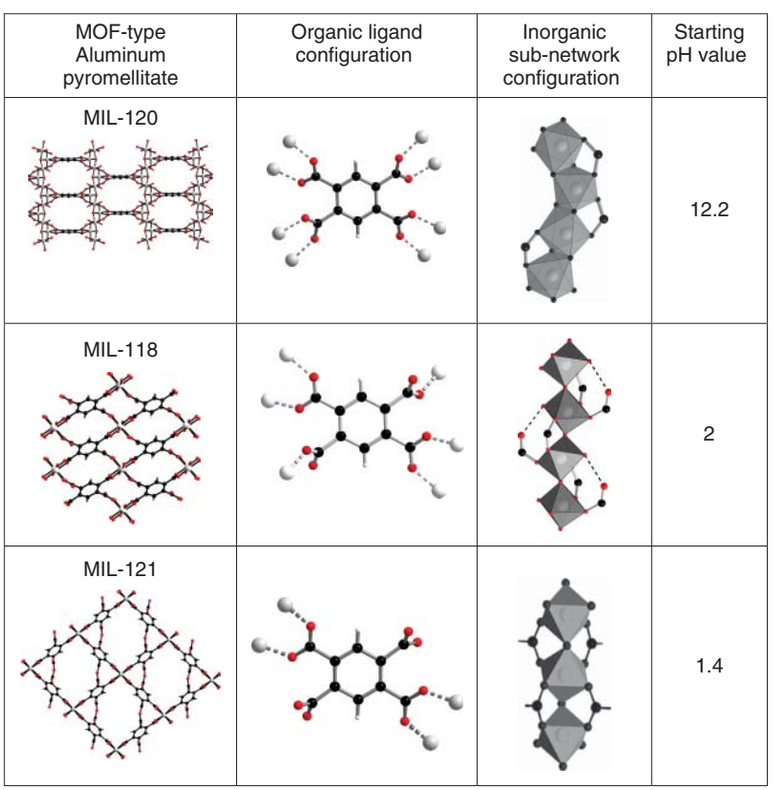


Figure 3 Influence of pH in the system $Al(NO_3)_3 \cdot 9H_2O/H_4BTEC/H_2O/NaOH$ on the formation of Al pyromellitate frameworks. (Reprinted with permission from Ref. 91. Copyright (2010) American Chemical Society.)

for MIL-118A into MIL-118B upon heating.[88] Both compounds exhibit different connectivities of the inorganic and organic building units and hence distinct PXRD patterns. Thermal heating can also lead to smaller structural changes, for example, of the organic or inorganic building units, which are not as readily detectable by X-ray diffraction. These can be confirmed, for example, by solid state NMR-spectroscopy[76] or by dissolving the activated compounds in deuterated solvents under acidic or basic conditions and carrying out ^{1}H- and ^{13}C-NMR-spectroscopic measurements.[65] Another possibility is to use in situ IR spectroscopy to follow the structural changes.[65] In MIL-53-COOH the thermal activation at elevated temperatures leads to the formation of carboxylic acid-anhydride groups and decarboxylation, which in turn modifies the structural flexibility of the framework (Figure 4a). The activation of CAU-1-NH_2 ($[Al_8(OH)_4(OCH_3)_8(1,4\text{-BDC-}NH_2)_6]\cdot x\,H_2O$) represents an even more complicated case. The synthesis conditions of the material must be carefully adjusted since prolonged reaction times (>3 min at 145 °C) lead to the methylation of the amino group that renders these groups unreactive for PSM. The inorganic building unit $\{Al_8(OH)_4(OCH_3)_8\}^{12+}$ can be modified while preserving the porosity of the framework. The thermal treatment under reduced pressure results only in the removal of the water molecules from the micropores, but the activation in air leads to the replacement of the $-OCH_3$ by $-OH$ groups and the inorganic building units $\{(Al_8(OH)_{12})\}^{12+}$ are formed (Figure 4).

While HT methods help to accelerate the discovery and synthesis optimization and allow establishing the field of formation they do not give any information about the crystallization process itself. Time-resolved crystallization studies using energy dispersive X-ray diffraction (EDXRD), small-angle X-ray scattering (SAXS)/wide-angle X-ray scattering (WAXS), and NMR-spectroscopy were carried out to learn more about the formation of Al-MOFs (Table 3). Diffraction measurements allow the

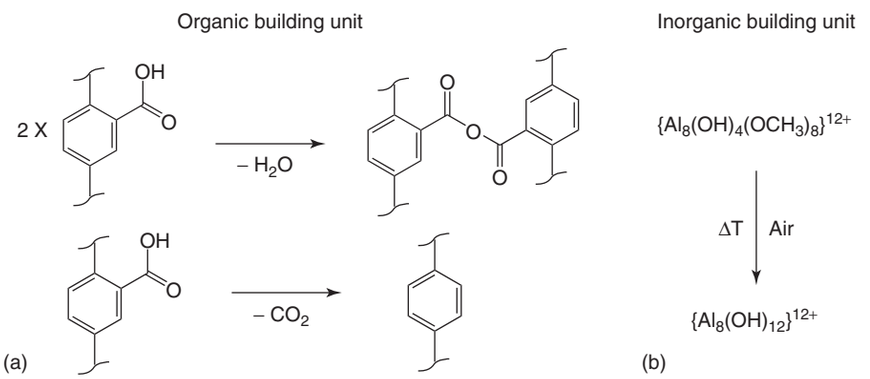


Figure 4 PSM reactions observed during the thermal activation of MIL-53-COOH (a) and CAU-1-NH_2 (b)

Table 3 List of crystallization studies of Al-MOFs and characterization methods applied

Ex-situ studies			
M-MIL-53; V-MIL-47	XRPD	Influence of metal ions on crystallization kinetics of isostructural M(III)-BDCs (M = Cr, Al)	103
MIL-96, -100, -110	XRPD	Influence of heating method, reaction time on the crystallization kinetics and phase formation	95
In-situ studies			
CAU-1-$(OH)_2$	EDXRD	Influence of heating methods on the kinetics	77
CAU-1-X	EDXRD	Effects of linker and heating methods on the kinetics X = $(OH)_2$, NH_2	100
MIL-53-NH_2 and MIL-101-NH_2	SAXS/WAXS	Evaluation of the competitive formation of Al-MIL-53-NH_2, Al-MOF-235-NH_2, and Al-MIL-101-NH_2	104
	SAXS/WAXS	Live encapsulation of Keggin polyanions, evaluation of the competitive formation of Al-MOF-235-NH_2 and Al-MIL-101-NH_2	105
CAU-13		Kinetics of the crystallization process	69
MIL-96 MIL-100 MIL-110	NMR	Determination of solution species under hydrothermal reaction conditions and correlation with building units observed in the MOFs	95

detection of crystalline intermediates and the assessment of individual reaction parameters, i.e., reaction rate constants and activation energies. These parameters are helpful to optimize the synthesis conditions of new compounds and to adjust the crystal size of the final product. NMR experiments allow the investigation of the solution species in order to understand the relationship between the chemistry occurring in solution and the topology of final crystalline structures. While such in-situ studies often require the use of special equipment, ex-situ studies can be more easily carried out under laboratory conditions and are fairly straightforward to conduct. Nevertheless the latter rely on the assumption that quenching and isolation does not lead to changes of the reaction products and are therefore not as reliable.

In one ex-situ study the influence of the metal ion on the formation rate of the isostructural compounds V-MIL-47, Al-MIL-53, and Cr-MIL-53 was studied.[103] Nucleation and crystal growth were found to decrease in the order MIL-47(V) > MIL-53(Al) > MIL-53(Cr). This trend correlates well with the reactivity (the lability) of the metal ions, which is a measure of simple complexation or ligand exchange and thus the deprotonation rate of H_2BDC seems to be fast and not the rate determining step in the reaction. In another ex-situ study the synthesis of benzenetricarboxylate-based compounds MIL-96, -100, and -110 was investigated.[98] Although the pH of the reaction mixture was previously shown to be a crucial factor, the authors were able to obtain with increasing reaction time MIL-100, MIL-110, and MIL-96 starting from the same reaction mixture.[98] This information and the possibility to use MW heating allowed the selective synthesis of MIL-100 or MIL-110.

Time resolved in-situ SAXS/WAXS measurements were employed, to determine the crystal growth kinetics of product formation in the system Al^{3+}/H_2BDC-NH_2/solvent.[103,104] In the first report, the influence of solvent, reactant concentration and reaction temperature was systematically investigated. When the synthesis is carried out in DMF at low reactant concentration, both MIL-53-NH_2 and MIL-101-NH_2 are observed. The increase of the reactant concentration or the replacement of DMF by water as solvent leads to the formation of MIL-53-NH_2. In the intermediate temperature range in DMF, MOF-235-NH_2 appears as a kinetically stable phase, which transforms into the thermodynamically more stable MIL-101-NH_2 as the reaction temperature rises. The DMF facilitates the dissolution of H_2BDC-NH_2, increasing the availability of the building blocks and thus favoring the formation of MOF-235-NH_2. The intermediate MOF-235-NH_2 phase could be isolated by quenching the reaction mixture at intermediate temperatures. In DMF/water mixtures, the MOF-235-NH_2 phase is hydrolyzed and the MIL-53-NH_2 phase is formed at high temperatures. The fast formation of MOF-235-NH_2 is supported by the higher rate of nucleation compared to crystal growth. In the second report, the encapsulation of Keggin polyoxometalate ions (POMs) in MIL-101-NH_2 was confirmed by the dramatic change of the relative intensities of the Bragg peaks after the addition of POM to the synthesis mixture. The crystal growth kinetics of MIL-101-NH_2 was almost unaffected by this addition. It has been inferred that the POM acts as nucleation sites and stabilizes the precursor MOF-235 phase that aggregates rapidly. When the crystallization of Al-MIL-101-NH_2 begins, such agglomerates separate and finally the POM nuclei are encapsulated in the cages of Al-MIL-101-NH_2.

Employing time-resolved in-situ EDXRD, the influence of the heating method (MW vs CE heating) on the crystallization process of CAU-1-$(OH)_2$ was investigated.[77] Complete crystallization was observed in the range 10–280 min depending on the reaction temperature and MW heating led to shorter induction periods as well as shorter reaction times compared to CE heating. The kinetic analysis of the data suggested that the reaction mechanism varied with the heating method. Results indicated a phase-boundary controlled reaction under CE heating and a diffusion-controlled reaction under MW heating. The influence of the linker molecule (H_2BDC-NH_2 vs H_2BDC-$(OH)_2$) on the rate of product formation was investigated in another set of EDXRD experiments.[100] Similar crystal growth rates were observed for both CAU-1-NH_2 and CAU-1-$(OH)_2$ using CE heating, while MW-assisted synthesis of CAU-1-NH_2 led to a shorter induction period as well as an acceleration of the crystal growth compared to CAU-1-$(OH)_2$. The acceleration in the crystal growth stage of CAU-1-NH_2 was attributed to a larger pre-exponential factor (about three times that of CAU-1-$(OH)_2$) as derived from the Arrhenius plot.

NMR-spectroscopy has also been used to investigate Al-MOFs, mainly by the groups of Taulelle[7,21,29,36,63,71,84–86,88,89,91,95] and Senker.[33,67,76,78,80,87] Solid state NMR spectroscopy on as-synthesized and activated compounds has been employed to characterize guest species in the pores,[36] the success and degree of PSM reactions,[67,76] or to confirm the correctness of a crystal structure determination. Recently, solid state NMR spectroscopy was also used to study the selectivity of host–guest interactions of acetone, water, and ethanol as probe molecules in the pores of three Al-MIL-53-X (X = H, NH_2, and NHCHO) derivatives.[33] Although a pronounced dynamical disorder of the guest molecules was observed, preferred binding of the acetone via a NH···OC hydrogen bond for the $-NH_2$ and the –NHCHO groups could be proven. At the same time ^1H–^1H through-space connectivities revealed a close vicinity of the acetone methyl groups to the benzene rings of the linkers. In contrast, for ethanol and water, the interaction with the anchor groups is too weak to compete with the thermal disorder at room temperature.

An almost unique possibility of NMR spectroscopy renders the investigation of Al species under solvothermal conditions in solution.[95] A detailed study on the formation mechanisms of three porous benzenetricarboxylate-based compounds MIL-96, MIL-100, and MIL-110 has recently been reported. These form under very similar reaction conditions but have distinct crystal structures containing different inorganic building units (Table 1, Figure 1). In-situ speciation in solution of both inorganic and organic parts during hydrothermal crystallization was monitored using ^{27}Al and ^{1}H NMR spectroscopy while the solids were characterized ex-situ by PXRD and scanning electron microscopy (SEM). Besides the dominant signal of the aluminum monomers (0–1 ppm), two additional small resonances at 4 and 7 ppm were assigned to two different types of Al dimers—a corner-shared μ_2-O and an edge-shared μ_2-O stabilized by two and one trimesate ligands, respectively. These units can be found in MIL-96 and MIL-100 structure for the first type of dimer and in MIL-110 structures for the second type of dimer. Based on these results a scheme of the reaction pathways occurring in solution was proposed.

Variable temperature PXRD monitoring of structural changes during the activation of the Al-MOFs has been reported in various studies. While during the thermal activation of rigid frameworks only changes in the relative reflection intensities are observed, in MIL-53 type compounds these studies are carried out to determine structural changes that lead to variation of reflection positions and relative intensities.[63–65] The structural flexibility of MIL-53 type compounds has also been studied by in-situ sorption experiments upon loading of guest species.[45] Recently different framework flexibilities, which depend on the nature of the metal ion incorporated was also used to confirm the formation of mixed metal (Al/V) MIL-53 materials: a gradual change from highly flexible (with easily induced phase transitions) to totally rigid structures upon increasing vanadium content was observed.[106]

4 STRUCTURES OF Al-BASED MOFs

In the structures of Al-MOFs exclusively octahedrally coordinated Al^{3+} ions are observed (Figure 1). Corner- and/or edge-sharing leads to the formation of Al–O clusters and chains. Only in the structure of CAU-4 isolated AlO_6 polyhedra are present (Figure 1, X). Three types of one-dimensional (1D) inorganic building units have been described, which are formed by *trans* or *cis* corner-sharing or edge-sharing of AlO_6 polyhedra. The formation of these inorganic building units depends strongly on the solvent and geometry of the linker employed in the synthesis. Thus building units I, II, III, VI, VIII, and IX are mainly observed in water or in mixed solvent systems containing water. The use of organic solvents leads to Al-MOFs with new inorganic building units (Figure 1, IV, V, VII, X) that can also contain organic solvent molecule (Figure 1, IV, V).

The most commonly observed structural motif is the one of *trans* corner-sharing polyhedra that leads to the formation of chains (Figure 1, I) as observed in MIL-53 and MIL-68 and their isoreticular compounds as well as in Al-PTP, MIL-118, MIL-122, CAU-8, and CAU-13. It is preferentially formed when linear linker molecules are employed. The structure of MIL-53 and its functionalized derivatives MIL-53-X/Y is of special interest since it shows a large structural flexibility, which strongly depends on the polarity, hydrophilicity, and acidity of functional group on the organic linker. Their presence leads to intraframework interactions that determine the flexibility of the framework upon the addition and removal of guest molecules (Figure 5),[64] which was reported to depend also on the synthesis method employed.[107] Thus electrochemically synthesized MIL-53 and MIL-53-NH_2 exhibited a diminished framework flexibility compared to solvothermally obtained samples. Temperature dependent framework flexibility is also observed in the absence of guest molecules. This was first demonstrated for unfunctionalized MIL-53 using neutron powder diffraction and inelastic

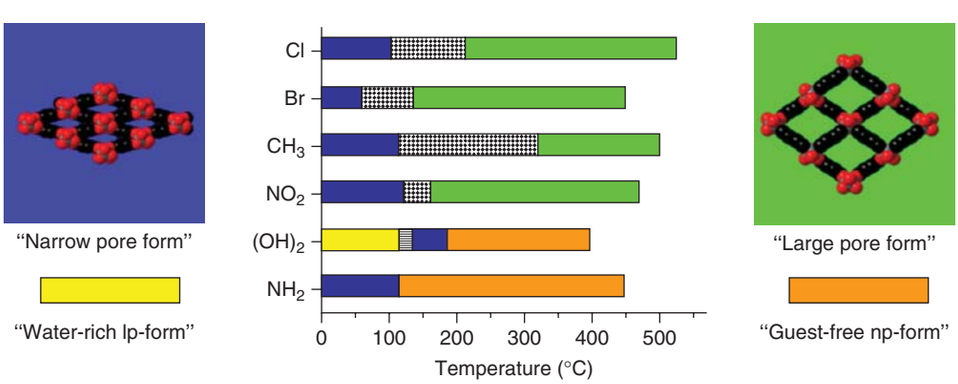


Figure 5 Temperature dependent structural changes observed in functionalized MIL-53 derivatives

neutron scattering techniques[108] and later by electron spin resonance spectroscopy.[109]

The pore diameter and the pore chemistry of MIL-53 can be modified by using linker molecules of different size or extended and functionalized linker molecules, respectively. Extension of the linker (Figure 1), for example, to naphthalene- of biphenyldicarboxylic acid leads to isoreticular MOFs exhibiting larger specific surface areas (e.g., DUT-4 and DUT-5),[72] while replacing the terephthalic acid by fumaric acid should result in a decrease of the pore size. Unfortunately for the latter case no structural information has been reported.[3] Surprisingly the framework is strongly effected and all three structures are rigid. The flexibility is also strongly diminished when *trans* 1,4-cyclohexanedicarboxylic acid is employed as the linker molecule as described in CAU-13.[69] Functionalization of the pore space and modulation of the structure are accomplished through the use of functionalized linker molecules such as terephthalic acid derivatives or 2,2′-bipyridinedicarboxylic acid (Table 1).[74]

The use of isophthalic acid (1,3-H_2BDC), a V-shaped linker molecule, leads to the formation of a helical inorganic building unit composed of *cis* corner-sharing AlO_6 polyhedra (Figure 1, II). This structural motif has been observed in the compounds CAU-10-X[82] and NOTT-300.[93] The connection of the chains by the organic linker molecules leads to the formation of 1D channels (Figure 6b). Functionalized CAU-10 derivatives with small functional groups, such as –OH, $-OCH_3$, $-NO_2$, $-NH_2$, or $-CH_3$ were also obtained. The functional groups lead to a modulation of the sorption properties, i.e., porosity and accessibility of the pores, which were further adjusted by synthesizing mixed-linker CAU-10 compounds.[83] In NOTT-300 ($[Al_2(OH)_2(BPTC)]$) a linker containing two fused 1,3-H_2BDC molecules, i.e., biphenyl-3,3′,5,5′-tetracarboxylic acid (3,3′,5,5′-H_4BPTC) was employed. The (μ-OH) hydroxyl groups interact with CO_2 and SO_2 molecules through the formation of hydrogen bonds that are reinforced by weak interactions with H-atoms of the aromatic rings.

Phthalic acid (1,2-H_2BDC) with vicinal –COOH groups leads to the formation of the third type of inorganic building unit, a chain of edge-sharing AlO_6 polyhedra (Figure 1, III) as observed in the CAU-15 and MIL-120. In both structures adjacent chains are connected through the linker molecules and layers are formed. In CAU-15 theses layers are arranged in an AA-type. The same layers were also observed in the structure of MIL-120, which contains a fully deprotonated linker 1,2,4,5-H_4BDC and thus two vicinal –COOH groups per linker molecule.[89] Hence adjacent layers are connected through the linker molecules, which leads to the formation of a 3D framework with 1D pores.

While the latter two structural motifs of chains of *cis* corner-sharing and edge-sharing AlO_6 polyhedra have only been observed employing geometrically restricted linker molecules, chains of *trans* corner-sharing AlO_6 polyhedra are also observed when other di-, tri-, and tetracarboxylic acid with increased flexibility are used in the synthesis. Thus the use of 4,4′-stilbenedicarboxylic acid or 4,4′-azobenzendicarboxylic acid results exclusively in the formation of the MIL-68 type structure (containing triangular and hexagonal channels), which is a framework polymorph of MIL-53 (Table 1, Figure 6e).[4,75] This compound has also been obtained using terephthalic acid, but no structure refinement has been carried out.[52] The larger linker molecules results in the formation of pores with a diameter in the range of 3 nm.[75] In the structure of Al-PTP, which contains large porphyrin-based tetracarboxylic linker molecules, the planar porphyrin units arrange the chains into an almost perfectly square array with every linker molecule connecting four different parallel chains (Figure 6f).[94] A very different arrangement of the Al–O chains is observed in the structure of CAU-8, which contains V-shaped, but rotationally flexible benzophenondicarboxylate ions.[81] Alternating layers of parallel Al–O-chains are arranged in an ABCDA stacking. The interconnection of these orthogonally oriented chains by the V-shaped dicarboxylate ions results in the formation a 3D framework structure containing 1D channels with a diameter of about 8 Å and small pores (~4 Å) (Figure 6c). The pore walls are lined by the keto-groups.

A rare case of a solid state transformation reaction has been observed in the MIL-118 series, which is obtained using benzene-1,2,4,5-tetracarboxylic acid as a linker.[88] The as synthesized compound MIL-118A ($[Al_2(OH)_2(H_2O)_2(BTEC)]$) contains also infinite chains of *trans* edge-sharing AlO_6 polyhedra but in contrast to the hitherto described structures a water molecule is present in the metal coordination sphere. The deprotonated linker ($BTEC^{4-}$) is not fully connected to the Al^{3+} ions and one carboxyl oxygen atom of two carboxylate functions each is hydrogen bonded to the terminal water molecule coordinating to the Al^{3+} ions. Thermal treatment leads to an irreversible structural transformation, the terminal water is removed and the previously nonbonded carboxylate groups are coordinating to aluminum. The structure of the resulting MIL-118B ($[Al_2(OH)_2(BTEC)]$) has small 1D pores and shows some framework flexibility upon reversible adsorption and desorption of water molecules under ambient conditions.

The use of benzene-1,3,5-tricarbocylic acid (1,3,5-H_3BTC) and its trimethyl ester has also been intensively studied and three materials MIL-96,[84] -100,[85] and -110[86] were obtained, that exhibit very distinct and complicated structures. The framework of MIL-96 is based on wave-shaped inorganic layers that contain 18-membered rings of *cis* and *trans* corner-sharing $AlO_4(OH)_2$ and $AlO_2(OH)_4$ polyhedra. The layers are connected via the trimesate ions to the trimeric $\{Al_3(\mu_3\text{-}O)(OH(H_2O)_2)\}$ building units thus forming a hexagonal framework containing three different

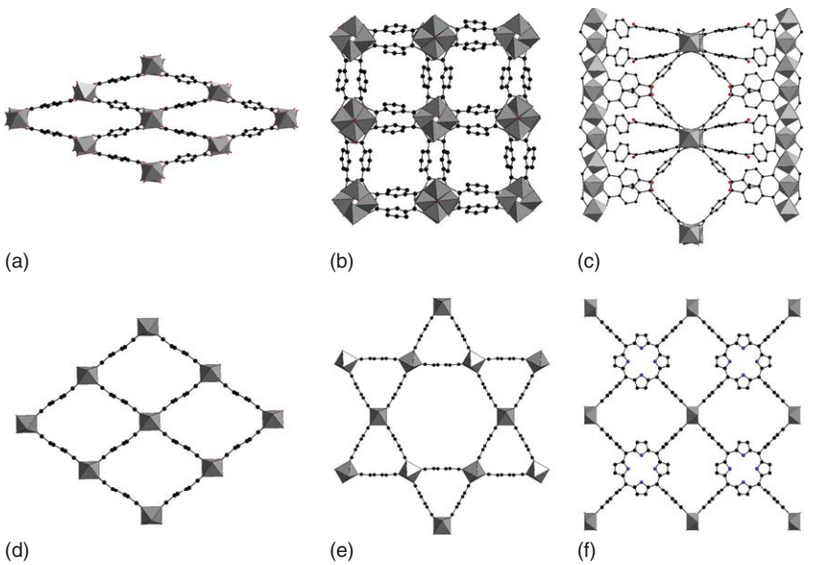


Figure 6 Structures of Al-MOFs containing chains of *trans* corner-sharing AlO_6 polyhedra: MIL-53 (large-pore and narrow-pore form, a and d), CAU-10 (b), CAU-8 (c), MIL-68 (e), and AlPTP (f)

kinds of cages. In MIL-100, only these trimeric inorganic building units are observed, which are connected through the timesate ions to form supertetrahedra. The connection of the supertetrahedra resembles the topology observed in the MTN-type zeolites and accordingly two types of mesoporous cages 25 and 29 Å in diameter and accessible through microporous windows of 5.5 and 8.6 Å are formed. The crystal structure of MIL-110 could be determined from a microdiffraction experiment using a $3 \times 3 \times 10\,\mu m$ sized single crystal. It contains a unique octameric inorganic building unit, consisting of edge- and corner-sharing AlO_6 polyhedra with some atomic disorder (Figure 1, IX).[86] The connection of the inorganic building units through the BTC^{3-} linker ions leads to a honeycomb-like network with hexagonal 16 Å channels.

Building units of similar complexity as described in the BTC^{3-}-containing MOFs have also been observed in the compounds synthesized from methanol or isopropanol. The solvent molecules are also incorporated in the final product. The use of methanol as a solvent resulted in the formation of two new series of Al-MOFs, the CAU-1 and the CAU-3 series containing octameric $\{Al_8(OH)_4(OCH_3)_8\}^{12+}$ and dodecameric $\{Al_{12}(OCH_3)_{24}\}^{12+}$ ring-shaped building units, respectively (Figure 1, IV and V). These units are each 12-fold connected to others.[73,76] The framework structures of CAU-1 and -3 can be best comprehended starting from a distorted body centered and cubic closed packing of these building units, respectively. The connection of these building units leads to the formation of pseudo-octahedral and tetrahedral cages. The functionality of the pores and the pore size has been modified by using functionalized or extended linker molecules.

An inorganic building unit that is related to a well known Al_{13}-cluster found in the basic aluminum chloride $[Al_{13}(OH)_{24}(H_2O)_{24}]Cl_{15} \cdot 13H_2O$ was described recently.[80,110] In CAU-6, columns of these condensed clusters (corner-sharing connectivity) are formed (Figure 1, VII). These are linked by the organic linker molecules, which results in the formation of sinusoidal trigonal channels with a diameter between 5 and 10 Å. The pores are partially occupied by chloride ions, 2-propanol, and water molecules in a non-ordered fashion, which results in the exceptional water sorption properties of CAU-6.

5 CONCLUSION

Al-MOFs have been intensively studied in both industry and academia during the last decade and the number of groups working on this topic has steadily increased. This is mainly due to the thermal and chemical stability of these compounds, but it could also be that the interesting, complex and challenging chemistry of aluminum is a reason, at least for academic groups. The rich chemistry of aluminum leads to unique inorganic building units, in some cases, which in turn result in new and fascinating MOF structures. This is especially true when reactions are carried out under non-aqueous conditions. For such systematic investigations of complex chemical systems high-throughput methods have been demonstrated to be

exceptionally helpful in order to discover new compounds, to optimize reaction conditions or to find chemical trends. Owing to the microcrystalline nature of the Al-MOFs, establishing structure–property relationships is not as straightforward as for other MOFs that more readily form single crystals. Nevertheless, it could be expected that in the next few years not only many new Al-MOFs will be described in the literature, but that the Al-MOFs will also find some applications in industry.

6 RELATED ARTICLES

Mechanochemical Approaches to Metal-Organic Frameworks; Porphyrinic Metal-Organic Frameworks; Postsynthetic Modification of Metal-Organic Frameworks; Recent Solid-State NMR Studies of Quadrupolar Nuclei in Metal-Organic Frameworks; Patterning Techniques for Metal-Organic Frameworks.

7 ABBREVIATIONS AND ACRONYMS

CAU = Christian-Albrechts Universität; CE = conventional electric; DUT = Dresden University of Technology; EDXRD = energy dispersive X-ray diffraction; MIL = Matériaux de l'Institut Lavoisier; MOF = Metal–organic framework; MW = microwave-assisted; NMR = nuclear magnetic resonance; POM = polyoxometalate; PSE = post-synthetic exchange; PSM = post-synthetic modification; PXRD = powder X-ray diffraction; SAXS = small-angle X-ray scattering; SEM = scanning electron microscope; WAXS = small-angle X-ray scattering; 1D = one-dimensional.

8 REFERENCES

1. A. U. Czaja, N. Trukhan, and U. Muller, *Chem. Soc. Rev.*, 2009, **38**, 1284.
2. A. Czaja, E. Leung, N. Trukhan, and U. Müller, 'Metal-Organic Frameworks', Wiley-VCH Verlag GmbH & Co. KGaA, 2011, p.337.
3. M. Gaab, N. Trukhan, S. Maurer, R. Gummaraju, and U. Müller, *Microporous Mesoporous Mater.*, 2012, **157**, 131.
4. T. Loiseau, G. Ferey, C. Volkringer, F. Taulelle, and M. Haouas, Preparation of porous crystallized aluminum aromatic azocarboxylate metal-organic frameworks for storage of liquids and gases, separation of gases, or as catalysts, WO 2010058124, 2010.
5. M. Gaab, A. Weber, M. Kostur, and U. Mueller (BASF), Process for coating support surface with porous metal-organic framework, WO 2012077030, 2012.
6. E. Leung, U. Mueller, N. Trukhan, H. Mattenheimer, G. Cox, and S. Blei (BASF), Process for preparing porous metal-organic frameworks based on aluminum fumarate, WO 2012042410, 2012.
7. T. Loiseau, G. Ferey, C. Volkringer, F. Taulelle, and M. Haouas, Hydrothermal preparation of porous crystallized aluminum carboxylate metal-organic frameworks for gas/liquid storage, gas separation or catalysis, WO 2010058123, 2010.
8. J. Pastre, U. Mueller, M. Schubert, C. Kiener, F. Teich, and F. Poplow (BASF), Closed reversible breathing apparatus having a metal organic framework, WO 2007101797, 2007.
9. H. Puetter, M. Schubert, I. Richter, U. Mueller, and N. Trukhan (BASF), Process for preparing porous metal organic frameworks, WO 2007131948, 2007.
10. I. Richter, M. Schubert, and U. Mueller (BASF), Porous metal organic framework and electrolyte based on pyrroles and pyridinones, WO 2007131955, 2007.
11. M. Savonnet, D. Farrusseng, C. Pinel, D. Bazer-Bachi, N. Bats, and V. Lecocq, Aluminum 2-azido-1,4-benzenedicarboxylate MIL-53-Al-N3 organic/inorganic hybrid solid and its preparation by post-modification of amine precursor, WO2011048280, 2011.
12. M. Schubert and U. Mueller (BASF), New metal-organic framework materials based on aluminum, iron, and chromium, WO 2008129051, 2008.
13. M. Schubert, U. Mueller, and C. Kiener (BASF), Preparation of aluminum-containing porous metalorganic framework materials and their use, WO 2008142059, 2008.
14. M. Schubert, U. Mueller, and C. Kiener (BASF), Method for the separation of carbon dioxide using a porous metal-organic framework material, WO 2008061958, 2008.
15. M. Schubert, U. Mueller, and C. Kiener (BASF), Porous metal-organic framework materials as drying agents, WO 2009092777, 2009.
16. M. Schubert, U. Mueller, and C. Kiener (BASF), Method for the separation of carbon dioxide using a porous metal-organic framework material, US 7556673, 2009.
17. M. Schubert, U. Mueller, and N. Trukhan (BASF), Metal oxides produced from metal-organic framework materials, WO 2007118843, 2007.
18. N. Trukhan, U. Mueller, J. Heimann, and A. Kindler (BASF), Metal-organic framework materials based on 2,5-furandicarboxylic acid or 2,5-thiophenedicarboxylic acid, WO 2011064307, 2011.
19. N. Trukhan, U. Mueller, J.-P. Melder, S. Brughmans, and T. Katz (BASF), Method for separating acid gases using metal-organic frameworks impregnated with amines, WO 2010106133, 2010.

20. C. Kiener, U. Mueller, M. Schubert, and F. Teich (BASF), Metal-organic frameworks in refrigeration/heating machines, EP2230288, 2010.
21. T. Loiseau, G. Ferey, C. Volkringer, F. Taulelle, and M. Haouas, Hydrothermal preparation of porous crystallized aluminum carboxylate metal-organic frameworks for gas/liquid storage, gas separation or catalysis, WO 2010058123, 2010.
22. I. M. Malkowsky, C. Kiener, I. Richter, M. Schubert, E. Leung, R. Moos, S. Achmann, and G. Hagen (BASF), Use of metal-organic framework materials for the production of humidity-sensitive layers for sensors, DE 102009047201, 2011.
23. M. Savonnet, D. Farrusseng, C. Pinel, B. D. Bazer, N. Bats, and V. Lecocq, Aluminum 2-azidoterephthalate (CAU-1-N3) organic/inorganic hybrid solid and its preparation from post-modification of its amine-containing precursor, WO 2011048282, 2011.
24. M. Savonnet, D. Farrusseng, C. Pinel, B. D. Bazer, N. Bats, and V. Lecocq, Method for preparing organic/inorganic hybrid functionalized solids having a triazole ring, FR2951726A, 2011.
25. M. Savonnet, D. Farrusseng, C. Pinel, B. D. Bazer, N. Bats, and V. Lecocq, Aluminum azidoterephthalate organic-inorganic hybrid MIL-53-Al-N_3 and its preparation, FR2951725, 2011.
26. BASF SE Press release 05.10.2010; C&EN October 11th, 18.
27. K. Maeda, Y. Kiyozumi, and F. Mizukami, *Angew. Chem. Int. Ed. Engl.*, 1994, **33**, 2335.
28. K. Maeda, J. Akimoto, Y. Kiyozumi, and F. Mizukami, *J. Chem. Soc. Chem. Commun.*, 1995, 1033.
29. C. Serre, J. A. Groves, P. Lightfoot, A. M. Z. Slawin, P. A. Wright, N. Stock, T. Bein, M. Haouas, F. Taulelle, and G. Férey, *Chem. Mater.*, 2006, **18**, 1451.
30. N. Stock and S. Biswas, *Chem. Rev.*, 2011, **112**, 933.
31. N. Stock, *Microporous Mesoporous Mater.*, 2010, **129**, 287.
32. M. Meilikhov, K. Yusenko, and R. A. Fischer, *Dalton Trans.*, 2009, 600.
33. J. Wack, R. Siegel, T. Ahnfeldt, N. Stock, L. Mafra, and J. Senker, *J. Phys. Chem. C*, 2013, **117**, 19991.
34. L. Alaerts, M. Maes, L. Giebeler, P. A. Jacobs, J. A. Martens, J. F. M. Denayer, C. E. A. Kirschhock, and D. E. De Vos, *J. Am. Chem. Soc.*, 2008, **130**, 14170.
35. M. Maes, F. Vermoortele, L. Alaerts, S. Couck, C. E. A. Kirschhock, J. F. M. Denayer, and D. E. De Vos, *J. Am. Chem. Soc.*, 2010, **132**, 15277.
36. M. Haouas, C. Volkringer, T. Loiseau, G. Ferey, and F. Taulelle, *Chem. Eur. J.*, 2009, **15**, 3139.
37. G. Ferey, M. Latroche, C. Serre, F. Millange, T. Loiseau, and A. Percheron-Guegan, *Chem. Commun.*, 2003, 2976.
38. S. Bourrelly, P. L. Llewellyn, C. Serre, F. Millange, T. Loiseau, and G. Ferey, *J. Am. Chem. Soc.*, 2005, **127**, 13519.
39. T. K. Trung, P. Trens, N. Tanchoux, S. Bourrelly, P. L. Llewellyn, S. Loera-Serna, C. Serre, T. Loiseau, F. Fajula, and G. Ferey, *J. Am. Chem. Soc.*, 2008, **130**, 16926.
40. S. Couck, J. F. M. Denayer, G. V. Baron, T. Remy, J. Gascon, and F. Kapteijn, *J. Am. Chem. Soc.*, 2009, **131**, 6326.
41. L. Hamon, C. Serre, T. Devic, T. Loiseau, F. Millange, G. Férey, and G. D. Weireld, *J. Am. Chem. Soc.*, 2009, **131**, 8775.
42. D. Himsl, D. Wallacher, and M. Hartmann, *Angew. Chem. Int. Ed.*, 2009, **48**, 4639.
43. A. Torrisi, R. G. Bell, and C. Mellot-Draznieks, *Cryst. Growth Des.*, 2010, **10**, 2839.
44. E. Stavitski, E. A. Pidko, S. Couck, T. Remy, E. J. M. Hensen, B. M. Weckhuysen, J. Denayer, J. Gascon, and F. Kapteijn, *Langmuir*, 2011, **27**, 3970.
45. S. Couck, E. Gobechiya, C. E. A. Kirschhock, P. Serra-Crespo, J. Juan-Alcañiz, A. Martinez Joaristi, E. Stavitski, J. Gascon, F. Kapteijn, G. V. Baron, and J. F. M. Denayer, *ChemSusChem*, 2012, **5**, 740.
46. N. Heymans, S. Vaesen, and G. De Weireld, *Microporous Mesoporous Mater.*, 2012, **154**, 93.
47. P. Serra-Crespo, E. Gobechiya, E. V. Ramos-Fernandez, J. Juan-Alcañiz, A. Martinez-Joaristi, E. Stavitski, C. E. A. Kirschhock, J. A. Martens, F. Kapteijn, and J. Gascon, *Langmuir*, 2012, **28**, 12916.
48. A. Boutin, M. A. Springuel-Huet, A. Nossov, A. Gedeon, T. Loiseau, C. Volkringer, G. Ferey, F. X. Coudert, and A. H. Fuchs, *Angew. Chem. Int. Ed.*, 2009, **48**, 8314.
49. M. Maes, F. Vermoortele, M. Boulhout, T. Boudewijns, C. Kirschhock, R. Ameloot, I. Beurroies, R. Denoyel, and D. E. De Vos, *Microporous Mesoporous Mater.*, 2012, **157**, 82.
50. B. Zornoza, A. Martinez-Joaristi, P. Serra-Crespo, C. Tellez, J. Coronas, J. Gascon, and F. Kapteijn, *Chem. Commun.*, 2011, **47**, 9522.
51. X. Si, C. Jiao, F. Li, J. Zhang, S. Wang, S. Liu, Z. Li, L. Sun, F. Xu, Z. Gabelica, and C. Schick, *Energy Environ. Sci.*, 2011, **4**, 4522.
52. Q. Yang, S. Vaesen, M. Vishnuvarthan, F. Ragon, C. Serre, A. Vimont, M. Daturi, G. De Weireld, and G. Maurin, *J. Mater. Chem.*, 2012, **22**, 10210.
53. F. Hinterholzinger, C. Scherb, T. Ahnfeldt, N. Stock, and T. Bein, *Phys. Chem. Chem. Phys.*, 2010, **12**, 4515.
54. S. Basu, M. Maes, A. Cano-Odena, L. Alaerts, D. E. De Vos, and I. F. J. Vankelecom, *J. Membr. Sci.*, 2009, **344**, 190.
55. Y. Hu, X. Dong, J. Nan, W. Jin, X. Ren, N. Xu, and Y. M. Lee, *Chem. Commun.*, 2011, **47**, 737.
56. X. Y. Chen, H. Vinh-Thang, D. Rodrigue, and S. Kaliaguine, *Ind. Eng. Chem. Res.*, 2012, **51**, 6895.

57. J. Nan, X. Dong, W. Wang, and W. Jin, *Microporous Mesoporous Mater.*, 2012, **155**, 90.
58. F. Zhang, X. Zou, X. Gao, S. Fan, F. Sun, H. Ren, and G. Zhu, *Adv. Funct. Mater.*, 2012, **22**, 3583.
59. L. Cao, K. Tao, A. Huang, C. Kong, and L. Chen, *Chem. Commun.*, 2013, **49**, 8513.
60. T. Rodenas, M. van Dalen, E. García-Pérez, P. Serra-Crespo, B. Zornoza, F. Kapteijn, and J. Gascon, *Adv. Funct. Mater.*, 2013, **24**, 249.
61. S. Sorribas, P. Gorgojo, C. Tellez, J. Coronas, and A. G. Livingston, *J. Am. Chem. Soc.*, 2013, **135**, 15201.
62. B. Zornoza, C. Tellez, J. Coronas, J. Gascon, and F. Kapteijn, *Microporous Mesoporous Mater.*, 2013, **166**, 67.
63. T. Loiseau, C. Serre, C. Huguenard, G. Fink, F. Taulelle, M. Henry, T. Bataille, and G. Ferey, *Chem. Eur. J.*, 2004, **10**, 1373.
64. S. Biswas, T. Ahnfeldt, and N. Stock, *Inorg. Chem.*, 2011, **50**, 9518.
65. N. Reimer, B. Gil, B. Marszalek, and N. Stock, *CrystEngComm*, 2012, **14**, 4119.
66. S. Biswas, T. Remy, S. Couck, D. Denysenko, G. Rampelberg, J. F. M. Denayer, D. Volkmer, C. Detavernier, and P. Van Der Voort, *Phys. Chem. Chem. Phys.*, 2013, **15**, 3552.
67. T. Ahnfeldt, D. Gunzelmann, T. Loiseau, D. Hirsemann, J. Senker, G. Ferey, and N. Stock, *Inorg. Chem.*, 2009, **48**, 3057.
68. J. Gascon, U. Aktay, M. D. Hernandez-Alonso, G. P. M. van Klink, and F. Kapteijn, *J. Catal.*, 2009, **261**, 75.
69. F. Niekiel, M. Ackermann, P. Guerrier, A. Rothkirch, and N. Stock, *Inorg. Chem.*, 2013, **52**, 8699.
70. A. Comotti, S. Bracco, P. Sozzani, S. Horike, R. Matsuda, J. Chen, M. Takata, Y. Kubota, and S. Kitagawa, *J. Am. Chem. Soc.*, 2008, **130**, 13664.
71. T. Loiseau, C. Mellot-Draznieks, H. Muguerra, G. Ferey, M. Haouas, and F. Taulelle, *C. R. Chim.*, 2005, **8**, 765.
72. I. Senkovska, F. Hoffmann, M. Fröba, J. Getzschmann, W. Böhlmann, and S. Kaskel, *Microporous Mesoporous Mater.*, 2009, **122**, 93.
73. H. Reinsch, M. Feyand, T. Ahnfeldt, and N. Stock, *Dalton Trans.*, 2012, **41**, 4164.
74. E. D. Bloch, D. Britt, C. Lee, C. J. Doonan, F. J. Uribe-Romo, H. Furukawa, J. R. Long, and O. M. Yaghi, *J. Am. Chem. Soc.*, 2010, **132**, 14382.
75. S. H. Lo, C. H. Chien, Y. L. Lai, C. C. Yang, J. J. Lee, D. S. Raja, and C. H. Lin, *J. Mater. Chem. A*, 2013, **1**, 324.
76. T. Ahnfeldt, N. Guillou, D. Gunzelmann, I. Margiolaki, T. Loiseau, G. Férey, J. Senker, and N. Stock, *Angew. Chem. Int. Ed.*, 2009, **48**, 5163.
77. T. Ahnfeldt, J. Moellmer, V. Guillerm, R. Staudt, C. Serre, and N. Stock, *Chem. Eur. J.*, 2011, **17**, 6462.
78. T. Ahnfeldt, D. Gunzelmann, J. Wack, J. Senker, and N. Stock, *CrystEngComm*, 2012, **14**, 4126.
79. P. Serra-Crespo, E. V. Ramos-Fernandez, J. Gascon, and F. Kapteijn, *Chem. Mater.*, 2011, **23**, 2565.
80. H. Reinsch, B. Marszalek, J. Wack, J. Senker, B. Gil, and N. Stock, *Chem. Commun.*, 2012, **48**, 9486.
81. H. Reinsch, M. Krüger, J. Marrot, and N. Stock, *Inorg. Chem.*, 2013, **52**, 1854.
82. H. Reinsch, M. A. van der Veen, B. Gil, B. Marszalek, T. Verbiest, D. de Vos, and N. Stock, *Chem. Mater.*, 2012, **25**, 17.
83. H. Reinsch, S. Waitschat, and N. Stock, *Dalton Trans.*, 2013, **42**, 4840.
84. T. Loiseau, L. Lecroq, C. Volkringer, J. Marrot, G. Ferey, M. Haouas, F. Taulelle, S. Bourrelly, P. L. Llewellyn, and M. Latroche, *J. Am. Chem. Soc.*, 2006, **128**, 10223.
85. C. Volkringer, D. Popov, T. Loiseau, G. Férey, M. Burghammer, C. Riekel, M. Haouas, and F. Taulelle, *Chem. Mater.*, 2009, **21**, 5695.
86. C. Volkringer, D. Popov, T. Loiseau, N. Guillou, G. Ferey, M. Haouas, F. Taulelle, C. Mellot-Draznieks, M. Burghammer, and C. Riekel, *Nat. Mater.*, 2007, **6**, 760.
87. H. Reinsch, M. Krüger, J. Wack, J. Senker, F. Salles, G. Maurin, and N. Stock, *Microporous Mesoporous Mater.*, 2012, **157**, 50.
88. C. Volkringer, T. Loiseau, N. Guillou, G. Ferey, M. Haouas, F. Taulelle, N. Audebrand, I. Margiolaki, D. Popov, M. Burghammer, and C. Riekel, *Cryst. Growth Des.*, 2009, **9**, 2927.
89. C. Volkringer, T. Loiseau, M. Haouas, F. Taulelle, D. Popov, M. Burghammer, C. Riekel, C. Zlotea, F. Cuevas, M. Latroche, D. Phanon, C. Knofelv, P. L. Llewellyn, and G. Ferey, *Chem. Mater.*, 2009, **21**, 5783.
90. H. Reinsch and N. Stock, *Microporous Mesoporous Mater.*, 2013, **171**, 156.
91. C. Volkringer, T. Loiseau, N. Guillou, G. Ferey, M. Haouas, F. Taulelle, E. Elkaim, and N. Stock, *Inorg. Chem.*, 2010, **49**, 9852.
92. C. Volkringer, T. Loiseau, N. Guillou, G. Ferey, and E. Elkaim, *Solid State Sci.*, 2009, **11**, 1507.
93. S. Yang, J. Sun, A. J. Ramirez-Cuesta, S. K. Callear, W. I. F. David, D. P. Anderson, R. Newby, A. J. Blake, J. E. Parker, C. C. Tang, and M. Schröder, *Nat. Chem.*, 2012, **4**, 887.
94. A. Fateeva, P. A. Chater, C. P. Ireland, A. A. Tahir, Y. Z. Khimyak, P. V. Wiper, J. R. Darwent, and M. J. Rosseinsky, *Angew. Chem. Int. Ed.*, 2012, **51**, 7440.
95. M. Haouas, C. Volkringer, T. Loiseau, G. Ferey, and F. Taulelle, *Chem. Mater.*, 2012, **24**, 2462.
96. M. Hartmann and M. Fischer, *Microporous Mesoporous Mater.*, 2012, **164**, 38.
97. E. Haque, N. A. Khan, C. M. Kim, and S. H. Jhung, *Cryst. Growth Des.*, 2011, **11**, 4413.
98. N. A. Khan, J. S. Lee, J. Jeon, C. H. Jun, and S. H. Jhung, *Microporous Mesoporous Mater.*, 2012, **152**, 235.

99. A. García Márquez, A. Demessence, A. E. Platero-Prats, D. Heurtaux, P. Horcajada, C. Serre, J.-S. Chang, G. Férey, V. A. de la Peña-O'Shea, C. Boissière, D. Grosso, and C. Sanchez, *Eur. J. Inorg. Chem.*, 2012, **2012**, 5165.

100. T. Ahnfeldt and N. Stock, *CrystEngComm*, 2012, **14**, 505.

101. C. Volkringer and S. M. Cohen, *Angew. Chem. int. Ed.*, 2010, **49**, 4644.

102. M. Kim, J. F. Cahill, H. Fei, K. A. Prather, and S. M. Cohen, *J. Am. Chem. Soc.*, 2012, **134**, 18082.

103. E. Haque, J. H. Jeong, and S. H. Jhung, *CrystEngComm*, 2010, **12**, 2749.

104. E. Stavitski, M. Goesten, J. Juan-Alcaniz, A. Martinez-Joaristi, P. Serra-Crespo, A. V. Petukhov, J. Gascon, and F. Kapteijn, *Angew. Chem. Int. Ed.*, 2011, **50**, 9624.

105. J. Juan-Alcaniz, M. Goesten, A. Martinez-Joaristi, E. Stavitski, A. V. Petukhov, J. Gascon, and F. Kapteijn, *Chem. Commun.*, 2011, **47**, 8578.

106. O. Kozachuk, M. Meilikhov, K. Yusenko, A. Schneemann, B. Jee, A. V. Kuttatheyil, M. Bertmer, C. Sternemann, A. Pöppl, and R. A. Fischer, *Eur. J. Inorg. Chem.*, 2013, **2013**, 4546.

107. A. Martinez Joaristi, J. Juan-Alcañiz, P. Serra-Crespo, F. Kapteijn, and J. Gascon, *Cryst. Growth Des.*, 2012, **12**, 3489.

108. Y. Liu, J.-H. Her, A. Dailly, A. J. Ramirez-Cuesta, D. A. Neumann, and C. M. Brown, *J. Am. Chem. Soc.*, 2008, **130**, 11813.

109. M. Mendt, B. Jee, N. Stock, T. Ahnfeldt, M. Hartmann, D. Himsl, and A. Pöppl, *J. Phys. Chem. C*, 2010, **114**, 19443.

110. W. Seichter, H. Mögel, P. Brand, and D. Salah, *Eur. J. Inorg. Chem.*, 1998, 795.

Polyrotaxane Metal-Organic Frameworks

Stephen J. Loeb and V. Nicholas Vukotic

University of Windsor, Windsor, ON, Canada

1	Introduction	115
2	Polyrotaxane Frameworks Containing Cucurbit[6]uril Wheels	115
3	Polyrotaxane Frameworks Containing DB24C8 Wheels	119
4	Polyrotaxane Frameworks Containing a Texas-Sized Molecular Box	126
5	Polyrotaxane Frameworks Containing a Cu^{I} Templated [2]Pseudorotaxane	127
6	Polyrotaxane Framework Containing Wheels with Donor Groups	128
7	Polyrotaxane Frameworks that Demonstrate Rotational Dynamics in the Solid-State	130
8	Summary and Look Forward	132
9	Related Articles	132
10	Abbreviations and Acronyms	132
11	References	132

1 INTRODUCTION

This chapter describes recent progress in the design, preparation, and solid-state structures of metal organic frameworks (MOFs)[1–7] which contain a mechanically interlocked molecule (MIM),[8–13] in the form of a rotaxane, as the linker. The idea of incorporating ligands with interpenetrated components into the framework of a solid-state material is motivated by the intriguing concept of transferring the beautiful dynamics and machine-like properties observed for MIM systems in solution[14–18] into the organized and coherent world of crystalline solids.[19] Although, the dream of mimicking such motion in the solid-state is only just starting to be realized,[20] a look back at the development of such materials[21–23] offers the casual reader and those new to the area, insight into the design process and, hopefully, a glimpse of the future potential of materials that display *robust dynamics*.[24]

These materials have previously been described by several names—e.g., metal-organic rotaxane framework (MORF)[25] or rotaxane coordination polymer (RCP)[21]—herein we use the more general term polyrotaxane framework (PRF). This work is arbitrarily divided into sections based on the rotaxane utilized as the linker for the PRF material and follows somewhat the historical timeline involved in their development. For each example, we have attempted to describe (i) the conditions required to prepare the material, (ii) the important details of the solid-state structure, including crystal symmetry and space group, (iii) any experiments used to study the physical properties of the material; including possible dynamics in the solid-state, and (iv) where appropriate, the thought process behind the design of a particular material.

2 POLYROTAXANE FRAMEWORKS CONTAINING CUCURBIT[6]URIL WHEELS

Cucurbiturils are an interesting family of macrocycles, consisting of glycoluril units linked together by methylene spacers. The result is a macrocyclic host with a very hydrophobic interior and an electron rich outer

Metal-Organic Framework Materials. Edited by Leonard R. MacGillivray and Charles M. Lukehart.
© 2014 John Wiley & Sons, Ltd. ISBN 978-1-119-95289-3

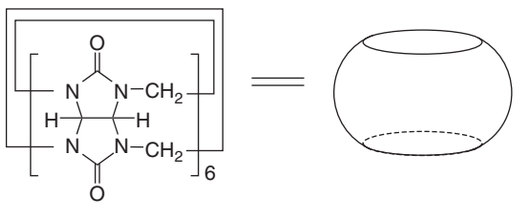


Figure 1 Line drawing of cucurbit[6]uril

rim of carbonyl oxygen atoms which can participate in hydrogen-bonding and ion–dipole interactions. Cucurbiturils are distinguished by the number of glycoluril units within the macrocycle; this is reflected by using a number in brackets to designate the number of glycoluril units i.e., cucurbit[6]uril is abbreviated to **CB[6]**. All the PRFs containing cucurbituril in this review, utilize **CB[6]** as it forms a strong host–guest interaction with diaminoalkane-based axles (Figure 1).

The axle–wheel interaction is so strong that one can actually isolate a [2]pseudorotaxane linker prior to PRF formation. This was accomplished by mixing 1 equivalent of *N,N′*-bis(4-pyridylmethyl)-1,4-diaminobutane dihydronitrate, **1**$(NO_3)_2$, and excess **CB[6]** in H_2O and allowing the mixture to stir overnight. Afterwards, undissolved **CB[6]** could be filtered off; while ^{1}H NMR spectroscopy of the filtrate in D_2O clearly exhibited the clean formation of the [2]pseudorotaxane [**1**⊂**CB[6]**]$^{2+}$ (Figure 2a). This filtrate was then placed in a diffusion tube and a solution of silver tosylate in MeOH was layered on top. After a week, colorless crystals of **PRF-1** with formula [Ag(**1**⊂**CB[6]**)][$C_7H_7SO_3$]$_3$·$(H_2O)_{11}$ were obtained.[26] **PRF-1** forms a linear, one-periodic framework consisting of Ag^I metal ions, and [**1**⊂**CB[6]**]$^{2+}$ linkers and crystallizes in the triclinic space group $P\bar{1}$. Each Ag^I centre is coordinated by two pyridyl groups of the rotaxane linker in a trans geometry (Figure 2b) to form a straight chain framework with a metal···metal distance of 20.2 Å between subunits (Figure 2c). Non-coordinating tosylate counterions and residual solvent molecules (H_2O) fill the voids remaining between aggregated chains in the framework.

Alternatively, one can increase the periodicity of the framework by using the same reaction conditions and changing the metal salt to silver nitrate. This resulted in the formation of colorless, plate-like crystals of **PRF-2** with formula [Ag(NO_3)(**1**⊂**CB[6]**$)_{1.5}$][NO_3]$_3$·$(H_2O)_{20}$ after 1 week.[26] **PRF-2** crystallizes in the orthorhombic space group *Cmca* and forms a two-periodic framework consisting of hexagonal nets of [**1**⊂**CB[6]**]$^{2+}$ linkers and Ag^I metal ions. Each Ag^I ion is coordinated to three [**1**⊂**CB[6]**]$^{2+}$ linkers and a single disordered nitrate ion to form a distorted tetrahedral geometry about the metal center (Figure 2d). The hexagon within the framework has an average side length of 20.9 Å and a distance of 38.0 Å from opposite

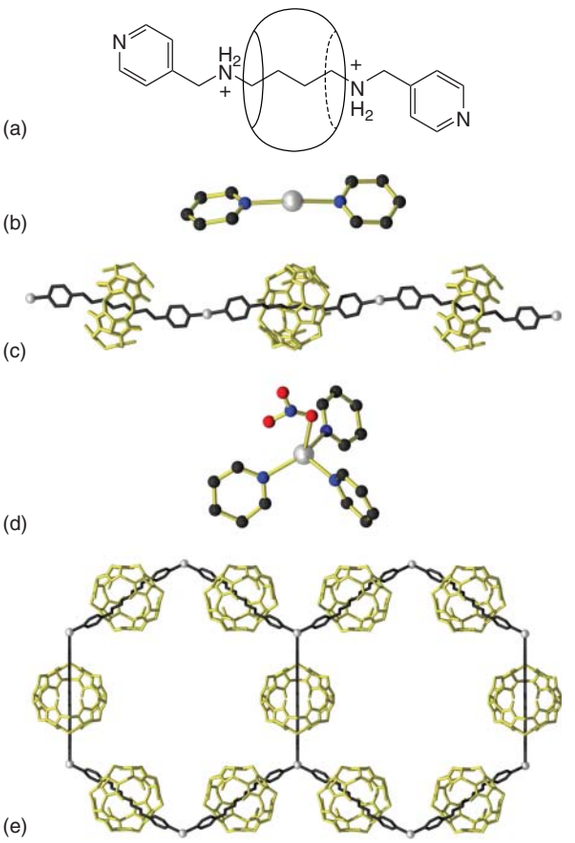


Figure 2 (a) [2]Pseudorotaxane linker [**1**⊂**CB[6]**]$^{2+}$ used to form **PRF-1** and **PRF-2**; (b) coordination environment of Ag^I center in **PRF-1**; (c) X-ray structure of the linear one-periodic framework of **PRF-1**; (d) coordination environment of Ag^I center in **PRF-2**; (e) X-ray structure of the hexagonal two-periodic framework of **PRF-2**

corners of the hexagon (Figure 2e). The two-periodic nets are stacked with an interlayer spacing of 9.9 Å and are also interpenetrated with another two-periodic net. The interlocking nets are positioned almost perpendicular to each other eliminating the large cavities that would have remained in the center of the hexagons. The remaining voids within the framework are filled with solvent (H_2O) and non-coordinated nitrate counterions.

One can also modify the terminal coordinating groups on the axle and the type of metal used to obtain different structural frameworks. Adding a slight excess of **CB[6]** to an aqueous solution of *N,N′*-bis(3-pyridylmethyl)-1,4-diaminobutane dihydronitrate, **2**$(NO_3)_2$, and stirring for 3 h under ambient conditions followed by filtering off undissolved **CB[6]**, allowed for formation of the [2]pseudorotaxane [**2**⊂**CB[6]**]$^{2+}$ (Figure 3a). The [2]pseudorotaxane was then isolated by reducing the volume of the solution via evaporation under vacuum, followed by addition of ethanol. **PRF-3** was obtained by placing

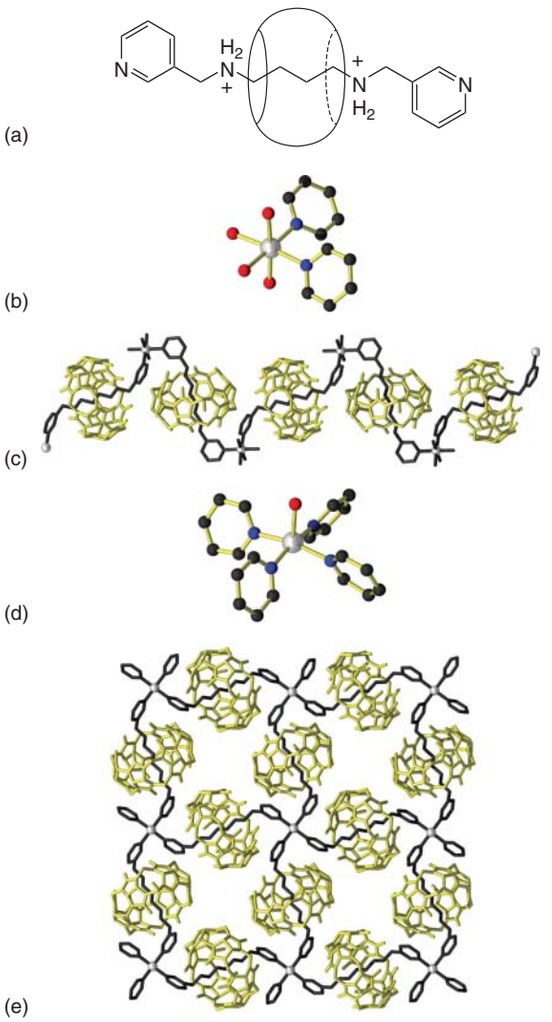


Figure 3 (a) [2]Pseudorotaxane linker [**2**⊂**CB[6]**]$^{2+}$ used to form **PRF-3** and **PRF-4**; (b) coordination environment of Co^{II} center in **PRF-3**; (c) X-ray structure of the zigzag one-periodic framework of **PRF-3**; (d) coordination environment of Cu^{II} center in **PRF-4**; (e) X-ray structure of the distorted square grid, two-periodic framework of **PRF-4**

an aqueous solution of $Co(NO_3)_2$ in a diffusion tube to which an aqueous solution of [**2**⊂**CB[6]**][NO_3]$_2$ was layered on top to produce red crystals with formula [$Co(H_2O)_4$(**2**⊂**CB[6]**)][NO_3]$_4$·(H_2O)$_{12}$.[27] **PRF-3** crystallized in the triclinic space group $P\bar{1}$ and forms a one-periodic framework consisting of Co^{II} metal ions and [**2**⊂**CB[6]**]$^{2+}$ linkers with alternating metal···metal distances of 16.9 and 17.1 Å, respectively. Each Co^{II} atom in the framework adopts an octahedral geometry with two pyridyl groups binding in a cis arrangement, while the remaining sites are occupied by four coordinated H_2O molecules (Figure 3b). The cis coordination of the terminal pyridyl groups on the metal center results in an abrupt change in direction leading to a zigzag conformation of the one-periodic framework (Figure 3c). The few voids in the structure are filled by H_2O molecules and non-coordinated nitrate anions.

The periodicity of the PRF formed by this linker can also be changed by simply using a different transition metal. Employing $Cu(NO_3)_2$ instead of $Co(NO_3)_2$ under the same reaction conditions resulted in blue crystals of **PRF-4** with formula [$Cu(H_2O)$(**2**⊂**CB[6]**)$_2$][NO_3]$_6$·(H_2O)$_{22.5}$.[27] **PRF-4** crystallized in the tetragonal space group *P*4/*n* and forms a two-periodic framework consisting of Cu^{II} metal ions and [**2**⊂**CB[6]**]$^{2+}$ linkers. Each Cu^{II} center within the framework adopts a distorted square pyramidal geometry with four pyridyl groups occupying the equatorial positions, while the axial position is occupied by an H_2O molecule (Figure 3d). The framework consists of non-interpenetrated, square grids with a metal···metal distance of 17.8 Å between rotaxane units (Figure 3e). The two-periodic grids are layered and highly undulating resulting in an interlayer spacing of 14.1 Å between layers. The remaining voids at the center of the grids are filled with 22 H_2O molecules and six non-coordinated nitrate anions per asymmetric unit.

By retaining the terminal 3-pyridylmethyl groups on the axle and extending the length of the internal alkyl chain to five carbons instead of four, one increases the flexibility of the ligand. This flexibility allows for the formation of a helical framework and shows how one can impart axial chirality into PRFs with achiral rotaxane linkers. Utilizing *N,N′*-bis(3-pyridylmethyl)-1,4-diaminopentane dihydronitrate, **3**(NO_3)$_2$, and similar reaction conditions to that used to make **PRF-1,** diffusion of silver nitrate into a solution of [**3**⊂**CB[6]**][NO_3]$_2$ resulted in colorless, crystals of **PRF-5** with formula [Ag(**3**⊂**CB[6]**)][NO_3]$_3$·(H_2O)$_x$.[28] **PRF-5** crystallized in monoclinic space group $P2_1/n$ and formed a one-periodic framework consisting of Ag^I metal ions and [**3**⊂**CB[6]**]$^{2+}$ linkers (Figure 4a). Each Ag^I center is coordinated by two pyridyl groups (Figure 4b) in a trans geometry with a more coplanar arrangement of the pyridyl rings when compared to the metal ligand fragment of **PRF-1**. The use of the longer diaminopentane axle and 3-pridylmethyl terminal groups resulted in a one-periodic helical framework (Figure 4c) as opposed to a linear or zigzag structure as in **PRF-1** and **PRF-3**. Each turn of the helix consists of two [**3**⊂**CB[6]**]$^{2+}$ linkers and two Ag^I ions with a metal···metal distance of 13.9 Å, with the helix propagating down the *b*-axis of the crystal with a pitch of 17.9 Å. It should be noted that **PRF-5** consists of both right- and left-handed helices within the material resulting in racemic crystals. The remaining voids in the structure are filled by H_2O molecules and non-coordinated nitrate anions.

In an effort to increase the periodicity of the PRF, Kim and coworkers altered their approach to utilize highly charged Tb(III) metal centers and modified the original 1,4-diaminobutane-based axle to possess

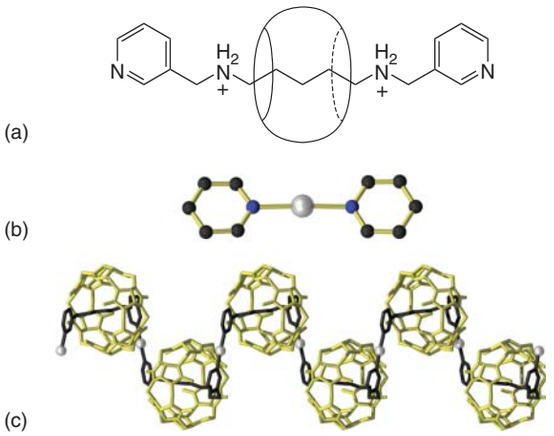


Figure 4 (a) [2]Pseudorotaxane linker [**3**⊂**CB[6]**]$^{2+}$ used to form **PRF-5**; (b) coordination environment of Ag^{I} center in **PRF-5**; (c) X-ray structure of the helical one-periodic framework of **PRF-5**

terminal 3-carboxybenzyl groups. This resulted in the first three-periodic PRF reported in the literature. To accomplish this, a slight excess of **CB[6]** was added to a solution of *N,N′*-bis(3-cyanobenzyl)-1,4-diaminobutane dihydronitrate in H_2O and the solution refluxed for 2 h, after which undissolved **CB[6]** was filtered off and the desired [2]pseudorotaxane isolated by evaporation and precipitation with ethanol. One equivalent of the [2]pseudorotaxane was then suspended in H_2O and placed in a stainless-steel bomb with 4.3 equivalents of $Tb(NO_3)_3{\cdot}5(H_2O)$ and ~0.1 equivalent of triethylamine. The bomb was subsequently sealed and heated to 150 °C for 3 days followed by slow cooling to room temperature after which large colorless crystals of **PRF-6** with formula $[Tb_2(H_2O)_4(\mathbf{4}\subset\mathbf{CB[6]})_3][\mathbf{4}\subset\mathbf{CB[6]}][NO_3]_4[OH]_4{\cdot}(H_2O)_{40}$ were obtained.[29] It should be noted that during this vigorous hydrothermal reaction the terminal 3-cyanobenzyl groups on the axle were converted to 3-carboxybenzyl groups which then coordinated to the available Tb^{3+} ions to form **PRF-6**. The ability of **CB[6]** to form strong [2]pseudorotaxanes in H_2O, even at elevated temperatures, allowed the use of hydrothermal synthesis whereas for other macrocyclic hosts the interaction between axle and wheel would have been completely eliminated under these very competitive solvent conditions.

PRF-6 crystallizes in the monoclinic space group $P2_1/c$ and forms a three-periodic framework consisting of Tb^{III} metal ions and [**4**⊂**CB[6]**] linkers (Figure 5a). Each Tb^{III} center can be described as having a distorted square *anti*-prismatic geometry and is part of a binuclear cluster which acts as a six-connected metal–ligand node. The binuclear Tb^{III} ions are linked by four bridging η^1,η'^1-carboxylate terminal groups, while two other η^2-chelating carboxylate groups and two H_2O molecules fill the remaining coordination sites (Figure 5b). This

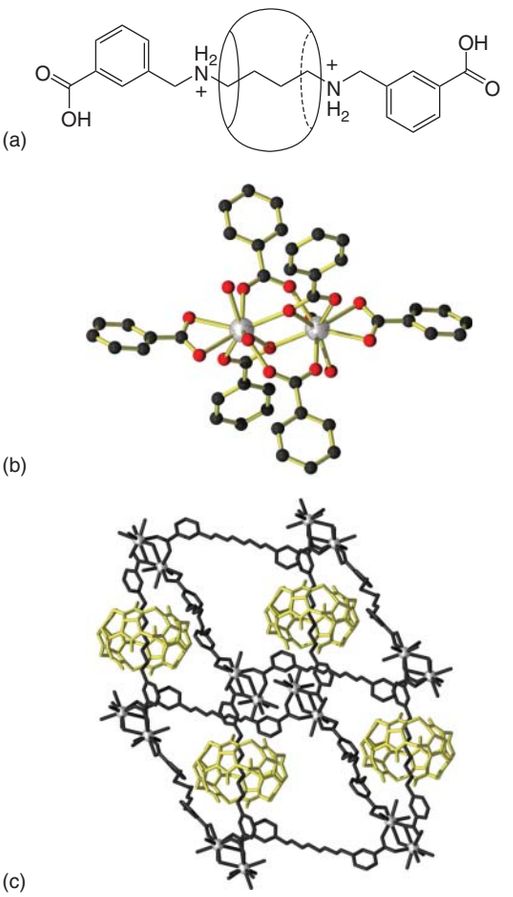


Figure 5 (a) [2]Pseudorotaxane linker [**4**⊂**CB[6]**]$^{2+}$ used to form **PRF-6**; (b) coordination environment of the Tb^{III} cluster in **PRF-6**; (c) X-ray structure of the primitive cubic, three-periodic framework of **PRF-5** (**CB[6]** macrocycles only shown in one direction of primitive cube for clarity)

results in a non-penetrated α-polonium-like network with a metal···metal distance between binuclear Tb^{III} centers of 3.97 and 17.4 Å between metal clusters which define the sides of the primitive cube (Figure 5c). Void space in the structure is filled with a single non-coordinating [2]pseudorotaxane supermolecule [**4**⊂**CB[6]**]$^{2+}$ per asymmetric unit, in addition to H_2O molecules and nitrate and hydroxide counterions. In addition, when an analogous axle was used with terminal 4-cyanobenzyl groups under the same reaction conditions with $Tb(NO_3)_3$, a PRF could be obtained with similar two-periodic hexagonal nets as in **PRF-2**.

While the PRFs developed by Kim and coworkers were some of the first examples of one-, two- and three-periodic frameworks with rotaxane linkers, very little material analysis (e.g., VT-PXRD) was reported to indicate the stability of these materials. However, recently

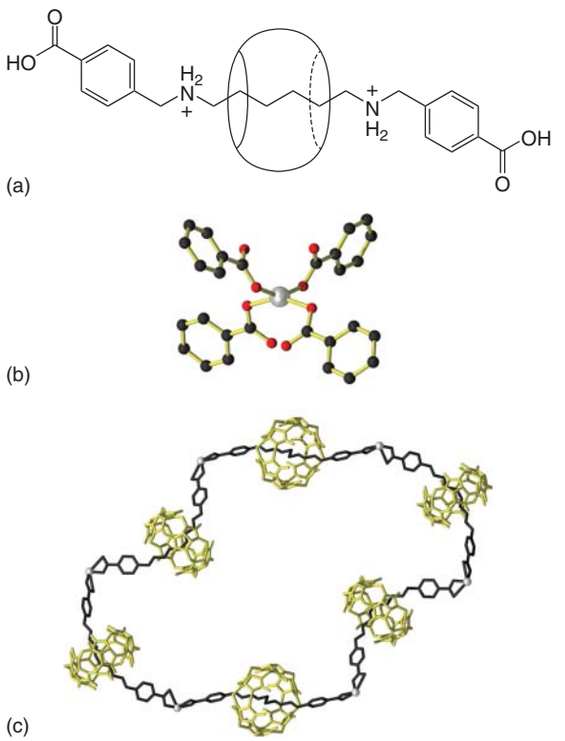


Figure 6 (a) [2]Pseudorotaxane linker [**5**⊂**CB[6]**]$^{2+}$ used to form **PRF-7**; (b) Coordination environment of Cu^{II} center in **PRF-7**; (c) X-ray structure of a distorted hexagonal unit which comprises the three-periodic framework of **PRF-7**

Su and coworkers used a longer 1,4-diaminohexane-based linker with terminal 4-carboxybenzyl groups in conjunction with **CB[6]** to form a series of isomorphous (Cu^{II}, Zn^{II}, Cd^{II}) three-periodic PRFs. To accomplish this, a slight excess of **CB[6]** was added to an aqueous solution of *N,N′*-bis(4-cyanobenzyl)-1,4-diaminohexane dihydronitrate followed by sonication and refluxing for 3 h, after which undissolved **CB[6]** was filtered off and the desired [2]pseudorotaxane isolated by evaporation and precipitation with ethanol. One equivalent of the isolated [2]pseudorotaxane was then suspended in H_2O and placed in a stainless-steel bomb with 1.9 equivalents of $Cu(NO_3)_3{\cdot}5(H_2O)$ and 3 drops of triethylamine. The bomb was subsequently sealed and heated to 170 °C for 72 h followed by slow cooling to room temperature, after which large green crystals of **PRF-7** were obtained with formula [Cu(**5**⊂**CB[6]**)][(**5**⊂**CB[6]**)·$(H_2O)_{13}$.[30] **PRF-7** crystallized in the monoclinic space group *C*2/*c* and formed a three-periodic framework consisting of Cu^{II} metal ions and [**5**⊂**CB[6]**] linkers (Figure 6a). Each Cu^{II} adopts a distorted tetrahedral geometry with four carboxylate linkers binding in an η^1 fashion to form a negatively charged metal node (Figure 6b). The resulting three-periodic framework can be described as having a *mok* topology consisting of distorted hexagonal sub-nets (Figure 6c) and threefold interpenetration. Each distorted hexagonal unit consists of two different rotaxane linkers (linear and bent). It was rationalized that during the vigorous reaction conditions a deprotonation–reprotonation equilibrium of the secondary ammonium ion resulted in a mixture of protonated rotaxane units (linear) and deprotonated rotaxane units (bent). VT-PXRD studies of **PRF-7** demonstrated that the material retained its diffraction pattern over 170 °C while thermogravimetric analysis (TGA) showed a loss of 7.3 wt% by 170 °C corresponding to thirteen interstitial H_2O molecules per asymmetric unit; this was followed by decomposition near 300 °C.

It should be noted that the flexible nature of the linkers used in conjunction with **CB[6]** to form **PRF-1**–**PRF-7** resulted in structures dictated almost entirely by the close-packing of the large **CB[6]** wheels. Unfortunately, this ultimately produces lattices with very limited amounts of the desirable void space (or free volume) required to allow large amplitude motions of the macrocyclic component within the structures.

3 POLYROTAXANE FRAMEWORKS CONTAINING DB24C8 WHEELS

Dibenzo[24]crown-8 (**DB24C8**) macrocycles are known to form [2]pseudorotaxanes with 1,2-bis(pyridinium)ethane axles. This motif has been used by Loeb *et al.* to form a variety of PRFs. Although the strength of the [2]pseudorotaxane adduct does not allow for aqueous or solvothermal synthesis it does come with some advantages. The **DB24C8** macrocycle allows for a higher degree of functionalization compared to **CB[6]** providing the opportunity to introduce functional groups into the PRF via the macrocycle. In addition, the electron-rich **DB24C8** macrocycle is known to exhibit intermolecular charge transfer with electron-poor, pyridinium-based axles, which allows one to infer the orientation of the macrocycle relative to the axle without detailed structural knowledge. This type of interaction could potentially be used for the creation of a MIM-based colorimetric switch in the solid-state.

Dissolving 1,2-bis(4,4′-bipyridinio)ethane tetrafluoroborate, **6**$(BF_4)_2$, in MeCN with 2 equivalents of **DB24C8** helps to push the equilibrium between free axle and wheel towards [2]pseudorotaxane formation. Adding 1 equivalent of $Co(BF_4)_2{\cdot}6(H_2O)$ to this mixture and subjecting it to slow evaporation produced yellow/orange crystals of **PRF-8** with formula $[Co(H_2O)_2(MeCN)_2$(**6**⊂**DB24C8**)$][BF_4]_4{\cdot}(MeCN)_2(H_2O)_2$ after 2 weeks.[31] **PRF-8** crystallized in the monoclinic space group $P2_1/c$ and forms a one-periodic framework consisting of Co^{II} metal ions and [**6**⊂**DB24C8**]$^{2+}$ linkers

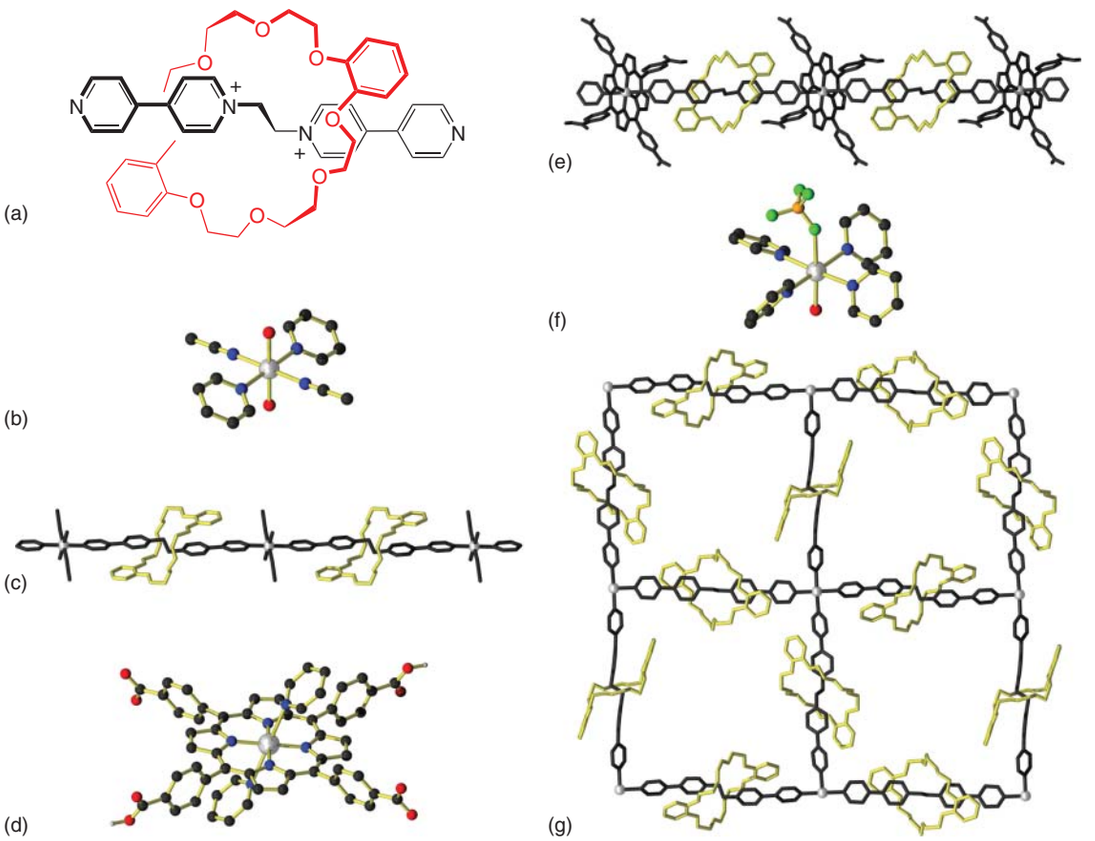


Figure 7 (a) [2]Pseudorotaxane linker [**6⊂DB24C8**]$^{2+}$ used to form **PRF-8**, **PRF-9**, and **PRF-10**; (b) coordination environment of Co^{II} center in **PRF-8**; (c) X-ray structure of the linear one-periodic framework of **PRF-8**; (d) coordination environment of [Zn^{II}(**TCPP**)]$^{2-}$ in **PRF-9**; (e) X-ray structure of the linear one-periodic framework of **PRF-9**; (f) coordination environment of Cd^{II} center in **PRF-10**; (g) X-ray structure of the square grid two-periodic framework of **PRF-10**

(Figure 7a). Each Co^{II} center adopts an octahedral geometry with two pyridyl groups of the rotaxane linkers binding in a trans arrangement, with the remaining equatorial sites occupied by two coordinated H_2O molecules and two coordinated MeCN molecules which also bind *trans* to one another (Figure 7b). This results in a linear one-periodic framework with a metal···metal distance of 22.1 Å between rotaxane units (Figure 7c); the **DB24C8** macrocycles adopt an S-conformation. This conformation allows both the electron rich aromatic groups of the macrocycle to π-stack effectively with both the electron-deficient pyridinium groups of the axle. The framework chains pack in a parallel arrangement with remaining void space filled by two MeCN molecules, two H_2O molecules, and four BF_4^- counterions per asymmetric unit.

One can control how these one-periodic chains organize relative to each other by using an ancillary ligand with external hydrogen-bond donor-/acceptor pairs such as *tetra*(4-carboxy)-phenyl-porphyrin (**TCPP**). One equivalent of **5**$(BF_4)_2$ was added to 4 equivalents of **DB24C8** in $CHCl_3$ and allowed to stir for 42 h after which an MeOH solution containing [Zn^{II}(**TCPP**)]$^{2-}$ was carefully layered on top to yield red crystals of **PRF-9** after a few days.[32] **PRF-9** consists of [Zn^{II}(**TCPP**)]$^{2-}$ metal nodes and [**6⊂DB24C8**]$^{2+}$ linkers with formula [Zn^{II}(**TCPP**)(**6⊂DB24C8**)]·$(H_2O)_4$] and crystallized in the monoclinic space group $P2_1/n$. Each Zn^{II} metal ion adopts a distorted octahedral geometry; four equatorial sites are bound to the porphyrin and the remaining axial sites are occupied by pyridyl units of the rotaxane linkers (Figure 7d). Each [Zn^{II}TCPP]$^{2-}$ unit acts simultaneously as an anionic bridging node and a hydrogen-bond donor/acceptor via the carboxy groups of the porphyrin. Overall, this results in a one-periodic framework with a metal···metal distance of 22.3 Å (Figure 7e). Deprotonation of two of the carboxy groups results in cooperative hydrogen-bonding between carboxylic/carboxylate groups of neighboring porphyrin molecules which allows for a way to organize the one-periodic framework chains in the solid-state. The remaining void space in **PRF-9** is free

from independent counterions and is filled with four H_2O molecules per asymmetric unit.

In order to increase the periodicity of these systems, Loeb and coworkers found that switching to a non-coordinating solvent (i.e., from MeCN to $MeNO_2$) during PRF synthesis allowed for formation of two-periodic frameworks. This was accomplished by dissolving **6**$(BF_4)_2$ in $MeNO_2$ and adding 2 equivalents of **DB24C8** with 1 equivalent of $Cd(BF_4)_2{\cdot}(H_2O)_6$. Vapor diffusion of *iso*-propyl ether into this reaction mixture produced light yellow crystals of **PRF-10** with formula $[Cd(H_2O)(BF_4)(\mathbf{6}{\subset}\mathbf{DB24C8})_2][BF_4]_5{\cdot}(MeNO_2)_{15}$.[31] **PRF-10** crystallizes in the triclinic space group *P*1and forms a two-periodic framework consisting of Cd^{II} metal ions and $[\mathbf{6}{\subset}\mathbf{DB24C8}]^{2+}$ linkers. Each Cd^{II} center adopts an octahedral geometry with four pyridyl groups of the rotaxane linkers binding in a square planar arrangement and the remaining axial sites occupied by one coordinated H_2O molecule and one coordinated BF_4^- anion (Figure 7f). The resulting open framework consists of non-interpenetrated two-periodic grids with a large metal···metal distance of 22.2 Å between rotaxane linkers (Figure 7g). The grids stack along the *c*-axis of the structure with alternating interlayer spacings of 12.0 and 10.0 Å. As a result, channels form along the *c*-axis that contains fifteen $MeNO_2$ molecules and five BF_4^- counterions per asymmetric unit. Thermogravimetric analysis was used to probe the stability of this material and although the material loses crystallinity as solvent is removed from the void, the rotaxane framework does not break down and lose the **DB24C8** macrocycles until over 250 °C. This demonstrates that although the macrocycle is only held in position by weak non-covalent interactions during [2]pseudorotaxane formation, a covalent or strong metal–ligand bond must be broken to release the interlocked wheel component from the framework.

The ability to functionalize **DB24C8** was used by Loeb and coworkers to determine if it was possible to obtain the same metal-organic framework by using the same axle but with an altered macrocycle. A tetraphenoxy derivative of **DB24C8** was synthesized (**TPDB24C8**) and employed under similar reaction conditions used to prepare **PRF-10**; **6**$(BF_4)_2$ was dissolved in $MeNO_2$ and mixed with 2 equivalents of **TPDB24C8** and half an equivalent of $Cd(BF_4)_2{\cdot}(H_2O)_6$ dissolved in an $MeNO_2$/MeOH mixture. Vapor diffusion of *iso*-propyl ether into this reaction mixture produced yellow crystals of **PRF-11** with formula $[Cd(H_2O)_2(\mathbf{6}{\subset}\mathbf{TPDB24C8})_2]\ [BF_4]_6{\cdot}(MeNO_2)_{23}$.[33] **PRF-11** crystallizes in the monoclinic space group *Pc* and forms a two-periodic framework consisting of Cd^{II} nodes and $[\mathbf{6}{\subset}\mathbf{TPDB24C8}]^{2+}$ linkers (Figure 8a) as well as naked $\mathbf{6}^{2+}$ axles. Each Cd^{II} center adopts an octahedral geometry with four pyridyl groups binding in a square planar arrangement, with the remaining axial sites occupied by two coordinated H_2O molecules (Figure 8b). The overall

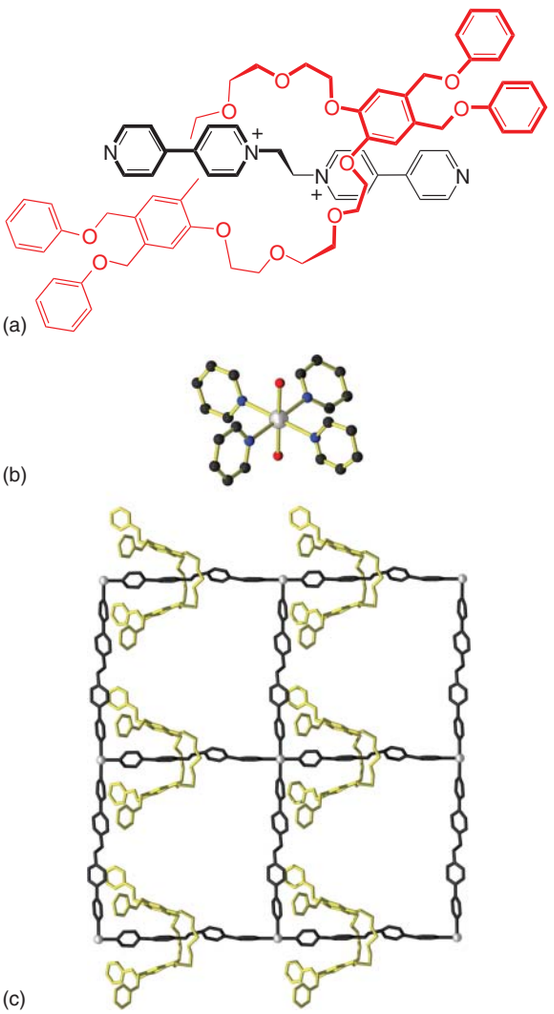


Figure 8 (a) [2]Pseudorotaxane linker $[\mathbf{6}{\subset}\mathbf{TPDB24C8}]^{2+}$ used to form **PRF-11**; (b) coordination environment of Cd^{II} center in **PRF-11**; (c) X-ray structure of the square grid, two-periodic framework of **PRF-11** containing rotaxane linkers $[\mathbf{6}{\subset}\mathbf{TPDB24C8}]^{2+}$ as well as naked $\mathbf{6}^{2+}$ linkers

result is a square grid which has the same topology and metal···metal distances as **PRF-10**, but with only half of the axles possessing a macrocycle (Figure 8c). This is likely due to the large size of the tetra-substituted macrocycle which adopts a C-conformation in **PRF-11** with the four $CH_2OC_6H_5$ groups of the macrocycle sheltering the naked $\mathbf{6}^{2+}$ linkers. Remaining voids in the structure are filled with 23 $MeNO_2$ molecules and six BF_4^- counterions, per asymmetric unit. **PRF-11** demonstrates how the interlocked macrocyclic component can be thought of as a supramolecular additive which does not perturb the structure of the framework. As such, it may be possible to use this as a method to tune the internal properties and/or structure of the cavities in porous PRFs—for example

making them hydrophobic or hydrophilic depending on what substituents are appended to the macrocycle.

Loeb and coworkers also found that modification of their traditional axle $\mathbf{6}^{2+}$ was possible by utilizing pyridine *N*-oxide terminal groups to form 1,2-bis-(4,4′-bipyridinio-mono-*N*-oxide)ethane tetrafluoroborate, $\mathbf{7}(BF_4)_2$. It was determined that under similar reaction conditions to **PRF-10**, a very different framework was obtained with this axle. Dissolving 1 equivalent of $Cd(BF_4)_2{\cdot}(H_2O)_6$ in $MeNO_2$ with 2 equivalents of $\mathbf{7}(OTf)_2$ and 6 equivalents of **DB24C8**, followed by vapor diffusion of *iso*-propyl ether into the reaction mixture produced orange crystals of **PRF-12** with formula $[Cd(OTf)_2(\mathbf{7})(\mathbf{7}\subset\mathbf{DB24C8})][OTf]_4{\cdot}(MeNO_2)_4$.[34] **PRF-12** crystallizes in the triclinic space group *P*1 and forms a two-periodic framework consisting of Cd^{II} nodes and $[\mathbf{7}\subset\mathbf{DB24C8}]^{2+}$ linkers (Figure 9a) as well as naked axles of $\mathbf{7}^{2+}$. Each Cd^{II} ion adopts an octahedral geometry with

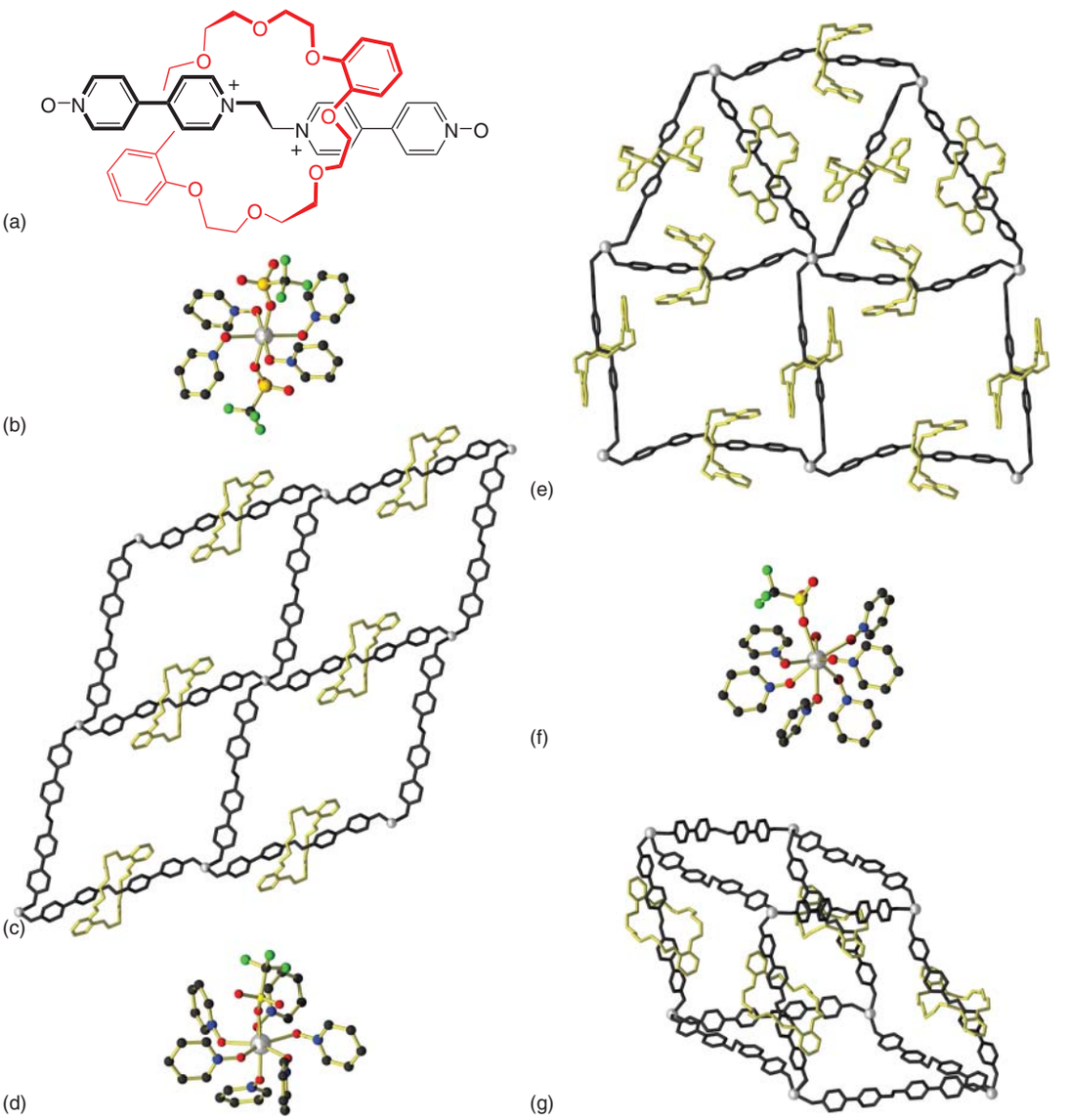


Figure 9 (a) [2]Pseudorotaxane linker $[\mathbf{7}\subset\mathbf{DB24C8}]^{2+}$ used to form **PRF-12**, **PRF-13**, and **PRF-14**; (b) coordination environment of Cd^{II} center in **PRF-12**; (c) X-ray structure of the distorted square grid, two-periodic framework of **PRF-12** containing rotaxane linkers $[\mathbf{7}\subset\mathbf{DB24C8}]^{2+}$ as well as naked $\mathbf{7}^{2+}$ linkers; (d) coordination environment of Yb^{III} center in **PRF-13**; (e) X-ray structure of the square and triangular forms which comprise layers in the three-periodic framework of **PRF-13**; (f) coordination environment of Sm^{III} center in **PRF-14**; (g) X-ray structure of the primitive cubic, three-periodic framework of **PRF-14** (**DB24C8** macrocycles only shown in one direction of the primitive cube for clarity)

four pyridine *N*-oxide ligands bound to the equatorial sites (two rotaxane linkers and two from naked axles of $\mathbf{7}^{2+}$) with the remaining axial sites occupied by two OTf anions (Figure 9b). The two different linkers form a two-periodic square net with a metal–metal separation of 22.5 Å (Figure 9c). As in **PRF-10**, only half of the linkers are composed of rotaxanes. In this case however, it cannot be attributed to a bulky macrocycle but instead to the less directional metal–ligand coordination bonds of the pyridine *N*-oxide coordinating groups. The resulting grids formed in **PRF-12** are layered in an alternating fashion in which the rotaxane linkers in one layer block openings in the adjacent layer eliminating the formation of channels. Remaining void space in **PRF-12** is filled with four OTf anions and four $MeNO_2$ molecules per asymmetric unit.

The combination of pyridine *N*-oxide axle $\mathbf{7}^{2+}$ and much larger oxophilic, lanthanide ions allowed for a higher coordination number and thus a desired increase in periodicity for this system. For example, slow diffusion of $Yb(OTf)_3$ dissolved in MeCN, into an MeCN solution containing $\mathbf{7}(OTf)_2$ and 3 equivalents of **DB24C8** resulted in large yellow crystals of **PRF-13** with formula $[Yb(OTf)(\mathbf{7}\subset\mathbf{DB24C8})_3][Cl][OTf]_7$ after 4 days.[35] **PRF-13** is a three-periodic framework consisting of Yb^{III} nodes and $[\mathbf{7}\subset\mathbf{DB24C8}]^{2+}$ linkers and crystallizes in the triclinic space group $P\bar{1}$. Each Yb^{III} metal center adopts a seven-coordinate pentagonal bipyramidal geometry, five pyridine *N*-oxide rotaxane linkers occupying the equatorial sites of the pentagonal plane while the residual axial sites are coordinated by another rotaxane linker and an OTf anion (Figure 9d). The rotaxanes bound to the equatorial sites result in two-periodic layers consisting of alternating square and triangular forms (Figure 9e), the layers are pillared by the rotaxanes bound to the axial site of the metal centers. The square forms in the layer allow for interpenetration of another lattice, while the triangular forms are too crowded to allow for penetration. It should also be noted that both the C- and S-conformations of the **DB24C8** macrocycle are observed in this structure, likely due to the flexibility of the crown ether and subtle crystal packing forces. The remaining void space in **PRF-13** is filled with OTf and Cl anions as well as crystallization solvents (MeCN and H_2O). The PXRD patterns of the desolvated material showed that the crystallinity of the sample was retained, while TGA again showed loss of the **DB24C8** macrocycle only above 240 °C, resulting from degradation of the framework.

Interestingly, when other lanthanide metals (Ln = Sm^{III}, Eu^{III}, Gd^{III}, Tb^{III}) were used under similar conditions, a very different series of isomorphous PRFs was formed. Adding 1 equivalent of $Ln(OTf)_3$ to an MeCN solution containing 2 equivalents of $\mathbf{7}(OTf)_2$ and 6 equivalents of **DB24C8**, resulted in large orange crystals of **PRF-14** with formula $[Ln(H_2O)(OTf)(\mathbf{7}\subset\mathbf{DB24C8})_3][Cl][OTf]_7$, after standing for 4 days.[35] **PRF-14** is a three-periodic framework consisting of Ln^{III} nodes and $[\mathbf{7}\subset\mathbf{DB24C8}]^{2+}$ linkers and crystallizes in the triclinic space group $P\bar{1}$. Each Ln^{III} metal center adopts an eight-coordinate geometry comprising six pyridine *N*-oxide rotaxane linkers, a single H_2O molecule, and OTf anion (Figure 9f). The resulting framework adopts an α-polonium-like network with Ln···Ln distances of 23.5 Å outlining the sides of the "cube" (Figure 9g). **PRF-14** is interpenetrated with another lattice with the remaining voids occupied by OTf and Cl anions in addition to crystallization solvents (MeCN and H_2O). This material exhibited similar stability to **PRF-13**, with a very similar TGA showing that there was retention of crystallinity after desolvation. While **PRF-13** and **PRF-14** are stable three-periodic frameworks, interpenetration and a plethora of independent counterions, limited the free volume available in these materials; a necessity for observing any large amplitude dynamic behavior of the macrocyclic component.

In an effort to eliminate the non-coordinating counterions that occupy much of the void space in lattices of PRFs, Loeb and coworkers developed a disulphonated crown ether $\mathbf{DSDB24C8}^{2-}$ to offset the dicationic charge on the bis-pyridinium axle. One equivalent of $\mathbf{6}(BF_4)_2$ was mixed with 2 equivalents of *anti*-$[Me_4N]_2$[**DSDB24C8**] and 1 equivalent of $[Cu_2(BnO)_4]$ in an MeOH/DMF mixture. This reaction mixture was subject to slow evaporation, which produced turquoise crystals of **PRF-15** with formula $[Cu_2(BnO)_4(\mathbf{6}\subset\mathbf{DSDB24C8})]$ $(MeOH)_2(DMF)$ after 1 week.[36] **PRF-15** crystallized in the triclinic space group *P1* and forms a one-periodic framework consisting of Cu^{II} paddlewheel nodes and [**6**⊂**DSDB24C8**] linkers (Figure 10a). The positively charged pyridinium groups of the axle are counteracted by the negative charges of the sulfonate groups on the macrocycle, resulting in a neutral, zwitterionic linker. Combining this with a neutral charge, metal node results in a framework which is also neutral and free from independent counterions. Each Cu^{II} ion is part of a binuclear complex and adopts a square pyramidal geometry with the equatorial sites bound by four benzoate groups which bridge two metal centers and the remaining axial sites coordinated to pyridine groups of the [**6**⊂**DSDB24C8**] linkers (Figure 10b). **PRF-15** has a metal···metal distance between rotaxane subunits of 21.6 Å with each $\mathbf{DSDB24C8}^{2-}$ macrocycle adopting the traditional S-conformation (Figure 10c). The one-periodic framework chains pack in a parallel arrangement with the remaining void space filled with two MeOH molecules and a single DMF molecule per asymmetric unit.

A neutral charge pseudorotaxane linker was a significant improvement over previous dicationic [2]pseudorotaxane linkers, however, increasing the periodicity of this system proved difficult. Consequently, a negatively charged [2]pseudorotaxane linker was developed by replacing one of the internal pyridinium rings of axle $\mathbf{6}^{2+}$ by a simple phenyl ring to create a monocationic pyridinium axle $\mathbf{8}^{+}$.

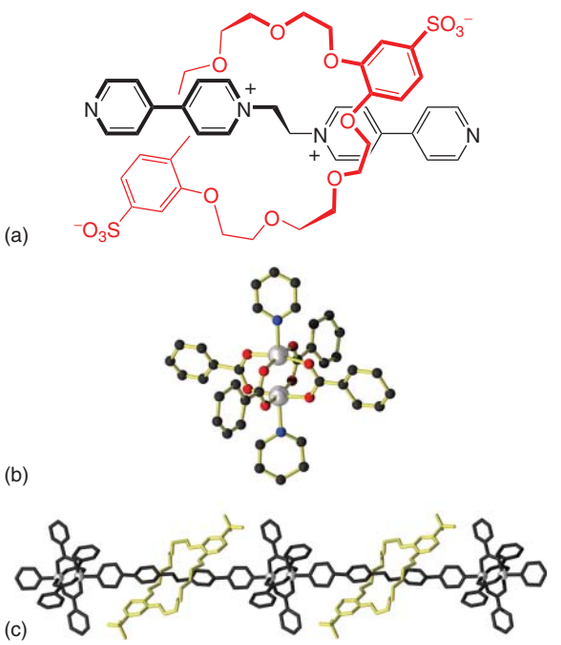


Figure 10 (a) [2]Pseudorotaxane linker [**6**⊂**DSDB24C8**] used to form **PRF-15**; (b) coordination environment of Cu^{II} paddlewheel cluster in **PRF-15**; (c) X-ray structure of the linear one-periodic framework of **PRF-15**

It was determined that $\mathbf{8}^{+}$ was still able to achieve significant [2]pseudorotaxane formation with a $\mathbf{DSDB24C8}^{2-}$ macrocycle to form an overall negatively charged [2]pseudorotaxane linker, [**8**⊂**DSDB24C8**]$^{-}$ (Figure 11a). This negatively charged linker was used to prepare **PRF-16**, **PRF-17**, and **PRF-18**.

PRF-16 was synthesized by mixing equimolar amounts of **8**(OTf), *anti*-$[Me_4N]_2$[**DSDB24C8**] and $Zn(NO_3)_2{\cdot}(H_2O)_6$ in MeOH and allowing the solution to stand for 3 days, after which a crop of pale yellow, crystals with formula [Zn(**8**⊂**DSDB24C8**)$(H_2O)_2$(MeOH)][NO_3]·$(MeOH)_2$ were isolated.[37] **PRF-16** crystallizes in the triclinic space group $P\bar{1}$ and forms a one-periodic framework consisting of Zn^{II} metal ions and [**8**⊂**DSDB24C8**]$^{-}$ linkers. Each Zn^{II} atom adopts an octahedral geometry with two coordinating pyridine groups from the rotaxane linkers and two H_2O molecules coordinated in a trans arrangement, with the remaining coordination sites occupied by a single MeOH molecule and a sulfonate group from a $\mathbf{DSDB24C8}^{2-}$ macrocycle (Figure 11b). **PRF-16** is a racemic, double-stranded, one-periodic framework with a Zn···Zn distance of 22.0 Å (Figure 11c). Two adjacent chains are joined together in a head-to-tail fashion by coordination of a sulfonate group of one unit to the Zn^{II} center of a neighboring unit, with the closest Zn···Zn distance being 9.17 Å. The $\mathbf{DSDB24C8}^{2-}$ macrocycles wrap around the charged pyridinium end of the axle, in a C-conformation, which presumably optimizes the non-covalent interactions between axle and wheel. Remaining voids in the structure are occupied by one nitrate counterion and two MeOH molecules per asymmetric unit.

While **PRF-16** demonstrated how [**8**⊂**DSDB24C8**]$^{-}$ could be used as a negatively charged [2]pseudorotaxane linker between positively charged metal centers, it did not contain the correct stoichiometry to form a neutral framework. In order to achieve a neutral framework with this singly charged linker, a two-periodic structure with dicationic metal centers would be required. This was accomplished by mixing 2 equivalents of **8**(OTf) and *anti*-$[Me_4N]_2$[**DSDB24C8**] with 1 equivalent of $Zn(NO_3)_2{\cdot}6(H_2O)$ in MeOH and allowing the solution to stand for 5 days. This resulted in a crop of pale yellow crystals of **PRF-17** with formula [Zn(**8**⊂**DSDB24C8**)$_2(H_2O)_2$]·$(H_2O)(CH_3NO_2)_{21}$.[37] **PRF-17** crystallized in the monoclinic space group *Cc* and forms a two-periodic framework consisting of Zn^{II} metal ions and [**8**⊂**DSDB24C8**]$^{-}$ linkers. Each Zn^{II} atom adopts an octahedral geometry with four pyridine groups from the rotaxane linkers coordinating to the equatorial sites with the remaining axial sites coordinated by two H_2O molecules (Figure 11d). With the correct stoichiometry, neutral, square grids are obtained in which the cationic Zn^{II} metal ions are counter-balanced by the anionic rotaxane linkers, with a metal···metal distance between rotaxane linkers of 22.0 Å. (Figure 11e). These charge neutral grids are stacked in an alternating AB fashion through hydrogen-bonding between axially coordinated H_2O molecules, with a layer spacing of 7.82 Å (Figure 11h). Large channels are formed at the center of these grids which are filled with numerous $MeNO_2$ solvent molecules. Immersion of **PRF-17** in $CHCl_3$ followed by treatment under mild vacuum at room temperature resulted in evacuation of the material (determined by TGA) to yield a porous solid with 42% void space. The stability of **PRF-17** was further determined by VT-PXRD, which showed that the material retained its original PXRD pattern up to 80 °C, after which a new layered structure formed, followed by decomposition at higher temperatures. This presumably was due to a loss of weak interlayer hydrogen-bonding from interstitial H_2O molecules, which held the layers in place.

Fortuitously, another PRF was isolated during the synthesis of **PRF-17** when excess $[Me_4N]_2[SO_4]$ was present, leading to the isolation of colorless, crystals of **PRF-18** with formula [Zn(**8**⊂**DSDB24C8**)$_2$][$(Zn(SO_4)(H_2O)_2(MeOH)_2)_2$]·$(CH_3NO_2)_{42}$.[37] **PRF-18** crystallized in the orthorhombic space group $Cmc2_1$ and forms a three-periodic framework consisting of Zn^{II} metal ions and [**8**⊂**DSDB24C8**]$^{-}$ linkers, in addition to $ZnSO_4$-based pillars. As in **PRF-17** the Zn^{II} atoms adopt an octahedral geometry with four pyridine groups from rotaxane linkers coordinating to the equatorial sites (Figure 11f)

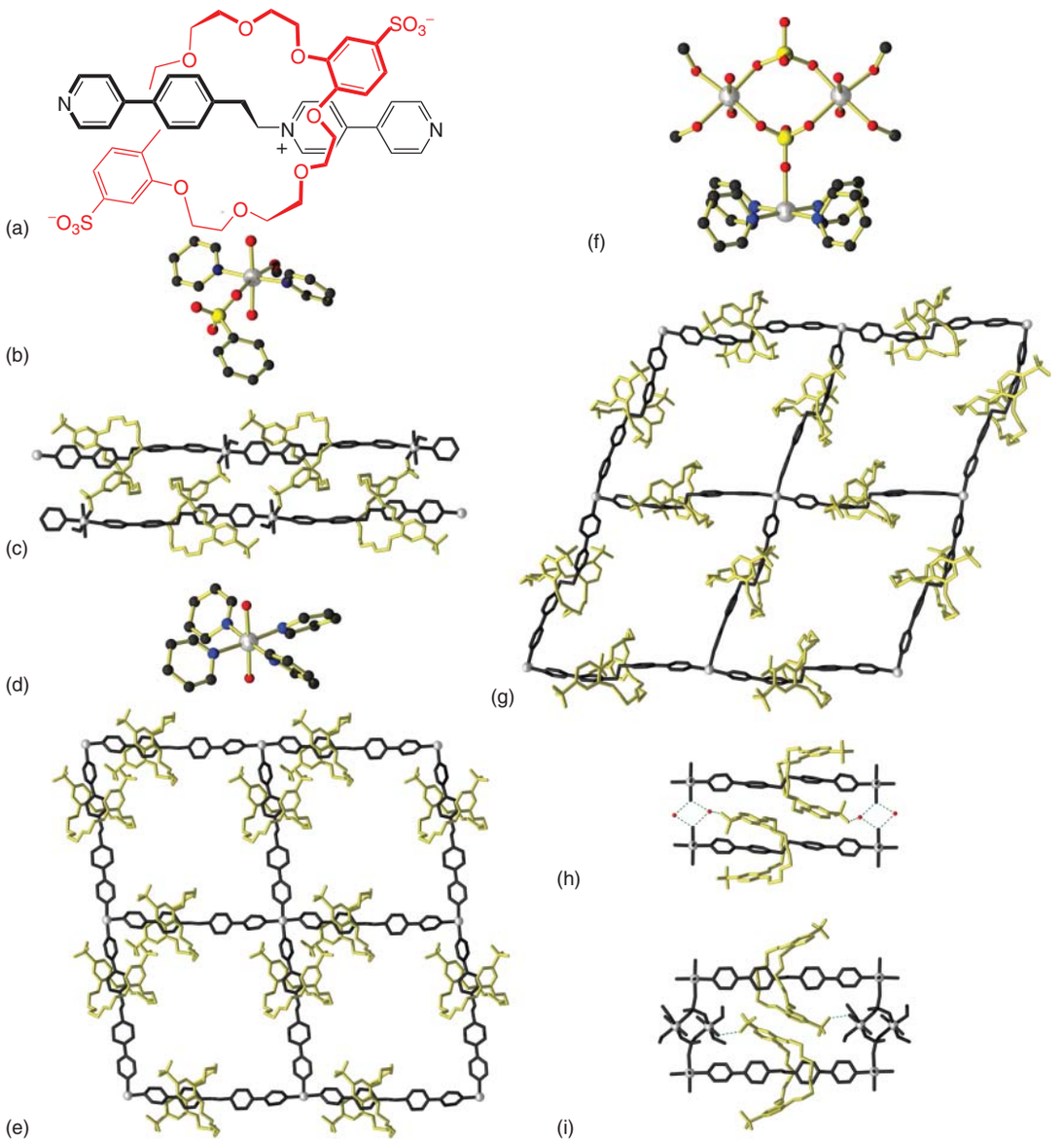


Figure 11 (a) [2]Pseudorotaxane linker [**8**⊂**DB24C8**]$^{-}$ used to form **PRF-16**, **PRF-17**, and **PRF-18**; (b) coordination environment of Zn^{II} center in **PRF-16**; (c) X-ray structure of the linear one-periodic framework of **PRF-16**; (d) coordination environment of Zn^{II} center in **PRF-17**; (e) X-ray structure of the square grid, two-periodic framework of **PRF-17**; (f) coordination environment of Zn^{II} center along with $ZnSO_4$-based pillars of **PRF-18**; (g) X-ray structure of the square grids within the three-periodic framework of **PRF-18**; (h) X-ray structure depicting how layers are pillared by interstitial water molecules in **PRF-17**; (i) X-ray structure depicting how the layers are pillared by inorganic $ZnSO_4$ in **PRF-18**

resulting in neutral square grids (Figure 11g). In contrast to **PRF-17,** these two-periodic grids are no longer stacked together by hydrogen-bonding interactions but are pillared by inorganic clusters of $(Zn(SO_4)(H_2O)_2(MeOH)_2)_2$, which results in a three-periodic structure with a larger layer spacing of 11.0 Å between metal centers (Figure 11i). In addition, there is also a significant difference in the orientation of the macrocycle in relation to the axle when comparing **PRF-17** to **PRF-18**. In **PRF-17**, the **DSDB24C8**$^{2-}$ macrocycle is π-stacked with the pyridinium group of the axle in a face-to-face interaction, (similar to that observed for almost every other rotaxane of this type) leading to charge transfer and the yellow color of the material. However in **PRF-18,** the **DSDB24C8**$^{2-}$ macrocycle is rotated by 90° and makes an edge-to-face π-interaction, preventing significant charge transfer and

resulting in a colorless material. Although a complete analysis of the stability and thermal properties of **PRF-18** was not possible, gentle heating of the **PRF-18** causes the material to change from colorless to yellow. This qualitative observation was rationalized as a thermally driven, irreversible phase change, in which the macrocyclic component was reoriented from an edge-to-face π-interaction to a π-stacked interaction within the material.

4 POLYROTAXANE FRAMEWORKS CONTAINING A TEXAS-SIZED MOLECULAR BOX

Sessler and coworkers have recently developed an imidazolium-based, electron-deficient macrocycle they dubbed the Texas-Sized Molecular Box, $\mathbf{TSMB}^{4+}$, which forms [2]pseudorotaxanes with well-known MOF linkers such as 2,6-naphthalene-dicarboxylate, $\mathbf{9}^{2-}$ and 1,4-benzene-dicarboxylate, $\mathbf{10}^{2-}$ as the axle.[38] When $\mathbf{9}^{2-}$ was utilized as the axle to form a [2]pseudorotaxane linker $[\mathbf{9}\subset\mathbf{TSMB}]^{2+}$ (Figure 12a), and combined with silver nitrate, a one-periodic **PRF** was obtained. This was accomplished by adding $AgNO_3$ to a solution containing $[\mathbf{TSMB}][PF_6]_4$ and **9** in DMF/MeCN/H_2O (1:1:1) followed by addition of triethylamine which precipitated a white solid that was removed by filtration. The resulting filtrate was subjected to slow evaporation for 4 weeks, after which colorless crystals of **PRF-19** with formula $[Ag_2(\mathbf{9}\subset\mathbf{TSMB})(\mathbf{9})][\mathbf{9}]\cdot(H_2O)_{16}$, were obtained.[39] **PRF-19** crystallizes in the triclinic space group $P\bar{1}$ and forms a one-periodic framework consisting of Ag^{I} metal ions and $[\mathbf{9}\subset\mathbf{TSMB}]^{2+}$ linkers as well as naked linkers of $\mathbf{9}^{2-}$. Each Ag^{I} center is coordinated by two carboxylate groups in a trans geometry (Figure 12b), one from a rotaxane linker and one from a naked axle, $\mathbf{9}^{2-}$, with metal···metal distances of 13.5 and 13.8 Å, respectively. The rotaxane units show strong donor–acceptor interactions, with less than 3.5 Å between π-stacked aromatic groups of the tetra-imidazolium macrocycle and the 2,6-naphthalene-based axle. The one-periodic framework chains propagate with every other linker being threaded through a tetra-imidazolium macrocycle. This allows for efficient packing in which the electron-deficient aromatic groups of the $\mathbf{TSMB}^{4+}$ in one chain π-stack to the electron-rich naked linkers of a neighboring chain (Figure 12c). Void space in the structure is filled with a non-coordinated axle, $\mathbf{9}^{2-}$, for charge balance and 16 H_2O molecules per asymmetric unit.

By utilizing the same [2]pseudorotaxane linker, $[\mathbf{9}\subset\mathbf{TSMB}]^{2+}$, with Zn^{II} metal ions, Sessler and coworkers were able to increase the periodicity of this system to obtain a three-periodic PRF. This was accomplished by mixing a solution containing $[\mathbf{TSMB}][PF_6]_4$, excess 2,6-naphthalene dicarboxylic acid and $Zn(NO_3)_2\cdot(H_2O)_6$ to

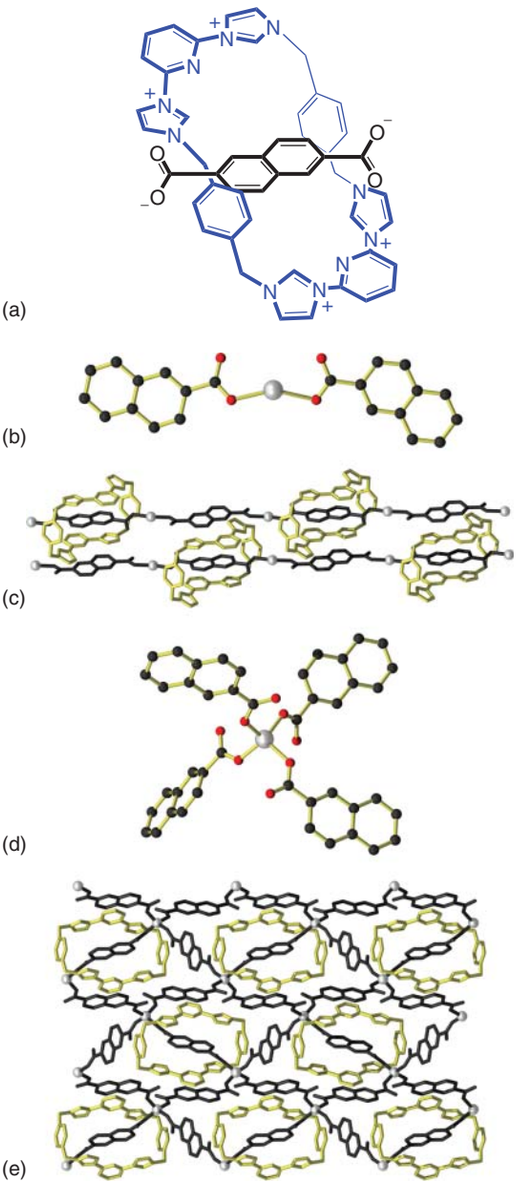


Figure 12 (a) [2]Pseudorotaxane linker $[\mathbf{9}\subset\mathbf{TSMB}]^{2+}$ used to form **PRF-19** and **PRF-20**; (b) coordination environment of Ag^{I} center in **PRF-19**; (c) X-ray structure of the linear one-periodic framework of **PRF-19**; (d) coordination environment of Zn^{II} center in **PRF-20**; (c) X-ray structure of the diamondoid three-periodic framework of **PRF-20** containing rotaxane linkers $[\mathbf{9}\subset\mathbf{TSMB}]^{2+}$ as well as naked $\mathbf{9}^{2-}$ linkers in a 1:3 ratio

a 1:1 solution of DMF/H_2O. After addition of triethylamine to this mixture, crystals of **PRF-20** with formula $[Zn_2(\mathbf{9}\subset\mathbf{TSMB})(\mathbf{9})_3]\cdot(H_2O)_6$ were isolated.[40] **PRF-20** crystallizes in the monoclinic space group $P2_1/c$ and forms a three-periodic framework consisting of Zn^{II} metal ions and $[\mathbf{9}\subset\mathbf{TSMB}]^{2+}$ linkers as well as naked linkers of $\mathbf{9}^{2-}$. Each Zn^{II} metal ion is coordinated by four carboxylate

groups in a tetrahedral geometry (Figure 12d) to form an interpenetrated, diamondoid network in which one out of every four linkers is encircled by a **TSMB**$^{4+}$ macrocycle (Figure 12e). **PRF-20** suffers from twofold interpenetration with the remaining voids in the structure filled by six interstitial H_2O molecules per asymmetric unit. Thermogravimetric analysis and PXRD measurements showed **PRF-20** to be thermally stable to 230 °C and retain its PXRD pattern after evacuation.

By utilizing a shorter linker, **10**$^{2-}$ and **TSMB**$^{4+}$ with lanthanide metal centers (Ln = Nd^{III}, Sm^{III}, Tb^{III}, and Eu^{III}) Sessler and coworkers were able to obtain a series of three-periodic PRFs. The Eu^{III} structure was obtained by layering a DMF solution containing [**TSMB**][PF_6]$_4$, **10**, and Eu(NO_3)$_3$ with tetramethylammonium hydroxide in an H_2O/DMF mixture to yield crystals of **PRF-21** with formula [Eu_2(**10**⊂ **TSMB**)(**10**)$_4$(H_2O)]·(H_2O)$_6$.[41] **PRF-21** crystallizes in the monoclinic space group $P2_1/c$ and forms a three-periodic framework consisting of Eu^{III} metal ions and [**10**⊂ **TSMB**]$^{2+}$ linkers as well as naked linkers of **10**$^{2-}$ (Figure 13a). There are two types of Eu^{III} environments that exist within this structure; 8- and 9-coordinate. The 8-coordinate environment consists of two η^2-chelating carboxylate groups, three η^1-coordinating carboxylate groups and a single H_2O molecule (Figure 13b). The nine-coordinate environment consists of three η^2-chelating carboxylate groups, a single η^1-coordinating carboxylate group and two H_2O molecules (Figure 13c). One out of every five **10**$^{2-}$ linkers in **PRF-21** is encircled by a **TSMB**$^{4+}$ macrocycle. The overall framework is charge neutral and results in two-periodic rectangular nets containing rotaxane linkers being pillared by naked **10**$^{2-}$ linkers (Figure 13d). **PRF-21** was also studied for its luminescent properties which showed the material to have a unique bright orange luminescence when compared to other lanthanide PRFs. Sessler and coworkers suggested that one may eventually be able to fine-tune the properties of these materials, by coupling interesting physical properties such as the luminescence observed in **PRF-21** with the dynamics of interlocked molecules.

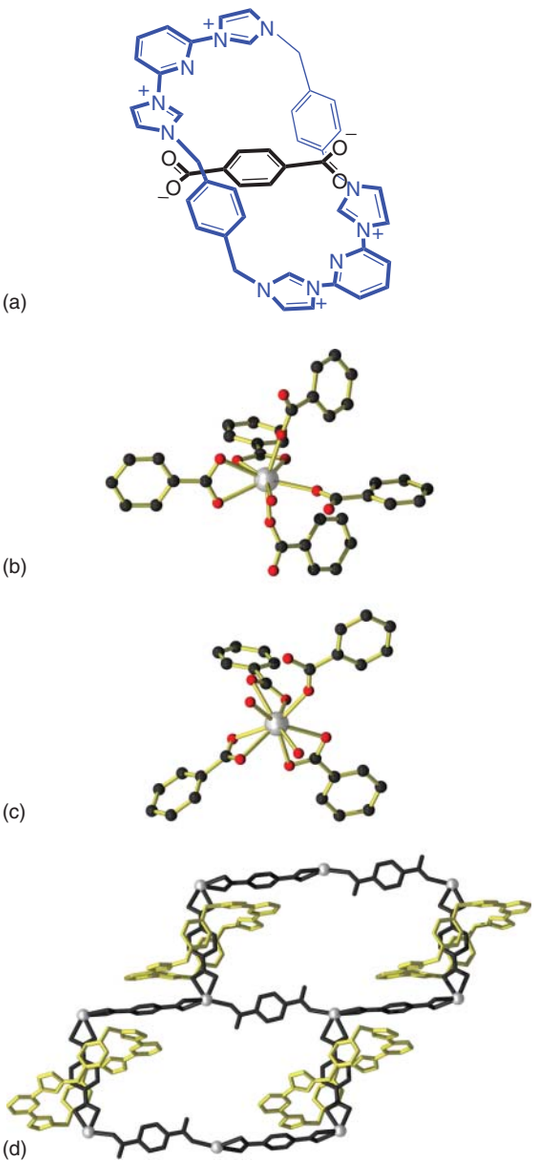


Figure 13 (a) [2]Pseudorotaxane linker [**10**⊂**TSMB**]$^{2+}$ used to form **PRF-21**; (b) coordination environment of eight-coordinate Eu^{III} center in **PRF-21**; (c) coordination environment of nine coordinate Eu^{III} center in **PRF-21**; (d) X-ray structure of the rectangular forms within the three-periodic framework of **PRF-21**

5 POLYROTAXANE FRAMEWORKS CONTAINING A Cu^{I} TEMPLATED [2]PSEUDOROTAXANE

Utilizing a Cu^{I} templated [2]pseudorotaxane linker, Stoddart, Sauvage, Yaghi, and coworkers were able to create a robust PRF capable of withstanding post synthetic modification. This was accomplished by adding a copper-coordinated phenanthroline-based macrocycle [Cu(**PM**)(MeCN)$_2$][PF_6] (**PM** = 1,10-Phenanthroline Macrocycle) into a solution of the axle **11** in CH_2Cl_2 to form [2]pseudorotaxane linker [Cu(**11**⊂**PM**)]$^{+}$ (Figure 14a). This linker was then added to a DEF solution of Zn(NO_3)$_2$·(H_2O)$_6$ and heated to 100 °C in a sealed tube for 48 h to yield red cubic crystals of **PRF-22** with formula [Zn_4O(Cu(**11**⊂**PM**))$_3$][PF_6]$_3$·(DEF)$_x$.[42] **PRF-22** crystallized in the monoclinic space group $P2_1/c$ and forms a three-periodic framework, consisting of inorganic Zn_4O clusters which are linked together by carboxylate terminated rotaxane linkers. The rotaxane linkers contain a single Cu^{I} metal ion which is coordinated in a distorted

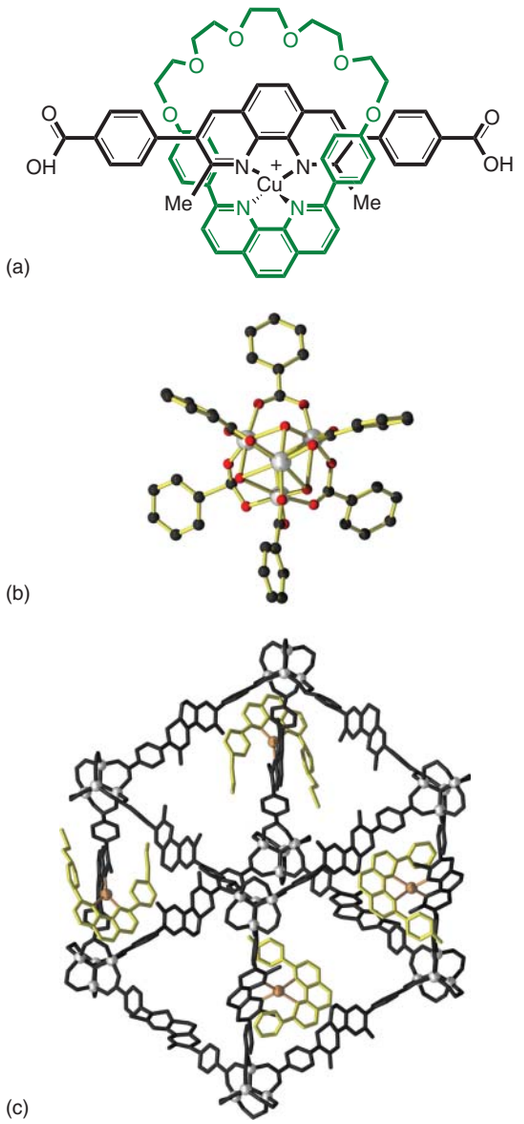


Figure 14 (a) [2]Pseudorotaxane linker [Cu(**11**⊂**PM**)]$^{+}$ used to form **PRF-22**; (b) coordination environment of the Zn_4O cluster in **PRF-22**; (c) X-ray structure of the primitive cubic, three-periodic framework of **PRF-22**; (**PM** macrocycles only shown in one direction of the primitive cube for clarity)

tetrahedral geometry to the 1,10-phenanthroline unit of the axle and a phenanthroline unit in the 30-membered **PM** macrocycle. Each Zn^{II} center is part of a Zn_4O cluster (Figure 14b) which forms a six-connected node resulting in a framework with *pcu* topology and an average Zn···Zn distance of 25.3 Å (Figure 14c). The resulting framework suffers from threefold interpenetration with the remaining voids filled with disordered PF_6 anions and DEF solvent molecules. Post synthetic modification was performed by exposing **PRF-22** to an oxone solution in CH_3CN at room temperature which resulted in oxidation of an unknown amount of Cu^{I} ions to Cu^{II}; this was confirmed qualitatively by EPR spectroscopy. The Cu^{I} ions within the rotaxane linkers which are oxidized to Cu^{II} were described as local electronic switches which alter the coordination geometry of the copper ions inside **PRF-22** by presumably shrinking and flattening of the coordination sphere. In addition, exposing **PRF-22** to KCN in MeOH resulted in 60% demetalation of the material with the remaining Cu^{I} being inaccessible in this highly interpenetrated framework. The degree of demetalation of **PRF-22** was confirmed by inductively coupled plasma mass spectrometry (ICP-MS) by quantifying the amount of Cu^{I} within the framework before and after treatment. Following the oxidation and demetalation experiments, **PRF-22** was shown to retain its crystallinity by PXRD. If this approach could be transferred to the bistable molecular switches developed by Sauvage *et al.* in which the transformation between Cu^{I} to Cu^{II} resulted in a reorientation of the macrocyclic wheel, this might be a viable methodology for incorporation of redox active molecular switches inside metal organic frameworks.

6 POLYROTAXANE FRAMEWORK CONTAINING WHEELS WITH DONOR GROUPS

All the examples of PRFs described to this point have taken advantage of the complexation of a linear, coordinating axle, and a macrocycle to form a [2]pseudorotaxane linker. While this strategy has led to numerous PRFs, it is not, however, the only option. Loeb and coworkers used a permanently interlocked [2]rotaxane with the ligand donors appended to the macrocyclic component rather than the axle to form a different style of PRF.

Reacting equal molar amounts of the [2]rotaxane linker $\mathbf{12}^{2+}$ with $Cd(BF_4)\cdot(H_2O)_6$ in MeCN, followed by vapor diffusion of *iso*-propyl ether into the reaction mixture produced yellow crystals of **PRF-23** with formula $[Cd_2Cl_4(H_2O)_4(\mathbf{12})][BF_4]_2\cdot(MeNO_2)_8$.[43] **PRF-23** crystallizes in the monoclinic space group $P2_1/c$ and forms a two-periodic framework consisting of binuclear Cd^{II} nodes $[(H_2O)_2Cd(\mu\text{-}Cl)_2Cd(H_2O)_2]$ and $\mathbf{12}^{2+}$ rotaxane linkers (Figure 15a). Each Cd^{II} center adopts an octahedral geometry in which the equatorial positions are occupied by two bridging Cl ions and two coordinated H_2O molecules while the axial positions are filled by 3-pyridyl donors from macrocycles of different rotaxane linkers (Figure 15b). The closest Cd···Cd distance within each node is 3.73 Å with a distance of 17.0 Å between metal nodes. The four 3-pyridyl appendages of a single macrocycle are coordinated to four different Cd^{II} ions to generate a two-periodic framework with the cavities of the crown ethers filled by independent and interlocked axles

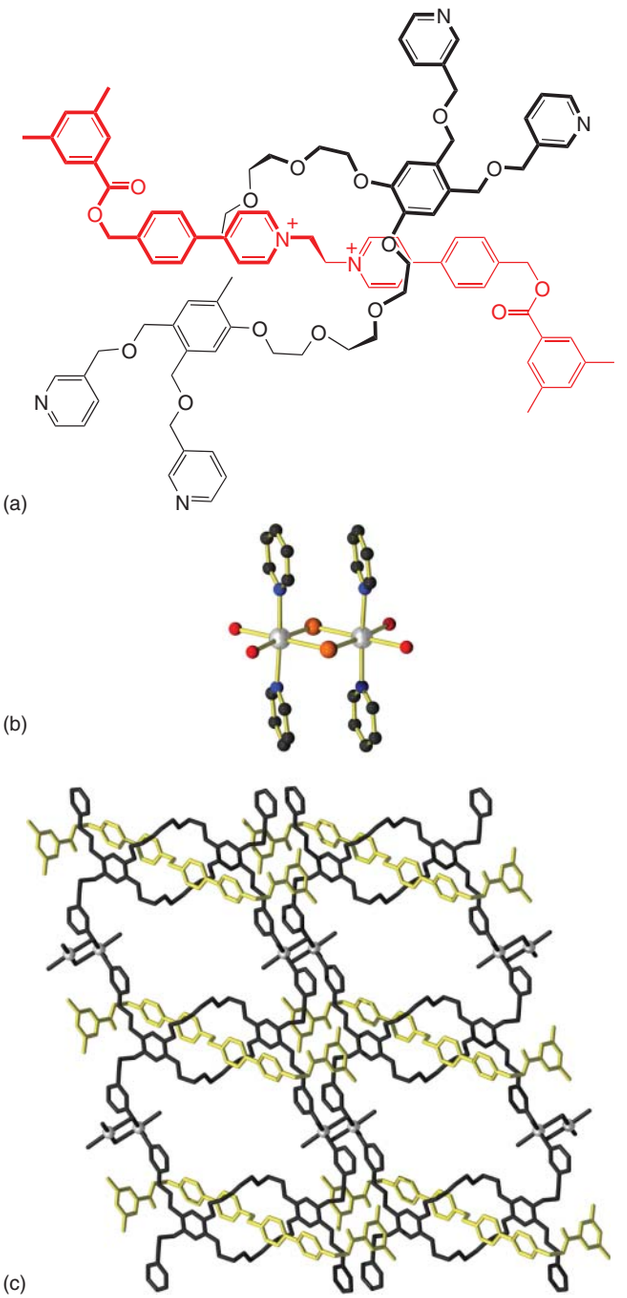


Figure 15 (a) [2]Rotaxane linker $\mathbf{12}^{2+}$ used to form **PRF-23**; (b) coordination environment of binuclear Cd^{II} nodes in **PRF-23**; (c) X-ray structure of the two-periodic framework of **PRF-23**

(Figure 15c). Remaining void space in **PRF-23** is filled by two BF_4 counterions and eight molecules of $MeNO_2$ per asymmetric unit.

Extending this new approach for constructing PRFs, Loeb and coworkers recently synthesized a permanently interlocked [2]rotaxane linker which contained coordinating groups on *both* the macrocyclic wheel and the terminal ends of the axle. The addition of thioether donors to the macrocycle as well as the terminal positions of the axle allowed for the formation of an interlocked hexadentate rotaxane linker $\mathbf{13}^{2+}$ (Figure 16a). Addition of linker $\mathbf{13}^{2+}$ to an MeCN solution of AgOTf resulted

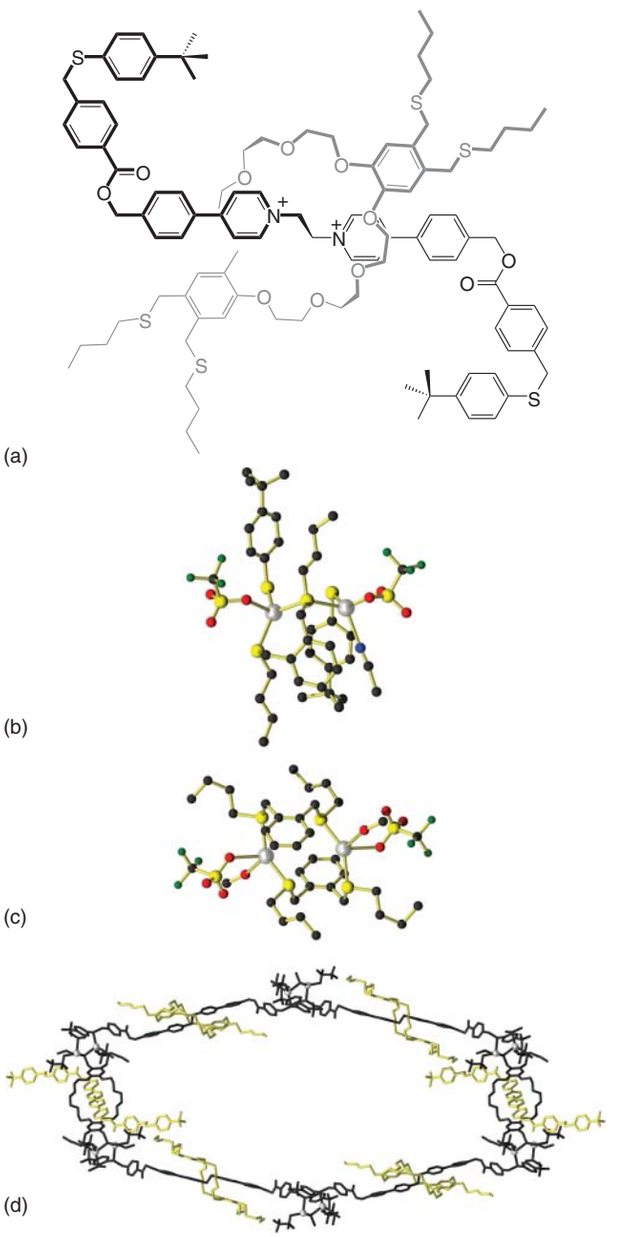


Figure 16 (a) [2]Rotaxane linker $\mathbf{13}^{2+}$ used to form **PRF-24**; (b) coordination environment of two unique Ag^{I} ions in a binuclear cluster used to form the distorted hexagonal net in **PRF-24**; (c) coordination environment of a binuclear Ag^{I} cluster; (d) X-ray structure of the distorted hexagonal forms within the interwoven framework of **PRF-24**

in the formation of crystals of **PRF-24**, with formula, $[Ag_6(\mathbf{13})_2(OTf)_6(MeCN)_2(MeOH)_2][OTf]_4\cdot(CH_3CN)_4$.[44] **PRF-24** crystallized in the monoclinic space group $P2_1/c$ and is the first example of a new type of lattice which contains *interwoven* frameworks resulting from interpenetration of frameworks due to the presence of an interlocked ligand in addition to traditional interpenetration of independent framework lattices. Two types of metal–ligand clusters exist within the structure; the first forms a node which links two axles and a single macrocycle together via thioether groups to form a hexagonal framework (Figure 16b). The metal–ligand cluster consists of two unique Ag ions. One adopts a distorted tetrahedral geometry bound to three thioether groups and a single OTf anion, while the other adopts a tetrahedral geometry bound to two thioether groups, a single OTf anion and a single MeCN molecule. The second metal-ligand cluster joins two macrocycles together to form one-periodic chain linking the hexagonal nets and consists of two identical Ag^I ions which adopt a tetrahedral geometry bound to two thioether groups from the macrocycle, a single OTf anion and a single MeOH molecule (Figure 16c). The overall topology of **PRF-24** can be described as hexagonal nets (Figure 16d) which are threaded through orthogonal hexagonal nets via their interlocked linkers as well as traditional interpenetration by independent nets. In addition, the *interwoven* nets are also knitted together by one-periodic chain made of linked macrocyclic components. Remaining void space in **PRF-24** is filled with OTf anions and MeCN solvent molecules.

PRF-23 and **PRF-24** demonstrate a novel way to create PRFs by using permanently interlocked rotaxanes which are connected by a mechanical linkage and not merely held together by relatively weak non-covalent interactions prior to PRF synthesis. This synthetic approach allows for the use of harsher reaction conditions since the linker cannot simply unthread when exposed to competitive solvation during PRF formation.

7 POLYROTAXANE FRAMEWORKS THAT DEMONSTRATE ROTATIONAL DYNAMICS IN THE SOLID-STATE

Even though **PRF-1** through **PRF-24** demonstrated numerous ways to incorporate rotaxanes into attractive one-, two-, and three-periodic structures, none of these materials demonstrated any actual dynamics related to large amplitude motion of the interlocked macrocycle. The demonstration of dynamic motion of the wheel component in the solid-state is crucial to the future development of molecular switches inside these materials and ultimately the ability of the material to function as a molecular machine. With this goal in mind, Loeb and coworkers offered a set of guidelines that might improve the chances of observing dynamics in future PRFs.

1. The combination of metal nodes and MIM linkers should result in a neutral, three-periodic, non-interpenetrated framework.
2. The MIM linker should be permanently interlocked.
3. The non-covalent interactions used to template MIM formation should be easily removed.
4. The MIM framework should be compact and rigid.
5. The system should be designed with a probe for verifying dynamics.

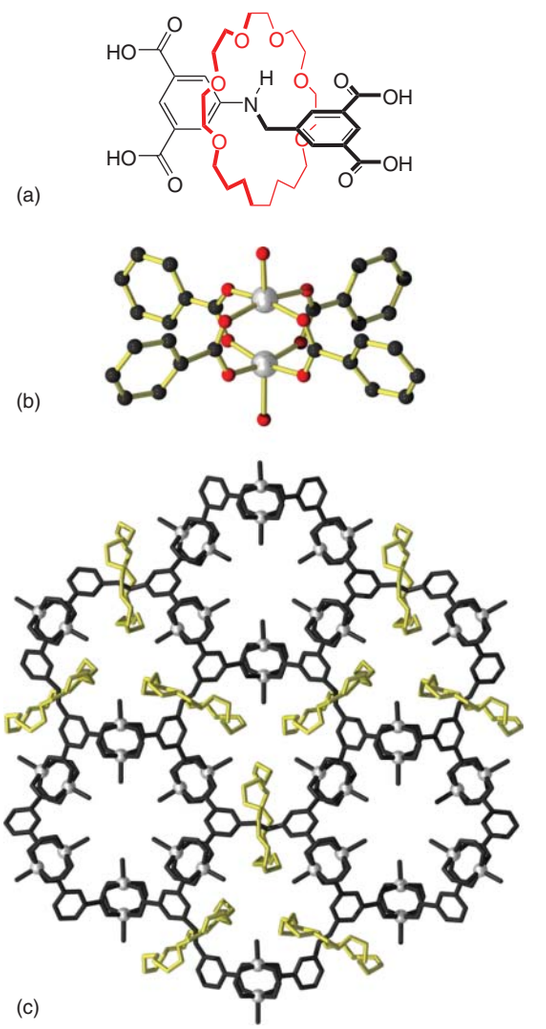


Figure 17 (a) [2]Rotaxane linker **14** used to form **PRF-25** (**UWDM-1**); (b) coordination environment of Cu^{II} paddlewheel cluster in **PRF-25**; (c) X-ray structure of the hexagonal channels within **PRF-25**

Following the above guidelines, Loeb and coworkers designed a neutral, aniline-based, permanently interlocked [2]rotaxane linker **14** (Figure 17a). This system utilized a charged anilinium axle to template the ring-closing metathesis reaction of a 24-membered crown ether macrocycle. Following [2]rotaxane formation, the anilinium could be easily neutralized to leave only a single NH···O interaction between the axle and macrocycle, thus removing the original template. Linker **14** was combined with 2 equivalents of $Cu(NO_3)_2{\cdot}3H_2O$ in a 3:2:2 mixture of DMF/EtOH/H_2O and heated to 65 °C for 48 h followed by slow cooling to room temperature to yield green crystals of **PRF-25** (published as **UWDM-1)** with formula $[Cu_2(\mathbf{14})(H_2O)_2]{\cdot}(H_2O)_3$.[20] **PRF-25** crystallized in the rhombohedral space group $R\bar{3}$ and adopts a rare β-phase of *nbo* topology. Each Cu center is involved in a binuclear paddlewheel unit bound by four carboxylate ligands and two axial H_2O molecules (Figure 17b). The overall structure consists of linked polyhedra composed of six paddlewheel units which result in hexagonal shaped channels in the material (Figure 17c). The majority of space in the channels is occupied by the macrocyclic component, with the remaining voids occupied by three H_2O molecules per asymmetric unit. The material was shown to be stable up to 250 °C by TGA and VT-PXRD measurements. Activation of the material resulted in removal of the

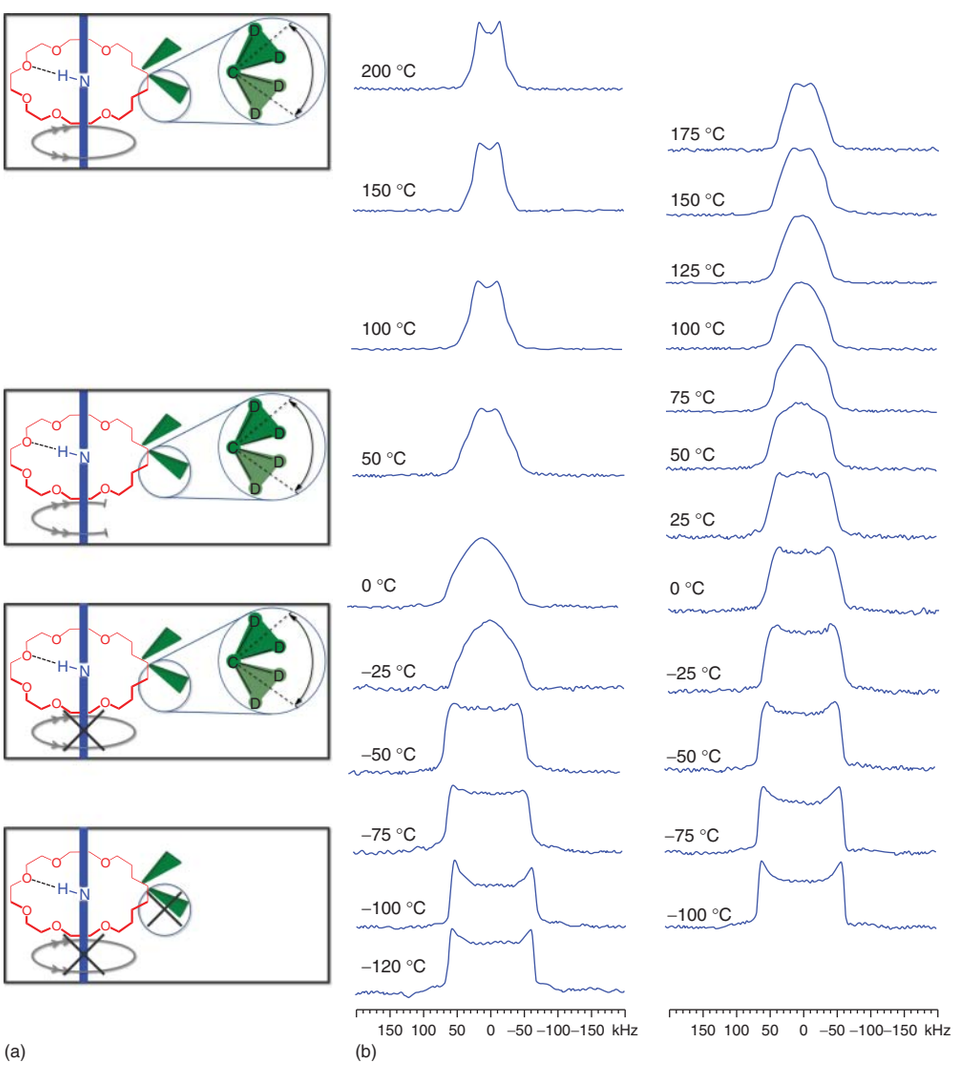


Figure 18 (a) Variable temperature ^{2}H SSNMR spectra of **PRF-25**$_{(24C6)}$ and depictions of various modes of motion for the macrocyclic ring; (from low to high) no motion that averages the ^{2}H quadrupolar interactions, conformational pseudo-axial/pseudo-equatorial interconversions, additional partial rotation of the ring, full rotation of the ring. (b) Variable temperature ^{2}H SSNMR spectra of **PRF-25**$_{(22C6)}$ depicting similar motions at correspondingly higher temperatures

H_2O molecules from both the channels and the Cu paddle-wheel units, thus providing the free space required for the macrocycle to be able to undergo motion unimpeded by neighboring molecular components within the framework.

In order to identify the dynamic nature of the macrocyclic component inside **PRF-25** a ^2H label was placed on the macrocycle and monitored by ^2H SSNMR spectroscopy. The VT-SSNMR spectra clearly indicated that a dense array of soft **24C6** macrocycles were able to rapidly rotate while mechanically linked to the rigid, three-periodic framework of **PRF-25** (Figure 18a). The motion was shown to be thermally driven and the rate of rotation of the macrocyclic component was estimated to be >10 MHz at temperatures >150 °C. This motion was shown to be completely reversible as cooling of the material caused reabsorption of H_2O molecules and halted the free rotation. **PRF-25** was the first known MOF material to show dynamic behavior of an interlocked component in the solid-state.

Following the success of **PRF-25**, Loeb and coworkers extended this series by utilizing the same axle with differently sized macrocycles, **22C6** and **B24C6**, to give isomorphous materials **PRF-25**$_{(22C6)}$ and **PRF-25**$_{(B24C6)}$. The dynamics of these two new MOFs proved to be different from the initial prototype **PRF-25**$_{(24C6)}$. When the 22-membered ring was utilized, higher temperatures were required to allow the smaller, tighter ring to display the same ^2H pattern of dynamics as the 24-membered ring (Figure 18b). Furthermore when the **B24C6** ring was utilized, ^2H SSNMR experiments showed the ring did not undergo free rotation of the substituted macrocyclic ring even at high temperatures. This result infers that the additional aromatic group of **B24C6** prevents rotation of the macrocycle by sterically locking the ring within the structure of the MOF framework. It should be noted that when the free aniline axle was used as the linker with no macrocycle the *NbO* structure of **PRF-25** was not formed; a structure with linked Cu_{24} nanoballs resulted instead. This was attributed to the increased flexibility of the axle when not encircled by the macrocycle.

8 SUMMARY AND LOOK FORWARD

The linkers and X-ray structures described in this chapter are beautiful examples of how researchers have approached the concept of organizing MIMs into the frameworks of crystalline solid-state materials. Recent examples, such as Loeb's **UWDM-1** series (**PRF-25**), demonstrate that, in principle, it should be possible to fabricate stable MOFs comprising components capable of large amplitude motion. It may then be possible to manipulate these components post-synthetically via some external perturbation similar to solution MIM systems, thus transferring the chemistry of interlocked molecular switches and machines into solid-state materials.

9 RELATED ARTICLES

Recent Solid-State NMR Studies of Quadrupolar Nuclei in Metal-Organic Frameworks; Single-Crystal to Single-Crystal Transformations in Metal-Organic Frameworks; Interpenetration and Entanglement in Coordination Polymers.

10 ABBREVIATIONS AND ACRONYMS

ICP-MS = inductively coupled plasma mass spectrometry; MIM = mechanically interlocked molecule; MOF = metal organic framework; MORF = metal-organic rotaxane framework; PRF = polyrotaxane framework; RCP = rotaxane coordination polymer; TCPP = *tetra*(4-carboxy)-phenyl-porphyrin; TGA = thermogravimetric analysis.

11 REFERENCES

1. H. Furukawa, K. E. Cordova, M. O'Keeffe, and O. M. Yaghi, *Science*, 2013, **341**, 974.
2. M. Eddaoudi, J. Kim, N. Rosi, D. Vodak, J. Wachter, M. O'Keeffe, and O. M. Yaghi, *Science*, 2002, **295**, 469.
3. S. Horike, S. Shimomura, and S. Kitagawa, *Nat. Chem.*, 2009, **1**, 695.
4. G. Ferey, C. Mellot-Draznieks, C. Serre, F. Millange, J. Dutour, S. Surble, and I. Margiolaki, *Science*, 2005, **309**, 2040.
5. C. E. Wilmer, M. Leaf, C. Y. Lee, O. K. Farha, B. G. Hauser, J. T. Hupp, and R. Q. Snurr, *Nat. Chem.*, 2012, **4**, 83.
6. J. Li, J. Yu, W. Lu, L. Sun, J. Sculley, P. B. Balbuena, and H. C. Zhou, *Nat. Commun.*, 2013, **4**, 1538.
7. E. D. Bloch, W. L. Queen, R. Krishna, J. M. Zadrozny, C. M. Brown, and J. R. Long, *Science*, 2012, **335**, 1606.
8. J. F. Stoddart, *Chem. Soc. Rev.*, 2009, **38**, 1802.
9. J. E. Beves, B. A. Blight, C. J. Campbell, D. A. Leigh, and R. T. McBurney, *Angew. Chem. Int. Ed.*, 2011, **50**, 9260.
10. J. F. Ayme, J. E. Beves, C. J. Campbell, and D. A. Leigh, *Chem. Soc. Rev.*, 2013, **42**, 1700.
11. V. Balzani, A. Credi, and M. Venturi, 'Devices and Machines: Concepts and Perspectives for the NanoWorld', Wiley-VCH, Weinheim, 2008.

12. R. S. Forgan, J. P. Sauvage, and J. F. Stoddart, *Chem. Rev.*, 2011, **111**, 5434.
13. B. Zheng, F. Wang, S. Dong, and F. Huang, *Chem. Soc. Rev.*, 2012, **41**, 1621.
14. A. Coskun, M. Banaszak, R. D. Astumian, J. F. Stoddart, and B. A. Grzybowski, *Chem. Soc. Rev.*, 2012, **41**, 19.
15. E. K. Kay, D. A. Leigh, and F. Zerbetto, *Angew. Chem. Int. Ed.*, 2007, **46**, 72.
16. V. Balzani, M. Gomez-Lopez, and J. F. Stoddart, *Acc. Chem. Res.*, 1998, **31**, 405.
17. A. C. Schalley, K. Beizai, and F. Vögtle, *Acc. Chem. Res.*, 2001, **34**, 465.
18. D. Nishimura, T. Oshikiri, Y. Takashima, A. Hashidzume, H. Yamaguchi, and A. Harada, *J. Org. Chem.*, 2008, **73**, 2496.
19. S. C. Vogelsberg and M. A. Garcia-Garibay, *Chem. Soc. Rev.*, 2012, **41**, 1892.
20. V. N. Vukotic, K. J. Harris, K. Zhu, R. W. Schurko, and S. J. Loeb, *Nat. Chem.*, 2012, **4**, 456.
21. V. N. Vukotic and S. J. Loeb, *Chem. Soc. Rev.*, 2012, **41**, 5896.
22. K. Kim, *Chem. Soc. Rev.*, 2002, **31**, 96.
23. S. J. Loeb, *Chem. Soc. Rev.*, 2007, **36**, 226.
24. X. H. Deng, A. M. Olson, J. F. Stoddart, and O. M. Yaghi, *Nat. Chem.*, 2010, **2**, 439.
25. S. J. Loeb, *Chem. Commun.*, 2005, 1511.
26. D. Whang and K. Kim, *J. Am. Chem. Soc.*, 1997, **119**, 451.
27. K. Park, D. Whang, E. Lee, J. Heo, and K. Kim, *Chem. Eur. J.*, 2002, **8**, 498.
28. D. Whang, J. Heo, C. Kim, and K. Kim, *Chem. Commun.*, 1997, 2361.
29. E. Lee, J. Heo, and K. Kim, *Angew. Chem. Int. Ed.*, 2000, **39**, 2699.
30. J. Liang, X. Wang, Y. Jiao, C. Qin, K. Shao, Z. Su, and Q. Wu, *Chem. Commun.*, 2013, **49**, 8555.
31. G. J. E. Davidson and S. J. Loeb, *Angew. Chem. Int. Ed.*, 2003, **42**, 74.
32. Y. Diskin-Posner, G. K. Patra, and I. Goldberg, *Eur. J. Inorg. Chem.*, 2001, 2515.
33. D. J. Mercer, J. Yacoub, S. K. Loeb, K. Zhu, and S. J. Loeb, *Org. Biomol. Chem.*, 2012, **10**, 6094.
34. D. J. Hoffart and S. J. Loeb, *Supramol. Chem.*, 2007, **19**, 89.
35. D. J. Hoffart and S. J. Loeb, *Angew. Chem. Int. Ed.*, 2005, **44**, 901.
36. L. K. Knight, V. N. Vukotic, E. Viljoen, C. B. Caputo, and S. J. Loeb, *Chem. Commun.*, 2009, 5585.
37. V. N. Vukotic and S. J. Loeb, *Chem. Eur. J.*, 2010, **16**, 13630.
38. H. Gong, B. M. Rambo, E. Karnas, V. M. Lynch, and J. L. Sessler, *Nat. Chem.*, 2010, **2**, 406.
39. H. Gong, B. M. Rambo, E. Karnas, V. M. Lynch, K. M. Keller, and J. L. Sessler, *J. Am. Chem. Soc.*, 2011, **133**, 1526.
40. H. Gong, B. M. Rambo, W. Cho, V. M. Lynch, M. Oh, and J. L. Sessler, *Chem. Commun.*, 2011, **47**, 5973.
41. H. Gong, B. M. Rambo, C. A. Nelson, V. M. Lynch, X. Zhu, and J. L. Sessler, *Chem. Commun.*, 2012, **48**, 10186.
42. A. Coskun, M. Hmadeh, G. Barin, F. Gándara, Q. Li, E. Choi, N. L. Strutt, D. B. Cordes, A. M. Z. Slawin, J. F. Stoddart, J. P. Sauvage, and O. M. Yaghi, *Angew. Chem.*, 2012, **124**, 2202.
43. D. J. Mercer, V. N. Vukotic, and S. J. Loeb, *Chem. Commun.*, 2011, **47**, 896.
44. N. C. Frank, D. J. Mercer, and S. J. Loeb, *Chem. Eur. J.*, 2013, **19**, 14076.

Photoreactive Metal-Organic Frameworks

Anjana Chanthapally and Jagadese J. Vittal

National University of Singapore, Singapore

1	Introduction	135
2	Formation of 1D CPs from Metal Complexes by [2+2] Cycloaddition Reactions	136
3	Photoreactive Ladder Polymers	137
4	Photoreactivity of 1D CPs Yielding 2D Structures	143
5	Photoreactivity of 1D CPs Yielding 3D Structures	145
6	Photoreactivity in 2D CPs	145
7	Photoreactive 3D CPs	150
8	Photoresponsive MOFs	153
9	Photo-Polymerization in CPs	154
10	Summary	155
11	Acknowledgments	155
12	Related Articles	155
13	Abbreviations and Acronyms	156
14	References	156

1 INTRODUCTION

For the past several decades, solid-state [2+2] cycloaddition reaction has been extensively studied.[1–11] The pioneering work of Schmidt and coworkers was mostly responsible for the birth of solid-state organic photochemistry as well as crystal engineering.[12–14] In the past decades, a number of photoreactive coordination polymers (CPs) and metal-organic frameworks (MOFs) have also been made by bringing the olefin bonds present in the spacer and terminal ligands closer in parallel to undergo photo-dimerization reactions.[15–17] The strength and directionality of the metal-coordination bond and the bridging nature of certain anions play prominent roles to direct the C=C bonds in the organic linkers, terminal ligands and/or guest molecules to satisfy the geometric criteria required for the cycloaddition reactions. Since the crystallization process is often controlled by the kinetic factors, it has been a challenge to obtain the desired photoreactive solids experimentally.[18–20] Apart from making photoreactive CPs and MOFs, this property has been recently engaged to control the pore size, surface area and functionalization for controlled guest release and sensing. A brief historical perspective of the photochemical dimerization reaction is provided in the next section.

1.1 Historic Background on the Solid-State [2+2] Cycloaddition Reaction

Crystallographic state and environmental factors influence the reactivity of the organic solids, than the intrinsic reactivity of the molecule. For example, *trans*-Cinnamic acid that merely isomerizes in solution, was found to dimerize in solid state, as early as 1889 by Leibermann.[21]

Schmidt and coworkers have extensively investigated the [2+2] cycloaddition reactions of different polymorphs that laid foundations for solid-state organic photochemistry as well as crystal engineering.[5] The photochemical reactivities of different polymorphic forms of organic solids containing C=C bonds have been found to form distinct products. For example, cinnamic acid was found to crystallize in three polymorphic forms and in all three, the olefins are packed as linear stacks and they

Metal-Organic Framework Materials. Edited by Leonard R. MacGillivray and Charles M. Lukehart.
© 2014 John Wiley & Sons, Ltd. ISBN 978-1-119-95289-3

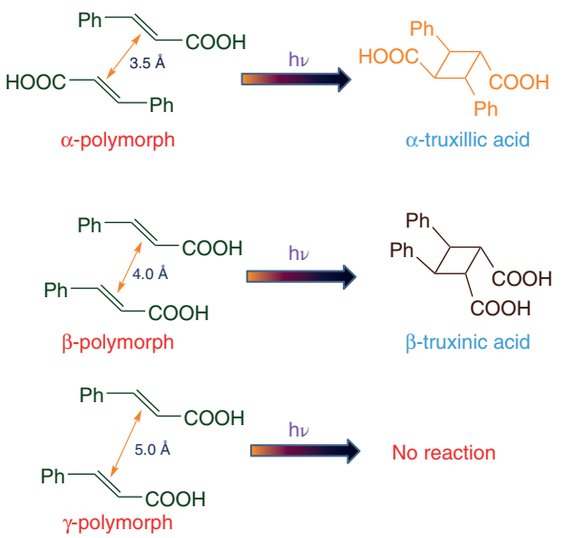


Figure 1 The reactivity of three polymorphic forms of cinnamic acids

differ in the repeat distance and symmetry of the packing as shown in Figure 1.[13]

A *head-to-tail* (HT) centro-symmetric relation was found between the monomers in the α-type polymorph that yields truxilic acid dimer. Whereas the β-type polymorph crystallizes with mirror symmetry, a *head-to-head* (HH) relation between the monomer molecules and on irradiation yields truxinic acid dimer. On the other hand, in the third γ-form the repeat distance >4.2 Å was found to be photostable. Schmidt postulated that the olefins should be aligned parallel with a distance <4.2 Å between the olefinic bond pairs and the reaction should take place with minimum atomic movement. The maximum distance criterion proposed in Schmidt's postulate may be related to maximum distance for interaction between the p_z orbital clouds that can be slightly larger than the sum of van der Waal's radii.[22,23]

This minimum movement of atoms or molecules in the solid state leading to the reaction is known as topochemical reaction.[24,25] Since the structure of the product is correlated with the geometry of the reactant solid in the crystal lattice, the stereochemistry of the product obtained in a solid state reaction is, in general, predictable. Most of the photodimerization reactions reported in the literature were found to follow these topochemical postulates of Schmidt.[4,6,12,15,21,26–28]

We intend to cover the following in this chapter. How the olefin pairs in the spacer and terminal ligands as well as guest molecules could be aligned for photochemical [2+2] cycloaddition reactions. In this process, two new σ-bonds are formed between the carbon atoms to yield cyclobutane rings during the photochemical reactions. This organic reaction has been responsible for a number of solid-state structural transformations owing to the change in the connectivity, dimensionality, and interpenetration. Thus, the sections are presented based on the dimensionality changes brought by the formation of cyclobutane rings from the reactive olefin pairs. Further, the changes in the physical and chemical properties accompanying the structural transformations are also discussed. In addition to the solid-state [2+2] cycloaddition reactions, other photochemical reactions such as *trans*-to-*cis* isomerization of azobenzenes, polymerizations, isomerizations and photodissociation reactions have also been presented in this chapter. Although a few classical works in this area have been covered for the sake of completeness, emphasis is given to the recent literature. This chapter is not intended to be comprehensive and hence any omission of literature was not intentional.

2 FORMATION OF 1D CPS FROM METAL COMPLEXES BY [2+2] CYCLOADDITION REACTIONS

2.1 Formation of 1D CP Through Ag···C Interactions

The intermolecular Ag···C bond formed during the [2+2] cycloaddition reaction between a discrete dinuclear Ag(I) complex $[Ag_2(4\text{-spy})_4(O_2CCF_3)_2]$ (**1**) is responsible for the formation of an interesting one-dimensional (1D) CP.[29] In **1** two $[Ag(4\text{-spy})_2(O_2CCF_3)]$ molecules are brought close together through Ag···Ag interactions and the resultant dimer has been stabilized by π···π contacts between the pyridyl groups. Although crisscrossed, the double bonds of the adjacent 4-spy ligands in the dimer are separated by 4.02 Å. On irradiation of ultraviolet (UV) light, the complex undergoes pedal motion forming the HH dimer product with *rctt* stereoisomer in the dimetallic complex $[Ag_2(4\text{-pyr-ph-cb})_2][(CO_2CF_3)_2]$ (**2**) where 4-pyr-ph-cb = *rctt*-1,2-bis(4-pyridyl)-3,4-bis(phenyl)cyclobutane. The argentophilic interaction in the product is lost, instead intermolecular Ag···C interactions connects the dimer complexes to form a 1D chain as shown in Figure 2.

2.2 Formation of 1D CP by the [2+2] Cycloaddition Reaction of a Dinuclear Zn(II) Complex

Chloro derivative of 4-spy (Cl-spy) was found to result in a chlorate bridged tetrahedral Ag(I) in $[Ag_2(Cl\text{-spy})_4(ClO_3)_2]$ (**3**) with four terminal Cl-spy ligands as shown below. Interestingly, the intermolecular packing brought 50% of the Cl-spy ligands to align in a HT manner with the neighboring Cl-spy ligands such that the C=C

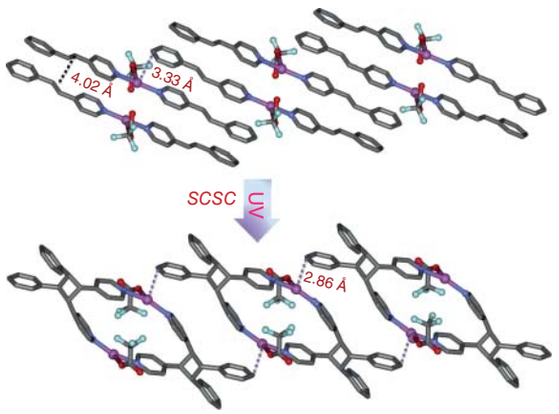


Figure 2 A view showing the transformation of discrete **1** to 1D CP, **2** owing to the formation of Ag···C interactions

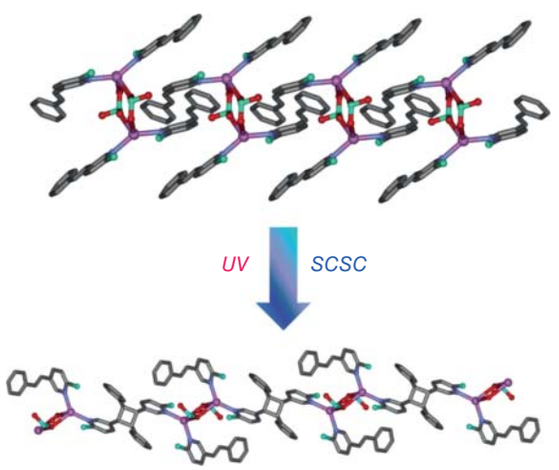


Figure 3 A perspective view showing the polymerization of **3** to a 1D CP through [2+2] cycloaddition reaction

bond pairs are separated by 3.77 Å, leaving the other terminal ligand photostable (Figure 3). UV irradiation of **3** resulted in a 1D CP in a single-crystal to single-crystal (SCSC) manner.[30]

2.3 1D CP from Photoreactive Hydrogen-Bonded Zwitter Ionic Metal Complexes

The utility of two photoreactive 1D hydrogen-bonded aggregates of metal complexes in the formation of 1D CPs are described here.[23–25]

The zwitter ionic Pb(II) complex [Pb(bpe-H)$_2$(TFA)$_4$] **(4)** (where TFA = trifluoroacetate anion) comprises [Pb(TFA)$_4$]$^{2-}$ anion and two bpe-H$^+$ cations. The coordinated monoprotonated bpe-H$^+$ cations and the neighboring oxygen atoms of the TFA ligands have complementary hydrogen bonds resulting in an infinitely organized 1D hydrogen-bonded aggregate in which pairs of bpe-H$^+$ cations are well-aligned in an HT manner as shown in Figure 4. These coordinated bpe-H$^+$ pairs undergo [2+2] cycloaddition reaction under UV light quantitatively to give the anticipated *rctt*-tpcb isomer.[31,32] In this process, the colorless block-like crystals turned into gel in 1–15 h and became powder after 25 h of exposure to UV light. Proton transfer occurs from bpe-H$^+$ to TFA anion with the elimination of two CF_3CO_2H during photodimerization yielding the expected 1D CP [Pb(*rctt*-tpcb)(TFA)$_2$] (**5**) (*rctt*-tpcb = regio *cis*, *trans*, *trans*-*tetrakis*(4-pyridyl)cyclobutane). The structure of the photo-product was determined after recrystallizing from methanol. The connectivity of the crystallized [Pb(*rctt*-tpcb)(TFA)$_2$] is slightly different from the expected structure owing to the reorganization of structures during crystallization.[31]

In another similar zwitter ionic Cd(II) complex, [Cd(bpe-H)$_2$(H_2O)(S_2O_3)$_2$] (**6**), two protonated [bpe-H]$^+$ ligands are bonded to Cd(II) in *trans*-manner.[33] The protons in the mono coordinated bpe-H$^+$ cations are hydrogen bonded to the neighboring thiosulfate oxygen atoms to form a hydrogen bonded 1D polymer. The C=C bonds in the well-aligned bpe-H$^+$ ligand pairs are separated by 3.72 Å. This compound showed quantitative [2+2] photocycloaddition as followed by ^{1}H-NMR (nuclear magnetic resonance) studies. As this is not an SCSC reaction, the proposed structure of the 1D CP is shown as depicted in the Figure 5.

3 PHOTOREACTIVE LADDER POLYMERS

Among the 1D CPs, only the ladder polymers can be designed to undergo [2+2] cycloaddition reaction within the structures. Either the poles or the rungs of the ladder can be manipulated for this purpose. The C=C bond containing spacer ligands can be utilized as poles in the ladders and can be brought closer in parallel by the judicious choice of the metal ions and the bridging anions. In some cases, argentophilic interaction has also been utilized without the need of bridging anions to bring two linear CPs and hence the C=C pairs. The bpe ligand is ideal for this purpose and thus, it has been studied extensively. Structural transformation of a ladder CP in general will yield another 1D ladder CP by [2+2] cycloaddition reaction, if the cyclobutane ring is formed within the ladder structure. A few such examples are illustrated below.

3.1 Carboxylate Bridged Ladder CPs

A simple photoreactive ladder CP [{(H_3CCO_2)(μ-O_2CCH_3)Zn}$_2$(μ-bpe)$_2$] (**7**) has two linear Zn(bpe) strands

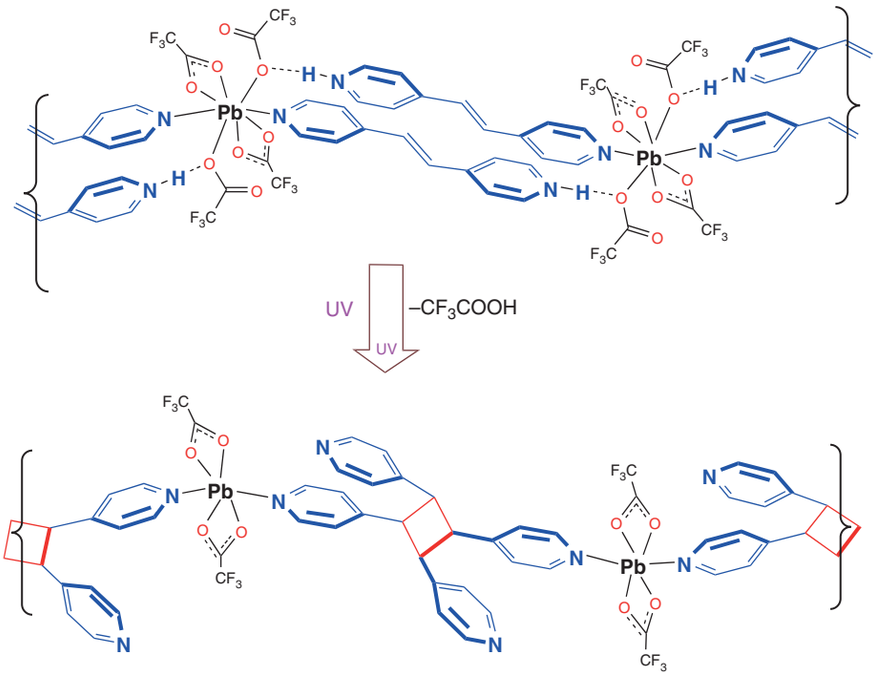


Figure 4 A zigzag hydrogen-bonded zwitter ionic Pb(II) complex, **4** undergoes polymerization reaction under UV light

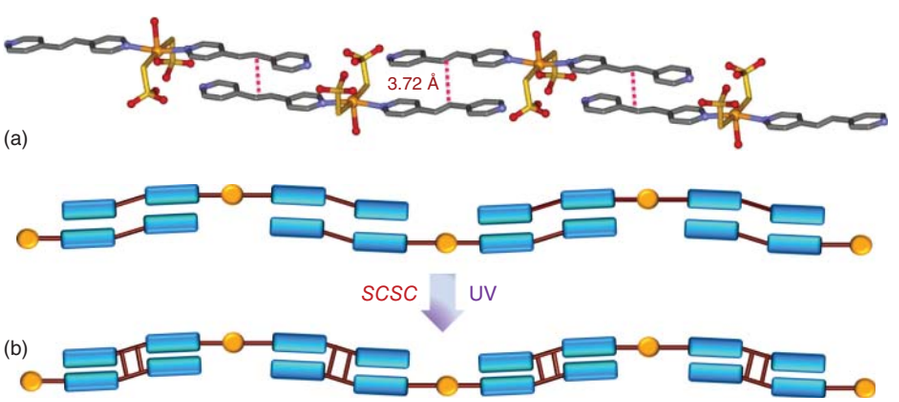


Figure 5 A view showing the packing of **6** in the solid (a) and a schematic diagram depicting the polymerization of a Cd(II) complex, **6** to a 1D CP by [2+2] cycloaddition reaction (b)

bridged by two acetate ligands. The distorted octahedral coordination geometry on each Zn(II) atom is completed by chelation of another OAc ligand. The bridging OAc ligands that control the distance between the linear Zn(bpe) strands are responsible for the photoreactivity. The distance between the well-aligned C=C bond pairs of the bpe ligands in the ladder is 3.66 Å. Quantitative conversion of the C=C bonds into cyclobutane rings under UV light has been confirmed from the ^{1}H-NMR data implying the formation of another 1D CP, but the single crystals were not preserved in the photoproduct to confirm its structure. On the contrary, [{(TFA)(μ-O_2CCH_3)Zn}$_2$(μ-bpe)$_2$] (**8**) has half of the OAc groups replaced by TFA anions and the single crystals were intact at the end of the UV experiment. The structure of the product was confirmed to be [{(TFA)(μ-O_2CCH_3)Zn}$_2$(*rctt*-tpcb)] **(9)** by single crystal X-ray crystallography (Figure 6). It appears that the fluorine atoms might have assisted to withstand the strain in the single crystals during the structural transformation.[34] These ladder polymers have also been obtained from

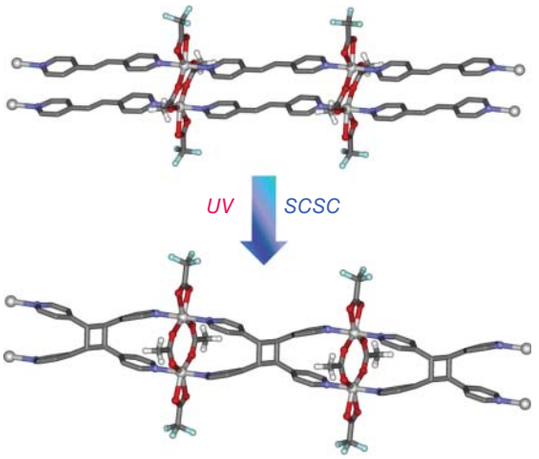


Figure 6 1D to 1D′ structural transformation in ladder structures

mechanochemical synthesis by grinding the stoichiometric ratios of reactants in the solid state.[35]

The benzoate anions can also be used as bridging ligands to bring a pair of [M(bpe)] (M = Cd(II) and Pb(II)) linear strands to make photoreactive ladder polymers.[36] For example, the Cd(II) 1D CP, $[Cd_2(\mu\text{-bpe})_2(\mu\text{-}O_2C\text{-}C_6H_4\text{-}p\text{-}Cl)_2(O_2C\text{-}C_6H_4\text{-}p\text{-}Cl)_2]$ (**10**) has been synthesized using *p*-chlorobenzoate as the clipping agent. In this case the [2+2] cycloaddition reaction was accompanied by SCSC structural transformation.[37] Of the various photoreactive Pb(II) ladder polymers with different benzoate ligands attempted, $[Pb_2(\mu\text{-bpe})_2(\mu\text{-}O_2C\text{-Ar})_2(O_2C\text{-Ar})_2]$ (**11**) (Ar = benzoate, 2-, 3-, and 4-methyl benzoates), the compound with 3-methylbenzoate ligand underwent SCSC transformation under UV light.[36] Hence, OAc and benzoate ligands have been proven to be effective bridging ligands to make photoreactive ladder polymers.

3.2 Metal Templated Photoreactive Ladder CPs

In the dinuclear Zn(II) complexes of a Schiff base ligand, the distance between the Zn(II) atoms are fixed at 3.1 Å. The donor atoms of the Schiff base ligand occupy all the equatorial positions of the two Zn(II) atoms leaving the axial positions available for the linear spacer ligands. When all the four axial positions in the dimer are occupied by bpe ligands, the photoreactive ladder structure contains well-aligned bpe pairs on both sides of the template in a serial manner as shown in Figure 7. UV irradiation of this compound showed quantitative cycloaddition reaction resulting in another 1D ladder structure.[27]

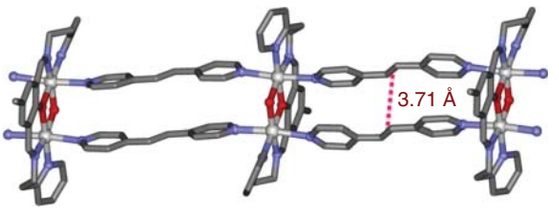


Figure 7 Perspective view of an infinitely aligned bpe pairs in a 1D CP containing Schiff base Zn(II) dimer building block

3.3 Ladder Polymer with the bpe Pairs Occupying the Rungs

It is also possible to construct a photoreactive ladder CP in which the bpe pairs occupying the rungs can be infinitely aligned one below the other in a parallel manner.[38] Such an unusual structure has been observed in $[Zn_2(1,2\text{-bdc})_2(bpe)]\cdot MeOH$ (**12**) (where 1,2-bdc is benzene-1,2-dicarboxylate). The nature of bonding of 1,2-bdc ligands controls the intrachain Zn···Zn separations to be 3.48 and 4.45 Å. One of the carboxylate groups in one 1,2-bdc ligand chelates a Zn (II) in $\mu_2{:}\eta^1{:}\eta^1$ manner and the other carboxylate group bridges two more Zn(II) atoms in $\mu_2{:}\eta^0{:}\eta^2$ manner in the 1D CP. Furthermore, each carboxylate group in the second 1,2-bdc bridges to two different Zn(II) atoms but overall bonded to three different Zn(II) atoms. Two adjacent [Zn(1,2-bdc)] strands are bridged by bpe rungs to form this unique ladder structure as shown in Figure 8. The nonbonding distances between the C=C bonds of the adjacent bpe ligands 3.85 and 4.03 Å are congenial for the photochemical reaction. Single crystal of this compound, upon UV irradiation under an Hg lamp (400 W) for 5 h, undergoes SCSC transformation to form $[Zn_2(1,2\text{-bdc})_2(rctt\text{-tpcb})_{0.5}]$ (**13**). Interestingly, the solvent is lost in this structural transformation and the interchain Zn···Zn distances changed to 3.57 and 4.43 Å.[38]

3.4 Step-Wise Double [2+2] Cycloaddition Reactions in Ladder Structures

The Ag(I) complex of the di-olefinic ligand, *N*,*N*′-bis(3-(4-pyridyl)acryloyl)-hydrazine (4-PAH) has been found to be photoreactive, assisted by Ag···Ag and Ag···π interactions. The ClO_4^- and NO_3^- anions were found to exert finer control over the selective orientation of olefinic groups for the photoreaction.[39] The 1D ladder CP, $[Ag(4\text{-PAH})(ClO_4)]$ (**14**) has face-to-face alignment of the 4-PAH ligands, and the crystal packing showed the alignment of the olefin pairs in an asymmetric manner between the two linear strands, assisted by the Ag···π (olefin) interactions as shown in Figure 9. Quantitative double [2+2] cycloaddition reaction between the two linear strands occurs by a stepwise mechanism under UV light

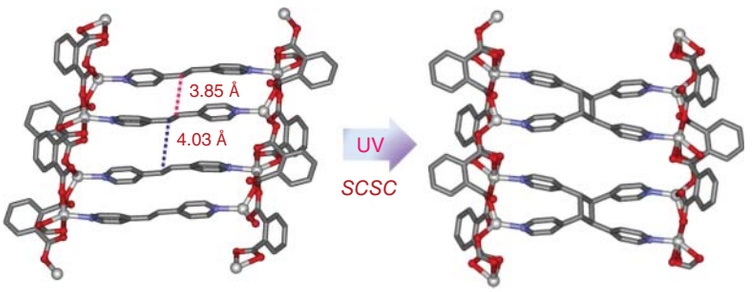


Figure 8 Schematic representation of the structural transformation of **12** to **13** by photodimerization reaction

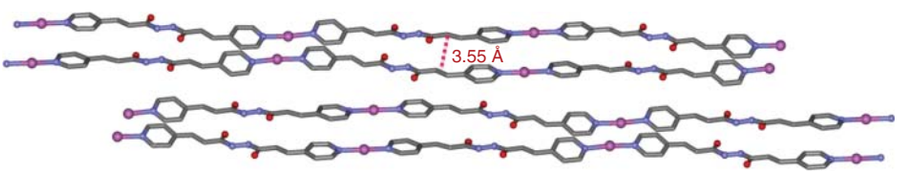


Figure 9 The alignment of the photoreactive olefin groups in 4PAH in Ag(I) 1D CP **14**

as revealed by the ^{1}H-NMR studies. Upon changing the counter anion to NO_3^-, similar double stranded pairs were retained. But, the interaction between the strands is so strong that the UV irradiation furnished only a mono-cyclobutane product.

3.5 Double [2+2] Cycloaddition Reactions in Ladder CPs

The bis-pyridyl derivatives of 1,3-pentadiene-3-one has conjugated dienes and can potentially undergo double [2+2] cycloaddition reactions, when they are aligned in a fact-to-face manner. The reaction of this ligand with $AgNO_3$ resulted in a 1D CP containing necklace like loops assisted by Ag···Ag interactions as shown in Figure 10a. The ligand exhibits *cisoid–transoid* conformation and as a consequence, only the C=C bonds with *cisoid* confirmation come closer between the interstrands. The other C=C bonds are 'out-of-phase' with each other. Although this solid exhibits quantitative [2+2] photoreaction, the nature of the photo-product is not known. In the absence of single crystal structure, it may be predicted that it may have 3D structure. When NO_3^- is replaced by ClO_4^- anion, a completely different packing pattern due to *cisoid–cisoid* conformation of the ligand is obtained (Figure 10b). The resulting linear 1D strands are paired up by Ag···Ag interactions to form ladder structure. This ladder compound yielded 100% double [2+2] cycloaddition product as assessed by the ^{1}H-NMR spectroscopy. But again, the X-ray structure of this 1D polymer is not known.[39]

3.6 Photoreactive Ladder Containing a Bio-Active Dicarboxylate

An unusual example of a transition metal ion to align a pair of C=C bonds in a biological active molecule is described here. Herein, a heterocyclic diolefin chelidonic acid (H_2CDO) has been incorporated into a 1D ladder polymer [Cu(CDO)(py)$_2$(H_2O)] (**15**) constructed from CDO anions with Cu(II) in the presence of pyridine.[40] The neighboring six membered CDO ligand pairs are aligned antiparallel with a distance of separation of 3.61 Å. This compound shows SCSC conversion under UV light as shown in Figure 11 and the color changed from blue to green in this process. The photo-dimerized product [Cu(EE1)(py)$_2$(H_2O)] (**16**) (where EE1 = organic cage dimer) showed the formation of a similar 1D CP but with the dimerized cage like ligand that can be extracted and recrystallized as sodium salt.

3.7 Structural Transformations of 1D Chains to Photoreactive Ladder Structures

Among the 1D CPs ladder structure is thermodynamically stable, but the experimental conditions employed often furnish kinetic products such as the solvated linear CPs. The removal of the solvent or guest molecules, in many cases, converts the kinetic linear polymers to the ladder structures. The absence of single crystal structures of the product renders this transformation unnoticed. If the ligand contains a C=C bond, then the ladder structure becomes photoreactive. Subsequently the formation of

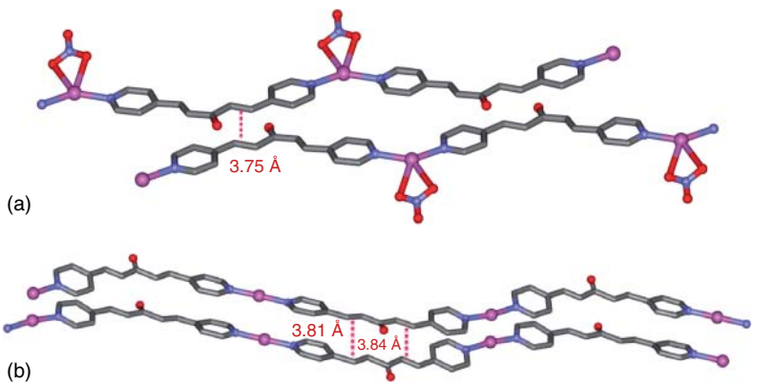


Figure 10 The alignment of 1,3-pentadiene-3-one in Ag(I) 1D CPs

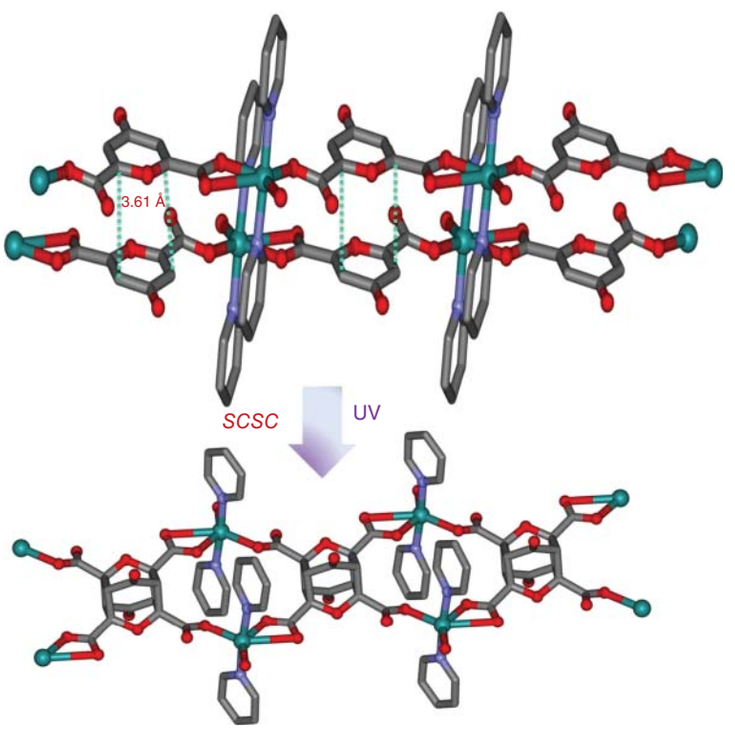


Figure 11 Transformation of **15** to **16** by double photo-cycloaddition of cyclic pairs

cyclobutane rings by UV irradiation can be used to confirm the formation of ladder polymer in the solid state by solution ^{1}H-NMR spectroscopy after dissolving the products in DMSO. Herein, a few photo reactive ladder polymers found in this way by thermal desolvation are described.

A 1D CP [Ag(μ-bpe)(H_2O)](TFA)·CH_3CN (**17**) was isolated as a kinetic product in one of the attempted syntheses of the ladder polymer [Ag_2(bpe)$_2$(TFA)$_2$] (**18**).[41] The Ag(I) atoms in the linear CP have a T-shaped geometry arising from two bpe spacers and an aqua ligand (Figure 12). A hydrogen-bonded sheet-like structure resulted owing to the O–H···O interactions between the coordinated water molecule and the oxygen atoms of the non-coordinated TFA anions. The C=C bonds of the bpe ligands are far away (5.15 Å) to satisfy the topochemical distance criterion. The aqua ligand can easily be lost in the atmosphere along with CH_3CN, thereby destroying the single crystals very easily. However, this desolvated powder showed quantitative formation of cyclobutane ring under UV light as confirmed by ^{1}H-NMR experiments.

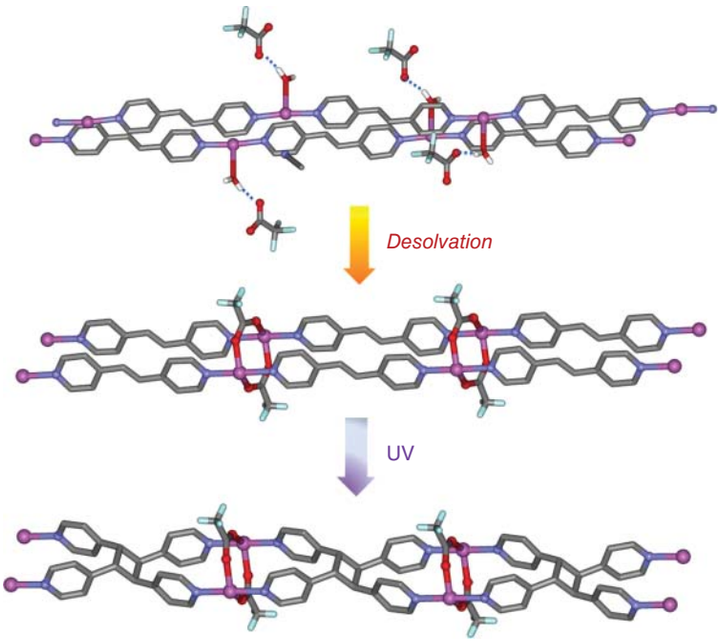


Figure 12 Rearrangement of a linear CP, **17** to a photoreactive ladder structure, **18** by desolvation

The loss of coordinatively bonded aqua ligands at such a low temperature suggests some kinds of structural transformation in the solid state. This photoreactivity confirms the formation of a thermodynamically stable ladder structure by the cooperative anisotropic molecular movements of the adjacent 1D chains occur during the desolvation process (Figure 12), which is stabilized by Ag···Ag and π···π interactions. A similar structural transformation of a linear CP [Cd(bpe)$(CH_3COO)_2(H_2O)$] (**19**) to a ladder structure by thermal dehydration was also successfully monitored because of its photoreactivity.[42]

The rearrangement of a kinetic product, namely, a linear CP [Pb(μ-bpe)$(O_2C\text{-}C_6H_5)_2]\cdot 2H_2O$ (**20**$\cdot 2H_2O$) to the ladder polymer [Pb_2(μ-bpe)$_2$(μ-$O_2C\text{-}C_6H_5)_2(O_2C\text{-}C_6H_5)_2$] (**21**) involves the thermal dehydration of the guest water molecules that aggregate to form a hydrogen-bonded 1D polymer in the crystal structure. In this case, the structural transformation to the photoreactive ladder structure was again confirmed by PXRD and the analysis of the UV irradiated product by ^{1}H-NMR spectroscopy in DMSO solution (Figure 13).[36]

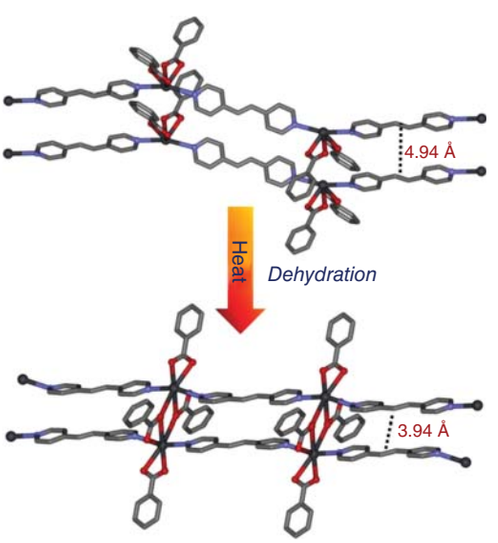


Figure 13 Transformation of a linear CP, **20**.$2H_2O$ to a photoreactive ladder structure, **21** upon dehydration of the water aggregate in the lattice

In another example how the photoreactivity has been successfully used to differentiate the ladder polymer from 2D CP is illustrated. In the [Cu$(O_2CCF_3)_2$(μ-bpe)(DMF)] (**22**) with linear chain structure, Cu(II) atom has distorted square pyramidal geometry with a DMF molecule occupying the apical position. When heated, the coordinated DMF starts leaving at 83.5 °C, well below the boiling point of DMF (153 °C) inferring a solid-state structural transformation from linear chain structure to a more stable one. But the single crystals were not maintained after the loss of DMF molecules. The structural changes due to the removal of DMF molecules by two different methods have been investigated by [2+2] cycloaddition reaction. When the single crystals were desolvated by heating,

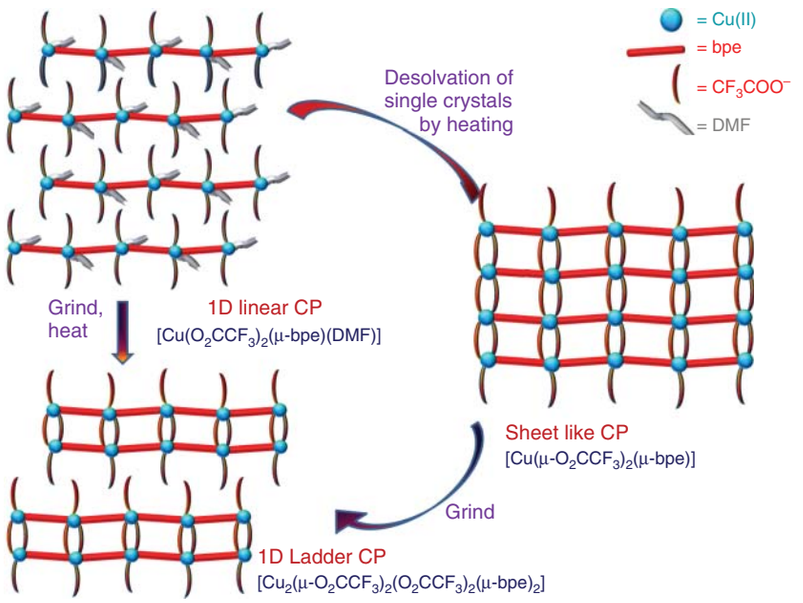


Figure 14 Sequence of desolvation and grinding on the structural transformation of **22**

the product exhibits a maximum of only ~80% reactivity as monitored by the ^{1}H-NMR spectra after dissolving the product in D_2O with a drop of acid in order to separate from the paramagnetic ions. Such an incomplete photo-conversion has been shown to take place only when the infinitely parallel alignment of the C=C bonds one below another present in the structure, for which the maximum yield has been theoretically calculated to be 82–87% based on the recurrence relations.[43–45] Hence, the solid state structure of the desolvated single crystals of **22** is proposed to be a 2D structure (Figure 14). When the single crystals were ground to powder and then heated to remove the DMF ligands, the product showed 100% photodimerization, which can be due to the formation of a ladder structure, $[Cu_2(\mu\text{-}O_2CCF_3)_2(O_2CCF_3)_2(\mu\text{-bpe})_2]$ (**23**). The formation of 2D and ladder structures was rationalized by the amount of cyclobutane ring formed from UV experiments. The thermal dehydration behavior of **22** could not have been predicted from the crystal packing or the topochemical principles. It is surprising that mechanochemical grinding can affect structural change from 2D sheet to ladder structure that has not been demonstrated before.[46]

4 PHOTOREACTIVITY OF 1D CPs YIELDING 2D STRUCTURES

Usually C=C bonds containing the spacer ligands have been employed to construct the photoreactive MOFs and CPs. The use of terminal ligands containing C=C bonds, such as 4-styrylpyridine (4-spy) for this purpose may be rather challenging. Furthermore, the C=C bonds in 4-spy can only be aligned in an HT manner between different polymeric strands, which will lead to higher dimensional structures. The formation of 1D CPs from the metal complexes of 4-spy was described earlier in Section 2.2. We describe the conversion of 1D CP to 2D sheet below.

4.1 The Use of 4-Styrylpyridine Ligand for Making a Photoreactive CP

In the linear 1D CP $[Cd(1,3\text{-bdc})(4\text{-spy})_2]$ (**24**) ($1,3\text{-}H_2bdc$ = 1,3-benzenedicarboxylic acid), the Cd(II) pairs are bonded to four 1,3-bdc ligands in a plane, in which one carboxylate of 1,3-bdc bridges two Cd(II) centers and the other carboxylate ligand chelates the next Cd(II) center and vice-versa. The two axial positions in each Cd(II) atom with octahedral geometry are filled by the 4-spy ligands and the pyridyl pairs are aligned parallel. However, the C=C bonds in the HT pairs are disoriented and too far apart to undergo a photochemical [2+2] cycloaddition reaction. On the other hand, the 4-spy ligands from neighboring chains interdigitate in an HT manner. A closer look at the packing reveals that one of the two 4-spy ligands is well-aligned with its partner from the neighboring strand with C···C distance of 3.86 Å. In other words, 50% of the 4-spy ligands can undergo HT dimerization above and below the 1D strands. Indeed, SCSC reaction occurs under UV light and the resultant

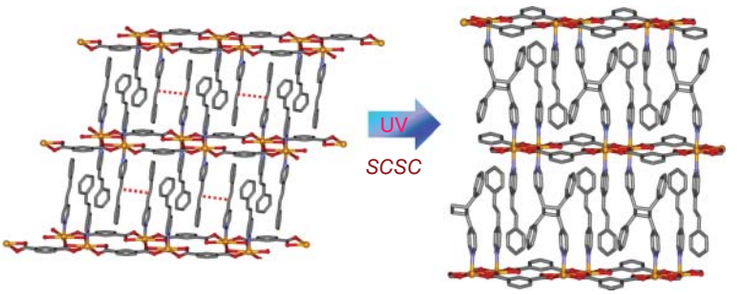


Figure 15 Formation of 2D sheet **25** from 1D CP **24** by partial photochemical reaction

compound [Cd(1,3-bdc)(4-spy)(HT-ppcb)$_{0.5}$] (**25**) (HT-ppcb = 1,3-bis(4′-pyridyl)2,4-bis(phenyl)cyclobutane) has 2D sheet structure as shown in Figure 15.[47]

4.2 Photoreactivity of a Triple-Stranded CP

The usual ladder structures are formed by a pair of polymeric strands bridged by various anions and/or spacer ligands. It is unusual to have three polymeric strands forming a ladder. Such a ladder can be considered as an intermediate (kinetic product) in the self-assembly of a 2D sheet. It will be interesting to investigate the photoreactivity of these triple-stranded ladders, if the C=C bonds in the three spacer ligands are aligned perfectly parallel satisfying Schmidt's criteria.

Indeed a photoreactive triple-stranded ladder, [$Pb_3(bpe)_3(O_2C\text{-}CF_3)_4(O_2CCH_3)_2$] **(26)** containing well-aligned three bpe spacer ligands has been investigated.[48] In this compound, Pb(II) in the central strand is bridged by an OAc and a TFA ligands, and the terminal Pb(II) atoms are chelated by TFA anions, thus arresting the formation of a 2D CP. This compound showed interesting photoreactivity. Irradiation of the single crystals of **26** under UV light for 10 h showed the expected 66% of dimerization of bpe, owing to the photodimerization between any two bpe molecules across the strands, leaving the third one unreacted. The percentage conversion with time was monitored by solution ^{1}H-NMR studies. When the photoirradiation was continued further, the compound showed quantitative photo-conversion of bpe to *rctt*-tpcb. Furthermore, grinding of the single crystals to powder form accelerates the second step to completion in 40 h.[48] It has been explained that there might be cooperative movements of these triple strands during the process that aligned the unreacted bpe between the intermolecular strands and thus the observed quantitative [2+2] cycloaddition as shown in Figure 16. Molecular movements have been proposed to understand this observation.[41,42]

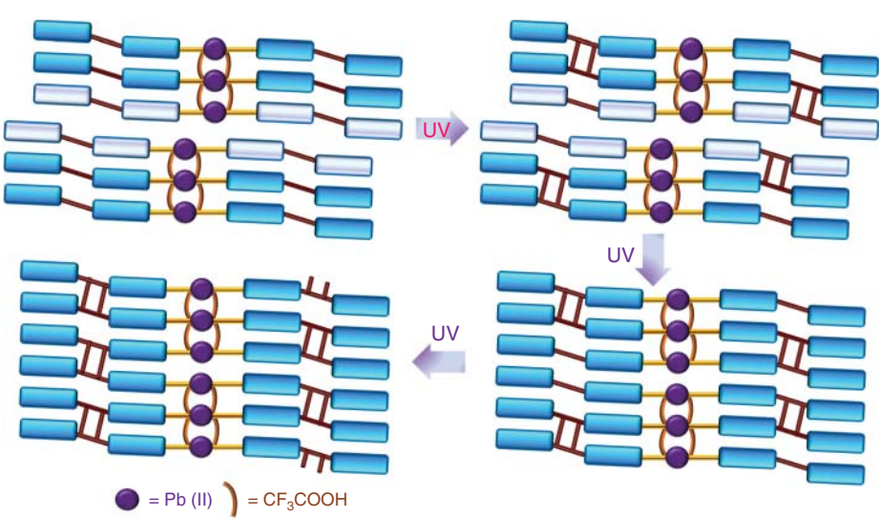


Figure 16 Photoreactivity of a triple stranded 1D CP, **26**

5 PHOTOREACTIVITY OF 1D CPs YIELDING 3D STRUCTURES

5.1 Photoreactivity of a 1D CP Containing Terminal bpe Pairs

In the two photoreactive 1D CPs, [M(1,2-chdc)$(bpe)_2(H_2O)_2]\cdot H_2O$ (M = Zn(II) **(27)**, Mn(II) **(28)**, 1,2-chdc = *trans*-1,2-cyclohexanedicarboxylate), the metal(II) in octahedral coordination geometry, is coordinated to two carboxylate oxygen atoms of chdc, two more sites are coordinated by the nitrogen atoms of bpe and the coordination sphere is completed by two aqua ligands. The 1D chain is formed by bridging the chdc ligands to two different metal ions, whereas the two bpe molecules act as terminal ligands and the non-coordinating nitrogen atoms are H-bonded to the aqua ligands in the neighboring chains. Such complementary hydrogen bonds align the C=C bonds of these two bpe in parallel with a C···C separation of 3.27 Å as shown in Figure 17. Cyclobutane rings are formed by the C=C bonds from neighboring bpe molecules quantitatively in an SCSC manner under UV light. The new bonds formed in the direction normal to the propagation of 1D CP transformed product into 3D network structure with **cds** topology.[49]

6 PHOTOREACTIVITY IN 2D CPs

6.1 Formation of rtct-Isomer in the Photodimerization of a Layer CP

The photoreactivity of an unusual crisscross alignment of the C=C bonds in adjacent CP layers is illustrated here. In the layer structure of $[Cd_2\ (fumarate)_2(H_2O)_4]$ **(29)** the building block comprises a Cd(II) dimer. Each Cd(II) is bonded to a chelating fumarate ion and two bridging fumarate anions form a Cd_2O_2 node as shown in Figure 18. Further connectivity of the $Cd_2(fumarate)_{4/2}$ dimer produced the expected (4,4) sheet structure. Each Cd(II) is further bonded to two aqua ligands in a *trans* manner. These coordinated water molecules are extensively hydrogen bonded to the adjacent layers. The adjacent layers are arranged in an ABAB manner leaving no voids in the structure. Interestingly, the olefinic groups of the fumarates in the adjacent layers are separated by a distance of 3.39 Å in a crisscross manner. Such antiparallel arrangements of C=C bonds usually undergo pedal-like motion in the organic crystals and 1D CPs, but highly unlikely in 2D layers. Hence, this cycloaddition reaction is expected to yield *rtct*-isomer, if observed. Indeed UV irradiation experiments yielded the unusual *rtct*-cyclobutane-1,2,3,4-tetracarboxylate in the quantitative yield as monitored by the appearance of the singlet at 3.31 ppm due to the cyclobutane C–H proton in the ^{1}H-NMR spectrum of the dissolved product. Owing to ABAB type of packing, cyclobutane ring formation can yield either bilayer structure, if the reaction occurs exclusively between two layers or 3D structure if C–C bonds are formed randomly on both sides of the layer. Since the single crystals did not survive during UV experiment, this interesting information has not been established.[50]

6.2 Photoreactivity of an Interpenetrated 2D CP Yielding Another Interpenetrated Sheet Structure

In the building block of a photoreactive twofold interpenetrated 2D layered structure of

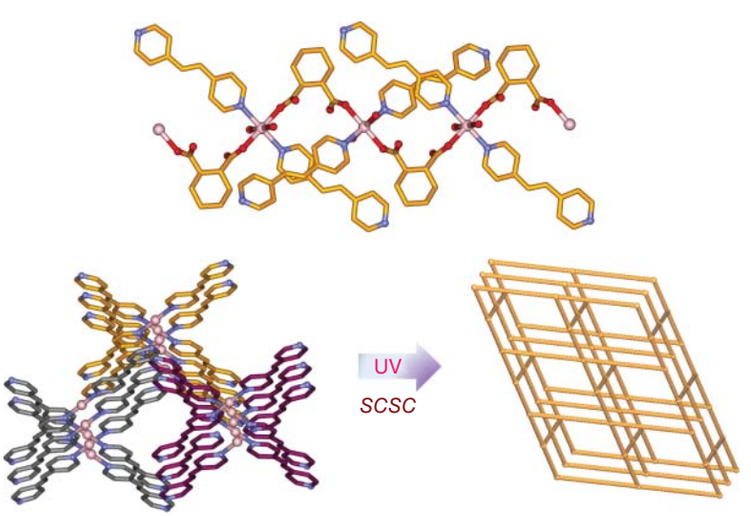


Figure 17 Schematic representation of transformation of 1D CP into 3D MOF through photo-cycloaddition

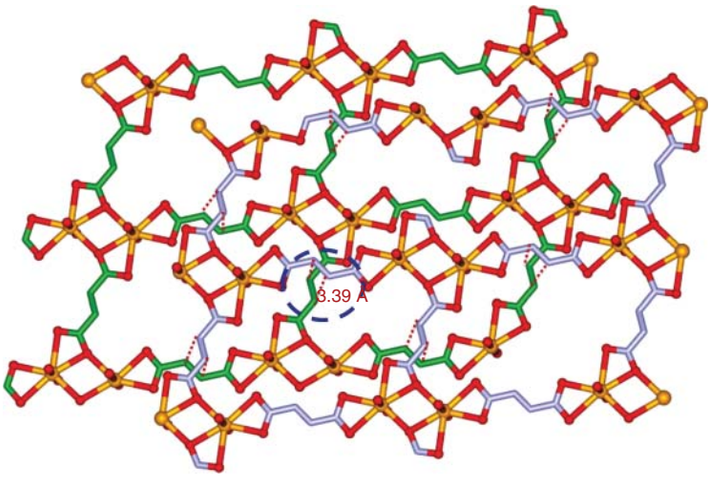


Figure 18 Photoreactivity of fumarates in 2D layered CP, **29**

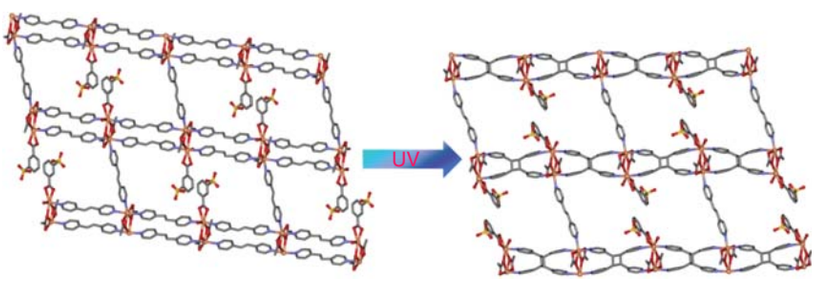


Figure 19 Photo-conversion of **30** to **31** upon UV irradiation

$[Cd_2(CH_3COO)_2(3\text{-sb})(bpe)_{2.5}(H_2O)]\cdot 4H_2O$ **(30)** (3-sb = 3-sulfonatobenzoate), two Cd(II) atoms are bridged by two OAc anions separated by 3.85 Å.[51] Each bridging OAc anion further chelates the other Cd(II) atom. Each Cd(II) is coordinated by two *trans* bpe ligands to furnish a 1D ladder chain. In one of the Cd(II) atoms, the hepta coordination geometry is completed by a chelating 3-sb anion and an aqua ligand. The equatorial position in the pentagonal bipyramid geometry of the second Cd(II) atom is completed by another bpe ligand bridging the neighboring ladder chains. This guided the formation of a brick wall type 2D structure (Figure 19), and the void created by this topology is minimized by twofold interpenetration. It is worth noted that the $[Cd_2(OAc)_2]$ unit controls the infinite parallel alignment of the bpe pairs and makes this crystal photoactive. The solution ^{1}H-NMR spectrum of the UV irradiated product showed that all these aligned bpe molecules reacted. The product $[Cd_2(CH_3COO)_2(3\text{-sb})(bpe)_{0.5}(4,4'\text{-tpcb})_2(H_2O)]\cdot 4H_2O$ **(31)** was independently synthesized by exposing the reaction mixture of **31** in solution under sunlight for several hours and then slowly evaporated at room temperature (RT). The structure determination by X-ray crystallography confirms that the interpenetrated 2D layer structure is preserved in the product. Another aspect of this reaction is that **31** was obtained only with a high power mercury lamp (300 W, $\lambda = 367$ nm) both in solution and the solid state after irradiation of 8 h but not using a low power UV lamp (30 W) with $\lambda = 253.7$ nm for 9 days.[51]

6.3 Thermal Cyclo-Reversion of Photoreacted 2D CPs

Reversible photochemical reactions have potential applications in optical storage and sensing, and hence the cleavage of the cyclobutane rings to the corresponding olefins is of great interest. Surprisingly, such cleavage of cyclobutane rings in CPs has never been observed. This property was investigated in a 2D CP by thermal treatment.[52] The asymmetric ligand, *trans*-2-(4′-pyridyl)vinylbenzoic acid (Hpvba) forms the following three photoreactive 2D CPs: $[Cd_2(pvba)_2(tbdc)(dmf)_2]$ **(32)**, $[Co_2(pvba)_2(tbdc)(dmf)_2(H_2O)_2]$ **(33)** and

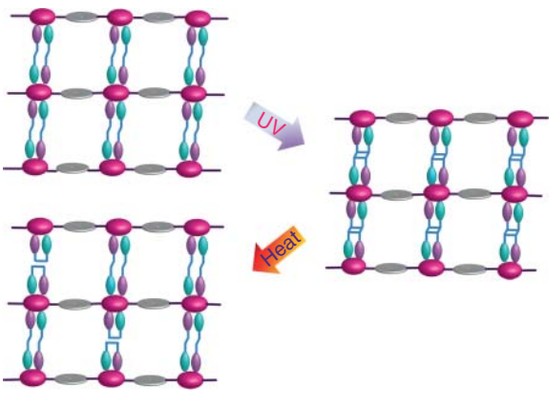


Figure 20 Schematic representation of 2D to 2D photo-transformation of **33** and its thermal reversibility

$[Ni_2(pvba)_2(tbdc)(dmf)_2(H_2O)_2]$ **(34)** where tbdc = 2,3,5,6-tetra-bromobenzene dicarboxylate. In the sheet structure, $[Cd_2(O_2C\text{-}C)_4(pyridyl)_2]$ core is the repeating unit connecting a pair of pvba ligands that are aligned parallel in an HT manner, whereas the tbdc ligands are arranged in the orthogonal direction. The C=C bonds in these pvba ligand pairs are well aligned for [2+2] cycloaddition reaction in the solid state under UV light, yielding the cyclobutane derivative quantitatively. This photochemical reaction has been accompanied by a solid-state structural transformation between two different sheet structures as shown in Figure 20.[52]

Further, the cyclobutane rings in the photo-dimerized product of **32** can be cleaved by heating to 220 °C for 12 h under vacuum in two different ways to yield a mixture of *trans*- and *cis*-isomers of pvba quantitatively as monitored by the ^{1}H-NMR spectroscopy. This transformation as depicted in Figure 20 appears to be the first attempt to reverse the cyclized product in CPs. From the integration of ^{1}H-NMR spectrum, the ratio between the *cis* and *trans* isomers has been observed to be 66.5 and 33.5% respectively. Formation of other isomer of pvba has also been supported by a new peak observed in photoluminescence (PL) spectrum at 370 nm, which is different from *trans* pvba and the dimer. Under similar conditions, the photo products of **33** and **34** showed scission of cyclobutanes up to 56 and 67%, respectively, of *trans* products.

6.4 Control of Pore Size and Gas Uptake Properties of a Photoreactive 2D CP

Pore surface modification is an important area in MOF chemistry as it finds applications in gas sorption. In this example, [2+2] cycloaddition reaction has been used as a post-synthetic method to modify the pore structure and surface area in a 2D CP.[53] In the photoreactive twofold interpenetrating 2D CP, $[Zn_2(moip)_2(bpe)_2(DMF)_2]$ **(35)** (H_2moip = 5-methoxy-isophthalic acid), the 1D polymer formed by $Zn_2(moip)_2$ is further linked to a pair of bpe ligands. These bpe pairs are oriented in parallel and the C=C bonds are separated by 3.71 Å. Twofold interpenetration occurs between these sheets forming a 3D structure and 1D channels are created with a cross-section of 3.2 × 4.5 Å with the solvent-accessible space of 27.0% of the unit cell volume. This compound showed quantitative photo-cycloaddition in an SCSC manner to form $[Zn_2(moip)_2(rctt\text{-tpcb})(DMF)_2]$ **(36)** under UV light. In this process, the size of the 1D channel has been enlarged owing to the cyclobutane formation as shown in Figure 21. Gas sorption studies of **35** showed no uptake of N_2 at 77 K probably owing to slow diffusion rate. On the contrary, the same compound showed better adsorption of CO_2 at higher temperature, 195 K. The activated precursor sample showed three-stepwise adsorptions with the initial uptake up to 0.06 kPa and followed by a steep rise from 0.06 to 1 kPa and then gradual pore filling at further increase in pressure of CO_2 and also showed a hysteresis at the step 0.06 kPa. On the other hand, the activated photo product **36** showed normal type-I isotherms without any discontinuous steps, attributed to the differences in the pore shape and the flexibility of the framework. Hence, it is possible to engineer the pore size and surface property through photoreactivity.[53]

6.5 Photoreactivity-Induced 2D to 2D′ and 3D to 3D′ Structural Transformations

A kinetic product $[Cd_2(bpe)_3(H_2O)_4(S_2O_3)_2]$ **(37)** was isolated during the synthesis of a 3D MOF.[33] The structure comprises 1D chains formed between Cd(II) and S (in μ_2 mode) from thiosulfate, and the alternating Cd(II) atoms are coordinated by two types of bpe ligands. One type of bpe is crosslinking the 'Cd(II)-S' chains forming a layer and the other type is monocoordinated to Cd(II) and hangs from other side without coordinating as shown in Figure 22. These 'dangling' bpe ligands from the adjacent 'Cd(II)-S' chains are perfectly aligned parallel and the C=C bonds are separated by a distance of 4.02 Å. Upon UV irradiation, this compound showed complete photoreactivity of these aligned bpe molecules as shown in Figure 22, which is almost 67% of the whole bpe molecules in the compound. This reaction is expected to generate another 2D layer structure through the formation of cyclobutane rings.

Similarly, the thermodynamic product $[Cd(bpe)S_2O_3]$ **(38)** was obtained by heating the reaction solution of **37** at 60 °C for 72 h. The structure is constructed from a tetranuclear $Cd_4(S_2O_3)_4$ secondary building unit (SBU) made by a Cd_4S_4 ring. The other two coordination sites

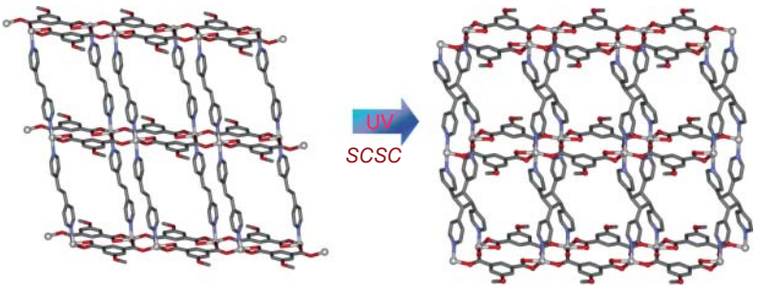


Figure 21 The manipulation of pores upon [2+2] photo-cycloaddition of bpe in **35**

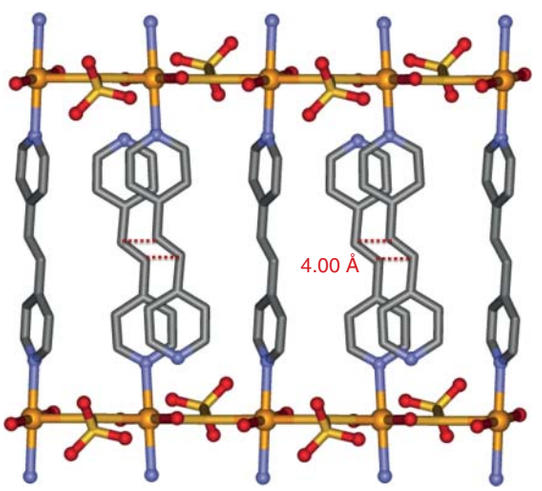


Figure 22 A perspective view showing the possible photoreactivity between the dangling bpe molecules in **37**

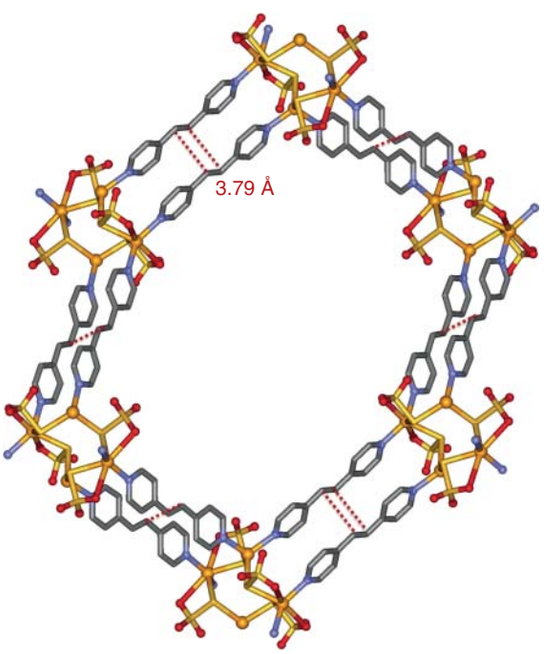


Figure 23 A perspective view showing the possible photoreactivity between the bpe molecules of a diamondoid ring in **38**

in each tetrahedral Cd(II) are occupied by bpe ligands. Overall, there are four pairs of bpe ligands tetrahedrally oriented in this tetranuclear cluster to produce fourfold interpenetrated diamondoid structure. Each bpe pair from two sulfur bridged Cd(II) atoms is aligned in parallel and separated by 3.79 Å (Figure 23). Upon UV irradiation, this compound showed up to ~80% photoreactivity and giving only *rctt*-isomer.[33]

6.6 Photoreactivity of 2D CP Yielding a 3D CP

In the unique 2D bilayered CP, $[Mn_2L_2(H_2O)_2] \cdot 3H_2O$ **(39)** (L = E-5-(2-(pyridin-4-yl)vinyl)isophthalic acid ligand), each distorted octahedral Mn(II) is coordinated to a chelated carboxylate O atoms, two *syn* and *anti* bridging O atoms from two different ligands, one N atom from fourth ligand, and a water molecule.[54] The 1D chain formed by Mn(II) carboxylates are further coordinated by pyridine groups from the neighboring ligands to result in the formation a 2D bilayer structure. These bilayers resulted from the *syn* and *anti* bridging carboxylates, are further packed in … AA … manner in the solid. The C=C bonds of the ligands are aligned parallel within the bilayer as well as between the bilayers in a *heat-to-tail* manner. The distance between the olefinic groups within the bilayer is 4.21 Å, whereas, the interlayer distance between the C=C bond pairs is shorter (3.68 Å) as shown in Figure 24. Upon irradiation under UV light, this 2D bilayer structure undergoes quantitative cycloaddition reaction between the layers in an SCSC manner and resulted in the formation of a 3D

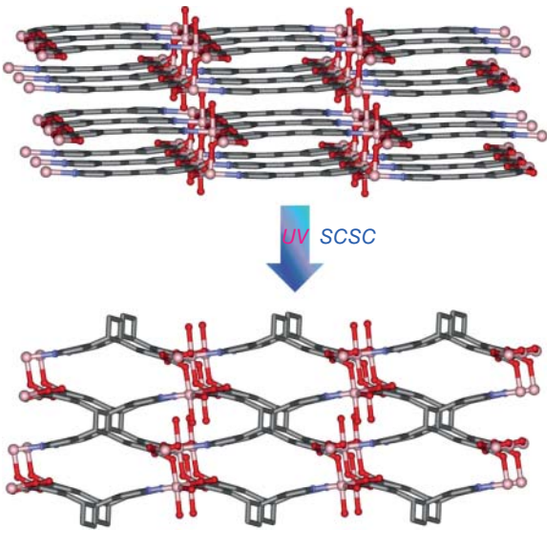


Figure 24 SCSC photo transformation of a 2D CP, **39** to a 3D MOF

MOF. Surprisingly, the coordinated water molecule does not destruct the single crystals during the cycloaddition reactions.[54]

6.7 Photoreactivity of 2D Interdigitated CP Leading to 3D MOF

We have discussed the usage of terminal ligands to make photoreactive CPs before (Sections 2.2, 4.1, and 5.1). Here the use of 4-spy for linking the 2D layers to form interpenetrated 3D structures by [2+2] cycloaddition reaction is illustrated.[55] The paddle-wheel SBU, $\{Zn_2(O_2C{-}C)_4\}$ has been found in two isotypical interdigitated photoreactive CPs, $[Zn_2(cca)_2(4\text{-spy})_2]$ **(40)** and $[Zn_2(ndc)_2(4\text{-spy})_2]$ **(41)**. The linear dicarboxylate ligands 4-carboxycinnamate (cca) or 2,6-naphthalenedicarboxylate (ndc) are connecting the paddle-wheel nodes to form the 2D layer structure with (4,4) connectivity. The two apical positions of each paddle-wheel building block are coordinated by the terminal 4-spy ligands. The 2D layers are interdigitated with each other owing to the long arm of this ligand. The C=C bonds of the terminal 4-spy ligands are aligned in *heat-to-tail* manner between the first and fourth layers with a distance of 3.85 Å. Of these two 2D MOFs, only the cca derivate shows [2+2] cycloaddition in an SCSC manner and the final structure of photoreacted compound, $[Zn_2(cca)_2(rctt\text{-}4\text{-ppcb})]$ **(42)** (where *rctt*-4-ppcb = 1,3-bis(4′-pyridyl)-2,4-bis(phenyl)cyclobutane) has been determined to be a triply interpenetrated MOF with α-Po topology. The reaction is depicted in Figure 25. This illustrates the use of the photoreactive terminal ligands to combine the 2D layers to form 3D structures by [2+2] photo-cycloaddition reactions.

6.8 Post-synthetic Modification to Fine-Tune the Sorption Behavior of a 2D CP

An example of modification of pore size and surfaces by [2+2] cycloaddition reaction was discussed in Section 6.4. In this work Kitagawa and coworkers demonstrated how to control the reactivity and pore surface of MOFs by photo-irradiation technique.[56] For this purpose, an interdigitated 2D CP $[Zn_2(abdc)_2(bpy)_2(DMF)_{1.5}]$ **(43)** using 5-amino-benzene-1,3-dicarboxylate (abdc) and 4,4′-bipyridine (bpy) was synthesized. The amino groups exposed on both sides of the pore created in the crystal packing are further diazotized followed by azidation with NaN_3 to get azido derivative. Surprisingly, this 2D CP containing azide group is thermally stable to 150 °C. But this is non-porous for oxygen sorption. On photo-irradiation at 77 K the adsorbed amount of oxygen was significantly improved owing to the loss of nitrogen and formation of triplet nitrene radicals in the pores. These results created a strategy to produce PCPs with reactive sites such as radicals and carbenes, which cannot be trapped by conventional synthetic conditions.[56] The details are depicted in Figure 26.

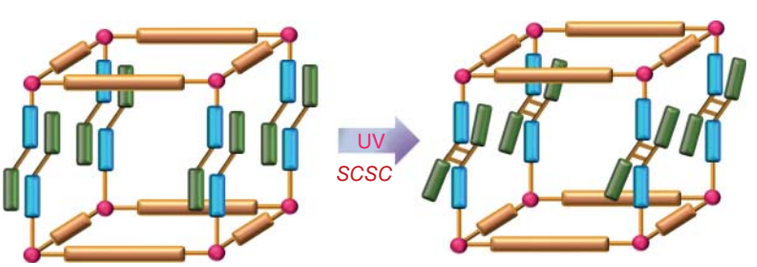


Figure 25 Schematic representation of the transformation a 2D interdigitated CP to a triply-interpenetrated 3D MOF. The interpenetration is not shown

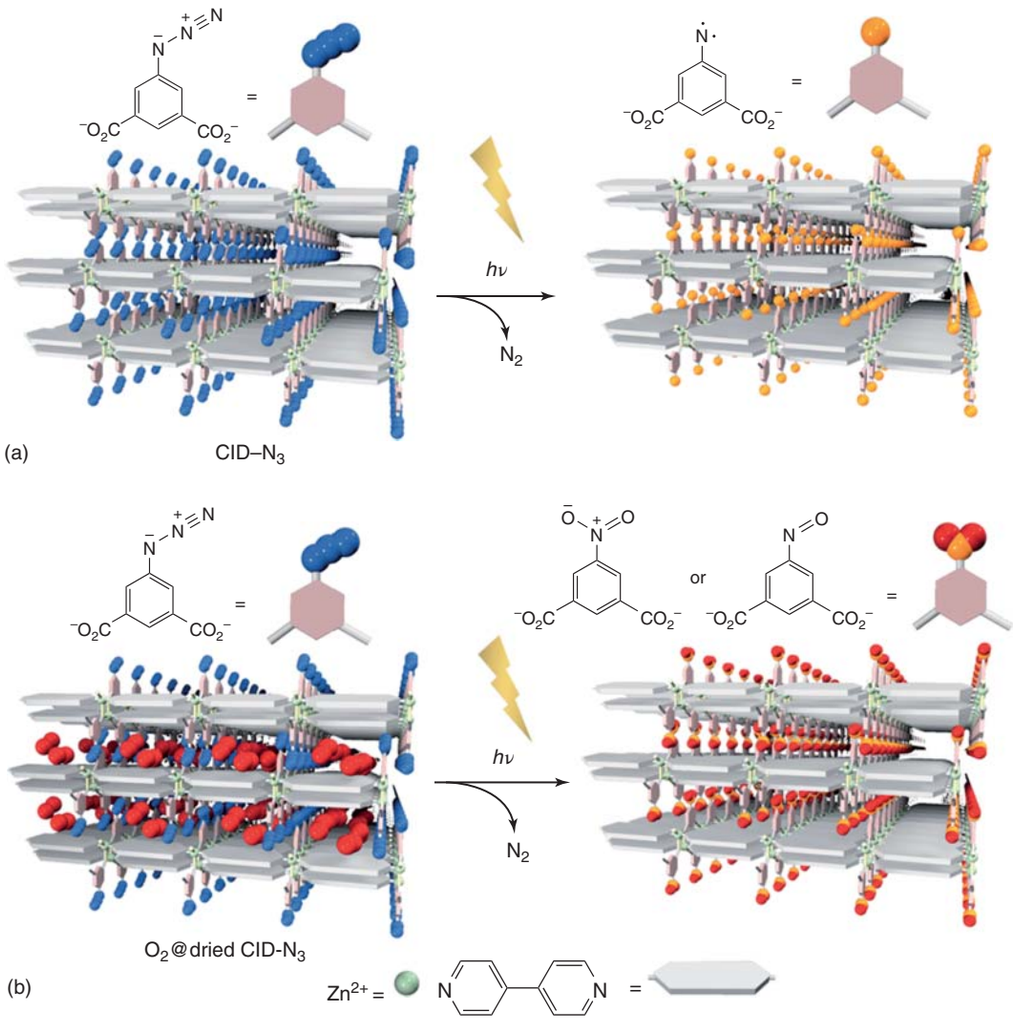


Figure 26 Schematic diagram illustrating the photoactivation of 2D CP, **43**. (a) Photoactivation of the azide moieties leads to the formation of triplet nitrenes on the pore surface. (b) Photochemical trapping of physisorbed oxygen molecules in the framework of dried **43** (Reprinted by permission from Macmillan Publishers Ltd: Nature Materials (Ref. 56). Copyright (2010).)

7 PHOTOREACTIVE 3D CPs

7.1 Post-synthetic Modification of Double-Pillared MOFs by [2+2] Cycloaddition Reaction

Post-synthetic modification of double-pillared MOFs by [2+2] photo cycloaddition was demonstrated in the following examples. Three photoreactive double-pillared MOFs, $[Zn_2(bpe)_2(muco)_2]\cdot DMF\cdot H_2O$ **(44)**, $[Zn_2(bpe)_2(bdc)_2]\cdot DMF$ **(45)** and $[Zn_2(bpe)_2(fum)_2]\cdot H_2O$ **(46)** (H_2muco = *trans*,*trans*-muconic acid, H_2bdc = 1,4-benzene dicarboxylic acid, and H_2fum = fumaric acid) have been investigated.[57] In these structures the layer is formed by the $\{Zn_2(O_2C\text{-}C)_4\}$ SBU in which each Zn(II) is chelated by a carboxylate and bridged by two carboxylates. These 2D layers are further double-pillared by the bpe ligands at the axial positions of Zn(II) atoms that are separated by 3.96 Å, to produce the 3D structure. This arrangement assists the bpe pairs to orient in parallel with the olefin groups separated by 3.79 Å (Figure 27). Upon irradiation under UV light, all these MOFs showed quantitative cycloaddition reaction across the double pillars as confirmed by solution ^{1}H-NMR spectral studies. Among the three, MOFs containing muco and bdc ligands underwent SCSC structural transformation. It has been shown that it is possible to modify the backbone of the spacer ligand without affecting the topology or porosity of the MOF during this structural transformation.[57]

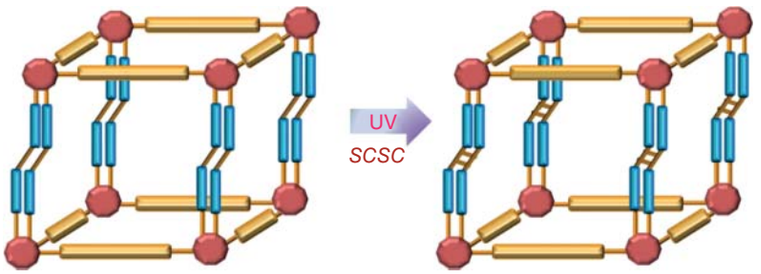


Figure 27 Schematic representation of post synthetic modification of 3D MOF using [2+2] photo-dimerization reaction

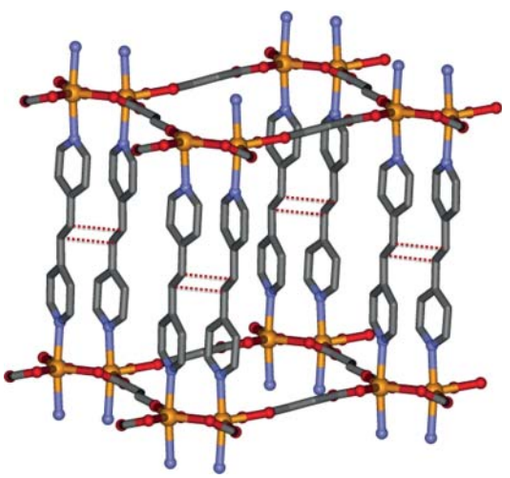


Figure 28 A portion of the photoreactive double-pillared MOF (**47**)

A similar Cd(II) analog, $[Cd_2(bpe)_2(fum)_2]$ **(47)** with a double-pillared MOF structure was also found to be photoreactive as shown in Figure 28.[58]

7.2 Photoreactive Double-Pillared MOFs with Conjugated C=C Bond Containing Ligands

So far spacer ligands containing single C=C bonds have been used extensively in photoreactive MOFs and ligands with two conjugated C=C bonds have been rarely used for this purpose. These ligands present many interesting possibilities for studying photoreactivity. (i) The 'face-to-face' aligned C=C bonds can undergo double [2+2] cycloaddition reaction. (ii) One C=C bond from each ligand can also take part in the cyclobutane formation, if the ligand pair is arranged in an 'out-of-phase' manner. (iii) If only one C=C bond pair is aligned between any two adjacent spacer ligands in a slip-stacked ("out-of-phase") manner forming a plane, then the photo-dimerization of these C=C bond pairs in the solid state is expected to furnish an organic polymer by [2+2] cycloaddition reaction. The first two situations have been encountered in the two photoreactive MOFs $[Zn_4(\mu_3\text{-}OH)_2(5\text{-}sipa)_2(1,4\text{-}bpeb)_2]\cdot 4H_2O$ **(48)** and $[Cd_2(1,3\text{-}pda)_2(1,4\text{-}bpeb)_2]$ **(49)** (5-H_3sipa = 5-sulfoisophthalic acid and 1,3-H_2pda = 1,3-phenylenediacetic acid) with the conjugated ligand, 1,4-bis[2-(4-pyridyl)ethenyl]benzene (bpeb).[59]

In the case of Zn(II) MOF, a 2D layer $[Zn_4(\mu_3\text{-}OH)_2(5\text{-}sipa)_2]$ with (6,3) connectivity related CdI_2 is formed by linking six equivalent 5-sipa with three equivalent $\{Zn_4(\mu_3\text{-}OH)_2\}$. Further the axial positions of these $\{Zn_4(\mu_3\text{-}OH)_2\}$ sheets are pillared by two pairs of bpeb ligands to form the double-pillared 3D network structure. Each bpeb pillar is arranged in between two other bpeb ligands, where one C=C bond is aligned 'in-phase' and the other in 'out of phase' manner satisfying the topochemical distance criteria. However, the 'in-phase' C=C bond pairs are crisscrossed and the 'out-of-phase' double bonds have parallel orientation. As a result, UV irradiation of this compound showed quantitative photoreaction between the 'out of phase' C=C pairs only and resulted in the formation of another 3D structure in an SCSC manner (Figure 29).[59]

In the case of Cd(II) MOF, **49** the (4,4) sheets formed by the $\{Cd_2(1,3\text{-}pda)_4\}$ are further pillared by the bpeb pairs to yield another double-pillared 3D structure. In the 'face-to-face' arrangement of the bpeb ligand-pairs, the C=C bonds are separated by 3.886 and 4.023 Å. The structural transformation takes place in an SCSC manner upon UV irradiation of these single crystals with the quantitative formation of double cyclobutane rings across bpeb pairs (Figure 29). This reaction is another example for the post-synthetic modification of double-pillar ligands into a single pillar by [2+2] cycloaddition reaction.[59]

7.3 Host–Guest Reactions in Pillared-Layer MOFs

The photoreactivity between the coordinated and guest bpe molecules present in the channels is described here. The layer structure of the pillared-layer CP $[Mn_2(HCO_2)_3(bpe)_2(H_2O)_2]$ $ClO_4\cdot H_2O\cdot$ bpe **(50)** is

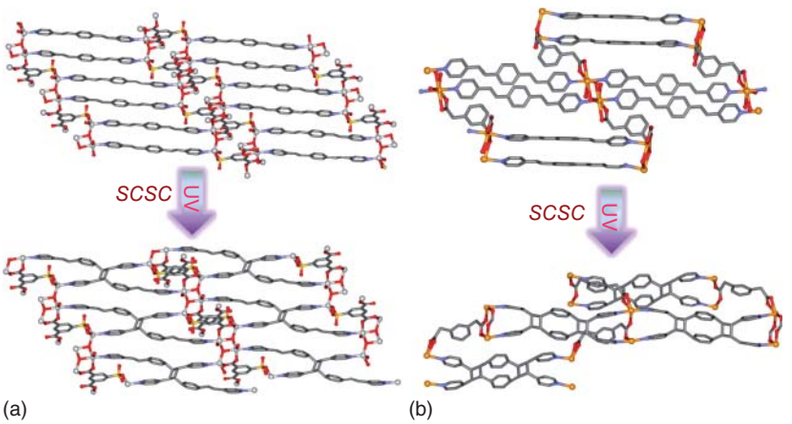


Figure 29 'Out of phase' photoreactivity of bpeb in **48** (a), and 'In-phase' photoreactivity of bpeb in **49** (b)

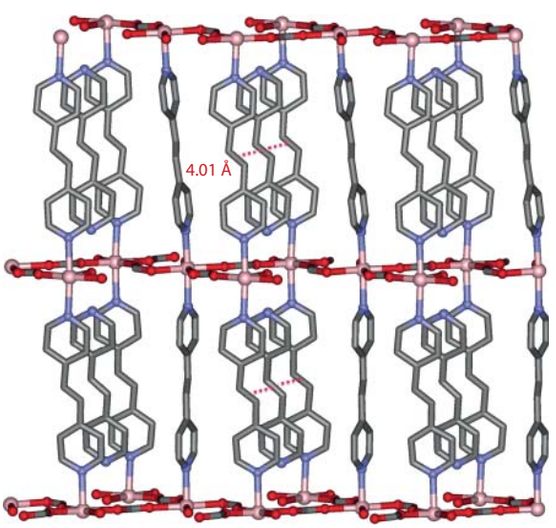


Figure 30 The alignment of bpe ligands and bpe guests in **50**

formed by $Mn_2(HCO_2)_3$ linked with bpe pillars.[60] Each Mn(II) is bonded to three other Mn(II) atoms through bridging formate ligands and an aqua ligand, whereas the two axial sites are occupied by the bpe ligands. Two different types of channels formed in this structure are occupied by the anions, lattice water and a guest bpe molecule. Incidentally, one of the coordinated bpe ligands is aligned parallel with a guest bpe (Figure 30) and further stabilized by the O–H···N hydrogen bonds with the aqua ligands. This pillared-layer is expected to be photoreactive to yield 66.7% cyclobutane product based on this host–guest interactions and was found to produce ~60% photo-product under UV light as monitored by the ^{1}H-NMR spectroscopy.[60] This appears to be the first [2+2] solid state photoreaction of a guest molecule with the framework structure.

7.4 Photoreactive Lanthanide-MOFs

Photoreactive CPs containing lanthanum(III) atoms with muconate ligands are described in this section. Muconate, an aliphatic linear spacer ligand with two conjugated C=C bonds in the backbone, offers mono and double cycloaddition as well as [4+4] cycloaddition products. The conversion of cyclobutane ring to cyclooctadiene by Cope rearrangement is another interesting reaction expected in this ligand system, whereas double [2+2] cycloaddition reaction can yield a highly strained ladderane structure.

Face-to-face parallel alignment between the muconate ligands has been achieved in two Ln(III) MOFs $[Ln_2(muco)_3(H_2O)_6]\cdot 2.5H_2O$ (H_2muco = *trans*,*trans*-muconic acid), Ln(III) = Er(III) **(51)** and Y(III) **(52)** in which the C=C bonds are separated by 3.60 Å and these compounds have been found to be photoreactive.[61] As mentioned earlier, identification of the photo product is challenging in these compounds in the absence of SCSC transformation. The solution ^{1}H-NMR spectroscopy has been routinely used to monitor the nature of products formed in the solids. Owing to the insoluble nature of some of these products, they are normally digested with acids to solubilize the organic moieties, and therefore, there is a possibility for these products to rearrange from one structure to another in this process in solution. Here the photo-irradiation of **51** showed the formation of ladderane structure with double [2+2] photo-cycloaddition reaction as shown in Figure 31, the reaction proceeds in an SCSC manner, where the single crystals are stable to 55% of photoreaction. This highly strained ladderane formation has also been characterized by other experimental evidences.[61] Similarly, isomorphs of the above structures have also been investigated and in all these compounds, the separation distance between the C=C bonds varies from 3.7 to 4.4 Å but not all are aligned in parallel.[62] However,

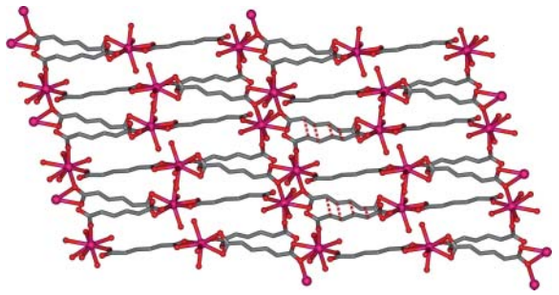


Figure 31 The structure of **51** that can produce ladderane structure upon UV irradiation is shown. The disordered atoms have been removed for clarity

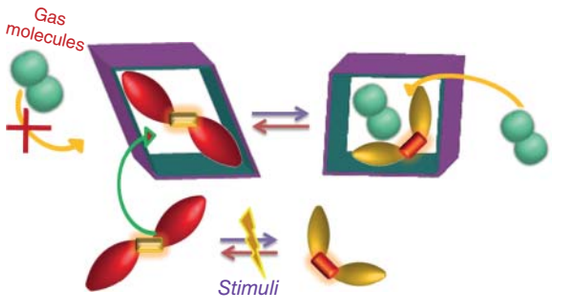


Figure 32 Reversible transformation of **53** by photo isomerization of azobenzene in the channels

all these compounds participated in the photoreaction as confirmed by ^{1}H-NMR spectral studies.

8 PHOTORESPONSIVE MOFs

8.1 Influence of Trans–Cis Isomerization on the Gas Adsorption Property of a MOF

The pore structure of the MOF $[Zn_2(bdc)_2(triethylenediamine)]$ (**53**) (pore size, 7.5×7.5 Å^2) is known to be deformed by the inclusion of certain aromatic guest molecules.[63] On the other hand, the *trans–cis* isomerization of azobenzene has been extensively investigated as photoresponsive materials.[26,64] Here how the *trans–cis* isomerization of azobenzene occupying the channels can influence the pore shape of a structurally dynamic MOF is nicely illustrated. The *trans* to *cis* isomerization under UV light changes the structure of MOF, whereas the thermal isomerization of *cis* to *trans* form results in a drastic switching of its adsorption property. The isomerization under UV light has been followed by the disappearance of the frequency at 690 cm^{-1} owing to the *trans* isomer and appearance of a new frequency at 697 cm^{-1} owing to the formation of *cis* isomer in the infra red (IR) spectroscopy. This isomerization is accompanied by the changes in the framework structure from orthorhombic to the tetragonal form (Figure 32). The nitrogen adsorption behavior is also changed owing to the dramatic change in the structure.[63]

8.2 Photoresponsive CO_2 Adsorption in 3D MOF

A MOF isostructural to MOF-5 was prepared with 2-(phenyldiazenyl)terephthalate ligand in the place of 1,4-benzenedicarboxylate. The cubic cavity was occupied by the azobenzene groups. The influence of the CO_2 gas uptake due to structural changes accompanied by the *trans–cis* isomerization was investigated. The CO_2 uptake in the original MOF sample in which the majority of azobenzene was present in *trans* form at RT was 22.9 cm^3 g^{-1} at 1 bar. After exposure to UV light for an hour the CO_2 uptake decreased to16.8 cm^3 g^{-1} and this corresponds to a 26.6% decrease in the CO_2 uptake. The CO_2 uptake was measured to be 10.5 cm^3 g^{-1} (an overall decrease of 53.9%) after sometime. This has been ascribed to the slow isomerization of *trans*-to-*cis* form arising from the steric hindrance among the azobenzene groups in the cavity. When this sample was kept in dark for a long time at 60 °C, the CO_2 uptake at 1 bar at RT has increased to 26.4 cm^3 g^{-1}, which might be due to the presence of *trans* isomer exclusively. This demonstrated reversible switching of CO_2 uptake owing to the two forms of azobenzene in the cavity (Figure 33).[65]

8.3 Dynamic Photo-Switching of Spacer Ligands in a MOF

Another dynamic light-induced structural changes that controls the CO_2 uptake was demonstrated in a triply interpenetrated pillared-layer structure $[Zn_2(AzDC)_2(bpe)]$ (**54**) (AzDC = 4,4′-azobenzene dicarboxylate). The 2D sheet formed by the paddle wheel SBU $Zn_2(O_2C\text{-}C)_4$ was further pillared by bpe ligands. Here although both carboxylates of AzDC ligands are bound to the metal strongly and not as pendant groups in the pores as noted before, the *trans*-to-*cis* isomerization, that is, the bending of azo groups and bpe, has been shown to occur on the local scale in a dynamic manner, irrespective of the use of broadband or filtered light sources. Overall, there was no structural change during this process as revealed by synchrotron X-ray diffraction studies. Further, on exposure to UV light, the MOF release 64% of the adsorbed CO_2 gas using broadband radiation and 42% desorption capacity under static conditions.[66]

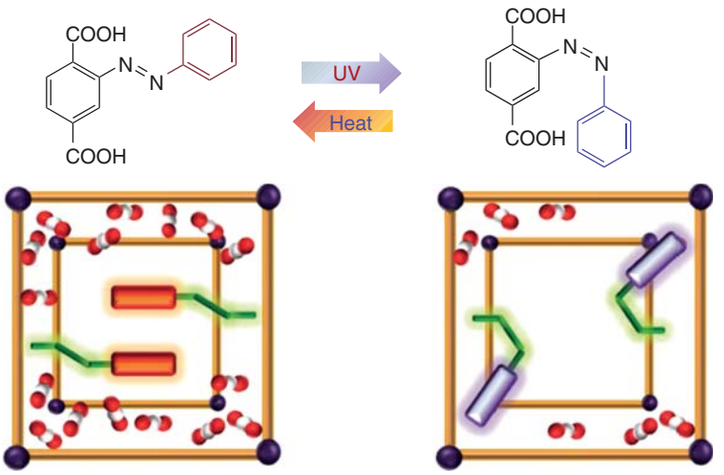


Figure 33 Influence of *trans*-to-*cis* isomerization of azo benzene groups on the porosity and CO_2 uptake

8.4 Light-Induced Release of Molecules from MOFs

Photothermal properties of gold nano-rods (GNRs) have been used to release the molecules from the MOFs along with the guest loading ability of the MOFs. Near infrared (NIR) light irradiation into the Plasmon bands of GNRs, electrons at the excited conduction band relax to the ground state, dissipating the excess energy into heat. Such localized heat release was designed to trigger molecular desorption or release by integrating the GNRs inside the MOFs in mesoscale so that the heat transfer will be effective. GNRs coated with Alumina was allowed to react in a microwave reactor with an organic ligand 1,4-naphthalenedicarboxylic acid H_2(1,4-ndc) as a linker to obtain a porous CP, GNR@[Al(OH)(1,4-ndc)]$_n$ (**55**). Metal@MOF composites were designed with controlled particle size for molecular release studies for the first time. For studying the molecular release, anthracene was loaded into the GNR@MOF composites by soaking it in cyclohexane solution for 24 h. The composites were washed to remove any excess surface molecules. The sample suspended in cyclohexane solution when irradiated with the Xenon lamp ($\lambda = 750$ nm) was found to release anthracene with time scale as compared to non-irradiated sample as depicted in Figure 34.[67]

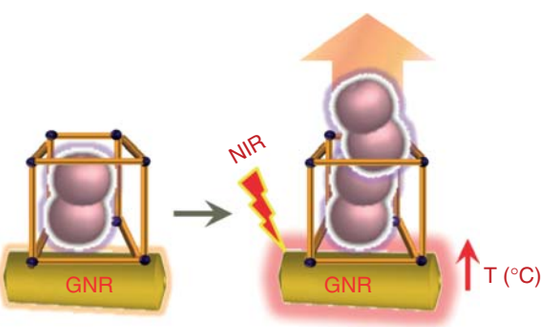


Figure 34 The light-induced release of molecules using the photoresponsive GNR incorporated within MOF

8.5 Photo-Isomerisation in 3D MOFs

Incorporation of photoactive metal complexes inside the MOFs provides specific environment without solvents. The solvothermal reaction of M(L)$(CO)_3$X with $MnCl_2$ (L = 2,2′-bipyridine-5,5′-dicarboxylate) furnished {Mn$(DMF)_2$[LRe$(CO)_3$Cl]} (**56**) and {Mn$(DMF)_2$[LMn$(CO)_3$Cl]} (**57**), which consists of L as linker and Mn(II) cation as node. The photoactive Re(diimine)$(CO)_3$Cl group shown in Figure 35(top), usually show ^{3}MLCT excited state character in solution. But in the constraints of space within MOF, the photo-induced excited state has been shown to be π–π* in character. Both metal complexes encapsulated in MOFs show *fac* and *mer* isomerism by photolysis as followed by solid-state Fourier transform infrared (FTIR) spectroscopy and confirmed by single crystal X-ray diffraction experiments (Figure 35).[68]

9 PHOTO-POLYMERIZATION IN CPs

Solid-state polymerization reactions have been investigated in Li(I), Na(I), K(I) acrylates and Ca(II), Ba(II) and Zn(II) methacrylates activated by ^{60}Co γ-rays.[69–77] Further, some of these compounds were also found to undergo thermal polymerization, but the final

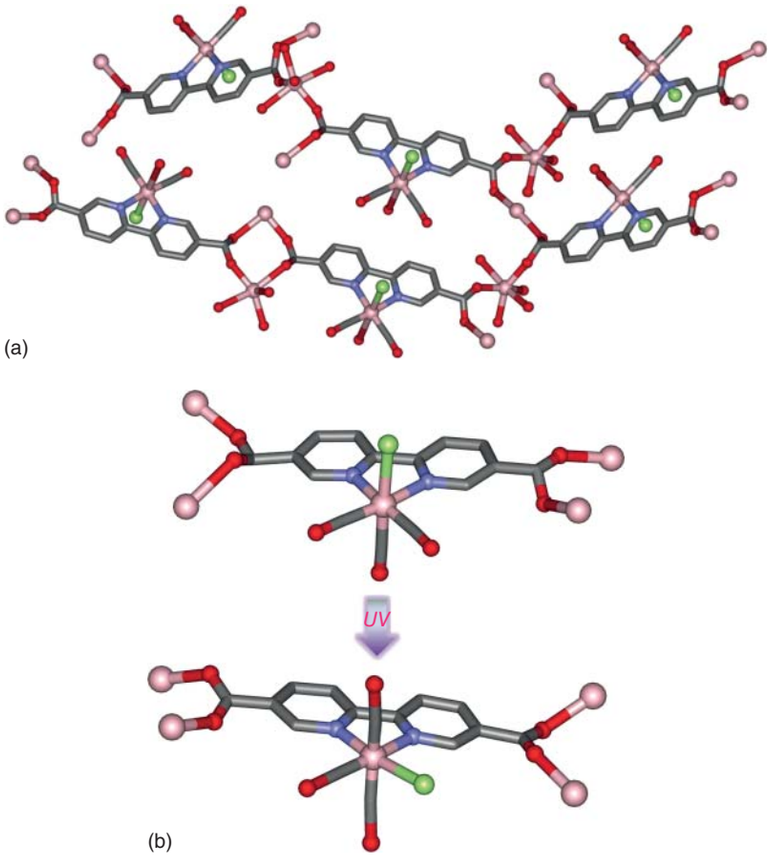


Figure 35 (a) Portion of the MOF and (b) the Mn complex spacer that is found to undergo photochemical isomerisation from *fac* to *mer*

structures of these compounds are not known since they do not retain their single crystallinity after the polymerization reaction.

10 SUMMARY

Various photochemical reactions occurring in CPs and MOFs have been discussed in this chapter. These result in interesting solid-state structural transformations affecting the connectivity, dimensionality, interpenetration and topology. Further [2+2] cycloaddition reactions have also been used for post-synthetic modification of surfaces to create reactive sites and radicals that are not possible by conventional synthetic routes, polymerization on the surfaces, *trans–cis* isomerization of the guest molecules in the cavities using the dynamic behavior of the structures, etc. Polymerization has also been observed in a number of CPs but the nature of the final products could only be predicted in the absence of crystal structures. Further, the [2+2] photochemical dimerization reaction has been used to follow the changes in the solid state, especially the formation of ladder structures from linear CPs, in the absence of crystal structures. Fortunately, most of the examples illustrated in this chapter maintain the single crystals at the end of the reactions to determine their solid state structures, thus allowing us to study the reactivity patterns unambiguously.

11 ACKNOWLEDGMENTS

The Ministry of Education, Singapore, is gratefully acknowledged for financial support through NUS FRC Grants R-143-000-562-112. We also thank nature publications for providing the copy right permissions for Figure 26.

12 RELATED ARTICLES

Porous Coordination Polymer Nanoparticles and Macrostructures; Mechanochemical Approaches

to Metal-Organic Frameworks; Postsynthetic Modification of Metal-Organic Frameworks; Gas Storage in Metal-Organic Frameworks; Open Metal Sites in Metal-Organic–Frameworks; Photoreactive Properties Hosted in Metal-Organic Frameworks; Single-Crystal to Single-Crystal Transformations in Metal-Organic Frameworks; Interpenetration and Entanglement in Coordination Polymers.

13 ABBREVIATIONS AND ACRONYMS

abdc = 5-amino-benzene-1,3-dicarboxylate; AzDC = 4,4′-azobenzene dicarboxylate; bdc = benzene dicarboxylic acid; Bpe = *trans*-1,2-bis(4-pyridyl)ethene or 4,4′-bipyridyl ethene; Bpeb = 1,4-bis[2-(4-pyridyl)ethenyl]benzene; Bpy = 4,4′-bipyridine; cca = 4-carboxycinnamate; CDO = chelidonic acid; chdc = *trans*-1,2-cyclohexanedicarboxylate; CP = coordination polymer; Calcd = calculated; cds = cadmium sulphide framework topology; CIF = Crystallographic Information File; CN = coordination number; CSD = Cambridge Structural Database; DMF = dimethylformamide; DMA = dimethylacetamide; DMSO = dimethylsulfoxide; DSC = differential scanning calorimetry; EtOH = ethanol; ESI-MS = electrospray ionisation mass spectrometry; FTIR = Fourier transform infrared; f.w = formula weight; GNR = gold nano rod; h = hour; HH = head to head; HT = head to tail; HTFA = trifluoroacetic acid; IR = infra red; MeCN = acetonitrile; MOF = metal-organic framework; moip = 5-methoxy-isophthalic acid; mp = melting point; MeOH = methanol; H_2muco = *trans*,*trans*-muconic acid; ndc = 2,6-naphthalenedicarboxylate; NIR = Near infrared NMR = nuclear magnetic resonance; OAc = acetate; PL = photoluminescence; pvba = *trans*-2-(4′-pyridyl)vinylbenzoic acid; *rctt*-tpcb = regio *cis*, *trans*, *trans*-*tetrakis*(4-pyridyl)cyclobutane; *rtct*-tpcb = regio *trans*, *cis*, *trans*-*tetrakis*(4-pyridyl)cyclobutane; RT = room temperature; SBU = secondary building unit; SCSC = single-crystal to single-crystal; 5-H_3sipa = 5-sulfoisophthalic acid; 4-spy = 4-styrylpyridine; tbdc = tetra bromodicarboxylic acid; TFA = trifluoroacetate; TGA = thermogravimetric analysis; UV = Ultraviolet; VT = variable temperature; XRPD = X-ray powder diffraction; 1D = one dimensional; 2D = two dimensional; 3D = three dimensional; 1,3-H_2pda = 1,3-phenylenediacetic acid.

14 REFERENCES

1. V. Ramamurthy and K. Venkatesan, *Chem. Rev.*, 1987, **87**, 433.
2. C. R. Theocharis and W. Jones, in 'Organic Solid State Chemistry', ed. G. R. Desiraju, Elsevier, 1987, p. 47.
3. B. S. Green, M. Lahav, and D. Rabinovich, *Acc. Chem. Res.*, 1979, **12**, 191.
4. W. Jones (ed.), 'Organic Molecular Solids: Properties and Applications', CRC Press, Boca Raton, 1997.
5. F. Toda, ed., 'Organic Solid State Reactions', Springer, Berlin, 2005.
6. A. E. Keating and M. A. Garcia-Garibay, in 'Organic and inorganic photochemistry', eds V. Ramamurthy and K. S. Schanze, Marcel Dekker, New York, 1998, p. 195.
7. K. Tanaka and F. Toda, *Chem. Rev.*, 2000, **100**, 1025.
8. F. Toda, *Acc. Chem. Res.*, 1995, **28**, 480.
9. E. Lee-Ruff and G. Mladenova, *Chem. Rev.*, 2003, **103**, 1449.
10. J. C. Namyslo and D. E. Kaufmann, *Chem. Rev.*, 2003, **103**, 1485.
11. J. Nishimura, Y. Nakamura, Y. Hayashida, and T. Kudo, *Acc. Chem. Res.*, 2000, **33**, 679.
12. M. D. Cohen, G. M. J. Schmidt, and F. I. Sonntag, *J. Chem. Soc. (Resumed)*, 1964, 2000.
13. G. M. J. Schimdt, *Pure Appl. Chem.*, 1971, **27**, 647.
14. G. R. Desiraju, J. J. Vittal, and A. Ramanan, 'Crystal Engineering. A Textbook', World Scientific, 2011.
15. G. K. Kole and J. J. Vittal, *Chem. Soc. Rev.*, 2013, **42**, 1755.
16. L. R. MacGillivray, G. S. Papaefstathiou, T. Frišćić, T. D. Hamilton, D.-K. Bučar, Q. Chu, D. B. Varshney, and I. G. Georgiev, *Acc. Chem. Res.*, 2008, **41**, 280.
17. K. Biradha and R. Santra, *Chem. Soc. Rev.*, 2013, **42**, 950.
18. M. Nagarathinam, A. M. P. Peedikakkal, and J. J. Vittal, *Chem. Commun.*, 2008, 5277.
19. M. Nagarathinam and J. J. Vittal, *Macromol. Rapid Commun.*, 2006, **27**, 1091.
20. J. J. Vittal, *Coord. Chem. Rev.*, 2007, **251**, 1781.
21. C. N. R. Rao and J. Gopalakrishnan, 'New Directions in Solid State Chemistry', 2nd edition, Edition en anglais edition, Cambridge University Press, 1997.
22. K. N. Houk, *Acc. Chem. Res.*, 1975, **8**, 361.
23. M. J. Bearpark, M. Deumal, M. A. Robb, T. Vreven, N. Yamamoto, M. Olivucci, and F. Bernardi, *J. Am. Chem. Soc.*, 1997, **119**, 709.
24. H. Morawetz, S. Z. Jakabhazy, J. B. Lando, and J. Shafer, *Proc. Natl. Acad. Sci. U. S. A.*, 1963, **49**, 789.
25. I. Halasz, *Cryst. Growth Des.*, 2010, **10**, 2817.
26. G. S. Kumar and D. C. Neckers, *Chem. Rev.*, 1989, **89**, 1915.
27. G. S. Papaefstathiou, I. G. Georgiev, T. Frišćić, and L. R. MacGillivray, *Chem. Commun.*, 2005, 3974.
28. R. Medishetty and J. J. Vittal, in 'Structure and Bonding', eds. B. Chen and G. Qian, Springer, London, 2014, Vol. 157, p. 105.

29. Q. Chu, D. C. Swenson, and L. R. MacGillivray, *Angew. Chem. Int. Ed.*, 2005, **44**, 3569.
30. S. Dutta, D.-K. Bučar, E. Elacqua, and L. R. MacGillivray, *Chem. Commun.*, 2013, **49**, 1064.
31. A. M. P. Peedikakkal, L. L. Koh, and J. J. Vittal, *Chem. Commun.*, 2008, 441.
32. A. M. P. Peedikakkal and J. J. Vittal, *Chem. Eur. J.*, 2008, **14**, 5329.
33. A. K. Paul, R. Karthik, and S. Natarajan, *Cryst. Growth Des.*, 2011, **11**, 5741.
34. N. L. Toh, M. Nagarathinam, and J. J. Vittal, *Angew. Chem. Int. Ed.*, 2005, **44**, 2237.
35. M. Nagarathinam and J. J. Vittal, *Aust. J. Chem.*, 2010, **63**, 589.
36. G. K. Kole, A. M. P. Peedikakkal, B. M. F. Toh, and J. J. Vittal, *Chem. Eur. J.*, 2013, **19**, 3962.
37. D. Liu, N.-Y. Li, and J.-P. Lang, *Dalton Trans.*, 2011, **40**, 2170.
38. Y.-C. Ou, W.-T. Liu, J.-Y. Li, G.-G. Zhang, J. Wang, and M.-L. Tong, *Chem. Commun.*, 2011, **47**, 9384.
39. R. Santra, K. Banerjee, and K. Biradha, *Chem. Commun.*, 2011, **47**, 10740.
40. J. F. Eubank, V. C. Kravtsov, and M. Eddaoudi, *J. Am. Chem. Soc.*, 2007, **129**, 5820.
41. M. Nagarathinam and J. J. Vittal, *Angew. Chem. Int. Ed.*, 2006, **45**, 4337.
42. M. Nagarathinam and J. J. Vittal, *Chem. Commun.*, 2008, 438.
43. J. Even and M. Bertault, *J. Chem. Phys.*, 1999, **110**, 1087.
44. K. D. M. Harris, J. M. Thomas, and D. Williams, *J. Chem. Soc. Faraday Trans.*, 1991, **87**, 325.
45. V. Kannan and G. R. Desiraju, *Proc. Indian Acad. Sci (Chem.Sci.)*, 1986, **96**, 351-362.
46. A. Chanthapally, W. T. Oh, and J. J. Vittal, *CrystEngComm*, 2013, **15**, 9324.
47. D. Liu, J.-P. Lang, and B. F. Abrahams, *Chem. Commun.*, 2013, **49**, 2682.
48. A. M. P. Peedikakkal and J. J. Vittal, *Inorg. Chem.*, 2010, **49**, 10.
49. Y. C. Ou, D. S. Zhi, W. T. Liu, Z. P. Ni, and M. L. Tong, *Chem. Eur. J.*, 2012, **18**, 7357.
50. A. Michaelides, S. Skoulika, and M. G. Siskos, *Chem. Commun.*, 2004, 2418.
51. X.-H. Miao and L.-G. Zhu, *Dalton Trans.*, 2010, **39**, 1457.
52. A. Chanthapally, G. K. Kole, K. Qian, G. K. Tan, S. Gao, and J. J. Vittal, *Chem. Eur. J.*, 2012, **18**, 7869.
53. H. Sato, R. Matsuda, M. H. Mir, and S. Kitagawa, *Chem. Commun.*, 2012, **48**, 7919.
54. M.-H. Xie, X.-L. Yang, and C.-D. Wu, *Chem. Eur. J.*, 2011, **17**, 11424.
55. R. Medishetty, L. L. Koh, G. K. Kole, and J. J. Vittal, *Angew. Chem. Int. Ed.*, 2011, **50**, 10949.
56. H. Sato, R. Matsuda, K. Sugimoto, M. Takata, and S. Kitagawa, *Nat. Mater.*, 2010, **9**, 661.
57. M. H. Mir, L. L. Koh, G. K. Tan, and J. J. Vittal, *Angew. Chem. Int. Ed.*, 2010, **49**, 390.
58. A. Michaelides, S. Skoulika, and M. G. Siskos, *CrystEngComm*, 2008, **10**, 817.
59. D. Liu, Z.-G. Ren, H.-X. Li, J.-P. Lang, N.-Y. Li, and B. F. Abrahams, *Angew. Chem. Int. Ed.*, 2010, **49**, 4767.
60. X.-Y. Wang, Z.-M. Wang, and S. Gao, *Chem. Commun.*, 2007, 1127.
61. A. Michaelides, S. Skoulika, and M. G. Siskos, *Chem. Commun.*, 2011, **47**, 7140.
62. A. Michaelides, S. Skoulika, and M. G. Siskos, *Chem. Commun.*, 2013, **49**, 1008.
63. N. Yanai, T. Uemura, M. Inoue, R. Matsuda, T. Fukushima, M. Tsujimoto, S. Isoda, and S. Kitagawa, *J. Am. Chem. Soc.*, 2012, **134**, 4501.
64. A. A. Beharry and G. A. Woolley, *Chem. Soc. Rev.*, 2011, **40**, 4422.
65. J. Park, D. Yuan, K. T. Pham, J.-R. Li, A. Yakovenko, and H.-C. Zhou, *J. Am. Chem. Soc.*, 2012, **134**, 99.
66. R. Lyndon, K. Konstas, B. P. Ladewig, P. D. Southon, P. C. J. Kepert, and M. R. Hill, *Angew. Chem. Int. Ed.*, 2013, **52**, 3695.
67. K. Khaletskaya, J. Reboul, M. Meilikhov, M. Nakahama, S. Diring, M. Tsujimoto, S. Isoda, F. Kim, K.-I. Kamei, R. A. Fischer, S. Kitagawa, and S. Furukawa, *J. Am. Chem. Soc.*, 2013, **135**, 10998.
68. A. J. Blake, N. R. Champness, T. L. Easun, D. R. Allan, H. Nowell, M. W. George, J. Jia, and X.-Z. Sun, *Nat. Chem.*, 2010, **2**, 688.
69. M. J. Vela, V. Buchholz, V. Enkelmann, B. B. Snider, and B. M. Foxman, *Chem. Commun.*, 2000, 2225.
70. M. J. Vela, B. B. Snider, and B. M. Foxman, *Chem. Mater.*, 1998, **10**, 3167.
71. M. Inoki, F. Akutsu, Y. Kitayama, Y. Kasashima, and K. Naruchi, *Macromol. Chem. Phys.*, 1998, **199**, 619.
72. M. Kudoh, F. Akutsu, E. Nakaishi, T. Kobayashi, K. Naruchi, and M. Miura, *Macromol. Rapid Commun.*, 1994, **15**, 239.
73. N. W. Alcock, P. de Meester, and T. J. Kemp, *J. Chem. Soc. Perkin Trans.*, 1979, **2**, 921.
74. F. M. Costaschuk, D. F. R. Gilson, and L. E. St. Pierre, *Macromolecules*, 1971, **4**, 16.
75. F. M. Costaschuk, D. F. R. Gilson, and L. E. St. Pierre, *Macromolecules*, 1970, **3**, 393.
76. M. J. Bowden, J. H. O'Donnell, and R. D. Sothman, *Die Makromol. Chem.*, 1969, **122**, 186.
77. J. H. O'Donnell and R. D. Sothman, *J. Polym. Sci. Part A: Polym. Chem.*, 1968, **6**, 1073.

Edible Metal-Organic Frameworks

Ross Stewart Forgan

University of Glasgow, Glasgow, UK

1	Introduction	159
2	Synthetic Considerations	159
3	Choice of Metal Ion	161
4	Choice of MOF Strut(s)	161
5	Conclusions and Outlook	170
6	Acknowledgments	170
7	Abbreviations and Acronyms	170
8	References	171

1 INTRODUCTION

Metal-organic frameworks (MOFs) are composed of metal or metal cluster joints connected in one, two, or three dimensions by multidentate organic linker ligands—the so-called struts—to form infinite crystalline network structures in which ordered arrays of nanoscale pores and/or channels are present.[1] MOFs that display permanent porosity, as a result of removing interstitial solvents or template molecules from their "hollow" interiors, have found application in numerous technologies because they possess very high internal surface areas and prodigious molecular storage capacities.[2] Active areas of research include the storage of gases (see ***Gas Storage in Metal-Organic Frameworks***), for example, carbon dioxide capture and hydrogen storage for energy applications, using MOFs to separate compounds of interest, carrying out heterogeneous catalysis within the pores of MOFs and, more recently, application in biomedical settings as drug delivery vectors.[3]

The principles behind using MOFs as drug delivery agents are simple—the porous MOF can encapsulate and store very large quantities of the bioactive compound and release it slowly upon administration.[4] This approach overcomes potential issues with the stability and solubility of the molecule of interest. MOFs have been shown (Figure 1) to encapsulate and slowly release drug molecules such as Ibuprofen,[5] Doxorubicin, Busulfan,[6] and Procainamide·HCl,[7] and research volume in this nascent field is expanding.

To date, the vast majority of research into medicinal application of MOFs has focused on ex vivo or in vitro experiments to assess their functionality and toxicity, with the exception of very promising recent studies into the intravenous dosing of iron-based MOF nanoparticle formulations into mice.[6,8] It would obviously be highly desirable for MOFs to be administered oral as well as intravenously to allow widespread public distribution of any marketable product, yet very little information abounds regarding *edible MOFs*. Clearly, for any MOF to be considered fit for human consumption, numerous factors must be considered during their design and synthesis, including choice of metal ion(s), linker(s), solvent(s), and synthetic method, and also the final particle size and modes of digestion and excretion if the MOF structure persists within the body. This chapter discusses the synthetic parameters that must be considered and also some recent advances in preparing MOFs that may be fit for human consumption.

2 SYNTHETIC CONSIDERATIONS

A wide range of techniques have been harnessed in the preparation of MOFs, including, but not limited to, solvothermal, hydrothermal, microwave, sonochemical, electrochemical, and mechanochemical (see ***Mechanochemical Approaches to Metal-Organic Frameworks***) syntheses, as well as simple batch-scale

Metal-Organic Framework Materials. Edited by Leonard R. MacGillivray and Charles M. Lukehart.
© 2014 John Wiley & Sons, Ltd. ISBN 978-1-119-95289-3

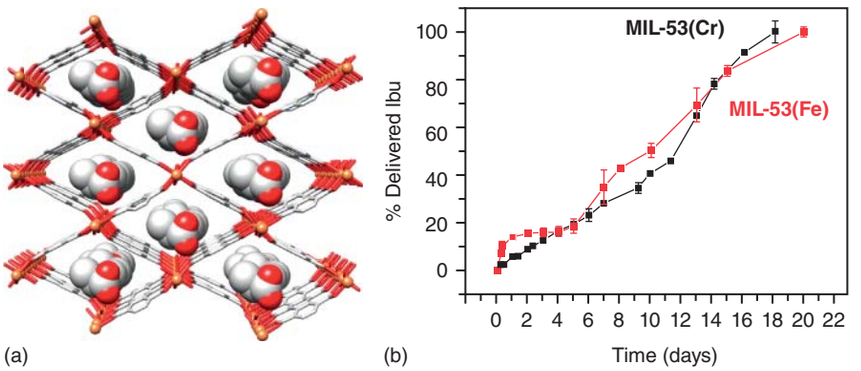


Figure 1 (a) The crystal structure of MIL-53(Fe), a flexible iron terephthalate MOF, loaded with Ibuprofen molecules (CCDC deposition EFEGOM). Solvent molecules and hydrogen atoms removed for clarity. (b) Release profiles of Ibuprofen (Ibu) from MIL-53(Fe) and MIL-53(Cr). (Reprinted with permission from Ref. 5. Copyright (2008) American Chemical Society.)

mixing.[9] The inclusion of interstitial solvents of crystallization within the pores of MOFs is ubiquitous in their synthesis, and, if MOFs are to be truly edible, it would be highly desirable to exclude harmful organic solvents altogether from their synthesis. Crystal morphology is also a factor that must be considered when assessing synthetic methodology with a view to end-user applications, for example, particle size may affect the rate of release of cargo loaded into MOFs upon ingestion.

An excellent illustrative example[10] of a synthetic optimization is that of MIL-88A nanoparticles for use in drug delivery applications. MIL-88A (MIL denotes Materials from Institut Lavoisier) is a flexible MOF composed of Fe(III) cations linked by fumarate dianions; fumaric acid is one of a series of endogenous diacids that play a role in the Krebs cycle in living cells (Section 4.2). Initial syntheses at the discovery stage involved solvothermal heating of iron(III) acetate and fumaric acid in methanol, a highly toxic solvent, which produced a microcrystalline material with a particle size range 2–25 μm. A systematic study of solvothermal reaction conditions found that water was a suitable replacement solvent in generating appreciable yields of crystalline material from $FeCl_3$ and fumaric acid, but with suboptimal control over the polydispersity of the particles that result from the hydrothermal preparation. Moving to a sonochemical approach in aqueous solution improved particle monodispersity but dramatically lowered yields, ruling it out for

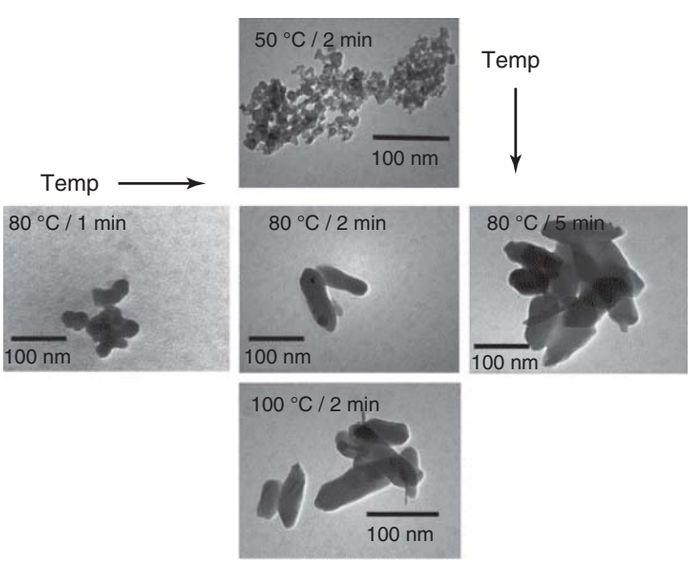


Figure 2 TEM images illustrate the effect of microwave reaction time and temperature on the size and morphology of MIL-88A nanoparticles. (Reproduced from Ref. 10 with permission from The Royal Society of Chemistry.)

bulk synthesis. Finally, microwave heating of aqueous solutions of MIL-88A precursors was examined and found to be a highly effective synthetic route, giving nanoparticles of controllable size and PDI values of less than 0.20 in yields of approximately 60%. MOF crystallite size can be adjusted (Figure 2) by varying the time, temperature, reagent concentration, and the pressure inside the reactor vessel during reactions.

This study is highly representative of a typical refinement of MOF preparation when a particular morphology is desirable to suit certain applications in that it requires an element of trial-and-error. Should the target application be drug delivery, the added considerations of both formulation and nontoxicity further restrict synthetic parameter space. For edible MOFs, water is obviously the most desirable solvent of choice, but organic solvents of relatively low toxicity, such as ethanol and ethyl acetate, which are ingested regularly by humans, may also be utilized. Some mechanochemical synthetic routes exclude solvent altogether (see ***Mechanochemical Approaches to Metal-Organic Frameworks***) and will also play an important role in the future synthesis of edible MOFs.

3 CHOICE OF METAL ION

The metal ions used to assemble MOFs are not only the prime structure-directing component but they also present arguably the greatest toxicity risk if they are to be ingested. While highly toxic metal ions, such as chromium, cadmium, and lead, should be excluded outright, one must consider the speciation of metal ions in the body if they are leached from the MOF. An obvious selection criterion would be limiting metal ions to those which are required bodily nutrients. Serre and Horcajada have collated toxicity data, as well as daily dose recommendations, of various metal ions that have been used in the assembly of MOFs.[4] It should again be noted that LD_{50} values for metal ions are usually only available for simple metal salts; these data act as a useful guide, but do not consider the speciation (oxidation state, ligand sphere) of metal ions upon metabolism of the MOF.

Metal ions with low toxicity that are poorly absorbed by the body, such as iron, magnesium, calcium, and zinc, are attractive candidates. Of these, iron and zinc have been extensively applied in MOF synthesis, perhaps owing to the kinetic lability of certain oxidation states and their affinity for carboxylate donors. Other metals are also suitable, depending on their toxicity in comparison to necessary dosage, but the toxicity of the MOF itself will originate from its metabolites, and so careful scrutiny of the speciation and breakdown of the MOF in the human body is obviously required.

4 CHOICE OF MOF STRUT(s)

As with the metal source, the organic linker molecules chosen to prepare the MOF must be nontoxic and biocompatible. In this regard, MOF struts can be classed as either (i) endogenous, if they are readily produced within the body in metabolic processes, or (ii) exogenous, if they are not. A much greater variety of ligands are available in comparison to metal ions; there are many subgroups of potential edible MOF struts that have been examined, some with inspiration from nature[11] and some not. A selection of MOFs prepared from ligands that one would expect to be nontoxic are described in the next sections on the condition that they do not contain heavy metal cations.

4.1 Exogenous Ligands

After nearly two decades of intensive research activity, there exist a great number of MOFs composed of myriad organic linkers. Most of these linkers, or struts, are synthetically derived and can be classified as exogenous, that is, they are not involved in any natural processes in the body. Despite this, many exogenous linkers will exhibit low toxicity, and a large proportion will have no available safety data whatsoever; clearly a considerable fraction of known MOFs will be composed of components suitable for human consumption, but their safety can only be determined after extensive testing.

One strut that has received particular scrutiny happens to be one of the most widely used in the synthesis of MOFs: terephthalic acid, also known as 1,4-benzenedicarboxylic acid. As one of the precursors of polyethylene terephthalate (PET), a polymer found in a range of food packaging, it is produced globally on a massive scale and is also the main component of some of the best-known MOFs, including MOF-5[12] (Figure 3a) and the MIL-53[5,13] series (Figure 3b). A wide range[14] of animal studies point to an LD_{50} value for terephthalic acid in rats of considerably greater than 1000 mg kg^{-1}—no matter the method of exposure—and it is considered of low risk to humans, although no experimental data are available.

If one assumes that terephthalate-based MOFs would be metabolized in the body simply to terephthalic acid, then perhaps examples with benign metals, for example, MIL-53(Fe), could be considered edible. This simplification does not consider any potential nanotoxicological health issues associated with the size of any persistent MOF particles. Similarly, trimesic acid (1,3,5-benzenetricarboxylic acid) is considered safe for human consumption, although toxicity data is based again on animal studies. Trimesic acid has been widely used as a MOF strut, with the copper trimesate HKUST-1[15] (Figure 3c) being examined for a number of applications.

Clearly, a number of the synthetically derived ligands that have been incorporated into MOFs will

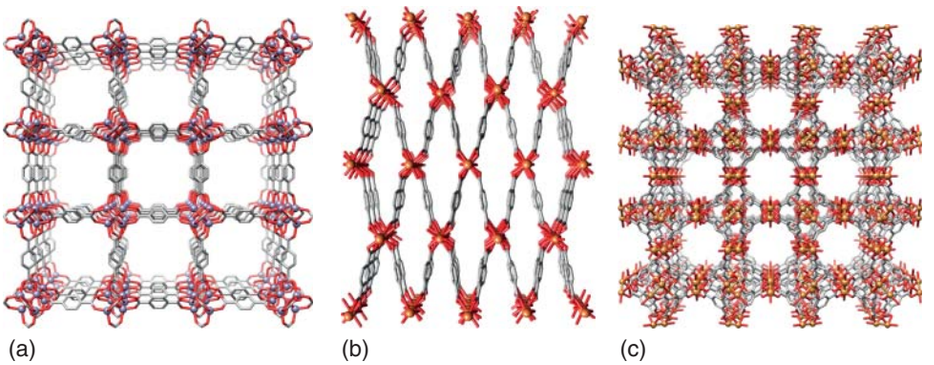


Figure 3 Solid-state structures of archetypal MOFs containing simple exogenous ligands. (a) MOF-5 (CCDC deposition SAHYIK), a cubic zinc terephthalate. (b) The flexible iron terephthalate, MIL-53(Fe)_lt (CCDC deposition POJTUE), in its hydrated, as-synthesized form. (c) HKUST-1 (CCDC deposition FIQCEN), a copper trimesate. Non-coordinated solvents and protons removed for clarity

be fit for human consumption. To ensure that any MOF—exogenous ligands or not—is suitable for a medical application, comprehensive testing on both the toxicity of the ligand itself and the speciation of metabolized MOF in the body are a necessity.

4.2 Endogenous Ligands

A number of simple carboxylic acids are known to be produced within the body, and so can be classed as endogenous ligands. Diacids such as fumaric, succinic, and malic acid are constantly synthesized and metabolized in cells during the Krebs cycle, whereas formic, oxalic, lactic, glutaric, and tartaric acid also play significant roles in biological processes (amino acids are discussed in Section 4.3). These endogenous linkers can be considered edible and have been extensively employed in MOF assembly—both transition metal and lanthanide formates with extended structures are commonplace, as well as metal oxalates, lactates, and tartrates—but this section focuses on a specific example, MIL-88A (Figure 4), which has found further application owing to its low toxicity and interesting properties.[16]

The optimized synthesis of MIL-88A, an iron(III) fumarate, has already been described in Section 2.[10] The structure of MIL-88-as (as stands for as-synthesized, Figure 4a) is composed of trimers of octahedral Fe^{3+} cations linked by one terminus of the fumarate dianions, with a central μ_3-O^{2-} ligand and three capping methanol solvent molecules generating an $[Fe_3O(O_2C\text{-}R)_6(solvent)_3]^+$ six-connected secondary building unit (SBU). Counterions and solvents are found in the pores of the material, which are linked by one-dimensional channels. The framework displays remarkable flexibility when solvents are exchanged or removed.[17] Drying the as-synthesized material at 150 °C yields a contracted form, MIL-88-dried, which can be rapidly resolvated under ambient conditions, for example, exposure to moisture yields the considerably expanded MIL-88-H_2O (Figure 4b).

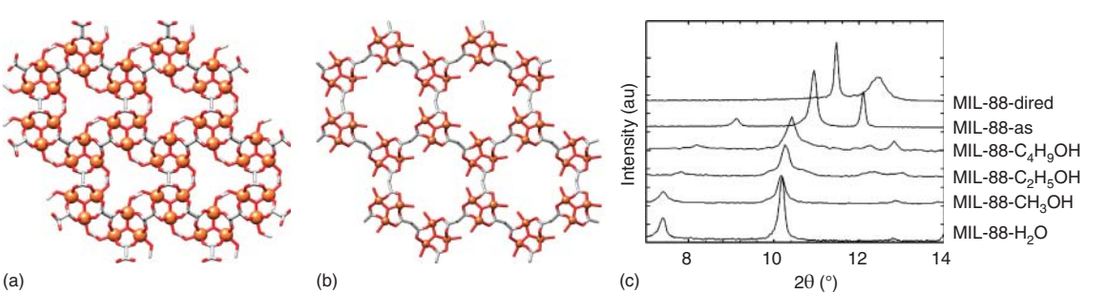


Figure 4 (a) The solid-state structure of MIL-88-as (CCDC deposition FAVKAP). (b) The solid-state structure of MIL-88-H_2O (CCDC deposition REZXIE01). Non-coordinated solvents, counterions, and protons removed for clarity. (c) Stacked partial powder X-ray diffraction patterns of MIL-88 samples with varying levels and types of solvation, illustrating the considerable flexibility of the framework with respect to the presence and removal of guest molecules. (Reprinted (adapted) with permission from Ref. 17. Copyright (2005) American Chemical Society.)

Powder X-ray diffraction analysis (Figure 4c) of a number of samples of MIL-88 with varying levels of solvation demonstrates the flexibility and robustness of the framework, as guest molecules are removed and introduced. The hexagonal space group $P\bar{6}2c$ is retained throughout, with the *a* axis increasing (9.26–13.87 Å) and the *c* axis decreasing (15.31–12.66 Å) in length as the unit cell volume doubles (1135–2110 $Å^3$) upon solvation. This guest-dependent flexibility has been exploited in the efficient (8% *w*/*w*) loading of the anticancer drug busulfan into MIL-88A, which can dually act as an MRI contrast agent as a result of the Fe^{3+} cations, as well as a drug delivery vector.[6]

4.3 Amino Acids

Amino acids have been incorporated into MOFs, as they are not only excellent metal binders with multiple coordination sites, but also readily available in enantiopure forms to facilitate the synthesis of homochiral MOFs, which have potential applications in enantioselective separations. MOFs prepared from simple amino acids usually exhibit lower dimensionality, as the stability of the bidentate NO chelating motif involving the carboxylate and amino moieties dominates, leaving only the second oxygen donor atom of the carboxylate to bridge into extended structures. Two general tactics have been employed in the pursuit of three-dimensional amino-acid frameworks: (i) use of an amino acid with a metal-binding side chain and (ii) incorporation of co-ligands. This section focuses on aspartic acid, which contains a $–CH_2COOH$ side chain.

The versatility of the aspartate ligand was exploited by Jacobson to prepare two extended nickel(II) species—a one-dimensional helical chain structure and a related three-dimensional net—by varying synthetic conditions (Figure 5).[18] Hydrothermal reaction of a mixture of $NiCl_2$, L-aspartic acid, and triethylamine at 150 °C yields a material formulated as $[Ni_2O(L\text{-}Asp)(H_2O)_2]\cdot 4H_2O$, a chiral helical structure wherein trimeric nickel units, chelated by aspartate dianions, are linked infinitely to form solely right-handed helices. Use of racemic aspartic acid as a starting material generates an analogous structure composed of an equal arrangement of left- and right-handed helices.

The aspartate dianion coordinates (Figure 5a) to five Ni^{2+} cations using all its donor atoms: four through monodentate coordination by carboxylate oxygen donors and a fifth by a tridentate *fac* motif through two carboxylate oxygen atoms (both of which bridge to a further Ni^{2+} unit) and the nitrogen atom. The handedness of the helices (Figure 5b) is dependent on the chirality of the aspartic acid starting material.

Carrying out the reaction at increased pH, achieved by the addition of further equivalents of triethylamine, results in the isolation of a three-dimensional network, $[Ni_{2.5}(OH)(L\text{-}Asp)_2]\cdot 6.55H_2O$. Analogous one-dimensional helices are observed, which are linked across the plane by $[Ni(L\text{-}Asp)_2]^{2-}$ subunits (Figure 5c) to yield a three-dimensional structure (Figure 5d), which is permanently porous with a BET surface area from N_2 uptake isotherm data of 157 $m^2\ g^{-1}$. This second aspartate dianion coordinates the linking Ni^{2+} ion in a *fac* motif through the

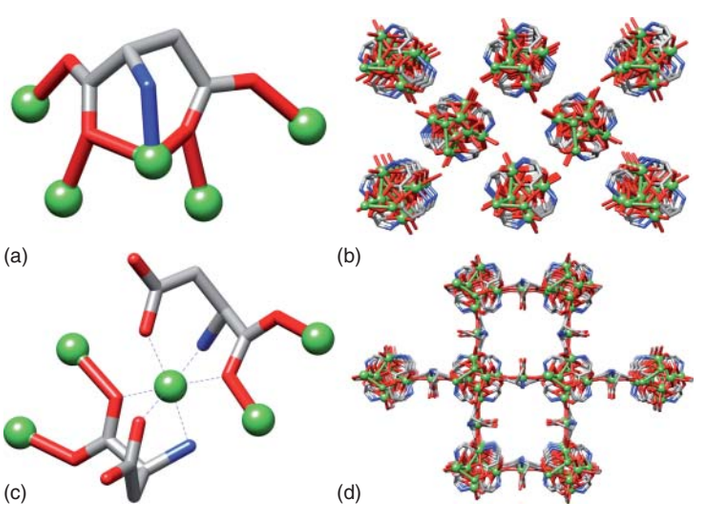


Figure 5 The solid-state structures of two related nickel aspartates. (a) The coordination of five Ni^{2+} cations to one aspartate ligand facilitates the formation of (b) homochiral helices in the packing arrangement of $[Ni_2O(L\text{-}Asp)(H_2O)_2]\cdot 4H_2O$ (CCDC deposition IVODOM). Linking of these helices through (c) further nickel aspartate coordination units yields (d) the three-dimensional homochiral framework $[Ni_{2.5}(OH)(L\text{-}Asp)_2]\cdot 6.55H_2O$ (CCDC deposition VEQBID), which is permanently porous. All non-coordinated solvents and protons removed for clarity

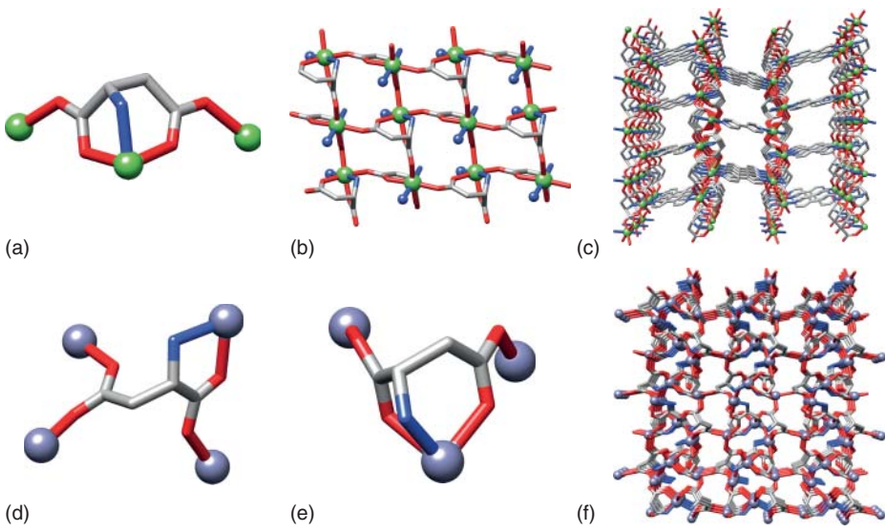


Figure 6 In the solid-state structure of $[Ni_2(L\text{-}Asp)_2(bipy)]\cdot CH_3OH\cdot H_2O$ (CCDC deposition PEPKUR), (a) each aspartate coordinates to three Ni^{2+} ions to form (b) two-dimensional sheets with free coordination sites (blue sphere) on each Ni^{2+} center, with 4,4′-bipyridine ligands linking the sheets to generate (c) a three-dimensional porous structure. The crystal structure of [Zn(L-Asp)] (CCDC deposition NUVLOG) is highly complex, with both (d) tetradentate aspartates and (e) tridentate aspartates, contributing to (f) a homochiral network. All solvents and protons removed for clarity

nitrogen atom and two carboxylate oxygen donors, while connecting the helices through further coordination of two Ni^{2+} atoms by one carboxylate unit, that is, these second aspartate ligands only link three Ni^{2+} cations.

Incorporation of secondary ligands can increase the pore space of amino acid-based MOFs. Rosseinsky *et al.* conceived a synthetic approach wherein pre-prepared $[Ni(Asp)_2]\cdot 3H_2O$ was combined hydrothermally with bidentate nitrogen donor ligands, such as 4,4′-bipyridine (bipy), to give extended structures.[19] The compound $[Ni_2(L\text{-}Asp)_2(bipy)]\cdot CH_3OH\cdot H_2O$, prepared hydrothermally in water/methanol mixtures, displays chiral Ni(L-Asp) sheets connected by the bipy ligands. The aspartate anions coordinate (Figure 6a) a Ni^{2+} cation in a tridentate *fac* motif through the nitrogen atom and one oxygen donor from each carboxylate group, with the second oxygen atom from the carboxylates coordinating to neighboring metal ions—each Ni^{2+} center is bound to three aspartates—forming (Figure 6b) a two-dimensional sheet structure. There remains one further coordination site on the Ni^{2+} cations, which is occupied by a nitrogen atom of the bipy auxiliaries that serve to link the sheets into a three-dimensional network (Figure 6c).

It should be noted that control of water content is key in retaining the enantiopurity of the material, as racemization of the L-Asp ligand occurs at high water:methanol ratios. The chirality of the framework endows it with enantioselective sorption properties in the vapor uptake of chiral diols, with an observed enantiomeric excess (ee) of 54% for the uptake of 2-methyl-2,4-pentanediol, which fits snugly within the chiral channels of the material and interacts via hydrogen bonding with the aspartate component of the framework.

One final example from the Rosseinsky group is a three-dimensional framework composed of an equal ratio of Zn^{2+} cations to Asp^{2-} anions.[20] This network is prepared in bulk by refluxing a mixture of $ZnCO_3$ and aspartic acid in aqueous methanol, yet single crystals of the material can be isolated from a solvothermal reaction involving $ZnCO_3\cdot 2ZnO\cdot 3H_2O$, aspartic acid and 4,4′-bipyridine in aqueous methanol. The bipy ligands do not take part in structure formation; presumably they act as a base rather than a component in the crystallization process. Unusually, three independent Zn^{2+} cations, with tetrahedral, trigonal bipyramidal, and octahedral geometries, in turn, are observed, while three crystallographically distinct aspartate anions (Figure 6d and e) are also present. Two have the same coordination motif, forming a bidentate chelate to a Zn^{2+} center through the nitrogen atom and one carboxylate oxygen donor, whereas the remaining three oxygen atoms each coordinate to a separate Zn^{2+} cation. The other aspartate ligand exhibits the same coordination motif as the Ni^{2+} cations in the previous example, binding one metal ion with a tridentate *fac* arrangement through the amine nitrogen and two carboxylate oxygens, with the remaining oxygen donors linking two further Zn^{2+} cations. While the complex network (Figure 6f) is nonporous—interstitial water molecules can be removed without damaging the framework, but the dehydrated material does not sorb H_2—it serves as an interesting example of a MOF composed solely of metal ions and amino acid linkers.

This final example sums up nicely many of the features of amino acid-based MOFs. Considerable complexity and homochirality can result from relatively simple linkers, yet auxiliary ligands are often required to induce permanent porosity. Care must be taken to ensure that these co-ligands are not harmful to health for these materials to form the basis of functional treatments.

4.4 Peptides

Peptide-based MOFs are the obvious next step from amino acid-based MOFs, offering a much greater diversity of possible linkers and coordination motifs as a result of the amide bond(s) between amino acid residues. Despite these observations, there are relatively few examples in the literature, and nearly all are limited to MOFs composed of simple dipeptides linked by divalent metal cations such as Zn(II) and the toxic heavy metals Cd(II) and Pb(II).

Two early zinc dipeptide frameworks (Figure 7) were reported by separate Japanese groups, with Zn^{2+} cations being linked by glycylglycine (gly-gly)[21] and glycylthreonine (gly-thr),[22] respectively. The structures of both MOFs involve an octahedral Zn^{2+} cation coordinated by (i) two NO chelates composed of the terminal NH_2 group and the amido oxygen atom and (ii) two monodentate oxygen atoms from the deprotonated terminal carboxylate unit, that is, each peptide coordinates two Zn^{2+} cations. In [Zn(gly–gly)$_2$], the bidentate NO chelates (Figure 7a) are disposed *trans* to one another with the carboxylate groups occupying the apical positions, forming two-dimensional sheets that are linked by hydrogen bonding through interstitial water molecules to form channels (Figure 7b). In [Zn(gly-thr)$_2$], the NO chelates are oriented (Figure 7c) *cis* to one another, as are the carboxylate groups. Two-dimensional sheets are again formed, with extensive hydrogen bonding arranging them in a perfect stack, forming porous channels (Figure 7d) along the crystallographic *c* axis.

Although both groups commented on the potentially porous nature of these frameworks, neither investigated their properties. Rosseinky *et al.* modified the synthesis of [Zn(gly-thr)$_2$], avoiding the use of barium salts as precipitants, and studied the absorption properties of the framework in detail.[23] Removal of methanol solvent molecules from the channels, by heating under vacuum, yields a rigid permanently porous material that exhibits a BET surface area, measured by CO_2 uptake isotherms, of 192 $m^2\ g^{-1}$. Interestingly, the material shows no uptake of N_2 and very little of CH_4, despite the main channels being lined with hydrophobic methyl units. This observation is attributed to the fact that relaxation of the pore surface is required to accommodate guests, with the large quadrupolar moment of CO_2 facilitating strong interaction between it and the polar internal surfaces as it diffuses through the framework.

The rigid structure of [Zn(gly-thr)$_2$] is in stark contrast to another zinc dipeptide framework prepared

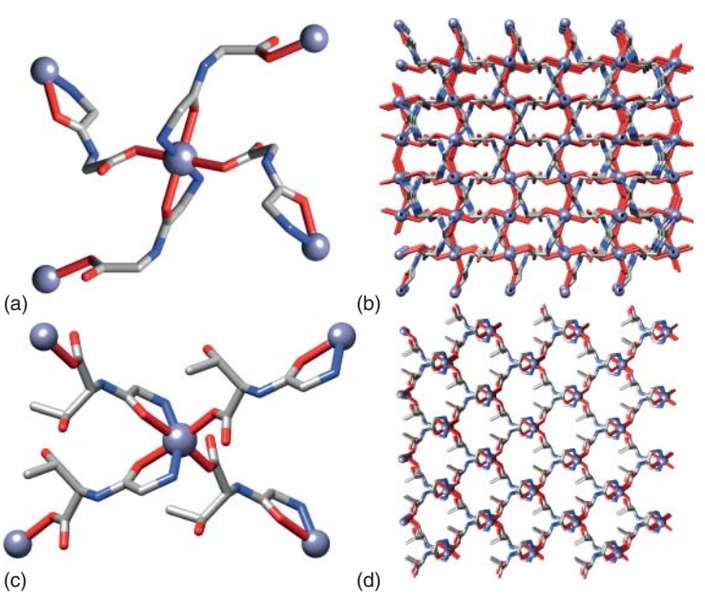


Figure 7 The crystal structure of [Zn(gly-gly)$_2$] (CCDC deposition TEXTOF) is composed of (a) octahedral Zn^{2+} cations linking four dipeptides into two-dimensional sheets that (b) stack to form a columnar arrangement. Similarly, the solid-state structure of [Zn(gly-thr)$_2$] (CCDC deposition MAFGUW) exhibits (c) octahedral Zn^{2+} cations linking the dipeptides in a slightly different arrangement, but still forming sheets that (d) hydrogen bond to form a permanently porous arrangement. All solvents and protons removed for clarity

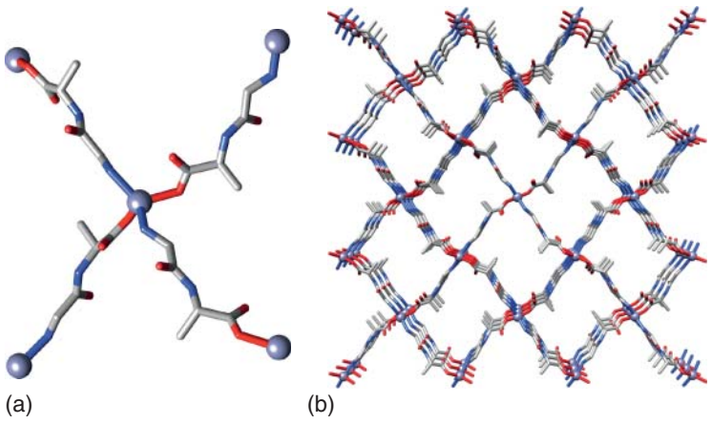


Figure 8 The solid-state structure of $[Zn(gly\text{-}ala)_2]$ (CCDC deposition BUWLEL) comprises (a) tetrahedrally coordinated Zn^{2+} cations, linking four gly-ala dipeptides by monodentate coordination to carboxylate oxygen atoms and amine nitrogen atoms into (b) two-dimensional sheets that form a perfectly stacked arrangement through inter-sheet hydrogen bonds. Solvents and hydrogen atoms removed for clarity

by the Rosseinsky group—$[Zn(gly\text{-}ala)_2]$—which shows remarkable guest-dependent flexibility.[24] Prepared from $Zn(NO_3)_2$ and the glycylalanine dipeptide in basic aqueous methanol, there are notable structural differences from the previously described frameworks. The Zn^{2+} cations are coordinated tetrahedrally (Figure 8a) to the dipeptides via two terminal carboxylate groups and two terminal amino moieties; both ends of each peptide coordinate Zn^{2+} units to again generate two-dimensional sheets. As the amido oxygen atoms of the gly-ala ligand are not involved in coordinating the Zn^{2+} cations, they are available to form hydrogen bonds with amido nitrogen atoms of adjacent layers to connect the framework sheets (Figure 8b) in a manner reminiscent of peptide β-sheet formation. The amide linkages also retain degrees of freedom, allowing the framework to exhibit adaptive porosity upon exposure to certain guests. Removal of interstitial methanol solvent molecules results in a marked transformation to a more amorphous phase, as measured by powder X-ray diffraction and solid-state ^{13}C NMR spectroscopy, with torsional changes in the peptide responsible for the structural shifts. The desolvated framework is again nonporous to N_2 and H_2 but will sorb polar substrates such as CO_2, H_2O, and methanol above a critical gate pressure that, when reached, triggers conformational rearrangements to open the pores of the material. This unusual substrate-dependent flexibility and porosity bear the hallmarks of the cooperative binding of guests by proteins, and this particular Zn-peptide framework lays the groundwork for adaptable synthetic materials to model biological systems.

While limited examples of metal-peptide frameworks exist, the ability to prepare both flexible and rigid MOFs with unusual functionality and properties, without incorporating secondary co-ligands, makes them materials where further study is essential. As complexity increases, care must be taken to ensure that the peptide linkers have no unwanted biological activity. Increasing the length of the peptide, however, brings with it the problem of flexible peptides chelating single metal ions. The challenge to synthetic chemists is to ensure that extended porous frameworks can continue to be selected for over discrete metal complexes.

4.5 Nucleobases

Nucleobases are a further class of endogenous biomolecules that can act as ligands, as they contain multiple heteroatomic sites—in particular nitrogen atoms—for metal coordination. Adenine especially has been exploited to produce a number of coordination polymers and MOFs. An initial report[25] described a coordination polymer, $[Cu_4(ad)_4(oxalate)_2]\cdot nH_2O$ (ad = adeninate), composed of Cu(II) cations and both adeninate and oxalate anions. Four adeninato ligands coordinate through their N3 and N9 atoms to two Cu(II) centers to form (Figure 9a) a water-capped paddlewheel SBU reminiscent of the ubiquitous copper acetate cluster, with framework extension occurring through coordination of further metal cations to the N7 atom to form a network with large void spaces (Figure 9b). Deprotonation of the N9 atom generates an anionic subunit related to the imidazolate ligand that has been extensively used in the assembly of the highly porous zeolitic imidazolate frameworks (ZIFs).[26]

Subsequently, Rosi *et al.* exploited the potential of adenine in MOF synthesis by preparing the so-called bio-MOF series, which have proven to exhibit some very exciting properties. Subjecting cobalt acetate and adenine to typical solvothermal conditions results in a MOF with the composition $[Co_2(ad)_2(OAc)_2]\cdot 2DMF\cdot 0.5H_2O$

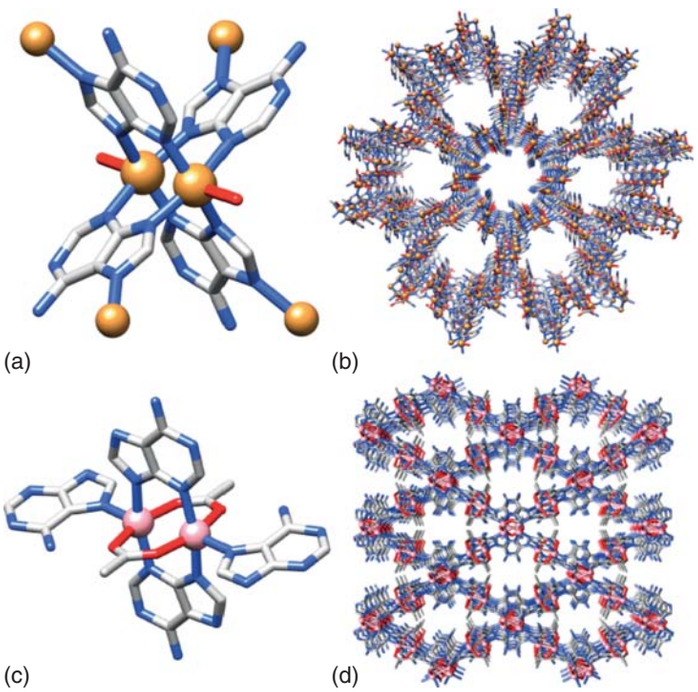


Figure 9 The crystal structure of $[Cu_4(ad)_4(oxalate)_2]\cdot nH_2O$ (CCDC deposition XACZEH) shows (a) four adenine ligands forming a Cu_2 paddlewheel with terminally bound water molecules. Further coordination to Cu^{2+} ions, also bound to oxalate anions, results in (b) an extended network with cylindrical channels. (c) In the crystal structure of bio-MOF-11 (CCDC deposition YUVSUE), each adenine unit acts as both a bidentate linker and a monodentate capping ligand to form a Co_2 paddlewheel SBU with two acetate ligands, generating (d) a highly porous extended network. All non-coordinated solvents and protons removed for clarity

(OAc = acetate), which has been termed bio-MOF-11.[27] The structure is composed of mixed-paddlewheel units (Figure 9c) wherein two Co^{2+} cations are bridged by two adeninate ligands, through coordination to the N3 and N9 atoms, and two acetate anions. Further linkage of these paddlewheels, through coordination of N7 atoms from two adjacent paddlewheels to the apical positions of the Co^{2+} cations, yields a three-dimensional framework (Figure 9d) with a BET surface area of 1040 $m^2\ g^{-1}$. Lining the cavities of bio-MOF-11 are numerous amino and pyrimidino functionalities; Lewis basic sites that serve to form significant interactions with CO_2 upon its sorption. This rich functionality of the adeninato ligand endows bio-MOF-11 with (i) a high CO_2 storage capacity, (ii) excellent CO_2 selectivity, and (iii) a high isosteric heat of sorption (Q_{st}) for CO_2, making adeninato-based MOFs prime candidates for carbon capture applications. An isostructural series incorporating Cu^{2+} cations with varying acids as co-ligands has also been reported.[28]

Introduction of multidentate co-ligands to bio-MOFs significantly increases their structural diversity. When 4,4′-biphenyldicarboxylic acid is combined with zinc acetate and adenine in dimethylformamide (DMF), solvothermal synthesis yields bio-MOF-1, which is formulated as $[Zn_8(ad)_4(BPDC)_6O]^{2-}\cdot 2[Me_2NH_2]^+$ (BPDC = 4,4′-biphenyldicarboxylate).[7] The network is composed of infinite columnar stacks of apex-sharing zinc-adeninate octahedral units (Figure 10a), themselves connected by BPDC ligands, to form a highly porous construct (Figure 10b) with a BET surface area of 1680 $m^2\ g^{-1}$ after removal of interstitial solvents. The framework is negatively charged, with dimethylammonium (DMA) cations generated by thermal decomposition of the DMF solvent balancing the charge. Exchange of these cations is a simple but highly effective method to post-synthetically modify the properties of bio-MOF-1 for a number of applications. In a striking example with implications for drug delivery technologies, the antiarrythmia drug Procainamide · HCl was absorbed into the framework in its protonated, cationic form, by soaking bio-MOF-11 in an aqueous solution of the drug, up to a loading of 0.22 g/g. The drug could then be fully released (Figure 10d) into a buffered aqueous solution, through a cation exchange process, over the course of 72 h.

By exchanging the DMA cations for increasingly larger ones, namely, tetramethylammonium (TMA), tetraethylammonium (TEA), and tetra-*n*-butylammonium (TBA), the available pore spaces of the bio-MOF-1 samples dramatically decrease, as indicated by the BET surface areas, measured by N_2 adsorption isotherms, of

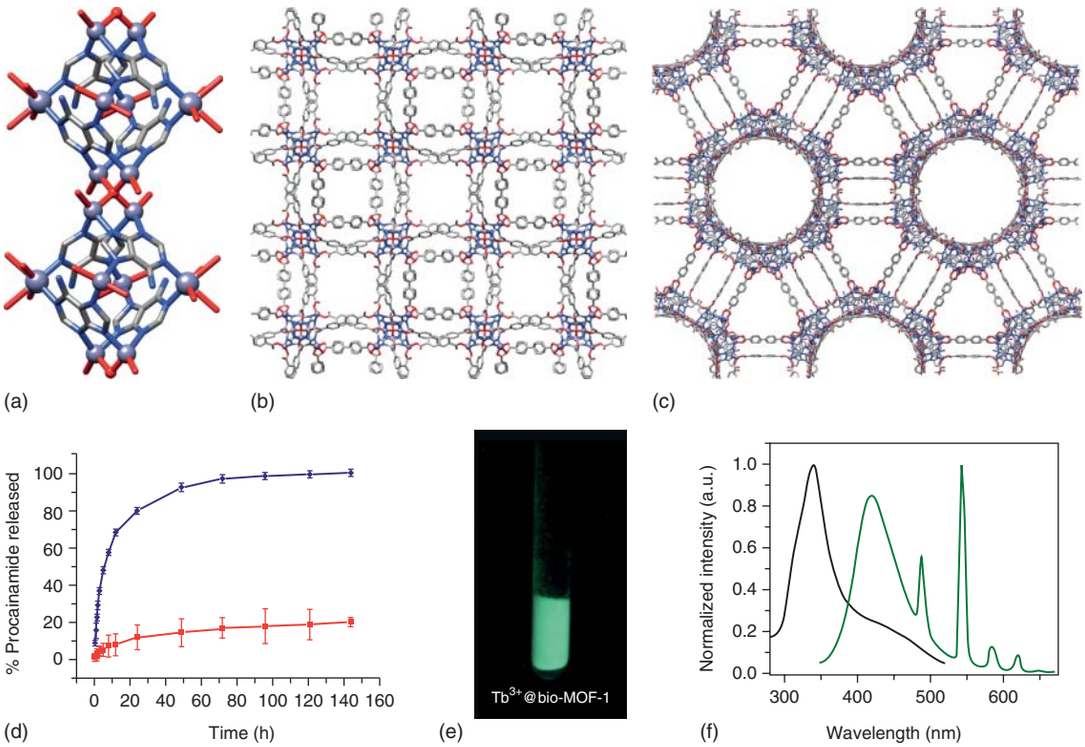


Figure 10 Structure and function of zinc-adeninate bio-MOFs. (a) The octahedral $[Zn_8(ad_4)]$ SBU taken from the crystal structure of bio-MOF-1 (CCDC deposition NUDLAA). In bio-MOF-1, each octahedral unit is linked horizontally by tetrahedral μ_4-O^{2-} ligands (shown as red spheres), whereas in bio-MOF-100, discrete μ_2-O^{2-}-capped SBUs allow greater framework extension. The remaining coordination sites on the Zn^{2+} cations are occupied by 4,4′-biphenyldicarboxylate linkers. (b) The packing structure of bio-MOF-1 in the solid state. (c) The packing structure of bio-MOF-100 in the solid state, showing mesoporous cylindrical channels (CCDC deposition SAPBIW). All counterions, solvents, and protons removed for clarity. (d) Drug release profiles of cationic Procainamide molecules from bio-MOF-1 in PBS buffer (blue, rapid cation exchange) and nanopure deionized water (red). (Reprinted with permission from Ref. 7. Copyright (2009) American Chemical Society.) (e) Luminescence of Tb^{3+}@bio-MOF-1 when excited at 365 nm. (f) Absorption and excitation spectra of Tb^{3+}@bio-MOF-1. (Reprinted with permission from Ref. 30. Copyright (2011) American Chemical Society.)

1680 $m^2\,g^{-1}$ (DMA), 1460 $m^2\,g^{-1}$ (TMA), 1220 $m^2\,g^{-1}$ (TEA), and 830 $m^2\,g^{-1}$ (TBA), in turn.[29] Surprisingly, the CO_2 uptake storage capabilities of the modified bio-MOFs did not follow the same trend as the surface areas, with bio-MOF-1-TMA exhibiting the largest CO_2 uptake at 273 K (4.46 mmol g^{-1}) and bio-MOF-1-TEA having the largest uptake at 313 K (1.66 mmol g^{-1}). This somewhat unexpected set of results can be rationalized by examining the isosteric heats of adsorption (Q_{st}) for CO_2 for the modified bio-MOF series—as surface areas and pore volumes decrease, the Q_{st} values *increase* from 22 to 31 kJ mol^{-1}. The bio-MOF-1 series is an illustrative example of the fact that smaller pores may be more suitable for CO_2 capture, as favorable interactions between the framework and the adsorbate can be promoted.

The organic cations of as-synthesized bio-MOF-1 can also be exchanged for inorganic ones.[30] Soaking samples in DMF solutions of lanthanide nitrate salts resulted in the incorporation of Tb^{3+}, Eu^{3+}, Sm^{3+}, or Yb^{3+} into samples of bio-MOF-1, with complete retention of both lanthanide incorporation and framework integrity achieved after soaking samples in aqueous solutions to remove residual DMF solvent. The organic component of the framework serves to sensitize lanthanide emission. Upon excitation (Figure 10e) with 365 nm radiation of samples dispersed in water, typical lanthanide excitation spectra (Figure 10f) were observed with λ_{em} values of 545–970 nm, that is, from orange all the way to NIR emission. This emission occurs despite the presence of the water, which has well-known quenching properties—the high luminescence lifetimes and quantum yields of the samples suggest a level of protection of the lanthanide cations from water by the MOF itself. The spatial dispersion of sensitized lanthanide cations within a high-surface area material, combined with a very sensitive near-IR emission profile, renders Yb^{3+}@bio-MOF-1 a prime candidate for oxygen-sensing applications. Indeed, exposure of O_2 gas to a dried sample mounted on a glass slide results in a reversible 40% attenuation of luminescence intensity.

A final example of an adenine containing bio-MOF is one which further illustrates the versatility of the series. Slightly modifying the synthetic conditions utilized to prepare bio-MOF-1 results in the isolation of bio-MOF-100, which is formulated as $[Zn_8(ad)_4(BPDC)_6O_2]^{4-}\cdot 4[Me_2NH_2]^+$.[31] Instead of the infinite columnar stacks of zinc-adeninate units, discrete octahedral $[Zn_8(ad)_4O_2]^{8+}$ SBUs are linked by BPDC ligands to form a mesoporous structure (Figure 10c) with a massive BET surface area of $4300\,m^2\,g^{-1}$. The very large pore volume of bio-MOF-100 can be rationalized by considering the much increased size of the zinc-adeninate building unit (14.2 Å in diameter) compared to the ubiquitous basic zinc acetate SBU (10.5 Å in diameter), which allows considerable framework expansion.

Nucleobases hold great potential as components for edible MOFs with a number of exciting properties, not least as drug delivery and bioimaging agents. In parallel with the amino acid MOFs described earlier, great care must be taken to ensure that co-ligands, which are often necessary to generate extended porous structures in concert with nucleobases, are also suitable for human consumption.

4.6 Carbohydrates

Carbohydrates, in particular simple sugar molecules, have long been known to act as ligands for metal cations, so it is perhaps surprising that more complex starches have not been utilized as multidentate ligands until recently. The cyclodextrins, cyclic arrangements of α,D-glucopyranosyl residues, have proven[32] to be highly effective ligands in the self-assembly of extended frameworks when linked by alkali metal cations.

γ-Cyclodextrin (γ-CD), which contains eight sugar residues and thus has a number of rotational symmetry operations, is particularly prone to forming MOFs linked by alkali metal cations. When γ-CD is dissolved in water alongside 8 equivalents of an alkali metal hydroxide, vapor diffusion of methanol into the solution results in the separation of colorless cubic crystals, which have been termed CD-MOFs. CD-MOFs 1–3, prepared from KOH, RbOH, and CsOH, in turn, are isostructural and display (Figure 11a) an array of $(\gamma\text{-CD})_6$ cubes held together by coordination of the alkali metal cations to the primary faces of the γ-CD units, with their associated counterions disordered throughout the porous network. These cubic substructures are themselves linked in a body-centered

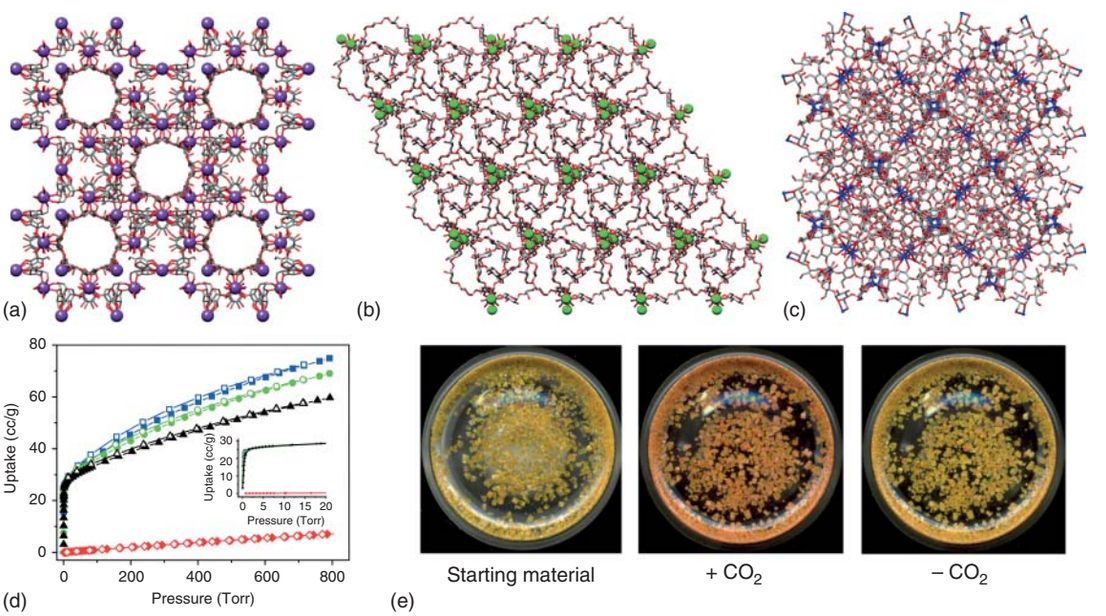


Figure 11 The structural diversity of the carbohydrate CD-MOFs is illustrated in packing images of (a) cubic $[(KOH)_2(\gamma\text{-CD})]_n$, generated from CCDC deposition LAJLAL, (b) trigonal $[SrBr_2(\gamma\text{-CD})]_n$, generated from CCDC deposition YAPSAL, and (c) tetragonal $[(RbOH)_5(\alpha\text{-CD})_2]_n$, generated from CCDC deposition MAMVED. All counterions, solvents, and protons removed for clarity. (d) CD-MOF-2 exhibits remarkably strong and selective uptake of CO_2, as evidenced by CO_2 uptake isotherms at 273 K (blue), 283 K (green), and 298 K (black) compared to CH_4 uptake at 298 K (red). (e) Incorporation of a pH indicator into CD-MOF-2 allows visual sensing of CO_2 chemisorption through carbonic acid formation, with crystals reversibly turning from yellow to orange upon binding. (Reprinted (adapted) with permission from Ref. 35. Copyright (2011) American Chemical Society.)

cubic packing arrangement by coordination of the metal ions to the secondary faces of the CDs, forming an extended structure of spherical pores 1.8 nm in diameter connected in all three dimensions by cylindrical channels of 0.9 nm in diameter. Changing either the metal salt[33] or the cyclodextrin[34] endows the resultant CD-MOFs with significant structural diversity, with offset 2D layer structures (NaOH + γ-CD), 3-D trigonal frameworks ($SrBr_2$ + γ-CD, Figure 11b), and highly complex interconnected 3D nets (RbOH + α-CD, Figure 11c) all observed. The multidenticities and varying symmetries of the cyclodextrins, combined with a range of coordination numbers available to the alkali and alkali earth metal cations, allow high connectivity and structural versatility—more examples surely await discovery.

Despite the metal–ligand bonding in the CD-MOFs being of a coordinative nature, much like the manner in which crown ethers bind alkali metal cations through repeating $-OCH_2CH_2O-$ chelate units, the resultant CD-MOFs are highly stable to removal of solvents and display permanent porosity, having BET surface areas, measured by N_2 uptake, of 1220 $m^2 g^{-1}$ (CD-MOF-1) and 1030 $m^2 g^{-1}$ (CD-MOF-2). Indeed, dehydrated single crystals of CD-MOF-2 were shown by single crystal and powder X-ray diffraction analyses to be highly crystalline a number of months after isolation and storage, and are only disassembled into their starting components by dissolution in water.

The high local concentration of nucleophilic hydroxyl groups lining the pore surfaces of CD-MOF-2 leads to an unusual reactivity toward CO_2.[35] Very steep, temperature independent adsorption isotherms (Figure 11d) recorded at low (<5 Torr) CO_2 partial pressures indicate that a chemisorptive phenomenon is occurring, with the reversible formation of a transient covalent bond, in the form of a carbonic acid moiety, observed by CP-MAS ^{13}C NMR spectroscopy. Post-synthetic incorporation of a pH-sensitive molecular probe into CD-MOF-2, which exhibits a color change (Figure 11e) upon formation of the carbonic acid group, yields a reusable, sustainable optical CO_2 sensor.

This series of CD-MOFs contains, as far as can be ascertained, the first example of a truly edible MOF prepared entirely from food-grade ingredients.[33] To assemble the edible MOF, food-grade potassium benzoate (manufactured as the preservative E212 and widely used in fruit juices and sodas) is dissolved in tap water alongside food-grade γ-cyclodextrin. To induce crystallization, Everclear, a drinkable alcoholic spirit distilled from grain that is essentially a 95% aqueous ethanol solution, is vapor diffused into the mixture. Colorless crystals of the edible MOF separate after approximately 1 week, whether the synthesis is carried out in the laboratory using specialized glassware, or in the kitchen using small drinking glasses and recycled food jars. The solid-state structure can be solved by single crystal X-ray diffraction and exhibits the same underlying framework as the other CD-MOFs, with the benzoate counterions residing within the γ-CD units. Upon dissolution of the crystals in mildly acidic aqueous media—resembling stomach acid—the framework dissociates to generate the γ-CD and potassium benzoate starting ingredients. In other words, the MOF is, as far as can be discerned from the literature, the first to be prepared entirely from food-grade ingredients, which will be initially digested back into them upon consumption, rendering it fit for human consumption. This author has even had the pleasure of preparing and tasting a small sample—starchy and slightly salty for those who are interested—and can report no ill effects!

5 CONCLUSIONS AND OUTLOOK

The examples detailed earlier illustrate the diversity in structures and properties of MOFs prepared from metals and ligands expected to be safe for human consumption. There are clearly numerous parameters that must be considered in the preparation of edible MOFs. Unless the MOF is shown to break down entirely into its constituent components upon ingestion, it is clearly highly unadvisable to consume it without comprehensive toxicity data, as the effects of persistent MOF particles on the human body are currently unknown and would be expected to vary with size and constitution. Synthetic chemists are increasingly preparing MOFs from biologically relevant ligands, such as amino acids, peptides, and nucleobases, whose inherent chirality, combined with many H-bonding and Lewis acid/base sites, can endow the resulting materials with unusual and desirable properties. Nonetheless, many simple synthetic polyacidic linkers, such as terephthalate, may still prove suitable for inclusion in edible MOFs, as standalone ligands or as auxiliaries to bioligands. As the potential applications of MOFs in biomedicine[4] are explored in more depth, alongside the continuing examination of new ligands and development of synthetic protocols, more and more edible MOFs will no doubt result.

6 ACKNOWLEDGMENTS

The author would like to thank the Royal Society for the award of a University Research Fellowship.

7 ABBREVIATIONS AND ACRONYMS

ad = adeninate; BET = Brunauer–Emmett–Teller; bipy = 4,4′-bipyridine; BPDC = 4,4′-biphenyldicarboxylate; CD = cyclodextrin; CP-MAS = cross polarization

magic angle spinning; DMA = dimethylammonium; DMF = dimethylformamide; MIL = Materials from Institut Lavoisier; MOF = metal-organic framework; NIR = near infrared; NMR = nuclear magnetic resonance; OAc = acetate; PDI = polydispersity index; PET = polyethylene terephthalate; SBU = secondary building unit; TBA = tetra-*n*-butylammonium; TEA = tetraethylammonium; TMA = tetramethylammonium; ZIF = zeolitic imidazolate framework.

8 REFERENCES

1. J. R. Long and O. M. Yaghi, *Chem. Soc. Rev.*, 2009, **38**, 1213, and other articles in this themed issue.
2. H.-C. Zhou, J. R. Long, and O. M. Yaghi, *Chem. Rev.*, 2012, **112**, 673, and other articles in this themed issue.
3. P. Horcajada, C. Serre, M. Vallet-Regì, M. Sebban, F. Taulelle, and G. Férey, *Angew. Chem., Int. Ed.*, 2006, **45**, 5974.
4. P. Horcajada, R. Gref, T. Baati, P. K. Allan, G. Maurin, P. Couvreur, G. Férey, R. E. Morris, and C. Serre, *Chem. Rev.*, 2012, **112**, 1232.
5. P. Horcajada, C. Serre, G. Maurin, N. A. Ramsahye, F. Balas, M. Vallet-Regí, M. Sebban, F. Taulelle, and G. Férey, *J. Am. Chem. Soc.*, 2008, **130**, 6774.
6. P. Horcajada, T. Chalati, C. Serre, B. Gillet, C. Sebrie, T. Baati, J. F. Eubank, D. Heurtaux, P. Clayette, C. Kreuz, J.-S. Chang, Y. K. Hwang, V. Marsaud, P.-N. Bories, L. Cynober, S. Gil, G. Férey, P. Couvreur, and R. Gref, *Nat. Mater.*, 2010, **9**, 172.
7. J. An, S. J. Geib, and N. L. Rosi, *J. Am. Chem. Soc.*, 2009, **131**, 8376.
8. T. Baati, L. Njim, F. Neffati, A. Kerkeni, M. Bouttemi, R. Gref, M. F. Najjar, A. Zakhama, P. Couvreur, C. Serre, and P. Horcajada, *Chem. Sci.*, 2013, **4**, 1597.
9. N. Stock and S. Biswas, *Chem. Rev.*, 2011, **112**, 933.
10. T. Chalati, P. Horcajada, R. Gref, P. Couvreur, and C. Serre, *J. Mater. Chem.*, 2011, **21**, 2220.
11. I. Imaz, M. Rubio-Martinez, J. An, I. Sole-Font, N. L. Rosi, and D. Maspoch, *Chem. Commun.*, 2011, **47**, 7287.
12. H. Li, M. Eddaoudi, M. O'Keeffe, and O. M. Yaghi, *Nature*, 1999, **402**, 276.
13. F. Millange, N. Guillou, R. I. Walton, J.-M. Grenèche, I. Margiolaki, and G. Férey, *Chem. Commun.*, 2008, 4732.
14. G. L. Ball, C. J. McLellan, and V. S. Bhat, *Crit. Rev. Toxicol.*, 2011, **42**, 28.
15. S. S. Y. Chui, S. M. F. Lo, J. P. H. Charmant, A. G. Orpen, and I. D. Williams, *Science*, 1999, **283**, 1148.
16. C. Serre, F. Millange, S. Surblé, and G. Férey, *Angew. Chem., Int. Ed.*, 2004, **43**, 6285.
17. C. Mellot-Draznieks, C. Serre, S. Surblé, N. Audebrand, and G. Férey, *J. Am. Chem. Soc.*, 2005, **127**, 16273.
18. E. V. Anokhina, Y. B. Go, Y. Lee, T. Vogt, and A. J. Jacobson, *J. Am. Chem. Soc.*, 2006, **128**, 9957.
19. R. Vaidhyanathan, D. Bradshaw, J.-N. Rebilly, J. P. Barrio, J. A. Gould, N. G. Berry, and M. J. Rosseinsky, *Angew. Chem., Int. Ed.*, 2006, **45**, 6495.
20. J. A. Gould, J. T. A. Jones, J. Bacsa, Y. Z. Khimyak, and M. J. Rosseinsky, *Chem. Commun.*, 2010, **46**, 2793.
21. T. Takayama, S. Ohuchida, Y. Koike, M. Watanabe, D. Hashizume, and Y. Ohashi, *Bull. Chem. Soc. Jpn.*, 1996, **69**, 1579.
22. E. Ueda, Y. Yoshikawa, N. Kishimoto, M. Tadokoro, H. Sakurai, N. Kajiwara, and Y. Kojima, *Bull. Chem. Soc. Jpn.*, 2004, **77**, 981.
23. C. Martí-Gastaldo, J. E. Warren, K. C. Stylianou, N. L. O. Flack, and M. J. Rosseinsky, *Angew. Chem., Int. Ed.*, 2012, **51**, 11044.
24. J. Rabone, Y.-F. Yue, S. Y. Chong, K. C. Stylianou, J. Bacsa, D. Bradshaw, G. R. Darling, N. G. Berry, Y. Z. Khimyak, A. Y. Ganin, P. Wiper, J. B. Claridge, and M. J. Rosseinsky, *Science*, 2010, **329**, 1053.
25. J. P. García-Terán, O. Castillo, A. Luque, U. García-Couceiro, P. Román, and L. Lezama, *Inorg. Chem.*, 2004, **43**, 4549.
26. K. S. Park, Z. Ni, A. P. Côté, J. Y. Choi, R. Huang, F. J. Uribe-Romo, H. K. Chae, M. O'Keeffe, and O. M. Yaghi, *Proc. Natl. Acad. Sci. U.S.A.*, 2006, **103**, 10186.
27. J. An, S. J. Geib, and N. L. Rosi, *J. Am. Chem. Soc.*, 2010, **132**, 38.
28. S. Pérez-Yáñez, G. Beobide, O. Castillo, J. Cepeda, A. Luque, A. T. Aguayo, and P. Román, *Inorg. Chem.*, 2011, **50**, 5330.
29. J. An and N. L. Rosi, *J. Am. Chem. Soc.*, 2010, **132**, 5578.
30. J. An, C. M. Shade, D. A. Chengelis-Czegan, S. Petoud, and N. L. Rosi, *J. Am. Chem. Soc.*, 2011, **133**, 1220.
31. J. An, O. K. Farha, J. T. Hupp, E. Pohl, J. I. Yeh, and N. L. Rosi, *Nat. Commun.*, 2012, **3**, 604.
32. R. A. Smaldone, R. S. Forgan, H. Furukawa, J. J. Gassensmith, A. M. Z. Slawin, O. M. Yaghi, and J. F. Stoddart, *Angew. Chem., Int. Ed.*, 2010, **49**, 8630.
33. R. S. Forgan, R. A. Smaldone, J. J. Gassensmith, H. Furukawa, D. B. Cordes, Q. Li, C. E. Wilmer, Y. Y. Botros, R. Q. Snurr, A. M. Z. Slawin, and J. F. Stoddart, *J. Am. Chem. Soc.*, 2012, **134**, 406.
34. J. J. Gassensmith, R. A. Smaldone, R. S. Forgan, C. E. Wilmer, D. B. Cordes, Y. Y. Botros, A. M. Z. Slawin, R. Q. Snurr, and J. F. Stoddart, *Org. Lett.*, 2012, **14**, 1460.
35. J. J. Gassensmith, H. Furukawa, R. A. Smaldone, R. S. Forgan, Y. Y. Botros, O. M. Yaghi, and J. F. Stoddart, *J. Am. Chem. Soc.*, 2011, **133**, 15312.

Mechanochemical Approaches to Metal-Organic Frameworks

Tomislav Friščić

McGill University, Montreal, QC, Canada

1	Introduction	173
2	Methods for the Mechanosynthesis of Coordination Bonds	174
3	Characterization of Mechanochemical Products	178
4	Synthetic Strategies for Extended Metal–Organic Structures	179
5	Porous MOFs by Mechanochemistry	184
6	Emergent Properties of Mechanochemically Obtained Metal-Organic Materials	185
7	Mechanistic Studies of Mechanochemical MOF Synthesis	187
8	Conclusions	190
9	Acknowledgments	190
10	Related Articles	190
11	Abbreviations and Acronyms	191
12	References	191

1 INTRODUCTION

1.1 Aim and Scope

Mechanochemical synthesis, i.e., chemical synthesis induced and/or sustained by the application of mechanical force,[1] is a well-known synthetic approach in the context of inorganic materials (e.g., mixed metal oxides such as ferrites, perovskites, etc.),[2] nanoparticles,[3] and alloying of otherwise immiscible metals or of metals and binary inorganic compounds.[4] Since 1990s it has become increasingly clear that mechanical force and agitation, in the form of milling or grinding, can also provide an excellent alternative to conventional solution-based and solvothermal methodologies for making organic molecules,[5] materials based on non-covalent interactions[6] (e.g., pharmaceutical cocrystals),[7] and materials based on coordination bonds, such as coordination polymers and open metal–organic frameworks (MOFs).[6,8] This brief overview aims to illustrate, by highlighting carefully selected recent examples, the current state of affairs in using mechanochemistry for the synthesis and transformation of extended metal–organic structures, specifically, coordination polymers and open MOFs,[9] as well as provide a basic introduction to mechanochemical techniques, synthetic strategies, and current understanding of reaction mechanisms underlying the transformations of metal–ligand bonds.

1.2 Why Mechanochemistry?

The continuous development of new structural designs for MOFs,[9] the rapidly increasing number of their potential applications (including hydrogen storage, carbon dioxide sequestration, light harvesting, and molecular sensing),[10] and the recent development of methods for commercial manufacture of several exemplary MOFs (e.g., the Basolite® series of products)[11]

Metal-Organic Framework Materials. Edited by Leonard R. MacGillivray and Charles M. Lukehart.
© 2014 John Wiley & Sons, Ltd. ISBN 978-1-119-95289-3

have highlighted the need to invent and develop new synthetic techniques that will allow the efficient screening for new MOF materials and topologies, as well as enable their synthesis in a scalable, but also atom-and energy-efficient and environmentally friendly manner. In the latter context, considerations[11] of safety, cost and environmental impact have highlighted the need to avoid thermally sensitive, toxic and often costly organic solvents, as well as employ safer and less expensive metal precursors in MOF synthesis. Thus, it is particularly desirable to avoid hazardous or corrosive metal nitrates and chlorides, and replace them with safer substances such as sulfates or oxides. In particular, using metal oxides as starting materials is expected to greatly improve synthetic procedures as the only reaction byproduct would, in many cases, be water. Furthermore, as oxides are primary products in the course of mineral and metal processing, such starting materials are likely to be inexpensive and readily accessible. Unfortunately, the poor solubility of metal sulfates and oxides, especially in organic solvents, seriously hinders their reactivity and impedes their use as reactants in commercial solvent-and solubility-dependent MOF syntheses. The described challenges of a more efficient and improved MOF synthesis are readily met by mechanochemical synthesis (mechanosynthesis). Mechanosynthesis allows to either completely avoid the use of solvent in a chemical synthesis, or reduce its amount to catalytic or near-stoichiometric level.[1,12] The absence of bulk solvent implies that mechanochemical reactions can readily take place regardless of the relative solubilities of starting materials and products, thus indicating the ability to use slightly soluble substances, such as metal oxides or carbonates, as starting materials for room-temperature syntheses of MOFs and coordination polymers. The recently introduced[12] mechanochemical techniques of liquid-assisted grinding (LAG) and of ion- and liquid-assisted grinding (ILAG)[1,6] are particularly attractive for that purpose. These experimental techniques have been developed with the intention to improve the reactivity of initially unreactive or low-yielding systems and optimize mechanochemical reactions for rapid (minutes to hours), quantitative, and room temperature synthesis without bulk solvents. Another benefit arising from avoiding bulk solvents via mechanosynthesis is excellent stoichiometric control, which is also observable for mechanosyntheses of cocrystals and organic molecules. Indeed, almost all examples provided in this brief overview involve reactions in which quantitative product yields were achieved using the exact stoichiometric amounts of reagents, i.e., without using excess reagents (ligand or metal precursor) that is often required in conventional solution-based or solvothermal synthesis.

2 METHODS FOR THE MECHANOSYNTHESIS OF COORDINATION BONDS

Currently there are four distinct experimental techniques for the mechanochemical synthesis of coordination polymers and MOFs: neat grinding, LAG or kneading[13] (also known under other names, such as solvent-drop grinding or solvent-assisted grinding), ILAG, and neat grinding followed by annealing.[14]

2.1 Neat grinding

Neat grinding is the simplest form of mechanosynthesis, and involves grinding a physical mixture of two or more reactants. Grinding reactions can often be performed manually, using a mortar and a pestle, although such approaches often yield results that are difficult to reproduce due to a number of variable parameters, including the strength of the experimenter, frequency of grinding, as well as the composition of the atmosphere, air humidity, and temperature of the surroundings. Alternatively, an electronically controlled laboratory mechanical ball mill can be employed, providing the ability to conduct reactions under well-controlled and reproducible conditions. Historically, neat grinding was the first method applied for the mechanosynthesis of metal–ligand bonds. In a particularly impressive early demonstration of the efficiency of mechanochemical synthesis, neat grinding was utilized to synthesize a tetranuclear metal–organic square and a hexanuclear metal–organic bowl by combining (ethylenediamine)platinum(II) nitrate with suitable di- and tri-pyridine ligands, respectively (Figure 1).[6]

Neat grinding has also been applied to the synthesis of one-dimensional and two-dimensional (1-D and 2-D, respectively) coordination polymers, as well as of three-dimensional (3-D) porous MOFs, such as metal carboxylates and zeolitic imidazolate frameworks (ZIFs). Although the area of mechanosynthesis of coordination compounds by neat grinding is still too small to allow broad generalizations, an array-based study of neat grinding reactions between diverse organic ligands and metal precursors indicates that neat grinding reactivity is favored with solid reactants that either have low melting points and/or are solvated.[1] Although neat grinding mechanochemical reactions are often considered to occur in a dry environment, it is noteworthy that most successful neat grinding reactions involve using hydrated metal salt precursors. It is likely that, when using hydrated acetates or chlorides as reagents, water or acid that is liberated during mechanochemical reaction could act as a liquid phase that facilitates the mechanochemical reaction, (as in LAG) and/or templates the formation of a porous structure. The surrounding atmosphere can have a strong effect on the course of neat grinding reactions, as grinding in open air is known to sometimes lead to

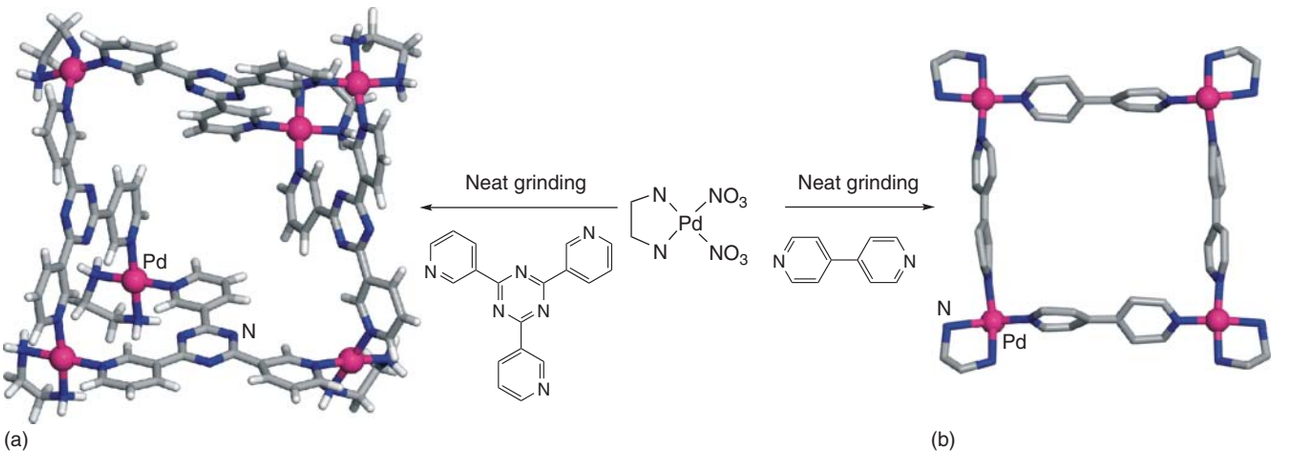


Figure 1 Mechanochemical construction of a molecular bowl (a) and a molecular square (b) by neat grinding

the formation of hydrated products due to absorption of moisture from air. Such behavior is exemplified by the grinding reaction of anhydrous reagents silver acetate and 1,4-diaminocyclohexane (**dace**)[1,14,15] which results in the formation of a hydrated coordination polymer $Ag(CH_3COO)(\mathbf{dace}) \cdot nH_2O$. Whereas mechanochemical reactions are commonly conducted in an electronically controlled ball mill, a simple and readily accessible experimental methodology was recently described, in which solid reaction mixture is mechanically agitated with steel balls (or BBs) using a laboratory vortexing mixer.[16] So far, such "vortex grinding" has been applied for several archetypal mechanochemical reactions, including the reaction of copper(II) acetate and isonicotinic acid to form the open copper(II) isonicotinate MOF (see also Section 5).

2.2 Grinding–Annealing

Heating of a monomeric metal complex initially obtained by neat grinding can lead to a subsequent coordination-driven polymerization to form a new product. For example, grinding of 3-cyanoacetylacetone with acetates of divalent transition metals leads to the formation of discrete monomeric metal β-diketonates with axially coordinated water molecules.[1,14] Annealing of these primary products results in the removal of coordinated water and the formation of 3-D metal–organic polymers. A different type of reactivity obtained by a neat grinding–annealing sequence was demonstrated as a follow-up to the mechanosynthesis of hydrogen-bonded pyridinium and imidazolium tetrachlorometallates(II) from corresponding organic hydrochlorides and metal chlorides. Thermal annealing of the resulting tetrachlorometallate(II) salts leads to the reversible loss of hydrogen chloride and the formation of 1-D coordination polymers consisting of metal chloride units connected to pyridine (or imidazole) ligands.[1,14]

2.3 Liquid-Assisted Grinding and Kneading

LAG and kneading were first introduced to mechanosynthesis in the context of forming hydrogen-bonded molecular cocrystals.[12] In contrast to neat grinding, LAG utilizes the addition of small quantities of a liquid phase to assist or enable the mechanochemical reaction. In cocrystal synthesis, LAG results in quantitative yields, short reaction times, and enables a greater scope of reactants and products.[6] For cocrystals, the enhancement of the mechanochemical reaction rate when using LAG as compared to neat grinding has been well established through a variety of techniques, including terahertz spectroscopy and X-ray powder diffraction (XRPD).[12] Products obtained by LAG often exhibit a high level of crystallinity, suggesting a means to avoid amorphous impurities that typically result from neat grinding. The mechanism through which a liquid accelerates mechanochemical reactivity and produces a highly crystalline product are not yet clear, but it is likely that it is related to enhanced molecular diffusion, particularly on the surface of the ground solids, and the plasticizing effect of the liquid phase.[7,12] Similar observations have been made in the context of coordination chemistry by LAG, where the addition of a liquid phase enhanced the rate of mechanochemical synthesis. This effect is illustrated by the mechanochemical synthesis of ethylenethiourea adducts of silver halides (Figure 2a).[1] Solution reaction of AgCl and ethylenethiourea yields a single product, $AgCl(ethylenethiourea)_{1.5}$, composed of 1-D polymeric cationic tapes of composition $[ClAg_4(ethylenethiourea)_6]^{3+}$, surrounded by Cl^- anions

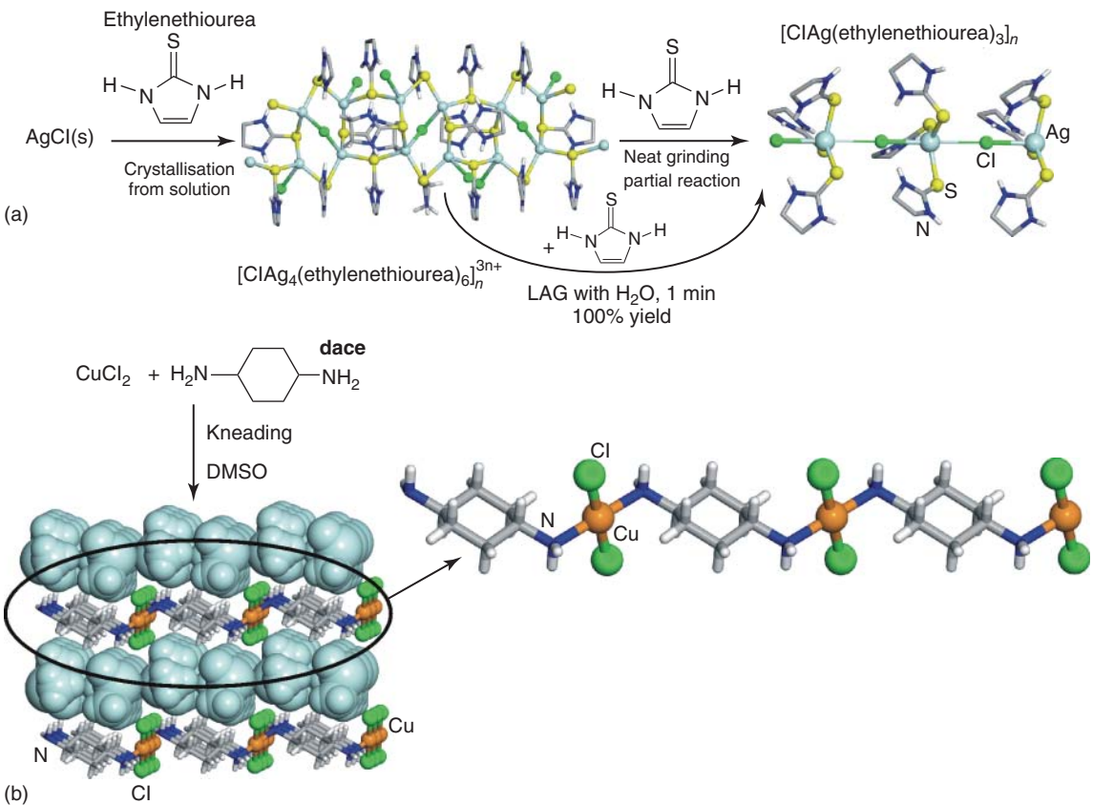


Figure 2 Examples of mechanochemical synthesis of a coordination polymer accelerated and directed by switching from neat grinding to LAG: (a) mechanochemical transformation of the $[ClAg_4(ethylenethiourea)_6]^{3+}$ coordination polymer into $AgCl(ethylenethiourea)_3$, accelerated by small quantities of water; (b) the construction of a metal–organic clay mimic material by kneading, with a single chain of the coordination polymer host $[Cu(\mathbf{dace})Cl_2]_n$ highlighted. Solvent molecules included between the layers of $[Cu(dace)Cl_2]_n$ are shown using a space-filling model

(Figure 2a). Neat grinding of this cationic polymer with further 1.5 equivalents of ethylenethiourea results in slow partial formation of a different product whose composition is $AgCl(ethylenethiourea)_3$. However, LAG in the presence of a small amount of water results in the quantitative formation of $AgCl(ethylenethiourea)_3$ product within 1 min. Enhancement of reactivity through adding catalytic amounts of a liquid phase was also observed in the reaction of silver iodide with ethylenethiourea. In this case, neat grinding did not lead to a reaction, whereas grinding with a small amount of water resulted in the quantitative formation of $AgI(ethylenethiourea)_2$ product which was structurally characterized by isostructurality to $AgBr(ethylenethiourea)_2$.

Whereas the first reports of LAG have often been described as grinding in the presence of "a few drops" of liquid, a recent attempt to quantify the effect of the added liquid phase on the mechanochemical reaction has led to the introduction of the parameter η, corresponding to the ratio of the volume of the added liquid (in μL) and the weight of solid reactants (in mg). The values of η associated with conventional LAG processes were empirically determined to lie between 0 and 1 $\mu L\,mg^{-1}$. The η parameter not only allows the characterization and consistent, quantitative reporting of LAG reaction conditions, it also permits a direct comparison between neat grinding (defined as $\eta = 0\,\mu L\,mg^{-1}$) reactions, LAG reactions, reactions in slurries ($\eta \sim 2$–$12\,\mu L\,mg^{-1}$), and solution-based or solvothermal synthesis ($\eta > 12\,\mu L\,mg^{-1}$).

LAG is particularly interesting for mechanochemical synthesis of porous frameworks and inclusion compounds, as the liquid can sometimes become incorporated into the final product as a guest and so direct (template) its structure.[12] One example of mechanochemical formation of a metal–organic host–guest complex is the kneading of copper(II) chloride and **dace** in the presence of *S*,*S*-dimethylsulfoxide (DMSO) or water, which leads to the simultaneous in situ formation of the 1-D coordination polymer host $[Cu(\mathbf{dace})Cl_2]$ and molecular inclusion to form inclusion compounds such as $[Cu(\mathbf{dace})Cl_2] \cdot n$DMSO (Figure 2b).[1,15] Importantly, the polymeric host itself is not obtainable by neat grinding

of $CuCl_2$ and **dace**. Both the DMSO and the water inclusion compound consist of layers of juxtaposed chains of [Cu(**dace**)Cl_2], separated by layers of included guest. Thermal desolvation provides the non-solvated polymer [Cu(**dace**)Cl_2]$_n$ which can reversibly include a variety of organic molecules upon kneading and suspension overnight. The same inclusion compounds could be prepared directly by kneading of $CuCl_2$ and **dace** in only a few cases, suggesting that the existence of coordination polymer layers of [Cu(**dace**)Cl_2]$_n$ is a prerequisite for inclusion, thus making this coordination polymer interesting as a metal–organic analog of layered clays with inclusion capabilities. The ability of LAG to enhance mechanochemical reactivity and lead to molecular inclusion has been recently exploited to screen for host–guest compounds of coordination polymers and porous MOFs from mixtures of reactants that do not readily react under neat grinding. For example, ball milling of ZnO and fumaric acid (**H_2fum**) with the bridging ligands 4,4′-dipyridyl (**bipy**) or *trans*-1,2-bis(4,-pyridyl)ethylene (**bpe**) in the presence of a space-filling liquid agent *N*,*N*-dimethylformamide (DMF) leads to a one-pot neutralization and self-assembly process to yield the anticipated pillared MOFs (Figure 3).[1]

The reaction yield was dependent on the amount of the space-filling liquid, leading to quantitative yields in the presence of sufficient DMF to fill the pores of the open framework. The mechanosynthesis of porous MOFs could also be conducted with other space-filling liquids, including environmentally more acceptable methanol, ethanol or 2-propanol, providing access to gram amounts of pillared MOFs within 30 min and at room temperature.[1] Thermogravimetric analysis of the mechanochemically prepared pillared MOFs revealed the loss of included guest upon heating. Subsequent XRPD analysis revealed the retention of the initial pillared MOF structure upon guest loss, indicating that the mechanochemically synthesized materials exhibit the structural robustness previously demonstrated for solvothermally synthesized samples.

2.4 Ion- and Liquid-Assisted Grinding (ILAG)

The ILAG[6,17] methodology represents an improvement of the LAG technique which is particularly useful in the synthesis of metal–organic materials directly from metal oxides. In particular, ILAG utilizes the addition of catalytic amounts of simple ionic salts as a means to induce, enhance, and direct mechanochemical synthesis starting from metal oxides. Whereas the synthesis of pillared MOFs based on relatively small fumarate anions and **bipy** (or **bpe**) bridging units was readily conducted by LAG, attempts to synthesize the large-pore pillared MOFs based on zinc terephthalate and diazabicyclo[2.2.2]octane (**dabco**) as a pillaring ligand in analogous way, i.e., by milling zinc oxide, terephthalic acid, **dabco,** and a space-filling agent, were unsuccessful. Instead, the addition of small amounts of ionic salts (about 100–1000 ppm with respect to the metal) was needed to enable the quantitative formation of the desired frameworks (Figure 4a). The use of nitrate salts as reaction additives (e.g., KNO_3 or NH_4NO_3) led to the formation of the porous framework based on square-grid zinc terephthalate sheets, while ionic additives containing the sulfate ion (e.g., Na_2SO_4 or $(NH_4)_2SO_4$) produced the supramolecular isomer of this MOF, based on zinc terephthalate sheets with a hexagonal (Kagome) topology. These unexpected structure-directing effects were accompanied

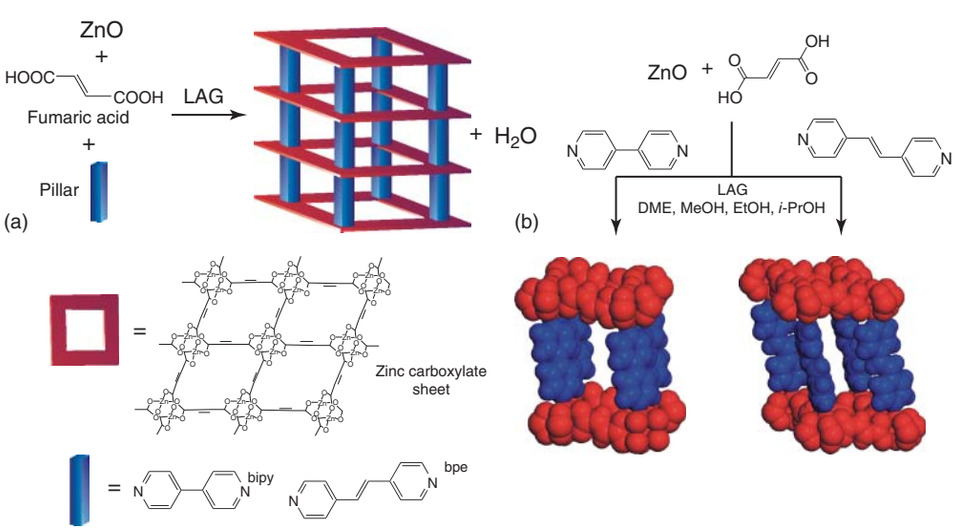


Figure 3 The synthesis of pillared porous MOFs by mechanochemical LAG synthesis starting from a metal oxide: (a) general schematic of the reaction and (b) examples of low-porosity pillared MOFs based on zinc fumarate, prepared by LAG

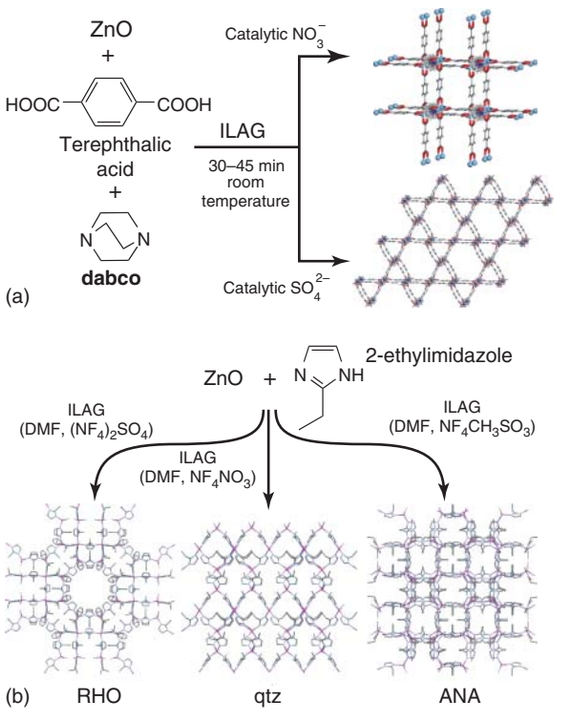


Figure 4 The synthesis of porous MOFs directly from a metal oxide using the mechanochemical ILAG technique: (a) the rapid (less than an hour) and quantitative synthesis of pillared MOFs enabled and directed by catalytic (about 100–1000 ppm) addition of nitrate or sulfate salts and (b) the quantitative formation of porous ZIFs from zinc oxide by grinding with two equivalents of 2-ethylimidazole. Analogous reactivity with 2-methylimidazole produced the popular material ZIF-8 and, with plain **Him**, several other open- and close-packed ZIF topologies

by the inclusion of salts in the MOF porous structure, revealed by solid-state nuclear magnetic resonance (NMR) and infrared spectroscopy. Subsequently, ILAG was used to enable the mechanochemical oxidation of cobalt and ruthenium complexes, and for the conversion of ZnO into ZIFs,[1] a family of porous MOFs which exploit a combination of tetrahedral metal ions (e.g., Zn^{2+}, Co^{2+}) and azolate anions to obtain porous metal–organic topologies analogous to those of zeolites (Figure 4b).[18] ILAG also enabled a rapid and environmentally friendly synthesis of the metallodrug bismuth subsalicylate,[19] the active component of the popular gastrointestinal drug Pepto-Bismol®, as well as of two further bismuth salicylates directly from Bi_2O_3. The outcome of the mechanochemical reactions, which are performed by ball milling in the presence of water and ammonium nitrate, was determined by the stoichiometric ratio of bismuth and salicylic acid in the reaction mixture. The quantitative reaction yield and purity of the products also facilitated the structural characterization of mechanochemical products using XRPD data, leading to the structural characterization of bismuth disalicylate monohydrate, an outstanding target from the 2002 Second Structure Determination by Powder Diffractometry Round Robin challenge (SDPDRR-2). The crystal structure revealed a non-porous 2-D MOF and corrected the previously proposed chemical composition which involved hydroxide ligands. The structure of bismuth disalicylate hydrate is currently the only known crystal structure for a bismuth salicylate complex without auxiliary organic ligands and, as a potential model for the bismuth subsalicylate active drug ingredient, it is in striking contrast to previously proposed models based on discrete oxo-cluster structures.[19]

3 CHARACTERIZATION OF MECHANOCHEMICAL PRODUCTS

Synthesis of metal–organic materials by mechanochemical grinding introduces additional challenges in terms of product characterization. In particular, the possibilities of low product solubility, as well as solvate formation, polymorphism or dissociation/association processes upon product dissolution make it difficult to reliably characterize a product of mechanosynthesis in any other way except in the solid form obtained immediately from the milling reaction. In that way, mechanosynthesis of coordination compounds, as well as of cocrystals, contrasts with organic mechanosynthesis where the product can typically be analyzed in solution after extraction from the solid reaction mixture. Consequently, most products of metal–organic mechanosynthesis are characterized primarily by XRPD, reflectance Fourier transform infrared (FTIR) spectroscopy and solid-state NMR spectroscopy. Although the latter two methods provide direct information on the chemical composition of the product, full structural characterization very often depends on the ability to obtain an identical product by single crystal growth from solution. In such cases, structural characterization is readily achieved through single crystal X-ray diffraction.[1] In cases where reaction in solution provides a different product than mechanosynthesis, it is, in principle, possible to obtain single crystals from solution by seeding it with fine powder of the grinding product.[1] This seeding strategy provides single crystals of the grinding product through heterogeneous nucleation. However, in cases where crystallization from solution consistently fails to provide single crystals of the desired solid phase, a possible alternative is given by methods for crystal structure solution from XRPD data. Indeed, the recent advances in laboratory technology and software have made structure determination from XRPD data, especially if aided by information gathered through spectroscopic, thermal or elemental analysis, a very viable and almost routine method for structural characterization of molecular materials.[20] An

example of complete structure determination from XRPD data is the porous interpenetrated pillared MOF with composition Zn_2(**fum**)$_2$(**bipy**), prepared by mechanochemical synthesis from zinc acetate, **H_2fum** and **bipy**.[1] The determination of the crystal structure for the related framework Zn_2(**fum**)$_2$(**bpe**) from XRPD data was facilitated by structural similarity to its copper(II) analog. Consequently, the structure of the zinc-based framework was obtained by the Rietveld refinement of the structural coordinates of the copper(II) analog to the XRPD pattern measured for the zinc product obtained by LAG.[1,14]

4 SYNTHETIC STRATEGIES FOR EXTENDED METAL–ORGANIC STRUCTURES

The experimental mechanochemical techniques for the synthesis of coordination polymers and MOFs, listed in Section 3, are readily applicable to a diversity of chemical processes leading to the formation of new metal–ligand bonds and associated extended structures. On the other hand, the chemical transformations underlying such processes allow them to be readily divided into four categories: (i) reactions of ligand addition in which the addition of a multi-topic ligand onto the metal center leads to the formation of an extended 1-, 2-, or 3-D structure; (ii) ligand exchange reactions, in which the formation of an extended structure is achieved by mechanochemically replacing simple ligands surrounding a metal center with multi-topic bridging ligands; (iii) acid–base proton-transfer reactions in which the formation of an extended architecture is associated with the protonation and expulsion of a ligand attached to a metal precursor, such as acetate, chloride, carbonate, or oxide; (iv) dehydration reactions[21] in which the loss of coordinated water on a metal center results in the polymerization of a small molecule complex.

4.1 Coordination Polymers by Ligand Addition

The mechanochemical addition of neutral ligands onto a metal-containing building block has been extensively used for the construction of simple coordination polymers. Possibly the first report[1] of a mechanochemically synthesized polymer corresponds to such a reaction, in which grinding of the pre-synthesized 1-D zigzag polymer of zinc bromide and pyrazine, $ZnBr_2$(pyrazine), with one more equivalent of pyrazine led to the formation of the 2-D square grid structure of $ZnBr_2$(pyrazine)$_2$. The bridging ligand that is very often used for mechanochemical syntheses of coordination polymers is **bipy**. For example, neat grinding of zinc chloride and **bipy** readily yielded the 2-D coordination polymer Zn(bipy)Cl_2. Interestingly, the product adopts only one out of three known polymorphic forms of the coordination polymer.[1] In contrast, the analogous 2-D sheet polymer [Co(**bipy**)Cl_2]$_n$ could not be obtained by neat grinding of anhydrous $CoCl_2$ and **bipy**. This polymer could, however, be obtained by neat grinding of $CoCl_2 \cdot 6H_2O$ and **bipy**, suggesting that the water produced by desolvation of the reagents might play a role in achieving mechanochemical reactivity (Figure 5). The construction of [Co(**bipy**)Cl_2]$_n$ from anhydrous $CoCl_2$ was possible by LAG, i.e., by adding a small quantity of ethanol to the grinding mixture. In a systematic study of the mechanosynthesis of coordination compounds James and co-workers[1] have utilized neat grinding of copper(II) acetylacetonate or hexafluoroacetylacetonate with **bipy** to construct 1-D polymers that are held together by axial Cu–N bonds. The product coordination polymers were obtained quantitatively and reliably identified by comparing their

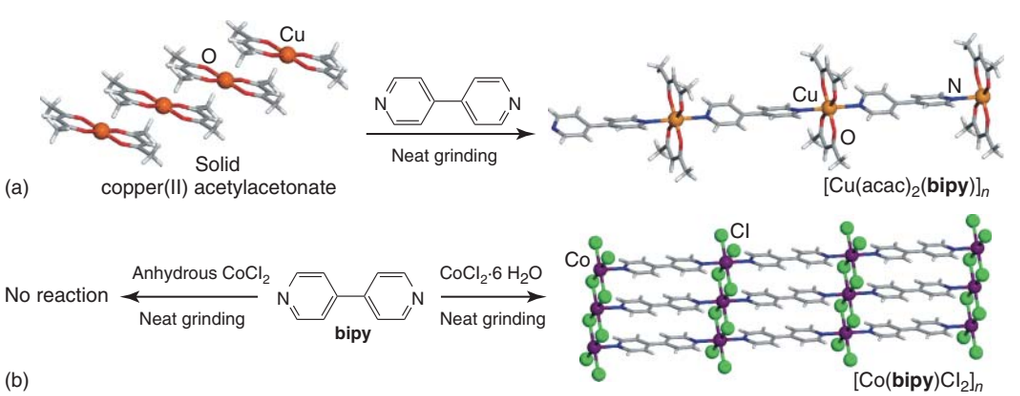


Figure 5 Two examples of the mechanochemical synthesis of coordination polymers by ligand addition reactions: (a) the synthesis of a 1-D coordination polymer from copper(II) acetylacetonate and **bipy** and (b) illustration of the difference in mechanochemical reactivity of **bipy** towards anhydrous $CoCl_2$ and $CoCl_2 \cdot 6H_2O$

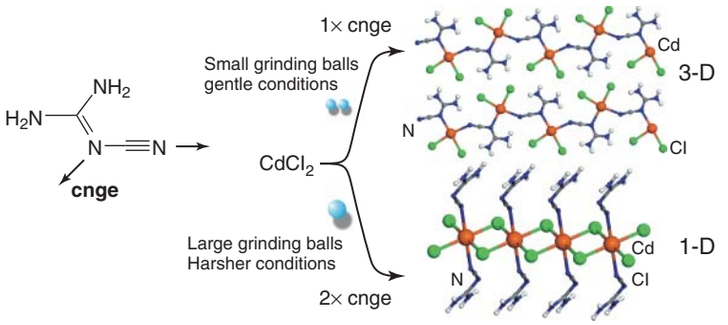


Figure 6 Controlling the mechanochemical synthesis of coordination polymers by variation of milling conditions: milling one equivalent of $CdCl_2$ with one equivalent of the **cnge** ligand leads to the formation of the 3-D framework Cd(**cnge**)Cl_2. Addition of a further equivalent of **cnge** to form the 1-D structure Cd(**cnge**)$_2Cl_2$ can be achieved only by milling with larger (heavier) steel balls, starting either directly from $CdCl_2$ or from Cd(**cnge**)Cl_2

XRPD patterns to those calculated for previously published crystal structures (Figure 5).

The ligand addition reactions[1,19] of $ZnCl_2$ or $CdCl_2$ with the non-symmetrical heteroditopic ligand cyanoguanidine (**cnge**, Figure 6) illustrate how the mechanosynthesis of coordination polymers can be manipulated by varying the conditions of neat milling, specifically the impact force and reaction mixture temperature. The **cnge** ligand provides two different binding sites, enabling the formation of polymers with different metal:ligand ratios and, hence, different dimensionality. Grinding of $ZnCl_2$ with one or two equivalents of **cnge** selectively provides the 1-D polymer Zn(**cnge**)Cl_2 or the discrete complex Zn(**cnge**)$_2Cl_2$, respectively. Similarly, the neat grinding of $CdCl_2$ and **cnge** in a 1:1 stoichiometric ratio provides the 3-D coordination polymer Cd(**cnge**)Cl_2. The product was always obtained as a pure phase and was structurally characterized using powder diffraction data. In contrast to $ZnCl_2$, neat grinding of $CdCl_2$ and **cnge** in the 1:2 stoichiometric ratio provided only a mixture of Cd(**cnge**)Cl_2 with excess ligand. The 1-D polymer Cd(**cnge**)$_2Cl_2$ could be obtained only through harsher grinding conditions, i.e., by employing heavier grinding balls (Figure 6). The difficulty to form 1-D Cd(**cnge**)$_2Cl_2$ was tentatively related to the higher dimensionality and, hence, kinetic stability of the 3-D Cd(**cnge**)Cl_2. Similar observations were also made in for the reaction of CdI_2 and **cnge**.

4.2 Coordination Polymers by Ligand Exchange

The first reported mechanochemical synthesis of a coordination polymer by design was based on a ligand exchange reaction involving the binuclear copper(II) acetate paddlewheel cluster.[1,14] Manual grinding of copper(II) acetate monohydrate with 1,3-bis(4-pyridyl)propane (**pn**) led to the replacement of copper-coordinated water molecules with bridging **pn** ligands, producing a water inclusion compound of a zigzag 1-D polymer (Figure 7a). The mechanochemical product was isostructural to the product of an analogous reaction in refluxing methanol which yielded a methanol inclusion compound. Isostructurality indicated that the water produced by mechanochemical ligand exchange probably became incorporated into the mechanochemical product as a guest. This was also supported by ^{13}C magic angle spinning-NMR spectrum of the mechanochemical product which was identical to the one of the methanol solvate, with the exception of NMR signals of the guest methanol molecules.

In the case of manual grinding of silver(I) acetate (AgOAc) and **dabco**, the neutral **dabco** ligand displaces the anionic acetate ligands coordinated to Ag^+ with simultaneous absorption of water from air to form the product Ag(**dabco**)$_2$(OAc) $\cdot$ $5H_2O$ (Figure 7b). The structure consists of cationic $[Ag(\textbf{dabco})_2(H_2O)]_n^{n+}$ chains with additional water molecules and acetate ions acting as inclusion guests.[1,13] The formation of a hydrated product upon grinding in air again serves to illustrate the significant impact that the surrounding atmosphere can have on mechanochemical synthesis using an open mortar-and-pestle setup.

4.3 Acid–Base Reactions

Reactions that include proton transfer are a powerful tool for the mechanochemical synthesis of coordination polymers and MOFs. Particularly noteworthy are reactions of metal acetate precursors with organic acids, which result in the formation of coordination polymers, accompanied by the release of acetic acid. Such reactivity was observed, e.g., between hydrated nickel(II) acetate and acetylenedicarboxylic acid (**H_2adc**), resulting in the formation of a hydrated 3-D coordination polymer

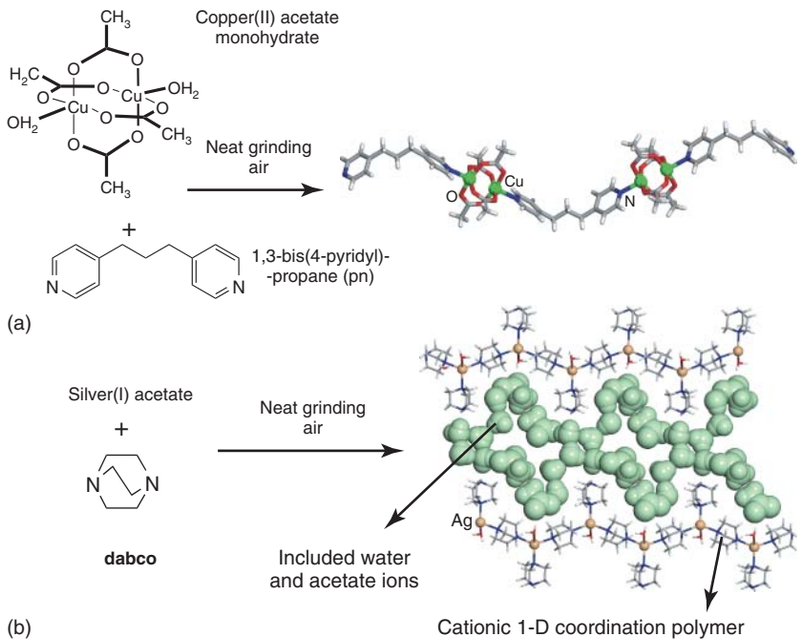


Figure 7 The synthesis of coordination polymers by ligand exchange reactions: (a) mechanochemical construction of a 1-D coordination polymer by exchange of the water ligands on the copper(II) acetate paddlewheel cluster and (b) the formation of a hydrated coordination polymer by neat manual grinding of AgOAc and **dabco** in air. Water and acetate guests are shown using a space-filling model

Ni(**adc**)$(H_2O)_2$.[1] The same product was also obtained by grinding of $\mathbf{H_2adc}$ with $Ni(NO_3)_2 \cdot 6H_2O$, revealing that very basic anions like acetates are not crucial for successful proton exchange in the solid state. Analogous reaction with zinc acetate leads to the formation of a previously unknown 3-D polymer Zn(**adc**)$(H_2O)_2$, identified by isostructurality to the Ni(II) analog, demonstrating how mechanosynthesis can be used to discover new metal–organic materials. This approach was extended to the synthesis of coordination polymers based on alkaline earth metals, specifically by grinding–annealing of magnesium or calcium acetate with $\mathbf{H_2adc}$.[14] The resulting materials Ca(**adc**) and Mg(**adc**) $\cdot 2H_2O$ were found to be isostructural to Sr(**adc**) and Mn(**adc**) $\cdot 2H_2O$. The acidic ligand in reactions with metal acetates does not need to be a carboxylic acid, as demonstrated by neat manual grinding reactions of transition metal acetates with **HCNacac** (3-cyanoacetylacetone) (Figure 8).[1] With acetates of Fe(II), Co(II), and Ni(II), proton transfer and ligand exchange directly yielded non-porous 3-D frameworks. Grinding of **HCNacac** with hydrated Mn(II), Cu(II), or Zn acetate, however, provided previously unknown mononuclear complexes Mn(**CNacac**)$_2 \cdot 2H_2O$, Cu(**CNacac**)$_2 \cdot H_2O$, and Zn(**CNacac**)$_2 \cdot H_2O$, respectively. Upon heating to 100 °C, these complexes lose water and form coordination polymers, illustrating the grinding–annealing dehydration route to coordination polymers (Figure 8).

Another example of the grinding–annealing synthetic technique is the thermal dehydrohalogenation of isomorphous 4,4′-bipyridinium salts of $FeCl_4^{2-}$, $CoCl_4^{2-}$, and $ZnCl_4^{2-}$ anions, prepared by neat grinding of 4,4′-bipyridinium chloride with $FeCl_2 \cdot 4H_2O$, $CoCl_2$ (or $CoCl_2 \cdot 6H_2O$), and $ZnCl_2$, respectively. The thermal step results in the reversible elimination of HCl gas and formation of a 1-D zigzag (in case of Zn) or 2-D sheet (in case of Fe and Co) polymers (Figure 9a). The dehydrohalogenation could also be achieved through the addition of an external base, such as KOH, rather than through heating (Figure 9b). While the use of external base is environmentally advantageous to thermal dehydrohalogenation, this advantage is somewhat offset by the need to remove the byproduct salt (e.g., KCl).[1]

4.4 Synthesis of Coordination Polymers and MOFs from Metal Oxides and Carbonates

So far, all discussed examples of acid–base reactions used to construct coordination polymers involve soluble metal salts as precursors. However, as mechanochemical reactivity is independent from the solubility of reactants, the use of slightly soluble but cleaner and readily available carbonate or oxide reactants is also possible.[1,6] With oxide reactants, the highly basic nature of the oxide ion provides a strong driving force for the

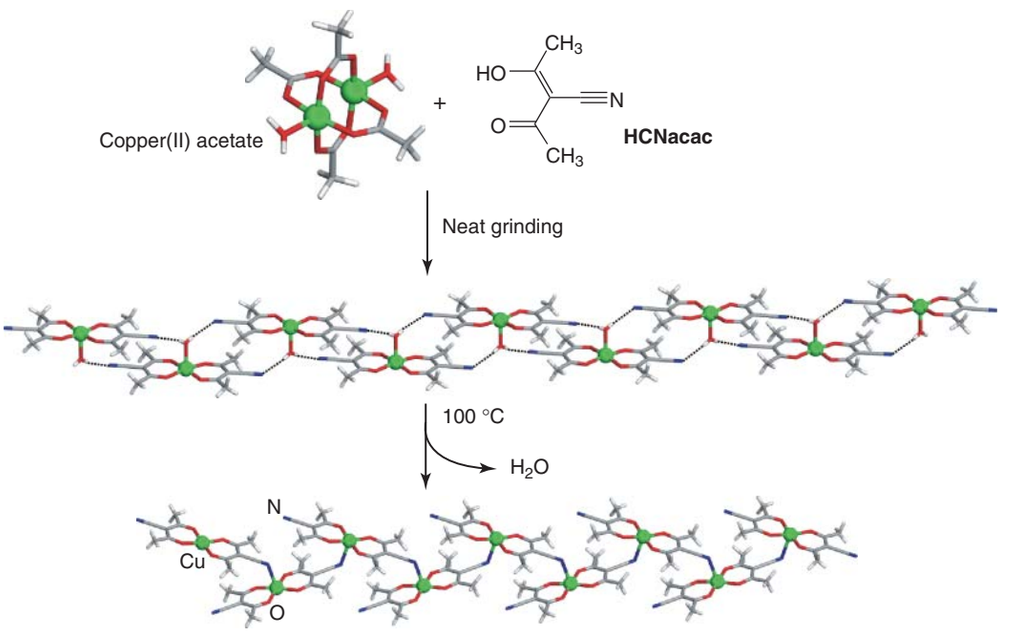


Figure 8 Synthesis of a coordination framework by a grinding–annealing procedure: reaction of copper(II) acetate monohydrate and **HCNacac** results in the formation of the monomeric complex Cu(**CNacac**)$_2 \cdot H_2O$ which subsequently, upon thermal treatment, loses water to form 1-D coordination polymer. Similar dehydration, leading to the formation of 2- and 3-D frameworks is also achievable through LAG with water-binding liquids, such as methanol (see Section 4.5)

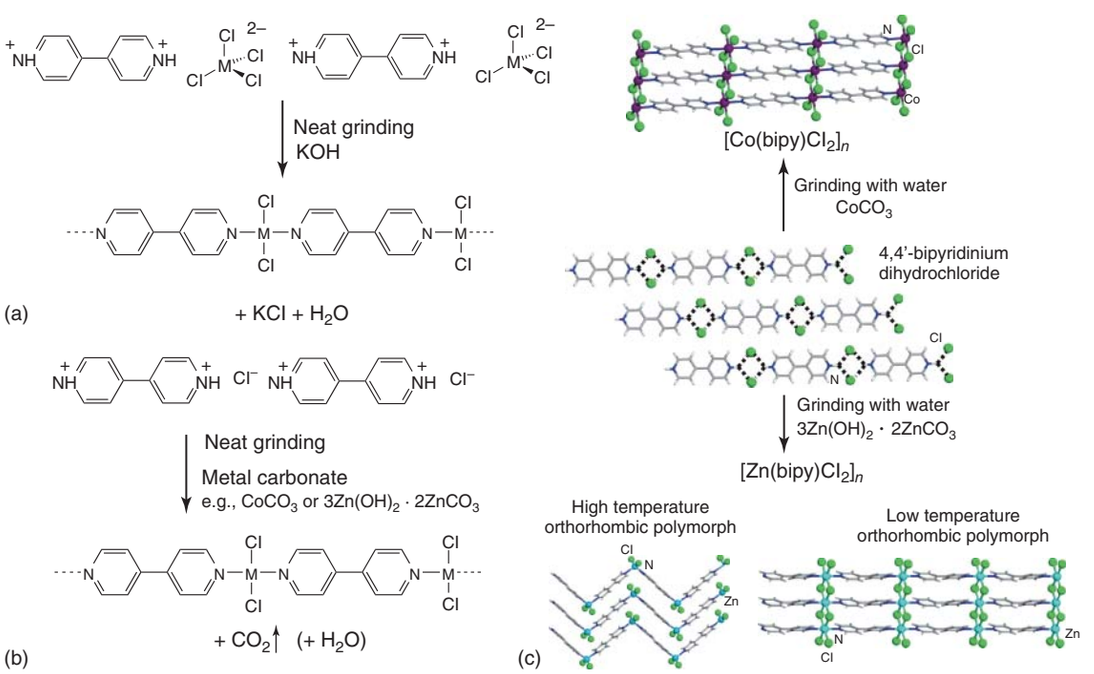


Figure 9 The synthesis of coordination polymers by acid–base reactions involving: (a) an external base, such a potassium hydroxide or (b) an internal base, in the form of a metal carbonate or hydroxide. (c) Illustration of the mechanochemical acid–base reactions leading to the formation of cobalt(II) and zinc coordination polymers

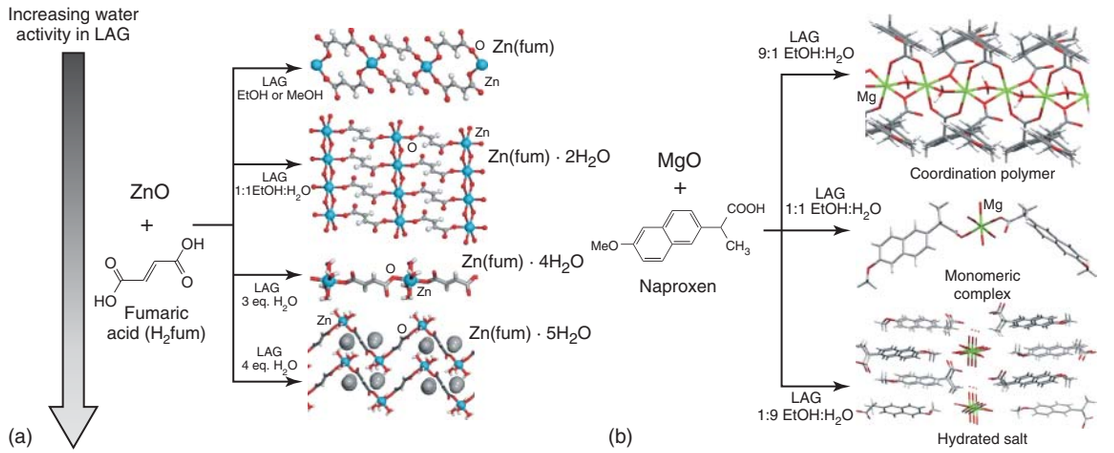


Figure 10 Controlling the outcome of mechanochemical synthesis by variation of water activity in the grinding liquid used for LAG: (a) the synthesis of zinc fumarate anhydrous and hydrated coordination polymers from ZnO and (b) screening for magnesium naproxen pharmaceutical derivatives of different levels of hydration and polymerization

mechanochemical reaction. For metal carbonates, the generation of gaseous CO_2 provides an additional driving force for the reaction (Figure 9c). Mechanochemical reactivity of metal oxides against organic ligands was first explored by Fernandez-Bertran, who obtained coordination polymers of Ag(I), Zn, Cd, and Hg(II) by neat grinding of respective metal oxides and **Him**.[1] Analogous reactions with oxides of other transition metals, Pb(II) or Mg could not be achieved, suggesting that the nd^{10} configuration of the metal ion was important for the reactivity. The construction of coordination polymers from metal carbonates was utilized in the synthesis of the 2-D sheet polymer $[Co(\mathbf{bipy})Cl_2]_n$ by LAG of cobalt(II) carbonate with bipyridinium chloride. The product was identical to the one constructed by kneading of $CoCl_2$ and **bipy** with water. Similarly, LAG of the basic zinc carbonate with bipyridinium chloride gave a mixture of two polymorphs of the $[Zn(\mathbf{bipy})Cl_2]_n$ polymer. This contrasts the neat grinding reaction of $ZnCl_2$ and **bipy** which yields only one polymorph, thus suggesting a surface templating effect in the reaction.

The reaction of ZnO with $\mathbf{H_2fum}$ was utilized to demonstrate rapid screening for coordination polymers using LAG.[19] Different liquid phases were found to steer the reaction towards the formation of different products. Quantitative yields allowed the structural characterization of anhydrous zinc fumarate and a previously not known zinc fumarate dihydrate directly from powder diffraction data. Furthermore, grinding of equimolar amounts of ZnO and $\mathbf{H_2fum}$ with three and four equivalents of water selectively produced the tetrahydrate and the pentahydrate forms of zinc fumarate, known to form concomitantly from solution.

The formation of different zinc fumarate coordination polymers by grinding with a different liquid phase was subsequently rationalized in a study using different mixtures of alcohols and water as grinding liquids. The composition of the product was found to be strongly correlated to the activity of water in the grinding liquid, suggesting a rational strategy to mechanochemically screen for hydrated coordination polymers by varying the activity of water in the grinding liquid. This was subsequently exploited in the pharmaceutical context, as a strategy to explore the phase space of hydrated magnesium complexes of the drug molecule naproxen (Figure 10). The formation of solid hydrates is of particular importance in developing pharmaceutical formulations and new solid form of pharmaceuticals. By controlling the water activity in the grinding liquid, we have generated four different magnesium derivatives of naproxen, simply by LAG of MgO and the drug. Structures of two thus generated materials have been obtained by re-crystallization and single crystal X-ray diffraction, and by structure determination from XRPD data from the material obtained directly by mechanochemical screening.[19]

4.5 Mechanochemical Dehydration

LAG offers an interesting alternative to grinding–annealing for achieving the formal dehydration of small molecule complexes and their association into extended structures. As demonstrated by Wang and coworkers,[21] mechanochemical milling of zinc oxide or copper(II) acetate monohydrate in the presence of water leads to the formation of corresponding hydrated metal isonicotinates, small discrete complexes of composition $M(\mathbf{ina})_2(H_2O)_4$ (where M = Zn or Cu). A second round of

milling, but now in the presence of methanol, a solvent well known to greatly reduce the activity of water, leads to the dehydration of the monomeric tetrahydrate complexes and their reversible polymerization to provide either the non-porous triply interpenetrated MOF Zn(**ina**)$_2$ with a diamondoid topology, or the open 2-D MOF Cu(**ina**)$_2$. Consequently, LAG with a solvent that exhibits a particularly high affinity for water can be used as a means of non-thermal dehydration and polymerization of small molecule complexes to form MOFs. Interestingly, the mechanochemical LAG dehydration is readily reversed by milling the two MOFs with water, yielding again the M(**ina**)$_2$(H_2O)$_4$ complexes.

5 POROUS MOFs BY MECHANOCHEMISTRY

The possibility to form a porous material through mechanochemical grinding was first demonstrated[1] in the acid–base reaction between copper acetate and **Hina**, which led to the construction of the open copper(II) isonicotinate framework Cu(**ina**)$_2$. Neat grinding resulted in the quantitative formation of the porous framework, with the acetic acid and water byproducts most likely included in the pores (Figure 11a). The same approach was subsequently used to construct the industrially relevant open framework HKUST-1 (pore diameter about 9 Å) by neat grinding of copper(II) acetate with trimesic acid.[14] As noted in Sections 2.3 and 2.4, the application of the LAG and ILAG techniques enabled the facile and rapid, topologically specific transformation of zinc oxide into microporous pillared MOFs based on zinc fumarate or terephthalate sheets.

The use of mechanochemistry to synthesize porous materials directly from metal oxides was recently extended to the construction of ZIFs (Figure 3). Whereas grinding of ZnO with solid **Him** is of very limited scope for the construction of ZIFs, modified methods such as LAG or ILAG lead to rapid and quantitative synthesis of a variety of close-packed and open-framework ZIFs. The grinding liquid and the ionic salt catalysts both enhance the reactivity of ZnO and **Him** ligands, and exert control over the final product topology. In that way, different grinding liquids and salt catalysts enable the topologically specific and quantitative formation of different ZIF architectures from the same reactants. This is illustrated in Figure 3 in the case of ZIFs based on 2-ethylimidazole, where different choices of ionic additive and grinding liquid lead to selective formation of frameworks with zeolite rho (RHO), analcime (ANA), and β-quartz (qtz) topologies.[1] It is noteworthy that the mechanosynthesis of ZIFs proceeds through a stepwise mechanism in which the most porous structures are formed first and subsequently transform to close-packed structures via intermediate architectures of intermediate porosity. Such transformation is reminiscent

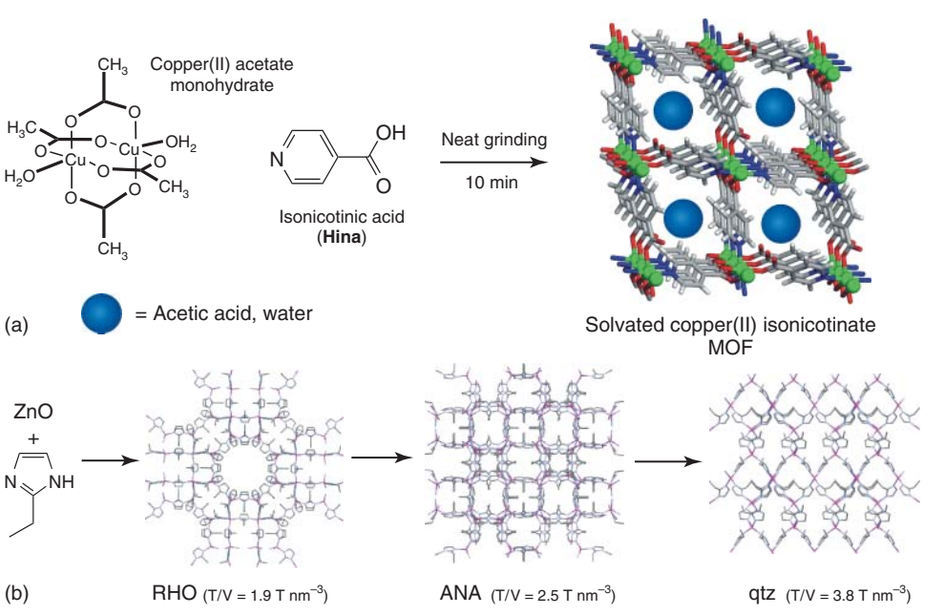


Figure 11 The first reported mechanochemical synthesis of a porous MOF, by neat grinding of copper(II) acetate hydrate with **Hina**. The acetic acid and water produced in the reaction become included in the open MOF product and can be removed by thermal treatment. The interconversion of porous and non-porous ZIF structures in the mechanochemical reaction of ZnO and 2-ethylimidazole. The sequence of structural transformations is consistent with the increasing density of tetrahedral centers (T) per unit volume (V) in the structures

of the Ostwald's rule of stages in which the less stable frameworks of low density (normally expressed as the ratio of tetrahedral sites per volume of the unit cell) transform to more stable, increasingly dense structures. The role of the salt additive in ZIF mechanosynthesis by ILAG is different than that in the synthesis of pillared MOFs. While the synthesis of pillared MOFs using ILAG clearly reveals an anion-related effect, ZIF synthesis strongly depends on the use of weakly acidic ammonium salts. The topological control in ILAG synthesis of ZIFs appears to arise from the ability of salt additives to control the rate of spontaneous interconversion of porous and non-porous structures, rather than from specific structure-templating effects (Figure 11b).[1,19]

The described mechanochemical methodologies have obvious advantages over solvothermal approaches used for porous MOF synthesis in terms of time (minutes vs days), temperature (near room-temperature vs 100–150 °C), and reactant choice (metal oxides vs soluble salts). Further advantages are the absence of bulk solvent and a wide choice of catalytic liquid phases, including ethanol, which is one of the more preferred solvents from a Green Chemistry perspective. The only waste product of the oxide-based reaction is water. The functional nature of porous MOFs obtained mechanochemically was recently investigated by Yuan and coworkers, who found that the Brunauer–Emmett–Teller (BET) surface area of the exemplary MOF HKUST-1 obtained by neat grinding of copper(II) acetate monohydrate with trimesic acid was comparable to that of samples obtained by conventional solution-based routes. Another study by Schlesinger and coworkers[22] compared neat and liquid-assisted mechanosynthesis with a variety of other procedures, involving room-temperature and reflux solution synthesis, solvothermal reactions, microwave-assisted synthesis, sonochemical, and electrochemical syntheses.[1] This comparative study revealed that the BET surface area and specific pore volume of HKUST-1 samples could be further increased if the reaction was conducted using LAG with DMF. The resulting porous properties were comparable to those obtained through solvothermal or microwave-assisted reactions. Similar observations have been made for the mechanochemically synthesized material MOF-14.

6 EMERGENT PROPERTIES OF MECHANOCHEMICALLY OBTAINED METAL-ORGANIC MATERIALS

6.1 Structural Dynamics under Mechanochemical Conditions

A recently reported effect in MOF chemistry, which might become of considerable importance, is the highly dynamic nature of the frameworks under conditions of LAG. For example, grinding of ZnO and terephthalic acid with water, DMF or methanol yields 1-D, 2-D, or 3-D forms of the zinc terephthalate polymer, respectively (Figure 12). Different forms were almost completely

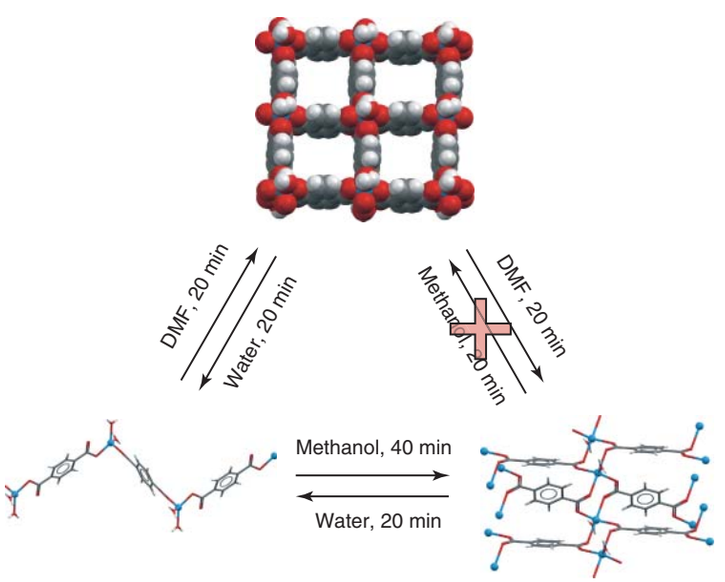


Figure 12 Illustration of the dynamic nature of coordination polymers and open MOFs under mechanochemical milling conditions. Milling with a suitable liquid phase leads to the formation of different open- and close-packed materials based on zinc terephthalate. Such high level of structural dynamics is not observed in analogous slurry experiments

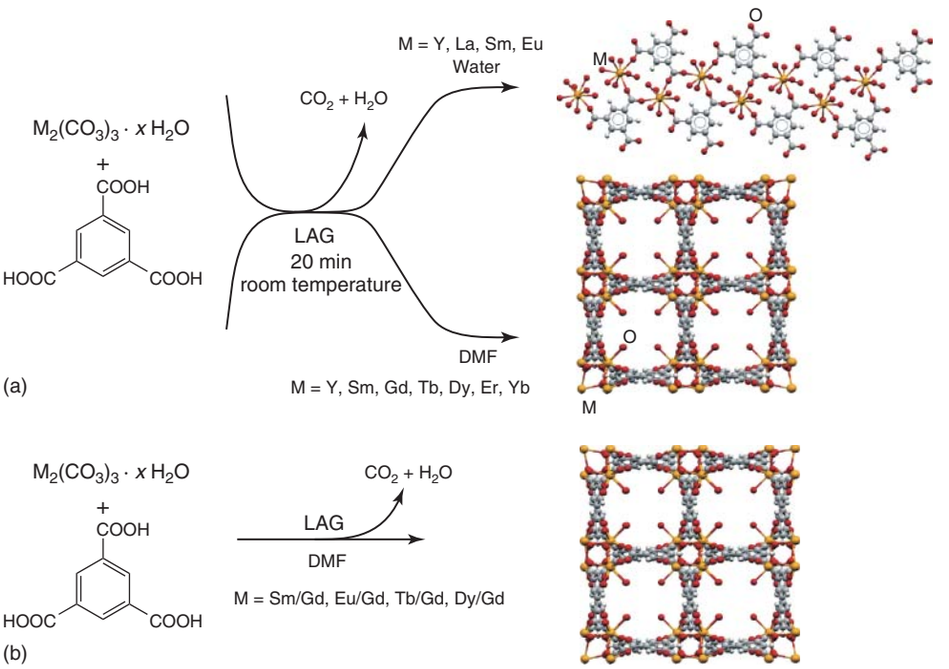


Figure 13 The formation of MOFs based on rare earth (lanthanide) ions by LAG with trimesic acid: (a) the formation of an open structure is dictated by LAG with DMF rather than water and (b) the formation of mixed-metal lanthanide MOFs containing selected pairs of metal ions

interconvertible by brief grinding with a suitable liquid and such fluxional behavior also permitted the construction of open pillared structures by addition of the bridging ligand such as **dabco** or **bipy**.[1] Such behavior is considerably different from solution-based chemistry, as the mechanochemically induced transformations do not readily occur by simple immersion of reactant materials in the bulk liquid.

6.2 Synthesis of Solid Solutions

Although isostructurality of components is often considered to be a very important factor in the synthesis of solid solutions, their formation via conventional solution-based methods is often hindered by the difference in solubility of individual components which leads to the preferential crystallization of separate components. The potential advantage of mechanochemistry for the construction of solid solutions of isostructural coordination polymers has been demonstrated by James and coworkers who constructed close-packed and open-framework materials by LAG reactions of rare earth metal carbonates and trimesic acid. In particular, LAG of each individual metal carbonate in the presence of water quantitatively yielded isostructural close-packed materials consisting of 1-D coordination polymers.[1] In contrast, LAG with DMF resulted in the formation of isostructural lanthanide MOFs based on an open 3-D architecture (Figure 13). The isostructurality of the 3-D MOF products suggested the possibility to form solid solutions. Indeed, grinding of different pairs of lanthanide metal carbonates (e.g., pairs Sm–Gd, Eu–Gd, Tb–Gd, and Dy–Gd) with trimesic acid resulted in the formation of mixed-lanthanide 3-D open frameworks isostructural to the ones obtained using individual metal carbonate reactants (Figure 13).[1]

The ability to mechanochemically form solid solutions of coordination polymers was exploited for the synthesis of metal–organic materials with controlled crystallographic lattice parameters and physical properties. Mechanochemical LAG of anhydrous $CoBr_2$ with **bipy** results in the quantitative formation of the 2-D sheet coordination polymer Co(**bipy**)Br_2. The coordination polymer is isostructural to Co(**bipy**)Cl_2 which is obtained by analogous reaction of anhydrous $CoCl_2$ (Figure 5). Correspondingly, LAG of different mixtures of anhydrous $CoCl_2$ and $CoBr_2$ yields solid solutions of the two coordination polymers, with overall composition Co(**bipy**)$Br_{2-x}Cl_x$. The solid solutions are homogeneous at length scales detectable by XRPD and UV/Vis spectroscopy, with the Br/Cl ratio determined by the relative amounts of $CoBr_2$ and $CoCl_2$ in the reaction mixture. The coordination polymer solid solutions are isostructural to the single phases Co(**bipy**)Cl_2 and Co(**bipy**)Br_2, but with lattice parameters

and UV/Vis absorption properties determined by the Br/Cl ratio. Specifically, the crystallographic lattice parameters and UV/Vis absorption of Co(**bipy**)$Br_{2-x}Cl_x$ were found to change in a continuous and linear fashion with x over the range 0–2.[1]

6.3 Binding of Carbon Dioxide upon Mechanochemical Treatment

Manual grinding of solid silver carbonate, Ag_2CO_3 with triphenylphosphine (PPh_3) in air and in the presence of liquid ethanol leads to the absorption of one equivalent of water (present in the form of air moisture) and one equivalent of CO_2 gas to yield bis(triphenylphosphino)silver(I) hydrogencarbonate (CCDC code OTAHUN) which can again release CO_2 upon thermal treatment. Monitoring of the reaction through solid-state infrared spectroscopy suggests a two-step mechanism involving the formation of the solid tetrakis(triphenylphosphino)silver(I) carbonate as the intermediate. Although this particular mechanochemical product is not an extended metal–organic structure, the ability to chemically bind carbon dioxide through a mechanochemical transformation of a metal–organic system is fascinating, especially when considering the growing importance of metal–organic materials for sequestration of waste carbon dioxide.[19]

7 MECHANISTIC STUDIES OF MECHANOCHEMICAL MOF SYNTHESIS

7.1 Stepwise Analysis

The mechanochemical synthesis of coordination polymers and MOFs does not necessarily need to proceed in a single step. Indeed, previous sections have already illustrated how the modification of mechanochemical milling force (upon milling of $CdCl_2$ and **cnge**) can induce the formation of crystalline intermediates that are detected in the reaction mixture through XRPD analysis or spectroscopic methods such as infrared or terahertz spectroscopy. The simplest approach to detect crystalline reaction intermediates in mechanosynthesis is by step-by-step analysis, i.e., by periodically halting the mechanochemical milling and analyzing the composition of the reaction mixture. Such analysis qualitatively revealed the stepwise transformation of ZIF topologies in ILAG synthesis of zinc 2-ethylimidazolate from ZnO, which was tentatively associated to relative thermodynamic stabilities of porous and non-porous frameworks (see also Section 5). Recently,[23] Raman spectroscopy was utilized to perform a quantitative step-by-step analysis of the mechanochemical LAG reaction of zinc oxide and **Him** with initially anhydrous DMF as the grinding liquid. The outcome of these measurements revealed "pseudo-fluid" behavior as the reaction progress was readily fitted to a second-order kinetic law. Moreover, the reaction rate was found to be linearly related to milling frequency, but independent of the temperature rise induced by extended milling. These observations indicated that the mechanochemical transformation is largely the result of a "contact reaction" taking place between reactant particles being brought into close contact through milling. In such a picture, the rapidly mixed solid mixture (or a thick slurry) behaves like a "pseudo-fluid" in which the reaction rate depends only on the frequency of reactive encounters between reactant particles, controlled by milling, rather than on reaction temperature or production of water during the reaction.

Another example of a stepwise mechanochemical reaction mechanism is the synthesis of the 1-D coordination polymer zinc fumarate tetrahydrate (Figure 14a). Whereas milling together of ZnO, **H_2fum** and three equivalents of water for about 45 min leads to the specific formation of the tetrahydrate phase, stopping the milling earlier reveals the presence of an intermediate pentahydrate phase. This stepwise process is explained by the rapid, liquid-assisted formation of the crystalline pentahydrate at early stages of the reaction in which water is abundant. The rapid formation of the pentahydrate phase, however, efficiently depletes the water in the reaction mixture and transforms the fast liquid-assisted reaction into a slower neat grinding process.[1] The resulting neat grinding process is speculated to proceed through an amorphous intermediate, deduced by the spontaneous formation of different coordination polymers by ageing of the partially reacted reaction mixture (Figure 14a). A similar stepwise mechanism was observed in the mechanochemical reaction of CuO and acetic acid, where the abundance of acetic early in the reaction leads to the formation of the intermediate crystalline acetic acid solvate of the copper(II) acetate paddlewheel cluster (Figure 14b).

A particularly interesting example of a stepwise mechanism in mechanosynthesis is given by neat grinding reaction of anhydrous $ZnCl_2$ with the aliphatic ligand **dabco**. The first reaction step is the formation of crystalline Zn(**dabco**)$Cl_2 \cdot 4H_2O$, which upon heating or further grinding transforms to the 1-D zigzag polymer $[Zn(\textbf{dabco})Cl_2]_n$. The latter was also obtained from solution and was characterized by single crystal X-ray diffraction (Figure 14c). The formation of an intermediate was ascribed to the hygroscopic nature of **dabco** under grinding conditions. Consequently, this reaction clearly demonstrates how the surrounding atmosphere can influence the course of a mechanochemical reaction. The active role of moisture in the formation of the intermediate was also confirmed by conducting the mechanosynthesis in dry air and with carefully dried reactants. Under such conditions, $[Zn(\textbf{dabco})Cl_2]_n$ formed directly, without observable

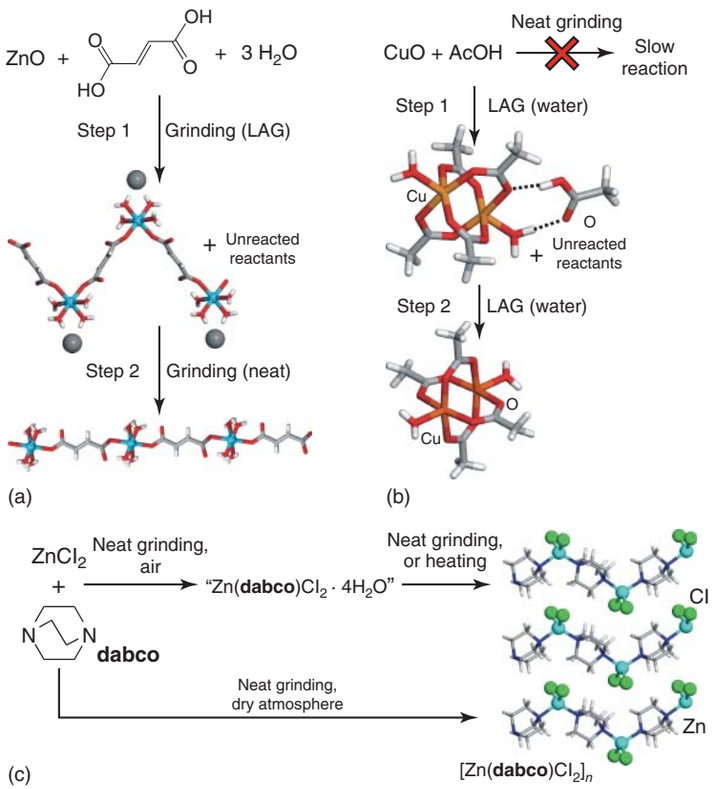


Figure 14 The stepwise reaction mechanism in the mechanochemical oxide-based LAG synthesis of: (a) zinc fumarate tetrahydrate coordination polymer and (b) copper(II) acetate monohydrate paddlewheel cluster. In such LAG reactions the stepwise nature of the mechanochemical process is associated with the large excess of liquid reactant present in the early stages of the reaction. (c) An example of the effect of surrounding atmosphere in the mechanism of mechanochemical formation of a coordination polymer: grinding $ZnCl_2$ and **dabco** in open air leads to the formation of the 1-D coordination polymer Zn(**dabco**)Cl_2 via a hydrated intermediate with a proposed formula Zn(**dabco**)$Cl_2 \cdot 4H_2O$. The same final product is obtained by grinding in a dry atmosphere, but without and observable crystalline intermediates

intermediates. That the sensitivity to moisture is largely related to **dabco** is also supported by the observation that neat grinding of anhydrous $ZnCl_2$ and **bipy** to form of a similar zigzag 1-D polymer proceeds in a single step.[14]

7.2 In Situ and Real-Time X-Ray Diffraction Studies

One of the major drawbacks of mechanochemical milling and grinding chemistry is the inability of real-time observing the transformation of reactants into products. As pointed out by Drebuschak and coworkers[24] *It is a challenge to understand the processes taking place in a powder sample during its grinding in a mill, or compacting, since one can neither measure local temperature, pressure, shear stresses, nor follow the changes in the diffraction patterns or vibrational spectra in situ.* Indeed, the ability of in situ monitoring mechanochemical reactions has been largely limited to temperature- and pressure-measurements on mechanically induced self-sustaining reactions, or on monitoring pressure changes in reactions adsorbing or releasing a gas. An example of the latter is the inorganic metathesis reaction kinetically analyzed by Urakaev and Boldyrev.[25] Very recently, however, the application of highly penetrating synchrotron X-ray radiation enabled an unprecedented technique for the real time in situ study of mechanochemical synthesis of porous MOFs by powder X-ray diffraction.[26] The excellent penetrating power of X-rays with a short wavelength (0.1 Å, corresponding to energies in the range of about 90 keV) enabled the recording of the powder diffraction patterns of reaction mixtures as these are being milled, with a time resolution in seconds. Such real-time and in situ structural studies have painted an unexpectedly dynamic picture of mechanochemical milling reaction, involving highly labile intermediate phases whose lifetime is less than a minute, dependent on milling conditions and environment, and whose chemical and particle size evolution could be measured in real time and in situ (Figure 15a–c). For the mechanochemical synthesis of the porous framework material ZIF-8 in situ studies have enabled the quantification of product formation rates for

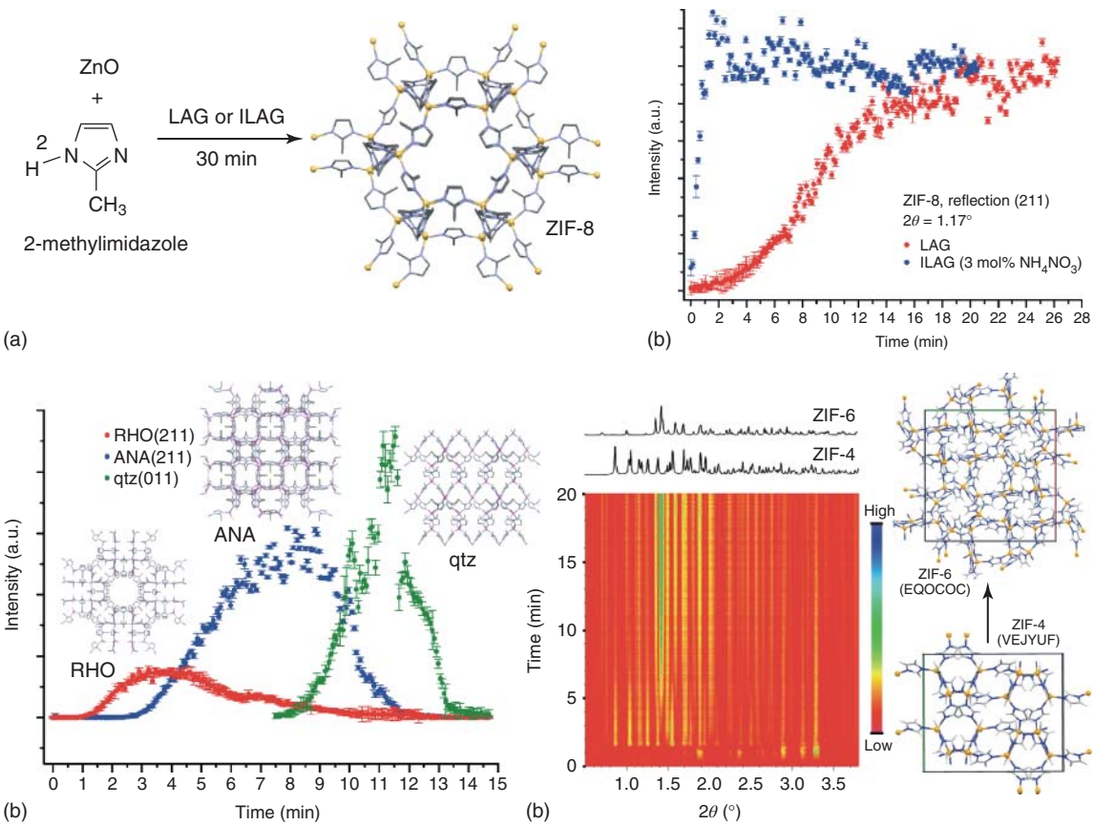


Figure 15 Mechanochemical formation of porous ZIFs investigated by time-resolved in situ powder X-ray diffraction methodology: (a) the quantitative synthesis of the popular ZIF-8 framework by LAG or ILAG reaction of ZnO with two equivalents of 2-methylimidazole; (b) kinetic curves for the LAG and ILAG syntheses of ZIF-8, based on monitoring the increase in intensity of a characteristic ZIF-8 (211) X-ray reflection during milling; (c) an example kinetic curve for the mechanochemical reaction of ZnO and 2-ethylimidazole, involving the sequential formation of three different ZIF topologies with decreasing porosity (see also Section 5) and (d) the time-resolved X-ray powder diffractogram (left) and schematic of the observed process (right) for the mechanochemical reaction of ZnO and **Him** in the presence of a reduced amount of DMF, which leads first to the formation of an open ZIF-4 structure which subsequently collapses to form the low-porosity ZIF-6

reactions conducted by LAG and by ILAG. Assuming Avrami-Erofe'ev kinetics switching from LAG to ILAG by salt addition led to a about 15-fold increase in the rate constant for product formation.

The in situ monitoring technique readily captured the formation and interconversion of ZIFs with different topologies upon mechanochemical ILAG reaction of ZnO and 2-ethylimidazole. Plotting the time-dependent intensities of the characteristic X-ray reflections for all involved materials provided the first insight into the kinetics of ZIF mechanosynthesis and transformation (Figure 15d). The real-time in situ monitoring of the milling reaction between **Him** and ZnO revealed strong dependence of the reaction behavior to reaction conditions. Neat grinding of the two reactants was observed to proceed in a single step to provide the discrete coordination tetramer of composition Zn_4(**im**)$_8$(**Him**). In contrast, ILAG with ethanol as the grinding liquid led to the rapid, one-step formation of the non-porous 3-D zinc imidazolate framework with *zni* topology. Replacing ethanol with DMF as the grinding liquid led to formation of the open framework structure known as ZIF-4, containing included DMF guests. However, reducing the amount of DMF led to a stepwise process in which the initially formed ZIF-4 is subsequently, within minutes, replaced by a low porosity structure known as ZIF-6 (Figure 15e,f).[26]

7.3 Scanning Electron Microscopy

There have been very few studies of the morphology of MOF particles obtained by mechanosynthesis. For example, scanning electron microscopy (SEM) images of zinc fumarate pillared MOFs obtained by LAG from ZnO, **H_2fum** and **bipy** reveal well-developed rectangular crystals with approximate size of 200 nm.[1] A similar observation

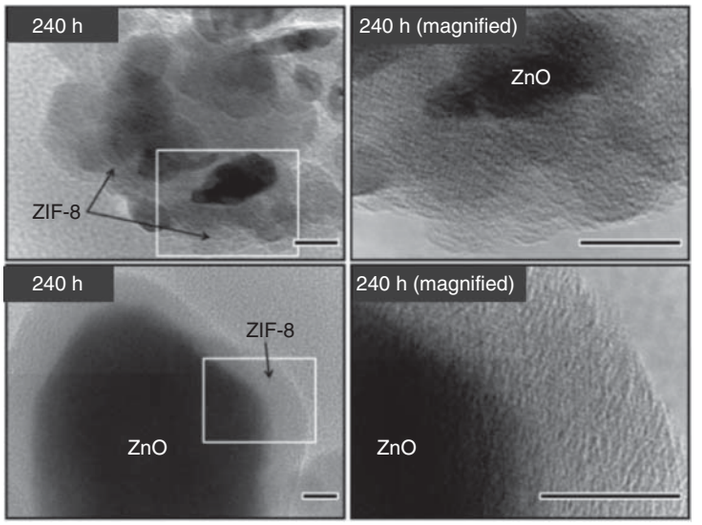


Figure 16 Field emission scanning electron microscopy (FESEM) images of product particles after 240 h milling of ZnO and 2-methylimidazole, leading to the formation of microporous zinc(2-methylimidazolate) ZIF-8. The images on the right represent the magnified frames from the left-side images. Scale bar is 500 nm. The formation of core-shell structures composed of ZnO and ZIF-8 is evident (Reproduced from reference 27.)

was also made for mechanochemically prepared microcrystals of zinc isonicotinate tetrahydrate, the monomeric precursor to interpenetrated diamondoid zinc isonicotinate framework, which exhibited well-developed needle- and rod-like morphologies.[21] Overall, the several existing SEM studies indicate that coordination polymers and MOFs prepared by LAG or ILAG will exhibit morphologically well-developed crystals with sizes in the range 100 nm–1 μm. The so far only systematic SEM study of particle development[27] during mechanochemical synthesis of MOFs has been conducted for the slow (up to 240 h milling) neat grinding reaction of ZnO and 2-methylimidazole to for ZIF-8. The study revealed that the transformation of ZnO particles into ZIF-8 can penetrate as far as 10 nm below the surface of the reactant oxide particle. Consequently, for small particles of ZnO it is possible to achieve the complete conversion into ZIF-8. For larger ZnO particles, or their agglomerates, the mechanochemical reaction leads to the formation of particles consisting of a core of zinc oxide surrounded by a shell of ZIF-8 (Figure 16).

8 CONCLUSIONS

Mechanochemical synthesis is a general and reliable approach to synthesize extended structures based on coordination bonds, and has very consistently improved the synthesis of diverse 1-D, 2-D, or 3-D coordination polymers and porous MOFs in terms of speed, energy, and solvent usage, as well as atom efficiency. The improved mechanochemical techniques of LAG and ILAG can reliably provide both easy and rapid access to porous MOFs directly from simplest precursors, as well as enable a means to probe structure templating effects that guide MOF assembly but are difficult, or even impossible, to detect in conventional solution-based or solvothermal synthesis. Moreover, the transformations of different MOF topologies upon mechanochemical milling have now become directly observable through a new technique for in situ and real-time reaction monitoring. These abilities suggest a rich and important future role of mechanochemistry in MOF chemistry, not only as a tool for the synthesis and screening of new materials, but also as a means to understand the fundamental factors controlling MOF topologies as well as processes underlying their self-assembly.

9 ACKNOWLEDGMENTS

The author acknowledges the support of McGill University, NSERC Discovery Grant and FRQNT Nouveaux Chercheurs grant.

10 RELATED ARTICLES

Porous Coordination Polymer Nanoparticles and Macrostructures; Synthesis and Structures of Aluminum-Based Metal-Organic Frameworks; Gas Storage in

Metal-Organic Frameworks; Single-Crystal to Single-Crystal Transformations in Metal-Organic Frameworks; Recent Solid-State NMR Studies of Quadrupolar Nuclei in Metal-Organic Frameworks; Interpenetration and Entanglement in Coordination Polymers.

11 ABBREVIATIONS AND ACRONYMS

AgOAc = silver(I) acetate; BET = Brunauer-Emmett-Teller; **bipy** = 4,4′-dipyridyl; **bpe** = *trans*-1,2-bis(4,-pyridyl)ethylene; **cnge** = cyanoguanidine; **dabco** = diazabicyclo[2.2.2]octane; **dace** = 1,4-diaminocyclohexane; DMF = *N*,*N*-dimethylformamide; DMSO = *S*,*S*-dimethylsulfoxide; FTIR = Fourier transform infrared; **H_2adc** = acetylenedicarboxylic acid; **H_2fum** = fumaric acid; **HCNacac** = 3-cyanoacetylacetone; **Him** = imidazole; **Hina** = isonicotinic acid; HKUST-1 = copper(II) trimesate; ILAG = ion- and liquid-assisted grinding; LAG = liquid-assisted grinding; MAS = magic angle spinning; MOF = metal–organic framework; NMR = nuclear magnetic resonance; OAc = acetate ion; **pn** = 1,3-bis(4-pyridyl)propane; PPh_3 = triphenylphosphine; SEM = scanning electron microscopy. XRPD = X-ray powder diffraction; ZIF = zeolitic imidazolate framework; 1-D = one-dimensional; 2-D = two-dimensional; 3-D = three-dimensional.

12 REFERENCES

1. S. L. James, P. Collier, I. Parkin, G. Hyatt, D. Braga, L. Maini, W. Jones, C. Bölm, A. Krebs, J. Mack, D. Waddell, W. Shearouse, A. G. Orpen, C. J. Adams, T. Friščić, J. W. Steed, and K. D. M. Harris, *Chem. Soc. Rev.*, 2012, **41**, 413.
2. V. Šepelák, A. Düvel, M. Wilkening, K.-D. Becker, and P. Heitjans, *Chem. Soc. Rev.*, 2013, **42**, 7507.
3. P. Baláž, M. Achimovičová, M. Baláž, P. Billik, Z. Cherkezova-Zheleva, J. Manuel Criado, F. Delogu, E. Dutková, E. Gaffet, F. J. Gotor, R. Kumar, I. Mitov, T. Rojac, M. Senna, A. Streletskii, and K. Wieczorek-Ciurowa, *Chem. Soc. Rev.*, 2013, **42**, 7571.
4. C. Suryanarayana, *Prog. Mater. Sci.*, 2001, **46**, 1.
5. G.-W. Wang, *Chem. Soc. Rev.*, 2013, **42**, 7668.
6. T. Friščić, *Chem. Soc. Rev.*, 2012, **41**, 3493.
7. A. Delori, T. Friščić, and W. Jones, *CrystEngComm*, 2012, **14**, 2350.
8. A. Lazuen-Garay, A. Pichon, and S. L. James, *Chem. Soc. Rev.*, 2007, **36**, 846.
9. S. R. Batten, N. R. Champness, X.-M. Chen, J. Garcia-Martinez, S. Kitagawa, L. Öhrström, M. O'Keeffe, M. P. Suh, and J. Reedijk, *CrystEngComm*, 2012, **14**, 3001.
10. H. Furukawa, K. E. Cordova, M. O'Keeffe, and O. M. Yaghi, *Science*, 2013, **341**. DOI:. DOI: 10.1126/science.1230444.
11. A. Czaja, E. Leung, N. Trukhan, and U. Müller, Industrial MOF synthesis, in 'Metal-Organic Frameworks: Applications from Catalysis to Gas Storage', 1st edition, ed. D. Farrusseng, Wiley-VCH, 2011.
12. T. Friščić and W. Jones, *Cryst. Growth Des.*, 2009, **9**, 1621.
13. D. Braga, L. Maini, and F. Grepioni, *Chem. Soc. Rev.*, 2013, **42**, 7638.
14. T. Friščić, Towards mechanochemical synthesis of metal-organic frameworks (MOFs): from coordination polymers and lattice inclusion compounds to porous materials, in 'Metal-Organic Frameworks: Design and Application', ed. L. R. MacGillivray, John Wiley & Sons, Inc., 2010.
15. D. Braga, S. L. Giaffreda, F. Grepioni, A. Pettersen, L. Maini, M. Curzi, and M. Polito, *Dalton Trans.*, 2006, 1249.
16. J. Stojaković, B. S. Farris, and L. R. MacGillivray, *Chem. Commun.*, 2012, **48**, 7958.
17. T. Friščić, *J. Mater. Chem.*, 2010, **20**, 7599.
18. J.-P. Zhang, Y.-B. Zhang, J.-B. Lin, and X.-M. Chen, *Chem. Rev.*, 2012, **112**, 1001.
19. T. Friščić, I. Halasz, V. Štrukil, M. Eckert-Maksić, and R. E. Dinnebier, *Croat. Chem. Acta*, 2012, **85**, 367.
20. K. D. M. Harris, Powder Diffraction Crystallography of Molecular Solids, in 'Advanced X-ray Crystallography', *Topics in Current Chemistry*, ed. K. Rissanen, Springer-Verlag, Berlin, 2012, Vol. 315, 133–177.
21. P. Wang, G. Li, Y. Chen, S. Chen, S. L. James, and W. Yuan, *CrystEngComm*, 2012, **14**, 1994.
22. M. Schlesinger, S. Schulze, M. Hietschold, and M. Mehring, *Micropor. Mesopor. Mater*, 2010, **132**, 121.
23. X. Ma, W. Yuan, S. E. J. Bell, and S. L. James, *Chem. Commun.*, 2014, **50**. DOI:. DOI: 10.1039/c3cc47898j.
24. T. N. Drebuschak, A. A. Ogienko, and E. V. Boldyreva, *CrystEngComm*, 2011, **13**, 4405.
25. F. K. Urakaev and V. V. Boldyrev, *Powder Technol.*, 2000, **107**, 197.
26. T. Friščić, I. Halasz, P. J. Beldon, A. M. Belenguer, F. Adams, S. A. J. Kimber, V. Honkimäki, and R. E. Dinnebier, *Nat. Chem.*, 2013, **5**, 66.
27. S. Tanaka, K. Kida, T. Nagaoka, T. Ota, and Y. Miyake, *Chem. Commun.*, 2013, **49**, 7884.

PART 2
Post-Modification

Postsynthetic Modification of Metal-Organic Frameworks

Andrew D. Burrows

University of Bath, Bath, UK

1	Introduction	195
2	Covalent Postsynthetic Modification	197
3	Dative Postsynthetic Modification	206
4	Inorganic PSM—Modification of the Metal Coordination Sphere	208
5	Conclusions	213
6	Related Articles	214
7	Abbreviations and Acronyms	214
8	References	214

1 INTRODUCTION

The synthesis and study of materials with structures consisting of metal centers or aggregates that are linked into extended networks by bridging organic ligands is an important and growing area of modern chemistry.[1] These materials are referred to by a number of different names including coordination polymers and metal–organic frameworks (MOFs) and, although there is considerable debate about how interchangeable these designations are,[2,3] this review uses the term *metal–organic framework* for any type of coordination network structure.

The current interest in MOFs is largely a consequence of their porosity. Many MOFs, especially those based on polycarboxylate and imidazolate linkers, show permanent porosity on removal of the solvent molecules from the pores and channels of the "as-synthesized" materials. This property has been utilized for a wide range of potential applications including hydrogen storage,[4] separations,[5] and heterogeneous catalysis.[6]

The properties of a MOF are related to the nature of the pores, and by introducing specific functional groups onto the pore surface, these properties can be tuned. Simple functional groups such as amines or halides can often be incorporated into a MOF through using the functionalized linker in the synthesis. This approach is, however, limited as many functional groups are not tolerant of the conditions used for MOF synthesis or lead to changes in the nature of the network formed. Postsynthetic modification (PSM) provides an alternative strategy to forming functionalized MOFs. In this approach, the nature of the pores is altered after synthesis of the MOF, thus allowing sensitive and/or coordinating groups to be introduced into the pores of a preformed network structure.

1.1 The Scope of Postsynthetic Modification

The idea of modifying the pores of a preformed extended network to tailor its properties was first suggested by Hoskins and Robson in 1990,[7] and the first reports of this being carried out in practice were published independently by the groups of Lee,[8] Kim,[9] and Williams[10] in 1999 and 2000. After this initial activity, the field lay largely dormant for several years before being revived by Wang and Cohen in 2007.[11]

As a general concept in MOF chemistry, PSM can refer to any change in a MOF following its synthesis. For the purposes of this review, however, PSM is divided into three categories, which are shown schematically in Figure 1. These are:

1. *Covalent PSM*: this involves covalent modification of a linker ligand and is the most well-developed type of PSM in MOF chemistry.
2. *Dative PSM*: this involves coordination of a metal center to a linker.

Metal-Organic Framework Materials. Edited by Leonard R. MacGillivray and Charles M. Lukehart.
© 2014 John Wiley & Sons, Ltd. ISBN 978-1-119-95289-3

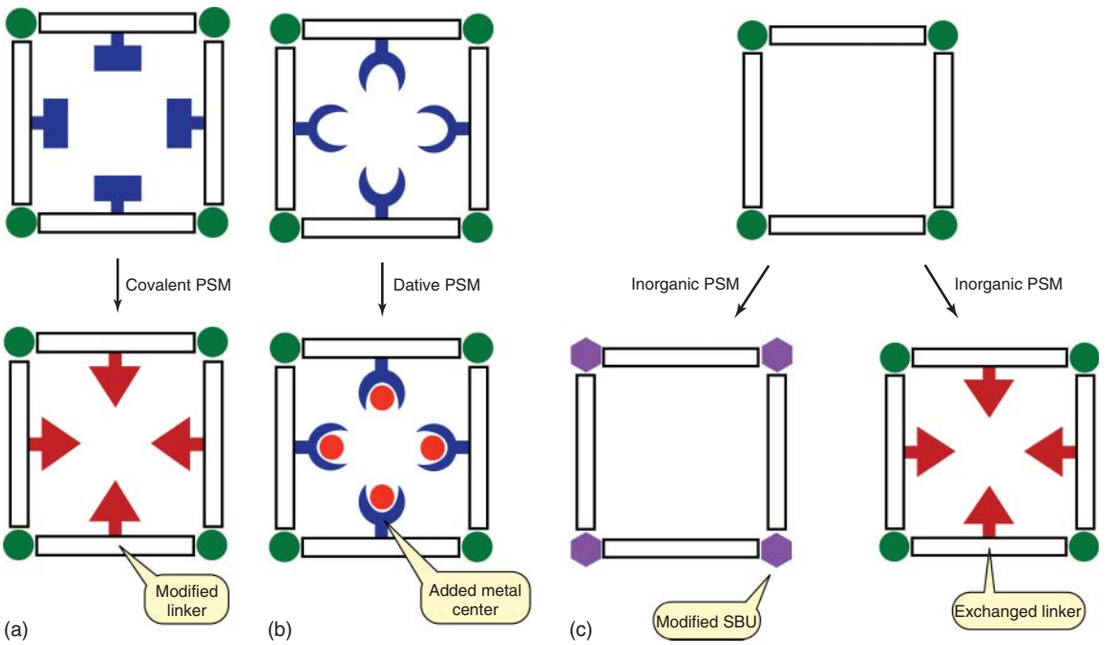


Figure 1 Schematic representation of the three categories of PSM covered in this review, showing (a) covalent PSM, (b) dative PSM, and (c) two types of inorganic PSM

3. *Inorganic PSM*: this involves a modification of the secondary building units (SBUs), which form the nodes of the MOF network, and includes substitution of the metal centers or linker ligands.

Other PSM transformations are possible, including exchange of guest molecules and/or counterions, but these are not dealt with here due to space constraints.

For covalent or dative PSM, the MOF normally needs to have a reactive group present on a linker. This group is referred to as a *tag*, and this is defined as a group or functionality that is stable and innocent during MOF formation, but that can be transformed by a PSM.[12] Sometimes, sequential PSM reactions are carried out. These are referred to as *tandem reactions*, and they typically involve either two or more consecutive covalent modifications or a covalent modification followed by a dative modification.

1.2 Metal–Organic Frameworks Commonly Used for PSM

Although PSM reactions have been carried out on a wide variety of MOFs, the systems that are most amenable to modification are those that form isoreticular series,[13] as in these cases, a tag group can typically be introduced into the structures without changing the nature of the network adopted. The MOF networks that have been most commonly used in PSM studies are those based on dicarboxylates and include $[Zn_4OL_3]$ (MOF-5),[13] $[Zn_4O(btb)_{4/3}L]$ (UMCM-1, btb = 4,4′,4″-benzene-1,3,5-triylbenzoate),[14] $[Zn_2L_2(dabco)]$ (DMOF-1, dabco = 1,4-diaza[2.2.2]bicyclooctane),[15] [M(OH)L] (MIL-53, M = Al, Cr, Fe, Ga, In),[16] $[M_3OF(H_2O)_2L_3]$ (MIL-101, M = Cr, Fe, Al),[17] [M(OH)L] (MIL-68, M = Ga, In),[18] and $[Zr_6O_4(OH)_4L_6]$ (UiO-66).[19] In the formulae, L is a dicarboxylate, and the acronym given is for the untagged version of the MOF, where L is 1,4-benzenedicarboxylate (bdc).

In this review, included solvent molecules are not included in the formulae presented unless they are coordinated. The acronym for a MOF in which the structural type can be formed by more than one metal is denoted with the framework metal in brackets, for example MIL-53(Al), and a MOF containing a ligand functionalized with a particular group has that functionality shown after the normal acronym. For example, a tagged version of MIL-101(Cr) containing 2-amino-1,4-benzenedicarboxylate (bdc-NH_2) in place of bdc is referred to as MIL-101(Cr)-NH_2.

1.3 Characterization

To be effective, PSM needs to take place without destroying the crystallinity of the MOF. Powder X-ray diffraction (PXRD) is generally employed to verify that the network structure remains unaltered during the PSM process, although in the case of flexible MOFs, such as those based on [Al(OH)(bdc)] (MIL-53), PSM

can alter the shape of the pores, and this is reflected in changes in the PXRD patterns. In some cases, PSM occurs in single-crystal to single-crystal (SC-SC) transformations, and thus can be followed by single crystal X-ray crystallography.[12,20,21] Even in these cases, however, disorder can prevent full information about the PSM process from being obtained from the crystal structure.

Many PSM reactions do not go to completion. For many PSM reactions, NMR spectroscopy generally provides the best evidence for the degree of conversion. Typically, the modified MOFs are digested by dissolving in acid or base and the resultant solutions analyzed by ^{1}H NMR spectroscopy,[11] although care needs to be taken to ensure that digestion does not alter the modified tag. Comparison of the integrals for the signals of the tagged and modified linkers allows the degree of conversion to be calculated. Solid-state NMR spectroscopy can also be informative,[22,23] although broad signals may limit the information available. Infrared spectroscopy has also been used to estimate the degree of conversion, and gas adsorption measurements provide insight into the effect of modification on BET surface areas.[24,25]

For PSM processes that involve introduction or exchange of metal centers, a range of spectroscopic techniques have been used to provide evidence of the metal centers and their environments. These include atomic absorption spectroscopy (AAS),[26] inductively coupled plasma atomic emission spectroscopy (ICP-AES),[27] energy-dispersive X-ray spectroscopy (EDX),[28] X-ray photoelectron spectroscopy,[29] and extended X-ray fine structure (EXAFS) spectroscopy.[30]

2 COVALENT POSTSYNTHETIC MODIFICATION

The majority of covalent PSM reactions occur on addition of a reagent, and these processes are discussed in Section 2.1. Covalent transformations can also take place on thermal or photochemical treatment, and these are described in Sections 2.2 and 2.3, respectively. Both thermolysis and photolysis can be used to reduce the size of a functional group and "unmask" a particular functional group. In these instances, Cohen has described the processes as postsynthetic deprotection (PSD) reactions.[31] Finally, electrochemical reactions are described briefly in Section 2.4.

2.1 PSM on Addition of a Reagent

The most studied type of PSM involves an organic transformation of a linking ligand, which takes place on addition of an appropriate reagent. The conversion of an amine to an amide on treatment with an acid anhydride or acid chloride was one of the first PSM reactions to be identified,[11] and this remains the most studied PSM process, with successful employment on MOFs based on zinc, gadolinium, aluminum, iron, zirconium, indium, and chromium. However, the scope of covalent PSM reactions has increased dramatically over the past few years, and reported processes are summarized in Table 1. Space limitations do not permit each type of reaction to be described in detail, and the interested reader is directed toward more comprehensive reviews in this area.[31,32]

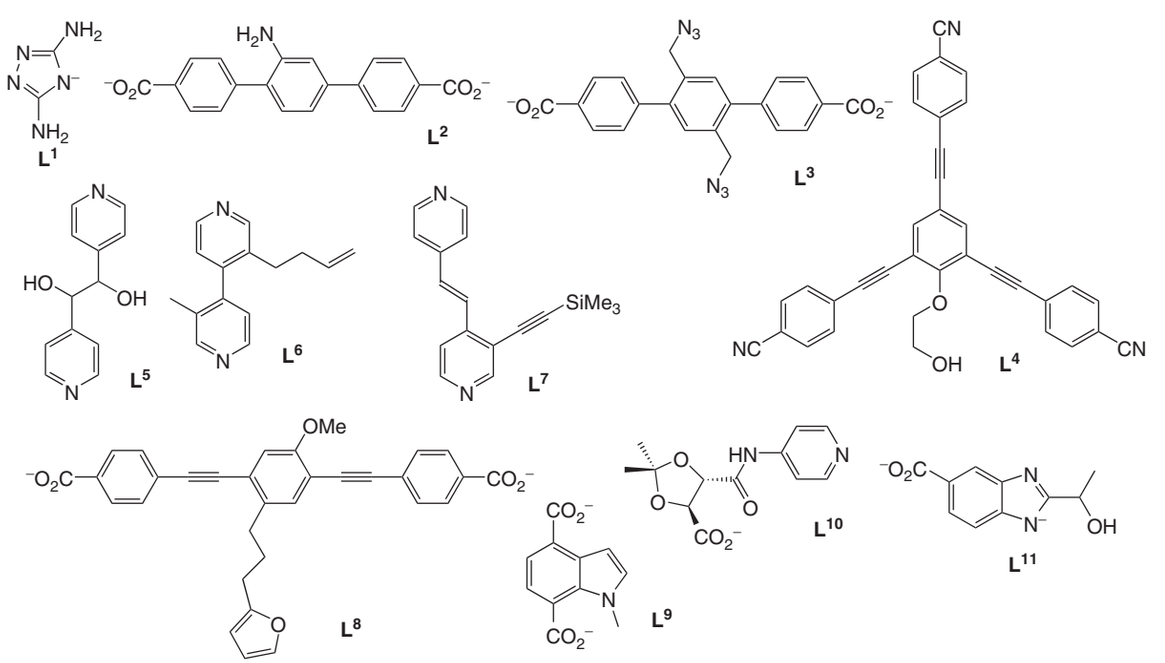


Table 1 Covalent PSMs requiring addition of a reagent

Starting MOF	Reagent	Tag	Modified tag	Degree of modification	Reference
$[Zn_4O(bdc\text{-}NH_2)_3]$, IRMOF-3	Acid anhydrides	$-NH_2$	$-NHC(O)R$	Dependent on R, up to 100%	11,33
$[Zn_2(bdc\text{-}NH_2)_2(dabco)]$, DMOF-1	Acid anhydrides	$-NH_2$	$-NHC(O)R$	Dependent on R, up to 100%	34,35
$[Zn_4O(btb)_{4/3}(bdc\text{-}NH_2)]$, UMCM-1-$NH_2$	Acid anhydrides	$-NH_2$	$-NHC(O)R$	Dependent on R, up to 100%	34,36
$[Gd_2(bdc\text{-}NH_2)_3(DMF)_4]$, MOF-LIC-1	$MeCO_2H$	$-NH_2$	$-NHC(O)H$	17% (1 h, 120 °C)	20
$[Al(OH)(bdc\text{-}NH_2)]$, MIL-53(Al)	HCO_2H	$-NH_2$	$-NHC(O)H$	~100% (3 h, 70 °C)	37
$[Al(OH)(bdc\text{-}NH_2)]$, MIL-53(Al)	Acid anhydrides	$-NH_2$	$-NHC(O)R$	Dependent on R, up to 91%	38
$[Al_4(OH)_2(OMe)_4(bdc\text{-}NH_2)_3]$, CAU-1-$NH_2$	Acetic anhydride	$-NH_2$	$-NHC(O)Me$	100% (3 h, RT)	39
$[Cu_3(btc\text{-}NH_2)_2]$, UHM-30	Acetic anhydride	$-NH_2$	$-NHC(O)Me$	Up to 92% (24 h, 55 °C)	40
$[Fe_3OF(H_2O)_2(bdc)_{2.49}(bdc\text{-}NH_2)_{0.51}]$	$[Pt(NH_3)_2Cl_2(OEt)(O_2CCH_2CH_2CO_2H)]$/1,1-carbonyldiimidazole	$-NH_2$	$-NHC(O)CH_2CH_2CO_2\{PtCl_2(OEt)(NH_3)_2\}$	37% (2 d, RT)	41
$[Cr_3OF(H_2O)_2(bdc\text{-}NH_2)_3]$, MIL-101(Cr)-$NH_2$	$PhN{=}NC_6H_4C(O)Cl$	$-NH_2$	$-NHC(O)C_6H_4N{=}NPh$	High (3 h, 130 °C, microwave)	42
$[Zr_6O_4(OH)_4(bdc\text{-}NH_2)_6]$, UiO-66-$NH_2$	Acid anhydrides	$-NH_2$	$-NHC(O)R$	Dependent on R, up to 100%	25,43
$[Zn_2(5\text{-aminotetrazolate})_3(H_2O)_3]$	$MeCO_2H$	$-NH_2$	$-NHC(O)Me$	67% (2 h, 160 °C)	44
$[Zn_2(5\text{-aminotetrazolate})_3(H_2O)_3]$	Trimesoyl chloride	$-NH_2$	$-NHC(O)C_6H_3(CO_2H)_2$-3,5	7% (1 h, RT)	44
$[Zn_4O(bdc\text{-}NH_2)_3]$	Nicotinyl chloride	$-NH_2$	$-NHC(O)C_5H_4N$-3	50% (5 d, 100 °C)	45
$[ZnF(\mathbf{L^1})]$	Nicotinyl chloride	$-NH_2$	$-NHC(O)C_5H_4N$-3	60% (5 d, 100 °C)	45
$[In(OH)(bdc\text{-}NH_2)]$, MIL-68(In)-$NH_2$	i. Fmoc-Pro/Ala-OH, ii. piperidine	$-NH_2$	$-NHC(O)$-Pro, $-NHC(O)$-Ala	~10% (i. 36 h, 38 °C, ii. 15 min, RT)	46
$[Gd_2(bdc\text{-}NH_2)_3(DMF)_4]$	EtNCO	$-NH_2$	$-NHCO_2H$	13% (1 h, 120 °C)	20
$[Zn_4O(bdc\text{-}NH_2)_3]$, IRMOF-3	RNCO	$-NH_2$	$-NHC(O)NHR$	Dependent on R, up to 71%	47
$[Zn_4O(bdc\text{-}NH_2)_3]$, IRMOF-3	Me_3SiNCO	$-NH_2$	$-NHC(O)NH_2$	100% (3 d, RT)	47
$[Zn_4O(bdc\text{-}NH_2)_3]$, IRMOF-3	Hacac	$-NH_2$	$-NHCMe{=}CHCOMe$	46% (24 h, 60 °C)	48
$[Zn_4O(bdc\text{-}NH_2)_3]$, IRMOF-3	$C_6H_4(OH\text{-}2)C(O)CH_2CHO$	$-NH_2$	$-NHCH{=}CHC(O)\text{-}C_6H_4OH$-2	90% (2 d, 61 °C)	48
$[Zn_4O(bdc\text{-}NH_2)_3]$, IRMOF-3	Fluorescein isothiocyanate (ArNCS)	$-NH_2$	$-NHC(S)NHAr$	Crystal surfaces only	49
$[Zr_6O_4(OH)_4(\mathbf{L^2})_6]$	Rhodamine B isothiocyanate (ArNCS)	$-NH_2$	$-NHC(S)NHAr$	Crystal surfaces only	50
$[Cr_3OF(H_2O)_2(bdc\text{-}NH_2)_3]$, MIL-101(Cr)-$NH_2$	EtNCO	$-NH_2$	$-NHC(O)NHEt$	100% (5 h, 70 °C)	51
$[Cr_3OF(H_2O)_2(bdc\text{-}NH_2)_3]$, MIL-101(Cr)-$NH_2$	$PhN{=}NC_6H_4NCO$	$-NH_2$	$-NHC(O)NHC_6H_4N{=}NPh$	High (3 d, 130 °C, microwave)	42
$[Al(OH)(bdc\text{-}NH_2)]$, MIL-53(Al)-$NH_2$	CCl_3O_2CCl	$-NH_2$	$-NCO$, and subsequently to ureas ($-NHC(O)NR_2$) and carbamates ($-NHCO_2R$)	90% in first step (18 h, RT), up to 100% in second step, dependent on R.	24
$[Al(OH)(bdc\text{-}NH_2)]$, MIL-53(Al)-$NH_2$	$C(S)Cl_2$	$-NH_2$	$-NCS$, and subsequently to thioureas ($-NHC(S)NR_2$) and thiocarbamates ($-NHC(S)OR$)	~90% in first step (18 h, 55 °C), up to 100% in second step, dependent on R.	24

$[Zn_2(cam)_2(apyr)]$	MeCHO	$-NH_2$	$-N{=}CHMe$	Not reported (2 d, RT)	52
$[Zr_6O_4(OH)_4(bdc\text{-}NH_2)_6]$, UiO-66-$NH_2$	MeCHO	$-NH_2$	$-NHCH(OH)Me$, $-NCH_2CH_2$	Up to 50% hemiaminal (24 h, RT), up to 60% aziridine (24 h, 85 °C)	53
$[Zn_4O(bdc\text{-}NH_2)_3]$, IRMOF-3	Salicylaldehyde	$-NH_2$	$-N{=}CHC_6H_4(OH\text{-}2)$	13% (7 d, RT)	54
$[Zn_4O(btb)_{4/3}(bdc\text{-}NH_2)]$	2-pyridinecarboxaldehyde	$-NH_2$	$-N{=}CHC_6H_4N\text{-}2$	100% (5 d, RT)	30
$[Zn_4O(bdc\text{-}NH_2)_3]$, IRMOF-3	i. RCHO, ii. $NaBH_3CN$	$-NH_2$	$-NHCH_2R$	Up to 67%, dependent on R (3 d, 50 °C)	55
$[Zn_4O(bdc\text{-}NH_2)_3]$, IRMOF-3	1,3-propanesultone	$-NH_2$	$-NHCH_2CH_2CH_2SO_2OH$	57% (24 h, 45 °C)	56
$[Zn_4O(bdc\text{-}NH_2)_3]$, IRMOF-3	2-methylaziridine	$-NH_2$	$-NHCH_2CH(Me)NH_2$	Mixture with 0, 1, and 2 additions (24 h, 45 °C)	56
$[Zn_4O(bdc\text{-}NH_2)_3]$, IRMOF-3	NO	$-NH_2$	$-NH\text{-}N(O){=}NOH$	44% (24 h, RT)	57
$[Zn_4O(btb)_{4/3}(bdc\text{-}NH_2)]$, UMCM-1-$NH_2$	NO	$-NH_2$	$-NH\text{-}N(O){=}NOH$	83% (24 h, RT)	57
$[Zn_2(bdc\text{-}NH_2)_2(dabco)]$, DMOF-1	^{t}BuONO, Me_3SiN_3	$-NH_2$	$-N_3$	100% (o/n, RT)	58,59
$[In(OH)(bdc\text{-}NH_2)]$, MIL-68(In)-$NH_2$	^{t}BuONO, Me_3SiN_3	$-NH_2$	$-N_3$	100% (o/n, RT)	58,59
$[Al_4(OH)_2(OMe)_4(bdc\text{-}NH_2)_3]$, CAU-1-$NH_2$	^{t}BuONO, Me_3SiN_3	$-NH_2$	$-N_3$	100% (o/n, RT)	59
$[Al(OH)(bdc\text{-}NH_2)]$, MIL-53(Al)-$NH_2$	^{t}BuONO, Me_3SiN_3	$-NH_2$	$-N_3$	100% (o/n, RT)	59
$[Fe_3OF(H_2O)_2(bdc\text{-}NH_2)_3]$, MIL-101(Cr)-$NH_2$	^{t}BuONO, Me_3SiN_3	$-NH_2$	$-N_3$	100% (o/n, RT)	59
$[Zn_4O(btb)_{4/3}(bdc\text{-}NH_2)]$, UMCM-1-$NH_2$	^{t}BuONO, Me_3SiN_3	$-NH_2$	$-N_3$	100% (o/n, RT)	60
$[Zn_4O(bdc)_x(bdc\text{-}NH_2)_{3-x}]$	^{t}BuONO, Me_3SiN_3	$-NH_2$	$-N_3$	100% (o/n, RT)	60
$[In(OH)(bdc)_{0.8}(bdc\text{-}N_3)_{0.2}]$	CO	$-N_3$	$-NCO$	100% (2 d, 120 °C)	61
$[Fe_3OF(H_2O)_2(bdc\text{-}NH_2)_{3-x}(bdc)_x]$, MIL-101(Fe)-$NH_2$	Br-BODIPY	$-NH_2$	$-NH$-BODIPY	21–40% (2 d, RT)	41
$[Zn_4O(bdc\text{-}NH_2)_3]$, IRMOF-3	Cyanuric chloride, NEt_3	$-NH_2$	$-NHC_3N_3Cl_2$	25% (1 d, RT)	62
$[Cr_3OF(H_2O)_2(bdc\text{-}NH_2)_3]$, MIL-101(Cr)-$NH_2$	i. $NaNO_2$, HCl, ii. I^-	$-NH_2$	$-I$	>95% (i. 3 h, 0–5 °C, ii. 3d, RT)	63
$[Cr_3OF(H_2O)_2(bdc\text{-}NH_2)_3]$, MIL-101(Cr)-$NH_2$	i. $NaNO_2$, HCl, ii. phenol	$-NH_2$	$-N{=}NC_6H_4OH$	>95% (i. 3 h, 0–5 °C, ii. 3d, RT)	63
$[Cr_3OF(H_2O)_2(bdc\text{-}NH_2)_3]$, MIL-101(Cr)-$NH_2$	$NaNO_2$, HBF_4	$-NH_2$	$-N_2^+\ BF_4^-$	>95% (3 h, 0–5 °C)	63
$[Cr_3OF(H_2O)_2(bdc\text{-}N_2)_3](BF_4)_3$	Heat	$-N_2^+\ BF_4^-$	$-F$	>95% (18 h, 100 °C)	63
$[Zn_4O(\mathbf{L}^3)_3]$	RC_2H, CuBr	$-N_3$	$-N_3C_2R$	Dependent on R, up to 100%	64
$[Zn_2(bdc\text{-}N_3)_2(dabco)]$	RC_2H, $Cu(NCMe)_4PF_6$	$-N_3$	$-N_3C_2R$	Dependent on R, up to 100%	58,59
$[In(OH)(bdc\text{-}N_3)]$	RC_2H, $Cu(NCMe)_4PF_6$	$-N_3$	$-N_3C_2R$	Dependent on R, up to 100%	58,59
$[Al(OH)(bdc\text{-}N_3)]$, MIL-53(Al)-N_3	RC_2H, $Cu(NCMe)_4PF_6$	$-N_3$	$-N_3C_2R$	Dependent on R, up to 100%	59
$[Al_4(OH)_2(OMe)_4(bdc\text{-}N_3)_3]$, CAU-1-$N_3$	RC_2H, $Cu(NCMe)_4PF_6$	$-N_3$	$-N_3C_2R$	Dependent on R, up to 100%	59
$[Fe_3OF(H_2O)_2(bdc\text{-}N_3)_3]$, MIL-101(Fe)-$N_3$	RC_2H, $Cu(NCMe)_4PF_6$	$-N_3$	$-N_3C_2R$	Dependent on R, up to 100%	59
$[Zn_4O(bdc)_{3-x}(bdc\text{-}N_3)_x]$	RC_2H, $CuI\{P(OEt)_3\}$	$-N_3$	$-N_3C_2R$	100% (14 h, 85 °C)	60
$[Zn_4O(btb)_{4/3}(bdc\text{-}N_3)]$	RC_2H, $CuI\{P(OEt)_3\}$	$-N_3$	$-N_3C_2R$	100% (14 h, 85 °C)	60
$[Zn_8O_2(adeninate)_4(bpdc\text{-}N_3)_6]^{4-}$, N_3-bio-MOF-100	Cyclooctyne derivatives	$-N_3$	$-N_3C_2RR'$	100% (o/n, RT)	65
$[Zn_2(mbdc\text{-}N_3)_2(bpy)_2]$, CID-$N_3$	i. UV, ii. O_2	$-N_3$	$-NO_2$, $-NO$	50% (10 h, 120 K)	21
$[Zn_4O\{bpdc\text{-}(CH_2N_3)_2\text{-}2,2'\}_3]$	PPh_3, H_2O	$-N_3$	$-NH_2$	100% (7 d, RT)	66

(*continued overleaf*)

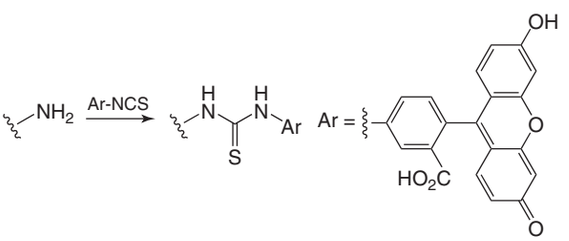
Table 1 (*Continued*)

Starting MOF	Reagent	Tag	Modified tag	Degree of modification	Reference
[Ag($\mathbf{L^4}$)]OTf	$O\{C(O)CF_3\}_2$ vapor	–OH	$-OC(O)CF_3$	100% (1 h, RT)	8
[Zn(tcpb)($\mathbf{L^5}$)]	Succinic anhydride	–OH	$-OC(O)CH_2CH_2CO_2H$	100% (3 d, 80 °C)	67
$[Zn_4O(sdc)_3]$	Br_2	–CH=CH–	–CHBrCHBr–	60% (24 h, 100 °C)	68
$[Zn_2(tdc)_2(\mathbf{L^6})]$	DMDO	$-CH=CH_2$	$-CHCH_2O$	100% (16 h, 4 °C)	69
$[Zn_2(tdc)_2(\mathbf{L^6})]$	i. DMDO, ii. EtSH	$-CH=CH_2$	$-CH(OH)CH_2SEt$	50% (5 h, 140 °C, microwave)	69
$[Zn_2(tdc)_2(\mathbf{L^6})]$	OsO_4, NMO	$-CH=CH_2$	$-CH(OH)CH_2OH$	>90% (5 d, RT)	70
$[Zn_2(tdc)_2(\mathbf{L^6})]$	$BH_3 \cdot SMe_2$	$-CH=CH_2$	$-CH_2CH_2BH_2$	>95% (16 h, 0 °C)	70
$[Zn_2(tdc)_2(\mathbf{L^6})]$	EtSH, UV	$-CH=CH_2$	$-CH_2CH_2SEt$	>95% (8 h, RT)	70
$[Zn_2(2,6\text{-ndc})_2(\mathbf{L^7})]$	i. NBu_4F, ii. RN_3, Cu(I)	$-CCSiMe_3$	$-C_2N_3R$	Crystal surfaces only	71
$[Zn_2(m\text{bdc-}OCH_2CCH)_2(bpy)_2]$	RN_3, $Cu(NCMe)_4ClO_4$	–CCH	$-C_2N_3R$	80% (24 h, RT)	72
$[Zr_6O_4(OH)_4(\mathbf{L^8})_6]$	$pTolCH_2N_3$, CuBr	–CCR	$-C_2N_3CH_2pTol$	98% (19 h, RT)	73
$[Zr_6O_4(OH)_4(\mathbf{L^8})_6]$	Maleimides	–Furan	Diels–Alder adducts	89–99%, dependent on R (7 d, 60 °C)	73
$[Zn_4O(bpdc\text{-}CHO)_3(H_2O)_2]$	NH_2NHAr	–CHO	–CH=NNHAr	60% (7 d, RT)	12
$[Zn_4O(bpdc\text{-}OMe)_{2.7}(bpdc\text{-}CHO)_{2.7}]$	NH_2NHAr	–CHO	–CH=NNHAr	100% (7 d, RT)	12
$[Zn(im\text{-}CHO)_2]$, ZIF-90	$NH_2CH_2CH_2OH$	–CHO	$-CH=NCH_2CH_2OH$	100% (3 h, 60 °C)	22
$[Zn(im\text{-}CHO)_2]$, ZIF-90	$NaBH_4$	–CHO	$-CH_2OH$	80% (24 h, 60 °C)	22
$[Zn(im\text{-}CHO)_2]$, ZIF-90	$(EtO)_3Si(CH_2)_3NH_2$	–CHO	$-CH=N(CH_2)_3Si(OEt)_3$	100% (30 min, 110 °C)	74
$[Zn(im\text{-}CHO)_{0.96}(im\text{-}Me)_{1.04}]$	$NH_2CH_2CH_2NH_2$	–CHO	$-CH=NCH_2CH_2NH_2$	46% (24 h, 80 °C)	75
$[Zn(mica)_2]$, SIM-1	$Me(CH_2)_{10}NH_2$	–CHO	$-CH=N(CH_2)_{10}Me$	22% (24 h, RT)	76
$[Cr_3OF(H_2O)_2(bdc)_3]$, MIL-101(Cr)	HNO_3, H_2SO_4	–H	$-NO_2$	100% (5 h, 0 °C)	51
$[Cr_3OF(H_2O)_2(bdc\text{-}NH_2)_3]$, MIL-101(Cr)-$NH_2$	$SnCl_2$, EtOH	$-NO_2$	$-NH_2$	100% (6 h, 70 °C)	51
$[Zn_4O(btb)_{4/3}(\mathbf{L^9})]$	$[Ph_2I]BF_4$, $Pd(OAc)_2$	–H	–Ph	100% (5 d, RT)	77
$[Al(OH)(bdc\text{-}NH_2)]$, MIL-53(Al)-$NH_2$	$MeOCH_2C(O)Cl$, $AlCl_3$	–H	$-CH_2Cl$	50% (3 h, 75 °C)	78
$[Cr_3OF(H_2O)_2(bdc)_3]$, MIL-101(Cr)	$MeOCH_2C(O)Cl$, $AlCl_3$	–H	$-CH_2Cl$	50% (5 h, 100 °C)	78
$[Cr_3OF(H_2O)_2(bdc)_{3-x}(bdc\text{-}CH_2Cl)_x]$	$LiPPh_2$	$-CH_2Cl$	$-CH_2PPh_2$	8% (12 h, −78 °C)	78
[Al(OH)(bdc)], MIL-53(Al)	Triflic anhydride, H_2SO_4	–H	$-SO_3H$	50% (1 h, RT)	79
$[Cr_3OF(H_2O)_2(bdc)_3]$, MIL-101(Cr)	Triflic anhydride, H_2SO_4	–H	$-SO_3H$	50% (1 h, RT)	79
$[Zr_6O_4(OH)_4(bdc\text{-}Br)_6]$, UiO-66-Br	CuCN	–Br	–CN	90% (10 min, 170 °C, microwave)	80
$[Zn_3O(\mathbf{L^{10}})_6]$, D-POST-1	MeI	$-C_5H_4N$	$-C_5H_4NMe^+I^-$	100% (2 h, RT)	9
$[Zn_4O(bpdc\text{-}CH_2SMe)_3]$	DMDO	$-CH_2SR$	$-CH_2S(O)R$, $-CH_2S(O)_2R$	Dependent on R, up to 100% (o/n, 40 °C)	81
$[Zn_3(\mathbf{L^{11}})_2(OH)_2]$	i. Heat, ii. Br_2	–CH(OH)Me	$-CH=CH_2$, then $-CHBr-CH_2Br$	Crystal surfaces only	82
$[Zn_3(Httca)_2(bpy)(H_2O)_2]$	Na[OMe]	$-CO_2H$	$-CO_2Na$	5 d, RT	83

bdc-X, 2-X-1,4-benzenedicarboxylate; dabco, 1,4-diaza[2.2.2]bicyclooctane; btb, 4,4′,4″-benzene-1,3,5-triylbenzoate; btc-X, 2-X-1,3,5-benzenetricarboxylate; cam, (+)-camphorate; apyr, 2-aminopyrazine; *m*bdc-X, 5-X-1,3-benzenedicarboxylate; bpdc-X, 2-X-4,4′-biphenyldicarboxylate; tcpb, 1,2,4,5-tetrakis(4-carboxyphenyl)benzene; sdc, *trans*-4,4′-stilbenedicarboxylate; tdc, 9,10-triptycenedicarboxylate; 2,6-ndc, 2,6-naphthalenedicarboxylate; im-X, 2-X-imidazolate; mica, 4-methyl-5-imidazole-carboxaldehyde; H_4ttca, 1,1′:2′,1″-terphenyl-4,4′,4″,5′-tetracarboxylic acid.

This type of covalent PSM reaction generally leads to an increase in the size of the substituent. The degree of conversion depends on the size of the introduced group and the larger this group, the lower the conversion. Thus, for example, Cohen and coworkers showed that the reaction of $[Zn_4O(bdc\text{-}NH_2)_3]$ (IRMOF-3) with an acid anhydride, RCO_2OR, gave complete conversion to the amide $[Zn_4O(bdc\text{-}NHC(O)R)_3]$ for R = Me, Et, Pr, Bu, and C_5H_{11}, but only 46% of the amine groups were modified with $R = C_9H_{19}$, and 20% were modified with $R = C_{16}H_{33}$ under identical conditions.[33] Notably, as the chain size increases, the modified MOFs become less sensitive to moisture and more hydrophobic.[38]

With particularly bulky substituents, the PSM process can be limited to the crystal surfaces. For example, Metzler-Nolte and coworkers investigated the reaction of IRMOF-3 with fluorescein isothiocyanate (ArNCS, equation 1) and used confocal laser scanning microscopy to show that fluorescence originated only from a very thin layer at the outer surfaces of the crystals. The steric bulk of the fluorescein group prevented the isocyanate from penetrating into the bulk of the crystals.[49]



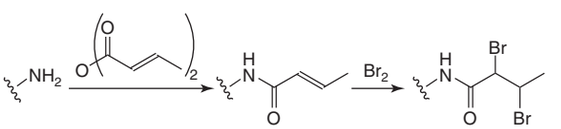
(1)

Higher degrees of conversion are generally observed for MOFs with larger pores. For example, use of $[Zn(btb)_{4/3}(bdc\text{-}NH_2)]$ (UMCM-1-NH_2) led to higher degrees of conversion on reaction with acid anhydrides than with IRMOF-3, whereas $[Zn_2(bdc\text{-}NH_2)_2(dabco)]$ (DMOF-1-NH_2), which has smaller pores, gave reasonable conversions only with short chain anhydrides.[34] However, the functional groups need to be accessible in order to react. Gamez and coworkers showed that when $[Gd_2(bdc\text{-}NH_2)_3(DMF)_4]$ reacts with acetic acid to give the methyl amide, only one of the three independent bdc-NH_2 groups in the structure could be modified due to steric constraints.[20]

Heating can also increase the degree of conversion, either conventionally or through use of microwave irradiation. Cohen and coworkers showed that $[Zr_6O_4(OH)_4(bdc\text{-}Br)_6]$ (UiO-66-Br) reacts with CuCN in DMF at 140 °C with 43% of the bromides converted to nitriles after 24 h. In contrast, microwave irradiation in *N*-methyl-2-pyrrolidone increased the conversion to 90% after only 10 min.[80] Ranocchiari and coworkers reported that vapor-phase PSM could be used to enhance the degree of modification while also decreasing reaction time. In this process, the reagent is in contact with the MOF only as a vapor. They reported that the reaction between IRMOF-3 and salicaldehyde vapor went to completion in 16 h whereas the conventional reaction using salicaldehyde in solution gave only 13% conversion.[84]

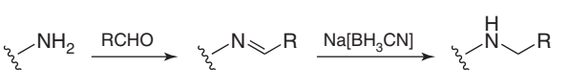
A postsynthetically modified MOF can be further modified by reaction with a second reagent. This leads to the possibility of tandem modifications, which involve two or even more sequential transformations, as shown schematically in Figure 2a.

For example, Wang and Cohen[85] showed that IRMOF-3 could be modified with crotonic anhydride to form an amide-functional MOF $[Zn_4O(bdc\text{-}NHC(O)\text{-}CH{=}CHMe)_3]$ containing alkenyl groups, which were themselves modified on treatment with bromine (equation 2).



(2)

Burrows and Keenan investigated tandem reactions on IRMOF-3, seeking to improve the scope of the reaction of an amine with an aldehyde by reducing the imine formed to give a product that is stable to hydrolysis. They showed that the imines generated on reaction with alkyl aldehydes were reduced to secondary amines on treatment with sodium cyanoborohydride (equation 3).[55]



(3)

The fact that many PSM reactions do not go to completion opens up the possibility of a second class of tandem process, during which the second reaction leads to modification of the tag groups that did not react during the first transformation. This is shown schematically in Figure 2b and is illustrated by the reaction of IRMOF-3 with crotonic anhydride, followed by acetic anhydride. If the first reaction is carried out for a limited amount of time, some but not all of the amino groups are modified. Subsequent reaction with the smaller acetic anhydride converts the remaining amino groups into amides.[85]

A judicious choice of reagents can lead to different reactions on the external surfaces and the interiors of crystals. Hupp and coworkers investigated tandem reactions starting with the (trimethylsilyl)ethynyl-functionalized MOF $[Zn_2(tcpb)_2(\mathbf{L}^7)]$ (tcpb = 1,2,4,5-tetrakis(4-carboxyphenyl)benzene). They showed that the trimethylsilyl groups on the crystal surfaces could be removed by reacting with aqueous potassium fluoride and that the primary alkyne products underwent copper-catalyzed [3+2] cycloaddition reactions with ethidium bromide monoazide (equation 4).[86]

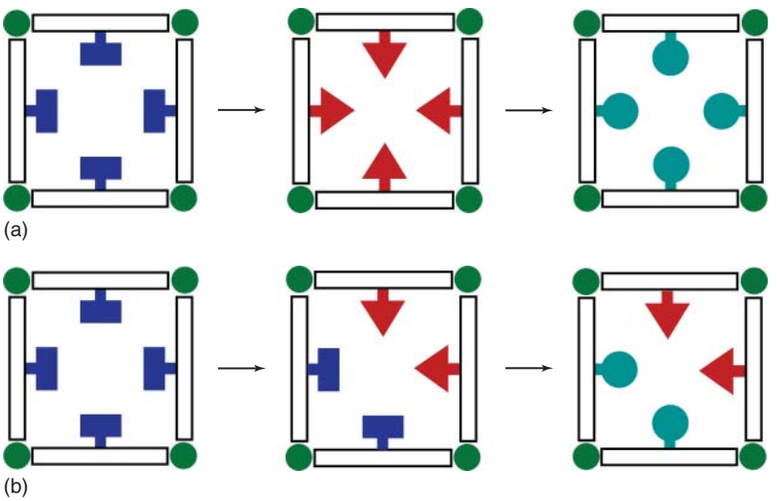
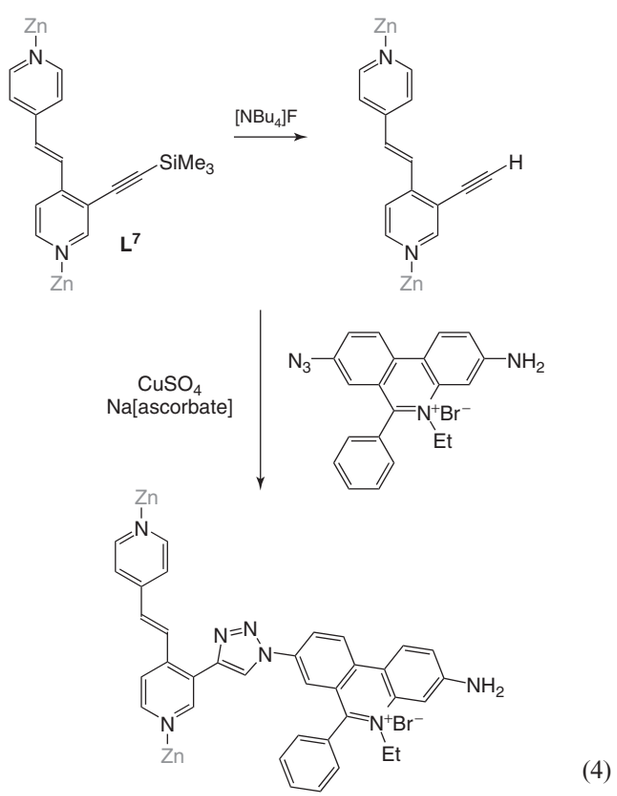


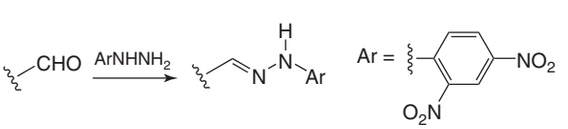
Figure 2 Schematic representation of tandem PSM reactions, showing two strategies for achieving tandem reactions: (a) sequential reactions and (b) partial conversion with a large reagent followed by conversion with a smaller reagent



(4)

The hydrophobic nature of the MOF prevents the reagent from penetrating into the pores. This surface-modified material was subsequently treated with NEt_4F to deprotect the interior alkynes, followed by benzyl azide, which converted the interior terminal alkynes into triazoles.

Low degrees of conversion in a PSM process can be problematic, especially if they are caused by pore-blocking, as this would limit diffusion within the modified MOF. This problem can be resolved using a mixed-component MOF approach.[32] Mixed-component MOFs are those which contain different linkers or metals with the same structural role. These include mixed-metal and mixed-ligand (also known as *multivariate*[87] or *MIXMOFs*[88]) MOFs. These systems can be thought of as solid solutions, in which the proportions of the ligands or metals can be adjusted or even controlled. Use of a mixed-linker approach in which only a small proportion of the linkers contain reactive tag groups reduces the problems of pore-blocking. For example, Burrows *et al.*[12] used an aldehyde-tagged 4,4′-biphenyldicarboxylate (bpdc-CHO) linker and showed that $[Zn_4O(bpdc\text{-}CHO)_3(H_2O)_2]$ reacts with 2,4-dinitrophenylhydrazine ($ArNHNH_2$) with conversion of 60% of the aldehyde groups into hydrazones (equation 5). The effect of the PSM reaction on the available pore space is shown in the space-filling structural diagrams in Figure 3. Use of the mixed-ligand MOF $[Zn_4O(bpdc\text{-}OMe)_{2.7}(bpdc\text{-}CHO)_{0.3}]$, containing fewer reactive tag groups, enabled the PSM reaction to proceed to completion.



(5)

Sometimes, this mixed-linker approach enables transformations to be studied on MOFs that cannot

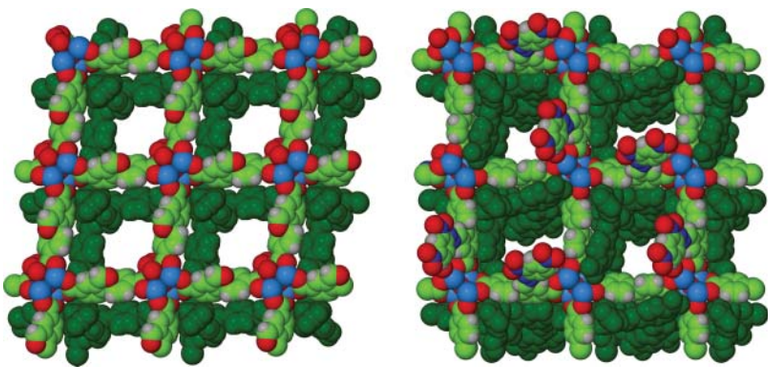
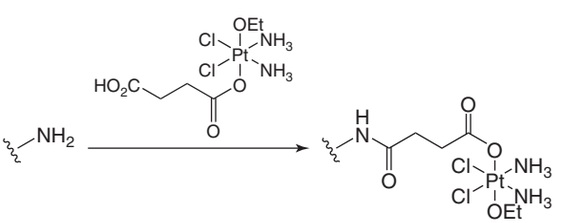


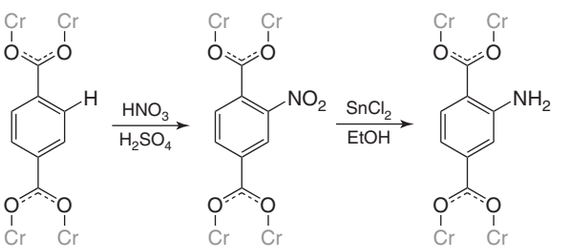
Figure 3 Space-filling diagrams of the structures of (a) $[Zn_4O(bpdc\text{-}CHO)_3(H_2O)_2]$ and (b) $[Zn_4O(bpdc\text{-}CHO)_{1.2}(bpdc\text{-}C{=}NNHAr)_{1.8}(H_2O)_2]$ (Ar = 2,4-dinitrophenyl), showing the effect of PSM on the pore size

easily be prepared otherwise. Lin and coworkers investigated iron(III) MOFs containing bdc-NH_2 and found that they were unable to prepare $[Fe_3OF(H_2O)_2(bdc\text{-}NH_2)_3]$, an analog of MIL-101(Fe), as a denser phase formed in preference. However, by using a mixture of H_2bdc and H_2bdc-NH_2 in the synthesis, they showed that up to 17% bdc-NH_2 can be incorporated into the MIL-101(Fe) structure. Thirty-seven percent of the amino groups of this material were then functionalized by reaction with the ethoxysuccinato-cisplatin prodrug (equation 6).[41]



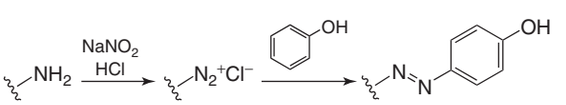
(6)

Many of the covalent PSM reactions in Table 1 were first carried out on zinc MOFs such as IRMOF-3, but recently, there has been a growing interest in the use of MOFs that are less moisture-sensitive, as these are likely to be easier to exploit for applications. This has also allowed the development of PSM reactions that are not feasible for zinc MOFs as the reaction conditions would lead to decomposition of the framework. For example, Stock and coworkers showed that MIL-101(Cr) is sufficiently stable to acid that the aromatic rings can be nitrated with a mixture of concentrated sulfuric and nitric acids at 0 °C, the reaction going to completion within 5 h. The resultant nitro groups were reduced to amines using tin(II) chloride in ethanol (equation 7).[51]



(7)

Burrows and coworkers treated MIL-101(Cr)-NH_2 with nitrite and an acid to form the diazonium salts and isolated the tetrafluoroborate. The chloride salt reacts with aqueous iodide to give MIL-101(Cr)-I and with phenol and sodium carbonate to give an azo-coupled product (equation 8). Heating the tetrafluoroborate salt led to MIL-101(Cr)-F.[63]



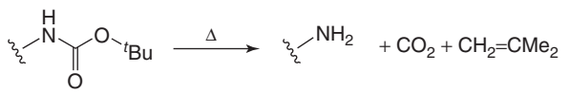
(8)

While the majority of PSM reactions are carried out on powders or crystals, the approach has also been used to modify membranes. For example, membranes of [Zn(im-CHO)$_2$] (ZIF-90) were functionalized by conversion of the aldehyde groups into imines on treatment with an appropriate amine and this was shown to give improvements in the H_2/CO_2 selectivity.[89]

2.2 Thermal PSM Reactions

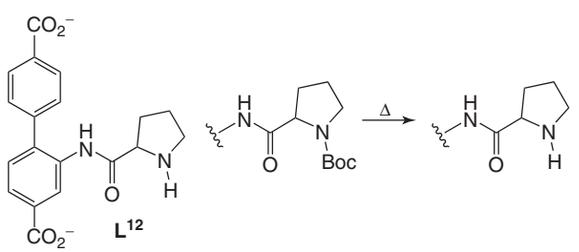
Thermal reactions can be used as deprotection processes to unveil functionalities. Telfer and coworkers showed that a *tert*-butylcarbamate-functionalized

4,4′-biphenyldicarboxylate (bpdc-NHBoc) could be incorporated into an IRMOF structure, giving $[Zn_4O(bpdc\text{-}NHBoc)_3]$. This forms a noninterpenetrated network due to the steric demands of the NHBoc group. On heating to 150 °C, the NHBoc group decomposed to a primary amine (equation 9), generating carbon dioxide and 2-methylpropene which were readily lost due to their volatility.[90]



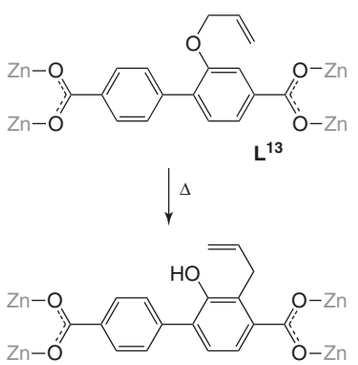
(9)

The group used a similar methodology (equation 10) to form a proline-functionalized IRMOF, $[Zn_4O(\mathbf{L^{12}})_3]$ which was shown to be an active catalyst for the asymmetric aldol reaction.[91]



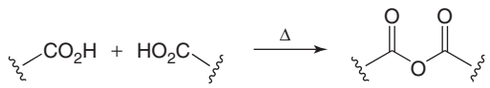
(10)

In addition to deprotection reactions, thermal treatment can lead to rearrangements. Richardson and coworkers showed that the allyloxy-functionalized MOF $[Zn_4O(\mathbf{L^{13}})_3]$ undergoes a solventless Claisen rearrangement on heating to 260 °C (equation 11). The progress of the reaction was followed by simultaneous thermogravimetric-differential thermal analysis.[92]



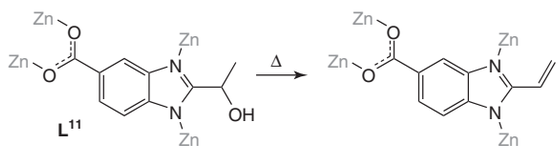
(11)

PSM can also be used to transform the connectivity in a MOF, by joining together two linker ligands. For example, Stock and coworkers showed that when [Al(OH)(bdc-CO_2H)] (MIL-53(Al)-CO_2H) was heated under reduced pressure, condensation of the carboxylic acid tags occurred to give acid anhydrides (equation 12).[93]



(12)

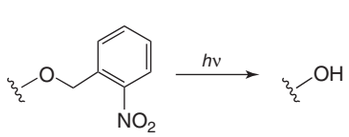
PSM protocols can be used to prepare ligands that cannot be synthesized using conventional methods. For example, 2-vinyl-1*H*-benzo[*d*]imidazole-carboxylic acid had not previously been reported before its synthesis within a MOF by alcohol dehydration on the zinc MOF $[Zn_3(\mathbf{L^{11}})_2(OH)_2]$ (equation 13). Subsequent attempts to prepare the acid without the use of the MOF as a protecting group were hindered by competing polymerization reactions.[82]



(13)

2.3 Photochemical PSM Reactions

Nitrobenzyl groups are often used as photocleavable protecting groups for alcohols. This is significant for MOF chemistry, as networks containing bdc-OH and bdc$(OH)_2$ can be difficult to prepare directly. Cohen and coworkers showed that one or two nitrobenzyl ether groups could be appended to bdc and that the resulting ligands could be combined with zinc(II) and H_3btb to form analogs of UMCM-1. On irradiation with laser light for 24 h, $[Zn_4O(btb)_{4/3}(bdc\text{-}OCH_2C_6H_4NO_2\text{-}2)]$ was converted quantitatively to $[Zn_4O(btb)_{4/3}(bdc\text{-}OH)]$ (equation 14), whereas for the photolysis of $[Zn_4O(btb)_{4/3}(bdc\text{-}\{OCH_2C_6H_4NO_2\}_2\text{-}2,3)]$, 75% conversion to $[Zn_4O(btb)_{4/3}\{bdc\text{-}(OH)_2\text{-}2,3\}]$ was observed.[94]



(14)

Telfer and coworkers showed that the same nitrobenzyl groups could be incorporated into bpdc linkers and that the resultant zinc MOF $[Zn_4O(bpdc\text{-}OCH_2C_6H_4NO_2\text{-}2)_3]$ has an IRMOF structure. Photolysis of powdered samples of this 2-nitrobenzyl ether with

Table 2 Dative PSMs

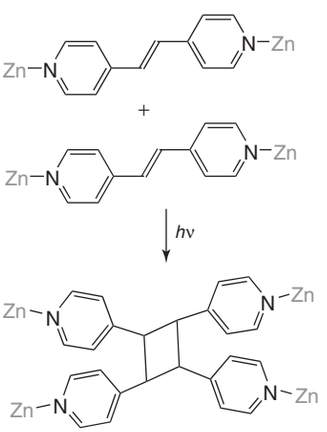
MOF	Reagent	Added group	Degree of modification	Reference
(a) Transformations involving addition of a metal fragment				
$[Zn_4O(bdc)_3]$, MOF-5	$Cr(CO)_6$	$Cr(CO)_3$	100% (5 d, 140 °C)	103
$[Zn_4O(bdc)_3]$, MOF-5	$Mo(CO)_6$	$Mo(CO)_3$	63% (5 d, 140 °C)	103
$[Zr_6O_4(OH)_4(bdc)_6]$, UiO-66	$Cr(CO)_6$	$Cr(CO)_3$	Not reported	104
$[Zn_4O(btb)_{4/3}(bdc\text{-}N{=}CH\text{-}C_5H_4N\text{-}2)]$	$[PdCl_2(NCMe)_2]$	$PdCl_2$	100% (12 h, RT)	30
$[Zn_4O(bdc\text{-}N{=}CH\text{-}CHO)_3]$	CuI/MeCN	CuI(NCMe)	100% (12 h, RT)	105
$[Zn_4O(bdc\text{-}SCH_2CH{=}CH_2)_3]$	$Pd(MeCN)_2Cl_2$	Pd^{II}	21% (5 d, RT)	106
$[Zn_4O(bdc\text{-}NH_2)_{2.94}(bdc\text{-}N{=}CHNC_5H_3N^iPr_2)_{0.06}]$	$[IrCl(cod)]_2$	IrCl	100% (2 h, RT)	107
[Al(OH)(bpydc)], MOF-253	$PdCl_2$	$PdCl_2$	Up to 83% (24 h, 65°C)	108
[Al(OH)(bpydc)], MOF-253	$Cu(BF_4)_2$	$Cu(BF_4)_2$	97% (24 h, 65°C)	108
[Al(OH)(bpydc)], MOF-253	$[RuCl_4(DMSO)_2]^-$	$RuCl_3(DMSO)$	Up to 13% (24 h, 78 °C)	109
$[Al(OH)(bdc\text{-}NH_2)_{1-x}(bdc\text{-}NHC(O)CH{=}CHCO_2H)_x]$	$Pd(OAc)_2$	"PdL_2"	Not reported	110
$[Zn(mbdc)(\mathbf{L}^{17})]$	$Cu(BF_4)_2$	Cu^+	25% (21 d, RT)	111
$[Ca_3\{P(C_6H_4CO_2\text{-}4)_3\}_2]$, PCM-10	$AuCl(SMe_2)$	AuCl	~100% (4 h, RT)	112
$[Zn_4O(bdc\text{-}NH_2)_{1.62}(bdc\text{-}NHMe{=}CHC(O)Me)_{1.38}]$	$NdCl_3$	$Nd(DMSO)_x$	100% (3 d, RT)	48
$[Zn_4O(bdc\text{-}NH_2)_{0.3}(bdc\text{-}NHCH{=}CHC(O)C_6H_4OH\text{-}2)_{2.7}]$	$NdCl_3$	$Nd(DMSO)_x$	33% (3 d, RT)	48
$[Zn_4O\{bdc\text{-}(SCH_2CH_2SMe)_2\text{-}2,5\}_3]$	$HgCl_2$	$HgCl_2$	24% (14 d, RT)	113
$[Zr_6O_4(OH)_4\{bdc\text{-}(SH)_2\text{-}2,5\}_6]$	$HgCl_2$	$HgCl_2$	30% (12 h, RT)	114
$[Zr_6O_4(OH)_4\{P(C_6H_4CO_2\text{-}4)_3\}_4]$	AuCl(tht)	AuCl	16% (24 h, 50 °C)	115
$[Zr_6O_4(OH)_4(bdc\text{-}NH_2)_{5.7}(bdc\text{-}N{=}CHNC_5H_3N^iPr_2)_{0.3}]$	$[IrCl(cod)]_2$	IrCl	100% (12 h, 40 °C)	107
(b) Transformations involving addition of a metal fragment accompanied by deprotonation				
$[Zr_6O_4(OH)_4(Hdcppy)_6]$, UiO-67-dcppy	$[Ir(OMe)(cod)]_2$	IrL	16% (24 h, 55 °C)	116
$[Zr_6O_4(OH)_4(Hdcppy)_6]$, UiO-67-dcppy	$[RhCl(cod)]_2$	RhL	20% (24 h, 55 °C)	116
$[Zn_2(Hdcppy)_2(dabco)]$, DMOF-1-dcppy	$[Ir(OMe)(cod)]_2$	IrL	10% (24 h, 55 °C)	116
$[Zn_2(Hdcppy)_2(dabco)]$, DMOF-1-dcppy	$[RhCl(cod)]_2$	RhL	28% (24 h, 55 °C)	116
$[Zn_2(Hdcppy)_2(bpy)]$, BMOF-1-dcppy	$[Ir(OMe)(cod)]_2$	IrL	16% (24 h, 55 °C)	116
$[Zn_2(Hdcppy)_2(bpy)]$, BMOF-1-dcppy	$[RhCl(cod)]_2$	RhL	26% (24 h, 55 °C)	116
$[Cd_3Cl_6(\mathbf{L}^{18})_3]$	$Ti(O^iPr)_4$	$Ti(O^iPr)_2$	33% (30 min, RT)	117
$[Cd_3(\mathbf{L}^{18})_4(NO_3)_6]$	$Ti(O^iPr)_4$	$Ti(O^iPr)_2$	25% (15 h, RT)	118
$[Zn(tcpb)(\mathbf{L}^5)]$	LiO^tBu	Li	100% (o/n, RT)	119
$[Zn(tcpb)(\mathbf{L}^5)]$	$Mg(OMe)_2$	Mg(OMe)	100% (o/n, RT)	119
$[Zn(tcpb)(\mathbf{L}^5)]$	$CuCl_2$	Cu^{2+}	Not reported	67
$[Cu_2(\mathbf{L}^{19})_2(H_2O)_2]$	$Ti(O^iPr)_4$	$Ti(O^iPr)_2$	100% (5 h, RT)	120
$[Cu_2(\mathbf{L}^{19})_2(H_2O)_2]$	$ZnMe_2$	Zn	90% (3 h, −78 °C)	120
$[Zn_4O(\mathbf{L}^{20})_3]$	$Ti(O^iPr)\{(OCH_2CH_2)_3N\}$	$Ti\{(OCH_2CH_2)_3N\}$	Up to 80% (RT)	121
$[Zn_4O(\mathbf{L}^{20})_3]$	$TiBz_4$	$TiBz_3$	Up to 45% (−30 °C)	121
$[Zn_4O(bdc\text{-}NH_2)_{2.6}(bdc\text{-}N{=}CH\text{-}C_6H_6OH\text{-}2)_{0.4}]$	$VO(acac)_2$	VO(acac)	100% (7 d, RT)	54
$[Zn_4O(bdc\text{-}NH_2)_{2.9}(bdc\text{-}N{=}CH\text{-}C_6H_6OH\text{-}2)_{0.1}]$	$NaAuCl_4$	$AuCl_2$	100% (1 h, RT)	122
$[Zn_4O(btb)_{4/3}(bdc\text{-}NH_2)_{0.65}\{bdc\text{-}NHCO\text{-}C_6H_3(OH\text{-}2)(CO_2H\text{-}6)\}_{0.35}]$	$Fe(acac)_3$	FeL	~50% (rapid, RT)	36
$[Zn_4O(btb)_{4/3}(bdc\text{-}NH_2)_{0.65}\{bdc\text{-}NHCO\text{-}C_6H_3(OH\text{-}2)(CO_2H\text{-}6)\}_{0.35}]$	$Cu(acac)_2$	CuL	~50% (rapid, RT)	36
$[Zn_4O(btb)_{4/3}(bdc\text{-}NH_2)_{0.5}\{bdc\text{-}NHCO\text{-}C_4N_2H_2(CO_2H\text{-}3)\}_{0.5}]$	$Fe(acac)_3$	FeL	~50% (rapid, RT)	36
$[Zn_4O(btb)_{4/3}(bdc\text{-}NH_2)_{0.5}\{bdc\text{-}NHCO\text{-}C_4N_2H_2(CO_2H\text{-}3)\}_{0.5}]$	$Cu(acac)_2$	CuL	~50% (rapid, RT)	36
$[Zn_4O(btb)_{4/3}\{bdc\text{-}NHCO\text{-}C_6H_3(OH\text{-}2)(CO_2H\text{-}6)\}]$	$In(acac)_3$	InL	~70% (4 h, RT)	123
$[Zn_4O(btb)_{4/3}\{bdc\text{-}NHCO\text{-}C_4N_2H_2(CO_2H\text{-}3)\}]$	$In(acac)_3$	InL	~70% (4 h, RT)	123
$[Cu_2(\mathbf{L}^{21})_2(MeOH)_2](NO_3)_4$	$Pd(OAc)_2$	PdL	76% (12 h, 66 °C)	29
$[Cr_3OF(H_2O)_{2-x}(dopamine)_x(bdc)_3]$	$VO(acac)_2$	VO(acac)	~100% (24 h, 50 °C)	124

bdc, 1,4-benzenedicarboxylate; btb, 4,4′,4″-benzene-1,3,5-triylbenzoate; bdc-X, 2-X-1,4-benzenedicarboxylate; bpydc, 2,2′-bipyridine-5,5′-dicarboxylate; Hdcppy, 2-phenylpyridine-5,4′-dicarboxylate; dabco, 1,4-diaza[2.2.2]bicyclooctane; bpy, 4,4′-bipyridyl; tcpb, 1,2,4,5-tetrakis(4-carboxyphenyl)benzene; Hacac, pentane-2,4-dione; cod, 1,5-cyclooctadiene; tht, tetrahydrothiophene.

laser light gave $[Zn_4O(bpdc\text{-}OH)_3]$, although with large single crystals, the reaction stopped at about 50% conversion.[95]

Azides can be photoactivated to form nitrenes. Kitagawa and coworkers used 5-azido-1,3-benzenedicarboxylate (*m*bdc-N_3) to form $[Zn_2(mbdc\text{-}N_3)_2(bpy)_2]$ (CID-N_3) and then irradiated this with ultraviolet radiation to convert the azide groups into nitrenes. The nitrene groups react with oxygen to give nitro- and nitroso- functionalities and with CO to give isocyanates.[21]

Alkenes are well-established to be able to undergo [2+2] photodimerization reactions in the solid state if the double bonds are close enough together, and this can happen in coordination networks. Lang and coworkers showed that both silver and cadmium coordination polymers containing *trans*-1,2-bis(4-pyridyl)ethylene (bpe) can undergo photodimerization, in the latter case in a SC-SC transformation.[96] Vittal and coworkers showed that compounds such as [Zn(bpe)(bdc)] formed interpenetrated three-dimensional (3D) networks with the double bonds from the two networks <4 Å apart. Following UV irradiation, the compounds were converted into the cyclobutane derivatives in SCSC transformations (equation 15).[97]

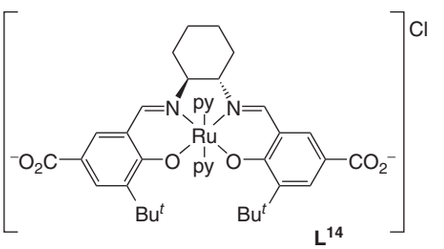


(15)

Champness and coworkers prepared the complexes *fac*-[M(bpydc)$(CO)_3$X] (M = Mn, Re; bpydc = 2,2′-bipyridine-5,5′-dicarboxylate) and reacted them with manganese(II) to form MOFs in which Mn(II) cations are the nodes and the diimine complexes are the linkers. On treatment with UV radiation, *fac* to *mer* isomerization was observed, as witnessed by IR spectroscopy and X-ray crystallography.[98]

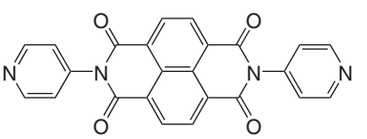
2.4 Electrochemical PSM Reactions

Electrochemical transformations in MOFs can involve redox processes on the nodes or the linkers. Lin and coworkers reported that the ruthenium complex **L**^{14} could be used as a linear dicarboxylate and that both doubly interpenetrated and noninterpenetrated supramolecular isomers of $[Zn_4O(\mathbf{L}^{14})_3]$ could be prepared. These could be reduced with $LiBEt_3H$, converting ruthenium(III) to ruthenium(II), and re-oxidized in air.[99] Although this process involves a change in metal oxidation state, the inclusion of ruthenium into the dicarboxylate means this formally involves a redox process on the linker.

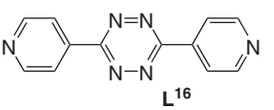


L^{14}

Hupp and coworkers prepared $[Zn_2(2,6\text{-}ndc)_2(\mathbf{L}^{15})]$ (2,6-ndc = 2,6-naphthalenedicarboxylate)[100,101] and $[Zn_2(2,6\text{-}ndc)_2(\mathbf{L}^{16})]$,[102] both of which form 3D structures with reducible pillaring ligands.



L^{15}

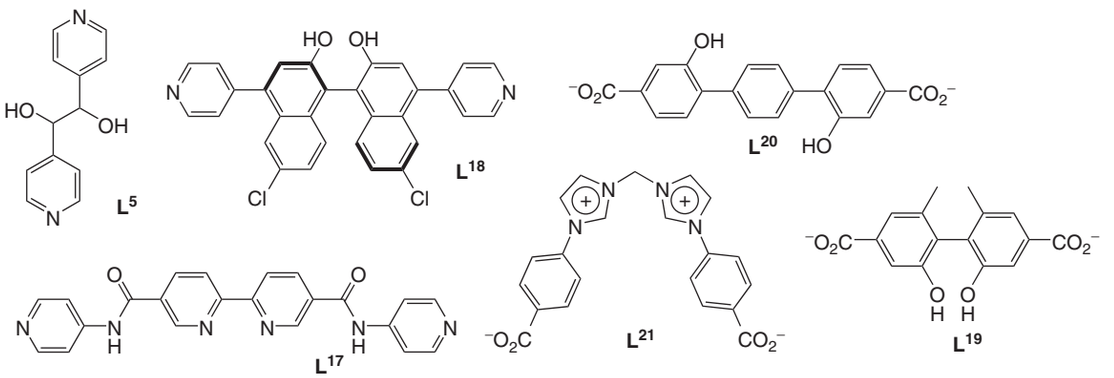


L^{16}

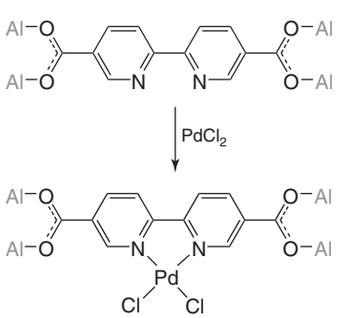
On treatment with lithium, sodium, or potassium naphthalenide, the **L**^{15} or **L**^{16} linkers were partially reduced, with the charges balanced by the included Group 1 cations. A small degree of reduction was found to enhance uptake of hydrogen.

3 DATIVE POSTSYNTHETIC MODIFICATION

Dative PSM involves the postsynthetic coordination of a metal center to one of the linker ligands. Examples of dative PSM reactions are summarized in Table 2.

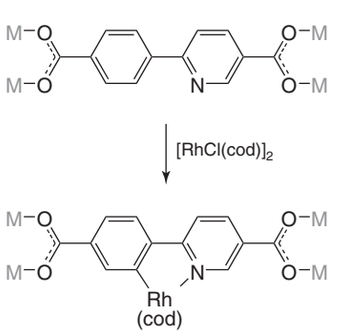


A number of groups have prepared MOFs that contain free ligand sites. For example, Long and coworkers prepared [Al(OH)(bpydc)] (MOF-253), then demonstrated that this reacts with $PdCl_2$ (equation 16) and $Cu(BF_4)_2$ to fill the majority of the bidentate 2,2′-bipyridyl sites.[108]



(16)

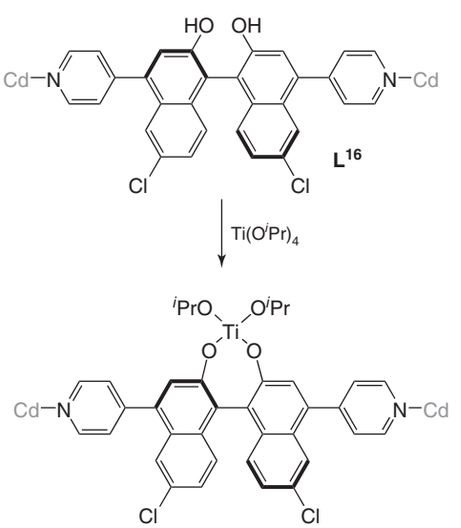
Cohen and coworkers have prepared zinc and zirconium MOFs containing 2-phenylpyridine-5,4′-dicarboxylate (dcppy) and shown they undergo cyclometalation reactions to introduce iridium and rhodium (equation 17) fragments.[116]



(17)

Even the aromatic ring of a bdc linker can act as a ligand. Kaye and Long[103] demonstrated that $[Zn_4O(bdc)_3]$ (MOF-5) reacts with $[Cr(CO)_6]$ to form $[Zn_4O\{bdc\text{-}Cr(CO)_3\}_3]$. Photolysis of this product in the presence of N_2 or H_2 led to substitution of one of the carbonyl groups and formation of $[Zn_4O\{bdc\text{-}Cr(CO)_2(N_2)\}_3]$ and $[Zn_4O\{bdc\text{-}Cr(CO)_2(H_2)\}_3]$, respectively.

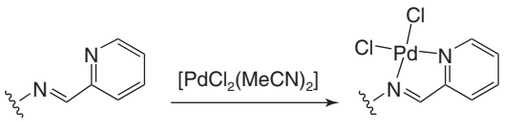
MOFs containing pendant hydroxyl groups can be metalated. For example, Lin and coworkers used dipyridyl-substituted binaphthol ligands as pillars in the preparation of the chiral cadmium MOF $[Cd_3Cl_6(\mathbf{L^{16}})_3]$. This product reacted with $Ti(OPr^i)_4$ with deprotonation of the hydroxyl groups (equation 18) to form a material that catalyzes the addition of diethylzinc to aromatic aldehydes.[117]



(18)

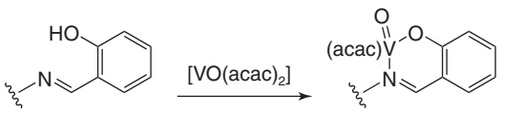
In another example, [Zn(tcpb)($\mathbf{L^5}$)] reacts with lithium *tert*-butoxide to lithiate the hydroxyl groups on the *N*,*N*-ditopic pillaring ligand.[100] Lithium-containing MOFs are of interest as calculations have shown they have enhanced H_2 storage potential.

Another common approach to dative PSM uses a covalent reaction to assemble a ligand and then reacts this with a metal center in the second half of a tandem process. For example, Yaghi *et al.* showed how an iminopyridine-functionalized UMCM-1 derivative, obtained by covalent PSM, reacts with $[PdCl_2(MeCN)_2]$ to give metallation of the bidentate coordination sites (equation 19).[61]



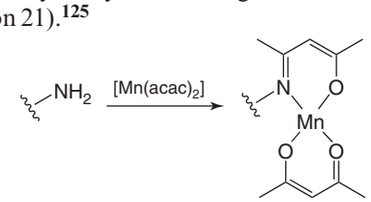
(19)

Rosseinsky and coworkers demonstrated that IRMOF-3 reacts with salicaldehyde in a covalent PSM process and that the product reacts with $[VO(acac)_2]$ to append a vanadyl group to the MOF (equation 20).[54]



(20)

Ahn and coworkers showed that it was possible to combine the PSM of an amine to form an imine-based ligand and coordination of a metal to this into a single step. They reported that IRMOF-3 reacts with $[Mn(acac)_2]$ to form a catalytically active manganese-functionalized MOF (equation 21).[125]



(21)

Other MOFs have been designed to sequester metal ions from solution. $[Zn_4O\{(bdc\text{-}SCH_2CH_2SMe)_2\text{-}2,5\}_3]$ is isoreticular with MOF-5 and is effective at removing Hg^{2+} from ethanol, with the concentration reduced from 84 ppm to 5 ppm after 6 days.[113]

4 INORGANIC PSM—MODIFICATION OF THE METAL COORDINATION SPHERE

Inorganic PSM involves modification of the SBU, or the way in which that connects to the linkers. In this review, inorganic PSM is divided into five areas: substitution of terminal ligands on the SBUs, reaction of an anionic part of the SBU, a redox reaction affecting the SBU, substitution of the metal centers, and substitution of the linker ligands. The last two of these areas have seen an increased focus over the past 2 years and arguably represent the fasting growing segments of PSM research.

4.1 Substitution of Labile Terminal Ligands

Many MOFs contain labile ligands, often coordinated solvent molecules, that are attached to the SBUs. These may be removed together with the solvent molecules included in the pores in the activation process to generate a porous material with open coordination sites. Alternatively, these labile ligands can be substituted for other ligands, and this substitution has often been used to enhance adsorption or catalytic properties. Examples of this type of PSM are summarized in Table 3. Many of these PSM reactions are carried out in two steps, with activation followed by complexation, and the conditions given in Table 3 refer to the second step.

The first example of this type of PSM reaction was reported by Williams and coworkers in 1999.[10] They demonstrated that the terminal water ligands in $[Cu_3(btc)_2(H_2O)_3]$ (btc = 1,3,5-benzenetricarboxylate, HKUST-1) could be removed by heating, and the activated material reacted with pyridine to form $[Cu_3(btc)_2(py)_3]$. Rosseinsky and coworkers looked at the analogous reaction with 4-(methylamino)pyridine (map) and showed it too could substitute for the water ligands to give $[Cu_3(btc)_2(map)_x(H_2O)_{3-x}]$.[126] They demonstrated that the 60%-functionalized material was able to adsorb NO, reversibly converting the secondary amine into an *N*-diazenium diolate. Subsequently, dithioglycol[127] and diamines[128] have been coordinated to the HKUST-1 copper(II) centers, with the products displaying enhanced activity for metal sequestration and CO_2 adsorption, respectively. The chromium MOF $[Cr_3OF(H_2O)_2(bdc)_3]$

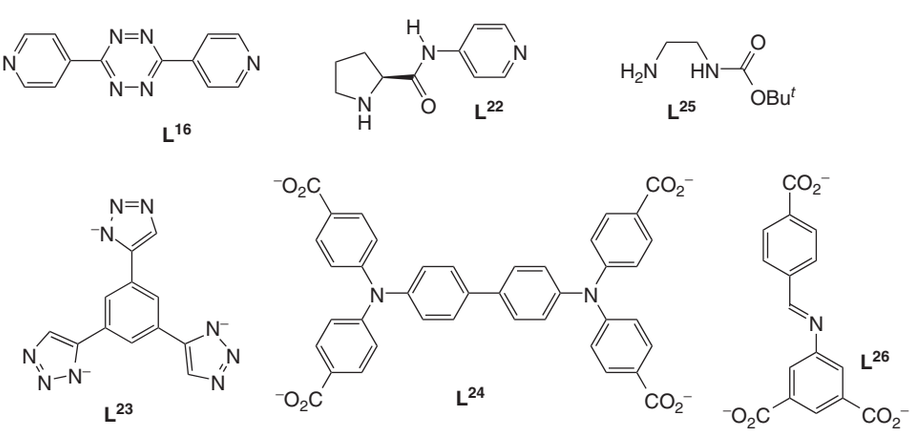


Table 3 PSMs involving substitution of a labile ligand or bonding to a coordinatively unsaturated metal center

Starting MOF	Substituted ligand	Incoming ligand	Degree of modification	Reference
$[Cu_3(btc)_2(H_2O)_3]$, HKUST-1	H_2O	py	100% (two-step process, second at RT)	10
$[Cu_3(btc)_2(H_2O)_3]$, HKUST-1	H_2O	map	Up to 97% (140 °C)	126
$[Cu_3(btc)_2(H_2O)_3]$, HKUST-1	H_2O	$HSCH_2CH_2SH$	Up to 75% (24 h, RT)	127
$[Cu_3(btc)_2(H_2O)_3]$, HKUST-1	H_2O	$NH_2CH_2CH_2NH_2$	80% (12 h, reflux)	128
$[Cu_3(btc)_2(H_2O)_3]$, HKUST-1	H_2O	3-picolylamine	67% (12 h, reflux)	128
$[Cu_3(btc)_2(H_2O)_3]$, HKUST-1	H_2O	4-picolylamine	50% (12 h, reflux)	128
$[Zn_2(tcpb)(DMF)_2]$	DMF	4-substituted pyridines	100% (24 h, RT)	129
$[Cr_3OF(H_2O)_2(bdc)_3]$, MIL-101(Cr)	H_2O	$NH_2CH_2CH_2NH_2$ and other diamines	Up to 100% (12 h, 111 °C)	130
$[Cr_3OF(H_2O)_2(bdc)_3]$, MIL-101(Cr)	H_2O	Dien	70% (8 h, 111 °C)	131
$[Cr_3OF(H_2O)_2(bdc)_3]$, MIL-101(Cr)	H_2O	**L**[22] and similar	90% (24 h, 61 °C)	132
$[Cr_3OF(H_2O)_2(bdc)_3]$, MIL-101(Cr)	H_2O	Dopamine, $NH_2CH_2CH_2SMe$	Mainly surfaces (24 h, 50 °C)	124
$[Cr_3OF(H_2O)_2(bdc)_3]$, MIL-101(Cr)	H_2O	**L**[25]	18% (12 h, 80 °C)	133
$H_3[(Cu_4Cl)_3(\mathbf{L}^{23})_8(DMF)_{12}]$, Cu-BTTri	DMF	$NH_2CH_2CH_2NH_2$	31% (12 h, 111 °C)	134
$H_3[(Cu_4Cl)_3(\mathbf{L}^{23})_8]$	—	Piperazine	100% (3 d, RT)	135
$[Zn_2(\mathbf{L}^{24})(H_2O)_2]$, SNU-30	H_2O	**L**[16]	80% (3 h, 100 °C)	136
$[Mg_2(dobdc)]$, MOF-74(Mg) [CPO-27(Mg)]	—	$[O^iPr]^-$, $ROCO_2R$	77% (111 °C)	137
$[Zn_2(dobdc)]$, MOF-74(Zn) [CPO-27(Zn)]	—	Histamine	77% (111 °C)	138
$[Zn_2(cam)_2(py)_2]$	py	Pyrazine	74% (7 d, RT)	139
$[Zn_2(cam)_2(py)_2]$	py	3-bromopyridine	86% (7 d, RT)	139
$[Nd_2(\mathbf{L}^{26})_2(DMF)_{2.8}(H_2O)_{1.2}]$	DMF	Wide range of ligands including THF, pyridine, imidazole, and Cl^-	100% (2 d, 50–100 °C)	140
$[Ca(C_4O_4)(H_2O)]$	H_2O	Cl^-	50% (2h, RT, ball-milling)	141

btc, 1,3,5-benzenetricarboxylate; py, pyridine; map, 4-(methylamino)pyridine; tcpb, 1,2,4,5-tetrakis(4-carboxyphenyl)benzene; bdc, 1,4-benzenedicarboxylate; dobdc, 2,5-dioxo-1,4-benzenedicarboxylate; cam, (+)-camphorate.

(MIL-101(Cr)) contains two coordinated labile water ligands per SBU and has been used in similar reactions to HKUST-1. For example, the reaction of MIL-101(Cr) with the catechol-functionalized amine dopamine gave a product containing catechol groups on the crystal surfaces, and these in turn were metalated on treatment with $[VO(acac)_2]$.[124]

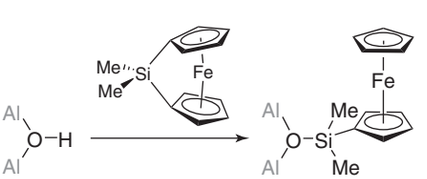
Tasiopoulos and coworkers showed that it was possible to substitute the terminal DMF ligands on the neodymium MOF $[Nd_2(\mathbf{L}^{26})_2(DMF)_{2.8}(H_2O)_{1.2}]$ for a wide range of terminal ligands, with the reactions all occurring in SC-SC transformations.[140]

Suh and coworkers reported that $[Zn_2(\mathbf{L}^{24})(H_2O)_2]$ (SNU-30) reacts with **L**[16].[136] The reaction occurs with substitution of the water molecules, although in this case each **L**[16] molecule displaced two water molecules, and in the product **L**[16] ligands bridge between pairs of zinc centers. The **L**[16] molecules can be removed by placing the crystals in DMF.

A related process was studied by Brammer and coworkers[139] They reported that heating the 2D MOF $[Zn_2(cam)_2(py)_2]$ led to elimination of pyridine, and conversion to a 3D MOF, with bridging carboxylate groups occupying the axial coordination sites. On reaction with pyrazine, the new Zn–O bonds were broken, with the bridging pyrazine linkers giving rise to a second 3D network. Overall, the two-step process leads to replacement of two terminal pyridine ligands by a bridging pyrazine linker.

4.2 Reaction at the Anionic Part of the SBU

[Al(OH)(bdc)] (MIL-53(Al)) contains infinite SBUs with hydroxide ions bridging between the Al^{3+} centers. Fischer and coworkers demonstrated that the hydroxide groups could be modified by reaction with 1,1′-ferrocenediyldimethylsilane (equation 22), with 25% of the hydroxyl groups converted into siloxy groups.[142]



(22)

Lillerud and coworkers demonstrated that on heating *in vacuo*, $[Zr_6O_4(OH)_4(bdc)_6]$, UiO-66, loses two equivalents of water from each SBU to form $[Zr_6O_6(bdc)_6]$ without loss of porosity.[143] Long and coworkers then showed that this material reacts with lithium *tert*-butoxide, with about 25% of the available sites on the SBUs occupied by O^tBu^- anions.[144] The modified material was shown to act as a solid-state electrolyte with potential application in Li-ion batteries. Larabi and Quadrelli[145] showed that the hydroxyl groups in the isoreticular network $[Zr_6O_4(OH)_4(bpdc)_6]$ (UiO-67, bpdc = 4,4′-biphenyldicarboxylate) could be deuterated, whereas the reaction with $[AuMe(PMe_3)]$ occurred to give $[Zr_6O_4(OH)_3(OAuPMe_3)(bpdc)_6]$.

4.3 Oxidation and Reduction of the Framework Metal Centers

Electrochemical PSMs of linking ligands were described in Section 2.4. Framework metal centers can also undergo postsynthetic oxidation and reduction. For example, Tarascon and coworkers reduced MIL-53(Fe) electrochemically in a cell with a lithium negative electrode. The process involves the uptake and removal of Li^+ ions together with the reversible reduction of iron(III) into iron(II).[146] Vimont and coworkers showed that $[Fe_3OF_{0.81}(OH)_{0.19}(H_2O)_2(btc)_2]$ (MIL-100(Fe)) undergoes a partial reduction from iron(III) to iron(II) on thermal treatment.[147] The presence of iron(II) enhances interactions with π-acceptor guests such as CO and alkenes.

Table 4 PSMs involving substitution of a metal center

Starting MOF	Substituted metal	Incoming metal	Degree of modification	Reference
$[Cd(bpy)_2(fds)]$	Cd	Cu	50% (30 d, RT, SC-SC)	150
$[Zn(bpy)_2(O_3SC_6H_4Fc\text{-}3)]$	Zn	Cd	60% (30 d, RT)	151
$[Zn(bpy)_2(O_3SC_6H_4Fc\text{-}3)]$	Zn	Pb	25% (30 d, RT)	151
$[Zn(bpy)_2(O_3SC_6H_4Fc\text{-}3)]$	Zn	Cu	50% (30 d, RT)	151
$[Zn_{0.4}Cd_{0.6}(bpy)_2(O_3SC_6H_4Fc\text{-}3)]$	Cd	Zn	33% (14 d, RT)	151
$Cd_{1.5}(H_2O)_3[(Cd_4O)_3(\mathbf{L^{27}})_8]$	Cd	Pb	100% (2 d, RT)	27
$Pb_{1.5}(H_2O)_3[(Pb_4O)_3(\mathbf{L^{27}})_8]$	Pb	Cd	100% (21 d, RT)	27
$Mn(H_3O)[(Mn_4Cl)_3(\mathbf{L^{28}})]$, POST-65	Mn	Co, Ni, Fe	100% (12 d, RT)	152
$Mn(H_3O)[(Mn_4Cl)_3(\mathbf{L^{28}})]$, POST-65	Mn	Cu	66% (12 d, RT)	152
$[Zn_5Cl_4(\mathbf{L^{29}})_3]$, MFU-4*l*	Zn	Co	80% (140 °C)	28
$[Zn_2(\mathbf{L^{30}})(DMF)_3]$, SNU-51	Zn	Cu	97% (4 d, RT)	153
$[Zn_4O(bdc)_3]$, MOF-5	Zn	Ni	25% (1 y, RT)	154
$[Zn_6(btb)_3(bpy)_3]$, SUMOF-1-Zn	Zn	Cu	95% (3 d, RT)	155
$[Zn_6(btb)_4(bpy)_3]$	Zn	Co, Cu, Ni	100% (1–2 d, RT)	156
$[Co_6(btb)_4(bpy)_3]$	Co	Zn, Cu, Ni	100% (1–2 d, RT)	156
$[Ni_6(btb)_4(bpy)_3]$	Ni	Cu	100% (14 d, RT)	156
$[Zn_2(tcpb)\{Mn(\mathbf{L^{31}})\}]$, Mn^{III}SO-MOF	Mn	Cr, Co	Two-step process: first step involves treatment with H_2O_2 (90%), second step 100%	157
$[Zn_2(tcpb)\{Mn(\mathbf{L^{31}})\}]$, Mn^{III}SO-MOF	Mn	Ni, Cu	Two-step process: first step involves treatment with H_2O_2 (90%), second step 86%	157
$[Zn_2(tcpb)\{Mn(\mathbf{L^{31}})\}]$, Mn^{III}SO-MOF	Mn	Zn	Two-step process: first step involves treatment with H_2O_2 (90%), second step 67%	157
$[Zn(\mathbf{L^{32}})(H_2O)_2](PF_6)_2$	Zn	Cu	100% (6 h, RT)	26
$[Cd(\mathbf{L^{32}})(H_2O)_2](PF_6)_2$	Cd	Cu	100% (6 h, RT)	26
$[Cu(\mathbf{L^{32}})(H_2O)_2](PF_6)_2$	Cu	Cd	53% (10 d, RT)	26
$[Zr_6O_4(OH)_4(bdc)_6]$, UiO-66	Zr	Ti	56% (15 d, 95 °C)	158,159
$[Zr_6O_4(OH)_4(bdc)_6]$, UiO-66	Zr	Hf	Low (5 d, 85 °C)	158
$(H_3O)_8[Cd_8\{Cd(\mathbf{L^{33}})\}_3]$, MMPF-5	Cd	Co	100% of porphyrin metal ions (5 d, 85 °C)	160
$[Zn_2\{Zn(\mathbf{L^{34}})\}\{Zn(\mathbf{L^{35}})\}]$	Zn	Co	100% SBU and $\mathbf{L}^{35}$ (24 h, 80 °C)	161
$[Zn_2\{Zn(\mathbf{L^{34}})\}\{Zn(\mathbf{L^{35}})\}]$	Zn	Ni	100% SBU only (24 h, 80 °C)	161
[Cd(tmpp)][$Cd_4(bpt)_4$]	Cd	Cu	100% (10 d, RT)	162
$[Zn_5(OAc)_4(\mathbf{L^{36}})_3]$	Zn	Co	20% (24 h, 60 °C)	163
$[Zn(im\text{-}Me)_2]$, ZIF-8	Zn	Mn	10% (24 h, 55 °C)	164
$[Zn(im\text{-}Cl_2\text{-}4,5)_2]$, ZIF-71	Zn	Mn	12% (24 h, 55 °C)	164

bpy, 4,4′-bipyridyl; fds, ferrocene-1,1′-disulfonate; Fc, ferrocenyl;tcpb, 1,2,4,5-tetrakis(4-carboxyphenyl)benzene; btb, 4,4′,4″-benzene-1,3,5-triylbenzoate; bdc, 1,4-benzenedicarboxylate; im-Me, 2-methylimidazolate; im-Cl_2-4,5, 4,5-dichloroimidazolate; bpt, biphenyl-3,4′,5-tricarboxylate; tmpp, tetra(*N*-methyl-4-pyridyl)porphine(4+).

Fischer and coworkers showed that [VO(bdc)] (MIL-47(V)) reacts with cobaltocene, [Co(η^5-$C_5H_5)_2$], to form [Co(η^5-$C_5H_5)_2$][VO(bdc)]$_2$.[148] In this process, cobaltocene is oxidized to cobaltocenium, and the framework contains a 1:1 mixture of vanadium(III) and vanadium(IV). Clet and coworkers demonstrated that MIL-47(V) can be formed with different proportions of vanadium(III) and vanadium(IV), depending on the activation protocol. They showed that the MOF containing only vanadium(III) is isostructural with the MIL-53 series and has a flexible structure, whereas MIL-47, which contains only vanadium(IV), has a rigid structure.[149]

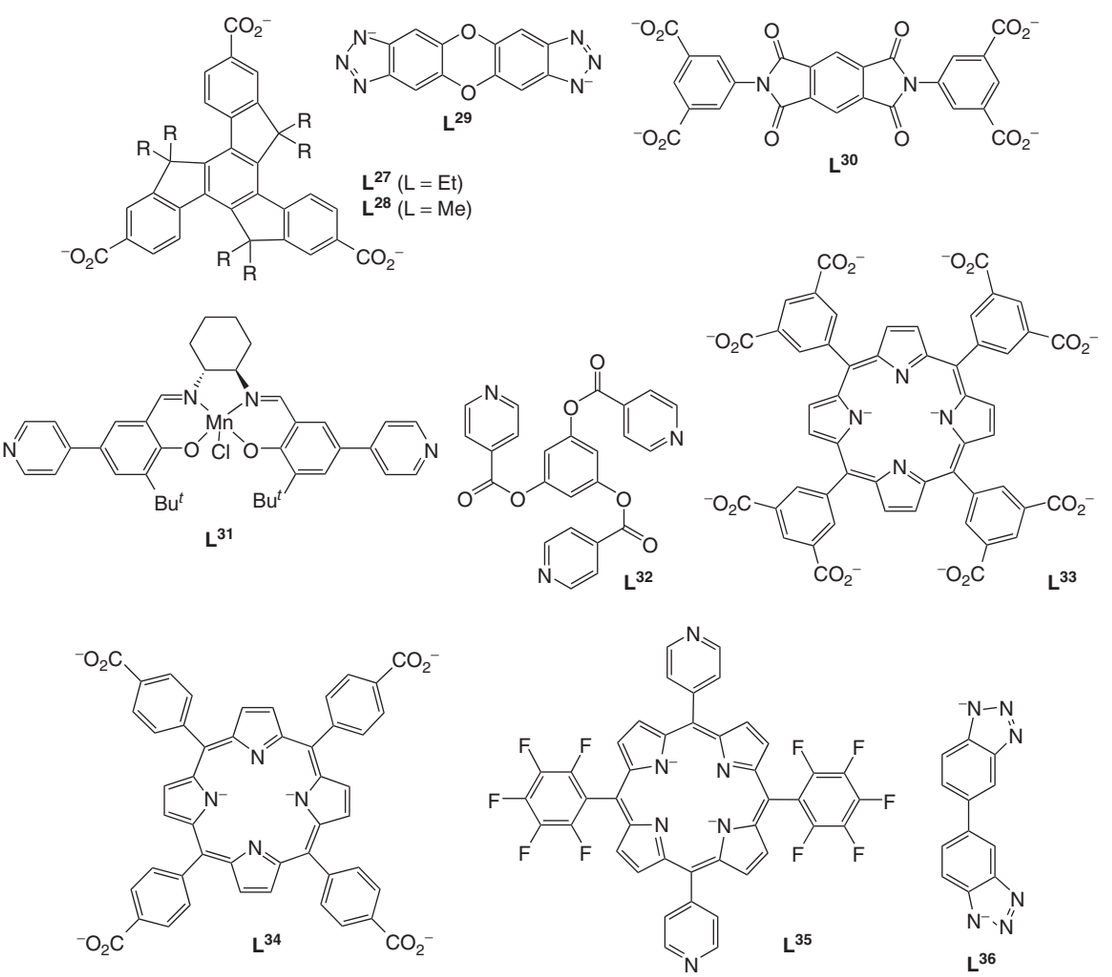
4.4 Substitution of Metal Centers

There have been a growing number of reports involving postsynthetic exchange of framework metal centers within a MOF, and these processes are summarized in Table 4.

The first examples of this type of PSM involved coordination networks with relatively weak bonds, and some of these processes were demonstrated to occur in a SC-SC manner. For example, the zinc(II) centers in [Zn(bpy)$_2$($O_3SC_6H_4$Fc-3)$_2$] (Fc = ferrocenyl) can be exchanged for cadmium(II), lead(II), and copper(II).[151]

Kim and coworkers demonstrated that $Cd_{1.5}(H_3O)_3[(Cd_4O)_3(\mathbf{L^{27}})_8]$ exchanges framework Cd^{2+} for Pb^{2+} while maintaining crystallinity. The substitution went to completion after 2 days in water, as witnessed by ICP-AES, but mixed Cd-Pb MOFs were observed using shorter reaction times. The substitution is reversible, although the reverse reaction was slower, with compete substitution of Pb^{2+} by Cd^{2+} taking 3 weeks.[27]

Metal exchange often does not go to completion, especially when the metal centers in the SBUs are structurally inequivalent. Four of the five zinc centers in $[Zn_5Cl_4(\mathbf{L^{29}})_3]$ could be exchanged for cobalt,[28] whereas only one of the five zinc centers in $[Zn_5(OAc)_4(\mathbf{L^{36}})_3]$ could be substituted.[163] In a similar manner, only one zinc center



in each SBU of MOF-5 can be replaced by Ni^{2+} even after a year.[154]

Suh and coworkers prepared $[Zn_2(\mathbf{L}^{30})(DMF)_3]$ (SNU-51) and showed that the zinc(II) centers could be exchanged for copper(II) centers without altering the gross structure. Direct reaction of copper(II) with $H_4\mathbf{L}^{30}$ gave a network with a different topology, illustrating the potential of PSM to form products that cannot be prepared by other means.[153]

Hupp and coworkers showed that the manganese center in the salen linker in $[Zn_2(tcpb)(\mathbf{L}^{31})]$ could be removed by treatment with hydrogen peroxide, with control of conditions enabling this reaction to occur only on the crystal surfaces.[165] The "de-manganated" MOF was modified by remetallating the salen struts with a range of other first row *d*-block ions giving a series of isoreticular MOFs. Most of these materials cannot be prepared directly due to competitive self-association.[157]

Zou and coworkers showed that the zinc(II) centers in $[Zn_6(btb)_4(bpy)_3]$ could be replaced by Co^{2+}, Ni^{2+}, and Cu^{2+}. The reversible reaction was possible for $[Co_6(btb)_4(bpy)_3]$, but not for the copper and nickel analogs.[156]

Cohen and coworkers demonstrated that metal exchange could be readily carried out on MOFs previously believed to be robust. They showed that Al^{3+} and Fe^{3+} ions were exchanged between MIL-53(Al)-Br and MIL-53(Fe)-Br and demonstrated that titanium(IV) and hafnium(IV) centers could be incorporated into the UiO-66 structure.[158] However, MIL-101(Cr) remained inert to metal exchange reactions. The Cohen group also showed that manganese could be introduced into the ZIF-8 and ZIF-71 structures through metal exchange.[164]

4.5 Substitution of Linker Ligands

Another fast growing area of PSM is the exchange of one linker for another, and examples of this type of transformation are given in Table 5.

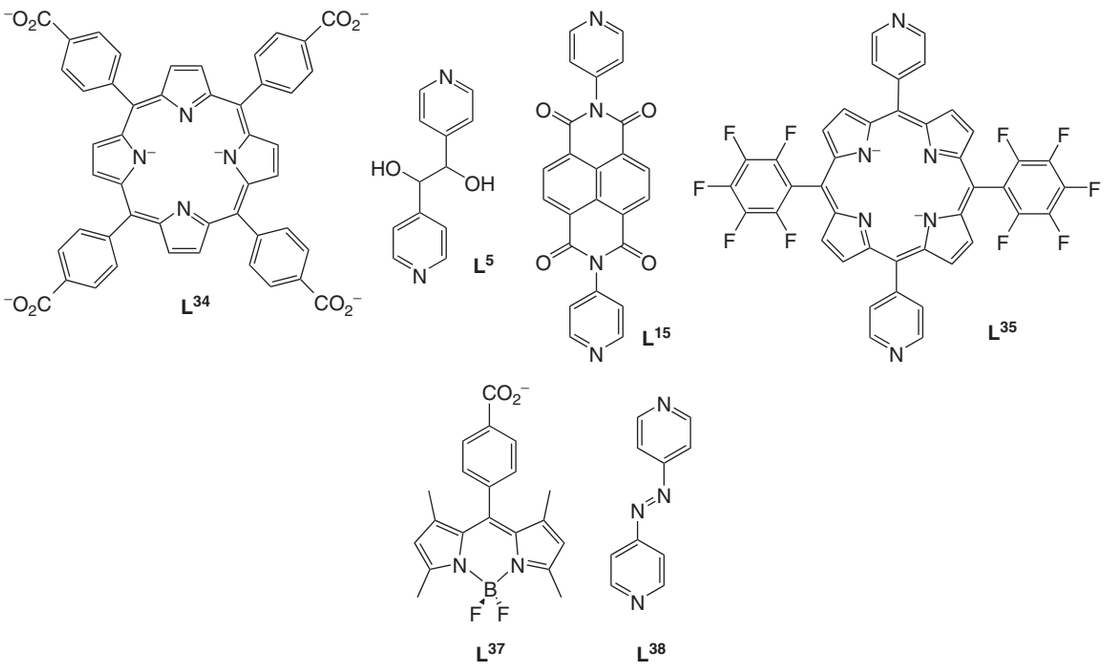
Choe and coworkers provided the first examples of this PSM process. They demonstrated that the porphyrin-based MOF $[Zn_2\{Zn(\mathbf{L}^{34})\}(\mathbf{L}^{15})]$ reacts with 4,4′-bipyridyl to form $[Zn_2\{Zn(\mathbf{L}^{34})\}(bpy)]$.[166] The transformation involves a decrease between layers from 21.2 to 12.8 Å, consistent with the shorter length of the bpy linker.

Cohen and coworkers used aerosol time-of-flight mass spectrometry (ATOF-MS) to show that UiO-66 derivatives could undergo postsynthetic ligand exchange.[167] They heated mixtures of UiO-66-NH_2 and UiO-66-Br and, by analyzing individual particles, demonstrated that the MOFs exchanged linkers. In addition, they showed that linker exchange can be carried out by treating, for example, UiO-66-Br with a salt of bdc-NH_2 in solution. This approach was also used to prepare previously unknown MOFs. For example, UiO-66 was treated with an

Table 5 PSMs involving substitution of a linking ligand

Starting MOF	Substituted linker	Incoming linker	Degree of modification	Reference
$[Zn_2\{Zn(\mathbf{L}^{34})\}(\mathbf{L}^{15})]$	$\mathbf{L}^{15}$	bpy	100% (2 h, RT)	166
$[Zr_6O_4(OH)_4(bdc\text{-}Br)_6]$, UiO-66-Br	bdc-Br	bdc-NH_2	76% (5 d, 85 °C)	167
$[Zr_6O_4(OH)_4(bdc\text{-}NH_2)_6]$, UiO-66-$NH_2$	bdc-NH_2	bdc-Br	43% (5 d, 85 °C)	167
$[Zr_6O_4(OH)_4(bdc)_6]$, UiO-66	bdc	bdc-N_3	50% (5 d, RT)	167
$[Zr_6O_4(OH)_4(bdc)_6]$, UiO-66	bdc	bdc-NH_2	67% (5 d, RT)	167
$[Zr_6O_4(OH)_4(bdc)_6]$, UiO-66	bdc	bdc-Br	48% (5 d, RT)	167
$[Zr_6O_4(OH)_4(bdc)_6]$, UiO-66	bdc	bdc-OH	48% (5 d, RT)	167
$[Zr_6O_4(OH)_4(bdc)_6]$, UiO-66	bdc	bdc-$(OH)_2$-2,5	42% (5 d, RT)	167
$[Zn(im\text{-}Cl_2\text{-}4,5)_2]$, ZIF-71	im-Cl_2-4,5	im-Br-4	35% (3 d, 55 °C)	158,164
$[Cd(im\text{-}Et)_2]$, CdIF-4	im-Et	im-NO_2	100% (2 d, 100 °C)	168
$[Cd(im\text{-}Et)_2]$, CdIF-4	im-Et	im-Me	100% (2 d, 100 °C)	168
$[Zn(im\text{-}Me)_2]$, ZIF-8	im-Me	im-Et	10–20% (3 d, 55 °C)	164
$[Zn(im\text{-}Me)_2]$, ZIF-8	im-Me	im	85% (7 d, 100 °C)	169
$[Zn_2(1,4\text{-}ndc)_2(dabco)]$	1,4-ndc	$\mathbf{L}^{37}$	Crystal surfaces only	170
$[Cu_3(btc)_2]$, HKUST-1	btc	$\mathbf{L}^{37}$	Crystal surfaces only	170
$[Zn(tcpb)(\mathbf{L}^{5})]$, DO-MOF	$\mathbf{L}^{5}$	bpy	100% (24 h, 80 °C)	171
$[Zn(tcpb)(\mathbf{L}^{5})]$, DO-MOF	$\mathbf{L}^{5}$	$\mathbf{L}^{38}$	100% (3 d, 80 °C)	171
[Ni(Hbtc)(bpy)]	bpy	dabco	100% (2 d, 100 °C)	172
$[Zn_2\{Zn(\mathbf{L}^{34})\}\{Zn(\mathbf{L}^{35})\}]$	$Zn(\mathbf{L}^{35})$	$H_2\mathbf{L}^{35}$	65% (24 h, 80 °C)	161
$[Zn_2\{Zn(\mathbf{L}^{34})\}\{Zn(\mathbf{L}^{35})\}]$	$Zn(\mathbf{L}^{35})$	$Al(\mathbf{L}^{35})^{+}$	51% (24 h, 80 °C)	161
$[Zn_2\{Zn(\mathbf{L}^{34})\}\{Zn(\mathbf{L}^{35})\}]$	$Zn(\mathbf{L}^{35})$	$Sn(\mathbf{L}^{35})^{2+}$	47% (24 h, 80 °C)	161
$[Zn_4O(bdc)_3]$, MOF-5	bdc	bdc-Br	53% (24 h, 85 °C)	173
$[Zn_4O(bdc\text{-}Br)_3]$, IRMOF-2	bdc-Br	bdc	41% (6 h, 85 °C)	173

bdc-X, 2-X-1,4-benzenedicarboxylate; bdc, 1,4-benzenedicarboxylate; im-Cl_2-4,5, 4,5-dichloroimidazolate; im-X, 2-X-imidazolate; 1,4-ndc, 1,4-naphthalenedicarboxylate; dabco, 1,4-diaza[2.2.2]bicyclooctane; btc, 1,3,5-benzenetricarboxylate; tcpb, 1,2,4,5-tetrakis(4-carboxyphenyl)benzene

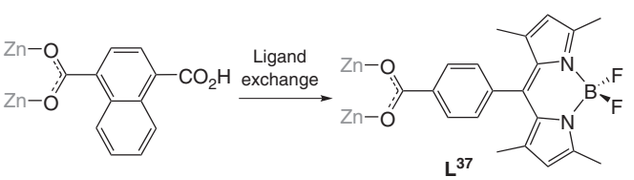


aqueous solution of 2-azido-1,4-benzenedicarboxylate to give UiO-66-N_3. In subsequent work, they demonstrated ligand exchange with other MOFs including MIL-53(Al) and MIL-68(In) analogs and [Zn(im-Cl_2-4,5)$_2$] (ZIF-71).[158]

In contemporary studies, Hupp and coworkers also showed that ligand exchange could occur in imidazolate networks, a process they termed *solvent-assisted linker exchange* (SALE). They demonstrated that the linkers in [Cd(im-Et)$_2$] could be exchanged for 2-nitroimidazolate and 2-methylimidazolate, the latter reaction generating a previously unreported material in a crystal-to-crystal transformation.[168] They subsequently showed that [Zn(im-Me)$_2$] (ZIF-8) undergoes linker exchange with imidazolate, with up to 85% completion.[169] Crucially, such transitions occur without change of phase, allowing for the synthesis of more porous networks that can be produced solvothermally.

Hupp and coworkers also demonstrated that the *N*,*N*-ditopic linker in [Zn(tcpb)(**L**^{5})] could be substituted by bpy with the reaction leading to a noninterpenetrated MOF.[171] This is in contrast to the direct synthesis of [Zn(tcpb)(bpy)], which gives a doubly interpenetrated MOF.

Kitagawa and coworkers recognized that the crystal surfaces of MOFs must contain coordinatively unsaturated ligands, such as dicarboxylates coordinated through a single carboxylate group. They studied substitution reactions of these surface ligands with monocarboxylates, selecting a carboxylate containing a fluorescent BODIPY dye (**L**^{37}) as a means of following the reaction. They showed that only the carboxylate-terminated surfaces of [Zn$_2$(1,4-ndc)$_2$(dabco)] (1,4-ndc = 1,4-naphthalenedicarboxylate) were fluorescent after modification (equation 23), whereas all surfaces of HKUST-1 became fluorescent.[170]



(23)

5 CONCLUSIONS

At the start of 1997, there were only a few isolated examples of PSM in coordination networks. Since then, however, PSM has developed into a powerful tool in the synthesis of functionalized MOFs. The range of possible covalent transformations has increased over the past few years from relatively simple transformations such as the conversation of amines to amides to more complex reactions including tandem processes and the unmasking of reactive groups. Furthermore, the range of MOFs amenable to these transformations has been extended from zinc-based systems based on MOF-5 to more robust and less moisture-sensitive networks such as those based on zirconium and chromium.

Although new covalent modifications continue to attract attention, much of the recent focus has been in inorganic transformations such as metal and linker exchange, and these processes have been shown to occur for many, although not all, networks.

PSM now routinely allows for the synthesis of MOFs that cannot be made by other routes, either because the functional groups are not tolerant of the synthetic conditions (covalent and dative PSM) or because direct synthesis leads to other phases (covalent and inorganic PSM). Furthermore, modified materials have been demonstrated to possess enhanced gas adsorption capacities and selectivities,[174,175] and higher catalytic activity[125,130,132] than their unmodified counterparts.

Future work is likely to see a greater emphasis on control of where the modifications occur. There are already examples of different PSM processes occurring on crystal surfaces and the interior,[86] as well as a few instances in which reaction is limited to specific sites within a MOF.[20,116] A growing emphasis on this area will eventually lead to greater control of the pore structure and provide the capability to tailor pores with a range of complementary functionalities. This structural control will in turn lead to greater control over properties such as catalysis and separations.

6 RELATED ARTICLES

Open Metal Sites in Metal-Organic-Frameworks; Metal Uptake in Metal-Organic Frameworks; Single-Crystal to Single-Crystal Transformations in Metal-Organic Frameworks.

7 ABBREVIATIONS AND ACRONYMS

AAS = atomic absorption spectroscopy; ATOF-MS = aerosol time-of-flight mass spectrometry; 2,6-ndc = 2,6-naphthalenedicarboxylate; bdc = 1,4-benzenedicarboxylate; bpdc = 1,3,5-benzenetricarboxylate; bpydc = 2,2′-bipyridine-5,5′-dicarboxylate; btb = 4,4′,4″-benzene-1,3,5-triylbenzoate; btc = 1,3,5-benzenetricarboxylate; 3D = three-dimensional; dabco = 1,4-diaza[2.2.2]bicyclo-octane; EDX = energy-dispersive X-ray spectroscopy; EXAFS = extended X-ray fine structure; Fc = ferrocenyl; ICP-AES = inductively coupled plasma atomic emission spectroscopy; MOF = metal–organic framework; PSD = postsynthetic deprotection; PSM = Postsynthetic modification; PXRD = Powder X-ray diffraction; 1,4-ndc = 1,4-naphthalenedicarboxylate; SALE = solvent-assisted linker exchange; SBU = secondary building unit; SC-SC = single-crystal to single-crystal; tcpb = 1,2,4,5-tetrakis(4-carboxyphenyl)benzene.

8 REFERENCES

1. *Chem. Rev.*, 2012, **112**(2) is dedicated to this type of compound.
2. D. J. Tranchemontagne, J. L. Mendoza-Cortés, M. O'Keeffe, and O. M. Yaghi, *Chem. Soc. Rev.*, 2009, **38**, 1257.
3. R. Robson, *Dalton Trans.*, 2008, 5113.
4. M. P. Suh, H. J. Park, T. K. Prasad, and D.-W. Lim, *Chem. Rev.*, 2012, **112**, 782.
5. J.-R. Li, J. Sculley, and H.-C. Zhou, *Chem. Rev.*, 2012, **112**, 869.
6. A. Corma, H. García, and F. X. Llabrés i Xamena, *Chem. Rev.*, 2010, **110**, 4606.
7. B. F. Hoskins and R. Robson, *J. Am. Chem. Soc.*, 1990, **112**, 1546.
8. Y.-H. Kiang, G. B. Gardner, S. Lee, Z. Xu, and E. B. Lobkovsky, *J. Am. Chem. Soc.*, 1999, **121**, 8204.
9. J. S. Seo, D. Whang, H. Lee, S. I. Jun, J. Oh, Y. J. Jeon, and K. Kim, *Nature*, 2000, **404**, 982.
10. S. S.-Y. Chui, S. M.-F. Lo, J. P. H. Charmant, A. G. Orpen, and I. D. Williams, *Science*, 1999, **283**, 1148.
11. Z. Wang and S. M. Cohen, *J. Am. Chem. Soc.*, 2007, **129**, 12368.
12. A. D. Burrows, C. G. Frost, M. F. Mahon, and C. Richardson, *Angew. Chem. Int. Ed.*, 2008, **47**, 8482.
13. M. Eddaoudi, J. Kim, N. Rosi, D. Vodak, J. Wachter, M. O'Keeffe, and O. M. Yaghi, *Science*, 2002, **295**, 469.
14. K. Koh, A. G. Wong-Foy, and A. J. Matzger, *Angew. Chem. Int. Ed.*, 2008, **47**, 677.
15. H. Chun, D. N. Dybtsev, H. Kim, and K. Kim, *Chem. Eur. J.*, 2005, **11**, 3521.
16. F. Millange, C. Serre, and G. Férey, *Chem. Commun.*, 2002, 822.
17. G. Férey, C. Mellot-Draznieks, C. Serre, F. Millange, J. Dutour, S. Surblé, and I. Margiolaki, *Science*, 2005, **309**, 2040.
18. C. Volkringer, M. Meddouri, T. Loiseau, N. Guillou, J. Marrot, G. Férey, M. Haouas, F. Taulelle, N. Audebrand, and M. Latroche, *Inorg. Chem.*, 2008, **47**, 11892.
19. J. H. Cavka, S. Jakobsen, U. Olsbye, N. Guillou, C. Lamberti, S. Bordiga, and K. P. Lillerud, *J. Am. Chem. Soc.*, 2008, **130**, 13850.
20. J. S. Costa, P. Gamez, C. A. Black, O. Roubeau, S. J. Teat, and J. Reedijk, *Eur. J. Inorg. Chem.*, 2008, **2008**, 1551.
21. H. Sato, R. Matsuda, K. Sugimoto, M. Takata, and S. Kitagawa, *Nat. Mater.*, 2010, **9**, 661.

22. W. Morris, C. J. Doonan, H. Furukawa, R. Banerjee, and O. M. Yaghi, *J. Am. Chem. Soc.*, 2008, **130**, 12626.
23. S. Yang, G. S. B. Martin, J. J. Titman, A. J. Blake, D. R. Allan, N. R. Champness, and M. Schröder, *Inorg. Chem.*, 2011, **50**, 9374.
24. C. Volkringer and S. M. Cohen, *Angew. Chem. Int. Ed.*, 2010, **49**, 4644.
25. M. Kandiah, S. Usseglio, S. Svelle, U. Olsbye, K. P. Lillerud, and M. Tilset, *J. Mater. Chem.*, 2010, **20**, 9848.
26. G. Mukherjee and K. Biradha, *Chem. Commun.*, 2012, **48**, 4293.
27. S. Das, H. Kim, and K. Kim, *J. Am. Chem. Soc.*, 2009, **131**, 3814.
28. D. Denysenko, T. Werner, M. Grzywa, A. Puls, V. Hagen, G. Eickerling, J. Jelic, K. Reuter, and D. Volkmer, *Chem. Commun.*, 2012, **48**, 1236.
29. G.-Q. Kong, X. Xu, C. Zou, and C.-D. Wu, *Chem. Commun.*, 2011, **47**, 11005.
30. C. J. Doonan, W. Morris, H. Furukawa, and O. M. Yaghi, *J. Am. Chem. Soc.*, 2009, **131**, 9492.
31. S. M. Cohen, *Chem. Rev.*, 2012, **112**, 970.
32. A. D. Burrows, *CrystEngComm*, 2011, **13**, 3623.
33. K. K. Tanabe, Z. Wang, and S. M. Cohen, *J. Am. Chem. Soc.*, 2008, **130**, 8508.
34. Z. Wang, K. K. Tanabe, and S. M. Cohen, *Inorg. Chem.*, 2009, **48**, 296.
35. Z. Wang and S. M. Cohen, *J. Am. Chem. Soc.*, 2009, **131**, 16675.
36. K. K. Tanabe and S. M. Cohen, *Angew. Chem. Int. Ed.*, 2009, **48**, 7424.
37. T. Ahnfeldt, D. Gunzelmann, T. Loiseau, D. Hirsemann, J. Senker, G. Férey, and N. Stock, *Inorg. Chem.*, 2009, **48**, 3057.
38. J. G. Nguyen and S. M. Cohen, *J. Am. Chem. Soc.*, 2010, **132**, 4560.
39. T. Ahnfeldt, D. Gunzelmann, J. Wack, J. Senker, and N. Stock, *CrystEngComm*, 2012, **14**, 4126.
40. K. Peikert, F. Hoffmann, and M. Fröba, *Chem. Commun.*, 2012, **48**, 11196.
41. K. M. L. Taylor-Pashow, J. Della Rocca, Z. Xie, S. Tran, and W. Lin, *J. Am. Chem. Soc.*, 2009, **131**, 14261.
42. A. Modrow, D. Zargarani, R. Herges, and N. Stock, *Dalton Trans.*, 2012, **41**, 8690.
43. S. J. Garibay and S. M. Cohen, *Chem. Commun.*, 2010, **46**, 7700.
44. Q. Yan, Y. Lin, P. Wu, L. Zhao, L. Cao, L. Peng, C. Kong, and L. Chen, *ChemPlusChem*, 2012, **78**, 86.
45. M. Savonnet, S. Aguado, U. Ravon, D. Bazer-Bachi, V. Lecocq, N. Bats, C. Pinel, and D. Farrusseng, *Green Chem.*, 2009, **11**, 1729.
46. J. Canivet, S. Aguado, G. Bergeret, and D. Farrusseng, *Chem. Commun.*, 2011, **47**, 11650.
47. E. Dugan, Z. Wang, M. Okamura, A. Medina, and S. M. Cohen, *Chem. Commun.*, 2008, 3366.
48. R. M. Abdelhameed, L. D. Carlos, A. M. S. Silva, and J. Rocha, *Chem. Commun.*, 2013, **49**, 5019.
49. M. Ma, A. Gross, D. Zacher, A. Pinto, H. Noei, Y. Wang, R. A. Fischer, and N. Metzler-Nolte, *CrystEngComm*, 2011, **13**, 2828.
50. F. M. Hinterholzinger, S. Wuttke, P. Roy, T. Preuße, A. Schaate, P. Behrens, A. Godt, and T. Bein, *Dalton Trans.*, 2012, **41**, 3899.
51. S. Bernt, V. Guillerm, C. Serre, and N. Stock, *Chem. Commun.*, 2011, **47**, 2838.
52. J. A. Rood, B. C. Noll, and K. W. Henderson, *Main Group Chem.*, 2009, **8**, 237.
53. W. Morris, C. J. Doonan, and O. M. Yaghi, *Inorg. Chem.*, 2011, **50**, 6853.
54. M. J. Ingleson, J. Perez Barrio, J.-B. Guilbaud, Y. Z. Khimyak, and M. J. Rosseinsky, *Chem. Commun.*, 2008, 2680.
55. A. D. Burrows and L. L. Keenan, *CrystEngComm*, 2012, **14**, 4112.
56. D. Britt, C. Lee, F. J. Uribe-Romo, H. Furukawa, and O. M. Yaghi, *Inorg. Chem.*, 2010, **49**, 6387.
57. J. G. Nguyen, K. K. Tanabe, and S. M. Cohen, *CrystEngComm*, 2010, **12**, 2335.
58. M. Savonnet, D. Bazer-Bachi, N. Bats, J. Perez-Pellitero, E. Jeanneau, V. Lecocq, C. Pinel, and D. Farrusseng, *J. Am. Chem. Soc.*, 2010, **132**, 4518.
59. M. Savonnet, E. Kockrick, A. Camarata, D. Bazer-Bachi, N. Bats, V. Lecocq, C. Pinel, and D. Farrusseng, *New J. Chem.*, 2011, **35**, 1892.
60. G. Tuci, A. Rossin, X. Xu, M. Ranocchiari, J. A. Van Bokhoven, L. Luconi, I. Manet, M. Melucci, and G. Giambastiani, *Chem. Mater.*, 2013, **25**, 2297.
61. J. G. Vitillo, T. Lescouet, M. Savonnet, D. Farrusseng, and S. Bordiga, *Dalton Trans.*, 2012, **41**, 14236.
62. Y. Yoo and H.-K. Jeong, *Chem. Eng. J.*, 2012, **181-182**, 740.
63. D. Jiang, L. L. Keenan, A. D. Burrows, and K. J. Edler, *Chem. Commun.*, 2012, **48**, 12053.
64. Y. Goto, H. Sato, S. Shinkai, and K. Sada, *J. Am. Chem. Soc.*, 2008, **130**, 14354.
65. C. Liu, T. Li, and N. L. Rosi, *J. Am. Chem. Soc.*, 2012, **134**, 18886.
66. S. Nagata, H. Sato, K. Sugikawa, K. Kokado, and K. Sada, *CrystEngComm*, 2012, **14**, 4137.
67. T. Gadzikwa, O. K. Farha, K. L. Mulfort, J. T. Hupp, and S. T. Nguyen, *Chem. Commun.*, 2009, 3720.
68. S. C. Jones and C. A. Bauer, *J. Am. Chem. Soc.*, 2009, **131**, 12516.
69. K. Hindelang, S. I. Vagin, C. Anger, and B. Rieger, *Chem. Commun.*, 2012, **48**, 2888.

70. K. Hindelang, A. Kronast, S. I. Vagin, and B. Rieger, *Chem. Eur. J.*, 2013, **19**, 8244.
71. T. Gadzikwa, G. Lu, C. L. Stern, S. R. Wilson, J. T. Hupp, and S. T. Nguyen, *Chem. Commun.*, 2008, 5493.
72. W. Zhu, C. He, P. Wu, X. Wu, and C. Duan, *Dalton Trans.*, 2012, **41**, 3072.
73. P. Roy, A. Schaate, P. Behrens, and A. Godt, *Chem. Eur. J.*, 2012, **18**, 6979.
74. A. Huang, N. Wang, C. Kong, and J. Caro, *Angew. Chem. Int. Ed.*, 2012, **51**, 10551.
75. J. A. Thompson, N. A. Brunelli, R. P. Lively, J. R. Johnson, C. W. Jones, and S. Nair, *J. Phys. Chem. C*, 2013, **117**, 8198.
76. J. Canivet and D. Farrusseng, *ChemCatChem*, 2011, **3**, 823.
77. T. Dröge, A. Notzon, R. Fröhlich, and F. Glorius, *Chem. Eur. J.*, 2011, **17**, 11974.
78. M. G. Goesten, K. B. Sai Sankar Gupta, E. V. Ramos-Fernandez, H. Khajavi, J. Gascon, and F. Kapteijn, *CrystEngComm*, 2012, **14**, 4109.
79. M. G. Goesten, J. Juan-Alcañiz, E. V. Ramos-Fernandez, K. B. S. S. Gupta, E. Stavitski, H. van Bekkum, J. Gascon, and F. Kapteijn, *J. Catal.*, 2011, **281**, 177.
80. M. Kim, S. J. Garibay, and S. M. Cohen, *Inorg. Chem.*, 2011, **50**, 729.
81. A. D. Burrows, C. G. Frost, M. F. Mahon, and C. Richardson, *Chem. Commun.*, 2009, 4218.
82. F. Sun, Z. Yin, Q.-Q. Wang, D. Sun, M.-H. Zeng, and M. Kurmoo, *Angew. Chem. Int. Ed.*, 2013, **52**, 4538.
83. J. Cao, Y. Gao, Y. Wang, C. Du, and Z. Liu, *Chem. Commun.*, 2013, **49**, 6897.
84. M. Servalli, M. Ranocchiari, and J. A.Van Bokhoven, *Chem. Commun.*, 2012, **48**, 1904.
85. Z. Wang and S. M. Cohen, *Angew. Chem. Int. Ed.*, 2008, **47**, 4699.
86. T. Gadzikwa, O. K. Farha, C. D. Malliakas, M. G. Kanatzidis, J. T. Hupp, and S. T. Nguyen, *J. Am. Chem. Soc.*, 2009, **131**, 13613.
87. H. Deng, C. J. Doonan, H. Furukawa, R. B. Ferreira, J. Towne, C. B. Knobler, B. Wang, and O. M. Yaghi, *Science*, 2010, **327**, 846.
88. W. Kleist, F. Jutz, M. Maciejewski, and A. Baiker, *Eur. J. Inorg. Chem.*, 2009, **2009**, 3552.
89. A. Huang and J. Caro, *Angew. Chem. Int. Ed.*, 2011, **50**, 4979.
90. R. K. Deshpande, J. L. Minnaar, and S. G. Telfer, *Angew. Chem. Int. Ed.*, 2010, **49**, 4598.
91. D. J. Lun, G. I. N. Waterhouse, and S. G. Telfer, *J. Am. Chem. Soc.*, 2011, **133**, 5806.
92. A. D. Burrows, S. O. Hunter, M. F. Mahon, and C. Richardson, *Chem. Commun.*, 2013, **49**, 990.
93. N. Reimer, B. Gil, B. Marszalek, and N. Stock, *CrystEngComm*, 2012, **14**, 4119.
94. K. K. Tanabe, C. A. Allen, and S. M. Cohen, *Angew. Chem. Int. Ed.*, 2010, **49**, 9730.
95. R. K. Deshpande, G. I. N. Waterhouse, G. B. Jameson, and S. G. Telfer, *Chem. Commun.*, 2012, **48**, 1574.
96. D. Liu, N.-Y. Li, and J.-P. Lang, *Dalton Trans.*, 2011, **40**, 2170.
97. M. H. Mir, L. L. Koh, G. K. Tan, and J. J. Vittal, *Angew. Chem. Int. Ed.*, 2010, **49**, 390.
98. A. J. Blake, N. R. Champness, T. L. Easun, D. R. Allan, H. Nowell, M. W. George, J. Jia, and X. Z. Sun, *Nat. Chem.*, 2010, **2**, 688.
99. J. M. Falkowski, C. Wang, S. Liu, and W. Lin, *Angew. Chem. Int. Ed.*, 2011, **50**, 8674.
100. K. L. Mulfort and J. T. Hupp, *J. Am. Chem. Soc.*, 2007, **129**, 9604.
101. K. L. Mulfort and J. T. Hupp, *Inorg. Chem.*, 2008, **47**, 7936.
102. K. L. Mulfort, T. M. Wilson, M. R. Wasielewski, and J. T. Hupp, *Langmuir*, 2009, **25**, 503.
103. S. S. Kaye and J. R. Long, *J. Am. Chem. Soc.*, 2008, **130**, 806.
104. S. Chavan, J. G. Vitillo, M. J. Uddin, F. Bonino, C. Lamberti, E. Groppo, K.-P. Lillerud, and S. Bordiga, *Chem. Mater.*, 2010, **22**, 4602.
105. J. Yang, P. Li, and L. Wang, *Catal. Commun.*, 2012, **27**, 58.
106. J. He, M. Zha, J. Cui, M. Zeller, A. D. Hunter, S.-M. Yiu, S.-T. Lee, and Z. Xu, *J. Am. Chem. Soc.*, 2013, **135**, 7807.
107. M. Pintado-Sierra, A. M. Rasero-Almansa, A. Corma, M. Iglesias, and F. Sánchez, *J. Catal.*, 2013, **299**, 137.
108. E. D. Bloch, D. Britt, C. Lee, C. J. Doonan, F. J. Uribe-Romo, H. Furukawa, J. R. Long, and O. M. Yaghi, *J. Am. Chem. Soc.*, 2010, **132**, 14382.
109. F. Carson, S. Agrawal, M. Gustafsson, A. Bartoszewicz, F. Moraga, X. Zou, and B. N. Martín-Matute, *Chem. Eur. J.*, 2012, **18**, 15337.
110. M. A. Gotthardt, A. Beilmann, R. Schoch, J. Engelke, and W. Kleist, *RSC Adv.*, 2013, **3**, 10676.
111. T. Jacobs, R. Clowes, A. I. Cooper, and M. J. Hardie, *Angew. Chem. Int. Ed.*, 2012, **51**, 5192.
112. A. J. Nuñez, L. N. Shear, N. Dahal, I. A. Ibarra, J. Yoon, Y. K. Hwang, J.-S. Chang, and S. M. Humphrey, *Chem. Commun.*, 2011, **47**, 11855.
113. J. He, K.-K. Yee, Z. Xu, M. Zeller, A. D. Hunter, S. S.-Y. Chui, and C.-M. Che, *Chem. Mater.*, 2011, **23**, 2940.
114. K.-K. Yee, N. Reimer, J. Liu, S.-Y. Cheng, S.-M. Yiu, J. Weber, N. Stock, and Z. Xu, *J. Am. Chem. Soc.*, 2013, **135**, 7795.
115. J. Václavík, M. Servalli, C. Lothschütz, J. Szlachetko, M. Ranocchiari, and J. A. Van Bokhoven, *ChemCatChem*, 2013, **5**, 692.

116. P. V. Dau, M. Kim, and S. M. Cohen, *Chem. Sci.*, 2013, **4**, 601.

117. C.-D. Wu, A. Hu, L. Zhang, and W. Lin, *J. Am. Chem. Soc.*, 2005, **127**, 8940.

118. C.-D. Wu and W. Lin, *Angew. Chem. Int. Ed.*, 2007, **46**, 1075.

119. K. L. Mulfort, O. K. Farha, C. L. Stern, A. A. Sarjeant, and J. T. Hupp, *J. Am. Chem. Soc.*, 2009, **131**, 3866.

120. K. S. Jeong, Y. B. Go, S. M. Shin, S. J. Lee, J. Kim, O. M. Yaghi, and N. Jeong, *Chem. Sci.*, 2011, **2**, 877.

121. J. Kim, D. O. Kim, D. W. Kim, J. Park, and M. S. Jung, *Inorg. Chim. Acta*, 2012, **390**, 22.

122. X. Zhang, F. X. Llabrés i Xamena, and A. Corma, *J. Catal.*, 2009, **265**, 155.

123. K. K. Tanabe and S. M. Cohen, *Inorg. Chem.*, 2010, **49**, 6766.

124. H. G. T. Nguyen, M. H. Weston, O. K. Farha, J. T. Hupp, and S. T. Nguyen, *CrystEngComm*, 2012, **14**, 4115.

125. S. Bhattacharjee, D.-A. Yang, and W.-S. Ahn, *Chem. Commun.*, 2011, **47**, 3637.

126. M. J. Ingleson, R. Heck, J. A. Gould, and M. J. Rosseinsky, *Inorg. Chem.*, 2009, **48**, 9986.

127. F. Ke, L.-G. Qiu, Y.-P. Yuan, F.-M. Peng, X. Jiang, A.-J. Xie, Y.-H. Shen, and J.-F. Zhu, *J. Hazard. Mater.*, 2011, **196**, 36.

128. C. Montoro, E. García, S. Calero, M. A. Pérez-Fernández, A. L. López, E. Barea, and J. A. R. Navarro, *J. Mater. Chem.*, 2012, **22**, 10155.

129. O. K. Farha, K. L. Mulfort, and J. T. Hupp, *Inorg. Chem.*, 2008, **47**, 10223.

130. Y. K. Hwang, D.-Y. Hong, J.-S. Chang, S. H. Jhung, Y.-K. Seo, J. Kim, A. Vimont, M. Daturi, C. Serre, and G. Férey, *Angew. Chem. Int. Ed.*, 2008, **47**, 4144.

131. S.-N. Kim, S.-T. Yang, J. Kim, J.-E. Park, and W.-S. Ahn, *CrystEngComm*, 2012, **14**, 4142.

132. M. Banerjee, S. Das, M. Yoon, H. J. Choi, M. H. Hyun, S. M. Park, G. Seo, and K. Kim, *J. Am. Chem. Soc.*, 2009, **131**, 7524.

133. B. Li, Y. Zhang, D. Ma, L. Li, G. Li, G. Li, Z. Shi, and S. Feng, *Chem. Commun.*, 2012, **48**, 6151.

134. A. Demessence, D. M. D'Alessandro, M. L. Foo, and J. R. Long, *J. Am. Chem. Soc.*, 2009, **131**, 8784.

135. A. Das, M. Choucair, P. D. Southon, J. A. Mason, M. Zhao, C. J. Kepert, A. T. Harris, and D. M. D'Alessandro, *Micropor. Mesopor. Mater.*, 2013, **174**, 74.

136. H. J. Park, Y. E. Cheon, and M. P. Suh, *Chem. Eur. J.*, 2010, **16**, 11662.

137. B. M. Wiers, M.-L. Foo, N. P. Balsara, and J. R. Long, *J. Am. Chem. Soc.*, 2011, **133**, 14522.

138. M. Inukai, S. Horike, D. Umeyama, Y. Hijikata, and S. Kitagawa, *Dalton Trans.*, 2012, **41**, 13261.

139. P. Smart, C. A. Mason, J. R. Loader, A. J. H. M. Meijer, A. J. Florence, K. Shankland, A. J. Fletcher, S. P. Thompson, M. Brunelli, A. H. Hill, and L. Brammer, *Chem. Eur. J.*, 2013, **19**, 3552.

140. M. J. Manos, E. J. Kyprianidou, G. S. Papaefstathiou, and A. J. Tasiopoulos, *Inorg. Chem.*, 2012, **51**, 6308.

141. S. Horike, Y. Kamitsubo, M. Inukai, T. Fukushima, D. Umeyama, T. Itakura, and S. Kitagawa, *J. Am. Chem. Soc.*, 2013, **135**, 4612.

142. M. Meilikhov, K. Yusenko, and R. A. Fischer, *J. Am. Chem. Soc.*, 2009, **131**, 9644.

143. L. Valenzano, B. Civalleri, S. Chavan, S. Bordiga, M. H. Nilsen, S. Jakobsen, K. P. Lillerud, and C. Lamberti, *Chem. Mater.*, 2011, **23**, 1700.

144. R. Ameloot, M. Aubrey, B. M. Wiers, A. P. Gómora-Figueroa, S. N. Patel, N. P. Balsara, and J. R. Long, *Chem. Eur. J.*, 2013, **19**, 5533.

145. C. Larabi and E. A. Quadrelli, *Eur. J. Inorg. Chem.*, 2012, **2012**, 3014.

146. G. Férey, F. Millange, M. Morcrette, C. Serre, M.-L. Doublet, J.-M. Grenèche, and J.-M. Tarascon, *Angew. Chem. Int. Ed.*, 2007, **46**, 3259.

147. H. Leclerc, A. Vimont, J.-C. Lavalley, M. Daturi, A. D. Wiersum, P. L. Llwellyn, P. Horcajada, G. Férey, and C. Serre, *Phys. Chem. Chem. Phys.*, 2011, **13**, 11748.

148. M. Meilikhov, K. Yusenko, A. Torrisi, B. Jee, C. Mellot-Draznieks, A. Pöppl, and R. A. Fischer, *Angew. Chem. Int. Ed.*, 2010, **49**, 6212.

149. H. Leclerc, T. Devic, S. Devautour-Vinot, P. Bazin, N. Audebrand, G. Férey, M. Daturi, A. Vimont, and G. Clet, *J. Phys. Chem. C*, 2011, **115**, 19828.

150. L. Mi, H. Hou, Z. Song, H. Han, H. Xu, Y. Fan, and S.-W. Ng, *Cryst. Growth Des.*, 2007, **7**, 2553.

151. L. Mi, H. Hou, Z. Song, H. Han, and Y. Fan, *Chem. Eur. J.*, 2008, **14**, 1814.

152. Y. Kim, S. Das, S. Bhattacharya, S. Hong, M. G. Kim, M. Yoon, S. Natarajan, and K. Kim, *Chem. Eur. J.*, 2012, **18**, 16642.

153. T. K. Prasad, D. H. Hong, and M. P. Suh, *Chem. Eur. J.*, 2010, **16**, 14043.

154. C. K. Brozek and M. Dinca, *Chem. Sci.*, 2012, **3**, 2110.

155. Q. Yao, J. Sun, K. Li, J. Su, M. V. Peskov, and X. Zou, *Dalton Trans.*, 2012, **41**, 3953.

156. X. Song, T. K. Kim, H. Kim, D. Kim, S. Jeong, H. R. Moon, and M. S. Lah, *Chem. Mater.*, 2012, **24**, 3065.

157. A. M. Shultz, A. A. Sarjeant, O. K. Farha, J. T. Hupp, and S. T. Nguyen, *J. Am. Chem. Soc.*, 2011, **133**, 13252.

158. M. Kim, J. F. Cahill, H. Fei, K. A. Prather, and S. M. Cohen, *J. Am. Chem. Soc.*, 2012, **134**, 18082.

159. C. Hon Lau, R. Babarao, and M. R. Hill, *Chem. Commun.*, 2013, **49**, 3634.

160. X.-S. Wang, M. Chrzanowski, L. Wojtas, Y.-S. Chen, and S. Ma, *Chem. Eur. J.*, 2013, **19**, 3297.

161. S. Takaishi, E. J. DeMarco, M. J. Pellin, O. K. Farha, and J. T. Hupp, *Chem. Sci.*, 2013, **4**, 1509.

162. Z. Zhang, L. Zhang, L. Wojtas, P. Nugent, M. Eddaoudi, and M. J. Zaworotko, *J. Am. Chem. Soc.*, 2012, **134**, 924.

163. P. Schmieder, D. Denysenko, M. Grzywa, B. Baumgärtner, I. Senkovska, S. Kaskel, G. Sastre, L.van Wüllen, and D. Volkmer, *Dalton Trans.*, 2013, **42**, 10786.

164. H. Fei, J. F. Cahill, K. A. Prather, and S. M. Cohen, *Inorg. Chem.*, 2013, **52**, 4011.

165. A. M. Shultz, O. K. Farha, D. Adhikari, A. A. Sarjeant, J. T. Hupp, and S. T. Nguyen, *Inorg. Chem.*, 2011, **50**, 3174.

166. B. J. Burnett, P. M. Barron, C. Hu, and W. Choe, *J. Am. Chem. Soc.*, 2011, **133**, 9984.

167. M. Kim, J. F. Cahill, Y. Su, K. A. Prather, and S. M. Cohen, *Chem. Sci.*, 2012, **3**, 126.

168. O. Karagiaridi, W. Bury, A. A. Sarjeant, C. L. Stern, O. K. Farha, and J. T. Hupp, *Chem. Sci.*, 2012, **3**, 3256.

169. O. Karagiaridi, M. B. Lalonde, W. Bury, A. A. Sarjeant, O. K. Farha, and J. T. Hupp, *J. Am. Chem. Soc.*, 2012, **134**, 18790.

170. M. Kondo, S. Furukawa, K. Hirai, and S. Kitagawa, *Angew. Chem. Int. Ed.*, 2010, **49**, 5327.

171. W. Bury, D. Fairen-Jimenez, M. B. Lalonde, R. Q. Snurr, O. K. Farha, and J. T. Hupp, *Chem. Mater.*, 2013, **25**, 739.

172. S. Jeong, D. Kim, X. Song, M. Choi, N. Park, and M. S. Lah, *Chem. Mater.*, 2013, **25**, 1047.

173. A. F. Gross, E. Sherman, S. L. Mahoney, and J. J. Vajo, *J. Phys. Chem. A*, 2013, **117**, 3771.

174. Z. Wang, K. K. Tanabe, and S. M. Cohen, *Chem. Eur. J.*, 2010, **16**, 212.

175. Y. E. Cheon and M. P. Suh, *Angew. Chem. Int. Ed.*, 2009, **48**, 2899.

PART 3
Properties and Applications

Functional Magnetic Materials Based on Metal Formate Frameworks

Ran Shang, Sa Chen, Zhe-Ming Wang and Song Gao

Peking University, Beijing, PR China

1	Introduction	221
2	Historical Comment and Some Earlier Works before 2000	222
3	The Dense Binary MFFs and Ternary Ones Incorporating Alkali Metal Ions	224
4	Metal Formate Frameworks Incorporating Ammonium Cations	224
5	The Porous Diamondoid MFFs of $[M_3(HCOO)_6]$	231
6	Magnetic MFFs with Coligands	234
7	Conclusions and Perspectives	237
8	Acknowledgment	237
9	Related Articles	237
10	Abbreviations and Acronyms	237
11	References	238

1 INTRODUCTION

The study of metal-organic frameworks (MOFs) has been proven to be one of the most intense areas of condensed matter in the past decades.[1–31] With both inorganic and organic components and the extended structures by coordination bonds,[4,5] these materials have shown great potential and various interesting properties and functionalities, such as porosity and the accompanied properties,[6–12] framework dynamics,[13,14] optical properties,[15–19] ferroelectrics,[20,21] and magnetism,[22–24] and their possible combinations.[15,16,25–29] Among them, magnetism[22–29] is the most actively studied one, owing to not only the fundamental interests of magnetic interactions and magneto-structural correlations but also the development of new functional molecule-based materials. The basic consideration for designing magnetic MOFs is the choice of spin carriers and bridges.[30,31] In other word, good bridging ligands that can effectively mediate the magnetic coupling between the local spin carriers are pivotal. So far, numerous short bridging ligands have been widely investigated,[22–31] including cyanide, oxalate, azide, and carboxylates. These magnetic MOFs display paramagnetism, long-range magnetic ordering, and low dimensional character showing a wide range of spin dynamics.

While numerous magnetic MOFs have been studied and reported, in this chapter, we choose metal formate frameworks (MFFs),[30–32] a relatively small but truly important class of MOFs, to give a unique perspective in the very wide research field of magnetic MOFs and their development in the past decades. The reasons for this choice are following. Firstly, formate is the smallest and simplest carboxylate and possesses all the functionalities of carboxylates. It can adopt various bridging modes (Figure 1) and has a small stereo effect, making it a good building block for constructing extended structures thus MOFs. Secondly, formate can act as a one- or three-atom connector depending on different coordination modes, thus mediate effective magnetic couplings, either ferro- or antiferromagnetic. Thirdly, what makes formate so special is that it is a good hydrogen-bonding acceptor thus facilitates the formation of hydrogen-bonding system, which plays a key role in the occurrence of structural transitions and ferroelectricity in such molecule-based

Metal-Organic Framework Materials. Edited by Leonard R. MacGillivray and Charles M. Lukehart.
© 2014 John Wiley & Sons, Ltd. ISBN 978-1-119-95289-3

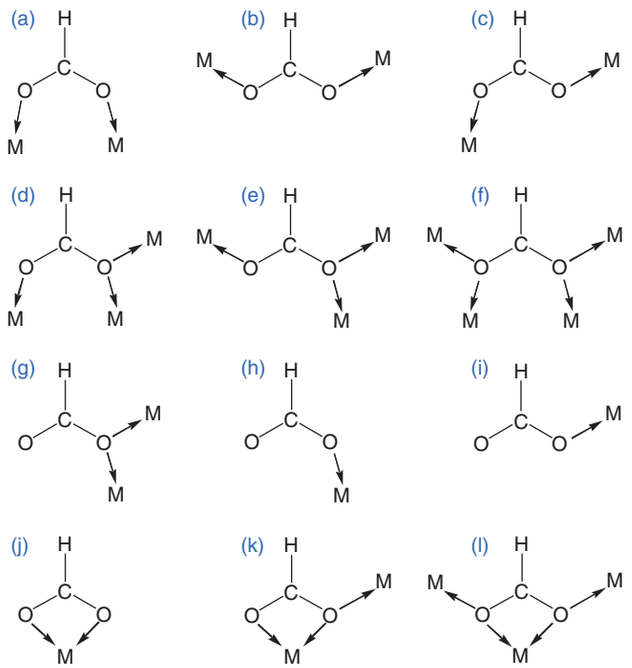


Figure 1 Some coordination modes of formate: (a) syn–syn, (b) anti–anti, (c) syn–anti, (d) syn–anti/syn, (e) anti–anti/syn, (f) anti/syn–anti/syn, (g) μ- or anti/syn-, (h) syn-, (i) anti-, (j) chelating, (k) chelating-anti, (k) anti-chelating-anti

systems.[20,21] The magnetic MFFs thus could serve as a platform for designing and constructing materials with multi-functionalities, in which the magnetism is combined with other functionalities such as ferroelectricity. Fourthly, these studies on MFFs and the achievements are also in accordance to the emerging realization[33–43] that MOFs themselves might display diversity in their physical properties and critical phenomena or phase transitions, probably as rich as the traditional materials such as oxides. Finally, formate has been less explored before in making magnetic MOFs, in contrast to those short ligands such as cyanide, azide, and oxalate, even acetate.

But this is still a quite large research field, so we limit our focus on the late 3d magnetic metals and lanthanides, though sometimes nonmagnetic or 4d/5d metals will be included if necessary. After this short introduction, we provide first a brief historical review (Section 2), to introduce the works on magnetic MFFs before 2000, by several selected earlier published results, then we review the later achievements obtained in the dense binary/ternary MFFs (Section 3), the MFFs incorporating ammonium cations (Section 4), the porous MFFs of $[M_3(HCOO)_6]$ (Section 5), and some selected magnetic MFFs with coligands (Section 6), respectively. Finally, we give the conclusions and perspectives (Section 7).

In most cases, we discuss structurally 3D frameworks, but some 1D and 2D ones will be included. That is, we might not follow the strictest definition of MOFs.[44] When describing the framework structures, we use the topological descriptions and notations[45,46] directly providing that they are simple, concise, and easily understandable, without further explanation. References 45, 46 could be consulted for these descriptions and notations. To save the space, we will use the abbreviations throughout the chapter as possible, and the most are listed below. Other abbreviations will be given when they appear first.

MFF for metal formate framework; AMFF for ammonium metal formate framework; M for metal; TM for transition metal; Ln for lanthanide; 1D/2D/3D for one-/two-/three-dimensional; SG for space group; HB for hydrogen bonding/bond; LRO for long-range ordering; PM/AF/WF/FO/FI for para-/antiferro-/weak ferro-/ferro-/ferri-magnet/magnetism/magnetic; J for magnetic coupling; PE/AFE/FE for para-/antiferro-/ferro-electric/electricity; T_N for Néel temperature; T_C for critical temperature and phase transition temperature; and HT/RT/LT for high/room/low temperature.

2 HISTORICAL COMMENT AND SOME EARLIER WORKS BEFORE 2000

Historically, the magnetic MFFs were explored around 1960–1970s, typically on the salts of metal formate dihydrate with formula $[M(HCOO)_2]\cdot 2H_2O$ (MFD) for divalent 3d metals.[47–63] This isostructural series possesses a 3D framework consisting of layers of (4,4) layer of $M(HCOO)_2$ linked by *trans*-$M(H_2O)_4(HCOO)_2$ units and all formato ligands within the layer are anti–anti (this will be the default for (4,4) layers below if not specially mentioned). They predominantly exhibit LRO of spin-canted AF or WF (Table 1). However, their magnetic behaviors are very interesting, probably because

Table 1 A collection of magnetic characteristics data for MFD and MFL

$M(HCOO)_2\cdot 2H_2O$	Mn	Fe	Co	Ni	Cu
Magnetism	WF	WF	WF	WF	AF
T_N in K	3.7	3.8	5.1	15.5	
Intralayer J_{M-M} in K	−0.35		−4.3	−8.6	−33
References			47–63		
$M(HCOO)_2\cdot 2L$	Mn	Fe	Co	Ni	
Magnetism	WF	WF	WF	WF	
T_N in K	3.8	7.9	6.34	15.0	
J_{M-M} in K	−0.34		−3.3		
References			64–72		

of the two steps of LRO, first occurring in the (4,4) layer, with the interlayer *trans*-$M(H_2O)_4(HCOO)_2$ units keeping PM state, then the 3D LRO. Very extensive and detailed magnetic investigations were continuously conducted, especially on the Mn member. In fact, this was beyond most of current research works on individual magnetic MOF. Other series in the formula of $M(HCOO)_2L_2$ (MFL),[64–72] where L is a coligand such as urea and formamide, also consists of similar (4,4) layers of $M(HCOO)_2$ linked by interlayer HBs, showing WF with quite similar T_N's to the MFD series (Table 1). Another very interesting example is copper formate tetrahydrate $[Cu(HCOO)_2]\cdot 4H_2O$ (CFT).[73–79] It has a layered structure, with the 2D water sheets interleaved by (4,4) sheets of $Cu(HCOO)_2$. The half number of water molecules coordinates to axial positions of Cu, and the other half hold by HBs. It is a nearly 2D $S = 1/2$ Heisenberg AF with $T_N = 17$ K, and an AFE with $T_C = 234$ K caused by the disorder–order transition of the HB system involving water molecules. CFT was thus subjected to very extensive studies. 3d metal formates without coligands were limited. Beside some Ca/Sr-Cu formate salts,[80–82] the interesting $Cu(HCOO)_2$, reported in 1993 or earlier,[83–85] has two FO polymorphs, α- and β-phases. Both compounds are 3D frameworks. The β-phase possesses a dense structure, consisting of (4,4) sheets of $Cu(HCOO)_2$ twinned together. Each anti–anti formate in one sheet, in fact, connects to one Cu atom of neighbor sheet via one oxygen, the ligand is thus anti–anti/syn, and the inter-sheet linkages are $Cu_2(\mu\text{-}O)_2$ dimers. The metastable β-phase could change to the α-phase, through the breakage of the anti Cu–O bonds of anti/syn-O end occurred for half number of formate and the formation of the syn Cu–O bonds of the anti-O end for another half number of formate, resulting in the structure of α-phase, in which the original (4,4) sheet is partially broken, and half numbers of anti–anti/syn formato bridges become anti–syn and another half anti-chelating-anti. The T_C's are 8.2 and 30.4 K for the α- and β-phases, respectively, in consistence with the structures, denser, stronger, and more Cu···Cu interactions for the β-phase. The T_C of 30.4 K for the β-$Cu(HCOO)_2$ is still very high for MFFs even now. MFFs incorporating ammonium cations were few then, with the published perovskites of $[CH_3NH_3][Cu(HCOO)_3]$,[86] $[(CH_3)_2NH_2][Cu(HCOO)_3]$,[87] and $[NH_2CHNH_2][Zn(HCOO)_3]$.[88] The ternary compound of $Cs[Co(HCOO)_3]$ was reported,[89] and it is also a perovskite. These were solely structural publications. In addition to those known divalent 3d MFFs, a perovskite framework of $Mn(HCOO)_3$ in which Mn is trivalent was reported in 1999.[90] The framework included carbon dioxide and/or formic acid guests in the cavities. It is an AF with T_N of 27 K. Ln MFFs,[91–96] with or without small coligands, are $Ln(HCOO)_3$, $Ln(HCOO)_3\cdot 2H_2O$, and $Ln(HCOO)_3\cdot 2HCONH_2$. $Ln(HCOO)_3$ possesses a 3D network that the chains composed by base-sharing Ln tricapped trigonal prisms are connected via capped formate ligands in anti-chelating mode. The frameworks of $Ln(HCOO)_3\cdot 2H_2O$ possess the chiral $(4^9\cdot 6^6)$ topology, and both syn–anti and anti–anti formate ligands are involved. $Ln(HCOO)_3\cdot 2HCONH_2$ has a perovskite-like framework, with all formate groups are anti–anti. However, most researches on these Ln MFFs focused on the crystal structures and spectra, and the magnetic behaviors were investigated very little.

This briefly historical comment and the several selected earlier MFF series cited here could lead to the following observations. First, the small formate ligand is really very beneficial for the formation of MOFs, even very dense ones such as β-$Cu(HCOO)_2$ and $Ln(HCOO)_3$. However, this point might be ignored by researchers for quite long time. A plausible reason, we suggest, might be the fact that a lot of polynuclear oxo-clusters involving carboxylate as well as formate ligands, such as the most popular dimers of $[M_2(\mu\text{-}RCOO)_4]$ and oxo-centered tri-nuclear complexes of $[M_3O(RCOO)_6L_3]$, received much attention then.[97] However, some interesting networks were also reported based on these units, such as the linkages of $[Mn_3O(HCOO)_6(HCOO)_3]$ units in $(K_2\{Mn(H_2O)_2[Mn_3O(HCOO)_9]_2\})_n$[98] via mono-nuclear Mn^{2+}. Second, formate could adapt very different coordination modes (Figure 1), such as syn–syn, anti–anti, syn–anti, syn–anti/syn, anti–anti/syn, anti/syn–anti/syn, and anti-chelating-anti, and these are all good bridging ones for constructing MOFs, with the anti–anti mode as the majority, and the (4,4) layer as the most common structural type or part for TM MFFs. Third, formate is a short bridge so it can mediate magnetic coupling effectively. This makes formate useful for magnetic MOFs. Fourth, coligands (we have just here cited literatures with some small coligands) or cationic components could be used to control and modulate the structures thus magnetic properties. Finally, formate is a good HB acceptor, thus helpful for the design and formation of HB systems. This is a very key point[20,21] for electric properties of MFFs, as that in CFT.[73–79] However, this importance has been only recognized again very recently, especially, when HB donors such as ammoniums, which were rarely used before for MFFs, are incorporated.

It should be mentioned that there are still continued, deeper, and detailed studies on these earlier MFF systems, such as MFD and MFL series, up to now,[99–104] even the structures redetermined in higher accuracy.[97] We have encountered that, in our experimental experience,[32] for many synthetic systems, the existence of small amount of water, even water absorbed from humid air during crystallization, led to easy contamination of MFD, in the final products, or even the MFD salts were the main products. Therefore, it is not surprised that the structures of MFD

have been reported again and again. However, we will not revisit these earlier MFFs below, if not necessary.

3 THE DENSE BINARY MFFs AND TERNARY ONES INCORPORATING ALKALI METAL IONS

The binary dense MFFs of $M(HCOO)_2$ (β- or γ-phases here, according to A. K. Powell; for the porous α-$M(HCOO)_2$, see Section 5) were mainly investigated by A. K. Powell *et al.* after 2000.[105–107] These materials had been reported earlier but structures unknown. Usually, two or more phases exist, and the structures complicated for these compounds with simple formula. β-$Mn(HCOO)_2$ was published in 2003.[106] Topologically β-$Mn(HCOO)_2$ has the same dense structure as that of β-$Cu(HCOO)_2$ described in Section 2, and it is an AF with $T_N = 8$ K. α-$Cd(HCOO)_2$ and β-$Cd(HCOO)_2$ have similar structures.[105] The 3D frameworks of β- and γ-$Fe(HCOO)_2$, β-$Zn(HCOO)_2$, and β-$Mg(HCOO)_2$ are all composed of chains,[105,107] in which the metal sites are linked by syn–anti/syn formates, further connected by anti–anti/syn interchain formate linkages, though the structural details are different. The dense structures for binary Co and Ni members are probably still unknown, or out of our awareness. Some binary Ln MFFs were reinvestigated.[102,103,108,109] The dense $Gd(HCOO)_3$ has just been found to possess strong magnetocaloric effect,[108] and $Sm(HCOO)_3$ was reported to show ferroelectricity because the structure is polar in SG *R*3*m*.[109]

Besides some earlier works,[89] only in recent years a few ternary MFFs incorporating alkali metal ions have been reported and their magnetism investigated. A chiral MFF of $[Na_3Mn_3(HCOO)_9]$ was reported by V. Paredes-García *et al.* in 2009.[110] The structure is a 3D network, in which the octahedral Mn centers are linked by syn–anti formates. The Mn-formate network has a quite complicated topology of $(3^3{\cdot}5^9{\cdot}6^3)$, and the network was also considered to be consisting of triangular Mn_3 building blocks, with the sodium locating above each Mn_3 triangle and linking to neighbor Mn sites by formates, which is now anti-chelating-anti if considering its coordination to Na^+. The material was suggested to show WF behavior around 30 K, and possible high degree of frustration in the lattice composed of Mn_3 triangles. In 2011, we reported two polymorphs of $K[Co(HCOO)_3]$, hexagonal phase and monoclinic one, and the irreversible transformation from the kinetic former to the thermodynamic stable later, in both solid and solution status.[111] The hexagonal phase has a chiral $(4^9{\cdot}6^6)$ Co–formate framework with hexagonal channels locating K^+ ions, and it could transform to the perovskite monoclinic phase, accompanied by changes from anti–anti to syn–anti of some formate bridges, and the alternations in magnetism from a spin-canted AF with $T_N = 8.3$ K to an AF with $T_N = 2.0$ K. Very recently, three MFFs of different Co/Na ratios were obtained using different ratios of the starting materials and solvents.[112] $[Na_2Co(HCOO)_4]$ possesses a 3D framework formed by (4,4) cobalt–formate layers connected by the interlayer zigzag tapes of edge-sharing $Na_2(\mu\text{-}O)_2$ dimers. The interaction between Co ions bridged by syn–anti formate is FO, and as the (4,4) Co-formate layers are well separated, no LRO occurred above 2 K. $[NaCo(HCOO)_3]$ is isostructural with the Mn analogous $[Na_3Mn_3(HCOO)_9]$ (this should be reduced to $[NaMn(HCOO)_3]$) but the Co/Na cations are statistically distributed in lattice. It displays AF interactions, and above 2 K, no magnetic LRO occurred, and no frustration observed. The structure of $[Na_2Co_7(HCOO)_{16}]$ is quite interesting and contains various Co···Co connections by formates in different coordination modes and was described as 10-membered cobalt rings connecting to 1D chains further expanding to 2D layers, all with Co···Co connections, and finally to 3D network by connections via interlayer Na^+ ions. The material showed AF LRO at 2.5 K.

It is noted that these simple binary metal formates, looked by their formula, and the further introduction of simple alkali ions can in fact provide dense magnetic MFFs with complicated structures and various magnetic behaviors. These systems are far from well explored and actually merit further investigation.

4 METAL FORMATE FRAMEWORKS INCORPORATING AMMONIUM CATIONS

Protonated amine cations or ammoniums (AH_n^{n+}) are perhaps the most popular and widely employed cationic templates or components for many chemical systems,[113–117] including many magnetic MOFs such as metal oxalates,[26,29,118] azides,[119–123] cyanides,[30,42,43] and dicyanamides.[124] The ammonium cations can transfer their structural information (size, shape, charge, etc.) into the formed architecture, thus control or template the structures of outcomes, and form HB interactions or systems.[32,114] However, before our works, the ammoniums have rarely been used in preparing MFFs, as aforementioned. In the past decade, we and other groups have systematically explored MFFs with ammonium cations, AMFFs, including mono-, di-, tri-, and poly-ammoniums.[32] While various framework structures (Figure 2) corresponding to different ammoniums employed have been obtained, they displayed interesting magnetic, dielectric/ferroelectric, mechanic properties, and possible multiferroics. These render them a very promising class of MOF-/molecule-based materials and the researches on these materials are currently active.

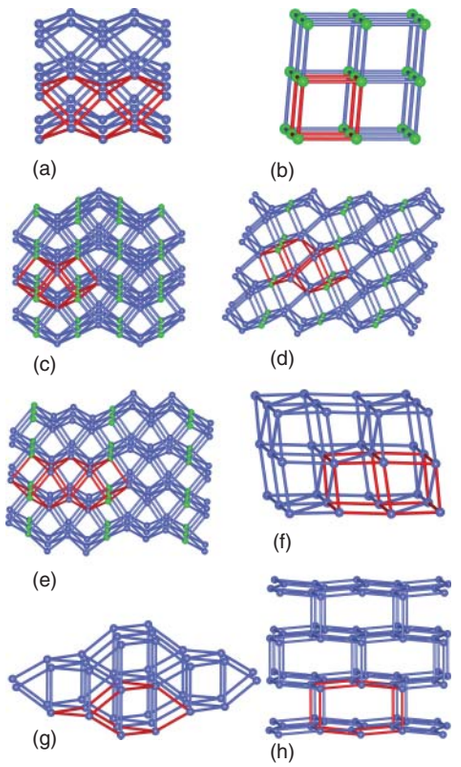


Figure 2 Topological plots of known AMFFs: (a) $(4^9{\cdot}6^6)$ framework of $[NH_4][M(HCOO)_3]$, and (b) $(4^{12}{\cdot}6^3)$ one of $[(CH_3)_2NH_2][M(HCOO)_3]$, (c) $(4^{12}{\cdot}6^3)(4^9{\cdot}6^6)$ one of $[dmenH_2][M(HCOO)_3]_2$ ($dmenH_2 = CH_3NH_2(CH_2)_2NH_2CH_3$), (d) $(4^{12}{\cdot}6^3)(4^9{\cdot}6^6)_2$ one of $[dptaH_3][M(HCOO)_3]_3$ ($dptaH_3 = NH_3(CH_2)_3NH_2(CH_2)_3NH_3$), (e) $(4^{12}{\cdot}6^3)(4^9{\cdot}6^6)_3$ one of $[tptaH_4][M(HCOO)_3]_4$, ($tptaH_4 = NH_3(CH_2)_3NH_2(CH_2)_3NH_2(CH_2)_3NH_3$), (f) perovskite-like one of some Ln AMFFs, and (g) diamond-like one of some Ln AMFFs, (h) pillared layered one in $[tmenH_2][Er(HCOO)_4]$ ($tmenH_2 = (CH_3)_2NH(CH_2)_2NH(CH_3)_2$), respectively. Spheres are metal ions, and sticks the formato bridges. Channels or cavities within the frameworks are highlighted. (Reproduced (a, b, c, and e) with permission from Ref. 32. © Wiley-VCH Verlag GmbH & Co. KGaA.)

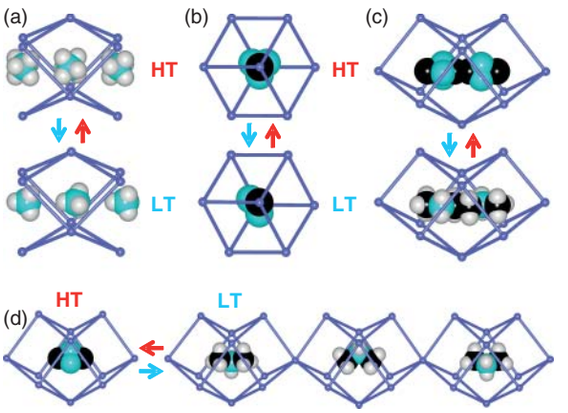


Figure 3 The order–disorder transitions in several AMFFs: (a) $[NH_4][Mn(HCOO)_3]$, (b) $[(CD_3)_2ND_2][Co(DCOO)_3]$, (c) $[dmenH_2][Zn(HCOO)_3]_2$, and (d) $[(CH_3)_2NH_2][Fe^{III}Fe^{II}(HCOO)_6]$, respectively. Channels or cavities are in topological view, as those in Figure 2. Cations are in space filling style. H-atoms of disordered cations are removed, except those in (a)

4.1 Structures

4.1.1 $[NH_4][M^{II}(HCOO)_3]$ and $[HONH_3][M^{II}(HCOO)_3]$ Series: Chiral Frameworks with $(4^9{\cdot}6^6)$ Topology

The employment of small ammonium cation NH_4^+ and $HONH_3^+$ resulted in MFFs[125–132] of the chiral $(4^9{\cdot}6^6)$ framework with the same topology as the aforementioned $K[Co(HCOO)_3]$[111] and $Ln(HCOO)_2{\cdot}2H_2O$.[92] In fact, both ammoniums have quite similar size to K^+ or water molecules. The octahedral metal ions within the framework are all 6-connected $(4^9{\cdot}6^6)$ nodes (Figure 2a), linked together by single anti–anti formato bridge. The framework can be described as parallel wavy (4, 4) sheets linked along the direction perpendicular to the sheets by the inter-sheet zigzag linkages, or one metal ion in one sheet links two metal ions of one neighbor sheet (above or below) in a *cis* mode. In other word, the framework is the three equivalent sets of the (4, 4) sheets, with their dihedral angles equal or close to 60°, merged together. These lead to hexagonal framework channels locating the ammonium cations. The chiral framework channel has wall made of rolled grids or bidirectional, triple-helix of $\cdots$M–OCHO–M–OCHO$\cdots$, showing a diameter of *ca.* 3 Å. The $[NH_4][M^{II}(HCOO)_3]$ compounds[125–131] belong to the polar SG $P\,6_322$ at RT and the NH_4^+ cations show quickly vibrational motion within the channels. The materials of this series undergo structural transitions on cooling, triggered by the disorder–order transition of NH_4^+ cations (Figure 3a), leading to an ordered structures in LT, in which the lattice becomes tripling, the SG changes to $P\,6_3$, and the unique channel in RT structure splits into three in LT, locating orderly arranged NH_4^+ cations showing different shifts with respect to the anionic framework, resulting in the spontaneous polarization.[126,127] The structural transition is thus PE to FE. Instead, in $[HONH_3][M^{II}(HCOO)_3]$,[132] the somewhat larger $HONH_3^+$ and the strong HB interactions between the cation and framework prohibit the phase transition, and all $HONH_3^+$ cations located orderly in lattice, though the framework is almost the same as that of $[NH_4][M^{II}(HCOO)_3]$.

4.1.2 *Perovskites of $[AH][M^{II}(HCOO)_3]$ Incorporating Mono-ammoniums, AH^+, with $(4^{12}\cdot6^3)$ Topology*

These are now the major AMFFs possessing several series[86–88,133–151] and we now can count 30∼40 published compounds, for the mono-ammoniums, AH^+, of 2–5 non-H atoms, $CH_3NH_3^+$,[86,133,134] $(CH_3)_2NH_2^+$,[87,133,135–144] $CH_3CH_2NH_3^+$,[133] $(CH_2)_3NH_2^+$ (azetidinium),[133,145,146] $C(NH_2)_3^+$ (guanidinium, Gua^+),[147,148] $NH_2CHNH_2^+$,[88,148] $C_3H_5N_2^+$ (imidazolium, ImH^+),[149] and divalent metal ions, Mn, Fe, Co, Ni, Cu, Zn, and Mg, and mixed metals such as Mn/Zn[150] and Al^{3+}/Na^+.[151] While the structural details and the lattice symmetries are different for different AH^+, the simple cubic (NaCl or α-Po type) framework of $[M^{II}(HCOO)_3^-]$ is the common feature (Figure 2b), and all formates are anti–anti. Within the framework cubic cavities locate the AH^+ cations, as the A-component of perovskite ABX_3 where B = M and X = $HCOO^-$. Both convenient N–H···O and weak C–H···O HBs are observed between the cation and the anionic framework. These AMFFs are MOF analogous to the inorganic perovskites such as FE $BaTiO_3$[152,153] and multiferroics $BiFeO_3$.[154,155] The $(4^{12}\cdot6^3)$ framework shows apparent breathing behavior[133] for accommodating AH^+ of different size by the change of the M–O–C angles, increasing with the increase of AH^+ size, and the cavity volume, and the total framework are usually less dense than the previous $(4^9\cdot6^6)$ one.[125–132] It has been observed that $(CH_3)_2NH_2^+$,[133,135–140] $(CH_2)_3NH_2^+$,[133,145,146] and ImH^+[149] in the structures are disordered at HT but on cooling the disorder–order transition occurred, with lattice symmetry lowering and ordered arrangement of the cations. For $[(CH_3)_2NH_2][M^{II}(HCOO)_3]$ series except the Cu member,[135–140] which is the most actively investigated now, the RT structures are in trigonal SG $R\bar{3}c$, in which the trigonally disordered cation is manifested by two methyl groups lying on the 3-axis connected by three equivalent positions of the central NH_2. In LT, the symmetry of the structures becomes monoclinic SG Cc, with two-fold disordered $(CH_3)_2NH_2^+$ (Figure 3b) probably because of crystal twinning in LT phases. For the series of $(CH_2)_3NH_2^+$,[133,145,146] the RT structures belong to orthorhombic $Pnma$, and the puckered ring cation $(CH_2)_3NH_2^+$ is apparently planar because of the fast dynamic flipping motion of the methylene opposite to N. In LT, this flipping motion was frozen, and the cations existed in resolved puckered rings, together with the lattice symmetry lowering to monoclinic $P2_1/n$ or $P2_1/c$, depending on metal ion. Very recently, it is reported that the ImH^+ cation in $[ImH][Mn^{II}(HCOO)_3]$[149] experienced order–disorder transition, from RT monoclinic phase in SG $P2_1/n$ to an HT tetragonal phase in SG $P\bar{4}2_1m$, resulted from the occurrence of rotation motion of ImH^+. The T_C of 435 K is high. Usually, the Mn, Fe, Co, Ni, Zn, and Mg members within the same series are isomorphs, but the Cu member may possesses different lattice symmetry and structure because of the Jahn–Teller effect of Cu^{2+} ion displaying 4+2 elongated octahedron, and the Cu–formate framework is composed of Cu–formate chains with short equatorial/basal Cu–O bond linked by the secondary long axial Cu–O bonds.[86,87,141,142,145,147] From the viewpoint of magnetism, the Cu members are low dimensional magnetism systems. Finally, a few neutral $M^{III}(HCOO)_3$ perovskites for Fe^{III}, Al^{III}, Ga^{III}, and In^{III}, with neutral guests of $HCOOH/CO_2/H_2O$ but not ammoniums, have been prepared and studied;[156] however, no magnetic properties reported for the magnetic members.

4.1.3 *Niccolite Frameworks and the Relevant Ones, Showing $(4^{12}\cdot6^3)(4^9\cdot6^6)_n$ $(n=1, 2, 3)$ Topologies*

We have extended our approach from mono- to poly-ammonium cations.[32,157–163] By employing linear di-, tri-, and tetra-ammonium cations in synthesis, novel bi-nodal AMFFs of $[AH_{n+1}][M(HCOO)_3]_{n+1}$ were formed with $(4^{12}\cdot6^3)(4^9\cdot6^6)_n$ topologies for $n=1$, 2, 3, respectively (Figure 2c–e). The $[dmenH_2][M(HCOO)_3]_2$ series,[162,163] where $dmenH_2^{2+}$ = di-protonated *N*,*N*′-dimethylethylenediamine, possesses a $(4^{12}\cdot6^3)(4^9\cdot6^6)$ $(n=1)$ framework topology, analogous to the minerals niccolite (NiAs) or colquiritte ($LiCaAlF_6$), representing the first MOF examples with such topology. The anionic framework contains two kinds of octahedral metal $(4^9\cdot6^6)$ and $(4^{12}\cdot6^3)$ nodes linked by anti–anti formate ligands and the $dmenH_2^{2+}$ cations located in the elongated, trigonally symmetric network cavities. Again, the framework could be considered to be (4,4) waved sheets merged together. The cation within the cavity is trigonally disordered with its two nitrogen atoms in six symmetry-related positions, forming HBs to the anionic framework. Disorder–order transition of the ammonium cation does occur for such systems. For $[dmenH_2][Zn(HCOO)_3]_2$, the trigonally disordered $dmenH_2^{2+}$ in HT $P\bar{3}1c$ phase became a completely extending, ordered cation in LT $C2/c$ phase (Figure 3c).[157,162] For tri- or tetra-ammoniums, metal–formate frameworks of $(4^{12}\cdot6^3)(4^9\cdot6^6)_n$ $(n=2, 3)$ topologies have been obtained.[157–160] These frameworks consist of $(4^{12}\cdot6^3)$ and $(4^9\cdot6^6)$ nodes in ratio of 1 to *n*, and the framework cavities are longer and longer to fit longer and longer ammonium cations. The niccolite AMFFs could also be constructed for mixed-valence/metal $Fe^{III}M^{II}$ but for mono-ammonium of $(CH_3)_2NH_2^+$ or maybe NH_4^+ with the formula of $[AH][Fe^{III}M^{II}(HCOO)_6]$ (M = Fe, Mn, Co), in which M^{2+} is the $(4^{12}\cdot6^3)$ node, whereas Fe^{3+} is the $(4^9\cdot6^6)$ node.[164–167] The $[(CH_3)_2NH_2][Fe^{III}Fe^{II}(HCOO)_6]$ has recently observed to experience an interesting phase transition around 155 K.[166] In the LT phase, the ammonium cation

displays three ordered orientations but in the RT ones, it is trigonally disordered (Figure 3d), with the LT lattice cell in SG $R\bar{3}c$, ninefold larger than the RT one in SG $P\bar{3}1c$.

4.1.4 *Lanthanide Formate Frameworks Incorporating Ammonium Cations*

The lanthanides have high coordination numbers and more variable coordination geometries, so it was expected that Ln AMFFs could show more various structure characters and topologies (Figure 2f–h), compared to the TM ones with fixed octahedral coordination geometry. Indeed, several chiral erbium–formate frameworks[168,169] of $[AH][Er(HCOO)_4]$ (Figure 4) for $AH^+ = NH_4^+$, $CH_3NH_3^+$, $NH_2CHNH_2^+$, Gua^+, ImH^+, $CH_3CH_2NH_3^+$, and $HOCH_3CH_2NH_3^+$ display at least two complicated framework topologies of $(3^6{\cdot}4^{15}{\cdot}5^7)$ and $(3^3{\cdot}4^6{\cdot}5^5{\cdot}6)$; however, the former is better understandable as perovskite-like (Figure 2f) and the later diamond-like (Figure 2g). It was very interesting to observe that, from this family, (i) as the ammonium cations become bulkier, the $[Er(HCOO)_4]$ frameworks are more expanded by shifting the coordinating modes of formates (some or all) from syn–anti (for short Er···Er distance) to anti–anti (for longer Er···Er distance) to chelating (for no limitation on Er···Er separation), thereby resulting in larger void space; (ii) the emergency of chirality in solids from such simple multiple acentric but achiral precursors, which was only occasionally encountered for AMFFs of TM or Mg.[125–132] For some AH^+ cations such as $NH_2CHNH_2^+$, other Ln members have been reported.[170,171] Diammoniums were also employed by us.[157,172] The two compounds, $[dmenH_2][Er(HCOO)_4]_2$ and $[tmenH_2][Er(HCOO)_4]_2$ ($tmenH_2$ = di-protonated *N*,*N*,*N*′,*N*′-tetramethylethylenediamine), represent two examples. The former has a perovskite-like (Figure 2f), whereas the later has pillared-layer one (Figure 2h). Both in fact have complicated framework topologies, $(3^6{\cdot}4^{15}{\cdot}5^7)$ for former including only anti–anti formates and $(3^3{\cdot}4^5{\cdot}5^4{\cdot}6^2)$ for later including chelating and anti–anti ones. A phase transition occurred for $[tmenH_2][Er(HCOO)_4]_2$ around 210 K,[172] in which the $tmenH_2^{2+}$ in the channels of the pillared-layer framework, showing rotational disorder of middle ethylene at RT, became two resolved ordered ones, together with the lattice doubling along *b* direction and symmetry alternations from SG *C* 2/*c* of RT phase to $P2_1/c$ of LT phase.

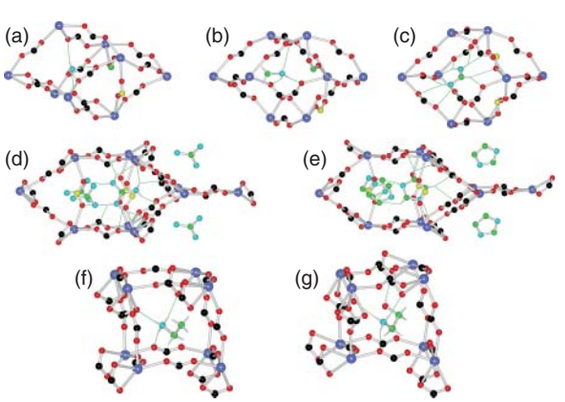


Figure 4 The view of cavities of the anionic Er–formate frameworks with the AH^+ template cations in chiral Ln AMFFs of $[AH][Er(HCOO)_4]$ for $AH^+ = NH_4^+$ (a), $CH_3NH_3^+$ (b), $NH_2CHNH_2^+$ (c), Gua^+ (d), ImH^+ (e), $CH_3CH_2NH_3^+$ (f), and $HOCH_3CH_2NH_3^+$ (g), respectively. Thin lines are O/N–H···O HBs, and H atoms of formate are omitted. (Reproduced from Ref. 168 with permission of The Royal Society of Chemistry. http://dx.doi.org/10.1039/C1CE05250K.)

The above survey of the published structures of AMFFs, if not all, has revealed the following points. (i) It is clear that the ammoniums can act as templates, and their shape, size, and HB geometries have important effects in directing the outcome framework structures. On the other hand, metal–formate frameworks show great conformity, malleability, and flexibility to match the ammonium cations incorporated. It is also interesting that many AMFFs in fact possess the structures similar to the typical minerals such as perovskite, niccolite, and diamond. (ii) For a specific ammonium, the AMFFs usually are isostructural or they are isomorphs for different metals. This provide not only the opportunity to study the AMFF properties based on the same structural type but also the possibility to obtain mixed metal systems though this kind of studies has just started. (iii) The ammoniums within the metal frameworks frequently display order–disorder transitions of various patterns and characters depending on the ammoniums, details of structures and HB systems within the materials. The structural phase transitions and critical phenomena trigged by these order–disorder transitions are of great importance and interest for the electric and mechanical properties of the materials[20,21,33–43] and even multi-functionalities when combining them with the intrinsic magnetic property of the frameworks with magnetic metal ions. To understand the details of such transitions, the extensively temperature-dependent structure studies are required.

4.2 Magnetism and Possible Multiferroics

The magnetic behaviors of many magnetic AMFFs have been investigated and analyzed quite carefully, and magneto-structural relationships established. Furthermore, some fascinating properties other than magnetic have been observed, for example, the structural phase transitions and the accompanied dielectric anomalies, AFE and FE, as well as mechanical properties. AMFFs therefore might be a new promising class of molecule-based multiferroics or multifunctional materials.

4.2.1 Magnetic Properties

Considering the very difference of TM and Ln AMFFs in magnetism, it is better to discuss their magnetic properties separately, first TM then Ln ones. 3D LRO of spin-canted AF or WF usually occurs in these TM AMFFs.[125–133,135–147,150,157–167] The T_N's are quite similar for the same kind of metal ion, that is, *ca.* 8, 10, 15, 30, and 5 K for divalent Mn, Fe, Co, Ni, and Cu members (Table 2, Figure 5a). This is because the metal–metal linkages are all single anti–anti formate bridges and the number of nearest neighbors around each magnetic site is always six, and the strengths of magnetic coupling via anti–anti formate bridge for the same metal ion are similar, regardless of the difference in framework structures. The typical values, in Kelvin, of these magnetic couplings, derived from the magnetic data of the perovskite $[Gua][M(HCOO)_3]$ series,[147] are −0.36 (Mn), −0.63 (Fe), −3.0 (Co), −7.3 (Ni), and −32.9 (Cu), respectively. These are all very close to that in MFD and MFL (Table 1) well investigated in earlier days, with the same anti–anti formate. However, the T_N's of these 3D AMFFs are nearly two times higher than the relevant ones of MFD or MFL. This is because of the dimensionality in both structures and magnetic interactions, 3D for AMFFs but 2D for MFD and related layered MFL compounds.[30–32] The high T_N's up to *ca.* 36 K for Ni AMFFs are quite impressive. The bending characteristics of anti–anti formate bridge leads to the tilting of the neighboring MO_6 octahedra. This structural feature, together with noncentrosymmetry between the magnetic M^{2+} ions bridged by $HCOO^-$, allow the occurrence of Dzyaloshinsky–Moriya interaction or antisymmetric exchange,[30,31,173–175] to give rise to spin-canted AF or WF. Besides the general characteristics of spin-canted AF,

Table 2 A collection of magnetic and electric characteristics data for some AMFFs

$[NH_4^+][M(HCOO)_3]$	Mn	Fe	Co	Ni	Cu
Magnetism	WF	WF	WF	WF	AF
T_N in K	8.4	9.4	9.8	29.5	2.9
J_{M-M} in K	−0.32	−0.62	−3.8	−7.6	
Electric property	FE	FE	FE	FE	AFE?
T_C in K	252	212	191	199	355
References			125–131		

The T_C for the PE–FE transitions of Zn and Mg members are 191 and 255 K, respectively.

$[AH][M(HCOO)_3]$	Mn	Fe	Co	Ni	Cu
Magnetism	WF	WF	WF	WF	W
[a] T_N in K	7.6		14.9	35.6	5.5
	8.8	10.0	14.2	34.2	4.5
[a] J_{M-M} in K	−0.34		−3.4	−7.3	−81[d]
	−0.36	−0.63	−3.0	−7.3	−32.9
Electric property	FE	FE	FE	FE	
[b, c] T_C in K	185	160	165	180	
			151		
References			133,135–144,147		

[a] $AH^+ = (CH_3)_2NH_2^+$ and Gua^+, and data in first line for $(CH_3)_2NH_2^+$, and in second line for Gua^+.
[b] For $(CH_3)_2NH_2^+$ only, and the second data of Co member is for the deuterated compound.
[c] The T_C for the PE–FE transitions of Zn and Mg members of $[(CH_3)_2NH_2][M(HCOO)_3]$ are 156 and 260 K, respectively.
[d] This is $2J$.

$[dmenH_2^+][M_2(HCOO)_6]$	Mn	Fe	Co	Ni	Cu
Magnetism	WF	WF	WF	WF	WF
T_N in K	8.6	19.8	16.8	33.6	6
J_{M-M} in K	−0.40	−1.0	−4.2	−10.1	−38.6
References			157,162,163		

The T_C for the phase transitions of Zn member is 299 K.

$[(CH_3)_2NH_2][Fe^{III}M^{II}(HCOO)_6]$	Mn	Fe	Co
Magnetism	WF	FI	WF
T_N in K	35	36.7	32
J_{M-M} in K	2.4		
References		164–166	

The T_C for the PE–AFE transition of $Fe^{III}Fe^{II}$ member is 155 K.

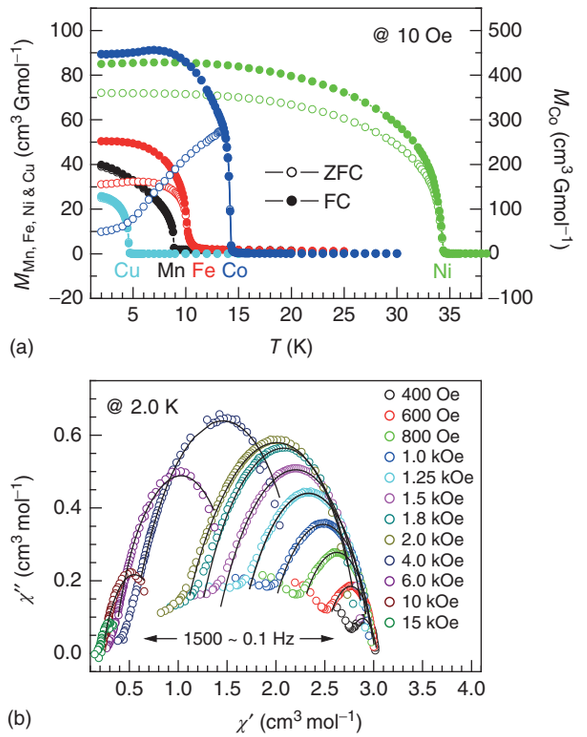


Figure 5 (a) Zero-field/field cooling magnetizations for the magnetic members (Mn, Fe, Co, Ni, and Cu) of [Gua][M(HCOO)$_3$] series. (Reproduced with permission from Refs. 32 and 147. Copyright, Wiley-VCH Verlag GmbH & Co. KGaA). (b) Cole–Cole plot of the ac susceptibility data of [tmenH$_2$][Er(HCOO)$_4$] under different bias dc fields at 2.0 K. (Reproduced from Ref. 172 with permission of The Royal Society of Chemistry. http://dx.doi.org/10.1039/C1DT10241A.)

abundant details in magnetism were observed. Hidden spin canting occurs in cases of [NH$_4$][Mn(HCOO)$_3$][125,127] and [(CH$_2$)$_3$NH$_2$][Mn(HCOO)$_3$][133] in which the lattices are tripled and doubled at LT because of the disorder–order transition of the ammoniums; quite large canting angles therefore quite large spontaneous magnetizations were observed for [Gua][Co(HCOO)$_3$],[147] [HONH$_3$][Co(HCOO)$_3$],[132] and [dmenH$_2$][Fe(HCOO)$_3$]$_2$,[157,162] which even has a high coercive field (H_C) of 11 kOe; some Co frameworks might show spin reorientation;[135] the Cu members[141,142,147,162] usually exhibited low dimensional character and slow magnetic relaxation, and so on. The mixed-valence/metal niccolites [(CH$_3$)$_2$NH$_2$][Fe^{III}M^{II}(HCOO)$_6$] series[164–166] displayed very interesting magnetic properties. [(CH$_3$)$_2$NH$_2$][Fe^{III}Fe^{II}(HCOO)$_6$] is a rare Néel N-type FI,[118] exhibiting negative magnetization with an asymmetric magnetization reversal in the hysteresis loop, because the two sublattices of different spin carriers, Fe^{III} and Fe^{II}, have different ordering rates with respect to temperature. [(CH$_3$)$_2$NH$_2$][Fe^{III}Mn^{II}(HCOO)$_6$] is an AF with small spin canting and [(CH$_3$)$_2$NH$_2$][Fe^{III}Co^{II}(HCOO)$_6$] an FI. Their T_N's are high, 37, 35, and 32 K for M = Fe^{II}, Mn^{II}, and Co^{II}, respectively, compared with most AMFFs containing divalent metal solely (Table 2). Finally, mixed metal systems probably provide another way to adjust the magnetism of AMFFs. For the series of perovskites of [CH$_3$NH$_3$][Mn$_{1-x}$Zn$_x$(HCOO)$_3$] solid solution,[150] the magnetism transfers from LRO of enhanced spin-canted AF for $x \geq 0.40$ to PM when $x \leq 0.30$, and the percolation limit was estimated experimentally, $x_P = 0.31(2)$ as expected by percolation theory for the simple cubic lattice.[176,177] Similar work has been performed for [NH$_4$][Mn$_{1-x}$Zn$_x$(HCOO)$_3$][130,131] and [NH$_4$][Mn$_{1-x}$Co$_x$(HCOO)$_3$].[128] Mixed metal systems for the earlier MFD or MFL have been also studied.[178–180]

It is well known that the 4f unpaired electrons in Ln^{3+} ions are well shielded, so the exchange interactions between Ln^{3+} ions are usually very weak. This is true for Ln AMFFs, which are usually PM down to 2 K, and in LT region, the temperature dependence of dc (direct current) susceptibilities is dominated by progressive depopulation of Stark levels.[157,168–172] However, the strong magnetic anisotropy of Ln^{3+} ions could lead to slow relaxation of the magnetization, and the so-called single molecule magnets (SMMs) or single ion magnets (SIMs), based on such slow relaxation behaviors, have received considerable attention and interest.[181–184] The zero-field relaxation of Ln AMFFs is usually faster than the employed frequencies. When a static bias field is applied, the fast relaxation mechanism is suppressed and slow relaxation could be observed, even for the most isotropic Gd^{3+} in [H$_2$NCHNH$_2$][Gd(HCOO)$_4$], in which the slowest magnetic relaxation in applied static fields might be originated from the phonon-bottleneck effect.[171] The two compounds, [dmenH$_2$][Er(HCOO)$_4$]$_2$ and [tmenH$_2$][Er(HCOO)$_4$]$_2$ (Figure 5b),[157,172] displayed field-dependent ac (alternate current) susceptibilities with complicated field-induced magnetic relaxation processes even magnetization history dependence, and the major slow ones are probably spin-lattice type, direct or Orbach processes of the two-level system for the Kramers ion Er^{3+}.

4.2.2 *Combination of Magnetism and Ferroelectricity and Possible Multiferroics*

In AMFFs, the ammonium cations, located in the framework cavities or channels, could be possibly disordered at HT and undergo disorder–order transitions on cooling, as described in Section 4.1. These could result in structural phase transitions with alteration in HB system and relevant dielectric anomalies even FE/AFE, similar to the molecule-based systems such as KDP[152,153] and those including ammonium components.[20,21,185–187]

Such AMFFs have been experimentally investigated are $[NH_4][M(HCOO)_3]$,[125–131] $[(CH_3)_2NH_2][M(HCOO)_3]$[135–144], $[(CH_2)_3NH_2][M(HCOO)_3]$[145,146], and $[(CH_3)_2NH_2][Fe^{III}Fe^{II}(HCOO)_6]$,[166] and theoretical studies were applied for $[Gua][Cu/Cr(HCOO)_3]$[188,189] in which the Cr compound is in fact a suppositional one.

The $[NH_4][M(HCOO)_3]$ series has been investigated mainly by us (Table 2).[125–131] Their T_N's of WF LRO are 8.0, 9.4, 9.8, 29.3, and 2.9 K for Mn, Fe, Co, Ni, and Cu members, respectively, and the T_C's of the PE–FE transitions are 252, 212, 191, 199, 191, 355 (possible PE–AFE), and 255 K for Mn, Fe, Co, Ni, Zn, Cu, and Mg, respectively. T_C is higher for TM of larger ionic radius, and this has been observed for the mixed metal systems of $[NH_4][Mn_{1-x}Zn_x(HCOO)_3]$ and $[NH_4][Mn_{1-x}Co_x(HCOO)_3]$ in which the averaged metal ionic radius could be adjusted. We have investigated the Mg and Cu members but the results have not been reported yet; however, their data could be tentatively given in Table 2 for comparison. The phase transitions are triggered by the disorder–order transitions of NH_4^+ cations and their displacement within the framework channels (Section 4.1). Dielectric hysteresis loops for Mn, Fe, Co, and Zn members are clearly observed for temperatures below T_C (Figure 6a). The concert shifts of NH_4^+ cations with respect to the anionic framework channels result in the spontaneous polarization thus FE in LT, and the spontaneous polarization could be estimated by the summation of dipoles resulted from such shifts of NH_4^+ within unit cell, with the values of 0.94–1.11 μCcm^{-2} for the $[NH_4][M(HCOO)_3]$ members at *ca.* 100 K, comparable to the experimental data. The systems are also highly anisotropic, with the *c* direction as the polarization axis. Mn and Fe members also display strong relaxor-like characteristics in their dielectric responses. Therefore, the magnetic members within the series show coexistence of magnetic and electric orderings in low temperature region. However, whether magnetoelectric (ME) effect exists in the magnetic members merits further investigation.

The $[(CH_3)_2NH_2][M(HCOO)_3]$ series was first prepared and magnetically characterized by us,[133,135] but their phase transitions and accompanied dielectric anomalies were investigated by A. K. Cheetham *et al.*,[136–144] and the series is now seemly a prototypical one for MOF- or molecule-based multiferroics. The T_N's of their WF LRO are 8.5, 20, 14.9, 35.6, and 5.2 K for the magnetic members Mn, Fe, Co, Ni, and Cu within the series, and the T_C's of the order–disorder transitions are 185, 160, 165, 180, 156, and 260 K for Mn, Fe, Co, Ni, Zn, and Mg (Table 2), respectively. However, whether the low temperature phases are FE or AFE had been controversial[136–139] until the dielectric hysteresis loop and SHG (second harmonic generation) effect for ferroelectrics were observed for the deuterated Co member, $[(CD_3)_2ND_2][Co(DCOO)_3]$ (Figure 6b),

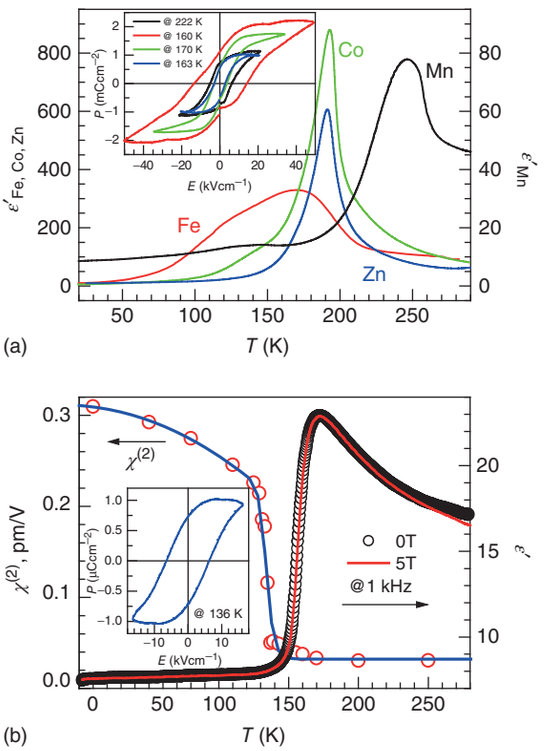


Figure 6 (a) Temperature-dependent traces of the real part of the dielectric permittivities, ε', for Mn, Fe, Co, and Zn members of $[NH_4][M(HCOO)_3]$, at 10 kHz, inset, electric hysteresis loops for the four materials at temperatures below their transition temperatures, all measurements for single crystals along *c* axis. (Reprinted with permission from Ref. 127. Copyright (2011) American Chemical Society). (b) Temperature-dependent traces of the real part of the dielectric permittivities, ε', and SHG effect for perovskite of $[(CD_3)_2ND_2][Co(DCOO)_3]$, inset, electric hysteresis loop at 136 K, all for single crystal along *a* axis. (Reproduced from data provided by the authors of Ref. 140, used with permission.)

below T_C of 151 K, reported by R.-G. Xiong *et al.*,[140] and the LT structure is polar, in monoclinic space group *Cc* (Section 4.1), and no ME effect was detected even under 5 T field. Possible ME effect has been recently reported for $[(CH_3)_2NH_2][Mn(HCOO)_3]$,[143] however, under very high magnetic fields and PM states.

The compounds of azetidinium series, $[(CH_2)_3NH_2][M(HCOO)_3]$, investigated by H. Kobayashi *et al.*,[145,146] were commonly found to exhibit very broad and extraordinarily large dielectric anomaly with ε' above 10^4, similar to the relaxor oxides. Structural phase transitions occurred near RT, from nonpolar structures to nonpolar ones, and coupled with the freezing of the ring-puckering molecular motion of azetidinium, within these materials. These might be related to the extremely large dielectric anomaly near RT. However, further investigation is required to clarify the microscopic mechanism of

the emergence of such giant dielectric anomaly in these systems.

The mixed-valence niccolites $[(CH_3)_2NH_2][Fe^{III}Fe^{II}(HCOO)_6]$ have been subjected to the variable temperature neutron diffraction studies, and both nuclear and magnetic structures determined.[166] The unprecedented disorder–order phase transition occurred at *ca.* 155 K, from HT to LT, involving a change in SG from $P\bar{3}1c$ to $R\bar{3}c$ and a tripling of the *c*-axis, with the ordering of the $(CH_3)_2NH_2^+$ cation, in three different orientations (Figure 3d). The occurrence of this phase transition is associated with an electric transition, from PE to AFE, showing somewhat ME effect owing to the magnetostriction effect when magnetic ordering occurred. The magnetic structure of this Néel N-Type FI unequivocally proved that the FI behavior is due to a noncompensation of the different Fe^{II} and Fe^{III} magnetic moments.

Besides these works, the mechanical studies of these AMFFs have emerged.[190–193] For example, resonant ultrasound spectroscopy has been used to study perovskites of $[(CH_3)_2NH_2][M(HCOO)_3]$ for M = Mn and Co.[190] Elastic and inelastic anomalies are evident at both the magnetic and electric ordering temperatures. Broadening of peaks above the ferroelectric transition implies the diminishing presence of a dynamic process caused by the ordering of $(CH_3)_2NH_2^+$ cation, and small elastic stiffening at low temperatures suggests weak magnetoelastic coupling in these materials. The dynamic process of $(CH_3)_2NH_2^+$ cation in $[(CH_3)_2NH_2][Zn(HCOO)_3]$ has also been investigated by NMR[191,192] techniques, suggesting the glassy behavior of the order–disorder transition. Young's modules of $[(CH_3)_2NH_2][M(HCOO)_3]$ shows an increase as a function of the crystal field stabilization energy (Ni > Co > Mn = Zn).[193] For $[NH_4][M(HCOO)_3]$ series, negative thermal expansion[126–131] and negative linear compressibility[194] have been all documented. We would like to emphasize, by our experimental experience, that the AMFFs crystals usually show quite good machining properties because of their 3D scaffold structures, and this is great beneficial for their practical use in making devices.

Strictly speaking, multiferroic materials should have ME effects that the two or more ferro properties can couple with each other. The magnetic AMFF compounds are good candidates for multiferroics. Computational studies[188,189] on $[Gua][Cu/Cr(HCOO)_3]$ proved this point because the ferromagnetic component is believed to be coupled to the spontaneous polarization and they are mutually reversible; however, this is waiting for experimental confirmation. Finally, Ln AMFFs might be expected to be good candidates for such materials.

5 THE POROUS DIAMONDOID MFFs OF $[M_3(HCOO)_6]$

The porous diamondoid $[M_3(HCOO)_6]$ family for M = divalent Mn, Fe, Co, Ni, Zn, and Mg, or α-$M(HCOO)_2$ phases according to A. K. Powell[105,195] is a very interesting and unique family of MFFs, having been received much attention. The syntheses of these compounds, firstly by us under ambient conditions,[32] need the participation of bulky ammoniums, such as triethylammonium; however, these bulky ammoniums act as negative templates to inhibit the formation of AMFFs discussed in Section 4, which acquired mono-ammoniums of smaller sizes or linear polyammoniums with suitable spacers of $(CH_2)_n$ with $n \leq 4$ between the ammonium group of NH_2 and/or NH_3. This negative template effect allowed us to prepare these compounds by simple solution chemistry methods under ambient temperature in the same or earlier time,[196–202] contrasted with the solvo-thermal routes by other groups.[203–207] The products are porous and quite thermally stable, thus show interesting gas/guest inclusion behavior and other properties that depend on or can be modulated by the guest molecules.

5.1 Structures, Porosity and Gas/Guest Inclusion Behaviors, and Thermal Stability

The compounds of the $[M_3(HCOO)_6]$ family are iso-structural (Figure 7a, b), belonging to the monoclinic SG $P2_1/c$ (some other authors[195,203–207] favored the other but nonstandard setting $P2_1/n$). The neutral porous framework is a diamondoid network[32,196–202] made of apex-sharing M-centered MM_4 tetrahedron nodes, in which all metal atoms are octahedral. The MM_4 node consists of one central M^{2+} ion, four apical M^{2+} ions, and six edges of $HCOO^-$ groups linking the metal ions in syn–anti/syn mode. The four central-apical M···M linkages, two have 2 μ-O + 1 syn–syn formate bridges and the other two have 1 μ-O + 2 syn–syn formate bridges, and the six apical-apical M···M linkages are single syn–anti formate one. These complicated metal–metal linkages may provide multiple super-exchange pathways and possible competition between them within the framework. The M–O bond distances agree well with the ionic radii of M^{2+} ions, and resulting in the framework size sequence from largest Mn member to smallest Ni one, with a change of *ca.* 20% in lattice volume.[32,200]

The openness and porosity of the framework lie in the channels in a honeycomb arrangement, with opening windows of *ca.* 4 × 5 Å and void space of *ca.* 30% of the crystal volume. The large nodes or thick walls forbid the interpenetration thus result in the permanent porosity of the frameworks, which has been proved by gas (N_2/H_2) adsorption experimental,[200–203] and the family shows a middle capacity of *ca.* 1% wt of H_2 storage. They also show

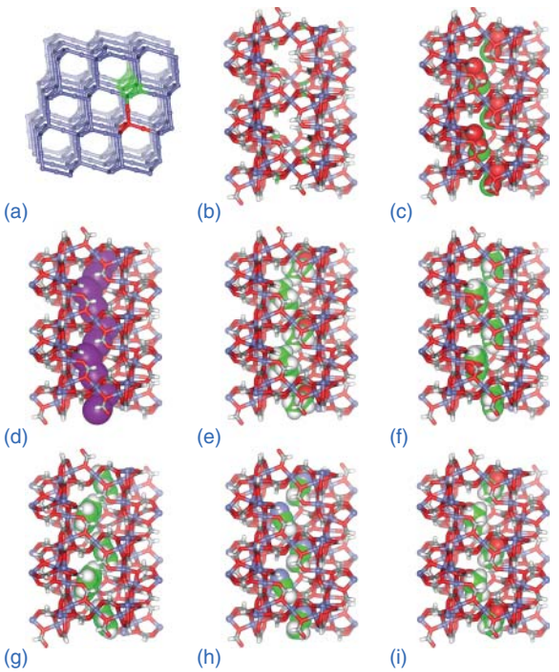


Figure 7 The structures of $[Fe_3(HCOO)_6](G)$: (a) the porous diamondoid framework of $[Fe_3(HCOO)_6]$ formed by the Fe-centered $FeFe_4$ tetrahedra as nodes (one highlighted) sharing apices and showing open channels, (b) the side views of one channel of apohost framework, (c–i) one channel (side view) with guest molecular arrays; H_2O/CH_3OH (c), iodine (d), THF (e), furan (f), benzene (g), acetonitrile (h), and acetone (i). Frameworks are in ball-stick model and the same framework orientation and guests highlighted in space filling model. Depth cueing is used to distinguish front and back. (Reproduced from Ref. 200. © Wiley-VCH Verlag GmbH & Co. KGaA.)

absorption for other gases of CO_2, C_2H_4, and so on.[204,205] The channel of the host framework has several important characteristics related to its inclusion properties.[32,200] First, the channel is zigzag like because of the different orientations of the formate groups and shows amphiphilic character because its inner wall is lined by alternate arrays of C–H groups and oxygen atoms. Therefore, the channel can include both hydrophilic and hydrophobic guests. Second, the M–O–M angles and the M···M distances can change to some extents, to conform the sizes of included guests, making the framework robust and flexible. Therefore, the porous frameworks can breathe to accommodate guests of different size but keep crystalline state. Finally, the achiral framework contains two kinds of channels; one is left-handed helical (*M*) and the other right-handed helical (*P*) because the twofold screw axis lies in the channels. The chiral channels may be expected to show some selectivity for chiral guests.

On the basis of such structural characters, the wide spectrum of guest inclusion and interesting inclusion behaviors were observed,[195–202,206–210] when exposing the apohost crystals of $[M_3(HCOO)_6]$ with empty channels to the vapor of different guests (Figure 7c–i). For instance, $[Mn_3(HCOO)_6]$ was observed to absorb over 40 kinds of guests,[196–199,208–210] which can be liquid or volatile solid, polar or nonpolar, enantiomer-pure or racemic mixtures, in fact, almost all of common solvents of suitable sizes in chemical laboratory could be included. The guest molecules form a zigzag array in the confined space of the channel and interplay with the host framework. On the one hand, the guest inclusion changes the size of the host frameworks. Small guests such as acetonitrile, acetone, iodine, furan, and imidazole made the host framework shrink, whereas large ones such as tetrahydrofuran (THF), benzene, and nitrobenzene expand it. The volume of the lattice can be modulated by guests as much as 11%, and the sample crystallinity still retains. On the other hand, the relevant size of the channel affects the arrangement of the guest molecules. Small guest molecules are allowed to rotate freely to find the energetic minimum positions and orientations because the channel is wide enough. Hence, among these guests, the polar one can form polar molecular array in one channel. For larger or longer guests such as nitrobenzene or chlorobenzene,[208] they are limited in two orientations. In addition, the kind of metal ions also has a subtle effect on the guest inclusion behavior probably via influencing the size of the void space. For example, the iodine inclusion compounds of $[Mn_3(HCOO)_6]$,[196] $[Fe_3(HCOO)_6]$,[200] and $[Zn_3(HCOO)_6]$[202] show different host–guest and guest–guest interactions even different iodine taking-up values. This host–guest interaction is mainly provided by the HB's between HB donors/acceptors of the guest molecule and acceptor/donors of framework. Guests in the channel also can have interactions between themselves. For example, it is interesting to observe that imidazole molecules form $(imidazole)_n$ chain via N–H···N hydrogen bonds between them[208] and this could be considered to be proton wire in the channel. Finally, it is true that chirality can be induced by inclusion of chiral guest molecules (R-/S-$CH_3C^*HClCH_2OH$) into the channel of an achiral framework $[Mn_3(HCOO)_6]$.[197] In this case, the R-/S-guest is ordered in the M-/P-channel and while disordered on two crystallographic orientations in the opposite-handed channels.

The porous frameworks are also thermally stable,[196–202,207,208] proved by both thermal analyses and variable temperature powder X-ray diffraction studies. The Mn and Zn frameworks keep the porous phase up to 220 and 150 °C, respectively, and then a phase transition, the collapse of the porous frameworks occurred. Other members, Fe, Co, and Ni, are thermally stable up to 270 °C, without any phase transition before the framework decomposition. The Mg member is reported very stable, up to 400 °C.[207] These frameworks are highly stable and do not

collapse upon the removal of the guest solvents in the as-prepared materials. The frameworks keep unchanged from RT down to 2 K, as revealed by the neutron diffraction for the Co member.[201]

5.2 Magnetism and Multi-functionalities

Because magnetic LRO and porosity are mutually exclusive in general, it remains a challenge to synthesize porous magnets. The examples, especially those with permanent porosity, are still few.[25] The magnetic members of $[M_3(HCOO)_6]$ family are porous magnets and the guest inclusion give further functionalities (chiral, electric, optical properties, etc.), providing a new approach to achieve multifunctional materials.

5.2.1 *Magnetism of Apohost $[M_3(HCOO)_6]$*

The magnetic members of apohost $[M_3(HCOO)_6]$ display different magnetic behaviors depending on the kind of metal ion or spin (Figure 8a).[195–201,208] The Mn, Fe, and Ni members are FI with T_C of 8.0, 16.1, and 2.7 K, respectively. The Co one is probably AF with spin canting probably associated with enhancement of the short-range correlation below 2 K, which needs to be proved by the further investigation. However, the T_C's of Co and Ni members of this family are much lower than the relevant AMFFs (Table 2). Mn and Ni members are soft magnets ($H_C \approx 0$ for Mn and 80 Oe for Ni), whereas the Fe compound is quite hard one with an H_C of 700 Oe. For Mn and Fe members, the detailed investigation on the magnetism in low field and low temperature region revealed that the two materials might display second magnetic transition below their T_C, indicating possible spin reorientation.[196–200] Because the framework is closely related to the pyrochlore structure except for the presence of the central metal site of the apex-shared tetrahedral nodes, and the framework possesses several exchange pathways between the metal sites with similar coupling strengths, the frameworks of $[Mn_3(HCOO)_6]$ and $[Fe_3(HCOO)_6]$ should be magnetic competition systems. On the basis of these observations, we think that the magnetic structures might not be simply collinear and non-collinear spin arrangement is possible, resulting in the possible spin reorientation or multiple magnetic transitions. The isomorphic character of the family indicates the possibility to obtain the mixed-metal porous frameworks with different ratios and kinds of metals. It can provide new porous materials with controllable pore size, various magnetic behavior, and further new guest-modulated magnetic properties. Indeed, this kind of modulation by mixing two metal ions has been realized in $[Fe_xZn_{3-x}(HCOO)_6]$.[208] When the $[Fe_3(HCOO)_6]$ framework is diluted by diamagnetic zinc ion, the lattice shrinks, and the series undergoes a systematic change from 3D magnetic LRO to spin glass then superPM (or possible SMM) and final PM, opening up a new way to design porous SMM or spin glass.

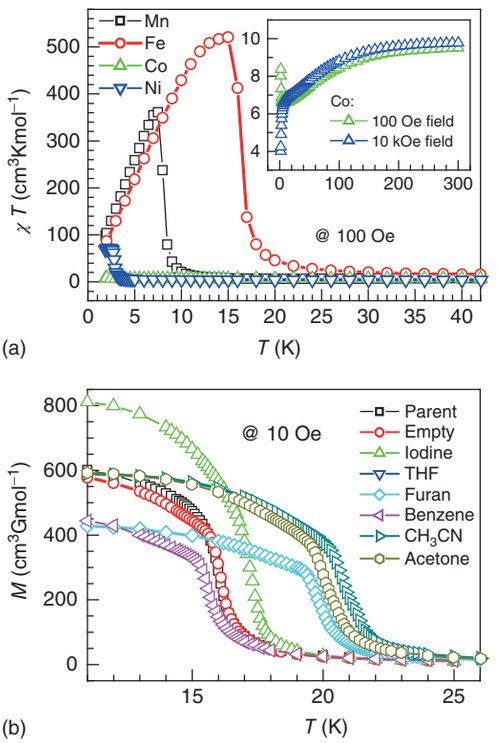


Figure 8 (a) The χT versus T traces for M = Mn, Fe, Co, and Ni members of $[M_3(HCOO)_6]$ between 2 and 40 K, inset, the traces for Co member under 100 Oe and 10 kOe fields. (Reproduced from Ref. 208. © Elsevier). (b) Field-cooling measurements of $[Fe_3(HCOO)_6](G)$ with the guest names shown under an applied field of 10 Oe. Parent is the parent compound with guests of methanol and water and Empty is the guest-free framework. (Reproduced from Ref. 31 with permission of The Royal Society of Chemistry. http://dx.doi.org/10.1039/B708122G.)

5.2.2 *Guest-dependent Magnetism of $[M_3(HCOO)_6](G)$ (G = guest)*

When the guest molecules are absorbed, the inclusion compounds $[M_3(HCOO)_6](G)$ are still show 3D magnetic LRO but they are guest-dependent (Table 3). The guest inclusion does not alternate the nature of the magnetic couplings but change their strength. The T_C's, H_C's, and remnant magnetizations (R_M's) can be smaller or larger than those of apohost compounds depending on the guest sizes and host–guest interactions. Magnetism of $[M_3(HCOO)_6](G)$ for M = Mn and Fe have been systematically investigated.[195–200,209,210] For $[Mn_3(HCOO)_6](G)$, T_C can be modulated by guests in range 4.8–9.7 K, compared to 8.0 K for apohost $[Mn_3(HCOO)_6]$. While for

Table 3 Guest-modulated magnetism (T_C) in $[Mn_3(HCOO)_6](G)$ and $[Fe_3(HCOO)_6](G)$

$[Mn_3(HCOO)_6](G)$		$[Fe_3(HCOO)_6](G)$	
Guest	T_C (K)	Guest	T_C (K)
As prepared, CH_3OH and H_2O	8.1	As prepared, CH_3OH and H_2O	16.0
Apohost	8.0	Apohost	16.1
Acetic acid	4.8	Formic acid	16
N,*N*-dimethyl formamide	7.2	Iodine	17.3
Furan	9.7	Tetrahydrofuran	18.8
Benzene	8.6	Furan	19.8
Iodine	7.1	Benzene	15.6
Ethanol	8.5	Acetonitrile	20.7
R-2-Cl-propan-1-ol	7.6	Acetone	20.0
S-2-Cl-propan-1-ol	7.6		
RS-2-Cl-propan-1-ol	8.3		

$[Fe_3(HCOO)_6](G)$, T_C changes from 15.6 to 20.7 K versus 16.1 K for the guest-free $[Fe_3(HCOO)_6]$ (Figure 8b). Higher H_C and for $[Fe_3(HCOO)_6](G)$ materials of higher T_C and R_M are also observed. On the basis of the currently available experimental observations, these guest-sensitive magnetic behaviors or the mechanism for guest-modulation lie in the changes in M–O–M angles of the host framework, where materials with large guests thus larger M–O–M angles[196] have lower T_C, and host–guest interactions, mainly the HB's, where the existence of stronger host–guest HB's seems to favor high T_C. Furthermore, enantiomer pure and racemic guests have a small but obviously different influence on the magnetism. Owing to the subtle difference in the molecular geometry of the host framework, the enantiomers lower T_C but the racemic ones raise T_C.[197] At the same time, the inclusion of chiral guest molecules into the channel of an achiral magnet is proven to be a possible and effective approach to obtain chiral magnets.

5.2.3 *Dielectric Anomalies and Ferroelectric Transition in $[Mn_3(HCOO)_6](G)$ ($G = H_2O$ and CH_3OH, CH_3CH_2OH)*

It is clear that the host framework of $[M_3(HCOO)_6]$ itself is rigid, thus usually display low and temperature-independent dielectric responses. However, the guest molecules in the framework channels should have large positional freedom, and if they are polar ones, the materials should display prominent dielectric properties. Indeed, this has been realized in the $[Mn_3(HCOO)_6](G)$ with the polar guests of H_2O and CH_3OH,[209] or CH_3CH_2OH.[210] The apohost framework $[Mn_3(HCOO)_6]$ showed no dielectric anomaly and low dielectric response, but interesting dielectric properties even ferroelectricity emerged for the guest inclusion materials. $[Mn_3(HCOO)_6](H_2O)(CH_3OH)$ displayed large dielectric drop around 120 K, indicating the possible liquid–solid phase transition or movement freezing of the guest molecules in the confined space of framework channel. The dielectric study on another guest inclusion compound, $[Mn_3(HCOO)_6](CH_3CH_2OH/D)$, revealed the PE–FE transition at 165 K. It is considered to be the first ferroelectric, porous magnets, showing magnetic and electric orderings below 8.5 K. Given the very wide spectrum of guest inclusion for the present porous magnets, the above achievements point out another new approach to design MOF-based multiferroic materials, in addition to multiferroic AMFFs discussed in Section 4.2.2.

6 MAGNETIC MFFs WITH COLIGANDS

In this section, we provide a short review on the magnetic MFFs incorporating coligands, from small or short ones to some large ones. The coligands can be used to adjust and control structures of MFFs, thus modulate the pathways, the strengths, and the dimensionalities of the magnetic couplings. A complete survey seemly is very difficult. We would like to introduce some selected examples and focus on those of magnetic late 3d metals, and hope this will be of help for designing and exploring new magnetic MOF materials with beautiful structures and interesting magnetism.

6.1 With Small/Short Coligands

Small coligands such as water, urea, and formamides were widely used to construct MFFs in earlier days (Section 2), and they usually acted as terminal ligands. Other small/short coligands used for MFFs are seemly limited. The smallest coligand might be hydroxyl except the μ_3-O in the most popular oxo-centered tri-nuclear complexes. The very recently reported $Cu_2(OH)_3(HCOO)$[211] represents an example. The compound consists of 2D triangular lattice of Cu^{2+} connected by μ_3-OH and μ_3-O

of HCOO, or the layer is composed of the elongated CuO_6 octahedra sharing their edges. The edges of the triangular lattice were not equivalent because of the Jahn–Teller effect of Cu^{2+} ion, resulted in quite complicated nonequivalent exchange paths. It displays AF LRO at 5.4 K, and a spin-flop transition was observed at about 20 kOe at 2 K, thereby indicating metamagnetic-like behavior. The saturation magnetization of almost 1/2 of the theoretical value at 2 K under 70 kOe might imply possible geometrical frustration for this triangular lattice. Some other frameworks such as $Co(HCOO)(OH)$[212] and $Fe_3(HCOO)_5Cl(H_2O)$,[105] both are 3D, have been synthesized, but no magnetism reported. However, it could be expected that such compounds with small OH^-, Cl^-, etc. probably exhibit good magnetic LRO properties because they are dense and involve more and strong magnetic interactions.

It is quite interesting to see that the formamide ($HCONH_2$) can act as bridging ligand and co-work with formate. $Co^{II}(HCOO)_2(HCONH_2)\cdot HCONH_2$ and $Na[Cr^{III}(HCOO)_4(HCONH_2)_2]\cdot 2H_2O$, reported by P. S. Mukherjee *et al.*,[213] possess neutral perovskite frameworks of $Co(HCOO)_2(HCONH_2)$ and $NaCr(HCOO)_4(HCONH_2)_2$, respectively, in which the bridging formamide acts as that of anti–anti formate. They are very similar to the perovskite AMFFs, however, in the cavities locate neutral formamide or water guests. The neutral guests could be removed and regained while the frameworks kept sustained, and the materials are highly thermally stable. Therefore, these are truly porous MFFs and porous magnets. The Co compounds, with or without guest, are spin-canted AF or WF at T_N's of *ca.* 10 K, and the NaCr one displays PM behavior. Unfortunately, no dielectric study was performed.

To our awareness, there are no or very rare reports involving cyanide and oxalate together with formate for 3d metals, probably because cyanide and oxalate possess much stronger coordinating ability that formate could not compete with. However, few examples incorporating octacynometalate Mo/W–CN units and Mn^{II} have been recently reported.[214,215] The constituents are complex. The frameworks are dense and complicated, dominated by Mo/W–CN–Mn linkages; however, syn–anti or anti–anti formates provide extra Mn···Mn linkages. The materials show FI LRO with high T_C's of 40~50 K,[214] and electrochemically switchable magnetism,[215] given the very strong magnetic couplings via cyanide bridges and the oxidation/reduction properties of Mo/W–CN units.

The short ligand azide possesses similar bridging modes and coordinating ability to formate.[31] In fact, the magnetic metal azide frameworks (MAFs) belong to a very large class of molecule-based magnetic materials,[30,31,119–123,216–219] well developed and extensively investigated, even several ammonium MAFs, AMAFs, have been known for quite long time.[119–123] The two compounds of $[(CH_3)_2NH_2][M(N_3)_2(HCOO)]$ (M = Fe, Co) seem to be the first examples incorporating formate and azide.[220] In the two complexes, the metal ions are three-fold bridged by two *end-on* azido and one syn–syn formato ligand, forming chains of $[M(N_3)_2(HCOO)^-]$ isolated by $(CH_3)_2NH_2^+$. Both compounds display similar metamagnetic properties below T_N's of 10 K arising from the strong intrachain FO but weak interchain AF interactions. Mixed formato/azido systems are deserved further investigation, for example, to construct the 3D frameworks incorporating ammoniums, parallel to AMFFs and AMAFs.

Pyrazine (pyz) and pyrimidine (pym) are neutral, short bridging ligands, and they could mediate effective magnetic exchange. Some MFFs involving such coligands have been investigated. The copper compounds $Cu(HCOO)_2(pyz)$[221,222] and $Cu(HCOO)_2(pym)$[223] are 3D frameworks consisting of (4,4) Cu-formate layers linked by interlayer pyz or pym. Formate ligands are all syn–anti in former but anti–anti in later; however, they are involved in the long axial Cu–O bonds. The main magnetic exchange paths thus are short equatorial Cu–pyz/pym–Cu linkages. Therefore, these material displays 1D AF behavior, different from the 2D magnetism for the copper formate di- or tetra-hydrate salts,[60,61,63,73] in which the (4,4) Cu-formate layer includes anti–anti formates but short equatorial $Cu–O_{HCOO}$ bonds. $Cu(HCOO)_2(pym)$ exhibits a transition to AF LRO below $T_N = 2.8$ K but $Cu(HCOO)_2(pyz)$ did not show magnetic LRO above 1.6 K.

For small terminal ligands of pyridine (py) and its derivatives, we just give an interesting example, the mixed-valence $Fe^{II}Fe^{III}$ compound of $[Fe^{II}_2Fe^{III}_2(HCOO)_{10}(4\text{-Mepy})_6]$.[224] The structure is made of (4,4) Fe-formate layers, and the interlayer interactions are π–π stacking between the aromatic parts of 4-Mepy coordinating to Fe. Owing to the mixed valence, the 2D system still shows AF LRO at T_C of 20 K, compared to 3.8 K for the Fe^{II} formate dihydrate[55,57,58] with very similar (4,4) Fe-formate layers, and 10 ~ 20 K for the Fe^{II} members of AMFF.[138,147,162]

Before finishing this part, we would like to introduce an $[Fe_3OMn]_n$ honeycomb layer compound including self-assembly of the popular μ_3-oxo trinuclear $[Fe^{III}_3O(HCOO)_6]$ units and their linking by $[Mn^{II}(HCOO)_3(H_2O)_3]$ fragments via syn–anti formates.[225] These 2D honeycomb layers are interlayer-connected by molecules of formic acid through an HB network. The structure has the voids space at the center of the hexagons and the interlayer region, filled by captured and exchangeable solvents. The magnetic property can be considered the AF between the Fe_3O trinuclear units, for which magnetism is governed by the strong superexchange interaction between Fe^{3+} spins of the Fe_3O units, and the Mn^{2+} ions.

6.2 With Large Ditopic or Polytopic Coligands

The bipyridyl ligands, well known for constructing MOFs, have been used as the coligand. The anhydrous $[M(HCOO)_2(4,4'\text{-bpy})]$ (M = Mn, Co, Ni, Cu; 4,4′-bpy = 4,4′-bipyridine) possess a 3D metal formate (anti–anti) diamondoid framework,[221,226,227] with the bpy pillars locating in the framework channels and coordinating metal sites. Instead, the hydrous compounds of $[M(HCOO)_2(4,4'\text{-bpy})](H_2O)_5$ (M = Co, Ni) are 3D $CdSO_4$ type framework constructed by anti–anti formate and 4,4′-bpy, with channels filled by water.[226,227] They are WF with T_N's lower than 10 K except the Ni compounds with T_N of *ca*. 20 K or higher. By employing longer bipyridyl ligand, 4,4′-bipyridylethylene (bpe), $[Mn_2(HCOO)_3(4,4'\text{-bpe})_3(H_2O)_2][(H_2O)$(anion) series[228] could be obtained. These are pillared layer structures with Mn–formate (anti–anti and syn–anti) herringbone (6, 3) layers pillared by 4,4′-bpe, with mono anions (ClO_4^-, NO_3^-, BF_4^-, Br^-, I^-) and lattice 4,4′-bpe molecules residing in between. The magnetic behaviors all indicate AF interactions, but a spin-flop transition happens under an external field, and the magnetic properties of this series can be finely tuned by different anions. Furthermore, on exposure to the UV light the lattice bpe molecules become photoactive and dimerize to tetrakis(4-pyridyl)-cyclobutane. This provides a good example of the design of the multifunctional materials using functional coligands.

Other N-based ligands have also been employed. An interesting example could be the series of $[M_2(HCOO)_3L_2](HCOO/NO_2)\cdot 2H_2O$, reported by X. H. Bu *et al.*,[229] where L is a rodlike ligand of 4,4′-bis(imidazol-1-yl)biphenyl and M = divalent Co, Ni, and Cu. The structures possess 2D metal formate (anti–anti and syn–anti) layers of Kagomé lattice perpendicularly pillared by L, forming 3D frameworks. The nickel member presents the spin-canting AF phenomenon, whereas cobalt and copper complexes are simply PMs with AF couplings.

Given the superiorities of carboxylate groups, carboxylate ligands have also been imported to metal formate systems, to create novel frameworks with various metal–metal linkages and nodes of clusters, even short coligands of hydroxyl and azide could be included.[230–232] While there are quite many published works, we here just selected the unusual examples of Mn/Mg-formate-cam,[233,234] where the chiral camphorate (cam) was employed. The $[M_3(HCOO)_4]_n^{2n+}$ porous framework with 3D Mn–O–Mn connectivity and open honeycomb channels were formed with the D-camphorate ligands attaching to the wall of the channel by coordination to metal sites. The magnetic investigation revealed dominant AF behavior for Mn compound. Similar Mn–formate–adc frameworks (adc = adamantane-1,3-dicarboxylate) could also be obtained, with the framework chirality induced by chiral camphoric acid or others in synthesis.[234,235]

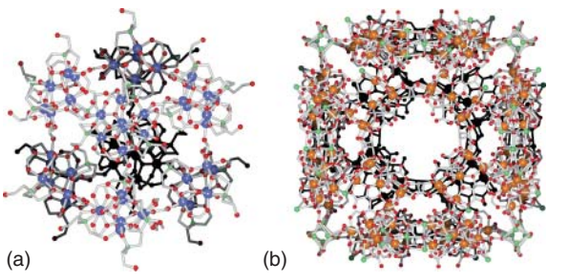


Figure 9 The cubic cages in $[Fe_{64}]$ (a) and $[Fe_{168}]$ (b). Depth cueing is used to distinguish front and back

Finally, we just introduce few examples of cages or frameworks having metal–formate clusters as apexes or nodes, or metal–formate–metal linkages, to illustrate the potential of formate for not only synthesizing clusters of high nuclearity but also linking these clusters. In these samples, polytopic or multipodal coligands are usually employed, and strong AF interactions are observed.

A nickel-sodium metal square cage of $[Ni_{16}Na_2]$[236] was synthesized with the help of *N*-methyldiethanolamine ($mdeaH_2$), which is one of the polypodal ligands having been previously proved to have the ability to form polynuclear clusters.[237,238] Each apex cluster of the square consists of four Ni ions arranged in a flattened tetrahedron. The Ni···Ni edges are linked by alkoxide arms of mdea, and the Ni···Ni edges from apical to basal positions are further crossed by *syn–syn* acetates. In the square, the Ni4 tetrahedra are linked by single anti–anti formate linking the two basal Ni atoms in the two opposite square edges, and along the other two square edges, they are linked by Na^+ via the Na–acetate bonds. In another example, an $[Fe^{III}{}_{64}]$ cubic cage[239] (Figure 9a) was prepared using formate together with de-protonated triethanolamine ($teaH_3$) ligands. The cubic cage contains 64 Fe^{3+} ions, 24 O^{2-}, 8 tea^{3-}, 24 $teaH^{2-}$, and 60 $HCOO^-$, thus totally 180 components. It consists of eight apexes of octanuclear $[Fe^{III}{}_8O_3(tea)(teaH)_3(HCOO)_6(HCOO)_{3/2}]$ unit with a propeller-like Fe_8O_3 core, further linked by 12 anti–anti formato ions as the edges of the cube. Both syn–syn formates and tea/teaH ligands contribute the formation of the octanuclear apex or node.

$[Co_6(BTC)_2(HCOO)_6(DMF)_6]$,[240] where BTC is 1,3,5-benzenetricarboxylate, which is a widely used ligand for building MOFs,[241–244] exhibits a 2D hexagonal network consisting of hexameric Co_6 ring clusters linked by triangular BTC. The Co_6 hexagonal cluster has six syn–anti/syn formates to link Co ions in a cyclic style, and in the framework the carboxylates of BTC syn–syn span the edges of Co_6 hexagon.

It is now come to $[Fe_{168}]$,[245] formulated as $Na_{96}[Na_{24}Fe_{168}(\text{L/D-Tart})_{96}(\mu_3\text{-O})_{48}(HCOO)_{144}]\cdot 310H_2O$. The introduction of L-tartrate and D-tartrate (Tart) into

the Fe^{3+}-formate system in the presence of a large amount of Na^+ cations led to the isolation of such unprecedented protein-sized chiral [Fe_{168}] cages linked by 2Na-caped Na_4O_4 cubanes (the capped Na is disordered, in two positions), forming a 3D zeolite-like framework of NbO-type topology (Figure 9b). The very large, complicated, and hierarchical or multilevel [Fe_{168}] cubic cages consist of wheel-like of [Fe_{28}] units or squares on its six faces and 2Na-caped Na_4O_4 cubanes on its 12 edges, and the [Fe_{28}] square is composed of four equivalent [Fe_7] trigonal prism, slight twisting and having an Fe^{3+} center, as the corners. Tartrate ligands provide the Fe···Fe linkages within the [Fe_7] unit and those between them, as well as the Fe···Na connections. Formates in syn–syn mode serve as Fe···Fe linkages within the [Fe_7] trigonal prism, but those in anti-μ_3 and anti/syn-μ_3 modes link Fe^{3+} of and [Fe_7] unit and Na^+ of 2Na-caped Na_4O_4 cubane units, forming the framework. Therefore, formates not only build the clusters but also connect the clusters into the MOFs.

7 CONCLUSIONS AND PERSPECTIVES

In conclusion, we have reviewed the state of art of the magnetic materials based on MFFs, mainly developed in the past decade. It has demonstrated that these materials, though belonging to a relatively small yet fundamentally important MOF class, do possess very diversity in their structures and more importantly in their charming properties. The binary or ternary dense MFFs with simple constituents in fact display complicated structures and various magnetic behaviors. AMFFs represent now the most actively investigated MFF systems because they have exhibited abundant and interesting magnetism, and di-/ferro-/antiferroelectric and mechanical properties, accompanying the structural phase transitions and critical phenomena triggered by various order–disorder transitions and patterns of the incorporated ammoniums, and the chirality, and possible combinations such as multiferroics. Especially, many AMFFs are MOF mimics or counter parts of the traditional inorganic materials such as perovskite, niccolite, and diamond. The porous diamondoid [$M_3(HCOO)_6$] MFFs have shown wide gas and guest inclusion behaviors, thus guest-modulated magnetism, guest-induced chirality, and guest-based electric polarization. Furthermore, combining coligands with formate definitely provides more opportunities to obtain MFFs with not only beautiful and fantastic architectures or structures but also interesting and appealing magnetic and other properties. This is truly a research field of multidimensionalities. In the view of synthetic and structural chemistry, different metal ions, cations, guests, and coligands could be employed and explored for the sake of acquiring various MFFs. On the other hand, the magnetic, electric, mechanical, and optical properties, and their combination or synergism, phase transitions, and critical phenomena and the underlying mechanisms, require extensive and deep investigations and characterizations upon the variables of temperature, pressure, stress, electric field, magnetic field, and so on, and wide cooperation. Finally, formate, as the smallest and simplest carboxylate, much cheap and less toxic thus more biocompatible and environment-friendly, having been previously more or less ignored, now comes back to our sight and awareness with its verified vital role in the construction of promising functional MOF materials. We look forward to the new development in this unique research area and believe more novel even amazing results will appear in the near future.

8 ACKNOWLEDGMENT

This work was supported by the NSFC (Grants 21171010, 21290170, and 21290171), and the National Basic Research Program of China (Grant 2009CB929403).

9 RELATED ARTICLES

Gas Storage in Metal-Organic Frameworks; Adsorption of Hydrocarbons and Alcohols in Metal-Organic Framework Materials; Metal-Organic Frameworks from Single-Molecule Magnets; Single-Crystal to Single-Crystal Transformations in Metal-Organic Frameworks; Interpenetration and Entanglement in Coordination Polymers.

10 ABBREVIATIONS AND ACRONYMS

AMFF = ammonium metal formate framework; CFT = copper formate tetrahydrate; HB = hydrogen bonding/bond; HT/RT/LT = high/room/low temperature J = magnetic coupling; Ln = lanthanide; LRO = long-range ordering; M = metal; MAF = metal azide framework; ME = magnetoelectric; MFF = metal formate framework; MOF = metal-organic framework; PE/AFE/FE = para-/antiferro-/ferroelectric/electricity PM/AF/WF/FO/FI = para-/antiferro-/weak ferro-/ferro-/ferri-magnet/magnetism/magnetic; SG = space group; SIM = single ion magnet; SMM = single molecule magnet; T_C = critical temperature and phase transition temperature; THF = tetrahydrofuran; TM = transition metal; T_N = Néel temperature; 1D/2D/3D = one-/two-/three-dimensional.

11 REFERENCES

1. H.-C. Zhou, J. R. Long, and O. M. Yaghi, *Chem. Rev.*, 2012, **112**, 673.
2. J. R. Long and O. M. Yaghi, *Chem. Soc. Rev.*, 2009, **38**, 1213.
3. C. Janiak and J. K. Vieth, *New J. Chem.*, 2010, **34**, 2366.
4. A. K. Cheetham and C. N. R. Rao, *Science*, 2007, **318**, 58.
5. C. N. R. Rao, A. K. Cheetham, and A. Thirumurugan, *J. Phys. Condens. Matter*, 2008, **20**, 083202.
6. M. P. Suh, H. J. Park, T. K. Prasad, and D.-W. Lim, *Chem. Rev.*, 2012, **112**, 782.
7. D. J. Collins and H.-C. Zhou, *J. Mater. Chem.*, 2007, **17**, 3154.
8. S. T. Meek, J. A. Greathouse, and M. D. Allendorf, *Adv. Mater.*, 2011, **23**, 249.
9. D. Farrusseng, S. Aguado, and C. Pinel, *Angew. Chem., Int. Ed.*, 2009, **48**, 7502.
10. J.-R. Li, J. Sculley, and H.-C. Zhou, *Chem. Rev.*, 2012, **112**, 869.
11. P. Horcajada, R. Gref, T. Baati, P. K. Allan, G. Maurin, P. Couvreur, G. Férey, R. E. Morris, and C. Serre, *Chem. Rev.*, 2012, **112**, 1232.
12. G. Férey, *Chem. Soc. Rev.*, 2008, **37**, 191.
13. S. Hhorike, S. Shimomura, and S. Kitagawa, *Nat. Chem.*, 2009, **1**, 695.
14. S. Kitagawa, R. Kitaura, and S. Noro, *Angew. Chem., Int. Ed.*, 2004, **43**, 2334.
15. O. Sato, J. Tao, and Y.-Z. Zhang, *Angew. Chem., Int. Ed.*, 2007, **46**, 2152.
16. C. Train, M. Gruselle, and M. Verdaguer, *Chem. Soc. Rev.*, 2011, **40**, 3297.
17. C. Wang, T. Zhang, and W. Lin, *Chem. Rev.*, 2012, **112**, 1084.
18. O. R. Evans and W. B. Lin, *Acc. Chem. Res.*, 2002, **35**, 511.
19. M. D. Allendorf, C. A. Bauer, R. K. Bhakta, and R. J. T. Houk, *Chem. Soc. Rev.*, 2009, **38**, 1330.
20. T. Hang, W. Zhang, H.-Y. Ye, and R.-G. Xiong, *Chem. Soc. Rev.*, 2011, **40**, 3577.
21. W. Zhang and R.-G. Xiong, *Chem. Rev.*, 2012, **112**, 1163.
22. E. Coronado and K. R. Dunbar, *Inorg. Chem.*, 2009, **48**, 3293.
23. J. S. Miller and D. Gatteschi, *Chem. Soc. Rev.*, 2011, **40**, 3065.
24. C. Rovira and J. Veciana, *CrystEngComm*, 2009, **11**, 2031.
25. P. Dechambenoit and J. R. Long, *Chem. Soc. Rev.*, 2011, **40**, 3249.
26. C. Train, R. Gheorghe, V. Krstic, L.-M. Chamoreau, N. S. Ovanesyan, G. L. J. A. Rikken, M. Gruselle, and M. Verdagure, *Nat. Mater.*, 2008, **7**, 729.
27. R. Ramesh, *Nature*, 2009, **461**, 1218.
28. S.-i. Ohkoshi, H. Tokoro, T. Matsuda, H. Takahashi, H. Irie, and K. Hashimoto, *Angew. Chem., Int. Ed.*, 2007, **46**, 3238.
29. E. Pardo, C. Train, H. Liu, L.-M. Chamoreau, B. Dkhil, K. Boubekeur, F. Lloret, K. Nakatani, H. Tokoro, S.-i. Ohkoshi, and M. Verdaguer, *Angew. Chem., Int. Ed.*, 2012, **51**, 8356.
30. D.-F. Weng, Z.-M. Wang, and S. Gao, *Chem. Soc. Rev.*, 2011, **40**, 3157.
31. X.-Y. Wang, Z.-M. Wang, and S. Gao, *Chem Commun.*, 2008, 281.
32. Z.-M. Wang, K.-L. Hu, S. Gao, and H. Kobayashi, *Adv. Mater.*, 2010, **22**, 1526.
33. I. E. Collings, A. B. Cairns, A. L. Thompson, J. E. Parker, C. C. Tang, M. G. Tucker, J. Catafesta, C. Levelut, J. Haines, V. Dmitriev, P. Pattison, and A. L. Goodwin, *J. Am. Chem. Soc.*, 2013, **135**, 7610.
34. A. L. Goodwin, M. Calleja, M. J. Conterio, M. T. Dove, J. S. O. Evans, D. A. Keen, L. Peters, and M. G. Tucker, *Science*, 2008, **319**, 794.
35. N. Lock, Y. Wu, M. Christensen, L. J. Cameron, V. K. Peterson, A. J. Bridgeman, C. J. Kepert, and B. B. Iversen, *J. Phys. Chem. C*, 2010, **114**, 16181.
36. Y. Wu, A. Kobayashi, G. J. Halder, V. K. Peterson, K. W. Chapman, N. Lock, P. D. Southon, and C. J. Kepert, *Angew. Chem., Int. Ed.*, 2008, **120**, 9061.
37. R. H. Baughman, S. Stafström, C. Cui, and S. O. Dantas, *Science*, 1998, **279**, 1522.
38. A. B. Cairns, J. Catafesta, C. Levelut, J. Rouquette, A. van der Lee, L. Peters, A. L. Thompson, V. Dmitriev, J. Haines, and A. L. Goodwin, *Nat. Mater.*, 2013, **12**, 212.
39. A. B. Cairns, A. Thompson, L. M. G. Tucker, J. Haines, and A. L. Goodwin, *J. Am. Chem. Soc.*, 2012, **134**, 4454.
40. K. W. Chapman, G. J. Halder, and P. J. Chupas, *J. Am. Chem. Soc.*, 2009, **131**, 17546.
41. T. D. Bennett, A. L. Goodwin, M. T. Dove, D. A. Keen, M. G. Tucker, E. R. Barney, A. K. Soper, E. G. Bithell, J.-C. Tan, and A. K. Cheetham, *Phys. Rev. Lett.*, 2010, **104**, 115503-1.
42. W. Zhang, Y. Cai, R. G. Xiong, H. Yoshikawa, and K. Awaga, *Angew. Chem., Int. Ed.*, 2010, **49**, 6608.
43. W. Zhang, H.-Y. Ye, R. Graf, H. W. Spiess, Y.-F. Yao, R.-Q. Zhu, and R.-G. Xiong, *J. Am. Chem. Soc.*, 2013, **135**, 5230.
44. S. R. Batten, N. R. Champness, X.-M. Chen, J. Garcia-Martinez, S. Kitagawa, L. Öhrström, M. O'Keeffe, M. P. Suh, and J. Reedijk, *Pure Appl. Chem.*, 2013, **85**, 1715.
45. A. F. Wells, 'Three-Dimensional Nets and Polyhedra', Wiley-Interscience, New York, 1977.
46. S. R. Batten and R. Robson, *Angew. Chem., Int. Ed.*, 1998, **37**, 1460.
47. K. Osaki and Y. Nakai, *J. Phys. Soc. Japan*, 1963, **18**, 919.

48. K. Osaki, Y. Nakai, and T. Watanabé, *J. Phys. Soc. Japan*, 1964, **19**, 717.
49. H. Abe, H. Morigaki, M. Matsuura, K. Torh, and K. Yamagata, *J. Phys. Soc. Japan*, 1964, **19**, 775.
50. H. Abe and K. Torh, *J. Phys. Soc. Japan*, 1965, **20**, 183.
51. K. Yamagata and H. Abe, *J. Phys. Soc. Japan*, 1965, **20**, 906.
52. K. Yamagata, *J. Phys. Soc. Japan*, 1967, **22**, 582.
53. R. D. Pierce and S. A. Friedberg, *Phys. Rev.*, 1968, **165**, 680.
54. J. Skalyo Jr., G. Shirane, and S. A. Friedberg, *Phys. Rev.*, 1969, **188**, 1037.
55. K. Takeda and K. Kawasaki, *J. Phys. Soc. Japan*, 1971, **31**, 1026.
56. P. Radhakrishna, B. Gillon, and G. Chevrier, *J. Phys. Condens. Matter*, 1993, **5**, 6447.
57. G. R. Hoy, S. de S. Barros, F. de S. Barros, and S. A. Friedberg, *J. Appl. Phys.*, 1965, **36**, 936.
58. R. D. Pierce and S. A. Friedberg, *Phys. Rev.*, 1971, **B3**, 934.
59. A. Kaufman, C. Afshar, M. Rossi, D. E. Zacharias, and J. P. Glusker, *Struct. Chem.*, 1993, **4**, 191.
60. R. L. Martin and H. Waterman, *J. Chem. Soc.*, 1959, 1359.
61. R. B. Flippen and S. A. Friedberg, *J. Chem. Phys.*, 1963, **38**, 2652.
62. M. Matsuura, H. W. J. Blöte, and W. J. Huiskamp, *Physica*, 1970, **50**, 444.
63. G. R. Wagner, R. T. Schumacher, and S. A. Friedberg, *Phys. Rev.*, 1966, **150**, 226.
64. Ridwan, *Jpn. J. Appl. Phys.*, 1992, **31**, 3559.
65. S. J. Rettig, R. C. Thompson, J. Trotter, and S. Xia, *Inorg. Chem.*, 1999, **38**, 1360.
66. K. Takeda, H. Deguchi, T. Hoshiko, and K. Yamagata, *J. Phys. Soc. Japan*, 1989, **58**, 3489.
67. K. Yamagata, Y. Saito, T. Abe, and M. Hashimoto, *J. Phys. Soc. Japan*, 1989, **58**, 3865.
68. K. Yamagata, Y. Saito, and T. Abe, *J. Phys. Soc. Japan*, 1989, **58**, 752.
69. K. Yamagata, T. Abe, Y. Higuchi, H. Deguchi, K. Takeda, K. Kanedo, H. Nojiri, and M. Motokawa, *J. Magn. Magn. Mater.*, 1992, **104–107**, 803.
70. H. Deguchi, T. Hoshiko, K. Takeda, and K. Yamagata, *J. Magn. Magn. Mater.*, 1990, **90–91**, 303.
71. K. Yamagata, N. Koyano, N. Ridwan, N. Achiwa, M. Fujino, Y. Iwata, and I. Shibuya, *J. Magn. Magn. Mater.*, 1992, **104–107**, 849.
72. M. Fujino, N. Achiwa, N. Koyano, I. Shibuya, N. Ridwan, and K. Yamagata, *J. Magn. Magn. Mater.*, 1992, **104–107**, 851.
73. H. Kobayashi and T. Haseda, *J. Phys. Soc. Jpn.*, 1963, **18**, 541.
74. K. Okada, *Phys. Rev. Lett.*, 1965, **15**, 252.
75. Y. Makita and I. Seo, *J. Chem. Phys.*, 1969, **51**, 3058.
76. G. R. Allen and J. F. Naglei, *J. Phys. C: Solid State Phys.*, 1975, **8**, 2788.
77. R. P. Canterford and F. Ninio, *J. Phys. C: Solid State Phys.*, 1975, **8**, 385.
78. K. Okada, M. I. Kay, D. T. Cromer, and I. Almodovar, *J. Chem. Phys.*, 1966, **44**, 1648.
79. N. Burger, H. Fuess, and P. Burlet, *Solid State Commun.*, 1980, **34**, 883.
80. M. J. Sanchis, P. Gómez-Romero, J.-V. Folgado, F. Sapiña, R. Ibáñez, A. Beltrán, J. García, and D. Beltrán, *Inorg. Chem.*, 1992, **31**, 2915.
81. A. G. Levya, G. Polla, P. K. de Perazzo, H. Lanza, and M. A. R. de Benyacar, *J. Solid State Chem.*, 1996, **123**, 291.
82. G. Polla, G. Levya, P. K. de Perazzo, H. Lanza, and M. A. R. de Benyacar, *J. Solid State Chem.*, 1995, **117**, 145.
83. F. Sapiña, M. Burgos, E. Escrivá, J.-V. Folgado, D. Marcos, A. Beltrán, and D. Beltrán, *Inorg. Chem.*, 1993, **32**, 4337.
84. N. Burger and H. Fuess, *Solid State Commun.*, 1980, **34**, 699.
85. G. A. Barclay and C. H. L. Kennard, *J. Chem. Soc.*, 1961, 3289.
86. E. Sletten and L. H. Jensen, *Acta Cryst.*, 1973, **B29**, 1752.
87. G. A. Nifontova, O. S. Filipenko, A. S. Astokhova, I. P. Lavrent'ev, and L. O. Atovmyan, *Koord. Khim.*, 1990, **16**, 218.
88. R. E. Marsh, *Acta Cryst.*, 1986, **C42**, 1327.
89. A. S. Antsyshkina, M. A. Poraikoshits, and V. N. Ostrikova, *Koord. Khim.*, 1988, **14**, 1268.
90. A. Cornia, A. Caneschi, P. Dapporto, A. C. Fabretti, D. Gatteschi, W. Malavasi, C. Sangregorio, and R. Sessoli, *Angew. Chem., Int. Ed.*, 1999, **38**, 1780.
91. P. Kistaiah, K. S. Murthy, L. Iyengar, and K. V. K. Rao, *J. Mater. Sci.*, 1981, **16**, 2321.
92. A. Pabst, *Can. Mineral.*, 1978, **16**, 437.
93. J. Legendziewicz, T. Glowiak, G. Oczko, and D. C. Ngoan, *J. Less Common Met.*, 1986, **125**, 45.
94. N. G. Furmanova, L. V. Soboleva, N. V. Belov, and L. M. Belyaev, *Kristallografiya*, 1981, **26**, 1315.
95. A. S. Antsyshkina, M. A. Porai-Koshits, and V. N. Ostrikova, *Koord. Khim.*, 1988, **14**, 850.
96. N. G. Furmanova, L. V. Soboleva, L. I. Khapaeva, and N. V. Belov, *Kristallografiya*, 1983, **28**, 62.
97. F. H. Allen and O. Kennard, 'Cambridge Structural Database, Version 5.33', Cambridge Crystallographic Data Centre, Cambridge, UK, 2012.
98. T. Lis and B. Jezowska-Trzebiatowska, *Acta Cryst.*, 1977, **B33**, 2112.
99. A. S. Lipton, M. D. Smith, R. D. Adams, and P. D. Ellis, *J. Am. Chem. Soc.*, 2002, **124**, 410.
100. H. Kageyama, D. I. Khomskii, R. Z. Levitin, and A. N. Vasil'ev, *Phys. Rev.*, 2003, **B67**, 224422.

101. J. Kong, J. Zon, and A. McBee, *Inorg. Chem.*, 2006, **45**, 977.
102. Y. B. Go and A. J. Jacobson, *Chem. Mater.*, 2007, **19**, 4702.
103. J.-M. Lin, Y.-F. Guan, D.-Y. Wang, W. Dong, X.-T. Wang, and S. Gao, *Dalton Trans.*, 2008, 6165.
104. T. Tajiri, S. Matsumoto, H. Deguchi, M. Mito, S. Takagi, C. Moriyoshi, K. Itoh, and K. Koyama, *J. Magn. Magn. Mater.*, 2007, **310**, e566.
105. M. Viertelhaus, PhD thesis, Institut für Anorganische Chemie, Universität Karlsruhe, 2003.
106. M. Viertelhaus, H. Henke, C. E. Anson, and A. K. Powell, *Eur. J. Inorg. Chem.*, 2003, 2283.
107. M. Viertelhaus, C. E. Anson, and A. K. Powell, *Z. Anorg. Allg. Chem.*, 2005, **631**, 2365.
108. G. Lorusso, J. W. Sharples, E. Palacios, O. Roubeau, E. K. Brechin, R. Sessoli, A. Rossin, F. Tuna, E. J. L. McInnes, D. Collison, and M. Evangelisti, *Adv. Mater.*, 2013, **25**, 4653.
109. D. Feng, Y. Che, and J. Zheng, *J. Rare Earth.*, 2012, **30**, 798.
110. V. Paredes-García, A. Vega, M. A. Novak, M. G. F. Vaz, D. A. Souza, D. Venegas-Yazigi, and E. Spodine, *Inorg. Chem.*, 2009, **48**, 4737.
111. Z.-M. Duan, Z.-M. Wang, and S. Gao, *Dalton Trans.*, 2011, **40**, 4465.
112. J.-P. Zhao, S.-D. Han, R. Zhao, Q. Yang, Z. Chang, and X.-H. Bu, *Inorg. Chem.*, 2013, **52**, 2862.
113. S.-T. Zheng, M.-H. Wang, and G.-Y. Yang, *Chem. Asian J.*, 2007, **2**, 1380.
114. P. J. Hagrman, D. Hagrman, and J. Zubieta, *Angew. Chem., Int. Ed.*, 1999, **38**, 2638.
115. A. K. Cheetham, G. Férey, and T. Loiseau, *Angew. Chem., Int. Ed.*, 1999, **38**, 3268.
116. C. S. Cundy and P. A. Cox, *Chem. Rev.*, 2003, **103**, 663.
117. J. Yu and R. Xu, *J. Mater. Chem.*, 2008, **18**, 4021.
118. M. Pilkington and S. Decurtins, in 'Crystal Design: Structure and Function', ed G. R. Desiraju, John Wiley & Sons Ltd, West Sussex, England, 2003, p.306.
119. T. Liu, Y.-F. Yang, Z.-M. Wang, and S. Gao, *Chem. Asian. J.*, 2008, **3**, 950.
120. F. A. Mautner, S. Hanna, R. Cortés, L. Lezama, M. G. Barandika, and T. Rojo, *Inorg. Chem.*, 1999, **38**, 4647.
121. M. A. S. Goher, J. Cano, Y. Journaux, M. A. M. Abu-Youssef, F. A. Mautner, A. Escuer, and R. Vicente, *Chem. Eur. J.*, 2000, **6**, 778.
122. F. A. Mautner, R. Cortés, L. Lezama, and T. Rojo, *Angew. Chem., Int. Ed.*, 1996, **35**, 78.
123. S. Saha, S. Koner, J.-P. Tuchagues, A. K. Boudalis, K.-I. Okamoto, S. Banerjee, and D. Mal, *Inorg. Chem.*, 2005, **44**, 6379.
124. S. R. Batten and K. S. Murray, *Coord. Chem. Rev.*, 2003, **246**, 103.
125. Z.-M. Wang, B. Zhang, K. Inoue, H. Fujiwara, T. Otsuka, H. Kobayashi, and M. Kurmoo, *Inorg. Chem.*, 2007, **46**, 437.
126. G.-C. Xu, X.-M. Ma, L. Zhang, Z.-M. Wang, and S. Gao, *J. Am. Chem. Soc.*, 2010, **132**, 9588.
127. G.-C. Xu, W. Zhang, X.-M. Ma, Y.-H. Chen, L. Zhang, H.-L. Cai, Z.-M. Wang, R.-G. Xiong, and S. Gao, *J. Am. Chem. Soc.*, 2011, **133**, 14948.
128. R. Shang, Z.-M. Wang and S. Gao, The 13th International Conference on Molecule-based Magnetism, Florida, United States, October, 2012.
129. Z.-M. Wang, The 5th Japanese-Russian Workshop on Open Shell Compounds and Molecular Spin Devices, Awaji, Japan, November, 2011.
130. X.-M. Ma, *BSc Thesis*, Peking University, 2009.
131. G.-C. Xu, X.-M. Ma, L. Zhang, Z.-M. Wang and S. Gao, *The 12th International Conference on Molecule-based Magnetism*, Beijing, China, October, 2010.
132. B. Liu, R. Shang, K.-L. Hu, Z.-M. Wang, and S. Gao, *Inorg. Chem.*, 2012, **51**, 13363.
133. Z.-M. Wang, B. Zhang, T. Otsuka, K. Inoue, H. Kobayashi, and M. Kurmoo, *Dalton Trans.*, 2004, 2209.
134. M. Boča, I. Svoboda, F. Renz, and H. Fuess, *Acta Cryst.*, 2004, **C60**, m631.
135. X.-Y. Wang, L. Gan, S.-W. Zhang, and S. Gao, *Inorg. Chem.*, 2004, **43**, 4615.
136. A. Rossin, A. Ienco, F. Costantino, T. Montini, B. D. Credico, M. Caporali, L. Gonsalvi, P. Fornasiero, and M. Peruzzini, *Cryst. Growth Des.*, 2008, **8**, 3302.
137. P. Jain, N. S. Dalal, B. H. Toby, H. W. Kroto, and A. K. Cheetham, *J. Am. Chem. Soc.*, 2008, **130**, 10450.
138. P. Jain, V. Ramachandran, R. J. Clark, H. D. Zhou, B. H. Toby, N. S. Dalal, H. W. Kroto, and A. K. Cheetham, *J. Am. Chem. Soc.*, 2009, **131**, 13625.
139. M. Sánchez-Andújar, S. Presedo, S. Yáñez-Vilar, S. Castro-García, J. Shamir, and M. A. Señarís-Rodríguez, *Inorg. Chem.*, 2010, **49**, 1510.
140. D.-W. Fu, W. Zhang, H.-L. Cai, Y. Zhang, J.-Z. Ge, R.-G. Xiong, S. D. Huang, and T. Nakamura, *Angew. Chem., Int. Ed.*, 2011, **50**, 11947.
141. Z. Wang, P. Jain, K.-Y. Choi, J. van Tol, A. K. Cheetham, H. W. Kroto, H.-J. Koo, H. Zhou, J. Hwang, E. S. Choi, M.-H. Whangbo, and N. S. Dalal, *Phys. Rev. B*, 2013, **87**, 224406.
142. P. J. Baker, T. Lancaster, I. Franke, W. Hayes, S. J. Blundell, F. L. Pratt, P. Jain, Z.-M. Wang, and M. Kurmoo, *Phys. Rev. B*, 2010, **82**, 012407.
143. W. Wang, L.-Q. Yan, J. -Z. Cong, Y. -L. Zhao, F. Wang, S.-P. Shen, T. Zou, D. Zhang, S. -G. Wang, X. -F. Han, and Y. Sun, *Sci. Rep.*, 2013, **3**, 2024.
144. B. Pato-Doldán, M. Sánchez-Andújar, L. C. Gómez-Aguirre, S. Yáñez-Vilar, J. López-Beceiro, C. Gracia-Fernández, A. A. Haghighirad, F. Ritter, S. Castro-García,

and M. A. Señarís-Rodríguez, *Phys. Chem. Chem. Phys.*, 2012, **14**, 8498.

145. B. Zhou, Y. Imai, A. Kobayashi, Z.-M. Wang, and H. Kobayashi, *Angew. Chem., Int. Ed.*, 2010, **50**, 11441.
146. Y. Imai, B. Zhou, Y. Ito, A. Kobayashi, Z.-M. Wang, and H. Kobayashi, *Chem. Asian J.*, 2012, **7**, 2786.
147. K.-L. Hu, M. Kurmoo, Z.-M. Wang, and S. Gao, *Chem. Eur. J.*, 2009, **15**, 12050.
148. A. Rossin, M. R. Chierotti, G. Giambastiani, R. Gobettob, and M. Peruzzini, *CrystEngComm*, 2012, **14**, 4454.
149. B.-Q. Wang, H.-B. Yan, Z.-Q. Huang, and Z. Zhang, *Acta Cryst.*, 2013, **C69**, 616.
150. R. Shang, X. Sun, Z.-M. Wang, and S. Gao, *Chem. Asian J.*, 2012, **7**, 1697.
151. A. Plutecka and U. Rychlewska, *Acta Cryst.*, 2009, **C65**, m75.
152. F. Jona and G. Shirane, 'Ferroelectric crystals', Pergamon Press, New York, 1962.
153. M. E. Lines and A. M. Glass, '*Principles and Applications of Ferroelectrics and Related Materials*', Clarendon Press, Oxford, 1977.
154. N. A. Spaldin, S.-W. Cheong, and R. Ramesh, *Phys. Today*, 2010, **63**, 38.
155. D. Khomskii, *Physics*, 2009, **2**, 20.
156. Y.-Q. Tian, Y.-M. Zhao, H.-J. Xu, and C.-Y. Chi, *Inorg. Chem.*, 2007, **46**, 1612.
157. M.-Y. Li, PhD Thesis, Peking University, 2011.
158. K.-L. Hu, PhD Thesis, Peking University, 2010.
159. Z.-M. Wang, R. Shang, K.-L. Hu, Z.-C. Jiang and S. Gao, *The 13th International Conference on Molecule-based Magnetism*, Florida, United States, October, 2012.
160. Z. M. Wang and S. Gao, *The 1st Asian Conference of Coordination Chemistry*, Okazaki, Japan, July, 2007.
161. Z.-C. Jiang, BSc Thesis, Peking University, 2007.
162. M.-Y. Li, M. Kurmoo, Z.-M. Wang, and S. Gao, *Chem. Asian J.*, 2011, **6**, 3084.
163. Z.-M. Wang, X.-Y. Zhang, S. R. Batten, M. Kurmoo, and S. Gao, *Inorg. Chem.*, 2007, **46**, 8439.
164. K. S. Hagen, S. G. Naik, B. H. Huynh, A. Masello, and G. Christou, *J. Am. Chem. Soc.*, 2009, **131**, 7516.
165. J.-P. Zhao, B.-W. Hu, F. Lloret, J. Tao, Q. Yang, X.-F. Zhang, and X.-H. Bu, *Inorg. Chem.*, 2010, **49**, 10390.
166. L. Cañadillas-Delgado, O. Fabelo, J. A. Rodríguez-Velamazán, M. Lemée-Cailleau, S. A. Mason, E. Pardo, F. Lloret, J. Zhao, X. Bu, V. Simonet, C. V. Colin, and J. Rodríguez-Carvajal, *J. Am. Chem. Soc.*, 2012, **134**, 19772.
167. Y.-Q. Tian, S.-Y. Yao, Y.-J. Guo, Y. Song, and G. Zhang, *Chin. J. Inorg. Chem.*, 2010, **26**, 385.
168. B. Liu, H.-B. Zheng, Z.-M. Wang, and S. Gao, *CrystEngComm.*, 2011, **13**, 5285.
169. B. Liu, PhD Thesis, Peking University, 2013.
170. X. Ma, J. Tian, H.-Y. Yang, K. Zhao, and X. Li, *J. Solid State Chem.*, 2013, **201**, 172.
171. A. Rossin, G. Giambastiani, M. Peruzzini, and R. Sessoli, *Inorg. Chem.*, 2012, **51**, 6962.
172. M.-Y. Li, B. Liu, B.-W. Wang, Z.-M. Wang, S. Gao, and M. Kurmoo, *Dalton Trans.*, 2011, **40**, 6038.
173. I. Dzyaloshinsky, *J. Phys. Chem. Solid*, 1958, **4**, 241.
174. T. Moriya, *Phys. Rev.*, 1960, **120**, 91.
175. T. Moriya, in 'Magnetism', eds G. T. Rado and H. Suhl, Academic Press, New York, 1963, Vol. **1**, p.85.
176. K. Christensen and N. R. Moloney, 'Complexity and Criticality', Imperial College Press, London, 2005.
177. A. Sur, J. L. Lebowitz, J. Marro, M. H. Kalos, and S. Kirkpatrick, *J. Stat. Phys.*, 1976, **15**, 345.
178. K. Zenmyoa, H. Kuboa, M. Tokitaa, K. Takedab, and K. Yamagata, *J. Magn. Magn. Mater.*, 2004, **277**, 281.
179. K. Takeda, O. Fujita, M. Hitaka, M. Mito, T. Kawae, Y. Higuchi, H. Deguchi, Y. Muraoka, K. Zenmyo, H. Kubo, M. Tokita, and K. Yamagata, *J. Phys. Soc. Japan*, 2000, **69**, 3696.
180. A. G. Leyva, G. Polla, D. Vega, R. Baggio, P. K. de Perazzo, M. A. R. de Benyacar, and M. T. Garland, *J. Solid State Chem.*, 2001, **157**, 23.
181. J. M. Clemente-Juan, E. Coronado, and A. Gaita-Ariño, *Chem. Soc. Rev.*, 2012, **41**, 7464.
182. T. Glaser, *Chem. Commun.*, 2011, **47**, 116.
183. D. N. Woodruff, R. E. P. Winpenny, and R. A. Layfield, *Chem. Rev.*, 2013, **113**, 5110.
184. R. Sessoli and A. K. Powell, *Coord. Chem. Rev.*, 2009, **253**, 2328.
185. H.-L. Cai, Y. Zhang, D.-W. Fu, W. Zhang, T. Liu, H. Yoshikawa, K. Awaga, and R.-G. Xiong, *J. Am. Chem. Soc.*, 2012, **134**, 18487.
186. D.-W. Fu, H.-L. Cai, Y.-M. Liu, Q. Ye, W. Zhang, Y. Zhang, X.-Y. Chen, G. Giovannetti, M. Capone, J.-Y. Li, and R.-G. Xiong, *Science*, 2013, **339**, 425.
187. W. Zhang, H.-Y. Ye, H.-L. Cai, J.-Z. Ge, R.-G. Xiong, and S. D. Huang, *J. Am. Chem. Soc.*, 2010, **132**, 7300.
188. A. Stroppa, P. Jain, P. Barone, M. Marsman, J. M. Perez-Mato, A. K. Cheetham, H. W. Kroto, and S. Picozzi, *Angew. Chem., Int. Ed.*, 2011, **50**, 5847.
189. A. Stroppa, P. Barone, P. Jain, J. M. Perez-Mato, and S. Picozzi, *Adv. Mater.*, 2013, **25**, 2284.
190. R. I. Thomson, P. Jain, A. K. Cheetham, and M. A. Carpenter, *Phys. Rev. B*, 2012, **86**, 214304-1.
191. T. Besara, P. Jain, N. S. Dalal, P. L. Kuhns, A. P. Reyes, H. W. Kroto, and A. K. Cheetham, *Proc. Natl. Acad. Sci.*, 2011, **108**, 6828.
192. T. Asaji and K. Ashitomi, *J. Phys. Chem. C*, 2013, **117**, 10185.
193. J.-C. Tan, P. Jain, and A. K. Cheetham, *Dalton Trans.*, 2012, **41**, 3949.

194. W. Li, M. R. Probert, M. Kosa, T. D. Bennett, A. Thirumurugan, R. P. Burwood, M. Parinello, J. A. K. Howard, and A. K. Cheetham, *J. Am. Chem. Soc.*, 2012, **134**, 11940.

195. M. Viertelhaus, P. Adler, R. Clérac, C. E. Anson, and A. K. Powell, *Eur. J. Inorg. Chem.*, 2005, 692.

196. Z.-M. Wang, B. Zhang, H. Fujiwara, H. Kobayashi, and M. Kurmoo, *Chem. Commun.*, 2004, 416.

197. Z.-M. Wang, B. Zhang, H. Fujiwara, T. Otsuka, H. Kobayashi and M. Kurmoo, *The 6th Conference of the Asian Crystallographic Association*, Hong Kong, China, 2004.

198. B. Zhang, Z.-M. Wang, M. Kurmoo, S. Gao, K. Inoue, and H. Kobayashi, *Adv. Funct. Mater.*, 2007, **17**, 577.

199. J. A. Stride, M. Kurmoo, and Z.-M. Wang, *Phys. B-Condens. Matter*, 2006, **385**, 465.

200. Z.-M. Wang, Y. Zhang, T. Liu, M. Kurmoo, and S. Gao, *Adv. Funct. Mater.*, 2007, **17**, 1523.

201. Z.-M. Wang, B. Zhang, M. Kurmoo, M. A. Green, H. Fujiwara, T. Otsuka, and H. Kobayashi, *Inorg. Chem.*, 2005, **44**, 1230.

202. Z.-M. Wang, Y. Zhang, M. Kurmoo, T. Liu, S. Vilminot, B. Zhao, and S. Gao, *Aust. J. Chem.*, 2006, **59**, 617.

203. D. N. Dybtsev, H. Chun, S. H. Yoon, D. Kim, and K. Kim, *J. Am. Chem. Soc.*, 2004, **126**, 32.

204. H. Kim, D. G. Samsonenko, M. Yoon, J. W. Yoon, Y. K. Hwang, J.-S. Chang, and K. Kim, *Chem. Commun.*, 2008, 4697.

205. D. G. Samsonenko, H. Kim, Y. Sun, G.-H. Kim, H.-S. Lee, and K. Kim, *Chem. Asian J.*, 2007, **2**, 484.

206. K. Li, D. H. Olson, J. Y. Lee, W. Bi, K. Wu, T. Yuen, Q. Xu, and J. Li, *Adv. Funct. Mater.*, 2008, **18**, 2205.

207. J. A. Rood, B. C. Noll, and K. W. Henderson, *Inorg. Chem.*, 2006, **45**, 5521.

208. Z.-M. Wang, B. Zhang, Y. J. Zhang, M. Kurmoo, T. Liu, S. Gao, and H. Kobayashi, *Polyhedron*, 2007, **26**, 2207.

209. H.-B. Cui, K. Takahashi, Y. Okano, H. Kobayashi, Z.-M. Wang, and A. Kobayashi, *Angew. Chem., Int. Ed.*, 2005, **44**, 6508.

210. H.-B. Cui, Z.-M. Wang, K. Takahashi, Y. Okano, H. Kobayashi, and A. Kobayashi, *J. Am. Chem. Soc.*, 2006, **128**, 15074.

211. W. Fujita, K. Kikuchi, and W. Mori, *Chem. Asian J.*, 2012, **7**, 2830.

212. Y.-L. Fu, J.-L. Ren, Z.-W. Xua, and S. W. Ng, *Acta Cryst.*, 2005, **E61**, m2395.

213. O. Sengupta, Y. Song, and P. S. Mukherjee, *Dalton Trans.*, 2009, 10343.

214. T.-W. Wang, J. Wang, S.-i. Ohkoshi, Y. Song, and X.-Z. You, *Inorg. Chem.*, 2010, **49**, 7756.

215. M. Okubo, K. Kagesawa, Y. Mizuno, D. Asakura, E. Hosono, T. Kudo, H. Zhou, K. Fujii, H. Uekusa, S.-i. Nishimura, A. Yamada, A. Okazawa, and N. Kojima, *Inorg. Chem.*, 2013, **52**, 3772.

216. Y.-F. Zeng, X. Hu, F.-C. Liu, and X.-H. Bu, *Chem. Soc. Rev.*, 2009, **38**, 469.

217. X.-Y. Wang, L. Wang, Z.-M. Wang, and S. Gao, *J. Am. Chem. Soc.*, 2006, **128**, 674.

218. O. Sengupta and P. S. Mukherjee, *Inorg. Chem.*, 2010, **49**, 8583.

219. Y.-F. Zeng, X. Hu, J.-P. Zhao, B.-W. Hu, E. C. Sañudo, F.-C. Liu, and X.-H. Bu, *Chem. Eur. J.*, 2008, **14**, 7127.

220. T. Liu, Y.-J. Zhang, Z.-M. Wang, and S. Gao, *Inorg. Chem.*, 2006, **45**, 2782.

221. J. L. Manson, J. G. Lecher, J. Gu, U. Geiser, J. A. Schlueter, R. Henning, X. Wang, A. J. Schultz, H.-J. Koo, and M.-H. Whangbo, *Dalton Trans.*, 2003, 2905.

222. M. Barquín, M. J. G. Garmendia, L. Larrínaga, E. Pinilla, and M. R. Torres, *Z. Anorg. Allg. Chem.*, 2005, **631**, 2210.

223. J. L. Manson, T. Lancaster, L. C. Chapon, S. J. Blundell, J. A. Schlueter, M. L. Brooks, F. L. Pratt, C. L. Nygren, and J. S. Qualls, *Inorg. Chem.*, 2005, **44**, 989.

224. J. Overgaard, E. Rentschler, G. A. Timco, and F. K. Larsen, *ChemPhysChem*, 2004, **5**, 1755.

225. A. S. Lytvynenko, S. V. Kolotilov, O. Cador, K. S. Gavrilenko, S. Golhen, L. Ouahab, and V. V. Pavlishchuk, *Dalton Trans.*, 2009, 3503.

226. X.-Y. Wang, H.-Y. Wei, Z.-M. Wang, Z.-D. Chen, and S. Gao, *Inorg. Chem.*, 2005, **44**, 572.

227. Y. Wang, R. Cao, W. Bi, X. Li, D. Yuan, and D. Sun, *Microporous Mesoporous Mater.*, 2006, **91**, 215.

228. X.-Y. Wang, Z.-M. Wang, and S. Gao, *Chem. Commun.*, 2007, 1127.

229. Z.-X. Li, J.-P. Zhao, E. C. Sañudo, H. Ma, Z.-D. Pan, Y.-F. Zeng, and X.-H. Bu, *Inorg. Chem.*, 2009, **48**, 11601.

230. B.-W. Hu, J.-P. Zhao, Q. Yang, X.-F. Zhang, and X.-H. Bu, *Sci China B Chem.*, 2009, **52**, 1451.

231. J.-P. Zhao, B.-W. Hu, Q. Yang, X.-F. Zhang, T.-L. Hu, and X.-H. Bu, *Dalton Trans.*, 2010, **39**, 56.

232. J.-P. Zhao, B.-W. Hu, Q. Yang, T.-L. Hu, and X.-H. Bu, *Inorg. Chem.*, 2009, **48**, 7111.

233. J. Zhang, S. Chen, H. Valle, M. Wong, C. Austria, M. Cruz, and X. Bu, *J. Am. Chem. Soc.*, 2007, **129**, 14168.

234. R. Morris and X. Bu, *Nat. Chem.*, 2010, **2**, 353.

235. J. Zhang, S. Chen, R. A. Nieto, T. Wu, P. Feng, and X. Bu, *Angew. Chem., Int. Ed.*, 2010, **49**, 1267.

236. B. Biswas, S. Khanra, T. Weyhermüller, and P. Chaudhuri, *Chem. Commun.*, 2007, 1059.

237. E. K. Brechin, *Chem. Commun.*, 2005, 5141.

238. G. Aromí and E. K. Brechin, *Struct. Bond.*, 2006, **122**, 1.

239. T. Liu, Y.-J. Zhang, Z.-M. Wang, and S. Gao, *J. Am. Chem. Soc.*, 2008, **130**, 10500.

240. J. He, Y. Zhang, Q. Pan, J. Yu, H. Ding, and R. Xu, *Microporous Mesoporous Mater.*, 2006, **90**, 145.

241. T. Loiseau, L. Lecroq, C. Volkringer, J. Marrot, G. Férey, M. Haouas, F. Taulelle, S. Bourrelly, P. L. Llewellyn, and M. Latroche, *J. Am. Chem. Soc.*, 2006, **128**, 10223.

242. O. M. Yaghi, H. Li, and T. L. Groy, *J. Am. Chem. Soc.*, 1996, **118**, 9096.

243. B. Chen, Y. Yang, F. Zapata, G. Lin, G. Qian, and E. B. Lobkovsky, *Adv. Mater.*, 2007, **19**, 1693.

244. S. S.-Y. Chui, S. M.-F. Lo, J. P. H. Charmant, A. G. Orpen, and I. D. Williams, *Science*, 1999, **283**, 1148.

245. Z.-M. Zhang, S. Yao, Y.-G. Li, R. Clérac, Y. Lu, Z.-M. Su, and E.-B. Wang, *J. Am. Chem. Soc.*, 2009, **131**, 14600.

Metal-Organic Frameworks from Single-Molecule Magnets

Athanassios D. Katsenis

National and Kapodistrian University of Athens, Athens, Greece

Euan K. Brechin

The University of Edinburgh, Edinburgh, UK

and

Giannis S. Papaefstathiou

National and Kapodistrian University of Athens, Athens, Greece

1	Introduction	245
2	2D MOFs from SMMs	247
3	3D MOFs from SMMs	253
4	Conclusion	255
5	Related Articles	256
6	Abbreviations and Acronyms	256
7	References	257

1 INTRODUCTION

During the last three decades, the field of molecular materials science has emerged from the bases set by classical molecular chemistry.[1–3] It is not only the ease of synthesis that makes molecular materials desirable, but the opportunity that they offer to finely tune properties by selecting the correct ingredients that these species are made of. Since most molecular materials are crystalline solids, the way that they are distributed in the solid state largely affects their properties. To this end, the principles set by supramolecular chemistry and crystal engineering provide the tools to control the synergistic effects between the molecules and finally tune the properties of the bulk molecular material.[4–6]

Metal–organic frameworks (MOFs) have emerged within the realm of the molecular world as leading materials for a series of industrial applications.[7] MOFs are crystalline hybrid organic–inorganic solids built from organic molecules and inorganic building blocks (metal ions or metal clusters) connected in space through coordination bonds to create extended polymeric frameworks. In other words, MOFs are polymeric coordination complexes often called coordination polymers. Contrary to the purely inorganic polymers (i.e., zeolites), MOFs are made under mild conditions (e.g., solution chemistry, solvothermal synthesis at low temperatures <300 °C) which are in general high yielding and scalable, features that make MOFs attractive targets for technological applications. The major advantage of MOFs over other traditional polymeric materials, such as zeolites, is the greater scope for tailoring these materials for specific applications, which is feasible because of their modular synthesis.[4] Their inherent modularity (i.e., the ability to modify the organic and/or inorganic components) imparts unique properties for a wide range of potential applications including gas storage, separation, catalysis, and sensing, placing them among the most interesting classes of solid-state materials.[8]

The easiest way to make a coordination polymer is to extend the coordination geometry of a metal ion using a linear organic bridge.[9] The coordination preferences of

Metal-Organic Framework Materials. Edited by Leonard R. MacGillivray and Charles M. Lukehart.
© 2014 John Wiley & Sons, Ltd. ISBN 978-1-119-95289-3

the metal ion and the steric requirements of the organic bridge dictate the way that the inorganic and the organic components will assemble to form the extended framework. At the early stages of this chemistry, the construction of topologically interesting frameworks of increasing dimensionality and complexity dominated.[10,11] While the field of coordination polymers was growing, pioneering work at the beginning of the century gave a new boost and a new outlook in this chemistry. Polynuclear metal complexes (i.e., metal clusters), in the form of oligonuclear metal carboxylates, were employed in MOF synthesis, instead of single metal ions.[12] In contrast to single metal ions, the metal clusters provided a means to fix the coordination environment around the nodes while the clusters imparted rigidity on the structures of the frameworks, giving rise to highly stable porous solids.

Polynuclear metal complexes or metal clusters existed before MOFs and constitute a distinctive field within the context of coordination chemistry.[13] Metal clusters are discrete entities consisting of at least three metal ions that are bridged by organic ligands. Over the years, several synthetic strategies have been developed for the isolation of such species,[14] with the "serendipitous self-assembly" of suitable bridging and terminal ligands with metal ions remaining the most prominent and productive approach.[13] Clusters based on paramagnetic metal ions are of special interest as they provide a means to study the magnetic properties originating from the intramolecular exchange coupling of the individual spin carriers (i.e., metal ions), which are in close proximity within the cluster. In 1993, the first polynuclear metal complex capable of storing magnetic information at the molecular level was discovered, and since then, many such complexes have been shown to act in a similar manner.[15,16] The literature pertaining to clusters built from paramagnetic metal ions can often be rather difficult to navigate for the nonspecialist, as the terminology employed (a blight on much modern chemistry!) can be a little confusing. Most commonly, these species are referred to as single-molecule magnets (SMMs) and molecular nanomagnets (MNMs).[17] The latter is a generic term that refers to any molecule possessing any interesting magnetic properties, whereas the former specifically refers to molecules that are bistable, exhibiting slow relaxation of the magnetization and hysteresis loops in magnetization versus field sweeps, below their blocking temperature (T_B), that are purely of molecular origin. In transition metal-based SMMs, this bistability originates from a (relatively) large spin ground state (S) that is split in zero field such that its largest $\pm M_s$ levels lie lowest in energy and its smallest $\pm M_s$ states highest in energy (a negative axial zero-field splitting, D). The resultant energy barrier (U) to reorient "spin-up" to "spin-down" is given by $S^2|D|$ and $(S^2-1/4)|D|$ for integer and noninteger spins, respectively. Relaxation proceeds via a thermally activated process ("up and over" the energy barrier) and via tunneling through the barrier (magnetic quantum tunneling, MQT).[18] Experimentally, this relaxation process is most easily determined through observation of temperature and frequency-dependent out-of-phase (χ'') AC susceptibility signals, as hysteresis is often not observed above 2 K, the temperature limit of most commercial SQUID magnetometers. An Arrhenius analysis of the AC data provides access to the effective barrier to magnetization relaxation (U_{eff}), which is normally a little smaller than the theoretical upper limit (U) due to the presence of MQT, a shortcut to magnetization reversal.

Although the magnetic properties of SMMs are of molecular origin, in the solid state, crystal-packing effects, which include weak interactions (e.g., hydrogen bonding and $\pi\cdots\pi$ interactions), may influence their magnetic response, especially at low temperatures. A decade ago, the tetranuclear SMM $[Mn_4O_3Cl_4(O_2CEt)_3(py)_3]$ was reported to form a supramolecular dimer in the solid state held together by six C–H···Cl bonds and one Cl···Cl interaction.[19] Although both the C–H···Cl and the Cl···Cl interactions are very weak, they induce antiferromagnetic coupling between the two SMMs resulting in different quantum behavior from that of the individual SMMs. Each $[Mn_4]$ within the dimer acts as a field bias on its neighbor, shifting the MQT resonances to new positions relative to the isolated $[Mn_4]$ molecules. More recently, similar behavior was also observed in a family of $[Mn^{III}{}_3O(R\text{-}sao)_3(X)(L)_{3-4}]$ ($saoH_2$ = salicylaldoxime; R = Et, Ph; X = RCO_2^-, ClO_4^-; L = solvent) SMMs.[20] The $[Mn_3]$ molecules self-assemble to form one-dimensional (1D), two-dimensional (2D), and three-dimensional (3D) hydrogen-bonded frameworks through multiple O–H···O and/or C–H···π interactions. Single crystal hysteresis loop measurements (Figure 1) demonstrated that these interactions are strong enough to cause a clear field bias, but too weak to transform the spin networks into classical antiferromagnets. The above results of exchange-coupled SMMs demonstrate that MQT can be controlled using weak exchange interactions, suggesting that supramolecular chemistry can be exploited to modulate the quantum physics of SMMs.

It is becoming self-evident that linking SMMs may alter their magnetic response providing access to materials with fascinating physical properties. In addition, the perspective of constructing MOFs from SMMs may also lead to dual- or multifunctional materials combing the inherent magnetic properties of the cluster-SMMs with the porosity of the framework, opening new frontiers in molecular magnetism and molecular recognition by offering the ability to study the interplay between magnetism and encapsulation of species within such frameworks. The controlled aggregation and organization of magnetic building blocks into designed 0–3D architectures, combining two fundamentally important and exciting areas of modern

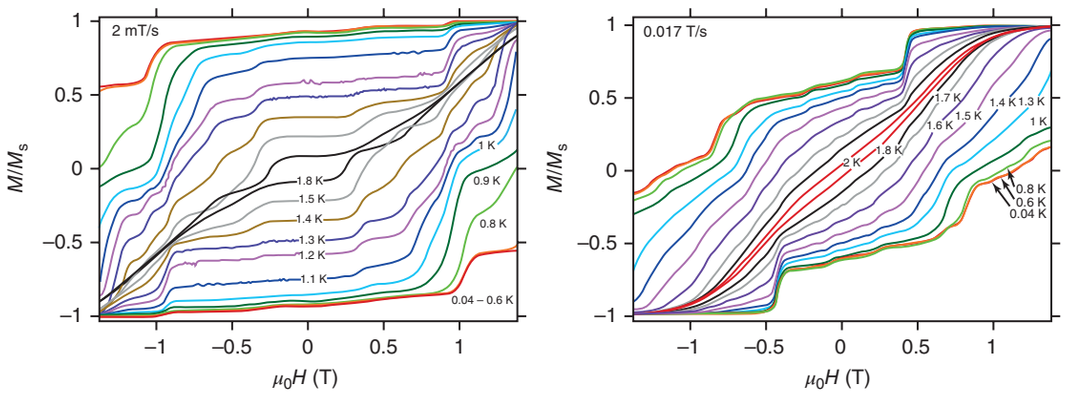


Figure 1 Magnetization versus field hysteresis loops, measured along the easy axis of magnetization, for a single crystal of $[Mn^{III}_3O(Et\text{-}sao)_3(ClO_4)(MeOH)_3]$ (left) and $[Mn_3O(Et\text{-}sao)_3(\mu_2\text{-}O_2Ph(CF_3)_2)(CH_3CH_2OH)(H_2O)_3]$ (right) at the indicated temperatures and field sweep rates. *M* is normalized to its saturation value

chemistry—molecular magnetism and supramolecular chemistry, is an extremely important facet of modern inorganic chemistry as such materials have long-term potential in areas that transcend chemistry, physics, and biology. Applications for molecule-based magnetic materials can be envisioned in low-temperature refrigeration, information storage, spintronics, molecular recognition, sensing and separations, biocompatible agents for use as contrast and polarizing agents in magnetic resonance imaging (MRI), and as agents for magnetic hyperthermic treatments. However, in order to make such applications feasible and to exploit the inherently interesting physics demonstrated by molecular magnets, they need to be easily addressable, that is, they should be organized in both the solution and the solid state. This is nontrivial. One potential way to circumvent this problem is to preorganize the magnets in the solid state by converting them into 1–3D arrays. The added bonus of this approach is that the scientist can choose to make the linker units innocent or noninnocent, the former maintaining the molecule-only properties, the latter offering adding functionality through intermolecular interactions that can be switched on and off.

While several 2D frameworks and many more 1D systems have been reported, literature examples of 3D SMM-MOFs are few and far between.[21] The purpose of this account is not to be comprehensive in listing all such examples, but rather to highlight some important/interesting examples possessing 2D and 3D networks while, when appropriate, introducing some pertinent 1D systems. We analyze the topological features of these systems providing details on some synthetic aspects and highlighting their basic magnetic properties.

2 2D MOFS FROM SMMS

2.1 MOFs based on $[Mn^{III}_3]$ and $[Mn^{III}_6]$ SMMs

Among a plethora of manganese clusters known today, the families of hexanuclear and trinuclear Mn^{III} SMMs of general formulae $[Mn^{III}_6O_2(R\text{-}sao)_6(O_2CR)_2(L)_{4-6}]$[22] ($[Mn_6]$) and $[Mn^{III}_3O(R\text{-}sao)_3(X)(L)_{3-4}]$[23] ($[Mn_3]$) ($saoH_2$ = salicylaldoxime; R = H, Me, Et etc; X = RCO_2^-, ClO_4^-; L = solvent) hold a prominent position as they contain more than 30 members each, allowing detailed magnetostructural correlations to be performed. The disklike triangular clusters consist of an $[Mn^{III}_3(\mu_3\text{-}O)]^{7+}$ core with three R-sao^{2-} ligands bridging the Mn^{III} ions along the edges of the triangle, whereas the anions and the solvent molecules are placed on either side of the disk, occupying the Jahn–Teller (JT) axes of the Mn^{III} ions. The hexanuclear clusters can be considered as two fused $[Mn_3]$ disks with the carboxylate anions and the solvent molecules occupying the two sides of the $[Mn^{III}_6(\mu_3\text{-}O)_2(R\text{-}sao)_6]^{2+}$ core. Therefore, each $[Mn_3]/[Mn_6]$ cluster carries six potential open coordination sites, three on each side, which are available for coordination to exo-dentate ligands capable of bridging the clusters. It has also been demonstrated that it is possible to significantly increase the ground spin state from $S = 4$ to $S = 12$ in $[Mn_6]$ and from $S = 2$ to $S = 6$ in $[Mn_3]$, enhancing the effective energy barrier for magnetization reversal (U_{eff}) to record levels. The origin of the antiferromagnetic to ferromagnetic (AF→F) switch between the Mn^{III} ions arises from an intracluster structural distortion of the $[Mn_3]/[Mn_6]$ molecule induced by the twisting of the (–Mn–N–O–) ring, as evidenced by the significant increases in the Mn–N–O–Mn torsion angles observed when derivatized salicylaldoximes were employed.

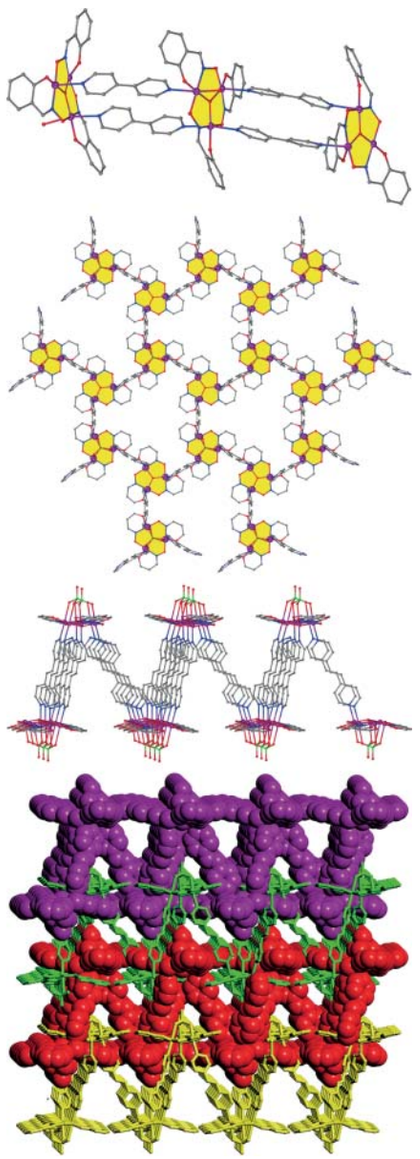


Figure 2 The structure of (**1**) (top), phase and side views of the layer in (**2**) and the supramolecular entanglement of the layers in (**2**) (bottom). All hydrogen atoms as well as many carbon atoms and solvent molecules have been removed for clarity. Color code: C, gray; O, red; N, blue; Mn, purple

Employment of the exo-dentate bridging ligands 4,4′-bipyridine (4,4′-bpy) and *trans*-1,2-bis(4-pyridyl)ethylene (4,4′-bpe) in $[Mn_3]$/$[Mn_6]$ chemistry afforded a 1D polymer and a 2D framework, respectively (Figure 2).[24,25] The $[Mn_3]$ triangles and the 4,4′-bpy ligands in $\{[Mn^{III}{}_3O(Et\text{-}sao)_3(4,4'\text{-}bpy)_2(MeOH)]ClO_4\}_n$ (**1**) have assembled to create a ladderlike $\{\text{-}[Mn_3]\text{-}(4,4'\text{-}bpy)_2\text{-}[Mn_3]\text{-}\}_n$ 1D polymer with two 4,4′-bpy molecules bridging between the $[Mn_3]$ disks. In $\{[Mn^{III}{}_3O(sao)_3(4,4'\text{-}bpe)_{1.5}]ClO_4\}_n$ (**2**), one 4,4′-bpe molecule is attached to each Mn^{III} ion, with all three being oriented on the same side of the $[Mn_3]$ disk, giving rise to the formation of an approximately 12.6 Å thick 2D framework possessing conical cavities within its body. Each cavity is big enough to host a $[Mn_3]$ unit from neighboring layers resulting in a unique interlocking of the layers that increases the dimensionality of the material from 2D to 3D. This supramolecular interlocking is based on host–guest and hydrogen bonding interactions and does not belong to the known topological and Euclidean entanglements.[26]

Although the $[Mn_3]$ core proved to be stable enough to maintain its structural integrity on reaction with pyridyl-type ligands, leading to polymeric materials, it achieved it by altering its local symmetry, which proved disadvantageous for the construction of magnetic materials, as the changes in the magnetic core dramatically reduced the Mn–N–O–Mn torsion angles resulting in the $[Mn_3]$ moieties within the materials possessing small or even diamagnetic spin ground states. In other words, the use of long pyridyl-type ligands flattened the triangular building blocks, promoting dominant AF exchange through the oximate bridges.

On the contrary, the employment of bis-carboxylate ligands, such as disodium iso-phthalate and disodium succinate, resulted in two polymeric species where the $[Mn_6]$ clusters retained their SMM behavior.[27] Complexes $[Mn^{III}{}_6O_2(Et\text{-}sao)_6(EtOH)_x(H_2O)_y(O_2C\text{–}Ph\text{–}CO_2)]_n$ (**3**) and $[Mn^{III}{}_6O_2(Et\text{-}sao)_6(EtOH)_4(H_2O)_2(O_2C\text{–}(CH_2)_2\text{–}CO_2)]_n$ (**4**) (x+y = 6, $HO_2C\text{–}Ph\text{–}CO_2H$ = isophthalic acid and $HO_2C\text{–}(CH_2)_2\text{–}CO_2H$ = succinic acid) are composed of $[Mn_6]$ SMMs spaced by the dicarboxylate ligands to create 1D coordination polymers. Following this approach, more bis-carboxylate-bridged 1D $[Mn_6]$ polymers were reported.[28–30] Since the incorporation of bis-carboxylate ligands resulted in polymeric species where the $[Mn_6]$ clusters retained their SMM behavior, higher dimensionality coordination polymers (i.e., 2D) were intentionally built from $[Mn_6]$ SMMs.[31] For this purpose, the tris-carboxylate ligand 1,3,5-benzene-tricarboxylic acid (trimesic acid, $tmaH_3$) was incorporated into blends of manganese/$saoH_2$ reaction mixtures. This reaction system was found to be sensitive to reaction conditions and, depending on the order that the starting materials were mixed, a 1D coordination polymer and a 2D framework were isolated. The structures of $[Mn_6O_2(sao)_6(tmaH)(MeOH)_{8.5}(H_2O)_{0.5}]_n$ (**5**) and $[Mn_6O_2(sao)_6(tma)_{0.66}(MeOH)_{3.33}(H_2O)_{1.33}]_n$ (**6**) are shown in Figure 3. Complex **5** consists of two types of $[Mn_6]$ clusters bridged by the $tmaH^{2-}$ ligands to form 1D chains. These chains are arranged in parallel, with the free carboxylic acids of the $tmaH^{2-}$ ligands participating in hydrogen bonding with neighboring chains, thus bridging them to create a 2D nonregular network with

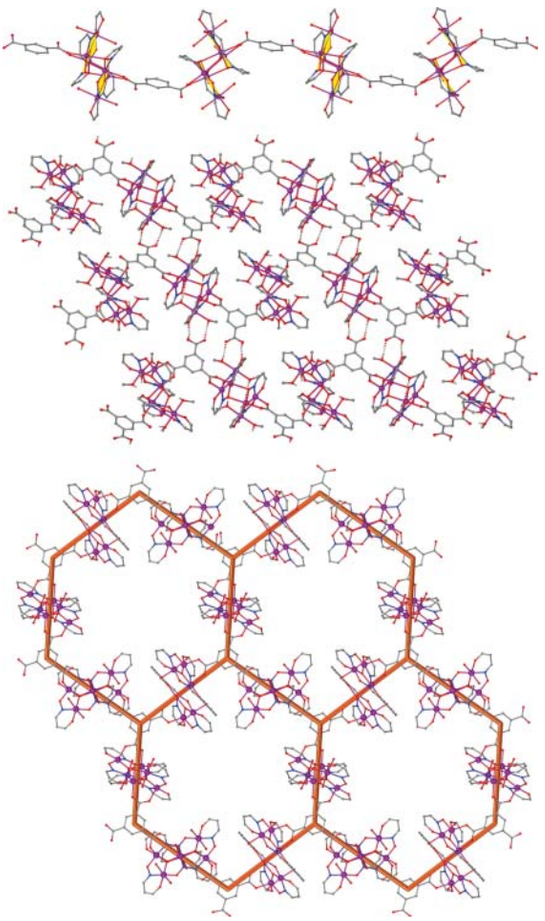


Figure 3 The structures of (**3**), (**5**), and (**6**) (from top to bottom). All hydrogen atoms as well as many carbon atoms and solvent molecules have been removed for clarity. Color code is same as in Figure 2

3,4L13 topology and point symbol $(4.6^2)_2(4^2.6^2.8^2)$. In this arrangement, the $[Mn_6]$ units serve either as bridges or as 4-connected nodes, and the $tmaH^{2-}$ ligands as 3-connected nodes. Complex (**6**) consists of three crystallographically independent $[Mn_6]$ clusters and tma^{3-} ligands that have assembled to create a regular (6,3) 2D framework with an **hcb** topology and point symbol 6^3, commonly known as honeycomb. In this inverted metal–organic framework (IMOF),[9] the tma^{3-} ligands serve as 3-connected nodes and the $[Mn_6]$ clusters as the spacers.

Alternating-current (AC) susceptibility measurements on (**3**), (**4**), (**5**), and (**6**) at low temperatures with the field oscillating at various frequencies were performed. A cusp in the real component χ' was found, which was accompanied by a nonzero imaginary component χ'' (Figure 4) at ~3.5, 4.3, 2.7, and 2.7 K for (**3**), (**4**), (**5**), and (**6**), respectively. The maxima for all complexes were strongly frequency-dependent, suggesting superparamagnetic blocking of the magnetization below the blocking temperatures (T_B), indicative of SMM behavior. Arrhenius plots constructed from the χ'' data afforded $\tau_0 = 1.6 \times 10^{-10}$ s and $U_{eff} = 48$ K for (**3**), $\tau_0 = 1.8 \times 10^{-10}$ s and $U_{eff} = 60$ K for (**4**), $\tau_0 = 3.3 \times 10^{-9}$ s and $U_{eff} = 32.84$ K for (**5**), and $\tau_0 = 5.6 \times 10^{-8}$ s and $U_{eff} = 24.54$ K for (**6**). The spin dynamics at low temperatures were investigated by calculating the frequency shift (k) of T_B. The presence of significant inter-$[Mn_6]$ interactions would be expected to slow down the spin dynamics at low temperatures and this would be manifested in a small frequency shift. Using the average T_B values of 3.5, 4.3, 2.7, and 2.69 K for (**3**), (**4**), (**5**), and (**6**), respectively, the frequency shift of T_B was calculated from $k = \Delta T_B \times (T_B \Delta \log f)^{-1}$, where ΔT_B is the change in T_B for the given change in frequency $\Delta \log f$, where $\Delta \log f = 2.4$ for (**3**) and (**4**) and 1.30 for (**5**) and (**6**). This provided values of 0.08 for (**3**) and (**4**), 0.19 for (**5**) and 0.24 for (**6**), which are within the range expected for ideal noninteracting superparamagnets ($0.1 \leq k \leq 1$) and close to those reported for the magnetically isolated $[Mn_6]$ complexes.[22] This suggests that the relaxation is in accordance with SMM behavior, and is not attributed to long-range interactions mediated through the polycarboxylate ligands.

2.2 MOFs based on $[Mn^{III}_2Mn^{II}_2]$ SMMs

Another interesting family of SMMs are those possessing the tetranuclear $[Mn^{III}_2Mn^{II}_2(\mu_3\text{-}O)_2(\mu\text{-}O)_4]$ core.[32] In this core, the four manganese ions are located at the corners of a defective double cubane (two cubanes sharing one face and each missing one vertex) and are either planar or very close to planarity. An interesting feature of this type of cluster is that the two Mn^{II} ions possess potentially open coordination sites (sites that terminal counter anions or solvent molecules are bound) enabling the clusters to be used as building blocks for the synthesis of extended frameworks. The exploitation of this type of cluster as building blocks has afforded four 2D frameworks, namely $\{[Mn_4(hmp)_6(dcn)_2](ClO_4)_2\}_n$ (**7**),[33] $\{[Mn_4(hmp)_4(Hpdm)_2(dcn)_2](ClO_4)_2\}_n$ (**8**),[33] $[Mn_4(hmp)_4Br_2(MeO)_2(dcn)_2]_n$ (**9**),[33] and $[Mn_4(hmp)_6\{Cu(pic)_2(ClO_4)_2\}_2]_n$ (**10**)[34] (Hhmp = 2-hydroxymethylpyridine, H_2pdm = pyridine-2,6-dimethanol, dcn^- = dicyanimide, Hpic = picolinic acid). Complexes (**9**) and (**10**) were synthesised by the reaction of a preisolated $[Mn^{III}_2Mn^{II}_2]$ SMM with sodium dicyanamide ($NaN(CN)_2$ or Nadcn) and copper picolinate $[Cu(pic)_2]\cdot 2H_2O$, respectively, whereas complexes (**7**) and (**8**) were isolated by a one-pot reaction from the starting materials in the presence of $NaN(CN)_2$. All complexes consist of a $[Mn^{III}_2Mn^{II}_2(\mu_3\text{-}O)_2(\mu\text{-}O)_4]$ core sitting on a center of inversion, which enforces planarity to the four manganese ions. The $[Mn^{III}_2Mn^{II}_2]$ units have assembled by either $N(CN)_2^-$

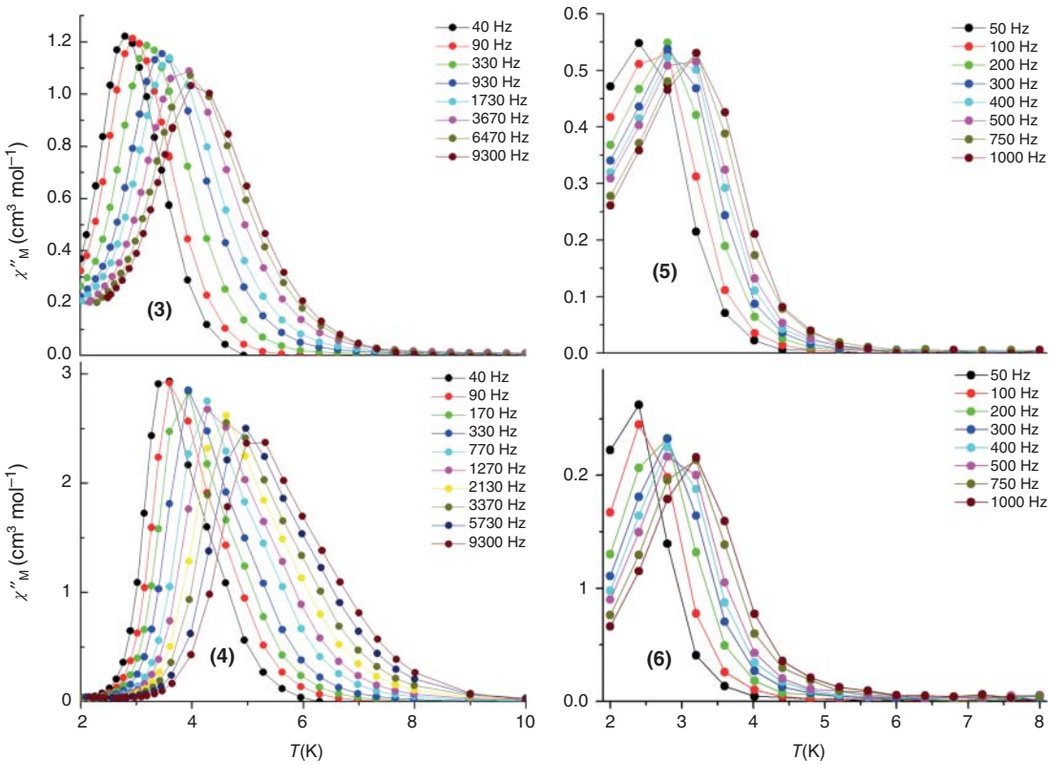


Figure 4 Plots of χ''_M versus T for complexes (**3**)–(**6**) at the indicated temperature and frequency ranges

(dcn$^-$) or $[Cu(pic)_2(ClO_4)_2]^{2-}$ anions to form 2D frameworks with an **sql** topology and point symbol $4^4.6^2$, commonly known as square grid (Figure 5). In this arrangement, the $[Mn^{III}_2Mn^{II}_2]$ units serve as four connected nodes with only the Mn^{II} ions acting as connection points while the dcn$^-$ or $[Cu(pic)_2(ClO_4)_2]^{2-}$ anions serve as linear bridges. Although the underlying networks of these 2D frameworks are the same, the $[Mn^{III}_2Mn^{II}_2]$ planes are oriented differently within the layers, a feature that largely affects the orientation of the JT axes of the Mn^{III} ions and subsequently the magnetic response of these materials. From the magnetic point of view, complexes (**8**) and (**10**) are best described as consisting of noninteracting SMMs (with $\tau_0 = 2.23 \times 10^{-7}$ s and $U_{eff} = 12.8$ K for (**8**) and $\tau_0 = 5.6 \times 10^{-10}$ s and $U_{eff} = 14$ K for (**10**)), whereas long-range magnetic order (canted antiferromagnetism) was observed for (**7**) below 4.6 K, and an interplay between SMM behavior and long-range magnetic order (canted antiferromagnetism) observed for complex (**9**) (see ***Functional Magnetic Materials Based on Metal Formate Frameworks***).

2.3 MOFs based on $[Mn^{III}_{11}Mn^{II}_6]$ SMMs

A rather unusual SMM comprising eleven Mn^{III} and six Mn^{II} ions was isolated serendipitously from the reaction of $Mn(O_2CCH_3)_2{\cdot}2H_2O$, $Mn(ClO_4)_2{\cdot}6H_2O$, NaN_3 and 1,3-propanediol (H_2pd) in a mixture of CH_3CN/pyridine (py).[35] This discrete entity was found to possess dominant ferromagnetic nearest-neighbor interactions between the metal centers giving rise to

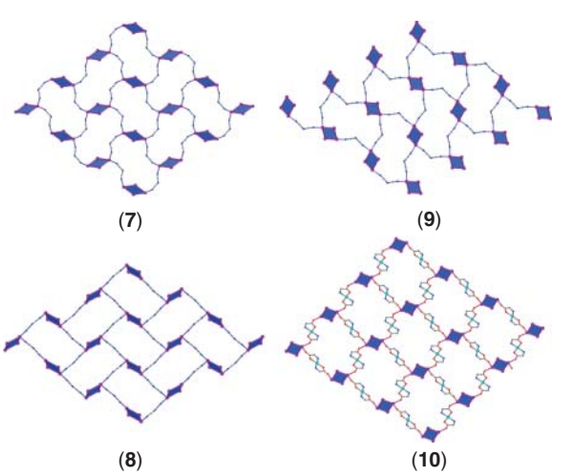


Figure 5 The structures of (**7**)–(**10**) emphasizing the $[Mn^{III}_2Mn^{II}_2]$ planes (blue rhombs) and the bridging anions (see text for details)

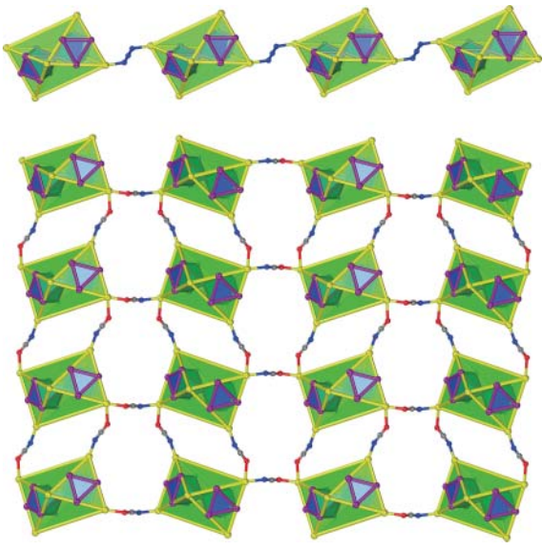


Figure 6 The structures of (**11**) (top) and (**12**) (bottom). Only the $[Mn^{III}{}_{11}Mn^{II}{}_{6}]$ core and the bridging anions are shown. Color code: C, gray; O, red; N, blue; Mn^{II}, yellow; Mn^{III}, purple

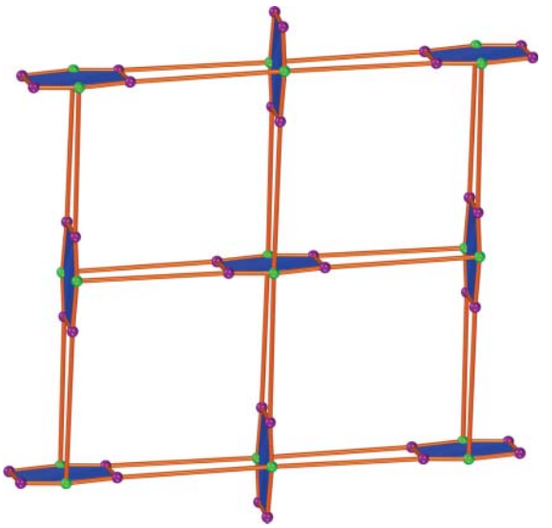


Figure 7 The doubly bridged nearly planar $[Co^{II}{}_{4}Ln^{III}{}_{2}]$ cores (in blue) in (**13**) and (**14**). Color code: Co, purple; Ln, green

a large spin ground state (of approximately $S \approx 37$). Single-crystal magnetization versus applied field studies revealed hysteresis loops below 0.7 K characteristic of SMM behavior; DC magnetization decay data affording $U_{eff} = 13$ K and $\tau_0 = 1.0 \times 10^{-13}$ s. By changing the reaction conditions, the 1D coordination polymer $[Mn_{17}O_8(N_3)_5(O_2CMe)(pd)_{10}(py)_6]_n$ (**11**) was obtained, whereas replacement of N_3^- by OCN^- resulted in the 2D MOF $[Mn_{17}O_8(OCN)_7(O_2CMe)_2(pd)_{10}(py)_4]_n$ (**12**) (Figure 6). Both polymeric species comprise the same core found in the discrete cluster. The $[Mn^{III}{}_{11}Mn^{II}{}_{6}]$ units in (**11**) are singly bridged by an end-on (EO) azide (N_3^-) to create a linear chain, whereas in (**12**), they are singly bridged by EO OCN^- anions to one dimension and doubly bridged by two EO OCN^- anions to the second dimension to form a 2D framework with an **sql** topology. None of the polymeric species exhibited any frequency dependence of their out-of-phase (χ'') AC susceptibility signals down to 1.8 K, suggestive of intercluster antiferromagnetic interactions.

2.4 MOFs based on [3d–4f] SMMs

Given that all paramagnetic lanthanide ions (Ln, 4f), except the f^7 and f^{14} congeners, possess anisotropic electron configurations, their incorporation within a 3d metal cluster may introduce enhanced anisotropy into the magnetic ground state of the molecule. Since anisotropy is vital in forming SMMs, the synthesis of such 3d–4f clusters is potentially exciting.[36] In line with these observations, two similar 2D MOFs comprising a $[Co^{II}{}_{4}Ln^{III}{}_{2}]$ core [Ln = Dy (**13**) or Ho (**14**)] were synthesized.[37] To this end, the bifunctional ligand 4′-(4-carboxyphenyl)-2,2′:6′,2″-terpyridine (HL), comprising a tridentate chelate terpyridine claw and a pendant carboxylic acid, was synthesized. Eight L^- anions wrap around the nearly planar $[Co^{II}{}_{4}Ln^{III}{}_{2}(CO_3)_4]^{6+}$ core with the carboxylate anions coordinated to the strongly Lewis acidic Ln^{III} ions and the terpyridine claws to Co^{II} ions. In this arrangement, a 2D framework with an **sql** topology forms from doubly bridged $[Co^{II}{}_{4}Ln^{III}{}_{2}]$ units in both directions (Figure 7). AC susceptibility measurements on (**13**) and (**14**) at low temperatures exhibited very weak frequency-dependent χ'' signals. When the AC susceptibility of **13** was repeated in the presence of an applied DC field, the χ'' maxima shifted to higher temperatures permitting calculation of $U_{eff} = 7.6$ K with $\tau_0 = 1.9 \times 10^{-6}$ s.

2.5 MOFs based on $[Dy^{III}{}_{2}]$ SMMs

Over the last decade, there has been a reignition of interest in Ln-based SMMs.[38,39] The large and unquenched orbital contribution to the magnetic moment and their numerous unpaired electrons potentially make paramagnetic Ln ions good candidates for constructing SMMs. However, as the 4f orbitals are contracted, the intramolecular exchange coupling in polynuclear Ln complexes is very weak and in most cases their magnetic properties are dominated by single-ion effects. A bifunctional ligand that promotes ferromagnetic interactions between Dy^{III} ions and leads to the isolation of a discrete $[Dy^{III}{}_{2}]$ SMM and a 2D framework composed of $[Dy^{III}{}_{2}]$ SMMs[40] is (2-hydroxy-3-methoxyphenyl)methylene (isonicotino)hydrazine (H_2hmi), a compartmental ligand able

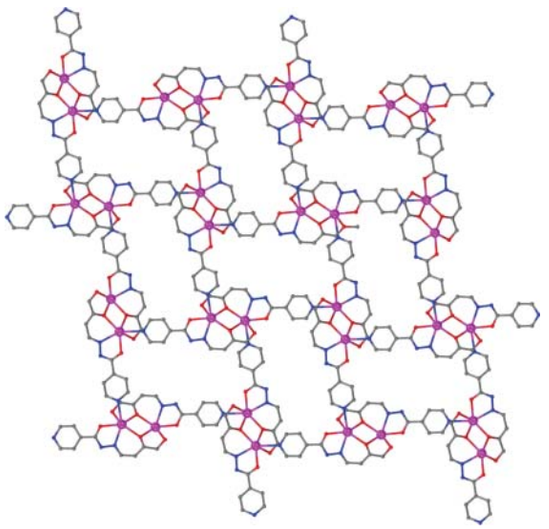


Figure 8 The structure of (**16**). All hydrogen atoms as well as many carbon atoms and solvent molecules have been removed for clarity. Color code: C, gray; O, red; N, blue; Dy, purple

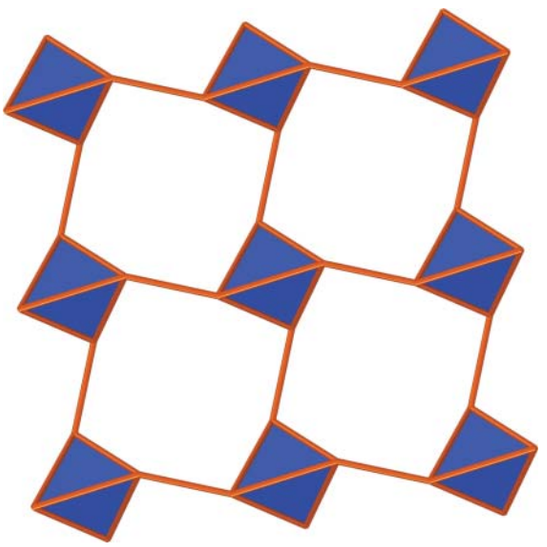


Figure 9 The augmented **sql** network in (**17**) and (**18**)

to host two Dy^{III} ions, and possessing a pendant pyridyl group capable of bridging the dinuclear units. The reaction of H_2hmi with $Dy(NO_3)_3{\cdot}5H_2O$ was found to be sensitive to reaction conditions, small changes leading to the discrete $[Dy_2(hmi)_2(NO_3)_2(MeOH)_2]$ (**15**) versus the 2D framework $[Dy_2(hmi)_2(NO_3)_2(MeOH)_2]_n$ (**16**). The two hmi^{2-} ligands in (**16**) wrap around the two Dy^{III} ions, being arranged in a head-to-tail manner with the pyridyl groups spanning across the Dy···Dy vector. In this arrangement, each $[Dy_2]$ unit serves as a linear bridge while it is bound to two pyridyl groups from neighboring dimers creating an **sql** network (Figure 8). Both DC magnetic susceptibility and magnetization measurements suggest the presence of intramolecular ferromagnetic interactions between the Dy^{III} ions. AC susceptibility measurements on (**15**) and (**16**) resulted in the calculation of U_{eff} and τ_0 values of 56 K and 3×10^{-7} s for (**15**) and 71 K and 7×10^{-8} s for (**16**).

2.6 MOFs based on $[Co^{II}_4]$ SMMs

Although octahedral Co^{II} ions can display large single-ion anisotropy and possess up to three unpaired electrons, Co^{II} SMMs are vastly outnumbered compared to those of Mn^{III}.[17] Two isomorphous 2D anionic frameworks based on $[Co^{II}_4]$ moieties were recently reported.[41] The $\{Cs_4[\mu\text{-}\{Co(glycol)(H_2O)_2\}\{Co_4(cit)_4\}]\}_n$ (**17**) and $\{Rb_4[\mu\text{-}\{Co(glycol)(H_2O)_2\}\{Co_4(cit)_4\}]\}_n$ (**18**) SMMs were prepared by treating a Co^{II} citrate (cit^{4-}) precursor with CsOH and RbOH, respectively, in the presence of ethylene glycol (glycol). The four Co^{II} ions and the four hydroxyl groups of the cit^{4-} anions within the $[Co_4(cit)_4]^{8-}$ core are arranged at alternate corners of a cube. All three carboxylate groups of the four cit^{4-} ligands provide peripheral ligation to the cubane core, whereas one carboxylate from each cit^{4-} ligand is further bonded to a $[Co(glycol)(H_2O)_2]^{2+}$ unit comprising an octahedral Co^{II} ion. In this arrangement, each $[Co_4(cit)_4]^{8-}$ unit is bound to four $[Co(glycol)(H_2O)_2]^{2+}$ while the latter simply bridges two $[Co_4(cit)_4]^{8-}$ units creating a 2D framework with an **sql** topology (Figure 9). The Cs^+, Rb^+, ethylene glycol, and H_2O molecules are differently disordered within the square cavities of (**17**) and (**18**), respectively, whereas the interlayer separation is 0.2 Å larger in (**17**) as compared to the respective interlayer separation in (**18**). The magnetic behaviors of (**17**) and (**18**) have been investigated from 300 K down to 90 mK. In each case, the ferromagnetically coupled $[Co_4]$ units within the 2D frameworks display SMM behavior manifested by frequency-dependent χ'' signals in out-of-phase AC susceptibility studies at approximately 4 K, with U_{eff} values of approximately 13 K. This is entirely analogous to that observed for molecular (0D) Co^{II} cubanes that are magnetically isolated and show little or no intermolecular interactions in the solid state. However, at lower temperatures, magnetic exchange between the cubane units and the single Co^{II} ions enforce a transition to a magnetically ordered phase between 0.20 and 0.25 K (see ***Functional Magnetic Materials Based on Metal Formate Frameworks***), the small differences in T_C being attributed to the difference in the nature of the s-block metal ion (Rb^+ or Cs^+) and the disordered solvent in the crystal lattice.

3 3D MOFs FROM SMMs

3.1 MOFs based on [Co^{II}_4] and [Co^{II}_5] SMMs

Further exploitation of the Co^{II} citrate chemistry led to the isolation of an anionic 3D MOF, which is based on [Co^{II}_4] cubanes and octahedral Co^{II} ions. $\{Na_4(H_2O)_{15}[\mu_3\text{-}\{Co(H_2O)_3\}_2\{Co_4(cit)_4\}]\}_n$ (**19**)[42] was obtained through the one-pot reaction of $CoSO_4{\cdot}7H_2O$, citric acid (H_4cit), and $(CH_3)_4NOH$ in H_2O. As in the previous 2D frameworks [complexes (**17**) and (**18**) in Section 2.6], (**19**) consists of $[Co_4(cit)_4]^{8-}$ cubanes and $[Co(H_2O)_3]^{2+}$ units comprising octahedral Co^{II} ions. Each $[Co_4(cit)_4]^{8-}$ is bound to six $[Co(H_2O)_3]^{2+}$, with the latter bridging three cubanes. In this arrangement, a 3D framework is constructed with an underlying topology of **ant** (anatase) and point symbol $(4^2.6)_2(4^4.6^2.8^8.10)$ (Figure 10). The DC magnetic susceptibility of (**19**) above 120 K is analogous to that observed for the magnetically isolated and structurally analogous [Co^{II}_4] SMMs, whereas below 20 K, ferromagnetic exchange between the [Co^{II}_4] unit and the single octahedral Co^{II} ions is observed. Frequency-dependent χ'' signals in out-of-phase AC susceptibility studies were observed below 6 K with an unusual crossover in the region ~3–4.5 K for AC oscillating fields in the range of 2–10 kHz, suggesting the presence of two relaxation processes. Magnetization versus applied field hysteresis loops, obtained on single crystals of (**19**) were observed below 0.6 K and were both temperature- and sweep-rate-dependent—having features different to those observed for discrete [Co^{II}_4] SMMs, suggesting the presence of intermolecular interactions to be an important contributory factor (see ***Functional Magnetic Materials Based on Metal Formate Frameworks***).

A similar $\{K_4(H_2O)_8[\{Co\}_2\{Co_4(Hcit)_2(cit)_2\}]\}_n$ (**20**)[43] anionic 3D framework with **ant** topology was obtained by the hydrothermal reaction of $Co(O_2CCH_3)_2{\cdot}4H_2O$ and citric acid in a H_2O/CH_3CH_2OH mixture in the presence of KOH. In this framework, the $[Co_4(Hcit)_2(cit)_2]^{6-}$ cubanes are connected to six tetrahedral Co^{II} ions, with the latter bridging three [Co^{II}_4] units. Magnetic measurements revealed that this framework is a canted antiferromagnet exhibiting antiferromagnetic interactions between the [Co^{II}_4] cubanes and the tetrahedral Co^{II} ions (see ***Functional Magnetic Materials Based on Metal Formate Frameworks***). Gas sorption isotherms for this 3D MOF revealed permanent microporosity with a Langmuir surface area of 939 $m^2\,g^{-1}$ and pore volume of 0.31 $cm^3\,g^{-1}$.

A 3D framework based on coplanar [Co^{II}_5] units was isolated under hydrothermal conditions from the reaction of $Co(NO_3)_2{\cdot}6H_2O$, benzophenone-2,4′-dicarboxylic acid (H_2bpdc), 1,4-diazabicyclo[2,2,2] octane (dabco), and KOH in H_2O.[44] $[Co_5(\mu_3\text{-}OH)_2(bpdc)_4(dabco)(H_2O)_2]$ (**21**) is built around a $[Co_5(\mu_3\text{-}OH)_2]^{8+}$ cluster comprising both octahedral and tetrahedral Co^{II} ions. The [Co^{II}_5] units are bridged by four $bpdc^{2-}$ dicarboxylates to form a square grid (**sql**) that is pillared by the neutral dabco ligands to create a **pcu** (primitive cubic, commonly known as α-Po) network with point symbol $4^{12}.6^3$ (Figure 11). The magnetic properties of the $[Co_5(\mu_3\text{-}OH)_2]^{8+}$ cluster are dominated by competing intramolecular antiferromagnetic exchange interactions. AC susceptibility measurements revealed a U_{eff} of 56.6 K with $\tau_0 = 8.74 \times 10^{-9}$ s, consistent with superparamagneticlike behavior. Nevertheless, further magnetic studies including zero-field-cooled (ZFC) and field-cooled (FC) magnetization measurements and hysteresis loop studies indicated the possible occurrence of long-range order consistent with a spin canted antiferromagnet.

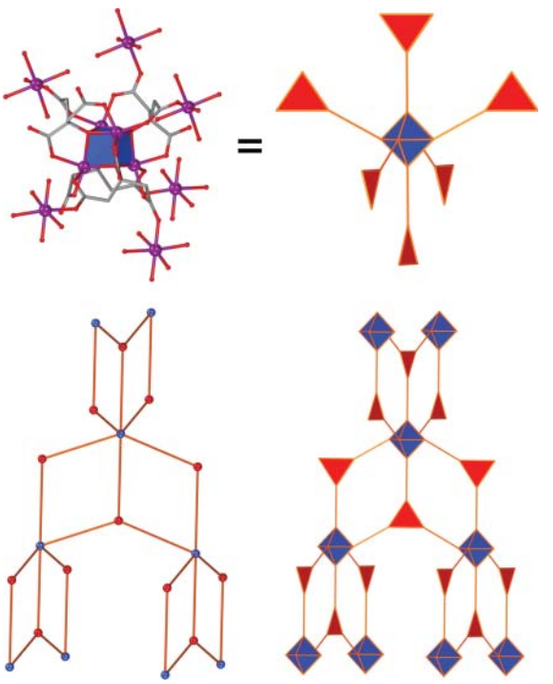


Figure 10 The augmented **ant** network found in (**19**) and (**20**)

3.2 MOFs based on [$Mn^{III}_2Mn^{II}_2$] SMMs

A 3D MOF based on the already-described [$Mn^{III}_2Mn^{II}_2$] core (Section 2.2) was obtained via the one-pot reaction between $Mn(ClO_4)_2{\cdot}6H_2O$ with Hhmp in CH_3CN in the presence of $NaN(CN)_2$ (Nadcn) and $(CH_3CH_2)_4NOH$.[45] $[Mn_4(hmp)_4(OH)_2Mn(dcn)_6]$ (**22**) consists of [$Mn^{III}_2Mn^{II}_2$] units and $[Mn(dcn)_6]^{4-}$ anions. As in the 2D frameworks (**7**)–(**10**), each of the two

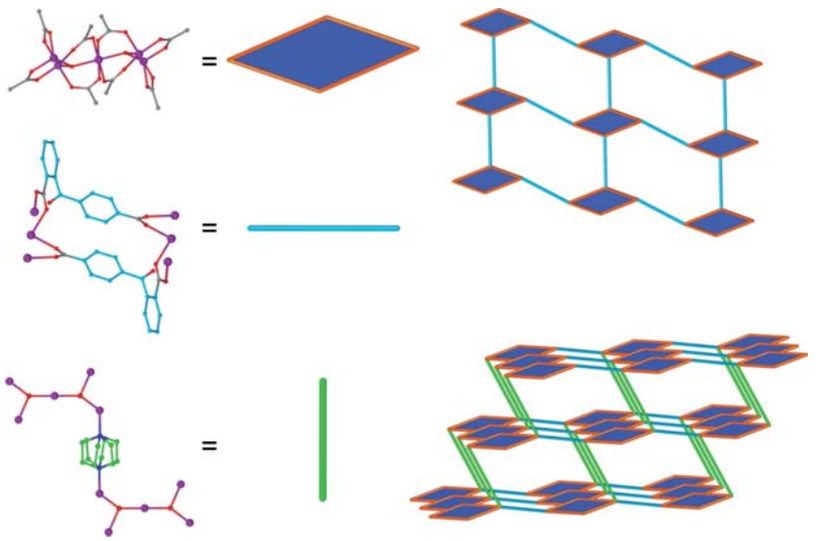


Figure 11 The pillared framework with a **pcu** topology found in (**21**)

Mn^{II} ions in the $[Mn^{III}_2Mn^{II}_2]$ moiety is bound to three dcn^- anions from three different $[Mn(dcn)_6]^{4-}$ units. In this arrangement, each $[Mn_4(hmp)_4(OH)_2]^{4+}$ is surrounded by six $[Mn(dcn)_6]^{4-}$ units with the latter also being surrounded by six $[Mn_4(hmp)_4(OH)_2]^{4+}$. Therefore, a six-connected **pcu** network forms (Figure 12), which is based on two different six-connected nodes (i.e., the $[Mn_4(hmp)_4(OH)_2]^{4+}$ and $[Mn(dcn)_6]^{4-}$ units). DC magnetic susceptibility measurements down to 30 K revealed the presence of ferromagnetic interactions within the $[Mn_4(hmp)_4(OH)_2]^{4+}$ core. AC magnetic susceptibility measurements revealed a frequency-independent peak in the in-phase (χ') and out-of-phase (χ'') signals at 4 and 4.1 K, respectively, indicating the presence of 3D magnetic ordering. Magnetization measurements at low applied fields below $T_C = 4.1$ K are consistent with an ordered ferrimagnetic phase in which the $S = 9$ $[Mn^{III}_2Mn^{II}_2]$ units are antiferromagnetically coupled with the $S = 5/2$ $[Mn^{II}(dcn)_6]^{4-}$ units.

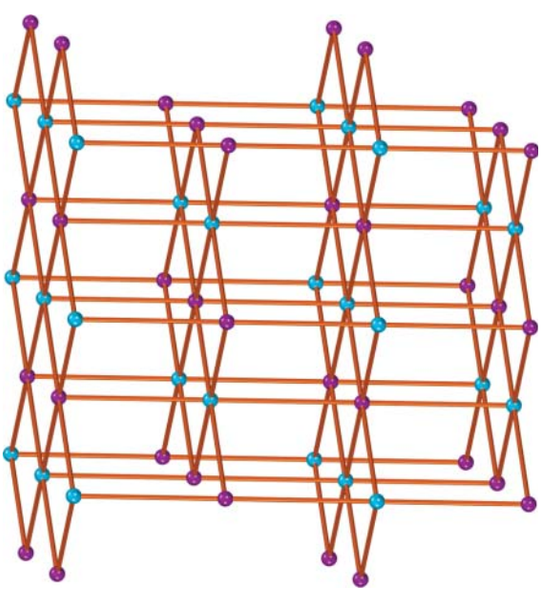


Figure 12 The **pcu** network found in (**22**). Light blue and purple spheres represent the six-connected $[Mn_4(hmp)_4(OH)_2]^{4+}$ and $[Mn(dcn)_6]^{4-}$, respectively

3.3 MOFs based on $[Mn^{II}Mn^{III}_3]_2$ SMMs

The new 3D framework $\{[Mn^{II}Mn^{III}_3O(Me\text{-}sao)_3(N_3)_3(dpp)_{1.5}]_2\}_n$ (**23**)[46] (dpp = 1,3-di-4-pyridylpropane, $saoH_2$ = salicylaldoxime) was obtained from the one-pot reaction of $Mn(ClO_4)_2{\cdot}6H_2O$ with Me-$saoH_2$ in a mixture of dimethylformamide/methanol in the presence of NaN_3. The $[Mn^{II}Mn^{III}_3]$ unit comprises the already-described disklike $[Mn^{III}_3(\mu_3\text{-}O)(R\text{-}sao)_3]^{2+}$ core (Section 2.1), which is capped by one Mn^{II} ion. The latter is connected to all three Mn^{III} ions through three EO N_3^-. Two such $[Mn^{II}Mn^{III}_3]$ units are loosely connected through the oximic oxygen atoms of the Me-sao^{2-} ligands ($Mn^{III}\cdots O$ distances of ~2.736 Å) to form a $[Mn^{II}Mn^{III}_3]_2$ cluster. Each Mn^{II} ion is further connected to three $N_{pyridyl}$ atoms from three different dpp ligands. In this arrangement, a **pcu** network forms, akin to those in Figures 11 and 12, with the $[Mn^{II}Mn^{III}_3]_2$ clusters serving as six-connected nodes and the dpp ligands as linear bridges. Two such **pcu** networks are grown within the empty cubic cavities of each other resulting in a 2-fold interpenetrated 3D

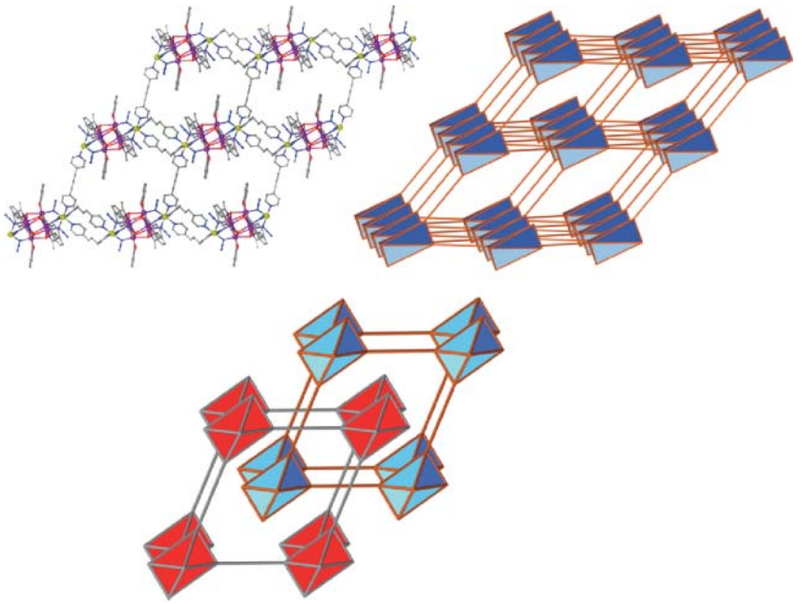


Figure 13 The two interpenetrated **pcu** networks in (**23**). Color code: C, gray; O, red; N, blue; Na, yellow; Mn, purple. Blue and red octahedra represent the $[Mn^{II}Mn^{III}{}_3]_2$ SMMs

framework (Figure 13) (see ***Interpenetration and Entanglement in Coordination Polymers***). Frequency-dependent χ'' signals were observed below ~4 K indicating superparamagneticlike behavior, with a temperature shift, $k = 0.13$ (the magnetic behavior is dominated by the molecules with little or no intermolecular interactions). Magnetization versus applied field hysteresis loops were observed below 1.8 K, which show stepwise magnetization and large coercivities, indicating significant quantum tunneling effects. Using both DC and AC decay data, the U_{eff} and τ_0 values of 37 K and 4.3×10^{-10} s were calculated, which are comparable to those calculated for complexes (**3**)–(**6**) (Section 2.1).

3.4 MOFs based on $[Mn^{III}{}_{12}Mn^{II}{}_7]$ SMMs

Two similar 3D frameworks comprising a $[Mn^{III}{}_{12}Mn^{II}{}_7]$ core were synthesized by the reaction of the trinuclear precursor $[Mn_3O(O_2CCH_3)_6(py)_3]\cdot py$ (py = pyridine) with either 1,3-propanediol (H_2pd) or 2-methyl-1,3-propanediol (H_2mpd) in CH_3CN.[47] $[Mn_{19}Na(\mu_4\text{-}O)_9(\mu_3\text{-}O)(\mu_3\text{-}OH)_3(O_2CMe)_9(pd)_9(H_2O)_3][OH]$ (**24**) and $[Mn_{19}Na(\mu_4\text{-}O)_9(\mu_3\text{-}O)(\mu_3\text{-}OH)_3(O_2CMe)_9(mpd)_9(H_2O)_3][OH]$ (**25**) have strikingly similar structures and magnetic properties. The Mn ions are arranged in a triangular-pyramidal-frustum manner, each being connected to three $[Na(O_2CCH_3)_6]^{5-}$ units, with the latter bridging three $[Mn^{III}{}_{12}Mn^{II}{}_7]$ clusters. In this arrangement, a 3D framework with an **srs** topology and point symbol 10^3 forms with both $[Mn^{III}{}_{12}Mn^{II}{}_7]$ and $[Na(O_2CCH_3)_6]^{5-}$ serving as three-connected nodes (Figure 14). Magnetization data below 10 K at various applied magnetic fields lead to the calculation of a large spin ground state $S \approx 23/2$ and a small but negative axial zero-field splitting parameter $D \approx -0.09\ \text{cm}^{-1}$. Single-crystal magnetization studies revealed hysteresis loops below 1.1 K with their coercivity increasing with decreasing temperature and increasing field sweep rate as expected for isolated SMMs.

4 CONCLUSION

In this account, we have reviewed those MOFs that are based on SMMs. Although both fields (i.e., MOFs and SMMs) have grown rapidly over the last two decades, SMM-based MOFs remain extremely rare with those possessing a 3D framework limited to just a handful of examples. MOFs are robust porous molecular materials based on polynuclear metal complexes with open framework structures enabling them to host a variety of molecules, gases, liquids, and solids that have been previously dissolved in an appropriate solvent. SMMs are most commonly based on polynuclear transition metal complexes possessing relatively large spin ground states, split in zero field to produce a barrier to magnetization reversal, that display fascinating spin relaxation dynamics

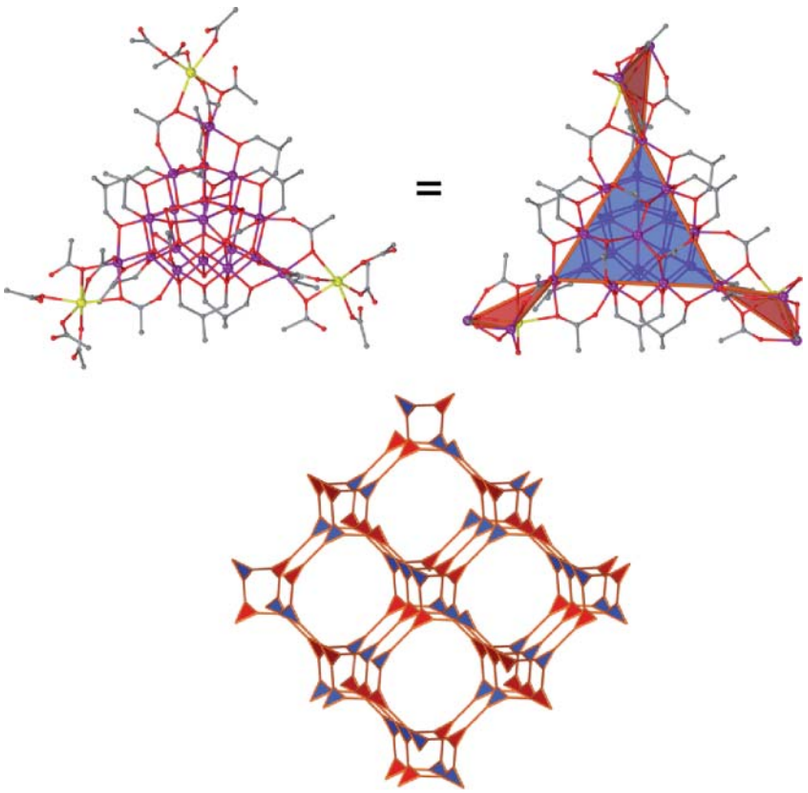


Figure 14 The **srs** network found in (**24**) and (**25**). Color code: C, gray; O, red; Na, yellow; Mn, purple. Blue and red triangles represent the $[Mn^{III}_{12}Mn^{II}_{7}]$ and the $[Na(O_2CCH_3)_6]^{5-}$ three-connected nodes

and have the ability to store magnetic information at the molecular level. Although the physics of these SMMs is intrinsically derived from intramolecular properties, these can be modulated by crystal-packing effects. The continued combination of these two molecular materials should therefore act to boost future efforts in both fields, as SMMs can transmit their magnetic properties to a MOF, whereas their incorporation within a framework, or the inclusion of additional guests within the pores of an SMM-MOF, may alter/modulate magnetic behavior. In other words, this class of molecular materials offers the opportunity to examine the chemistry and physics of intriguing molecule-based complexes in a somewhat more controlled manner than has hitherto been possible. Most SMMs are easily obtained in large yields employing standard benchtop coordination chemistry using solution methods. They are therefore ideal candidates to serve as building blocks for the construction of MOFs. This also suggests that an alternative way to obtain an SMM-based MOF would be to employ exo-dentate bridging ligands, including metalloligands, to a reaction blend known to result in an SMM.

The magnetic properties of previously reported SMM-based MOFs have shown behaviors varying from zero intermolecular interactions through to LRMO. This scale is truly enormous and the potential to discover many fascinating new molecule-based materials within it is ripe for exploration and exploitation (see ***Functional Magnetic Materials Based on Metal Formate Frameworks***). When truly porous SMM-MOFs are synthesized, the ability to study the interplay between magnetism and structure and the encapsulation of species (e.g., small radicals) within the pores of such frameworks will be realized. We close this account with the hope that this will inspire chemists to make such materials.

5 RELATED ARTICLES

Functional Magnetic Materials Based on Metal Formate Frameworks; Interpenetration and Entanglement in Coordination Polymers.

6 ABBREVIATIONS AND ACRONYMS

FC = field-cooled; LRMO = long-range magnetic order; MNM = molecular nanomagnet; MOF =

Metal–organic framework; MQT = magnetic quantum tunneling; MRI = magnetic resonance imaging; SMM = single-molecule magnet; ZFC = zero-field-cooled; 1D = one-dimensional; 2D = two-dimensional; 3D = three-dimensional.

7 REFERENCES

1. P. Ball (ed), 'Designing the Molecular World: Chemistry at the Frontier', Princeton University Press, Princeton, 1994.
2. N. Hall (ed), 'The New Chemistry', Cambridge University Press, Cambridge, 2000.
3. M. D. Hollingsworth, *Science*, 2002, **295**, 2410.
4. J. Michl (ed), 'Modular Chemistry', Kluwer Academic Publishers, Dordrecht, 1997.
5. M. J. Zaworotko, *Chem. Soc. Rev.*, 1994, **23**, 283.
6. J.-M. Lehn, 'Supramolecular Chemistry – Concepts and Perspectives', Wiley-VCH, Weinheim, 1995.
7. A. U. Czaja, N. Trukhan, and U. Müller, *Chem. Soc. Rev.*, 2009, **38**, 1284.
8. R. J. Kuppler, D. J. Timmons, Q.-R. Fang, J.-R. Li, T. A. Makal, M. D. Young, D. Yuan, D. Zhao, W. Zhuang, and H.-C. Zhou, *Coord. Chem. Rev.*, 2009, **253**, 3042.
9. G. S. Papaefstathiou and L. R. MacGillivray, *Coord. Chem. Rev.*, 2003, **246**, 169.
10. M. J. Zaworotko, *Chem. Commun.*, 2001, 1.
11. B. Moulton and M. J. Zaworotko, *Chem. Rev.*, 2001, **101**, 1629.
12. M. Eddaoudi, D. B. Moler, H. Li, B. Chen, T. M. Reineke, M. O'Keeffe, and O. M. Yaghi, *Acc. Chem. Res.*, 2001, **34**, 319.
13. R. E. P. Winpenny, *Dalton Trans.*, 2002, 1.
14. G. S. Papaefstathiou and S. P. Perlepes, *Comments Inorg. Chem.*, 2002, **23**, 249.
15. R. Sessoli, H.-L. Tsai, A. R. Schake, S. Wang, J. B. Vincent, K. Folting, D. Gatteschi, G. Christou, and D. N. Hendrickson, *J. Am. Chem. Soc.*, 1993, **115**, 1804.
16. R. Sessoli, D. Gatteschi, A. Caneschi, and M. A. Novak, *Nature*, 1993, **365**, 141.
17. G. Aromí and E. K. Brechin, *Struct. Bond.*, 2006, **122**, 1.
18. D. Gatteschi, R. Sessoli, and J. Villain, 'Molecular Nanomagnets', Oxford University Press, Oxford, 2006.
19. W. Wernsdorfer, A. Aliaga-Alcalde, D. N. Hendrickson, and G. Christou, *Nature*, 2002, **416**, 406.
20. R. Inglis, G. S. Papaefstathiou, W. Wernsdorfer, and E. K. Brechin, *Aust. J. Chem.*, 2009, **62**, 1108.
21. I.-R. Jeon and R. Clérac, *Dalton Trans.*, 2012, **41**, 9569.
22. R. Inglis, L. F. Jones, C. J. Milios, S. Datta, A. Collins, S. Parsons, W. Wernsdorfer, S. Hill, S. P. Perlepes, S. Piligkos, and E. K. Brechin, *Dalton Trans.*, 2009, 3403.
23. R. Inglis, S. M. Taylor, L. F. Jones, G. S. Papaefstathiou, S. P. Perlepes, S. Datta, S. Hill, W. Wernsdorfer, and E. K. Brechin, *Dalton Trans.*, 2009, 9157.
24. C. C. Stoumpos, R. Inglis, G. Karotsis, L. F. Jones, A. Collins, S. Parsons, C. J. Milios, G. S. Papaefstathiou, and E. K. Brechin, *Cryst. Growth Des.*, 2009, **9**, 24.
25. R. Inglis, A. D. Katsenis, A. Colins, F. White, C. J. Milios, G. S. Papaefstathiou, and E. K. Brechin, *CrystEngComm*, 2010, **12**, 2064.
26. L. Carlucci, G. Ciani, and D. M. Proserpio, *Coord. Chem. Rev.*, 2003, **246**, 247.
27. L. F. Jones, A. Prescimone, M. Evangelisti, and E. K. Brechin, *Chem. Commun.*, 2009, 2023.
28. M. Haryono, M. Kalisz, R. Sibille, R. Lescouëzec, C. Fave, G. Trippe-Allard, Y. Li, M. Seuleiman, H. Rousselière, A. M. Balkhy, J.-C. Lacroix, and Y. Journaux, *Dalton Trans.*, 2010, **39**, 4751.
29. G.-Y. An, A.-L. Cui, and H.-Z. Kou, *Inorg. Chem. Commun.*, 2011, **14**, 1475.
30. K. N. Lazarou, Y. Sanakis, A. K. Boudalis, M. Pissas, V. Psycharis, and C. P. Raptopoulou, *Polyhedron*, 2013, **52**, 917.
31. A. D. Katsenis, R. Inglis, A. Prescimone, E. K. Brechin, and G. S. Papaefstathiou, *CrystEngComm*, 2012, **14**, 1216.
32. O. Roubeau and R. Clérac, *Eur. J. Inorg. Chem.*, 2008, 4325.
33. H. Miyasaka, K. Nakata, Y. Nakazawa, L. Lecren, T. Fujisaki, M. Yamashita, C. Coulon, K. Sugiura, and R. Clérac, *J. Am. Chem. Soc.*, 2006, **128**, 3770.
34. I.-R. Jeon, R. Ababei, L. Lecren, Y.-G. Li, W. Wernsdorfer, O. Roubeau, C. Mathoniere, and R. Clérac, *Dalton Trans.*, 2010, **39**, 4744.
35. E. E. Moushi, T. C. Stamatatos, W. Wernsdorfer, V. Nastopoulos, G. Christou, and A. J. Tasiopoulos, *Inorg. Chem.*, 2009, **48**, 5049.
36. R. E. P. Winpenny, *Chem. Soc. Rev.*, 1998, **27**, 447.
37. Y. Liu, Z. Chen, J. Ren, X.-Q. Zhao, P. Cheng, and B. Zhao, *Inorg. Chem.*, 2012, **51**, 7433.
38. L. Sorace, C. Benelli, and D. Gatteschi, *Chem. Soc. Rev.*, 2011, **40**, 3092.
39. D. N. Woodruff, R. E. P. Winpenny, and R. A. Layfield, *Chem. Rev.*, 2013, **113**, 5110.
40. P.-H. Lin, T. J. Burchell, R. Clérac, and M. Murugesu, *Angew. Chem., Int. Ed.*, 2008, **47**, 8848.
41. E. Burzuri, J. Campo, L. R. Falvello, E. Forcen-Vazquez, F. Luis, I. Mayoral, F. Palacio, C. S. d. Pipaon, and M. Tomas, *Chem. Eur. J.*, 2011, **17**, 2818.
42. K. W. Galloway, M. Schmidtmann, J. Sanchez-Benitez, K. V. Kamenev, W. Wernsdorfer, and M. Murrie, *Dalton Trans.*, 2010, **39**, 4727.

43. S. Xiang, X. Wu, J. Zhang, R. Fu, S. Hu, and X. Zhang, *J. Am. Chem. Soc.*, 2005, **127**, 16352.

44. S. Hu, J.-L. Liu, Z.-S. Meng, Y.-Z. Zheng, Y. Lan, A. K. Powell, and M.-L. Tong, *Dalton Trans.*, 2011, **40**, 27.

45. H. Miyasaka, K. Nakata, K. Sugiura, M. Yamashita, and R. Clerac, *Angew. Chem., Int. Ed.*, 2004, **43**, 707.

46. H.-L. Tsai, C.-I. Yang, W. Wernsdorfer, S.-H. Huang, S.-Y. Jhan, M.-H. Liu, and G.-H. Lee, *Inorg. Chem.*, 2012, **51**, 13171.

47. E. E. Moushi, T. C. Stamatatos, W. Wernsdorfer, V. Nastopoulos, G. Christou, and A. J. Tasiopoulos, *Angew. Chem. Int. Ed.*, 2006, **45**, 7722.

Open Metal Sites in Metal-Organic-Frameworks

Yabing He

Zhejiang Normal University, Jinhua, PR China

and

Banglin Chen

University of Texas at San Antonio, San Antonio, TX, USA

1	Introduction	259
2	Porous MOFs with OMSs for Gas Storage	261
3	Porous MOFs with OMSs for Selective Gas Separation	269
4	Porous MOFs with OMSs for Sensing Small Molecules	273
5	Porous MOFs with OMSs for Heterogeneous Catalysis	274
6	Conclusion	277
7	Acknowledgments	278
8	Related Articles	278
9	Abbreviations and Acronyms	278
10	References	278

1 INTRODUCTION

Metal–organic frameworks (MOFs) or porous coordination polymers (PCPs) have attracted considerable research interest in the past two decades. Such materials are readily self-assembled from metal ions or metal-containing clusters [generally termed as *secondary building units* (SBUs)] with organic bridging ligands through metal coordination bonds. The modular nature and mild synthesis conditions endow them with great advantages over other porous materials. For example, the pore size can be tuned systematically by selecting the diverse metal-containing SBUs and rich organic linkers. Furthermore, the pore surface can be functionalized by immobilization of different recognition sites such as open metal sites (OMSs, also referred to as *unsaturated metal centers*, *exposed metal sites*, *accessible metal sites*) and organic functional groups. These attractive characteristics have led to an enormous application potential for MOFs in gas storage, separation, sensing, and catalysis (see ***Metal-Organic Frameworks for Removal of Harmful Gases***, ***Gas Storage in Metal-Organic Frameworks***, ***Adsorption of Hydrocarbons and Alcohols in Metal-Organic Framework Materials***, and ***Photoreactive Metal-Organic Frameworks***).

Immobilization of OMSs into the pore surface of MOFs is one commonly used strategy for pore surface engineering because OMSs play very important roles in their specific recognition of small molecules. Immobilization of OMSs has been attempted with other porous solids such as zeolites and carbon-based materials through ion exchange and impregnation, but in these cases, the OMSs are not uniformly isolated and the local environment around the OMSs is not clear. This situation changed with the emergence of porous MOFs. Taking advantage of well-defined pore structures of MOFs, OMSs can be incorporated into the pore surface with a completely uniform arrangement.

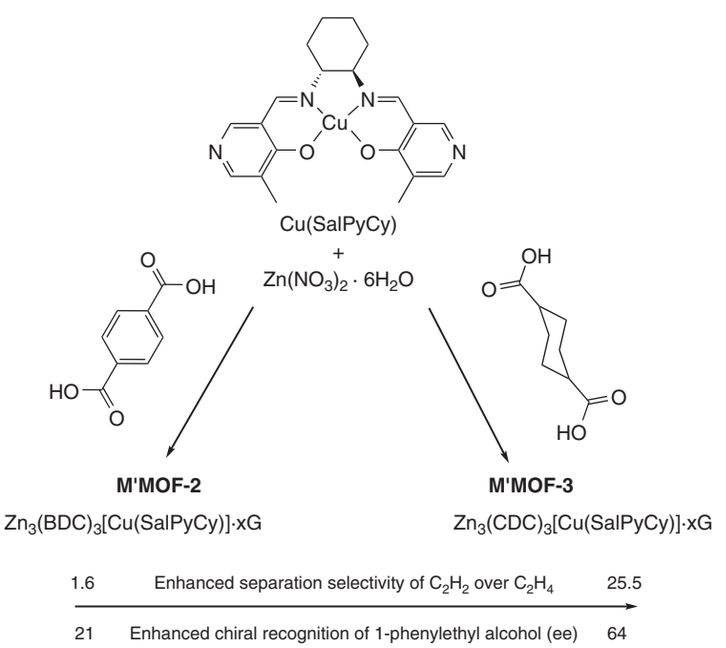
The term *open metal sites* was first used by Chen *et al.* in 2000.[1] They synthesized a porous MOF (MOF-11) based on the dicopper paddle wheel SBUs and 1,3,5,7-adamantane tetracarboxylate. The rigid MOF architecture

Metal-Organic Framework Materials. Edited by Leonard R. MacGillivray and Charles M. Lukehart.
© 2014 John Wiley & Sons, Ltd. ISBN 978-1-119-95289-3

allows for complete removal of guests including terminal water molecules to yield an anhydrous framework with periodic arrays of OMSs. The absence of water ligands on Cu is clearly confirmed by single-crystal X-ray structure analysis. Compared to the hydrated form, the Cu–OCO distance is shorter (1.935 Å) and the Cu–Cu distance (2.49 Å) is significantly shortened in the anhydrous compound. Owing to genesis of exposed metal sites after the removal of axially coordinated solvent molecules, the dicopper paddle wheel cluster has become one of the commonly used SBUs in the isoreticular synthesis of MOFs.[2]

Aside from the removal of terminally coordinated solvent molecules bound at metal nodes to create OMSs, as discussed above, a more rational approach is to use metalloligand as building block. Kitagawa group employed this approach to construct three three-dimensional (3D) coordination frameworks where different OMSs were immobilized on the pore surfaces.[3] The reaction of H_4salphdc (H_4salphdc = *N*,*N*′-phenylenebis(salicylideneimine)dicarboxylic acid) and $Cu(OAc)_2 \cdot H_2O$ afforded the Schiff base type metalloligand $[Cu(H_2salphdc)] \cdot H_2O$, which was then complexed with $Zn(NO_3)_2 \cdot 6H_2O$ to yield the 3D MOF $[Zn_3(OH)_2(L^{Cu})_2] \cdot 2DMF$ ($L^{Cu} = [Cu(salphdc)]^{2-}$ DMF = *N*,*N*′-dimethylformamide). In this framework, one Zn atom is coordinated to two hydroxide anions and two carboxylate oxygen atoms of L^{Cu} and the other Zn atom is coordinated to two hydroxide anions and four carboxylate oxygen atoms of L^{Cu} to form an infinite chain, which is further connected by L^{Cu} to form a 3D network with 1D large channels of approximately 14×14 Å^2. Interestingly, the Cu(II) ions from the L^{Cu} are coordinatively unsaturated, and are embedded regularly in the pore wall of a 3D porous framework with an intermetallic distance of 6.1 Å. More importantly, the Cu(II) metal ions can be replaced by the other metal ions such as Co(II) and Ni(II). So, these three compounds are very good examples illustrating that the OMSs can be rationally immobilized in the pore surface via the metalloligand approach. With this strategy, our group has realized several mixed metal–organic frameworks (M'MOFs) with rationally immobilized OMSs for gas storage and separation.[4–6] As shown in Scheme 1, the metalloligand [Cu(SalPyCy)] was treated with either H_2BDC (benzene-1,4-dicarboxylic acid) or H_2CDC (cyclohexane-1,4-dicarboxylic acid) along with $Zn(NO_3)_2 \cdot 6H_2O$ under solvothermal conditions to afford two M'MOF (**M'MOF-2** and **M'MOF-3)**. Amazingly, the subtle tuning of the micropores by the change of BDC in **M'MOF-2** to CDC in **M'MOF-3** led to significantly enhanced C_2H_2/C_2H_4 separation and chiral recognition of 1-phenylethyl alcohol.[5]

In this chapter, different strategies to introduce OMSs onto the pore surface of MOFs were described, and the potential applications of MOFs with OMSs in H_2, CH_4, C_2H_2 storage, gas separation, chemical sensing, and catalysis were illustrated, respectively.



Scheme 1 Metalloligand approach for the construction of two M'MOFs. **M'MOF-3** shows better C_2H_2/C_2H_4 gas separation and chiral separation than **M'MOF-2**

2 POROUS MOFs WITH OMSs FOR GAS STORAGE

2.1 Porous MOFs with OMSs for H_2 Storage

Hydrogen is widely considered to be a potential alternative to fossil fuels for mobile applications because of its environmental benefit and high gravimetric energy density. Unfortunately, its volumetric energy density under ambient conditions is extremely low for practical applications. For onboard use, hydrogen must be compressed to very high pressures or stored cryogenically, both of which cost energy and substantially increase vehicle weight. Therefore, the utilization of hydrogen in automobiles relies on the development of low-cost light-weight materials that can reversibly and rapidly store hydrogen near ambient conditions at a density equal to or higher than liquid hydrogen.

Since the first report of hydrogen adsorption on a porous MOF in 2003,[7] porous MOFs have been extensively studied for hydrogen storage over the past two decades. The main problem of use of these materials as H_2 storage sorbents is weak van der Waals interaction energy between H_2 and the surface of these sorbents (typically 5–8 kJ mol^{-1}), which has limited their gas storage capacities to low temperature (often 77 K) and high pressure (up to 90 bar). In fact, none of the MOFs developed so far satisfies the proposed DOE (Department of Energy) target at non-cryogenic temperatures. Therefore, frameworks exhibiting strong binding interactions are needed to facilitate H_2 adsorption at room temperature. Theoretically, an energy of interaction of about 15–20 kJ mol^{-1} has been suggested for porous materials to maintain a good balance between high capacity at ambient temperatures and fast hydrogen adsorption–desorption kinetics. Experimentally, efficient methods to improve the hydrogen sorption affinities have been explored, including generation of OMSs, fabrication of framework interpenetration,[8,9] construction of pore sizes comparable to hydrogen molecules,[10] and doping of frameworks with metal centers and nanoparticles by spillover effect.[11,12] In particular, extensive effort has being undertaken to generate porous MOFs bearing high concentrations of coordinatively unsaturated open metal centers, because neutron powder diffraction (NPD) and inelastic neutron scattering (INS) studies have verified that in most cases, H_2 first binds at these sites.[13–17] For example, NPD studies on a D_2-loaded **HKUST-1** sample, a MOF that was first synthesized in 1999 by Chui *et al.*,[18] identified six distinct D_2 adsorption sites within the nanoporous structure, and the first D_2 adsorption site in **HKUST-1** was located at the open copper site in the paddle wheel units.[13] The short Cu$\cdots$D$_2$ distance of 2.39 Å indicates appreciable interaction between a hydrogen molecule and the d^9 Cu(II) center.

Since there have been several excellent review papers already summarizing the research efforts on hydrogen storage in MOFs,[19–21] in the following sections, we only discuss a few of representative MOFs with OMSs that have been reported for H_2 storage, with special focus placed on the methods for generating OMSs.

A copper-tetracarboxylate framework **MOF-505** was synthesized by the self-assembly of the dicopper paddle wheel SBUs and 3,3′,5,5′-biphenyltetracarboxylic acid (H_4bptc).[22] There exist two different polyhedral cages in the framework, which are arranged in an alternating manner (Figure 1a). To investigate the hydrogen adsorption properties, the acetone-exchanged sample was evacuated step-by-step at room temperature for 15 h (Stage I, desolvation), at 70 °C for 15 h (stage II, partial dehydration), and at 120 °C for 12 h (stage III, complete dehydration). Each stage of activation is accompanied by distinct change in

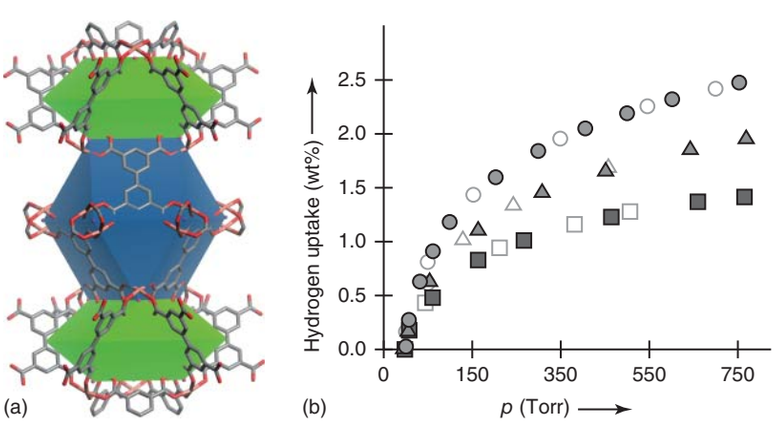


Figure 1 (a) Two different polyhedral cages and (b) H_2 isotherms for **MOF-505** after three different activation stages: stage I (25 °C, squares), stage II (70 °C, triangles), and stage III (120 °C, circles) (Reproduced with permission from Ref. 22. © Wiley-VCH Verlag GmbH & Co. KGaA, 2005.)

sample color from light blue to deep purple, consistent with the change in the coordination environment of the metal sites. At Stage I, the sample loses 42% of the weight, and the H_2 uptake is 1.41 wt%, whereas at the later stage, the hydrogen uptake increases up to 2.47%, despite only a 10% mass loss (Figure 1b). The experimental results indicate that the created open copper sites have a favorable impact on the hydrogen sorption capacity of **MOF-505a**.

To determine the effect of OMSs within a MOF on H_2 adsorption, Suh and coworkers synthesized three porous isoreticular MOFs (**SNU-4**, **SNU-5′**, and **SNU-5**) with the same NbO-type net topology.[23] The formation of OMSs can be controlled by precisely selecting different activation conditions. It was observed that in the presence of OMSs, the MOF clearly has a higher H_2 adsorption on both gravimetric and volumetric bases, probably due to a stronger interaction between OMSs with H_2 molecules, because the reduction of framework mass cannot completely explain the enhanced volumetric uptake. Note that for isostructural materials, volumetric capacity calculations can elucidate the effects of OMSs without discriminating against the additional mass.

To investigate the role of pore size, ligand functionalization, and exposed metal sites on the hydrogen adsorption, Schröder and coworkers synthesized a series of copper-carboxylate frameworks (**NOTT-100** to **NOTT-108**) having the same NbO topology that were formed from a range of polyphenyl tetracarboxylates and $[Cu_2(COO)_4]$ paddle wheel SBUs.[24] The pore sizes can be controlled and tuned by the polyaromatic backbones. Elongation of the ligand dramatically increases pore diameter along the *c* axis from 10.0 Å in **NOTT-100** to 32.0 Å in **NOTT-102**. All desolvated materials exhibit high H_2 adsorption due to the large pore volumes as well as the presence of open copper sites. In the case of **NOTT-107**, introducing methyl groups to create smaller pores can increase the heat of H_2 adsorption and thus uptake at low pressure; however, it also reduces the free volume and thus negatively affects the high-pressure H_2 adsorption capacity. NPD studies on D_2-loaded **NOTT-101** clearly identify three adsorption sites for this material: at the exposed open copper sites, at the pocket formed by three $[Cu_2(CO_2)_4]$ paddle wheels, and at the cusp of three phenyl rings. The exposed copper site is found to be the strongest adsorption site in the pore, but its adsorption heat is only slightly higher than those for other sites.

Although numerous MOFs with appreciable hydrogen uptakes have been constructed from dicopper paddle wheel SBUs and tetracarboxylate ligands, the OMSs in these MOFs are often misaligned. In 2008, Zhou and coworkers reported two copper-tetracarboxylate frameworks **PCN-12** and **PCN-12′** (PCN = porous coordination network) that were synthesized by the solvothermal reaction of $Cu(NO_3)_2 \cdot 6H_2O$ and H_4mdip (5,5′-methylenediisophthalate).[25] **PCN-12** consists of cuboctahedral cages with all the OMSs aligned, whereas in **PCN-12′**, the OMSs are out of alignment. The dissimilar alignments of OMSs significantly affect the hydrogen uptakes of these two MOFs. **PCN-12** has an exceptionally high hydrogen uptake of 3.05 wt% at 77 K and 1 atm, 27% higher than that of **PCN-12′** under the same conditions (2.40 wt%), although they have the same atom-to-atom connectivity. Evidently, this higher hydrogen uptake of **PCN-12**, compared to **PCN-12′**, is ascribed to the "close packing" alignment of OMSs in the framework, namely, the formation of cuboctahedral cages and the unique alignment of open metals sites in each cuboctahedral cage. The INS spectrum of **PCN-12** indicates that H_2 strongly prefers available copper sites to other binding sites.

From a fundamental perspective, systematic studies of the gas sorption properties of a family of isostructural materials containing unsaturated coordination sites are necessary in order to gain insight into the effect of different metal substitution on gas uptake capacities. Currently, the examples are mainly limited to a small number of systems such as **MMOF-74** (M = Zn, Mg, Co, Mn, Ni, Fe, Cu; labeled as **CPO-27-M** by Dietzel *et al.*), and $M_3(BTC)_2$ (M = Cu, Zn, Mo, Fe, Cr, Ru, Ni).[26] Using a tritopic tetraazole-based bridging ligand H_3BTT (1,3,5-benzenetristetrazolate), Long and coworkers constructed three isostructural MOFs (Mn-BTT, Cu-BTT, and Fe-BTT)[14–16] and systematically investigated their H_2 sorption properties. Structurally, these frameworks consist of truncated octahedral cages defined by six chloride-centered square-planar $[M_4Cl]^{7+}$ units and eight triangular planar BTT^{3-} bridging ligands. Each cage shares its square faces with six neighboring cages, generating a network structure closely related to that of sodalite (Figure 2a). Solvothermal reaction of H_3BTT with $MnCl_2 \cdot 4H_2O$ affords solvated Mn-BTT.[14] The solvent molecules in the pores can only be partially removed by solvent exchange with methanol and subsequent evacuation without a collapse of the framework, yielding a material Mn-BTT with an exceptional H_2 capacity of 2.2 wt% at 77 K and 1.2 bar and a high initial adsorption enthalpy of 10.1 kJ mol^{-1}. At 77 K and 90 bar, the total H_2 uptake reaches 6.9 wt% or 60 g L^{-1}. The latter value is only 11 g L^{-1} lower than the density of liquid hydrogen at 1 atm and 21 K. PND experiments indicate that the strong adsorption at low loadings is due to H_2 molecules binding directly to unsaturated Mn^{2+} site within the framework with a distance of 2.27 Å. However, this desolvated material Mn-BTT still retains some residual methanol molecules, such that very few strong binding sites are accessible. In order to obtain a structure with more OMSs, an isostructural MOF Cu-BTT was synthesized by replacement of Mn^{2+} with Cu^{2+}, which can be fully desolvated to give a higher density of exposed OMSs for H_2 binding, due to the Jahn–Teller effect of Cu^{2+} ions.[15] The enthalpy of H_2 adsorption for Cu-BTT starts out slightly lower than that of Mn-BTT

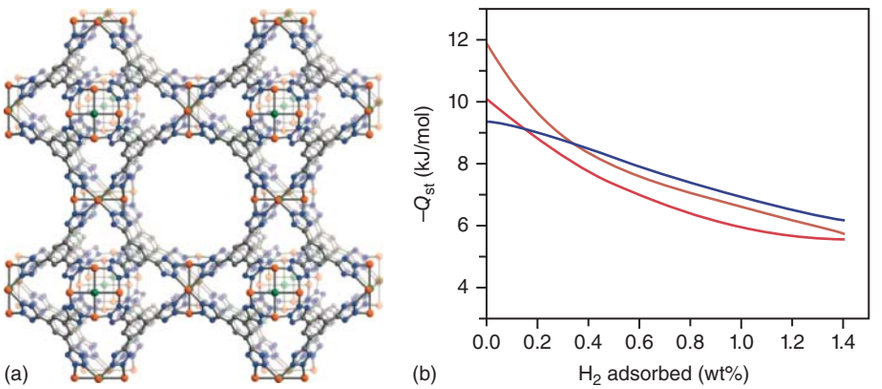


Figure 2 (a) A portion of the single-crystal X-ray structure of M-BTT and (b) the isosteric heat of adsorption as a function of hydrogen uptake in Fe-BTT (orange), Mn-BTT (red), and Cu-BTT (blue) (Reproduced from Ref. 16 with permission from The Royal Society of Chemistry. DOI: 10.1039/C0SC00179A.)

(9.5 vs 10.1 kJ mol^{-1} at zero coverage), but then quickly surpasses it as more H_2 is adsorbed. The improved overall adsorption enthalpy in Cu-BTT is attributed to an increased number of OMSs, which was further confirmed by NPD experiments. Using high-throughput synthetic methodology to screen conditions, the same group synthesized a rare Fe^{2+}-based MOF by treatment of $FeCl_2$ and H_3BTT in a mixture of DMF and DMSO under solvothermal conditions,[16] whose structure is isotypic with those of the manganese- and copper-containing analogs discussed above. On soaking the compound in methanol and heating under dynamic vacuum, most of the solvent can be removed to yield a material Fe-BTT, in which approximately 30% of the framework Fe^{2+} centers still retain a bound methanol molecule. Hydrogen adsorption measurements show an initial isosteric heat of adsorption of 11.9 kJ mol^{-1} (Figure 2b), which is higher than those of the manganese- and copper-containing analogs, and is among the largest recorded for H_2 binding in a MOF. As a comparison, the highest Q_{st} value of MOFs reported so far is 15.1 kJ mol^{-1} for **SNU-15′**.[27] Such high initial heat of adsorption is associated with the presence of open Fe^{2+} coordination sites within the $[Fe_4Cl]^{7+}$ clusters of the framework providing a strong interaction with H_2. Sensibly, compared to the Mn^{2+} ions, the greater charge density (charger-to-radius ratio) of the exposed Fe^{2+} cations induces stronger binding toward H_2 molecules, whereas in the case of Cu-BTT, the Jahn–Teller effect of Cu^{2+} ions leads to a longer Cu^{2+}–H_2 interaction distance, and accordingly a low initial adsorption heat, although Cu^{2+} ion is smaller than Fe^{2+} ion. Experimentally, the neutron diffraction studies clearly show that the strongest binding sites reside just 2.17(5) Å from the framework Fe^{2+} cations, which is the shortest metal–D_2 distance yet observed in a MOF. This study highlights the great promise of immobilization of greater polarizing power of cations in isostructural materials to improve the H_2 binding affinity.

Another example is four isostructural lanthanide–organic frameworks [Ln(TPO)] built from a phosphine-oxide-based tricarboxylate (H_3TPO = tris-(4-carboxylphenyl)phosphine oxide).[28] The inorganic SBU is a binuclear Ln cluster bridged by four carboxylates of TPOs with one DMF solvent molecule on the terminal position of each Ln center. The coordinated DMF molecule can be completely eliminated after the careful activation, thus giving rise to OMSs within the framework capable of providing strong interaction with the incoming gas molecules. Because all compounds have the identical network structures, it is expected that as the atomic number of lanthanides increases from Nd^{3+} to Gd^{3+}, the molecular mass becomes heavier and hence gravimetric gas adsorption tends to gradually diminish. However, the H_2 sorption experiments show that the gravimetric uptake increases when moving from Nd^{3+} to Gd^{3+}, which is sharply contrary to the predicted trend toward higher gravimetric adsorption capacity for the lighter metal in a series of isostructural materials. This experimental observation is believed to be related with enhanced BET surface areas and charge density. When going from Nd^{3+} to Gd^{3+}, the ionic radius of lanthanide ions undergoes a steady reduction, and consequently, the charge density becomes pronounced, thus increasing binding strengths between the frameworks and guest molecules, and accordingly gravimetric uptakes.

In the examples discussed above, the OMSs are generated by removal of coordinated solvent molecules from metal-based nodes. In contrast, Ma and Zhou reported a MOF **PCN-9** ($H_2[Co_4(\mu_4\text{-}O)(TATB)_{8/3}]$, TATB = 4,4′,4″-*s*-triazine-2,4,6-triyltribenzoate) with entatic metal centers (EMCs).[29] The EMCs have the potential to bind the substrates without the removal of

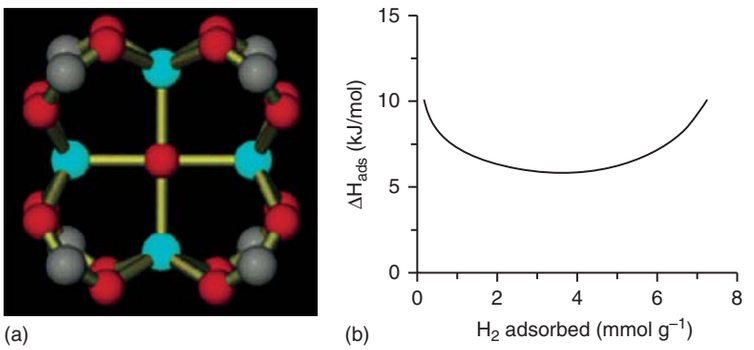


Figure 3 (a) The $Co_4(\mu_4\text{-}O)(CO_2)_8$ SBU in **PCN-9** and (b) the isosteric heat of H_2 adsorption for **PCN-9** (Reprinted with permission from Ref. 28. Copyright (2010) American Chemical Society.)

terminal ligands. As shown in Figure 3a, all four Co atoms in a square-planar $Co_4(\mu_4\text{-}O)$ SBU are in an entatic state, analogous to the active center in hemoglobin, and are ready to bind a substrate to achieve an octahedron coordination. After desolvation, **PCN-9** exhibits a H_2 uptake of 1.53 wt% at 77 K and 1 atm. At low coverage, the heat of H_2 adsorption of **PCN-9** is 10.1 kJ mol^{-1} (Figure 3b), which is higher than that of **MOF-5** (5.2 kJ mol^{-1}), **HKUST-1** (6.6 kJ mol^{-1}), and **MOF-74** (8.3 kJ mol^{-1}). Evidently, this remarkable enhancement of gas affinity is due to the EMCs, which was supported by IR spectra studies using the cyanide and CO as probe molecules.

Another promising approach for creating the OMSs in the MOFs is the metalloligand or preconstructed building block approach, which involves a two-step self-assembly process, namely, an organic ligand is first complexed with metal ions to make a discrete metalloligand, which are then used as linkers and are connected by another metal ions used as nodes to construct MOFs. By this metalloligand approach, different OMSs can be rationally immobilized in the pore surfaces. For example, a solvothermal reaction of functionalized metallo-Schiff complex $[Cu(H_2Pyen)](NO_3)_2$, H_2BDC and $Zn(NO_3)_2 \cdot 6H_2O$ led to the formation of **M'MOF-1** $[Zn_3(BDC)_3Cu(Pyen)]$.[4] The framework is composed of trinuclear $[Zn_3(COO)_6]$ SBUs bridged by BDC moieties to form 3^6 tessellated 2D sheets that are further pillared by the Cu(Pyen) units to build the 3D network (Figure 4a–c). Remarkably, there exist rationally immobilized copper centers within the two types of micropores: curved pores of about 5.6×12.0 $Å^2$ in the direction of the crystallographic *c* axis (Figure 4d) and irregular ultramicropores in the direction of the crystallographic *b* axis (Figure 4e). After desolvation, each immobilized copper center has two potential open sites for binding hydrogen molecules, thus resulting in a high hydrogen adsorption enthalpy of 12.29 ± 0.53 kJ mol^{-1} at zero coverage (Figure 4f). More significantly, the different adsorption kinetics for H_2 and D_2 was observed (Figure 4g), and therefore, **M'MOF-1** might be utilized for the kinetics sieving separation of H_2/D_2.

Besides, the other approach for creating OMSs in the MOFs is postfunctionalization of a parent MOF such as postsynthetic cation exchange, and framework reduction (see ***Postsynthetic Modification of Metal-Organic Frameworks***). For example, Champness and coworkers reported a doubly interpenetrated anionic MOF material **NOTT-200** in which the framework exhibited a big hysteretic hydrogen adsorption.[30] However, when the charge-balancing counterions H_2ppz^{2+} (ppz = piperazine) were exchanged with Li^+, the resulting MOF **NOTT-201** showed not only the typical Type-I isotherms with no hysteresis but also enhanced H_2 adsorption capacity as well as increased H_2 adsorption enthalpy. Framework reduction can also provide OMSs in the form of cations that balance negative charge of the reduced ligands. With this strategy, Hupp *et al.*[31] prepared a ~5 mol% Li^+-doped MOF $[Zn_2(NDC)_2(diPyNI)]$ (diPyNI = *N*,*N*′-di-(4-pyridyl)-1,4,5,8-naphthalenetetracarboxydiimide, NDC = 2,6-naphthalenedicarboxylate) by direct reduction with lithium metal in DMF, which presented nearly double of H_2 adsorption capacity at 1 atm as well as greater isosteric heat of H_2 adsorption compared with that of the undoped parent MOF. At 1 atm, the enhancement in H_2 uptake corresponds to the uptake of as many as 60 hydrogen molecules per added Li^+, which is greater than the maximum number of hydrogen molecules capable of directly interacting with the free cations. Apparently, this cannot be explained solely by direct H_2-cation binding, and other factors such as framework displacement and/or strut polarizability also contribute to the H_2 uptake enhancement. Later, they have also observed that H_2 binding intensity with the framework-reduced materials decreases in the order of $Li^+ > Na^+ > K^+$ whereas H_2 uptake increases in the opposite order.[32] The authors attributed the behavior to the structural changes arising

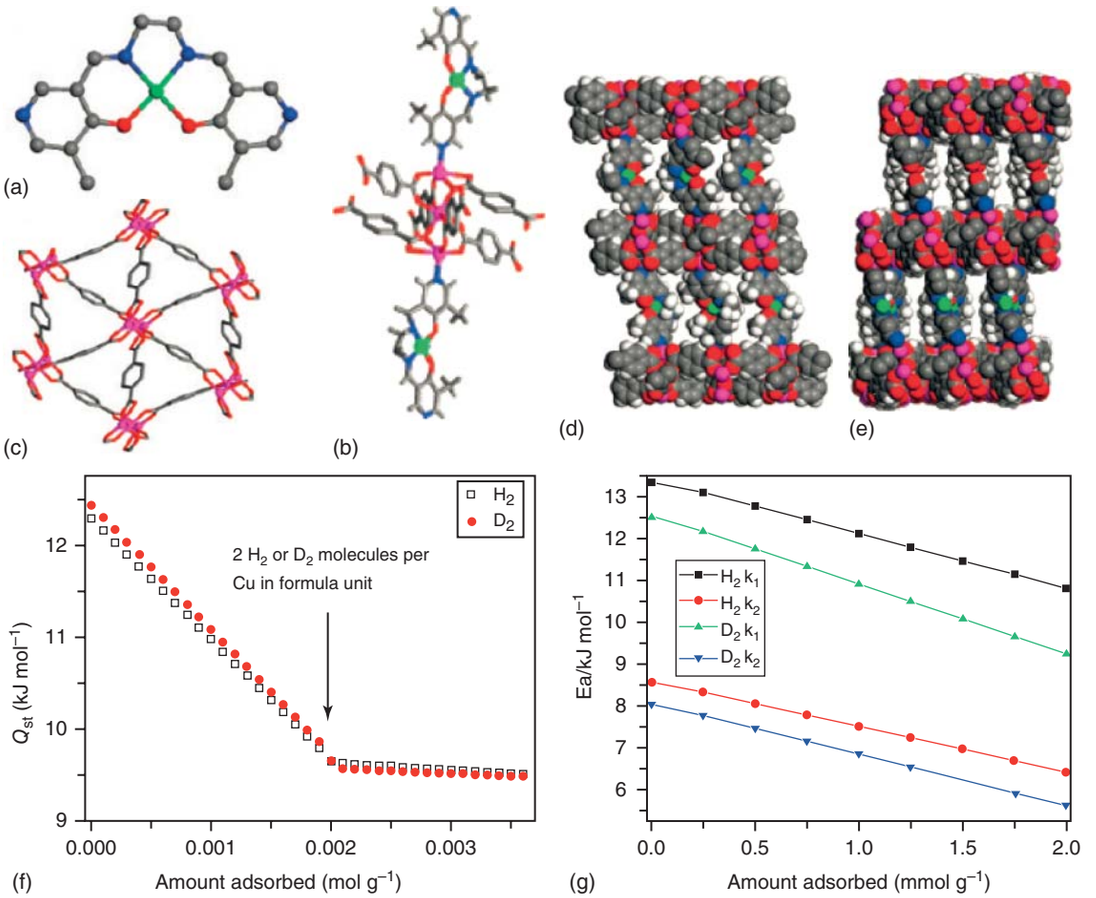


Figure 4 Single-crystal X-ray structure of **M'MOF-1** showing that the framework is composed of trinuclear $[Zn_3(COO)_6]$ SBUs (b) bridged by BDC moieties to form 3^6 tessellated 2D sheets (c) that are further pillared by the Cu(Pyen) units (a) to form a 3D network having curved pores of about 5.6×12.0 Å^2 along the *c* axis (d) and irregular ultramicropores along the *b* axis (e). Variation of isosteric enthalpy of adsorption (f) and activation energy (g) with amount adsorbed for H_2 and D_2 on **M'MOF-1** (Reprinted with permission from Ref. 4. Copyright (2008) American Chemical Society.)

from framework reductions. Therefore, the effect of the cations may be more structural than electronic.

2.2 Porous MOFs with OMSs for Methane Storage

As with hydrogen, methane is also considered a promising energy carrier for mobile applications due to its relative abundance and less adverse effect on the environment. However, the lack of efficient storage methods has prevented the widespread use of methane in motor vehicles. Adsorption in porous materials is considered to be one promising method as moderately high-density methane storage can be achieved at relatively mild conditions, namely, ambient temperature and moderate pressure (30–60 bar). The success of adsorption storage relies on the development of efficient adsorbent materials.

Among the diverse materials for methane storage, porous MOFs are definitely very unique and promising due to their exceptionally high surface areas, tunable pore sizes, and functionalizable pore walls. Since Kitagawa and coworkers in 1997 reported the first example of the high-pressure methane sorption on the porous MOF material $[Co_2(4,4'\text{-bipyridine})_3(NO_3)_4]$,[33] a number of researchers have been trying to develop MOF materials with higher methane sorption capacity. A variety of factors influence the ability of porous MOFs to adsorb methane, such as surface area, pore size, ligand functionalization, and heat of adsorption, and so on. Apparently, a highly porous MOF cannot take up a large amount of methane volumetrically because of their significantly low framework densities and weak gas-framework interactions. It has been suggested that to maximize the methane storage within porous MOFs at room temperature, some functional sites such as OMSs need to be immobilized onto the pore surfaces while at the same time the pore space should be optimized.[34]

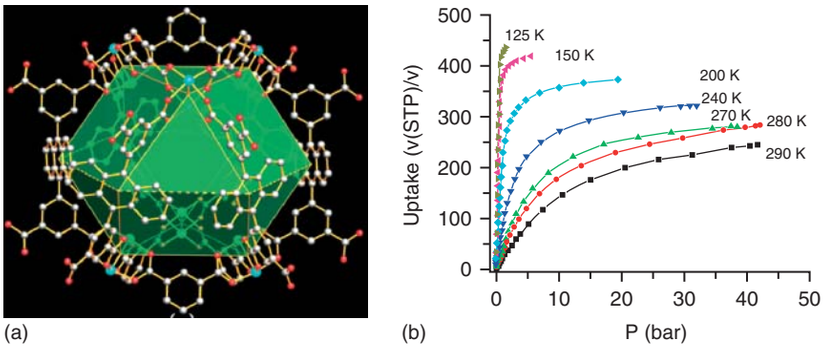


Figure 5 (a) Squashed cuboctahedral cages and (b) absolute high-pressure methane sorption isotherms at various temperatures (Reprinted with permission from Ref. 32. Copyright (2008) American Chemical Society.)

In the following sections, we will focus on a few MOF materials with the high volumetric methane uptakes, and the impact of OMSs on methane storage and delivery.

In 2008, a microporous material **PCN-14** was synthesized by the self-assembly of 5,5′-(9,10-anthracediyl)diisophthalate (adip) and dicopper paddle wheel SBUs.[35] The framework has two remarkable structural features: (i) Every 12 adip ligands connect 6 paddle wheel SBUs to form a squashed cuboctahedral cage (Figure 5a), bridging the anthracenyl rings in close proximity (2.6 Å between an H atom and the center of a phenyl ring from the adjacent anthracenyl group). Such an orientation of organic linkers within the framework system leads to the enhanced van der Waals potential pocket where methane can interact strongly with the frameworks. (ii) The removal of coordinated water molecules from the terminal sites of the dicopper paddle wheel SBUs results in the formation of open copper sites that are approximately oriented toward the center of the cuboctahedral cages so as to maximize electrostatic interactions with guest species. The combination of small pore diameter and available OMSs permits a high absolute volumetric methane uptake of 230 cm^3 (STP) cm^{-3} at 290 K and 35 bar (Figure 5b), which is 28% higher than the widely referred *DOE target* of 180 cm^3 (STP) cm^{-3} for methane storage. Recently, Snurr and coworkers used a high-throughput computational screening method to identify a MOF **NOTT-107** with a high methane uptake and predicted a potential storage capacity of 213 cm^3 (STP) cm^{-3} at 298 K and 35 bar.[36] The reason for such a high methane uptake in **NOTT-107** is believed to be similar to the one behind **PCN-14**.

To investigate the role of OMSs in methane adsorption and the influence of the specific metal on the properties of the materials, in 2009, Zhou and coworkers[37] studied methane adsorption in a series of **MMOF-74** materials (M = Mg, Mn, Co, Ni, Zn), one of the most well-studied families of MOFs bearing the highest concentration of OMSs reported so far. **ZnMOF-74** was first synthesized by Rosi *et al.*,[38] and subsequently other analogs were reported.[39–42] Each of these materials is composed of M^{2+} ions generating the infinite helical SBUs bound by 2,5-dioxido-1,4-benzenedicarboxylate (DOBDC) resulting in a 1D hexagonal pore structure of ~1.1 nm in diameter. On thermal treatment, the terminal water molecule can be removed, leaving the metal atom with an open coordination site toward an empty channel that can be taken by an adsorbed guest molecule. Thus, this MOF series represents an ideal system for studying the role of different open metals on the adsorption of different gas molecules.[42–46] Of the five isostructural MOFs investigated, **NiMOF-74** exhibited the highest absolute methane storage capacity of 200 cm^3 (STP) cm^{-3} at 300 K and 35 bar, indicating that the specific metal that is employed has a certain effect on the methane adsorption capacity. The neutron diffraction experiments clearly reveal that the OMSs are the primary methane adsorption sites and play a major role in the adsorption of methane.

In 2011, we reported a new copper-carboxylate framework **UTSA-20** of a novel *zyg* topology, exhibiting the excess (absolute) volumetric methane storage capacity of 178 (195) cm^3 (STP) cm^{-3} at 300 K and 35 bar (Figure 6b).[34] **UTSA-20** was formed by the self-assembly of a noncoplanar hexacarboxylate organic linker H_6bhb (H_6bhb = 3,3′,3″,5,5′5″-benzene-1,3,5-triyl-hexabenzoic acid) with dicopper paddle wheel $[Cu_2(CO_2)_4]$ SBUs. Two different types of 1D channels are formed within the framework with the potential open copper sites exposed to the pore surfaces: rectangular pores with dimension of 3.4 × 4.8 Å and cylindrical pores with a diameter of 8.5 Å (Figure 6a). Computational investigations indicate that besides the open copper sites, the linker channel sites are also one of primary methane adsorption sites, and that the methane binding at the linker channel sites is even stronger than that at OMSs because the methane molecule is well-sandwiched between two bhb linker potential surfaces. The combination of the two adsorption sites (open copper

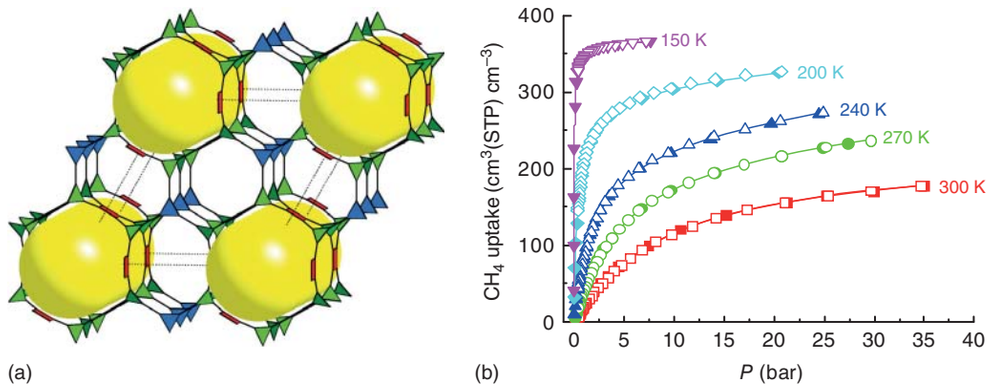


Figure 6 (a) The pore structure of **UTSA-20** along the *c* axis and (b) excess high-pressure methane sorption isotherms of **UTSA-20** at various temperatures (Reproduced with permission from Ref. 34. © Wiley-VCH Verlag GmbH & Co. KGaA, 2011.)

sites and linker channel sites) contributes to ~90% of the experimental uptake at 298 K and 35 bar. The remaining ~10% may be easily attributed to additional secondary binding sites that exhibit lower heats of adsorption. The methane storage density of 0.222 g cm^{-3} in micropores in **UTSA-20** at 300 K and 35 bar is equivalent to the density of compressed methane at 300 K and 340 bar. Such high methane storage density is attributed to the full utilization of both open copper sites and the pore space.

The materials discussed above are best performing adsorbents for methane storage. However, when evaluating the performance of an adsorbent for vehicular application, the deliverable capacity of methane gas is more important because it determines the driving range of natural gas vehicles (NGVs). Note that **NiMOF-74a** has the second high volumetric methane uptake of 200 cm^3 (STP) cm^{-3}; however, the deliverable amount of methane, referred to as the difference in the amount of methane adsorbed between 5 and 35 bar, is only 84 cm^3 (STP) cm^{-3}, less than a half of the absolute uptake. The relatively high retention of methane in **NiMOF-74a** at low pressures can be explained considering that it possesses the highest density of OMSs. Therefore, to maximize the deliverable capacity of the sorbent, it is necessary to minimize the amount of methane stored at unusable pressure, that is, below 5 bar. Because the OMSs play the most important roles for the methane storage below 5 bar, pursuing MOFs with high density of OMSs will be not a good strategy to target MOFs with high methane delivery.

2.3 Porous MOFs with OMSs for C_2H_2 Storage

Acetylene is a very important raw material for various industrial chemicals, consumer products, and oxy-acetylene cutting in metal fabrication. Owing to the very explosive nature, acetylene storage needs to be released under a pressure of 0.2 MPa. Thus, its safe and efficient storage has become a key concern. Since the first account of acetylene adsorption in a microporous metal–organic material $[Cu_2(pzdc)_2(pyz)]$,[47] MOFs have been widely studied as potential acetylene storage candidates. The early research studies on the MOFs for acetylene storage have mainly focused on those with small pores to enhance their acetylene adsorption enthalpies, which has however limited their uptake capacities with the highest ever reported being 106 cm^3 (STP) g^{-1}.[48] To facilitate acetylene adsorption at ambient temperature, some specific sites such as OMSs,[44,49] and hydrogen bond acceptors,[47] need to be immobilized within porous MOFs to enhance their interactions with acetylene molecules and thus maximize the storage capacities at ambient temperature.

Recognizing the importance of the OMSs in gas storage, our research group has examined six prototypical microporous MOFs for acetylene storage,[49] namely **HKUST-1**, **MOF-505**, **MOF-508**, **MIL-53**, **MOF-5**, and **ZIF-8**, which can be classified into three types of pore structures featuring OMSs (**HKUST-1** and **MOF-505**), small pores (**MOF-508** and **MIL-53**), and large pores (**MOF-5** and **ZIF-8**), respectively. Of these MOF materials investigated, those with large pore or small pores are evidently not favorable for acetylene storage, whereas those with open copper sites take up a significantly large amount of acetylene (Figure 7b). At 295 K and 1 atm, the amounts of C_2H_2 adsorbed in **HKUST-1** and **MOF-505** reach 201 and 148 cm^3 (STP) g^{-1}, respectively, significantly higher than those of other MOFs examined without OMSs. Rietveld analysis of the C_2D_2-loaded **HKUST-1** clearly showed that the first and second strongest acetylene binding sites, respectively, were located at the axial position of dicopper paddle wheel units and the entrance window of the small cage (Figure 7a). The open copper site density of 4.96 mmol g^{-1} in **HKUST-1** will contribute to ~55% of the total gravimetric storage capacity of 201 cm^3 (STP) g^{-1} at room temperature and 1 atm. The exceptionally

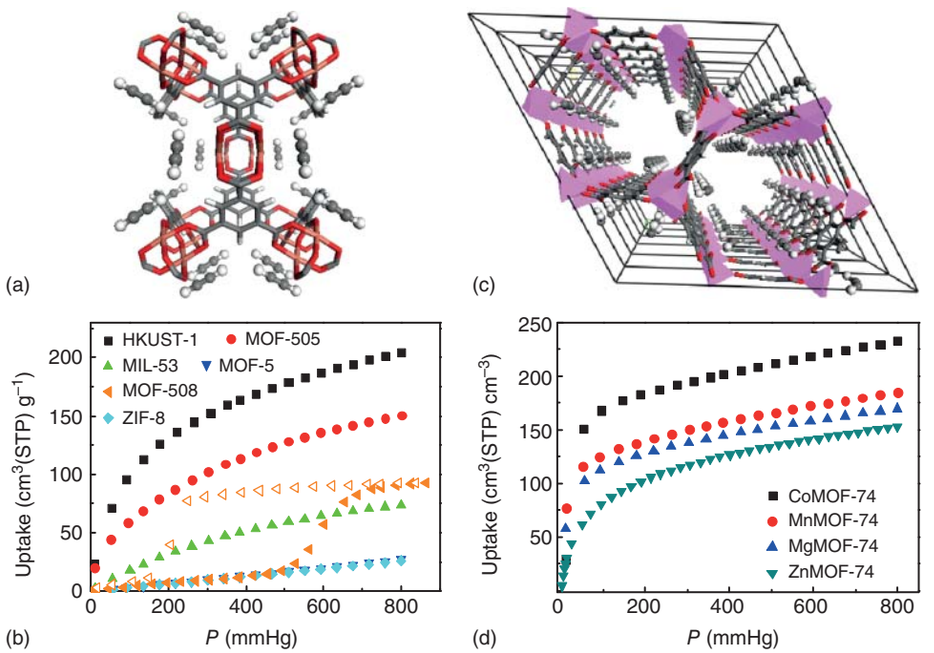


Figure 7 (a) The crystal structure of one C_2D_2 *per* Cu-loaded **HKUST-1** exhibiting the open copper sites for the recognition of acetylene molecules. (b) Acetylene adsorption isotherms of microporous MOFs at 295 K (**MOF-508** at 290 K). (c) The crystal structure of 0.54 C_2D_2 *per* Co-loaded **CoMOF-74** along the *c* axis exhibiting the high density of adsorbed acetylene molecules in *pseudo*-1D arrays. (d) C_2H_2 adsorption isotherms of **MMOF-74** (M = Co, Mn, Mg, and Zn) at 295 K

high acetylene storage capacity of **HKUST-1** at room temperature and atmosphere pressure highlights the bright promise of the immobilization of OMSs to target some useful microporous MOF materials as practical acetylene storage media.

Realizing that OMSs play a very important role to direct their bonding with acetylene molecules, as well exemplified in **HKUST-1** and **MOF-505**,[49] a new highly porous **MOF-505** analog [Cu_2(EBTC)] was constructed in which a triple bond was incorporated into the organic linker EBTC (1,1′-ethynebenzene-3,3′,5,5′-tetracarboxylate).[50] The activated MOF shows the extraordinarily high C_2H_2 uptakes of 252 and 160 cm^3 (STP) g^{-1} under 1 bar and at 273 and 295 K, respectively, which are systematically higher than those of 177 and 148 cm^3 (STP) g^{-1} found in **MOF-505**. Since both frameworks (Cu_2(EBTC) and **MOF-505**) have similar OMSs and pore window sites, the arrangement of these open copper metal sites and their orientation with respect to each other are believed to play crucial roles in such differential interactions with acetylene guest molecules. Concretely, the open copper sites deviate from linearity in **MOF-505**, whereas the open copper sites are oppositely aligned in Cu_2(EBTC), which enforces their stronger interactions with the adsorbed acetylene molecules. Another possible reason for the higher acetylene uptake of Cu_2(EBTC) might be attributed to the C≡C bonds, which enhances their interactions with acetylene molecules through weak π–π interactions.

In searching for other MOFs with high density of OMSs, we notice that the isostructural series **MMOF-74** (M = Zn, Co, Mn, Mg) have much higher densities of OMSs than **HKUST-1** (7.13–7.59 vs 4.36 mmol cm^{-3}). By examining these MOF series, we realized **CoMOF-74** as the highest volumetric acetylene storage material ever reported with the uptake of 230 cm^3 (STP) cm^{-3} at 295 K and 1 atm (Figure 7d).[44] The OMSs within this series of isostructural MOFs exhibit differential interactions with acetylene molecules in which Co^{2+} has the highest interactions with acetylene. Neutron diffraction studies of C_2D_2-loaded **CoMOF-74** evidenced the open Co^{2+} sites as the preferential adsorption sites (Figure 7c), which was further supported by the first principle calculations.

Recently, a new porous MOF **ZJU-5** was constructed based on a new tetracarboxylate H_4PDDI (H_4PDDI = 5,5′-(pyridine-2,5-diyl)diisophthalic acid) with Lewis basic pyridyl sites and dicopper paddle wheel units.[51] The activated **ZJU-5a** takes up extraordinarily high acetylene of 290 cm^3 (STP) g^{-1} and 193 cm^3 (STP) g^{-1} under 1 bar at 273 and 298 K, respectively. The acetylene storage capacity of 290 cm^3 (STP) g^{-1} at 273 K is the highest ever reported thus far among porous materials. In addition, **ZJU-5a** also exhibits very high methane storage capacity, reaching 190 cm^3 (STP) cm^{-3} under 35 bar and

300 K. Such high gas adsorption properties of **ZJU-5a** are attributed to its unique structural features combining the open copper sites, Lewis basic pyridyl sites, and suitable pore spaces.

3 POROUS MOFs WITH OMSs FOR SELECTIVE GAS SEPARATION

3.1 Postcombustion CO_2 Capture

The escalating level of atmospheric CO_2 is a subject of widespread public concern associated to global warming and climate change, and there is an urgent need to develop efficient and cost-effective methods for CO_2 capture and sequestration (CCS). Studies have revealed that the concentration of CO_2 in the atmosphere has increased from about 310 ppm to over 380 ppm during the last half century. About one-third of the CO_2 released to the atmosphere was from postcombustion flue gas generated from coal-fired power plants. Typically, these power plants produce flue gas at 1 atm with a CO_2 concentration of <15%, depending on the fuel used in the process. Such a low partial pressure makes the capture and separation of CO_2 very challenging. The state-of-the-art technology to capture CO_2 makes use of liquid amine-based absorbents to chemically adsorb CO_2; however, this technology suffers from the drawbacks of the corrosive nature of the solvents, and high energy demand for solvent regeneration because of the strong interactions of CO_2 with these absorbents. In this regard, adsorption-based processes appear to be attractive due to their low energy requirements, thus stimulating extensive efforts to find suitable adsorbents for removing CO_2 from flue gas. Numerous studies have demonstrated that MOFs with multifunctional groups, such as OMSs[42] and Lewis basic sites,[52,53] interact strongly with CO_2, and are particularly effective in CO_2 capture and separation from binary mixtures of CO_2 and N_2.[54,55]

Generally, the CO_2 uptake capacity in MOFs at high pressure is correlated with the pore volume of MOFs,[56] indicating that MOFs with ultrahigh porosity such as **MOF-210**[57] and **NU-100**[58] would be desirable for the precombustion process. However, the amount of CO_2 uptake at low pressure is usually associated with the CO_2 binding affinity. Thus, for postcombustion CO_2 capture, MOFs with high CO_2 affinity would be more desirable. To enhance the low-pressure binding affinity of MOFs toward CO_2, one approach that has been widely explored is to build structures bearing exposed OMSs on the pore surfaces, in which the OMSs serve as charge dense binding sites for CO_2 owing to the greater quadrupole moment and polarizability of CO_2 relative to N_2. In the following section, we briefly discuss the CO_2 sorption properties of several typical MOFs with OMSs.

One of the most widely studied MOF materials bearing OMSs is **HKUST-1**. The as-synthesized form of the framework contains weakly bound water molecules on the axial coordination sites of each Cu^{2+} metal center, which can be easily removed by heating the compound in vacuum to afford open Cu^{2+} sites pointing toward the interior of the cavity for binding guest molecules. A relatively high zero-coverage isosteric heat of CO_2 adsorption of 29.2 kJ mol^{-1} has been achieved for such sites. Note that CO_2 adsorption capacities of **HKUST-1** are quite differently reported by various authors, most likely due to the sample purity and/or the degree of sample activation. Llewellyn *et al.*[59] investigated the CO_2 adsorption properties within the chromium-based MOFs **MIL-100** and **MIL-101**. These two materials feature exposed Cr^{3+} sites after the removal of the terminal H_2O molecules originally bound to the metal centers. The high heats of adsorption of CO_2 at low coverage (44 and 63 kJ mol^{-1} for **MIL-101** and **MIL-100**, respectively) are attributed to the coordination of the CO_2 molecules onto the Lewis acid chromium sites. Bae *et al.*[60] suggested that OMSs improve the CO_2/CH_4 selectivity in carborane-based MOFs by comparing samples with and without OMSs. Snurr and coworkers used both experiments and simulations to screen a diverse set of MOFs for low-pressure CO_2 uptakes.[61] Among the 14 MOFs that they considered, those having a high density of OMSs such as **MgMOF-74** and **NiMOF-74** have the highest CO_2 capacities at 0.1 atm and 298 K, which are 5.95 and 4.07 mol kg^{-1}, respectively.

Recently, many studies have been focusing on the CO_2 adsorption properties of MOFs from the **MOF-74** series, one of the most well-studied families of MOFs bearing coordinately unsaturated OMSs that can be systematically varied without affecting the underlying framework structure. Thus, it is possible to study how properties change with variation of just the framework metal cations. Matzger and coworkers utilized this opportunity and examined the CO_2 adsorption properties of Zn, Co, Ni, and Mg analogs of **MOF-74**.[42] The high density of OMSs embedded in the 1D pore channels affords high adsorption capacity for CO_2 at 0.1 bar and 296 K, ranging from 5.8 wt% in **ZnMOF-74** to 23.6 wt% in **MgMOF-74**, respectively. In fact, the value for **MgMOF-74** represents the highest low-pressure gravimetric and volumetric adsorption capacity for CO_2 among known MOFs, despite its relatively low surface areas (1495 m^2 g^{-1}). In particular, among the four compounds studied, **MgMOF-74** shows an exceptional CO_2 affinity of 47 kJ mol^{-1}, due to a stronger ionic character of Mg–O bonds. High resolution powder X-ray diffraction data have been used to elucidate the binding sites and conformation of the CO_2 molecules in **NiMOF-74**.[62] Importantly, the diffraction data following dosing with CO_2 reveal that the guest molecules are indeed end-on coordinated via η^1(O) to the open Ni^{2+} sites in the framework, clearly demonstrating the role of

the metal in binding. The Ni–O distance of 2.29(2) Å is significantly shorter than the sum of the van der Waals radii of Ni and O of 3.1 Å, indicative of a strong interaction. The CO_2 molecule appears to be slightly distorted from its usual linear structure with a bent O–C–O angle of 162(3)°. Dietzel *et al.*[63] found a preferential adsorption of CO_2 over CH_4 or N_2 under dynamic conditions using **NiMOF-74** powder. Britt *et al.*[64] showed that **MgMOF-74** powder takes up 8.9 wt% CO_2 during breakthrough experiments with an 80% CH_4/20% CO_2 mixture at atmospheric pressure and room temperature, and is easily regenerated under relatively mild conditions. More recently, computational simulations suggested that the binding affinity of CO_2 for **MMOF-74** can be tuned by metal substitution and that **TiMOF-74** and **VMOF-74** have higher CO_2 binding affinity than **MgMOF-74**.[65] The origin of such a strong binding is thought to be a local electric field generated by a positive charge of the OMS that stabilizes CO_2 and orbital interactions of the lone pair of CO_2 with the empty d-levels of metals as in a coordination bond, but demonstration of synthetic feasibility has yet to be seen.

One alternative strategy that has been pursued to create the OMSs is postsynthetic insertion of metal ions. For example, Yaghi and coworkers[66] constructed an aluminum-based MOF material [Al(OH)(bpydc)] (**MOF-253**, bpydc = 2,2′-bipyridine-5,5′-dicarboxylate) lined with open 2,2′-bipyridine (2,2′-bpy) chelating groups along the 1D pores (Figure 8a). Considering that insertion of metal ions to the 2,2′-bpy coordination sites can create electronic dipoles on the pore that render the material suitable for gas separation, they inserted $PdCl_2$ and $Cu(BF_4)_2$ in the MOF by soaking the MOF solid in acetonitrile solutions of $PdCl_2$ and $Cu(BF_4)_2$, respectively. The Cu^{2+}-loaded material [Al(OH)(bpydc)] · 0.97$Cu(BF_4)_2$ indeed exhibited the higher CO_2 uptake at 298 K and 1 bar despite a decreased surface area, as well as a dramatic increase in the CO_2/N_2 selectivity from 2.8 to 12.0, compared with the bare framework (Figure 8b). The average isosteric heat of CO_2 adsorption was also found to increase from 23 to 30 kJ mol^{-1} on insertion of $Cu(BF_4)_2$, suggesting that a more suitable chemical environment for CO_2 binding is facilitated by the insertion of $Cu(BF_4)_2$ into the channels of the framework.

It should be mentioned herein that a dual functionality strategy has also been widely explored to enhance CO_2–MOF interaction, namely, simultaneous immobilization of OMSs and Lewis basic sites (LBS) into the framework. It has been well-known that the LBS sites, such as $-NH_2$, amide, can afford large dipole–quadrupole interactions with CO_2 molecules. Taking as an example, a *rht*-type MOF **Cu-TDPAT** featuring a high density of both OMSs (1.76 nm^{-3}) and Lewis basic sites (3.52 nm^{-3}) was built from a LBS-rich hexacarboxylate ligand H_6TDPAT (TDPAT = 2,4,6-tris(3,5-dicarboxyphenylamino)-1,3,5-triazine) and dicopper paddle wheel units.[67] Remarkably, such a dual functionality results in its large adsorption capacity and strong binding affinity toward CO_2. At 298 K, **Cu-TDPAT** takes up 6.2 and 25.8 wt% of CO_2 at 0.1 and 1.0 atm, respectively, significantly higher than all *rht*-type structures reported previously. The IAST CO_2/N_2 selectivity as high as 79 was achieved for a 10:90 CO_2–N_2 gas mixture at a total pressure of 1 atm. A very high adsorption enthalpy of 42.2 kJ mol^{-1} at zero loading is clearly indicative of strong adsorbate–adsorbent interactions. Another analogous example of **NOTT-112** was reported recently, which is constructed using a triazole-containing linker (5,5′,5″-(4,4′,4″-(benzene-1,3,5-triyl)tris(1H-1,2,3-triazole-4,1-diyl))triisophthalic acid, H_6BTTI).[68] The activated **NOTT-122a** shows a high CO_2 uptake of 20.4 wt% at 298 K and 1 atm. Such a high CO_2 uptake is attributed to the combination of the OMSs and the polar pore environment created by the triazole groups in this particular framework.

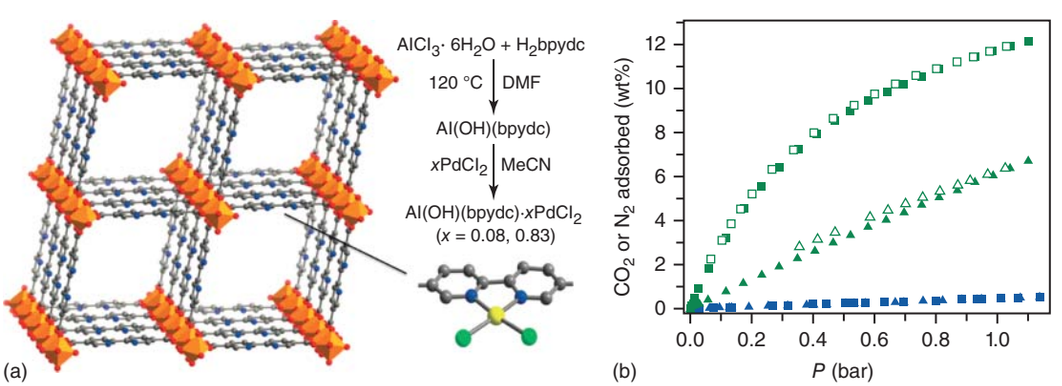


Figure 8 (a) Synthesis and representative structure of [Al(OH)(bpydc)], with subsequent insertion of $PdCl_2$ into open bpy ligand sites. (b) Adsorption isotherms collected at 298 K for uptake of CO_2 in [Al(OH)(bpydc)] (green triangles) and [Al(OH)(bpydc)] · 0.97$Cu(BF_4)_2$ (green squares) and for the uptake of N_2 in [Al(OH)(bpydc)] (blue triangles) and [Al(OH)(bpydc)] · 0.97$Cu(BF_4)_2$ (blue squares) (Reprinted with permission from Ref. 66. Copyright (2010) American Chemical Society.)

3.2 Separation of Light Hydrocarbons

Light hydrocarbons are very important energy resources and raw chemicals, and their separations are at all times one of very important and energy-intensive tasks in petroleum-chemical industry. Traditional cryogenic distillation is a reliable and dominant technology for their separations, but the necessary low temperature and high pressure make it an energy-intensive separation scheme because of their similar sizes and close relative volatilities. Replacing large-scale cryogenic distillation with higher-temperature separation processes could potentially save tremendous amounts of energy. Adsorption-based separation is regarded to be one of the promising energy- and cost-effective options. Furthermore, tremendous cost and energy savings are expected if one is able to design an adsorbent with improved properties for their separations. In this context, MOFs with OMSs have shown great potential for separating these challenging mixtures. In fact, **HKUST-1**, an archetypal example of a MOF with OMSs, has been widely explored for the adsorptive separations of ethylene/ethane,[69–71] propylene/propane,[72–76] and isobutene/isobutane[77] couples. The open copper sites in **HKUST-1** function as electron acceptors capable of forming π bonds with the double bonds in the olefin molecules, resulting in the preferential affinity toward unsaturated gas molecules and thus selective adsorptive separation of olefin/paraffin gas mixtures. In the following sections, we discuss a few of representative examples of MOFs with OMSs for adsorptive separation of light hydrocarbons.

Preferential adsorption of propylene over propane was observed in **FeMIL-100**.[78] The valence of Fe centers generated after activation depends on the activation temperature. Only Fe(III) sites are formed on activation at temperature below 423 K under high vacuum, whereas reduced Fe(II) sites are generated at higher temperature. Importantly, the sorption affinity for propylene over propane is found to be valence-dependent on the Fe centers at low pressures. In the presence of only Fe(III) sites, similar adsorption enthalpies (30 kJ mol^{-1}) were observed for propane and propylene. The introduction of Fe(II) sites dramatically enhanced the heat of adsorption of propylene at low coverage (70 kJ mol^{-1}), whereas that of propane remained almost unchanged. Breakthrough experiments gave a separation factor of 28.9 for propylene over propane on the sample activated at 523 K, but 5.1 for the one activated at 423 K. This result indicates that the presence of Fe(II) sites can dramatically improve the separation performance due to its softer metal character.

Nineteen different MOFs including the ones with OMSs and mixed MOFs (M'MOFs) were selected to evaluate their efficacy for the following six different adsorptive separation tasks: (i) separation of CH_4 with 99%+purity from an equimolar four-component $CH_4/C_2H_2/C_2H_4/C_2H_6$ mixture; (ii) fractionating a four-component $CH_4/C_2H_2/C_2H_4/C_2H_6$ mixture to obtain each of the constituents in a nearly pure form; (iii) fractionating a six-component $CH_4/C_2H_2/C_2H_4/C_2H_6/C_3H_6/C_3H_8$ mixture to obtain each of the constituents in a nearly pure form; (iv) separation of an equimolar C_2H_4/C_2H_6 mixture for production of C_2H_4 of 99.5%+purity and C_2H_6 of 99%+purity; (v) separation of an equimolar C_3H_6/C_3H_8 mixture for production of C_3H_6 of 99.5%+purity and C_3H_8 of 99%+purity; and (vi) selective removal of C_2H_2 from a C_2H_2/C_2H_4 mixture containing 1% C_2H_2 to produce a C_2H_4 product containing <40 ppm C_2H_2. It is found that MOFs with high density of OMSs such as **FeMOF-74**, **CoMOF-74**, and **MgMOF-74** are versatile adsorbents that can be used in all of the above-mentioned separation tasks.[79] Clearly, this study indicates that the OMSs play the most important roles to differentiate their interactions with these light hydrocarbons, although tuning the pore sizes, curvatures, and porosities, to a certain extent, can also adjust their separation capacities.

MOF-74 series is still one of the most intensively studied MOFs for adsorptive separation of light hydrocarbons. **MgMOF-74** has been suggested by Deng and coworkers as a possible candidate for adsorptive separation of ethylene/ethane and propylene/propane couples on the basis of the single-component adsorption isotherms.[80] Shortly afterward, Snurr and coworkers systematically investigated the propylene/propane separation in a series of isostructural frameworks **MMOF-74** (M = Co, Mn, Mg).[45] Among the compounds studied, **CoMOF-74** exhibits the highest thermodynamic propylene/propane selectivity due to strongest π-complexation interactions between the open Co^{2+} sites and the propylene molecules. Most remarkably, the propylene/propane selectivity increases with increasing pressure. The unusual behavior is attributed to the proper match between the size of the propylene molecules and the pore size. The selective adsorption of propylene over propane was further confirmed by breakthrough experiments using an equimolar mixture of propylene and propane with a considerable C_3H_6 separation capacity. Recently, Long and coworkers reported that **FeMOF-74** exhibited the excellent performance for separation of light hydrocarbons.[81] Breakthrough experiments showed that this material can efficiently separate an equimolar mixture of ethylene and ethane into the pure component gases of 99–99.5% purity (Figure 9a), and an equimolar propylene–propane gas mixture into 100% pure propane and >99% pure propylene (Figure 9b). NPD experiments revealed that the unsaturated hydrocarbons (acetylene, ethylene, and propylene) display the *side-on* binding modes with Fe–C distances in the range of 2.42–2.60 Å, whereas the interactions of both ethane and propane with metal cations in **FeMOF-74** are even weaker with the elongated Fe–C distance of ~3 Å (Figure 9c). More recently, Long and coworkers also systematically investigated a series of isostructural **MMOF-74** (M = Mg, Mn, Fe, Co, Ni, Zn) for selective adsorptive separation of ethylene over ethane and

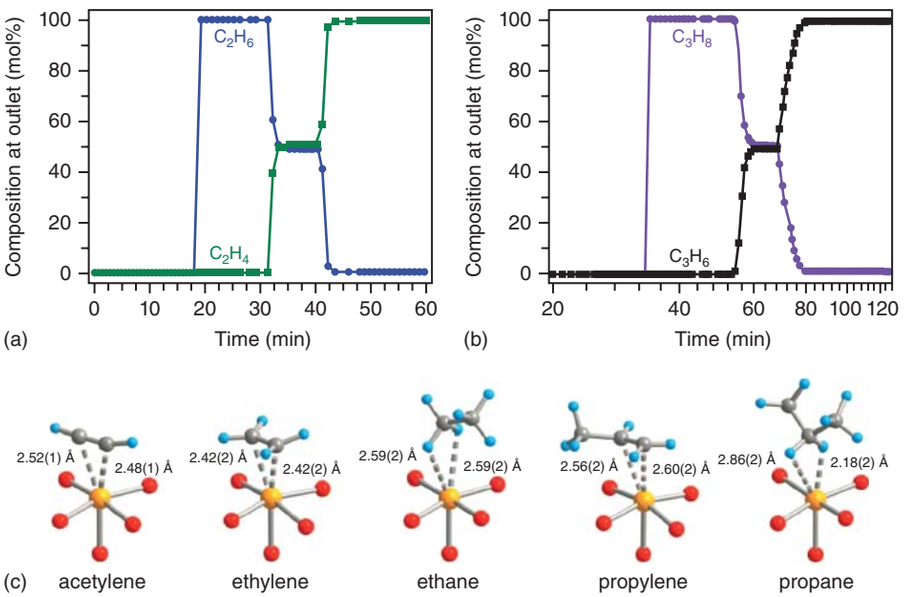


Figure 9 Experimental breakthrough curves for the adsorption of equimolar (a) ethane/ethylene and (b) propane/propylene mixtures flowing through a 1.5-mL bed of **FeMOF-74** at 318 K with a total gas flow of 2 mL min^{-1} at atmospheric pressure. After breakthrough of the olefin and return to an equimolar mixture composition, a nitrogen purge was applied, leading to desorption of the olefin. (c) The first coordination spheres for the iron centers in the solid-state structures obtained on dosing **FeMOF-74** with acetylene, ethylene, ethane, propylene, and propane (From Ref. 81. Reprinted with permission from AAAS.)

propylene over propane at higher temperature (45 °C).[46] Of these MOFs, **FeMOF-74** and **MnMOF-74** exhibit the highest selectivity for the separation of ethylene/ethane and propylene/propane mixtures, respectively. Rietveld analysis of gas-loading **CoMOF-74** revealed that the unsaturated hydrocarbons ethylene and propylene bind the Co^{2+} ions in *side-on* manner, with Co–C distance of 2.60 and 2.66/2.73 Å, respectively. The metal-olefin bond lengths for **CoMOF-74** is longer than the Fe–C distances of 2.42 Å for ethylene and 2.56/2.60 Å for propylene in **FeMOF-74**,[81] consistent with the lower Q_{st} values and IAST selectivities in **CoMOF-74**.

3.3 Separation and Purification of C_2H_2

Acetylene is a very important molecule that is widely used as a starting material for many chemical products and electronic materials. The separation and purification of C_2H_2 is therefore highly needed to promote its wide applications. Zhang *et al.*[82] constructed a rod-packing microporous MOF with 1D pores along *a* axis of about 6.2×5.7 $Å^2$ by the solvothermal reaction of $Zn(NO_3)_2 \cdot 6H_2O$ and 1,2,4-H_3BTC (1,2,4-BTC = benzene-1,2,4-tricarboxylate). The terminal water molecules can be readily removed to generate the OMSs. The resulting MOF takes up the different amounts of C_2H_2, CO_2, and CH_4, indicating its potential application for the separation of C_2H_2/CH_4 and CO_2/CH_4. The Henry's law selectivities for C_2H_2/CH_4 and CO_2/CH_4 mixtures at 296 K are 14.7 and 4.5, respectively. It is thought that the OMSs in the framework contribute significantly to the stronger interactions between acetylene molecules with pore surfaces. In fact, the acetylene adsorption enthalpy of 28.1 kJ mol^{-1} at low coverage is even higher than that of 24.0 kJ mol^{-1} of **ZnMOF-74** with well-orientated open Zn^{2+} sites.[44] This MOF also exhibits different adsorption behavior with respect to different alcohols. The methanol adsorption isotherm exhibits two-step adsorption, whereas those for ethanol, *n*-propanol, and *i*-propanol do not, indicating the small methanol molecules stepwisely bind to the two different OMSs.

To take advantage of the framework interpenetration to tune the micropores, and the metalloligand to immobilize the OMSs in the pore, Zhang *et al.*[83] realized a microporous MOF **M'MOF-20** via the M'MOF approach for highly selective separation of methane from C_2H_2 and CO_2. **M'MOF-20** is composed of dizinc paddle wheel units bridged by four biphenyl-4,4′-dicarboxylate (BPDC) to 2D square-grid layers. The axial sites of the paddle wheels are coordinated by the nitrogen atoms of the metalloligands Cu(Pyen), connecting the 2D layers into a 3D structure. Notably, the triple framework interpenetration tunes the micropores to 3.9 Å, and open copper sites immobilized within the framework are accessible to gas molecules. As a result, the triple framework interpenetration and the open copper sites collaboratively induce

much stronger interactions with C_2H_2 and CO_2 than CH_4, thus resulting in high CO_2/CH_4 and C_2H_2/CH_4 Henry's law selectivities of 6.8 and 34.9, respectively. The uniqueness of the M'MOF approach to systematically tune micropores and immobilize OMSs to induce their differential interactions with gas molecules has enabled M'MOFs to be promising microporous materials for the adsorptive separation of gas molecules.

To immobilize both OMSs and Lewis basic pyridyl sites into a microporous MOF, Xu *et al.*[84] synthesized **UTSA-50** by the solvothermal reaction of $Cu(NO_3)_2 \cdot 6H_2O$ and 3,5-PDC (3,5-pyridinedicarboxylate). The desolvated framework **UTSA-50a** features the open copper sites and Lewis basic pyridyl sites, which collaboratively leads to a high acetylene adsorption enthalpy of 39.4 kJ mol^{-1}, 10 and 20 kJ mol^{-1} larger than the corresponding ones for CO_2 and CH_4, respectively. As a result, **UTSA-50a** takes up a moderately high amount of acetylene gas molecules of 91 cm^3 (STP) g^{-1} at 296 K and 1 atm, and exhibits the highly selective separation of C_2H_2/CH_4 and C_2H_2/CO_2 with the Henry's Law selectivity of 68.0 and 13.3, respectively, at 296 K. The C_2H_2/CH_4 separation selectivity of 68 is the highest ever reported thus far.

4 POROUS MOFs WITH OMSs FOR SENSING SMALL MOLECULES

There has been extensive interest in the recognition and sensing of small chiral/achiral organic molecules, cations, and anions because of their important roles in biological and environmental systems. In this regard, MOFs are certainly very promising luminescent sensing materials because both the inorganic and organic components constituting MOFs can provide platforms to generate luminescence. Once luminescent metal sites and/or organic linkers are incorporated into MOFs, the recognition event can be readily transduced into an external luminescence intensity change. Furthermore, the modular nature of MOFs in principle allows for the facile and ordered incorporation of various recognition elements into pore surfaces such as OMSs, NH_2, and OH, thus providing more dimensions to improve the sensitivity and selectivity of the luminescent MOFs toward guest molecules. Presented below were a few representative examples of luminescent MOFs with OMSs for the sensing of small organic molecules and anions.

To make use of luminescent open Eu^{3+} sites for the sensing of small molecules, Chen *et al.*[85] synthesized a microporous Eu(BTC)(H_2O) with 1D channels of about 6.6 × 6.6 Å along the *c* axis, which is accessible to a variety of small molecules. Thermal activation leads to the formation of the guest-free phase Eu(BTC), whose pore surfaces are lined with luminescent open Eu^{3+} sites (Figure 10a). The activated Eu(BTC) exhibits the characteristic transitions of the Eu^{3+} ion at 590, 616, and 698 nm, when excited at 285 nm, which are ascribable to the $^5D_0$-$^7F_1$, $^5D_0$-$^7F_2$, and $^5D_0$-$^7F_4$ transitions, respectively. Remarkably, its PL spectrum was found to be heavily dependent on the solvent molecules. Particularly, DMF and acetone exhibit the most significant luminescence enhancing and quenching, respectively (Figure 10b–c). Furthermore, a gradual decrease in the fluorescence intensity was observed on the addition of acetone to 1-propanol emulsion of Eu(BTC), and the emission intensity of the $^5D_0$-$^7F_2$ transition of Eu^{3+} at 616 nm versus the volume ratio of acetone could be well-fitted with a first-order exponential decay. Such solvent-dependent luminescence properties are of interest for the sensing of DMF and acetone small molecules. The authors speculated that the binding interaction of the open Eu^{3+} sites with guest solvent molecules plays a crucial role, and the weakly coordinated 1-propanol molecules on the Eu^{3+} sites are gradually replaced by DMF and acetone molecules, leading to their luminescence enhancement and diminishment, respectively. It is expected that if the pore sieving function is further introduced to the framework, such a luminescent OMS strategy may lead to some highly sensitive sensors for selective detection of small molecules.

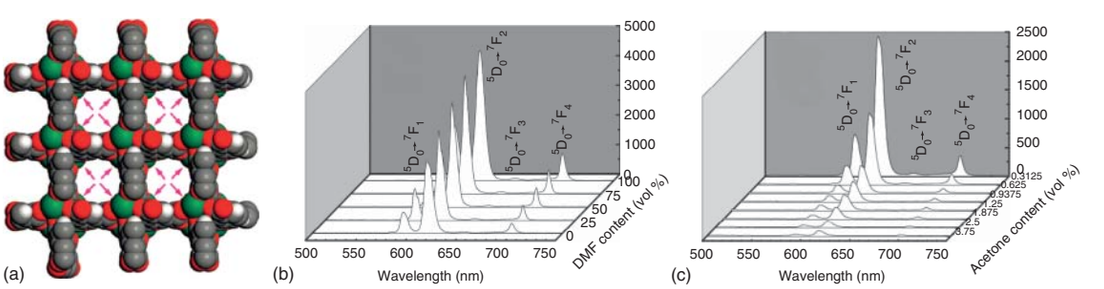


Figure 10 (a) Single-crystal X-ray structure of Eu(BTC) showing uniformly immobilized accessible Eu^{3+} sites within the framework, and the PL spectra of Eu(BTC) 1-propanol emulsion in the presence of various content of (b) DMF and (c) acetone solvents (Reproduced with permission from Ref. 85. Wiley-VCH Verlag GmbH & Co. KGaA, 2007.)

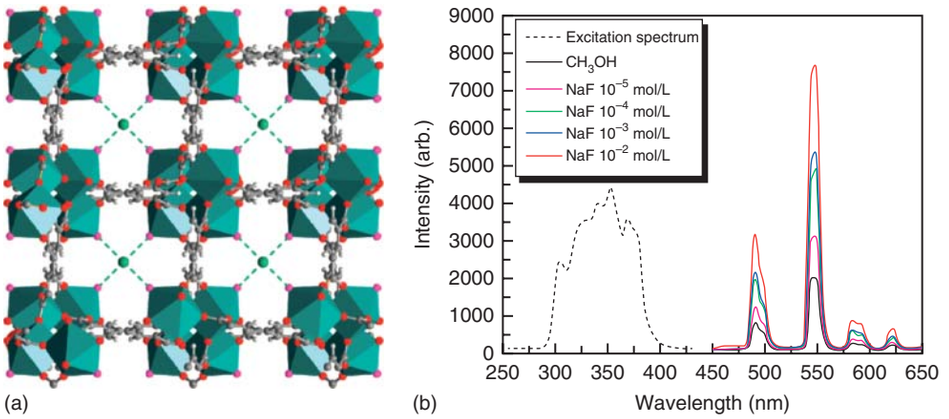


Figure 11 Single-crystal X-ray structure of a luminescent hybrid material Tb(BTC) activated in methanol-containing NaF with the model of fluoride (green) at the center of the channel involving its hydrogen bonding interaction with terminal methanol molecules. (b) Excitation (dotted) and PL spectra (solid) of Tb(BTC) solid activated in different concentrations of NaF methanol solution (Reprinted with permission from Ref. 87. Copyright (2008) American Chemical Society.)

To extend the sensing function of luminescent MOFs into the NIR region, the NIR luminescent MOF $[Yb(BPT)(H_2O)(DMF)_{1.5}(H_2O)_{1.25}]$ was constructed by the solvothermal reaction of $Yb(NO_3)_3{\cdot}6H_2O$ and H_3BPT (BPT = biphenyl-3,4′,5-tricarboxylate).[86] There exist 1D square channels of about 7.2×7.2 Å along the *c* axis. After thermal activation, open Yb^{3+} sites within solvent-free MOF Yb(BPT) are accessible for their recognition of small molecules. When excited at 326 nm, the activated MOF exhibits typical NIR emission from the $^2F_{5/2}$-$^2F_{7/2}$ transition of the Yb^{3+} ion at 980 nm. Similar to the above-mentioned Eu(BTC), its PL spectrum is largely dependent on the solvent molecules, particularly in the case of DMF and acetone, which exhibit the most significant enhancing and quenching effects, respectively. The fluorescence decrease is nearly proportional to the acetone concentration, and the fluorescence quenching by acetone is diffusion controlled. This work indicates the bright promise of NIR luminescent MOFs, which can be developed and applied in the sensing of substrates in biological systems.

Given the richness of N–H and O–H containing organic linkers and terminal organic solvents within MOFs to induce hydrogen bonding interactions with anions, microporous MOFs are expected to be very promising materials for the recognition and sensing of anions. Chen *et al.*[87] demonstrated the first prototypical luminescent MOF **MOF-76** [Tb(BTC)·G] (BTC = benzene-1,3,5-tricarboxylate, G = guest solvent) for the recognition and sensing of F^- ions. There are 1D channels of about 6.6×6.6 Å^2 along the *c* axis in which the terminal solvent molecules partially occupy the pores. Significantly, the terminal solvent molecules can be removed by thermal activation, and the methanol molecules can be incorporated in the terminal positions of Tb^{3+} ions in the activated sample [Tb(BTC)], providing the platform of inducing differential hydrogen bonding interactions with various anions (Figure 11a). When the activated sample was impregnated in methanol with different anions such as F^- Cl^- Br^- CO_3^{2-} and SO_4^{2-} the luminescence intensity of the anion-incorporated sample is significantly enhanced, particularly for the F^- incorporated one (Figure 11b). It is speculated that the anions, immobilized within micropores, can form hydrogen bonding with the terminal methanol molecules, thus diminishing the quenching effects of O–H bond stretching within the terminal methanol molecules, and consequently enhancing the luminescence intensity of the framework. Evidently, in the case of F^- ion, the stronger hydrogen bonding interaction between the F^- ions and methanol has led to its higher luminescence enhancement.

5 POROUS MOFs WITH OMSs FOR HETEROGENEOUS CATALYSIS

Since Fujita and coworkers[88] reported the first MOF-based catalysis on cyanosilylation of aldehydes by a 2D MOF $[Cd(4,4'\text{-bpy})_2](NO_3)_2$, the field of catalysis using MOFs has experienced an impressive growth.[89] MOFs constructed from metal ions or metal-containing clusters and multitopic organic ligands inherently have metal ions at the nodes of the frameworks. Some metal ions at the nodes such as square-planar paddle wheel units $[M_2(CO_2)_4]$ and trigonal prismatic clusters $[M_3O(CO_2)_6]$ have labile coordinated solvent molecules, which can be easily removed or replaced by substrates without losing the structural integrity of the

frameworks. Such metal nodes with open coordination sites can be utilized as a Lewis acid catalyst in chemical transformations. In addition, the modularity of MOFs allows for the introduction of extra OMSs via the use of metalloligands (see ***Porphyrinic Metal-Organic Frameworks***). Examples include Ti-BINOLate, metallosalen, and metalloporphyrin.

Aside from gas storage and separation applications, **HKUST-1** has also shown activity in a growing number of Lewis-acid-catalyzed reactions such as benzaldehyde cyanosilylation,[90] isomerization of α-pinene oxide,[91] citronellal cyclization,[91] rearrangement of ethylene ketal of 2-bromopropiophenone,[91] Friedländer quinoline synthesis,[92] and oxidation of hydroquinone to *p*-benzoquinone.[93] Compared to **HKUST-1**, **MIL-101** is more active for benzaldehyde cyanosilylation.[94] **MgMOF-74** exhibited excellent catalytic performance in cycloaddition of CO_2 to styrene oxide under relatively mild reaction conditions (2.0 MPa, and 373 K) with close to 100% selectivity to carbonate.[95] Generally, for the efficient synthesis of cyclic carbonate from CO_2 and epoxide, Lewis acid catalyst and cocatalyst were required to activate epoxide and CO_2, respectively, but **MgMOF-74** functioned exceptionally well without any additive. The authors speculated that the five oxygen atoms from the organic linkers located around magnesium atoms can function as a base despite the low basicity, whereas open metal magnesium is well-known to function as a Lewis acid site.

Long and coworkers[96] reported a rigid 3D MOF $Mn_3[(Mn_4Cl)_3(BTT)_8(CH_3OH)_{10}]_2$ with two different types of exposed Mn(II) sites residing in the open channels: site I has one chloride and four bridging tetrazolate ligands, and site II is bound by just two tetrazolate ligands. This MOF has been discussed for H_2 adsorption in the previous section. To demonstrate that the Mn(II) sites can serve as potential Lewis acid sites, the compound was examined in Lewis-acid-promoted reactions: carbonyl cyanosilylation and Mukaiyama aldol reaction between an aldehyde and a silyl enolate. It was found that the compound can catalyze the cyanosilylation of aromatic aldehydes and ketones, as well as the more demanding Mukaiyama aldol reaction in a size-selective manner. Interestingly, in the latter case, the Mn(II) centers are still active even in the presence of a highly coordinating solvent such as DMF. This is presumably due to a synergistic effect wherein the Mn(II) centers activate the carbonyl substrate whereas DMF molecules activate the silyl enolate.

Construction of catalytically active homochiral MOFs having open metal coordination sites at the nodes of the frameworks was initiated by Lin and coworkers in 2001.[97] Using an enantiopure bisphosphonate H_4L, they synthesized a series of homochiral lanthanide–organic frameworks with a general formula of $[Ln(H_2L)(H_3L)(H_2O)_4]\cdot xH_2O$ (H_4L = 2,2′-diethoxy-1,1′-binaphthalene-6,6′-bisphosphonic acid, Ln = La, Ce, Pr, Nd, Sm, Gd, Tb, $x = 9–14$). The resulting MOFs have a 2D lamellar structure, which is further extended to 3D network via interdigitation of the binaphthyl rings from the adjacent layers. Despite such an interdigitation, the framework still has large chiral channels with a largest dimension of 12 Å. Because the desolvated Sm compound has accessible metal ions at the nodes, its catalytic activity was examined in several Lewis acid-promoted reactions including cyanosilylation of aldehydes, ring opening of *meso*-carboxylic anhydrides, and Diels–Alder reactions. The yield was moderate to good, but the enantioselectivity was disappointingly negligible. Such a low enantioselectivity is due to the chiral environment that is too remote from catalytically active Sm centers. To introduce a chiral moiety in close vicinity to open accessible metal nodes, Kaskel and coworkers[98] prepared two chiral tricarboxylic acids (chirBTB-1 and chirBTB-2) in which a well-known chiral auxiliary oxazolidinone attached to the *ortho* position of the benzoates, and used them to construct two homochiral MOFs, Zn_3(chirBTB-1)$_2$ and Zn_3(ChirBTB-2)$_2$. The resulting two MOFs exhibit the completely different pore structures, depending on the nature of the chiral oxazolidinone. Significantly, the metal sites at nodes are accessible for potential substrates, and are surrounded by the chiral oxazolidinone subunits, thus providing a proper chiral environment right near the metal centers for asymmetric Lewis acid catalysis. The catalytic activities of both MOFs were examined in the asymmetric Mukaiyama aldol reactions of aldehydes with 1-methoxy-1-(trimethylsiloxy)-2-methyl-1-propene. The observed *ee* values of the reaction depend on the solvents used. While no enantioselectivity was observed for benzaldehyde in CH_2Cl_2 using Zn_3(chirBTB-1)$_2$ as a catalyst, 9% *ee* was observed in *n*-heptane. For the same catalytic reaction, Zn_3(ChirBTB-2)$_2$ showed comparable *ee* values, 8 and 6% in CH_2Cl_2 and *n*-heptane, respectively. Despite the relatively low enantioselectivity, this is an interesting approach for the asymmetric catalysis harnessing OMSs at the nodes and chiral auxiliaries positioned near the metal nodes.

To extend the MOF catalysis from liquid phase to gas phase, Xu and coworkers prepared a metal–organic polymer $[Cu(mipt)(H_2O)](H_2O)_2$ (mipt = 5-methylisophthalate) and examined its catalytic activity for oxidation of CO to CO_2.[99] In the structure, the dicopper paddle wheel clusters are interconnected by bent mipt linkers to form an undulating 2D sheet, which are eclipsed to each other to form a microporous framework with two types of open channels. Importantly, on dehydration, the resulting Lewis acid copper sites are accessible for catalytic transformation, which has been confirmed by FTIR spectroscopy using CO as a probe molecule. A ν(C–O) stretching band was observed at 2113 cm^{-1} after ^{12}CO adsorption, which was assigned to CO adsorbed onto Lewis acid copper sites. The dehydrated MOF exhibits high catalytic activity for the oxidation of CO to CO_2.

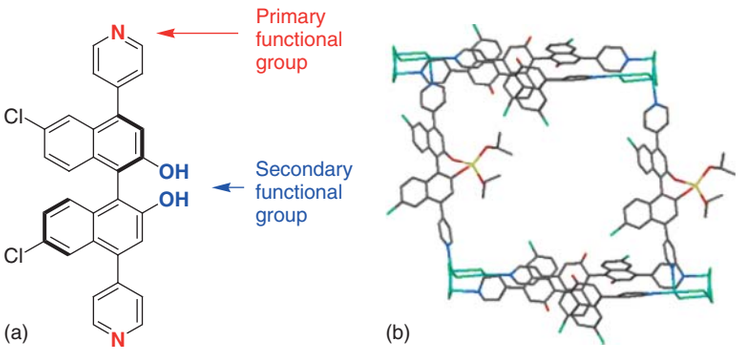


Figure 12 (a) The molecular structure of the bridging ligand and (b) schematic representation of the active (BINOLate)Ti(O^iPr)$_2$ catalytic sites in the open channels (Reprinted with permission from Ref. 100. Copyright (2005) American Chemical Society.)

At 200 °C, the CO conversion reaches 100%. As a comparison, the activity is similar to or higher than that reported for CuO or CuO/Al_2O_3. Although room temperature oxidation of CO is reported over CuO, the catalytic activity is lost on exposing the sample to atmospheric air for a very short time. The nanoCuO shows much higher activity at 105 °C than the present MOF, whereas their activities are almost similar above 130 °C.

The examples discussed above mainly rely on the intrinsic catalytic activity of the metal connecting points. Nevertheless, a more rational strategy for rationally immobilizing catalytically active OMSs within porous MOFs is to incorporate well-established organometallic catalyst units into the linkers of a framework such as BINOLate, metallosalen, and metalloporphyrin.

Lin and coworkers[100] used an axially chiral bridging ligand (*R*)-6,6′-dichloro-2,2′-dihydroxyl-1,1′-binaphthyl-4,4′-bipyridine (Figure 12a) to construct a homochiral porous MOF. The ligand contains the bipyridyl primary functionality connecting with structural metal ions, and orthogonal chiral 2,2′-dihydroxy secondary functionality producing asymmetric catalytic sites on treatment with Ti(O^iPr)$_4$. Structurally, the octahedrally coordinated Cd(II) ions are doubly bridged by the chlorides to form 1D zigzag chains of $[Cd(\mu\text{-}Cl)_2]_n$ that serve as SBUs, which are further extended into a noninterpenetrating 3D network by coordination of the metal ions to pyridyl groups. Although two-thirds hydroxyl groups are shielded by neighboring naphthyl rings, the remaining third are exposed to the open channels, thus facilitating the formation of catalytically active Lewis acidic titanium complex on postsynthesis modification with Ti(O^iPr)$_4$ (Figure 12b). The Ti-coordinated framework can catalyze the addition of diethyl zinc to aldehydes with complete conversion and high *ee* ranging from 80 to 93%, which is comparable to that of the homogeneous counterpart. The size selectivity of the catalysts was demonstrated by a series of contrast tests using dendritic aldehydes of varying sizes. Specifically, the homogeneous catalyst BINOL-Ti(O^iPr)$_4$ showed similar catalytic activity for all dendritic aldehydes regardless of the dendron size, whereas the yield and *ee* of the reaction catalyzed by the Ti-coordinated framework decreased when the size of dendritic aldehydes increased, which suggested the catalysis mainly occurred inside the open channels of MOF.

To incorporate the metallosalen complex into the framework, Hupp and coworkers reported a microporous homochiral pillared-layer MOF as an highly effective enantioselective catalyst for olefin epoxidation.[101] A solvothermal reaction between a chiral (salen)Mn complex (*R*,*R*)-(−)-1,2-cyclohexanediamino-*N*,*N*′-bis(3-*tert*-butyl-5-(4-pyridyl)salicylidene)$Mn^{III}Cl$ (Figure 13a) with $Zn(NO_3)_2 \cdot 6H_2O$ and 4,4-biphenyldicarboxylic acid afforded this MOF with double framework interpenetration. Despite interpenetration, the crystal structure exhibits channels along the crystallographic *a* and *c* direction with dimensions of 6.2×6.2 Å^2 and 6.2×15.7 Å^2, respectively, ensuring accessibility of the Mn(III) sites for catalysis (Figure 13b). The catalytic activity was examined in the enantioselective epoxidation of 2,2-dimethyl-2*H*-chromene using 2-(*tert*-butylsulfonyl)iodosylbenzene as oxidant. The corresponding epoxide was obtained in good yield (70%) and enantioselectivity (82%). Compared to the free (salen)Mn complex, the MOF shows only slightly lower enantioselectivity, presumably due to the loss of flexibility in the salen ligand on framework immobilization or to the electronic effect arising from coordination of the pyridyl groups to Zn metal nodes. Furthermore, the MOF was cycled and reused three times, displaying only a slight decrease in activity and no loss in enantioselectivity. The remarkable stability over its homogeneous counterpart is ascribed to the special separation of the active centers, which prevents an oxidation of the salen ligand by other manganese–salen complexes. The size selectivity experiments with two competitive reagents [a large porphyrinic substrate (Figure 13a) and ethyl 4-vinyl benzoate] indicated

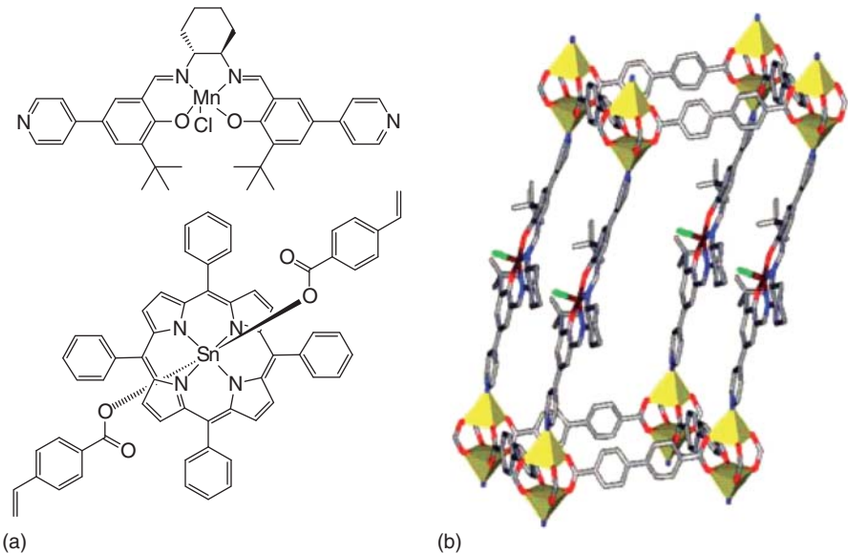


Figure 13 (a) The molecular structures of (*R*,*R*)-(−)-1,2-cyclohexanediamino-*N*,*N*′-bis(3-*tert*-butyl-5-(4-pyridyl)salicylidene)$Mn^{III}Cl$ and a large porphyrinic substrate and (b) a POVRAY view of a single network unit (Reproduced from Ref. 101 with permission from The Royal Society of Chemistry. DOI: 10.1039/B600408C.)

that at the beginning, a significant fraction of the catalysis occurs on exterior surface of the MOF, but at later stages, catalysis occurs chiefly inside the pores of the MOF. Evidently, the recyclability, easy separation, and extended catalyst lifetime and substrate size selectivity certainly makes this MOF a better catalyst than the free metalloligand. Expanding this strategy, Lin and coworks[102] recently reported a series of isoreticular chiral MOFs, which were constructed by linking $Zn_4O(COO)_6$ SBUs and chiral Mn–salen-derived dicarboxylic acids. By changing the length of the ligands, together with controlling the framework interpenetration, the channel sizes of the resulting MOFs can be systematically tuned, thus providing an opportunity for studying their structure-catalytic activity relationships. The catalytic activities were examined in asymmetric epoxidation of a variety of unfunctionalized olefins. It was found that the reaction rate increased as the channel sizes of the frameworks increased, suggesting that the diffusion of the substrates and oxidant played an important role in determining the reaction rate. When pore channels are large enough to facilitate the diffusion of reactants and products, the catalytic activity of the chiral MOFs is mainly limited by the intrinsic reactivity of the catalytic molecular building blocks.

To incorporate metalloporphyrin building blocks into the pore surface of the porous MOFs, Wu and coworkers[103] constructed three isostructural porous metalloporphyrinic frameworks (MPFs) of tbo topology (**ZJU-18**: $[Mn_5Cl_2(MnCl\text{-}OCPP)(DMF)_4(H_2O)_4]\cdot 2DMF\cdot 8CH_3CO_2H\cdot 14H_2O$; **ZJU-19**: $[Mn_5Cl_2(Ni\text{-}OCPP)(H_2O)_8]\cdot 7DMF\cdot 6CH_3CO_2H\cdot 11H_2O$; and **ZJU-20**: $[Cd_5Cl_2(MnCl\text{-}OCPP)(H_2O)_6]\cdot 13DMF\cdot 2CH_3CO_2H\cdot 9H_2O$) using octatopic metalloporphyrin ligands metal 5,10,15,20-tetrakis(3,5-biscarboxylphenyl)porphyrin (M-H_8OCPP) (M = Mn(III)Cl or Ni(II)), and examined their catalytic activities for oxidation of alkylbenzenes (Figure 14). Of these three MPFs, **ZJU-18** consisting of Mn(III)porphyrin units coordinated to manganese-containing SBUs exhibited highly efficient and selective oxidation of alkylbenzene. Furthermore, in terms of the catalytic activities, **ZJU-18** is very superior to the molecular counterpart Mn(III)Cl-Me_8OCPP, indicating that such a porous MPF enhanced their catalytic activities by blocking the formation of the catalytically inactive dimetalloporphyrinic species.

6 CONCLUSION

We have summarized the latest developments in the area of pore surface engineering of porous MOFs by immobilization of OMSs. The ability to more rationally immobilize the OMSs on the pore surface has featured the emerging porous MOFs as very promising media for diverse applications in gas storage and separation, chemical sensing, and heterogeneous catalysis, where OMSs play very important role in differential or specific recognition of small molecules. It is thus expected that by immobilization of OMSs on the pore surface, some practically useful

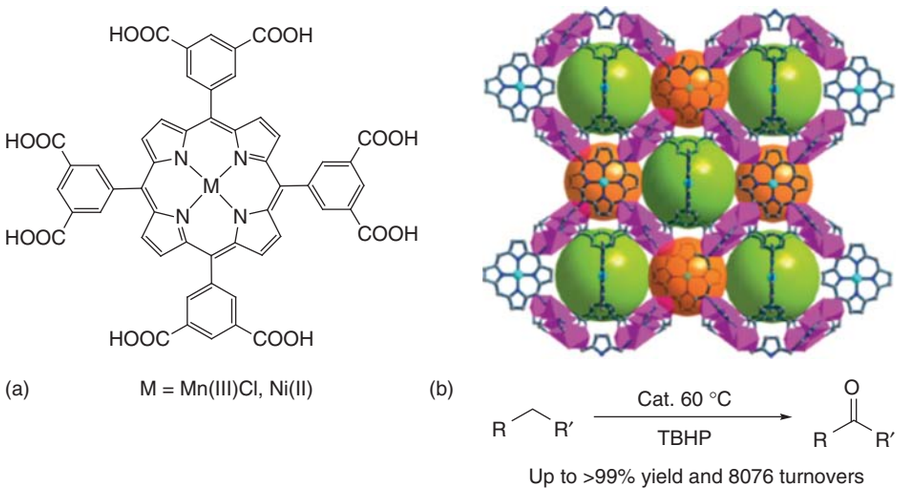


Figure 14 The molecular building blocking metal 5,10,15,20-tetrakis(3,5-biscarboxylphenyl)porphyrin (M-H_8OCPP) (M = Mn(III)Cl or Ni(II)) (a) used to construct porous MPFs for catalytic oxidation of alkylbenzenes (b) (Reprinted with permission from Ref. 103. Copyright (2012) American Chemical Society.)

MOFs will be targeted and implemented in industrial usage in the near future.

7 ACKNOWLEDGMENTS

This work was supported by an AX-1730 from Welch Foundation (BC).

8 RELATED ARTICLES

Metal-Organic Frameworks for Removal of Harmful Gases; Gas Storage in Metal-Organic Frameworks; Adsorption of Hydrocarbons and Alcohols in Metal-Organic Framework Materials; Photoreactive Metal-Organic Frameworks.

9 ABBREVIATIONS AND ACRONYMS

adip = 5,5′-(9,10-anthracediyl)diisophthalate; BPDC = biphenyl-4,4′-dicarboxylate; BPT = biphenyl-3,4′,5-tricarboxylate; bpydc = 2,2′-bipyridine-5,5′-dicarboxylate; BTC = benzene-1,3,5-tricarboxylate; CCS = CO_2 capture and sequestration; diPyNI = *N*,*N*′-di-(4-pyridyl)-1,4,5,8-naphthalenetetracarboxydiimide; DOBDC = 2,5-dioxido-1,4-benzenedicarboxylate; DOE = Department of Energy; EBTC = 1,1′-ethynebenzene-3,3′,5,5′-tetracarboxylate; EMC = entatic metal center; G = guest solvent; H_2BDC= benzene-1,4-dicarboxylic acid; H_2CDC = cyclohexane-1,4-dicarboxylic acid; H_3BTT = 1,3,5-benzenetristetrazolate; H_3TPO = tris-(4-carboxylphenyl)phosphine oxide; H_4bptc = 3,3′,5,5′-biphenyltetracarboxylic acid; H_4mdip = 5,5′-methylene-diisophthalate; H_4PDDI = 5,5′-(pyridine-2,5-diyl)diisophthalic acid; H_4salphdc = *N*,*N*′-phenylenebis (salicylideneimine)dicarboxylic acid; H_6bhb = H_6bhb = 3,3′,3″,5,5′5″-benzene-1,3,5-triyl-hexabenzoic acid; INS = inelastic neutron scattering; LBS = Lewis basic sites; M'MOF = mixed metal–organic framework; mipt = 5-methylisophthalate; MOF = Metal–organic framework; MPF = metalloporphyrinic framework; NDC = 2,6-naphthalenedicarboxylate; NGV = natural gas vehicle; NPD = neutron powder diffraction; OMS = open metal site; PCN = porous coordination network; PCP = porous coordination polymer; ppz = piperazine; SBU = secondary building unit; TATB = 4,4′,4″-*s*-triazine-2,4,6-triyltribenzoate; TDPAT = 2,4,6-tris(3,5-dicarboxyphenylamino)-1,3,5-triazine; 1,2,4-BTC = benzene-1,2,4-tricarboxylate; 2,2′-bpy = 2,2′-bipyridine; 3,5-PDC = 3,5-pyridinedicarboxylate; 3D = three-dimensional.

10 REFERENCES

1. B. Chen, M. Eddaoudi, T. M. Reineke, J. W. Kampf, M. O'Keeffe, and O. M. Yaghi, *J. Am. Chem. Soc.*, 2000, **122**, 11559.

2. B. Chen, M. Eddaoudi, S. T. Hyde, M. O'Keeffe, and O. M. Yaghi, *Science*, 2001, **291**, 1021.
3. R. Kitaura, G. Onoyama, H. Sakamoto, R. Matsuda, S.-I. Noro, and S. Kitagawa, *Angew. Chem. Int. Ed.*, 2004, **43**, 2684.
4. B. Chen, X. Zhao, A. Putkham, K. Hong, E. B. Lobkovsky, E. J. Hurtado, A. J. Fletcher, and K. M. Thomas, *J. Am. Chem. Soc.*, 2008, **130**, 6411.
5. S. Xiang, Z. Zhang, C.-G. Zhao, K. Hong, X. Zhao, D.-L. Ding, M.-H. Xie, C.-D. Wu, R. Gill, K. M. Thomas, and B. Chen, *Nat. Commun.*, 2012, **2**, 204.
6. M. C. Das, Q. Guo, Y. He, J. Kim, C.-G. Zhao, K. Hong, S. Xiang, Z. Zhang, K. M. Thomas, R. Krishna, and B. Chen, *J. Am. Chem. Soc.*, 2012, **134**, 8703.
7. N. L. Rosi, J. Eckert, M. Eddaoudi, D. T. Vodak, J. Kim, M. O'Keeffe, and O. M. Yaghi, *Science*, 2003, **300**, 1127.
8. S. Ma, D. Sun, M. Ambrogio, J. A. Fillinger, S. Parkin, and H.-C. Zhou, *J. Am. Chem. Soc.*, 2007, **129**, 1858.
9. B. Kesanli, Y. Cui, M. R. Smith, E. W. Bittner, B. C. Bockrath, and W. Lin, *Angew. Chem. Int. Ed.*, 2005, **44**, 72.
10. L. Pan, M. B. Sander, X. Huang, J. Li, M. Smith, E. Bittner, B. Bockrath, and J. K. Johnson, *J. Am. Chem. Soc.*, 2004, **126**, 1308.
11. Y. Li and R. T. Yang, *J. Am. Chem. Soc.*, 2006, **128**, 726.
12. Y. Li and R. T. Yang, *J. Am. Chem. Soc.*, 2006, **128**, 8136.
13. V. K. Peterson, Y. Liu, C. M. Brown, and C. J. Kepert, *J. Am. Chem. Soc.*, 2006, **128**, 15578.
14. M. Dincă, A. Dailly, Y. Liu, C. M. Brown, D. A. Neumann, and J. R. Long, *J. Am. Chem. Soc.*, 2006, **128**, 16876.
15. M. Dincă, W. S. Han, Y. Liu, A. Dailly, C. M. Brown, and J. R. Long, *Angew. Chem. Int. Ed.*, 2007, **46**, 1419.
16. K. Sumida, S. Horike, S. S. Kaye, Z. R. Herm, W. L. Queen, C. M. Brown, F. Grandjean, G. J. Long, A. Dailly, and J. R. Long, *Chem. Sci.*, 2010, **1**, 184.
17. Y. Yan, I. Telepeni, S. Yang, X. Lin, W. Kockelmann, A. Dailly, A. J. Blake, W. Lewis, G. S. Walker, D. R. Allan, S. A. Barnett, N. R. Champness, and M. Schröder, *J. Am. Chem. Soc.*, 2010, **132**, 4092.
18. S. S.-Y. Chui, S. M.-F. Lo, J. P. H. Charmant, A. G. Orpen, and I. D. Williams, *Science*, 1999, **283**, 1148.
19. M. P. Suh, H. J. Park, T. K. Prasad, and D.-W. Lim, *Chem. Rev.*, 2012, **112**, 782.
20. L. J. Murray, M. Dincă, and J. R. Long, *Chem. Soc. Rev.*, 2009, **38**, 1294.
21. J. L. C. Rowsell and O. M. Yaghi, *Angew. Chem. Int. Ed.*, 2005, **44**, 4670.
22. B. Chen, N. W. Ockwig, A. R. Millward, D. S. Contreras, and O. M. Yaghi, *Angew. Chem. Int. Ed.*, 2005, **44**, 4745.
23. Y.-G. Lee, H. R. Moon, Y. E. Cheon, and M. P. Suh, *Angew. Chem. Int. Ed.*, 2008, **47**, 7741.
24. X. Lin, I. Telepeni, A. J. Blake, A. Dailly, C. M. Brown, J. M. Simmons, M. Zoppi, G. S. Walker, K. M. Thomas, T. J. Mays, P. Hubberstey, N. R. Champness, and M. Schröder, *J. Am. Chem. Soc.*, 2009, **131**, 2159.
25. X.-S. Wang, S. Ma, P. M. Forster, D. Yuan, J. Eckert, J. J. Lpez, B. J. Murphy, J. B. Parise, and H.-C. Zhou, *Angew. Chem. Int. Ed.*, 2008, **47**, 7263.
26. C. R. Wade and M. Dincă, *Dalton Trans.*, 2012, **41**, 7931.
27. Y. E. Cheon and M. P. Suh, *Chem. Commun.*, 2009, 2296.
28. W. R. Lee, D. W. Ryu, J. W. Lee, J. H. Yoon, E. K. Koh, and C. S. Hong, *Inorg. Chem.*, 2010, **49**, 4723.
29. S. Ma and H.-C. Zhou, *J. Am. Chem. Soc.*, 2006, **128**, 11734.
30. S. Yang, X. Lin, A. J. Blake, G. S. Walker, P. Hubberstey, N. R. Champness, and M. Schröder, *Nat. Chem.*, 2009, **1**, 487.
31. K. L. Mulfort and J. T. Hupp, *J. Am. Chem. Soc.*, 2007, **129**, 9604.
32. K. L. Mulfort and J. T. Hupp, *Inorg. Chem.*, 2008, **47**, 7936.
33. M. Kondo, T. Yoshitomi, K. Seki, H. Matsuzaka, and S. Kitagawa, *Angew. Chem. Int. Ed.*, 1997, **36**, 1725.
34. Z. Guo, H. Wu, G. Srinivas, Y. Zhou, S. Xiang, Z. Chen, Y. Yang, W. Zhou, M. O'Keeffe, and B. Chen, *Angew. Chem. Int. Ed.*, 2011, **50**, 3178.
35. S. Ma, D. Sun, J. M. Simmons, C. D. Collier, D. Yuan, and H.-C. Zhou, *J. Am. Chem. Soc.*, 2008, **130**, 1012.
36. C. E. Wilmer, M. Leaf, C. Y. Lee, O. K. Farha, B. G. Hauser, J. T. Hupp, and R. Q. Snurr, *Nat. Chem.*, 2012, **4**, 83.
37. H. Wu, W. Zhou, and T. Yildirim, *J. Am. Chem. Soc.*, 2009, **131**, 4995.
38. N. L. Rosi, J. Kim, M. Eddaoudi, B. Chen, M. O'Keeffe, and O. M. Yaghi, *J. Am. Chem. Soc.*, 2005, **127**, 1504.
39. P. D. C. Dietzel, Y. Morita, R. Blom, and H. Fjellvåg, *Angew. Chem. Int. Ed.*, 2005, **44**, 6354.
40. P. D. C. Dietzel, B. Panella, M. Hirscher, R. Blom, and H. Fjellvåg, *Chem. Commun.*, 2006, 959.
41. P. D. C. Dietzel, R. Blom, and H. Fjellvåg, *Eur. J. Inorg. Chem.*, 2008, **2008**, 3624.
42. S. R. Caskey, A. G. Wong-Foy, and A. J. Matzger, *J. Am. Chem. Soc.*, 2008, **130**, 10870.
43. W. Zhou, H. Wu, and T. Yildirim, *J. Am. Chem. Soc.*, 2008, **130**, 15268.
44. S. Xiang, W. Zhou, Z. Zhang, M. A. Green, Y. Liu, and B. Chen, *Angew. Chem. Int. Ed.*, 2010, **49**, 4615.
45. Y.-S. Bae, C. Y. Lee, K. C. Kim, O. K. Farha, P. Nickias, J. T. Hupp, S. T. Nguyen, and R. Q. Snurr, *Angew. Chem. Int. Ed.*, 2012, **51**, 1857.
46. S. J. Geier, J. A. Mason, E. D. Bloch, W. L. Queen, M. R. Hudson, C. M. Brown, and J. R. Long, *Chem. Sci.*, 2013, **4**, 2054.

47. R. Matsuda, R. Kitaura, S. Kitagawa, Y. Kubota, R. V. Belosludov, T. C. Kobayashi, H. Sakamoto, T. Chiba, M. Takata, Y. Kawazoe, and Y. Mita, *Nature*, 2005, **436**, 238.
48. D. Tanaka, M. Higuchi, S. Horike, R. Matsuda, Y. Kinoshita, N. Yanai, and S. Kitagawa, *Chem. Asian. J.*, 2008, **3**, 1343.
49. S. Xiang, W. Zhou, J. M. Gallegos, Y. Liu, and B. Chen, *J. Am. Chem. Soc.*, 2009, **131**, 12415.
50. Y. Hu, S. Xiang, W. Zhang, Z. Zhang, L. Wang, J. Bai, and B. Chen, *Chem. Commun.*, 2009, 7551.
51. X. Rao, J. Cai, J. Yu, Y. He, C. Wu, W. Zhou, T. Yildirim, B. Chen, and G. Qian, *Chem. Commun.*, 2013, **49**, 6719.
52. J. An, S. J. Geib, and N. L. Rosi, *J. Am. Chem. Soc.*, 2010, **132**, 38.
53. R. Vaidhyanathan, S. S. Iremonger, G. K. H. Shimizu, P. G. Boyd, S. Alavi, and T. K. Woo, *Science*, 2010, **330**, 650.
54. K. Sumida, D. L. Rogow, J. A. Mason, T. M. McDonald, E. D. Bloch, Z. R. Herm, T.-H. Bae, and J. R. Long, *Chem. Rev.*, 2012, **112**, 724.
55. Z. Zhang, Y. Zhao, Q. Gong, Z. Li, and J. Li, *Chem. Commun.*, 2013, **49**, 653.
56. A. R. Millward and O. M. Yaghi, *J. Am. Chem. Soc.*, 2005, **127**, 17998.
57. H. Furukawa, N. Ko, Y. B. Go, N. Aratani, S. B. Choi, E. Choi, A. Ö. Yazaydin, R. Q. Snurr, M. O'Keeffe, J. Kim, and O. M. Yaghi, *Science*, 2010, **329**, 424.
58. O. K. Farha, A. Ö. Yazaydın, I. Eryazici, C. D. Malliakas, B. G. Hauser, M. G. Kanatzidis, S. T. Nguyen, R. Q. Snurr, and J. T. Hupp, *Nat. Chem.*, 2010, **2**, 944.
59. P. L. Llewellyn, S. Bourrelly, C. Serre, A. Vimont, M. Daturi, L. Hamon, G. D. Weireld, J.-S. Chang, D.-Y. Hong, Y. K. Hwang, S. H. Jhung, and G. Férey, *Langmuir*, 2008, **24**, 7245.
60. Y.-S. Bae, A. M. Spokoyny, O. K. Farha, R. Q. Snurr, J. T. Hupp, and C. A. Mirkin, *Chem. Commun.*, 2010, **46**, 3478.
61. A. Ö. Yazaydın, R. Q. Snurr, T.-H. Park, K. Koh, J. Liu, M. D. LeVan, A. I. Benin, P. Jakubczak, M. Lanuza, D. B. Galloway, J. J. Low, and R. R. Willis, *J. Am. Chem. Soc.*, 2009, **131**, 18198.
62. P. D. C. Dietzel, R. E. Johnsen, H. Fjellvåg, S. Bordiga, E. Groppo, S. Chavan, and R. Blom, *Chem. Commun.*, 2008, 5125.
63. P. D. C. Dietzel, V. Besikiotis, and R. Blom, *J. Mater. Chem.*, 2009, **19**, 7362.
64. D. Britt, H. Furukawa, B. Wang, T. G. Glover, and O. M. Yaghi, *Proc. Natl. Acad. Sci.*, 2009, **106**, 20637.
65. J. Park, H. Kim, S. S. Han, and Y. Jung, *J. Phys. Chem. Lett.*, 2012, **3**, 826.
66. E. D. Bloch, D. Britt, C. Lee, C. J. Doonan, F. J. Uribe-Romo, H. Furukawa, J. R. Long, and O. M. Yaghi, *J. Am. Chem. Soc.*, 2010, **132**, 14382.
67. B. Li, Z. Zhang, Y. Li, K. Yao, Y. Zhu, Z. Deng, F. Yang, X. Zhou, G. Li, H. Wu, N. Nijem, Y. J. Chabal, Z. Lai, Y. Han, Z. Shi, S. Feng, and J. Li, *Angew. Chem. Int. Ed.*, 2011, **51**, 1412.
68. Y. Yan, M. Suyetin, E. Bichoutskaia, A. J. Blake, D. R. Allan, S. A. Barnett, and M. Schröder, *Chem. Sci.*, 2013, **4**, 1731.
69. Q. M. Wang, D. Shen, M. Bülow, M. L. Lau, S. Deng, F. R. Fitch, N. O. Lemcoff, and J. Semanscin, *Microporous Mesoporous Mater.*, 2002, **55**, 217.
70. T. M. Nicholson and S. K. Bhatia, *J. Phys. Chem. B*, 2006, **110**, 24834.
71. S. Wang, Q. Yang, and C. Zhong, *Sep. Purif. Technol.*, 2008, **60**, 30.
72. J. W. Yoon, I. T. Jang, K.-Y. Lee, Y. K. Hwang, and J.-S. Chang, *Bull. Kor. Chem. Soc.*, 2010, **31**, 220.
73. A. Wagener, M. Schindler, F. Rudolphi, and S. Ernst, *Chem. Ing. Tech.*, 2007, **79**, 851.
74. M. Jorge, N. Lamia, and A. E. Rodrigues, *Colloids Surf. A*, 2010, **357**, 27.
75. N. Lamia, M. Jorge, M. A. Granato, F. A. AlmeidaPaz, H. Chevreau, and A. E. Rodrigues, *Chem. Eng. Sci.*, 2009, **64**, 3246.
76. A. F. P. Ferreira, J. C. Santos, M. G. Plaza, N. Lamia, J. M. Loureiro, and A. E. Rodrigues, *Chem. Eng. J.*, 2011, **167**, 1.
77. M. Hartmann, S. Kunz, D. Himsl, and O. Tangermann, *Langmuir*, 2008, **24**, 8634.
78. J. W. Yoon, Y.-K. Seo, Y. K. Hwang, J.-S. Chang, H. Leclerc, S. Wuttke, P. Bazin, A. Vimont, M. Daturi, E. Bloch, P. L. Llewellyn, C. Serre, P. Horcajada, J.-M. Grenèche, A. E. Rodrigues, and G. Férey, *Angew. Chem. Int. Ed.*, 2010, **49**, 5949.
79. Y. He, R. Krishna, and B. Chen, *Energy Environ. Sci.*, 2012, **5**, 9107.
80. Z. Bao, S. Alnemrat, L. Yu, I. Vasiliev, Q. Ren, X. Lu, and S. Deng, *Langmuir*, 2011, **27**, 13554.
81. E. D. Bloch, W. L. Queen, R. Krishna, J. M. Zadrozny, C. M. Brown, and J. R. Long, *Science*, 2012, **335**, 1606.
82. Z. Zhang, S. Xiang, X. Rao, Q. Zheng, F. R. Fronczek, G. Qian, and B. Chen, *Chem. Commun.*, 2010, **46**, 7205.
83. Z. Zhang, S. Xiang, K. Hong, C. D. Madhab, H. D. Arman, M. Garcia, J. U. Mondal, K. M. Thomas, and B. Chen, *Inorg. Chem.*, 2012, **51**, 4947.
84. H. Xu, Y. He, Z. Zhang, S. Xiang, J. Cai, Y. Cui, Y. Yang, G. Qian, and B. Chen, *J. Mater. Chem. A*, 2013, **1**, 77.
85. B. Chen, Y. Yang, F. Zapata, G. Lin, G. Qian, and E. B. Lobkovsky, *Adv. Mater.*, 2007, **19**, 1693.
86. Z. Guo, H. Xu, S. Su, J. Cai, S. Dang, S. Xiang, G. Qian, H. Zhang, M. O'Keeffe, and B. Chen, *Chem. Commun.*, 2011, **47**, 5551.
87. B. Chen, L. Wang, F. Zapata, G. Qian, and E. B. Lobkovsky, *J. Am. Chem. Soc.*, 2008, **130**, 6718.

88. M. Fujita, Y. J. Kwon, S. Washizu, and K. Ogura, *J. Am. Chem. Soc.*, 1994, **116**, 1151.

89. A. Corma, H. García, and F. X. L. I. Xamena, *Chem. Rev.*, 2010, **110**, 4606.

90. K. Schlichte, T. Kratzke, and S. Kaskel, *Microporous Mesoporous Mater.*, 2004, **73**, 81.

91. L. Alaerts, E. Séguin, H. Poelman, F. Thibault-Starzyk, P. A. Jacobs, and D. E. D. Vos, *Chem. Eur. J.*, 2006, **12**, 7353.

92. E. Pérez-Mayoral and J. Čejka, *ChemCatChem*, 2011, **3**, 157.

93. Y. Wu, L.-G. Qiu, W. Wang, Z.-Q. Li, T. Xu, Z.-Y. Wu, and X. Jiang, *Transit. Met. Chem.*, 2009, **34**, 263.

94. A. Henschel, K. Gedrich, R. Kraehnert, and S. Kaskel, *Chem. Commun.*, 2008, 4192.

95. D.-A. Yang, H.-Y. Cho, J. Kim, S.-T. Yang, and W.-S. Ahn, *Energy Environ. Sci.*, 2012, **5**, 6465.

96. S. Horike, M. Dincă, K. Tamaki, and J. R. Long, *J. Am. Chem. Soc.*, 2008, **130**, 5854.

97. O. R. Evans, H. L. Ngo, and W. Lin, *J. Am. Chem. Soc.*, 2001, **123**, 10395.

98. K. Gedrich, M. Heitbaum, A. Notzon, I. Senkovska, R. Frçhlich, J. R. Getzschmann, U. Mueller, F. Glorius, and S. Kaskel, *Chem. Eur. J.*, 2011, **17**, 2099.

99. R.-Q. Zou, H. Sakurai, S. Han, R.-Q. Zhong, and Q. Xu, *J. Am. Chem. Soc.*, 2007, **129**, 8402.

100. C.-D. Wu, A. Hu, L. Zhang, and W. Lin, *J. Am. Chem. Soc.*, 2005, **127**, 8940.

101. S.-H. Cho, B. Ma, S. T. Nguyen, J. T. Hupp, and T. E. Albrecht-Schmitt, *Chem. Commun.*, 2006, 2563.

102. F. Song, C. Wang, J. M. Falkowski, L. Ma, and W. Lin, *J. Am. Chem. Soc.*, 2010, **132**, 15390.

103. X.-L. Yang, M.-H. Xie, C. Zou, Y. He, B. Chen, M. O'Keeffe, and C.-D. Wu, *J. Am. Chem. Soc.*, 2012, **134**, 10638.

Gas Storage in Metal-Organic Frameworks

Muwei Zhang, Hao Li, Zachary Perry and Hong-Cai Zhou

Texas A&M University, College Station, TX, USA

1	Introduction	283
2	Metal-Organic Frameworks: Porosity, Surface Area, and Functionalization	283
3	Hydrogen Storage in MOFs	285
4	Carbon Dioxide Capture in MOFs	287
5	Methane Storage in MOFs	290
6	Storage of Other Gases in MOFs	297
7	Conclusion	299
8	Acknowledgments	299
9	Related Articles	299
10	Abbreviations and Acronyms	299
11	References	299

1 INTRODUCTION

For the past few decades, porous materials have been extensively investigated in scientific and technological research owing to their capability to adsorb and interact with atoms, ions, and molecules.[1] Particularly, metal-organic frameworks (MOFs) have gained a tremendous amount of attention because of their novel structures and their diverse applications.[2] MOFs are a novel category of inorganic–organic hybrid crystalline porous materials with an infinite framework structure consisting of metal ions/clusters (also known as secondary building units, or SBUs) and organic linkers (ligands). Owing to the inexhaustible variability of the SBUs and ligands, enormous surface areas and pore volumes, and the convenient functionalization by pre- or postsynthetic modifications (PSMs), MOFs are widely applied in many areas such as gas storage,[3] gas separation,[4] carbon dioxide capture,[5] catalysis,[6] sensors,[7] drug delivery,[8] photosensitive materials,[9] and magnetic materials.[10]

Gas storage in solids has become an ever more important technology[11] attributable to the current worldwide interest of exploring alternative renewable energy resources and global concern about the environmental problems from the escalating level of anthropogenic CO_2 emissions. There are many advantages of gas storage in solid materials rather than simple physical compression in a tank, where the former requires a much lower operational pressure but, in many cases, yields a larger storage density.[12] Highly porous materials, such as carbon-based materials,[13] porous silica,[14,15] zeolites,[16,17] MOFs,[2] covalent-organic frameworks,[18] and porous polymer networks,[19,20] have provided a great variety of structural architectures suitable for gas storage. Among all those candidates, MOFs appear to be one of the most attractive adsorbents for gases because of their large gas uptake capacities and the tunable nature of their components. This chapter will focus on the gas storage properties of MOFs, whereas the other potential MOF applications will be illustrated in detail elsewhere in this book.

2 METAL-ORGANIC FRAMEWORKS: POROSITY, SURFACE AREA, AND FUNCTIONALIZATION

MOFs [also known as porous coordination networks (PCNs) or porous coordination polymers] are essentially three-dimensional coordination polymers in which the metallic centers are connected by polytopic organic linkers.[21,22] Provided that the organic linkers possess a certain degree of rigidity, the resulting framework usually exhibits a permanent inner porosity (i.e., pores remain intact and accessible to guest molecules) on the removal

Metal-Organic Framework Materials. Edited by Leonard R. MacGillivray and Charles M. Lukehart.
© 2014 John Wiley & Sons, Ltd. ISBN 978-1-119-95289-3

of the guest molecules in its pores. It is this permanent porosity of the framework that provides room for gas storage. Figure 1 illustrates an example of the architecture and porosity of MOF-5,[23] one of the earliest MOFs to be structurally characterized. Its metal clusters (Zn_4O SBUs) connect with six carboxylates to form an octahedral unit. The rigidity of the organic linker, 1,4-benzenedicarboxylate (bdc), in combination with the SBU, generates large three-dimensional channels inside its structure, giving an 8.0-Å channel diameter.

The porous nature of a solid can be categorized according its pore size. Pore sizes smaller than 2 nm are defined as micropores; pores ranging between 2 and 50 nm are mesopores; and pores larger than 50 nm are termed macropores.[1] Their pore size and shape significantly affect their abilities to perform the desired functions, especially for gas storage. Specifically, microporous MOFs with uniform cavities appear to be particularly promising for gas storage.[24]

The adhesion between the surfaces within the pores and the guest molecules is defined as adsorption. Unlike absorption in which the guest molecules permeate or dissolve through the entire absorbent, adsorption only occurs on the surface of the adsorbent. With respect to a given gas molecule, surface area can be calculated from its adsorption isotherm. Langmuir surface area[25] and Brunauer–Emmett–Teller (BET) surface area[26] are usually utilized to describe MOF porosity. To achieve larger surface areas, many ultraporous MOFs have recently been reported, with Langmuir surface area as high as $10\,400\ m^2 \cdot g^{-1}$ (in MOF-210, Ref. 27) and BET surface area as high as $7140\ m^2 \cdot g^{-1}$ (in NU-110E, Ref. 28).

While the gas storage capacities of a MOF are closely related to its surface area, surface functionality is another significant factor that considerably affects its gas adsorption behavior. In order to achieve better framework properties, *functionalization* of the frameworks appears to be necessary for gas storage and is done by presynthetic modification or PSM.[29] Presynthetic modification of MOFs can typically be achieved by ligand design, whereas PSM can be accomplished by direct functionalization of the framework. Many different functionalization units can

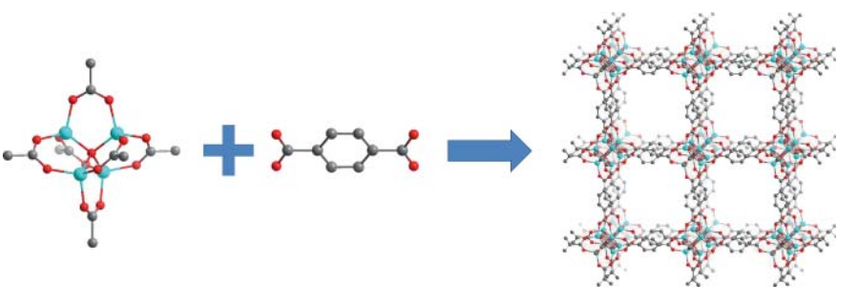


Figure 1 The representation of the structure and porosity of MOF-5,[23] where the gray, red, and cyan spheres represent C, O, and Zn, respectively. H atoms were omitted for clarity

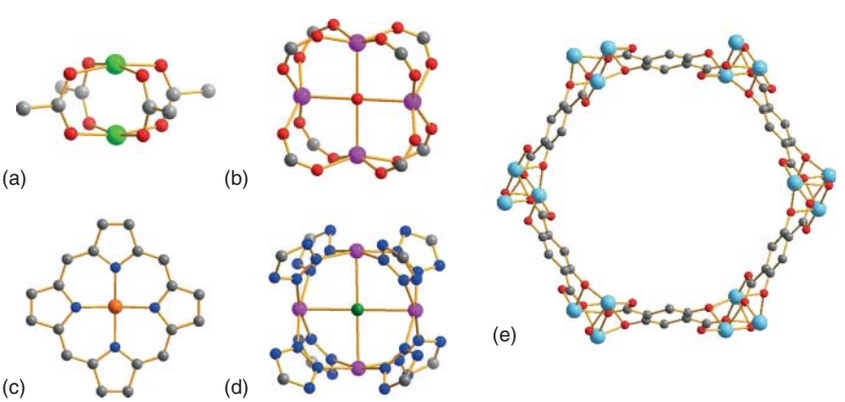


Figure 2 The illustration of some representative UMCs. (a) A dicopper paddlewheel structure with unsaturated copper centers.[30] (b) A $Co_4(\mu_4\text{-O})(\text{carboxylate})_8$ SBU with unsaturated cobalt centers.[31] (c) A metalloporphyrin moiety with unsaturated iron center.[40] (d) A $Mn_4(\mu_4\text{-Cl})(\text{tetrazolate})_8$ SBU with unsaturated manganese centers.[41] (e) The Mg-MOF-74 (CPO-27) structure with unsaturated magnesium centers[42]

be incorporated into MOFs for the purpose of improving the interaction between the adsorbate (gas molecules) and adsorbent (MOFs).

Among the functional aspects generally considered, unsaturated metal centers (UMCs, also known as open metal sites) are of special interest because of the interactions between the open sites of the metal ions and adsorbates, such as hydrogen,[30,31] methane,[32] carbon dioxide,[33,34] sulfur dioxide,[35] oxygen,[36] acetylene,[37] ethylene,[38] propene,[39] and many others. Figure 2 demonstrates some commonly seen UMCs in MOF chemistry, where the interactions between these UMCs and gas molecules will be illustrated in the subparts.

3 HYDROGEN STORAGE IN MOFS

Fossil fuels and other biologically produced resources have provided sufficient energy to run society for centuries. However, with the current rate of population growth, it is estimated that supply of gasoline products will run short of demand in the near future. It is imperative that researchers should search for an alternative energy source as the replacement of the current petroleum-based energy infrastructure. Hydrogen fuel is a zero-emission fuel that has already been applied in electrochemical cells and combustion engines in order to power vehicles and electric devices. Even though hydrogen is not a primary energy resource yet, its gravimetric energy density is almost three times higher than that of gasoline.[43] The National Aeronautics and Space Administration (NASA) has been using liquid hydrogen to propel its space shuttles into orbit since the 1970s. Currently, some vehicles, such as buses, shuttles, and trains, already run on hydrogen.

Hydrogen is not a naturally occurring source of energy such as fossil fuels, and it has to be first produced and then stored before it can be used. The storage and transportation of hydrogen is one of the most significant challenges that confront the hydrogen economy. Methods of hydrogen storage include many approaches, but they can be primarily divided into two categories: physical storage and chemical storage. Conventional physical storage typically involves the production of compressed hydrogen by high pressure or cryogenic conditions, but the low volumetric energy density and high operational cost have significantly restrained their large-scale applications. Chemical storage of H_2 involves the utilization of various chemicals, including metal hydrides, borane,[44] and, more recently, imidazolium ionic liquids.[45] These methods still suffer from many drawbacks, including high production cost, unfavorable kinetics requiring heating cycles, and susceptibility to contamination by impurities.[46]

MOFs appear to be competitive materials for hydrogen storage because of their large specific surface area and tunable surface properties. MOF-5 (Ref. 23, Figure 1) is one of the early examples of representative MOFs that have been investigated for hydrogen storage purposes.[46] The uniformity of three-dimensional micropores has resulted in a 4.5 wt% hydrogen uptake at 78 K and 20 bar. In order to achieve a higher storage density of hydrogen in MOFs, many functionalization units can be incorporated into the framework. Both experimental and computational studies show that the UMCs are particularly promising features to improve the interaction between H_2 and the framework and hence enhance the H_2 storage density and heat of adsorption. The UMCs are generated on the activation of materials when the solvents and other volatile components are removed from the cavities, leaving coordination sites exposed on the pore surfaces. Maximization of these sites through ligand design and activation methods should work constructively to increase H_2 uptake.

The interaction between H_2 molecules and exposed metal ions has been studied for decades. The initial motivation to study this type of interaction came from the activation and cleavage of hydrogen by metal centers for important chemical reactions. The discovery of metal–H_2 complexes has enabled chemists to examine the coordination nature of the σ donors, such as a H_2 molecule. The σ-electrons of H_2 can coordinate to a vacant metal d orbital, whereas its empty σ^* orbital can receive electrons from an occupied metal d orbital.[47] This type of interaction has dictated the side-on coordination mode of the H_2 molecule, where the H_2 σ and σ^* bonds can fully interact with the metal d orbitals (Figure 3).

The interaction between H_2 molecules with the UMCs in MOFs has also been observed. The Mn-btt MOF (Figure 4a) consists of the $Mn_4(\mu_4\text{-Cl})$ SBUs (Figure 2d) connected by the 1,3,5-tris(2H-tetrazol-5-yl)benzene ligand. Unsaturated Mn centers are generated on the MOF activation. Neutron scattering diffraction experiments were performed to study the interaction between D_2 and the framework. The two strongest binding sites for D_2 at low loading can be assigned to sites I and II in Figure 4(b). Particularly, site I is located just 2.27 Å from the Mn^{2+} ions, indicating the existence of the strong metal–H_2 interaction in this MOF.[41] Similarly, the D_2 molecules also bind to the UMCs in a side-on manner, implying the σ-donor nature of

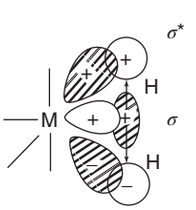


Figure 3 The illustration of interactions between H_2 molecule and a metal ion. (Reprinted with permission from Ref. 47. Copyright (1988) American Chemical Society.)

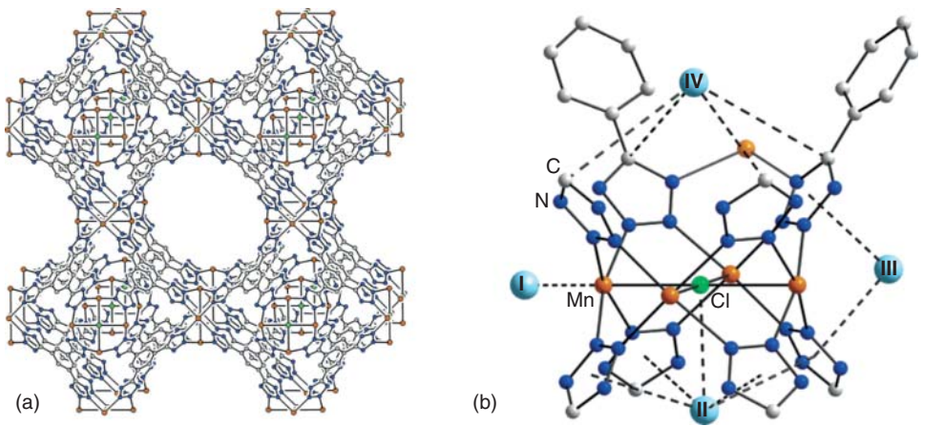


Figure 4 (a) The representation of the crystal structure of the Mn-btt MOF. (b) The strongest D_2-binding sites within this MOF. Light blue spheres represent the D_2 centroids, whereas the orange spheres represent the unsaturated Mn centers. (Reprinted with permission from Ref. 41. Copyright (2006) American Chemical Society.)

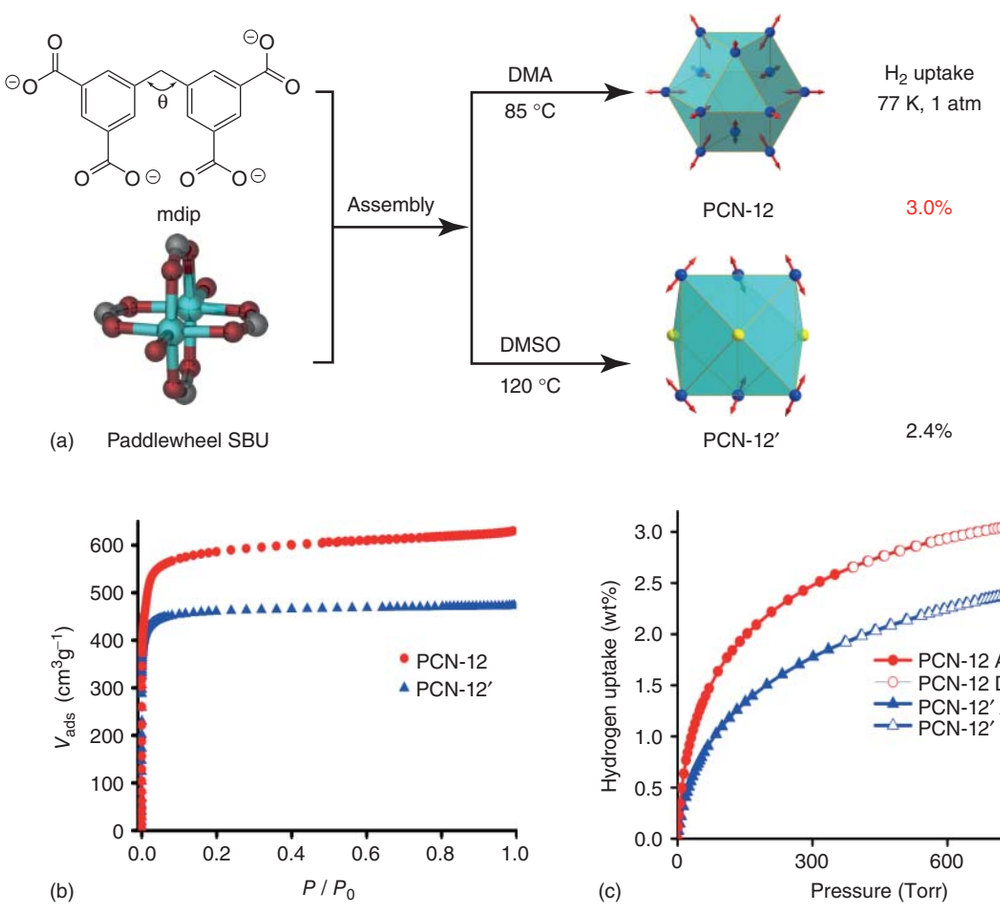


Figure 5 (a) The formation and UMC alignments of the two polymorphic MOFs, PCN-12, and PCN-12′. (b) N_2 adsorption isotherms for PCN-12 and PCN-12′. (c) H_2 adsorption isotherms for PCN-12 and PCN-12′. (Reproduced with permission from Ref. 30. © Wiley-VCH Verlag GmbH & Co. KGaA, Weinheim, 2008.)

a H_2 ligand. In addition, in Figure 4(b), sites III and IV are the third and fourth strongest D_2-binding sites. These sites become evident only when the D_2 loading is high. The high density of UMCs in Mn-btt MOF significantly contributes to its large H_2 uptake. Its hydrogen uptake is 2.2 wt% at 77 K and 1.2 bar and 5.1 wt% at saturation (40 bar).

The strategy of increasing the number of nearest neighboring UMCs to each H_2-hosting cavity in order to enhance the H_2 uptake appears to be very efficient. PCN-12, the current record holder for H_2 storage at 77 K and 1 bar, was designed and synthesized based on this strategy.[30] PCN-12 consists of dicopper paddlewheel SBUs connected by the 5,5′-methylene-di-isophthalate (mdip) ligand (Figure 5a). A polymorphic framework, PCN-12′, can also be synthesized with the same ligand but different solvothermal conditions. Both exhibit permanent porosity (Figure 5b). Even though the two MOFs are isomeric, the hydrogen uptakes between them are remarkably different (Figure 5c). PCN-12 possesses a hydrogen uptake of 3.05 wt% at 77 K and 1 bar, which is the highest among all MOFs, in contrast to an uptake of 2.40 wt% for PCN-12′ under the same conditions. This difference is attributed to the dissimilar alignment of UMCs in the two polymorphs (Figure 5a).[30]

In summary, MOFs are promising materials for H_2 storage because of their inherent porosity and the wide variety of surface functionalities that can be applied to tune for optimum sorption. Specifically, the presence of UMCs significantly contributes to the H_2 uptake capacity and the heat of adsorption. Table 1 lists some representative MOFs for H_2 uptake at 77 K and different pressures.

4 CARBON DIOXIDE CAPTURE IN MOFS

Elimination of CO_2 from mixed component gas streams has been extensively investigated because of escalating concern about the environmental and climatic impact of greenhouse gas emissions.[51] The sharply rising level of atmospheric CO_2 has become one of the most urgent and challenging problems confronting our civilization, and it is the attributed cause of many environmental problems, such as global warming and ocean acidification. In order to reduce anthropogenic CO_2 emissions, various carbon capture and sequestration (CCS) techniques have emerged as means to selectively remove CO_2 from the existing emission resources, primarily from the flue gas of fossil fuel-powered plants.[52] Traditional methods of CCS include the utilization of aqueous alkanolamines, such as monoethanolamine or triethanolamine solutions, to capture CO_2 selectively from flue gas.[53] Regardless of their large CO_2 capacity and affinity, this process suffers from a series of complications that have considerably limited their large-scale application, such as the high regeneration cost arising from the large heat capacity of aqueous alkanolamine solutions, in addition to the toxicity, unpleasant smell, and corrosive nature of amine compounds.[54]

As an alternative solution, many solid porous materials have been shown to be promising candidates to overcome the downsides of aqueous alkanolamine solutions. Different from the process of CO_2 *absorption* into alkanolamine solutions, the utilization of solid materials is a process of CO_2 *adsorption* onto the inner surface of their cavities. MOFs are especially promising materials for selective elimination of CO_2 with high efficiency, low toxicity, and effective cost. Figure 6 shows the high pressure CO_2 uptake of some representative MOFs at room temperature (298 K). Among all the selected MOFs, MOF-177 has the largest uptake, probably because it possesses the highest surface area (BET surface area of 4500 $m^2 \cdot g^{-1}$) among them.[48] The large surface area of this framework ensures enough space for CO_2 diffusion and adsorption, where its CO_2 capacity reaches 33.5 $mmol \cdot g^{-1}$ at 42 bar.[55] Presumably, MOFs with larger cavities and surface areas may result in an additional increase of CO_2 uptake. The CO_2

Table 1 Representative MOFs H_2 uptake at 77 K

MOF	Ligand	Metal	BET surface area ($m^2 \cdot g^{-1}$)	H_2 uptake (wt%)	Pressure (bar)	Functionalization	Reference
MOF-5	bdc	Zn	2300	4.5	20	NA	46
MOF-177	btb	Zn	4500	7.5	70	NA	48
MIL-101	bdc	Cr	5500	6.1	60	UMC	49
Mn-btt	btt	Mn	2100	2.2	1.2	UMC	41
				5.1	40	UMC	41
PCN-12	mdip	Cu	1943	3.05	1	UMC	30
PCN-12′	mdip	Cu	1577	2.40	1	UMC	30
PCN-68	ptei	Cu	5109	1.87	1	UMC	3
				7.32	50	UMC	3
NU-100/PCN-610	ttei	Cu	6143	9.95	56	UMC	50

bdc, 1,4-benzenedicarboxylate; btt, tris(2H-tetrazol-5-yl)benzene; mdip, 5,5′-methylene-di-isophthalate; ptei, 5,5′-((5′-(4-((3,5-dicarboxyphenyl)ethynyl)phenyl)-[1,1′:3′1″-terphenyl]-4,4″-diyl)-bis(ethyne-2,1-diyl))diisophthalate; ttei, 5,5′,5″-(((benzene-1,3,5-triyltris(ethyne-2,1-diyl))tris(benzene-4,1-diyl))tris-(ethyne-2,1-diyl))triisophthalate

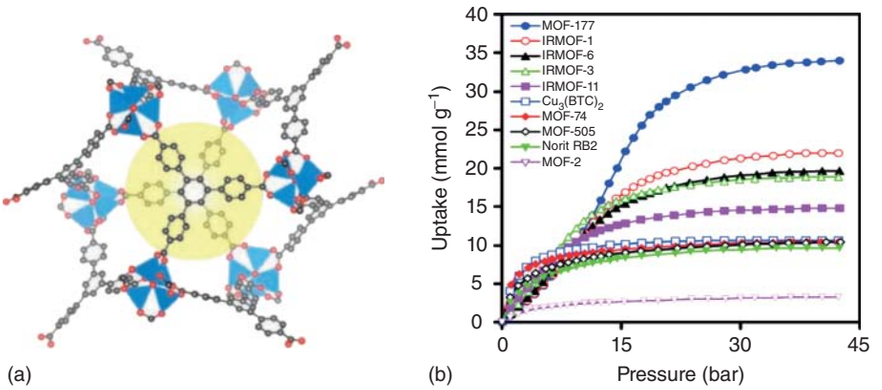


Figure 6 (a) The crystal structure of MOF-177. (b) The high pressure CO_2 uptake of some representative MOFs. (Reprinted with permission from Ref. 55. Copyright (2005) American Chemical Society.)

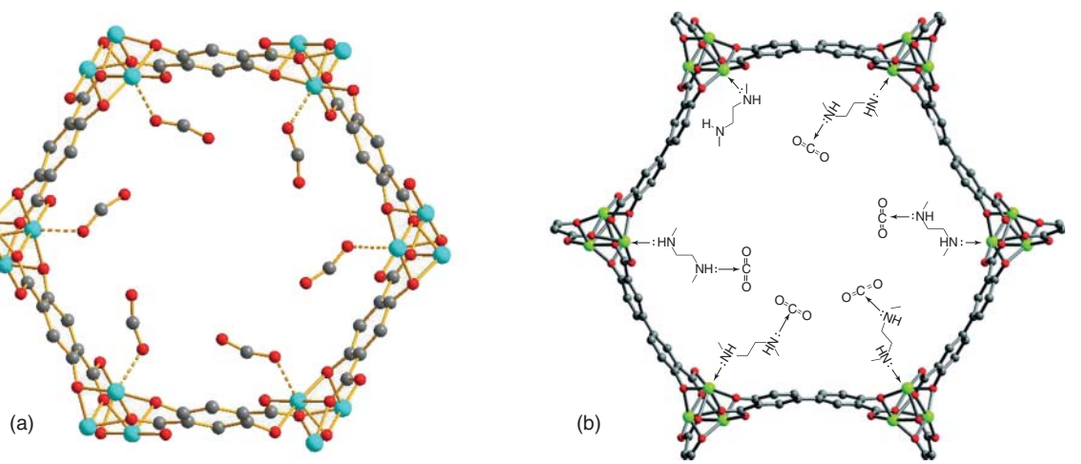


Figure 7 The functionalization of MOFs and their interactions with CO_2. (a) The crystallographic structure of Ni-MOF-74 in the presence of CO_2, where the CO_2 coordinates to unsaturated nickel centers in an end-on manner.[53,60] (b) The introduction of Lewis base (mmen) into an analogous Mg-MOF with larger cavities, where the mmen coordinates to the unsaturated magnesium centers. (Figure 7b: Reprinted with permission from Ref. 5. Copyright (2012) American Chemical Society.)

capacity of MOF-210 (Ref. 27) with a BET surface area of 6240 $m^2 \cdot g^{-1}$ reaches 65.2 $mmol \cdot g^{-1}$ at 50 bar, which makes it the MOF with the highest CO_2 capacity at high pressure to date.[53]

While the high pressure CO_2 capacity is closely related to the porosity of the framework, the low pressure uptake is more dependent on the interaction between CO_2 and the framework. Materials with a highly functionalized inner surface typically demonstrate high CO_2 capacity. Incorporation of functional units, such as UMCs,[56,57] Lewis bases,[5,54,58] and, more recently, single molecular traps (SMTs),[52,59] into the frameworks appears to be very efficient ways to reinforce the interaction between CO_2 and the adsorbents, increasing the framework selectivity of CO_2 over N_2. Among all MOFs, M-MOF-74 series[56,57,60] (also known as CPO-27-M,[42] Figure 2e) have been intensively studied for CO_2 uptake recently owing to their abundance of UMCs. Crystallographic study shows that CO_2 coordinates to the UMCs in a distinctive end-on manner (Figure 7a), which has significantly increased the CO_2 affinity of the framework.[60] The appropriate pore size and high density of UMCs have made them promising materials for low pressure CO_2 capture. Particularly, one of its members, Mg-MOF-74, possesses the highest CO_2 uptake for MOFs at ambient temperature so far.[53]

Introduction of Lewis bases into frameworks is another efficient way to improve their CO_2 affinity. The basic units can be incorporated by presynthetic ligand design[58] or PSM.[5] Figure 7(b) demonstrates an example of postsynthetic incorporation of polyamine units

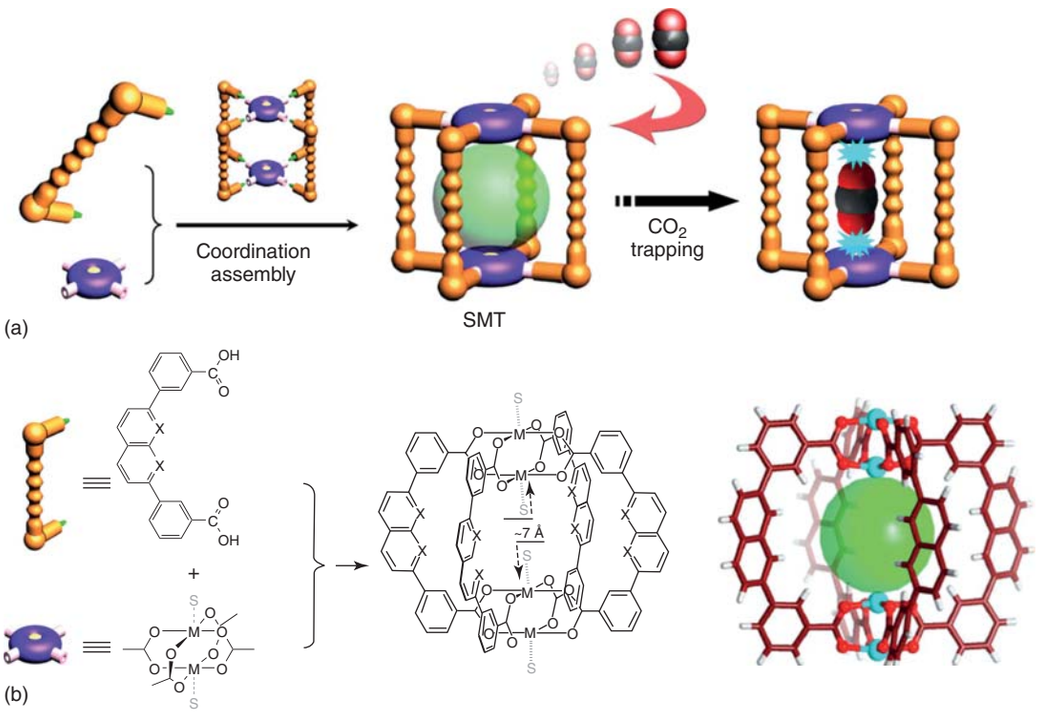


Figure 8 (a) The representation of the design and construction of a SMT for CO_2 adsorption. The organic ligands are shown in orange and the UMCs shown in purple. The green sphere represents the cavity for CO_2 capture. (b) The representation of construction of discreet SMT units as MOPs and their crystal structures. In the scheme, X = N or CH, M = Cu or Mo, S = Solvent. (Reprinted by permission from Macmillan Publishers Ltd: *Nature Communication* (Ref. 59), copyright (2013).)

into a framework. In this work, an elongated analog of Mg-MOF-74 was prepared, and the subsequent functionalization with *N*,*N*′-dimethylethylenediamine (mmen) has yielded a framework exhibiting an extraordinarily large CO_2 capacity, especially at low pressures.[5] This MOF has a CO_2 capacity of 2.0 mmol·g^{-1} at 0.39 mbar and room temperature, which makes it an attractive adsorbent for low pressure CO_2 capture.

Even though a great amount of effort has been made to enhance surface functionalities, optimal design of porous materials that are tailored for CO_2 capture still remains largely challenging. In recent years, SMTs[52,59] have emerged as a novel way to precisely control the CO_2 selectivity of the framework from the molecular level. An SMT is a predesigned cavity in a porous material with customized size and surface properties, which are exactly desirable for CO_2 capture (Figure 8a).[59] CO_2 is a linear molecule with partial positive charge located on its center and partial negative charge on its end. It is conceivable that two positively charged centers separated by a specific distance will selectively interact with CO_2 via electrostatic forces, whereas the negatively charged groups surrounding the carbon atom in the CO_2 molecule will further increase this interaction. Particularly, an SMT can be constructed by placing two UMCs (such as metal paddlewheels, Figure 2a) 6.4–8.0 Å apart from each other in a parallel position. This SMT should only hold one CO_2 molecule in each cavity and will have minimal interactions with other gases (such as N_2 or CH_4), affording an extremely high selectivity of CO_2 over other gases.

The SMTs can be synthesized as discrete units or incorporated into an extended network. Figure 8(b) demonstrates the design and preparation of a discrete SMT unit based on a metal-organic polyhedra (MOP), whose cavity is exactly suitable for the capture of one CO_2 molecule. MOPs are another category of crystalline porous material consisting of metal ions/clusters (or SBUs) and organic linkers. Different from the infinitely extended nature and the three-dimensional architecture of MOFs, MOPs typically appear as zero-dimensional discrete cages with a fixed shape and a confined cavity.[61] An SMT MOP was constructed from two-paddlewheel SBUs surrounded by four organic ligands with a bridging angle of 0°, yielding a lantern-shaped structure (Figure 8b). The size of its cavity was determined by its crystal structure, and its large preference of CO_2 over other gases was experimentally confirmed.[59]

Regardless of their excellent CO_2 selectivity, the CO_2 capacities of MOPs are relatively low because of their limited porosities. Incorporating SMTs into extended

frameworks (such as MOFs) with a larger porosity appears to be an efficient way to construct frameworks with both high affinity and storage capacity of CO_2. The incorporated SMT units will ensure the efficient transport of CO_2 inside the framework cavities. As an example of SMT-incorporated framework, PCN-88 was prepared from a ligand with two types of carboxylate groups: two parallel carboxylates for the formation of SMTs and another two for the formation of an extended framework (Figure 9a).[59] This ligand was devised by functionalizing the SMT MOP ligand (Figure 8b) with two additional carboxylate groups. Through the formation of dicopper paddlewheel SBUs, PCN-88 (Figure 9c) was successfully constructed with built-in SMTs analogous to the discreet MOP SMT units. As shown in Figure 9(b), this framework has a significant uptake of CO_2 but very limited uptakes of methane and nitrogen, and it exhibits a high selectivity of CO_2 over N_2 and CH_4. It is worth mentioning that the low pressure CO_2 uptake capacity of PCN-88 at ambient temperature ranks among the highest for MOFs constructed from pure carboxylate ligands[59] (excluding M-MOF-74 series from ligands with –OH moieties, Table 2).

In order to further investigate the efficiency of the incorporated SMTs for CO_2 uptake, control experiments were accomplished by deliberate obstruction of the SMTs in PCN-88 (Figure 9d). Consequently, PCN-88′ was synthesized by one-pot reaction of the ligand and copper salt in the presence of pyrazine, and it has an identical structure with that of PCN-88 except that the SMTs were blocked by the pyrazine molecules. A significant difference of CO_2 uptake between PCN-88 and PCN-88′ at lower pressures (especially <0.2 atm) was observed, which should probably be attributed to the existence of SMTs in the PCN-88 framework. This is particularly valuable for CO_2 separation from flue gas, where the partial pressure of CO_2 is about 0.15 atm.[53]

The customized interaction between SMTs and CO_2 indicates that increasing the density of SMTs in a MOF will further improve the CO_2 selectivity of this framework. A guest-responsive MOF PCN-200 was rationally designed and synthesized for the purposes of selective capture of CO_2 over N_2 under flue gas conditions. Different from the lantern-shaped SMT in PCN-88, this MOF possesses elastic SMTs that accommodate CO_2 but *exclude* N_2 molecules.[52] Its crystal structure includes one-dimensional channels along the *c*-axis located on a center of inversion (Figure 10a). In the as-synthesized samples of PCN-200, noncoordinating water molecules occupy the pores and are stabilized by strong hydrogen bonding. The as-synthesized sample can be easily activated by heating or applying vacuum, generating permanent cavities with diameters of 4.4 Å in the structure. Single-component gas isotherms reveal that this material can selectively adsorb CO_2 molecules, excluding N_2 and many other gases. At 195 K and 1 bar, saturation of CO_2 can be observed in PCN-200, where four molecules of CO_2 can be crystallographically identified in each unit cell (1.78 $mmol \cdot g^{-1}$), implying full occupation of CO_2 in all the existing pores at these conditions (Figure 10b). Interestingly, this material still retains 75% of its maximum uptake capacity (three molecules of CO_2 per unit cell, Figure 10b) at ambient temperature. It should be noted that the significantly greater density of PCN-200 compared to many other MOFs has resulted in a high volumetric uptake capacity of 129 $g \cdot L^{-1}$.[52] Despite its low porosity, the presence of SMTs, large density, high stability, and low production cost have made PCN-200 a promising solid adsorbent for industrial CCS processes.

In summary, MOFs are promising materials for CO_2 capture owing to their large surface area and many possibilities for functionalization. Table 2 lists some representative MOFs for CO_2 uptake at room temperature. For these materials, the high pressure CO_2 uptake is closely correlated to their surface areas, whereas the low pressure CO_2 uptake is associated with the functionalized units on their surface, including UMCs, Lewis bases, and SMTs, which increase the strength of framework–CO_2 interactions.

5 METHANE STORAGE IN MOFS

Methane, the main component of natural gas (>95%), is another competitive candidate to replace petroleum in automobiles owing to its natural abundance, clean burning process, and considerable heat of combustion. However, owing to practical limitations to the safe and convenient storage of methane, its application in vehicles still remains challenging. Traditional ways to store methane involve liquefaction at low temperature (LNG, liquefied natural gas) and compression at high pressure (CNG, compressed natural gas) at room temperature. These methods not only require the use of expensive cryogenic vessels or thick-walled cylindrical tanks but also suffer from significantly lower volumetric energy density (22.2 and 9.2 $MJ \cdot L^{-1}$, respectively) than that of gasoline (34.2 $MJ \cdot L^{-1}$).[63] Solid adsorbents are being investigated to overcome the downsides of the traditional methods for methane storage. In 2000, to propel the development in this field, the US Department of Energy (DOE) set the target for methane storage at 180 v(STP) v^{-1} at 298 K and 35 bar. (The v(STP) v^{-1} refers to the equivalent volume of methane per volume of the adsorbent material.) MOFs stand out from various porous materials such as zeolites and activated carbons because of their intriguing structures, high surface areas, and regular and tunable pore sizes. All the intrinsic characteristics of MOFs contribute to their high methane storage capacities. In this section, a detailed description of several representative MOFs will be presented in terms of their chemical structures, methane uptake performances,

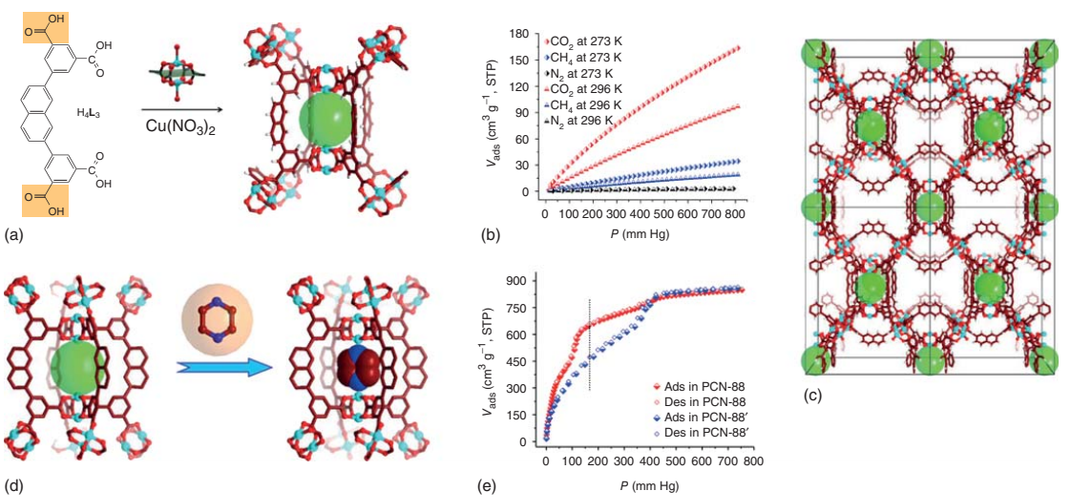


Figure 9 (a) The representation of the construction of a SMT unit in an extended framework. The carboxylates highlighted in orange form the linkages extending to the 3D framework. The green sphere represents the free space inside the built-in SMTs. (b) The CO_2, CH_4, and N_2 adsorption isotherms of PCN-88 at different temperatures (273 and 296 K). (c) The crystal structure of PCN-88. (d) The representation of the synthesis of PCN-88′, where a pyrazine molecule was introduced into the cavity of PCN-88 to block the SMT. (e) The CO_2 adsorption isotherms of PCN-88 and PCN-88′ at 196 K, indicating the significant contribution of SMTs for CO_2 uptake. (Reprinted by permission from Macmillan Publishers Ltd: *Nature Communication* (Ref. 59), copyright (2013).)

Table 2 Representative MOFs for room temperature (298 K) CO_2 uptake

MOF	Ligand	Metal	BET surface area ($m^2 \cdot g^{-1}$)	CO_2 capacity ($mmol \cdot g^{-1}$)	Pressure (bar)	Functionalization	Reference
MOF-5	bdc	Zn	2300	18.7	40	NA	62
MOF-177	btb	Zn	4500	33.5	42	NA	55
MOF-210	bte and bpdc	Zn	6240	65.2	50	NA	27
Mg-MOF-74	dobdc	Mg	1174	8.5	1	UMC	57
Bio-MOF-1	Adenine and bpdc	Zn	1680	3.4	1	Lewis base	58
mmen-Mg_2(dobpdc)	dobpdc	Mg	70	2.0	0.00039	Lewis base	5
PCN-88	ndda	Cu	3308	4.2	1	UMC and SMT	59
PCN-200	tzc and dpp	Cu	N/A	1.2	1	SMT	52

bdc, 1,4-benzenedicarboxylate; btb, 4,4′,4″-benzene-1,3,5-triyl-tribenzoate; bte, 4,4′,4″-(benzene-1,3,5-triyl-tris(ethyne-2,1-diyl))-tribenzoate; bpdc, 4,4′-biphenyldicarboxylate; dobdc, 2,5-dioxido-1,4-benzenedicarboxylate; dobpdc, 4,4′-dioxido-3,3′-biphenyldicarboxylate; ndda, 5,5′-(naphthalene-2,7-diyl)diisophthalate; tzc, tetrazolate-5-carboxylate; dpp, 1,3-di(4-pyridyl)propane

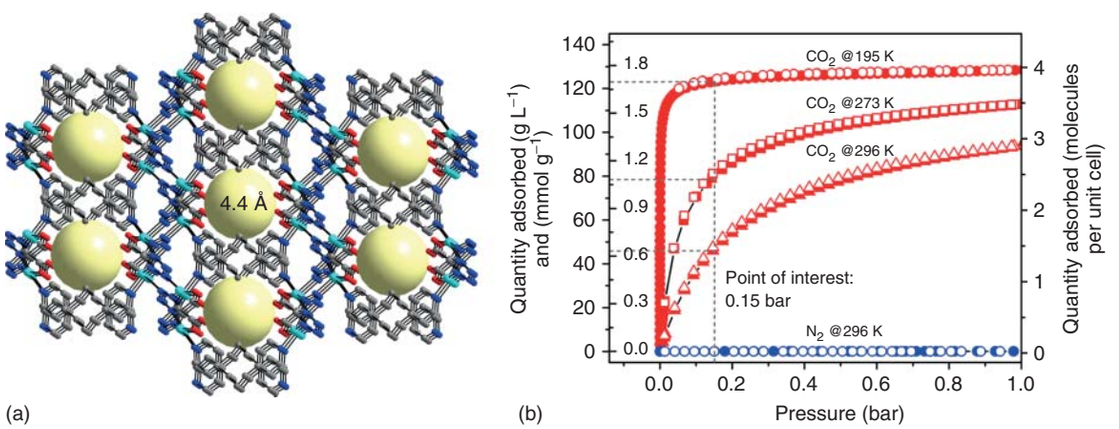


Figure 10 (a) Crystal structure of PCN-200 and its channels along *c*-axis. (b) Gas adsorption isotherms for CO_2 and N_2 of PCN-200. CO_2 at 195 K (red circles), 273 K (rectangles), and 296 K (triangles) and N_2 at 296 K (blue circles). (Reproduced with permission from Ref. 52. © Wiley-VCH Verlag GmbH & Co. KGaA, Weinheim, 2012.)

and interactions with methane. A compilation of their compositions, surface areas, pore volumes, and methane adsorption capacities is provided in Table 3. These MOFs serve as a guide to designing porous adsorbents with high performance.

IRMOF-993, a theoretical MOF based on 9,10-anthracene dicarboxylate (adc^{2-}), was predicted to have a methane storage capacity of 181 v v^{-1}, surpassing the DOE target (180 v v^{-1}).[70] However, attempts to synthesize IRMOF-993 experimentally only gave rise to PCN-13.[63] PCN-13, deviating significantly from the expected performance of IRMOF-993, exhibited very limited methane uptake and selective adsorption of hydrogen and oxygen over nitrogen and carbon monoxide, owing to the confined pore size (~3.5 Å). To build MOFs with a considerable methane-adsorption capacity, another ligand, 5,5′-(9,10-anthracenediyl)diisophthalate ($adip^{4-}$), was chosen to enlarge the pore size. The self-assembly of tetratopic carboxylate $adip^{4-}$ and dicopper paddlewheel SBU under solvothermal reaction conditions produced a MOF designated PCN-14, which bears *nbo* net topology. PCN-14 consists of squashed cuboctahedral cages, which are built from 12 $adip^{4-}$ ligands and 6 dicopper paddlewheels. These microscopic cages are very suitable for methane storage because the close proximity between anthracenyl rings enhances the dispersive interaction between adsorbates and pore surfaces, thus creating very good van der Waals potential pockets (the pocket dimension is comparable to the kinetic diameter of methane) for methane molecules. Moreover, the removal of solvent molecules from the axial coordinating sites of dicopper paddlewheels leads to the formation of UMCs, which permit stronger Coulomb attraction between exposed Cu ions and slightly polarized methane molecules. These advantageous properties endow PCN-14 with an excellent ability to store methane. Its total methane uptake is 230 v v^{-1} at 290 K and 35 bar, surpassing the DOE target by 28%. It is currently the record holder in terms of volumetric methane uptake in a solid porous material, to the best of our knowledge (Figure 11 and Scheme 1).

Table 3 Representative MOFs for room temperature CH_4 uptake

MOF	Surface area ($m^2 \cdot g^{-1}$)		Pore volume ($cm^3\ g^{-1}$)	Condition		Methane uptake capacity		Reference
	BET	Lang.		*P* (bar)	*T* (K)	wt%	v(STP) v^{-1}	
Cu_2(adip) [PCN-14]	1753	2176	0.87	35	290	15.3[a]	220[a]	64
Cu_2(sbtc) [PCN-11]	1931	2442	0.91	25	298	14.0[a]	171[a]	65
$Cu_3(btc)_2$ [HKUST-1]	1502	2368	0.82	35	304	10.2[b]	165[b]	66
Ni_2(dhtp) [Ni-MOF-74]	1027		0.54	49.7 (35)	298	11.9[a]	195[a](190)[a]	32, 56
Mg_2(dhtp) [Mg-MOF-74]	1332			58.3 (35)	298	13.7[a]	169[a](149)[a]	32, 56
Mn_2(dhtp) [Mn-MOF-74]	1102			35	298		158[a]	32
Co_2(dhtp) [Co-MOF-74]	1056			35	298		174[a]	32
Zn_2(dhtp) [Zn-MOF-74]	885			35	298		171[a]	32
Cu_2(tmbdi) [NOTT-107]	1822		0.767	35	298		185	67
Cu_3(bhb) [UTSA-20]	1156		0.63	35	298		178[a]	68
Cu_2(btei) [PCN-61]	3000	3500	1.36	35	298	15.7[a]	145[a]	3
Cu_2(ntei) [PCN-66]	4000	4600	1.63	35	298	15.1[a]	100[a]	3
Cu_2(ptei) [PCN-68]	5109	6033	2.13	35	298	15.7[a]	99[a]	3
$C_{36}H_{21}Cu_3N_9O_{15}$ [NU-125]	3120		1.29	58	298		228[b]	69

adip, 5,5′-(9,10-anthracenyl)di-isophthalate; sbtc, *trans*-stilbene-3,3′,5,5′-tetracarboxylate; btc, benzene-1,3,5-tricarboxylate; dhtp, 2,5-dihydroxyterphthalate; tmbdi, 5,5′-(2,3,5,6-tetramethylbenzene-1,4-diyl)di-isophthalate; bhb, 3,3′3″,5,5′5″-benzene-1,3,5-triyl-hexabenzoate; btei, 5,5′5″-benzene-1,3,5-triyltris(1-ethynyl-2-isophthalate); ntei, 5,5′5″-(4,4′4″-nitrilotris(benzene-4,1-diyl)tris(ethyne-2,1-diyl))triisophthalate; ptei, 5,5′-((5′-(4-((3,5-dicarboxyphenyl)ethynyl)phenyl)-[1,1′:3′1″-terphenyl]-4,4″-diyl)-bis(ethyne-2,1-diyl)) diisophthalate.

[a]Excess uptake

[b]Total uptake

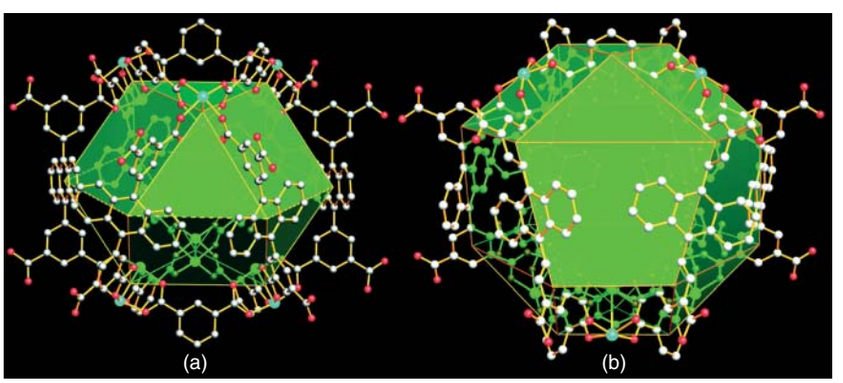
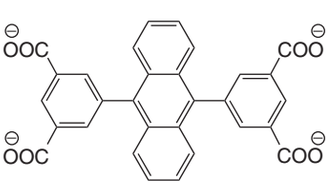


Figure 11 (a) Squashed cuboctahedral cage. (b) Microscopic cage with 18 vertices, 30 edges, and 20 faces. Color scheme: C, gray; Cu, turquoise; and O, red. (Reprinted with permission from Ref. 64. Copyright (2007) American Chemical Society.)



Scheme 1 The structure of $adip^{4-}$ ligand in PCN-14

PCN-11, another benchmark MOF, that shows very high excess methane uptake [171 cm^3(STP)/cm^3] at 298 K, is built from a double bond-coupled bis(isophthalate) ligand named *trans*-stilbene-3,3′,5,5′-tetracaboxylate ($sbtc^{4-}$). Solvothermal reaction of $Cu(NO_3)_2$ with *trans*-stilbene-3,3′,5,5′-tetracaboxylic acid (H_4sbtc) generates this network structure, which has stable porosity. PCN-11 also contains microporous cages and UMCs, similar to PCN-14.[65] There are two types of pores in PCN-11.[71] The small pore in the octahedral cage has a dimension of about 7 Å, whereas the large pore in the elongated cuboctahedral cage is 10 Å by 16 Å. Grand canonical Monte Carlo (GCMC) simulation studies of the adsorption sites in PCN-11 indicates that methane

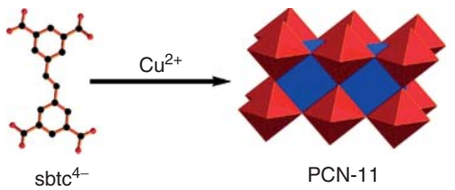


Figure 12 Ligand and 3D framework of PCN-11 viewed as a polyhedron model (red: octahedral cage; blue: elongated cuboctahedral cage). Hydrogen atoms were omitted for clarity. Color scheme: carbon, black; oxygen, red. (Reprinted with permission from Ref. 65. Copyright (2008) American Chemical Society.)

molecules mainly populate at unsaturated Cu sites and the cage window-opening sites.[71] The binding energies at these two types of sites are both approximately 25 kJ·mol^{-1}. Normally, the magnitude at the unsaturated Cu sites is expected to be higher than that at open cage window sites owing to the enhanced Coulomb interaction induced by the exposed Cu ion. The unusually high affinity at cage window sites can be explained by the good symmetry and geometric match between the cage window and the methane molecule, which gives rise to multiple surface interactions and results in increased binding energy (Figure 12).

HKUST-1 is one of the most widely studied MOF structures.[72] It is composed of dicopper paddlewheel SBUs and carboxylate organic linker 1,3,5-benzenetricarboxylate (btc). Self-assembly of the dicopper tetracarboxylate SBUs generates a network with fourfold symmetric nanochannels viewed from the [100] direction. HKUST-1 exhibits a high excess methane adsorption [~160 cm^3 (STP)/cm^3] at 35 bar and room temperature.[66] Similar to the adsorption mechanism of PCN-14 and PCN-11, HKUST-1 mainly traps methane molecules at unsaturated Cu centers and the van der Waals potential pocket, which has multiple surface interactions with methane molecules.[71]

The M-MOF-74 series (Figure 2e) also possesses a large methane uptake because of the exceptionally high density of UMCs (4.5 sites nm^{-3}).[32] It is calculated that saturating these metal sites with methane molecules could generate adsorption capacity in the range of 160–174 v v^{-1}. In order to clarify the influence of UMCs on methane uptake, the M-MOF-74 series [M_2(dhtp), M = Mg, Mn, Co, Ni, Zn; dhtp = 2,5-dihydroxyterephthalate] were synthesized, and their methane adsorption was investigated.[32] M-MOF-74 bears one-dimensional channels with diameters of approximately 13.6 Å, which can easily be approached by methane molecules. Among the five M-MOF-74 variants studied, Ni-MOF-74 exhibits the highest absolute methane storage capacity of ~200 cm^3 (STP)/cm^3, surpassing the DOE target by 10%. Neutron diffraction studies indicate that methane molecules primarily bind at the UMCs in M-MOF-74. The calculated binding energies are larger than those of typical adsorption sites in classical MOFs, which accords with the measured higher heat of adsorption. However, two disadvantages of M-MOF-74 are quite apparent. At low pressures, there is a relatively large amount of methane (~105 v v^{-1} at 5 bar) remaining in the framework, owing to the high heat of adsorption. This significantly restricts the application of M-MOF-74 as a methane storage material. In addition, the heaviness of the metal elements and the high density of UMCs make M-MOF-74 less attractive in terms of weight capacity. Nevertheless, M-MOF-74, especially Ni-MOF-74, is still noteworthy for its design and high methane uptake (Figure 13).

NOTT-107 has also been identified as an efficient methane adsorbent through a high throughput screening

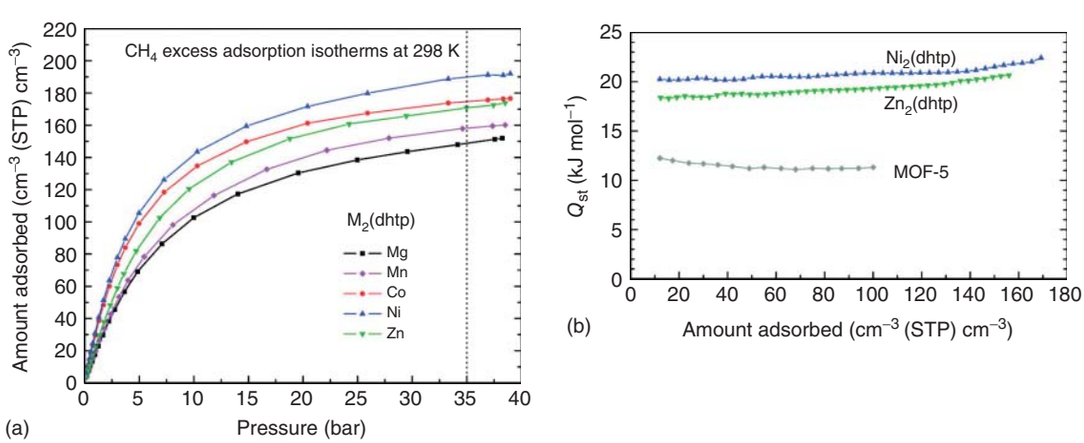
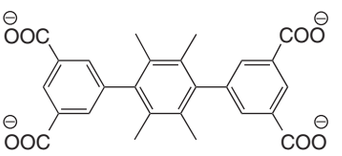


Figure 13 (a) Excess CH_4 adsorption isotherms of M_2(dhtp) at 298 K. (b) The experimental Q_{st} of Ni_2(dhtp) and Zn_2(dhtp) (the error bar is ±5%). The Q_{st}'s of Mg_2(dhtp), Mn_2(dhtp), and Co_2(dhtp) fall between the two curves and, thus, are not shown for clarity. The Q_{st}'s of MOF-5 (from Zhou *et al.*[73]) are also plotted for comparison. (Reprinted with permission from Ref. 32. Copyright (2009) American Chemical Society.)

of potential MOF candidates. The structure of NOTT-107 is very similar to that of PCN-14. It is based on dicopper paddlewheel SBUs and 5,5′-(2,3,5,6-tetramethylbenzene-1,4-diyl)di-isophthalate. The methyl groups on the central phenyl ring of NOTT-107 stretch into the pores of the framework, reducing the pore diameter to 7.0 Å, which is analogous to the role played by the phenyl rings of anthracenyls in PCN-14. These structural features can account for the potential methane uptake (213 v v^{-1} at 35 bar and 298 K) of NOTT-107 predicted by GCMC simulation using the universal force field. The small pore size creates opportunities for the methane molecules to closely interact with the surrounding multiple surfaces (creating van der Waals potential pockets), thus leading to a strong framework–adsorbate interaction and high methane uptake capacity. In order to compare simulated results, a sample of NOTT-107 was prepared and its methane adsorption tested.[67] It turned out that the experimental methane uptake (~196 v v^{-1}) was lower than the predicted. Incomplete activation may be responsible for the discrepancy. Note the experimental BET surface area was 1770 $m^2 \cdot g^{-1}$, whereas the simulated one was 2207 $m^2 \cdot g^{-1}$, which helps support the above explanation (Scheme 2).



Scheme 2 The structure of $tmbdi^{4-}$ ligand in NOTT-107

UTSA-20, a MOF based on dicopper paddlewheel SBUs and 3,3′,3″,5,5′,5″-benzene-1,3,5-triyl-hexabenzoate (bhb^{6-}), was built to immobilize high density UMCs and appropriate pore spaces within a framework for methane adsorption.[68] Two types of one-dimensional channels are found in UTSA-20. One is a rectangular pore with dimensions of 3.4 × 4.8 $Å^2$, whereas the other is a cylindrical pore with a diameter of 8.5 Å. More interestingly, the UMCs are exposed to the pores so that methane molecules can approach these binding sites more easily. The BET surface area (1156 $m^2 \cdot g^{-1}$) obtained from the N_2 sorption isotherm at 77 K only falls in the moderate range, but the methane adsorption capacity was determined to be very high (178 v v^{-1}). It was discovered that the full occupation of the UMCs in UTSA-20 with methane only accounts for around 50% of the overall methane uptake. Therefore, there must be other favorable binding sites that contribute the observed high methane storage capacity. GCMC simulation revealed some reasons behind this fact. It was found that the distances between two adjacent bhb^{6-} linkers that construct the pores within the channel are appropriate to allow methane molecules to be "sandwiched" between the two bhb^{6-} potential surfaces.[68] The UMCs along with the sandwiched binding sites were calculated to account for approximately 90% of the total experimental methane adsorption amount at 298 K and 35 bar. The other 10% may come from the adsorption occurring at the secondary binding sites (Figure 14).

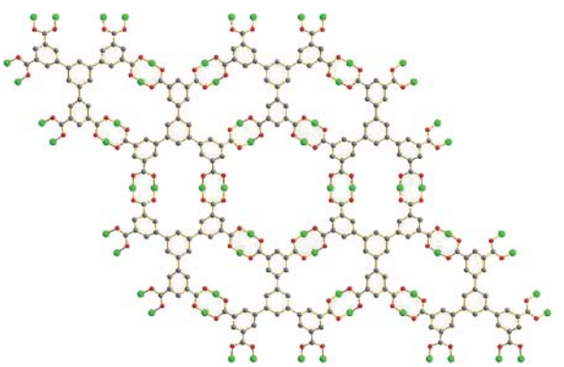


Figure 14 The crystal structure of UTSA-20, where the gray, red, and green spheres represent C, O, and Cu, respectively. H atoms were omitted for clarity

Apart from the density of UMCs and van der Waals potential pockets, surface area is another factor that largely affects the efficacy of gas adsorption application of MOFs.[74] To synthesize frameworks with high surface areas, a general strategy is to increase the length of the ligands. However, frameworks with extended ligands tend to collapse easily on the removal of supporting solvent molecules.[3] It has been discovered that introducing mesopores with microwindows into MOFs can alleviate the accompanying instability.[74] Furthermore, dendritic ligands, being more branched, will produce MOFs that can tolerate more extended ligands.[19] PCN-6X (framework formula Cu_3L, L = btei, PCN-61; ntei, PCN-66; ptei, PCN-68; ttei, PCN-610), a (3,24)-connected MOF series, is based C_3 symmetric dendritic ligands. The networks are built up from three types of polyhedra: cuboctahedra (cub-O_h), truncated tetrahedral (T-T_d) and truncated octahedra (T-O_h). Among them, only the size of cub-O_h remains unchanged as the ligands extend, confining the open window sizes of the T-T_d and T-O_h in microscale.[3] Although the surface area increases with the extension of ligands, the PCN-6X series maintains its framework stability. PCN-6X series exhibits impressive surface areas. Amidst them, PCN-68 has a Langmuir surface area >6000 $m^2 \cdot g^{-1}$, which is one of the highest records for MOFs, accounting for the high gravimetric methane uptake capacity at high pressure (>60 bar). However, PCN-61 shows a larger methane adsorption capacity in the low to medium pressure range (<30 bar) than PCN-68 because of the better methane–framework interaction coming from more suitable pore space. The volumetric methane capacity of

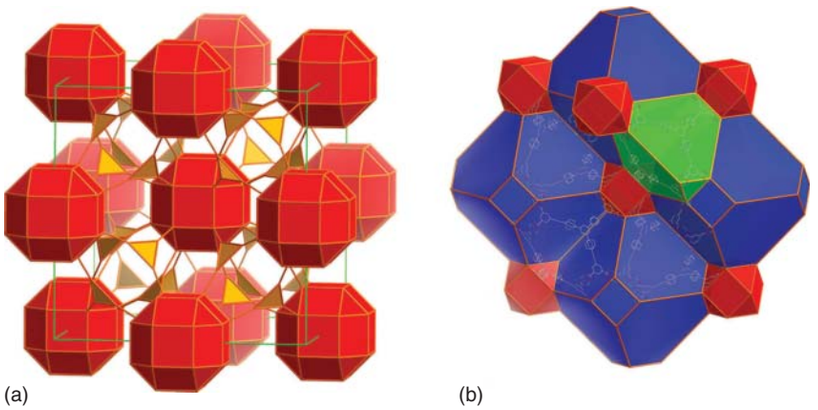


Figure 15 (a) (3,24)-connected network in PCN-68. (b) 3D polyhedra packing in PCN-68. Color scheme: red, cuboctahedra; green, truncated tetrahedra; blue, truncated octahedra. (Reproduced with permission from Ref. 3. © Wiley-VCH Verlag GmbH & Co. KGaA, Weinheim, 2010.)

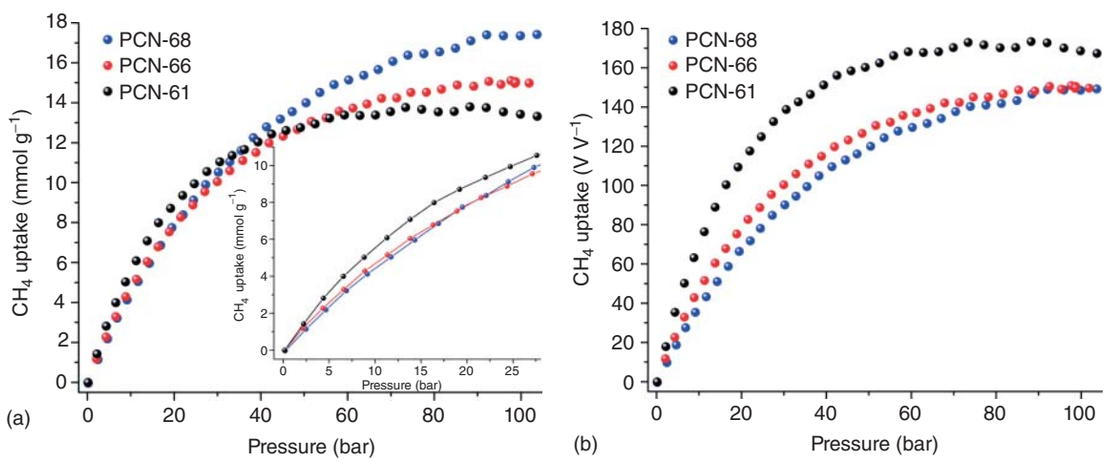


Figure 16 (a) Gravimetric and (b) volumetric capacities of methane adsorption in the PCN-6X series at 298 K. The inset in (a) shows the medium-pressure region enlarged. (Reproduced with permission from Ref. 3. © Wiley-VCH Verlag GmbH & Co. KGaA, Weinheim, 2010.)

PCN-61, PCN-66, and PCN-68 are 145, 110, and 99 v v^{-1}, respectively (Figures 15 and 16).

Regardless of the numerous advantages of MOFs for methane storage, it may still be problematic to realize their commercialization in vehicular systems owing to the following technical barriers: (i) the material ought to possess a considerable deliverable capacity, which refers to the difference between the amount of gas adsorbed at the highest pressure and at the lowest pressure; (ii) the adsorbent must be synthesized on a large scale and must be robust enough to go through repetitive adsorption–desorption cycles.[69] Bearing these objectives in mind, a new MOF named NU-125 was synthesized on a gram scale in high yield and is composed of dicopper paddlewheel SBUs and hexa-carboxylate ligands L^{6-} (Figure 17). The above two types of building "bricks" link to each other in a paddlewheel manner, producing a noncatenated structure with *rht* topology.[69] NU-125 has a deliverable methane capacity of 174 v v^{-1} at 298 K (58 bar to 5.8 bar), which is equivalent to 67% of the amount delivered by CNG tanks. Moreover, methane isotherm measurement results showed no apparent variation between cycles during the stability test, proving the robustness of the material. All these advantageous properties of NU-125 make it another step toward the implementation of MOF materials into automobiles as fuel carriers.

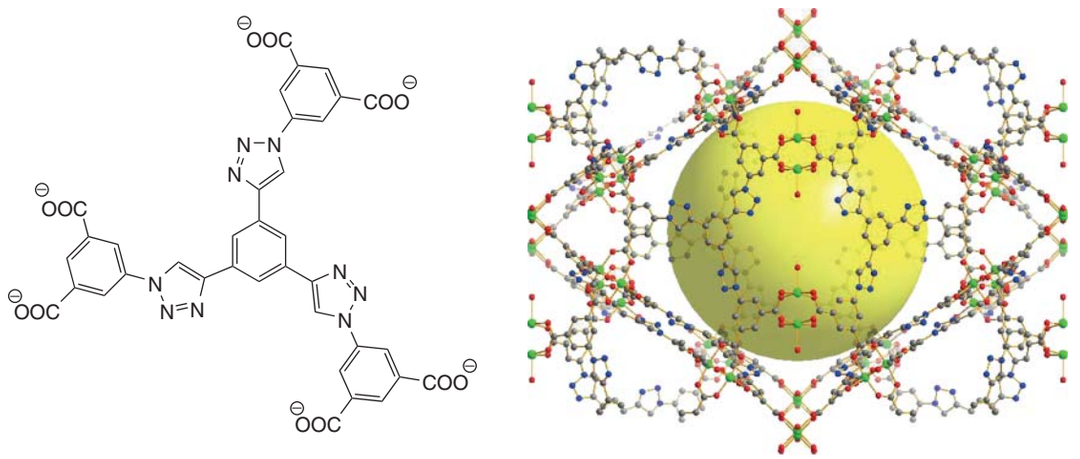


Figure 17 The chemical structure of the ligand and the crystal structure of NU-125

In summary, MOFs have received wide attention in the field of methane storage owing to their advantageous features. The abovementioned MOFs offer great enlightenments in designing new porous materials with excellent methane uptake performances. We believe laboratory achievements can eventually be applied in industrial methane storage applications after overcoming all the obstacles on the road to commercialization.

6 STORAGE OF OTHER GASES IN MOFS

In contrast to the intensively studied solid adsorbents for energy-related applications, the storage materials for other gases, such as oxygen, nitric oxide (NO), ethylene, and acetylene, are less studied but are arguably much closer to commercialization because of their biomedical or industrial applications.[11] For instance, materials for the storage and controlled delivery of NO can serve as exogenous NO resources for prophylactic and therapeutic purposes. This section will selectively introduce the storage of a few other gases in MOFs, including oxygen[36] and some hydrocarbons.[4,38]

6.1 Oxygen Storage in MOFs

Oxygen is not only one of the most important molecules for life but also one of the most widely used chemicals in the world for industrial and medical applications. Traditionally, the industrial separation of O_2 from the air involves the extremely energy-consuming cryogenic distillation processes.[36] Aerobic organisms can selectively take up O_2 from the air at ambient temperature and pressures with the assistance of oxygen-transport metalloproteins, such as hemoglobin, hemerythrin, or hemocyanin.[75] This selectivity results from the UMCs (iron or copper) located in the active sites of metalloproteins. Similarly, the UMCs, especially unsaturated iron centers, will significantly facilitate this process in MOFs as well. The M-MOF-74 series are renowned for their high density of UMCs, and Fe-MOF-74 was reported as an efficient adsorbent for O_2 storage and O_2/N_2 separation owing to the existence of unsaturated Fe(II) centers.[36] This MOF was synthesized by air-free procedures, and it has a BET surface area of 1360 $m^2 \cdot g^{-1}$. After a full activation, Fe-MOF-74 [also known as Fe_2(dobdc)] preferentially binds O_2 over N_2 at all temperatures.

As shown in Figure 18(c), at 298 K, an extremely steep rise of O_2 adsorption isotherm occurs at very low pressure, where the O_2 uptake quickly rises to 9.3 wt% when the pressure is still less than 0.01 bar. This is probably due to the strong interaction between the O_2 and the unsaturated Fe(II) centers in the framework. A higher pressure will not increase the O_2 uptake significantly afterward. The O_2 uptake slightly increased to 10.4 wt% at 1 bar. The gradual increase at higher pressures probably results from a saturation of O_2 for all the available UMCs in this MOF and the subsequent O_2 uptake is merely physisorption on the surface of the framework.[36] Stoichiometric study shows that the adsorption of each O_2 molecule corresponds to two iron centers at this temperature. The O_2 adsorption at room temperature is *not* fully reversible. Mossbauer spectroscopy shows that an oxidation state change on the iron centers were observed when O_2 was introduced, indicating the existence of high spin Fe(III) ions. This illuminates the chemisorption nature of O_2 binding to the unsaturated iron centers, where the one molecule of O_2 receives two electrons from two Fe(II) centers, producing two Fe(III) centers and a peroxide anion (O_2^{2-}). This can be further corroborated by the crystallographic data (Figure 18b and e), where the O_2 is coordinated to iron centers in an asymmetric side-on

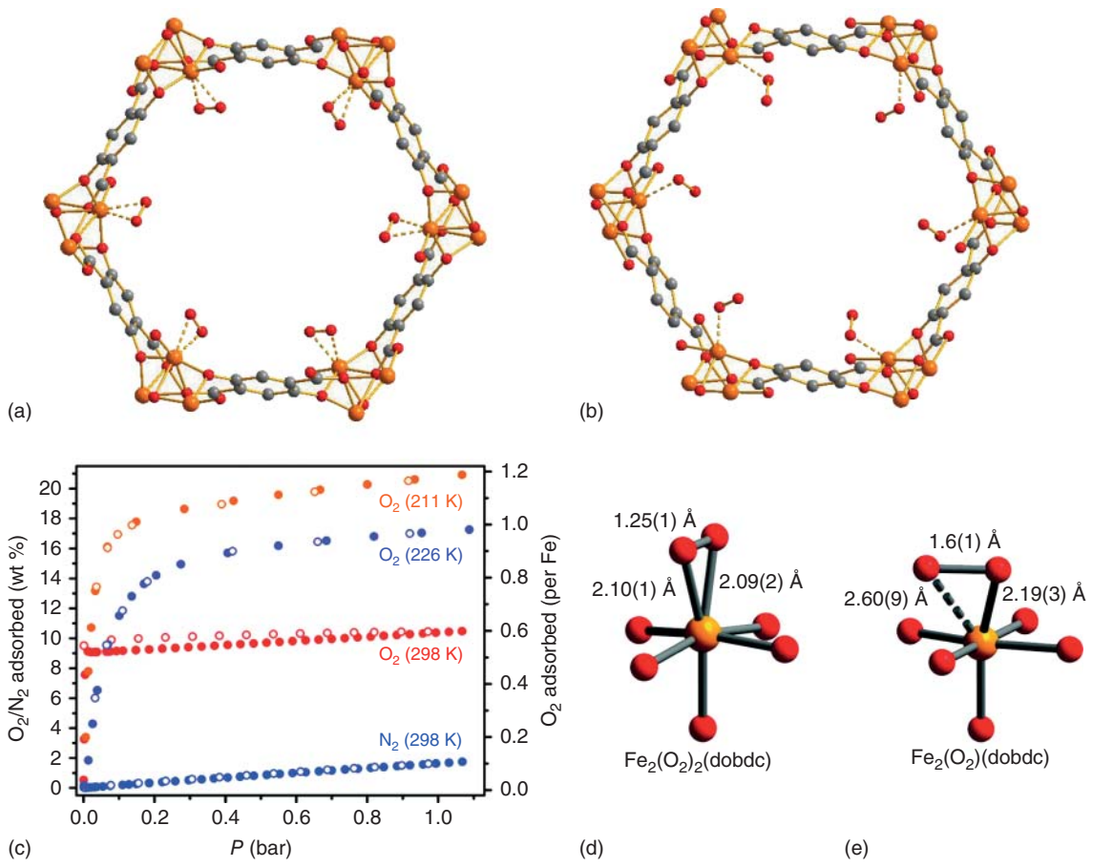


Figure 18 (a) The representation of crystal structure of Fe-MOF-74 with O_2 at 100 K. O_2 was bond in a side-on manner at this temperature. (b) The crystal structure of Fe-MOF-74 with O_2 at 298 K. At this temperature, the ferrous centers were oxidized to the ferric ions, and they were bonded to a peroxide anion. (c) Excess O_2 adsorption isotherms collected for Fe-MOF-74 at 211 K (orange), 226 K (purple), and 298 K (red) and N_2 adsorption at 298 K (blue). (d) The coordination sphere of iron centers with O_2 at 100 K. (e) The coordination sphere of iron centers with O_2 at 298 K. (c–e: Reprinted with permission from Ref. 36. Copyright (2011) American Chemical Society.)

mode with the O–O bond length 1.6 Å, consistent with the bond length of O–O single bond in peroxide compounds. This asymmetric side-on mode resembles the coordination manner of peroxide in the biological systems.[76]

At lower temperature, Fe-MOF-74 has an increased O_2 uptake of 18.2 wt% at 211 K, corresponding to one molecule of O_2 for each iron center, and its O_2 adsorption becomes fully reversible. Mossbauer spectroscopy indicates a partial electron transfer from each Fe(II) centers to the weakly bonded O_2, generating a dioxygen species somewhere between the neutral molecule and the superoxide (O_2^-).[36] This can be substantiated by the crystallographic data (Figure 18a and d) as well, where the O_2 is coordinated to iron centers in a symmetric side-on mode with the O–O bond length 1.25 Å. This bond length lies between the bond length of a free O_2 molecule (1.2071 Å) and a superoxide (1.28 Å), implying the partial electron transfer from the iron centers to the O_2. The presence of unsaturated iron centers in MOFs has not only largely increased the O_2 affinity and capacity but also shed some light on the biomimetic attributes of MOFs.

6.2 Storage of Other Hydrocarbons in MOFs

UMCs are also effective in the storage and separation of hydrocarbons. The separation of olefin/paraffin mixtures with similar sizes and boiling points is of vital importance in the petroleum industry. The traditional way of industrial separation of olefins and paraffins involves low temperature distillation, where the utilization of cryogenic conditions makes this process very energy consuming.[77] Alternatively, MOFs with adjustable pore sizes and tunable pore surface functionalities may be able to separate olefins and paraffins with high energy efficiency and low cost. The redox-active Fe-MOF-74 also exhibits a high efficiency in the separation of low molecular weight

alkanes, alkenes, and alkynes, owing to the existence of its unsaturated iron centers.[4,38] Determination of interactions between the hydrocarbons and adsorbents were carried out by neutral diffractions. Unsaturated hydrocarbons, such as acetylene, ethylene, and propylene, coordinate to the unsaturated iron centers in a side-on manner. The binding strength of the hydrocarbons to unsaturated iron centers increases in the following series: methane < ethane < propane < propylene < acetylene < ethylene.[4]

7 CONCLUSION

MOFs as a growing category of porous materials are of great impact for recent research on inorganic chemistry. Owing to their well-defined structures, large permanent porosities, and variety in functionalization, MOFs are especially promising materials for the storage of various gases, including hydrogen, carbon dioxide, methane, oxygen, ethylene, acetylene, and many others. A great number of MOFs with various functionalization units (UMCs, Lewis bases, and SMTs) have been synthesized for the purposes of gas storage. The current research on MOFs may provide a practical way to solve many longstanding yet urgent issues confronting us, such as utilization of renewable energy, lowering anthropogenic carbon emissions, and other uses.

8 ACKNOWLEDGMENTS

This work was supported as part of the Center for Gas Separations Relevant to Clean Energy Technologies, an Energy Frontier Research Center funded by the US Department of Energy (DOE), Office of Science, Office of Basic Energy Sciences under Award Number DE-SC0001015, part of the Hydrogen and Fuel Cell Program under Award Number DE-FC36-07G017033, and part of the Methane Opportunities for Vehicular Energy (MOVE) Program, an ARPA-e project under Award Number DE-AR0000249. The authors thank Mr. Mathieu Bosch for revising this chapter.

9 RELATED ARTICLES

Edible Metal-Organic Frameworks; Metal-Organic Frameworks for Removal of Harmful Gases; Postsynthetic Modification of Metal-Organic Frameworks; Open Metal Sites in Metal-Organic-Frameworks; Adsorption of Hydrocarbons and Alcohols in Metal-Organic Framework Materials.

10 ABBREVIATIONS AND ACRONYMS

bdc = 1,4-benzenedicarboxylate; BET = Brunauer–Emmett–Teller; btc = 1,3,5-benzenetricarboxylate; CCS = carbon capture and sequestration; CNG = compressed natural gas; DOE = Department of Energy; GCMC = Grand canonical Monte Carlo; LNG = liquefied natural gas; mdip = 5,5′-methylene-di-isophthalate; mmen = *N*,*N*′-dimethylethylenediamine; MOF = metal-organic framework; MOP = metal-organic polyhedra; NASA = National Aeronautics and Space Administration; NO = nitric oxide; PCN = porous coordination network; PSM = postsynthetic modification; SBU = secondary building unit; SMT = single molecular trap; UMC = unsaturated metal center.

11 REFERENCES

1. M. E. Davis, *Nature*, 2002, **417**, 813.
2. H.-C. Zhou, J. R. Long, and O. M. Yaghi, *Chem. Rev.*, 2012, **112**, 673.
3. D. Yuan, D. Zhao, D. Sun, and H.-C. Zhou, *Angew. Chem. Int. Ed.*, 2010, **49**, 5357.
4. E. D. Bloch, W. L. Queen, R. Krishna, J. M. Zadrozny, C. M. Brown, and J. R. Long, *Science*, 2012, **335**, 1606.
5. T. M. McDonald, W. R. Lee, J. A. Mason, B. M. Wiers, C. S. Hong, and J. R. Long, *J. Am. Chem. Soc.*, 2012, **134**, 7056.
6. C.-D. Wu, A. Hu, L. Zhang, and W. Lin, *J. Am. Chem. Soc.*, 2005, **127**, 8940.
7. A. Lan, K. Li, H. Wu, D. H. Olson, T. J. Emge, W. Ki, M. Hong, and J. Li, *Angew. Chem. Int. Ed.*, 2009, **48**, 2334.
8. P. Horcajada, T. Chalati, C. Serre, B. Gillet, C. Sebrie, T. Baati, J. F. Eubank, D. Heurtaux, P. Clayette, C. Kreuz, J.-S. Chang, Y. K. Hwang, V. Marsaud, P.-N. Bories, L. Cynober, S. Gil, G. Ferey, P. Couvreur, and R. Gref, *Nat. Mater.*, 2010, **9**, 172.
9. K. C. Stylianou, R. Heck, S. Y. Chong, J. Bacsa, J. T. A. Jones, Y. Z. Khimyak, D. Bradshaw, and M. J. Rosseinsky, *J. Am. Chem. Soc.*, 2010, **132**, 4119.
10. M. Wriedt, A. A. Yakovenko, G. J. Halder, A. V. Prosvirin, K. R. Dunbar, and H.-C. Zhou, *J. Am. Chem. Soc.*, 2013, **135**, 4040.
11. R. E. Morris and P. S. Wheatley, *Angew. Chem. Int. Ed.*, 2008, **47**, 4966.
12. R. J. Kuppler, D. J. Timmons, Q.-R. Fang, J.-R. Li, T. A. Makal, M. D. Young, D. Yuan, D. Zhao, W. Zhuang, and H.-C. Zhou, *Coord. Chem. Rev.*, 2009, **253**, 3042.
13. J. Lee, J. Kim, and T. Hyeon, *Adv. Mater.*, 2006, **18**, 2073.
14. D. Zhao, J. Feng, Q. Huo, N. Melosh, G. H. Fredrickson, B. F. Chmelka, and G. D. Stucky, *Science*, 1998, **279**, 548.

15. G. S. Attard, J. C. Glyde, and C. G. Goltner, *Nature*, 1995, **378**, 366.
16. C. J. H. Jacobsen, C. Madsen, J. Houzvicka, I. Schmidt, and A. Carlsson, *J. Am. Chem. Soc.*, 2000, **122**, 7116.
17. N. Wang, Z. K. Tang, G. D. Li, and J. S. Chen, *Nature*, 2000, **408**, 50.
18. A. P. Côté, A. I. Benin, N. W. Ockwig, M. O'Keeffe, A. J. Matzger, and O. M. Yaghi, *Science*, 2005, **310**, 1166.
19. T. Ben, H. Ren, S. Ma, D. Cao, J. Lan, X. Jing, W. Wang, J. Xu, F. Deng, J. M. Simmons, S. Qiu, and G. Zhu, *Angew. Chem. Int. Ed.*, 2009, **48**, 9457.
20. D. Yuan, W. Lu, D. Zhao, and H.-C. Zhou, *Adv. Mater.*, 2011, **23**, 3723.
21. D. Zhao, D. J. Timmons, D. Yuan, and H.-C. Zhou, *Acc. Chem. Res.*, 2010, **44**, 123.
22. F. A. Almeida Paz, J. Klinowski, S. M. F. Vilela, J. P. C. Tome, J. A. S. Cavaleiro, and J. Rocha, *Chem. Soc. Rev.*, 2012, **41**, 1088.
23. H. Li, M. Eddaoudi, M. O'Keeffe, and O. M. Yaghi, *Nature*, 1999, **402**, 276.
24. Q.-R. Fang, T. A. Makal, M. D. Young, and H.-C. Zhou, *Comments Inorg. Chem.*, 2010, **31**, 165.
25. I. Langmuir, *J. Am. Chem. Soc.*, 1916, **38**, 2221.
26. S. Brunauer, P. H. Emmett, and E. Teller, *J. Am. Chem. Soc.*, 1938, **60**, 309.
27. H. Furukawa, N. Ko, Y. B. Go, N. Aratani, S. B. Choi, E. Choi, A. Ö. Yazaydin, R. Q. Snurr, M. O'Keeffe, J. Kim, and O. M. Yaghi, *Science*, 2010, **329**, 424.
28. O. K. Farha, I. Eryazici, N. C. Jeong, B. G. Hauser, C. E. Wilmer, A. A. Sarjeant, R. Q. Snurr, S. T. Nguyen, A. Ö. Yazaydın, and J. T. Hupp, *J. Am. Chem. Soc.*, 2012, **134**, 15016.
29. S. M. Cohen, *Chem. Rev.*, 2011, **112**, 970.
30. X.-S. Wang, S. Ma, P. M. Forster, D. Yuan, J. Eckert, J. J. López, B. J. Murphy, J. B. Parise, and H.-C. Zhou, *Angew. Chem. Int. Ed.*, 2008, **47**, 7263.
31. S. Ma and H.-C. Zhou, *J. Am. Chem. Soc.*, 2006, **128**, 11734.
32. H. Wu, W. Zhou, and T. Yildirim, *J. Am. Chem. Soc.*, 2009, **131**, 4995.
33. D. Britt, H. Furukawa, B. Wang, T. G. Glover, and O. M. Yaghi, *Proc. Natl. Acad. Sci. U.S.A.*, 2009, **106**, 20637.
34. L.-C. Lin, J. Kim, X. Kong, E. Scott, T. M. McDonald, J. R. Long, J. A. Reimer, and B. Smit, *Angew. Chem.*, 2013, **125**, 4506.
35. D. Britt, D. Tranchemontagne, and O. M. Yaghi, *Proc. Natl. Acad. Sci. U.S.A.*, 2008, **105**, 11623.
36. E. D. Bloch, L. J. Murray, W. L. Queen, S. Chavan, S. N. Maximoff, J. P. Bigi, R. Krishna, V. K. Peterson, F. Grandjean, G. J. Long, B. Smit, S. Bordiga, C. M. Brown, and J. R. Long, *J. Am. Chem. Soc.*, 2011, **133**, 14814.
37. S. Xiang, W. Zhou, J. M. Gallegos, Y. Liu, and B. Chen, *J. Am. Chem. Soc.*, 2009, **131**, 12415.
38. S. J. Geier, J. A. Mason, E. D. Bloch, W. L. Queen, M. R. Hudson, C. M. Brown, and J. R. Long, *Chem. Sci.*, 2013, **4**, 2054.
39. Y.-S. Bae, C. Y. Lee, K. C. Kim, O. K. Farha, P. Nickias, J. T. Hupp, S. T. Nguyen, and R. Q. Snurr, *Angew. Chem. Int. Ed.*, 2012, **51**, 1857.
40. D. Feng, Z.-Y. Gu, J.-R. Li, H.-L. Jiang, Z. Wei, and H.-C. Zhou, *Angew. Chem. Int. Ed.*, 2012, **51**, 10307.
41. M. Dincă, A. Dailly, Y. Liu, C. M. Brown, D. A. Neumann, and J. R. Long, *J. Am. Chem. Soc.*, 2006, **128**, 16876.
42. P. D. C. Dietzel, R. Blom, and H. Fjellvåg, *Eur. J. Inorg. Chem.*, 2008, **2008**, 3624.
43. D. Zhao, D. Yuan, and H.-C. Zhou, *Energy Environ. Sci.*, 2008, **1**, 222.
44. L. Schlapbach and A. Zuttel, *Nature*, 2001, **414**, 353.
45. M. P. Stracke, G. Ebeling, R. Cataluña, and J. Dupont, *Energy Fuels*, 2007, **21**, 1695.
46. N. L. Rosi, J. Eckert, M. Eddaoudi, D. T. Vodak, J. Kim, M. O'Keeffe, and O. M. Yaghi, *Science*, 2003, **300**, 1127.
47. J. Kubas Gregory, *Acc. Chem. Res.*, 1988, **21**, 120.
48. H. K. Chae, D. Y. Siberio-Perez, J. Kim, Y. Go, M. Eddaoudi, A. J. Matzger, M. O'Keeffe, and O. M. Yaghi, *Nature*, 2004, **427**, 523.
49. M. Latroche, S. Surblé, C. Serre, C. Mellot-Draznieks, P. L. Llewellyn, J.-H. Lee, J.-S. Chang, S. H. Jhung, and G. Férey, *Angew. Chem. Int. Ed.*, 2006, **45**, 8227.
50. O. K. Farha, A. Özgür Yazaydın, I. Eryazici, C. D. Malliakas, B. G. Hauser, M. G. Kanatzidis, S. T. Nguyen, R. Q. Snurr, and J. T. Hupp, *Nat. Chem.*, 2010, **2**, 944.
51. P. N. Pearson and M. R. Palmer, *Nature*, 2000, **406**, 695.
52. M. Wriedt, J. P. Sculley, A. A. Yakovenko, Y. Ma, G. J. Halder, P. B. Balbuena, and H.-C. Zhou, *Angew. Chem. Int. Ed.*, 2012, **51**, 9804.
53. K. Sumida, D. L. Rogow, J. A. Mason, T. M. McDonald, E. D. Bloch, Z. R. Herm, T.-H. Bae, and J. R. Long, *Chem. Rev.*, 2011, **112**, 724.
54. W. Lu, J. P. Sculley, D. Yuan, R. Krishna, Z. Wei, and H.-C. Zhou, *Angew. Chem. Int. Ed.*, 2012, **51**, 7480.
55. A. R. Millward and O. M. Yaghi, *J. Am. Chem. Soc.*, 2005, **127**, 17998.
56. P. D. C. Dietzel, V. Besikiotis, and R. Blom, *J. Mater. Chem.*, 2009, **19**, 7362.
57. A. O. Z. R. Yazaydın, R. Q. Snurr, T.-H. Park, K. Koh, J. Liu, M. D. LeVan, A. I. Benin, P. Jakubczak, M. Lanuza, D. B. Galloway, J. J. Low, and R. R. Willis, *J. Am. Chem. Soc.*, 2009, **131**, 18198.
58. J. An, S. J. Geib, and N. L. Rosi, *J. Am. Chem. Soc.*, 2009, **131**, 8376.
59. J.-R. Li, J. Yu, W. Lu, L.-B. Sun, J. Sculley, P. B. Balbuena, and H.-C. Zhou, *Nat. Commun.*, 2013, **4**, 1538.

60. P. D. C. Dietzel, R. E. Johnsen, H. Fjellvag, S. Bordiga, E. Groppo, S. Chavan, and R. Blom, *Chem. Commun.*, 2008, 5125.
61. J.-R. Li and H.-C. Zhou, *Nat. Chem.*, 2010, **2**, 893.
62. J.-S. Choi, W.-J. Son, J. Kim, and W.-S. Ahn, *Microporous Mesoporous Mater.*, 2008, **116**, 727.
63. T. A. Makal, J.-R. Li, W. Lu, and H.-C. Zhou, *Chem. Soc. Rev.*, 2012, **41**, 7761.
64. S. Ma, D. Sun, J. M. Simmons, C. D. Collier, D. Yuan, and H.-C. Zhou, *J. Am. Chem. Soc.*, 2007, **130**, 1012.
65. X.-S. Wang, S. Ma, K. Rauch, J. M. Simmons, D. Yuan, X. Wang, T. Yildirim, W. C. Cole, J. J. López, A. D. Meijere, and H.-C. Zhou, *Chem. Mater.*, 2008, **20**, 3145.
66. I. Senkovska and S. Kaskel, *Microporous Mesoporous Mater.*, 2008, **112**, 108.
67. C. E. Wilmer, M. Leaf, C. Y. Lee, O. K. Farha, B. G. Hauser, J. T. Hupp, and R. Q. Snurr, *Nat. Chem.*, 2012, **4**, 83.
68. Z. Guo, H. Wu, G. Srinivas, Y. Zhou, S. Xiang, Z. Chen, Y. Yang, W. Zhou, M. O'Keeffe, and B. Chen, *Angew. Chem. Int. Ed.*, 2011, **50**, 3178.
69. C. E. Wilmer, O. K. Farha, T. Yildirim, I. Eryazici, V. Krungleviciute, A. A. Sarjeant, R. Q. Snurr, and J. T. Hupp, *Energy Environ. Sci.*, 2013, **6**, 1158.
70. T. Düren, L. Sarkisov, O. M. Yaghi, and R. Q. Snurr, *Langmuir*, 2004, **20**, 2683.
71. H. Wu, J. M. Simmons, Y. Liu, C. M. Brown, X.-S. Wang, S. Ma, V. K. Peterson, P. D. Southon, C. J. Kepert, H.-C. Zhou, T. Yildirim, and W. Zhou, *Chem.—Eur. J.*, 2010, **16**, 5205.
72. S. S.-Y. Chui, S. M.-F. Lo, J. P. H. Charmant, A. G. Orpen, and I. D. Williams, *Science*, 1999, **283**, 1148.
73. W. Zhou, H. Wu, M. R. Hartman, and T. Yildirim, *J. Phys. Chem. C*, 2007, **111**, 16131.
74. D. Zhao, D. Yuan, D. Sun, and H.-C. Zhou, *J. Am. Chem. Soc.*, 2009, **131**, 9186.
75. E. G. Kovaleva, M. B. Neibergall, S. Chakrabarty, and J. D. Lipscomb, *Acc. Chem. Res.*, 2007, **40**, 475.
76. A. Karlsson, J. V. Parales, R. E. Parales, D. T. Gibson, H. Eklund, and S. Ramaswamy, *Science*, 2003, **299**, 1039.
77. R. B. Eldridge, *Ind. Eng. Chem. Res.*, 1993, **32**, 2208.

Metal-Organic Frameworks for Removal of Harmful Gases

Jian Liu, B. Peter McGrail, Denis M. Strachan and Jun Liu

Pacific Northwest National Laboratory, Richland, WA, USA

Jian Tian

Texas A&M University, College Station, TX, USA

and

Praveen K. Thallapally

Pacific Northwest National Laboratory, Richland, WA, USA

1	Introduction	303
2	CO_2 Capture	305
3	Inorganic Toxic Gas Removal	309
4	Volatile Organic Compounds Adsorption	310
5	Radioactive Gas Immobilization	313
6	Perspectives and Conclusions	315
7	Acknowledgments	317
8	Related Articles	317
9	Abbreviations and Acronyms	317
10	References	317

1 INTRODUCTION

Metal organic frameworks (MOFs) or porous coordination polymers (PCPs) are an important class of solid-state materials that offer great potential for unraveling many challenges in the areas of energy and health.[1–4] The conceptual approach for synthesizing these materials is based on the self-assembly of cationic systems acting as nodes with polytopic organic ligands acting as linkers. As an analogy to zeolite frameworks, this approach to hybrid material construction allows the design of specific nanometer-scale framework geometries with particular pore structures and highest surface area known to date.[5,6] In contrast to zeolites, for which a relatively limited number of structures exist (178 to date), hybrid materials take advantage of the versatile coordination chemistry, polytopic linkers that make it possible to design an almost infinite variety of structures. Another key advantage is when self-assembly fails during the synthesis with functional linkers, the post-functionalization of a parent material appears to be a very valuable alternative. This approach consists of modifying the organic part of the hybrid material by a chemical reaction that takes place within the porous framework. Therefore, the structural nanoporosity of these materials places them at the frontier between zeolites and mesoporous materials.[7–9]

Metal-organic frameworks can be synthesized with a wide variety of metal cations and a large choice of functionalized organic linkers by use of various synthesis methods, such as solvothermal (hydrothermal), microwave heating,[10] ultrasonic,[11] mechanochemical,[12] electrochemical synthesis,[13] and the spray-drying.[14] However, only the conventional solvothermal (hydrothermal) method is well studied for MOF synthesis. In a typical solvothermal synthesis, both organic and inorganic precursors are dissolved in solvent

Metal-Organic Framework Materials. Edited by Leonard R. MacGillivray and Charles M. Lukehart.
© 2014 John Wiley & Sons, Ltd. ISBN 978-1-119-95289-3

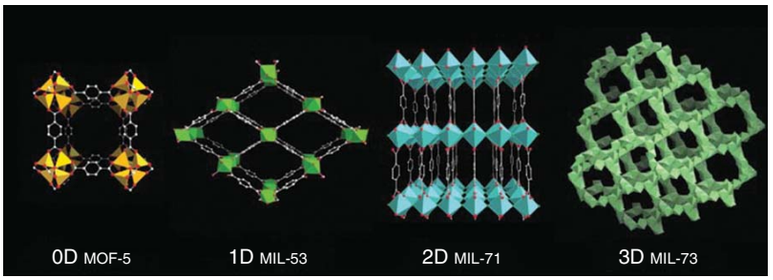


Figure 1 Examples of MOFs with various dimensionalities (Reproduced Ref. 4 with permission of The Royal Society of Chemistry. http://dx.doi.org/10.1039/B618320B.)

mixtures and sealed in a closed vessel under autogeneous conditions. Parameters like solvent combinations, pH, reactant concentration, temperature, and reaction time are important for producing the desired MOF with 0D to 3D network structures. Figure 1 shows some MOF examples with different dimensionalities.[4]

Over 10 000 MOF structures have been included in the Cambridge Structural Database (CSD), and many of them possess unique adsorption properties, including moderate heats of adsorption, chemical and morphological variety, and unprecedented porosity and surface area that provide great potential to revolutionize adsorption processes.[3] Many comprehensive reviews have been published on the synthesis and characterization of MOFs.[2,3,15,16] However, it is the applications for which MOFs are envisioned that motivate the rapid growth of research interest in MOFs.

Energy and environment are two important topics and are critical challenges for humans. On the one hand, MOFs have been extensively studied as novel adsorbents for energy storage, such as H_2 and CH_4 storage for clean-energy vehicles.[17–20] These applications have taken advantage of the extraordinarily high surface areas and large pore volumes of MOFs, which contain favorable gas molecules sites. Therefore, many large organic linkers with multiple benzene rings and extended length, such as the 4,4′,4″-benzene-1,3,5-triyltribenzoate (BTB) and another linker with multiple phenyl rings, 4,4′,4″-(benzene-1,3,5-triyl-tris(benzene-4,1-diyl)) tribenzoate (BBC), have been used to synthesize MOFs with extra-large surface areas and pore volumes.

In addition to larger organic linkers, activating MOFs with supercritical fluid is another option to increase surface areas and pore volumes. Supercritical activation can eliminate the solvent surface tension and prevent the pore collapse that would otherwise occur upon removal of organic solvents with heat. This activation method can help thoroughly remove residual solvent inside a MOF and increase their surface area to an even larger value than just the use of solvent exchange.[21] Moreover, unique characteristics of MOFs, such as the considerable structural flexibility, the ability to include accessible cation sites, and the variability of organic functional moieties, allow for intriguing gas storage behavior.[22–26]

On the other hand, a significant amount of research has been done to investigate the application of MOFs in removing harmful components from gas streams to protect the environment (see Table 1). The number of publications on the application of MOFs in environmental protection has increased exponentially during the last decade, as shown in Figure 2. The first class of harmful gases discussed here is the greenhouse gases—mainly CO_2. The higher the concentration of CO_2 in the atmosphere,

Table 1 List of harmful gases of environmental interest discussed

	CO_2, Fluorocarbons[a]	$H_2S/SO_x/NO_x/NH_3$	Aldehydes, ketones, benzene, etc.,	Xe, Kr, Rn, and I_2
Greenhouse gases	X Refs. 30–63	—	—	—
Inorganic toxic gases	—	X Refs. 27, 64–78	—	—
VOCs	—	—	X Refs. 28, 79–91	—
Radioactive gases	—	—	—	X Refs. 15, 29, 92–122

[a] Fluorocarbons were excluded from this chapter because of no (or/) limited experimental data results using MOFs.

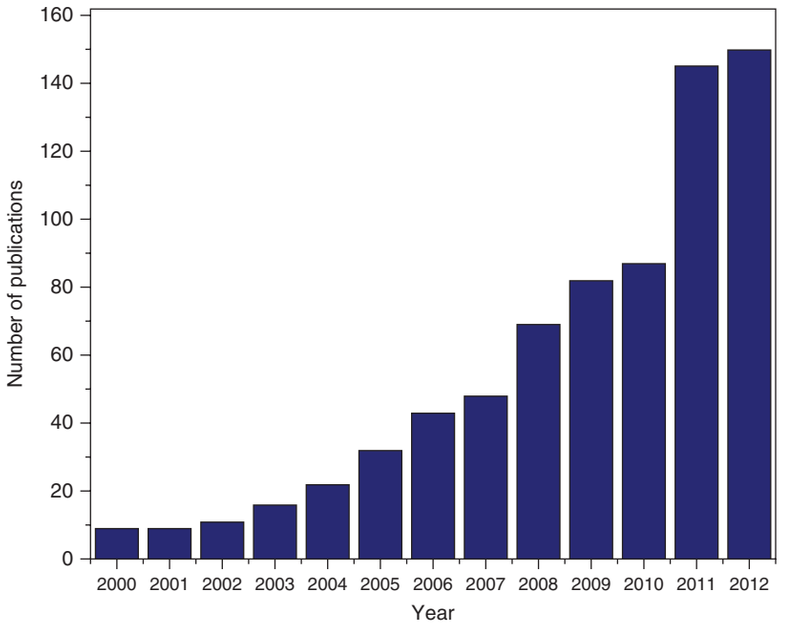


Figure 2 Number of publications on the use of MOFs in environment-related applications from 2000 to 2012. The data were obtained from the Web of Science database with English topic keyword search method on June 24th, 2013. The actual numbers of publications could be larger

the more heat will be retained inside the atmosphere, which leads to temperature increases and climate changes.[4]

The second class of harmful gases are inorganic toxic gases that include SO_x, NO_x, H_2S, and NH_3. These gases can be toxic to humans, animals, and plants that are present in various gas streams.[27] Therefore, it is important to remove these toxic gases to minimize release to the environment.

The third class of harmful gases includes volatile organic compounds (VOCs), such as formaldehyde, benzene, toluene, and certain ketones. These VOCs are a threat to human health, as well as to the environment, because of their involvement in photochemical pollution.[28]

The fourth class of harmful gases to be discussed are the radioactive gases potentially emitted during nuclear fuel reprocessing and reactor operations. Radioactive Kr, Xe, and I are the most common radioactive gases potentially found in a typical off-gas from a nuclear power plant. Removing and immobilizing the radioactive Xe and Kr reduces radioactive contamination to civil dwellings and possibly provide a new source of valuable noble gases for many industries.[29]

The content to follow will be presented in the order of CO_2 capture, acid-gas removal, VOC adsorption, and radioactive gas adsorption in MOFs, as we described above. The intention is not to present a complete review and summary on all the related research published in the literature, but to try giving a flavor of the research in which MOFs are used to adsorb these harmful gases and share some perspectives on the progress and challenges of this research topic.

2 CO_2 CAPTURE

The global warming effect is mainly caused by the anthropogenic emission of CO_2 into the atmosphere.[30] Some research results reveal that the concentration of CO_2 in the atmosphere has increased from about 310 ppm (parts per million) to over 380 ppm during the last half century, and it may soon reach 400 ppm for the first time in human existence, as shown by the Keeling curve in Figure 3.[31] A significant amount of CO_2 was released from coal-fired power plants in the United States. A typical 600 MW power plant can release over 8000 tons of CO_2 every day.[32] Therefore, to capture CO_2 from these main sources is an effective and convenient way to reduce CO_2 emissions, because a CO_2 capture unit only needs to be added to existing power plants. The current technique used in industry to remove CO_2 from flue gas is amine solution scrubbing. The regeneration of the amine solutions requires large amounts of energy because of the high heat capacity of the solution. Compared to the conventional amine solution scrubbing method, physisorption is an economical and promising method to separate CO_2 from flue gases. Many adsorbents have been developed and studied

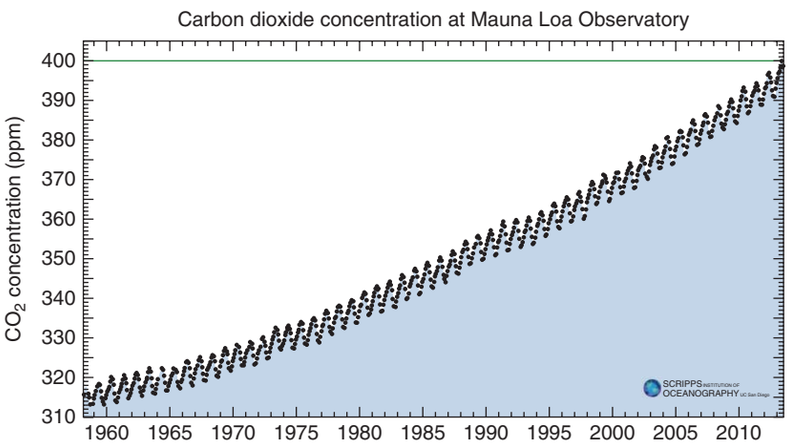


Figure 3 CO_2 concentration in the atmosphere (Reproduced by permission of Scripps Institution of Oceanography, University of California at San Diego.)

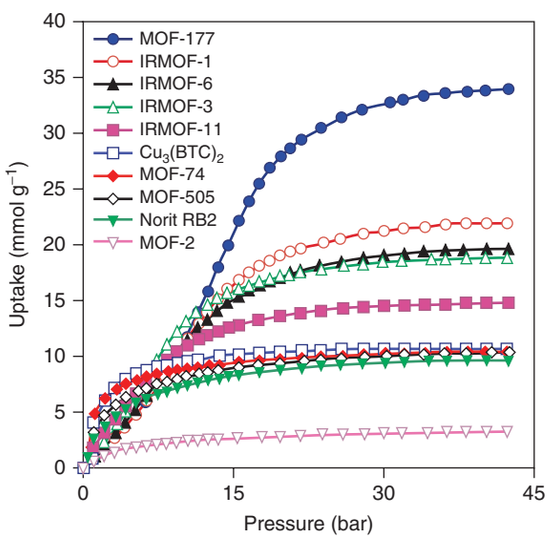


Figure 4 Gravimetric CO_2 capacities for several MOFs (and an activated carbon Norit RB2 as a reference) determined at ambient temperature and pressures up to 42 bar (Reprinted with permission from Ref. 40. Copyright (2005) American Chemical Society.)

for CO_2 capture, such as activated carbon, zeolites, and modified porous silica.[33–35] The common shortcomings for these traditional adsorbents are either low CO_2 capacities or difficult regeneration processes.

Many MOFs have higher saturated CO_2 capacities compared to those of the conventional adsorbents.[36–39] Yaghi's group published a pioneering work in 2005 on CO_2 adsorption in over 10 MOFs at pressures up to 4.5 MPa at ambient temperature. As shown in Figure 4, their results showed that MOF-177 can adsorb CO_2 to more than 30 mol kg^{-1}, which is promising for CO_2 storage.[40] However, because the CO_2 partial pressures in flue gases are usually around 15 kPa, it is of greater importance to understand CO_2 adsorption in MOF materials at low-pressures than at high pressures. In addition, the major component of flue gas is the remaining N_2 after combustion. It is important to study the selectivity between CO_2 and N_2 adsorption in MOFs, as well. More importantly, the existence of water in flue gas cannot be neglected, because even trace amounts of water influence gas adsorption in adsorbents, such as some zeolites and MOFs.[41,42]

Yazaydin *et al.*[43] used both experiments and simulation to screen MOFs for the highest CO_2 capacities at about 10 kPa. They found that the Mg/DOBDC and Ni/DOBDC (also known as Mg-MOF-74 and Ni-MOF-74 or CPO-27-Mg and CPO-27-Ni) have the highest CO_2 capacities at 10 kPa and 298 K at 587 kPa and 4.07 mol kg^{-1}, respectively. Instead of the surface area or the free volume, the authors found that MOFs with a high density of unsaturated metal centers (UMCs), such as Mg/DOBDC and Ni/DOBDC, were promising candidates for CO_2 capture from flue gas in which CO_2 partial pressure was about 10 kPa. The DOBDC series of MOFs had 1D pores with a uniform pore size of 1.1 to 1.2 nm after the depletion of solvent molecules, as shown in Figure 5. Unsaturated metal centers, which can enhance gas adsorption, especially under low-pressure conditions, were located inside the pores and exposed to guest gas molecules after removing the original coordinated solvent molecules, such as water molecules.[44,45] In addition, Caskey *et al.*[46] found that UMCs substitution in the DOBDC series MOFs can significantly impact their CO_2 capacities at the low-pressure region. This substitution effect may have been caused by the differences in the ionic character of the metal–oxygen bonds.

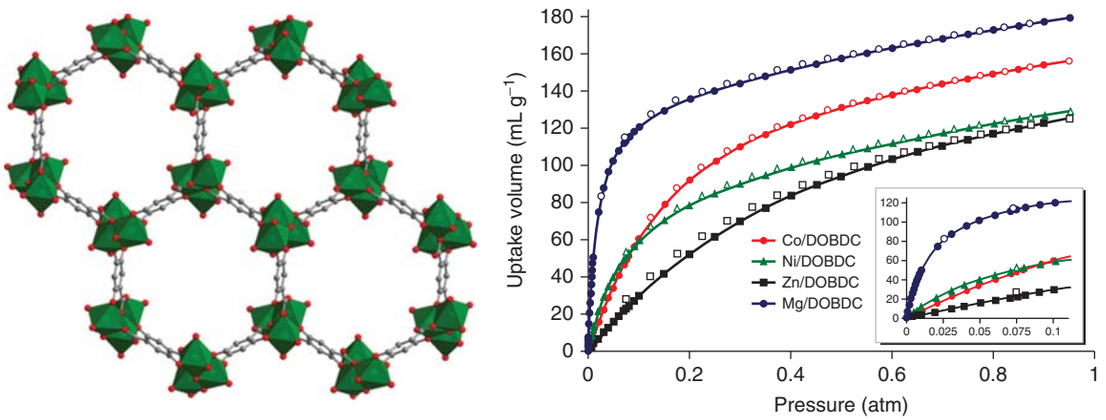


Figure 5 The 1D cylindrical channels present in the M/DOBDC structure. M = Zn, Ni, Co, Mg, Mn, or Fe; Metal center: green polyhedral; C: gray ball; O: red ball. CO_2 isotherms for four of the DOBDC series MOFs are included, as well. (Adapted with permission from Refs. 54 and 46. Copyright (2012 and 2008) American Chemical Society.)

It is important to have a MOF that can selectively adsorb CO_2 over N_2, because the majority of flue gas is composed of N_2. Liu and Smit[47] investigated seven MOFs, including CuBTC, MIL-47 (V), IRMOF-1, IRMOF-12, IRMOF-14, IRMOF-11, and IRMOF-13, for the separation performance of CO_2 over N_2 using Grand Canonical Monte Carlo (GCMC) simulations. CO_2 was preferentially adsorbed than N_2 in all the MOFs, with CuBTC showing the highest CO_2/N_2 selectivity. They also found that pore size played an important role in the selective adsorption of CO_2 over N_2. The effect of the electrostatic interactions became less evident compared to the effects of pore size, because both CO_2 and N_2 molecules have quadruple moments, so the electrostatic interactions help increase the adsorption for both of them. Wu *et al.*[48] substituted all the hydrogen atoms with O–Li groups in the aromatic rings of IRMOF-1 and obtained a Li-modified IRMOF-1 (here on words chem-4Li MOF). This hypothetical MOF was found to have an extraordinarily high CO_2/N_2 selectivity of 395 (CO_2:N_2 = 15.6:84.4), which is two orders of magnitude higher than that of the original IRMOF-1. This is believed to be caused by the strong electrostatic interactions between the gas molecules and the lithium atoms in the framework.

Although simulation research has shown that it is possible to construct new MOFs or modify existing MOFs to achieve very high CO_2/N_2 selectivity, some reported experimental studies showed much lower CO_2/N_2 selectivities for many MOFs. Bastin *et al.*[49] synthesized a microporous MOF-508b and obtained a CO_2/N_2 selectivity of 4 for a 50:50 mixture of CO_2 and N_2 at a total pressure of 1 bar through a fixed-bed. Basu *et al.*[50] mixed several MOFs, including CuBTC, ZIF-8, and MIL-53, into a polymer film and achieved a CO_2/N_2 selectivity of about 25 for a 10:90 mixture of CO_2 and N_2. Li *et al.*[51] synthesized a robust zeolitic MOF material that selectively adsorbed CO_2 over N_2. The selective CO_2 adsorption was caused by the small channels in the zeolitic MOF, which distinguish the two gases with kinetic diameters. Bae *et al.*[52] reported a way to enhance the CO_2/N_2 selectivity of a Zn-based MOF by cavity modification with a pyridine derivative. Their results showed that the modified MOF had a theoretical CO_2/N_2 selectivity of 28 at 100 kPa with an equimolar mixture composed of CO_2 and N_2. However, the modified MOF had a much lower CO_2 capacity, which is $<0.02\ mol\ kg^{-1}$ at 15 kPa, compared to the original MOF. Recently, Dickey *et al.*[53] reported that it is reasonable to use single-component isotherms plus the ideal adsorbed solution theory (IAST) to predict CO_2/N_2 mixtures adsorption results, because the predicted results agreed well with those obtained from GCMC simulations. This study provided an alternative method to preliminarily screen MOFs for CO_2/N_2 separation based only on single-component isotherms. Nonetheless, it is still critical to use experiments to study the real CO_2/N_2 mixture separation with a column breakthrough method for industrial applications.

Liu *et al.*[54] reported an experimental study on Ni/DOBDC to remove 15% CO_2 from a mixture of N_2 with a small amount of water (3% RH at 25 °C). Their results showed that a trace amount of water affected CO_2 adsorption capacity, as well as CO_2/N_2 selectivity of the Ni/DOBDC. The CO_2 capacity of the Ni/DOBDC cannot be fully recovered after water adsorption, even with heating. However, Ni/DOBDC retained a CO_2 capacity of $2.2\ mol\ kg^{-1}$ and a CO_2/N_2 selectivity of 22 at 15 kPa CO_2 with 3% RH water.

As mentioned above, selectivity between H_2O and CO_2 is important in the use of MOFs to separate CO_2 from flue gas, because a typical flue gas is saturated with water vapor. Some research work shows that a small amount of

water can enhance CO_2 adsorption in HKUST-1.[55] The enhanced CO_2 uptake is caused by interactions between the quadruple moment of CO_2 and the electric field created by the coordinated water molecules. However, further increasing water loading on the HKUST-1 results in considerable uncoordinated water molecules that can block pore space and cause the HKUST-1 to adsorb less CO_2 than the dry sample.

On the other hand, Liu *et al.*[56] reported that neither the HKUST-1 nor the Ni/DOBDC adsorbed significant amounts of CO_2 when water loadings were high, though water did not affect CO_2 adsorption in HKUST-1 and Ni/DOBDC as much as in traditional zeolites. In addition, it was much easier to remove water from Ni/DOBDC with heat regeneration. Therefore, the Ni/DOBDC adsorbed more CO_2 than traditional zeolites under moist conditions. More importantly, Ni/DOBDC had a reasonable hydrothermal stability. Kizzie *et al.*[57] studied CO_2/N_2 breakthrough phenomena for the DOBDC series of MOFs. They measured saturated capacities of CO_2 for the hydrated DOBDC series of MOFs after regeneration, observing significant decreases in capacities for the Mg/DOBDC and Zn/DOBDC, but much less significant decreases for the Ni/DOBDC and Co/DOBDC compared to the original samples.

By attaching hydrophobic moieties with post-modification method or generating MOFs with hydrophobic ligands, one can obtain MOFs with more hydrophobicity. Yang *et al.*[58] synthesized some fluorinated metal–organic frameworks (FMOFs) in which hydrogen atoms were substituted with fluorine atoms in all ligands. These fluorinated MOFs had enhanced thermal stability and hydrophobicity compared to their non-fluorinated analogs. Farha *et al.*[59] replaced the coordinated solvent molecules in a 3D MOF with various cavity modifiers, including pyridine and its derivatives. The resulting tailored cavities show different adsorption properties, and this post-synthetic modification method can be adopted to cover hydrophilic surfaces in some MOFs with hydrophobic molecules, such as pyridine, to reduce H_2O effects on CO_2 adsorption.

Some MOFs were recently found to be water and heat stable. For example, Li *et al.*[60] reported a series of cobalt-adeninate bio-MOFs that have high water stability and the stability increased as the aliphatic chain length increased. Moreover, the bio-MOF-14 had a unique molecular sieving property that allowed it to adsorb only CO_2, but not N_2, at near room temperature. In addition, Cavka *et al.*[61] reported a new zirconium-based MOF, UiO-66, with high surface area with unprecedented stability, as shown in Figure 6. The decomposition temperature for the UiO-66 was as high as 540 °C, and it was stable in boiling water. The high stability was based on the combination of strong Zr–O bonds and the ability of the inner Zr_6-cluster to rearrange reversibly upon removal or addition of μ_3-OH groups, without any changes in the connecting carboxylates. Huang *et al.*[62] found that by adding two methyl groups on the benzene ring of the benzendicarboxylate acid, one could obtain a modified MOF, UiO-66-$(CH_3)_2$, with enhanced stability, larger CO_2 adsorption capacity, and higher selectivity toward CO_2/N_2, compared to the original UiO-66. Walton's group synthesized UiO-66 analogs with amino-, nitro-, methoxy-, and naphthyl-substituted ligands. They found that water adsorption in

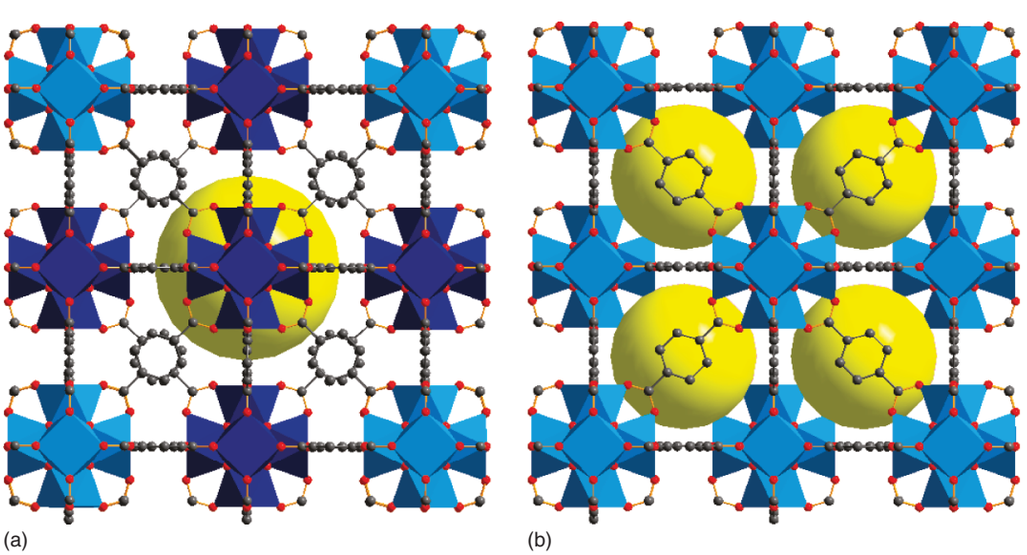


Figure 6 Illustration of the water and heat-stable MOF UiO-66(Zr) structure. (a) Octahedral cage; (b) tetrahedral cages. Hydrogen atoms on the organic linkers were omitted for clarity. The large yellow spheres represent the void regions inside the cages. (Reprinted with permission from Ref. 61. Copyright (2008) American Chemical Society.)

the naphthyl-substituted UiO-66 was reduced, and this modified UiO-66 did not suffer from water adsorption effects when used to CO_2 capture from flue gas.[63]

3 INORGANIC TOXIC GAS REMOVAL

The toxicity of SO_2 causes growing environmental concerns, because it can be further oxidized in the atmosphere to produce acid rain. Traditional processes for capturing SO_2, including limestone scrubbing, ammonia scrubbing, and organic solvents absorption, have been limited by some inherent disadvantages, such as producing a lot of wastewater. In this regard, MOF materials have drawn recent attention, in that they can efficiently, reversibly, and economically capture SO_2 without generating a lot of byproducts. Recently, Schröder and coworkers reported a chemically and thermally stable porous MOF (NOTT-300) that showed high capacity and selectivity for CO_2 and SO_2 gases.[64] The structure of NOTT-300 was configured as 1D square-shaped channels with hydroxyl groups protruding into them, endowing the pore environment with free hydroxyl groups in four directions that are binding sites for SO_2 molecules. Strikingly, NOTT-300 has shown a maximum SO_2 capacity of $8.1\,mmol\,g^{-1}$ (at 273 K and 100 kPa), representing the highest value observed so far for MOFs. Moreover, the adsorbed SO_2 can be readily released, and the NOTT-300 regenerated at ambient temperatures without the need for heating, indicating an easy-on/easy-off capture system. Thallapally *et al*.[65] studied SO_2 and H_2S adsorption in some Prussian blue analogs, $M_3[Co(CN)_6]_2 \cdot nH_2O$ (M = Co, Zn). They showed that the $Co_3[Co(CN)_6]_2$ can adsorb a significant amount of SO_2 and H_2S, with capacities of 10 and 4.5 wt% at 100 kPa, respectively. They also showed that these Prussian blue analogs can retain their crystallinity after exposure to acidic gases. However, other research showed that exposure to acidic gases, such as SO_2, with humidity can affect the crystallinity of MOFs and lead to reduced CO_2 capacities.[66,67]

Metal-organic framework materials have also been investigated for removal of H_2S in their use for the purification of natural gas. De Weireld and coworkers have examined two types of MOFs, exhibiting small or large pores, for H_2S sorption.[68] These MOFs demonstrated distinct behavior toward H_2S sorption. The adsorption of H_2S in the large-pore series (MIL-100 and MIL-101) was very large, but appeared to be partially irreversible. In contrast, the small-pore series (MIL-47(V) and MIL-53(Al, Cr)) exhibited perfectly reversible one- or two- step adsorption behavior under H_2S pressure, except for the Fe analog. These studies demonstrated that a judicious choice of crystal structures and metal centers led to MOFs that were stable and easily regenerable after H_2S sorption, which represented a first step toward the use of MOFs for the purification of gases containing H_2S impurities.

Besides SO_x and H_2S adsorption in MOFs, NO_x adsorption has also been investigated by researchers. Particularly, the adsorption of NO in MOFs is of great importance in some biological applications; it is an important biological signaling molecule. Morris' group studied the NO adsorption in the Ni/DOBDC and Co/DOBDC, and they found that each UMC in the structure coordinated to one NO molecule.[69] The extremely high adsorption capacity (7 mmol of NO/g of MOF) and good storage stability made this MOF ideal for NO storage. More importantly, the entire reservoir of stored gas was recoverable given a trigger from water molecules. At about the same time, another group from France also showed that the Ni/DOBDC could reversibly adsorb NO, and the slow displacement of NO molecules by H_2O molecules made the Ni/DOBDC a promising candidate for NO delivery inside biological tissues.[70] Morris's group then carefully investigated the feasibility of NO delivery using several well-known MOFs, including Ni/DOBDC, Co/DOBDC, HKUST-1 (CuBTC), MIL-53 (Al), and MIL-53 (Cr), as the carriers.[71] Their preliminary data showed that the MOFs they studied were stable in water and biological fluid. The toxicology study indicated that the MOFs were acceptable for use in healthcare applications, and the authors proposed that MOFs composed of iron carboxylate should have less toxicology concern and, therefore, had a promising future in biological applications.[71] Different from NO adsorption in MOFs, the adsorption of NO_2 in MOFs was usually reactive. Bandosz's group found that a composite of CuBTC and graphite oxide (GO) had enhanced NO_2 breakthrough capacity compared to the CUBTC and GO separately under dry conditions.[72] The improvement was due to the increased porosity and the reactive adsorption of NO_2 on copper, which led to the formation of bidentate and monodentate nitrates. Under moist conditions, the NO_2 capacity of the composite decreased because of the competition from water molecules binding to copper sites. The same group used more stable MOFs, UiO-66 and UiO-67, and conducted a similar NO_2 adsorption study on them.[73] The larger pore size of the UiO-67 was found to have a positive impact on the adsorption of NO_2 under moist conditions, while it had the opposite effect under dry conditions. Moreover, the authors found that under moist conditions, a large amount of water retained on the UiO-67 facilitated the formation of nitrous and nitric acids, which led to the collapse of its structure. Meanwhile, the UiO-66 was more stable under the same conditions, because the UiO-66 had smaller pores, so NO_2 molecules were blocked from getting into the pores by water molecules, which prevented the formation of nitric acid.

Capturing basic toxic gases, such as ammonia from air, is another potentially promising application of

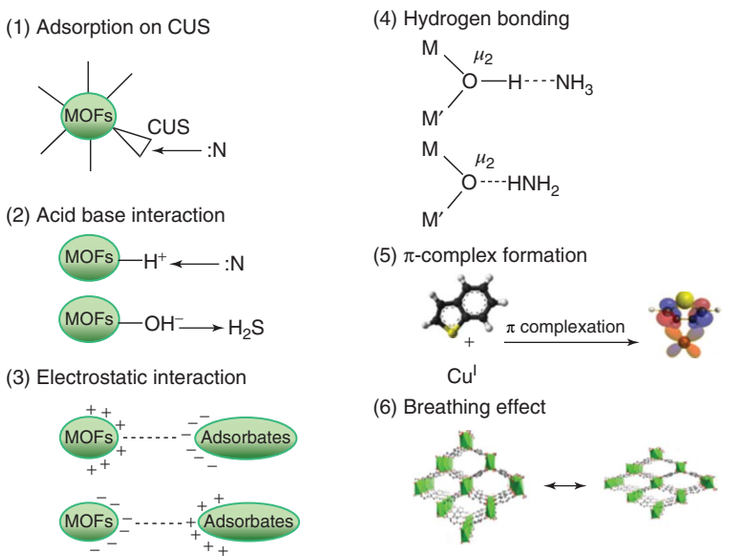


Figure 7 Important mechanisms for the adsorption of toxic gases in MOFs. (Reproduced from Ref. 78. © Elsevier, 2013.)

MOFs. Only a few studies have reported on the adsorption of ammonia by MOFs. Britt *et al.*[27] investigated several benchmark MOFs, including MOF-5, IRMOF-3, MOF-74, MOF-177, MOF-199, and IRMOF-62, for the adsorptive removal of ammonia. They reported that these MOFs outperformed activated carbon in kinetic breakthrough measurements. Yaghi and coworkers examined the dynamic loading capacity of ammonia in the M-MOF-74 (M = Co, Mg, Ni, and Zn) series under both dry and humid conditions.[74] All analogs had capacities equivalent to or higher than traditional zeolites and BPL activated carbon, among which Mg-MOF-74 and Co-MOF-74 had the highest capacities under dry conditions. Notably, these MOFs retained a significant portion of the adsorbed ammonia when the materials were exposed to dry air during a desorption experiment. Peterson *et al.*[75] found that the $Cu_3(BTC)_2$ had an ammonia capacity of 6–9 mol kg^{-1} at saturation, which was among the highest reported values. However, much of the capacity was due to chemical reactions with the structure of the $Cu_3(BTC)_2$ that could not be fully recovered by regeneration. Saha and Deng[76] reported similar structure degradations for MOF-5 and MOF-177 after ammonia adsorption, and suggested that the loss of MOF crystalline structures was caused by the hydrogen bonding between ammonia molecules and the Zn_4O clusters, which is similar to how water molecules interfere with the MOF frameworks. In order to screen promising MOF adsorbents for ammonia capture under humid conditions, Snurr's group calculated the binding energies for ammonia and water to 21 functional groups. They found that R-COOCu and R-COOAg were the top two candidates for ammonia capture under humid conditions because they had the largest difference in binding energies between ammonia and water molecules.[77]

In order to better understand toxic gas adsorption in MOFs, the interaction mechanisms need to be investigated. As pointed out by Khan and co-authors[78] in a recent review, the variety of chemical compositions of MOFs has led to different strategies towards adsorption of various hazardous compounds through specific interactions. For example, UMCs have been used to bind polarizable toxic gases, such as H_2S, NH_3, and SO_2. In addition, incorporation of acidic/basic species and metals into MOFs dramatically improves the adsorption capacity for various toxic compounds through acid–base interaction and π-complex formation, respectively. Some important mechanisms for the adsorption of toxic gases in MOFs are summarized in Figure 7. As one can see, besides the mechanism mentioned above, hydrogen bonding and breathing effects also play a key role in toxic gas adsorption in MOFs.

4 VOLATILE ORGANIC COMPOUNDS ADSORPTION

Volatile organic compounds represent a broad class of airborne organic compounds that can be found in industry exhaust and everyday life. Volatile organic compounds are considered both indoor and outdoor air pollutants. The main concern indoors is the potential for VOCs to adversely impact the health of people that are

exposed. The main concern outdoors is their ability to create photochemical smog under certain conditions.[79] There are thousands of different chemicals classified as VOCs. Some of the dangerous and commonly found VOCs are formaldehyde (carcinogen), benzene (carcinogen), toluene (causes neurological damage), xylene (causes neurological damage), and perchloroethylene (causes central nervous system damage). These VOCs pose well-known and serious health risks to humans and the environment, even at trace levels (ppt–ppm).[80] Therefore, to monitor and detect these compounds is of great importance to human health. The current adsorbents used to remove VOCs, such as carbonaceous adsorbents, zeolites, silicates, and polymeric resins, are limited by problems related to rigorous regeneration conditions, slow kinetics, low surface areas, and unacceptable stability.[28]

Metal-organic framework materials have been proposed to remove VOCs, though compared to small molecules, such as H_2, CH_4, and CO_2, only a limited number of studies reported about the adsorption of larger organic molecules in MOFs. A systematic study has been done by Luebbers *et al*.[28] on the use of IRMOF-1 to adsorb a variety of VOCs, mainly alkanes, alkylbenzenes, and some common organic solvents. It was noted that the adsorption enthalpies vary linearly with the increase in chain length for a series of *n*-alkanes and alkylbenzenes. The same research group functionalized the IRMOF-1 with trifluoromethoxy and methyl groups to improve the stability and measured VOCs adsorption in the functionalized IRMOF-1. They found that the functionalized IRMOF-1 had significantly reduced capacities and heats of adsorption compared to those of the IRMOF-1. These differences were due to chemical and geometric changes in the pore apertures of the materials.

Luebbers *et al*.[81] also studied VOC adsorption in ZIF-8 using an inverse gas chromatography methodology. They observed that aromatic compounds, branched alkanes, and heavily halogenated compounds elute very quickly as very sharp peaks, indicating a molecular sieving effect that prevented these large molecules from entering the narrow apertures of the framework crystal. However, *n*-alkane molecules, which are smaller and more linear compared to the molecules just mentioned, can be adsorbed into the ZIF-8 even if the *n*-alkanes had kinetic diameters greater than the reported ZIF-8 pore aperture size of 0.34 nm. These results showed a surprising flexibility of the ZIF-8 framework. In addition, a significant enhancement in the adsorption of alkenes over their corresponding alkanes was observed for the ZIF-8. These enhancements were caused by the polarizability of the π-electrons and the interactions of the induced dipole with the framework structure. The ability for ZIF-8 to discriminate in the adsorption of both branched versus linear alkanes and paraffins versus olefins, along with its exceptional stability, indicated a great potential for it to be used in related separation applications.

Besides alkanes and alkenes, adsorption of benzene in MOFs has also been studied. Amirjalayer *et al*.[82] used quantum mechanical methods to study benzene adsorption in MOF-5. They demonstrated that benzene molecules interact strongly with the inorganic vertex of the MOF-5 framework with heats of adsorption at about 42 kJ mol^{-1}, as compared to light molecules, such as H_2 or CH_4. Kolokolov *et al*.[83] investigated the dynamics of benzene entrapped in the MIL-47(V) by quasielastic neutron scattering (QENS) and solid-state ^2H NMR, combined with molecular simulations. They obtained excellent agreement between QENS and molecular simulations on the quantitative study of molecular motion of fluids adsorbed in MIL-47(V). They found that benzene molecules confined in the MIL-47 move in a corkscrew fashion; that is, move along axis by short jumps, as shown in Figure 8. This

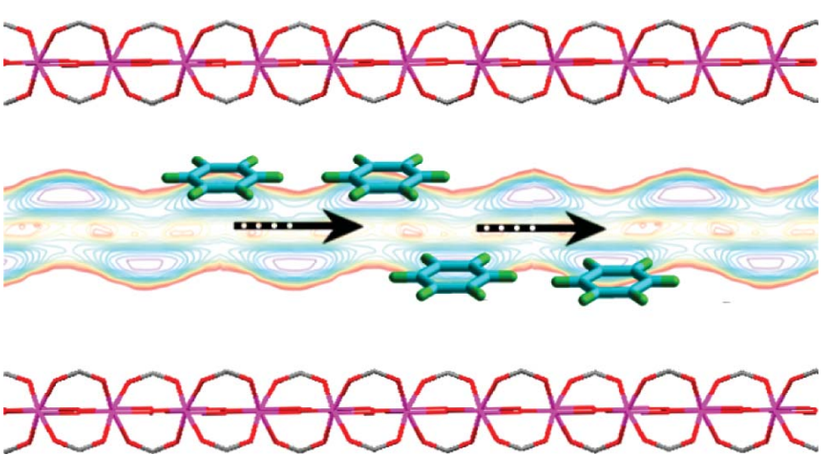


Figure 8 Benzene inside MIL-47(V) moves along the channels axis by short-length jumps (Reprinted with permission from Ref. 83. Copyright (2012) American Chemical Society.)

phenomenon may be used to design a kinetic separation process of benzene with MIL-47(V) as a novel adsorbent.

In regard to the separation of benzene, Zeng *et al.*[84] studied the adsorption behavior of thiophene and benzene in the CuBTC and IRMOF-1 using GCMC simulations. Their simulation results of binary adsorption of thiophene and benzene showed that thiophene adsorbs preferentially near the metal sites of the MOF at low coverage, while benzene tended to distribute throughout the pore space. The CuBTC was found to be a promising candidate to separate the mixtures of thiophene and benzene.

Xylene separation with MOFs recently became a popular topic. Finsy *et al.*[85] studied gas-phase adsorption of C_8 alkyl aromatics in the MIL-47. In the Henry's law region, *p*-xylene, *m*-xylene, *o*-xylene, and ethylbenzene (EB) had comparable Henry's law constants and adsorption enthalpies. However, individual C_8 alkyl aromatics packed differently in the constrained environment of the MIL-47 pores, which can be used to achieve molecular separation. The authors found that the adsorption selectivity among the xylene isomers increased with degree of pore filling; that is, the more molecules present in the pores, the more the ordering of these molecules became important. Therefore, adsorption selectivity was strongly dependent on pressure and temperature, which provided a way to optimize the adsorption process.

The MIL-53 (Al) has also been studied for the adsorption and separation of C_8 alkyl aromatic components by Finsy and his colleagues.[86] They observed expected framework breathing during the adsorption of C_8 alkyl aromatic molecules. At low pressures, adsorption caused the MIL-53 (Al) framework to contract. In the limited space of the closed form of the MIL-53 (Al) framework, only a single-file arrangement of molecules could be accommodated. At much higher pressures, the pores of the MIL-53 (Al) reopened. In the open form of the MIL-53 (Al) framework, the space was sufficiently large for the xylene isomers to be adsorbed in pairs, leading to a twofold increase in the capacity. This breathing phenomenon strongly affected the separation of xylene mixtures. Below the transition pressure, no separation could be achieved; at pressures higher than the transition pressure, the adsorption selectivity increased with the degree of pore filling.

Gu *et al.*[87] prepared a capillary column coated with the MIL-101 and achieved a baseline separation of *p*-xylene, *o*-xylene, *m*-xylene, and EB, as shown in Figure 9. The excellent selectivity originated from the host–guest interactions, UMCs, and suitable polarity of the MIL-101. Their results indicated that the MIL-101 is very promising for high-resolution capillary gas chromatography.

Long's group recently reported a MOF, $Fe_2(BDP)_3$ (BDP = 1,4-benzenedipyrazolate), a highly stable framework with triangular channels that can separate the hexane isomers based on the degree of branching, as shown in Figure 10.[88] The adsorption isotherms

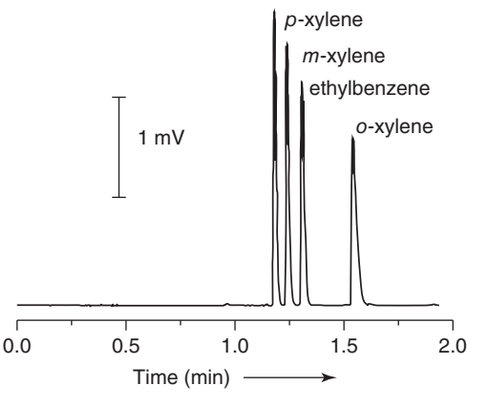


Figure 9 GC separation of xylene isomers and EB on a MIL-101 coated capillary column (15 m long × 0.53 mm long) at 160 °C under an N_2 flow rate of 3 mL min^{-1}. No temperature programming was used (Reproduced from Ref. 87. © Wiley-VCH Verlag GmbH & Co. KGaA, 2010.)

and calculated isosteric heats of adsorption indicated an adsorption selectivity order of *n*-hexane > 2-methylpentane > 3-methylpentane > 2,3-dimethylbutane ≈ 2,2-dimethylbutane. This was consistent with the varying abilities of the isomers to wedge along the triangular corners of the structure. The authors used both the column breakthrough and molecular simulation to confirm this molecular origin of the selectivity. Based on the adsorption selectivity of the $Fe_2(BDP)_3$, the authors proposed to separate only the two most valuable, di-branched isomers from the other three to economically achieve a potential fuel with high octane numbers.

Formaldehyde is another VOC that is considered to cause cancer and other diseases in human beings. Iswarya *et al.*[89] studied formaldehyde adsorption in MOF-5 (or IRMOF-1), and they found a linear increase in response to the concentration of formaldehyde. Maihom *et al.*[90] used density functional theory (DFT) to study the stability of monomeric formaldehyde encapsulated in the lithium-decorated MOF, Li-MOF-5. Their calculation results showed that the oligomerization of formaldehyde in Li-MOF-5 was reversible, suggesting that Li-MOF-5 may be a good candidate for preserving formaldehyde in its monomeric form. The Li cation interacted with formaldehyde in a way similar to the Na cation in zeolites, which is known to prevent formaldehyde from self-polymerizing.

Post-synthesis modification or functionalization can help increase the capacities of a variety of VOCs for MOFs. Ma *et al.*[91] functionalized porous MOFs by encapsulating Keggin-type Polyoxometalates (POMs) and further modified the inclusion state via ion exchange. They showed that both POMs (through hydrogen bondings) and alkali metal cations (through polar interactions) played important roles in increasing the adsorption capacity of MOFs for a wide range of VOCs.

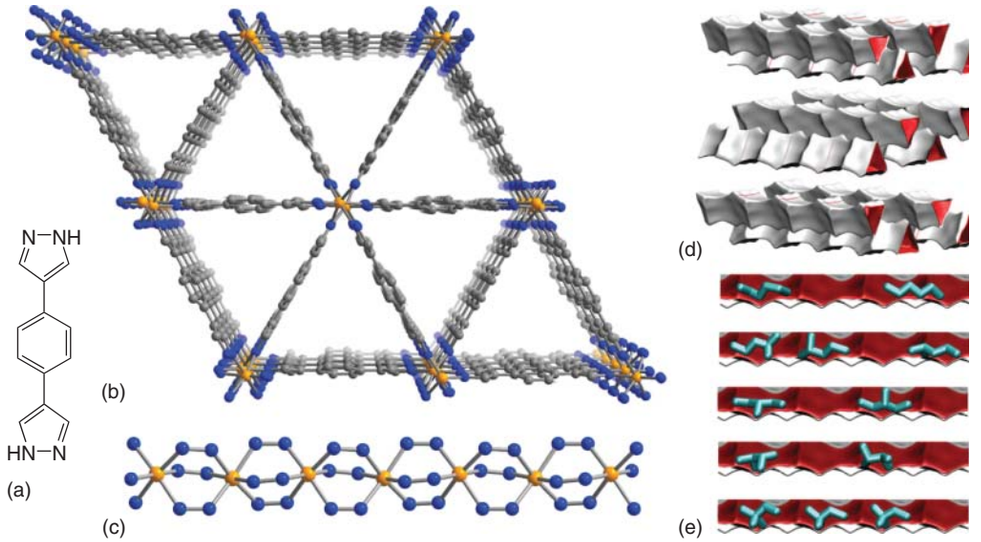


Figure 10 (a) Depiction of the bridging ligand precursor H_2BDP. (b) The structure of $Fe_2(BDP)_3$ viewed along the [001] direction. Orange, blue, and gray spheres represent Fe, N, and C atoms, respectively; H atoms are omitted for clarity. (c) A perpendicular view of the 1D chains of pyrazolate-bridged FeIII octahedra, excluding C and H atoms. (d) The van der Waals surfaces associated with the corrugated triangular channels running through the structure. (e) Snapshots of the hexane isomers within the channels of $Fe_2(BDP)_3$ for a loading of four molecules per unit cell at 160 °C. (From Ref. 88. Reprinted with permission from AAAS.)

5 RADIOACTIVE GAS IMMOBILIZATION

Nuclear fission results in fission products including those volatile under the conditions of used nuclear fuel reprocessing and medical isotope production. The radionuclides that have been identified as important to capture from reprocessing off-gas streams are ^{129}I, ^{127}Xe, and ^{85}Kr.[92]

Of the iodine isotopes, ^{129}I is a particularly long-lived isotope with a half-life of 1.57×10^7 years that must be captured and reliably stored. Typically, ^{131}I (half life = 8.02 d) has decayed to innocuous levels by the time nuclear fuels are ready to be processed. Therefore, while it can directly affect human metabolic processes, it is at such low concentrations that it does not pose a health risk.[93] Therefore, the main dose consequences have to calculated on the long-lived ^{129}I. Current methods of capturing I_2 by porous adsorbents include the use of silver-exchanged zeolites.[94] These materials lack high adsorption capacities because of their relatively low surface areas. The use of silver metal also draws some concerns related to cost and environmental impact.

There have been a few studies of I_2 sorption on MOFs, and, in those reports, the adsorption of I_2 is not particularly strong.[95–97] ZIF-8 was selected by a research group from Sandia National Laboratory as a novel adsorbent for I_2 because of its suitable pore aperture size, large surface area, and high chemical and thermal stability. They found that up to 5.4 I_2 molecules were captured inside each cage, and the I_2 adsorption was mainly due to favorable interactions with the organic linker of the ZIF-8, as shown in Figure 11. The increase of I_2 loadings resulted in a reduction of long-range crystallinity, but the cage connectivity was retained.[98] ZIF-8 maintained its high I_2 adsorption capacity when it was extruded into pellets. ZIF-8 consists of tetrahedrally coordinated Zn atoms linked by 2-methylimidazole ligands. It has a network similar to an expanded sodalite structure. The β-cages are connected through six membered-ring apertures with a diameter of 0.34 nm, which is slightly larger than the molecular size of iodine (0.335 nm).[99] The small pores of the ZIF-8 can limit I_2 from escaping after adsorption. Therefore, this adsorption in the ZIF-8 allows I_2 to be isolated, and incorporated into appropriate waste forms.[100] The same group from Sandia National Laboratory further prepared a novel glass-composite material waste form by mixing and sintering the I_2-containing MOFs with Bi-Zn-O low-temperature sintering glasses and silver metal flakes. I_2 is sequestered in-situ during the heating process, with no evidence of iodine loss by the formation of AgI.[101]

Bennett *et al.*[102] reported the synthesis and characterization of a new ZIF, ZIF-mnIm, which has an identical topology to the ZIF-8, but with a different organic linker. They determined I_2 adsorption in the ZIF-mnIm and compared the performance with those of known ZIF frameworks. They found that the ZIF-69 had the highest initial adsorption, but poor retention because of the large pore aperture. The authors also showed that mechanical grinding of loaded samples significantly increased the I_2

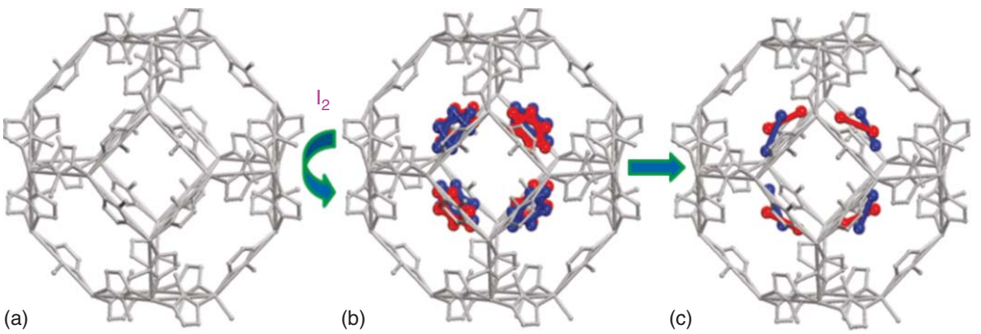


Figure 11 (a) Ball-and-stick model of the activated cage prior to I_2 loading. (b) Two individual molecular I_2 adsorption sites refined inside the β-cage, "Ia" (blue) and "Ib" (red). (c) Actual molecular arrangement (H atoms have been omitted for clarity). (Reprinted with permission from Ref. 98. Copyright (2011) American Chemical Society.)

retention temperature to 100 °C. Although ZIF-8 was overall the best candidate with regard to I_2 uptake and retention, ZIF-mnIm displayed the greatest change in retention temperature after grinding. The use of grinding may enable MOFs to act as permanent storage media, not just for I_2, but for other harmful guest species. Few other research groups published studies on I_2 adsorption in liquid phase by MOFs target for luminescent applications by reversible adsorption of I_2 and, therefore, are beyond the scope of our topic.[97,103,104]

Separating low concentrations of Xe and Kr from air is an important step in removing radioactive ^{127}Xe and ^{85}Kr from the off-gas streams from the reprocessing of spent nuclear fuels.[105] The current method to separate these radioactive gases is cryogenic distillation, which is energy-intensive and may be expensive to install. In contrast, separation of Xe and Kr by selective adsorption at near room temperature could be more energy efficient and less expensive overall. One of the main concerns with storage of cryogenically separated ^{85}Kr in stainless steel canisters at elevated pressures is the Rb that is formed as the ^{85}Kr decays. Rubidium is a liquid at waste storage temperatures and, as a liquid, is very corrosive. The use of adsorbents improves this technology in two ways. First, it allows more gas to be stored in the canister at lower pressures. Second, the decay product Rb would be isolated in the adsorbents, thereby reducing the corrosion concerns. Previous research has shown that NaA and NaX zeolites are selective adsorbents for Xe over Kr, with selectivities of approximately four to six, but they have low Xe capacities.[106–109]

The storage of noble gases was demonstrated in some MOFs, though research to date is somewhat limited.[15] Recently, Thallapally *et al.*[110] reported that Ni/DOBDC has a Xe capacity of 4.16 mol kg^{-1} at 100 kPa and 298 K. Moreover, Liu *et al.*[29] used a column breakthrough method to study the low concentration Xe and Kr adsorption in MOFs. For the first time, their experimental results showed that the Ni/DOBDC was able to separate 400 ppm Xe from 40 ppm Kr mixture in air, with a Xe/Kr overall selectivity of 7.3. Fernandez *et al.*[111] showed that they could switch the Xe/Kr selectivity for a microporous fluorinated MOF by adjusting temperatures. The fluorinated MOF had a pore size which was very close to the molecular size of Kr, but a little smaller than the atomic size of Xe. By reducing the temperature from room temperature to 233 K, Kr adsorption capacity increased, whereas Xe molecules could adsorb into the pores because of the shrinkage of the pore aperture.[112] This reversed selectivity could be used to selectively separate Kr from Xe in a typical nuclear power plant off-gas. This may be important since the molar content of non-radiactive Xe in irradiated nuclear fuel is about ten times that of Kr.

The adsorption affinity of Xe and Kr is directly related to the interaction strength between MOFs and the noble gas molecules, and the affinity can be adjusted by functionalization of ligands. Dorcheh *et al.*[113] monitored the interaction strength between different noble gases and MOFs, including HKUST-1 MFU-4l and ZIF-8, by thermal desorption spectroscopy (TDS). The TDS results show that MFU-4l and HKUST-1 are potential candidates for separation and storage of Kr and Xe, based on the significant difference in the final desorption temperature for Xe and Kr on the two MOFs. Allendorf and coworkers show that the uptakes of Xe and Kr can be affected by the polarizable functional groups and is evident from their results with a series of monohalogenated isoreticular MOFs.[114]

A few computer simulation studies have been reported in which MOF candidates have been screened for Xe and Kr separation. Greathouse *et al.*[115] used GCMC simulation to investigate Xe and Kr separation in IRMOF-1. Ryan *et al.*[116] studied Xe and Kr separation in several MOFs, also using a GCMC simulation method. Both these studies showed that small pores were desirable for MOFs to have high Xe/Kr selectivity. Along the same lines, Bae *et al.*[117] reported that MOF-505 has high Xe/Kr selectivities, because of the presence of small pores that

favor the Xe adsorption and Xe/Kr selectivities. This observation was supported further by molecular simulation in which MOFs with pore-limiting diameters slightly above the kinetic diameter of Xe/Kr were shown to have high Xe/Kr selectivities. Moreover, Snurr's group reported a work on screening the Xe/Kr selectivity for 137 000 hypothetical MOFs.[118] They found that the MOFs with polar functional groups tend to have higher Xe/Kr selectivities compared to those that do not have polar functional groups. Moreover, the Xe/Kr selectivity is maximized when the MOF structures have pore morphologies resembling tubes of uniform pore width, as shown in Figure 12.

Gurdal and Keskin[119] used molecular simulations to assess both the adsorption-based and permeation-based separation performances of various MOFs for Xe/Kr and Xe/Ar separations. They observed a trade-off between adsorption-based selectivity and working capacity. Large pore materials with low adsorption selectivities, such as IRMOF-1, exhibited high working capacities. They also found that the MOFs examined in their study could be better membrane materials than Zeolites because of higher permeation selectivities and gas permeabilities. In another work, the same authors[120] also computed adsorption and diffusion of Xe/Kr and Xe/Ar mixtures in several MOFs using both computationally demanding mixture simulations (GCMC and MD) and theoretical correlations (IAST). Their results showed that IAST predicts the mixture adsorption well for both Xe/Kr and Xe/Ar in all MOFs. Separation properties of MOFs, such as adsorption selectivity, working capacity, diffusion selectivity, permeation selectivity, and gas permeability, can be accurately predicted by applying theoretical correlations. The agreement between theory and simulations was best at zero loading, since correlation effects were negligible at low loadings. The authors pointed out that heterogeneity factors, such as existence of different pore sizes, shapes, loading, and composition of the adsorbates were critical to the theoretical correlations in IAST.

Recently, Greathouse and coworkers[121] screened 16 MOFs for selective adsorption of noble gases from air using GCMC simulations. The ability of these MOFs to selectively adsorb noble gases in the presence of air was probed by comparing mixture selectivities at Henry's Law region and 100 kPa pressure. Based on their results, they proposed that MOFs with pore geometries similar in size to the targeting gas molecule show unusually large adsorption capacity toward the targeting gas, as well as unusually high selectivities in the presence of competing gases. Therefore, the authors think optimization of the pore dimensions should lead to MOFs having a Kr/N_2 selectivity superior to zeolites, for which the best reported was around three.[108,122]

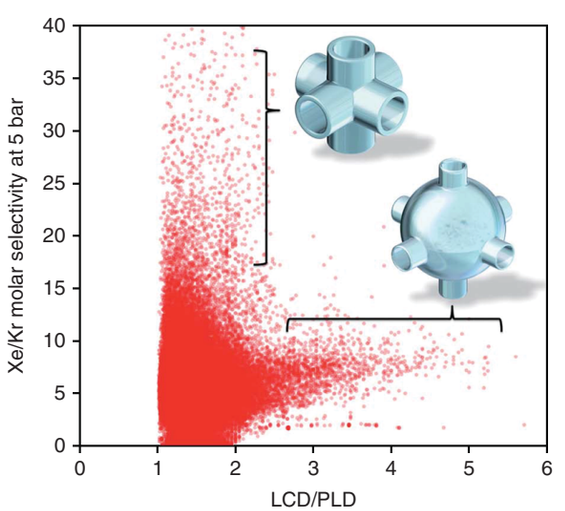


Figure 12 In all of the 137 000 hypothetical MOFs, the least Xe-selective MOFs had large cavities connected by narrow channels (largest cavity diameter, LCD/pore limiting diameter, PLD ratio >2), while the best MOFs had tube-like pore morphologies (LCD/PLD ratio between 1 and 2). The selectivity has been cutoff at 40 for clarity. (Reproduced Ref. 118 with permission of The Royal Society of Chemistry. http://dx.doi.org/10.1039/C2SC01097F.)

6 PERSPECTIVES AND CONCLUSIONS

Metal-organic frameworks have shown great potential for the removal of toxic gases from air and other gas streams. Some MOFs can effectively separate CO_2 from N_2 because of their high CO_2 capacities and CO_2/N_2 selectivities. Some MOFs can even maintain significant amount of CO_2 capacity under moist conditions. Moreover, these properties can be adjusted and controlled by pore structure and chemical composition design. However, the key to capturing CO_2 from flue gas is economic feasibility. Considering the scale of the carbon capture problem, as we described in the main text, an affordable adsorbent must found before optimizing any process to realize the CO_2 capture task with physical adsorption. Therefore, scale up of MOF synthesis and cost of MOF production are the two major challenges for their application in CO_2 capture and other gas separation applications, as well. One possible way to approach these two challenges is to use less expensive raw chemicals to produce the organic ligands and to recycle the solvents during the synthesis of MOFs and solvent exchange process.

The key for the inorganic toxic gas removal with MOFs is to enhance the toxic gas capacities and the strength of interactions between toxic gas molecules and MOF structures. The cost of MOFs can be justified here, because first removing toxic gas can directly reduce the threats to human health. In addition, the concentrations of these toxic gases are on the order

of ppm to parts per billion (ppb), so a relatively small quantity of MOFs can be used to process large volumes of gases containing toxic gases. The concerns now shift to the question of whether MOFs can retain the toxic gas molecules strongly enough that no desorption occurs before an adsorbent regeneration. The toxicity of MOFs should also be further studied before MOFs can be practically used in biological systems to deliver NO.

The research on VOC adsorption in MOFs is still at its early stage. Experimental studies can only be found on alkane and alcohol adsorption in MOFs. The adsorption of some critical VOCs, such as benzene and formaldehyde, has been studied with molecular simulation or theoretical calculation. Therefore, experimental investigation of the removal of VOCs with MOFs as novel adsorbents, especially VOCs with higher threat to environmental and human health, is urgently needed. An experiment and simulation combinatorial screening study will be important to start the exploration of MOFs for the removal of VOCs.

In regard to the radioactive gas adsorption in MOFs, the next focus could be how to enhance the selectivity between radioactive gases, such as Xe and Kr. The higher the selectivity an adsorbent has, the higher purities can be achieved for both components after an appropriate separation process. High purity is obviously desirable if one wants to find an alternative source of these valuable and useful gases. Another reason to have high selectivity is that ^{85}Kr is the noble gas isotope that survives the relatively long fuel storage times prior to reprocessing. The molar concentration of Xe is about 10 times that of Kr. The capacity of a Kr-storage system would be increased if the Xe could be economically separated and released or recovered for beneficial use elsewhere. Normal microporous adsorbents, including many MOFs, preferably adsorb Xe over Kr because of larger molecular size and polarizability of Xe. In addition, it is also necessary to find some other MOFs that have higher iodine capacities than that of ZIF-8. Modification of current MOFs with polar functional groups or substances that can react with iodine will be another way to improve vapor phase iodine removal with MOFs.

Compared to traditional adsorbents, such as zeolites and carbonaceous materials, MOFs have extraordinary surface areas, controllable pore sizes, and topologies. Most importantly, the chemical compositions and the functionalization of the ligands of MOFs can be designed and various properties can be achieved through the design or post-synthesis of MOFs. Other than these advantages, MOFs are crystalline materials that can be well studied with molecular simulations. Thousands of hypothetical MOFs can be investigated for various applications even before they are synthesized. Fundamental theory, such as the reticular chemistry, can be used to predict and design MOFs with properties to suit a wider range of gas adsorption applications. However, MOFs also have disadvantages that need to be addressed before they can be used in practical applications. The first concern is the stability of MOFs, including the thermal stability and water stability. An example of stable MOFs is ZIF-8 in which the Zn–N bond is stronger than the Zn–O bond and leads to higher stability. However, the number of organic ligands with *N*-containing bonding sites is limited. UiO-66, another recently discovered Zirconium-based MOF, has shown extraordinary stability toward both heat and water. However, many MOFs with superior gas adsorption properties, such as Mg-MOF-74, are not stable enough for extended usage, which is critical if MOFs are to be used industrially. A possible reason to explain the huge difference between the stability of UiO-66 and the stability of MOF-5 is the difference in the coordination numbers for the metal atoms, even though the organic ligand is the same in these two MOFs. The coordination number of Zn in the MOF-5 is 4, while the coordination number of Zr in the UiO-66 is 8. All of the eight coordination bonds are between Zr and O, and none of them are between Zr and solvent molecules, like in the MOFs with UMCs. More coordination bonds means that more energy is needed to dissociate the structure and that leads to better overall stability. Actually, this trend has already been indicated in a hydrothermal stability map of MOFs.[123] Therefore, to explore secondary building units with higher coordination numbers may be a straightforward, yet not an easy, way to create MOFs with enhanced stability.

The next challenge in the development of MOFs is the cost of synthesis. Currently, there are five MOFs available from Sigma-Aldrich® and they are manufactured by BASF®. The average price for the commercial MOFs is \$6–\$30 g^{-1}, depending on the type and quantity of MOF. At this moment, these commercial MOFs are only affordable for research purposes, versus large-scale applications. The scale-up of the MOF synthesis is definitely a way to reduce the unit cost, but landing an appropriate application is actually the real driving force for the scale-up MOF synthesis. Almost all MOFs are now synthesized in batch reactors from hydrothermal or solvothermal reactions; it is possible to increase the productivity and reduce the unit cost of MOFs with some well-controlled continuous flow mode reactors.[124] Exploring alternative sources for the organic ligands, such as raw petroleum products, also shows promise for cost reduction of MOF production, because the costs for the organic ligands is at least one-third of the total cost to synthesize MOFs.

In summary, MOFs are promising novel adsorbents for harmful gas separation and removal. Tremendous research work has been done on improving the performance of MOFs, such as adsorption capacity and selectivity. As we mentioned above, with respect to

different harmful gases, different key factors exist. The core value remains to be in exploring beneficial and appropriate applications for MOFs with unique properties. Meanwhile, how to increase the stability of current MOFs or create new MOFs having better stability and similar or better adsorption properties and how to reduce the cost of MOFs to make their costs competitive with those of the benchmark adsorbents, such as synthetic zeolites, are two critical challenges along the pathway to the future discovery and applications of MOFs for the removal of harmful gases.

7 ACKNOWLEDGMENTS

PKT and DMS would like to thank the U.S. Department of Energy (DOE), Office of Nuclear Energy for their support, in particular, Dr. James Bresee who has direct project oversight responsibilities. The authors would also like to thank Dr. Terry Todd (Idaho National Laboratory) and Dr. Robert Jubin (Oak Ridge National Laboratory) for their continued programmatic support and guidance. In addition PKT and JL would like to thank Office of Basic Energy Sciences, Division of Materials Sciences and Engineering (Award KC020105-FWP12152). Pacific Northwest National Laboratory is a multiprogram national laboratory operated for the U.S. Department of Energy by Battelle Memorial Institute under Contract DE-AC05-76RL01830.

8 RELATED ARTICLES

Porous Coordination Polymer Nanoparticles and Macrostructures; Fluorinated Metal-Organic Frameworks (FMOFs): Concept, Construction, and Properties; Photoreactive Metal-Organic Frameworks; Functional Magnetic Materials Based on Metal Formate Frameworks; Interpenetration and Entanglement in Coordination Polymers; Mesoporous Metal-Organic Frameworks; Open Metal Sites in Metal-Organic-Frameworks; Gas Storage in Metal-Organic Frameworks; Adsorption of Hydrocarbons and Alcohols in Metal-Organic Framework Materials; Metal Uptake in Metal-Organic Frameworks.

9 ABBREVIATIONS AND ACRONYMS

BBC = 4,4′,4″-(benzene-1,3,5-triyl-tris (benzene-4,1-diyl)) tribenzoate; BTB = 4,4′,4″-Benzene-1,3,5-triyltribenzoate; CSD = Cambridge Structural Database; DFT = Density functional theory; EB = ethylbenzene; FMOF = fluorinated metal–organic framework; GCMC = Grand Canonical Monte Carlo; GO = Graphite oxide; I_2 = Iodine; IAST = Ideal adsorbed solution theory; LCD = Largest cavity diameter; MOFs = Metal–organic frameworks; PCP = Porous coordination polymers; PLD = Pore limiting diameter; POMs = Polyoxometalates; ppb = Parts per billion; ppm = Parts per million; QENS = Quasielastic neutron scattering; TDS = Thermal desorption spectroscopy; UMCs = Unsaturated metal centers; VOCs = Volatile organic compounds; 3D three-dimensional.

10 REFERENCES

1. J. R. Li, J. Sculley, and H. C. Zhou, *Chem. Rev.*, 2012, **112**, 869.
2. S. Kitagawa, R. Kitaura, and S. Noro, *Angew. Chem. Int. Ed.*, 2004, **43**, 2334.
3. J. L. C. Rowsell and O. M. Yaghi, *Micropor. Mesopor. Mater.*, 2004, **73**, 3.
4. G. Ferey, *Chem. Soc. Rev.*, 2008, **37**, 191.
5. H. Furukawa, N. Ko, Y. B. Go, N. Aratani, S. B. Choi, E. Choi, A. O. Yazaydin, R. Q. Snurr, M. O'Keeffe, J. Kim, and O. M. Yaghi, *Science*, 2010, **329**, 424.
6. O. K. Farha, I. Eryazici, N. C. Jeong, B. G. Hauser, C. E. Wilmer, A. A. Sarjeant, R. Q. Snurr, S. T. Nguyen, A. O. Yazaydin, and J. T. Hupp, *J. Am. Chem. Soc.*, 2012, **134**, 15016.
7. J. R. Li, R. J. Kuppler, and H. C. Zhou, *Chem. Soc. Rev.*, 2009, **38**, 1477.
8. J. Liu, P. K. Thallapally, B. P. McGrail, D. R. Brown, and J. Liu, *Chem. Soc. Rev.*, 2012, **41**, 2308.
9. O. M. Yaghi, J. L. C. Rowsell, E. C. Spencer, J. Eckert, and J. A. K. Howard, *Science*, 2005, **309**, 1350.
10. C. P. Li, Y. L. Tian, and Y. M. Guo, *Inorg. Chem. Commun.*, 2008, **11**, 1405.
11. M. Klimakow, P. Klobes, A. F. Thunemann, K. Rademann, and F. Emmerling, *Chem. Mater.*, 2010, **22**, 5216.
12. A. M. Joaristi, J. Juan-Alcaniz, P. Serra-Crespo, F. Kapteijn, and J. Gascon, *Cryst. Growth Des.*, 2012, **12**, 3489.
13. A. Carne-Sanchez, I. Imaz, M. Cano-Sarabia, and D. Maspoch, *Nat. Chem.*, 2013, **5**, 203.
14. Y. Liu, J. H. Her, A. Dailly, A. J. Ramirez-Cuesta, D. A. Neumann, and C. M. Brown, *J. Am. Chem. Soc.*, 2008, **130**, 11813.
15. U. Mueller, M. Schubert, F. Teich, H. Puetter, K. Schierle-Arndta, and J. Pastréa, *J. Mater. Chem.*, 2006, **16**, 626.
16. S. L. James, *Chem. Soc. Rev.*, 2003, **32**, 276.

17. N. L. Rosi, J. Eckert, M. Eddaoudi, D. T. Vodak, J. Kim, M. O'Keeffe, and O. M. Yaghi, *Science*, 2003, **300**, 1127.
18. J. L. C. Rowsell and O. M. Yaghi, *Angew. Chem. Int. Ed.*, 2005, **44**, 4670.
19. M. Eddaoudi, J. Kim, N. Rosi, D. Vodak, J. Wachter, M. O'Keeffe, and O. M. Yaghi, *Science*, 2002, **295**, 469.
20. S. Q. Ma, D. F. Sun, J. M. Simmons, C. D. Collier, D. Q. Yuan, and H. C. Zhou, *J. Am. Chem. Soc.*, 2008, **130**, 1012.
21. A. P. Nelson, O. K. Farha, K. L. Mulfort, and J. T. Hupp, *J. Am. Chem. Soc.*, 2009, **131**, 458.
22. C. Serre, C. Mellot-Draznieks, S. Surblé, N. Audebrand, Y. Filinchuk, and G. Férey, *Science*, 2007, **315**, 1828.
23. S. Surblé, C. Serre, C. Mellot-Draznieks, F. Millange, and G. Férey, *Chem. Commun.*, 2006, **3**, 284.
24. S. S. Y. Chui, S. M. F. Lo, J. P. H. Charmant, A. G. Orpen, and I. D. Williams, *Science*, 1999, **283**, 1148.
25. P. D. C. Dietzel, B. Panella, M. Hirscher, R. Bloma, and H. Fjellvåg, *Chem. Commun.*, 2006, 959.
26. P. M. Forster, J. Eckert, B. D. Heiken, J. B. Parise, J. W. Yoon, S. H. Jhung, J. S. Chang, and A. K. Cheetham, *J. Am. Chem. Soc.*, 2006, **128**, 16846.
27. D. Britt, D. Tranchemontagne, and O. M. Yaghi, *Proc. Natl. Acad. Sci. U. S. A.*, 2008, **105**, 11623.
28. M. T. Luebbers, T. Wu, L. Shen, and R. I. Masel, *Langmuir*, 2010, **26**, 11319.
29. J. Liu, P. K. Thallapally, and D. M. Strachan, *Langmuir*, 2012, **28**, 11584.
30. H. Q. Yang, Z. H. Xu, M. H. Fan, R. Gupta, R. B. Slimane, A. E. Bland, and I. Wright, *J. Environ. Sci.*, 2008, **20**, 14.
31. http://keelingcurve.ucsd.edu/
32. G. D. Pirngruber and D. Leinekugel-le-Cocq, *Ind. Eng. Chem. Res.*, 2013, **52**, 5985.
33. K. T. Chue, J. N. Kim, Y. J. Yoo, S. H. Cho, and R. T. Yang, *Ind. Eng. Chem. Res.*, 1995, **34**, 591.
34. J. L. Soares, H. J. Jos, and R. F. P. M. Moreira, *Braz. J. Chem. Eng.*, 2003, **20**, 75.
35. E. Diaz, E. Munoz, A. Vega, and S. Ordonez, *Chemosphere*, 2008, **70**, 1375.
36. H. L. Li, M. Eddaoudi, M. O'Keeffe, and O. M. Yaghi, *Nature*, 1999, **402**, 276.
37. Q. Y. Yang, C. Y. Xue, C. L. Zhong, and J. F. Chen, *AIChe J.*, 2007, **53**, 2832.
38. B. Arstad, H. Fjellvag, K. O. Kongshaug, O. Swang, and R. Blom, *Adsorption*, 2008, **14**, 755.
39. R. Vaidhyanathan, S. S. Iremonger, K. W. Dawson, and G. K. U. Shimizu, *Chem. Commun.*, 2009, **35**, 5230.
40. A. R. Millward and O. M. Yaghi, *J. Am. Chem. Soc.*, 2005, **127**, 17998.
41. D. W. Breck, 'Zeolite Molecular Sieves: Structure, Chemistry, and Use', Wiley, New York, 1973.
42. F. Brandani and D. M. Ruthven, *Ind. Eng. Chem. Res.*, 2004, **43**, 8339.
43. A. O. Yazaydin, R. Q. Snurr, T. H. Park, K. Koh, J. Liu, M. D. LeVan, A. I. Benin, P. Jakubczak, M. Lanuza, D. B. Galloway, J. J. Low, and R. R. Willis, *J. Am. Chem. Soc.*, 2009, **131**, 18198.
44. P. D. C. Dietzel, Y. Morita, R. Blom, and H. Fjellvag, *Angew. Chem. Int. Ed.*, 2005, **44**, 6354.
45. D. J. Collins and H. C. Zhou, *J. Mater. Chem.*, 2007, **17**, 3154.
46. S. R. Caskey, A. G. Wong-Foy, and A. J. Matzger, *J. Am. Chem. Soc.*, 2008, **130**, 10870.
47. B. Liu and B. Smit, *Langmuir*, 2009, **25**, 5918.
48. D. Wu, Q. Xu, D. H. Liu, and C. L. Zhong, *J. Phys. Chem. C*, 2010, **114**, 16611.
49. L. Bastin, P. S. Barcia, E. J. Hurtado, J. A. C. Silva, A. E. Rodrigues, and B. Chen, *J. Phys. Chem. C*, 2008, **112**, 1575.
50. S. Basu, A. Cano-Odena, and I. F. Vankelecom, *J. Sep. Purif. Technol.*, 2011, **75**, 15.
51. J. R. Li, Y. Tao, Q. Yu, X. H. Bu, H. Sakamoto, and S. Kitagawa, *Chem. Eur. J.*, 2008, **14**, 2771.
52. Y. S. Bae, O. K. Farha, J. T. Hupp, and R. Q. Snurr, *J. Mater. Chem.*, 2009, **19**, 2131.
53. A. N. Dickey, A. O. Yazaydin, R. R. Willis, and R. Q. Snurr, *Can. J. Chem. Eng.*, 2012, **90**, 825.
54. J. Liu, J. Tian, P. K. Thallapally, and B. P. McGrail, *J. Phys. Chem. C*, 2012, **116**, 9575.
55. A. O. Yazaydin, A. I. Benin, S. A. Faheem, P. Jakubczak, J. J. Low, R. R. Willis, and R. Q. Snurr, *Chem. Mater.*, 2009, **21**, 1425.
56. J. Liu, Y. Wang, A. I. Benin, P. Jakubczak, R. R. Willis, and M. D. LeVan, *Langmuir*, 2010, **26**, 14301.
57. A. C. Kizzie, A. G. Wong-Foy, and A. J. Matzger, *Langmuir*, 2011, **27**, 6368.
58. C. Yang, X. P. Wang, and M. A. Omary, *J. Am. Chem. Soc.*, 2007, **129**, 15454.
59. O. K. Farha, K. L. Mulfort, and J. T. Hupp, *Inorg. Chem.*, 2008, **47**, 10223.
60. T. Li, D. L. Chen, J. E. Sullivan, M. T. Kozlowski, J. K. Johnson, and N. L. Rosi, *Chem. Sci.*, 2013, **4**, 1746.
61. J. H. Cavka, S. Jakobsen, O. Unni, N. Guillou, C. Lamberti, S. Bordiga, and K. P. Lillerud, *J. Am. Chem. Soc.*, 2008, **130**, 13850.
62. Y. T. Huang, W. P. Qin, Z. Li, and Y. W. Li, *Dalton Trans.*, 2012, **41**, 9283.
63. G. E. Cmarik, M. Kim, S. M. Cohen, and K. S. Walton, *Langmuir*, 2012, **28**, 15606.
64. S. H. Yang, J. L. Sun, A. J. Ramirez-Cuesta, S. K. Callear, W. I. F. David, D. P. Anderson, R. Newby, A. J. Blake, J. E. Parker, C. C. Tang, and M. Schröder, *Nat. Chem.*, 2012, **4**, 887.

65. P. K. Thallapally, R. K. Motkuri, C. A. Fernandez, B. P. McGrail, and G. S. Behrooz, *Inorg. Chem.*, 2010, **49**, 4909.
66. J. Liu, A. I. Benin, A. M. B. Furtado, P. Jakubczak, R. R. Willis, and M. D. LeVan, *Langmuir*, 2011, **27**, 11451.
67. S. Han, Y. G. Huang, T. Watanabe, S. Nair, K. S. Walton, D. S. Sholl, and J. C. Meredith, *Microporous Mesoporous Mater.*, 2013, **173**, 86.
68. L. Hamon, C. Serre, T. Devic, T. Loiseau, F. Millange, G. Férey, and G. De Weireld, *J. Am. Chem. Soc.*, 2009, **131**, 8775.
69. A. C. McKinlay, B. Xiao, D. S. Wragg, P. S. Wheatley, I. L. Megson, and R. E. Morris, *J. Am. Chem. Soc.*, 2008, **130**, 10440.
70. F. Bonino, S. Chavan, J. G. Vitillo, E. Groppo, G. Agostini, C. Lamberti, P. D. C. Dietzel, C. Prestipino, and S. Bordiga, *Chem. Mater.*, 2008, **20**, 4957.
71. N. J. Hinks, A. C. McKinlay, B. Xiao, P. S. Wheatley, and R. E. Morris, *Microporous Mesoporous Mater.*, 2010, **129**, 330.
72. B. Levasseur, C. Petit, and T. J. Bandosz, *ACS Appl. Mater. Interfaces*, 2010, **2**, 3606.
73. A. M. Ebrahim, B. Levasseur, and T. J. Bandosz, *Langmuir*, 2013, **29**, 168.
74. T. G. Glover, G. W. Peterson, B. J. Schindler, D. Britt, and O. M. Yaghi, *Chem. Eng. Sci.*, 2011, **66**, 163.
75. G. W. Peterson, G. W. Wagner, A. Balboa, J. Mahle, T. Sewell, and C. J. Karwacki, *J. Phys. Chem. C*, 2009, **113**, 13906.
76. D. Saha and S. G. Deng, *J. Colloid Interface Sci.*, 2010, **348**, 615.
77. K. C. Kim, D. C. Yu, and R. Q. Snurr, *Langmuir*, 2013, **29**, 1446.
78. N. A. Khan, Z. Hasan, and S. H. Jhung, *J. Hazard. Mater.*, 2013, **244–245**, 444.
79. Volatile Organic Compounds: Technical Overview, US Environmental Protection Agency. http://www.epa.gov/iaq/voc2.html
80. R. Atkinson, *Atmos. Environ.*, 2000, **34**, 2063.
81. M. T. Luebbers, T. J. Wu, L. J. Shen, and R. I. Masel, *Langmuir*, 2010, **26**, 15625.
82. S. Amirjalayer and R. Schmid, *J. Phys. Chem. C*, 2012, **116**, 15369.
83. D. I. Kolokolov, H. Jobic, A. G. Stepanov, J. Ollivier, S. Rives, G. Maurin, T. Devic, C. Serre, and G. Férey, *J. Phys. Chem. C*, 2012, **116**, 15093.
84. Y. P. Zeng, X. M. Zhu, Y. Yuan, X. B. Zhang, and S. G. Ju, *Sep. Purif. Technol.*, 2012, **95**, 149.
85. V. Finsy, H. Verelst, L. Alaerts, D. De Vos, P. A. Jacobs, G. V. Baron, and J. F. Denayer, *J. Am. Chem. Soc.*, 2008, **130**, 7110.
86. V. Finsy, C. E. A. Kirschhock, G. Vedts, M. Maes, L. Alaerts, D. E. De Vos, G. V. Baron, and J. F. M. Denayer, *Chem. Eur. J.*, 2009, **15**, 7724.
87. Z. Y. Gu and X. P. Yan, *Angew. Chem. Int. Ed.*, 2010, **49**, 1477.
88. Z. R. Herm, B. M. Wiers, J. A. Mason, J. M. van Baten, M. R. Hudson, P. Zajdel, C. M. Brown, N. Masciocchi, R. Krishna, and J. R. Long, *Science*, 2013, **340**, 960.
89. N. Iswarya, M. G. Kumar, K. S. Rajan, and J. B. B. Rayappan, *J. Appl. Sci.*, 2012, **12**, 1681.
90. T. Maihom, S. Choomwattana, P. Khongpracha, M. Probst, and J. Limtrakul, *ChemPhysChem*, 2012, **13**, 245.
91. F. J. Ma, S. X. Liu, D. D. Liang, G. J. Ren, F. Wei, Y. G. Chen, and Z. M. Su, *J. Solid State Chem.*, 2011, **184**, 3034.
92. R. C. Ewing and F. N. von Hippel, *Science*, 2009, **325**, 151.
93. W. E. Lee, M. I. Ojovan, M. C. Stennett, and N. C. Hyatt, *Adv. Appl. Ceram.*, 2006, **105**, 3.
94. K. W. Chapman, P. J. Chupas, and T. M. Nenoff, *J. Am. Chem. Soc.*, 2010, **132**, 8897.
95. J. P. Lang, Q. T. Xu, R. X. Yuan, and B. F. Abrahams, *Angew. Chem. Int. Ed.*, 2004, **43**, 4741.
96. Z. M. Wang, Y. J. Zhang, T. Liu, M. Kurmoo, and S. Gao, *Adv. Funct. Mater.*, 2007, **17**, 1523.
97. M. H. Zeng, Q. X. Wang, Y. X. Tan, S. Hu, H. X. Zhao, L. S. Long, and M. Kurmoo, *J. Am. Chem. Soc.*, 2010, **132**, 2561.
98. D. F. Sava, M. A. Rodriguez, K. W. Chapman, P. J. Chupas, J. A. Greathouse, P. S. Crozier, and T. M. Nenoff, *J. Am. Chem. Soc.*, 2011, **133**, 12398.
99. R. Vaidhyanathan, S. S. Iremonger, G. K. H. Shimizu, P. G. Boyd, S. Alavi, and T. K. Woo, *Science*, 2010, **330**, 650.
100. D. R. Haefner and T. J. Tranter, 'Methods of Gas Phase Capture of Iodine from Fuel Reprocessing Off-Gas: A Literature Survey; INL/EXT-07-12299', Idaho National Laboratory, Idaho Falls, 2007.
101. D. F. Sava, T. J. Garino, and T. M. Nenoff, *Ind. Eng. Chem. Res.*, 2012, **51**, 614.
102. T. D. Bennett, P. J. Saines, D. A. Keen, J. C. Tan, and A. K. Cheetham, *Chem. Eur. J.*, 2013, **19**, 7049.
103. Q. K. Liu, J. P. Ma, and Y. B. Dong, *Chem. Commun.*, 2011, **47**, 7185.
104. W. W. He, S. L. Li, G. S. Yang, Y. Q. Lan, Z. M. Su, and Q. Fu, *Chem. Commun.*, 2012, **48**, 10001.
105. F. G. Kerry, 'Industrial Gas Handbook: Gas Separation and Purification', CRC Press, Boca Raton, 2007.
106. K. Munakata, T. Fukumatsu, S. Yamatsuki, K. Tanaka, and M. Nishikawa, *J. Nucl. Sci. Technol.*, 1999, **36**, 818.
107. J. Izumi, 'Handbook of Zeolite Science and Technology', Marcel Dekker, New York, 2003.

108. R. E. Bazan, M. Bastos-Neto, A. Moeller, F. Dreisbach, and R. Staudt, *Adsorption*, 2011, **17**, 371.

109. K. Munakata, S. Kanjo, S. Yamatsuki, A. Koga, and D. Ianovski, *J. Nucl. Sci. Technol.*, 2003, **40**, 695.

110. P. K. Thallapally, J. W. Grate, and R. K. Motkuri, *Chem. Commun.*, 2012, **48**, 347.

111. C. A. Fernandez, J. Liu, P. K. Thallapally, and D. M. Strachan, *J. Am. Chem. Soc.*, 2012, **134**, 9046.

112. S. Q. Ma, D. F. Sun, X. S. Wang, and H. C. Zhou, *Angew. Chem. Int. Ed.*, 2007, **46**, 2458.

113. A. Soleimani Dorcheh, D. Denysenko, D. Volkmer, W. Donner, and M. Hirscher, *Microporous Mesoporous Mater.*, 2012, **162**, 64.

114. S. T. Meek, S. L. Teich-McGoldrick, J. J. Perry IV, J. A. Greathouse, and M. D. Allendorf, *J. Phys. Chem. C*, 2012, **116**, 19765.

115. J. A. Greathouse, T. L. Kinnibrugh, and M. D. Allendorf, *Ind. Eng. Chem. Res.*, 2009, **48**, 3425.

116. P. Ryan, O. M. Farha, L. J. Broadbelt, and R. Q. Snurr, *AIChe J.*, 2011, **57**, 1759.

117. Y. S. Bae, B. G. Hauserb, Y. J. Colónc, J. T. Huppb, O. K. Farhab, and R. Q. Snurr, *Micropor. Mesopor. Mater.*, 2013, **169**, 176.

118. B. J. Sikora, C. E. Wilmer, M. L. Greenfield, and R. Q. Snurr, *Chem. Sci.*, 2012, **3**, 2217.

119. Y. Gurdal and S. Keskin, *Ind. Eng. Chem. Res.*, 2012, **51**, 7373.

120. Y. Gurdal and S. Keskin, *J. Phys. Chem. C*, 2013, **117**, 5229.

121. M. V. Parkes, J. J. Perry, C. L. Staiger, M. D. Allendorf, and J. A. Greathouse, *Phys. Chem. Chem. Phys.*, 2013, **15**, 9093.

122. F. H. Tezel, H. O. Tezel, and D. M. Ruthven, *J. Colloid Interface Sci.*, 1992, **149**, 197.

123. J. J. Low, A. I. Benin, P. Jakubczak, J. F. Abrahamian, S. A. Faheem, and R. R. Willis, *J. Am. Chem. Soc.*, 2009, **131**, 15834.

124. P. M. Schoenecker, G. A. Belancik, B. E. Grabicka, and K. S. Walton, *AIChE J.*, 2013, **59**, 1255.

Adsorption of Hydrocarbons and Alcohols in Metal-Organic Framework Materials

Debasis Banerjee, Benjamin J. Deibert, Hao Wang and Jing Li

Rutgers University, Piscataway, NJ, USA

1	Introduction	321
2	Physisorption, Mechanisms, and Methods	321
3	Adsorption in MMOFs	323
4	Hydrocarbon Adsorption and Separation	326
5	Alcohol Adsorption and Separation	333
6	Conclusion and Outlook	337
7	Acknowledgments	337
8	Related Articles	337
9	Abbreviations and Acronyms	337
10	References	338

1 INTRODUCTION

Metal-organic frameworks (MOFs) or coordination polymers are crystalline materials composed of infinite arrays of single metal cations (primary building unit or PBU) or metal clusters (secondary building unit or SBU) connected by functionalized organic linkers forming chains, layers, or three-dimensional (3-D) frameworks.[1–3] A large variety of metal centers and functionalized organic linkers are used to construct MOFs under a variety of synthetic conditions giving rise to unprecedented structural diversity.[2–6] A subclass of MOFs known as microporous metal-organic frameworks (MMOFs), is characterized by having an ordered and well-defined pore structure with micrometer pore dimensions (<2 nm); typically these materials exhibit extended 3-D frameworks (Figure 1).[3,7] MMOFs offer many appealing features, including but not limited to high internal surface area and pore volume, structural flexibility, and functionalized pore surfaces.[3,7–9] Moreover, these physical features can be systematically and deliberately modified to enhance targeted properties and achieve improved performances in various applications such as gas adsorption and separation, catalysis, and chemical sensing.[1,2,7,10–17]

Using MMOFs as a medium for gas storage and separation has received considerable attention in the past few years, particularly as an adsorbent for H_2 and CO_2, and in hydrocarbon adsorption and separation.[7,9,11] Adsorption-based separation is an important process for hydrocarbon mixtures in the petrochemical industry. While zeolite-based molecular sieves have been successfully applied for such commercial applications since the middle of the past century,[7,18–20] MMOFs offer distinct advantages, thanks to their adjustable pore dimensions, unique pore geometries, and functionalized pore surfaces.[7,18] In this chapter, we give a concise summary of the various aspects of hydrocarbon and alcohol adsorption and separation using MMOFs as the adsorbent.

2 PHYSISORPTION, MECHANISMS, AND METHODS

The adsorption of gases or liquids can be divided into two broad categories, chemisorption and physisorption. Chemisorption, as the name suggests, occurs when an adsorbent material forms a chemical bond with a corresponding adsorbate. Metal hydrides and complex hydrides, in which hydrogen is chemically bonded to the metal atoms in bulk, is a representative example of the chemisorption process.[21] In contrast, the physisorption process can be described by the adsorbate forming

Metal-Organic Framework Materials. Edited by Leonard R. MacGillivray and Charles M. Lukehart.
© 2014 John Wiley & Sons, Ltd. ISBN 978-1-119-95289-3

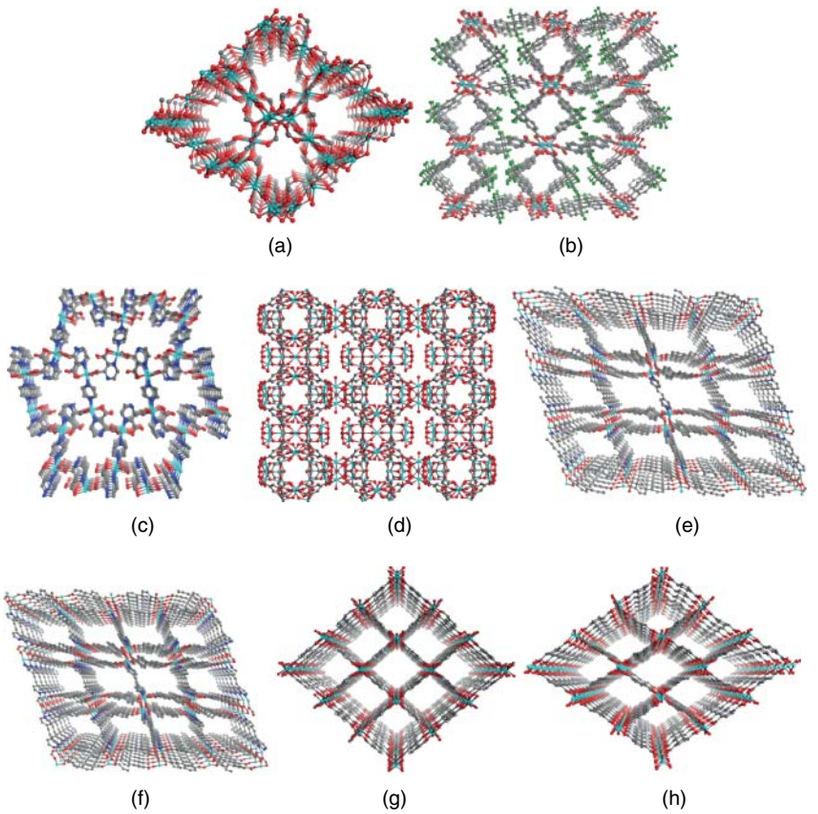


Figure 1 Selected crystal structures of guest-free MMOFs that exhibit commensurate adsorption behavior: (a) $[Co_3(fa)_6]$, (b) $[Cu(hfipbb)(H_2hfipbb)_{0.5}]$, (c) $[Cu_2(pzdc)_2(pyz)]$, (d) $[Al_{12}O(OH)_{18}(H_2O)_3(Al_2(OH)_4)(btc)_6]$ (MIL-96), (e) $[Zn_2(bpdc)_2(bpee)]$ (RPM3-Zn), (f) $[Zn_2(bpdc)_2(bpe)]$ (RPM4-Zn), (g) $[V^{IV}O(bdc)]$ (MIL-47), and (h) $[Al^{III}(OH)(bdc)]$ (MIL-53ht). All structures are projected along the channel's direction except (e), which has two types of accessible cages. Color scheme: metal center (cyan), O (red), C (gray), N (blue), and hydrogen is omitted for clarity. The names for the abbreviated linkers can be found in the abbreviation section of the book chapter. (Reprinted with permission from Ref. 7. Copyright (2012) American Chemical Society.)

weak van der Waals interactions with the pore surface of the adsorbent material. Physisorption is the prevailing mechanism by which adsorbates interact with the pore surfaces of adsorbents such as MMOFs.[7,9,11] This process is often beneficial for practical applications as it is associated with complete reversibility owing to fast adsorption/desorption kinetics.[7,9]

Physisorption-based adsorption and separation processes are of primary interest for various applications, including H_2 storage,[11] carbon capture and sequestration,[9] and hydrocarbon separations.[7,18] Physisorption based separation of adsorbate mixtures can occur through a variety of mechanisms, including equilibrium, steric, kinetic, or some combination of these in more complex systems.[22,23] In equilibrium processes, separation is based on differences in the relative amounts of the adsorbates within the adsorbent once equilibrium has been established. The process is dictated by the differences in the isotectic heats of adsorption (Q_{st}) between the different adsorbate molecules and the adsorbent.[7,24] In the case of steric mechanisms, the separation happens as a consequence of morphological exclusion or molecular sieving effects, that is, when larger or branched adsorbates cannot fit through the pore openings, whereas smaller or linear species can.[25] Lastly, separations can be achieved based on the kinetic mechanism: adsorbates with much faster adsorption and transport rates will be effectively separated out from adsorbates with lower rates during an adsorption process.[26]

For a typical physisorption process, the interaction energy between the adsorbate and the adsorbant's pore surface is low owing to weak van der Waals interactions. These interactions can be enhanced by modifying the pore surface via introduction of coordinatively unsaturated metal centers, also known as open metal sites, or functional groups, such as amines.[9,27,28] These special sites interact with the adsorbed molecules via electronic interactions, increasing the total uptake and interaction energy. For example, CO_2 can be selectively adsorbed with respect to N_2 using the above-mentioned "pore surface engineering" techniques as a result of carbon dioxide's

large quadrupole moment.[9] Recent findings suggest a new approach for the selective adsorption of CO_2 over N_2 where the geometry of the organic linker is responsible for the selectivity. In this particular case, the adsorbed CO_2 sits in a pocket between two phenyl rings and undergoes favorable quadrupole–aromatic π interactions leading to selective CO_2 uptake.[29]

Adsorption processes are generally characterized by taking gravimetric or volumetric gas adsorption isotherm measurements.[30,31] The gravimetric method, which requires the use of a sensitive microbalance and pressure gauge, allows the adsorbed amount to be measured directly from the difference in weight after pressure-dependent buoyancy corrections. This method is more accurate at or near room temperature as the adsorbate is not in direct contact with the thermostat, making it difficult to control and measure the exact temperature of the adsorbing species. The volumetric method relies on the ideal gas equation and is the preferable method when performing cryogenic and high temperature adsorption isotherms.[31] The adsorbed amount is calculated from the difference of the total amount of gas admitted to the sample holder with the adsorbent, and the amount of gas in the free space. The free space measurement is generally taken by introducing a nonadsorbing gas, such as helium, before or after each measurement at room temperature and also at the experimental temperature. The use of helium gas can be avoided by introducing alternative techniques such as NOVA (NO void analysis), or using differential measurements that rely on the introduction of a reference cell during the measurement.[32]

Many industrially important hydrocarbons are liquids at room temperature and ambient pressure, thus the procedure for liquid adsorption generally involves gas chromatography (GC) techniques.[33,34] An inert solvent, which is not adsorbed and does not have any effect on the adsorbate, is used a carrier solvent. The adsorbate flow is measured by monitoring the mixing of adsorbent with the solvent. Alternatively, a vapor bubbler can be used to generate vapors of a given hydrocarbon from its liquid phase using nitrogen as the carrier gas.[7,25,26,35,36] Comparable levels of adsorption can be achieved for both liquid- and vapor-phase adsorbates for a range of adsorbate concentrations, temperatures, and pressures.[37,38]

The adsorption and separation properties of a particular adsorbent largely depend on the adsorbate, including its morphology, composition, polarity, polarizability, diffusivity, and other properties. In the following sections we will describe adsorption and separation in MMOFs, focusing mainly on industrially important hydrocarbons and alcohols. We also discuss the concepts of commensurate and incommensurate adsorption in MMOFs and their implications toward adsorption-related properties.

3 ADSORPTION IN MMOFs

Ever since the inception of MMOFs, research has been primarily directed toward using these materials for the adsorption and separation of different adsorbates under various conditions. Early work concentrated on synthesizing MMOFs for applications related to the storage of different gases, including H_2, CH_4, and CO_2.[9,11,39] One such example is cubic $[Zn_4O(bdc)_3]$ (bdc = terephthalate), or MOF-5, which was found to have a gravimetric H_2 uptake capacity of 7.1 wt% at 77 K and 40 bar.[40,41] The MMOFs that are promising for H_2 storage generally possess at least one of the following characteristics: high surface area, catenated frameworks, open metal sites, or metal ion doping in porous anionic frameworks.[11] The presence of open metal sites in the adsorbent leads to higher uptakes and heat of adsorption values owing to the stronger interactions between adsorbed H_2 and the open metal sites.[42] Another strategy for increasing interaction and uptake is doping alkali metal ions into anionic or redox active frameworks.[43] Similar strategies are also applied for CO_2 adsorption in MMOFs; the high polarizability and quadrupole moment of CO_2 leads to stronger interactions with the pore surface when containing unsaturated metal ions or amine functional groups.[8,9] Zeolitic imidazolate frameworks (ZIFs) are a subclass of MMOFs, built on divalent metal ions, such as Co(II) and Zn(II), and N-based imidazolate linkers, that show promising CO_2 storage properties.[44] The imidazolate linker contains two nitrogen atoms and is present in high density throughout the structure as a result of being the only linker ligand. The nitrogen atoms of imidazolate interact strongly with CO_2, leading to a framework that is intrinsically efficient at binding CO_2 molecules.

Preferential adsorption of CO_2 over other gas components is essential for CO_2 capture in a number of industrial separation processes. Apart from modulating pore size, strategies to increase the absorption selectivity of CO_2 in MMOFs often include functionalizing the pore surface with strongly polarizing groups, such as amines or open metal sites, and ligand geometry modifications.[9] A large number of MMOFs have been tested for CO_2 selectivity at 0.15 bar of CO_2 and 0.85 bar of N_2, a typical post-combustion flue gas composition in industry. Among the various MMOFs tested so far, $[M_2(dobdc)]$ (M = Mg, Mn, Fe, Co, Ni, Zn, dobdc = 2,5-dioxido-1,4-benzenedicarboxylate) has been of particular interest. This material has a relatively large surface area and a high density of unsaturated M^{2+} cation sites that can selectively interact with CO_2 as shown by a number of spectroscopic studies, including powder neutron diffraction and in situ infrared spectroscopy.[9,28] However, MMOFs with open metal sites, such as $M_2(dobdc)$, perform poorly as a CO_2-selective material in presence of water vapor, a component of post-combustion flue gases, as a result of competition from water molecules for the open metal sites.[45]

In addition to adsorption and separation of H_2 and CO_2, MMOFs are promising for many other types of gas or liquid adsorption and separation applications, including Kr, Xe, O_2, NO_x, NH_3, SO_2, alcohols, and various hydrocarbons.[7,18,46,47] The separation of hydrocarbons is a commercially important process and largely determines the price of petroleum-based products in the global market. Porous materials, mainly zeolite molecular sieves, are employed as an energy-saving alternative to cryogenic distillation processes for separating hydrocarbons. As previously mentioned, MMOFs offer numerous advantages over traditional zeolite molecular sieves for industrially relevant separation applications. Indeed, many recent reports have emerged demonstrating that MMOFs have great promise for separations involving small hydrocarbons, hexane isomers, and C_8 xylene isomers.[48–50] The progress of hydrocarbon separations using various types of MMOFs is described in a concise manner in Section 4.

3.1 Commensurate Adsorption

Commensurate adsorption is a phenomenon that occurs when the molecular size and shape of the adsorbate coincide with that of the adsorption sites, and the amount adsorbed at equilibrium is compatible with the crystal symmetry and pore structure of the adsorbent.[7] The phenomenon was first observed during diffraction studies of adsorbed noble gas and small molecules, such as CH_4, Kr, Xe, H_2, and D_2, on 2-D graphite surfaces.[51–53] It was characterized by neutron diffraction, high resolution X-ray scattering, density functional theory (DFT), and molecular simulations.[53] In the later part of the past century, the concept of commensurate adsorption was extended to crystalline porous materials such as aluminosilicates, zeolites, and silicates.[54,55] Understanding the phenomenon in porous materials is much more complex in nature than in the case of surface adsorption. In porous materials, the interaction between the adsorbate and the host framework takes place entirely inside the pores, and as a result, obtaining direct evidence of commensurate adsorption is difficult.[55] While examples of locating the adsorbates inside the pores of a host framework using direct methods, such as single crystal or powder X-ray diffraction (PXRD) studies, do exist,[56,57] indirect methods, such as molecular simulation and gas adsorption studies, are more commonly employed to identify and describe commensurate adsorption.[58–60] An early example of commensurate adsorption was found in case of *p*-xylene (*p*X) adsorption in ZSM-5 (orthorhombic Pnma, $a = 20.07(2)$, $b = 19.92(2)$, $c = 13.42(2)$ Å, and Si/Al = 0.86). The framework has a 2-D pore structure with two intersecting straight and sinusoidal channels along crystallographic [010] and [100], respectively, as defined by 10-membered ring topology.[54] A careful analysis of the crystal structure reveals that there are distinct adsorption sites: the straight channel, the sinusoidal channel, and their intersection. As a direct consequence of intrinsic symmetry, there are a total of four straight channels, sinusoidal channels, and intersecting sites per unit cell of ZSM-5. The gas-adsorption data show two independent adsorption sites per unit cell of the adsorbent. Single crystal X-ray diffraction data and molecular simulation studies show that four molecules were adsorbed in the channel intersection area with their methyl groups oriented toward the straight channel, whereas four more molecules were adsorbed in the sinusoidal channel for a total of eight molecules adsorbed per unit cell.

With the advent of MMOFs, the concept of commensurate adsorption was extended to the adsorption studies related to these porous frameworks.[7,58–61] Commensurate adsorption is more commonplace in MMOFs than traditional aluminosilicates and zeolites in the room temperature region, especially for the ultramicroporous (pore diameter <7 Å) and supermicroporous (7 Å <pore diameter <20 Å) frameworks with small pores or zigzag-shaped channels.[7] Apart from that aspect, MMOFs distinguish themselves from zeolites by their extraordinary structural diversity owing to the availability of a large number of metal centers, functionalized organic linkers, and chemical tunability leading to pore surface modifications. A number of MMOF examples have demonstrated adsorbate molecules being commensurately adsorbed in the pores (also conventionally known as freezing/locking), with a good majority of them featuring 1-D channels with cavities, or cages with distinct shapes (see Figure 1).[7,62]

Kitagawa and coworkers[61,63] reported an early example of commensurate adsorption of acetylene in a microporous framework, $[Cu_2(pzdc)(pyz)]$ (pzdc = pyrazine-2,3-dicarboxylate, pyz = pyrazine), consisting of 1-D cylindrical channels with a cross section of $\sim 4 \times 6$ Å (Figure 2). The adsorption isotherm collected at variable temperature shows that the uptake reaches saturation loading of 42 $cm^3\ g^{-1}$ between 5 and 60 kPa of pressure. The maximum uptake corresponds to one molecule per pore segment or two molecules of adsorbate per unit cell. Interestingly, CO_2, which has a similar kinetic diameter of 3.3 Å, shows significantly less uptake at similar temperature and pressure regions. The position of the C_2H_2 molecules adsorbed in the host framework was confirmed by the maximum entropy method (MEM) and Rietveld analysis using the synchrotron PXRD method. Each acetylene molecule is involved in strong hydrogen bonding between the uncoordinated oxygen atoms of the linker in the pore surface, and the hydrogen atoms of the acetylene molecule, resulting in a significantly higher enthalpy of adsorption than that of CO_2. In this case, the channel shape and the nature of the pore surface, along with the orientation and size of the adsorbate, allows a perfect fit within each segment.[7,61]

The microporous $[M_3(fa)_6]$ (M = Mg, Mn, Co, Ni, fa = HCOO or formate) family perhaps represents the best-studied case of commensurate adsorption (Figure 3).[7,59,62]

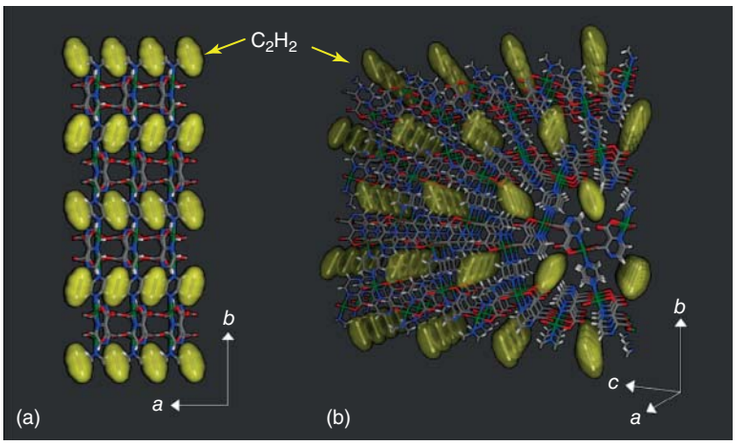


Figure 2 The C_2H_2-loaded $[Cu_2(pzdc)_2(pyz)]$ structure (170 K) from MEM/Rietveld analysis. (a) View along the *c*-axis. (b) Perspective view along the *a*-axis. Color scheme: Cu (green), O (red), C (gray), N (blue), and H (white). (Reproduced from Ref. 61. © Nature Publishing Group.)

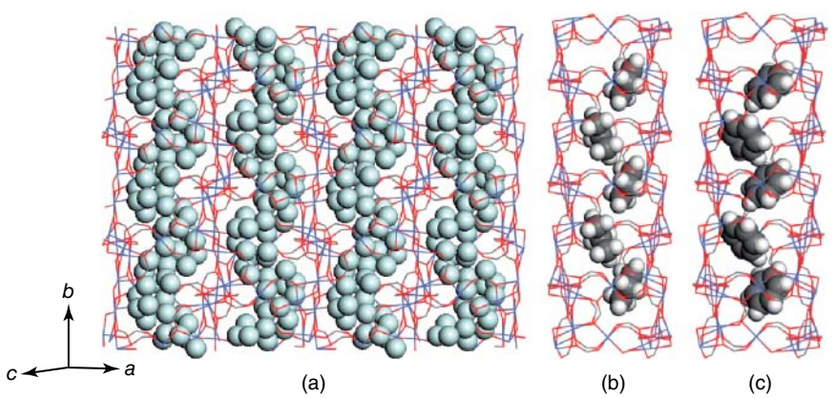


Figure 3 The simulated gas adsorption in the $[Co_3(fa)_6]$ structure. The 1-D channels run along the crystallographic *b*-axis. (a) He at 1 K and 760 torr; (b) propane at 303 K and 684 torr; and (c) benzene at 303 K and 61.4 torr. Color scheme: Co (blue), O (red), C (gray), He (powder blue), and H (white). (Reprinted with permission from Ref. 7. Copyright (2012) American Chemical Society.)

The isostructural 3-D $[M_3(fa)_6]$ series consists of a diamondoid (octahedral) framework connectivity, with 1-D sinusoidal channels along the crystallographic *b*-axis. Simulated He filling models revealed the sinusoidal, or as popularly termed, "zigzag" nature of the channel with the length of each "zig" (or "zag") sections estimated to be around 7.1 Å. Each unit cell contains a total of four distinct segments, or a pair of "zigzag" units, with each segment having a diameter of approximately 5.5 Å and a window opening of 4.5 Å. Experimental studies show that light alcohols, such as ethanol, propanol, and butanol, and alkanes, such as ethane, propane, and *n*-butane, show adsorption of approximately four molecules per unit cell. The associated simulation data shows that the packing position of these molecules is commensurate with the zigzag-shaped segments, also confirming the results obtained from the helium adsorption simulation. The commensurate adsorption is believed to be a direct consequence of the correlation between the segment length and the length of the adsorbate molecules.[7,59]

Similar adsorption behavior is also reported in the case of $[Cu(hfipbb)(H_2hfipbb)_{0.5}]$($H_2hfipbb$ = 4,4′-(hexafluoroisopropylidene)bis(benzoic acid), a guest free, rigid, 3-D framework with a paddle wheel SBU.[25,64] The 1-D channel of the framework is composed of oval-shaped cages of diameter ~5.1 Å, connected by small necks with a diameter of ~3.2 Å; each of the cages is ~7.3 Å in length along the channel. Such pore characteristics offer unique adsorption behavior for the framework, with exclusion of all branched hydrocarbons and any paraffin or olefins longer than C_4. The "cage" effect leads to commensurate adsorption for smaller molecules such as propane and

n-butane, where one adsorbate molecule fits in the cage of the channel.[7,25] Other MMOFs that exhibit commensurate adsorption of hydrocarbons and alcohols include $[Zn_2(bpdc)_2(bpee)]$ (RPM3-Zn) and $[Zn_2(bpdc)_2(bpe)]$ (RPM4-Zn) (RPM = Rutgers Recyclable Porous Materials, bpdc = biphenyl-4,4′-dicarboxylate, bpee = 1,2-bis(2-pyridyl)ethylene)).[62–69]

3.2 Incommensurate Adsorption

Incommensurate adsorption, or as the name suggests, "non-commensurate" adsorption, happens when there are size or symmetry mismatches between the adsorbate and the pores of the adsorbent. The phenomenon was first observed and quantified for the surface adsorption of organic molecules on layered substrates, with an incommensurate–commensurate transition occurring as a function of physical parameters such as temperature and pressure.[53]

Traditional zeolite-based molecular sieves most commonly exhibit incommensurate adsorption. This can be attributed to two main criteria: (1) the dimensions of their channels or cages are, on average, much larger than that of the adsorbate molecules and (2) symmetry mismatches are often present.[7] For example, zeolite-Y exhibits incommensurate adsorption for benzene and toluene molecules adsorbed within its super cage (Figure 4).[70] The incommensurate adsorption type depends also on external parameters such as temperature. Single crystal and PXRD studies on the *n*-hexane-loaded silicate-I MFI-type zeolite shows that at room temperature the adsorbed molecules are dynamically disordered and distributed over the entire channel, whereas at sufficiently low temperature, the adsorbate becomes well ordered within the channel, which is commensurate with the framework type.[71]

A transition to incommensurate adsorption is often observed in MMOFs that exhibit commensurate adsorption. A classic example is the aforementioned $[M_3(fa)_6]$ series.[7,26,58,59] This framework does in fact exhibit commensurate adsorption for short linear alkanes C_1–C_3, but the adsorption becomes incommensurate from *n*-C_4 onwards, as suggested by gas-adsorption and simulation experiments.[7,59] The incommensurate adsorption happens as the chain length of the adsorbate exceeds the segment length of the channel. The $[Cu_2(pzdc)(pyz)]$-type frameworks demonstrate another example of the commensurate–incommensurate transition as a result of structural modifications.[72] Based on the gas-adsorption data, replacement of the small pyz linker by bpy (bpy = 4,4′-bipyridine), a longer linker, leads to incommensurate adsorption of adsorbates such as N_2 and CO_2. Interestingly, in situ synchrotron-based PXRD studies show that the framework undergoes a structural transformation with the accommodation of different guest molecules.[72]

4 HYDROCARBON ADSORPTION AND SEPARATION

The separation of hydrocarbons is one of the most important chemical processes routinely carried out in the petrochemical industry.[7,18] Hydrocarbons, as the name suggests, are exclusively made up of carbon and hydrogen atoms that can be broadly classified based on their chemical nature: alkanes or paraffins (general formula – C_nH_{2n+2}, example: ethane, C_2H_6), alkenes or olefins (general formula – C_nH_{2n}, example: ethene, C_2H_4), alkynes (general formula – C_nH_{2n-2}, example: acetylene, C_2H_2) and aromatic hydrocarbons, such as toluene and xylenes. Among the many types of hydrocarbon adsorption and separations, separations involving small hydrocarbons (C_1–C_4), isomers of hexane, and C_8-aromatics (*ortho*-xylene or *o*X, *meta*-xylene or *m*X, *para*-xylene or *p*X, and ethyl benzene or EB) have received considerable attention because of their role in various

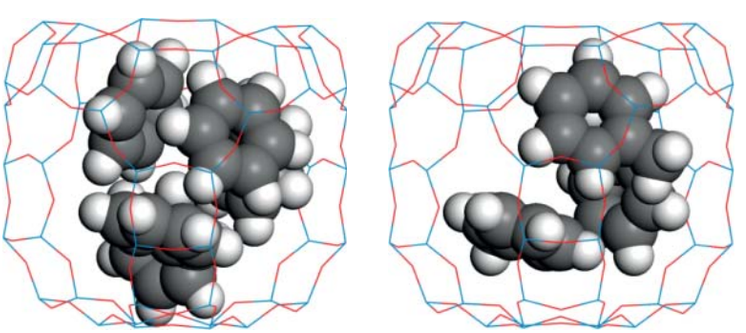


Figure 4 Random packing of (a) benzene and (b) toluene in a single super cage of zeolite-Y. Color scheme: Si (blue), O (red), C (gray sphere), and H (white sphere). (Reprinted with permission from Ref. 7. Copyright (2012) American Chemical Society.)

aspects of the petrochemical and chemical industries, such as being primary building blocks for polymers, and in natural gas and petroleum purification and production processes. Cryogenic distillation and molecular sieves such as zeolites have been employed for their separation thus far; however, both methods are inefficient with respect to cost and energy usage owing to the difficulties in separating molecules with such similar physical properties, including size and boiling point.[73,74] Recently, a number of publications regarding the adsorption and separation of hydrocarbons by different types of MMOFs have emerged (see Table 2 for examples); the unique and tunable pore geometries of MMOFs make them rational and promising candidates for further advancing the state-of-the-art separation technologies. We will focus further discussion on representative examples of various types of hydrocarbon adsorption and separations using MMOFs.[7–9,18]

4.1 Separation of C_1 Hydrocarbons

Small hydrocarbons are essential for the petrochemical and chemical industries because of their pivotal role as fuel and chemical building blocks. Methane, the simplest of all hydrocarbons, is the principal component of natural gas and is a cleaner alternative to gasoline. A plethora of examples are reported on methane storage in MMOFs and can be found in various literature reviews.[10,18,75] In 1997, Kitagawa and coworkers[76] reported the very first methane adsorption in an MMOF, $[Co_2(bpy)_3(NO_3)_4]$, with a moderate uptake of 52 $cm^3\ g^{-1}$ at 298 K and 3 MPa. In 2001, the first systematic study was carried out on a porous, pillared MMOF series with the general formula $[Cu_2(L)_2(dabco)]$ (L = fma, bdc, sdc, bpdc, fma = fumarate, sdc = styrenedicarboxylate, dabco = 1,4-diazabicyclo[2.2.2]-octane), which features a copper paddle wheel SBU.[77–81] Among these frameworks, $[Cu_2(sdc)_2(ted)]$ shows the highest uptake capacity of 213 $cm^3\ g^{-1}$ at 298 K and 3.5 MPa, which is consistent with its higher surface area and pore size with respect to other members of the family. Several other MMOFs have been investigated for methane uptake since then, including members of the IRMOF, PCN, USTA, and M-MOF-74 series (IRMOF = isoreticular metal-organic framework, PCN = porous coordination networks, USTA = University of Texas San Antonio, M = Mg, Mn, Co, Ni, Zn).[48,82–87] Of these, the M-MOF-74 series represents the most widely studied system and is comprised of isostructural 3-D frameworks formed by 2,5-dihydroxyterephthalate (dobdc), with 1-D hexagonal channels and a high concentration of open metal sites on the pore surfaces after activation.[28] This MMOF series shows methane storage capacities ranging between 149 and 190 $cm^3\ g^{-1}$, with the Ni analog exhibiting the highest uptake. Neutron powder diffraction studies on the methane-adsorbed Ni-MOF-74 reveal the open metal sites as the primary adsorption sites.[48]

4.2 Separation of C_2–C_3 Hydrocarbons

As mentioned earlier, the adsorption and separation of various C_2 and C_3 hydrocarbons using MMOFs have been investigated.[7,18,49,50,85–87] The size and shape of different hydrocarbon molecules that are only one carbon difference in length are very similar, and as such it is intrinsically difficult to separate them by molecular sieving. The M-MOF-74 series (M = Fe, Mg, Co, Ni, Mn, Zn), in addition to being thoroughly evaluated for methane storage, has been extensively studied for these separations.[50,88,89] It was found that the open metal sites on the pore surfaces of this material lead to preferential binding of adsorbate molecules.[50,89] The adsorption isotherms collected on C_2 and C_3 paraffins and olefins show similar trends for M = Fe, Co, Ni, Mn, Zn, with the uptake reaching one molecule per metal center at saturation loading. The saturation loading for the Mg analogue is less than one as a result of incomplete activation or the presence of an amorphous phase.[89] The trend for uptake and heat of adsorption is propene > propane > ethylene > ethane, matching with the order of polarizability of the molecules. Neutron diffraction studies on the guest-adsorbed M-MOF-74 (M = Mn, Fe, Co) show different types of interactions based on the electronic nature of the adsorbates. For example, ethane interacts with the open metal center in an "end on" manner, with the deuterium atoms interacting with the open metal sites forming a metal–alkane complex. For unsaturated hydrocarbons, the interaction happens in a "side-on" manner between the π bond of the molecule and the open metal sites. The bond distances between the π bond of the adsorbate and the MOF's metal centers vary based on the differences in the absorbates' heat of adsorption (Figure 5).[50,89] Breakthrough experiments conducted on Fe-MOF-74 confirmed the separation of C_2 and C_3 olefins from C_2 and C_3 paraffins under industrially relevant conditions (Figure 6).[50] A breakthrough experiment is typically conducted by passing a mixture of gas or liquid adsorbate through a solid adsorbent, to effect separation of one or more components of the mixture as it travels though the solid.

Chen and coworkers[85–88] reported a series of flexible heterometallic MMOFs (USTA series) based on a zinc paddle wheel SBU and copper metalloligands for the separation of small hydrocarbons by systematically tuning the pore sizes of the MMOFs. The tuning of pore size and shape, which is typically achieved by changing or modifying the linker ligands, is important for size selective separations involving small hydrocarbons. They found that replacement of the rigid bdc linker by its flexible saturated analog, CDC (1,4-cyclohexanedicarboxylate), leads to enhanced selectivity in the separation of acetylene over ethylene.[87] Another flexible MMOF recently reported by Li and coworkers,[90] $[Zn_2(bpdc)_2(bpee)]$, shows enhanced separation of C_1–C_4 paraffins and both C_2 isomer pairs (C_2H_2–C_2H_4 and C_2H_4–C_2H_6) at room temperature. Raman spectroscopy and ab initio DFT calculations show

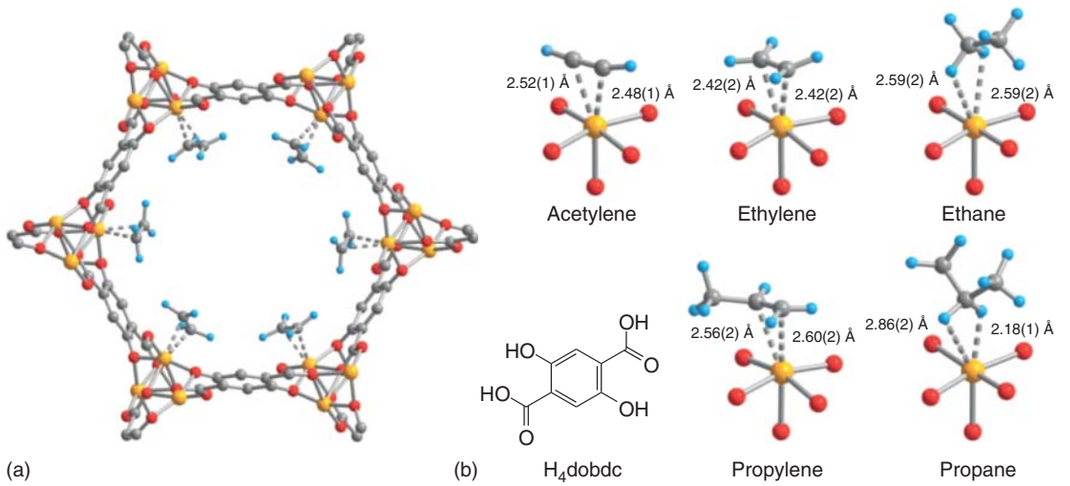


Figure 5 (a) The view of $Fe_2(dobdc)\cdot 2C_2D_4$ along [001] direction, showing an ethylene molecule bound to the open coordination site at each iron(II) center as determined by analysis of neutron powder diffraction data; orange, red, gray, and blue spheres represent Fe, O, C, and D atoms, respectively. (b) The interaction of the open metal site with C_2–C_3 hydrocarbons. (Reproduced with permission from Ref. 50. Copyright 2012 American Association of Advancement of Science.)

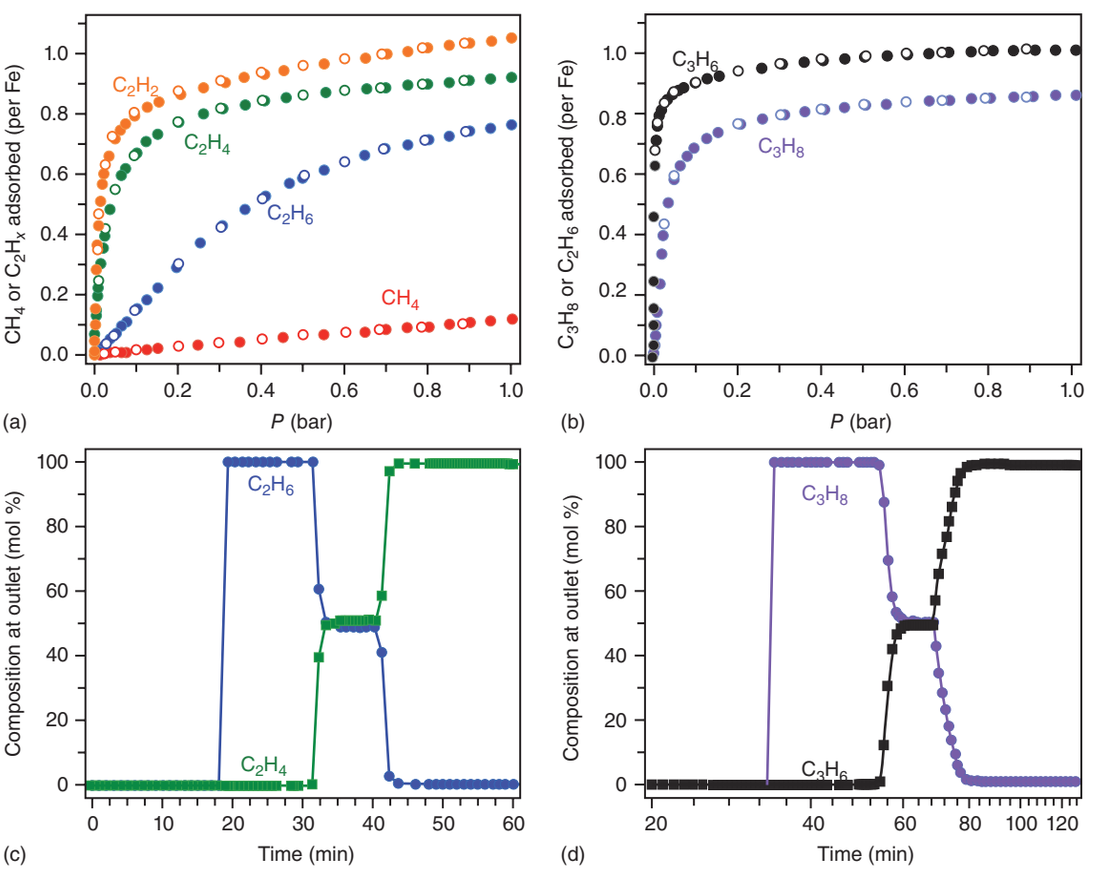


Figure 6 Single component gas adsorption isotherms for (a) methane, ethane, ethylene, and acetylene and (b) propane and propene at 318 K in $Fe_2(dobdc)$. The filled and open circles represent adsorption and desorption data, respectively. (c) and (d) represent experimental breakthrough curves for the adsorption of equimolar ethane/ethylene and propane/propylene mixtures. (Reproduced with permission from Ref. 50. Copyright 2012 American Association of Advancement of Science.)

that the separation behavior of this compound originates as a result of hydrogen bonding between the adsorbate and the free C=O group of the bpdc linker in the framework, which leads to gas-induced structural changes (flexibility) and its associated gate-opening pressure. Gate-opening pressure is a unique phenomenon for flexible frameworks, where the pore dimension changes as a function of variation of external stimuli, such as external pressure of the adsorbate. Such change depends on the chemical and electronic nature of the adsorbate for a particular system and can be applied for selective separation of adsorbates as a function of different pressure ranges.[91]

Li and coworkers[26] also recently reported the separation of propene and propane using zinc-based ZIFs, utilizing the different rates of adsorption of the two molecules (Figure 7). The ZIF series, as previously mentioned in Section 2.2, is comprised of 3-D frameworks formed upon divalent metals with tetrahedral coordination geometry and imidazole ligands.[44] Apart from their chemical and thermal stability, ZIFs also lack Lewis and Bronsted acid sites that can result in the unwanted catalytic polymerization of olefins inside the pores and thus represent an interesting class of materials for olefin/paraffin separation. ZIF-8, $[Zn(2\text{-mim})_2]$ (2-mim = 2-methylimidazole), adsorbs almost same amount of propane and propene (155 and 160 mg g^{-1} at 30 °C and 600 torr, respectively) with similar Q_{st} at low loadings (34 and 30 kJ mol^{-1}), indicating similar types of adsorbate–adsorbent interactions in both systems. Their almost identical interaction energies make thermodynamic separation improbable; however, as their individual rates of adsorption are quite different, kinetic separation becomes a feasible process. The diffusion rate coefficient (D), which is defined as the ratio of diffusion rates between propane and propene, is 125 at 30 °C, indicating a large activation barrier for the diffusion of propene. Two isostructural ZIFs, namely $[Zn(2\text{-cim})_2]$ and $[Zn(2\text{-bim})_2]$ (2-cim = 2-chloroimidazole, 2-bim = 2-bromoimidazole), also demonstrate similar kinetic separations, but to a lesser extent. The activation energies needed for propene and propane to pass through the pore openings of $[Zn(2\text{-cim})_2]$ were calculated to be 9.7 and 74.1 kJ mol^{-1} respectively,

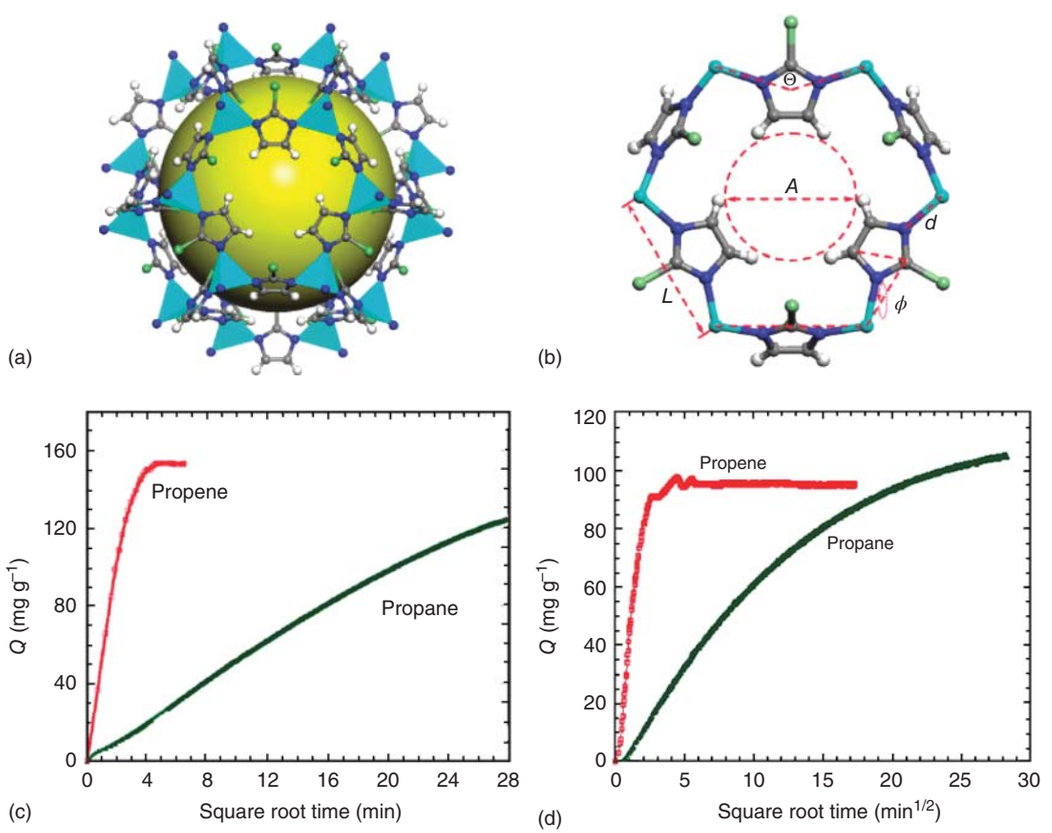


Figure 7 (a) View of the pore opening along one threefold axis in $[Zn(2\text{-cim})_2]$ and $[Zn(2\text{-bim})_2]$. (b) Size. C: gray; H: white; N: blue; Zn: light blue; and Cl or Br (or methyl in ZIF-8 or $[Zn(2\text{-mim})_2]$): light green. All disordered solvent molecules were removed for clarity. Yellow sphere indicate the cavity inside the cages (~12.5 Å in diameter). (c) Propene and propane uptake by ZIF-8 (left) and $[Zn(2\text{-cim})_2]$ (right) as a function of square root of time. (Reprinted with permission from Ref. 26. Copyright (2009) American Chemical Society.)

which results in lower rates of adsorption for propane compared to propene.[26] The large difference in activation energies likely arise from the effective size of the pore openings, a phenomenon that was previously witnessed in several eight-membered ring (8MR) zeolites where separation capabilities depend largely on the window size of the cages.[35,92,93] Other representative MMOFs, such as HKUST-1 and MIL-100, also show separation characteristics for propane and propene via preferential adsorption of unsaturated propene at the open metal sites.[94,95]

4.3 Separation of C_4 Hydrocarbons

A unique case of adsorptive separation occurs in the case of [Cu(hfipbb)(H_2hfipbb)$_{0.5}$] (previously described in Section 3.1) (Figure 8).[7,25,64] This MMOF's segmented channels and small pore diameters lead to the separation of normal short chain hydrocarbons (C_4 or less) from all branched and long chain hydrocarbons (>C_4) by a size exclusion effect. The straight 1-D channel is composed of a periodic array of cages with small necks at intervals of 7.3 Å, a length that is greater than that of the *n*-C_4 hydrocarbons (~6.5 Å), but less than the *n*-C_5 (7.7 Å) and longer hydrocarbons. As a result, normal C_1–C_4 paraffins and olefins can fit within the cage, but C_5 and larger cannot. Although the neck is large enough to allow the passage of normal alkanes longer than C_4, there is not enough space for the larger adsorbate to reach equilibrium, whereas the branched paraffins and olefins are excluded from entering the channels altogether. Zeolite molecular sieves that adsorb *n*-C_4 hydrocarbons also adsorb normal longer chain hydrocarbons; it is only due to the unique pore architecture of this MMOF that results in this desirable adsorption selectivity with a cutoff in carbon chain length.

4.4 Separation of C_6 Hydrocarbons

Paraffins with six carbon atoms (C_6 series) have a total of five structural isomers based on the degree of branching: normal hexane (nHEX), 2-methylpentane (2-MP), 3-methylpentane (3-MP), 2,3-dimethylbutane (23-DMB), and 2,2-dimethylbutane (22-DMB).[7,49] Recent changes related to gasoline production regulation requires that the benzene content be no greater than 1%; this results in a necessary increase in the amount of branched hydrocarbons present in gasoline in order to maintain or increase the quality of the gas. Branched hydrocarbons are preferable to straight-chain hydrocarbons in gasoline because they burn more efficiently and have a higher octane number (RON – Research Octane Number).[19,96] Effective separation of branched hexane isomers from the linear species is thus of significant importance. Current processes involve increasing the amount of branched isomers by molecular sieving followed by catalytic isomerization of the left over nHEX. An ideal molecular sieve should selectively separate the dibranched isomers, 23-DMB and 22-DMB, which have the highest octane ratings, from their monobranched and normal isomers. The adsorptive separation of these three different hexane isomers, nHEX, 3-MP, and 22-DMB, in [Zn(bdc)(ted)$_{0.5}$] has been investigated using both experimental and molecular simulation methods.[59,97,98] [Zn(bdc)(ted)$_{0.5}$] is a 3-D MMOF with two types of intersecting channels. The large channel, with a cross section of ~7.5 × 7.5 Å, is present along the crystallographic [100] direction, whereas the two smaller

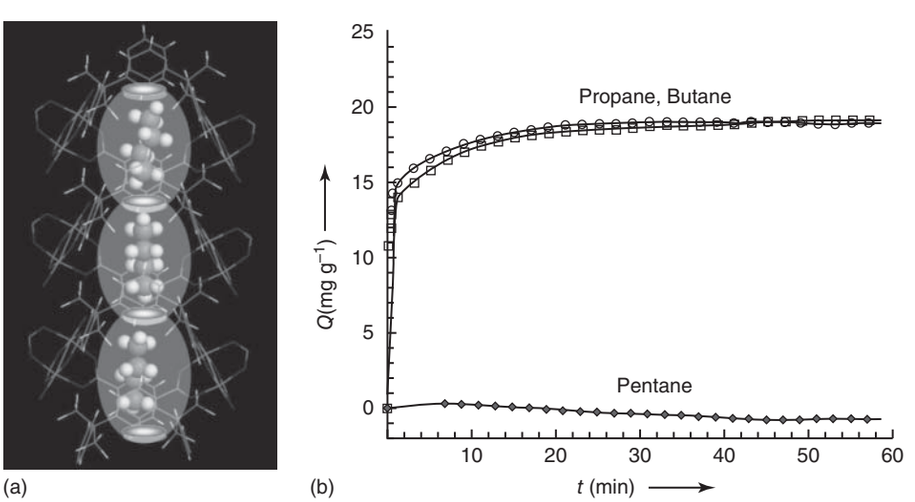


Figure 8 (a) Arrangement of butane molecules in the microchannel of [Cu(hfipbb)(H_2hfipbb)$_{0.5}$]. (b) Adsorption of propane, butane, and pentane at 90 °C and 650 torr as a function of time. *Q* is the weight of hydrocarbon molecules adsorbed in the adsorbent. (Reproduced from Ref. 25. © Wiley-VCH Verlag GmbH & Co. KGaA, 2006.)

channels of dimension ~3.8 × 3.8 Å are present along the other two crystallographic directions.[99,100] The larger channel is able to accommodate each of the three specified types of hexane isomers, whereas the smaller channels can only adsorb the linear nHEX molecules, leading to a hold-up of the nHEX. The nHEX molecules also strongly interact with the pore surfaces of the framework owing to equilibrium effects. The net result is that $[Zn(bdc)(ted)_{0.5}]$ adsorbs significantly higher amounts of nHEX than it does 3-MP or 22-DMB and serves as a potential candidate for separation via breakthrough experiments.[97]

Recently, Long and coworkers[49] reported an iron-based MMOF, $[Fe_2(bdp)_3]$ (bdp^{2-} = 1,4-benzenedipyrazolate), that has triangular shaped channels formed by the rigid, nearly planar bdp^{2-} linker (Figure 9a). The vertices of the channels are formed by octahedral Fe(III) chains, with the shape and size of the linker defining the channel's topography. The metal … metal triangle edge length is 13.25(2) Å and forms sharply angled openings running along the corners of the channel. Such openings along the channel could provide strong van der Waals contacts for normal alkanes, whereas the branched alkanes will occupy the pore space. This material also exhibits high thermal and chemical stabilities; the PXRD patterns show no loss of crystallinity after being submerged in boiling acidic and basic aqueous solutions (pH 2–10) for extended periods of time. The activated material shows a typical microporous structure and has a BET (Brunauer–Emmett–Teller) surface area of 1230 $m^2 g^{-1}$. The hexane adsorption isotherms were collected at the

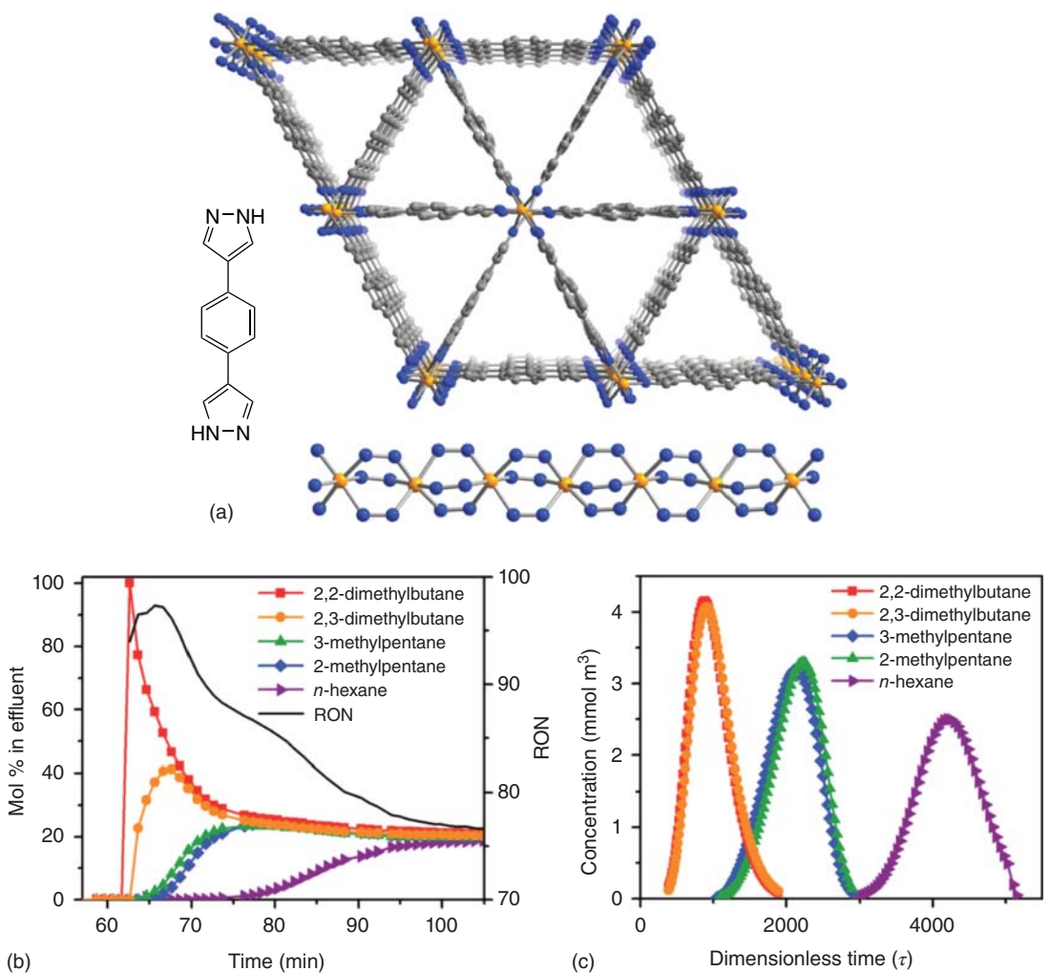


Figure 9 (a) The structure of $Fe_2(bdp)_3$ along [001] direction. The 1-D chains of pyrazolate-bridged Fe(III) octahedra, excluding C and H atoms, are shown in the bottom. (b) Separation of an equimolar mixture of hexane isomers running through a packed bed of $Fe_2(bdp)_3$ at 160 °C. Experimental breakthrough data, together with the RON calculated for the eluted mixture at 1 bar. (c) Pulsed chromatogram data calculated based on the single component isotherms of the hexane isomers at different temperature (130 °C, 160 °C, and 200 °C). (Reproduced with permission from Ref. 49. Copyright 2013 American Association of Advancement of Science.)

temperature that ranges between 100 and 200 °C, which is the condition typical for industrial separations. The single component adsorption isotherms and calculated heats of adsorption reveal an adsorption selectivity order based on the degree of branching: nHEX > 2-MP > 3-MP > 23-DMB ≈ 22-DMB. Breakthrough experiments, conducted at 160 °C with an equimolar mixture of all five isomers, reveal that dibranched isomers emerge first from a packed bed of the activated material, followed by the monobranched analogs, and finally the nHEX (Figure 9b and c). Molecular simulations employing configurational-bias Monte Carlo (CBMC) method were employed to estimate the origin of the separation and showed that the van der Waals overlap decreases with the degree of branching. This means that the number of carbon atoms that can effectively interact with the pore surface decreases with degree of branching, resulting in weak interactions and less time in the sample bed.[49]

4.5 Separation of C_8 Hydrocarbons

The C_8-based xylene isomers, *o*X, *m*X, *p*X, and EB, are important raw materials for the chemical industry. The most noteworthy, *p*X, is the basic building block for polyethylene terephthalate, which is used for materials such as resins and polyester fibers.[101] The general source for all of the xylene isomers is crude oil, which requires separation to isolate the compounds. Cryogenic distillation-based separation is difficult to perform because of their closely related boiling points (137–149 °C, Table 1) and as such, molecular sieving-based separation is the preferred choice.[102] One of the best materials for this separation is Faujasite-based zeolite, which allows the selectivity toward each isomer to be modified by changing the metal ion present in the zeolite.[103]

In the search for more efficient separation materials, MMOFs belonging to the MIL series (Materials of "Institut Lavoisier") have recently been investigated and showed promising results.[37,101,104–106] MIL-47(V), having the activated framework formula [VO(bdc)], is composed of 1-D chains of corner-sharing VO_6 octahedra interconnected by the bdc linker (Figure 10).[68] The activated framework, where the vanadium metal center undergoes oxidation from V^{3+} to V^{4+}, has straight 1-D channels with a diamondoid cross section parallel to the crystallographic [100] axis, with repetitive segments of cages of dimension 9.7 × 8.2 Å. As a result of change in metal valance, the corner-sharing μ_2-OH groups are replaced by corner-sharing μ_2-oxo groups. Both liquid and vapor phase adsorption studies of C_8 xylene isomers on activated MIL-47(V) were carried out by De Vos and coworkers.[37,104] In the case of liquid adsorption at room temperature, *p*X and *o*X show higher uptakes with respect to *m*X and EB.[37] Variable-temperature (333, 383, and 423 K) vapor phase adsorption produced results that are consistent with the liquid adsorption observations.[104] All four isomers have similar adsorption enthalpies; the higher adsorption loading of *p*X and *o*X is attributed to them having more effective $\pi-\pi$ interactions with the framework's aromatic linkers, as confirmed by Rietveld analysis of synchrotron PXRD patterns of MIL-47(V) samples that were saturated with the individual C_8 aromatic isomers at room temperature, and

Table 1 The physical properties of different industrially important hydrocarbon molecules

Adsorbates		Melting point (K)	Boiling point (K)	Dipole moment $\times 10^{18}$/esu cm	Polarizability $\times 10^{25}$ cm^{-3}	Kinetic diameter (Å)	Density[(a)]	
Formula	Name						g L^{-1}	g cm^{-3}
CH_4	Methane	90.7	111.6	0	25.93	3.8	0.66	—
C_2H_2	Acetylene	192.4[(b)]	188.4	0	33.3–39.3	3.3	1.10	—
C_2H_4	Ethylene	104.0	169.5	0	42.52	4.163	1.18	—
C_2H_6	Ethane	90.4	184.5	0	44.3–44.7	4.443	1.26	—
C_3H_6	Propylene	88	225.5	0.366	62.6	4.7	1.75	—
C_3H_8	Propane	85.5	231	0.084	62.9–63.7	4.3–5.1	1.88	—
C_4H_{10}	*n*-Butane	133–139	272.6	0.05	82.0	4.7	2.49	—
C_5H_{12}	*n*-Pentane	143	309.0	0	99.0	4.5	—	0.63
C_6H_{14}	*n*-Hexane	178	341.8	0	119	4.3	—	0.65
	3-Methylpentane	155.15	336.3	N/A	N/A	5.5	—	0.66
	2-Methylpentane	113–127	333.4	0.1	N/A	N/A	—	0.65
	2,2′-Dimethylbutane	171–175	322.8	N/A	N/A	6.2	—	0.65
	2,3-Dimethylbutane	137–149	331.1	N/A	N/A	N/A	—	0.66
C_8H_{10}	*p*-Xylene	286	411.4	0.1	137–149	5.8	—	0.86
	o-Xylene	249	417.6	0.640	141–149	6.8	—	0.88
	m-Xylene	225	412.2	0.37	142	6.8	—	0.86
	Ethyl benzene	178	409.2	0.59	142	5.8	—	0.87

[(a)]298 K, 1 atm
[(b)]sublimating point
N/A, not available.

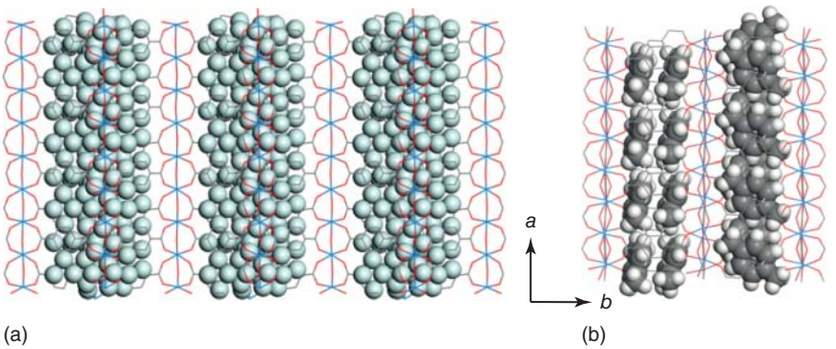


Figure 10 The simulated gas adsorption in the MIL-47 structure shown in two directions. (a) He at 1 K and 760 torr; (b) *p*-Xylene at 303 K and 11.7 torr. Color scheme: V (light blue), O (red), C (gray), He (powder blue), and H (white). (Reprinted with permission from Ref. 7. Copyright (2012) American Chemical Society.)

high temperature grand canonical Monte Carlo molecular simulations.[37,104] The adsorption of EB is markedly different than all three xylene isomers as the framework experiences significant lattice distortions. The bulky ethyl group of the adsorbate molecules align themselves in a diagonal direction of the channel segment so that each ethyl group is situated as far away as possible from each other. Such an arrangement greatly abates the $\pi-\pi$ interactions between the pore[37,104] surface and the adsorbate.

Another member of MIL series, MIL-53, having the formula $[M^{III}(OH)(bdc)]$ (M = Al, Cr, Fe, Ga), adopts the same structural topology as MIL-47*as* (*as* = as synthesized), with corner-sharing $MO_4(OH)_2$ (M = Al, Cr, Fe, Ga) octahedra connected by bdc linkers to form a 3-D framework with straight 1-D channels and a diamondoid-shaped cross section.[69,107–110] The pore size and volume vary, based on the metal center and the structural form of the framework. The frameworks belonging to the MIL-53 series show significant "breathing behavior" upon hydration–dehydration cycle owing to the presence of the corner-sharing hydroxyl group in the SBU and its interaction with the adsorbed water molecules. The single component liquid adsorption characteristics of MIL-53 are similar to that of MIL-47, showing preferential adsorption of *o*X and *p*X over *m*X and EB.[38] The uptake reaches a plateau at ~45–46 wt% at a bulk concentration of ~0.2 M and ~0.5 M for *o*X and *p*X, respectively. Rietveld analysis of activated MIL-53 samples with the different C_8 isomers adsorbed shows drastic changes to the lattice parameters. The arrangement of *o*X within the pore allows both of its methyl groups to interact closely with the framework's carboxylate groups, leading to the strongest interaction among the different isomers. On the other hand, *m*X and *p*X have only one methyl group in close proximity to the carboxylate groups resulting in weaker interactions. The presence of the bulky ethyl group in EB leads to the weakest adsorbate–adsorbent binding among them all. Vapor phase adsorption of the xylene isomers at 110 °C shows a two-step adsorption profile with significant hysteresis, indicating changes in the crystal structure during adsorption, which is different from what was observed in case of liquid adsorption experiments.[106] Indeed, Rietveld analysis of the PXRD patterns of *o*X adsorbed MIL-53(Al) at different loadings shows structural transformations between several phases, including MIL-53*as* (Al) (dominating at very low loadings), MIL-53iX (Al) (dominating at intermediate loadings), and MIL-53ht (Al) (dominating at high loadings). Similar studies conducted on MIL-53ht (Fe) show that the material can separate *o*X, *m*X, and *p*X under chromatographic conditions. Using heptane as the eluent at 293 K, elution of *p*X occurred before either of the other two isomers. Crystallographic studies on the individual isomer-loaded framework revealed similar host–guest and guest–guest-type interactions of the *o*X and *m*X isomers, with a distinctly different set of interactions for their *p*X counterpart, indicating the major role of the pore surface–adsorbate interactions in separation process.[101] Apart from the MIL series, other unrelated MMOFs have also demonstrated adsorption-based separation of the xylene isomers, some of which can be referenced in Table 2.

5 ALCOHOL ADSORPTION AND SEPARATION

The adsorption and separation of various types of alcohol molecules has recently received wide-spread attention, especially with the advent of biofuels where the separation of alcohol and water is essential for production. Representative examples of alcohol adsorption in MMOFs are compiled in Table 3.

One of the earliest examples of selective adsorption of alcohols was reported by Yaghi and coworkers[127] on $[Zn_2(btc)(NO_3)]$ (btc = 1,3,5-benzenetricarboxylate), which possesses a 3-D framework topology. The removal of coordinated guest molecules leads to the formation of

Table 2 The adsorption of industrially important hydrocarbon molecules in various MMOFs

Adsorbate		MOF	T (K)	P or relative concentration%	Uptake	References
Ethane		$[V^{IV}O(bdc)]$ (MIL-47)	303	25 bar	6.0 molec/UC	111
		$[Fe^{III}(OH)(bdc)]$ (MIL-53-Fe)	303	30 bar	6.6 mmol g^{-1}	112
		$Ag_2[Cr_3O(OOCC_2H_5)_6(H_2O)_3]_2[\alpha\text{-}SiW_{12}O_{40}]$	298	0.7 P/P_0	~0.2 mol mol^{-1}	113
		$[Cu(hfipbb)(H_2hfipbb)_{0.5}]$	298	760 torr	1.2wt%	25
		$Fe_2(dobdc)$	318	1 bar	0.7/Fe	50
		$[Co_3(fa)_6]$	303	684 torr	64 mg g	62
Ethylene		$Ag_2[Cr_3O(OOCC_2H_5)_6(H_2O)_3]_2[\alpha\text{-}SiW_{12}O_{40}]$	298	0.3 P/P_0	~2.0 mol mol^{-1}	113
		$[Zn(bim)_2]$ (ZIF-7)	298	1 bar	4 molec/cage	114
		$Fe_2(dobdc)$	318	1 bar	0.9/Fe	50
Acetylene		$Ag_2[Cr_3O(OOCC_2H_5)_6(H_2O)_3]_2[\alpha\text{-}SiW_{12}O_{40}]$	298	~0.03P/P_0	~1.2 mol mol^{-1}	113
		$[Mn_3(fa)_6]$	298	1 bar	51.2 cc(STP) g^{-1}	115
		$[Mg_3(fa)_6]$	298	1 bar	65.7 cc(STP) g^{-1}	115
		$[Cu_2(pzdc)_2\ (pyz)]\cdot 2H_2O$	300	1 bar	42 cc(STP) g^{-1}	61
		$Fe_2(dobdc)$	318	1 bar	~1/Fe	50
Propane		$[V^{IV}O(bdc)]$ (MIL-47)	303	10 bar	4.5 molec/UC	111
		$Ag_2[Cr_3O(OOCC_2H_5)_6(H_2O)_3]_2[\alpha\text{-}SiW_{12}O_{40}]$	298	0.7 P/P_{00}	~0.2 mol mol^{-1}	113
		$[Zn(bim)_2]$ (ZIF-7)	298	1 bar	4 molec/cage	114
		$[Co_3(fa)_6]$	303	684 torr	91 mg g^{-1}	62
		$Fe_2(dobdc)$	318	1 bar	1/Fe	50
		$[Cu(hfipbb)(H_2hfipbb)_{0.5}]$	298	0.063 P/P_0	2.6 wt%	25
Propylene		$Ag_2[Cr_3O(OOCC_2H_5)_6(H_2O)_3]_2[\alpha\text{-}SiW_{12}O_{40}]$	298	0.4 P/P_0	~2.0 mol mol^{-1}	113
		$[Zn(bim)_2]$ (ZIF-7)	298	1 bar	4 mo/cage	114
		$[Cu(hfipbb)(H_2hfipbb)_{0.5}]$	298	0.019 P/P_0	2.0 wt%	25
		$[Co_3(fa)_6]$	303	684 torr	87 mg g^{-1}	62
		$Fe_2(dobdc)$	318	1 bar	0.8/Fe	50
Hexane isomers	*n*-Hexane	$[Al^{III}(OH)(bdc)]$ (MIL-53-Al)	313	0.95 P/P_0	2.4 molec/UC	116
		$[Cr^{III}(OH)(bdc)]$ (MIL-53-Cr)	313	0.95 P/P_0	3.0 molec/UC	111
		$Ag_2[Cr_3O(OOCC_2H_5)_6(H_2O)_3]_2[\alpha\text{-}SiW_{12}O_{40}]$	303	100 torr	54 mg g^{-1}	113
		$[Mg_3(fa)_6]$	298	1 P/Po	8.5 wt%	115
		$Fe_2(bdp)_3$	403	100 mbar	1.4 mmol g^{-1}	49
		$[Co_3(fa)_6]$	303	100 torr	102 mg g^{-1}	62
	2-Methyl-pentane	$Fe_2(bdp)_3$	403	100 mbar	1.3 mmol g^{-1}	49
	3-Methyl-pentane	$Fe_2(bdp)_3$	403	100 mbar	1.3 mmol g^{-1}	49
	2,3-Dimethyl-butane	$Fe_2(bdp)_3$	403	100 mbar	1.3 mmol g^{-1}	49
	2,2-Dimethyl-butane	$Fe_2(bdp)_3$	403	100 mbar	1.3 mmol g^{-1}	49
Xylene isomers	*p*-Xylene	$[V^{IV}O(bdc)]$ (MIL-47)	298	0.8 M	37 wt%	104
		$[Al^{III}(OH)(bdc)]$ (MIL-53-Al)	298	0.55 M	43 wt%	106
		$Ag_2[Cr_3O(OOCC_2H_5)_6(H_2O)_3]_2[\alpha\text{-}SiW_{12}O_{40}]$	303	6.0 torr	124 mg g^{-1}	113
		$[Co_3(fa)_6]$	303	6.0 torr	48 mg g^{-1}	62
	o-Xylene	$[V^{IV}O(bdc)]$ (MIL-47)	298	0.8 M	35 wt%	104
		$[Al^{III}(OH)(bdc)]$ (MIL-53-Al)	298	0.55 M	46 wt%	106
		$Ag_2[Cr_3O(OOCC_2H_5)_6(H_2O)_3]_2[\alpha\text{-}SiW_{12}O_{40}]$	303	3.9 torr	130 mg g^{-1}	113
	m-Xylene	$[V^{IV}O(bdc)]$ (MIL-47)	298	0.8 M	30 wt%	104
		$[Al^{III}(OH)(bdc)]$ (MIL-53-Al)	298	0.55M	25 wt%	106
Ethylbenzene		$[V^{IV}O(bdc)]$ (MIL-47)	298	0.8 M	17 wt%	34
		$[Al^{III}(OH)(bdc)]$ (MIL-53-Al)	298	0.55 M	16 wt%	106
		$[Co_3(fa)_6]$	303	5.8 torr	130 mg g^{-1}	62

Table 3 The adsorption of industrially important alcohols in various MMOFs

Adsorbate	MOF	T (K)	P or R.C.%	Uptake	References
Methanol	$[Cu_2(pzdc)_2(dpyg)]$	298	1.0 P/P_0	6.2 mmol g^{-1}	117
	$[Cu_2(pzdc)(bpee)]$	298	1.0 P/P_0	35 cc g^{-1}	118
	$[Cd(4\text{-btapa})_2(NO_3)_2]$	298	0.9 P/P_0	130 cc(STP) g^{-1}	119
	$[Ni(bpe)_2(N(CN)_2)](N(CN)_2)$	298	0.9 P/P_0	85 cc(STP) g^{-1}	120
	[Cu(etz)]	298	1.0 P/P_0	175 mg g^{-1}	121
	$[Ce(tci)(H_2O)]$	298	0.9 P/P_0	2 molec/UC	122
	$[Zn_2(bpdc)_2(bpee)]\cdot 2DMF$	303	85 torr	126 mg g^{-1}	7
	$Cu_4O(OH)_2(Me_2trzpba)_4$	298	0.9 P/P_0	14 mmol g^{-1}	123
	$[Zn_2(bptc)]$	298	1.0 P/P_0	10 wt%	124
	$[Cu(gla)(4,4'\text{-bipy})_{0.5}]$	298	0.96 P/P_0	2.1 mmol g^{-1}	125
	$[Zn_2(bdc)_2(dabco)]\cdot 4DMF\cdot 0.5H_2O$	298	0.42 P/P_0	5.02 mg g^{-1}	126
	[Zn(tbip)]	298	90 torr	110 mg g^{-1}	36
Ethanol	[Cu(etz)]	298	1.0 P/P_0	245 mg g^{-1}	121
	$[Ni(bpe)_2(N(CN)_2)](N(CN)_2)$	298	0.9 P/P_0	32 ccg^{-1}	120
	$[Zn_2(bpdc)_2(bpee)]$ 2DMF	303	41 torr	115 mg g^{-1}	7
	$[Zn_2(bpdc)_2(bpe)]$ 2DMF	303	41 torr	82 mg g^{-1}	7
	$[Zn_2(bdc)_2(dabco)]\cdot 4DMF\cdot 0.5H_2O$	298	0.42 P/P_0	418 mg g^{-1}	126
	[Zn(tbip)]	303	41 torr	106 mg g^{-1}	36
n-Propanol	$[Zn_2(bpdc)_2(bpee)]$ 2DMF	303	12 torr	143 mg g^{-1}	7
	$[Zn_2(bpdc)_2(bpe)]$ 2DMF	303	12 torr	126 mg g^{-1}	7
	[Zn(tbip)]	303	12 torr	143 mg g^{-1}	36
isopropanol	$[Zn_2(bdc)_2(dabco)]\cdot 4DMF\cdot 0.5H_2O$	308	0.9 P/P_0	160 cc(STP) g^{-1}	126
n-Butanol	$[Zn_2(bpdc)_2(bpee)]$ 2DMF	303	3.5 torr	152 mg g^{-1}	7
	$[Zn_2(bpdc)_2(bpe)]$ 2DMF	303	3.5 torr	128 mg g^{-1}	7
	[Zn(tbip)]	303	3.5 torr	168 mg g^{-1}	7
n-Pentanol	$[Zn_2(bpdc)_2(bpee)]$ 2DMF	303	1.2 torr	155 mg g^{-1}	7
	$[Zn_2(bpdc)_2(bpe)]$ 2DMF	303	1.2 torr	106 mg g^{-1}	7
	[Zn(tbip)]	303	1.2 torr	108 mg g^{-1}	36

DMF = dimethylformamide.

open metal sites that were shown to selectively bind small alcohol molecules, such as methanol, ethanol, 1-propanol, and 1-butanol, while excluding non-alcohols such as chloroform and acetonitrile. Breakthrough experiments were performed with a packed column gas chromatograph using the activated MOF as the column's packing material. The results showed preferential adsorption of methanol over larger alcohols as a result of morphologic selectivity. Another early example of selective alcohol adsorption was observed with the cobalt-based porous zeotype metalloporphyrin framework, PIZA-1, which has the formula $[CoT(p\text{-}CO_2)PPCo_{1.5}]$ (PIZA = porphyrinic Illinois zeolite analog; $H_4T(p\text{-}CO_2)PP$ = meso-tetrakis(4-carboxyphenyl)porphine or H_2tcpp).[128] The framework consists of two types of oval-shaped channels having dimensions of $\sim 9 \times 7$ Å and 14×7 Å, with an open metal site functionalized hydrophilic pore surface. These hydrophilic pore surfaces are responsible for PIZA-1's high adsorption selectivity toward water (162 ml 100 g^{-1} after a 3-week exposure) and alcohols. Interestingly, PIZA-1 can selectivity adsorb alcohols as a function of their hydrophobicity and steric mass with a general uptake trend of: methanol > ethanol > propanol ≫ butanol > hexanol. The adsorption selectivity also extends to linear and branched alcohols as a function of steric hindrance, with the linear alcohols being preferentially adsorbed.

In addition to the presence of open metal sites, the nature of the pore surface also plays an important role in selective adsorption and separation of alcohols as is demonstrated by $[Zn(bdc)(ted)_{0.5}]$, an MMOF previously described in Section 4.4. The activated MMOF selectively adsorbs methanol, ethanol, and dimethylether (DME) over water at room temperature and pressure (Figure 11).[100] The material shows a high uptake for methanol, adsorbing 520 mg g^{-1} at 25 °C and 60 torr; the adsorption profile increases linearly with pressure until capillary condensation takes effect resulting in a sharp rise at higher pressures and temperatures. A similar adsorption profile has also been observed for ethanol, with an uptake of ~418 mg g^{-1}. The calculated heat of adsorption for methanol at low loadings (59.5 kJ mol^{-1}) is lower than that of ethanol (65.8 kJ mol^{-1}), which is consistent with the energy contribution from the nonbonding interaction related to the additional $-CH_2$ group. While the interaction of ethanol with the pore surface is energetically favored, methanol has a higher overall uptake, which is attributed to more efficient packing of the smaller methanol molecules within the pore. The adsorption of DME does not show any capillary condensation at higher pressure regions and has

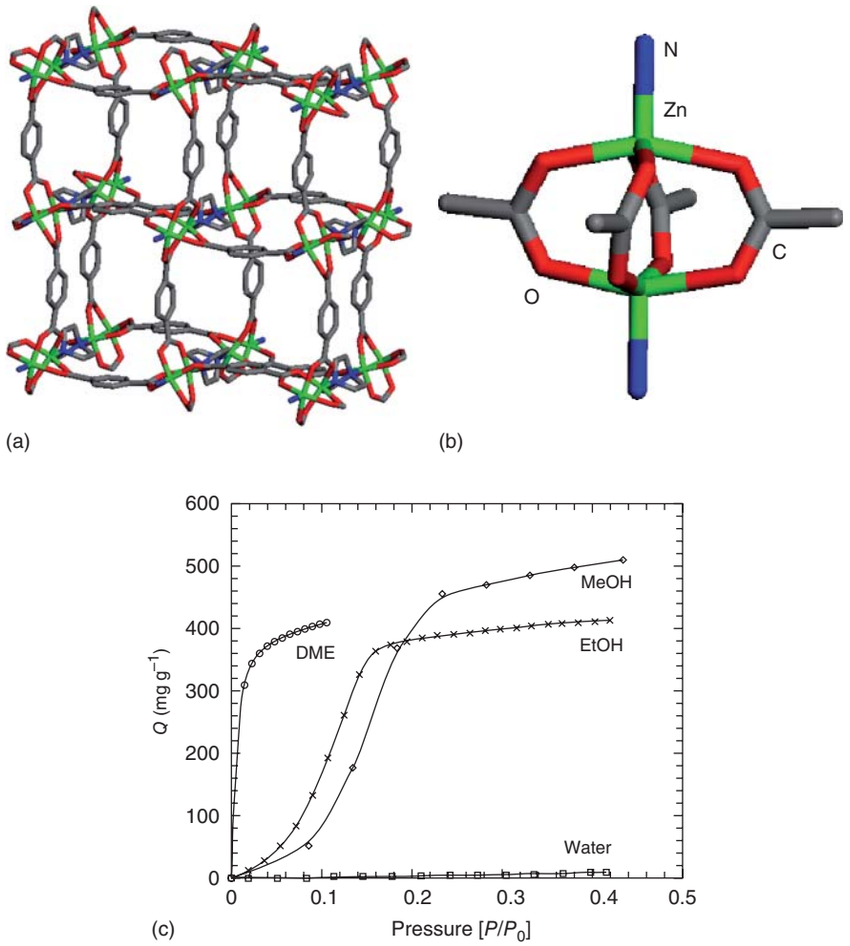


Figure 11 (a) View of the crystal structure of $[M(bdc)(ted)_{0.5}]$, (M = Cu, Zn). Zn and Cu (green), O (red), N (blue), and C (gray). For clarity, solvent molecules are omitted. (b) The paddle-wheel $Zn_2(COO)_4(ted)_2$ SBU unit. (c) Comparison of MeOH, EtOH, DME, and water adsorption isotherms for $[Zn(bdc)(ted)_{0.5}]$ plotted as a function of relative pressure (P/P_0). (Reproduced from Ref. 100. © Wiley-VCH Verlag GmbH & Co. KGaA, 2007.)

a much lower heat of adsorption ($\sim$30 kJ mol^{-1}). This phenomenon is explained by the presence of H-bonding between the alcohol's –OH protons and the MMOF's carboxylate-group oxygen atoms, effectively increasing the overall uptakes for methanol and ethanol. Interestingly, $[Zn(bdc)(ted)_{0.5}]$ adsorbs very small amounts of water ($\sim$6 mg g^{-1} at $P/P_0 = 0.42$) demonstrating the hydrophobic nature of the pore surface.

The selective adsorption of DME over methanol is observed in microporous [Zn(tbip)] (tbip = 5-tert-butylisophthalate), representing an interesting example of equilibrium adsorption.[36] [Zn(tbip)] is a guest-free MMOF with a hexagonal closed packed 1-D channel with a diameter of $\sim$4.5 Å. The 3-D framework is comprised of zinc metal centers tetrahedrally coordinated to the tbip linkers. The tbip linkers arrange themselves in such a way that the hydrophobic tertiary butyl groups stick out into the channel. The adsorption experiments conducted on the material shows absorption of methanol and DME, but essentially no uptake of water (<1 mg g^{-1} at room temperature and $P/P_0 = 0.65$). The adsorption profiles of methanol and DME are markedly different as well. Adsorption of DME shows a typical type I adsorption profile, whereas methanol does not get adsorbed until a certain pressure threshold is exceeded, which is almost entirely attributed to capillary condensation. Thus, the selective adsorption of DME over methanol is possible using Zn(tbip) below this threshold pressure and temperature.

The effect of alcohol adsorption in flexible frameworks such as RPM-3 and RPM-4 has also been investigated.[48] The results of these studies show a stepwise adsorption of alcohols as a function of pressure. Recently, several groups have tested MMOFs for separation of various alcohols from water for biofuel purification.[129–132] For

example, Chance and coworkers reported the single component adsorption profiles of water and different types of alcohols such as methanol, ethanol, and 1-butanol.[132] ZIFs (ZIF-8, ZIF-71, ZIF-90) used in the study contain $-CH_3$, $-Cl$, and $-CHO$ functionalized imidazole linkers, respectively, forming a hydrophobic pore surface for the first two and a hydrophilic pore surface for ZIF-90. The single component water adsorption isotherms show very low uptake for ZIF-8 and ZIF-71 ($<4\,mmol\,g^{-1}$ at saturation uptake), whereas ZIF-90 exhibits a sinusoidal-type adsorption curve with steep rise in adsorption after a pressure threshold ($0.4P/P_0$ with a saturation uptake of $20\,mmol\,g^{-1}$). The single component adsorption isotherms for alcohols show similar sinusoidal-type adsorption curves, resulting from different types of adsorbate–adsorbent interactions at different pressure points. The length of the base of the sinusoidal curves vary based on the nature of the alcohol, with longer chain alcohols such as 1-butanol showing a steep rise in adsorption at lower pressure regions with respect to smaller alcohol molecules, such as methanol and ethanol. As a result, the separation of larger alcohol (e.g., 1-butanol)–water pairs is deemed more practical. Employing the ideal adsorbed solution theory IAST, the calculated sorption selectivity of a vapor phase mixture of 1-butanol and water (0.25 mol% 1-butanol and 99.75 mol% water) reaches 290; the higher 1-butanol uptake over water is a result of the negligible initial alcohol sorption plateau.

6 CONCLUSION AND OUTLOOK

MMOFs have emerged as a promising new type of adsorbent material with potential applications in gas storage, separation, and purification. The rich chemistry and nearly infinite variations of pore characteristics in MMOFs highlight their distinct advantages for separation-related applications over traditional zeolite-based molecular sieves and other types of sorbent materials. The adsorbate–adsorbent interactions in MMOFs can be tuned in a number of ways, including but not limited to the incorporation of open metal sites, functional groups, and post-synthetic modifications. MMOFs have been investigated for several aspects of hydrocarbon and alcohol adsorption and separation with encouraging results as detailed in this chapter. Current research focuses on understanding and enhancing interactions between the pore surface and the adsorbate molecules. In this regard, commensurate adsorption, a phenomenon related to the morphological correlations between the adsorbate and adsorbent, is of fundamental importance. The MMOFs exhibiting commensurate adsorption behavior generally possess 1-D open channels with distinctly shaped segments/cavities or have pore windows that correlate with the geometry of the adsorbate molecules. Further research in this direction will offer additional valuable insight into adsorbate–adsorbent interactions and fuel our search for more efficient, robust, and selective porous solids.

7 ACKNOWLEDGMENTS

This work is supported in full by the US Department of Energy, Office of Basic Energy Sciences, Materials Sciences and Engineering Division through grant DE-FG02-08ER46491.

8 RELATED ARTICLES

Gas Storage in Metal-Organic Frameworks; Metal-Organic Frameworks for Removal of Harmful Gases; Mesoporous Metal-Organic Frameworks; Open Metal Sites in Metal-Organic-Frameworks.

9 ABBREVIATIONS AND ACRONYMS

as = as synthesized; bdc = terephthalate; bdp = 1,4-benzenedipyrazolate; BET = Brunauer–Emmett–Teller; bipy = 4,4′-bipyridine (also bpy); bpdc = biphenyl-4,4′-dicarboxylate; bpe = 1,2-bis(2-pyridyl)ethane; bpee = 1,2-bis(2-pyridyl)ethylene); bpy = 4,4′-bipyridine; btc = 1,3,5-benzenetricarboxylate; btapa = 1,3,5-benzenetricarboxyate tris[*N*-(4-pyridyl)amide]; CBMC = configurational-bias Monte Carlo; dabco = 1,4-diazabicyclo[2.2.2]-octane); DFT = density functional theory; DME = dimethylether; dobdc = 2,5-dioxido-1,4-benzenedicarboxylate; dpyg = 1,2-di(4-pyridyl)-glycol; EB = ethyl benzene; etz = 3,5-diethyl-1,2,4-triazole; fma = fumarate; GC = gas chromatography; gla = *R*-2-methylglutarate; H_2hfipbb = 4,4′-(hexafluoroisopropylidene)bis(benzoic acid); H_4T(*p*-CO_2)PP = meso-tetrakis(4-carboxyphenyl)porphine; IRMOF = isoreticular metal-organic framework; *m*X = *meta*-xylene; MEM = maximum entropy method; MIL = Materials of "Institut Lavoisier"; MMOF = microporous metal-organic framework; MOF = Metal-organic framework; nHEX = normal hexane; NOVA = NO void analysis; *o*X = *ortho*-xylene; *p*X = *para*-xylene; PCN = porous coordination networks; PIZA = porphyrinic Illinois zeolite analog; PXRD = powder X-ray diffraction; pyz = pyrazine; pzdc = pyrazine-2,3-dicarboxylate; Q_{st} = isotectic heats of adsorption; RON = Research Octane Number; RPM = Rutgers Recyclable Porous Materials; SBU = secondary

building unit; sdc = styrenedicarboxylate; tbip = 5-tert-butylisophthalate; tci = tris(2-carboxyethyl) isocyanurate; ted = triethylenediamine; USTA = University of Texas San Antonio; ZIF = Zeolitic imidazolate framework; 2-bim = 2-bromoimidazole; 2-cim = 2-chloroimidazole; 2-mim = 2-methylimidazole; 2-MP = 2-methylpentane; 22-DMB = 2,2-dimethylbutane; 23-DMB = 2,3-dimethylbutane; 3-D = three-dimensional; 3-MP = 3-methylpentane.

10 REFERENCES

1. H. C. Zhou, J. R. Long, and O. M. Yaghi, *Chem. Rev.*, 2012, **112**, 673.
2. M. O'Keeffe and O. M. Yaghi, *Chem. Rev.*, 2012, **112**, 675.
3. N. Stock and S. Biswas, *Chem. Rev.*, 2012, **112**, 933.
4. K. J. Gagnon, H. P. Perry, and A. Clearfield, *Chem. Rev.*, 2012, **112**, 1034.
5. J. P. Zhang, Y. B. Zhang, J. B. Lin, and X. M. Chen, *Chem. Rev.*, 2012, **112**, 1001.
6. W. Zhang and R. G. Xiong, *Chem. Rev.*, 2012, **112**, 1163.
7. H. H. Wu, Q. H. Gong, D. H. Olson, and J. Li, *Chem. Rev.*, 2012, **112**, 836.
8. J. R. Li, J. Sculley, and H. C. Zhou, *Chem. Rev.*, 2012, **112**, 869.
9. K. Sumida, D. L. Rogow, J. A. Mason, T. M. McDonald, E. D. Bloch, Z. R. Herm, T. H. Bae, and J. R. Long, *Chem. Rev.*, 2012, **112**, 724.
10. R. B. Getman, Y. S. Bae, C. E. Wilmer, and R. Q. Snurr, *Chem. Rev.*, 2012, **112**, 703.
11. M. P. Suh, H. J. Park, T. K. Prasad, and D. W. Lim, *Chem. Rev.*, 2012, **112**, 782.
12. P. Horcajada, R. Gref, T. Baati, P. K. Allan, G. Maurin, P. Couvreur, G. Ferey, R. E. Morris, and C. Serre, *Chem. Rev.*, 2012, **112**, 1232.
13. M. Yoon, R. Srirambalaji, and K. Kim, *Chem. Rev.*, 2012, **112**, 1196.
14. Y. J. Cui, Y. F. Yue, G. D. Qian, and B. L. Chen, *Chem. Rev.*, 2012, **112**, 1126.
15. L. E. Kreno, K. Leong, O. K. Farha, M. Allendorf, R. P. Van Duyne, and J. T. Hupp, *Chem. Rev.*, 2012, **112**, 1105.
16. C. Wang, T. Zhang, and W. B. Lin, *Chem. Rev.*, 2012, **112**, 1084.
17. A. Betard and R. A. Fischer, *Chem. Rev.*, 2012, **112**, 1055.
18. Y. B. He, W. Zhou, R. Krishna, and B. L. Chen, *Chem. Commun.*, 2012, **48**, 11813.
19. K. Huddersman and M. Klimczyk, *AIChE J.*, 1996, **42**, 405.
20. D. W. Breck, 'Zeolite Molecular Sieves, Structure, Chemistry and Use', John Wiley & Sons, Inc., New York, 1974, p.771.
21. J. Graetz, *Chem. Soc. Rev.*, 2009, **38**, 73.
22. R. T. Yang, 'Adsorbents: Fundamentals and Applications', John Wiley & Sons, Inc., Hoboken, 2003.
23. J. U. Keller and R. Staudt, 'Gas Adsorption Equilibria, Experimental Methods and Adsorptive Isotherms', Springer Science+Business Media, Inc., Boston, 2005.
24. J. Moellmer, E. B. Celer, R. Luebke, A. J. Cairns, R. Staudt, M. Eddaoudi, and M. Thommes, *Micropor. Mesopor. Mat.*, 2010, **129**, 345.
25. L. Pan, D. H. Olson, L. R. Ciemnolonski, R. Heddy, and J. Li, *Angew. Chem. Int. Ed.*, 2006, **45**, 616.
26. K. Li, D. H. Olson, J. Seidel, T. J. Emge, H. Gong, H. Zeng, and J. Li, *J. Am. Chem. Soc.*, 2009, **131**, 10368.
27. P. D. C. Dietzel, R. E. Johnsen, H. Fjellvag, S. Bordiga, E. Groppo, S. Chavan, and R. Blom, *Chem. Commun.*, 2008, 5125.
28. S. R. Caskey, A. G. Wong-Foy, and A. J. Matzger, *J. Am. Chem. Soc.*, 2008, **130**, 10870.
29. A. M. Plonka, D. Banerjee, W. R. Woerner, Z. J. Zhang, N. Nijem, Y. J. Chabal, J. Li, and J. B. Parise, *Angew. Chem. Int. Edit.*, 2013, **52**, 1692.
30. R. S. Mikhail and E. Robens, 'Microstructure and Thermal Analysis of Solid Surfaces', John Wiley & Sons, Ltd, Chichester, 1983.
31. K. S. W. Sing, D. H. Everett, R. A. W. Haul, L. Moscou, R. A. Pierotti, J. Rouquerol, and T. Siemieniewska, *Pure Appl. Chem.*, 1985, **57**, 603.
32. S. Lowell, J. E. Shields, M. A. Thomas, and M. Thommes, 'Characterization of Porous Solids and Powders: Surface Area, Porosity and Density', Springer, 2006.
33. M. Maes, L. Alaerts, F. Vermoortele, R. Ameloot, S. Couck, V. Finsy, J. F. M. Denayer, and D. E. De Vos, *J. Am. Chem. Soc.*, 2010, **132**, 2284.
34. M. Maes, F. Vermoortele, L. Alaerts, S. Couck, C. E. A. Kirschhock, J. F. M. Denayer, and D. E. De Vos, *J. Am. Chem. Soc.*, 2010, **132**, 15277.
35. D. H. Olson, X. Yang, and M. A. Camblor, *J. Phys. Chem. B*, 2004, **108**, 11044.
36. L. Pan, B. Parker, X. Huang, D. H. Olson, Lee, and J. Li, *J. Am. Chem. Soc.*, 2006, **128**, 4180.
37. L. Alaerts, C. E. A. Kirschhock, M. Maes, M. A.van der Veen, V. Finsy, A. Depla, J. A. Martens, G. V. Baron, P. A. Jacobs, J. F. M. Denayer, and D. E. De Vos, *Angew. Chem. Int. Ed.*, 2007, **46**, 4293.
38. L. Alaerts, M. Maes, L. Giebeler, P. A. Jacobs, J. A. Martens, J. F. M. Denayer, C. E. A. Kirschhock, and D. E. De Vos, *J. Am. Chem. Soc.*, 2008, **130**, 14170.
39. W. Zhou, *Chem. Rec.*, 2010, **10**, 200.
40. S. S. Kaye, A. Dailly, O. M. Yaghi, and J. R. Long, *J. Am. Chem. Soc.*, 2007, **129**, 14176.
41. H. Li, M. Eddaoudi, M. O'Keeffe, and O. M. Yaghi, *Nature*, 1999, **402**, 276.

42. M. Dinca, W. S. Han, Y. Liu, A. Dailly, C. M. Brown, and J. R. Long, *Angew. Chem. Int. Edit.*, 2007, **46**, 1419.
43. K. L. Mulfort, T. M. Wilson, M. R. Wasielewski, and J. T. Hupp, *Langmuir*, 2009, **25**, 503.
44. R. Banerjee, A. Phan, B. Wang, C. Knobler, H. Furukawa, M. O'Keeffe, and O. M. Yaghi, *Science*, 2008, **319**, 939.
45. A. C. Kizzie, A. G. Wong-Foy, and A. J. Matzger, *Langmuir*, 2011, **27**, 6368.
46. J. Liu, P. K. Thallapally, and D. Strachan, *Langmuir*, 2012, **28**, 11584.
47. D. Britt, D. Tranchemontagne, and O. M. Yaghi, *Proc. Natl. Acad. Sci. U. S. A.*, 2008, **105**, 11623.
48. H. Wu, W. Zhou, and T. Yildirim, *J. Am. Chem. Soc.*, 2009, **131**, 4995.
49. Z. R. Herm, B. M. Wiers, J. A. Mason, J. M.van Baten, M. R. Hudson, P. Zajdel, C. M. Brown, N. Masciocchi, R. Krishna, and J. R. Long, *Science*, 2013, **340**, 960.
50. E. D. Bloch, W. L. Queen, R. Krishna, J. M. Zadrozny, C. M. Brown, and J. R. Long, *Science*, 2012, **335**, 1606.
51. P. W. Stephens, P. A. Heiney, R. J. Birgeneau, P. M. Horn, D. E. Moncton, and G. S. Brown, *Phys. Rev. B*, 1984, **29**, 3512.
52. I. Gameson and T. Rayment, *Chem. Phys. Lett.*, 1986, **123**, 150.
53. P. Bak, *Rep. Prog. Phys.*, 1982, **45**, 587.
54. D. H. Olson, G. T. Kokotailo, S. L. Lawton, and W. M. Meier, *J. Phys. Chem.*, 1981, **85**, 2238.
55. B. Smit and T. L. M. Maesen, *Nature*, 1995, **374**, 42.
56. S. Y. Zhen and K. Seff, *Micropor. Mesopor. Mat.*, 2000, **39**, 1.
57. G. H. Jeong, Y. Kim, and K. Seff, *Langmuir*, 2004, **20**, 9354.
58. D. Olson, A. Lan, J. Seidel, K. Li, and J. Li, *Adsorption*, 2010, **16**, 559.
59. R. Krishna and J. M.van Baten, *Mol. Simulat.*, 2009, **35**, 1098.
60. B. Smit and T. L. M. Maesen, *Chem. Rev.*, 2008, **108**, 4125.
61. R. Matsuda, R. Kitaura, S. Kitagawa, Y. Kubota, R. V. Belosludov, T. C. Kobayashi, H. Sakamoto, T. Chiba, M. Takata, Y. Kawazoe, and Y. Mita, *Nature*, 2005, **436**, 238.
62. K. Li, D. H. Olson, J. Y. Lee, W. Bi, K. Wu, T. Yuen, Q. Xu, and J. Li, *Adv. Funct. Mater.*, 2008, **18**, 2205.
63. M. Kondo, T. Okubo, A. Asami, S.-i. Noro, T. Yoshitomi, S. Kitagawa, T. Ishii, H. Matsuzaka, and K. Seki, *Angew. Chem. Int. Ed.*, 1999, **38**, 140.
64. L. Pan, M. B. Sander, X. Y. Huang, J. Li, M. Smith, E. Bittner, B. Bockrath, and J. K. Johnson, *J. Am. Chem. Soc.*, 2004, **126**, 1308.
65. J. M. Zhang, H. H. Wu, T. J. Emge, and J. Li, *Chem. Commun.*, 2010, **46**, 9152.
66. T. Loiseau, L. Lecroq, C. Volkringer, J. Marrot, G. Ferey, M. Haouas, F. Taulelle, S. Bourrelly, P. L. Llewellyn, and M. Latroche, *J. Am. Chem. Soc.*, 2006, **128**, 10223.
67. A. J. Lan, K. H. Li, H. H. Wu, L. Z. Kong, N. Nijem, D. H. Olson, T. J. Emge, Y. J. Chabal, D. C. Langreth, M. C. Hong, and J. Li, *Inorg. Chem.*, 2009, **48**, 7165.
68. K. Barthelet, J. Marrot, D. Riou, and G. Férey, *Angew. Chem. Int. Ed.*, 2002, **41**, 281.
69. T. Loiseau, C. Serre, C. Huguenard, G. Fink, F. Taulelle, M. Henry, T. Bataille, and G. Férey, *Chem. Eur. J.*, 2004, **10**, 1373.
70. S. M. Auerbach, L. M. Bull, N. J. Henson, H. I. Metiu, and A. K. Cheetham, *J. Phys. Chem.*, 1996, **100**, 5923.
71. H. Morell, K. Angermund, A. R. Lewis, D. H. Brouwer, C. A. Fyfe, and H. Gies, *Chem. Mater.*, 2002, **14**, 2192.
72. R. Matsuda, R. Kitaura, Y. Kubota, T. C. Kobayashi, M. Takata, and S. Kitagawa, *Micropor. Mesopor. Mat.*, 2010, **129**, 296.
73. J. Kager, D. M. Ruthven, and D. N. Theodorou, 'Diffusion in Nanoporous Materials', John Wiley & Sons, Inc., New York, 2012, p.902.
74. J. Cejka, H. V. Bekkum, A. Corma, and F. Schuth, 'Introduction to Zeolite Science and Practice', Elsevier, Amsterdam, 2007, p.1094.
75. K. Konstas, T. Osl, Y. X. Yang, M. Batten, N. Burke, A. J. Hill, and M. R. Hill, *J. Mater. Chem.*, 2012, **22**, 16698.
76. M. Kondo, T. Yoshitomi, K. Seki, H. Matsuzaka, and S. Kitagawa, *Angew. Chem. Int. Edit.*, 1997, **36**, 1725.
77. K. Seki, *Phys. Chem. Chem. Phys.*, 2002, **4**, 1968.
78. K. Seki and W. Mori, *J. Phys. Chem. B*, 2002, **106**, 1380.
79. K. Seki, *Chem. Commun.*, 2001, 1496.
80. K. Seki, S. Takamizawa, and W. Mori, *Chem. Lett.*, 2001, 332.
81. K. Seki, S. Takamizawa, and W. Mori, *Chem. Lett.*, 2001, 122.
82. S. Q. Ma, D. F. Sun, J. M. Simmons, C. D. Collier, D. Q. Yuan, and H. C. Zhou, *J. Am. Chem. Soc.*, 2008, **130**, 1012.
83. D. Zhao, D. Q. Yuan, A. Yakovenko, and H. C. Zhou, *Chem. Commun.*, 2010, **46**, 4196.
84. I. Daems, G. V. Baron, S. Punnathanam, R. Q. Snurr, and J. F. M. Denayer, *J. Phys. Chem. C*, 2007, **111**, 2191.
85. M. C. Das, Q. S. Guo, Y. B. He, J. Kim, C. G. Zhao, K. L. Hong, S. C. Xiang, Z. J. Zhang, K. M. Thomas, R. Krishna, and B. L. Chen, *J. Am. Chem. Soc.*, 2012, **134**, 8703.
86. M. C. Das, H. Xu, S. C. Xiang, Z. J. Zhang, H. D. Arman, G. D. Qian, and B. L. Chen, *Chem. Eur. J.*, 2011, **17**, 7817.
87. S. C. Xiang, Z. J. Zhang, C. G. Zhao, K. L. Hong, X. B. Zhao, D. R. Ding, M. H. Xie, C. D. Wu, M. C. Das, R. Gill, K. M. Thomas, and B. L. Chen, *Nat. Commun.*, 2011, **2**, 1.

88. Y. B. He, R. Krishna, and B. L. Chen, *Eng. Environ. Sci.*, 2012, **5**, 9107.

89. S. J. Geier, J. A. Mason, E. D. Bloch, W. L. Queen, M. R. Hudson, C. M. Brown, and J. R. Long, *Chem. Sci.*, 2013, **4**, 2054.

90. N. Nijem, H. H. Wu, P. Canepa, A. Marti, K. J. Balkus, T. Thonhauser, J. Li, and Y. J. Chabal, *J. Am. Chem. Soc.*, 2012, **134**, 15201.

91. S. Aguado, G. Bergeret, M. P. Titus, V. Moizan, C. Nieto-Draghi, N. Bats, and D. Farrusseng, *New J. Chem.*, 2011, **35**, 546.

92. D. H. Olson, M. A. Camblor, L. A. Villaescusa, and G. H. Kuehl, *Micropor. Mesopor. Mat.*, 2004, **67**, 27.

93. R. Krishna and J. M.van Baten, *J. Phys. Chem. C*, 2010, **114**, 18017.

94. N. Lamia, M. Jorge, M. A. Granato, F. A. A. Paz, H. Chevreau, and A. E. Rodrigues, *Chem. Eng. Sci.*, 2009, **64**, 3246.

95. J. W. Yoon, Y.-K. Seo, Y. K. Hwang, J.-S. Chang, H. Leclerc, S. Wuttke, P. Bazin, A. Vimont, M. Daturi, E. Bloch, P. L. Llewellyn, C. Serre, P. Horcajada, J.-M. Grenèche, A. E. Rodrigues, and G. Férey, *Angew. Chem. Int. Ed.*, 2010, **49**, 5949.

96. K. Huddersman and M. Klimczyk, *J. Chem. Soc. Faraday Trans.*, 1996, **92**, 143.

97. P. S. Bárcia, F. Zapata, J. A. C. Silva, A. E. Rodrigues, and B. Chen, *J. Phys. Chem. B*, 2007, **111**, 6101.

98. D. Dubbeldam, C. J. Galvin, K. S. Walton, D. E. Ellis, and R. Q. Snurr, *J. Am. Chem. Soc.*, 2008, **130**, 10884.

99. D. N. Dybtsev, H. Chun, and K. Kim, *Angew. Chem. Int. Ed.*, 2004, **43**, 5033.

100. J. Y. Lee, D. H. Olson, L. Pan, T. J. Emge, and J. Li, *Adv. Funct. Mater.*, 2007, **17**, 1255.

101. R. El Osta, A. Carlin-Sinclair, N. Guillou, R. I. Walton, F. Vermoortele, M. Maes, D.de Vos, and F. Millange, *Chem. Mater.*, 2012, **24**, 2781.

102. X. H. Gu, J. H. Dong, T. M. Nenoff, and D. E. Ozokwelu, *J. Membr. Sci.*, 2006, **280**, 624.

103. M. O. Daramola, A. J. Burger, M. Pera-Titus, A. Giroir-Fendler, S. Miachon, J. A. Dalmon, and L. Lorenzen, *Asia-Pac. J. Chem. Eng.*, 2010, **5**, 815.

104. V. Finsy, H. Verelst, L. Alaerts, D. E. De Vos, P. A. Jacobs, G. V. Baron, and J. F. M. Denayer, *J. Am. Chem. Soc.*, 2008, **130**, 7110.

105. J. M. Castillo, T. J. H. Vlugt, and S. Calero, *J. Phys. Chem. C*, 2009, **113**, 20869.

106. V. Finsy, C. E. A. Kirschhock, G. Vedts, M. Maes, L. Alaerts, D. E. De Vos, G. V. Baron, and J. F. M. Denayer, *Chem. Eur. J.*, 2009, **15**, 7724.

107. C. Serre, F. Millange, C. Thouvenot, M. Noguès, G. Marsolier, D. Louër, and G. Férey, *J. Am. Chem. Soc.*, 2002, **124**, 13519.

108. F. Millange, C. Serre, and G. Ferey, *Chem. Commun.*, 2002, **8**, 822.

109. T. R. Whitfield, X. Wang, L. Liu, and A. J. Jacobson, *Solid State Sci.*, 2005, **7**, 1096.

110. M. Vougo-Zanda, J. Huang, E. Anokhina, X. Wang, and A. J. Jacobson, *Inorg. Chem.*, 2008, **47**, 11535.

111. N. Rosenbach Jr, A. Ghoufi, I. Deroche, P. L. Llewellyn, T. Devic, S. Bourrelly, C. Serre, G. Ferey, and G. Maurin, *Phys. Chem. Chem. Phys.*, 2010, **12**, 6428.

112. P. L. Llewellyn, P. Horcajada, G. Maurin, T. Devic, N. Rosenbach, S. Bourrelly, C. Serre, D. Vincent, S. Loera-Serna, Y. Filinchuk, and G. Férey, *J. Am. Chem. Soc.*, 2009, **131**, 13002.

113. S. Uchida, R. Kawamoto, H. Tagami, Y. Nakagawa, and N. Mizuno, *J. Am. Chem. Soc.*, 2008, **130**, 12370.

114. C. Gucuyener, J.van den Bergh, J. Gascon, and F. Kapteijn, *J. Am. Chem. Soc.*, 2010, **132**, 17704.

115. D. G. Samsonenko, H. Kim, Y. Sun, G.–. H. Kim, H.-S. Lee, and K. Kim, *Chem. Asian J.*, 2007, **2**, 484.

116. T. K. Trung, P. Trens, N. Tanchoux, S. Bourrelly, P. L. Llewellyn, S. Loera-Serna, C. Serre, T. Loiseau, F. O. Fajula, and G. R. Férey, *J. Am. Chem. Soc.*, 2008, **130**, 16926.

117. R. Kitaura, K. Fujimoto, S.-i. Noro, M. Kondo, and S. Kitagawa, *Angew. Chem. Int. Ed.*, 2002, **41**, 133.

118. T. K. Maji, K. Uemura, H.–. C. Chang, R. Matsuda, and S. Kitagawa, *Angew. Chem. Int. Ed.*, 2004, **43**, 3269.

119. S. Hasegawa, S. Horike, R. Matsuda, S. Furukawa, K. Mochizuki, Y. Kinoshita, and S. Kitagawa, *J. Am. Chem. Soc.*, 2007, **129**, 2607.

120. T. K. Maji, R. Matsuda, and S. Kitagawa, *Nat. Mater.*, 2007, **6**, 142.

121. J.-P. Zhang and X.-M. Chen, *J. Am. Chem. Soc.*, 2008, **130**, 6010.

122. S. K. Ghosh, S. Bureekaew, and S. Kitagawa, *Angew. Chem. Int. Ed.*, 2008, **47**, 3403.

123. J. Lincke, D. Lassig, J. Moellmer, C. Reichenbach, A. Puls, A. Moeller, R. Glaser, G. Kalies, R. Staudt, and H. Krautscheid, *Micropor. Mesopor. Mat.*, 2011, **142**, 62.

124. X. Lin, A. J. Blake, C. Wilson, X. Z. Sun, N. R. Champness, M. W. George, P. Hubberstey, R. Mokaya, and M. Schröder, *J. Am. Chem. Soc.*, 2006, **128**, 10745.

125. B. Chen, Y. Ji, M. Xue, F. R. Fronczek, E. J. Hurtado, J.U. Mondal, C. Liang, and S. Dai, *Inorg. Chem.*, 2008, **47**, 5543.

126. K. Uemura, Y. Yamasaki, Y. Komagawa, K. Tanaka, and H. Kita, *Angew. Chem.*, 2007, **119**, 6782.

127. O. M. Yaghi, C. E. Davis, G. M. Li, and H. L. Li, *J. Am. Chem. Soc.*, 1997, **119**, 2861.

128. M. E. Kosal, J. H. Chou, S. R. Wilson, and K. S. Suslick, *Nat. Mater.*, 2002, **1**, 118.

129. J. K. Sun, M. Ji, C. Chen, W. G. Wang, P. Wang, R. P. Chen, and J. Zhang, *Chem. Commun.*, 2013, **49**, 1624.

130. T. Borjigin, F. X. Sun, J. L. Zhang, K. Cai, H. Ren, and G. S. Zhu, *Chem. Commun.*, 2012, **48**, 7613.

131. J. A. Gee, J. Chung, S. Nair, and D. S. Sholl, *J. Phys. Chem. C*, 2013, **117**, 3169.

132. K. Zhang, R. P. Lively, M. E. Dose, A. J. Brown, C. Zhang, J. Chung, S. Nair, W. J. Koros, and R. R. Chance, *Chem. Commun.*, 2013, **49**, 3245.

Metal Uptake in Metal-Organic Frameworks

Michaele J. Hardie

University of Leeds, Leeds, UK

1	Introduction	343
2	Grafting onto Framework	343
3	Uptake of Metals into MOF Pores	352
4	Transmetallation	357
5	Conclusions	359
6	Related Articles	359
7	Abbreviations and Acronyms	359
8	References	359

1 INTRODUCTION

Metal-organic frameworks (MOFs) are 3D coordination polymers with robust and porous structures. They are constructed from linker ligands that bridge between metal cations or between clusters of metal cations to create a framework structure.[1,2] Connecting points within a framework are often referred to as framework nodes or connecting nodes. Two early examples of 3D coordination polymers and MOFs are shown in Figure 1, namely [Cu(tetra-(4-cyanophenyl)methane)]$^+$, which has a diamond-like framework with tetrahedral Cu(I) and ligand nodes,[1] and [$Zn_4O(bdc)_3$] (bdc = 1,4-benzenedicarboxylate), which is commonly known as MOF-5 where a tetrameric Zn(II) metal cluster acts as the node.[2] The porous nature of MOFs and other porous coordination polymers means that they function as solid-state hosts able to take up additional molecules or ions through their pores. In this chapter, the uptake of metals and metal-containing moieties by MOFs will be reviewed.

Metals in MOFs have a fundamental structural role as framework nodes, but may also impart additional functionality such as magnetism, luminescence, Lewis acid catalysis, and guest binding at coordinatively unsaturated metal sites.[3,4] Uptake of additional metals by a MOF may introduce new functionality, or alter functionality, and thus finds a variety of potential applications. For example, luminescence or color changes for sensing; applications in catalysis; ion exchange; removal of metal contaminants from the atmosphere or solution; altering gas-binding properties of a MOF by creation of electric dipoles on the framework surface; and ion transport for battery applications.

Metal uptake may occur through a number of different mechanisms including: grafting of metals or metal-containing species onto the framework of the MOF itself; cation exchange within anionic MOFs; and pore absorption of metal-containing guest molecules. Related to this is metal cation metathesis, also referred to as transmetallation, where metal cations within the framework are substituted for a different cation usually with retention of the gross original framework structure. Both grafting and transmetallation are examples of post-synthetic modification (PSM) where the solid-state MOF framework is chemically altered.[5]

2 GRAFTING ONTO FRAMEWORK

The majority of MOFs and coordination polymers form in a manner that is coordinatively saturated with respect to the ligand, that is, each metal-binding site within a ligand is bound to a metal. This is not always the case, however, and metal-binding groups may be left unencumbered within a MOF either by design or through serendipity, and thus be available for grafting a metal cation in a PSM. Strategies for generating MOFs with pendant-binding sites include manipulating hard–soft metal-binding preferences; post-synthetic demetallation of nonstructural metal site; post-synthetic conversion of

Metal-Organic Framework Materials. Edited by Leonard R. MacGillivray and Charles M. Lukehart.
© 2014 John Wiley & Sons, Ltd. ISBN 978-1-119-95289-3

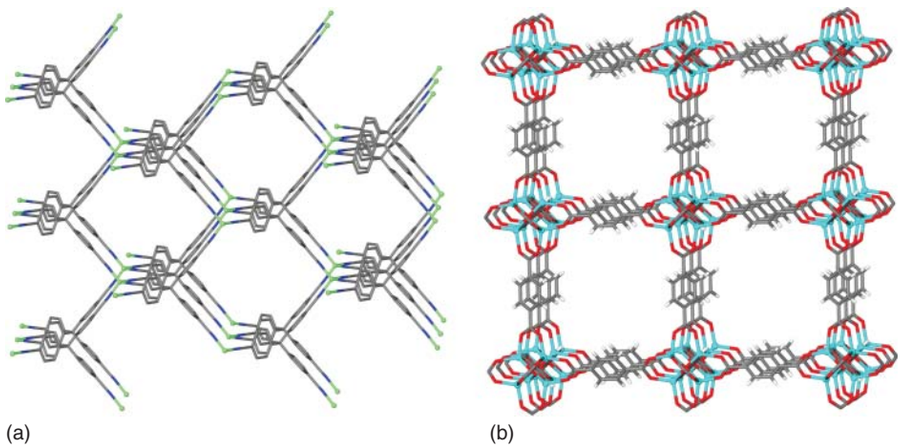


Figure 1 Archetypal coordination polymer or metal-organic framework structures: (a) diamondoid structure of [Cu(tetra-(4-cyanophenyl)methane)]$^{+}$; (b) structure of $[Zn_4O(bdc)_3]$, MOF-5

other pendant functional groups to ligand groups; and the use of organometallic metal-binding possibilities inherent in some linker ligands. Examples are summarized in Table 1.

2.1 Hard–Soft Ligands for Pendant Ligand Sites

One strategy for generating MOFs with pendant-binding sites is to use the hard–soft ideas of coordination chemistry. Essentially these are that hard metal cations which are not particularly polarizable and may have high oxidation states preferentially interact with hard donor atoms that are likewise of low to moderate polarizability. Conversely, soft metal cations that are typically larger and more polarizable prefer soft ligands with polarizable donor atoms, to form predominantly covalent bonds. Thus, a ligand with both hard and soft donor atoms can be paired with a hard metal for MOF construction, leaving pendant soft donor atoms. As an example, a MOF constructed from Ca(II) and *tris*(*p*-carboxylated)triphenylphosphine has hard–hard Ca(II)-carboxylate structural nodes, and the pendant soft phosphine is able to bind the soft metal Au(I) through a PSM.[6] Most examples, however, of this hard–soft approach utilize S or N donors as the pendant ligand site, Charts 1 and 2.

2.1.1 Thiols and Thioethers

Benzene-1,4-dicarboxylic acid (H_2bdc) is one of the most commonly utilized ligands in MOF chemistry, being the linker ligand for MOF-5. Deprotonated carboxylic acids or carboxylates are hard donors and are frequently coupled with Zn(II), a hard metal, for MOFs. Sulfur is a typical soft atom donor and Xu, Hunter, and coworkers have employed benzene-1,4-dicarboxylic acid ligands with additional thioether groups to generate a series of MOFs with pendant thiol or thioether groups. Tetrakis(methylthio-)-1,4-benzenedicarboxylic acid (H_2tmbd, Chart 1) and Zn(II) form the complex $[Zn_4O(H_2O)_3(tmbd)_3]$ with the anticipated open zinc-carboxylate structure and free methylthio groups. This demonstrates that hard–soft principles can be used to build MOF-type materials with pendant ligand groups;[65] however, this material was not robust to solvent loss so could not be investigated for soft metal uptake. The MOF [Pd(tmbd)], on the other hand, has a robust 3D framework with methylthio-lined channels.[7] Heating [Pd(tmbd)] and $HgCl_2$ in benzene at 100 °C for 48 h resulted in a stoichiometric uptake of $HgCl_2$ to give adduct [Pd(tmbd)]·$HgCl_2$. A further example is the MOF-5 analog $[Zn_4O(metbd)_3]$ (metbd = 2,5-bis-(2-(methylthio)ethylthio)-1,4-benzenedicarboxylate, Chart 1), which has chelating thioether groups lining the MOF channels and is able to uptake $HgCl_2$ from ethanol solution at room temperature.[8] In both of these examples, the $HgCl_2$ binding was reversible, as it could be washed out with a polar solvent such as acetonitrile at moderately elevated temperate.

While the thioether-lined MOFs show reversible binding of Hg(II), thiols are more likely to show stronger interactions. The Zr(IV)-based MOF $[Zr_6O_4(OH)_4(dmbd)_6]$[9] (dmbd = 2,5-dimercapto-1,4-benzenedicarboxylate, Chart 1) has a 12-connected framework with $dmbdc^{2-}$ linear linkers between $Zr_6O_4(OH)_4$ clusters. Tetrahedral-cage cavities within $[Zr_6O_4(OH)_4(dmbd)_6]$ are

Table 1 Selected examples of metal uptake in MOFs through grafting and pore uptake[a]

Material	Metal(s) taken up in post-synthetic processes	Reagent(s) employed	Property or application	References
Direct or indirect grafting (Section 2)				
$[Ca_2\{tris(p\text{-}carboxyl)triphenylphosphine\}]$	Au(I)	$(Me_2S)AuCl$	Hydrocarbon separations	6
[Pd(tmbd)]	Hg(II)	$HgCl_2$	Heavy metal sequestering	7
$[Zn_4O(metbd)_3]$	Hg(II)	$HgCl_2$	Heavy metal sequestering	8
$[Zr_6O_4(OH)_4(dmbd)_6]$	Hg(II), Hg(0)	$HgCl_2$, Hg(g)	Heavy metal sequestering, sensing	9
$[Zn_4O(dtabc)_3]$	Pd(II), Ru(III), Au(I), Ir(III), Pt(II), Ag(I), Cu(II), Ni(II), Co(II), Mn(II)	$PdCl_2$, $RuCl_3$, $AuCl_3$, AuCl, $IrCl_3$, $PtCl_2$, $AgNO_3$, $CuCl_2$, $NiCl_2$, $Co(NO_3)_2$, $MnCl_2$	Sensing	10
$[Eu(pdc)_{1.5}(DMF)]$	Mn(II), Cu(II), Co(II)m Zn(II), Cd(II)	$M(NO_3)_2$	Sensing	11
[Al(OH)(bpydc)]	Pd(II), Cu(II)	$PdCl_2$, $Cu(BF_4)_2$	Gas storage	12
[Al(OH)(bpydc)]	Ru(III)	$[RuCl_4(DMSO)][(DMSO)_2H]$	Catalysis	13
[Zn(isophtalate)(bispybpy)]	Cu(I)	$CuCl_2$		14
$[Zr_6O_4(OH)_4(tcpp\text{-}H_2)_3]$	Fe(III)	$FeCl_3$		15
$[Cd_3Cl_6(pybinol)_3]$	Ti(IV)	$Ti(O^iPr)_4$	Catalysis	16
$[Cu_2(dcbinol)(H_2O)_2]$	Ti(IV), Zn(II)	$Ti(O^iPr)_4$ or $ZnMe_2$	Catalysis	17
$[Zn_4O(dpdiol)_3]$	Cu(II)	$CuCl_2$		18
$[Zn(btp)(dped)_2]$	Li(I), Mg(II)	$Li(O^tBu)$, $Mg(OMe)_2$	Gas binding	19
[Al(OH)(hbd)]	Li(I)	Lithium diisopropylamide	Gas binding	20
$[Cu_2(imc)_2(MeOH)_2]$	Pd(II)	$Pd(OAc)_2$	Catalysis	21
$[Zn_4O(bdc)_3]$ (MOF-5)	Cr(0)	$Cr(CO)_6$		22
$[Zr_6O_4(OH)_4(bdc)_6]$	Cr(0)	$Cr(CO)_6$	Photoreactivity	23
$[Ni_2(dhbd)]$	Mo(0)	$Mo(CO)_6$	Catalysis	24
[Al(OH)(bdc)]	Fe(II)	1,1′-Ferrocenediyl-dimethylsilane	Redox catalysis	25
$[Zn_4O(NH_2bdc)_3]$ (IRMOF-3)	Fe(II)	Ferrocene carboxylic anhydride	Redox activity	26
$[Zn_4O(NH_2bdc)_3]$ (IRMOF-3)	V(IV)	Salicylaldehyde then $VO(acac)_2$	Catalysis	27
$[Zn_4O(NH_2bdc)_3]$ (IRMOF-3)	Nd(III), Y(III)	3-(2-Hydroxyphenyl)-3-oxopropanal then MCl_3	Near IR-emission	28

(*continued overleaf*)

Table 1 (*Continued*)

Material	Metal(s) taken up in post-synthetic processes	Reagent(s) employed	Property or application	References
$[Zr_6O_4(OH)_4(bpdc)_6]$	Mg(I), Au(0)	MeMgBr, $MeAu(PMe_3$		
$[Zr_6(OH)_8(OH)_8(TBAPy)_2]$	Zn(II), Al(III)	$ZnEt_2$, $AlMe_3$	Catalysis	30
$[(Zn_4O)_3(NH_2bdc)_3(btb)_4]$	Pd(II)	2-Pyridinecarboxaldehyde, $[Pd(CH_3CN)_2Cl_2]$		31
$[Cr_3F(H_2O)O(bdc)_2]$, MIL-101	V(IV)	Dehydration, dopamine, $VO(acac)_2$	Catalysis	32
MnSO-MOF	Cr(II), Co(II), Mn(II), Ni(II), Cu(II), Zn(II)	Aq. H_2O_2, then M(II) salts	Catalysis	33
$[Cd_4(btp)_4]$	Na(I), Ba(II), Mn(II), Cd(II)	NaCl, $BaCl_2$, $MnCl_2$ and $CdCl_2$	Gas binding	34
$[Zn_4O(bdc)_{3-x}(btb)_x]$ (ligand doped MOF-5)	Pd(II)	$Pd(OAc)_2$	Catalysis	31
Pore uptake and/or cation exchange (Section 3)				
$[Zn_3(O)L_6]$	Ru(II)	$[Ru(2,2'\text{-bipyridine})_3]^{2+}$		35
$[H_2ppz][In_2L_2]$ (NOTT-208)	Li(I)	LiCl	Gas storage	36,37
$[Me_2NH_2]_{48}[In_{48}(\text{imidazole-dicarboxylate})_{90}]$	Na(I), Li(I), Mg(II)	$M(NO_3)_x$	Gas storage	38
$(NH_2Me_2)_2[Mn_3(L)_2]$	Co(II), Cu(II), Ni(II), Zn(II), Li(I), Na(I), Mg(II)	$M(NO_3)_x$	Selective metal uptake	39
$[Zn_8(ad)_4(bpdc)_6O]\cdot 2Me_2NH_2$	Tb^{3+}, Sm^{3+}, Eu^{3+}, Yb^{3+}	$M(NO_3)_3$	Luminescence	40 (see also 41–46)
$[Zr_6O_4(OH)_4(bdc)_6]$	Li(I)	Li(O^{t}Bu)	Solid electrolyte	47 (see also 48–51)
$[Zn_2(ndc)_2(dipyni)]$	Li(I), Na(I), K(I)	Li(0), metal napthalenides	Gas storage	52–54
[Zn(4-pyridyl-4-phenyl-diketonate)$_2$]	Fe(II)	$Fe(acac)_3$	Luminescence quenching	55
$[Zn_4O(bdc)_3]$ (MOF-5)	Fe(II)	$Fe(C_5H_5)_2$		56
[Al(OH)bdc]	Fe(II)	$Fe(C_5H)_2$, $Fe(C_5H_5)(C_5H_4COH)$		57
$[Cr_3F(H_2O)O(bdc)_2]$ (MIL-101)	Fe(II), Ru(II)	Perfluorinated and dimeric phthalocyanine complexes	Catalysis	58
$[Cr_3F(H_2O)O(bdc)_2]$ (MIL-101)	Fe(II)	Iron tetrasulfophthalocyanine	Catalysis	59
$[Cu_3(btc)_2]$ (HKURST-1)	Li(I), Na(I), Al(III)	$LiBH_4$, $NaAlH_4$	Gas storage	60–62

[a] For similar summaries of complex uptake before nanoparticle formation (Section 3.3.2); and transmetallations (Section 4), see references 63 and 64, respectively.

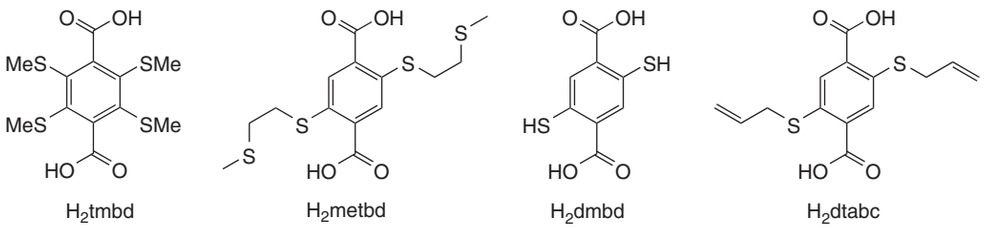


Chart 1 Thioether and thiol derivatized bridging benzene-1,4-dicarboxylic acid ligands for MOF synthesis leaving pendant S-donor groups

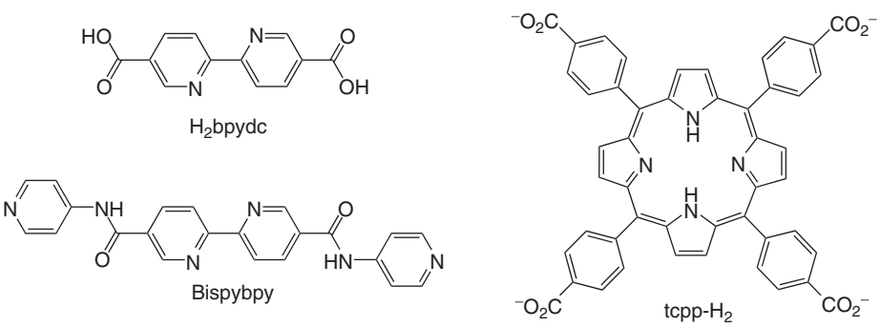


Chart 2 Ligands for MOF synthesis leaving pendant N-donor groups

lined with thiol groups, Figure 2, and the MOF binds either Hg(II) from aqueous solution or gaseous Hg(0). Treatment of an acidified aqueous solution of $Hg(NO_3)_2$ with solid $[Zr_6O_4(OH)_4(dmbd)_6]$ leads to removal of 99.9% of the mercury from solution, through binding at the thiol sites.

Photoluminescence may be quenched in the presence of heavy metals, and in these examples, Hg(II) or Hg(0) uptake can be monitored by emission spectra as the fluorescence of the Zn-carboxylate or Zr-carboxylate MOFs is quenched in the presence of mercury. This suggests potential applications for these materials in monitoring the presence of mercury contamination and in its removal.

The related MOF $[Zn_4O(dtabc)_3]$ (dtabc = 2,5-dithioalloxy-1,4-benzenedicarboxylate, Chart 1), which is isorecticular with MOF-5, exhibits photoluminescence quenching when soaked in solutions containing one of a range of different metal salts, namely $PdCl_2$, $RuCl_3$, $AuCl_3$, AuCl, $IrCl_3$, $PtCl_2$, $AgNO_3$, $CuCl_2$, $NiCl_2$, $Co(NO_3)_2$, and $MnCl_2$ suggesting metal uptake by the MOF in each case.[10] $PdCl_2$ also showed a unique response in the visible region. Immersion of $[Zn_4O(dtabc)_3]$ in an acetonitrile solution of $Pd(NCCH_3)_2Cl_2$ resulted in a color change from light yellow to dark red within several minutes. This color change was not observed for other transition metals, and also occurred with Pd(II) in the presence of other transition metals. Thus, the material acts as a simple visual sensor for the presence of Pd(II). Interaction between the Pd(II) and the olefin groups of the ligand $dtabc^{2-}$ was indicated by Raman spectroscopy. Sensing of metal cations has also

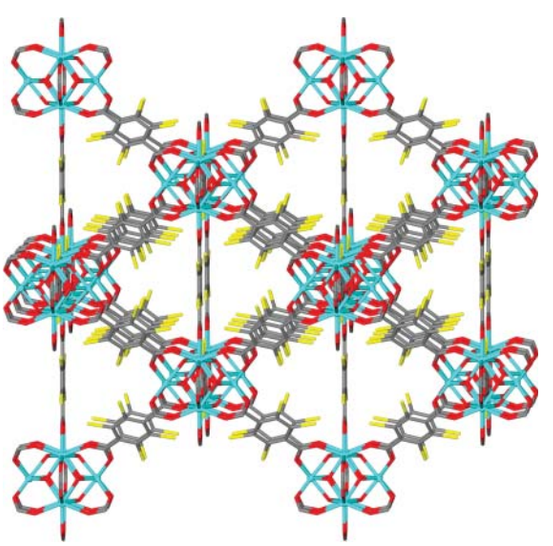


Figure 2 Structure of $[Zr_6O_4(OH)_4(dmbd)_6]$ with thiol S atoms shown in yellow. Owing to disorder, each apparent thiol group has 50% occupancy. These thiol groups bind Hg(II) or Hg(0)[9]

been demonstrated for $[Eu(pdc)_{1.5}(DMF)]$ (pdc = pyridine-1,3-dicarboxylate; DMF = dimethylformamide), a MOF with a pendant pyridyl group available for metal uptake.[11]

2.1.2 Ligands with N or P Donor Atoms

The hard–soft metal-ligand approach was also employed by Long, Yaghi, and coworkers using 2,2′-bipyridine-5,5′-dicarboxylate ($bpydc^{2-}$, Chart 2) paired with Al(III).[12] Al(III) is a hard metal and preferentially interacts with the carboxylate groups rather than the softer 2,2′-bipyridine. The resultant MOF, [Al(OH)(bpydc)], has an extended MIL-53-type structure with channels lined with unmetalled, and potentially chelating, 2,2′-bipyridine groups. The Al(III) nodes in [Al(OH)(bpydc)] impart a high degree of chemical and thermal stability. Soaking the desolvated MOF in either acetonitrile solutions of $PdCl_2$ or $Cu(BF_4)_2$ led to metal uptake, with pXRD showing retention of the MOF structure. The Pd(II) environment in the doped MOF was probed using X-ray absorption fine structure (EXAFS), which gave Pd–N and Pd–Cl bond distances in good agreement with the analogous molecular compound [Pd(2,2′-bipyridine)Cl_2] and demonstrates that the $PdCl_2$ has indeed been grafted onto the walls of the MOF framework. The copper loaded MOF showed a significantly enhanced ability to bind CO_2, with an increased average isosteric heat of adsorption.

2,2′-Bipyridine is a versatile metal-binding agent, and catalytically active Ru(III) can be bound at the bpy groups of the same MOF, [Al(OH)(bpydc)]. Treating crystalline [Al(OH)(bpydc)] with $[RuCl_4(DMSO)][(DMSO)_2H]$ (DMSO = dimethylsulfoxide) in ethanol at reflux gives $[Al(OH)(bpydc)]\cdot 0.13[RuCl_3(DMSO)]$.[13] The ruthenated MOF catalyzed the oxidation of primary and secondary alcohols, with high conversion levels under mild conditions.

Functionalized 2,2′-bipyridine ligands were also employed in the synthesis of the MOF [Zn(iso)(bispybpy)] (iso = isophthalate/benzene-1,3-dicarboxylate; bispybpy = *N*,*N*′-bis(pyridin-4-yl)-2,2′-bipyridine-5,5′-dicarboxamide), which has an unusual self-catenating framework structure. The Zn(II) nodes are only coordinated by bridging isophthalate anions and the monodentate pyridyl groups of the bispybpy ligand, leaving chelating sites empty. Immersion of the MOF in a DMF solution of $CuCl_2$ results in the uptake of Cu(I) at the bipyridine sites, Figure 3, in a single crystal-to-single crystal (SCSC) manner.[14]

The macrocyclic effect can also be employed. MOF $[Zr_6O_4(OH)_4(tcpp\text{-}H_2)_3]$ (tcpp-H_2 = tetra(carboxyphenyl) porphyrin, Chart 2) is constructed using unmetallated porphyrin square planar tectons. The MOF can be quantitatively metalled in an SCSC manner to form $[Zr_6O_4(OH)_4(tcpp\text{-}FeCl)_3]$ by immersion in a DMF solution of $FeCl_3$ at 100 °C.[15] Interestingly, this MOF could not be formed directly using a premetallated H_4tcppFeCl precursor.

2.2 Pendant Alcohols and Carbenes

Direct post-synthetic grafting of catalytically active metal species onto the framework of MOFs has also been effected using ligands groups where initial deprotonation of the metal-binding group is required. This usually occurs simultaneously with metallation.

Lin and coworkers reported the chiral MOF $[Cd_3Cl_6(pybinol)_3]$ where pybinol is the pyridine-decorated chiral binol ligand (*R*)-6,6′-dichloro-2,2′-dihydroxy-1,1′-binaphthyl-4,4′-bipyridine shown in Chart 3.[16] The

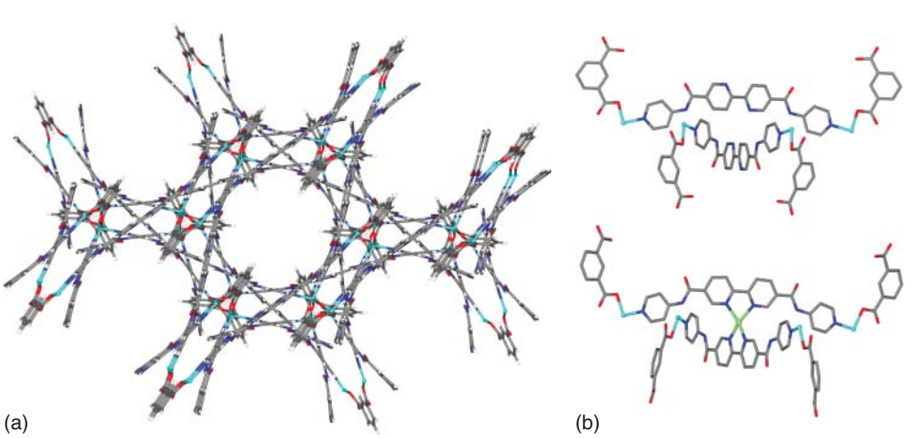


Figure 3 (a) Crystal structure of [Zn(iso)(bispybpy)]; (b) unmetalled bipyridine groups of [Zn(iso)(bispybpy)] shown at top, with Cu(I) uptake shown in bottom figure[14]

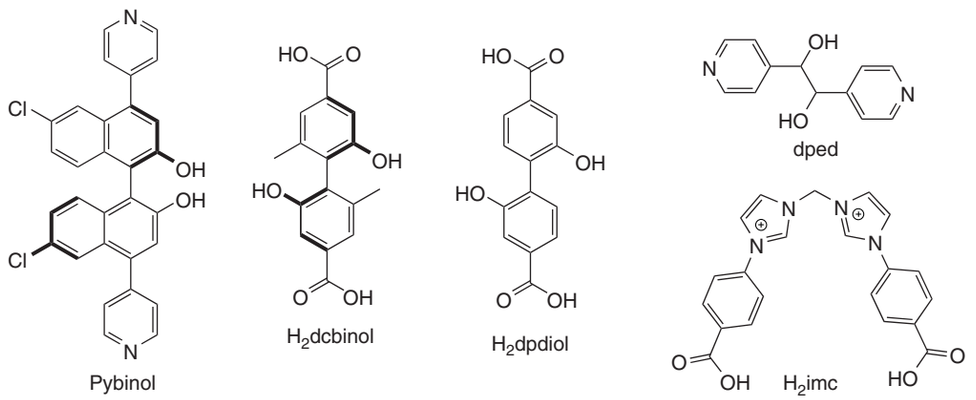


Chart 3 Ligands for MOF synthesis leaving available hydroxyl or carbene groups

structure features channels lined by the binol groups, some of which form strong OH … O hydrogen bonds between adjacent ligands, but one-third of which do not show strong supramolecular interactions. Treatment of $[Cd_3Cl_6(pybinol)_3]$ with $Ti(O^iPr)_4$ results in the formation of catalytically active binolate-$Ti(O^iPr)_2$ sites within the MOF. This catalyzes the addition of $ZnEt_2$ to aromatic aldehydes with complete conversion and enantiomeric excess values comparable to those seen in homogeneous systems. A similar approach was adopted by Jeong *et al.*[17] who reported a chiral Cu-carboxylate MOF from (*S*)-2,2′-dihydroxy-6,6′-dimethyl(1,1′-biphenyl)-4,4′-dicarboxylic acid (H_2dcbinol). The MOF $[Cu_2(dcbinol)(H_2O)_2]$ has an NbO-type structure with very large 2 × 2 × 2 nm pores and pendant diol groups that can be metalled through treatment with $Ti(O^iPr)_4$ or $ZnMe_2$. The metalled $[Cu_2(dcbinol)(H_2O)_2]$ MOFs were shown to catalyze hetero-Diels–Alder reactions with enhanced stereoselectivity, which was attributed to the reactions occurring within the exaggerated chiral environment near the metallation sites.

Other examples of the metallation of pendant alcohol groups occur for $[Zn_4O(dpdiol)_3]$ (dpdiol = diphenyl-2,2′-dihydroxy-4,4′-dicarboxylate, Chart 3), which is isorecticular with MOF-5, and takes up $CuCl_2$ from DMF solution,[18] and $[Zn(btp)(dped)_2]$ (btp = benzene-1,3,4,6-tetra(4-phenylcarboxylate); dped =1,2-di-4-pyridyl-1,2-ethanediol, Chart 3) with readily accessible diol groups (Figure 4), which can bind Li(I) or Mg(II).[19] The metallated $[Zn(btp)(dped)_2]$ MOFs showed modestly enhanced H_2 storage properties over the parent MOF. Likewise, the MIL-53 analog [Al(OH)(hbd)] (hbd =2-hydroxy-benzene-1,4-dicarboxylate) has a pendant hydroxyl on the bridging ligand and treatment with lithium diisopropylamide results in partial lithiation of these groups.[20] Again, lithiation of the MOF resulted in enhanced H_2-binding properties.

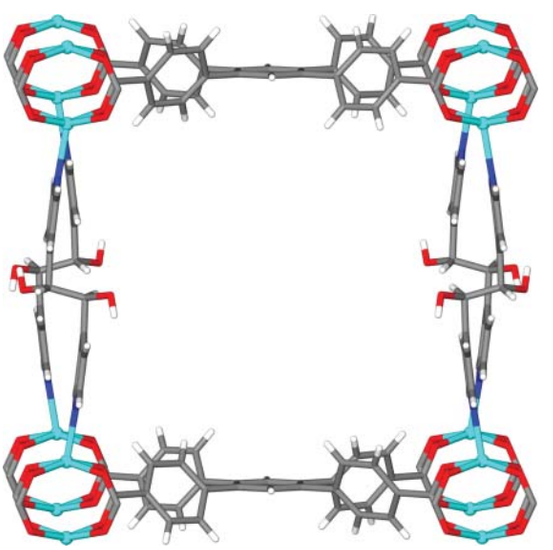
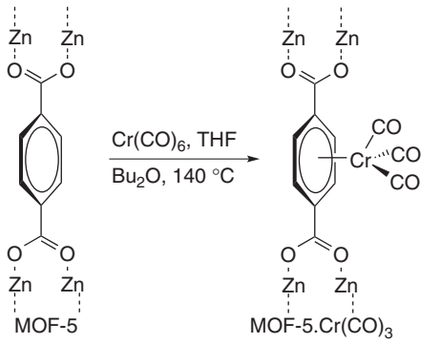


Figure 4 Section of the crystal structure of $[Zn(btp)(dped)_2]$. Only one disorder position is shown for each bridging ligand for the sake of clarity. The pendant alcohol groups directed into the MOF cavities can form R–O–M bonds with M = Li(I) and Mg(II)[19]

The complex $[Cu_2(imc)_2(MeOH)_2]$ (imc =1*H*-imidazolium,3,3′-methylenebis[1-(4-carboxyphenyl)], Chart 3) is a 2D coordination polymer where the linker ligand features *bis*-imidazolium residues.[21] Deprotonation of the imidazolium groups creates *N*-heterocyclic carbenes that are excellent σ-donor ligands.[66] Treatment of $[Cu_2(imc)_2(MeOH)_2]$ with $Pd(OAc)_2$ results in Pd(II) being grafted onto the coordination polymer at the *bis*-carbenes, with around 76% of the imidazolium groups being palladated. The Pd(II)-doped material behaved as a catalyst for Sukuki–Miyaura coupling reactions.



Scheme 1 Direct metallation of arene rings of MOF-5[22]

2.3 Uptake of Organometallics

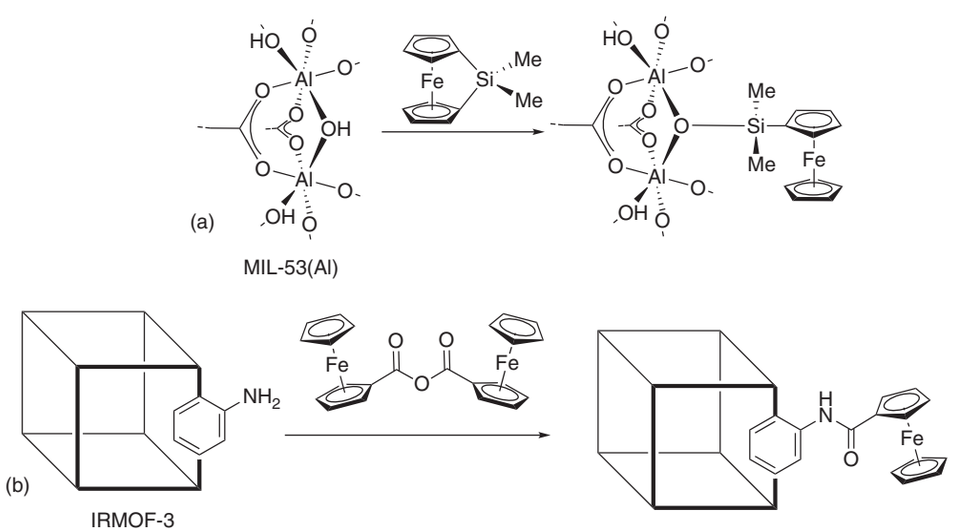
2.3.1 Grafting onto Arene Rings

Direct metal uptake in MOFs can occur by utilizing the arene rings of the linker ligands in MOF structures to form organometallic complexes with appropriate metal complex precursors. For example, MOF-5 may be metallated through reaction with $Cr(CO)_6$ in a sealed tube reaction.[22] The infrared spectrum of the metallated MOF exhibits new ν_{co} stretches corresponding to those of molecular $(H_2bdc)Cr(CO)_3$ indicating that the bdc^{2-} walls of MOF-5 are binding $Cr(CO)_3$ in an η^6 manner, Scheme 1. The MOF-5·$Cr(CO)_6$ complex displays further reactivity, and one CO ligand can be exchanged for an N_2 or H_2 ligand under photolysis conditions. $Cr(CO)_3$ fragments can also be grafted onto arene groups of MOF $[Zr_6O_4(OH)_4(bdc)_6]$ (UiO-66).[23] Similarly, the MOF $[Ni_2(dhbd)]$ (dhbd = 2,5-dihydroxybenzene-1,4-dicarboxylate) can be metallated through chemical vapor deposition (CVD) with sublimation of $Mo(CO)_6$ into the MOF pores.[24] Again infrared spectroscopy supports the formation of $(dhbd)Mo(CO)_3$ species on the MOF framework, and microanalysis indicates that half of the $dhbd^{2-}$ ligands are metallated. This material was degraded under an atmosphere of dihydrogen-hydrogen sulfide to give a heterogeneous catalyst for hydrodesulfurization reactions.

Organometallic reagents are also used for pore doping of metal complexes through CVD or immersion methods before reduction to form metal nanoparticles within the MOFs. The reagents are contained within the MOF pores rather than chemisorbed to its surface, more details can be found in Section 3.3.

2.3.2 Grafting onto Other Pendant Functional Groups

Organometallic fragments can be directly grafted onto MOFs through PSM of appropriate pendant functional groups. Fisher and coworkers demonstrated that the bridging hydroxides in crystalline [Al(OH)(bdc)], MIL-53(Al), will react with the silane group of 1,1′-ferrocenediyl-dimethylsilane in the vapor phase to form a tethered ferrocene, Scheme 2(a).[25] The ferrocene decorated MIL-53(Al) showed activity as a redox catalyst, demonstrating that such strategies can be used to develop redox active MOFs. A further example of tethering a ferrocene fragment onto a MOF utilizes a pendant amine group on the organic linker. MOF $[Zn_4O(NH_2bdc)_3]$ (NH_2bdc = 2-amino-benzene-1,4-dicarboxylate), also referred to as IRMOF-3 as it is isorecticular with MOF-5, has pendant



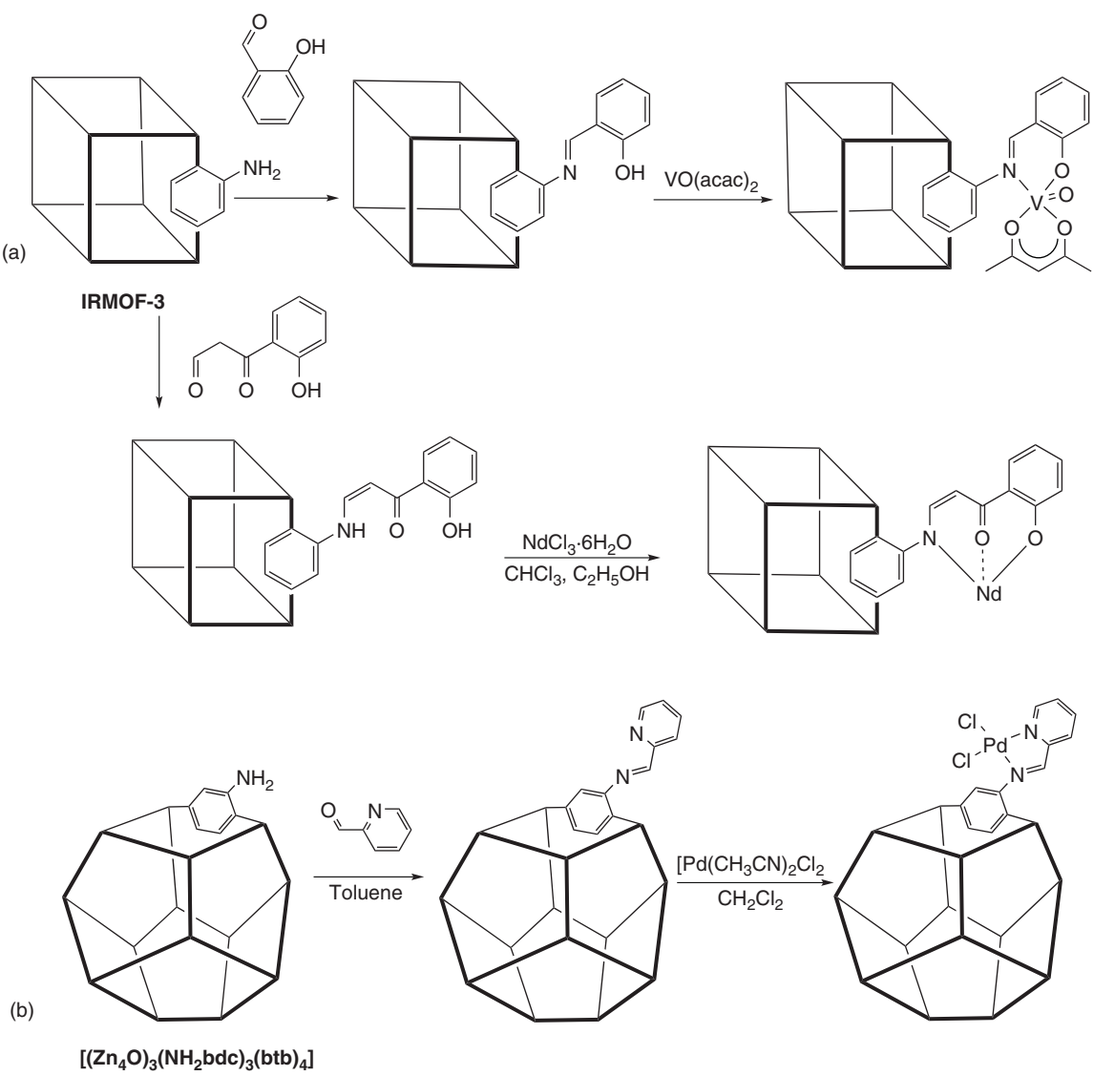
Scheme 2 Attaching ferrocene moieties onto (a) MIL-53(Al)[25] and (b) IRMOF-3[26]

amine groups. Burrows, Marken, and coworkers reacted IRMOF-3 with ferrocenecarboxylic anhydride to tether ferrocene through an amide linker, Scheme 2(b).[26]

Pendant hydroxide ligands in a MOF can also be directly metalled with organometallic reagents. Quadrelli has demonstrated that the bridging hydroxides of MOF $[Zr_6O_4(OH)_4(bpdc)_6]$ (bpdc = 1,1′-biphenyl-4,4′-dicarboxylate) can undergo various PSMs. These include grafting of MgBr using the Grignard reagent MeMgBr, and grafting of $Au(PMe_3)$ through treatment with $MeAu(PMe_3)$.[29] Farha and Hupp have recently reported a Zr-based MOF, $[Zr_6(\mu_3\text{-}OH)_8(OH)_8(TBAPy)_2]$ (TBAPy = 1,3,6,8-tetrakis(*p*-benzoate)pyrene) where 1D hexagonal channels are lined by terminal hydroxide ligands.[30] Vapor-phase atomic layer deposition techniques were used to treat this MOF with $ZnEt_2$ or $AlMe_3$, with the grafted metal species shown to bind at the terminal hydroxides. Metal loading occurred at an average of 0.5 Zn per Zr or 1.4 Al per Zr, and the metallated MOFs were active catalysts.

2.4 PSM Creation of Pendant Ligand Site

The pendant amine groups of IRMOF-3 have also been utilized in two-step PSM procedures where the initial step creates a ligand group, followed by metal binding, Scheme 3. Rosseinsky and coworkers derivatized IRMOF-3 by treatment with salicylaldehyde, which converted *ca.* 13% of the amine groups to the imine, salicylidene.[27] Each of these salicylidene units can be subsequently metalled through treatment with $VO(acac)_2$, Scheme 3(a). The



Scheme 3 Two-step PSM to attach metal complexes to (a) IRMOF-3,[27,28] and (b) $[(Zn_4O)_3(NH_2bdc)_3(btb)_4]$[67]

vanadyl-derived IRMOF-3 material thus formed was an active catalyst for the oxidation of cyclohexene, but the catalyst had poor turnover frequency and showed loss of framework integrity. A very high degree of amine conversion was found by Silva, Rocha, and coworkers who reacted IRMOF-3 with 3-(2-hydroxyphenyl)-3-oxopropanal to covert 90% of the amine groups to chelating ligand groups, Scheme 3(a).[28] Lanthanide metal uptake in some of these positions, specifically Nd^{3+} and Y^{3+}, converts the MOF into a near-infrared emitter.

Pendant amine functionality has also been used by Yaghi and coworkers in the heteroleptic MOF $[(Zn_4O)_3(NH_2bdc)_3(btb)_4]$ where btb = benzene-1,3,5-tris(benzene-4-carboxylate), which has an edge-sharing cage structure shown schematically in Scheme 3(b). Treatment with 2-pyridinecarboxaldehyde coverts the amines to an iminopyridyl, and quantitative metallation was achieved by subsequent reaction with $[Pd(CH_3CN)_2Cl_2]$, Scheme 3(b).[67]

An alternative approach is to utilize coordinatively unsaturated metal sites of a MOF to anchor additional bifunctional ligand groups. MIL-101(Cr), $[Cr_3F(H_2O)O(bdc)_2]$, is a chromium and benzene-1,4-dicarboxylate (bdc)-based MOF,[68] which can be dehydrated, removing aquo ligands and thus exposing coordinatively unsaturated Cr(III) cations. PSM with dopamine grafts the dopamine to the Cr(III) centers via its amine groups, leaving catechol groups of the dopamine available for a secondary PSM.[32] These catechols can then be metallated with $VO(acac)_2$. The material is an active catalyst for oxidation of organo-sulfide and, in contrast to an analogous homogeneous catalyst, shows selectivity for the sulfoxide product.

Not all metal cations within an as-synthesized MOF are structural. Selective removal of a nonstructural metal cation creates unmetalled ligand sites that can be used for subsequent metal uptake. This approach has been elegantly demonstrated by Hupp, Nguyen, and coworkers using a bis(pyridyl)-derived Mn(III)salen as a tecton for MOF synthesis. The Mn(III) is not a connecting node of the MnSO-MOF MOF framework, which has Zn(II) connecting nodes, Scheme 4.[33] The Mn(III) can be selectively removed by treatment with aqueous H_2O_2, which reduced the Zn:Mn ratio from 2:1 to *ca*. 20:1. Exposure of the manganese-depleted material to solutions containing M(II) salts, where M = Cr, Co, Mn, Ni, Cu, Zn, gave immediate color changes indicating metal uptake by the MOF. Remetallation occurred quantitatively to at levels close to quantitative, although the uptake of Cu(II) was at a higher level than anticipated. This was attributed to some Zn(II) sites within the framework being replaced by Cu(II). Such transmetallation phenomena in MOFs in covered in more detail in Section 4.

2.5 Ion Pair Grafting

Ion pair grafting involves both anionic and cationic uptakes at different specific site within a MOF. The MOF $[Cd_4(btp)_4]$ (btp = biphenyl-3,4′,5-tricarboxylate) was reported by Zaworotko and coworkers to form a [Cd(tetra(*N*-methyl-4-pyridyl)porphine)] template guest occupying half the MOF cavities.[34] The metal chlorides, NaCl, $BaCl_2$, $MnCl_2$, and $CdCl_2$, can each be grafted to the MOF in a SCSC manner, with the metal cation binding at carboxylate sites of the framework and the chlorides binding at the axial Cd(II) coordination site of the Cd(II)-porphyrin guest, Figure 5. These materials showed improved CO_2 uptake and selectivity over CH_4 compared with the parent.

2.6 Ligand Defect Approach

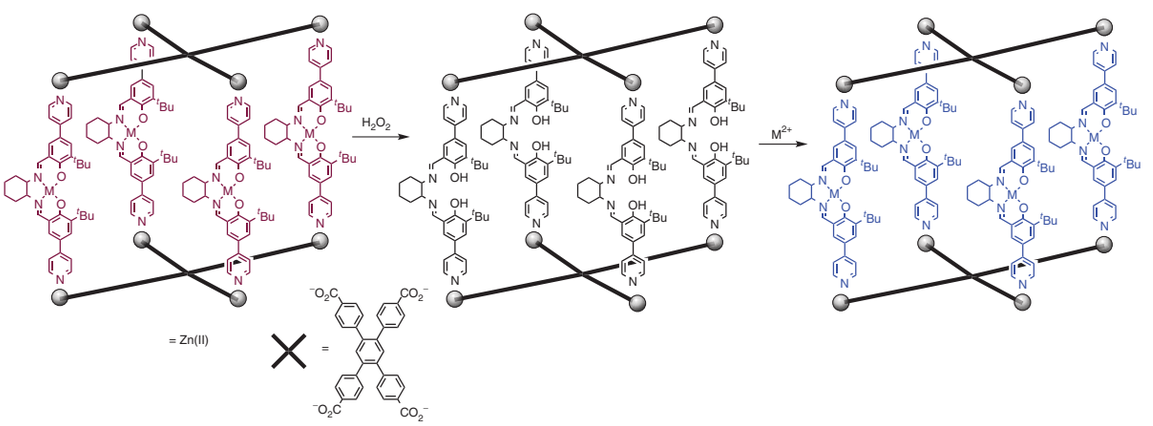
A novel approach to produce MOFs with pendant ligand sites is to introduce defects into the MOF lattice through copolymerization with two ligands. A "defective" analog of MOF-5 can be synthesized by doping in 5–10 mol% of H_3btb (btb =1,3,5-tris(4-carboxyphenyl)benzene) during the synthesis of MOF-5. The resultant $[Zn_4O(bdc)_{3-x}(btb)_x]$ MOF retains MOF-5-like connectivity but contains 5–10% btb each of which has a pendant carboxylic acid site, as only two of the three carboxylates are engaged in framework formation.[31] Treating this material with a CH_2Cl_2 solution of $Pd(OAc)_2$ resulted in an uptake of Pd(II), which was attributed to Pd(OAc) binding at the free carboxylates. The palladated MOF behaved as a catalyst. While similar treatment of pure MOF-5 with $Pd(OAc)_2$ did not result in notable Pd(II) uptake, other authors have reported pore uptake of other Pd(II) species such as $Pd(acac)_2$ into the pores of MOF-5 where there is no grafting to the framework.[63,69,70]

3 UPTAKE OF METALS INTO MOF PORES

MOFs are porous materials and while much of the focus of MOF development has been uptake of gaseous guest molecules, uptake of other neutral or charged guest species into the MOF pores is also well established. Some examples are given in Table 1.

3.1 Cation Exchange

MOFs with anionic frameworks have cationic guests for charge balance. Exchange of such cations is a further mechanism for uptake of metals into MOFs. This may involve exchange of a guest cation for a different guest cation, or the new cation may also bind to the framework. An early study from Kim and coworkers reports



Scheme 4 Demetallation and remetallation of salen struts of MnSO-MOF[33]

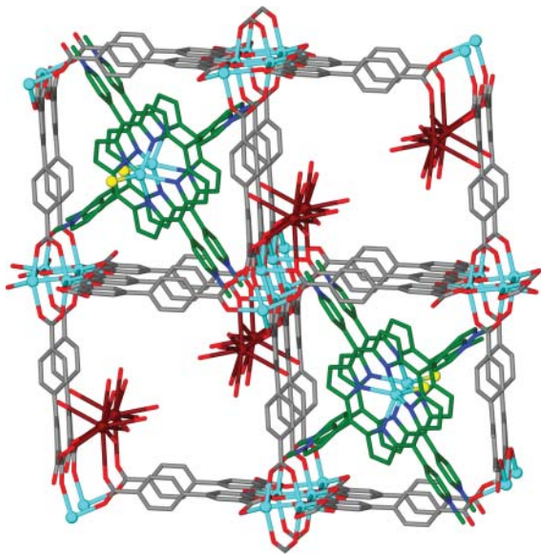


Figure 5 Anion and cation uptake showing binding of hydrated Ba^{2+} (shown in dark red) at $[Cd_4(btp)_4]$ MOF framework and binding of Cl^- (shown in yellow) by the guest Cd-porphyrin (in green)[34]

the cation exchange of H_3O^+ for $[Ru(2,2'\text{-bipyridine})_3]^{2+}$ in a homochiral Zn-based MOF with large channels.[35] Uptake of the metal complex occurs with a degree of enantioselectivity, with a 66% enantiomeric excess of the Δ isomer of $[Ru(2,2'\text{-bipyridine})_3]^{2+}$ being bound within the channels. Most reported examples, however, have investigated the exchange of organic ammonium or alkylammonium cations that reside within framework channels for a transition or main group metal cation.[36–43,71,72]

Champness, Schröder, and coworkers report the lithiation of a series of In(III)-based MOFs with tetracarboxylate ligands through exchange of the as-synthesized organic counter-cation $Me_2NH_2^+$ or Hppz (ppz = piperazine).[36,37] Immersion of the crystalline MOFs in a water/acetone solution of LiCl resulted in the $Me_2NH_2^+$ or Hppz cations being exchanged for Li(I) and H_3O^+ in a SCSC transformation. The Li(I) cations are bound to the framework, Figure 6. This has a marked effect on the hydrogen-binding properties of the MOFs with both an increase in percentage uptake and a significant increase in the isosteric heat of adsorption. Eddaoudi and coworkers have similarly reported enhanced H_2 binding through exchange of an organic counter-cation for Li(I) or Mg(II).[38]

Dalgarno, Thallapally, and coworkers also report a system where exchange of an organic cation for a transition metal cation also leads to grafting of the metal onto the MOF framework.[39] Complex $(NH_2Me_2)_2[Mn_3(L)_2]\cdot 9DMF$, where L = tetrakis[4-(carboxyphenyl)oxamethyl]methane, has an anionic $[Mn_3(L)_2]^{2-}$ framework charge balanced by organic cations. The organic cations can be exchanged for a variety of divalent metal cations. For Co(II), Cu(II), and Ni(II), the exchange takes place in a SCSC manner, and the counter-cation exchange is accompanied by both new metal sites being grafted onto the framework along with transmetallation (Section 4) to give frameworks with Mn:M stoichiometry of *ca*. 1:3. This process involves metal-carboxylate bond breakage and formation, occurs in two different manners, and is shown for Co(II) uptake in Figure 7.

Luminescence behavior in MOFs is another property that can be modulated through uptake of metal cations. The MOF itself may have inherent luminescence, or luminescent metals cations can be introduced. For example, the $Me_2NH_2^+$ cations that occupy the 1D channels of MOF $[Zn_8(ad)_4(bpdc)_6O]$. $2Me_2NH_2$ (ad = adeninate; bpdc = biphenyldicarboxylate) can be exchanged for the lanthanide cations, Tb^{3+}, Sm^{3+}, Eu^{3+}, or Yb^{3+} by soaking the as-synthesized MOF in DMF solutions of the nitrate salts of the lanthanides.[40] Lanthanides are luminescent; however, their emissions may be quenched in water and the design of luminescent lanthanide complexes or materials includes an antenna component. When suspended in water, the lanthanide-doped $[Zn_8(ad)_4(bpdc)_6O]$ materials displayed visible (for Ln = Tb, Sm, Eu) and near infrared (Ln = Yb) luminescence, demonstrating that the MOF is an effective luminescence sensitizer. MOFs constructed from lanthanide cations are often themselves luminescent, a property that may be moderated by uptake of other metal cations. Dong and coworkers report a luminescent, anionic Gd(II)-carboxylate MOF with guest $[Mn(H_2O)_6]^{2+}$ as the counter-cation.[44] The $[Mn(H_2O)_6]^{2+}$ can be partly exchanged for $[Tb(H_2O)_8]^{3+}$, which can in turn be exchanged for $[Eu(H_2O)_8]^{3+}$ and the original material regenerated by further cation exchange. The presence of different cations changes the luminescent properties; hence, luminescence of this MOF is tuneable through having different counter-cation compositions. Similar luminescence effects through reversible cation exchange are seen in related lanthanide-MOFS, and uptake of certain metals such as Fe(III) and Cu(II) leads to quenching of the fluorescence.[45]

Quenching or enhancement of luminescence within MOFs through metal cation uptake is a potential mechanism for the development of sensors. Sensors require selective guest uptake or a measurable response selective for a specific guest. Various luminescent MOFs with an ability to take up metal cations through cation exchange or other mechanisms, have shown sensor-like luminescence responses for targeted metals including Fe(III),[41,45] Cu(II),[42,45,46] Mg(II),[73] and Ag(I).[46]

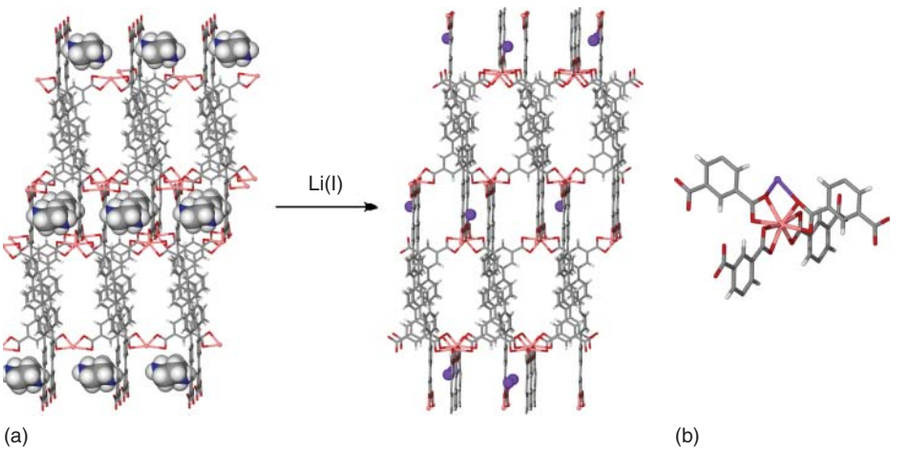


Figure 6 (a) Cation exchange of the organic Hppz cation (shown in space filling mode) for Li(I) (purple spheres); (b) highlight showing binding of Li(I) to framework. In(III) shown as pink spheres[37]

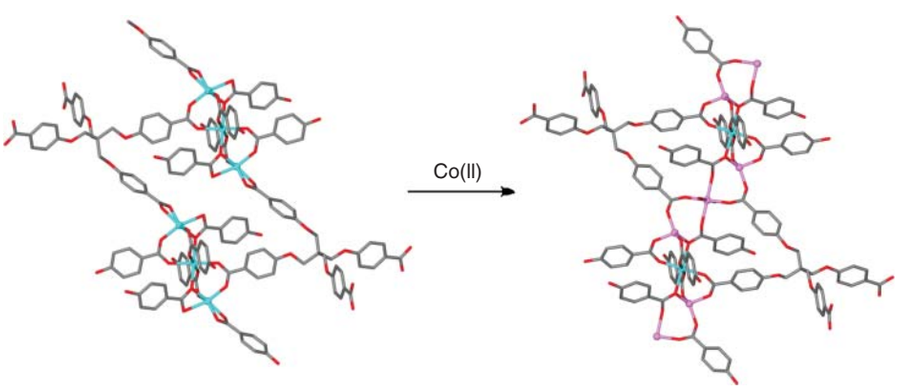


Figure 7 Metal cation grafting and transmetallation through cation exchange in $(NH_2Me_2)_2[Mn_3(L)_2]$, only fragments of most ligands are shown for clarity and same ligand fragments are shown in both figures. Mn = blue, Co = pink

3.2 Chemical Modification of MOF that Induces Cation Uptake

Another approach to metallation of a MOF is to chemically render a neutral MOF anionic with concomitant cation uptake to balance the charge. This can be achieved through grafting of an anionic group onto the MOF framework or through reduction of the framework.

MOF UiO-66, $[Zr_6O_4(OH)_4(bdc)_6]$, can be dehydrated to give a Zr_6O_6 cluster core with unsaturated Zr(IV) sites. Treatment of the dehydrated UiO-66 with lithium *t*-butoxide results in the butoxide anions being grafted onto the Zr(IV) sites, and the material must incorporate Li(I) cations in order to achieve charge balance.[47] The lithium butoxide-grafted UiO-66 is an ionic conductor with mobile Li(I) cations; hence, it may be suitable as a solid electrolyte for Li-based batteries. Similar studies investigating the potential of MOFs as electrolytes in lithium batteries have targeted coordinatively unsaturated Mg(II) sites.[48] There is currently considerable interest in MOFs as electrode materials for lithium ion batteries, owing to their ability to uptake and release Li(I) ions.[47–51]

Another approach to metallation of a MOF is to chemically reduce a neutral MOF with concomitant cation uptake to balance the charge, which has been pursued by Hupp and coworkers.[52–54] Remarkably, reduction of the twofold interpenetrating MOF $[Zn_2(ndc)_2(dipyni)]$ (ndc = 2,6-napthalenedicarboxylate; dipyni = *N*,*N*′-di-(4-pyridyl)-1,4,5,8-napthalenetetracarboxydiimide) can be achieved by direct reaction with Li(0) in DMF.[52] H_2 uptake is enhanced at an optimal Li(I) loading of ~5 mol%, and the hydrogen adsorption and desorption profile is hysteretic indicative of dynamic framework behavior. Such dynamic behavior was not observed in the unmetalled MOF. This MOF can also

be reduced by treatment with metal naphthalenides where the metal is Li(I), Na(I), or K(I), leading to uptake of the metals as counter-cations.[53,54] While there was a percentage increase in H_2 uptake for the metalled MOFs, there was little change in the isosteric heat of adsorption.

3.3 Pore Loading by Metal Complexes

3.3.1 Complexes and Ion Pairs in Pores

Metal complex can themselves be taken up as guests in the pores or channels of a MOF, which can alter properties such as gas binding or luminescence, or introduce new functionality such as catalysis. For example, a recently reported Zn-based MOF with an NbO-type structure can take up $[Fe(acac)_3]$ from solution, and this quenches the luminescence of the MOF.[55] Kim and coworkers report that ferrocene, $[Fe(\eta^5\text{-}C_5H_5)_2]$, can be sublimated into the pores of MOF-5 to give a well-ordered structure with efficiently packed pores, Figure 8.[56] Ferrocene is also strongly absorbed by MIL-53, [Al(OH)bdc], as is ferrocenealdehyde.[57]

Larger metal complexes such as metallophthalocyanines have also been reported to be absorbed from solution into the pores of MIL-101(Cr). Immersion techniques have been employed to effect the uptake of mononuclear and dinuclear metallophthalocyanine complexes to form catalytically active MOF-pthalocyanine materials.[58,59] For example, approximately 1.2 molecules per pore of [RuPcF16] (PcF16 = perfluorophthalocyanine) can be incorporated into MIL-101(Cr) and this material is an order of magnitude more active as an oxidation catalyst for tetralin than is free [RuPcF16].[58]

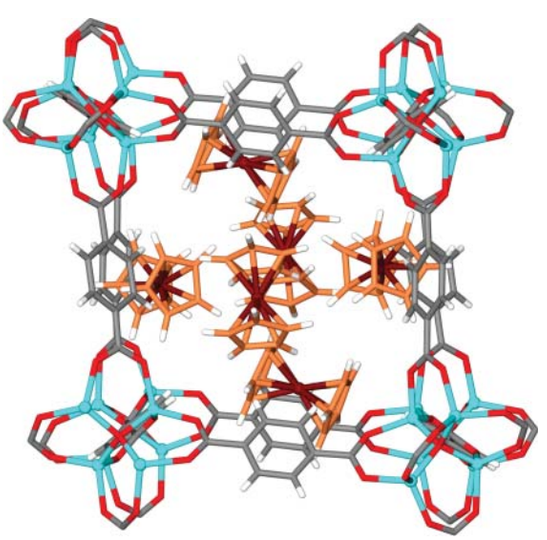


Figure 8 Crystal structure showing six ferrocene molecules in the smaller pore of MOF-5 in complex $[Fe(\eta^5\text{-}C_5H_5)_2]_7{\cdot}[Zn_4O(bdc)_3]$. The larger pore contains eight ferrocene molecules[56]

Small hydrogen-rich metal-containing species such as $LiBH_4$[60] and $NaAlH_4$[61,62] can be bound in the pores of $[Cu_3(btc)_2]$ (dehydrated HKUST-1, btc = benzene-1,3,5-tricarboxylate). An alternative approach to the problem of hydrogen storage is chemisorption where such hydrides release H_2 on heating, and the H_2 release characteristics of the hydrides embedded in MOFs were distinct from that of bulk hydrides.

Polyoxometallates are high nuclearity metal clusters, often anionic, and hybrid materials where polyoxometallates that are encapsulated by MOFs are emerging as novel catalytic materials, as recently reviewed by Gascon and coauthors.[70] The majority of these hybrid materials are formed by growth of the MOF around the polyoxometallate; however, there are also reports of polyoxometallates being taken up by MIL-101(Cr) through post-synthetic treatment.[68,74] MIL-101(Cr) has a particularly open mesoporous structure, large enough to allow passage of polyoxometallates.

3.3.2 Nanoparticles in MOFs

A number of research groups have investigated the uptake of redox active metal complexes as a precursor to the formation of metal nanoparticles inside MOFs. This area has recently been reviewed by Suh and co-workers,[63] hence only representative examples will be discussed. In most examples, pores within the MOF are loaded with a metal complex or salt through CVD or through immersion of the MOF in a solution containing the complex, and subsequent chemical reduction gives the metal nanoparticle embedded in the MOF. The MOFs with embedded nanoparticles may have enhanced H_2 storage because of $M{-}H_2$ interactions to the particles,[69,75,76] and they are effective solid-state catalysts.[69,77–80]

Fischer, and others, have demonstrated that CVD with volatile organometallic species is an effective method of pore loading MOFs.[81,82] Examples of organometallic complexes that can be loaded into MOF-5 are shown in Chart 4.[76,78,79,81,82] Vapor deposition is particularly effective at ensuring a high degree of pore loading, giving, for example, six ferrocene molecules per MOF cube pore.[81] Hydrogenolysis[77–79,82] or thermal decomposition[76] of the loaded MOFs in selected systems gives nanoparticles embedded in the MOF.

Pore loading can also be achieved through soaking the MOF in a solution containing a metal complex. For example, MOF-5 will uptake $Pd(acac)_2$ from a $CHCl_3$ solution,[69] MIL-100(Al) ($[Al_3F(H_2O)O(btc)_2]$) binds $[PdCl_4]^{2-}$ from aqueous acid,[75] and MIL-100(Cr) binds $[PtCl_6]^{2-}$ from a water/hexane mix.[80] Again, treatment with H_2 at an appropriate temperature results in the formation of metal nanoparticles within the pores.

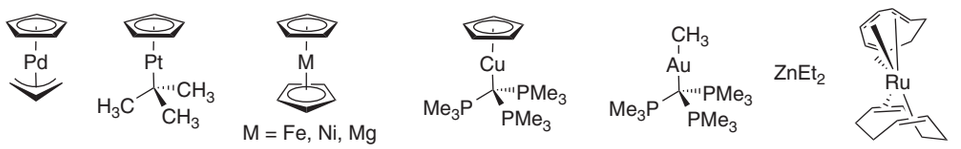


Chart 4 Examples of organometallic complexes that can be pore-loaded in MOF-5

The MOF system can itself be designed to both uptake the metal-containing nanoparticle precursor and effect the chemical reduction to a nanoparticle. The 1D coordination chain structures of [Ni(cyc)(bpdc)] (cyc = 3,10-dimethyl-hexaazacyclotetradecane) features Ni(II)cyc macrocycles linked by dicarboxylate bpdc ligands. These pack in a braided arrangement in the crystal lattice to form a robust porous solid. Immersion in a methanolic solution of $AgNO_3$ results in Ag(I) uptake and concomitant Ag(0) nanoparticle formation, with the Ni(II) acting as the reductant, noting that the cyc macrocycle stabilizes the unusual Ni(III) oxidation state.[83]

Similar methodologies can be used to embed quantum dots inside MOFs. The MOF $[Zn(Meim)_2]$ (ZIF-8; Meim = imidazolate-2-methyl) can be loaded with $[(CH_3)_3NGaH_3]$ through CVD, with three guest molecules per ZIF-8 pore.[84] The included $[(CH_3)_3NGaH_3]$ was reacted with ammonium gas at two different temperatures to give firstly cyclotrigallane, and then GaN quantum dots embedded in the pores.

4 TRANSMETALLATION

Transmetallation, or metal metathesis, in MOFs is a PSM that involves the substitution of one type of metal cation for another. This area has been recently reviewed by Hupp and coworkers.[64] The metal cation may be a structural node,[85–93] hence, an integral part of the framework structure, or a nonstructural metal action embedded in a ligand,[91,94,95] or terminal with respect to the framework structure.[96] There have been a number of recent reports of transmetallations in MOFs, which may occur concurrently with other metal uptake phenomena such as guest cation exchange and metal cation grafting. Most examples of metal cation methathesis in MOF involve immersion of a solid MOF in a solution of the alternative metal salt. Cohen, however, has demonstrated that the mixing in water of solid samples of two isostructural MIL-53 analogs, each with different metal nodes, results in metal methathesis between the solid particles.[86] Many of the known examples of metal metathesis involve MOFs with the labile d^{10} metal cations Zn(II), Cd(II), and Hg(II) as structural nodes.[87–95] It should be noted that linker ligands within MOFs have also been reported to undergo post-synthetic exchange.[86] Metathesis within MOFs is likely to be related to be related to the degree of lability in M–L bonding, however, has been documented to occur for both relatively labile M–N bonds and more inert M–carboxylate bonds. Such metal/ligand metathesis offers a novel mechanism for accessing MOFs that cannot be synthesized directly from their constituent components.[85,86,91]

One of the first examples of metal metathesis in MOFs was reported by Long. MOF $[Mn(DMF)_6]_3[(Mn_4Cl)_3(btt)_8(H_2O)_{10}]_2 \cdot m(CH_3OH)$ (btt = 1,3,5-benzenetristetrazolate) has guest $[Mn(DMF)_6]^{2+}$ counter-cations. On heating, the MOF loses solvent and transforms to $Mn_3[(Mn_4Cl)_3(btt)_8(MeOH)_{10}]_2$ in an SCSC manner. In the desolvated MOF, the charge-balancing Mn(II) is now bound to the framework in an "extra-framework," that is, non-node position, Figure 9.[96] The exposed Mn(II) gives the desolvated MOF enhanced H_2-binding properties. Long and coworkers have shown that this extra-framework cation position can be exchanged for other cations. Such transmetallation with Fe(II) or Co(II) leads to an increase in enthalpy of hydrogen adsorption compared with the parent compound.[97] Other cations, including Li(I), Cu(I),

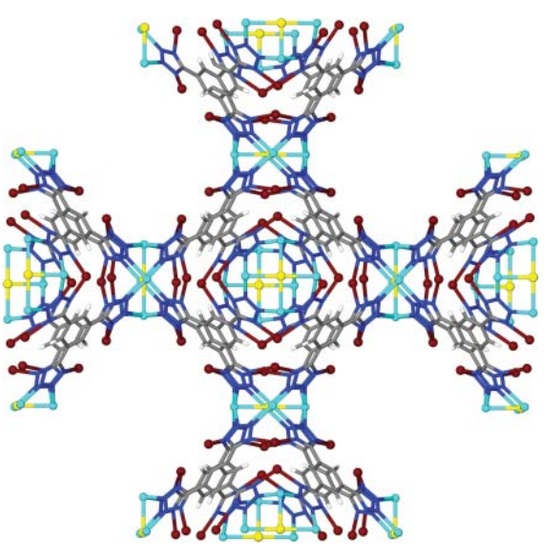


Figure 9 Crystal structure of $Mn_3[(Mn_4Cl)_3(btt)_8(MeOH)_{10}]_2$, with "extra-framework" Mn(II) positions shown in dark red and disordered coordinating solvent excluded for clarity. These extra-framework Mn(II) cations can be transmetallated for Fe(II), Co(II), or other cations. Light blue = framework Mn(II), yellow = Cl^-[96]

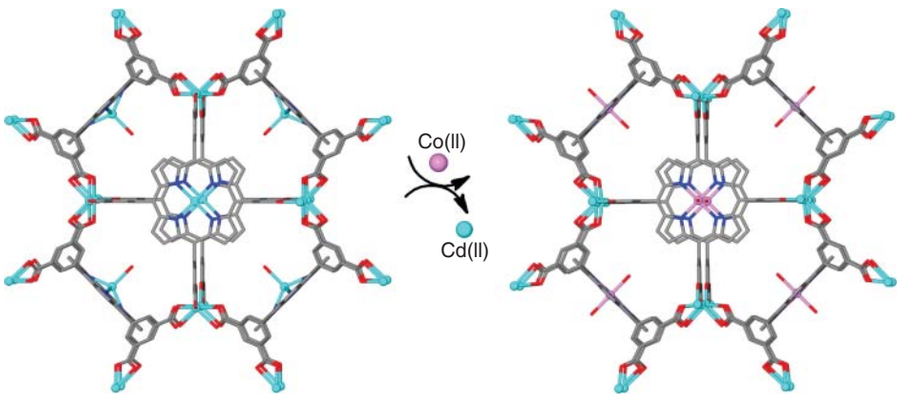


Figure 10 Exchange of nonstructural Cd(II) cations for Co(II) in MOF $[Cd_2(tdcpp)(Cd)(H_2O)]$. Disorder is not shown for the sake of clarity. Light blue = Cd(II); pink = Co(II)[95]

Ni(II), Cu(II), and Zn(II) can also be exchanged into the extra-framework position.

An early report of a complete transmetallation where all framework cations were swapped was reported by Kim and coworkers with the MOF $\{Cd_{1.5}(H_3O)_3\}$ $[(Cd_4O)_3(hett)_8]$ (hett = ethyl substituted truxene tricarboxylate).[89] A complete Cd(II) to Pb(II) exchange occurs in an SCSC manner on soaking the MOF in an aqueous $Pb(NO)_3$ solution, with the exchange 98% complete after only 2 h. The exchange was completely reversible; however, the reverse ion exchange was slower taking 3 weeks to complete. Mukherjee and Biradha[90] report an isostructural series of 2D coordination polymers $[M(btnic)(H_2O)_2].2(anion)$ (M(II) = Cu, Co, Cd, or Zn; bttn = benzene-1,3,5-triyltriisonicotinate) with kagome dual structures, that show SCSC metal metathesis behavior on immersion in methanol solutions of alternative metal salts. Exchange of Zn(II) for Cu(II) was effected within 6 h using $Cu(NO_3)_2$, whereas exchange of Cd(II) for Cu(II) was much slower, and only 53% complete after 10 days. Exchange of Cu(II) by Zn(II) or Cd(II) was not found to occur.

Zaworotko's $[Cd_4(btp)_4]\cdot[Cd(porph)]$ (porph = tetra(*N*-methyl-4-pyridyl)porphine) system discussed in Section 2.5 may undergo a stepwise metal metathesis, replacing the Cd(II) cations for Cu(II).[91] Immersion of $[Cd_4(btp)_4][Cd(porph)]$ crystals in a methanol solution of $Cu(NO_3)_2$ for 10 days leads to a complete exchange of Cd(II) for Cu(II) to give a new MOF with additional metal sites, $[Cu_8(X)_4(btp)_4][Cu(porph)]\cdot 4NO_3\cdot$solvent (X = OH^-, CH_3O^-). This MOF was inaccessible by direct synthesis and the transformation was irreversible. The degree of metathesis could be controlled through using a mixture of $Cd(NO_3)_2/Cu(NO_3)_2$ in the immersion solution. A 4:1 or 8:1 Cd/Cu ratio resulted in complete exchange of the nonstructural Cd(II) bound within the porphyrin, and only incomplete exchange of the framework carboxylate-bound Cd(II) cations. Interestingly, when metathesis was incomplete, then a degree of reversibility was observed for the system. Ma and coworkers have also shown that nonstructural cations within a porphyrin can be exchanged.[95] MOF $[Cd_2(tdcpp)(Cd)]$ (tdcpp = tetrakis(3,5-dicarboxyphenyl)porphine) is shown in Figure 10 with both structural Cd(II) nodes and nonstructural Cd(II) cations sitting above the plane of the porphyrin. Exchange of the nonstructural Cd(II) cations can be effected with Co(II), and these smaller cations sit flat in the plane of the porphyrin, Figure 10, and their presence converts the material into an active catalyst.

In an insightful piece of work by Lah and colleagues investigated transmetallation and epitaxial growth in the isostructural MOFs series $[M_6(btb)_4(4,4'\text{-bipyridine})_3]$ [M(II) = Zn, Co, Cu, Ni].[87] Transmetallation occurs from the Zn(II) MOF to the Co(II), Cu(II), or Ni(II) analog; however, the reverse transmetallation to the Zn(II) complex occurs only from Co(II). The Co(II) may be converted to the Cu(II) or Ni(II) and the Ni(II) to the Cu(II). Transmetallations occur from the outside of the crystal and proceed into the interior, allowing for isolation of core-shell crystals with macroscopic domains of different MOFs, simply by collecting the crystals before transmetallation is complete. The outside-in mechanism is consistent with the progress of other dynamic structural events in MOFs.[98] The least thermodynamically stable MOFs, the Zn(II) analog, can be epitaxially grown from a solution of $Zn(NO_3)_2$, H_3btb, and 4,4′-bpy onto the surface of crystals of the more thermodynamically stable MOFs to form $[Zn_6(btb)_4(4,4'\text{-bipyridine})_3]@[M_6(btb)_4(4,4'\text{-bipyridine})_3]$ (M = Co, Cu or Ni) core-shell crystals. The reverse was not the case, and attempts to use the least thermodynamically stable $[Zn_6(btb)_4(4,4'\text{-bipyridine})_3]$ as a seed crystal for epitaxial growth resulted in transmetallation of the Zn(II).

5 CONCLUSIONS

MOFs and coordination polymers are solid-state materials that display a range of inherent adaptabilities, including host–guest properties, structural dynamic behavior, and post-synthetic chemical modification. Recent research has shown that many MOFs have the ability to uptake metals and metal complexes through a variety of phenomena, including grafting directly onto the MOF framework, uptake into pores through host–guest binding or ion exchange, and transmetallation where metal cations inherent to the MOF framework structure are swapped. Metal uptake may occur through SCSC, crystalline powder-to-crystalline powder, and single crystal-to-crystalline powder transformations. While the uptake of metal complexes is known to occur through exposing the solid MOF to vapors of the metal complex, the majority of examples occur with the metal species introduced via immersion of the solid MOF in a solution of the metal species. It is therefore worth noting that some of these uptake phenomena are likely to be solvent-mediated and may involve concerted small-scale dissolution and recrystallization of the MOF as has been demonstrated for some anion-exchange processes in MOFs.[99] The uptake of metals or metal complexes by MOFs allows for the manipulation of MOF properties in a number of areas including luminescence and sensing, catalysis, gas binding, and cation exchange and binding; hence, it will be an important and fruitful area in the continued development of MOF chemistry.

6 RELATED ARTICLES

Postsynthetic Modification of Metal-Organic Frameworks; Open Metal Sites in Metal-Organic-Frameworks; Gas Storage in Metal-Organic Frameworks; Single-Crystal to Single-Crystal Transformations in Metal-Organic Frameworks; Porphyrinic Metal-Organic Frameworks.

7 ABBREVIATIONS AND ACRONYMS

acac = acetylacetonate; ad = adeninate; bdc = benzene-1,4-dicarboxylate; bispybpy = *N*,*N*′-bis(pyridin-4-yl)-2,2′-bipyridine-5,5′-dicarboxamide; bpdc = 1,1′-biphenyl-4,4′-dicarboxylate; bpydc = 2,2′-bipyridine-5,5′-dicarboxylate; btb = benzene-1,3,5-tris(benzene-4-carboxylate); btc = benzene-1,3,5-tricarboxylate; btp = biphenyl-3,4′,5-tricarboxylate; btt = 1,3,5-benzenetristetrazolate; CVD = chemical vapor deposition; cyc = 3,10-dimethyl-hexaazacyclotetradecane; dcbinol = (*S*)-2,2′-dihydroxy-6,6′-dimethyl(1,1′-biphenyl)-4,4′-dicarboxylate; dhbd = 2,5-dihydroxybenzene-1,4-dicarboxylate; dipyni = *N*,*N*′-di-(4-pyridyl)-1,4,5,8-napthalenetetracarboxydiimide; dmbd = 2,5-dimercapto-1,4-benzenedicarboxylate; dpdiol = diphenyl-2,2′-dihydroxy-4,4′-dicarboxylate; dped = 1,2-di-4-pyridyl-1,2-ethanediol; DMF = *N*,*N*′-dimethylformamide; DMSO = dimethylsulfoxide; dtabc = 2,5-dithioalloxy-1,4-benzenedicarboxylate; EXAFS = X-ray absorption fine structure; Et = ethyl; hbd = 2-hydroxy-benzene-1,4-dicarboxylate; HKURST-1 = $[Cu_3(btc)_2(H_2O)_2]$; imc = 1*H*-imidazolium,3,3′-methylenebis[1-(4-carboxyphenyl)]; IRMOF-3 = $[Zn_4O(NH_2bdc)_3]$; iso = isophthalate (benzene-1,3-dicarboxylate); Ln = lanthanide; Me = methyl; Meim = imidazolate-2-methyl; metbd = 2,5-bis-(2-(methylthio)ethylthio)-1,4-benzenedicarboxylate; MIL-53(Al) = [Al(OH)(bdc)]; MIL-100(M) = $[M_3F(H_2O)O(btc)_2]$, M = Al, Cr; MIL-101(Cr) = $[Cr_3F(H_2O)O(bdc)_2]$; MOF = metal-organic framework; MOF-5 = $[Zn_4O(bdc)_3]$; ndc = 2,6-napthalenedicarboxylate; NH_2bdc = 2-amino-benzene-1,4-dicarboxylate; OAc = acetate; PcF16 = perfluorophthalocyanine; pdc = pyridine-1,3-dicarboxylate; porph = tetra(*N*-methyl-4-pyridyl)porphine; ppz = piperazine; Pr = propyl; PSM = post-synthetic modification; pybinol = (*R*)-6,6′-dichloro-2,2′-dihydroxy-1,1′-binaphthyl-4,4′-bipyridine; SCSC = single crystal-to-single crystal; TBAPy = 1,3,6,8-tetrakis(*p*-benzoate)pyrene; tcpp-H_2 = tetra(carboxyphenyl)porphyrin; tdcpp = tetrakis(3,5-dicarboxyphenyl)porphine; tmbd = tetrakis(methylthio-)-1,4-benzenedicarboxylate; UiO-66 = $[Zr_6O_4(OH)_4(bdc)_6]$; ZIF-8 = $[Zn(Meim)_2]$

8 REFERENCES

1. R. Robson, *Dalton Trans.*, 2000, **21**, 3735.
2. O. M. Yaghi, M. O'Keeffe, N. W. Ockwig, H. K. Chae, M. Eddaoudi, and J. Kim, *Nature*, 2003, **423**, 705.
3. H.-C. Zhou, J. R. Long, and O. M. Yaghi, *Chem. Rev.*, 2012, **112**, 673.
4. C. Janiak and J. K. Vieth, *New J. Chem.*, 2010, **34**, 2366.
5. S. M. Cohen, *Chem. Rev.*, 2012, **112**, 970.
6. A. J. Nuñez, L. N. Shear, N. Dahal, I. A. Ibarra, J. Yoon, Y. K. Hwang, J.-S. Chang, and S. M. Humphrey, *Chem. Commun.*, 2011, **47**, 11855.
7. X.-P. Zhou, Z. Xu, M. Zeller, and A. D. Hunter, *Chem. Commun.*, 2009, 5439.
8. J. He, K.-K. Yee, Z. Xu, M. Zeller, A. D. Hunter, S. S.-Y. Chui, and C.-M. Che, *Chem. Mater.*, 2011, **23**, 2940.
9. K.-K. Yee, N. Reimer, J. Liu, S.-Y. Cheng, S.-M. Yiu, J. Weber, N. Stock, and Z. Xu, *J. Am. Chem. Soc.*, 2013, **135**, 7795.

10. J. He, M. Zha, J. Cui, M. Zeller, A. D. Hunter, S.-M. Yiu, S.-T. Lee, and Z. Xu, *J. Am. Chem. Soc.*, 2013, **135**, 7807.
11. B. Chen, L. Wang, Y. Xiao, F. R. Fronczek, M. Xue, Y. Cui, and G. Qian, *Angew. Chem. Int. Ed.*, 2009, **48**, 500.
12. E. D. Bloch, D. Britt, C. Lee, C. J. Doonan, F. J. Uribe-Romo, H. Furukawa, J. R. Long, and O. M. Yaghi, *J. Am. Chem. Soc.*, 2010, **132**, 14382.
13. F. Carson, S. Agrawal, M. Gustafsson, A. Bartoszewicz, F. Moraga, X. Zou, and B. Martín-Matute, *Chem. Eur. J.*, 2012, **18**, 15337.
14. T. Jacobs, R. Clowes, A. I. Cooper, and M. J. Hardie, *Angew. Chem. Int. Ed.*, 2012, **51**, 5192.
15. W. Morris, B. Volosskiy, S. Demir, F. Gándara, P. L. McGrier, H. Furukawa, D. Cascio, J. F. Stoddart, and O. M. Yaghi, *Inorg. Chem.*, 2012, **51**, 6443.
16. C.-D. Wu, A. Hu, L. Zhang, and W. Lin, *J. Am. Chem. Soc.*, 2005, **127**, 8940.
17. K. S. Jeong, Y. B. Go, S. M. Shin, S. J. Lee, J. Kim, O. M. Yaghi, and N. Jeong, *Chem. Sci.*, 2011, **2**, 877.
18. D. Rankine, A. Avellaneda, M. R. Hill, C. J. Doonan, and C. J. Sumby, *Chem. Commun.*, 2012, **48**, 10328.
19. K. L. Mulfort, O. M. Farha, C. L. Stern, A. A. Sarjeant, and J. T. Hupp, *J. Am. Chem. Soc.*, 2009, **131**, 3866.
20. D. Himsl, S. Wallacher, and M. Hartmann, *Angew. Chem. Int. Ed.*, 2009, **48**, 4639.
21. G.-Q. Kong, X. Xuan, C. Zou, and C.-D. Wu, *Chem. Commun.*, 2011, **47**, 11005.
22. S. S. Kaye and J. R. Long, *J. Am. Chem. Soc.*, 2008, **130**, 806.
23. S. Chavan, J. G. Vitillo, M. J. Uddin, F. Bonino, C. Lamberti, E. Groppo, K.-P. Lillerud, and S. Bordiga, *Chem. Mater.*, 2010, **22**, 4602.
24. C. Larabi, P. K. Nielsen, S. Helveg, C. Thieuleux, F. B. Johansson, M. Brorson, and E. A. Quadrelli, *ACS Catal.*, 2012, **2**, 695.
25. M. Meilikhov, K. Yusenko, and R. A. Fisher, *J. Am. Chem. Soc.*, 2009, **131**, 9644.
26. J. E. Halls, A. Hernán-Gómez, A. D. Burrows, and F. Marken, *Dalton Trans.*, 2012, **41**, 1475.
27. M. J. Ingleson, J. P. Barrio, J.-B. Guilbaud, Y. Z. Khimyak, and M. J. Rosseinsky, *Chem. Commun.*, 2008, 2680.
28. R. M. Abdelhameed, L. D. Carlos, A. M. S. Silva, and J. Rocha, *Chem. Commun.*, 2013, **49**, 5019.
29. C. Larabi and E. A. Quadrelli, *Eur. J. Inorg. Chem.*, 2012, 3014.
30. J. E. Mondloch, W. Bury, D. Fairen-Jimenez, S. Kwon, E. J. DeMarco, M. H. Weston, A. M. Sarjeant, S. T. Nguyen, P. C. Stair, R. Q. Snurr, O. M. Farha, and J. T. Hupp, *J. Am. Chem. Soc.*, 2013, **135**, 10294.
31. T. H. Park, A. J. Hickman, K. Koh, S. Martin, A. G. Wong-Foy, M. S. Sanford, and A. J. Matzger, *J. Am. Chem. Soc.*, 2011, **133**, 20138.
32. H. G. T. Nguyen, M. H. Weston, O. K. Farha, J. T. Hupp, and S. T. Nguyen, *CrystEngComm*, 2012, **14**, 4115.
33. A. M. Shultz, A. A. Sarjeant, O. K. Farha, J. T. Hupp, and S. T. Nguyen, *J. Am. Chem. Soc.*, 2011, **133**, 13252.
34. Z. Zhang, W.-Y. Gao, L. Wojtas, S. Ma, M. Eddaoudi, and M. J. Zaworotko, *Angew. Chem. Int. Ed.*, 2012, **51**, 9330.
35. J. S. Seo, D. Whang, H. Lee, S. I. Jun, J. Oh, Y. J. Jeon, and K. Kim, *Nature*, 2000, **404**, 982.
36. S. Yang, X. Lin, A. J. Blake, G. S. Walker, P. Hubberstey, N. R. Champness, and M. Schröder, *Nat. Chem.*, 2009, **1**, 487.
37. S. Yang, G. S. B. Martin, J. J. Titman, A. J. Blake, D. R. Allan, N. R. Champness, and M. Schröder, *Inorg. Chem.*, 2011, **50**, 9374.
38. F. Nouar, J. Eckert, J. F. Eubank, P. Forster, and M. Eddaoudi, *J. Am. Chem. Soc.*, 2009, **131**, 2864.
39. J. Tian, L. V. Saraf, B. Schwenzer, S. M. Taylor, E. K. Brechin, J. Liu, S. J. Dalgarno, and P. K. Thallapally, *J. Am. Chem. Soc.*, 2012, **134**, 9581.
40. J. An, C. M. Shade, D. A. Chengelis-Czegan, S. Petoud, and N. L. Rosi, *J. Am. Chem. Soc.*, 2011, **133**, 1220.
41. S. Dang, E. Ma, Z.-M. Sun, and H. Zhang, *J. Mater. Chem.*, 2012, **22**, 16920.
42. Y.-W. Li, J.-R. Li, L.-F. Wang, B.-Y. Zhou, Q. Chen, and X.-H. Bu, *J. Mater. Chem. A*, 2013, **1**, 495.
43. S. Liu, J. Li, and F. Luo, *Inorg. Chem. Commun.*, 2010, **13**, 870.
44. P. Wang, J.-P. Ma, Y.-B. Dong, and R.-Q. Huang, *J. Am. Chem. Soc.*, 2007, **129**, 10620.
45. P. Wang, J. P. Ma, and Y. B. Dong, *Chem. Eur. J.*, 2009, **15**, 10432.
46. F. Luo and S. R. Batten, *Dalton Trans.*, 2010, **39**, 4485.
47. R. Amelot, M. Aubrey, B. M. Wiers, A. P. Gómora-Figueroa, S. N. Patel, N. P. Balsara, and J. R. Long, *Chem. Eur. J.*, 2013, **19**, 5533.
48. B. M. Wiers, M.-L. Foo, N. P. Balsara, and J. L. Long, *J. Am. Chem. Soc.*, 2011, **133**, 14522.
49. C. Y. Cheng, S. J. Fu, C. J. Yang, W. H. Chen, K. J. Lin, G. H. Lee, and Y. Wang, *Angew. Chem. Int. Ed.*, 2003, **42**, 1937.
50. G. Combarieu, M. Morcrette, F. Millange, N. Guillou, J. Cabana, C. P. Grey, I. Margiolaki, G. Ferey, and J.-M. Tarascon, *Chem. Mater.*, 2009, **21**, 1602.
51. K. Saravanan, M. Nagarathinam, P. Balaya, and J. J. Vittal, *J. Mater. Chem.*, 2010, **20**, 8329.
52. K. L. Mulfort and J. T. Hupp, *J. Am. Chem. Soc.*, 2007, **129**, 9604.
53. K. L. Mulfort and J. T. Hupp, *Inorg. Chem.*, 2008, **47**, 7936.
54. K. L. Mulfort, T. M. Wilson, M. R. Wasielewski, and J. T. Hupp, *Langmuir*, 2009, **25**, 503.
55. G.-G. Hou, Y. Liu, Q.-K. Liu, J.-P. Ma, and Y.-B. Dong, *Chem. Commun.*, 2011, **47**, 10731.

56. H. Kim, H. Chun, G.-H. Kim, H.-S. Lee, and K. Kim, *Chem. Commun.*, 2006, 2759.
57. M. Meilikhov, K. Yusenko, and R. A. Fisher, *Dalton Trans.*, 2009, 600.
58. E. Kockrick, T. Lescouet, E. V. Kudrik, A. B. Sorokin, and D. Farrusseng, *Chem. Commun.*, 2011, **47**, 1562.
59. O. V. Zalomaeva, K. A. Kovalenko, Y. A. Chesalov, M. S. Mel'gunov, V. I. Zaikovskii, V. V. Kaichev, A. B. Sorokin, O. A. Kholdeeva, and V. P. Fedin, *Dalton Trans.*, 2011, **40**, 1441.
60. W. Sun, S. Li, J. Mao, Z. Guo, H. Liu, S. Dou, and X. Yu, *Dalton Trans.*, 2011, **40**, 5673.
61. R. K. Bhakta, J. L. Herberg, B. Jacobs, A. Highley, R. Behrens Jr, N. W. Ockwig, J. A. Greathouse, and M. D. Allendorf, *J. Am. Chem. Soc.*, 2009, **131**, 13198.
62. V. Stavila, R. K. Bhakta, T. M. Alam, E. H. Majzoub, and M. D. Allendorf, *ACS Nano*, 2012, **6**, 9807.
63. H. R. Moon, D.-W. Lim, and M. P. Suh, *Chem. Soc. Rev.*, 2013, **42**, 1807.
64. M. Lalonde, W. Bury, O. Karagiardi, Z. Brown, J. T. Hupp, and O. K. Farha, *J. Mater Chem. A*, 2013, **1**, 5453.
65. X.-P. Zhou, Z. Xu, M. Zeller, A. D. Hunter, S. S.-Y. Chui, and C.-M. Che, *Inorg. Chem.*, 2008, **47**, 7459.
66. W. A. Herrmann, *Angew. Chem. Int. Ed.*, 2002, **41**, 1290.
67. C. J. Doonan, W. Morros, H. Furukawa, and O. M. Yaghi, *J. Am. Chem. Soc.*, 2009, **131**, 9492.
68. G. Férey, C. Mellot-Draznieks, C. Serre, F. Millange, J. Dutour, S. Surblé, and I. Margiolaki, *Science*, 2005, **309**, 2040.
69. M. Sabo, A. Henschel, H. Fröde, E. Klemm, and S. Kaskel, *J. Mater. Chem.*, 2007, **17**, 3827.
70. J. Juan-Alcañiz, J. Gascon, and F. Kapteijn, *J. Mater. Chem.*, 2012, **22**, 10102.
71. T.-Z. Zhang, Z.-M. Zhang, Y. Lu, H. Fu, and E.-B. Wang, *CrystEngComm*, 2013, **15**, 459.
72. K. Akhbari and A. Morsali, *Dalton Trans.*, 2013, **42**, 4786.
73. B. Zhao, H.-L. Gao, X.-Y. Chen, P. Cheng, W. Shi, D.-Z. Liao, S.-P. Yan, and Z.-H. Jiang, *Chem. Eur. J.*, 2006, **12**, 149.
74. N. V. Maksimchuk, K. A. Kovalenko, S. S. Arzumanov, Y. A. Chesalov, M. S. Melgunov, A. G. Stepanov, V. P. Fedin, and O. A. Kholdeeva, *Inorg. Chem.*, 2010, **49**, 2920.
75. C. Zlotea, R. Campesi, F. Cuevas, E. Leroy, P. Dibandjo, C. Volkringer, T. Loiseau, G. Férey, and M. Latroche, *J. Am. Chem. Soc.*, 2010, **132**, 2991.
76. D.-W. Lim, J. W. Yoon, K. Y. Ryu, and M. P. Suh, *Angew. Chem. Int. Ed.*, 2012, **51**, 9814.
77. F. Schröder, D. Esken, M. Cokoja, M. W. E. Van den Berg, O. I. Lebedev, G. V. Tendeloo, B. Walaszek, G. Buntkowsky, H.-H. Limbach, B. Chaudret, and R. A. Fischer, *J. Am. Chem. Soc.*, 2008, **130**, 6119.
78. Y. K. Park, S. B. Choi, H. J. Nam, D.-Y. Jung, H. C. Ahn, K. Choi, H. Furukawa, and J. Kim, *Chem. Commun.*, 2010, **46**, 3068.
79. S. Proch, J. Herrmannsdörfer, R. Kempe, C. Kern, A. Jess, L. Seyfarth, and J. Senker, *Chem. Eur. J.*, 2008, **14**, 8204.
80. A. Aijaz, A. Karkamkar, Y. J. Choi, N. Tsumori, E. Rönnebro, T. Autrey, H. Shioyama, and Q. Xu, *J. Am. Chem. Soc.*, 2012, **134**, 13926.
81. S. Hermes, F. Schröder, S. Amirjalayer, R. Schmid, and R. A. Fischer, *J. Mater. Chem.*, 2006, **16**, 2464.
82. S. Hermes, M.-K. Schröter, R. Schmid, L. Khodeir, M. Muhler, A. Tissler, R. W. Fischer, and R. A. Fischer, *Angew. Chem. Int. Ed.*, 2005, **44**, 6237.
83. H. R. Moon, J. H. Kim, and M. P. Suh, *Angew. Chem. Int. Ed.*, 2005, **44**, 1261.
84. D. Esken, S. Turner, C. Wiktor, S. B. Kalidindi, G. V. Tendeloo, and R. A. Fischer, *J. Am. Chem. Soc.*, 2011, **133**, 16370.
85. Y. Kim, S. Das, S. Bhattacharya, S. Hong, M. G. Kim, M. Yoon, S. Natarajan, and K. Kim, *Chem. Eur. J.*, 2012, **18**, 16642.
86. M. Kim, J. F. Cahill, H. Fei, K. A. Prather, and S. M. Cohen, *J. Am. Chem. Soc.*, 2012, **134**, 18082.
87. X. Song, T. K. Kim, H. Kim, D. Kim, S. Jeong, H. R. Moon, and M. S. Lah, *Chem. Mater.*, 2012, **24**, 3065.
88. T. K. Prasad, D. H. Hong, and M. P. Suh, *Chem. Eur. J.*, 2010, **16**, 14043.
89. S. Das, H. Kim, and K. Kim, *J. Am. Chem. Soc.*, 2009, **131**, 3814.
90. G. Mukherjee and K. Biradha, *Chem. Commun.*, 2012, **48**, 4293.
91. Z. Zhang, L. Wojtas, M. Eddaoudi, and M. J. Zaworotko, *J. Am. Chem. Soc.*, 2013, **135**, 5982.
92. S. Huang, X. Li, X. Shi, H. Hou, and Y. Fan, *J. Mater. Chem.*, 2010, **20**, 5695.
93. Z.-J. Zhang, W. Shi, Z. Niu, H.-H. Li, B. Zhao, P. Cheng, D.-Z. Liao, and S.-P. Yan, *Chem. Commun.*, 2011, **47**, 6425.
94. Z. Zhang, L. Zhang, L. Wojtas, P. Nugent, M. Eddaoudi, and M. J. Zaworotko, *J. Am. Chem. Soc.*, 2011, **134**, 924.
95. X.-S. Wang, M. Chrzanowski, L. Wojtas, Y.-S. Chen, and A. Ma, *Chem. Eur. J.*, 2013, **19**, 3297.
96. M. Dincă, A. Dailly, Y. Liu, C. M. Brown, D. A. Neumann, and J. R. Long, *J. Am. Chem. Soc.*, 2006, **128**, 16876.
97. M. Dincă and J. R. Long, *J. Am. Chem. Soc.*, 2007, **129**, 11172.
98. B. F. Abrahams, M. J. Hardie, B. F. Hoskins, R. Robson, and G. A. Williams, *J. Am. Chem. Soc.*, 1992, **114**, 10641.
99. X. Cui, A. N. Khlobystov, X. Chen, D. H. Marsh, A. J. Blake, W. Lewis, N. R. Champness, C. J. Roberts, and M. Schröder, *Chem. Eur. J.*, 2009, **15**, 8861.

Photoreactive Properties Hosted in Metal-Organic Frameworks

Victoria J. Richards, Thomas J. Reade, Michael W. George and Neil R. Champness

University of Nottingham, Nottingham, UK

1	Introduction	363
2	Guest Detection	364
3	Chemical Modification of MOFs Using Photochemical Processes	365
4	Modification of Photochemical Processes Using MOFs	367
5	Conclusion	370
6	Acknowledgment	370
7	Related Articles	370
8	Abbreviations and Acronyms	370
9	Further Reading	370
10	References	370

1 INTRODUCTION

The field of metal–organic frameworks, typically called MOFs, represents one of the largest and most topical areas of current chemical research.[1] MOFs are prepared from the combination of metal cations, most commonly d- or f-block metals, and ligands capable of bridging metal centers to create polymeric framework structures.[2–4] Thus, the synthesis of MOFs relies on a basic understanding of the coordination bond and has developed from the long-established field of coordination polymers.[5] The first use of the term coordination polymer can be traced back to 1916[6] and one many even consider Prussian Blue as the first member of this now vast field of study.[7] However, the field began to grow following seminal papers by Robson in the early 1990s[2,3] followed by significant developments by Kitagawa[8] and Yaghi.[4]

The key features of MOFs that make them so attractive to researchers from so many fields are their regular structure and the positioning of components in three-dimensional space. Although such positioning occurs within molecular crystals, logical strategies to create well-controlled spacing and positioning of molecules are still in their infancy, despite the famous rallying call to crystal engineers from Maddox in 1988.[9] The beauty of MOFs lies in the fact that through a basic understanding of coordination chemistry, tracing all the way back to the original discoveries of Werner, the careful chemist can use relatively robust and predictable coordination bonds to position different components of a polymeric structure with respect to one another. This important feature of MOFs allows researchers to manipulate structure at the molecular scale within polymeric framework structures and hence to modify the material properties of the resulting structures. It is this basic premise that underscores the promise of MOFs in so many fields.[1] Thus, MOFs have found application in a wide variety of disciplines from gas storage[10–12] to drug delivery[13] and materials with magnetic properties.[14]

There are many excellent reviews[15–20] outlining the plethora of structural and material properties of MOFs, but this chapter focuses on the incorporation of photoactive components within MOFs. The opportunities to incorporate photoactive species within frameworks are readily achievable when one considers the building-block methodology[2,3] and the plethora of metal cations and ligands that can be exploited. Although it is possible to simply incorporate fluorescent metal cations, such as lanthanides or ligands, these systems have been excellently reviewed recently.[21] Similarly, photodimerization of ligands within MOFs has also been extensively reviewed and will not be

Metal-Organic Framework Materials. Edited by Leonard R. MacGillivray and Charles M. Lukehart.
© 2014 John Wiley & Sons, Ltd. ISBN 978-1-119-95289-3

covered in this contribution.[22,23] This chapter focuses on the use of photochemical processes in the development of new materials and processes in MOFs.

2 GUEST DETECTION

Exploiting the building-block methodology, it is easy to envisage the inclusion of chemical moieties within the framework structure whose photochemical properties can be modified by guest inclusion. In principal, any selectivity of guest inclusion induced by the framework structure can be used to prepare MOFs that can act as selective sensors for guest species. This approach has been demonstrated by a number of examples for a variety of systems including detection of volatile organic compounds (VOCs),[24] explosives,[25–27] small molecules,[28–30] anions,[31] and even biological systems such as spores.[32]

A particularly elegant study of luminescent sensing in MOFs, by Kitagawa *et al.*,[24] reported a $[Zn_2(1,4\text{-}BDC)_2(dpNDI)]$ (bdc, 1,4-benzenedicarboxylate; dpNDI, *N*,*N*′-di(4-pyridyl)-1,4,5,8-naphthalenediimide) framework that takes advantage of the photoactive nature of the NDI ligand to afford effective and sensitive sensing of a class of VOCs, specifically tropospheric air pollutants. While the as-synthesized framework demonstrates very weak fluorescence with a very low quantum yield, adsorption of VOCs by the material affords guest-dependent multicolor fluorescence with intense emissions in the visible region (Figure 1). Such characteristic distinctions are observed as a result of the induced-fit structural

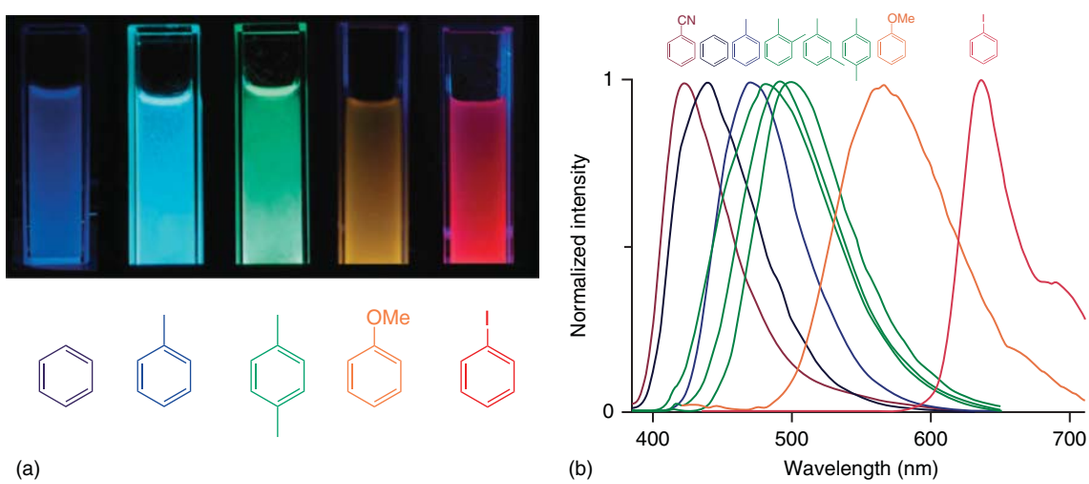


Figure 1 (a) Resulting luminescence of $[Zn_2(1,4\text{-}BDC)_2(dpNDI)]$ suspended in each VOC after excitation at 365 nm and (b) height-normalized luminescent spectra with incorporation of each VOC; excitation at 370 nm. (Reproduced with permission from Ref. 24. © Nature Publishing Group, 2011.)

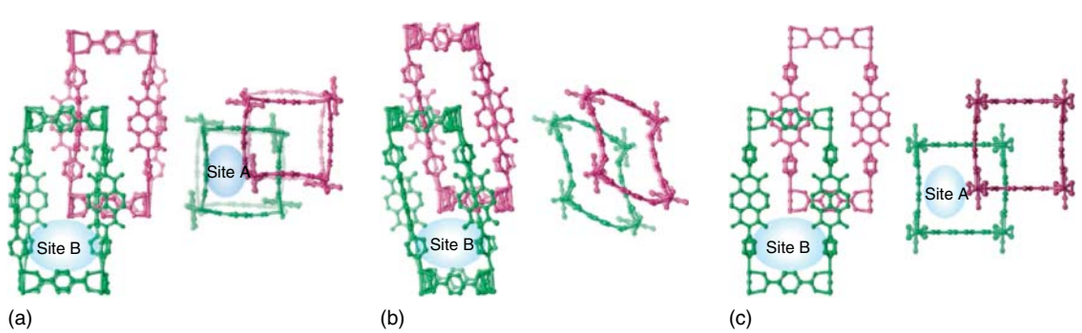


Figure 2 Illustration of the structural dynamics of the framework-crystal structures of $[Zn_2(1,4\text{-}BDC)_2(dpNDI)]$ hosting different guests: (a) 4 DMF molecules, (b) 1 DMF molecule, and (c) 2.5 toluene molecules. (Reproduced with permission from Ref. 24. © Nature Publishing Group, 2011.)

transformations of the interpenetrated framework. That is, two distinct MOF nets are entangled in such a manner as to offer two sites for adsorbate binding (sites A and B, Figure 2). Structural shifts of the two interpenetrated nets with respect to one other occur in order to maximize NDI–guest interactions. This results in a gradual red-shift in emission intensities as the electron-donating abilities of the VOC guest increases.

The basic concepts of using luminescent MOFs to detect target guest molecules has also been exploited to develop materials that act as explosive detectors.[25–27] The highly luminescent MOF $[Zn_2(bpdc)_2(bpee)]$ (bpdc = 4,4′-biphenyldicarboxylate; bpee = 1,2-bipyridylethene) has been shown to be capable of acting as a very fast and fully reversible detector of trace explosives 2,4-dinitrotoluene (DNT) and 2,3-dimethyl-2,3-dinitrobutane (DMNB).[25] The bpdc and bpee linkers provide both the source of luminescence and the chemical sensing element through their highly conjugated π-systems. On exposure to DNT and DMNB vapors, adsorption of each of these guests results in significant quenching of the framework's fluorescence (85% and 84%, respectively; Figure 3), and although the mechanism of this quenching effect is not yet fully understood, it is thought to proceed through a redox quenching mechanism similar to that in conjugated polymer systems.

3 CHEMICAL MODIFICATION OF MOFS USING PHOTOCHEMICAL PROCESSES

An intriguing feature of incorporating photoactive groups within MOFs is the possibility of using light to initiate chemical transformations within the framework environment and hence to exploit the framework environment to potentially stabilize unusual chemical species. This principle is demonstrated in a remarkable study by Kitagawa *et al.*, which shows the use of MOFs to stabilize highly reactive species within a MOF matrix.[33]

Reaction of 5-azidoisophthalic acid with $Zn(NO_3)_2.2H_2O$ and 4,4′-bipyridine affords a framework structure that incorporates azide moieties that protrude into a one-dimensional channel running through the framework structure. Irradiation of this material in a vacuum environment leads to cleavage of the azide moiety to generate a highly unusual and reactive nitrene species supported on the frameworks' isophthalate struts. Approximately 35–40% conversion was achieved, depending on the precise experimental conditions used, and established by IR spectroscopy and the identification of the triplet state of nitrene by electron spin resonance (ESR) spectroscopy. The identification of the nitrene within the MOF environment is particularly remarkable considering its highly reactive nature. The reactivity of the photogenerated nitrene species was established via the photoirradiation of the precursor azide-bearing MOF in an atmosphere of O_2. This leads to the formation of nitro- and nitroso-functionalized isophthalate struts through the reaction of the nitrene with oxygen.

A similar strategy of using photoactivation to cleave what may be viewed as protecting groups can similarly be used in the postsynthetic modification of MOFs.[34–36] Cohen *et al.* demonstrated[35] the use of a catechol-bearing terephthalic acid ligand, 2-((2-nitrobenzyl)oxy)terephthalic acid, into a MOF through the protection of the catechol moiety with nitrobenzyl

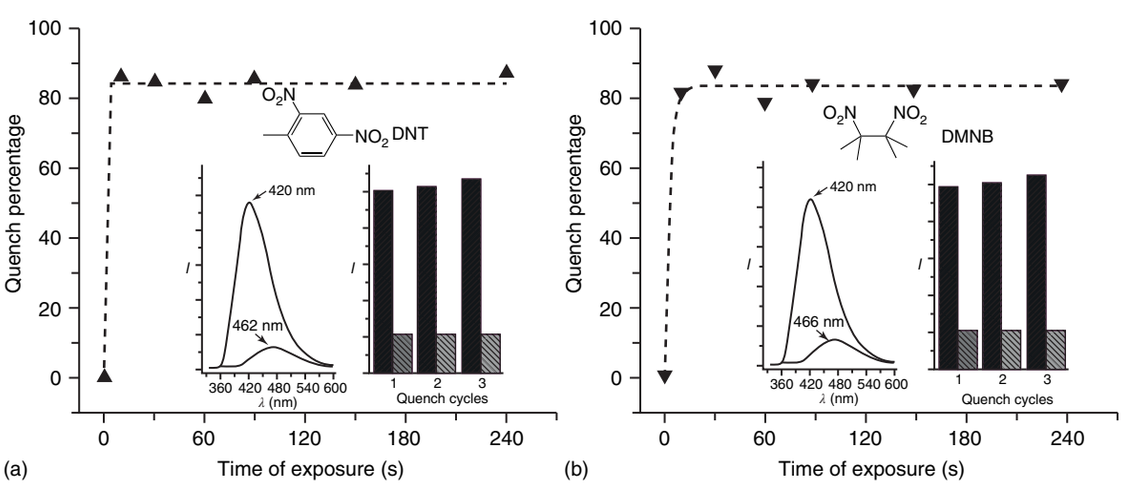


Figure 3 Time-dependant fluorescence quenching by (a) DNT and (b) DMNB. Insets: (left) corresponding fluorescence spectra before and after exposure to the analyte vapors for 10 s, and (right) three consecutive quench/regeneration cycles. (Reproduced with permission from Ref. 25. © Wiley-VCH Verlag GmbH & Co. KGaA, 2009.)

groups. Such an approach is essential due to the ability of catecholate moieties to act as ligands that would compete with the carboxylate groups used to create the framework structure. The nitrobenzyl groups can be subsequently cleaved from the catecholate moiety via photoirradiation of the MOF resulting in release of 2-nitrosobenzaldehyde and formation of a catechol-bearing MOF material. This MOF can be subsequently functionalized through reaction with [Fe(acac)$_3$] (where acac = acetylacetonate), leading to coordination of Fe^{3+} cations to the catecholate moiety. Cohen's study nicely illustrates the potential of using photoactivated processes for the postsynthetic modification of MOFs, allowing the introduction of competing coordinating groups in a systematic manner.

Modification of the photochemical properties of specific groups can also be achieved through their incorporation within MOFs and can also lead to identification and characterization of photoinitiated isomerization products. For example, we have studied the behavior of the M(diimine)(CO)$_3$X (M = Re, Mn, X = Cl, Br) moiety by incorporating it within the MOF by using a dicarboxylate-functionalized bipyridyl ligand, 2,2′-bipyridine-5,5′-dicarboxylate.[37] The 2,2′-bipyridine-5,5′-dicarboxylate ligand binds both the M(CO)$_3$X moiety through the 2,2′-bipyridyl group and forms a MOF through reaction of the carboxylate groups with Mn(II) salts (Figure 4). The photoreactivity and nature of the photoexcited state of the M(diimine)(CO)$_3$X moiety is modified by incorporation within the MOF environment. Picosecond time-resolved IR (TRIR) studies of the Re(diimine)(CO)$_3$Cl incorporating MOF reveal the formation of both ^{3}MLCT and ^{3}IL (intraligand) $\pi-\pi^*$ states. However, the MLCT bands are not stable and decay rapidly (*ca.* 20 ps) concurrent with further growth of the IL $^3\pi-\pi^*$. Furthermore, the TRIR spectra obtained 1 ns after laser excitation shows only the presence of IL $^3\pi-\pi^*$ states. The $^3\pi-\pi^*$ state of Re(bpy)(CO)$_3$Cl is not normally accessible in solution as it is higher in energy than the commonly observed ^{3}MLCT state. The change in the properties of the M(diimine)(CO)$_3$X (M = Re, Mn) moiety can be explained by a change in environment and absence of solvent from the photoactive species. Indeed, a key factor in the understanding of the photophysics of coordination compounds is the influence of solvent, which is often difficult to decouple; thus, the MOF environment provides a unique environment to elucidate these fundamental properties, whether photoreactivity or chemical reactivity.

The MOFs formed from reaction of M(2,2′-bipyridine-5,5′-dicarboxylate)(CO)$_3$X (M = Re, Mn, X = Cl, Br) with Mn(II), {Mn(DMF)$_2$[(2,2′-bipyridine-5,5′-dicarboxylate)M(CO)$_3$X]}$_n$ adopt a *fac*-arrangement at the M(diimine)(CO)$_3$X moiety, as commonly seen for

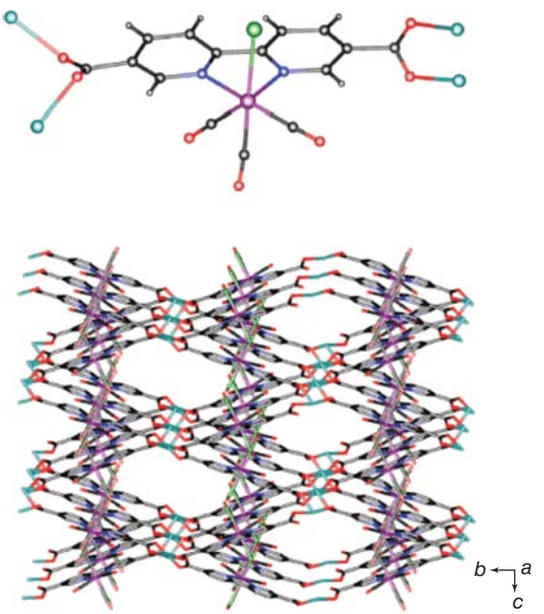


Figure 4 View of the M(2,2′-bipyridine-5,5′-dicarboxylate)(CO)$_3$X ligand (above) that is used to create a complex-bearing MOF (below) through reaction of the carboxylate groups with Mn(II) salts. (Reproduced with permission from Ref. 37. © Nature Publishing Group, 2010.)

such species. *Fac*-isomers of M(diimine)(CO)$_3$X species can undergo photoinduced CO loss and subsequent isomerization to the corresponding *mer*-isomer on irradiation with higher-energy UV light. Irradiation of the MOF, where M = Re, {Mn(DMF)$_2$[(2,2′-bipyridine-5,5′-dicarboxylate)Re(CO)$_3$X]}$_n$, for 22 h at 200 K leads to the observation of a weak IR band at *ca.* 2132 cm^{-1} due to the production of free CO in the MOF. Monitoring by IR spectroscopy reveals that warming of this sample to above 250 K leads to the formation of the corresponding *mer*-isomer of the M(diimine)(CO)$_3$X species. In the case of {Mn(DMF)$_2$[(2,2′-bipyridine-5,5′-dicarboxylate)Re(CO)$_3$Cl]}$_n$, approximately 10% conversion to the *mer*-isomer is observed. In contrast, the corresponding MOF that incorporates Mn(diimine)(CO)$_3$Cl, {Mn(DMF)$_2$[(2,2′-bipyridine-5,5′-dicarboxylate)Mn(CO)$_3$Cl]}$_n$ undergoes 25% conversion from *fac*- to *mer*-isomer and this allowed direct characterization of the isomerization product by single crystal X-ray diffraction experiments (Figure 5).[37]

A related study by Long *et al.*[38] also developed the idea of using photochemical processes to modify the interior of a MOF. Drawing comparisons to traditional matrix isolation studies, the authors used MOF-5[39,40] as a substrate on which to bind Cr(CO)$_3$ moieties to the struts

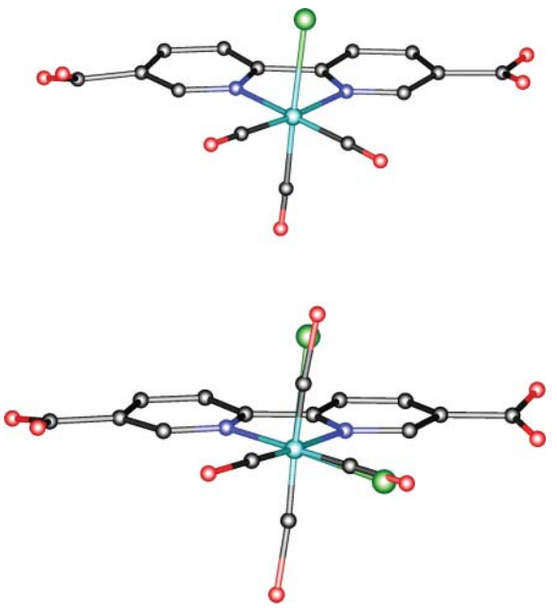


Figure 5 View of the photoinduced isomerization of the Mn(2,2′-bipyridine-5,5′-dicarboxylate)$(CO)_3Cl$ moiety from the *fac*-isomer (above) to the *mer*-isomer (below) within $\{Mn(DMF)_2[(2,2'\text{-bipyridine-5,5}'\text{-dicarboxylate})Mn(CO)_3Cl]\}_n$. Single crystal X-ray diffraction reveals approximately 25% conversion (*fac*- to *mer*-isomer) by observation of chloride occupancy of the equatorial positions of the complex (shown in green in the lower image). (Reproduced with permission from Ref. 37. © Nature Publishing Group, 2010.)

of the framework (Figure 6). This was achieved by reacting MOF-5 with $Cr(CO)_6$ to afford a framework, $\{Zn_4O[(\eta^6\text{-}1,4\text{-benzenedicarboxylate})Cr(CO)_3]_3\}_n$, in which $Cr(CO)_3$ moieties are coordinated to the benzene units of the 1,4-benzenedicarboxylate ligands. The structure could also be considered as (1,4-benzenedicarboxylate)$Cr(CO)_3$ ligands bridging Zn_4O secondary building units (SBUs). Although not characterized by single crystal X-ray studies, the compound was authenticated by a variety of techniques including IR spectroscopy. The latter technique was used to probe the reaction of the chromium moieties with N_2 or H_2 following photolysis using 450-nm light of the $(\eta^6\text{-aryl})Cr(CO)_3$ moiety under a flow of the appropriate gas. Reaction at the chromium center to afford $\{Zn_4O[(\eta^6\text{-}1,4\text{-benzenedicarboxylate})Cr(CO)_2(N_2)]_3\}_n$ or $\{Zn_4O[(\eta^6\text{-}1,4\text{-benzenedicarboxylate})Cr(CO)_2(H_2)]_3\}_n$ was confirmed by IR spectroscopy (Figure 7). Both compounds exhibit enhanced stability with respect to molecular analogues such that in the case of the dihydrogen complex, the MOF-supported compound is stable for up to two weeks at 25 °C in comparison to a matter of minutes for molecular analogues, $(\eta^6\text{-aryl})Cr(CO)_2(H_2)$. As for the nitrene-bearing MOF discussed above, it is clear that the MOF provides an excellent environment to stabilize highly reactive species. In part, this is due to inhibition of decomposition pathways that involve reactions of two of the reactive species due to the rigidity of the framework.

4 MODIFICATION OF PHOTOCHEMICAL PROCESSES USING MOFS

Just as the MOF can modify the chemical reactivity of species contained within, or as part of, the framework, so it is also possible to modify photochemical processes of the substituents of the framework. The modification of the favored excited for M(diimine)$(CO)_3X$ moieties incorporated within MOFs is highlighted above.[37] Hupp has developed studies that demonstrate intraframework energy transfer through careful design of framework components. Hupp, Nguyen *et al*.[39] combined

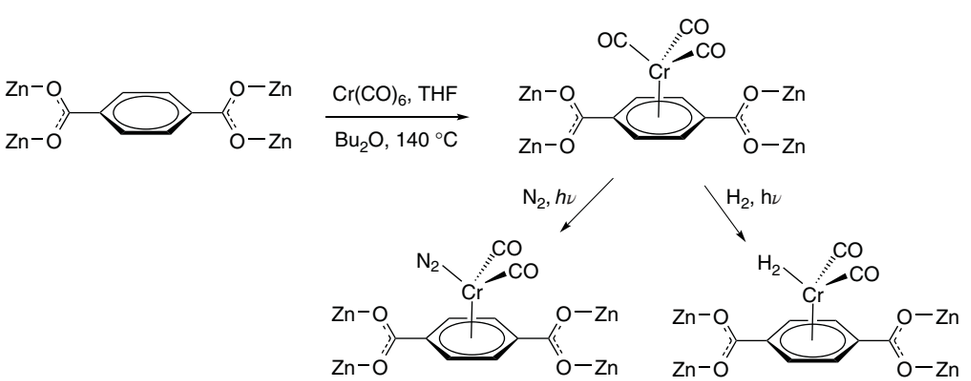


Figure 6 Reaction of MOF-5 with $Cr(CO)_6$ affords $\{Zn_4O[(\eta^6\text{-}1,4\text{-benzenedicarboxylate})Cr(CO)_3]_3\}_n$, which undergoes photoinitiated reactions with N_2 or H_2

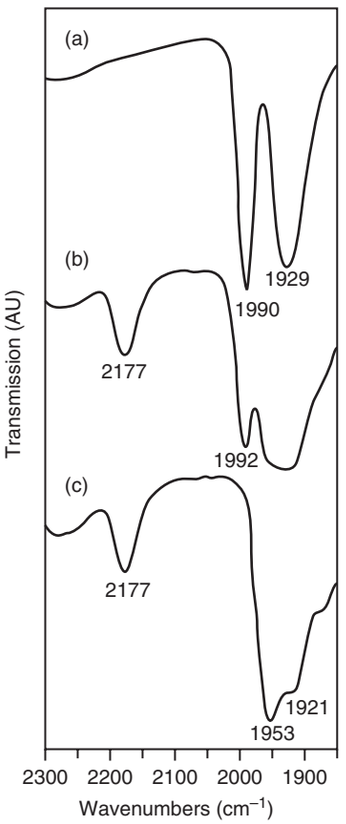


Figure 7 IR spectra confirming the reaction of $\{Zn_4O[(\eta^6\text{-}1,4\text{-benzenedicarboxylate})Cr(CO)_3]_3\}_n$ during irradiation with 450-nm light for (a) 0, (b) 2, and (c) 5 h under a flow of N_2 to afford $\{Zn_4O[(\eta^6\text{-}1,4\text{-benzenedicarboxylate})Cr(CO)_2(N_2)]_3\}_n$. (Reprinted with permission from Ref. 38. Copyright (2008) American Chemical Society.)

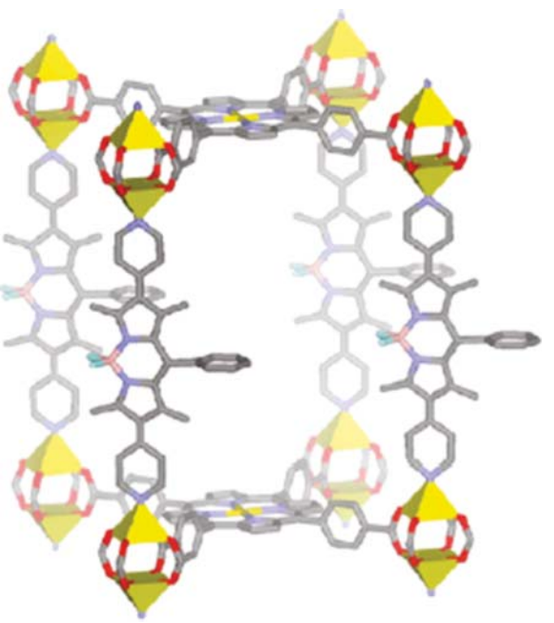


Figure 8 View of a Zn(II)-based MOF that combines a tetracarboxylate-derived porphyrin with a bis-pyridyl substituted BODIPY (difluoro-boron-dipyrromethene) ligand. (Reprinted with permission from Ref. 41. Copyright (2011) American Chemical Society.)

a tetracarboxylate-derived porphyrin with a bis-pyridyl substituted BODIPY (difluoro-boron-dipyrromethene) derivative in a Zn(II) MOF, named BOP (Figure 8). The strategy of combining carboxylate and pillaring pyridyl donors in a MOF mimics early examples of MOFs.[40] Excitation of the BOP MOF at 543 nm, a wavelength at which the BODIPY ligand adsorbs, does not result in typical BODIPY emission. However, luminescence was readily observed in the region 650–710 nm, consistent with emission from the Zn porphyrin moiety, indicating that energy is efficiently transferred within the BOP MOF, from the BODIPY strut to the porphyrin group. This hypothesis was further demonstrated by studies of a related MOF in which the porphyrin ligand was replaced by a nonchromophoric pentaaryl-tetracarboxylate ligand. This second MOF exhibited fluorescence at 596 nm consistent with typical BODIPY fluorescence. Thus, the study clearly demonstrated intraframework energy transfer opening the possibility of developing related materials.

In elegant studies by Lin *et al.*,[42–45] a series of MOFs containing $\{M[4,4'\text{-}(HO_2C)_2\text{-bipy}]_2(bipy)\}^{2+}$ building blocks (M = Ru or Os) are reported, mirroring related studies using $\{M[4,4'\text{-}(HO_2C)_2\text{-bipy}](CO)_3Cl\}$ (M = Re, Mn),[37] discussed above. Reaction of these transition metal-bearing ligands with Zn(II) affords MOF structures that both exhibit steady-state emission spectra at $\lambda_{max} \approx 620$ nm for M = Ru and $\lambda_{max} \approx 720$ nm for M = Os.[42] It is also possible to prepare MOFs in which small proportions, up to 2.6%, of the ruthenium building-blocks are replaced by osmium components. This has a significant effect on the lifetimes of the emissive state reducing it from 171 ns for the parent Ru-based MOF to 29 ns for the 2.6% Os-doped MOF and 8 ns for the purely Os-MOF. These studies demonstrate clear evidence for intraframework energy transfer in the mixed Ru/Os MOFs.

Lin's strategy for incorporating photoactive tris-bipy Ru(II)/Os(II) units within MOFs was further exploited to study diffusion effects[43] in a MOF of formula $\{Zn_2L^{Ru}{}_{0.5}(BPDC)_2\}_n$ {where L^{Ru} = Ru(2,2′-bipy)$_2$ (2,2′-bipyridine-5,5′-dicarboxylate) and BPDC = 4,4′-biphenyldicarboxylate}. In this case, the photoactive component does not represent every strut in the MOF but is distributed randomly throughout the structure. This allows the porous framework to act as a host for guest species including small amine species, NEt_3, NPr_3, and

NBu_3, which are capable of acting to quench the luminescence of the Ru-bearing struts. The dynamics of diffusion of the amine species were probed using time-dependent luminescence quenching measurements demonstrating that Fickian diffusion was followed throughout the MOF environment. This compelling study illustrates how species diffuse through, and interact with, MOF environments, a subject of great interest to many applications of MOFs.

The same principle of using metal-bearing ligands was employed to prepare frameworks that incorporate $[Ir(ppy)_2(5,5'\text{-}(HO_2C)_2\text{-bipy})]^+$ ligands (ppy = 2-phenylpyridine) within a UiO-67 framework structure of formula $\{Zr_6(\mu^3\text{-}O)_4(\mu^3\text{-}OH)_4(bpdc)_{5.94}([Ir(ppy)_2(5,5'\text{-}(O_2C)_2\text{-bipy})])_{0.06}\}_n$.[45] An analogous reaction using $[Ir(ppy)_2(5,5'\text{-(dibenzoate)}_2\text{-bipy})]^+$ with $ZrCl_4$ affords a framework that incorporates iridium complexes as each strut of the MOF,[46] with charge balance obtained through the incorporation of $O_2CCF_3^-$ anions. The larger length of the ligands in this case allows incorporation of the bulky $Ir(ppy)_2$ species on each strut, which is not achieved with smaller metal-bearing ligands such as $[Ir(ppy)_2(5,5'\text{-}(HO_2C)_2\text{-bipy})]^+$. These two Ir-bearing MOFs, $\{Zr_6(\mu^3\text{-}O)_4(\mu^3\text{-}OH)_4(bpdc)_{5.94}([Ir(ppy)_2(5,5'\text{-}(HO_2C)_2\text{-bipy})])_{0.06}\}_n$ and $\{Zr_6(\mu^3\text{-}O)_4(\mu^3\text{-}OH)_4([Ir(ppy)_2(5,5'\text{-(dibenzoate)}_2\text{-bipy})]_6)\}_n$, can be used to generate platinum nanoparticles within the MOF pores.[46] It is known that NEt_3 can reductively quench the photoexcited state $[Ir(ppy)_2(bpy)]^{+*}$ to generate the reduced radical $[Ir(ppy)_2(bpy^{\bullet-})]$, which can in turn reduce $PtCl_4^{2-}$ to generate Pt nanoparticles.[47] Lin's study elegantly demonstrates that this process can proceed within the MOF pores to afford nanoparticles whose size is controlled to some degree by the MOF cavity size (Figure 9). In some instances, the Pt nanoparticles were found to be larger than the calculated pore dimensions due to distortions of the framework on nanoparticle generation.

A related approach has been developed by Rosseinsky *et al*.[48] who have exploited meso-tetra(4-carboxylphenyl)porphyrin as a bridging ligand through reaction with $AlCl_3.6H_2O$ to afford a porphyrin-bearing MOF, $\{(tetra(4\text{-carboxy-phenyl})porphyrin)[AlOH]_2(DMF_3\text{-}(H_2O)_2)\}_n$. This porous, water-stable, MOF exhibits optical properties, both absorption and fluorescence, consistent with those of the porphyrin moiety. The properties of the MOF were demonstrated by studying the

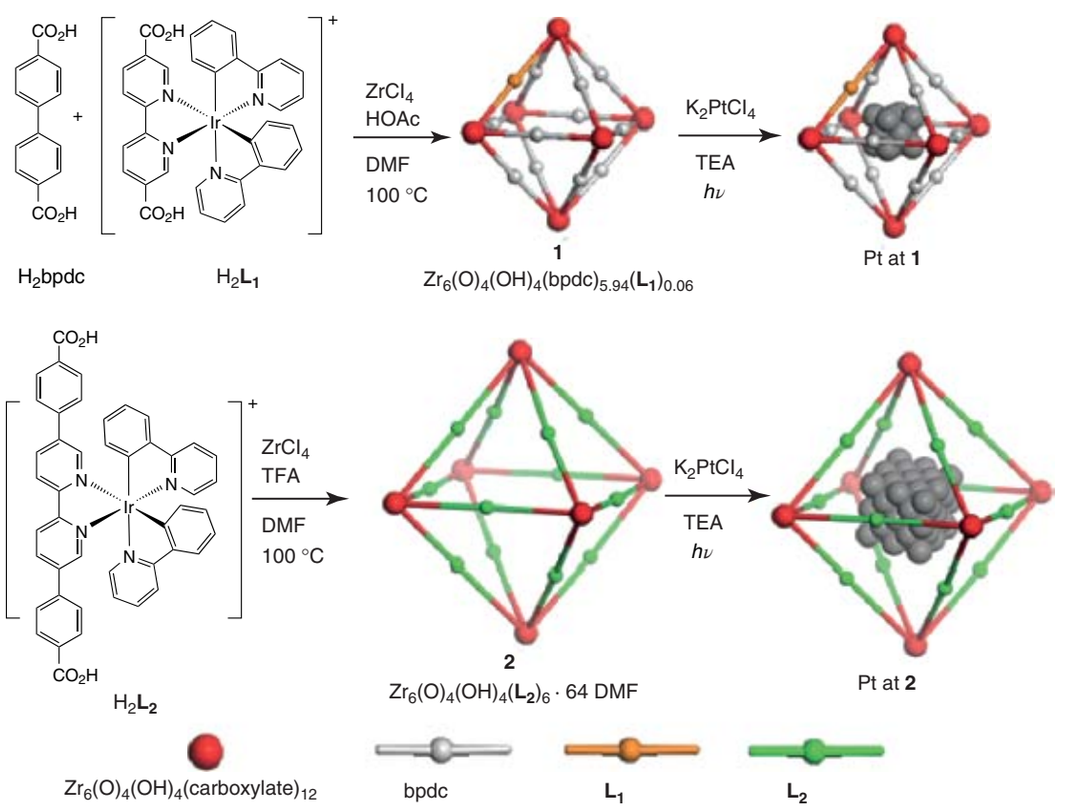


Figure 9 $[Ir(ppy)_2(bpy)]$-bearing MOFs and their use to form Pt nanoparticles. (Reprinted with permission from Ref. 46. Copyright (2012) American Chemical Society.)

photochemical generation of H_2 by the system. In particular, photoexcitation of the porphyrin ligand facilitated reduction of guest methyl viologen to its corresponding radical cation and, in turn, accompanying oxidation of ethylenediaminetetraacetic acid (EDTA). The methyl viologen radical cation is able to transfer its additional electron to colloidal platinum facilitating hydrogen evolution. Although the process is not as efficient as analogous solution-based processes, possibly due to restricted flow of guests through MOF channels, the study indicates that the use of MOFs is a viable strategy for developing photochemical processes in framework environments.

5 CONCLUSION

Photochemical reactions of species contained within MOF environments have a rich and exciting future. Whether the photoactive species are a fundamental constituent of the MOF, that is, part of the framework, or whether they are a guest within channels or pores, it is clear that the MOF environment can affect the properties of that species. This can be manifested simply by alteration of the excited states of the species or radical modification of the photochemical reactivity of the species.

At the simplest level, the environment of the MOF can be used to modify the fluorescence of a guest species and as a result be used as a sensor to detect guest species. However, the MOF environment can have a much greater role to play and can stabilize highly unusual species such as nitrenes[24] or (η^6-aryl)$Cr(CO)_2(N_2)$ complexes[38] and modify the reactivity of metal complexes such as the isomerization of M(diimine)$(CO)_3X$ moieties.[37] The reactivity of species within the framework can also be used to generate new frameworks through postsynthetic modification processes.[35,36] All of these studies illustrate the great potential of using photochemical processes as a synthetic tool and this has been further illustrated by recent studies that demonstrate photoinitiated reactions within MOF pores generating nanoparticles[46] and initiating H_2 production.[48]

In conclusion, it can be seen that through careful design, the incorporation of photoactive units within a MOF can affect the photoreactivity and hence chemical reactivity of the MOF itself, leading to the stabilization of unusual species. In turn, this modification of photochemical properties can be used to induce unusual reactivity and allow modification of guest properties all within a highly tailored environment. It is difficult to envisage other chemical systems in which such a controlled, and potentially designed, environment as that seen in MOFs can be used in such a manner. This relatively new field of MOF research has many promising aspects that exploit the fundamental design principles of the building-block methodology and thus developing photoreactivity within MOFs can only have a bright future.

6 ACKNOWLEDGMENT

N.R.C. gratefully acknowledges the receipt of a Royal Society Wolfson Merit Award.

7 RELATED ARTICLES

Photoreactive Metal-Organic Frameworks; Porphyrinic Metal-Organic Frameworks; Postsynthetic Modification of Metal-Organic Frameworks.

8 ABBREVIATIONS AND ACRONYMS

DMNB = 2,3-dimethyl-2,3-dinitrobutane; DNT = 2,4-dinitrotoluene; EDTA = ethylenediaminetetraacetic acid; ESR = electron spin resonance; MOF = metal–organic framework; SBU = secondary building unit; TRIR = time-resolved IR; VOC = volatile organic compound.

9 FURTHER READING

O. K. Farha, A. M. Shultz, A. A. Sarjeant, S. T. Nguyen, and J. T. Hupp, *J. Am. Chem. Soc.*, 2011, **133**, 5652.

10 REFERENCES

1. N. R. Champness, *Dalton Trans.*, 2011, **40**, 10311.
2. B. F. Hoskins and R. Robson, *J. Am. Chem. Soc.*, 1990, **112**, 1546.
3. R. Robson, B. F. Abrahams, S. R. Batten, R. W. Gable, B. F. Hoskins, and J. P. Liu, *ACS Symp. Ser.*, 1992, **499**, 256.
4. H. Li, M. Eddaoudi, M. O'Keeffe, and O. M. Yaghi, *Nature*, 1999, **402**, 276.
5. S. R. Batten, N. R. Champness, X.-M. Chen, J. Garcia-Martinez, S. Kitagawa, L. Öhrstrom, M. O'Keeffe, M. P. Suh, and J. Reedijk, *CrystEngComm*, 2012, **14**, 3001.
6. Y. Shibata, CAN 11:5339, *J. Coll. Sci. Imp. Univ. Tokyo*, 1916, **37**, 1.
7. B. F. Hoskins, R. Robson, and N. V. Y. Scarlett, *J. Chem. Soc. Chem. Commun.*, 1994, 2025.
8. M. Kondo, T. Yoshitomi, K. Seki, H. Matsuzaka, and S. Kitagawa, *Angew. Chem. Int. Ed.*, 1997, **36**, 1725.
9. J. Maddox, *Nature*, 1988, **335**, 201.
10. X. Lin, J. Jia, P. Hubberstey, M. Schröder, and N. R. Champness, *CrystEngComm*, 2007, **9**, 438.

11. X. Lin, N. R. Champness, and M. Schröder, *Top. Curr. Chem.*, 2010, **293**, 35.
12. J. R. Li, Y. Mab, M. C. McCarthy, J. Sculley, J. Yu, H. K. Jeong, P. B. Balbuena, and H. C. Zhou, *Coord. Chem. Rev.*, 2011, **255**, 1791.
13. P. Horcajada, C. Serre, G. Maurin, N. A. Ramsahye, F. Balas, M. Vallet-Regí, M. Sebban, F. Taulelle, and G. Férey, *J. Am. Chem. Soc.*, 2008, **130**, 6774.
14. M. Kurmoo, *Chem. Soc. Rev.*, 2009, **38**, 1353.
15. J.-P. Zhang, Y.-B. Zhang, J.-B. Lin, and X.-M. Chen, *Chem. Rev.*, 2012, **112**, 1001.
16. S. A. Barnett and N. R. Champness, *Coord. Chem. Rev.*, 2003, **246**, 145.
17. T. Uemura, N. Yanai, and S. Kitagawa, *Chem. Soc. Rev.*, 2009, **38**, 1228.
18. D. J. Tranchemontagne, J. L. Mendoza-Cortes, M. O'Keeffe, and O. M. Yaghi, *Chem. Soc. Rev.*, 2009, **38**, 1257.
19. Z. Wang and S. M. Cohen, *Chem. Soc. Rev.*, 2009, **38**, 1315.
20. K. A. Cychosz, R. Ahmad, and A. J. Matzger, *Chem. Sci.*, 2010, **1**, 293.
21. M. D. Allendorf, C. A. Bauer, R. K. Bhakta, and R. J. T. Houk, *Chem. Soc. Rev.*, 2009, **38**, 1330.
22. D. K. Bucar, G. S. Papaefstathiou, T. D. Hamilton, Q. L. Chu, I. G. Georgiev, and L. R. MacGillivray, *Eur. J. Inorg. Chem.*, 2007, 4559.
23. G. K. Kole and J. J. Vittal, *Chem. Soc. Rev.*, 2013, **42**, 1755.
24. Y. Takashima, V. Martínez Martínez, S. Furukawa, M. Kondo, S. Shimomura, H. Uehara, M. Nakahama, K. Sugimoto, and S. Kitagawa, *Nature Comm.*, 2011, **2**, 168.
25. A. Lan, K. Li, H. Wu, D. H. Olson, T. J. Emge, W. Ki, M. Hong, and J. Li, *Angew. Chem. Int. Ed.*, 2009, **48**, 2334.
26. S. Pramanik, C. Zheng, X. Zhang, T. J. Emge, and J. Li, *J. Am. Chem. Soc.*, 2011, **133**, 4153.
27. H. Xu, F. Liu, Y. Cui, B. Chen, and G. Qian, *Chem. Commun.*, 2011, **47**, 3153.
28. Y.-Q. Huang, B. Ding, H.-B. Song, B. Zhao, P. Ren, P. Chen, H.-G. Wang, D.-Z. Liao, and S.-P. Yan, *Chem. Commun.*, 2006, 4906.
29. B. Chen, Y. Yang, F. Zapata, G. Lin, G. Qian, and E. B. Lobkovsky, *Adv. Mater.*, 2007, **19**, 1693.
30. M. M. Wanderley, C. Wang, C. D. Wu, and W. Lin, *J. Am. Chem. Soc.*, 2012, **134**, 9050.
31. B. L. Chen, L. B. Wang, F. Zapata, G. D. Qian, and E. B. Lobkovsky, *J. Am. Chem. Soc.*, 2008, **130**, 6718.
32. H. Xu, X. Rao, J. Gao, J. Yu, Z. Wang, Z. Dou, Y. Cui, Y. Yang, B. Chen, and G. Qian, *Chem. Commun.*, 2012, **48**, 7377.
33. H. Sato, R. Matsuda, K. Sugimoto, M. Takata, and S. Kitagawa, *Nature Mater.*, 2010, **9**, 661.
34. Z. Wang and S. M. Cohen, *Chem. Soc. Rev.*, 2009, **38**, 1315.
35. K. K. Tanabe, C. A. Allen, and S. M. Cohen, *Angew. Chem. Int. Ed.*, 2010, **49**, 9730.
36. R. K. Deshpande, G. I. N. Waterhouse, G. B. Jameson, and S. G. Telfer, *Chem. Commun.*, 2012, **48**, 1574.
37. A. J. Blake, N. R. Champness, T. L. Easun, D. R. Allan, H. Nowell, M. W. George, J. Jia, and X.-Z. Sun, *Nature Chem.*, 2010, **2**, 688.
38. S. S. Kaye and J. R. Long, *J. Am. Chem. Soc.*, 2008, **130**, 806.
39. S. S. Kaye, A. Dailly, O. M. Yaghi, and J. R. Long, *J. Am. Chem. Soc.*, 2007, **129**, 14176.
40. M. Eddaoudi, J. Kim, N. Rosi, D. Vodak, J. Wachter, M. O'Keeffe, and O. M. Yaghi, *Science*, 2002, **295**, 469.
41. C. Y. Lee, O. K. Farha, B. J. Hong, A. A. Sarjeant, S. T. Nguyen, and J. T. Hupp, *J. Am. Chem. Soc.*, 2011, **133**, 15858.
42. C. A. Kent, B. P. Mehl, L. Ma, J. M. Papanikolas, T. J. Meyer, and W. Lin, *J. Am. Chem. Soc.*, 2010, **132**, 12767.
43. C. Wang and W. Lin, *J. Am. Chem. Soc.*, 2011, **133**, 4232.
44. C. A. Kent, D. Liu, L. Ma, J. M. Papanikolas, T. J. Meyer, and W. Lin, *J. Am. Chem. Soc.*, 2011, **133**, 12940.
45. C. Wang, Z. G. Xie, K. E. deKrafft, and W. Lin, *J. Am. Chem. Soc.*, 2011, **133**, 13445.
46. C. Wang, K. E. deKrafft, and W. Lin, *J. Am. Chem. Soc.*, 2012, **134**, 7211.
47. J. I. Goldsmith, W. R. Hudson, M. S. Lowry, T. H. Anderson, and S. Bernhard, *J. Am. Chem. Soc.*, 2005, **127**, 7502.
48. A. Fateeva, P. A. Chater, C. P. Ireland, A. A. Tahir, Y. Z. Khimyak, P. V. Wiper, J. R. Darwent, and M. J. Rosseinsky, *Angew. Chem. Int. Ed.*, 2012, **51**, 7440.

Semiconducting Metal-Organic Frameworks

Zhengtao Xu

City University of Hong Kong, Hong Kong, PR China

1	Introduction	373
2	The Taming of the Sulfur	375
3	The Two-Step Strategy: the Divide-and-Conquer of Crystallinity and Functionality	378
4	Turning Insolubility on its Head	380
5	Conclusion	382
6	Acknowledgments	383
7	Related Articles	383
8	Abbreviations and Acronyms	383
9	References	383

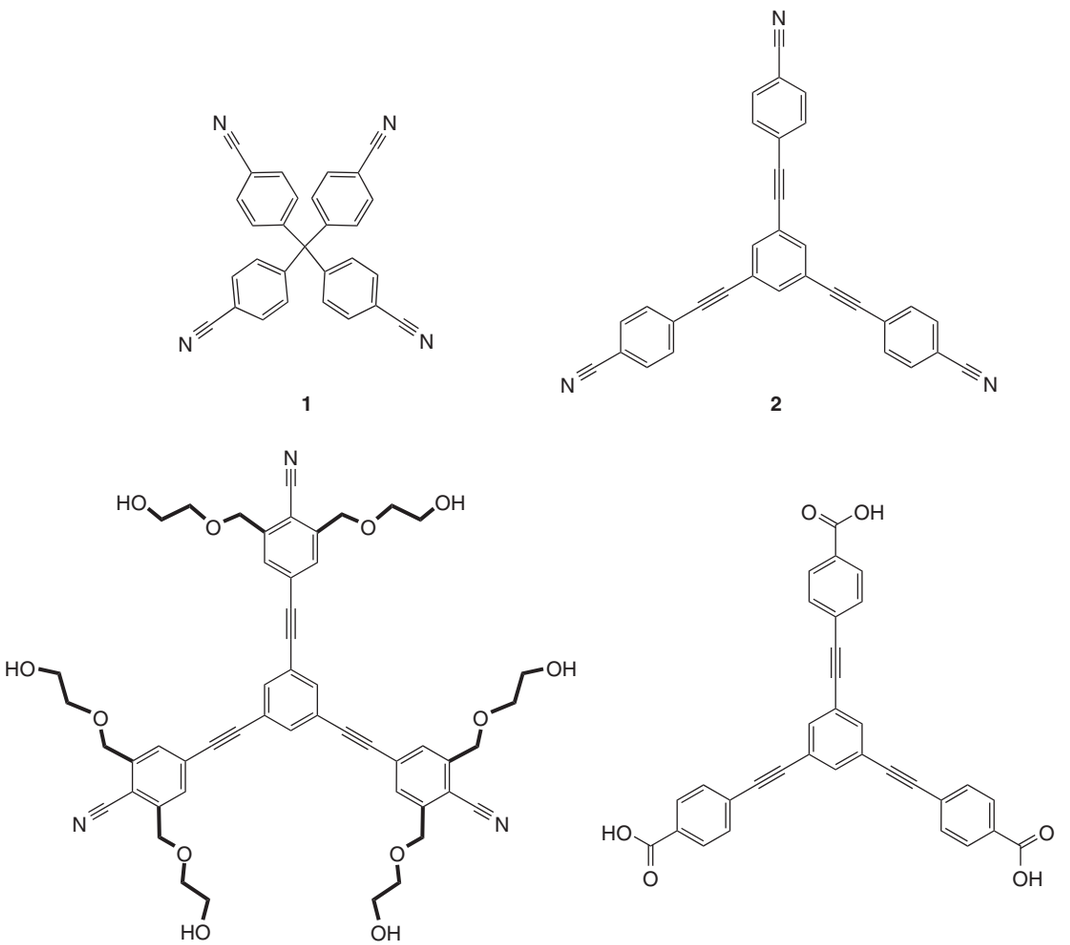
1 INTRODUCTION

Semiconductor becomes a misleading term when its definition all hinges on the intermediate ability to conduct electrical current (e.g., about 10^{-4} to 10^{6} S m^{-1}). In a simple demonstration, one could blend metal and insulator particles to give conductivities in the said range. Such a seemingly "semiconducting" mixture/composite, obviously, is scientifically and technologically a far cry from the bona fide semiconductors, which are more properly defined by the energy gap in the electronic band structures. In chemical terms, energy bands arise from the interaction of the large number of atomic/molecular orbitals in a solid-state (e.g., infinite) ensemble. In general, strong, covalentlike interactions between the building units are crucial for achieving large band dispersion to offer the significant, bandlike conducting behaviors as seen in the technological powerhouse of inorganic semiconductors.

Such a statement spells an interesting challenge for the making of semiconducting metal–organic frameworks. On one hand, crystallization of such frameworks largely depends on the weak or ionic interactions between the metal ions and the organic linkers (e.g., metal–nitrile, metal–carboxylate bonds), and the resultant electronic interaction between the metal and ligand is generally insignificant. Stronger, more effective interactions, such as the metal–thiolate bond, however, would likely prevent the formation of crystalline, well-defined framework products. In spite of the challenge, more and more attention is drawn to the field of semiconducting metal–organic frameworks, because of its potentially great academic and technological implications. Presently, the number of reported semiconductive framework compounds continues to grow, and recent reviews are available that focus on electrical conductivity[1,2] or electronic interaction[3] in coordination nets. This presentation is necessarily interpretive and selective, and it is driven partly by the lack of a systematic account of synthetic strategies that are broadly applicable for achieving the targeted property of semiconductivity and electroactivity within porous metal–organic frameworks (e.g., by addressing the above-mentioned dilemma of bond strength and crystallinity). Instead of listing individual, isolated cases, we select syntheses and products that are representative or implicative of general methodological importance. Also, this work heavily leans toward the synthetic aspect, leaving out other advanced topics such as bulk heterojunctions (for solar cell and other device applications), thin film processing, and battery/electrode technology that are especially relevant for porous semiconductive materials. We start off with a brief overview of metal–organic frameworks in general.

"Rigidity" is the best one-word summary for the developments in the research of porous framework materials. After all, the opening scene was set by the very rigid tetrapod tetrakis(4-cyanophenyl)methane (molecule **1** in Scheme 1), which coordinated with Cu(I) to form a diamondlike net that, quite surprisingly at the time, contained large void space.[4] Nowadays, it has become

Metal-Organic Framework Materials. Edited by Leonard R. MacGillivray and Charles M. Lukehart.
© 2014 John Wiley & Sons, Ltd. ISBN 978-1-119-95289-3



Scheme 1 Four examples of rigid molecular scaffolds for building open frameworks: **1**, **2**, and **4** are multiarm nitrile or carboxylic acid molecules without additional functional units, whereas **3** is a bifunctional molecule equipped with six flexible ether-alcohol side chains

almost axiomatic that, for substantial porosity in the framework product, the best bet is with rigid, multidirectional building blocks [see Scheme 1 for the additional examples: the tris(4-cyanophenylethynyl)benzene of **2**,[5] the hydroxyl-laced **3**,[6] and the tricarboxylic acid of **4**[7–9]]. But absolute rigidity does not exist. Even networks of most rigid aromatic linkers often exhibit dynamic behaviors (e.g., breathing effects and dynamic guest transport, see ***Single-Crystal to Single-Crystal Transformations in Metal-Organic Frameworks***) indicative of substantial framework flexibility. Moreover, too much rigidity is uncalled-for. The departure from rigidity started early in the game, to wit, in the form of an aromatic nitrile backbone coupled with the supple ethylene ether side chains (e.g., **3** in Scheme 1).[6,10,11] The crux here is to select a side chain (or other secondary groups) that is compatible with the primary ligand–metal interaction for network construction, and therefore, lends itself to further modification within the framework product. The power and popularity of this two-step strategy of crystallization and functionalization are best seen in the recent surge in the practice of postsynthesis modifications (PSM, see ***Postsynthetic Modification of Metal-Organic Frameworks***).[10,12–16] Rigid bifunctional building blocks, as exemplified by molecules such as **3**, will remain dominant for a long time to come, because of the rich potential to produce functional porous structures, and to achieve the many desirable properties expected of porous frameworks.

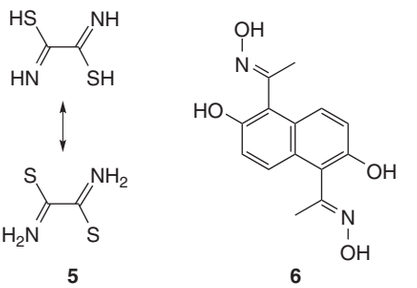
Such an overview of the field naturally connects to a definition of framework materials. Porous materials are not new—activated carbon, zeolites, and many resin systems are among the diverse examples long in wide practical uses. The recent craze in porous framework research is partly driven by the appeal of rational design associated with the modular assembly process using distinct, prefabricated building blocks. Although the ability to correlate molecular and crystal structures remains far from perfection, the selection of shape and function in the molecular building blocks does lend considerable

control over the connectivity and porous features of the prospective frameworks. Also, the building blocks, such as most organic molecules, often allow for rather systematic modifications (e.g., in the form of a side chain), while maintaining the basic linker characteristics to produce the desired framework type.

A definition for such a specific class of porous framework materials, therefore, ought to emphasize two key features: (i) the distinct modular nature in the synthetic process; and (ii) the possibility of chemical modification of the building blocks. In this light, activated carbon may not qualify as a framework material (e.g., it is not a COF—covalent organic framework[17]), mainly because of the lack of distinct, modular building units on which the structure is based. Zeolites, on the other hand, often sport distinct cage/polyhedron units, but these are not the building units, one started off within the synthetic process—instead, zeolites are often made from the rudimentary compounds of Si, Al, and the like (rather, the cages are formed in situ). The modular nature of the synthesis is consequently not as clear-cut. In addition, the inorganic scaffolds of zeolites do not as readily accommodate added functional group. Altogether, zeolites hardly fit in the system of framework materials thus specifically defined. Definitions are, however, seldom definitive. The purpose here is not to stir bookish debates on semantics, but rather to highlight and to promote the practical spirit in the exercises of modular synthesis and multifunctional building blocks.

2 THE TAMING OF THE SULFUR

One such exercise is to combine semiconductivity and porosity in metal–organic frameworks (and other framework materials). Electrical conductivity largely precedes porosity as a topic of study in coordination



5 6

Scheme 2 Two tautomeric forms—iminothiol (top) and thioamide (bottom) of rubeanic acid (**5**) and the structure of molecule **6**. Notice that the thiol and phenol groups are mitigated in their metal-binding ability by the adjacent electron-withdrawing imine and oxime units, respectively

polymers. Earliest examples include Kanda's rubeanato-Cu(II) system[18] (see **5** in Scheme 2 for the structure of rubeanic acid—i.e., dithiooxamide; see Figure 1 for a structural model later proposed[19]) and Dewar's polymeric complex based on Cu(II) and the dioxime of 1,5-diacetyl-2,6-dihydroxynaphthalene (molecule **6** in Scheme 2).[20] For instance, the Cu(II)-rubeanate exhibited a resistivity of 2.5×10^5 ohm cm^{-1} at 30 °C, with a bandgap of 0.3 eV (from conductivity data determined between −10 and 80 °C). Further studies on rubeanic acid derivatives with substituents (e.g., ethyl and 2-hydroxylethyl) on the $-NH_2$ unit led to a two-dimensional grid type (Figure 1) that is typical of these complexes.[19,21–25] Although some structural models and X-ray powder patterns[21] were made available, detailed accounts of structural studies (e.g., by X-ray methods) would be even more helpful, especially in regard of the interesting properties of proton conductivity[22–24] and electrocatalysis (for ethanol oxidation[25]) that have been reported of these rubeanate frameworks.

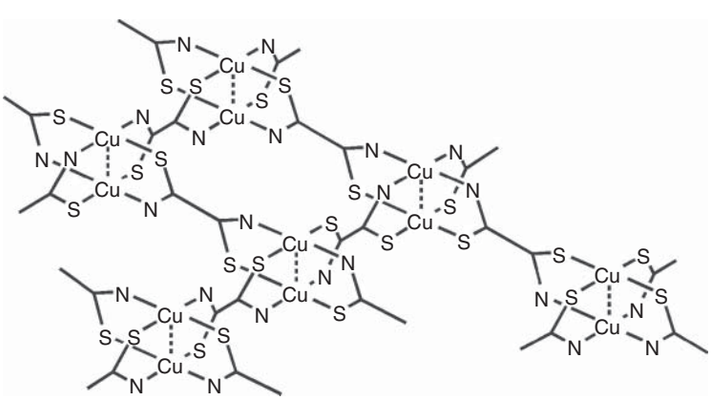
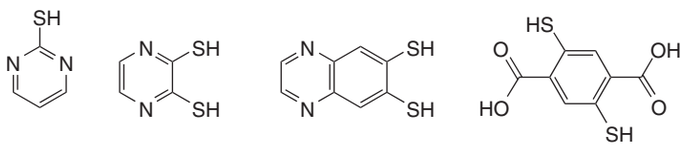


Figure 1 The structural model of a 2D network of Cu(II) rubeanate. The Cu(II) dimer adopts a common paddle-wheel-like coordination geometry



7 **8** **9** **10**, DMBD

Scheme 3 Structures of pyrimidine-2-thiol (**7**), 2,3-pyrazinedithiol (**8**), quinoxaline-6,7-dithiol (**9**), and 2,5-dimercaptobenzene dicarboxylic acid (**10**). Like molecules **5** and **6**, the thiol donor are conjoined with electron-withdrawing groups (e.g., the pyrimidine unit in **7**) to temper its interaction with metal ions, and to promote the formation of ordered networks

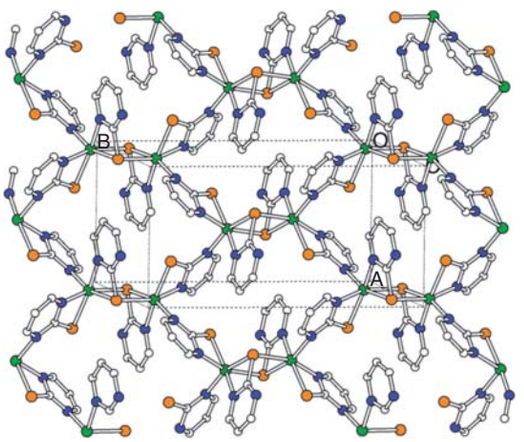


Figure 2 A 2D network from **7** and Ni(II). The composition is $Ni_2(C_4N_2H_3S)_4$. Orange spheres: S; blue: N; green: Ni; open spheres: C

The Cu(II)-rubeanate system can be related to an effective approach to attenuate the very strong sulfur–metal interaction, and to enhance the crystalline order of the framework solid. The tempering effect on the thiol unit is easily seen in the electron-withdrawing imine unit in the iminothiol form (Scheme 2). In many cases, by coupling the thiol (–SH) group to an electron-deficient unit, well-ordered single crystal structures can be obtained. Some early works built on pyrimidine-2-thiol (i.e., **7** in Scheme 3)[26] and pyridine-2-thiol.[27] For example, molecule **7** and Ni(II) formed a close-packed (nonporous) 2D network featuring distinct $Ni_2(C_4N_2H_3S)_4$ units that are linked via the Ni^{II}–N coordinate bonds (i.e., the Ni–S bonds are all confined within the bimetallic unit, Figure 2). A pressed powder sample from ground crystals was found to be semiconductive with an electrical conductivity of 5.00×10^{-3} S cm^{-1} at 28 °C which increased with temperature. The bulk transport behavior, as well as the antiferromagnetic coupling across the dimer units ($J = 7.3$ cm^{-1}), thus indicate effective electronic interaction across the Ni^{II}–N links in this particular system.

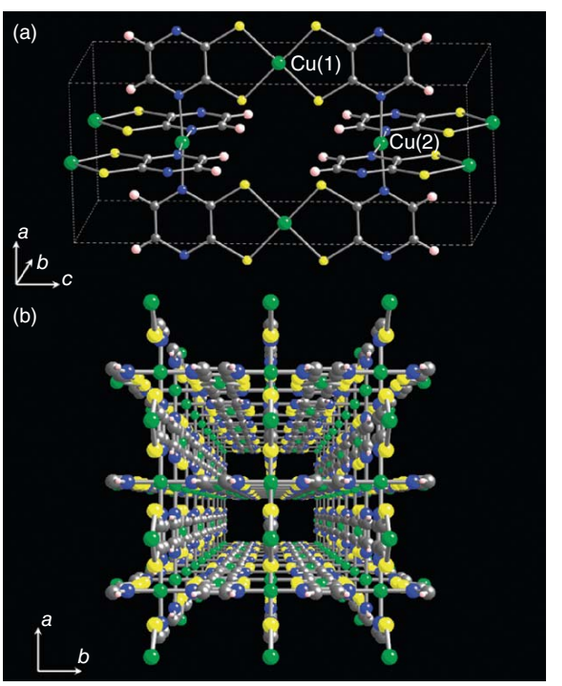


Figure 3 Crystal structure of $Cu[Cu(pdt)_2]$ (pdt is **8**): (a) local bonding features; (b) a perspective view showcasing the channels. Color code: green, Cu; yellow, S; gray, C; blue, N; pink, H. (Reprinted with permission from Ref. 28. Copyright (2009) American Chemical Society.)

Later works on 2,3-pyrazinedithiol (pdt, i.e., molecule **8** in Scheme 3) achieved open frameworks that combine remarkable porous features and semiconductive properties. For example, the crystal structure of $Cu[Cu(pdt)_2]$ (Figure 3) builds on planar Cu(II)-dithiolene units of $Cu(pdt)_2$ that, in turn, bind a second set of Cu(II) centers (via the Cu^{II}–N interactions) to produce a 3D tetragonal grid featuring 1D channels.[28] An electrical conductivity of 6×10^{-4} S cm^{-1} at 300 K was reported of this compound, with an activation energy (bandgap) of 193 meV determined from the temperature dependence of the conductivity. The charge bistability between $Cu^{I}[Cu^{III}(pdt)_2]$ and $Cu^{II}[Cu^{II}(pdt)_2]$ was postulated

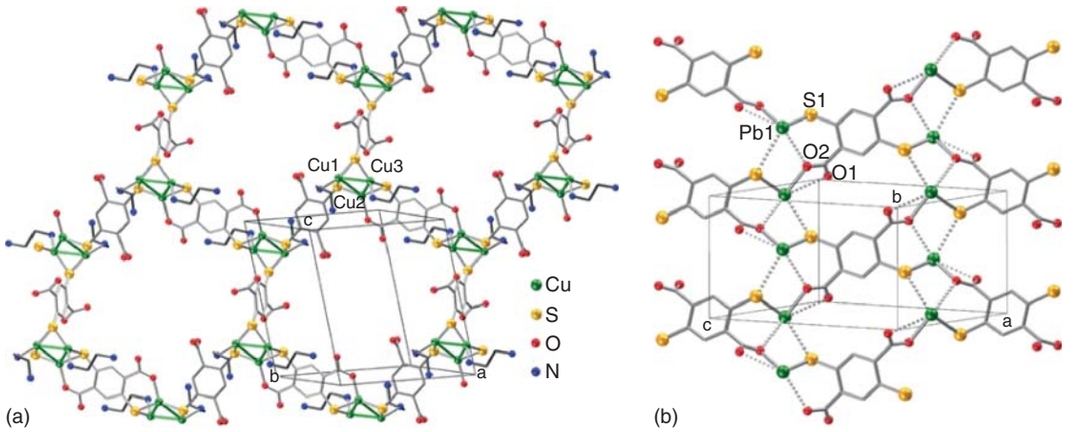


Figure 4 (a) An overview of the 2D network of CuDMBD (uncoordinating en species in the channels are omitted): normal bonding distances (2.177–2.302 Å) are observed for all the six Cu–S contacts around the Cu(I) trimer. (b) The 2D network in PbDMBD (the en molecule chelating the Pb^{2+} ion is removed for clarity). Two Pb–S (2.679 and 3.306 Å) contacts are present, the longer one marked by the dotted line

as contributing to the electrical conductivity. Another work on the isostructural $Cu[Ni(pdt)_2]$ solid by Allendorf and Long systematically characterized the porosity feature (e.g., surface area ~400 $m^2\,g^{-1}$), and revealed the *p*-type transport property with I_2-doping resulting in a 10^4-fold increase in conductivity to approximately $1 \times 10^{-4}\,S\,cm^{-1}$.[29] Like in the above $Ni_2(C_4N_2H_3S)_4$ compound, the metal–N links (i.e., Cu^{II}–N) prove to be effective in mediating the electronic coupling across the transition metal–thiolate building units of $Cu(pdt)_2$ and $Cu(pdt)_2$. Looking ahead, we foresee a versatile class of porous electroactive frameworks to be made from wider range of building blocks that integrate the thiol donor function (or even nitrogen-based donors, such as the porous and conductive metal–triazolate frameworks recently reported[30]) and electron-withdrawing N-heterocycle functions (e.g., quinoxaline-6,7-dithiol;[31] molecule **9** of Scheme 3).

More distinct bifunctional character is found in the combination of thiol and carboxyl groups. The DMBD building block (molecule **10** of Scheme 3), for example, was initially used to exploit the hard-and-soft strategy in network construction.[32] The carboxyl groups, besides tempering the metal–thiol interaction so as to generate better-ordered networks, can be selectively engaged by very hard metal ions [e.g., Al(III),[33–36] Cr(III),[37–39] Eu(III),[32] and Zr(IV)[40]], whereas the –SH groups remain free-standing as versatile functionality for the solid framework. The general efficacy of this approach was demonstrated by how DMBD interacts (using 1,2-ethylenediamine as the solvent) with the increasingly harder ions of Cu^+, Pb^{2+}, and Eu^{3+} to form the networks of $Cu_6(DMBD)_3(en)_4(Hen)_6$, $Pb_2(DMBD)(en)_2$, and $Eu_2(H_2DMBD)_3(DEF)_4$ (abbreviated as CuDMBD, PbDMBD, and EuDMBD; en and Hen: 1,2-ethylenediamine, used as a solvent, and its monoprotonated cation; DEF: *N*,*N*-diethylformamide,used as a solvent). Notably, in CuDMBD, half of the carboxylate units remain uncoordinated, whereas the thiolate groups fully bond to the Cu(I) centers (of the triangular Cu_3 cluster) to form a 2D Cu(I)–thiolate net (Figure 4a); with the slightly harder Pb(II) in PbDMBD, both the mercapto and the carboxylic groups are fully bonded to the Pb^{2+} ions (Figure 4b); in EuDMBD, the very hard Eu(III) only coordinate with the carboxyl groups, leaving the thiol groups as free-standing units on the 3D Eu(III)–carboxylate network (Figure 5). Notably, the CuDMBD, with the very strong, interconnecting Cu–S interactions, features an optical

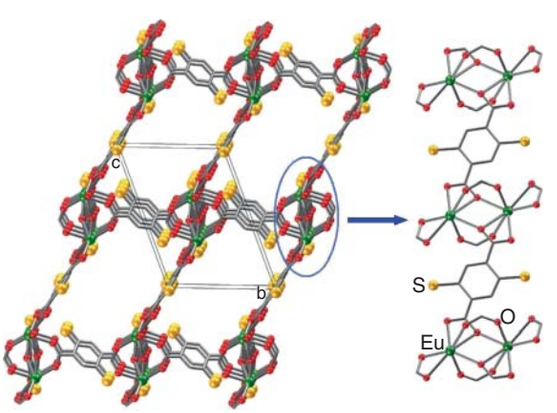


Figure 5 View of the 3D net of EuDMBD along the *a* axis (left, the DEF molecules are omitted), and the connection of the $Eu_2(COO)_6$ units shown along the *a* axis (right) to highlight the free-standing thiol units

absorption edge at significant lower energy (1.61 eV) than those of PbDMBD (2.43 eV) and EuDMBD (2.58 eV), indicating the effective electronic interactions across the metal–thiolate bridges. This study thus illustrated the rich solid-state structural features and potential functions offered by the carboxyl–thiol combination, although permanent porosity (as characterized by gas adsorption) was not reported for these early exemplary networks.

Dincă and coworkers recently explored along the line of sulfur–carboxyl combination, and achieved network systems with stable porous features.[41,42] For example, both the carboxyl and the thiol groups are fully bonded to the Mn(II) centers in compound MnDMBD [composition: Mn_2(DMBD)], forming a 3D framework with 1D channel-like voids (Figure 6).[42] The sulfur atoms participate in infinite one-dimensional Mn–S chains, which were credited with the significant charge mobility observed [e.g., between 0.001 $cm^2\,V^{-1}\,s^{-1}$ and 0.01 $cm^2\,V^{-1}s^{-1}$, as measured by the FP-TRMC (flash-photolysis time-resolved microwave conductivity) and TOF (time-of-flight) methods]. The structural integrity of an activated sample of Mn_2(DMBD) was verified by powder X-ray diffraction (PXRD), and N_2 adsorption isotherm measurements indicated a Brunauer–Emmett–Teller (BET) surface area of 978 $m^2\,g^{-1}$, thus demonstrating the robust porosity of this semiconductive MOF.

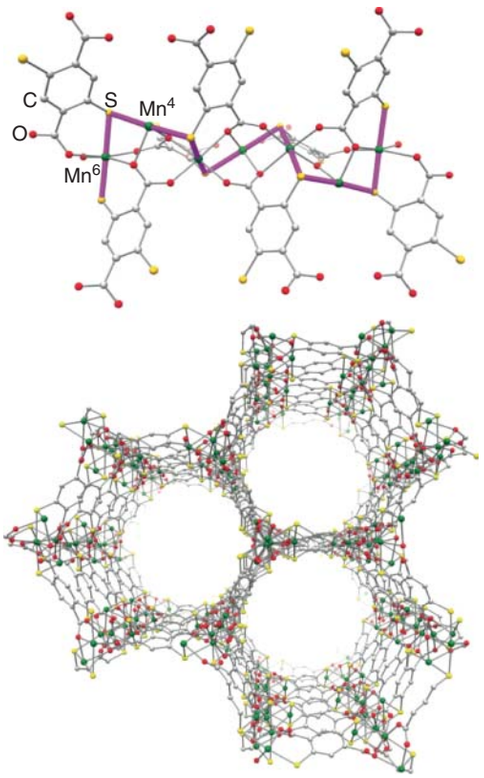


Figure 6 Bonding connectivity in the crystal structure of MnDMBD (top) with the 1D Mn–S chain marked in pink and an overview (bottom) showing infinite 1D empty channels. (Reprinted with permission from Ref. 42. Copyright (2013) American Chemical Society.)

3 THE TWO-STEP STRATEGY: THE DIVIDE-AND-CONQUER OF CRYSTALLINITY AND FUNCTIONALITY

The ZrDMBD system, on the other hand, points to a different approach to building metal–thiolate links into MOF structures (Figure 7). Unlike the common "shake and bake" recipe, a two-step method, in keeping with the PSM spirit (see ***Postsynthetic Modification of Metal-Organic Frameworks***) as initially embodied by molecule **3**, can be designed by invoking the hard-and-soft principle. First, the carboxyl groups of DMBD selectively reacts with the chemically very hard Zr(IV) ions to set up the porous scaffold of ZrDMBD, whereas the soft mercapto (–SH) groups remain the free-standing functional units. Like many other Zr-MOF systems, the ZrDMBD framework (of the UiO-66 topology[43]) thus assembled features robust porosity: the activated ZrDMBD sample displayed typical type-I gas adsorption isotherms with a BET surface area of 513 $m^2\,g^{-1}$, and it is stable even to water and 2M nitric acids. In the second step, metal ions can be introduced into the pores of ZrDMBD to react with the thiol groups and install the metal–thiolate links. The very strong-binding thiol groups enable the uptake of diverse metal ions for broad functions (see ***Metal Uptake in Metal-Organic Frameworks***)—for example, for removing heavy metal ions, and for creating semiconductive/electroactive properties and catalytic sites (e.g., mimicking the iron–sulfur, copper–sulfur proteins). Moreover, the versatile organic transformations by thiols also allow for convenient postcrystallization (postsynthetic) modifications,[10,12–15] for example, covalent cross-linking inside the pores for synergizing the studies of organic polymers and solid-state frameworks, and reacting with other reagents (e.g., H_2O_2, Br_2) for further functional modifications.

Besides the thiol (–SH) group as showcased by DMBD, the thioether function (R–S–R) offers a useful alternative to team up with the carboxylic acid unit, so as to explore the hard-and-soft chemistry and the two-step strategy for network construction. Compared with thiols, thioethers are weaker donors. Being less disruptive, they allow a wider range of metal ions to be selectively bound by the carboxyl moiety for constructing the porous net: aside from the very hard Eu(III), Al(III), and Zr(IV), one can also use softer ones such as Pb(II), Zn(II), and Cu(II).[44–49] The unbonded, free-standing thioether donors in the resultant framework can then take up a wide range of soft

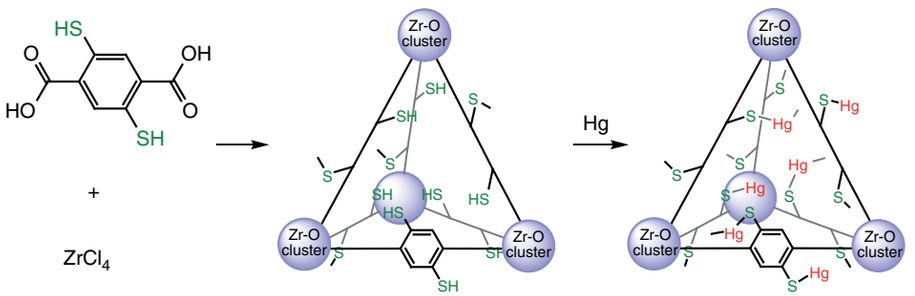


Figure 7 The synthetic scheme for the ZrDMBD network (same topology as UiO-66; simplified as a tetrahedral cage unit) and the uptake of Hg species (vapor or Hg^{2+} in water) to install the covalent metal–thiolate links throughout the network. The electronic properties of framework can thus be conveniently tuned by the very diverse metal guests that can be entered to link up the thiol donors

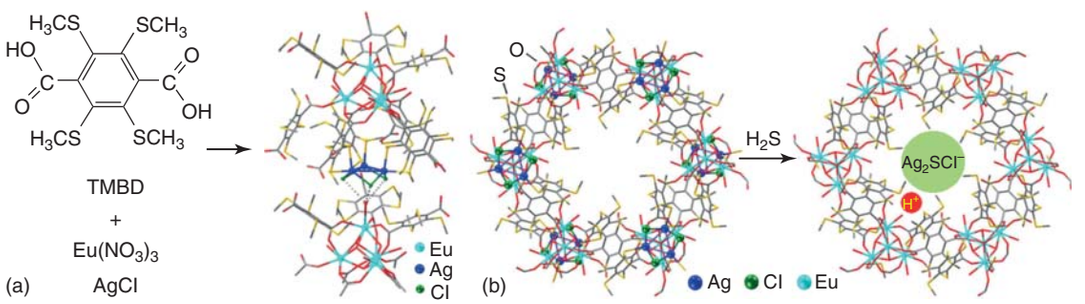


Figure 8 (a) The synthetic scheme of EuTMBD–AgCl, showing the local bonding features of the carboxyl-bound Eu_4O_4 cluster and sulfur-bound AgCl trimer in the X-ray single crystal structure. (b) A view of the single crystal structures of EuTMBD–AgCl along the channel direction before (left) and after (right) treatment by H_2S gas: the EuTMBD host net holds up in the process, whereas the AgCl moiety reacts to form disordered Ag_2SCl^- species which are located at the central region of the channel

metal species (e.g., $HgCl_2$, $PdCl_2$). Because of the generally labile nature of the thioether-metal coordination, the metal species thus uploaded into the pores can be readily involved in various transformations for functionalization purposes.

The close bearing on the semiconductive property is illustrated by the EuTMBD–AgCl framework system (Figure 8).[50] In this microporous composite system, the TMBD molecule extends the hard carboxylate groups to Eu(III) to form the 3D scaffold of the host net, while encapsulating the AgCl component using its soft sulfur side arms. When the network solid was treated by H_2S, the AgCl moiety was converted into the dark-colored Ag_2S species, while leaving the hard host net intact and upstanding. This hard-and-soft approach serves to conjoin the rich electronic/semiconductive properties of metal chalcogenides and the tunable size/function of coordination host net. In other words, the semiconductive property does not have to be directly borne by the host net (see also, e.g., a GaN-loaded MOF composite[51]). Instead, by adjusting the amount of the uploaded metal species, one can aim to form a continuous subdomain of the chalcogenide component to effect the charge transport throughout the composite solid matrix. As highly porous MOF scaffolds (e.g., with up to 70–90% of void fraction) become routinely accessible, even by partially (e.g., 50%) filling the void, one can conceivably result in a subsidiary net of the chalcogenide moiety that is extended in 1D or higher dimensionality (see also ***Mesoporous Metal-Organic Frameworks***); the remaining void space would be substantial, so much as that it maintains the high surface area and porous properties of the monolithic chalcogenide-MOF composite.

Besides small molecules such as H_2S, larger organic, aromatic thiol molecules are interesting and handy choices as guest species. In other words, the metal–thiolate subdomain thus installed within the porous MOF host serves to obviate the tendency to close-pack in the solid state, a tendency that is seen in the growing number of extended metal thiolate structures reported to date.[26,27,52–57] The many thiol molecules available, together with the highly tunable pore size/geometry of the crystalline host nets, will likely allow for tailoring the size, shape, and distribution of the metal thiolate species at the molecular level. Not only can one thus reliably impose high surface area on these electronically interesting systems,

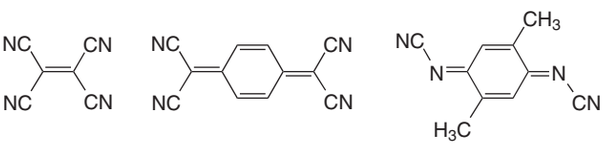
but also rationally impact the reactivity and materials properties associated with the subsidiary nets made of the metal–thiolate components.

In a broader perspective, the concept of subsidiary net construction readily encompasses a wide range of other linker systems (i.e., to be introduced as a subsidiary, guest linker into the metal-laden host net). Of relevance to the making of semiconducting/conducting networks are the well-known electron acceptor molecules, for example, tetracyanoquinodimethane (TCNQ), *N*,*N*′-dicyanoquinodiimine (DCQNI), and analogs (molecules **11**, **12**, and **13** in Scheme 4).[58,59] Besides being used to interact with electron donors (e.g., tetrathiafulvalene, TTF)[60–62] to make molecular organic metals, the cyano (–CN) groups on these organonitriles can bind metal ions, and many of the coordination networks thus formed present electronically interesting properties.[63–66] For example, the close-packed diamondoid network compound (sixfold interpenetrated), $(DM\text{-}TCNQI)_2Cu$ was reported to be electronically conductive in the year 1986[67] [a few years before Robson's seminal report[4] on the open framework of Cu(I)–TCPM]. However, porous and semiconductive networks of these acceptor organonitrile–metal systems have not been reported, possibly due to the relatively weak metal–nitrile bonds and the packing habits associated with the linkers used. By installing a subsidiary net of conductive organonitrile–metal component [e.g., Cu(TCNQ)] within a highly porous MOF matrix, one could therefore create a functional composite system that unifies the high surface area of the host net and the conductive properties of the subsidiary net.

In the context of subsidiary net construction, the sulfur-functionalized frameworks as host systems offer obvious advantages. First, the sulfur donor effectively anchors the metal species within the host net (other ways of loading metal species into MOF pores are also known[14,51,68–80]), minimizing their leaching out of the pores and preventing the formation of the chalcogenide or metal–thiolate components outside of the MOF crystals. With the anchoring of the sulfur donors, one can hope for the formation of uniform and monolithic composite throughout the MOF matrix. Also, the sulfur donors recover their (largely) free-standing state after the first iteration of subnet formation, and thus are ready to take up metal species again for further rounds of subnet formation, so as to increase its volume fraction (e.g., relative to the host net), and to fine-tune the conductive and porous characters of the overall composite crystal system.

4 TURNING INSOLUBILITY ON ITS HEAD

In their earlier papers, Wolczanski and coworkers demonstrated the strongly electroactive nature of



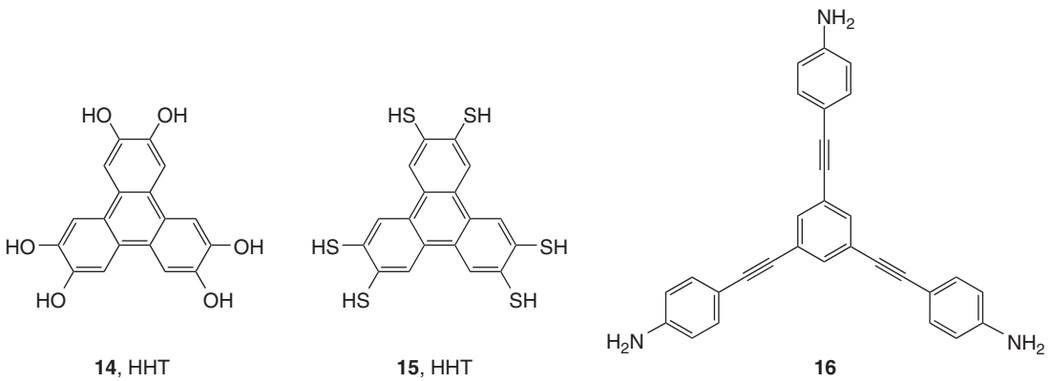
11, TCNE **12**, TCNQ **13**, DM-DCNQI

Scheme 4 Three organocyanide molecules (TCNE, TCNQ, and DM-DCNQI) used as electron acceptors in organic metals and conductive coordination networks

a series of covalent metal–organic networks (CMON) based on metal–aryloxide connections.[81–85] For example, strong, covalent titanium/quinone linkages were chosen as the crucial connections to encourage intermetallic electronic communication (i.e., $Ti^{IV}–OC_6H_4O–Ti^{IV} \leftrightarrow Ti^{III}{\leftarrow}O{=}CC_4H_4C{=}O{\rightarrow}Ti^{III}$) throughout these densely packed (nonporous) solid-state networks. More recently, Yaghi and coworkers reported porous 2D frameworks based on the highly conjugated tricatecholate, 2,3,6,7,10,11-hexahydroxytriphenylene (HHT, molecule **14** in Scheme 5), and metal ions (Co^{2+} or Ni^{2+}).[86] The crystal structures (Figure 9) of these metal–catecholates (M–CATs) consist of two types of lamellar domains. In one, Co(II) is chelated to two HHTP linkers to form a 2D honeycomb sheet, and the HHT therein exist in the semiquinone form with the charge of each deprotonated HHT being −3; in the other layer, the HHT is not oxidized and each takes on three Co(II), with each of the latter being sealed off by four water molecules to give the isolated complex of $Co_3(HHT)(H_2O)_{12}$. Argon gas adsorption measurements at 87 K reveal the BET surface areas for Co and Ni–CAT-1 to be 490 and 425 $m^2\ g^{-1}$, respectively. The microcrystalline sample of Cu–CAT-1 showed high electrical conductivity and charge storage capacity.

Growing single crystals for these semiconducting frameworks is, however, exceptionally challenging. Single crystals good for regular diffractometers are hard to come by, and synchrotron radiation or powder diffraction methods are often necessary for elucidating the crystal structures. To some degree, a dilemma exists between conductivity and the crystalline order: efficient charge transports call for strong metal–linker interaction, and it is such strong interaction that tends to frustrate the formation of ordered, crystalline networks. In fact, the large majority of crystalline MOFs are based on the relatively labile donors such as carboxylate and pyridinyl units; crystalline networks based on the stronger metal–aryloxide and metal–thiolate links remain, by comparison, few and far between.

But porosity does not have to entail crystallinity. As is well illustrated by the growing field of porous polymer frameworks,[87–96] in which molecular building blocks with rigid and open geometry are often found to polymerize to form open, porous covalent structures with large pores and surface areas (e.g., up to 5000 $m^2\ g^{-1}$,[97] about 10 times that



Scheme 5 The HTT molecule (**14**), together with two other rigid, trigonal molecules (**15** and **16**), for directly reacting with metal species (e.g., $PtCl_2$ for **15** and $BiCl_3$ for **16**) to produce covalent metal–organic networks with porous and semiconductive properties

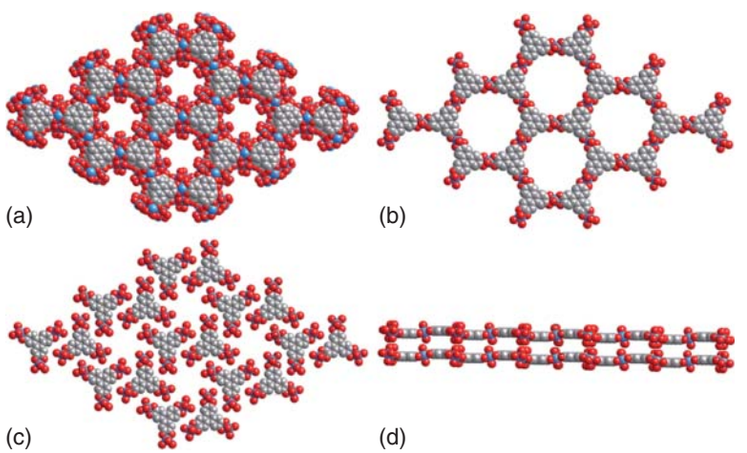


Figure 9 Space filling drawings of the single-crystal structure of Co–CAT-1. (a) Overview along the *c* axis. (b) Extended layer of Co–CAT-1. (c) Layer of the trinuclear complexes $Co_3(HTTP)(H_2O)_{12}$ (d) Side view of two adjacent layers. Color code: Co, blue; C, gray; O, red. (Reprinted with permission from Ref. 86. Copyright (2012) American Chemical Society.)

of activated carbon). Once again, the rigidity factor comes into play—only this time, the polymerization process directly involves the formation of the very strong covalent bonds. With carefully chosen building blocks, reaction conditions can at times be found to give products with significant structural order (e.g., as per X-ray powder diffraction) in the porous framework products. One major forte of these polymer framework solids is their stability, as is seen in the covalent triazine-based frameworks (CTFs)[88–90] and the diamondlike networks based on tetraphenylmethane building blocks;[97,98] both systems withstand high temperatures (e.g., up to 400 °C) and strong acid/base treatments, with stability of the former (i.e., CTFs) further highlighted in a recently reported application for electrochemical energy storage device, in which the CTF system continues to hold up after thousands of electrochemical cycles.[99]

The connection to metal–organic systems is therefore obvious—for example, to directly react metal species with thiol building blocks that are of open and rigid structures. The reaction will be fast, and the resultant metal–thiolate frameworks less-ordered than the regular MOF crystals, but significant porosity is likely to be enforced by the rigid and open character of the building units. In such a simple, one-pot recipe, porosity can be integrated with the versatile electronic/semiconducting properties of the metal–thiolate systems. In other words, one turns the insolubility issue on its head. By relenting on the mandate of crystallinity, one sidesteps the dilemma between bonding strength and conductive properties, and thus comes to achieve electroactive/conductive properties in robust covalent frameworks that are structurally less-ordered but present strong porous character and high surface area for practical applications.

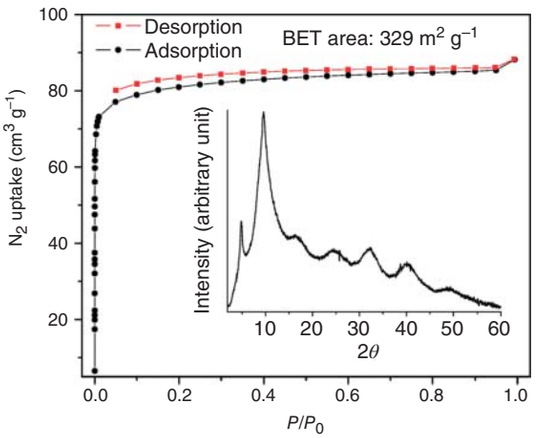


Figure 10 N_2 (273 K) adsorption/desorption isotherms for an activated HTT-Pt sample; inset: a PXRD pattern of an as-made sample of HTT-Pt

Among the many rigid thiol molecules, the triphenylene hexathiol molecule (**15**, HTT in Scheme 5) is illustrative. The advantages provided by a molecule such as HTT are obvious. Besides the very rigid, symmetrical imposed by the fused aromatic core of triphenylene unit, the chelating dithiolene unit of HTT is poised to form rigid, well-defined bonding motifs with metal ions;[100,101] the sulfur atoms are fully conjugated with triphenylene core to provide conductive pathways in the prospective solid-state frameworks. Moreover, the synthesis of HTT (or its thioester as the protected form) is highly feasible—it has already been well-established in the literature.[102,103]

Experiments on HTT and $PtCl_2$ attest to the potential efficacy of this approach.[104] Simply by reacting the hexaanion of HTT (e.g., 0.12 mmol, generated in situ from the hexabutyryl thioester of HTT in NaOH/methanol) and $Pt(CH_3CN)_2Cl_2$ (0.18 mmol) under N_2 in a methanol/DMA(*N*,*N*-dimethylacetamide) solution at 90 °C for several hours, one obtained a black solid product of HTT-Pt in high yield (over 90%). The as-made solid of HTT-Pt features a composition of $(HTT)_{2.0}Pt_{3.0}Na_{2.0}$, and shows a series of broadened X-ray diffraction peaks indicative of a honeycomb-like structure (inset of Figures 10 and 11). The crystalline order was maintained after activation by Soxhlet-extracting with methanol (in air), and the activated sample exhibits a BET area over 300 $m^2\,g^{-1}$ (Figure 10). Moreover, the Na^+ ion in the pores of HTT-Pt can be exchanged with Li^+ and Cs^+ in water solutions; and the anionic framework can be oxidized by I_2 to give a nearly neutral framework of $(HTT)_{2.0}Pt_{3.0}$ (with HTT being trianionic). Both ion exchange and I_2 treatment do not compromise the overall structural integrity of the HTT-Pt host framework, and the porous character (e.g., with comparable BET surface areas) continues to hold up as a result.

5 CONCLUSION

A summary of the large field of porous semiconductive frameworks would normally be a daunting task. But a summary for this work is not; only one word is needed for each of three synthetic methods identified. (i) Tempering: for example, of the bonding strength of thiols by carboxyl and other electron-withdrawing groups; (ii) severing: for example, the crystallization of the host net from the installation of the metal–thiolate subsidiary net, as in the spirit of the hard-and-soft or the two-step approach; and (iii) mixing: for example, rigid open thiol building blocks with metal species to directly produce semiconductive frameworks that are less-ordered but retain substantial porous features. Among the three methods, rigid and multidirectional molecular building blocks uniformly embody a consistent, crucial design element. With careful functionalization (as in the carboxyl–thiol or carboxyl–thioether combination), such rigid building blocks prove to be especially versatile in tackling the electronic properties and other topical issues in the field of porous framework materials.

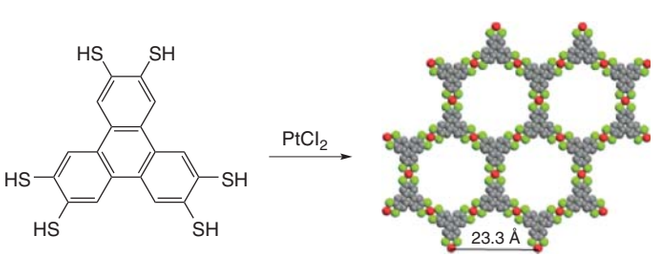


Figure 11 A schematic for the reaction between the HTT molecule and $PtCl_2$, with the resultant framework of HTT-Pt shown as a single net modelled on standard bonding geometries

6 ACKNOWLEDGMENTS

This work is supported by City University of Hong Kong (Project 7002723) and the Research Grants Council of HKSAR (GRF Project 103212). ZX acknowledges the Alexander von Humboldt Foundation for a Humboldt Research Fellowship for Experienced Researchers (host: Prof. Markus Antonietti). The preliminary results on HTT-Pt were obtained with technical assistance from Mr. Jieshun Cui (as part of his PhD dissertation). Figure 1 was redrawn by Mr. Yan Lung Wong.

7 RELATED ARTICLES

Electrochemical Properties of Metal-Organic Frameworks; Mesoporous Metal-Organic Frameworks; Metal Uptake in Metal-Organic Frameworks; Post-synthetic Modification of Metal-Organic Frameworks; Single-Crystal to Single-Crystal Transformations in Metal-Organic Frameworks.

8 ABBREVIATIONS AND ACRONYMS

BET = Brunauer–Emmett–Teller; CMON = covalent metal–organic networks; CTF = covalent triazine-based framework; DCQNI = *N*,*N*′-dicyanoquinodiimine; DEF = *N*,*N*-diethylformamide; DMA = *N*,*N*-dimethylacetamide; FP-TRMC = flash-photolysis time-resolved microwave conductivity; HHT = 2,3,6,7,10,11-hexahydroxytriphenylene; M–CAT = metal–catecholate; PSM = postsynthesis modifications; PXRD = powder X-ray diffraction; TCNQ = tetracyanoquinodimethane; TOF = time-of-flight; TTF = tetrathiafulvalene.

9 REFERENCES

1. G. Givaja, P. Amo-Ochoa, C. J. Gómez-García, and F. Zamora, *Chem. Soc. Rev.*, 2012, **41**, 115.
2. C. H. Hendon, D. Tiana, and A. Walsh, *PCCP*, 2012, **14**, 13120.
3. Z. Xu, *Coord. Chem. Rev.*, 2006, **250**, 2745.
4. B. F. Hoskins and R. Robson, *J. Am. Chem. Soc.*, 1989, **111**, 5962.
5. G. B. Gardner, D. Venkataraman, J. S. Moore, and S. Lee, *Nature*, 1995, **374**, 792.
6. Y.-H. Kiang, G. B. Gardner, S. Lee, and Z. Xu, *J. Am. Chem. Soc.*, 2000, **122**, 6871.
7. M. P. Suh, H. J. Choi, S. M. So, and B. M. Kim, *Inorg. Chem.*, 2003, **42**, 676.
8. N. Kobayashi and M. Kijima, *J. Mater. Chem.*, 2008, **18**, 1037.
9. H. Furukawa, N. Ko, Y. B. Go, N. Aratani, S. B. Choi, E. Choi, A. O. Yazaydin, R. Q. Snurr, M. O'Keeffe, J. Kim, and O. M. Yaghi, *Science*, 2010, **329**, 424.
10. Z. Xu, S. Lee, Y.-H. Kiang, A. B. Mallik, N. Tsomaia, and K. T. Mueller, *Adv. Mater.*, 2001, **13**, 637.
11. Z. Xu, Y.-H. Kiang, S. Lee, E. B. Lobkovsky, and N. Emmott, *J. Am. Chem. Soc.*, 2000, **122**, 8376.
12. J. S. Seo, D. Whang, H. Lee, S. I. Jun, J. Oh, Y. J. Jeon, and K. Kim, *Nature*, 2000, **404**, 982.
13. P. Brunet, E. Demers, T. Maris, G. D. Enright, and J. D. Wuest, *Angew. Chem. Int. Ed.*, 2003, **42**, 5303.
14. C.-D. Wu, A. Hu, L. Zhang, and W. Lin, *J. Am. Chem. Soc.*, 2005, **127**, 8940.
15. Z. Wang and S. M. Cohen, *J. Am. Chem. Soc.*, 2007, **129**, 12368.
16. L. Ma, J. M. Falkowski, C. Abney, and W. Lin, *Nat. Chem.*, 2010, **2**, 838.
17. A. P. Cote, A. I. Benin, N. W. Ockwig, M. O'Keeffe, A. J. Matzger, and O. M. Yaghi, *Science*, 2005, **310**, 1166.
18. S. Kanda and S. Kawaguchi, *J. Chem. Phys.*, 1961, **34**, 1070.
19. S. Kanda, A. Suzuki, and K. Ohkawa, Energy and Charge Transfer Organic Semiconductors: Proceedings of the U.S.-Japan Seminar, 1974, p. 85.
20. M. J. S. Dewar and A. M. Talati, *J. Am. Chem. Soc.*, 1963, **85**, 1874.
21. M. Fujishima, S. Kanda, T. Mitani, and H. Kitagawa, *Synth. Met.*, 2001, **119**, 485.
22. Y. Nagao, R. Ikeda, S. Kanda, Y. Kubozono, and H. Kitagawa, *Mol. Cryst. Liq. Cryst. Sci. Technol., Sect. A*, 2002, **379**, 89.
23. H. Kitagawa, Y. Nagao, M. Fujishima, R. Ikeda, and S. Kanda, *Inorg. Chem. Commun.*, 2003, **6**, 346.
24. Y. Nagao, T. Kubo, K. Nakasuji, R. Ikeda, T. Kojima, and H. Kitagawa, *Synth. Met.*, 2005, **154**, 89.
25. L. Yang, S. Kinoshita, T. Yamada, S. Kanda, H. Kitagawa, M. Tokunaga, T. Ishimoto, T. Ogura, R. Nagumo, A. Miyamoto, and M. Koyama, *Angew. Chem. Int. Ed.*, 2010, **49**, 5348.
26. Y. Zhao, M. Hong, Y. Liang, R. Cao, J. Weng, S. Lu, and W. Li, *Chem. Commun.*, 2001, 1020.
27. W. Su, M. Hong, J. Weng, R. Cao, and S. Lu, *Angew. Chem. Int. Ed.*, 2000, **39**, 2911.
28. S. Takaishi, M. Hosoda, T. Kajiwara, H. Miyasaka, M. Yamashita, Y. Nakanishi, Y. Kitagawa, K. Yamaguchi, A. Kobayashi, and H. Kitagawa, *Inorg. Chem.*, 2009, **48**, 9048.
29. Y. Kobayashi, B. Jacobs, M. D. Allendorf, and J. R. Long, *Chem. Mater.*, 2010, **22**, 4120.

30. F. Gándara, F. J. Uribe-Romo, D. K. Britt, H. Furukawa, L. Lei, R. Cheng, X. Duan, M. O'Keeffe, and O. M. Yaghi, *Chem. Eur. J.*, 2012, **18**, 10595.
31. R. Bolligarla, S. N. Reddy, G. Durgaprasad, V. Sreenivasulu, and S. K. Das, *Inorg. Chem.*, 2013, **52**, 66.
32. J. He, C. Yang, Z. Xu, M. Zeller, A. D. Hunter, and J. Lin, *J. Solid State Chem.*, 2009, **182**, 1821.
33. T. Ahnfeldt, D. Gunzelmann, T. Loiseau, D. Hirsemann, J. Senker, G. Férey, and N. Stock, *Inorg. Chem.*, 2009, **48**, 3057.
34. T. Ahnfeldt, N. Guillou, D. Gunzelmann, I. Margiolaki, T. Loiseau, G. Férey, J. Senker, and N. Stock, *Angew. Chem. Int. Ed.*, 2009, **48**, 5163.
35. H. Reinsch, B. Marszalek, J. Wack, J. Senker, B. Gil, and N. Stock, *Chem. Commun.*, 2012, **48**, 9486.
36. H. Reinsch, M. Feyand, T. Ahnfeldt, and N. Stock, *Dalton Trans.*, 2012, **41**, 4164.
37. G. Férey, C. Mellot-Draznieks, C. Serre, F. Millange, J. Dutour, S. Surble, and I. Margiolaki, *Science*, 2005, **309**, 2040.
38. L. Hamon, C. Serre, T. Devic, T. Loiseau, F. Millange, G. Férey, and G. De Weireld, *J. Am. Chem. Soc.*, 2009, **131**, 8775.
39. C. Serre, F. Millange, C. Thouvenot, M. Nogues, G. Marsolier, D. Loueer, and G. Férey, *J. Am. Chem. Soc.*, 2002, **124**, 13519.
40. M. Kim and S. M. Cohen, *CrystEngComm*, 2012, **14**, 4096.
41. T. C. Narayan, T. Miyakai, S. Seki, and M. Dincă, *J. Am. Chem. Soc.*, 2012, **134**, 12932.
42. L. Sun, T. Miyakai, S. Seki, and M. Dincă, *J. Am. Chem. Soc.*, 2013, **135**, 8185.
43. J. H. Cavka, S. Jakobsen, U. Olsbye, N. Guillou, C. Lamberti, S. Bordiga, and K. P. Lillerud, *J. Am. Chem. Soc.*, 2008, **130**, 13850.
44. X.-P. Zhou, Z. Xu, M. Zeller, A. D. Hunter, S. S.-Y. Chui, and C.-M. Che, *Inorg. Chem.*, 2008, **47**, 7459.
45. X.-P. Zhou, Z. Xu, M. Zeller, and A. D. Hunter, *Chem. Commun.*, 2009, 5439.
46. A. D. Burrows, C. G. Frost, M. F. Mahon, and C. Richardson, *Chem. Commun.*, 2009, 4218.
47. X.-P. Zhou, Z. Xu, J. He, M. Zeller, A. D. Hunter, R. Clérac, C. Mathonière, S. S.-Y. Chui, and C.-M. Che, *Inorg. Chem.*, 2010, **49**, 10191.
48. J. He, K.-K. Yee, Z. Xu, M. Zeller, A. D. Hunter, S. S.-Y. Chui, and C.-M. Che, *Chem. Mater.*, 2011, **23**, 2940.
49. J. He, M. Zha, J. Cui, M. Zeller, A. D. Hunter, S.-M. Yiu, S.-T. Lee, and Z. Xu, *J. Am. Chem. Soc.*, 2013, **135**, 7807.
50. X.-P. Zhou, Z. Xu, M. Zeller, A. D. Hunter, S. S.-Y. Chui, C.-M. Che, and J. Lin, *Inorg. Chem.*, 2010, **49**, 7629.
51. D. Esken, S. Turner, C. Wiktor, S. B. Kalidindi, G. Van Tendeloo, and R. A. Fischer, *J. Am. Chem. Soc.*, 2011, **133**, 16370.
52. E. Neofotistou, C. D. Malliakas, and P. N. Trikalitis, *Inorg. Chem.*, 2007, **46**, 8487.
53. D. L. Turner, T. P. Vaid, P. W. Stephens, K. H. Stone, A. G. DiPasquale, and A. L. Rheingold, *J. Am. Chem. Soc.*, 2008, **130**, 14.
54. X.-Y. Tang, H.-X. Li, J.-X. Chen, Z.-G. Ren, and J.-P. Lang, *Coord. Chem. Rev.*, 2008, **252**, 2026.
55. K.-H. Low, V. A. L. Roy, S. S.-Y. Chui, S. L.-F. Chan, and C.-M. Che, *Chem. Commun.*, 2010, **46**, 7328.
56. S. L.-F. Chan, K.-H. Low, G. K.-M. So, S. S.-Y. Chui, and C.-M. Che, *Chem. Commun.*, 2011, **47**, 8808.
57. E. J. Mensforth, M. R. Hill, and S. R. Batten, *Inorg. Chim. Acta*, 2013, **403**, 9.
58. D. S. Acker, R. J. Harder, W. R. Hertler, W. Mahler, L. R. Melby, R. E. Benson, and W. E. Mochel, *J. Am. Chem. Soc.*, 1960, **82**, 6408.
59. N. Martín, J. L. Segura, and C. Seoane, *J. Mater. Chem.*, 1997, **7**, 1661.
60. F. Wudl, D. Wobschall, and E. J. Hufnagel, *J. Am. Chem. Soc.*, 1972, **94**, 670.
61. M. Bendikov, F. Wudl, and D. F. Perepichka, *Chem. Rev.*, 2004, **104**, 4891.
62. J. Ferraris, D. O. Cowan, V.Walatka Jr, and J. H. Perlstein, *J. Am. Chem. Soc.*, 1973, **95**, 948.
63. C. Avendano, Z. Zhang, A. Ota, H. Zhao, and K. R. Dunbar, *Angew. Chem. Int. Ed.*, 2011, **50**, 6543.
64. Z. Zhang, H. Zhao, H. Kojima, T. Mori, and K. R. Dunbar, *Chem. Eur. J.*, 2013, **19**, 3348.
65. R. S. Potember, T. O. Poehler, and D. O. Cowan, *Appl. Phys. Lett.*, 1979, **34**, 405.
66. B. F. Abrahams, R. W. Elliott, T. A. Hudson, and R. Robson, *Cryst. Growth Des.*, 2013, **13**, 3018.
67. A. Aumüller, P. Erk, G. Klebe, S. Hünig, J. U. v. Schütz, and H.-P. Werner, *Angew. Chem. Int. Ed. Engl.*, 1986, **25**, 740.
68. H. R. Moon, J. H. Kim, and M. P. Suh, *Angew. Chem. Int. Ed.*, 2005, **44**, 1261.
69. M. J. Ingleson, J. P. Barrio, J.-B. Guilbaud, Y. Z. Khimyak, and M. J. Rosseinsky, *Chem. Commun.*, 2008, 2680.
70. K. L. Mulfort, O. K. Farha, C. L. Stern, A. A. Sarjeant, and J. T. Hupp, *J. Am. Chem. Soc.*, 2009, **131**, 3866.
71. B. Chen, L. Wang, Y. Xiao, F. R. Fronczek, M. Xue, Y. Cui, and G. Qian, *Angew. Chem. Int. Ed.*, 2009, **48**, 500.
72. M. H. Alkordi, Y. Liu, R. W. Larsen, J. F. Eubank, and M. Eddaoudi, *J. Am. Chem. Soc.*, 2008, **130**, 12639.
73. C. J. Doonan, W. Morris, H. Furukawa, and O. M. Yaghi, *J. Am. Chem. Soc.*, 2009, **131**, 9492.
74. K. K. Tanabe and S. M. Cohen, *Angew. Chem. Int. Ed.*, 2009, **48**, 7424.
75. M. Sabo, A. Henschel, H. Fröde, E. Klemm, and S. Kaskel, *J. Mater. Chem.*, 2007, **17**, 3827.

76. T. Ishida, M. Nagaoka, T. Akita, and M. Haruta, *Chem. Eur. J.*, 2008, **14**, 8456.

77. T. Uemura, D. Hiramatsu, K. Yoshida, S. Isoda, and S. Kitagawa, *J. Am. Chem. Soc.*, 2008, **130**, 9216.

78. F. Schröder, D. Esken, M. Cokoja, M. W. E.van den Berg, O. I. Lebedev, G. Van Tendeloo, B. Walaszek, G. Buntkowsky, H.-H. Limbach, B. Chaudret, and R. A. Fischer, *J. Am. Chem. Soc.*, 2008, **130**, 6119.

79. M. Meilikhov, K. Yusenko, and R. A. Fischer, *Dalton Trans.*, 2009, 600.

80. M. Müller, X. Zhang, Y. Wang, and R. A. Fischer, *Chem. Commun.*, 2009, 119.

81. T. P. Vaid, E. B. Lobkovsky, and P. T. Wolczanski, *J. Am. Chem. Soc.*, 1997, **119**, 8742.

82. T. P. Vaid, J. M. Tanski, J. M. Pette, E. B. Lobkovsky, and P. T. Wolczanski, *Inorg. Chem.*, 1999, **38**, 3394.

83. J. M. Tanski, T. P. Vaid, E. B. Lobkovsky, and P. T. Wolczanski, *Inorg. Chem.*, 2000, **39**, 4756.

84. J. M. Tanski and P. T. Wolczanski, *Inorg. Chem.*, 2001, **40**, 2026.

85. J. M. Tanski and P. T. Wolczanski, *Inorg. Chem.*, 2001, **40**, 346.

86. M. Hmadeh, Z. Lu, Z. Liu, F. Gándara, H. Furukawa, S. Wan, V. Agustyn, R. Chang, L. Liao, F. Zhou, E. Perre, V. Ozolins, X. Duan, B. Dunn, Y. Yamamto, O. Terasaki, and O. M. Yaghi, *Chem. Mater.*, 2012, **24**, 3511.

87. P. M. Budd, B. Ghanem, K. Msayib, N. B. McKeown, and C. Tattershall, *J. Mater. Chem.*, 2003, **13**, 2721.

88. P. Kuhn, M. Antonietti, and A. Thomas, *Angew. Chem. Int. Ed.*, 2008, **47**, 3450.

89. P. Kuhn, A. Thomas, and M. Antonietti, *Macromolecules*, 2009, **42**, 319.

90. S. Ren, M. J. Bojdys, R. Dawson, A. Laybourn, Y. Z. Khimyak, D. J. Adams, and A. I. Cooper, *Adv. Mater.*, 2012, **24**, 2357.

91. Z. Xie, C. Wang, K. E.de Krafft, and W. Lin, *J. Am. Chem. Soc.*, 2011, **133**, 2056.

92. N. B. McKeown and P. M. Budd, *Macromolecules*, 2010, **43**, 5163.

93. Z. Xiang and D. Cao, *J. Mater. Chem. A*, 2013, **1**, 2691.

94. P. Kaur, J. T. Hupp, and S. T. Nguyen, *ACS Catalysis*, 2011, **1**, 819.

95. Y. Zhang and S. N. Riduan, *Chem. Soc. Rev.*, 2012, **41**, 2083.

96. A. Thomas, *Angew. Chem. Int. Ed.*, 2010, **49**, 8328.

97. T. Ben, H. Ren, S. Ma, D. Cao, J. Lan, X. Jing, W. Wang, J. Xu, F. Deng, J. M. Simmons, S. Qiu, and G. Zhu, *Angew. Chem. Int. Ed.*, 2009, **48**, 9457.

98. H. Ren, T. Ben, E. Wang, X. Jing, M. Xue, B. Liu, Y. Cui, S. Qiu, and G. Zhu, *Chem. Commun.*, 2010, **46**, 291.

99. K. Sakaushi, G. Nickerl, F. M. Wisser, D. Nishio-Hamane, E. Hosono, H. Zhou, S. Kaskel, and J. Eckert, *Angew. Chem. Int. Ed.*, 2012, **51**, 7850.

100. C. W. Dirk, M. Bousseau, P. H. Barrett, F. Moraes, F. Wudl, and A. J. Heeger, *Macromolecules*, 1986, **19**, 266.

101. T. Kambe, R. Sakamoto, K. Hoshiko, K. Takada, M. Miyachi, J.-H. Ryu, S. Sasaki, J. Kim, K. Nakazato, M. Takata, H. Nishihara, *J. Am. Chem. Soc.*, 2013, **135**, 2462.

102. K. Li, Z. Xu, H. Xu, and J. M. Ryan, *Chem. Mater.*, 2005, **17**, 4426.

103. K. Li, PhD thesis, George Washington University (Washington, DC), 2006.

104. J. Cui, Z. Xu, *Chem. Commun.* 2014, **50**, 3986.

Patterning Techniques for Metal-Organic Frameworks

Paolo Falcaro and Mark J. Styles

Commonwealth Scientific and Industrial Research Organisation (CSIRO), Clayton South, VIC, Australia

1	Introduction	387
2	Positioning MOFs, the Different Methods	388
3	Conclusions and Future Outlook	397
4	Acknowledgments	398
5	Abbreviations and Acronyms	398
6	References	398

1 INTRODUCTION

Of all the different functional materials, porous and ultraporous materials are an important class of responsive materials for a variety of different applications.[1] Despite the potential of this class of materials, the positioning protocols have been broadly investigated only for specific subclasses (e.g., mesoporous coatings[2]); for other porous materials, the research is still in a primordial stage (e.g., thermally rearranged polymers[3]). In the case of metal-organic frameworks (MOFs), also called porous coordination polymers, an increasing number of studies on controlling the location of such ultraporous materials have been recently reported.[4] MOFs are an emerging class of ultraporous hybrid materials that originate through the self-assembly of metallic nodes coordinating polydentate bridging ligands (usually carboxylate, sulfonate, or phosphonate). Once the proper synthetic conditions are found, the resulting material presents high porosity due to a precise, geometrically arranged network.[5–9] A schematic of a generic cubic arrangement is proposed in Figure 1h.

Owing to their large surface area, tunable pore size, chemistry, and topology, MOFs have been extensively studied as they are very promising for a variety of applications.[12] Although MOFs have been mainly investigated for their outstanding gas storage properties[13] and separation,[8] these porous crystals hold much promise in sensing,[14] micro- and nano-electronics,[15,16] micromotors,[17] as well as biological and medical applications.[12,18,19] The precise design of the framework, as well as engineering via heterogeneous functionalization, enable the fabrication of stimuli-responsive materials with a variety of functional properties.[20–25]

Owing to the fervent research activity in this field, an increasing number of reviews are available, providing comprehensive overviews of different aspects related to MOFs, such as their synthesis,[26–28] postsynthetic modification techniques,[29] concepts/properties,[30,31] and possible applications.[32,33] The fabrication of MOF films was an essential first step for the production of MOF-based devices. The research groups of Fisher,[34,35] Kitagawa,[36] and the Sanchez and Férey[37–39] are examples of pioneers who have proposed protocols that have led to progress in this field. However, the incorporation of these self-assembled structures into a device is a complex task,[40] and only a few cases have been reported of MOFs being used in miniaturized devices.[15] Recent progress in MOF patterning technology has enabled the achievement of a limited number of versatile and fast patterning techniques. The control of their growth and position on a variety of substrates and the ability to tune the crystal orientation, quality, and size are currently major challenges in the field. In this chapter, we review the recent progress in positioning MOFs and controlling the location of active functional species within MOFs.

Metal-Organic Framework Materials. Edited by Leonard R. MacGillivray and Charles M. Lukehart.
© 2014 John Wiley & Sons, Ltd. ISBN 978-1-119-95289-3

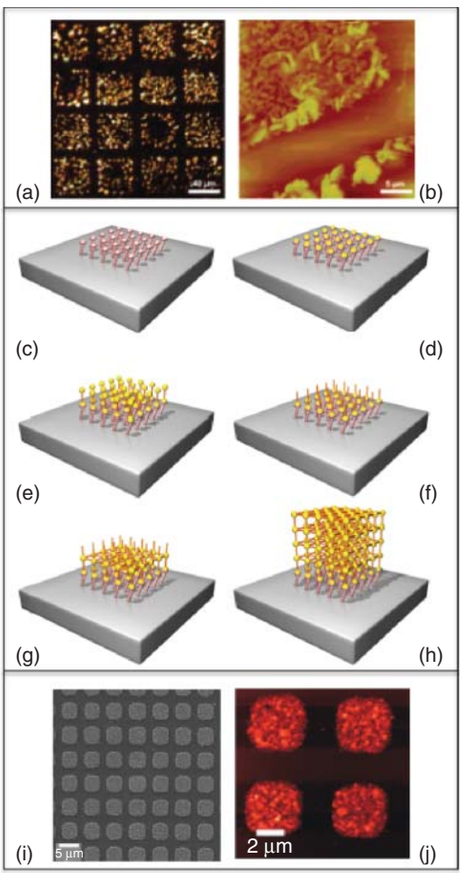


Figure 1 (a) Optical microscope and (b) an AFM image of a patterned self-assembled monolayer (SAM) of 16-mercaptohexadecanoic acid and 1H,1H,2H,2H-perfluorododecane thiol on Au(111) after a solvothermal growth of MOF-5. (Reproduced with permission from Ref. 10.) (c–h) The layer-by-layer approach for growing thin MOF films on SAM-functionalized substrates; the functionalization is shown in pink. The technique involves repeated cycles of immersion in solutions of the metal precursor (yellow balls) and of the organic ligand (orange sticks) with washing between each step. (Reproduced with permission from Ref. 4.) After several cycles, the MOF crystal is formed (h). (i) SEM and (j) AFM images of patterned Cu-ADA MOF thin films after layer-by layer deposition multistep procedure (16 cycles) on a patterned SAM gold substrate via microcontact printing (μCP) using 1-hexadecanethiol (HDT) (squares). (Reprinted with permission from Ref. 11. Copyright (2011) American Chemical Society.)

2 POSITIONING MOFs, THE DIFFERENT METHODS

Self-assembly presents a spontaneous mechanism for the preparation of materials with complex architectures. In this context, self-assembly represents an ideal process to build up a framework with defined porosity without the need for further processing.[15] However, due to the intrinsic nature of the spontaneous organization, control over the growth and position of the MOF self-assembly presents an open challenge.[40]

The current MOF patterning protocols have been mainly based on a bottom-up approach and only recently has the top-down approach been explored as a potential patterning methodology. Nature provides evidence that crystallization processes can be carefully controlled[41] and research in the use of self-assembly for device fabrication is in progress.[42] However, for MOFs, the investigation of patterning protocols is in its infancy. The ideal fabrication technique for MOFs would enable control over the crystal position, size, orientation, and lattice quality in a fast and inexpensive process. A strong adhesion between the ultraporous crystals and different substrates would also be desirable. The majority of the protocols presented in the literature allow the control over several aspects; however, further progress is required to accomplish all of the suggested goals. Here, we summarize the proposed methodologies in three main streams, taking advantage of:

Promoting agents to assist the nucleation in specific locations. This fabrication method involves directly controlling the MOF position using a specific agent (e.g., seeding method or controlled film growth). Such an agent plays an active role, enhancing/promoting the MOF nucleation/growth process in selected areas.

External controls to drive the nucleation in confined areas. The external control can be any external driving force promoting the growth of MOFs (e.g., electrochemical approach) or controlling/depositing the amount of MOF precursors in precise locations (e.g., microcontact printing and evaporation-induced growth).

Preformed MOFs that can be precisely located, using an external control. With this two-step approach (synthesis of MOFs and then relocation), the positioning can be permanently or dynamically achieved (e.g., photolithography assisted fabrication as permanent localization and patterning using a magnetic field as dynamic localization).

2.1 Promoting Agents

2.1.1 Controlled Thin Film Growth

The first step for the fabrication of MOF-based devices is usually the ability to prepare MOF coatings. Several reviews on the formation of MOF films have recently been published;[34,35,43] however, here we focus on the ability to position and pattern MOFs for device applications. Thin MOF films were initially prepared using self-assembled organic monolayers (SAMs[44]) as promoting agents in combination with solvothermal processes.[10] MOF-5 building units were bound to the SAM's carboxylic acid surface groups forming a 500-nm thick polycrystalline

film that was selectively patterned[10] using the microcontact printing (μCP[45]) lithographic method (Figure 1a, b). It has been shown that the SAM layer is crucial for the fabrication of thin MOF films with preferential orientation.[46–48] Bein *et al*. showed that the out-of-plane crystal orientation depends on whether the SAM is terminated by the COOH– or the OH– groups.[46]

Controlled MOF film crystallization was achieved by Fischer's group[49–52] through a layer-by-layer (LbL[53]) or liquid phase epitaxy (LPE[54]) technique. Ultrathin MOF films (also called SURMOFs[35]) are built by immersing the substrate into alternate mixtures of the metal precursor and the organic ligand; this induces the formation of crystals preferentially oriented along the out-of-plane direction. (The preferential growth produced by the LbL process is illustrated in (Figure 1 c–h.) The resultant MOF films have a smooth surface (roughness in the order of a few molecules) due to the accurate control over the formation process.[43] Further progress producing both out-of-plane and in-plane order was achieved by the Langmuir Blodgett method.[55,56]

Using the layer-by layer growth technique on SAM functionalized surfaces, Terfort's group[11,57] produced patterned MOF thin films. The Cu-based MOF films, prepared from Cu-carboxylate dimer secondary building units (SBUs) and 4,4-azobenzene dicarboxylate ligands (ADA), were grown from patterns functionalized with 1-hexadecanethiol (HDT) SAM on a gold substrate using the μCP[45] approach. Localized preferential crystal growth of Cu-ADA MOF on the HDT SAM surface, leaving the surrounding bare gold surface clear, is shown in the SEM image (Figure 1i,j). The Cu-ADA MOF was observed growing on the disordered HDT-μCP-deposited SAM surface, whereas no growth was detected on an ordered HDT surface. This result confirms the importance of the substrate surface for the development and quality of MOF crystallization.[11]

The advantage of LbL synthesis is that it can produce MOF thin films with crystal ordering in both the in-plane and out-of-plane directions. The thickness of the films is well-controlled by the number of cycles completed during fabrication, and the position of the MOF films can then be determined through patterning of the SAM combined with a μCP fabrication technique.

2.1.2 Seeding Method

The concept of using seeds to induce controlled nucleation of MOFs has been successfully implemented to master MOF formation on a variety of substrates. The nucleation has been obtained using nano- or microparticles of the MOF itself ("homogeneous" seeding); however, more recently, MOFs have been grown from nano- or micro-ceramic seeds ("heterogeneous" seeding).

An example of controlled ZIF-7 (Zn(benzimidazolate)$_2$)[58] growth promoted on ZIF-7 seeds was reported by Caro and coworkers.[59] The authors observed that diethylamine allows for the controlled growth of ZIF-7 rods when $ZnCl_2$ is used as the precursor for the coordinating metal centers.[59] This phenomenon was successfully used to induce directional growth of ZIF-7 membranes from layers of randomly oriented ZIF-7 nanoparticles on a ceramic substrate. The ZIF-7 nanoparticle (40–140 nm) seeded substrates subsequently undergo a secondary growth step in a DMF solution of $ZnCl_2$, benzimidazole, and diethylamine, through a microwave-assisted autoclave (100 °C). After 45 min, the membrane shows a defined orientation along the *c* (out-of-plane) axis, and its thickness is observed to increase nearly linearly with the treatment time.[59]

The seeding approach based on heterogeneous nucleation of MOF crystals has been recently reported.[24,60,61] Buso *et al.*[60] described the fast nucleation of monodispersed MOF-5 microcrystals obtained using carboxy- and amino-functionalized SiO_2 nanoparticles as nucleating agents. Using the silica nanoparticles, MOF-5 formation occurs ten times faster than the conventional solvothermal synthesis when ceramic seeds are used under stirring conditions. A drop of the colloidal solution with functionalized SiO_2 nanoparticles was cast on flat silicon substrates, leaving a bed of ceramic seeds, before the substrate was immersed in the MOF-growing solution.[60] This approach showed preferential MOF growth in areas defined by the location of the particles. In this context, it is important to highlight that several lithographic techniques can be used for precise control of particle location.[62,63] Different parameters including substrate, solvent, and evaporation rate can be used to control the self-assembly of silica-based particles in precise locations.[64,65]

In 2011, the same research group reported on a novel class of zinc phosphate hydrate (α-hopeite) microparticles as exceptional nucleating agents for the fast formation of MOF-5.[24,61] These seeds form spontaneously within the starting MOF-5 precursor solution when a surfactant (Pluronic F-127) is added. In the presence of the DRMs, the authors measured a three times faster MOF-5 growth than the traditional solvothermal approach. Additionally, the α-hopeite particles can be effectively isolated from the precursor solution and used as seeds to induce localized MOF growth on a variety of substrates. With this method, MOF-5 crystals were easily grown on flat silicon and alumina substrates. Subsequently, the seeds were used to control the growth on these substrates, and also on more complex 3D geometries. An epoxy-based membrane (SU-8) previously lithographed with arrays of vertical microchannels via deep X-ray lithography (DXRL)[66] was used. The ceramic seeds were introduced inside the lithographed channels, and then the seeded 3D structure was immersed in an MOF-5 precursor solution. MOF-5 crystals were

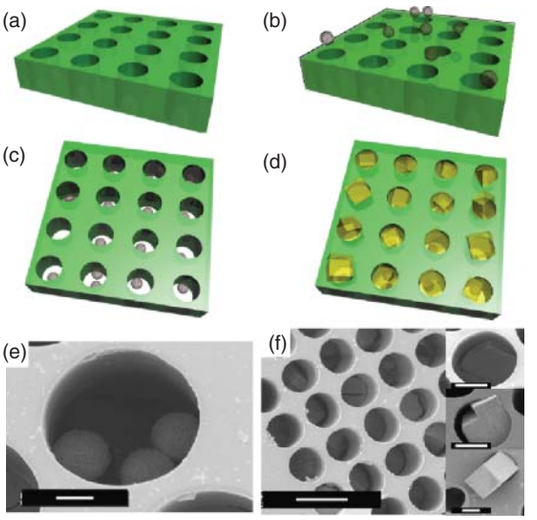


Figure 2 (a–d) Schematics of the protocol used to spatially manipulate ceramic seeds for MOF-5 formation. (a) Patterned membrane with a uniform distribution of wells on a commercial epoxy-resist (SU-8). (b) Drops of the ceramic seeds were pipetted onto the lithographed substrate. (c) The substrate was vacuum dried to draw the seeds into the cylindrical wells. (d) The seeded substrate was then placed into a MOF-5 growing medium to induce the MOF formation within the wells. (e) SEM of zinc-based seeds positioned in the wells of a SU-8 lithographed membrane after vacuum drying (scale bar, 10 μm); the wells are 40 μm in diameter and 100-μm deep. (f) MOF-5 crystal growth within several lithographed wells after 5-h solvothermal reaction (scale bar, 50 μm). Insets show crystals emerging from a well at different growth stages (scale bar, 20 μm). (Reproduced from Ref. 24. © Nature Publishing Group.)

observed to preferentially form inside the channels throughout the thickness of the membrane (Figure 2).[24]

Other studies have subsequently proposed the use of different ceramic seeds for heterogeneous nucleation. Although further studies are needed to fully understand the potential of this approach, the heterogeneous nucleation represents an effective and inexpensive method to induce controlled MOF growth.

There are a number of advantages to the seeding methods described here. These typically include low moisture sensitivity, low substrate sensitivity, availability of lithographic methods for positioning nano- and micro-particles, relatively short MOF growth times, and the potential to incorporate functionality within the seeds themselves.

2.2 Fabrication Methods Requiring External Control

2.2.1 Electrochemical Approach

The first study on high-quality patterns achieved using an external electric field was reported by Ameloot *et al.*[67]; the authors showed that this procedure was efficient in inducing the controlled growth of MOFs, confining the porous crystals in precise locations. The authors used a well-known MOF structure called HKUST-1 synthesized in 1999 by Chui *at al.*[68] This MOF is based on Cu^{II} cations coordinating tricarboxylic ligand (1,3,5-benzenetricarboxylic acid, BTC), and is also known as $Cu_3(BTC)_2$.

In the approach proposed by Ameloot, a copper microelectrode is immersed in a solution containing the ligand (BTC) for the preparation of the HKUST-1; methyltributylammonium methyl sulfate (MTBS) electrolyte. When a voltage is applied, the copper microelectrode releases metal ions into the solution containing the ligand, and the two precursors produce the corresponding Cu-based MOF. The naked metallic area naturally provides a high concentration of metal ions and the nucleation and growth of MOF crystals is enhanced in such areas, as depicted in Figure 3. As a consequence of the preferential growth on the bare copper, a continuous coating of

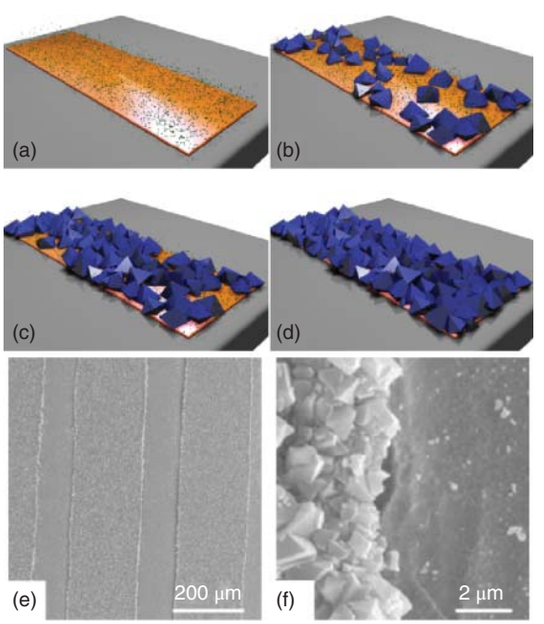


Figure 3 (a–d) Schematic of the electrodeposition-based lithographic technique[4] to deposit HKUST-1 on copper substrates proposed by Ameloot *et al.*[67] (a) A copper anode (orange substrate) was used to release Cu cations (small, green dots). (b) The ligand (BTC) in solution can react with the metal cations growing the MOF crystals (blue), where the probability that the reaction will occur is higher (anode). (c) Over time, the metal precursor density remains higher where the anode remains bare, hence allowing for MOF growth on these areas. (d) Using this mechanism, a highly dense MOF crystal coating can be achieved in selected regions. (e) SEM measurements performed on the patterned regions and (f) detail showing the preferential growth of $Cu_3(BTC)_2$ MOFs on metal. (Reprinted with permission from Ref. 67. Copyright (2009) American Chemical Society.)

MOF can be prepared. HKUST-1 crystal coatings with a controlled thickness in the 1–20 μm range were obtained. The roughness of the coating depends on the crystal size distribution; therefore, for thicker films, a better control of the thickness was achieved. This straightforward technique was used to control MOF coating formation on top of a quartz crystal microbalance.[67] The proposed MOF-based microsystem was used as a humidity sensor, providing evidence that an electrochemical method can be combined with standard lithographic techniques for the microfabrication of miniaturized electrodes.

In 2010, the same research group proposed further progress, combining controlled evaporative conditions with the electrochemical procedure.[69] A substrate (glass slide) was functionalized with a trimethylsilane, a precursor widely used to modify the water affinity because of the hydrophobic termination. Afterward, a mask was applied on top of the hydrophobic substrate and copper was evaporated on top of the mask. With this fabrication process, copper patterns were easily prepared. The BTC ligand and silver nitrate were dissolved in dimethyl sulfide and then spin-coated on top of the patterned substrate. A preferential dewetting of the mixture was induced by the exposed methyl-functionalized areas; the solution preferentially wets the region covered by copper. Using this approach, it was possible to confine the electrochemical reaction in 50×50 μm areas. Interestingly, the deposition of silver occurring during the same electrochemical process was helpful for anchoring the 100–200 nm $Cu_3(BTC)_2$ MOF crystals to the substrate.[69]

Advantages of the electrochemical deposition technique are that it can be performed in a relatively short amount of time (compared to other procedures such as LbL), a limited amount of reactants is required, a high density of crystals is obtained on the metallic surfaces, and the scanning microscope images provide evidence that crystal growth is confined to the defined regions. The technique could possibly be applied to a variety of MOFs using a suitable lithographed metal pattern. Furthermore, lithographic methods for the fabrication of complex metallic micro- and nano-structures are widely available. Importantly, in regard to lithography, electrochemical methods are suitable for the preparation of a variety of metallic micro- and nano-structures in the first fabrication step; therefore, the same technique can be used to grow the MOFs on such structures. This fabrication method can be considered inexpensive (due to the limited amount of chemicals used) and versatile and is therefore very promising for industrial applications.

2.2.2 *Microcontact Printing and Evaporation-Induced Growth*

A variety of parameters can be used to control MOF formation. Following this consideration, MOF synthesis techniques have increasingly been extended beyond the standard solvothermal approach, which depend on different variables such as precursors, concentration, and temperature. An important role is also played by the solvent used during the MOF reaction. In particular, by controlling the solvent evaporation process, the MOF formation kinetics can be varied. The same process has been used for other self-assembled materials such as mesoporous films.[70] In the field of MOFs, the controlled evaporation approach has been successfully coupled to contact lithographic methods, such as microprinting and dip-pen lithography. The generated patterns are made of MOF single crystals grown in specific locations with a precision in the micron scale.

Ameloot *et al.*[71] successfully stabilized the MOF precursor for HKUST-1 by replacing the standard ethanol/water solvent with dimethyl sulfoxide (DMSO). This unconventional solvent in MOF synthesis has a strong affinity toward metal ions and allows for the formation of hydrogen bonded solvate structures with tricarboxylic ligand. Taking advantage of the reversible stabilizing effect, the authors discovered that during the conventional solvothermal route, the formation of HKUST-1 was triggered by solvent evaporation at 100 °C. By means of microcontact printing, the MOF precursor solution was confined in precise areas and then, controlling the evaporation of the solvent, the formation of MOF crystals was triggered in specific regions. The method was accomplished using the "lithographically controlled wetting" (LCW[72]) technique. The microlithographed polydimethylsiloxane (PDMS) stamp is wet with the MOF precursor solution, and the stamp is subsequently placed on the target platform (Figure 4a–d). Thanks to the capillary forces, the MOF precursor solution is maintained exclusively underneath the stamp protrusions; this condition is needed to control the growth of the MOF crystals in controlled areas. Subsequently, the evaporation is performed at 100 °C. With this method, separated MOF crystals have been successfully grown in an ordered manner (Figure 4a–d). The authors observed that a preferred orientation on the HKUST-1 crystals along the [111] direction was obtained. This result was irrespective of the substrate surface chemistry, and the same crystal orientation was observed in the case of silanol, vinyl, or carboxylic acid substrate surface groups. Owing to the evidence that no crystal formation occurs under the same temperature conditions when the process is performed in a closed vessel (evaporation blocked), the authors demonstrated that evaporation is the main driving force for MOF nucleation, not the process temperature.

Evaporation-induced MOF growth combined with a precise control of the MOF precursor solution volume in a precise location offers a powerful tool to master single crystal localization with high spatial accuracy. This approach also offers the possibility of controlling MOF crystal formation by tuning the volume of the precursor solution. In the papers by Bellido *et al.*[73] and Carbonell *et al.*,[74] examples of how to chemically functionalize the

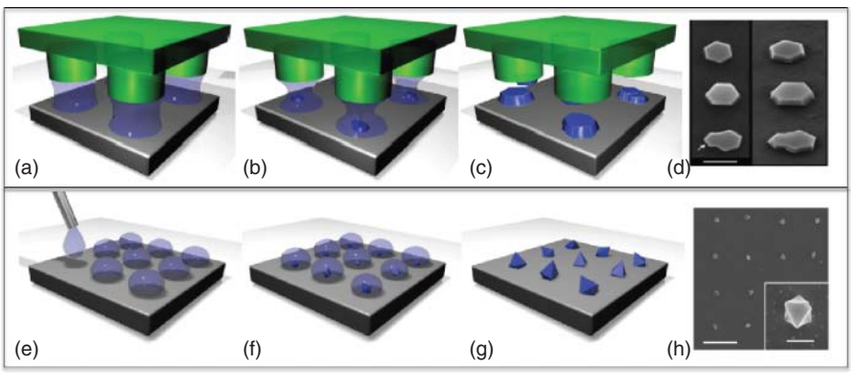


Figure 4 (a–c) Schematic showing a HKUST-1 pattern obtained using controlled and confined solvent evaporation. (d) Patterned deposition of HKUST-1 crystals (scale bar 1 μm). (Reproduced with permission from Refs. 4, 71) (e–g) Schematic of microcontact printing method using microfluidic pens or AFM tips to fabricate single crystal MOF arrays. (h) FESEM image of an array of HKUST-1 single crystals formed on a gold substrate prepared with CH_3-terminated functional groups. Scale bar 5 μm and inset 500 nm. (Reprinted with permission from Ref. 74. Copyright (2011) American Chemical Society.)

tip of an atomic force microscope (AFM) or a microfluidic pen are reported. Femtoliter droplets of MOF precursor solution were deposited onto specified locations substrates (Figure 4e–h). The deposition technique used is known as dip-pen nanolithography.[75] The miniaturized droplets act as microreactors for MOF nucleation and growth. Again, the traditional ethanol/water solvent mixture used for the room temperature synthesis of HKUST-1 was substituted with DMSO.[74]

As a support, Bellido *et al.*[73] used gold substrates functionalized with monolayers of 16-mercaptohexadecanoic acid and 1-octanethiol to grow HKUST-1 crystals at specific locations. The authors controlled crystal growth in the 150–650 nm range by tuning the solvent evaporation rate through incubation of the substrates in a closed vessel saturated with solvent vapours.[73] In this study, the controlled deposition of a single crystal per droplet of each solution was not achieved yet; however, the experiment demonstrated the potential of this technique to obtain crystal arrays with a spatial resolution in the micron scale.

Carbonell *et al.*[74] used a microfluidic pen for the deposition of arrays of MOF precursor solution droplets. For this sophisticated deposition, the authors found that the contact angle of the droplets is a critical factor in obtaining controlled precipitation of an MOF single crystal per droplet. If the contact angle is increased due to $-CF_3$ and $-CH_3$ functionalized surfaces, single crystals are formed, whereas more hydrophilic surfaces decorated with different functional groups (i.e., $-NH_3$, $-COOH$, and $-OH$) tend to increase the MOF nucleation density on the contact surface.[74] Controlling these parameters, HKUST-1 single crystals are obtained in the 0.5–1.2 μm range. Precise control over the edge dimension of the single crystals can be obtained by varying the microdroplet volume. The authors also observed that HKUST-1 single crystals tend to grow preferentially oriented along their [111] direction when forming on hydrophobic $-CH_3$ and $-CF_3$ SAMs.[74] While dip-pen nanolithography is a highly precise fabrication technique, it is normally considered time-expensive, although recent progress has shown the advantage of a parallel probe for high-throughput deposition.[75]

You and coworkers[76] combined the depolymerize/repolymerize ability of coordination polymers with a standard method of micromolding in capillaries (MIMIC[77]). With this approach, they created bidimensional micro-arrangements of highly luminescent reticular superstructures on a silica substrate. Coordination polymers can be reversibly depolymerized by dissolving them in a strong coordination solvent; then, they can be reconfigured into their initial macrostructure by controlled removal of the solvent. If this reversible process is performed within the microcavities of a lithographed micromold, microstructures of the coordination polymer reproducing the mold patterns can be fabricated.[76] A clear solution was obtained by dissolving zinc-coordinated 4,4′-di(4-pyridyl)cyanostilbene in an excess of pyridine. The solution was then introduced into rectangular capillaries in conformal contact with a patterned PDMS mold and a ceramic substrate (glass). The excess pyridine diffused into the PDMS walls, inducing repolymerization of the zinc-coordinated 4,4′-di(4-pyridyl)cyanostilbene within the PDMS cavities. The PDMS mold was then removed from substrate, leaving ordered coordination polymer microstructures on the silica substrate (Figure 5).

The authors observed that the polymer microstructures replicated the shape of the capillaries with minimal deformation. The fabricated patterns showed birefringence properties under cross-polarized illumination conditions,

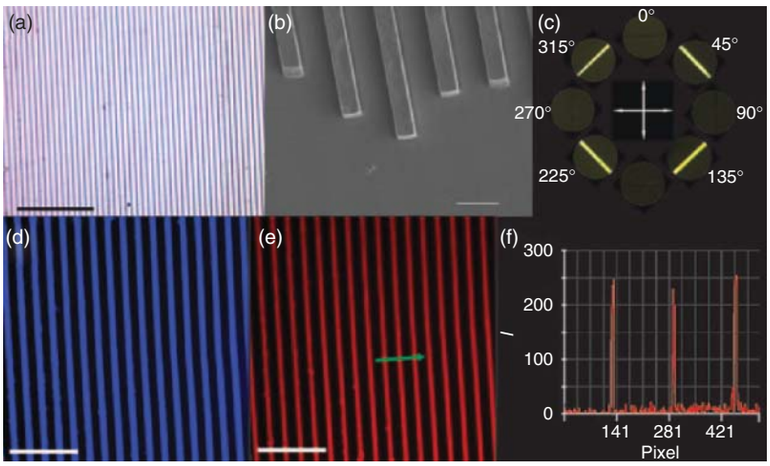


Figure 5 (a) Optical microscopy and (b) SEM image of coordination polymer roads (scale bar 100 and 10 μm, respectively. (c) Optical microscopy image of a single road collected under cross-polarization conditions. The road shows birefringence at every 45° rotation with respect to the polarizer. (d–e) fluorescence image and (f) fluorescence profile of the pattern. (Reproduced from Ref. 76. © Wiley-VCH Verlag GmbH & Co. KGaA, 2010.)

indicating the directional order of the microfabricated structure.[76]

Using the μCP technique, Gassensmith *et al.*[78] were able to pattern the surface of a single MOF-5 crystal using a stamp made of a functionalized silicon wafer. The authors first prepared the azide-terminated monolayer that was then patterned with a PDMS stamp loaded with a copper-catalyzed alkyne-azide. The resulting carboxylic acid pattern provides a nucleating surface for MOF growth once the substrate is immersed in MOF-5 precursor solution (a solution of DMF, therephthalic acid, and zinc nitrate). The resulting substrates showed 40-nm thick uniform MOF films on the carboxyl-terminated surfaces, whereas no MOF formation was detected on the azide surfaces. Continued immersion in the MOF-5 growing medium formed MOF film monoliths that could be removed from the substrate; the crystals were presenting a patterned surface according with Figure 6.[78]

Advantages of the microcontact printing process include the low cost associated with the patterning methodology and the relatively low amount of reactants involved. Fine control of the crystal orientation has been achieved, and the high precision and straightforward methodology (referring in particular to the work of Ameloot *et al.*[71]) offers the opportunity to pattern large surfaces.

2.2.3 Digital Microfluidics

Digital microfluidics is a rapidly emerging technology that enables small droplets of solution (<1 μL) to be independently manipulated on the surface of a hydrophobic substrate using software-controlled electronic signals. The major advantage of this technique is that only selected areas of the substrate come into contact with the solution, meaning that contact with other features of the substrate, such as electrical connections that may be sensitive to corrosion, can be avoided. The droplet actuation technology is relatively inexpensive and allows all fluidic elementary operations (droplet dispensing, splitting, merging, transport, and mixing) to be performed on-chip using reconfigurable pathways.

Witters *et al.*[79] have described an implementation of digital microfluidics, which enables large arrays of MOF crystals to be rapidly and accurately printed. Their methodology consists of a modular two-plate digital microfluidic device in which the bottom plate of the assembly, containing the electronics, is dedicated to transport of micro- to nanoliter-sized "mother droplets". Droplet actuation is achieved by the electrowetting-on-dielectric (EWOD) principle, in which an imbalance in the interfacial tension between a liquid droplet and an electrode coated with a dielectric layer is used to propel the droplet. The hydrophilic substrate onto which the MOF crystals are to be printed is coated with a patterned hydrophobic layer (e.g., Teflon AF), forming hydrophilic-in-hydrophobic micropatches, and constitutes the top plate of the device. Mother droplets are generated on-chip from a fluid reservoir, and then transported over these micropatches, dispensing femtoliter droplets into the hydrophilic micropatches in the process, as shown in Figure 7.

Witters *et al.*[79] have demonstrated that by removing the top plate after printing and controlling the evaporation rate of the solution contained in the micropatches, large grids of single MOF crystals can be grown with high spatial control, high monodispersity, and high crystal orientation ([1 1 1] direction) (Figure 7e–g). Furthermore, the

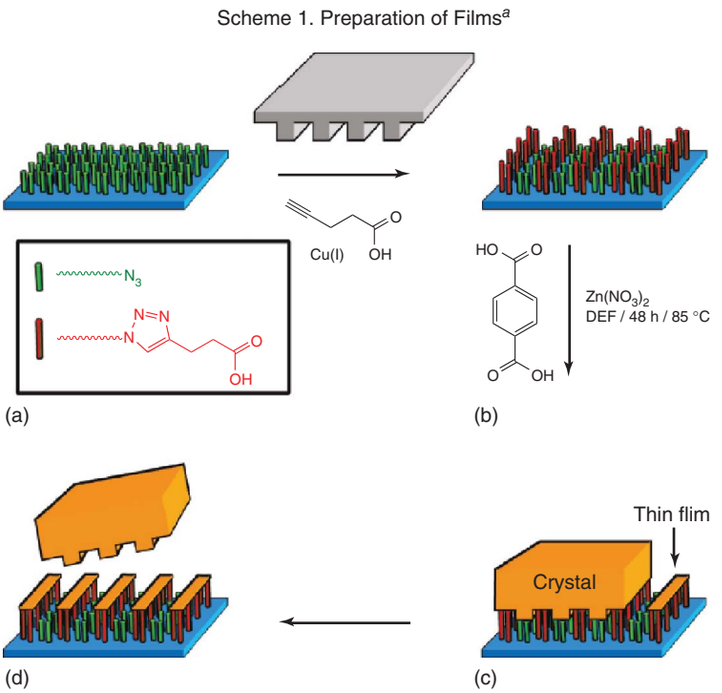


Figure 6 Schematic of the process proposed by Gassensmith *et al.*[78] (a) A silicon wafer is functionalized with a monolayer of alkylazide. (b) With the microcontact printing of an alkyl precursor (pentynoic acid), the click chemistry is used to graft the carboxy functionalization. (c) Subsequently, the substrate is immersed in the MOF-5 growing solution; thin films and large crystals are obtained. Crystal larger than 0.5 mm can be removed from the substrate showing a pattern on the surface. (Reprinted with permission from Ref. 78. Copyright (2011) American Chemical Society.)

size of the MOF crystals was shown to be controlled by the size of the micropatches in which they are grown.

Witters *et al.*[80] have also demonstrated that this digital microfluidic methodology can be used to deposit thin, dense, polycrystalline films within the micropatches using a LbL technique. In this instance, droplets of a metal salt solution, an organic ligand solution, and clean rinsing solvent are repeatedly dispensed from on-chip fluid reservoirs and transported over the micropatches in the top plate by the actuation electrodes in the bottom plate. Using this approach, micropatches with thicknesses of around 550 nm can be grown after an equivalent of 40 LbL cycles.

2.3 Fabrication Methods that Require External Control to Position Preformed MOFs

2.3.1 MOFs and Magnetic Particles for Dynamic Relocation

An effective method for spatial control of MOFs is the preparation of MOF composites (also called framework composites, FCs)[81] embedding magnetic particles/fibers.[82] This class of ultraporous composite magnetic materials is named magnetic framework composites (MFCs).[81] The ability to locate a variety of materials using an external magnetic field has previously been reported using a variety of magnetic responsive nano- and microparticles.[83–89] Although MOFs with interesting magnetic properties can be prepared using precursor elements such as Mn, Co, and Fe as the coordination metals,[90–94] no evidence of spatial control has been reported for these "pure" magnetic MOF crystals. Subsequent studies have focused on the integration of MOFs with magnetic particles and fibers (MFCs).[23,81,95,96]

In 2011, Lohe and coworkers[95] reported the preparation and use of MFC for catalysis and drug delivery. The MFC were prepared via a two-step approach, where the surface of the 10–20 nm iron oxide nanoparticles were initially grafted with the MOF precursors in order to induce the heterogeneous nucleation of MOF crystals. The resulting AlOH(2,6-naphthalenedicarboxylate)[97] MFC was used as a catalyst in the cyanosilylation of benzaldehyde to produce cyanohydrins.[94] Compared with traditional filtration methods, magnetic separation of the catalyst improved the efficiency of catalyst recovery. The authors also used the MFC for drug molecule storage (ibuprofen). Magnetic HKUST-1 composites were loaded with the drug, thanks to the porous framework. Using an alternating magnetic

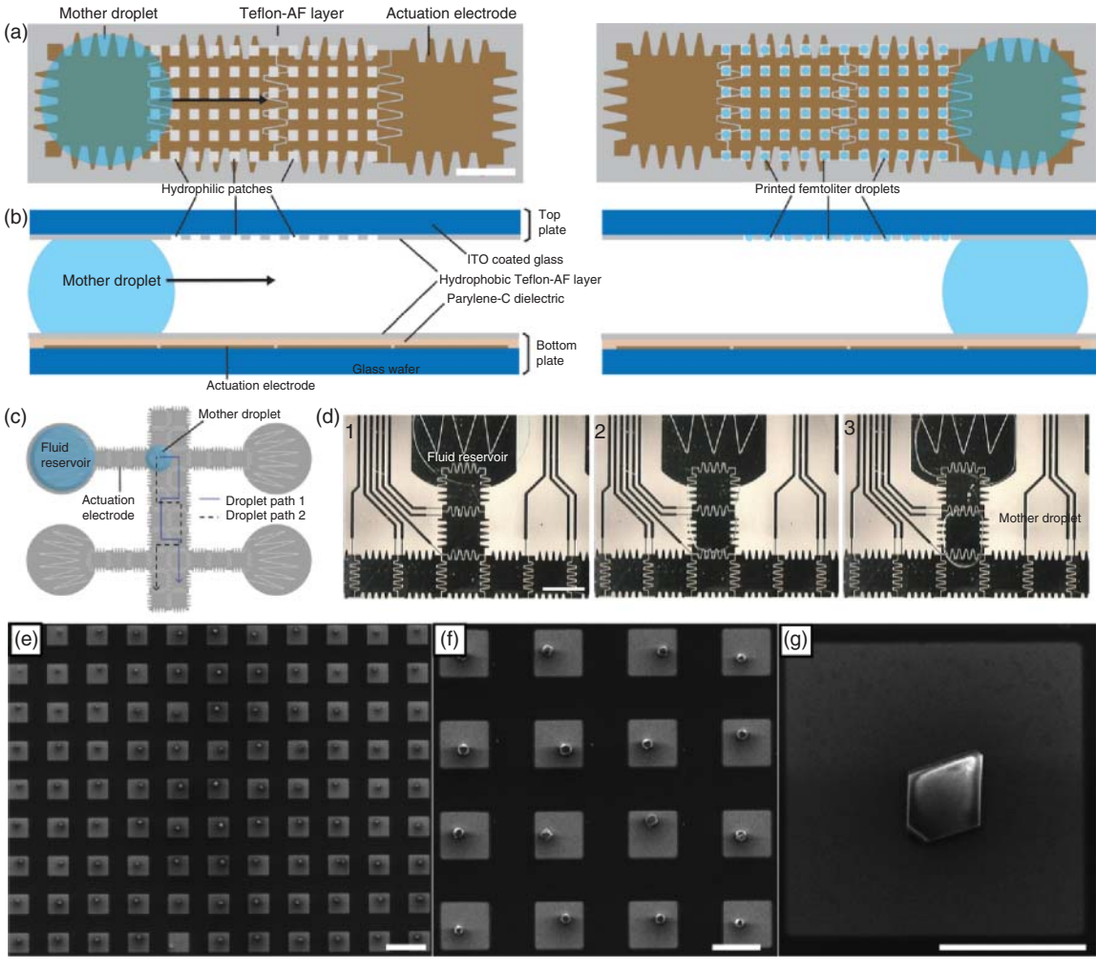


Figure 7 (a) Top view (scale = 700 μm) and (b) side view of a digital microfluidic chip implemented by Witters *et al.*[79] for printing of MOF crystals. Mother droplets are transported over arrays of hydrophilic-in-hydrophobic micropatches, dispensing femtoliter droplets of solution into the micropatches in the process. (c) Schematic drawing of two different paths that could be taken by a mother droplet by applying different actuation sequences to the electrodes. (d) Sequence of frames from a movie demonstrating on-chip dispensing of a mother droplet from a fluid reservoir (scale = 1.4 mm). (e–g) SEM images of single HKUST-1 crystal arrays produced by controlled evaporation. The square-shaped micropatches (20 × 20 μm) are ITO in a hydrophobic Teflon-AF matrix, over which a mother droplet has passed. Highly monodisperse single crystals can be observed after controlled evaporation of the solution. Scale bars represent 40 (e), 20 (f), and 10 μm (g). (Reproduced from Ref. 79. © Wiley-VCH Verlag GmbH & Co. KGaA, 2012.)

field, the magnetic particles heated up, increasing the drug release kinetics.[94] This methodology offers a control over the composite location and drug delivery rate.

During the same year, Ke *et al.*[96] integrated Fe_3O_4 particles in HKUST-1 for targeted drug delivery. The composites were synthesized by combining 50–150 nm Fe_3O_4 nanorods with Cu-based MOF. The MOF was acting as an open porous network to store nimesulide, a particular type of cancer drug. The main improvement of Ke and coworkers was the use of superparamagnetism. This class of material has a low residual magnetization, preventing particle agglomeration that would cause undesirable embolisms.[95]

Other MFCs were recently used by Falcaro *et al.*[23]; 50-nm carbon-coated cobalt particles were used for the dynamic spatial control of MOF-5 nanocomposite. The MFCs were prepared using a one-pot procedure in which the carbon-coated cobalt nanoparticles were added to a solution containing the MOF-5 precursors and a surfactant (Pluronic, F127) to prevent premature sedimentation. Within 24 h of solvothermal reaction, dark cubic crystals formed. The authors also demonstrated that they were able to direct the location of the MOF crystal growth using static magnetic fields to collect the Co MFCs (Figure 8) and placing the nanocomposite in a fresh MOF-5 precursor

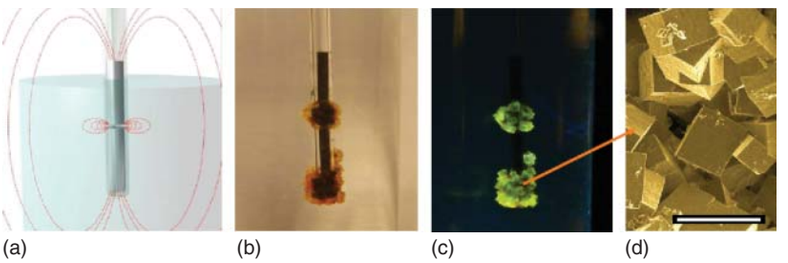


Figure 8 (a) Scheme showing 1-mm capillary containing two magnetic bars. This probe was used as a magnetic finger to collect Co FCs. (b) Picture under visible light showing that the magnetic composite Co FC seeds are preferentially positioned to where the magnetic field lines are most dense. The seeds grow further when placed in a MOF-5 growing medium and the solvothermal approach is used. The crystal clusters are then impregnated with fluorescein isothiocyanate, turning the crystals orange. (c) Picture under UV light (365 nm) of the dye-doped crystal clusters. (d) SEM image of the crystal clusters (scale bar 200 μm). (Reproduced from Ref. 23. © Wiley-VCH Verlag GmbH & Co. KGaA, 2011.)

solution. This secondary growth step uses the homogeneous nucleation method in combination with MFCs collected with a small magnet.[23]

The loss of surface area due to the magnetic particles was limited; the authors measured a 4% decrease. This would make the composite an interesting material for applications requiring porous materials for uptake, storage, catalytic, and sensing properties. Further progress in the field of positioning MFCs has been achieved by the same research group.[98] A mixed component MOF[99] was synthesized in DEF in the presence of H_2bdc and 2-aminoterephthalic acid (H_2Abdc),[100] zinc nitrate, and carbon-coated cobalt nanoparticles. Single MOF particles were isolated and a 50-μm cubic MFC was injected into a microfluidic circuit showing that a single particle can be relocated within the circuit and the MOF properties can be provided on demand. The ability to control the growth position or spatial manipulation of MOF crystals and the ability to activate the functionality of the ultraporous crystal on demand has shown great potential for the fabrication of integrated platforms.

2.3.2 *Films from Colloidal MOF Solutions*

Ferey and Sanchez *et al.*[37–39] reported an alternative method of preparing MOF films; the proposed method requires a colloidal solution containing preformed MOF crystals. Tunable film thickness of the MOF film in the range 40 nm–1 μm was obtained, thanks to dip-coating deposition. Stable, homogeneous, monodispersed colloidal solutions of MIL-101(Cr),[101] MIL-89 (Fe),[102] and ZIF-8 (Zn)[58] were prepared by controlling the hydrothermal synthesis. The film thickness was adjusted by controlling the withdrawal speed and the number of depositions. Washing and drying steps were performed between each coating. Because a single deposition step forms one or two MOF crystal layers, the roughness of the films is minimized through the careful design of the preformed MOF nanoparticles. The resulting films showed good transparency and optical transmittance >96%, confirming the homogeneity of the MOF coating.[37,38,100,103,104]

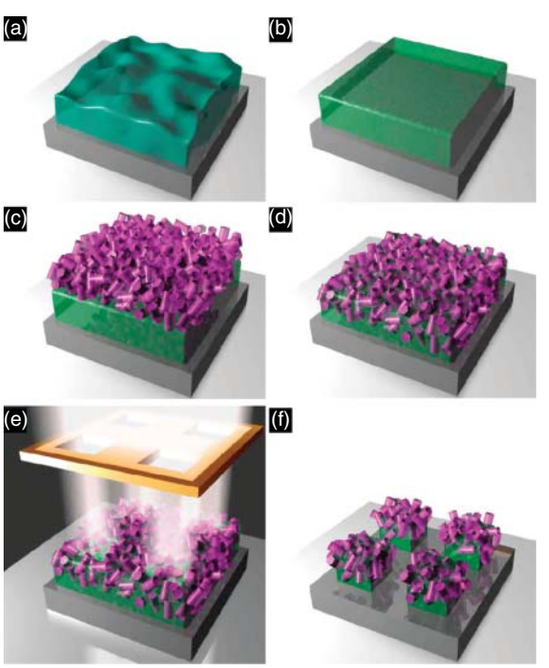


Figure 9 Fabrication process: phenyltriethoxysilane (PhTES) solution is drop-cast onto a silicon wafer (a) and heated until set (b). ZIF-9 powder is spread across the PhTES surface (c), heated to adhere the crystals (d) and then repeated to achieve a dense coverage. The surface is then exposed to lithographic X-ray beam (e) and rinsed with ethanol, etching unexposed areas to leave behind the patterned surface (f). (Reproduced from Ref. 105 with permission of The Royal Society of Chemistry.)

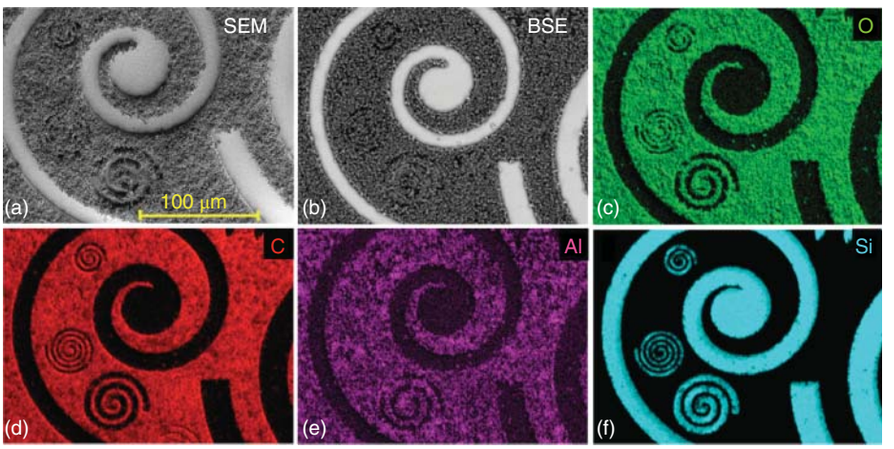


Figure 10 (a) SEM and (b) backscattered image, showing the patterning ability of the imprint technique utilized by Doherty *et al.*[18] (c–f) Energy dispersive X-ray analysis of NH_2-MIL-53(Al) MOF pattern showing the presence of oxygen (c), carbon (d), and aluminum (e) from the MOF, and silicon (f) from the substrate. (Reproduced from Ref. 18. © Wiley-VCH Verlag GmbH & Co. KGaA, 2013.)

The advantage of these films is that they can be produced relatively quickly and the thickness can be carefully tailored; however, they feature polydispersed crystallinity as opposed to the more controlled but slower LbL thin film formation technique.

2.3.3 *Photolithography using Preformed MOF Crystals*

While methods such as electrochemical growth, microcontact printing, and digital microfluidics constitute bottom-up approaches to the formation of patterned MOF surfaces, in that the MOF crystals are induced to grow on a prepatterned surface, photolithography can be used as a top-down approach to pattern a surface already coated with MOF crystals. This method offers the significant advantages of very high spatial control over the features of the pattern, and of making the patterning process independent of the MOF synthesis, allowing a wider range of synthesis conditions to be used.

Photolithography techniques employ a wide range of photon energies, from the visible spectrum right up to hard X-rays, and hence offer the possibility to pattern MOF surfaces in different ways. For example, Dimitrakakis *et al.*[105] have demonstrated how DXRL can be used to selectively cross-link a phenyltriethoxysilane (PhTES) sol–gel matrix heavily loaded with ZIF-9 particles, which are largely stable under such radiation. In this work, thin PhTES films were drop-cast on cleaned and dried silicon wafers (Figure 9a), heated until the film was observed to have dried out (Figure 9b), and allowed to cool. Preprepared ZIF-9 powder was then manually spread on the PhTES film to achieve a homogenous coverage (Figure 9c), before being heated again to soften the sol–gel layer and secure the ZIF-9 particles (Figure 9d). The samples were exposed for a limited time to synchrotron X-rays through the apertures of a mask (Figure 9d). After gentle rinsing in ethanol, the unexposed regions of the PhTES layer were completely etched away, leaving behind well-defined pillars on the silica wafer surface (Figure 9f). Using UV-photolithography, Lu *et al.*[106] have demonstrated how a layer of photoresist material can be used to achieve selective chemical etching and hence patterning of an underlying film of ZIF-8. As a proof of concept, the MOF coatings were used to sense H_2, thanks to its optical response.

An alternative approach to photolithographic patterning of MOF surfaces has recently been described by Doherty *et al.*,[18] in which substrates coated in layers of photoresist material patterned by UV lithography are used to graft or imprint a variety of MOF crystals into the prepatterned surface (Figure 10). Since in this case, the imprinting technique is independent from the lithography process, it is suitable for almost all MOF materials. This protocol is highly versatile, fast, and cheap and the MOF chemical functionality is not affected by the process.

3 CONCLUSIONS AND FUTURE OUTLOOK

Progress in MOF technology has shown the potential to bring these ultraporous crystals into the area of device fabrication. Patterning methodologies is a very recent research trend in the field of MOFs, and in the past few years, important progress has been made in identifying different routes/mechanisms to control the position of the ultraporous crystals on substrates. These different methods

Table 1 Example of different MOF and related pattering techniques used for achieving control over the location of the porous crystals

Type of MOF	Type of patterning method used	References
HKUST-1	Self-assembly monolayer by microcontact printing	11
	Electrochemical	66, 67
	Microcontact printing	69, 71, 72
	Microfluidic	77, 78
	Dynamic localization	92, 93
MOF-5	Self-assembly monolayer	10
	Heterogeneous seeds	44, 59
	Microcontact printing	76
	Dynamic localization	79
CU-ADA	Self-assembly monolayer by Microcontact printing	56
ZIF-9	Photolithography	58
ZIF-8	Photolithography	18, 104
MIL-53 (Al), ZIF 67	Photolithography	18
DUT-4, DUT-5	Dynamic localization	92
Mixed component	Dynamic localization	96

rely on different strategies: positioning promoting agents to facilitate the crystal growth (chemical functionalization or nucleation seeds); controlling the growth through the use of external controls (electrochemistry, microcontact); positioning preformed MOF (or MOF composites) using either external magnetic field or photopatterning techniques.

Table 1 reports examples of different MOFs prepared using various patterning techniques described in this chapter.

Among the different lithographic techniques, photolithography appears to be a very promising approach. However, further advances are required to satisfy important criteria needed for commercial device fabrication. In fact, a fast preparation protocol, using a cheap approach with the ability to position any MOF onto any substrate is what would be required to take full advantage of MOF technology.[4] Although several of the features can be now achieved by a limited number of approaches, the control of the crystal orientation is still an open challenge. Another crucial aspect that needs to be considered is the accurate identification of the mechanical properties and durability which represent the key to the advancement of new technologies.[4,107]

4 ACKNOWLEDGMENTS

P.F. acknowledges the Australian Research Council (ARC) for support from the DECRA Grant DE120102451 and the CSIRO Office of the Chief Executive (OCE) Science Leader Scheme and the AM TCP for support. M.J.S. acknowledges the support of CSIRO through the OCE Science Program.

5 ABBREVIATIONS AND ACRONYMS

AFM = atomic force microscope; BTC = 1,3,5-benzenetricarboxylic acid; DMSO = dimethyl sulfoxide; DXRL = deep X-ray lithography; EWOD = electrowetting-on-dielectric; FC = framework composite; HDT = 1-hexadecanethiol; LbL = layer-by-layer; LCW = lithographically controlled wetting; LPE = liquid phase epitaxy; MFC = magnetic framework composite; MIMIC = micromolding in capillaries; MOF = metal-organic framework; MTBS = methyltributylammonium methyl sulfate; PDMS = polydimethylsiloxane; PhTES = phenyltriethoxysilane; SAM = self-assembled organic monolayer; SBU = secondary building unit; STM = scanning tunneling microscope; μCP = microcontact printing.

6 REFERENCES

1. M. E. Davis, *Nature*, 2002, **417**, 813.
2. P. Innocenzi, T. Kidchob, P. Falcaro, and M. Takahashi, *Chem. Mater.*, 2008, **20**, 607.
3. S. H. Han, C. M. Doherty, B. Marmiroli, H. Jin Jo, D. Buso, A. Patelli, P. Schiavuta, P. Innocenzi, Y. Moo Lee, A. W. Thornton, A. J. Hill, and P. Falcaro, *Small*, 2013, **9**(13), 2277.
4. P. Falcaro, D. Buso, A. J. Hill, and C. M. Doherty, *Adv. Mater.*, 2012, **24**, 3153.
5. H. Li, M. Eddaoudi, M. O'Keeffe, and O. M. Yaghi, *Nature*, 1999, **402**, 276.
6. J. Della Rocca, D. Liu, and W. Lin, *Acc. Chem. Res.*, 2011, **44**, 957.
7. C. Petit and T. J. Bandosz, *Adv. Funct. Mater.*, 2011, **21**, 2108.
8. J. R. Li, R. J. Kuppler, and H. C. Zhou, *Chem. Soc. Rev.*, 2009, **38**, 1477.
9. G. Ferey, *Chem. Soc. Rev.*, 2008, **37**, 191.
10. S. Hermes, F. Schröder, R. Chelmowski, C. Wöll, and R. A. Fischer, *J. Am. Chem. Soc.*, 2005, **127**, 13744.
11. J. L. Zhuang, K. Lommel, D. Ceglarek, I. Andrusenko, U. Kolb, S. Maracke, U. Sazama, M. Fröba, and A. Terfort, *Chem. Mater.*, 2011, **23**, 5366.
12. M. O'Keeffe, *Chem. Soc. Rev.*, 2009, **38**, 1215.
13. Y. H. Hu and L. Zhang, *Adv. Mater.*, 2010, **22**, E117.

14. S. Achmann, G. Hagen, J. Kita, I. M. Malkowsky, C. Kiener, and R. Moos, *Sensors*, 2009, **9**, 1574.
15. M. D. Allendorf, A. Schwartzberg, V. Stavila, and A. A. Talin, *Chem. Eur. J.*, 2011, **17**, 11372.
16. J. Gómez-Herrero and F. Zamora, *Adv. Mater.*, 2011, **23**, 5311.
17. Y. Ikezoe, G. Washino, T. Uemura, S. Kitagawa, and H. Matsui, *Nat. Mater.*, 2012, **11**, 1081.
18. C. M. Doherty, G. Grenci, R. Riccò, J. I. Mardel, J. Reboul, S. Furukawa, S. Kitagawa, A. J. Hill, and P. Falcaro, *Adv. Mater.*, 2013, **25**, 4701.
19. A. C. McKinlay, R. E. Morris, P. Horcajada, G. Ferey, R. Gref, P. Couvreur, and C. Serre, *Angew. Chem. Int. Ed.*, 2010, **49**, 6260.
20. S. Horike, S. Shimomura, and S. Kitagawa, *Nat. Chem.*, 2009, **1**, 695.
21. A. Modrow, D. Zargarani, R. Herges, and N. Stock, *Dalton Trans.*, 2011, **40**, 4217.
22. D. Buso, J. Jasieniak, M. D. H. Lay, P. Schiavuta, P. Scopece, J. Laird, H. Amenitsch, A. J. Hill, and P. Falcaro, *Small*, 2012, **1**, 80.
23. P. Falcaro, F. Normandin, M. Takahashi, P. Scopece, H. Amenitsch, S. Costacurta, C. M. Doherty, J. Liard, M. D. H. Lay, F. Lisi, A. J. Hill, and D. Buso, *Adv. Mater.*, 2011, **23**, 3901.
24. P. Falcaro, A. J. Hill, K. M. Nairn, J. Jasieniak, J. I. Mardel, T. J. Bastow, S. C. Mayo, M. Gimona, D. Gomez, H. J. Withfield, R. Riccò, A. Patelli, B. Marmiroli, H. Amenitsch, T. Colson, L. Villanova, and D. Buso, *Nat. Commun.*, 2011, **2**, A237.
25. T. J. Bandosz and C. Petite, *Adsorption*, 2011, **17**, 5.
26. W. Lin, W. J. Rieter, and K. M. L. Taylor, *Angew. Chem. Int. Ed.*, 2009, **48**, 650.
27. A. M. Spokoyny, D. Kim, A. Sumrein, and C. A. Mirkin, *Chem. Soc. Rev.*, 2009, **38**, 1218.
28. N. Stock and S. Biswa, *Chem. Rev.*, 0000. DOI: dx.doi.org/10.1021/cr200304.
29. S. M. Cohen, *Chem. Sci.*, 2010, **1**, 32.
30. G. Férey, *Chem. Soc. Rev.*, 2009, **38**, 1284.
31. C. Janiak and J. K. Vieth, *New J. Chem.*, 2010, **34**, 2366.
32. U. Mueller, M. Schubert, F. Teich, H. Puetter, K. Schierle-Arndt, and J. Pastré, *J. Mater. Chem.*, 2006, **16**, 626.
33. A. U. Czaja, N. Trukhan, and U. Müller, *Chem. Soc. Rev.*, 2009, **38**, 1284.
34. O. Shekhah, J. Liu, R. A. Fisher, and C. Wöll, *Chem. Soc. Rev.*, 2011, **40**, 1081.
35. D. Zacher, R. Shmid, C. Wöll, and R. A. Fisher, *Angew. Chem. Int. Ed.*, 2011, **50**, 176.
36. R. Makiura and H. Kitagawa, *Eur. J. Inorg. Chem.*, 2010, 3715.
37. P. Horcajada, C. Serre, D. Grosso, C. Boissière, S. Perruchas, C. Sanchez, and G. Férey, *Adv. Mater.*, 2009, **21**, 1931.
38. A. Demessence, P. Horcajada, C. Serre, C. Boissière, D. Grosso, C. Sanchez, and G. Férey, *Chem. Commun.*, 2009, **101**, 7149.
39. A. Demessence, C. Boissière, D. Grosso, P. Horcajada, C. Serre, G. Férey, G. J. A. A. Soler-Illia, and C. Sanchez, *J. Mater. Chem.*, 2010, **20**, 7676.
40. K. Sakakibara, J. P. Hill, and K. Ariga, *Small*, 2011, **7**, 1288.
41. T. Douglas, *Science*, 2003, **299**, 1192.
42. E. C. P. Smits, S. G. J. Mathijssen, P. A. van Hal, S. Setayesh, T. C. T. Geuns, K. A. H. A. Mutsaers, E. Cantatore, H. J. Wondergem, O. Werzer, R. Resel, M. Kemerink, S. Kirchmeyer, A. M. Muzafarov, S. A. Ponomarenko, B. de Boer, P. W. M. Blom, and D. M. de Leeuw, *Nature*, 2008, **455**, 956.
43. A. Bétard and R. Fischer, *Chem. Rev.*, 2012. DOI: doi.org/10.1021/cr200167v.
44. M. Mrksich and G. M. Whitesides, *Trends Biotechnol.*, 1995, **13**, 228.
45. J. C. Love, L. A. Estroff, J. K. Kriebel, R. G. Nuzzo, and G. M. Whitesides, *Chem. Rev.*, 2005, **105**, 1103.
46. E. Biemmi, C. Scherb, and T. Bein, *J. Am. Chem. Soc.*, 2007, **129**, 8054.
47. C. Scherb, A. Schödel, and T. Bein, *Angew. Chem. Int. Ed.*, 2008, **47**, 5777.
48. D. Zacher, K. Yusenko, A. Bétard, S. Henke, M. Molon, T. Ladnorg, O. Shekhah, B. Schüpbach, T. de los Arcos, M. Krasnopolski, M. Meilikhov, J. Winter, A. Terfort, C. Wöll, and R. A. Fischer, *Chem. Eur. J.*, 2011, **17**, 1448.
49. O. Shekhah, H. Wang, T. Strunskus, P. Cyganik, D. Zacher, R. Fischer, and C. Wöll, *Langmuir*, 2007, **23**, 7440.
50. O. Shekhah, H. Wang, S. Kowarik, F. Schreiber, M. Paulus, M. Tolan, C. Sternemann, F. Evers, D. Zacher, R. A. Fischer, and C. Wöll, *J. Am. Chem. Soc.*, 2007, **129**, 15118.
51. C. Munuera, O. Shekhah, H. Wang, C. Wöll, and C. Ocal, *Phys. Chem. Chem. Phys.*, 2008, **10**, 7257.
52. O. Shekhah, H. Wang, M. Paradinas, C. Ocal, B. Schüpbach, A. Terfort, D. Zacher, R. A. Fischer, and C. Wöll, *Nat. Mater.*, 2009, **8**, 481.
53. G. Decher, J. D. Hong, and J. Schmitt, *Thin Solid Films*, 1992, **210–211**, 831.
54. H. Nelson, *RCA Rev.*, 1963, **24**, 603.
55. R. Makiura, S. Motoyama, Y. Umemura, H. Yamanaka, O. Sakata, and H. Kitagawa, *Nat. Mater.*, 2010, **9**, 565.
56. S. Motoyama, R. Makiura, O. Sakata, and H. Kitagawa, *J. Am. Chem. Soc.*, 2011, **133**, 5640.

57. J. L. Zhuang, D. Ceglarek, S. Pethuraj, and A. Terfort, *Adv. Funct. Mater.*, 2011, **21**, 1442.
58. K. S. Park, Z. Ni, A. P. Cote, J. Y. Choi, R. Huang, F. J. Uribe-Romo, H. K. Chae, M. O'Keeffe, and O. M. Yaghi, *Proc. Natl. Acad. Sci. U.S.A.*, 2006, **103**(27), 10186.
59. Y. S. Li, H. Bux, A. Feldhoff, G. L. Li, W. S. Yang, and J. Caro, *Adv. Mater.*, 2010, **22**, 3322.
60. D. Buso, K. A. Nairn, M. Gimona, A. J. Hill, and P. Falcaro, *Chem. Mater.*, 2011, **23**, 929.
61. D. Buso, A. J. Hill, T. Colson, H. J. Whitfield, A. Patelli, P. Scopece, C. M. Doherty, and P. Falcaro, *Cryst. Growth Des.*, 2011, **11**, 5268.
62. J. Zhang, Y. Li, X. Zhang, and B. Yang, *Adv. Mater.*, 2010, **22**, 4249.
63. J. A. Rogers and H. H. Lee, 'Unconventional Nanopatterning Techniques and Applications', John Wiley & Sons, Inc., Hoboken, NJ, 2008, Chap. 15.
64. S. M. Yang, S. G. Jang, D. G. Choi, S. Kim, and H. K. Yu, *Small*, 2006, **2**, 458.
65. P. Innocenzi, P. Falcaro, and L. Malfatti, 'From Water Droplet to Nanotechnology', Springer, 2013. ISBN: 978-1-84973-664-0.
66. P. Innocenzi, L. Malfatti, and P. Falcaro, *Soft Matter*, 2012, **8**, 3722.
67. R. Ameloot, L. Stappers, J. Fransaer, L. Alaerts, B. F. Sels, and D. E. De Vos, *Chem. Mater.*, 2009, **21**, 2580.
68. S. S. Y. Chui, S. M. F. Lo, J. P. H. Charmant, A. G. Orpen, and I. D. Williams, *Science*, 1999, **283**, 1148.
69. R. Ameloot, L. Pandey, M. Van der Auweraer, L. Alaerts, B. F. Sels, and D. E. De Vos, *Chem. Commun.*, 2010, **46**, 3735.
70. C. J. Brinker, Y. Lu, A. Sellinger, and H. Fan, *Adv. Mater.*, 1999, **11**, 579.
71. R. Ameloot, E. Gobechiya, H. Uji-i, J. A. Martens, L. Alaerts, B. F. Sels, and D. E. De Vos, *Adv. Mater.*, 2010, **22**, 2685.
72. M. Cavallini and F. Biscarini, *Nano Lett.*, 2003, 3,1269.
73. E. Bellido, S. Cardona-Serra, E. Coronado, and D. Ruiz-Molina, *Chem. Commun.*, 2011, **47**, 5175.
74. C. Carbonell, I. Imaz, and D. Maspoch, *J. Am. Chem. Soc.*, 2011, **133**, 2144.
75. D. S. Ginger, H. Zhang, and C. A. Mirkin, *Angew. Chem. Int. Ed.*, 2004, **43**, 30.
76. Y. You, H. Yang, J. W. Chung, J. H. Kim, Y. Jung, and S. Y. Park, *Angew. Chem. Int. Ed.*, 2010, **49**, 3757.
77. Y. Xia and G. M. Whitesides, *Annu. Rev. Mater. Sci.*, 1998, **28**, 153.
78. J. J. Gassensmith, P. M. Erne, W. F. Paxton, C. Valente, and J. F. Stoddart, *Langmuir*, 2011, **27**, 1341.
79. D. Witters, N. Vergauwe, R. Ameloot, S. Vermeir, D. De Vos, R. Puers, B. Sels, and J. Lammertyn, *Adv. Mater.*, 2012, **24**, 1316.
80. D. Witters, S. Vermeir, R. Puers, B. F. Sels, D. E. De Vos, J. Lammertyn, and R. Ameloot, *Chem. Mater.*, 2013, **25**, 1021.
81. C. M. Doherty, D. Buso, A. J. Hill, S. Furukawa, S. Kitagawa, and P. Falcaro, *Acc. Chem. Res.*, 2014. DOI: 10.1021/ar400130a.
82. R. Ricco, L. Malfatti, M. Takahashi, A. J. Hill, and P. Falcaro, *J. Mater. Chem. A*, 2013, **1**, .
83. C. S. Lee, H. Lee, and R. M. Westervelt, *Appl. Phys. Lett.*, 2001, **79**, 3308.
84. T. Ji, V. G. Lirtsman, Y. Avny, and D. Davidov, *Adv. Mater.*, 2001, **13**, 1253.
85. S. Palacin, P. C. Hidber, J. P. Bourgoin, C. Miramond, C. Fermon, and G. M. Whitesides, *Chem. Mater.*, 1996, **8**, 1316.
86. T. Deng, G. M. Whitesides, M. Radhakrishnan, G. Zabow, and M. Prentiss, *Appl. Phys. Lett.*, 2001, **78**, 1775.
87. A. Snezhko and I. S. Aranson, *Nat. Mater.*, 2011, **10**, 698.
88. M. Reches and E. Gazit, *Nat. Nanotechnol.*, 2006, **1**, 195.
89. G. Frasca, F. Gazeau, and C. Wilhelm, *Langmuir*, 2009, **25**, 2348.
90. D. Maspoch, D. Ruiz-Molina, K. Wurst, N. Domingo, M. Cavallini, F. Biscarini, J. Tejada, C. Rovira, and J. Veciana, *Nat. Mater.*, 2003, **2**, 190.
91. S. Qiu and G. Zhu, *Coord. Chem. Rev.*, 2009, **253**, 2891.
92. D. Maspoch, D. Ruiz-Molina, and J. Veciana, *Chem. Soc. Rev.*, 2007, **36**, 770.
93. D. W. Ryu, W. R. Lee, J. W. Lee, J. H. Yoon, H. C. Kim, E. K. Koh, and C. S. Hong, *Chem. Commun.*, 2010, **46**, 8779.
94. A. Centrone, T. Harada, S. Speakman, and T. A. Hatton, *Small*, 2010, **6**, 1598.
95. M. R. Lohe, K. Gedrich, T. Freudenberg, E. Kockrick, T. Dellmann, and S. Kaskel, *Chem. Commun.*, 2011, **47**, 3075.
96. F. Ke, Y. P. Yuan, L. G. Qiu, Y. H. Shen, A. J. Xie, J. F. Zhu, X. Y. Tian, and L. D. Zhang, *J. Mater. Chem.*, 2011, **21**, 3843.
97. T. Loiseau, C. Mellot-Draznieks, H. Muguerra, G. Férey, M. Haouas, and F. C. R. Taulelle, *Chimie*, 2005, **8**, 765.
98. P. Falcaro, F. Lapierre, B. Marmiroli, M. Styles, Y. Zhu, M. Takahashi, A. J. Hill, and C. M. Doherty, *J. Mater. Chem. C*, 2013, **1**, 42.
99. A. D. Burrows, *CrystEngComm*, 2011, **13**, 3623.
100. W. Kleist, F. Jutz, M. Maciejewski, and A. Baiker, *Eur. J. Inorg. Chem.*, 2009, 3552.
101. G. Férey, C. Mellot-Draznieks, C. Serre, F. Millange, J. Dutour, S. Surblé, and I. Margiolaki, *Science*, 2005, **309**, 2040.
102. C. Serre, F. Millange, S. Surbl, and G. Frey, *Angew. Chem. Int. Ed.*, 2004, **43**, 6286.
103. C. Sanchez, P. Belleville, M. Popall, and L. Nicole, *Chem. Soc. Rev.*, 2011, **40**, 696.

104. D. Grosso, *J. Mater. Chem.*, 2011, **21**, 17033.

105. C. Dimitrakakis, B. Marmiroli, H. Amenitsch, L. Malfatti, P. Innocenzi, G. Grenci, L. Vaccari, A. J. Hill, B. P. Ladewig, M. R. Hill, and P. Falcaro, *Chem. Commun.*, 2012, **48**, 7483.

106. G. Lu, O. K. Farfa, W. Zhang, F. Huo, and J. T. Hupp, *Adv. Mater.*, 2012, **24**, 3970.

107. H. D. Espinosa, B. C. Prorok, and M. Fischer, *J. Mech. Phys. Solids*, 2003, **51**, 47.

Metal-Organic Frameworks in Mixed-Matrix Membranes

Harold B. Tanh Jeazet and Christoph Janiak

Heinrich-Heine-Universität, Düsseldorf, Germany

1	Introduction	403
2	Metal–Organic Frameworks in Mixed-Matrix Membranes	407
3	Conclusion	414
4	Acknowledgments	414
5	Related Articles	414
6	Abbreviations and Acronyms	414
7	References	414

1 INTRODUCTION

Metal–organic frameworks (MOFs) receive continuous attention[1–5] due to their high and tunable porosity, which promises applications, such as gas storage,[6–9] separation processes,[10–12] drug delivery,[13] heterogeneous catalysis,[14,15] heat transformation,[16,17] and so on. MOFs are also highly promising additives for polymer membranes.[18–20] Ligands with a broad variety of functionalities are possible with MOFs, which enable MOFs to interact well with the polymer material in order to obtain hybrid materials, so-called mixed-matrix membranes (MMMs) with improved separation properties.

Membrane processes are very important in our everyday life, but also in industry, for example, for water and waste water treatment, in medical applications, or separation of petrochemicals. Membrane processes are an energy saving method for the separation of mixtures, which occur in nearly all production processes in the chemical industry. Membrane-based devices are much smaller and work at lower temperatures compared to conventional separation facilities with distillation, extraction, or adsorption processes. Classical separation methods used for purification of chemical products, notably distillation, extraction, and crystallization are energy and cost intensive. Over 50% of the energy costs in the chemical industry are used for the separation of gaseous or liquid mixtures.[21] With membrane technology, the costs for difficult separations, for example, of azeotropic mixtures, can be reduced significantly.[22] The worldwide membrane market has a growth of approximately 10–15% each year.[23] Membrane processes applied on industrial scale are natural gas treatment (removal of CO_2 before the natural gas can be passed to the pipeline), hydrogen isolation and recovery (i.e., in cracking processes), oxygen enrichment from air (medical devices), and nitrogen enrichment from air (used as protecting atmosphere for oxygen-sensitive compounds).[24] Other membrane-based processes with fast growing market relevance are vapor recovery systems,[25] monomer recovery units, for example, ethylene/N_2 or propylene/N_2 separation,[26,27] the dehydration of organic solvents, and the removal of polar low-molecular-weight components in equilibrium reactions.[28]

In membranes with pore sizes of >2 nm, the separation is based on size exclusion, and thus, these membranes are suited for separation of components with sufficient size difference, for example, in dialysis, waste water treatment, and functional clothing.[29–31] For separation of components with comparable sizes or the separation of ions from water, solution-diffusion membranes are used.[32]

The solution-diffusion mechanism is based on the principle that the mixture component with higher solubility and higher diffusion rate permeates preferentially through the membrane, independent of the component sizes.[33,34] Solution-diffusion membranes feature free volume sites that cannot be occupied by polymer chains due to restricted motion and packing density of the polymer chains. The

Metal-Organic Framework Materials. Edited by Leonard R. MacGillivray and Charles M. Lukehart.
© 2014 John Wiley & Sons, Ltd. ISBN 978-1-119-95289-3

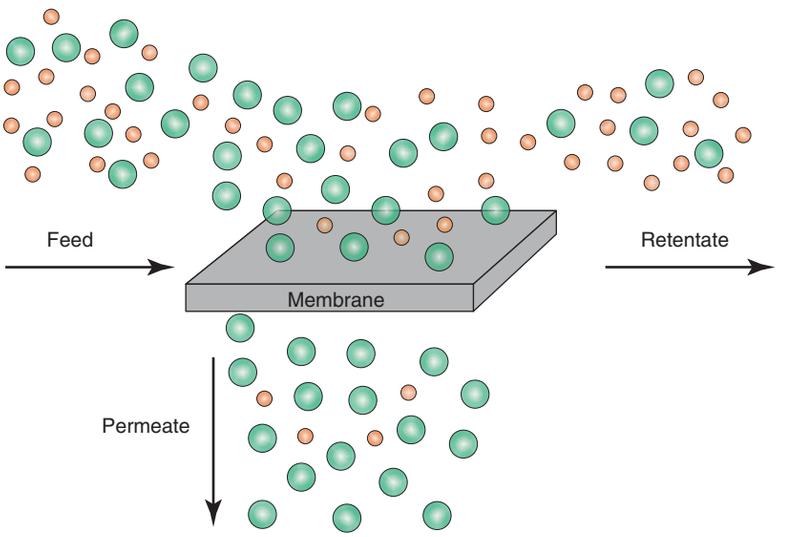


Figure 1 Gas separation with membrane. The feed mixture flows along the membrane and the feed components diffuse into and through the membrane at different rates. (Reproduced from Ref. 36, © MDPI AG (Basel, Switzerland) 2012.)

components are transported through the membrane by successive movement between the transient free volume gaps close to the feed side and those close to the permeate side owing to thermal motion of segments of the polymer chains.[35]

A membrane-based separation of gas mixtures is schematically shown in Figure 1. The gas mixture (feed) is passed over the membrane. The component that permeates preferentially is concentrated in the permeate, whereas the retained component is enriched in the retentate. Which component is preferentially permeating depends on the solubility of the components in the polymer matrix and the diffusion rate of the components through the membrane. The driving force for permeation is given by the difference of chemical potentials of the components on feed and permeates side and depends on pressure, temperature, and concentration difference.[34,37,38]

The important separation characteristics of a membrane are permeability P and selectivity α. Permeability is a measure of the quantity of permeate, whereas the selectivity describes its quality (mole fraction of preferentially permeating component in the permeate).[35]

The permeability (permeance) P is defined as the gas flow rate multiplied by the thickness of the membrane, divided by the area and by the pressure difference across the membrane (Equation 1). The permeability is given in the unit *barrer* or *gas permeation unit (GPU)* (Equations 2 and 3).

$$\text{Permeability } (P) = \frac{\text{gas flow rate} \times \text{membrane thickness}}{\text{membrane area} \times \text{pressure difference}} \tag{1}$$

The unit barrer is a non-SI unit in the cgs system for the gas permeability P of thin materials in honor of the New Zealand chemist Richard M. Barrer (1910–1996), who was a leader in research on the diffusion of gases. The permeability P of 1 barrer corresponds to the flow rate of 10^{-10} cubic centimeters per second (volume at standard temperature and pressure, 0 °C and 1 atm), times 1 cm of membrane thickness, per square centimeter of membrane area, and centimeter of mercury difference in pressure between both sides of the membrane. That is, a permeability of 1 barrer = 10^{-10} cm^2 s^{-1} cmHg^{-1} (Equation 2), or, in SI units, 7.50062×10^{-18} m^2 s^{-1} Pa^{-1} with 1 cm = 10^{-2} m, 1 cmHg = 10 Torr = 1.333223×10^3 Pa.

$$P(1 \text{ barrer}) = 10^{-10} \frac{\text{cm}^3 \text{ (STP)} \cdot \text{cm}}{\text{cm}^2 \cdot \text{s} \cdot \text{cmHg}} \tag{2}$$

The gas permeance of a membrane can be given in GPU (Equation 3) instead of *barrer* in order to express the productivity of a material.

$$P(1 \text{ GPU}) = 10^{-6} \frac{\text{cm}^3 \text{ (STP)} \cdot \text{cm}}{\text{cm}^2 \cdot \text{s} \cdot \text{cmHg}} \tag{3}$$

For experiments with gas mixtures, the gas selectivity α is calculated by Equation 4,

$$\alpha_{i,j} = \frac{Y_i / Y_j}{X_i / X_j} \tag{4}$$

where Y_i and Y_j are the mole fractions of the gases i and j produced in the permeate, whereas X_i and X_j are their corresponding mole fractions in the feed.

From single-gas experiments with permeabilities P_i (for preferentially permeating gas) and P_j, the ideal gas selectivity $\alpha_{i,j}$ is calculated according to Equation 5, thereby, assuming that both gases i and j would not affect each other in their permeation behavior.

$$\alpha_{i,j} = \frac{P_i}{P_j} \tag{5}$$

There are different types of materials that are suitable for membrane application. Inorganic membranes such as ceramic membranes of metal oxides (γ-Al_2O_3, ZrO_2, TiO_2, or $ZrTiO_4$), perovskites or zeolites, porous carbon membranes, metal membranes, or porous glass membranes[39] have exceptionally high permeability and selectivity together with thermal and chemical stabilities. However, manufacturing procedures are more complicated (e.g., require support treatment, zeolite crystallization, thermal programming for pyrolysis, and a controlled inert gas atmosphere in terms of flow, pressure, and composition) and there is a lower reproducibility for membrane properties associated with high cost and low mechanical stability. This makes the production of inorganic membranes more difficult than for polymer membranes.[39–41]

Therefore, most commercial solution-diffusion membranes contain polymer materials,[42–45] which can be divided into rubbery and glassy polymers. Glassy polymers show very attractive separation characteristics. Rubbery polymers show comparably low selectivity with high permeability for common gas pairs such as O_2/N_2, H_2/CH_4, CO_2/CH_4, and so on.[46,47] Of the glassy polymers, polyimides have been found to be very promising as membrane materials because they have good separation characteristics, offer good thermal and chemical resistance, and are easy to process.[35] Additionally, they can be easily functionalized and therefore customized for any given separation problem.

Solution-diffusion membranes already find application in removal of CO_2 from natural gas, dehydration of organic solvents, desalination, removal of polar low-molecular-weight components in equilibrium reactions, oxygen or nitrogen enrichment from air as well as in vapor recovery systems and several more.[48–51]

Natural gas treatment is of the highest industrial interest.[52] Currently, <5% of the plants processing natural gas employ membrane technology, mainly for removal of carbon dioxide.[53] Processing costs can be reduced significantly by substitution or extension of the commonly used amine absorption plants[54] by membrane separation processes. Natural gas is composed of mainly methane (75–90%) and some higher hydrocarbons. Unfortunately, a significant number of natural gas resources cannot be exploited due to the high amount of CO_2 (up to 30%) and other undesirable impurities (water, nitrogen, hydrogen sulfide, etc.), as they lead to corrosion of the pipelines.[49] The specifications for natural gas delivery to the US national pipeline grid[55] demand carbon dioxide contents of <2%.

A membrane material is well-suited for separation, when both permeability and selectivity are high. Unfortunately, improvement of the permeability often is gained in conjunction with a loss of selectivity, or vice versa.[43,46,56] The most common approaches for membrane modification are shown in Figure 2. Usually, at least two polymers are blended together, to take advantage of the different properties of those components. For example, it was found that monomers having bulky substituents restrict chain mobility and simultaneously chain packing, and lead to

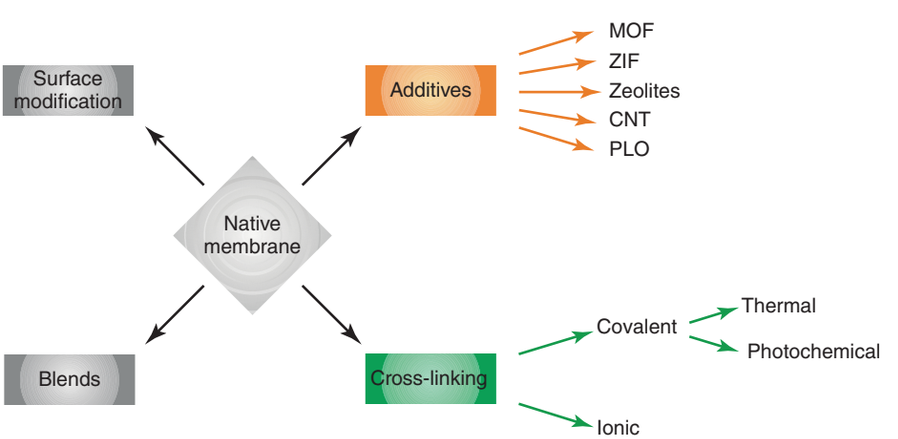


Figure 2 Different approaches to improve polymeric membrane materials. Notes: MOF = metal–organic frameworks; ZIF = zeolitic imidazolate frameworks; CNT = carbon nanotubes; PLO = porous layer oxides. (Reproduced from Ref. 36, © MDPI AG (Basel, Switzerland) 2012.)

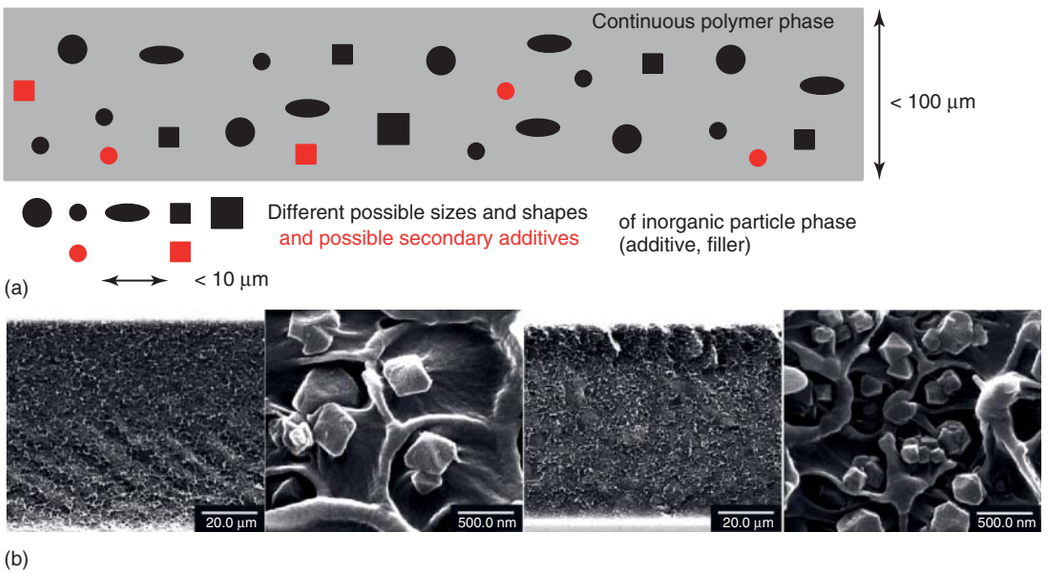


Figure 3 (a) Schematic representation of a mixed-matrix membrane indicating the different possible sizes, shapes, and components for the inorganic filler materials (e.g., MOFs, ZIFs, and nanotubes). (b) Scanning electron microscopy (SEM) cross-sections of MIL-101-polysulfone MMMs with 7.5 wt% MIL-101 (left) and 16 wt% MIL-101 loading (right) (for MIL-101, see Figure 7c and accompanying text). (Reprinted from Ref. 78 with permission of The Royal Society of Chemistry. DOI: 10.1039/C2CC16628C.)

significantly improved selectivity as well as permeability.[57] Today, most copolymers consist of alternating bulky and flexible monomer units.[43]

Although permeability and selectivity are the main criteria for classification of the separation characteristics of a membrane, the membranes are required to be thin but nonetheless stable, and they are desired to be low in cost. In addition to mechanical stability, the chemical resistance against the feed mixture is of great importance.

Unmodified ("native"), polymeric membranes often show strong plasticization effects when exposed to high partial pressures of CO_2,[58,59] hydrocarbons,[60,61] or ethylene oxide.[62] Plasticization increases the intermolecular distance and molecular motion of the polymer chains due to a decrease in inter- and/or intramolecular attractive forces. Consequently, the permeability for all feed components increases, whereas the selectivity decreases. Strong plasticization can even lead to a partial dissolution of the membrane.[63] Hydrocarbons present in natural gas can reduce the selectivity by 30–50% due to plasticization.[58,64] Plasticization can be limited by cross-linking the polymer chains through either covalent or ionic bonds (Figure 2) but will not be detailed here further (see Ref. 36 instead).[61,62,65–74]

Another approach to improve the separation characteristics of a membrane is the implementation of additives. MMMs consist of an inorganic or inorganic–organic hybrid material in the form of micro- or nanoparticles (discrete or dispersed phase) incorporated into a polymer matrix (continuous phase) (Figure 3).[79,80] The use of two materials with different flux and selectivity allows to better design a gas separation membrane through the synergistic combination of easy processability of the polymer and superior gas separation performance of inorganic materials. Different types of inorganic additives, impermeable and permeable ones, for example, zeolites,[79,81–84] MOFs,[18–20,85–88] carbon nanotubes (CNTs),[89–97] or porous layered oxides (PLOs)[98–104] can be used as filler materials.[18–20,79,80]

First MMMs were studied in the 1980s and are more and more investigated in recent years.[105–113] MMMs receive attention as a possibility to enhance the properties of pure polymer membranes.[114] Separation properties with MMMs can be above the Robeson upper bond (Figure 4),[46,47] which is a plot of permeability versus selectivity for most industrial relevant gas mixtures. Porous inorganic fillers can counteract the trade-off between selectivity and permeability, which is typical for pure polymer membranes.

However, zeolites form problematic aggregates that create defects, especially in glassy polymer matrices.[115] Several attempts of modifying the surface of the zeolites to chemically bond them to the polymer chains and avoid macrovoid formation have been made, which often led to a considerable decrease of the gas permeability due to the rigidification of the polymer chains near the zeolite surface.[116,117] Also modification of the zeolite surface by using amino functionalized siloxane to induce the formation of hydrogen bonds has been used.[118]

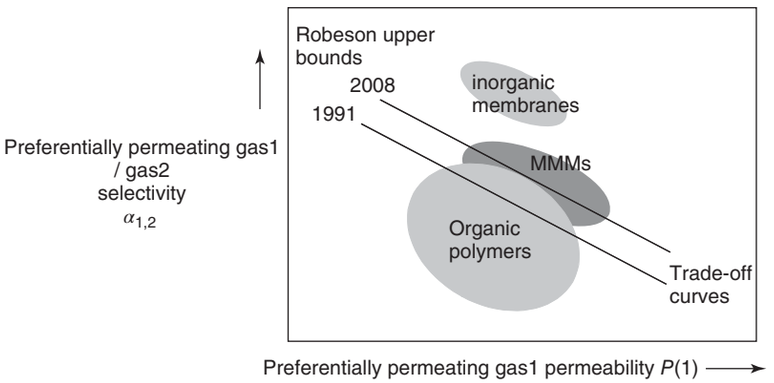


Figure 4 Schematic presentation of the trade-off between permeability and selectivity with the 1991 and 2008 Robeson upper bounds.[46,47] In most cases, the technologically attractive region lies around or above the Robeson upper bound

2 METAL–ORGANIC FRAMEWORKS IN MIXED-MATRIX MEMBRANES

MOFs offer various advantages over zeolites or other porous inorganic additives:[119–123] Organic ligands are an inherent part of MOFs and allow MOF particles to interact better with the polymer material and its functionalities. This way, the formation of gaps between the "inorganic" filler and the organic polymer phase, which leads to loss in selectivity, can be avoided. Also, the MOF surface properties can be easily tuned by (postsynthetic) functionalization if necessary. Moreover, MOFs also have higher pore volumes and lower density than zeolites, and therefore, their effect on the membrane properties can be more pronounced for a given mass loading. For MMMs, a perfect interaction between the two components is highly important in order to achieve optimized separation properties of the hybrid material. Table 1 provides a summarized overview on MOFs studied for gas separations in MMMs and selected examples will be briefly described in the text.

Incorporation of the MOF 4,4′-bipyridine-hexafluorosilicate-copper(II) (Cu-BPY-HFS)[124] (Figure 5a) into a Matrimid® 5218 membrane increased the gas permeabilities and selectivities for pure gases (from single-gas experiments) and gas mixtures of CH_4/N_2 but decreased the ideal CO_2/CH_4 and H_2/CH_4 selectivities.[127]

Cu-BTC MOF[125] (Figure 5b) as additive in an asymmetric membrane of Matrimid® 9725 or of 3:1 Matrimid®/polysulfone Utrason S 6010 N blend showed a higher CO_2 permeance compared to the unfilled membrane in mixed gas permeation experiments.[129,130] The binary gas mixtures CO_2/CH_4 and CO_2/N_2 were studied for CO_2 concentrations from 10 to 75 vol.%. The permeance of the preferential permeating gas CO_2 and, hence, the CO_2 selectivity increased with the filler loading. Noteworthy, the CO_2/CH_4 selectivity α_{CO_2/CH_4} dropped linearly when the CO_2 content increased from 10 to 75 vol.%. The slope of this selectivity drop did not depend on the $[Cu_3(BTC)_2]$ additive content.[129,130] This could be due to plasticization phenomena with higher CO_2 content.

Cu-BTC[125] (Figure 5b) was spun into MMM hollow fibers with a polyimide prepared from 4,4-oxydianiline (ODA) and pyromellitic dianhydride (PMDA). Hydrogen, H_2 permeance, and selectivity of H_2 with respect to N_2, CO_2, O_2, and CH_4 increased with increased Cu-BTC loading. At 6 wt% Cu-BTC, the permeance of H_2 was higher by 45%, and its ideal selectivity from other gases was up by a factor of 2–3 compared to pure polyimide.[131]

Cu-BTC[125] (Figure 5b) or ZIF-8[136,137] (Figure 6a) and the zeolite silicalite-1 (S1C) were combined in a MMM with polysulfone Udel® P-3500[133] for the separation of CO_2/N_2, CO_2/CH_4, O_2/N_2, and H_2/CH_4 mixtures. For some of these gas mixtures, the combined-filler MMM showed a synergetic enhancement in selective gas transport when compared either to the pure polymer or to the MMM with only one filler type. All fillers, at the same loading of 16 wt%, increase the CO_2 permeability when compared to that of the bare polymer in the two CO_2-containing mixtures. However, the maximum separation selectivities for CO_2/CH_4 and CO_2/N_2 mixtures ($\alpha_{CO_2/CH_4} = 22.4$ with $P = 8.9$ barrer for CO_2, and $\alpha_{CO_2/N_2} = 38.0$ with $P = 8.4$ barrer for CO_2) were obtained only for Cu-BTC when combined with S1C in a PSF MMM.[133]

When the same Cu-BTC/ZIF-8/S1C single- or double-additive MMMs were applied to O_2/N_2 and H_2/CH_4 separations, for which the mechanism is based mainly on diffusion and not on adsorption differences, the combination of Cu-BTC and S1C significantly enhanced the selectivities of O_2 or H_2, respectively. This may be due to an improved diffusion through zeolite crystals from the synergy with Cu-BTC.[133]

Table 1 MOF-based mixed-matrix membranes

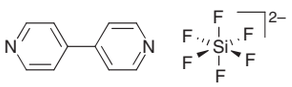
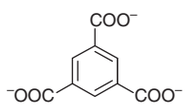
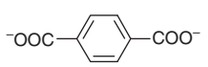
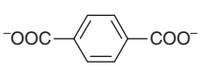
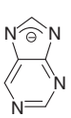
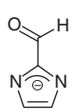
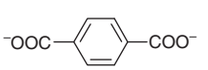
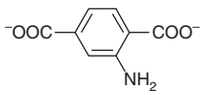
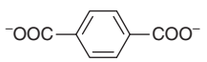
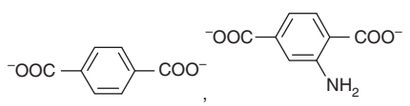
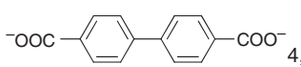
MOF metal	MOF linker (MOF acronym)	Polymers[(a)]	Gas or gas mixture	References
Cu	 4,4′-bipyridine and hexafluorosilicate (Cu-HFS-BIPY) (see Figure 5a)	Matrimid® 5218	H_2, N_2, O_2, CH_4, CO_2, CO_2/CH_4, H_2/CO_2, CH_4/N_2	127
Cu	 benzene-1,3,5-tricarboxylate, (trimesate, BTC) (HKUST-1, Cu-BTC, $Cu_3(BTC)_2$ or MOF-199) (see Figure 5b)	PSF, PDMS Matrimid® 9725, PSF Utrason S 6010 N PMDA-ODA 6FDA-ODA PSF Udel® P-3500	H_2, N_2, O_2, CH_4, CO_2 CO_2/CH_4, CO_2/N_2 H_2, N_2, O_2, CH_4, CO_2 CO_2/CH_4, O_2/N_2, H_2/CH_4, CO_2/CH_4, CO_2/N_2	128 129,130 131 132 133
Cu	25% NH_2-BDC + 75%BTC (NH_2-MOF-199)	6FDA-ODA	CO_2/CH_4	132
Cu	 benzene-1,4-dicarboxylate (terephthalate, BDC) (Cu-BDC)	PVAc	He, N_2, O_2, CH_4, CO_2	134
Zn	 benzene-1,4-dicarboxylate (terephthalate, BDC) (MOF-5 or IRMOF-1) (see Figure 5c)	Matrimid® 5218	H_2, N_2, O_2, CH_4, CO_2, H_2/CO_2, N_2/CH_4, CO_2/CH_4	135
Zn	 2-methylimidazolate(Meimi) (ZIF-8) (see Figure 6a)	Matrimid® 5218 Matrimid® 9725 PPEES PSF Udel® P-3500 Ultem® 6FDA-DAM	H_2, N_2, O_2, CH_4, CO_2, C_3H_8, H_2/CO_2, CO_2/CH_4 CO_2/CH_4, CO_2/N_2 CO_2 O_2/N_2, H_2/CH_4, CO_2/CH_4, CO_2/N_2 CO_2, N_2, CO_2/N_2, C_3H_6, C_3H_8, C_3H_6/C_3H_8	140–142 130 143 133 144 145
Zn	 purinate(ZIF-20) (see Figure 6b)	PSF Udel® P-3500	O_2/N_2	146
Zn	 2-carboxyaldehyde imidazolate(ZIF-90) (see Figure 6c)	Matrimid® 5218, Ultem® 1000, 6FDA-DAM	CO_2, CH_4, CO_2/CH_4, CO_2/N_2	123
Mn	 formiate($Mn(HCOO)_2$) (see Figure 7a)	PSF	H_2, N_2, O_2, CH_4, CO_2	128
Al	 benzene-1,4-dicarboxylate (terephthalate, BDC) (MIL-53(Al)) (see Figure 7b)	Matrimid® 9725	CO_2/CH_4, CO_2/N_2	130

Table 1 *(Continued)*

MOF metal	MOF linker (MOF acronym)	Polymers[(a)]	Gas or gas mixture	References
Al	 2-amino-terephthalate (NH_2-BDC) (NH_2-MIL-53(Al))	PSF Udel® P-3500	CO_2/CH_4	147
Cr	 benzene-1,4-dicarboxylate (terephthalate, BDC) (MIL-101(Cr)) (see Figure 7c)	PSF Utrason S 6010 N	O_2, N_2, CH_4, CO_2	36,78
Zr	 benzene-1,4-dicarboxylate (terephthalate, BDC), 2-amino-terephthalate (NH_2-BDC) (UiO-66 = Zr-BDC), (NH_2-UiO-66 = Zr-NH_2-BDC)	6FDA-ODA	CO_2/CH_4	132
Zr	 4,4′-biphenyl-dicarboxylate (BPDC) (UiO-67, Zr-BPDC)	6FDA-ODA	CO_2/CH_4	132

[(a)]See Table 2 for polymer repeat units.

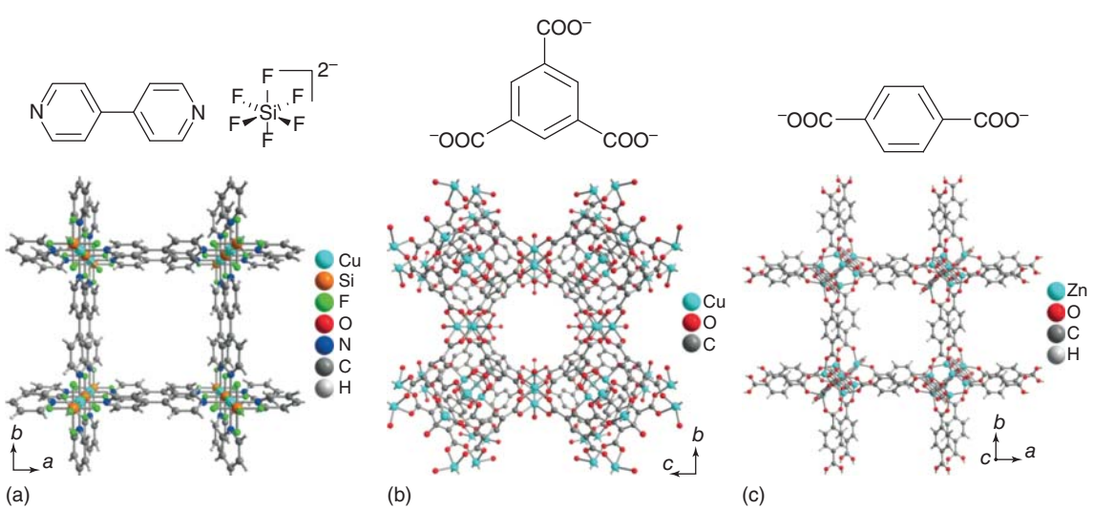


Figure 5 Linkers and sections of the packing diagrams of (a) Cu-BPY-HFS, [Cu(μ-SiF_6)(μ-4,4′-bipy)$_2$] (BPY = 4,4′-bipyridine, HFS = hexafluorosilicate),[124] (b) Cu-BTC, [Cu_3(BTC)$_2$(H_2O)$_3$] (BTC = benzene-1,3,5-tricarboxylate),[125] and (c) MOF-5 (IRMOF-1), [Zn_4(μ$_4$-O)(BDC)$_3$] (BDC = benzene-1,4-dicarboxylate, terephthalate)[126]

MOF-5[126] (Figure 5c) nanocrystals showed a strong affinity to Matrimid® 5218. Single-gas permeabilities of H_2, CO_2, O_2, N_2, and CH_4 approximately doubled from the pure polymer with MOF-5 loadings of 30 wt%. The increase was ascribed to the MOF-5 porosity. Tests with binary CH_4-containing gas mixtures for the 30% MOF-5 MMM revealed an increase in selectivity for CH_4. The larger solubility of CO_2 and N_2 in the polymer matrix was seen as the reason to favor enhanced CH_4 transport.[135]

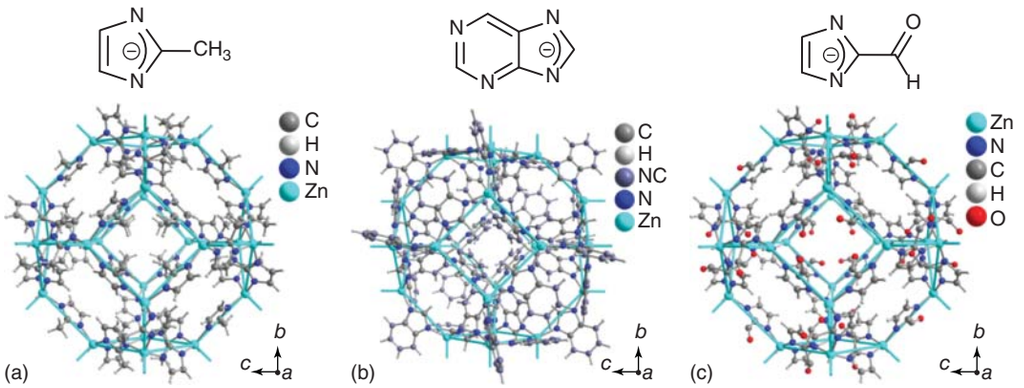


Figure 6 Linkers and sections of the packing diagrams, emphasizing the cuboctahedral β-cage, which is depicted by blue topological lines connecting the Zn atoms, of (a) ZIF-8 [Zn(2-methylimidazolate)$_2$],[136,137] (b) ZIF-20 [Zn(purinate)$_2$],[138] and (c) ZIF-90, [Zn(2-carboxyaldehyde imidazolate)$_2$][139]

Zeolitic imidazolate framework-8 (ZIF-8, Figure 6a)[136,137] was incorporated with loadings up to 80% (w/w) into Matrimid® 5218, which are much higher than the typical loadings achieved with selected zeolite materials.[140] The ZIF-8/Matrimid® MMMs permeabilities were tested for H_2, CO_2, O_2, N_2, CH_4, C_3H_8, and gas mixtures of H_2/CO_2 and CO_2/CH_4 and increased as the ZIF-8 loading increased to 40% (w/w). It was suggested that the addition of ZIF-8 nanoparticles to Matrimid® increases the distance between polymer chains and thereby creates a higher free volume in the polymer matrix. For the majority of gas pairs (O_2/N_2, CH_4/N_2, H_2/O_2, H_2/CO_2, H_2/N_2), there was no significant change in the ideal selectivity until 40 wt% ZIF-8 loading. At higher loadings of 50 and 60 wt%, the permeability decreased for all gases and the selectivities increased. Ideal selectivities of gas pairs containing gases of different size, such as H_2/O_2, H_2/CO_2, H_2/CH_4, CO_2/CH_4, CO_2/C_3H_8, and H_2/C_3H_8, improved with the 50 wt% ZIF-8 loading through a shift from polymer- to ZIF-8-controlled gas transport process. ZIF-8 can selectively transport smaller gas molecules such as H_2 and CO_2.[140]

An asymmetric MMM of Matrimid® 9725 and ZIF-8 (or MIL-53(Al), see below) exhibited a higher CO_2 permeance than the unfilled membrane in mixed gas permeation experiments.[130] MOF fillers with 10, 20, and 30 wt% were loaded in Matrimid®. Binary gas mixtures CO_2/CH_4 and CO_2/N_2 with CO_2 concentrations from 10 to 75 vol.% were investigated and the results compared to Cu-BTC/Matrimid®[129] or MIL-53(Al).[130] The permeance of the preferentially permeating gas CO_2 increased with the filler loading in the binary mixtures in all three cases, but the CO_2 selectivity only increased slightly in the case of Cu-BTC or MIL-53(Al) and remained almost constant for ZIF-8. The CO_2/CH_4 selectivity $\alpha_{CO2/CH4}$ showed a constant drop with the increase of CO_2 content from 10 to 75 vol.% for all three additives. The drop in selectivity was independent of the filler content. Increase in CO_2 permeability was assigned to the extra pore network of the MOF fillers. Scanning electron microscopy cross-section images showed the MOF filler well distributed and embedded in the polymer matrix even for the 30 wt% loaded membranes.[129,130]

MMMs made of poly-(1,4-phenylene ether-ether-sulfone) (PPEES) and ZIF-8 with filler loadings of 10, 20, and 30 wt% were studied for CO_2 diffusion using pulsed field gradient (PFG) NMR techniques.[143] The self-diffusion coefficient increased from 2.1×10^{-8} cm^2 s^{-1} for the pristine PPEES membrane to 9.3×10^{-8} cm^2 s^{-1} for the 30 wt% ZIF-8/PPEES-MMM. ZIF-8 provides Langmuir adsorption sites for CO_2 molecules, thus, the gas adsorption in the MMM increases with the filler content.[143]

Combining ZIF-8[136,137] and silicalite-1 in polysulfone Udel® P-3500 (ZIF-8/S1C-PSF MMM) did not improve the separation results compared to either S1C-PSF or ZIF-8-PSF alone in MMMs for CO_2/CH_4 and CO_2/N_2 gas mixtures. The relatively large silicalite-1 crystals probably could not be intercalated between small ZIF-8 particles. ZIF-8 alone produced the highest increase of CO_2 permeability, which can be attributed to its textural properties and its small particle size, which however gave poorly dispersed aggregates.[133] For O_2/N_2 and H_2/CH_4 gas separation, a ZIF-8-PSF MMM produced the best selectivity-permeability results compared to a Cu-BTC or S1C-PSF MMM. This may be due to an increase in free volume (as suggested for ZIF-8-polyimide MMMs)[140] together with an efficient molecular separation effect (based on diffusion differences) because of the small pore aperture window of ZIF-8 (3.4 Å, 0.34 nm) compared to Cu-BTC (6 Å, 0.6 nm) and S1C (5.5 Å, 0.55 nm).[133]

Different sonication powers were applied on ZIF-8[136,137] nanoparticles for the preparation of ZIF-8/Matrimid® nanocomposite membranes with the aim of

investigating the effect of typical membrane processing conditions on the structure, the interfacial morphology, and the gas separation performance. It was shown that ultrasonication generates significant changes in the shape, size distribution, and structure of ZIF-8 particles suspended in an organic solvent during membrane processing. Although there were significant changes in the particle morphology, there were only minor losses in crystallinity and microporosity as proven from powder X-ray diffraction, synchrotron X-ray pair distribution function analysis, and nitrogen physisorption. Dynamic light scattering and electron microscopy showed that ZIF-8 nanoparticles undergo substantial Ostwald ripening when subjected to high-intensity ultrasonication. Composite films prepared with both direct (high-intensity) and indirect (low-intensity) sonication showed good adhesion between the polymer and ZIF-8 phases. However, films prepared using indirect sonication exhibit drastic agglomeration of nanoparticles, whereas direct sonication produced ripened nanoparticles with variable dispersion. The ripened particles gave lower pore volumes and lower surface areas compared to the as-synthesized material. ZIF-8/Matrimid® composite membranes prepared from the two different sonication methods showed significant differences in microstructure. Permeation measurements in membranes fabricated with high-intensity sonication showed strong enhancement in permeability of CO_2 and increased CO_2/CH_4 selectivity, in agreement with the Maxwell model. In contrast, composite membranes prepared with low-intensity sonication were found to be defective.[141]

Small and less agglomerated ZIF-20 (Figure 6b)[138] with 8 wt% in a polysulfone Udel® P-3500 mixed-matrix membrane gave a better separation of an equimolar O_2/N_2 mixture than the pure polymer. The increase in O_2/N_2 selectivity from 4.7 (±0.4) to 6.7 (±0.5) in the MMM could be reasoned by the difference in kinetic diameter (d_k) between O_2 ($d_k = 0.343$ nm) and N_2 ($d_k = 0.368$ nm).[146]

Submicrometer-sized particles of ZIF-90 (Figure 6c)[139] were used to fabricate nanocomposite membranes with three different polyimides (Ultem® 1000, Matrimid® 5218, and 6FDA-DAM, Tables 1 and 2).[123] Scanning electron microscopy revealed well-dispersed MOF crystals with an excellent adhesion to the polyimides and no interfacial voids. Ultem® and Matrimid® MMMs showed significantly enhanced CO_2 permeability without any loss of CO_2/CH_4 selectivity. ZIF-90 with the highly permeable polymer 6FDA-DAM gave significant enhancements in both CO_2 permeability and CO_2/CH_4 selectivity. Membranes containing smaller particles showed slightly better results. The performance of ZIF-90/6FDA-DAM MMM exceeded the polymer upper bound for polymeric membrane performance from 1991,[46] and reached the technologically attractive region (Figure 4).[123]

The CO_2/CH_4 binary mixture gas permeation properties of pure 6FDA-DAM and 15 wt% ZIF-90/6FDA-DAM membranes revealed an enhanced gas separation performance of the MMM. The CO_2/CH_4 mixed gas selectivity of the ZIF-90 MMM was higher than the ideal selectivity measured by single-component gas permeation, presumably because of selective sorption and diffusion of CO_2 in the ZIF-90 crystals.[123] Also, a ZIF-90/6FDA-DAM membrane showed an ideal CO_2/N_2 selectivity of 22 compared to 14 for pure 6FDA-DAM, indicating the possibility for separation of CO_2 from flue gases.[123]

The MOF $Mn(HCOO)_2$[75] (Figure 7a) as PSF-MMM showed high adsorption affinity for H_2 only. Higher loadings reduced the gas solubility, but increased the permeability, indicating defective membranes with interfacial voids.[128]

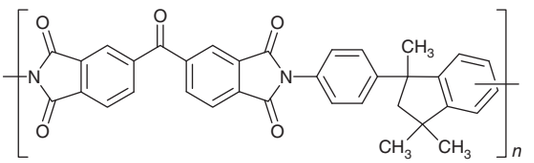
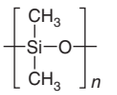
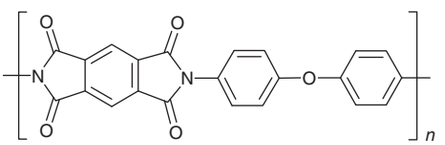
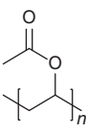
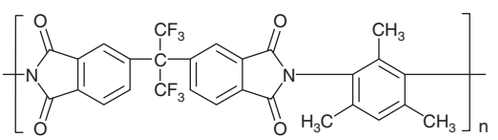
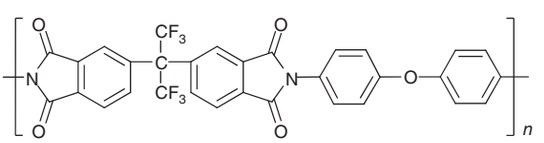
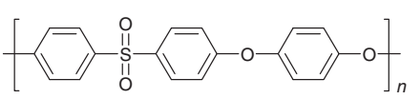
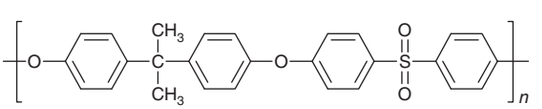
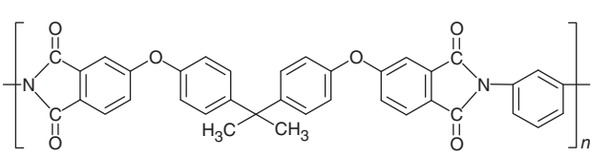
An asymmetric membrane from MIL-53(Al)[76] (Figure 7b) (or Cu-BTC or ZIF-8, see above and Table 1) and Matrimid® 9725 showed a higher CO_2 permeability than the unfilled membrane in mixed gas permeation experiments.[130] Preferentially, permeation of CO_2 increased with the filler loading for all thre MOFs in the binary gas mixtures CO_2/CH_4 and CO_2/N_2 with CO_2 concentrations from 10 to 75 vol.%. Yet, the CO_2 selectivity increased only slightly in the case of Cu-BTC or MIL-53(Al) and remained almost constant for ZIF-8. Under the same conditions, the CO_2 permeability remained invariant with the type of MOF for the CO_2/N_2 gas mixture. The CO_2/CH_4 selectivity α_{CO_2/CH_4} dropped linearly when the CO_2 fraction increased from 10 to 75 vol.% for all three MOFs. The decrease in selectivity was essentially independent of the MOF filler content.[129,130]

A variant of MIL-53(Al), namely compound NH_2-MIL-53(Al) with the 2-aminobenzene-1,4-dicarb oxylate linker (NH_2-BDC) but the same structure as MIL-53(Al), was used to fabricate nanocomposite membranes with PSF Udel® P-3500. The homogeneously distributed NH_2-MIL-53(Al) particles showed excellent adhesion with the polysulfone. The CO_2/CH_4 separation selectivity of NH_2-MIL-53(Al)/PSF-MMM increased with pressure, which was traced to the flexibility of the NH_2-MIL-53(Al) filler.[147]

MMMs with the water-stable MOF MIL-101(Cr)[77] (Figure 7c) in polysulfone Ultrason S 6100 N exhibited a remarkable four-fold increase (compared to pure PSF) in the permeability of O_2 to technically needed values above 6 barrer and a simultaneous high selectivity for O_2 over N_2 of 5–6. The MIL-101(Cr) particles showed long-term hydrothermal stability and very good adhesion with polysulfone (Figure 3b).[78]

Single-gas experiments of MIL-101(Cr)/PSF membranes with CO_2, CH_4, and N_2 at different MOF loadings showed increases in gas permeabilities with increasing MIL-101(Cr) weight percentage in PSF (Figure 8). CO_2 is the preferentially permeating gas with permeability

Table 2 Polymer acronyms and repeat units

Matrimid®, polyimide		PDMS, polydimethylsiloxane	
PMDA-ODA, polyimide (PMDA: pyromellitic dianhydride, ODA: 4,4′-oxydianiline)		PVAc, poly(vinyl acetate)	
6FDA-DAM, polyimide (6FDA: 2,2′-bis(3,4-carboxyphenyl)hexafluoropropane dianhydride, DAM: diaminomesitylene)			
6FDA-ODA, polyimide 6FDA: 2,2′-bis(3,4-carboxyphenyl)hexafluoropropane dianhydride, ODA: 4,4′-oxydianiline			
PPEES, poly-(1,4-phenylene ether-ether-sulfone)			
PSF, polysulfone			
Ultem®, polyimide			

increases from about 5 to over 35 barrer from pure PSF to 20 wt% MIL-101/PSF. The increase for CO_2 also raises the ideal selectivities for CO_2/CH_4 and CO_2/N_2 from about 20 to 25.[36]

The CO_2 permeability is rather invariant to the thickness of the membrane (Figure 9a), whereas the CH_4 and N_2 permeabilities decrease when the membrane becomes thicker for the same high (14 and 19 wt%)

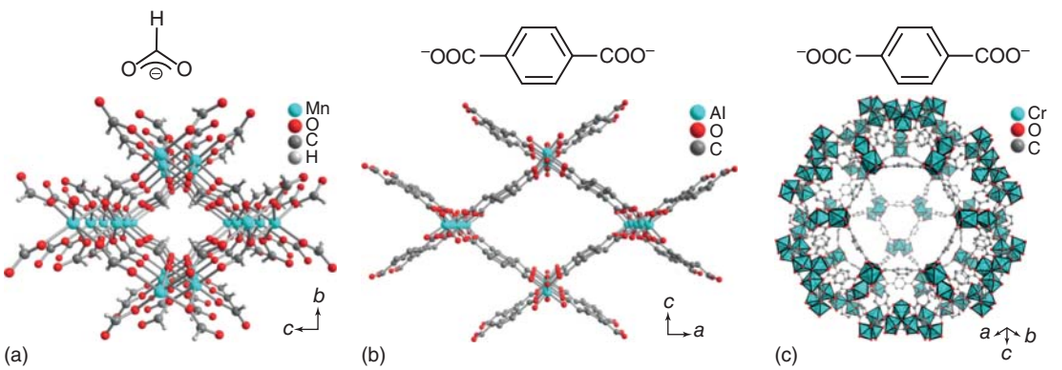


Figure 7 Linkers and sections of the packing diagrams of (a) $Mn(HCOO)_2$ (manganese formiate),[75] (b) MIL-53(Al), [Al(μ-OH)(BDC)] (BDC = benzene-1,4-dicarboxylate, terephthalate),[76] and (c) MIL-101(Cr), $[Cr_3(\mu_3\text{-}O)(F,OH)(BDC)_3(H_2O)_2]$[77]

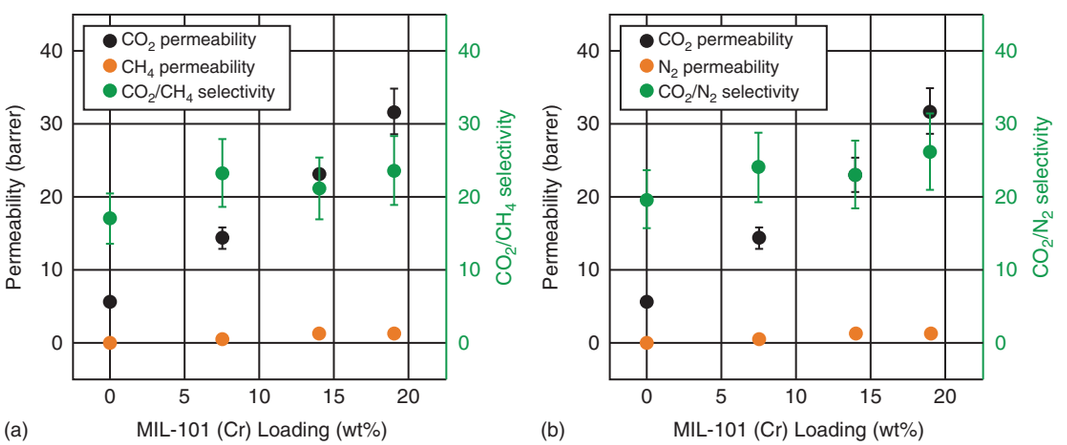


Figure 8 Single-gas CO_2, CH_4, and N_2 permeabilities and ideal (a) CO_2/CH_4 and (b) CO_2/N_2 selectivities of pure PSF and MIL-101/PSF membranes with different MIL wt% loadings (averaged values for different membrane thicknesses). (Reproduced from Ref. 36, © MDPI AG (Basel, Switzerland) 2012.)

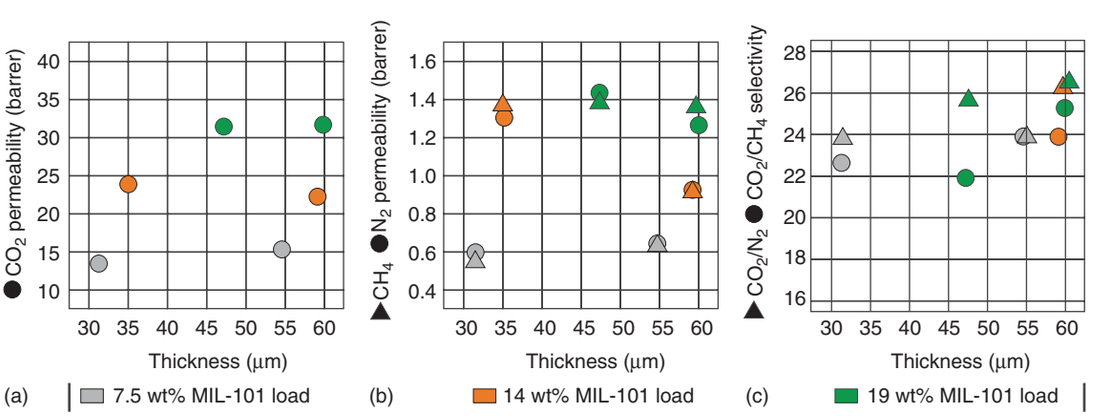


Figure 9 (a) Single-gas CO_2; (b) CH_4 and N_2 permeabilities; (c) ideal CO_2/CH_4 and CO_2/N_2 selectivities for MIL-101(Cr)/PSF membranes at different MIL wt% loadings and membrane thicknesses. (Reproduced from Ref. 36, © MDPI AG (Basel, Switzerland) 2012.)

MIL-101(Cr) loading (Figure 9b). Hence, the ideal CO_2/CH_4 and CO_2/N_2 selectivities increase with the membrane thickness, in particular for at higher (19 wt%) MOF loading (Figure 9c).[36]

3 CONCLUSION

Mixed-matrix membranes with MOFs as additives (fillers) exhibit enhanced permeabilities and possibly also selectivities when compared to the underlying pure polymer. Matrimid® and polysulfone are popular polymer matrices for MOF fillers. MOF particle adhesion to these organic polymers does not represent a problem. Permeability increases can be traced to MOF porosity. Crucial permeability-selectivity factors worth further investigation are, among others, filler content, filler (nano)size and dispersion, functional gas-binding groups in filler (e.g., amines for CO_2), water-stability of MOF filler (many popular MOFs such as MOF-5 and Cu-BTC are not moisture stable)[148–152] as well as mixed gases with different volume fractions instead of single gases. Addition of MOFs to polymers in MMMs easily yields performances similar to the best polymeric membranes and higher selectivities than those reported to date for any pure MOF membrane for the respective separation. MOF-polymer MMMs allow for an easier synthesis and handability compared to pure MOF membranes.[153–157]

4 ACKNOWLEDGMENTS

The authors thank the Anton-Betz-Stiftung for their support.

5 RELATED ARTICLES

Metal-Organic Frameworks for Removal of Harmful Gases; Gas Storage in Metal-Organic Frameworks; Adsorption of Hydrocarbons and Alcohols in Metal-Organic Framework Materials.

6 ABBREVIATIONS AND ACRONYMS

CNT = carbon nanotube; GPU = gas permeation unit; MMM = mixed-matrix membrane; MOF = Metal–organic framework; ODA = 4,4-oxydianiline; PFG = pulsed field gradient PLO = porous layered oxide; PMDA = pyromellitic dianhydride; PPEES = poly-(1,4-phenylene ether-ether-sulfone);

7 REFERENCES

1. Introduction to special MOF issue: J. R. Long and O. M. Yaghi, *Chem. Soc. Rev.*, 2009, **38**, 1213.
2. K. Biradha, *New J. Chem.*, 2010, **34**, 2353.
3. Introduction to special MOF issue: H. C. Zhou, J. R. Long, and O. M. Yaghi, *Chem. Rev.*, 2012, **112**, 673.
4. S. Kitagawa and S. Natarajan, *Eur. J. Inorg. Chem.*, 2010, 3685.
5. C. Janiak and J. K. Vieth, *New J. Chem.*, 2010, **34**, 2366.
6. J.-R. Li, R. J. Kuppler, and H.-C. Zhou, *Chem. Soc. Rev.*, 2009, **38**, 1477.
7. M. Paik Suh, H. J. Park, T. K. Prasad, and D.-W. Lim, *Chem. Rev.*, 2012, **112**, 782.
8. H. Wu, Q. Gong, D. H. Olson, and J. Li, *Chem. Rev.*, 2012, **112**, 836.
9. L. J. Murray, M. Dincă, and J. R. Long, *Chem. Soc. Rev.*, 2009, **38**, 1294.
10. Z. Zhang, Y. Zhao, Q. Gong, Z. Li, and J. Li, *Chem. Commun.*, 2013, **49**, 653.
11. J.-R. Li, J. Sculley, and H.-C. Zhou, *Chem. Rev.*, 2012, **112**, 869.
12. G. Férey, C. Serre, T. Devic, G. Maurin, H. Jobic, P. L. Llewellyn, G. De Weireld, A. Vimont, M. Daturif, and J.-S. Chang, *Chem. Soc. Rev.*, 2011, **40**, 550.
13. P. Horcajada, R. Gref, T. Baati, P. K. Allan, G. Maurin, P. Couvreur, G. Férey, R. E. Morris, and C. Serre, *Chem. Rev.*, 2012, **112**, 1232.
14. J.-Y. Lee, O. K. Farha, J. Roberts, K. A. Scheidt, S. T. Nguyen, and J. T. Hupp, *Chem. Soc. Rev.*, 2009, **38**, 1450.
15. M. Yoon, R. Srirambalaji, and K. Kim, *Chem. Rev.*, 2012, **112**, 1196.
16. C. Janiak and S. K. Henninger, *Chimia*, 2013, **67**, 419.
17. S. K. Henninger, F. Jeremias, H. Kummer, and C. Janiak, *Eur. J. Inorg. Chem.*, 2012, 2625.
18. H. B. Tanh Jeazet, C. Staudt, and C. Janiak, *Dalton Trans.*, 2012, **41**, 14003.
19. B. Zornoza, C. Tellez, J. Coronas, J. Gascon, and F. Kapteijn, *Microporous Mesoporous Mater.*, 2013, **166**, 67.
20. G. Dong, H. Li, and V. Chen, *J. Mater. Chem. A*, 2013, **1**, 4610.
21. C. J. King, Separation processes, introduction, in 'Ullmann's Encyclopedia of Industrial Chemistry', John Wiley and Sons, Inc., Hoboken, NJ, USA, 2000 .
22. J. C. Davis, R. J. Valus, R. Eshraghi, and A. E. Velikoff, *Sep. Sci. Tec.*, 1993, **28**, 463.
23. H. Strathmann, *AIChE J.*, 2001, **47**, 1077.
24. W. J. Koros and R. Mahajan, *J. Membrane Sci.*, 2000, **175**, 181.

25. K. Ohlrogge and K. Stürken, in 'Membrane Technology in the Chemical Industry', eds. S. P. Nunez and K.-V. Peinemann, Wiley-VCH, Weinheim, 2001.
26. R. W. Baker, *Ind. Eng. Chem. Res.*, 2002, **41**, 1393.
27. BORSIG Membrane Technology GmbH http://www.borsig-china.com/#productrecovery (accessed Mar 2014).
28. Sulzer Chemtech AG http://www.sulzerchemtech.com (accessed Mar 2014).
29. M. Kondo, M. Komori, H. Kita, and K. Okamoto, *J. Membrane Sci.*, 1997, **133**, 133.
30. S. M. Holmes, M. Schmitt, C. Markert, R. J. Plaisted, J. O. Forrest, P. N. Sharratt, A. A. Garforth, C. S. Cundy, and J. Dwyer, *Chem. Eng. Res. Des.*, 2000, **78**, 1084.
31. A. W. C. Van den Berg, L. Gora, J. C. Jansen, M. Makkee, and T. Maschmeyer, *J. Membrane Sci.*, 2003, **224**, 29.
32. C. A. Scholes, G. W. Stevens, and S. E. Kentish, *Fuel*, 2012, **96**, 15.
33. T. Graham, *J. Chem. Soc.*, 1867, **20**, 235.
34. W. J. Koros and G. K. Fleming, *J. Membrane Sci.*, 1993, **83**, 1.
35. N. Schmeling, R. Konietzny, D. Sieffert, P. Rölling, and C. Staudt, *Beilstein J. Org. Chem.*, 2010, **6**, 789.
36. K. Hunger, N. Schmeling, H. B. Tanh Jeazet, C. Janiak, C. Staudt, and K. Kleinermanns, *Membranes*, 2012, **2**, 727.
37. R. W. Baker, 'Membrane Technology and Applications' 2nd edition, Wiley, Chichester, UK, 2004.
38. D. R. Paul and Y. P. Yampol'skii, 'Polymeric Gas Separation Membranes', CRC Press, Boca Raton, FL, USA, 1994.
39. H. Strathmann, 'Introduction to Membrane Science and Technology', Wiley-VCH, Weinheim, Germany, 2011.
40. G. Saracco, H. W. J. P. Neomagus, G. F. Versteeg, and W. P. M. van Swaaij, *Chem. Eng. Sci.*, 1999, **54**, 1997.
41. A. Julbe, Zeolite membranes—synthesis, characterization and application, in 'Introduction to Zeolite Science and Practice' 3rd edition, eds. J. Cejka, H. Bekkum, A. Corma and F. Schüth, Elsevier B.V., Amsterdam, The Netherlands, 2007, p.181.
42. E. Staude, 'Membranen und Membranprozesse', Wiley-VCH, Weinheim, Germany, 1992.
43. G. Maier, *Angew. Chem., Int. Ed.*, 1998, **37**, 2961.
44. L. G. Lin, Y. Z. Zhang, and Y. Kong, *Fuel*, 2009, **88**, 1799.
45. B. Bolto, M. Hoang, and Z. L. Xie, *Chem. Eng. Process.*, 2011, **50**, 227.
46. L. M. Robeson, *J. Membrane Sci.*, 1991, **62**, 165.
47. L. M. Robeson, *J. Membrane Sci.*, 2008, **320**, 390.
48. K. Ohlrogge and K. Stürken, The separation of organic vapors from gas streams by means of membranes, in 'Membrane Technology', Wiley-VCH, Weinheim, Germany, 2001, p.69.
49. R. W. Baker, *Ind. Eng. Chem. Res.*, 2002, **41**, 1393.
50. R. W. Spillman, *Chem. Eng. Prog.*, 1989, **85**, 41.
51. H. Ohya, V. V. Kudryavtsev, and S. I. Semenova, 'Polyimide Membranes: Applications, Fabrications and Properties', CRC Press, Boca Raton, FL, USA, 1996.
52. N. Y. Du, H. B. Park, M. M. Dal-Cin, and M. D. Guiver, *Energy Environ. Sci.*, 2012, **5**, 7306.
53. R. W. Baker and K. Lokhandwala, *Ind. Eng. Chem. Res.*, 2008, **47**, 2109.
54. A. L. Kohl and R. B. Nielsen, 'Gas Purification' 5th edition, Gulf Professional Publishing, Houston, TX, USA, 1997.
55. R. H. Hugman, E. H. Vidas and P. S. Springer, Chemical Composition of Discovered and Undiscovered Natural Gas in the Lower-48 United States. Project Summary. Final report, 1 November 1988–31 March 1990; Technical Report No. PB-91-144600/XAB; Energy and Environmental Analysis, Inc.: Arlington, VA, USA, 1 November, 1990.
56. L. M. Robeson, W. F. Burgoyne, M. Langsam, A. C. Savoca, and C. F. Tien, *Polymer*, 1994, **35**, 4970.
57. K. Tanaka, M. Okano, H. Kita, K.-i. Okamoto, and S. Nishi, *Polym. J.*, 1994, **26**, 1186.
58. C. Staudt-Bickel and W. J. Koros, *J. Membrane Sci.*, 1999, **155**, 145.
59. M. Wessling, S. Schoeman, T. van der Boomgaard, and C. A. Smolders, *Gas Sep. Pur.*, 1991, **5**, 222.
60. J. H. Kim, W. J. Koros, and D. R. Paul, *J. Membrane Sci.*, 2006, **282**, 21.
61. C. Staudt-Bickel and W. J. Koros, *J. Membrane Sci.*, 2000, **170**, 205.
62. B. Schiewe, C. Staudt-Bickel, A. Vuin, and G. Wegner, *ChemPhysChem*, 2001, **2**, 211.
63. J. Z. Ren, C. Staudt-Bickel, and R. N. Lichtenthaler, *Sep. Purif. Tech.*, 2001, **22–23**, 31.
64. D. Q. Vu, W. J. Koros, and S. J. Miller, *Ind. Eng. Chem. Res.*, 2001, **41**, 367.
65. F. Pithan, C. Staudt-Bickel, S. Hess, and R. N. Lichtenthaler, *ChemPhysChem*, 2002, **3**, 856.
66. B. Cao, H. Hinode, and T. Kajiuchi, *J. Membrane Sci.*, 1999, **156**, 43.
67. S. Matsui and D. R. Paul, *J. Membrane Sci.*, 2002, **195**, 229.
68. M. S. McCaig and D. R. Paul, *Polymer*, 1999, **40**, 7209.
69. M. E. Rezac and B. Schöberl, *J. Membrane Sci.*, 1999, **156**, 211.
70. A. Bos, I. G. M. Punt, M. Wessling, and H. Strathmann, *Sep. Purif. Technol.*, 1998, **14**, 27.
71. A. Bos, I. G. M. Punt, M. Wessling, and H. Strathmann, *J. Polym. Sci. B Polym. Phys.*, 1998, **36**, 1547.
72. H. Kita, T. Inada, K. Tanaka, and K.-i. Okamoto, *J. Membrane Sci*, 1994, **87**, 139.

73. M. E. Rezac, E. Todd Sorensen, and H. W. Beckham, *J. Membrane Sci.*, 1997, **136**, 249.
74. C. T. Wright and D. R. Paul, *J. Membrane Sci.*, 1997, **124**, 161.
75. D. N. Dybtsev, H. Chun, S. H. Yoon, D. Kim, and K. Kim, *J. Am. Chem. Soc.*, 2004, **126**, 32.
76. T. Loiseau, C. Serre, C. Huguenard, G. Fink, F. Taulelle, M. Henry, T. Bataille, and G. Férey, *Chem. Eur. J.*, 2004, **10**, 1373.
77. G. Férey, C. Mellot-Draznieks, C. Serre, F. Millange, J. Dutour, S. Surble, and I. Margiolaki, *Science*, 2005, **309**, 2040.
78. H. B. T. Jeazet, C. Staudt, and C. Janiak, *Chem. Commun.*, 2012, **48**, 2140.
79. T. S. Chung, L. Y. Jiang, Y. Li, and S. Kulprathipanja, *Prog. Polym. Sci.*, 2007, **32**, 483.
80. D. Bastani, N. Esmaeili, and M. Asadollahi, *J. Ind. Eng. Chem.*, 2013, **19**, 375.
81. T. T. Moore and W. J. Koros, *J. Mol. Struct.*, 2005, **739**, 87.
82. R. Mahajan and W. J. Koros, *Polym. Eng. Sci.*, 2002, **42**, 1420.
83. Y. Li, T. S. Chung, C. Cao, and S. Kulprathipanja, *J. Membrane Sci.*, 2005, **260**, 45.
84. B. D. Reid, F. A. Ruiz-Trevino, I. H. Musselman, K. J. Balkus Jr, and J. P. Ferraris, *Chem. Mater.*, 2001, **13**, 2366.
85. K. Biradha, *New J. Chem.*, 2010, **34**, 2353.
86. M. J. Zaworotko, *New J. Chem.*, 2010, **34**, 2355.
87. K. Hindson, *Eur. J. Inorg. Chem.*, 2010, **2010**, 3683.
88. S. Kitagawa and S. Natarajan, *Eur. J. Inorg. Chem.*, 2010, **2010**, 3685.
89. A. I. Skoulidas, D. S. Sholl, and J. K. Johnson, *J. Chem. Phys.*, 2006, **124**, 054708:1.
90. D.-Y. Kang, H. M. Tong, J. Zang, R. P. Choudhury, D. S. Sholl, H. W. Beckham, C. W. Jones, and S. Nair, *ACS Appl. Mater. Interfaces*, 2012, **4**, 965.
91. A. Fonseca, S. Reijerkerk, J. Potreck, K. Nijmeijer, Z. Mekhalif, and J. Delhalle, *Desalination*, 2010, **250**, 1150.
92. S. Kim, T. W. Pechar, and E. Marand, *Desalination*, 2006, **192**, 330.
93. T. Liu, Y. Tong, and W.-D. Zhang, *Compos. Sci. Technol.*, 2007, **67**, 406.
94. A. Pantano, G. Modica, and F. Cappello, *Mater. Sci. Eng. A*, 2008, **486**, 222.
95. P. S. Goh, B. C. Ng, A. F. Ismail, M. Aziz, and Y. Hayashi, *J. Colloid Interface Sci.*, 2012, **386**, 80.
96. D.-Y. Kang, C. W. Jones, and S. Nair, *J. Membrane Sci.*, 2011, **381**, 50.
97. H. Cong, J. Zhang, M. Radosz, and Y. Shen, *J. Membrane Sci.*, 2007, **294**, 178.
98. H.-K. Jeong, W. Krych, H. Ramanan, S. Nair, E. Marand, and M. Tsapatsis, *Chem. Mater.*, 2004, **16**, 3838.
99. J. R. Johnson and W. J. Koros, *Taiwan Inst. Chem. Eng.*, 2009, **40**, 268.
100. C. Yang, W. H. Smyrl, and E. L. Cussler, *J. Membrane Sci.*, 2004, **231**, 1.
101. J. A. Sheffel and M. Tsapatsis, *J. Membrane Sci.*, 2007, **295**, 50.
102. J. Choi and M. Tsapatsis, *J. Am. Chem. Soc.*, 2009, **132**, 448.
103. C. Rubio, C. Casado, P. Gorgojo, F. Etayo, S. Uriel, C. Téllez, and J. Coronas, *Eur. J. Inorg. Chem.*, 2010, 159.
104. A. Galve, D. Sieffert, E. Vispe, C. Téllez, J. Coronas, and C. Staudt, *J. Membrane Sci.*, 2011, **370**, 131.
105. Q. Hu, E. Marand, S. Dhingra, D. Fritsch, J. Wen, and G. Wilkes, *J. Membrane Sci.*, 1997, **135**, 65.
106. C. M. Zimmerman, A. Singh, and W. J. Koros, *J. Membrane Sci.*, 1997, **137**, 145.
107. R. Mahajan and W. J. Koros, *Ind. Eng. Chem. Res.*, 2000, **39**, 2692.
108. L. Y. Jiang, T. S. Chung, C. Cao, Z. Huang, and S. Kulprathipanja, *J. Membrane Sci.*, 2005, **252**, 89.
109. T. S. Chung, L. Y. Jiang, Y. Li, and S. Kulprathipanja, *Prog. Polym. Sci.*, 2007, **32**, 483.
110. P. Bernardo, E. Drioli, and G. Golemme, *Ind. Eng. Chem. Res.*, 2009, **48**, 4638.
111. T. T. Moore, R. Mahajan, D. Q. Vu, and W. J. Koros, *Angew. Chem., Int. Ed.*, 2004, **50**, 311.
112. G. Langhendries and G. V. Baron, *J. Membrane Sci.*, 1998, **141**, 265.
113. P. Gorgojo, D. Sieffert, C. Staudt, C. Tellez, and J. Coronas, *J. Membrane Sci.*, 2012, **411**, 146.
114. T. C. Merkel, B. D. Freeman, R. J. Spontak, Z. He, I. Pinnau, P. Meakin, and A. J. Hill, *Science*, 2002, **296**, 519.
115. T. T. Moore and W. J. Koros, *J. Mol. Struct.*, 2005, **739**, 87.
116. R. Mahajan and W. J. Koros, *Polym. Eng. Sci.*, 2002, **42**, 1420.
117. J. M. Duval, A. J. B. Kemperman, B. Folkers, M. H. V. Mulder, G. Desgrandchamps, and C. A. Smolders, *J. Appl. Polym. Sci.*, 1994, **54**, 409.
118. T. W. Pechar, S. Kim, B. Vaughan, E. Marand, M. Tsapatsis, H. K. Jeong, and C. J. Cornelius, *J. Membrane Sci*, 2006, **277**, 195.
119. R. D. Noble, *J. Membrane Sci.*, 2011, **378**, 393.
120. J. R. Li, Y. G. Ma, M. C. McCarthy, J. Sculley, J. M. Yu, H. K. Jeong, P. B. Balbuena, and H. C. Zhou, *Coord. Chem. Rev.*, 2011, **255**, 1791.
121. D. H. Liu and C. L. Zhong, *J. Mater. Chem.*, 2010, **20**, 10308.
122. S. T. Meek, J. A. Greathouse, and M. D. Allendorf, *Adv. Mater.*, 2011, **23**, 249.
123. T. H. Bae, J. S. Lee, W. L. Qiu, W. J. Koros, C. W. Jones, and S. Nair, *Angew. Chem., Int. Ed.*, 2010, **49**, 9863.

124. S. Noro, S. Kitagawa, M. Kondo, and K. Seki, *Angew. Chem., Int. Ed.*, 2000, **39**, 2082.

125. S. S.-Y. Chui, S. M.-F. Lo, J. P. H. Charmant, A. G. Orpen, and I. D. Williams, *Science*, 1999, **283**, 1148.

126. H. Li, M. Eddaoudi, T. L. Groy, M. O'Keeffe, and O. M. Yaghi, *Nature*, 1999, **402**, 276.

127. Y. F. Zhang, I. H. Musseman, J. P. Ferraris, and K. J. Balkus, *J. Membrane Sci.*, 2008, **313**, 170.

128. A. Car, C. Stropnik, and K. -V. Peinemann, *Desalination*, 2006, **200**, 424.

129. S. Basu, A. Cano-Odena, and I. F. J. Vankelecom, *J. Membrane Sci.*, 2010, **362**, 478.

130. S. Basu, A. Cano-Odena, and I. F. J. Vankelecom, *Sep. Purif. Technol.*, 2011, **81**, 31.

131. J. Hu, H. P. Cai, H. Q. Ren, Y. M. Wei, Z. L. Xu, H. L. Liu, and Y. Hu, *Ind. Eng. Chem. Res.*, 2010, **49**, 12605.

132. O. G. Nik, X. Y. Chen, and S. Kaliaguine, *J. Membrane Sci.*, 2012, **413–414**, 48.

133. B. Zornoza, B. Seoane, J. M. Zamaro, C. Tellez, and J. Coronas, *ChemPhysChem*, 2011, **12**, 2781.

134. R. Adams, C. Carson, J. Ward, R. Tannenbaum, and W. Koros, *Microporous Mesoporous Mater.*, 2010, **131**, 13.

135. E. V. Perez, K. J. Balkus, J. P. Ferraris, and I. H. Musselman, *J. Membrane Sci.*, 2009, **328**, 165.

136. X.-C. Huang, Y.-Y. Lin, J.-P. Zhang, and X.-M. Chen, *Angew. Chem., Int. Ed.*, 2006, **45**, 1557.

137. K. S. Park, Z. Ni, A. P. Côté, J. Y. Choi, R. Huang, F. J. Uribe-Romo, H. K. Chae, M. O'Keeffe, and O. M. Yaghi, *Proc. Natl. Acad. Sci. U.S.A.*, 2006, **103**, 10186.

138. H. Hayashi, A. P. Côté, H. Furukawa, M. O'Keeffe, and O. M. Yaghi, *Nature Mater.*, 2007, **6**, 501.

139. W. Morris, C. J. Doonan, H. Furukawa, R. Banerjee, and O. M. Yaghi, *J. Am. Chem. Soc.*, 2008, **130**, 12626.

140. M. J. C. Ordonez, K. J. Balkus, J. P. Ferraris, and I. H. Musselman, *J. Membrane Sci.*, 2010, **361**, 28.

141. J. A. Thompson, K. W. Chapman, W. J. Koros, C. W. Jones, and S. Nair, *Microporous Mesoporous Mater.*, 2012, **158**, 292.

142. Q. Song, S. K. Nataraj, M. V. Roussenova, J. C. Tan, D. J. Hughes, W. Li, P. Bourgoin, M. A. Alam, A. K. Cheetham, S. A. Al-Muhtaseb, and E. Sivaniah, *Energy Environ. Sci.*, 2012, **5**, 8359.

143. K. Diaz, L. Garrido, M. Lopez-Gonzalez, L. F. del Castillo, and E. Riande, *Macromolecules*, 2010, **43**, 316.

144. Y. Dai, J. R. Johnson, O. Karvan, D. S. Sholl, and W. J. Koros, *J. Membrane Sci.*, 2012, **401–402**, 76.

145. C. Zhang, Y. Dai, J. R. Johnson, O. Karvan, and W. J. Koros, *J. Membrane Sci.*, 2012, **389**, 34.

146. B. Seoane, J. M. Zamaro, C. Tellez, and J. Coronas, *RSC Adv.*, 2011, **1**, 917.

147. B. Zornoza, A. Martinez-Joaristi, P. Serra-Crespo, C. Tellez, J. Coronas, J. Gascon, and F. Kapteijn, *Chem. Commun.*, 2011, **47**, 9522.

148. F. Jeremias, V. Lozan, S. Henninger, and C. Janiak, *Dalton Trans.*, 2013, **42**, 15967.

149. A. Khutia, H. U. Rammelberg, T. Schmidt, S. Henninger, and C. Janiak, *Chem. Mater.*, 2013, **25**, 790.

150. F. Jeremias, A. Khutia, S. K. Henninger, and C. Janiak, *J. Mater. Chem.*, 2012, **22**, 10148.

151. J. Ehrenmann, S. K. Henninger, and C. Janiak, *Eur. J. Inorg. Chem.*, 2011, 471.

152. J. J. Low, A. I. Benin, P. Jakubczak, J. F. Abrahamian, S. A. Faheem, and R. R. Willis, *J. Am. Chem. Soc.*, 2009, **131**, 15834.

153. S. Aguado, J. Canivet, and D. Farrusseng, *J. Mater. Chem.*, 2011, **21**, 7582.

154. S. Aguado, C. -H. Nicolas, V. Moizan-Basle, C. Nieto, H. Amrouche, N. Bats, N. Audebrand, and D. Farrusseng, *New J. Chem.*, 2011, **35**, 41.

155. J. Gascon and F. Kapteijn, *Angew. Chem., Int. Ed.*, 2010, **49**, 1530.

156. H. Bux, F. Liang, Y. Li, J. Cravillon, M. Wiebcke, and J. Caro, *J. Am. Chem. Soc.*, 2009, **131**, 16000.

157. Y.-S. Li, F.-Y. Liang, H. Bux, A. Feldhoff, W.-S. Yang, and J. Caro, *Angew. Chem., Int. Ed.*, 2010, **49**, 548.

Electrochemical Properties of Metal-Organic Frameworks

Frédéric Jaouen and Adina Morozan

Université Montpellier II, Montpellier, France

1	Introduction	419
2	Electrochemical Response of MOFs	420
3	Electrochemical Applications of Pristine MOFs	430
4	Sacrificial MOFs for Electrochemical Applications	436
5	Conclusions	438
6	Acknowledgments	438
7	Related Articles	438
8	Abbreviations and Acronyms	439
9	References	439

1 INTRODUCTION

Metal–organic frameworks (MOFs) are crystalline microporous hybrid networks comprising coupling units (metal ions or metal–oxo units) coordinated by electron-donating multidentate organic ligands. They were first defined by Yaghi and coworkers in 1995,[1,2] following the pioneering works of Tomic[3] and Hoskins and Robson.[4,5] MOFs display the highest specific surface areas reported to date for porous materials (up to 6200 $m^2 g^{-1}$),[6,7] large internal pore volumes with well-defined and tunable pore sizes and apertures, as well as high thermal, chemical, and mechanical stability in some instances.[8] Coordination polymers (see ***Porous Coordination Polymer Nanoparticles and Macrostructures***) would be also addressed as MOFs, except for the metal-free structures that by definition cannot be included in this family.[9–11] Within the large structural variety offered by MOFs, the entire framework is always supported by coordination bonds and/or other weak cooperative interactions such as H-bonding, π–π stacking, and van der Waals interaction. Thus, an obvious advantage of MOFs over other porous solid materials with high specific surface area is the chemical versatility offered by the choice of the organic ligand. Another specificity of MOFs is their degree of mechanical flexibility, which is a consequence of the rather weak bonds forming the crystalline structure.[12] This allows a significant and often reversible deformation of the structure when subjected to various external factors such as guest molecules, temperature, or pressure.[13,14]

Comprehensive review papers have summarized the fast-paced research efforts in the field of MOF synthesis, chemistry, and structure, as well as their application in various areas.[7,14–17] The investigation of MOFs in the field of electrochemistry is quite recent but expanding, as recently reviewed.[18] The physicochemical properties provided either independently by the inorganic and organic components or *via* synergistic effects offer vast possibilities to tailor MOFs for a given application. They have already been designed for use in electrochemical devices for energy storage and conversion (supercapacitors, batteries, fuel cells, and electrolyzers), for metal-center-based electrocatalysis in general, and for ion conduction in solid-state electrolytes. The highly accessible and coordinatively unsaturated transition-metal centers present in MOFs offer a promising platform for bioinspired electrocatalysis, with potentially more active or robust catalytic sites compared to isolated coordination complexes.[19] While most MOFs are based on divalent cations (Ni^{II}, Cu^{II}, Zn^{II}) offering thereby a restricted choice of electrochemical redox activities, a number of MOFs now include trivalent cations (Fe^{III}, Al^{III}, Cr^{III}),[20,21] whereas polyoxometalate-metal–organic

Metal-Organic Framework Materials. Edited by Leonard R. MacGillivray and Charles M. Lukehart.
© 2014 John Wiley & Sons, Ltd. ISBN 978-1-119-95289-3

framework (POMOF) or metaloporphyrin MOF composites (see ***Porphyrinic Metal-Organic Frameworks***) enable one to include the redox pairs of high-valence metal ions (Mo, W, V) and also to dissociate structural metal nodes from catalytic metal nodes.[22] The latter approach is advantageous from a robustness viewpoint.

Electrochemical phenomena, in a broad sense, involve charge transfer in electrolytes. One can distinguish between electrodics focused on the electron transfer across the electrode–electrolyte interface and ionics concerning the transport of ions in electrolytes in the presence of an electric field.[23] In general, MOFs display poor electron conductivity that would a priori exclude them from being used as electrode materials or electrocatalysts. However, coupled ion/electron transfer within the MOF may sometimes overcome this limitation,[24,25] at least for applications where the required current densities are moderate. Electrons can be conducted in MOFs via a hopping mechanism between redox centers. Either the metal centers[22,26] or the ligands[27,28] may provide the redox processes required for such a conduction mechanism. Thus, the direct synthesis or postsynthetic modification[29] of redox-active MOFs is of special interest (see ***Postsynthetic Modification of Metal-Organic Frameworks***), as it could lead to enhanced electronic conductivity.[30,31] In a nutshell, combined porosity, fully accessible embedded redox centers, and non-negligible electronic conductivity brighten the possible application of MOFs as electrode materials for rechargeable batteries[32,33] or as electrocatalysts.[34–36] Moreover, if supported on a electron-conductive support, MOF particles with electron conductivities larger than *ca*. 10^{-6} to 10^{-5} S m^{-1} are not expected to result in significant Ohmic losses in most operating electrochemical devices, whereas conductivities typically larger than *ca*. 10^{-3} to 10^{-2} S m^{-1} are necessary for the high volumetric current densities produced in fuel cells.[18] The electronic conductivity of MOFs spans from 10^{-12} to 10^{4} S m^{-1}, but most MOFs have conductivities close to or above the minima stated above.[37]

Herein, the electrochemical properties of MOFs are reviewed, including their redox behaviors and their properties for electrocatalysis, charge storage as well as ion conduction. In parallel to the investigation of pristine MOFs, novel nanomaterials derived from MOFs have shown appropriate properties for various electrochemical applications. In this second approach, MOFs are merely utilized as chemical precursors for the synthesis of, for example, novel metal, metal oxide,[38–41] or carbon nanostructures.[42–46] This review briefly summarizes this second aspect and provides appropriate references.

2 ELECTROCHEMICAL RESPONSE OF MOFS

When considered as a metal-cation porous host, MOFs are subject to electrochemical oxidation or reduction, which can be electrochemically reversible or irreversible depending on the kinetics of the electron transfer. Moreover, application of an electric potential above certain limits may result in unstable responses if the metal-ion/ligand coordination is broken or if the 2D or 3D structure is irreversibly modified. In contrast to the case of free metal cations diffusing toward and reacting at an electrode surface, a reductive or oxidative event in the bulk of a MOF does not require the diffusion of metal cations but obviously requires electron transport and may also be accompanied by ionic transport for the conservation of electroneutrality.[24,25] As mentioned in the introduction, the electronic conductivity in a given MOF is controlled by the metal-cation nature and by its coordination chemistry. This is due to the electron-hopping mechanism from one metal-ion center to the next. The internal ionic conductivity of MOFs is also controlled by ligand-ion interactions and hydrophilicity and also by additional factors, such as ligand acido-basic properties, MOF functionalization, and MOF-guest molecule interactions when conductivity is promoted by a second phase.[47–50] In the following sections, the electrochemical behavior of various MOFs is perused from the perspectives of ionic transport and redox response.

2.1 Ion-Size Effects

Owing to the well-defined pore network and narrow pore apertures in MOFs, size exclusion or diffusion effects of counter ions are expected to play an important role in the electrochemical response of MOFs. The nature of the ions present in the electrolyte has been shown to affect the electrochemical response of MOFs. This is first illustrated for the reduction of a Cu-MOF and a Zn-MOF in contact with different anion/cation couples in acetonitrile (MeCN).[24,25] These two MOFs were synthesized from terephtalic acid and copper or zinc salts. As shown in Figure 1(a) for the Cu-MOF, only poorly defined cathodic waves were visible in Bu_4NPF_6/MeCN (curve A).[24] In contrast, in Et_4NClO_4/MeCN and especially $LiClO_4$/MeCN, two well-defined reduction steps were recorded at +0.05 V and −0.65 V versus Ag/AgCl (curves B and C, respectively). By comparison, the standard redox potentials given versus Ag/AgCl for copper are E^0 (Cu^{II}/Cu^0) = +0.13 V, E^0 (Cu^{II}/Cu^{I}) = −0.06 V, and E^0 (Cu^{+I}/Cu^0) = +0.31 V.

Moreover, in the case of the $LiClO_4$/MeCN electrolyte, a prominent third reduction peak around −1.75 V versus Ag/AgCl appeared, corresponding to the bulk reduction of the Cu-MOF to Cu^0. The propagation of the redox reaction inside the Cu-MOF with the reduction of Cu^{II} centers into Cu^{I} or Cu^0 must be accompanied by the transport of the supporting-electrolyte cations into the solid microporous lattice. The electrochemical response was obviously related to the cation size, which is in the order $Bu_4N^+ > Et_4N^+ > Li^+$. Expectedly, the smallest cation resulted in the most intense electrochemical

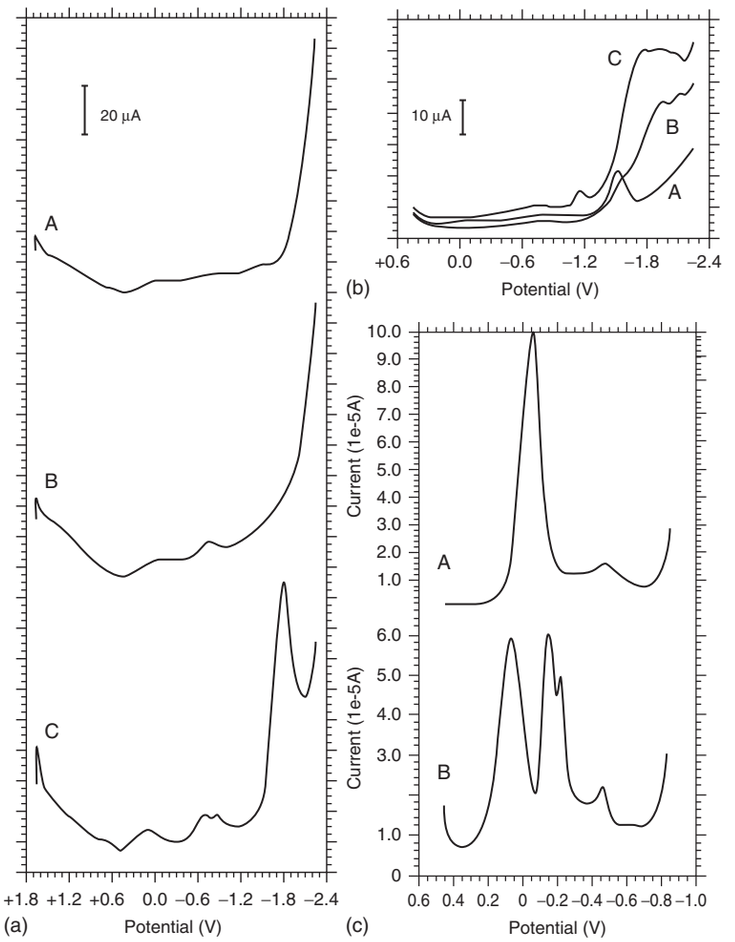


Figure 1 Effect of the nature of the electrolyte on the electrochemical response of a Cu-MOF and Zn-MOF based on terephtalic acid. (The potential-step increment was 4 mV and square-wave amplitude 25 mV. Potentials are given versus Ag/AgCl.) (a) Square-wave voltammetry (frequency 5 Hz) of the Cu-MOF in: (A) 0.1 M Bu_4NPF_6/MeCN, (B) 0.1 M Et_4NClO_4/MeCN, and (C) 0.1 M $LiClO_4$/MeCN (Reproduced from Ref. 24. © Elsevier, 2006.) (b) Square-wave voltammetry (frequency 5 Hz) of the Zn-MOF in: (A) 0.1 M Bu_4NPF_6/MeCN, (B) 0.1 M Et_4NClO_4/MeCN, and (C) 0.1 M $LiClO_4$/MeCN. (Reprinted with permission from Ref. 25. Copyright (2007) American Chemical Society.) (c) Square-wave voltammetry (frequency 2 Hz) of the Cu-MOF in: (A) 0.5 M acetate buffer and (B) 0.5 M acetate buffer + 0.05 M NaCl. Potential scan initiated at +0.45 V in the negative direction. (Reprinted with permission from Ref. 25. Copyright (2007) American Chemical Society.)

response, Figure 1(a). A similar cation-size dependency was established from the voltammetric response of the parent Zn-MOF.[25] As shown in Figure 1(b) for the Zn-MOF in Bu_4NPF_6/MeCN electrolyte, an isolated and least intense peak is seen at −1.53 V versus Ag/AgCl. In contrast, in Et_4NClO_4/MeCN or $LiClO_4$/MeCN electrolytes, more intense reduction peaks were observed from −1.8 to −2.15 V. Another example of cation-size effect was reported for the Cu^{II}-based MOF $[Cu_3(btc)_2]$ (also known as HKUST-1 or MOF-199), for which the reduction of Cu^{II} to Cu^{I} was more facile and started at a higher potential in 0.1 M LiCl than in 0.1 M KCl aqueous electrolytes (Figure 6 in Ref. 51), in agreement with the smaller ionic radius of Li^+.

In aqueous electrolyte, and for an oxidation reaction (cations diffusing out of the MOFs), the cation-size effect was different. The terephtalic-acid-based Cu-MOF investigated in 0.1 M $LiNO_3$, $NaNO_3$, or KNO_3 electrolytes showed similar cyclic voltammograms (CVs) with two reduction waves at −0.065 and −0.2 V versus Ag/AgCl, followed by an intense and well-defined oxidation peak at +0.1 V in the reverse scan (Figure 5 in Ref. 25). However, the latter had the lowest intensity in 0.1 M $LiNO_3$ and the highest intensity in 0.1 M KNO_3. Thus, the intensity of this oxidation peak increased with increasing ionic radius of the cations ($K^+ > Na^+ > Li^+$). Such a counter-intuitive effect is also discussed for Prussian blue (PB) in Section 3.1. In aqueous electrolyte as well, the effect of

the addition of chloride anions was investigated for the same Cu-MOF. A single reduction peak was observed at −0.05 V versus Ag/AgCl in 0.5 M acetate buffer (Figure 1c, curve A), whereas two separate reduction peaks at +0.05 and −0.15 V were observed in 0.5 M acetate buffer + 0.05 M NaCl (Figure 1c, curve B). These reduction peaks are ascribed to the single-electron reduction of Cu^{II}.

Next, the role of the supporting-electrolyte's anion on the voltammetric response of MOFs was reported for the commercially available Fe^{III}–btc MOF (Basolite™ F300 from BASF).[52] The intensity of the Fe^{III}/Fe^{II} redox peak was *ca.* twice stronger in 0.1 M HCl than in 0.1 M HNO_3 aqueous electrolytes (Figure 3A in Ref. 52). Yet another example of anion-size effect was reported for two dithiolene-based MOFs, $Cu[Ni(pdt)_2]$ and $Cu[Cu(pdt)_2]$.[31] The voltammetric response in MeCN was more intense and better defined with the small anion Br^- than with PF_6^- (Figure 2). The difference is major for $Cu[Cu(pdt)_2]$ (Figure 2c and d). When comparing these two MOFs in Bu_4NBr, the current was *ca.* 20 times larger with $Cu[Ni(pdt)_2]$ than with $Cu[Cu(pdt)_2]$. The authors explained this on the basis of particle size, only 150 nm for the former MOF but 2–3 μm for the latter. This suggests that anion diffusion and/or electron conduction within the MOF limited the electrochemical reaction to the outer shell in the larger $Cu[Cu(pdt)_2]$-MOF particles.

The electrochemical processes occurring during the oxidoreduction of metal centers were modeled and compared to experimental data.[25] Charge conservation requires the ingress of cations in the microporous solid during the reduction of Cu^{II} (equation 1), where M^+ is the electrolyte's cation:

$$[Cu^{II}R]_n + nM^+ + ne^- \rightarrow [Cu^{I}(M^+)R]_n \qquad (1)$$

The authors analyzed chronoamperometric data on the basis of models developed for coupled cation and electron transfer from the particle/electrode/electrolyte interface and into the body of the MOF. The electron transport was assumed to take place via a series of Faradaic reactions involving immobile redox centers. The chronoamperometric curves recorded at the mild reductive potential of −250 mV could be fitted with this model. Values of diffusion coefficients of $D(e^-) = 2{\cdot}10^{-11}$ cm^2 s^{-1}; $D(Li^+) = 1.4{\cdot}10^{-7}$ cm^2 s^{-1}; $D(Na^+) = 4.4{\cdot}10^{-8}$ cm^2 s^{-1}; and $D(K^+) = 4.1{\cdot}10^{-8}$ cm^2 s^{-1} were estimated. These diffusion coefficients are close to those reported for the same cations in microporous zeolites.

In conclusion, MOFs obviously show electrochemical response but the latter is strongly influenced by the coupling between the electrolyte nature and the MOF porous network scaffold due to size exclusion, confinement, or charge conservation effects. The requirements for the electrochemical accessibility of metal centers include (i) electron and (ii) ion transport necessary for electroneutrality. Moreover, solvated ions present sizes that are commensurate with the smallest apertures found in microporous MOFs. The choice of the MOF structure and electrolyte nature must therefore be carefully reflected.

2.2 Reversibility of the Redox Response of MOFs or MOF Composites

In this section, pure MOF systems as well as composites comprising MOF-encapsulated redox-active materials or interpenetrated networks are considered (see ***Interpenetration and Entanglement in Coordination Polymers*** and ***Patterning Techniques for Metal-Organic Frameworks***). The reversibility and stability of their electrochemical response are discussed. Stability may be defined as a retained electrochemical response on repeated cycling, whereas electrochemical reversibility is linked to the concept of fast electron transfer at the

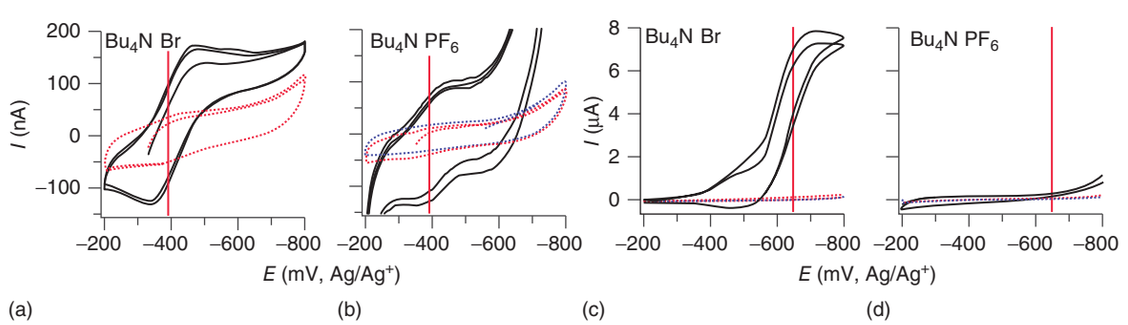


Figure 2 Anion-size effect on the cyclic voltammograms of: (a, b) $Cu[Ni(pdt)_2]$ and (c, d) $Cu[Cu(pdt)_2]$. (The electrolytes are 0.1 M Bu_4NBr or Bu_4NPF_6 in MeCN. Scan rate is 10 mV s^{-1}. The dotted blue line corresponds to the bare Pt disk electrode whereas the red dotted line corresponds to the Pt electrode after polishing off the deposited MOF. The red vertical lines indicate the position of $E_{1/2}$ for the $[Ni(pdt)_2]^{2-/1-}$ redox couple in (A, B) and for $[Cu(pdt)_2]^{2-/1-}$ redox couple in (C, D)). (Reproduced with permission from Ref. 31. Copyright (2010) American Chemical Society.)

Table 1 Theoretical characteristics for the cyclic voltammograms of various redox systems

$i = f(E)$	$\Delta E_p = E_{p,a} - E_{p,c}$ (mV)	Peak current (i_p)	$i_{p,a}/i_{p,c}$	FWHM (mV)
1. Nernstian system	$=59/n$	$\propto v^{1/2}$	—	$>113/n$
2. Quasi-reversible system	$>59/n$	$\propto v^{1/2}$	—	—
3. Irreversible system	$>59/n$; each E_p value shifts by $30/\alpha$ per decade of v and by $60/\alpha$ per decade of k^0	$\propto v^{1/2}$	—	$>95.4/\alpha$
4. Nernstian system with surface-confined species[(a)]	$=0$	$\propto v$	1	$=90.6/n$
5. Quasi-reversible system with surface-confined species	$\neq 0$	$\propto v$	1	—
6. Irreversible system with surface-confined species[(a)]	$\neq 0$	$\propto v$	1	$=62.5/\alpha$

[(a)] Assuming a Langmuir isotherm.

electrolyte/electrode interface. In order to classify the various electrochemical responses reported in the literature, the most important theoretical results regarding the cyclic voltammetry of reversible, quasi-reversible, and irreversible electrochemical systems are summarized in Table 1.[23]

For a Nernstian reversible system where n is the number of electrons exchanged in the redox reaction, the difference between the potential corresponding to the peak of anodic current ($E_{p,a}$) and that corresponding to the peak of cathodic current ($E_{p,c}$) is $59/n$ (in millivolt). It is scan-rate-independent. The reactive species are located in the electrolyte and diffuse toward the electrode in order to react. This defines a square root dependence of the peak current on the scan rate, v, which is characteristic for a diffusion control. Quasi-reversible systems are defined as systems where the charge transfer is sufficiently fast so that the electrode is only slightly polarized and both the oxidation and reduction reactions must still be taken into account. The response is found in-between that of a reversible and a totally irreversible system, depending on the exact value of the standard rate constant k^0 of the reaction. For totally irreversible electrochemical systems (slow charge transfer), the peak-to-peak distance (ΔE_p) increases with increased scan rate and also increases with decreased value of the kinetic constant k^0 describing the redox reaction. As an example, the value of $E_{p,c}$ decreases by $30/\alpha$ for a one-decade increase of v, and decreases by $60/\alpha$ for a one-decade decrease in k^0 (where α is the charge transfer coefficient). The value for the peak current is still proportional to the square root of v, due to the diffusion-controlled reaction rate when the electrode is sufficiently polarized to drive the reactions.

In the case of strongly adsorbed or covalently attached redox species, the latter do not need to diffuse in the electrolyte before reacting at the electrode or electroactive surface of materials. The current is now proportional to the scan rate, v, independently of the reversible or irreversible nature of the redox reaction. Moreover, the electric charge below the peak corresponds to the amount of species adsorbed or fixed on the electrode; hence, the ratio $i_{p,a}/i_{p,c}$ is equal to one. This surface-confined hypothesis is likely to match the case of redox species found in many MOFs, unless the electron transfer through the MOFs is very slow. If the electrons must diffuse or be conducted in a complex way to the immobile redox species, the case becomes equivalent to that of redox species diffusing toward an electrode. In the case of surface-confined species for a Nernstian redox system, there is no shift in potential between $E_{p,a}$ and $E_{p,c}$ while the full-width-at-half-maximum (FWHM) of either the cathodic or anodic wave is equal to $90.6/n$. Strong interactions may however increase this theoretical value.[23] Last, surface-confined species defining an irreversible redox system result in a peak current being still proportional to the scan rate, but the peak potentials are now far from the formal redox potential, due to the slow kinetics. The shapes of the oxidation or reduction wave become also highly asymmetric around the peak. The FWHM value for the reduction wave is related to the cathodic charge transfer coefficient, α (and vice versa for the anodic wave).

Reported redox equilibria in MOF or MOF-composite materials are now reviewed. The reversibility or irreversibility of these different redox couples is summarized in Table 2.

2.2.1 Ferrocene

The ferrocene (Fc) redox couple has a theoretical standard potential E^0 (Fc^+/Fc) = 0.5 V versus SCE (saturated calomel electrode). A quasi-reversible electrochemical response with a peak-to-peak separation of *ca.* 0.06 V was reported by Fischer and coworkers after immobilization and trapping of ferrocene species (1,1′-ferrocenediyl-dimethylsilane) inside the channels of an Al-based MOF [Al(OH)(bdc)].[57] The $E_{1/2}$ value [$E_{1/2} = (E_{p,a} + E_{p,c})/2$] was +0.24 V versus SCE (compared to +0.18 V versus SCE for the pure ferrocene species) and the current waves were very broad and had low intensity. Later, Zn^{II} and Al^{III} dicarboxylate-based frameworks were postsynthetically functionalized with covalently attached

Table 2 Reversibility (or not) of redox reactions for various MOFs in various electrolytes

MOF	Redox pair, *n*	Electrolyte	Scan rate ($mV\ s^{-1}$)	$E_{1/2}$ (mV vs SCE)	ΔE_p (mV)	Reversible? Diffusion?	References
Fc-functionalized $[Zn_4O(bdc\text{-}H_2)(btb)_{4/3}]$	Fc^+/Fc, 1	0.1 M NBu_4PF_6 in dichloroethane	10–100	+680	100	QR DL & SC	29
Fc-functionalized $[Al(OH)(bdc\text{-}NH_2)]$	Fc^+/Fc, 1	0.1 M NBu_4PF_6 in dichloroethane	10–100	+680	100–120	QR DL	29
Fe(btc)	Fe^{III}/Fe^{II}, 1	pH < 1 0.1–0.5 M HCl	50	+480	70–90	R DL	52
$Cu_3(btc)_2$	Cu^{II}/Cu^{I}, 1	pH 6, 0.1 M phosphate buffer	50	−140	180	I SC?	35
Cu-bipy-btc	Cu^{II}/Cu^{I}, 1	pH 6, 0.1 M phosphate buffer	20	−190	115	I SC?	35
MIL-101(Cr)	Cr^{III}/Cr^{II}, 1	pH 2.2 aqueous H_2SO_4 solution	10–750	+256	16	R SC	53
$[Ni_2(bimb)_2(Mo^{VI}{}_4Mo^{V}{}_2O_{19})]$	Mo^{VI}/Mo^{V}	1 M H_2SO_4	30–50	+436 +163	60 60	QR SC	54
Z-POMOF1 (ε-type Keggin $Mo_{12}O_{40}$)	Mo^{VI}/Mo^{V}, 2 Mo^{VI}/Mo^{V}, 2 Mo^{VI}/Mo^{V}, 2	pH 2 (1 M LiCl + HCl)	10–200	+180 +26 −151	20 43 43	QR SC	22
PW_{11}@MIL-101(Cr)	W^{VI}/W^{V}	pH 2.2 aqueous H_2SO_4 solution	X-200	−518 −734	100 100	QR DL	53
$Co_2(bpy)_3(ox)(As_2W_{18}O_{62})\cdot 2(H_2bpy)$	W^{VI}/W^{V} W^{VI}/W^{V} W^{VI}/W^{V}	1 M H_2SO_4	80–500	−550 −280 −50	240 200 200	I SC	55
$[Ag(bipy)]_2[Ag(bipy)(H\text{-}bipy)][P_2W_{18}O_{62}][H_2bipy]$	W^{VI}/W^{V} W^{VI}/W^{V} W^{VI}/W^{V}	1 M H_2SO_4	50	−390 −244 −135	100 100 100	I DL	56

R, reversible; QR, quasi-reversible; I, irreversible; DL, diffusion limited; SC, surface confined.

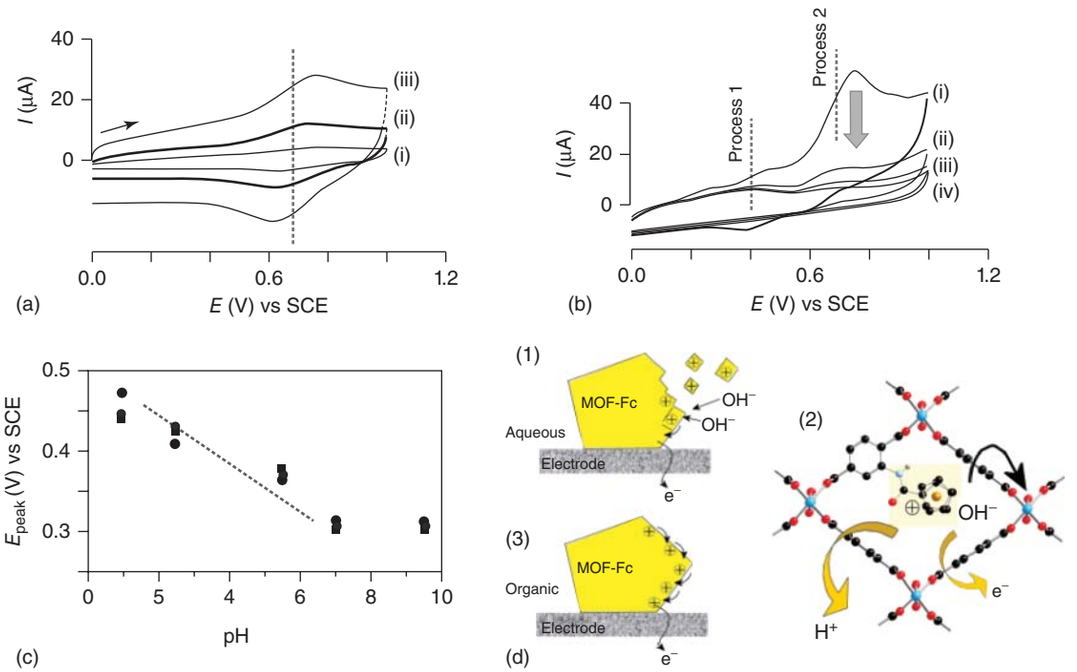


Figure 3 Electrochemical response of the ferrocene-functionalized $[Zn_4O(bdc\text{-}NH_2)(btb)_{4/3}]$ MOF. (a) Cyclic voltammograms for the ferrocene-functionalized MOF immobilized on pyrolytic graphite (electrolyte: dichloroethane with 0.1 M NBu_4PF_6; scan rates: (i) 10, (ii) 35, and (iii) 100 mV s^{-1}). (b) Cyclic voltammograms of the ferrocene-functionalized MOF immobilized on pyrolytic graphite (electrolyte: aqueous 0.1 M phosphate buffer pH 1; scan rate 20 mV s^{-1}; the first four scans are shown). (c) Plot of the peak potential for process 1 versus pH (scans i–iii). The dashed line corresponds to 30 mV pH^{-1}. (d) (1) Schematic description of the ferrocene-functionalized MOF reactivity in aqueous electrolyte; (2) drawing of the pore redox process involving: removal of one electron, fast expulsion of one proton, and hydroxide attack; (3) schematic description of the ferrocene-functionalized MOF reactivity in organic electrolyte. (Reproduced by permission of The Royal Society of Chemistry, Ref. 29.)

ferrocene redox groups through an amine to amide functional group interconversion.[29] The investigated MOFs were $[Zn_4O(bdc\text{-}NH_2)(btb)_{4/3}]$ (UMCM-1-NH_2) and $[Al(OH)(bdc\text{-}NH_2)]$ (MIL-53-NH_2). The pores were functionalized throughout the MOF structure. Similar voltammetric responses were observed for both MOFs and are exemplified in Figure 3 for the Zn^{II}-based MOF.

In organic electrolyte (Figure 3a), a well-defined and stable redox process was observed and assigned to the oxidation and reduction of ferrocene groups immobilized on the surface of MOF particles. The position of the oxidation and reduction peaks was independent of the scan rate, indicative of fast electron transfer. However, the value of *ca.* 100 mV for ΔE_p indicates (Table 1) that at least one of the species involved in the redox reaction is not attached to the surface. The peak current for the oxidation of ferrocene in $[Zn_4O(bdc\text{-}NH_2)(btb)_{4/3}]$ was indeed found to be proportional to $v^{0.78}$, which is a result in-between the theoretical predictions for diffusion-limited ($v^{1/2}$) and surface-confined reaction (v). For ferrocene in $Al(OH)(bdc\text{-}NH_2)$, the exponent value of 0.56 was found, in agreement with the theoretical value of 1/2 expected for a diffusion-limited process.

In aqueous electrolyte, two distinct processes are observed (Figure 3b). Process 1 was assigned to near-surface immobilized ferrocene groups whereas process 2 occurred at higher potential and exhibited a rapid decay on cycling. The larger magnitude of the initial charge below this second peak probably reflects a bulk phenomenon associated with an irreversible chemical modification of the functionalized MOF framework. As shown in Figure 3c, ferrocene oxidoreduction during process 1 shows a shift of *ca.* 30 mV pH^{-1}. This implies the involvement of less than one proton per transferred electron. The same pH dependency was observed for the redox peak of process 2. The expulsion of protons following ferrocene oxidation results in the formation of hydroxyl groups in the pores. These resulting hydroxyl ions are thought to considerably weaken the framework, resulting in the electrochemically driven MOF disintegration in aqueous electrolyte (decay of process 2, see Figure 3d).

2.2.2 *Iron*

The standard potential of the noncomplexed ferri-ferro redox pair is $E^0(Fe^{III}/Fe^{II}) = +0.53$ V versus SCE.

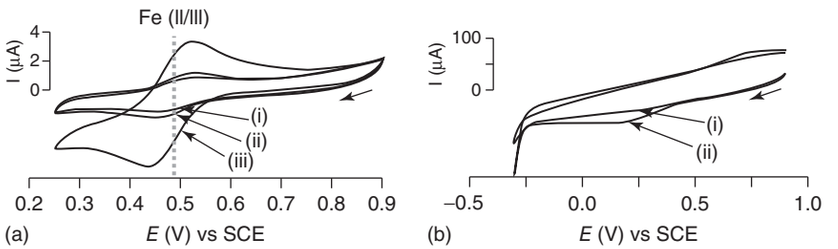


Figure 4 Cyclic voltammograms of Fe^{III}–btc in acid medium on two different substrates: (a) platinum disk in aqueous HCl solution at concentrations of (i) 0.1, (ii) 0.2, and (iii) 0.5 M; (b) basal plane pyrolytic graphite, (i) without and (ii) with Fe^{III}–btc (scan rate 50 mV s^{-1}). (Reproduced from Ref. 52. © Elsevier, 2010.)

The commercial Fe^{III}–btc MOF (Basolite F300) was investigated in acid medium.[52] While no redox features were observed in 0.1 M KCl, a well-defined redox pair was observed for Fe^{III}–btc deposited on platinum in 0.1 M HCl (Figure 4a). The $E_{1/2}$ value was +0.48 V versus SCE and found independent of the acid concentration, that is, the protons are not involved in the redox process. The latter information, combined with a ΔE_p value of *ca.* 60 mV, suggests that the redox process is not surface-confined and corresponds in fact to a dissolution plus redox reaction of free Fe cations. When deposited on pyrolytic graphite, only a very weak signal was detected (Figure 4b). The redox behavior of iron cations present in PB and Prussian blue analogs (PBA) are discussed in the context of rechargeable batteries (Section 3.1).

2.2.3 Copper

The Cu^{II}–btc MOF (also labeled MOF-199, HKUST-1, or Basolite C300) belongs to the most iconic MOFs and has been extensively studied.[58] Cyclic voltammetry of Cu^{II}–btc MOF immobilized onto carbon in 0.1 M KCl showed two redox peaks.[59] The charge below these peaks are however highly asymmetric between oxidation and reduction, and irreversible oxidation of the MOF framework may be at play. The authors assigned the peaks at −0.14 and +0.02 V versus SCE to the redox reaction Cu^{II}/Cu^{I}. This is in line with the standard potential E^0 (Cu^{II}/Cu^{I}) of −0.08 V versus SCE. The second pair of peak currents with positions of −0.45 and −0.102 V versus SCE was assigned to the redox reaction Cu^{I}/Cu^{0}. This assignment seems to be incorrect at least for the oxidation peak, with respect to the nonmatching standard potential for this redox couple, E^0 (Cu^{+I}/Cu^{0}) = +0.28 V versus SCE.

In contrast to the previous study, only one redox pair was observed for Cu^{II}–btc MOF in N_2-saturated 0.1 M phosphate buffer (Figure 5d).[35] The coordination chemistry, X-ray diffraction pattern (XRD), and scanning electron microscope (SEM) image of the as-synthesized MOF are shown in Figure 5(a–c). Each copper atom is coordinated to four oxygen atoms of carboxylate groups, whereas each btc ligand holds three dimeric Cu paddle wheel, to form a 3D structure. The $E_{1/2}$ value was *ca.* −0.15 V versus SCE and could be assigned to the Cu^{II}/Cu^{I} equilibrium. The peak separation ΔE_p was *ca.* 180 mV, indicative of irreversible electron transfer (Table 2).

Recently, Szanyi *et al.*[60] reported the coexistence of mixed-valence states for Cu in the same commercial MOF-199. After annealing in vacuum at 200 °C, the Cu^{II}–btc MOF showed the coexistence of Cu^{I} and Cu^{II} oxidation states, as evidenced by CO and NO selective molecular probes, respectively. The highest concentration of Cu^{I} sites was found after annealing at 200 °C in vacuum, whereas annealing under reductive atmosphere (CO or H_2) surprisingly resulted in a twofold decrease in the concentration of the Cu^{I} sites.

For a Cu-terephtalic acid MOF, cyclic voltammetry in aqueous solution at pH 4.85 resulted in two overlapping cathodic waves at −0.25 and −0.50 V versus SCE and a single oxidation peak at +0.33 V versus SCE.[25] The latter was associated with the oxidation of copper metal formed at low potential ($E < -0.35$ V vs SCE) and disappeared when the lower potential boundary was restricted to −0.25 V versus SCE. Square-wave voltammetry resulted in a better resolution of the various cathodic peaks, with three resolved peaks at −0.14, −0.17, and −0.20 V versus SCE.

For the MOF $[Cu_2(bpdc)_2(dpq)_2(H_2O)]\cdot H_2O$ obtained from the hydrothermal reaction of copper chloride with the mixed ligands bpdc and dpq, the redox couple observed at −100/+50 mV versus SCE in pH 2 (phosphate buffer) was attributed to Cu^{II}/Cu^{I}.[26] The charge below the reduction peak was much larger than that below the oxidation peak, possibly due to the instability of the reduced form of copper, which may undergo a fast chemical oxidation in an aqueous solution of pH 2.

2.2.4 Chromium

The first electrochemical study in acidic medium of the 3D porous Cr^{III}-terephthalate MOF (MIL-101) discovered by Férey and coworkers[21] was recently completed and

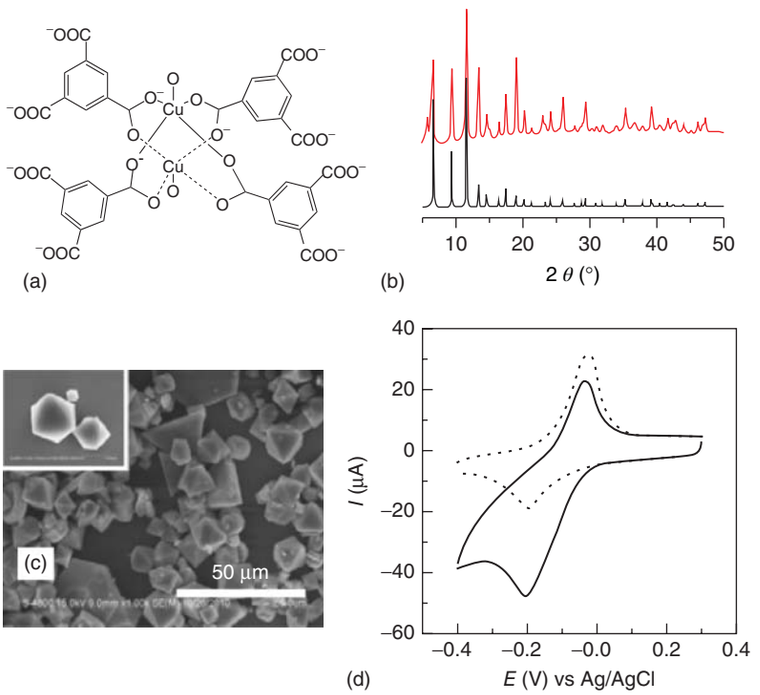


Figure 5 Characterization of Cu^{II}–btc MOF and its electrochemical properties: (a) coordination of Cu atoms; (b) XRD pattern of as-prepared Cu^{II}–btc (red curve) and simulated one (black curve); (c) SEM image of Cu^{II}–btc; (d) cyclic voltammogram of Cu^{II}–btc on glassy carbon in 0.1 M phosphate buffer (pH 6.0) saturated with N_2 (dotted line) or O_2 (solid line), scan rate 50 mV s^{-1}. (Reproduced from Ref. 35. © Elsevier, 2012.)

the reversible surface-controlled redox signal with a peak potential at 0.496 V versus SHE (standard hydrogen electrode) was attributed to the redox equilibrium Cr^{III}/Cr^{II} of the chromium nodes.[53] As illustrated in Figure 6a, the cathodic peak is not observed in the first scan (gray line) but only starting from the second cycle. Both the reduction and oxidation peaks are observed on subsequent cycles, with increased intensity until they stabilized, indicating that reorganization and/or wetting of the MOF layer was necessary. As an indication of the reversibility of the redox process, the cathodic and anodic peak potentials remained constant for scan rates ranging from 10 to 750 mV s^{-1}, with $\Delta E_p = 16 \pm 5$ mV. The cathodic and anodic peak current intensities increased linearly with scan rate, as expected for a surface-confined reversible redox reaction (Table 1). The number of electrons exchanged in the redox process was

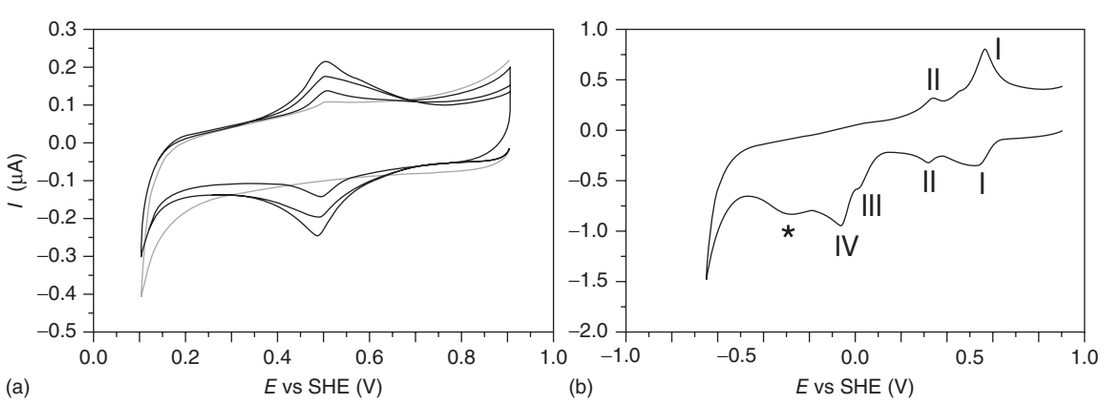


Figure 6 Cyclic voltammograms of MIL-101 immobilized on pyrolytic graphite: (a) in the range +0.1 to +0.9 V versus SHE; (b) in the range −0.65 to +0.9 V versus SHE (electrolyte: H_2SO_4 aqueous solution pH 2.2, scan rate: 100 mV s^{-1}). (Reproduced from Ref. 53. © Elsevier, 2013.)

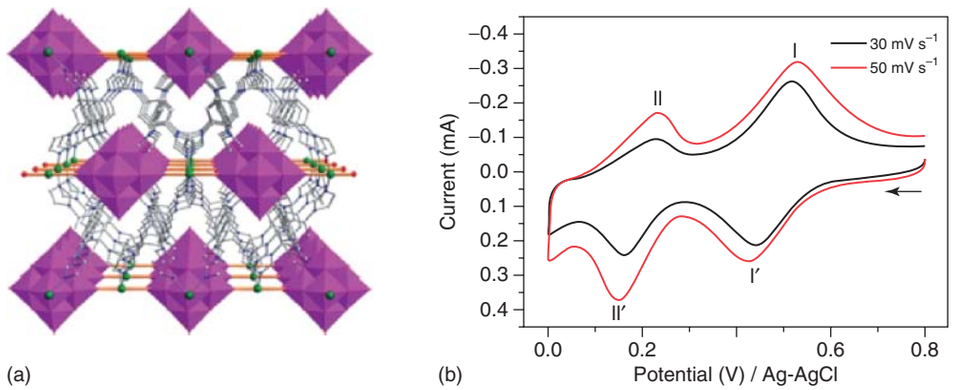


Figure 7 Structure and cyclic voltammetry of the POMOF $[Ni_2(bimb)_2(Mo^{VI}{}_4Mo^{V}{}_2O_{19})]$: (a) three-dimensional framework along the *b* axis (pink polyhedra = $[Mo_6O_{19}]^{4-}$ polyoxoanions, green dots = Ni^{2+}); (b) cyclic voltammograms of the POMOF carbon paste electrode in 1 M H_2SO_4 at different scan rates. (Reproduced from Ref. 54 with permission of The Royal Society of Chemistry. DOI: 10.1039/C0CE00259C.)

found to be one, on the basis of the FWHM of the peak (Table 1). One additional redox pair as well as two cathodic waves were detected when the potential was scanned down to −0.65 V versus SHE instead of +0.1 V (Figure 6b). The redox couple II features a reversible response with ΔE_p = 14 mV and $E_{1/2}$ of +0.328 V versus SHE. Signal III features an irreversible cathodic peak. These signals were assigned to lower oxidation states of chromium.

2.2.5 *Polyoxometalate (Mo, W)—MOF Composites*

These composites (labeled POMOFs) comprise polyoxometalates (POMs) linked to one another through bridging organic linkers.[61–63] Highly oxidized transition metals such as W^{VI}, Mo^{VI}, or V^{V} engaged in ionic bonds with oxygen atoms form the POM oxyanion clusters. The latter display multiple and subsequent redox equilibria, and POMs are excellent electrocatalysts for several important reactions. The electrochemical behavior of a series of four distinct POMOFs, constructed from $[Mo_6O_{18}(O_3AsPh)_2]^{4-}$ polyoxoanions and Cu^{I}-ligand MOFs [four different bis(triazole) ligands from triazolpropane triazol-hexane] were similar except for small shifts of the redox potentials.[64] As an example, the CV for $[Cu^{I}{}_4(L3)_4Mo_6O_{18}(O_3AsPh)_2]$ showed two reversible redox pairs I–I′ and II–II′ with $E_{1/2}$ values of −0.028 and +0.279 V, respectively. The redox peaks I–I′ and II–II′ might be ascribed to the As_2Mo_6 cluster. When the scan rate was varied from 20 to 200 mV s^{-1}, the peak separation ΔE_p increased, which can be explained by irreversible electron transfer. In contrast, the electron transfer is usually quasi-reversible for polyoxomolybdates not embedded in MOFs.[65–67]

A more intense and reversible redox behavior was obtained with a POMOF based on the hexamolybdate anion.[54] The $[Ni_2(bimb)_2(Mo^{VI}{}_4Mo^{V}{}_2O_{19})]$ POMOF was synthesized, in which each $(Mo^{VI}{}_4Mo^{V}{}_2O_{19})^{4-}$ anion is surrounded by four nickel cations, forming an interpenetrated network that can be considered as a combination of six-connected Ni-nodes and four-connected nodes for the $[Mo_6O_{19}]^{4-}$ anions (Figure 7a). Cyclic voltammetry of this compound in 1 M H_2SO_4 electrolyte revealed two well-resolved redox pairs assigned to Mo^{VI}/Mo^{V} with $E_{1/2}$ values of +0.436 and +0.163 V versus SCE, ΔE_p values of *ca.* 60 mV and peak currents proportional to the scan rate (Figure 7b). This redox system can thus be described as a quasi-reversible surface-confined system (Tables 1 and 2).

The CVs in Ar-purged 1 M LiCl + HCl electrolyte (pH 1) of another series of POMOFs containing POM building blocks connected by btc-linkers showed two redox waves characteristic of the reversible oxidoreduction of Mo centers.[63] The compound $(tba)_3[PMo^{V}{}_8Mo^{VI}{}_4O_{36}(OH)_4Zn_4](btc)_{4/3}\cdot 6H_2O$ (labeled $\varepsilon(trim)_{4/3}$) was analyzed, as well as two other compounds (labeled $\varepsilon_2(trim)_2$ and $[\varepsilon(trim)]_\infty$) showing different stoichiometries and topologies. The redox waves were centered at *ca.* +0.12 V versus SCE for $\varepsilon(trim)_{4/3}$ and $\varepsilon_2(trim)_2$ and −0.1 to −0.12 V versus SCE for $\varepsilon_2(trim)_2$ and $\varepsilon(trim)_{4/3}$.

Another example of POMOF involving an ε-type Keggin POM and a Zn^{II}–bdc MOF was reported by Dolbecq and coworkers.[22] The compound $(tba)_3[PMo^{V}{}_8Mo^{VI}{}_4O_{36}(OH)_4Zn_4(bdc)_2]\cdot 2H_2O$ (Z-POMOF1) was synthesized and identified as an insoluble compound. The structure consists of three interpenetrated networks, with tba as counter-cations and space-filling agents stabilizing the structure. The Keggin ions are capped by four Zn^{II} ions and three tba^+ cations for electroneutrality. The electrochemical activity of the inorganic unit was conserved in Z-POMOF1, but with clear changes

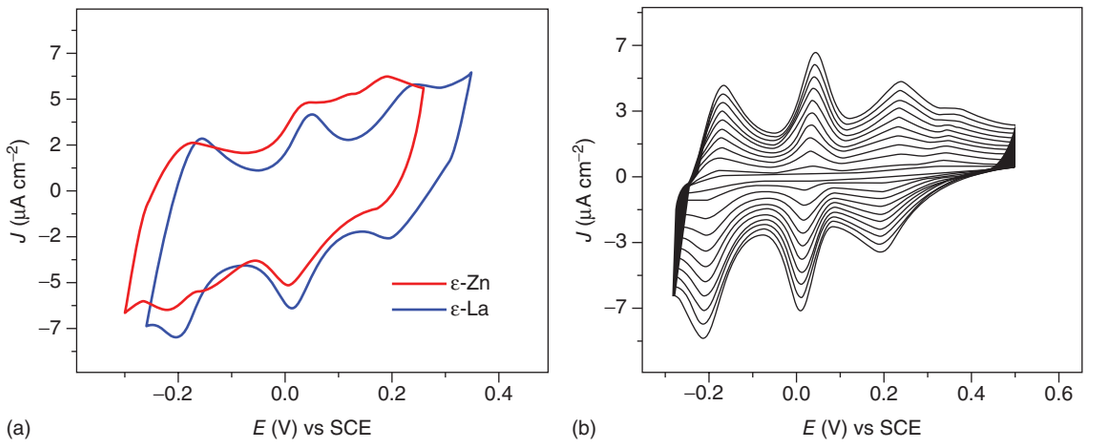


Figure 8 Electrochemical response of a Z-POMOF1 based on the ε-type Keggin POM $Mo_{12}O_{40}$ and Zn^{II}–bdc MOF: (a) comparison of the redox waves for Z-POMOF1 (ε-Zn) and the chloride salt of ε-La (no MOF) (scan rate 200 mV s^{-1}, pH 2 medium 1M LiCl/HCl, carbon paste electrode); (b) response of Z-POMOF1 for different scan rates, from 10 to 200 mV s^{-1} (pH 2 medium 1M LiCl/ HCl, carbon paste electrode). (Reproduced with permission from Ref. 22. Copyright (2009) American Chemical Society.)

compared to the chloride salt of the same inorganic unit, ε-La (Figure 8a). The latter shows three quasi-reversible redox pairs assigned to subsequent Mo^{VI}/Mo^{V} redox equilibria. Z-POMOF1 also shows three redox pairs but with a shift toward lower potential of the upper wave, as well as a splitting of the lower wave. The reversibility of the redox reactions was maintained intact in this example, with similar ΔE_p values in Z-POMOF1 and ε-La. Once the Mo^{V} centers were preoxidized, the redox peaks became more intense, and the electrochemical response to the scan rate is shown in Figure 8b. Linearity was observed between the current and scan rate, as expected for surface-confined processes.

The three redox equilibria seen in Figure 8b for the Keggin structure $Mo_{12}O_{40}$ have been described in the literature by equations (2–4):

$$PMo^{VI}{}_{12}O_{40} + 2e^- + 2H^+ \Longleftrightarrow H_2PMo^{VI}{}_{10}Mo^{V}{}_2O_{40} \quad (2)$$

$$H_2PMo^{VI}{}_{10}Mo^{V}{}_2O_{40} + 2e^- + 2H^+ \Longleftrightarrow H_4PMo^{VI}{}_8Mo^{V}{}_4O_{40} \quad (3)$$

$$H_4PMo^{VI}{}_8Mo^{V}{}_4O_{40} + 2e^- + 2H^+ \Longleftrightarrow H_6PMo^{VI}{}_6Mo^{V}{}_6O_{40} \quad (4)$$

The positions of the redox waves in Figure 8b correspond to those observed for the same POM deposited, for example, on carbon nanotubes.[67] It can be seen from equations (2–4) that POM reduction is accompanied by proton transfer, at least in electrolytes with sufficiently low pH.[68] This results in a shift of the redox equilibria of 60 mV pH^{-1}, as predicted from the Nernst equation. Since the redox reactions involve proton diffusion, the redox systems are therefore not strictly speaking surface-confined processes. However, if the proton concentration is sufficiently high, this will not be a limiting factor and the peak currents were indeed proportional to the scan rate (Suppl. Inf. of Ref. 22); that is, the systems behaved as surface-confined ones. The nonzero peak splitting observed in Figure 8b for the three redox waves thus indicates that the system was quasi-reversible (Tables 1, 2).

The electrochemical investigation of composite materials based on POMs encapsulated inside the framework MIL-101 was reported by de Sousa *et al.* in 2013.[53] MIL-101 is suited for the encapsulation of various guest materials due the large cavities available in its structure.[21] The two Keggin-type encapsulated POMs were $K_7[PW_{11}O_{39}]\cdot 10H_2O$ (PW_{11}) and $K_8[SiW_{11}O_{39}]\cdot 13H_2O$ (SiW_{11}). Their study showed that the guest POMs did not affect the electrochemical behavior of the MOF (Cr^{III}/Cr^{II} couple, see Figure 6a). Two additional redox pairs specific for the POMs appeared in the range −0.65 to 0.0 V versus SHE. In contrast to the linearity observed between peak current and scan rate for the same POMs not encapsulated in MIL-101, the peak current intensities for the POMOF composites were proportional to the square root of the scan rate. This indicates that the redox processes were controlled by diffusion.

Another POMOF based on one hand on the Wells–Dawson POM ($[As_2W_{18}O_{62}]^{6-}$) and on the other hand on a MOF synthesized from cobalt, bipyridine, and oxalate was synthesized and characterized electrochemically. In this POMOF structure, the POM was noncoordinating and simply regularly occupied the channels of the 3D MOF. Cyclic voltammetry in 1 M H_2SO_4 revealed three redox pairs assigned to the POM polyanion, with ΔE_p values of *ca.* 0.20 V in each case.[55] This

might be ascribed to irreversible redox reactions. The peak currents were proportional to the scan rate, indicating surface-confined redox centers (Table 2).

Yet another POMOF based on the Wells–Dawson POM ($[P_2W_{18}O_{62}]^{6-}$) and on the other hand on a MOF synthesized from Ag and bipy showed the three redox pairs in 1 M H_2SO_4 characteristic for the POM.[56] The peak current was proportional to the square root of the scan rate, indicating a diffusion-limited redox process.

3 ELECTROCHEMICAL APPLICATIONS OF PRISTINE MOFs

3.1 MOFs as Electrode Materials for Rechargeable Batteries and Supercapacitors

The first successful use of a MOF as a rechargeable intercalation electrode was reported by Férey *et al*.[32] Its stability relies on the strong metal–oxygen bonds obtained with Fe^{III}. The MOF $Fe^{III}(OH)_{0.8}F_{0.2}(bdc)\cdot H_2O$ (MIL-53(Fe)·H_2O) was successfully investigated as a positive electrode for a Li-ion battery. A maximum lithium uptake of 0.6 Li per Fe atom could be reached on discharge, resulting in a capacity of 75 mAh g^{-1}. It was shown that a local atomic reversible rearrangement around Fe occurred on electrochemical cycling, showing the flexible structure of this MOF. Other MOFs comprising transition-metal phosphates and oxalate-anion organic linkers have also been synthesized and investigated as cathode materials for Li-ion batteries.[69,70] These hybrid materials display a layered structure with straight channels, appropriate for fast insertion/extraction of alkali cations. A specific capacity of *ca*. 70 mAh g^{-1} was achieved at 0.4 °C rate (1 °C rate being defined as full charge or discharge in 1 h) for the compound $K_{2.5}[(V^{IV}O)_2(HPO_4)_{1.5}(PO_4)_{0.5}(C_2O_4)]$, which can be compared to the theoretical capacity of 108 mAh g^{-1} as calculated from the compound's structure (assuming the full removal of 2 K^+ ions).[69] Potassium cations were partially replaced by Li^+ during the first cycles. Cyclic voltammetry showed a redox couple with peaks at 3.83 and 4.18 V versus Li^+/Li; ascribed to the V^V/V^{IV} equilibrium.

Several MOFs have also been used in innovative ways to form Li-ion battery anodes that store Li^+ either via the intercalation or via the conversion–reaction mechanism. The group of Tarascon reported an initial specific capacity of 300 mAh g^{-1} for a Li^I-terephthalate MOF in 1 M $LiPF_6$ carbonate electrolytes.[71] Perhaps even more important, the reaction between the lithiated Li^I-terephthalate MOF and electrolyte was three times less exothermic than that for LiC_6, thereby affording a distinct safety improvement. Next, a Li^I-pyridinedicarboxylate MOF showed reversible Li extraction/insertion with a specific capacity of 160 mAh g^{-1} at a rate of C/5.[72] A first report on a MOF supporting the conversion-reaction mechanism with Lithium was published by Li *et al*.[73] The $Zn_4O(btb)_2$ MOF synthesized with different morphologies showed a large irreversible loss during the first cycle, but retained the same capacity during cycles 2–50. The gravimetric capacity was limited to 100–110 mA h g^{-1} in cycles 2–50, compared to 400 mA h g^{-1} observed during the first charge. Saravanan *et al*.[33] reported on a more successful application of formate MOFs, such as $Zn_3(HCOO)_6$, $Co_3(HCOO)_6$ and $Zn_{1.5}Co_{1.5}(HCOO)_6$, for Li-storage. The best results were obtained with $Zn_3(HCOO)_6$ (Figure 9a). After 60 cycles, the capacity of 560 mA h g^{-1} was retained (Figure 9b), corresponding to 9.6 Li atoms per repetitive unit of the MOF. The proposed conversion mechanism is described by equations (5) and (6):

$$Zn_3(HCOO)_6 + 6Li^+ + 6e^- \Longleftrightarrow 3Zn + 6HCOOLi \quad (5)$$

$$3Zn + 3Li^+ + 3e^- \Longleftrightarrow 3LiZn \quad (6)$$

The MOF reacts first with Li^+ to form Zn nanoparticles and lithium-formate MOF during the first charge, followed by LiZn alloy formation on deep charge. On the subsequent discharge, the alloy is transformed back into metal nanoparticles and then into zinc-formate MOF.

The next example of MOF application for batteries relates to the nonaqueous Li-S battery, whose positive electrode implies the reversible reduction of sulfur metal to polysulfides and eventually, Li_2S. In spite of a high theoretical capacity, this battery system needs to overcome several challenges, including solubility of intermediate polysulfide products, and the insulating character of metallic sulfur. Hence, sulfur needs to be supported on a conductive support with, ideally, a porous network designed to capture the soluble polysulfide compounds and prohibit their diffusion into the battery separator/electrolyte.[75] A chromium trimesate MOF, [MIL-100(Cr) or $Cr_3O(btc)_2X$, with X = OH or F], was investigated as a sulfur host.[74] The sulfur-impregnated MOF showed a sharp decline in capacity over the two first cycles but lower capacity fading over cycles 2–1000 as compared to mesoporous carbons as S-host (Figure 9c). The lower capacity fading could be related to the lower amount of polysulfide species released in the electrolyte. A composite MOF/carbon obtained by planetary ball-milling was necessary to overcome the insulating character of the MOF itself. The level of impregnation of the MOF by sulfur was controlled so as to leave some free space for dilatation on sulfur lithiation. Sulfur impregnation in the MOF was revealed by the change in BET surface area, with 1485 m^2 g^{-1} for the MOF and 360 m^2 g^{-1} for the MOF-S composite.

Increasing pressure on Li resources, its high cost, and uneven global distribution have raised awareness for more sustainable rechargeable battery systems.[76] Recent

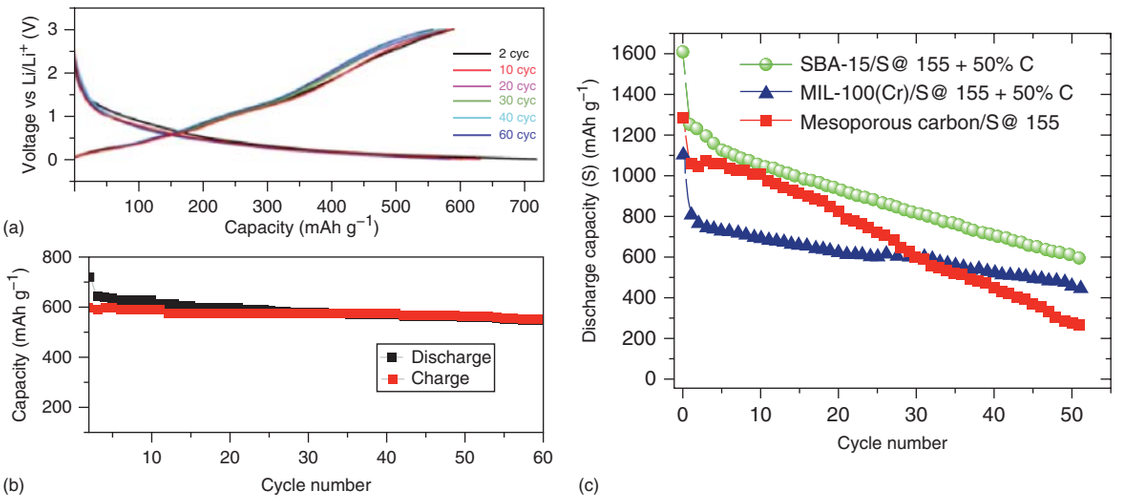


Figure 9 MOF application as negative electrode in rechargeable Li-ion (left) and positive electrode in rechargeable Li-S battery (right). Electrochemical evaluation of $Zn_3(HCOO)_6$ MOF: (a) 2nd to 60th charge–discharge cycle, (b) Capacity versus cycle number (the constant current for charge/discharge was 60 mA g^{-1}, corresponding to 0.11 °C rate, 1 °C referring to a capacity of 520 mA g^{-1} in 1 h). (Reproduced by permission of The Royal Society of Chemistry, Ref. 33). Electrochemical evaluation of MIL100(Cr)-S composite: (c). Cycling performance of the composites (MIL100(Cr)–S + 50% C; mesoporous carbon–S; mesoporous silica SBA15–S + 55% C) in 1 M Li organic electrolyte at a discharge rate of C/10. (Reproduced by permission of The American Chemical Society, Ref. 74.)

reports on Na^+ battery materials hold great promise.[77–79] The larger ionic radius of Na^+ relative to Li^+ however requires a host material with optimized pore network in order to reach appropriate mobility of the sodium ion. PB and PBA have been used as pigments starting in the early eighteenth century, well before their metal–organic nature was understood. PB, with general formula $KFe_2(CN)_6$ or $Fe_7(CN)_{18}$, consists of a cubic structure of Fe^{II} and Fe^{III} ions coordinated with C and N atoms from the cyano-groups, respectively (Figure 10).

The interstitial sites of the cubic structure allow for the fast electrochemical insertion/extraction of alkali cations.[80,81] Moreover, Fe^{II} may be replaced by other metal cations (e.g., Mn^{II}, Co^{II}, Ni^{II}, Cu^{II}, Zn^{II}), leading to a wide variety of PBA. Such materials have recently shown interesting properties as positive electrode materials for the reversible insertion/extraction of Na^+.[82–84] Alkali cation insertion is triggered by the reduction of Fe^{III} into Fe^{II} and, in PBA, by the additional reduction of the second metal.[82,83]

For PB, the mechanism may be written as in equation (7), where A is an alkali metal:

$$Fe^{III}{}_4[Fe^{II}(CN)_6]_3 + 4e^- + 4A^+ \Longleftrightarrow A_4Fe^{II}{}_4[Fe^{II}(CN)_6]_3 \quad (7)$$

This leads to a theoretical capacity of 103–109 mAh g^{-1} depending on the number of coordinating water molecules in the structure. Here, only 4/7 of the Fe atoms are redox active. For PBAs, the mechanism may in its simplest form be described as in equation (8):[80]

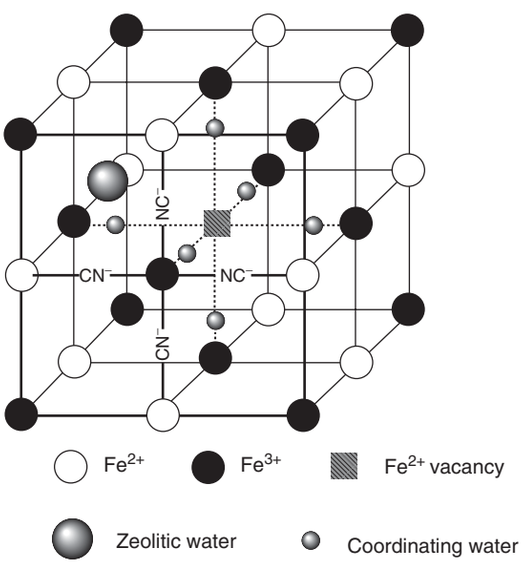


Figure 10 The ideal structure of the insoluble form of Prussian blue, $Fe_4[Fe(CN)_6]_3$. 1/4 of the Fe^{II} sites are unoccupied, for electroneutrality. (Reproduced from Ref. 80. © Elsevier, 1999.)

$$M^{III}Fe^{III}(CN)_6 + 2e^- + 2A^+ \Longleftrightarrow A_2M^{II}Fe^{II}(CN)_6 \quad (8)$$

The equivalent theoretical capacity is *ca.* 200 mAh g^{-1}. Hence, these structures are potential competitors to the state-of-the-art Li-ion cathode materials ($LiCoO_2$ and $LiFePO_4$ showing 140 and 170 mAh g^{-1} capacity,

respectively) used in rechargeable batteries designed for portable and automotive application and may also be used in batteries designed for grid-scale peak power shaving and electrochemical energy storage of renewable electricity sent to the grid. The required characteristics for the latter application are low cost, long cycle life, and capability of handling fast charge or discharge rates.

In organic electrolyte (carbonates + 1 M $NaClO_4$), a reversible capacity of 100 mAh g^{-1} at a rate of C/20 was reported for PB. Two reversible redox peaks were observed and ascribed to low-spin Fe^{II}/Fe^{III} bonded to C and high-spin Fe^{II}/Fe^{III} bonded to N. During the discharge, two plateaus were accordingly observed. In contrast, PBAs based on Mn, Co, Ni, Cu, and Zn showed a single redox peak and discharge plateau, and capacities of 45–70 mAh g^{-1}.[82] The simultaneous presence of K^+ and Na^+ alkali cations in the above study may have impacted the electrochemical capacity. A higher capacity of 135 mAh g^{-1} at a rate of 0.6 °C was reported for a Co-hexacyanoferrate (HCF) in 1 M $NaClO_4$ carbonate electrolyte.[85] Two plateaus were observed during the discharge, suggesting a two-electron mechanism. The capacity measured at an ultrafast rate of 60 °C was still 120 mAh g^{-1}. On the basis of lattice contraction and expansion, the first plateau was ascribed to Fe reduction and the second to Co reduction. After 100 cycles, the capacity had decreased to *ca*. 100 mAh g^{-1}. A Mn-HCF also showed a high capacity of 110–120 mAh g^{-1} in organic electrolyte containing Na^+.[86] On the other hand, Zn, the heaviest of the 3d transition metals, resulted in a lower capacity of 50–55 mAh g^{-1} for Zn-HCF.[83] In the particular Zn-HCF investigated in Ref. 83 ($Zn^{II}_3[Fe^{III}(CN)_6]_2$), Zn was however electrochemically inactive and only Fe changed its redox state. PBAs have also been investigated in aqueous electrolytes.[84,87,88] The specific capacity of Cu-HCF and Ni-HCF was *ca*. 50–60 mAh g^{-1}, but showed interesting life cycle on insertion/extraction of K^+ and NH_4^+. There was no measurable loss after 500 cycles of Na^+ or K^+ insertion in Ni-HCF.[84] The capacity was still *ca*. 40 mAh g^{-1} at 40 °C charging rate. The larger instability of these PBAs with Li^+ was interpreted in term of the Stokes radius of the hydrated alkali cations. Li^+ has a larger Stokes radius than K^+ or NH_4^+ (*ca*. 2.4 and 1.2 Å, respectively).[84] Similar observations had been reported earlier in organic electrolyte.[81,89]

PB and PBAs have been recently used in innovative ways in Li-ion batteries.[90,91] The composite obtained from the archetypal $LiMn_2O_4$ cathode material and PB showed in organic electrolyte capacities of *ca*. 120 and 50 mAh g^{-1} at rates of 0.2 and 10 °C, respectively, whereas the $LiMn_2O_4$ cathode showed, in the same order, capacities of 110 and then only 17 mAh g^{-1}. Next, a core-shell composite made of two PBAs (Ni-HCF shell on a Cu-HCF core) showed better cyclability than the Cu-HCF alone.[91] Cu-HCF shows two redox processes, one for Cu^{II}/Cu^{I} and the other for Fe^{III}/Fe^{II}, but has poor stability due to a phase transition in its highly reduced state.[91,92] In $LiClO_4$ carbonate electrolyte, the core-shell Ni-HCF/Cu-HCF composite showed a capacity of 100 and 65 mAh g^{-1} initially and after 50 cycles, respectively, whereas the Cu-HCF showed corresponding values of 120 and then only 24 mAh g^{-1}. In conclusion, PBAs are promising materials for the positive electrode of rechargeable batteries for various alkali metals and their performance compares well with those of other compounds presently considered, for example, Na-ion batteries.[76]

MOFs with high surface area, tunable pore size, and high density of redox centers are also potential candidates as electrode materials for electrochemical capacitors.[93–95] A capacity of 150–200 F g^{-1} in 1 M LiOH aqueous electrolyte was reported for a Co-terephthalate-based MOF, with stability over 1000 cycles.[93] A Mn-HCF MOF was used to form a composite material with MnO_2, resulting in a gravimetric capacitance of 225 F g^{-1} in 0.5 M Na_2SO_4 aqueous electrolyte.[95] The authors reported a composite material with a core-shell structure involving a Mn-HCF core and a thin MnO_2 layer, obtained after electrooxidation at 1.7 V versus Ag/AgCl. Cyclic voltammetry of this composite could be deconvoluted in contributions arising from Mn-HCF and MnO_2 (Figure 7 in Ref. 95).

3.2 MOFs as Electrocatalysts

Several POMOFs have shown interesting electrocatalytic activity for the hydrogen evolution reaction (HER).[63] A series of three POMOFs based on oxomolybdate anions showed activity for the HER at pH 1. The redox properties of these MOFs were previously discussed in Section 2.2. The electrocalytic reduction process revealed an onset potential of *ca*. +0.3 V versus RHE at pH 1, which is thermodynamically impossible. One possible explanation for this onset potential significantly above 0 V versus RHE is a local pH within the POMOFs being lower than that in the bulk electrolyte.[63] Two other POMOFs based on oxomolybdate anions exhibited some electrocatalytic activity toward the HER in 0.5 M H_2SO_4 but with high onset overpotentials of −0.5 V.[96]

The oxygen reduction reaction (ORR) is another paramount reaction for fuel cells and metal–air batteries, and much limiting the energy efficiency of these systems due to its slow kinetics. The high density of coordinatively unsaturated metal ions in MOFs and improved robustness compared to isolated metal complexes offers a platform for bioinspired catalysts free of precious metal elements. Recently, several pristine MOF structures have shown some activity for the ORR.[34,35] It is well-known that porphyrins may be used as building blocks to form 2D or 3D MOFs.[97,98] A composite MOF structure $(G\text{-dye–FeP})_n$ comprising pyridine-functionalized graphene (reduced graphene oxide sheets functionalized with donor–π–acceptor dye containing pyridinium

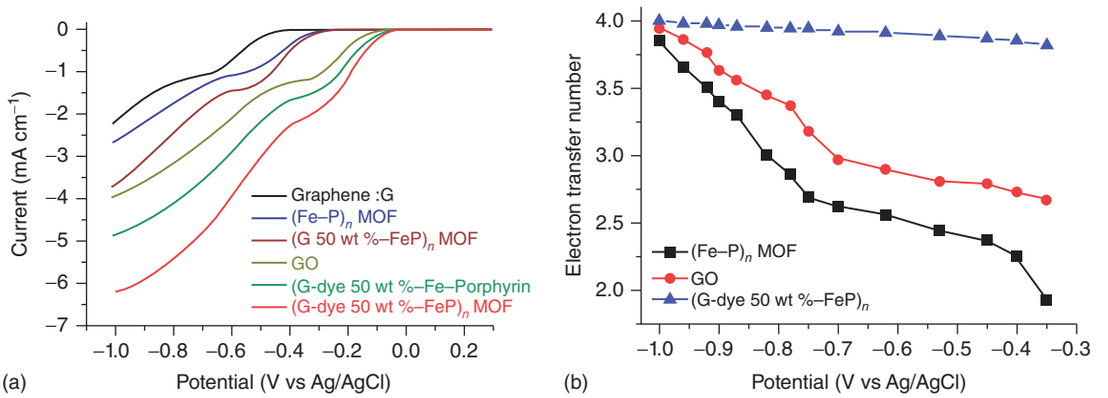


Figure 11 Electrocatalytic activity for the ORR on graphene-iron porphyrin MOF composites: (a) RDE voltammograms of graphene, $(Fe–P)_n$ MOF, (G 50 wt% –FeP)$_n$ MOF, G-dye 50 wt% –Fe–Porphyrin (G-dye 50 wt% –FeP)$_n$ MOF, and graphene oxide-GO (rotation rate of 2000 rpm, electrolyte 0.1 M KOH); (b) the dependence of the electron transfer number on the potential for (G-dye 50 wt% –Fe–P)$_n$ MOF, $(Fe–P)_n$ MOF and GO as a function of the electric potential. (Reproduced with permission from Ref. 34. Copyright (2010) American Chemical Society.)

moieties, and labeled G-dye) and an iron porphyrin [5,10,15,20-tetrakis(4-carboxyl)-iron-porphyrin; labeled FeP] was recently reported for its interesting catalytic activity toward the ORR in alkaline medium with an onset potential of *ca.* 0.93 V versus RHE (Figure 11a).[34] G-dye was used as a building block for the assembly of MOF. The larger bond polarity due to nitrogen ligands in the G-dye, the catalytically active iron porphyrin, and the framework porosity acted synergistically to afford a near 4-electron ORR pathway (Figure 11b).

Another example of a MOF-based electrocatalyst for the ORR is given by $Cu_3(btc)_2$ (Figure 5d) and by Cu^{II}–bipy–btc. The bipy auxiliary ligand was necessary to stabilize the structure in aqueous medium, as the Cu^{II}–btc MOF [$Cu_3(btc)_2$] was not stable enough.[35] A large increase in the reduction current in O_2-saturated medium attests

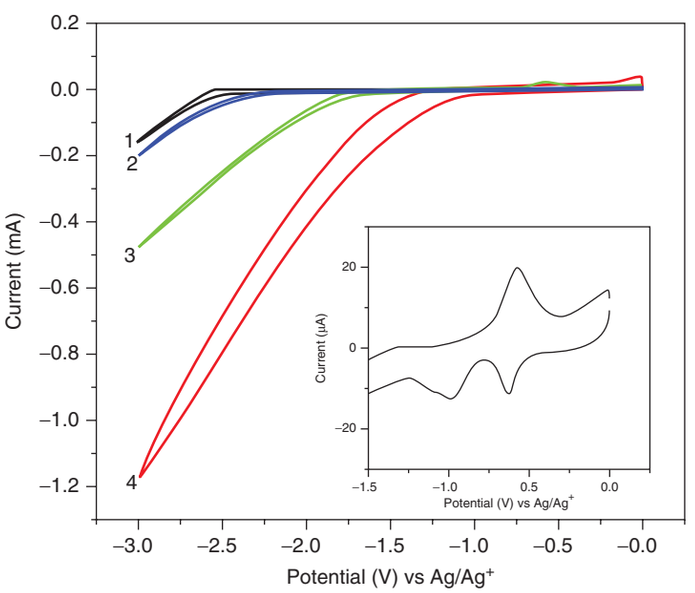


Figure 12 Electrocatalytic reduction of CO_2 by $Cu_3(btc)_2$ in aprotic electrolyte. Cyclic voltammogram of: (1) bare GC, (2) bare GC in presence of CO_2, (3) $Cu_3(btc)_2$-coated GC, and (4) $Cu_3(btc)_2$-coated GC in presence of CO_2, in a solution containing 0.01 M TBATFB/DMF, scan rate 50 mVs^{-1}. Inset: cyclic voltammogram of $Cu_3(btc)_2$-coated GC in CO_2-saturated DMF. (Reproduced from Ref. 59. © Elsevier, 2012.)

the electrocatalysis of the ORR. A stable electrocatalytic behavior of the Cu^{II}–bipy–btc MOF was obtained at pH 6 with an onset potential for the ORR of *ca.* −0.10 V versus Ag/AgCl. The reduction of Cu^{II} to Cu^{I} coincided with the onset potential for the ORR in the O_2-saturated electrolyte. The redox pair at −0.15 V versus Ag/AgCl was assigned to Cu^{II}/Cu^{I} and the onset potential for the ORR again coincided with the redox potential, suggesting Cu^{I} as the catalytic site for the ORR. The short Cu–Cu distance in these MOFs (Figure 5a) also suggests a bimetallic catalytic centre for the ORR.

Electrochemical conversion of captured CO_2 into valuable chemicals or fuels is a topic of interest in electrocatalysis. The $Cu_3(btc)_2$ MOF deposited as a uniform film on glassy carbon was shown to electrochemically reduce CO_2 to oxalate anions through the dimerization of CO_2 radical anions in DMF solution.[59] The oxalate anions then abstracted protons from the solvent to ultimately form oxalic acid. Cyclic voltammetry (Figure 12) revealed that the onset potential for the CO_2 reduction started at much more positive potentials for the $Cu_3(btc)_2$-coated GC electrode (−0.9 V vs Ag/Ag^+) than for the bare GC electrode (−2.1 V vs Ag/Ag^+). The cathodic current density at, for example, −2.5 V versus Ag/Ag^+ was also significantly higher. Seemingly, the catalytic activity was triggered by the reduction of Cu^{II} to Cu^{I}, which occurs at −0.62 V versus Ag/Ag^+ in the CO_2-saturated DMF solution (inset of Figure 12).

Electrooxidation of liquid fuels is the logical pending facet of their electrosynthesis. The first example of the utilization of a noble-metal-free MOF-based material as a catalyst for ethanol electrooxidation was reported by Kitagawa's group.[36] The MOF was *N*,*N*′-bis(2-hydroxyethyl)dithiooxamidato-copper(II) [$(HOC_2H_4)_2$dtoaCu]. Cyclic voltammetry showed one redox couple (peak I) centered at 0.35 V versus Ag/AgCl and ascribed to Cu^{I}/Cu^{II} oxidation, and an irreversible wave (peak II) at 0.71 V versus Ag/AgCl attributed to Cu^{II}/Cu^{III} oxidation (Figure 13). Addition of ethanol resulted in an increase of the redox peak, ascribed to some ethanol oxidation and charge transfer to Cu atoms, and in a sustained ethanol oxidation current starting at 0.62 V versus Ag/AgCl (corresponding to 0.82 V vs SHE). The product of ethanol oxidation was acetaldehyde (two-electron oxidation), instead of the full six-electron oxidation to CO_2. This is a serious drawback, which adds on the high overpotential for ethanol oxidation (the ethanol–acetaldehyde standard equilibrium potential is −0.21 V versus RHE).

Nitrate and nitrite originating from fertilizers are highly oxidizing species and their electrochemical reduction could be an option for denitrification. Cu-based MOFs and several POMOFs have shown substantial electrochemical activity for nitrite reduction, as expected from the catalytic properties of POM anions.[18,26,55,99] A 3D

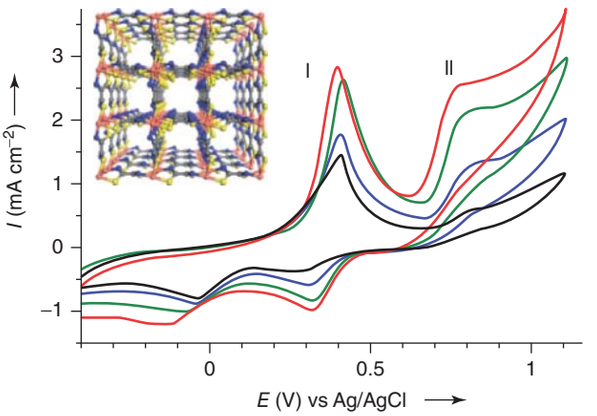


Figure 13 Ethanol electrooxidation by the Cu^{II}-MOF [$(HOC_2H_4)_2$dtoaCu]. Cyclic voltammograms of a glassy carbon electrode coated with Cu^{II}-MOF in 0.5 M H_2SO_4 containing different concentrations of ethanol (from inner to outer curve: 0.0, 0.5, 1.0, and 2.0 M), scan rate 100 mV s^{-1}. Inset: the crystal structure of [$(HOC_2H_4)_2$dtoaCu]. (Reproduced from Ref. 36. © Wiley-VCH Verlag GmbH & Co. KGaA, 2010.)

Cu-based POMOF $[Cu^{I}(pci)Mo_2{}^{V}O_5]$ incorporating small polyoxomolybdate anions showed significant electrocatalytic activity toward the reduction of nitrite in acidic medium.[99] Two other POMOFs with electrocatalytic activity for the same reaction are $Co_2(bpy)_3(ox)(As_2W_{18}O_{62}) \cdot 2(H_2bpy) \cdot 2H_2O$,[55] as well as the POMOF previously discussed in Section 2.2.5, namely $Cu^{I}{}_4(L3)_4Mo_6O_{18}(O_3AsPh)_2$.[64]

3.3 MOFs for Proton-Conductive Membranes in Fuel Cell

Proton conductivity is a key property required for fuel cell applications. Proton conductivities reached with state-of-the-art materials for low- and high-temperature polymer electrolyte membrane fuel cells (PEMFCs), sulfonated fluoro-polymers (e.g., Nafion®) and phosphoric-acid-doped polybenzimidazole membranes are typically 10 S m^{-1} at 80 °C and 100% relative humidity (RH), and 5–20 S m^{-1} at 150 °C and 0% RH, respectively.[100–102] MOFs entered this field of research in 2003.[103] With regard to the design of a better proton-conducting material, the investigated approaches can be classified into three types: (i) pristine MOFs; (ii) MOFs loaded with guest molecules (imidazole or triazole) or incorporating inorganic nanostructures (POMs); and (iii) postsynthesis functionalized MOFs. Proton conductivity of the various MOF systems discussed in this section is given, in the order of appearance in the text, in Table 3.

3.3.1 Approach (i)

Kitagawa's group reported proton conductivity for several MOFs of the type M(OH)(bdc–R) with M =Al, Fe;

Table 3 Proton conductivities of various metal–organic frameworks

MOF systems	Proton conductivity (S m^{-1})	T (°C)	Relative humidity (%)	References
Al(OH)(bdc–OH)	1.9×10^{-4}	80	95	47
Al(OH)(bdc–H)	3.6×10^{-5}	80	95	47
Al(OH)(bdc–NH_2)	4.1×10^{-6}	80	95	47
Fe(OH)(bdc–$(COOH)_2$)	7×10^{-4}	80	95	47
Ferrous oxalate dihydrate	1.3×10^{-1}	25	98	104
$[(Zn_{0.25})_8O][Zn_6(L)_{12}(H_2O)_{29}(DMF)_{69}(NO_3)_2]_n$; L = carboxy-phenyl-imidazolium	2.3×10^{-1}	25	95	105
PCMOF-5	2.5×10^{-1}	60	98	106
$[Zn(l\text{-}L_{Cl})(Cl)](H_2O)_2$	4×10^{-3}	30	98	48
$[Zn(d\text{-}L_{Cl})(Cl)](H_2O)_2$	4×10^{-3}	30	98	48
PCMOF-2½	2.1	85	90	107
β-PCMOF-2	1.3×10^{-1}	85	90	107
β-PCMOF-2	10^{-4}	100	0	108
β-PCMOF-2 loaded with 1,2,4-triazole	5×10^{-2}	150	0	108
Fe-MIL-101-NH2-SPPO	10	25	98	109
Fe-MIL-101-NH2-SPPO	25	90	98	109
$[Al(\mu_2\text{-}OH)(1,4\text{-ndc})]_n$ loaded with imidazole	2.2×10^{-3}	120	0	110
$(NH_4)_2[Zn_2(ox)_3]\cdot3H_2O$ loaded with adipic acid	8×10^{-1}	25	98	111
$[Mo_5P_2O_{23}][Cu(phen)(H_2O)]_3\cdot5H_2O$	2.2×10^{-3}	3	98	112
Cr-MIL-101 loaded with $CsHSO_4$	1	200	0	113
H_2SO_4@MIL-101	1	150	0.13	114
H_3PO_4@MIL-101	3×10^{-1}	150	0.13	114
Sulfated MIL-53(Al)	3×10^{-1}	20	100	115

R = H, NH_2, OH, or $(COOH)_2$.[47] The proton conductivity increased over 2 orders of magnitude with increased acidity of the R-group. The same group reported a higher conductivity of 0.13 S m^{-1} for a ferrous oxalate dihydrate MOF[104] and an even higher value with a MOF synthesized from a carboxy-phenyl-imidazolium ligand and a hitherto unknown Zn_8O metal cluster (Table 3).[105] The Zn_8O cluster coordinated to six ligands formed an overall 3D structure with channels occupied by DMF and water molecules. The latter are believed to sustain the Grotthuss-type conduction mechanism for the protons originating from the methylene groups of the imidazolium ligand. A similarly high conductivity of 2.5×10^{-1} S m^{-1} at 60 °C and 98% RH was reported for PCMOF-5 ($[La(H_5L)(H_2O)_4]$, with L = 1,2,4,5-tetrakis-phosphonomethylbenzene). The high proton conductivity was explained on the basis of noncoordinating diprotic phosphonic acid groups lining the pores and crystallographically located intra-pore water molecules as well as free water molecules.[106]

Sahoo *et al*.[48] investigated the role of halogens (Br or Cl) on the proton conductivity of chiral Zn-based MOFs. Only the MOFs involving Cl-atoms, enantiomers with respect to the ligand backbone (d or l amino acid derivative) showed proton conductivity (Table 3).

Recently, Shimizu's group reported enhanced proton conduction in a MOF by isomorphous ligand replacement.[107] They modified the structure of a previously investigated MOF [Na_3(2,4,6-trihydroxy-1,3,5-benzene-trisulfonate), labeled β-PCMOF-2] to host triazole molecules, as will be discussed in Section 3.3.2.[108] The replacement of 2,4,6-trihydroxy-1,3,5-benzenetrisulfonate ligand molecules in the MOF structure by 1,3,5-benzenetriphosphonic acid ligand molecules increased the proton conductivity by *ca*. 1.5 order of magnitude (Table 3). The new MOF was labeled PCMOF-2½ and its proton conductivity reached 2.1 S m^{-1} at 90% RH and 85 °C (Table 3). On the replacement of the trianionic ligand molecules in β-PCMOF2 by trianionic and also triprotic ligand molecules, the pores became partially lined with hydrogen phosphonate groups rather than with exclusively nonprotonated sulfonate groups, which enhanced the proton conduction.

Another approach involves hybrid polymer-MOF membranes. An excellent proton conductivity of 25 S m^{-1} at 98% RH and 90 °C (Table 3) was obtained with a mixed-matrix of Fe-MIL-101-NH_2 and a sulfonated polymer.[109] The Fe-MIL-101-NH_2 MOF, 3D $[Fe_3(O)(bdc\text{-}NH_2)_3(OH)(H_2O)_2]\cdot pH_2O$, adhered well to sulfonated poly (2,6-dimethyl-1,4-phenylene oxide) (SPPO) via acid-amine chemical bonds. The MOF crystals alone have an octagonal shape (Figure 14a) but are connected via chemical bonds in the mixed-matrix membrane, Figure 14b. The optimum content of MOF in the polymer was found to be 6 wt%, resulting in a conductivity of 10 S m^{-1} at room temperature, against 8 S m^{-1} for the pure SPPO polymer membrane and only 2.8×10^{-5} S m^{-1} for the pure MOF. A mechanism for the conduction of protons in the hybrid MOF-polymer membrane was proposed and involved generation of protons by the acidic sulfonimide groups and Grotthuss-type conduction in the MOF crystals where the

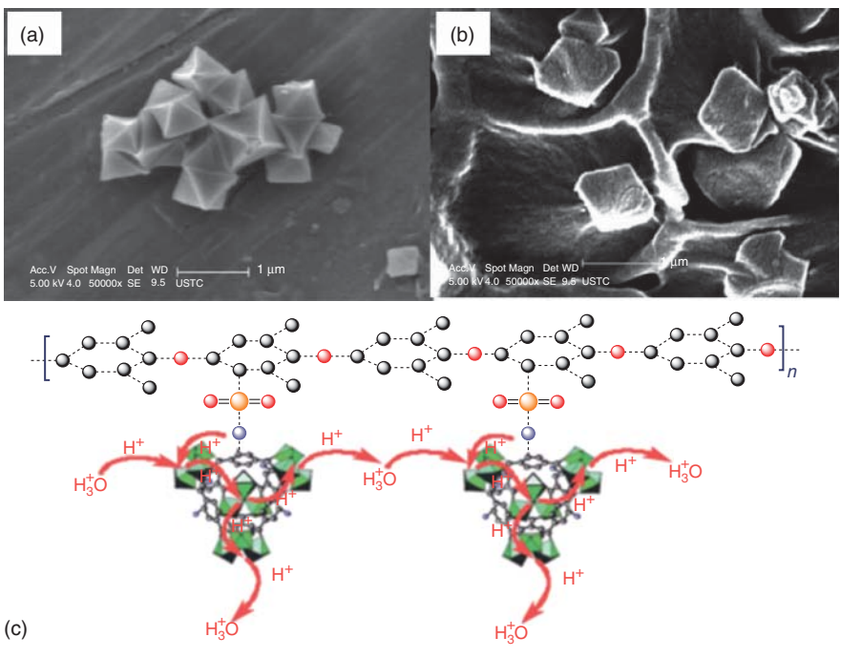


Figure 14 SEM images of: (a) Fe-MIL-101-NH_2 crystals and (b) the cross-section of the Fe-MIL-101-NH_2-PPO-SO_2Cl membrane. (c) Schematic illustration of the possible pathway of proton transfer in the membranes. S, O, C, and N are represented as orange, red, gray, and blue, respectively, H atoms are omitted. (Reproduced from Ref. 109 with permission of The Royal Society of Chemistry. DOI: 10.1039/C2CC37045J.)

water is bound to an otherwise open coordination Fe^{III} site (Figure 14).

3.3.2 *Approach (ii)*

Shimizu and coworkers investigated β-PCMOF-2 loaded with the guest molecule 1,2,4-triazole (Tz).[108] The as-synthesized MOF showed poor proton conductivity, but with a loading of Tz molecules, the conductivity increased by 2–3 orders of magnitude (Table 3). The proton mobility in *N*-heterocycles such as imidazole or triazole and the electrochemical stability of the latter had been previously demonstrated.[116]

Al-based porous frameworks were also reported to moderately conduct protons above 100 °C through the incorporation of imidazole (Im) within the pores.[110] A higher proton-conductive MOF was obtained by introducing adipic acid in a layered oxalate-bridged framework $(NH_4)_2[Zn_2(ox)_3]\cdot 3H_2O$.[111] Also, hybrid materials comprising a MOF and POMs were investigated.[112]

Ponomareva *et al.*[113] introduced the acid salt $CsHSO_4$ into a Cr-based MOF (known under the label Cr-MIL-101), $Cr_3O(H_2O)Y(bdc)_{0.15}HNO_3\cdot 13H_2O$, where Y = F or NO_3, and devoid of proton-conductive properties, reporting a significant value of proton conductivity for high temperature hybrid electrolytes. Similar values have been reported more recently by the same group for the impregnation of the same MOF by the nonvolatile acids H_2SO_4 and H_3PO_4.[114] The acid molecules are strongly trapped in the pores of the hosting MOF and cannot be removed either on heating or on hydration of the MOF in a humid atmosphere.

3.3.3 *Approach (iii)*

The regular structure of MOFs can serve as a scaffold to anchor acidic groups and to form efficient proton transfer pathways.[111,117] Goesten *et al.*[115] functionalized the MOF MIL-53(Al) (aluminum terephthalate-MOF) in a postsynthesis step by reacting it at room temperature in a solution of H_2SO_4–Tf_2O in nitromethane (Tf_2O = trifluoromethanesulfonic anhydride). Sulfoxy-acid moieties covalently bonded to the aryl carbons of the organic linker were generated for approximately 50% of the terephthalate linking units and a proton conductivity of *ca.* 3×10^{-1} S m^{-1} at 20 °C and 100% RH was observed for the sulfated MIL-53(Al) material.

4 SACRIFICIAL MOFs FOR ELECTROCHEMICAL APPLICATIONS

MOFs can also be used as sacrificial materials to form, for example, microporous carbon or metal and

metal oxide nanoparticles that are subsequently used for their charge-storage properties in electrochemical double layer capacitors (EDLCs)[42,43,46,118–122] as well as negative electrode in Li-ion batteries.[38,123,124] Moreover, the use of MOFs as sacrificial precursors for the synthesis of ORR catalysts was first reported in 2010.[125] MOFs may be coined as sacrificial if they are subjected to a process during which they are transformed into a single or multiphase material that no longer displays a MOF crystalline structure. Such MOF-derived materials may present morphologies or structures otherwise difficult to reach. While numerous physical or chemical processes may be applied to transform MOFs, thermal processes in inert, reducing, or oxidizing atmospheres have been the most ubiquitous one so far.

4.1 Electrochemical Supercapacitors

Carbon materials with a specific surface area up to 3447 $m^2\ g^{-1}$ have been obtained by thermal decomposition of MOFs[42,118–120] or MOF–organic precursor composites.[43,46,121,122] To date, two Zn-based MOFs, MOF-5 [$Zn_4O(bdc)_3$] and ZIF-8 [$Zn(2\text{-methylimidazole})_2$], have been investigated as major sacrificial MOFs.[126] Pyrolysis of Fe- or Ni-based MOFs seems to result either in more graphitic carbon with low surface area or in carbon nanotubes.[119,127] The electrochemical capacitance obtained with MOF-derived carbons compares well with typical values of gravimetric capacitance obtained with activated carbons, which are 100–120 F g^{-1} in organic electrolytes and 150–300 F g^{-1} in aqueous electrolytes, respectively.[128] The largest capacitances reported by Hu *et al*.[42] in basic and organic electrolytes from galvanostatic charge–discharge curves at 0.25 A g^{-1} were 274 and 168 F g^{-1}, respectively, obtained with a KOH-activated MOF-derived carbon having a surface area of 2222 $m^2\ g^{-1}$. In acidic medium, capacitances of 200 F g^{-1} at 0.25 A g^{-1} were obtained with samples having surface areas of 2169 and 3405 $m^2\ g^{-1}$.[43]

4.2 Rechargeable Batteries

The conversion-reaction mechanism taking place on Li insertion/extraction in Si or Sn, for example, leads to theoretical capacities for the negative electrode of 4200 and 990 mAh g^{-1}, respectively. These values, while much higher than that of graphite (372 mAh g^{-1}), are usually not reached due to challenges of cyclability and volume expansion that are intrinsic to the conversion mechanism (equation 9).

$$M_xO_y + 2yLi^+ + 2ye^- \leftrightarrow xM + yLi_2O \qquad (9)$$

Nanostructured metal/metal oxides are needed to overcome these challenges, and MOF may play a key role in generating such controlled nanostructures.[38,123,124] Liu *et al*.[124] synthesized Co_3O_4 nanoparticles with agglomerate structure and low surface area by calcination at 600 °C of a Co-based MOF, $Co_3(ndc)_3(dmf)_4$. After mixing with a conductive phase and subsequent testing as the negative electrode in a Li-ion battery, a reversible capacity of 965 mA h g^{-1} was obtained after 50 cycles. The capacity for Li storage compared favorably to that of nonagglomerated cobalt-oxide nanostructures,[123] reveling the unique feature of sacrificial MOFs to improve the performance of cobalt oxide materials in Li-ion batteries.

Nano/micro Co_3O_4 materials for EDLCs electrodes were also prepared by Zhang *et al*.[129] by calcination at 450 °C of another MOF, cobalt$(bdc)_2$. Cyclic voltammetry in 6 M KOH showed two redox pairs, ascribed to the Co_3O_4–CoOH and CoOH–CoO_2 couples. Gravimetric capacitances of 210 and 179 F g^{-1} were reported at scan rates of 5 and 30 mV s^{-1}, respectively. Higher calcination temperatures (550 and 650 °C) lead to decreased capacitance, probably due to increased particle size of the resulting materials.

Mixed transition metal oxide materials with a spinel structure were considered as well.[130] By calcination of appropriate MOF precursors at 450 °C, AMn_2–ptcda, Zhao *et al*.[38] synthesized the spinel oxides AMn_2O_4 (A = Zn, Co, or Ni) with a unique gypsum-flower-like morphology derived from the pristine MOFs. The measured electrode capacity was comparable to, but not better than, results obtained with the $ZnMn_2O_4$ material formed by the coprecipitation method followed by calcination (initial capacity of 800 mA h g^{-1}, and *ca*. 500 mA h g^{-1} after 30 cycles).[130]

Moreover, a general strategy for the synthesis of carbon-supported metal or metal oxide nanoparticles starting from MOFs was reported by Poddar's group.[39] The authors found a correlation between the redox potential of the metal^{n+}/metal redox couple and the ability of a metal^{n+}-based MOF to form metal nanoparticles on pyrolysis. Cu^{II} and Co^{II} have redox potentials of +0.34 and −0.28 V versus SHE, whereas Zn^{II}, Mn^{II}, and Mg^{II} have much lower potentials of −0.76, −1.18, and −2.37 V versus SHE, respectively. It was concluded from experimental results that metal cations with a potential above *ca*. −0.27 V SHE could react with the organic ligands of the MOFs to be reduced to zero oxidation state during pyrolysis in inert atmosphere, whereas others resulted in metal oxide nanoparticles after pyrolysis.

4.3 ORR in Aqueous Electrolyte (Polymer Electrolyte Membrane or Alkaline Fuel Cell)

Liu's group from Argonne National Laboratory pioneered the use of MOF as a sacrificial precursor for preparing ORR catalysts.[44,125] The original MOF structure was not preserved after the thermal activation above

600 °C, but it played a key role in generating a high density of catalytic sites with proper accessibility for oxygen. The choice of cobalt imidazolate MOF precursor was explained by its analogous structure with the CoN_4 (or FeN_4) macromolecules precursors for nonprecious metal catalysts for the ORR.[131]

Shortly thereafter, ZIF-8 (a Zn-based zeolithic imidazolate framework) was selected for its high nitrogen content and high microporous surface area (1700 m^2 g^{-1}) in order to form an ORR catalyst precursor when mixed with 1,10-phenanthroline or TPTZ and ferrous acetate.[45,132] An optimized Fe/N/C-catalyst hosting FeN_x active sites was prepared from the pyrolysis in argon at 1050 °C, then in ammonia at 950 °C, of the catalyst precursor obtained by low-energy planetary ball-milling of ZIF-8, phenanthroline, or TPTZ, and ferrous acetate mixed in optimized ratios. H_2–O_2 polymer electrolyte membrane (PEM) fuel cell tests with the optimized cathode catalyst yielded a current density of 1.2–1.3 A cm^{-2} at 0.6 V and a peak power density of 0.91 W cm^{-2}. A cation-exchange reaction was observed between Zn^{II} and Fe^{II} during the wet impregnation step of ZIF-8, Fe^{II}-acetate, and TPTZ.[132] This exchange was found to be detrimental for the final catalyst and depended on the stability of the iron–ligand complex. The Fe^{II}-phenanthroline complex being much more stable than the Fe^{II}-TPTZ, the metal-exchange reaction was not observed with phenanthroline. The metal-exchange reaction between a MOF and metal cations present in the electrolyte is a general process that may lead to a modification of the pristine MOF or to its complete dissolution, depending on the metal-cation concentration and nature.[133,134]

Further modifications of the synthesis method were explored by replacing ZIF-8 with a commercially available Fe-btc MOF (F300, 1500 m^2 g^{-1}).[135] Major negative changes of the electrocatalytic activity of the resulting catalyst were observed by the substitution of ZIF-8 with F300, whereas replacing Fe^{II}-acetate by Fe^{II}–phthalocyanine or replacing phenanthroline by polyaniline resulted in minor changes in the electrochemical performance of the resulting catalysts. Therefore, the MOF chemistry obviously plays a key role in the synthesis of nonprecious metal catalysts via pyrolytic steps. The iron atoms native of F300 agglomerate during the heat treatment and catalyze graphitization, resulting in excess Fe and low microporous surface area after pyrolysis, in contrast to Fe^{II}-acetate/phenanthroline/ZIF-8 precursors where Fe is present at only *ca*. 1 wt% whereas Zn atoms native of the MOF conveniently forms volatile products at high temperature.

Recently, a metaloporphyrin MOF was successfully used to pyrolytically synthesize a highly active ORR catalyst.[136] In contrast to other Fe-based MOFs, the pyrolysis at 700–1000 °C of the polymerized Fe^{II}-5, 10,15,20-tetrakis-(3,5-di-thio-phen-2-yl-phenyl)porphyrin (PFeTTPP) resulted in high-surface-area carbon structures (760–900 m^2 g^{-1}) with embedded Fe-based active sites that revealed a high activity for the ORR in acidic electrolyte. H_2–O_2 PEM fuel cell tests with the PFeTTPP cathode catalyst pyrolyzed at 700 °C yielded a current density of *ca*. 0.6 A cm^{-2} at 0.6 V and a peak power density of 0.73 W cm^{-2} at 0.4 V.

5 CONCLUSIONS

The electrochemical investigation of MOFs is a recent and blossoming but complex field of research. It would be advantageous to conduct synthetic efforts and electrochemical evaluation as much as possible in parallel, in order to identify early the potentials of such materials. The electrochemical evaluation of MOFs or MOF-based materials is however not straightforward, due to (i) the microporous or micro-mesoporous nature of MOFs and lack of macropores, as well as (ii) their usually poor electron conductivity. It is therefore easy to underestimate the intrinsic electrochemical properties of a given MOF for a given application if the ionic or electronic paths leading to the active sites within the MOF are nonpercolating, or poor. Pristine MOFs or hybrid materials comprising pristine MOFs have now shown interesting properties at par with state-of-the-art materials in several electrochemical applications, but an example of a clear-cut advantage brought by pristine MOFs is still awaited. Materials derived from MOFs, for example, through pyrolysis in inert or reactive atmosphere, is another interesting topic with promising results. Overall, the field is quite promising with yet largely unexplored possibilities in combining MOFs with more conventional materials used in electrochemistry in order to take advantage of specific properties of both materials, or of synergetic effects.

6 ACKNOWLEDGMENTS

The authors are grateful for the funding by *Agence Nationale de la Recherche* under contract ANR 2011 CHEX 004-01.

7 RELATED ARTICLES

Porous Coordination Polymer Nanoparticles and Macrostructures; Mesoporous Metal-Organic Frameworks; Porphyrinic Metal-Organic Frameworks; Postsynthetic Modification of Metal-Organic Frameworks; Open Metal Sites in Metal-Organic-Frameworks.

8 ABBREVIATIONS AND ACRONYMS

bdc = 1,4-benzenedicarboxylate; bimb = 1,4-bis(1-imidazolyl)benzene; bipy = bipyridine; bpdc = *para*-biphenyldicarboxylate; bpy = 4,4′-bipyridine; btb = 1,3,5-benzenetribenzoate; btc = benzene-1,3,5-tricarboxylate; CV = cyclic voltammogram; dmf = *N*,*N*′-dimethyl-formamide; dpq = dipyrido[3,2-d:2′,3′-f]quinoxaline; EDLC = electrochemical double layer capacitor; FWHM = full-width-at-half-maximum; HCF = hexacyanoferrate; HER = hydrogen evolution reaction; L3 = 1,5-bis(1,2,4-triazol-1-yl)pentane; MOF = Metal–organic framework; ndc = 2,6-naphthalene-dicarboxylate; ORR = oxygen reduction reaction; ox = oxalate; PB = cyclic voltammogram; PBA = Prussian blue analogs; pci = pyridine-4-carboxylic ion; pdt = pyrazine-2,3-dithiolate; PEM = polymer electrolyte membrane; PEMFC = polymer electrolyte membrane fuel cell; POM = polyoxometalate; POMOF = polyoxometalate-metal–organic framework; ptcda = perylene-3,4,9,10-tetracarboxylic dianhydride; RH = relative humidity; SCE = full-width-at-half-maximum; SEM = scanning electron microscope; SHE = scanning electron microscope; SPPO = sulfonated poly (2,6-dimethyl-1,4-phenylene oxide); tba = tetrabutylammonium; TPTZ = 2,4,6-tris-(2-pyridyl)-*s*-triazine; XRD = X-ray diffraction pattern.

9 REFERENCES

1. O. M. Yaghi and H. L. Li, *J. Am. Chem. Soc.*, 1995, **117**, 10401.
2. O. M. Yaghi, G. M. Li, and H. L. Li, *Nature*, 1995, **378**, 703.
3. E. A. Tomic, *J. Appl. Polym. Sci.*, 1965, **9**, 3745.
4. B. F. Hoskins and R. Robson, *J. Am. Chem. Soc.*, 1989, **111**, 5962.
5. B. F. Hoskins and R. Robson, *J. Am. Chem. Soc.*, 1990, **112**, 1546.
6. H. Furukawa, N. Ko, Y. B. Go, N. Aratani, S. B. Choi, E. Choi, A. O. Yazaydin, R. Q. Snurr, M. O'Keeffe, J. Kim, and O. M. Yaghi, *Science*, 2010, **329**, 424.
7. W. Xuan, C. Zhu, Y. Liu, and Y. Cui, *Chem. Soc. Rev.*, 2012, **41**, 1677.
8. K. S. Park, Z. Ni, A. P. Cote, J. Y. Choi, R. Huang, F. J. Uribe-Romo, H. K. Chae, M. O'Keeffe, and O. M. Yaghi, *Proc. Natl. Acad. Sci. U.S.A.*, 2006, **103**, 10186.
9. C. Janiak, *Dalton Trans.*, 2003, 2781.
10. R. Robson, *Dalton Trans.*, 2008, 5113.
11. K. Biradha, A. Ramana, and J. J. Vittal, *Cryst. Growth Des.*, 2009, **9**, 2969.
12. G. Férey, *Chem. Soc. Rev.*, 2008, **37**, 191.
13. S. Keskin and S. Kizilel, *Ind. Eng. Chem. Res.*, 2011, **50**, 1799.
14. R. J. Kuppler, D. J. Timmons, Q.-R. Fang, J.-R. Li, T. A. Makal, M. D. Young, D. Yuan, D. Zhao, W. Zhuang, and H.-C. Zhou, *Coord. Chem. Rev.*, 2009, **253**, 3042.
15. S. Kitagawa, R. Kitaura, and S.-I. Noro, *Angew. Chem. Int. Ed.*, 2004, **43**, 2334.
16. J. L. C. Rowsell and O. M. Yaghi, *Microporous Mesoporous Mater.*, 2004, **73**, 3.
17. J. L. C. Rowsell and O. M. Yaghi, *J. Am. Chem. Soc.*, 2006, **128**, 1304.
18. A. Morozan and F. Jaouen, *Energy Environ. Sci.*, 2012, **5**, 9269.
19. A. Mantion, L. Massüger, P. Rabu, C. Palivan, L. B. McCusker, and A. Taubert, *J. Am. Chem. Soc.*, 2008, **130**, 2517.
20. H. Chevreau, T. Devic, F. Salles, G. Maurin, N. Stock, and C. Serre, *Angew. Chem. Int. Ed.*, 2013, **52**, 5056.
21. G. Férey, C. Mellot-Draznieks, C. Serre, F. Millange, J. Dutour, S. Surblé, and I. Margiolaki, *Science*, 2005, **309**, 2040.
22. L. M. Rodriguez-Albelo, A. R. Ruiz-Salvador, A. Sampieri, D. W. Lewis, A. Gómez, B. Nohra, P. Mialane, J. Marrot, F. Sécheresse, C. Mellot-Draznieks, R. N. Biboum, B. Keita, L. Nadjo, and A. Dolbecq, *J. Am. Chem. Soc.*, 2009, **131**, 16078.
23. A. J. Bard and L. R. Faulkner, 'Electrochemical Methods: Fundamental and Applications', John Wiley & Sons, Inc., New York, 2001.
24. A. Domenech, H. Garcia, M. T. Domenech-Carbo, and F. Llabres-i-Xamena, *Electrochem. Commun.*, 2006, **8**, 1830.
25. A. Domenech, H. Garcia, M. T. Domenech-Carbo, and F. Llabres-i-Xamena, *J. Phys. Chem. C*, 2007, **111**, 13701.
26. H. Y. Lin, X. Wang, H. Hu, B. Chen, and G. Liu, *Solid State Sci.*, 2009, **11**, 643.
27. K. L. Mulfort and J. T. Hupp, *J. Am. Chem. Soc.*, 2007, **129**, 9604.
28. T. L. A. Nguyen, T. Devic, P. Mialane, E. Rivière, A. Sonnauer, N. Stock, R. Demir-cakan, M. Morcrette, C. Livage, J. Marrot, J. M. Tarascon, and G. Ferey, *Inorg. Chem.*, 2010, **49**, 10710.
29. J. E. Halls, A. Hernán-Gómez, A. D. Burrows, and F. Marken, *Dalton Trans.*, 2012, **41**, 1475.
30. N. Lopez, H. Zhao, A. Ota, A. V. Prosvirin, E. W. Reinheimer, and K. R. Dunbar, *Adv. Mater.*, 2010, **22**, 986.
31. Y. Kobayashi, B. Jacobs, M. D. Allendorf, and J. R. Long, *Chem. Mater.*, 2010, **22**, 4120.
32. G. Férey, F. Millange, M. Morcrette, C. Serre, M.-L. Doublet, J.-M. Greneche, and J.-M. Tarascon, *Angew. Chem. Int. Ed.*, 2007, **46**, 3259.

33. K. Saravanan, M. Nagarathinam, P. Balaya, and J. J. Vittal, *J. Mater. Chem.*, 2010, **20**, 8329.
34. M. Jahan, Q. Bao, J.-X. Yang, and K. P. Loh, *J. Am. Chem. Soc.*, 2010, **132**, 14487.
35. J. Mao, L. Yang, P. Yu, X. Wei, and L. Mao, *Electrochem. Commun.*, 2012, **19**, 29.
36. L. Yang, S. Kinoshita, T. Yamada, S. Kanda, H. Kitagawa, M. Tokunaga, T. Ishimoto, T. Ogura, R. Nagumo, A. Miyamoto, and M. Koyama, *Angew. Chem. Int. Ed.*, 2010, **49**, 5348.
37. G. Givaja, P. Amo-Ochoa, C. J. Gomez-Garcia, and F. Zamora, *Chem. Soc. Rev.*, 2012, **41**, 115.
38. J. Zhao, F. Wang, P. Su, M. Li, J. Chen, Q. Yang, and C. Li, *J. Mater. Chem.*, 2012, **22**, 13328.
39. R. Das, P. Pachfule, R. Banerjee, and P. Poddar, *Nanoscale*, 2012, **4**, 591.
40. C.-Y. Su, A. M. Goforth, M. D. Smith, P. J. Pellechia, and H.-C.zur Loye, *J. Am. Chem. Soc.*, 2004, **126**, 3576.
41. J. Zhao, M. Li, J. Sun, L. Liu, P. Su, Q. Yang, and C. Li, *Chem.—Eur. J.*, 2012, **18**, 3163.
42. J. Hu, H. Wang, Q. Gao, and H. Guo, *Carbon*, 2010, **48**, 3599.
43. H.-L. Jiang, B. Liu, Y.-Q. Lan, K. Kuratani, T. Akita, H. Shioyama, F. Zong, and Q. Xu, *J. Am. Chem. Soc.*, 2011, **133**, 11854.
44. S. Ma, G. A. Goenaga, A. V. Call, and D.-J. Liu, *Chem.—Eur. J.*, 2011, **17**, 2063.
45. E. Proietti, F. Jaouen, M. Lefevre, N. Larouche, J. Tian, J. Herranz, and J.-P. Dodelet, *Nat. Commun.*, 2011, **2**, 416.
46. B. Liu, H. Shioyama, T. Akita, and Q. Xu, *J. Am. Chem. Soc.*, 2008, **130**, 5390.
47. A. Shigematsu, T. Yamada, and H. Kitagawa, *J. Am. Chem. Soc.*, 2011, **133**, 2034.
48. S. C. Sahoo, T. Kundu, and R. Banerjee, *J. Am. Chem. Soc.*, 2011, **133**, 17950.
49. F. Jaouen, E. Proietti, M. Lefevre, R. Chenitz, J.-P. Dodelet, G. Wu, H. T. Chung, C. M. Johnston, and P. Zelenay, *Energy Environ. Sci.*, 2011, **4**, 114.
50. S.-L. Li and Q. Xu, *Energy Environ. Sci.*, 2013, **6**, 1656.
51. S. Loera-Serna, M. A. Oliver-Tolentino, M. D. L. López-Núñez, A. Santana-Cruz, A. Guzmán-Vargas, R. Cabrera-Sierra, H. I. Beltrán, and J. Flores, *J. Alloys Compd.*, 2012, **540**, 113.
52. K. F. Babu, M. A. Kulandainathan, I. Katsounaros, L. Rassaei, A. D. Burrows, P. R. Raithby, and F. Marken, *Electrochem. Commun.*, 2010, **12**, 632.
53. P. M. P. de Sousa, R. Grazina, A. D. S. Barbosa, B.de Castro, J. J. G. Moura, L. Cunha-Silva, and S. S. Balula, *Electrochim. Acta*, 2013, **87**, 853.
54. G.-S. Yang, H.-Y. Zang, Y.-Q. Lan, X.-L. Wang, C.-J. Jiang, Z.-M. Su, and L.-D. Zhu, *CrystEngComm*, 2011, **13**, 1461.
55. Y. Yang, S. Liu, C. Li, S. Li, G. REn, F. Wei, and Q. Tang, *Inorg. Chem. Commun.*, 2012, **17**, 54.
56. H. Pang, J. Peng, J. Sha, A. Tian, P. Zhang, Y. Chen, and M. Zhu, *J. Mol. Struct.*, 2009, **921**, 289.
57. M. Meilikhov, K. Yusenko, and R. A. Fischer, *J. Am. Chem. Soc.*, 2009, **131**, 9644.
58. S. S.-Y. Chui, S. M.-F. Lo, J. P. H. Charmant, A. G. Orpen, and I. D. Williams, *Science*, 1999, **283**, 1148.
59. R. S. Kumar, S. S. Kumar, and M. A. Kulandainathan, *Electrochem. Commun.*, 2012, **25**, 70.
60. J. Szanyi, M. Daturi, G. Clet, D. R. Baer, and C. H. F. Peden, *Phys. Chem. Chem. Phys.*, 2012, **14**, 4383.
61. C. Streb, C. Ritchie, D.-L. Long, P. Koegerler, and L. Cronin, *Angew. Chem. Int. Ed.*, 2007, **46**, 7579.
62. S.-T. Zheng, H. Zhang, and G.-Y. Yang, *Angew. Chem. Int. Ed.*, 2008, **47**, 3909.
63. B. Nohra, H. El Moll, L. M. Rodriguez Albelo, P. Mialane, J. Marrot, C. Mellot-Draznieks, M. O'Keeffe, R. N. Biboum, J. Lemaire, B. Keita, L. Nadjo, and A. Dolbecq, *J. Am. Chem. Soc.*, 2011, **133**, 13363.
64. B. Liu, J. Yang, G.-C. Yang, and J.-F. Ma, *Inorg. Chem.*, 2013, **52**, 84.
65. P. Wang, X. Wang, and G. Zhu, *Electrochim. Acta*, 2000, **46**, 637.
66. E. Völker, E. J. Calvo, and F. J. Williams, *J. Electroanal. Chem.*, 2012, **673**, 1.
67. Y. Song, E. Wang, Z. Kang, Y. Lan, and C. Tian, *Mater. Res. Bull*, 2007, **42**, 1485.
68. M. Sadakane and E. Steckhan, *Chem. Rev.*, 1998, **98**, 219.
69. M. Nagarathinam, K. Saravanan, E. J. H. Phua, M. V. Reddy, B. V. R. Chowdari, and J. J. Vittal, *Angew. Chem. Int. Ed.*, 2012, **51**, 5866.
70. A. S. Hameed, M. Nagarathinam, M. Schreyer, M. V. Reddy, B. V. R. Chowdari, and J. J. Vittal, *J. Mater. Chem. A*, 2013, **1**, 5721.
71. M. Armand, S. Grugeon, H. Vezin, S. Laruelle, P. Ribière, P. Poizot, and J. M. Tarascon, *Nat. Mater.*, 2009, **8**, 120.
72. L. Gou, H.-X. Zhang, X.-Y. Fan, and D.-L. Li, *Inorg. Chim. Acta*, 2013, **394**, 10.
73. X. Li, F. Cheng, S. Zhang, and J. Chen, *J. Power Sources*, 2006, **160**, 542.
74. R. Demir-Cakan, M. Morcrette, F. Nouar, C. Davoisne, T. Devic, D. Gonbeau, R. Dominko, C. Serre, G. Ferey, and J.-M. Tarascon, *J. Am. Chem. Soc.*, 2011, **133**, 16154.
75. X. Ji, K. T. Lee, and L. F. Nazar, *Nat. Mater.*, 2009, **8**, 500.
76. V. Palomares, P. Serras, I. Villaluenga, K. B. Hueso, J. Carretero-González, and T. Rojo, *Energy Environ. Sci.*, 2012, **5**, 5884.
77. D. A. Stevens and J. R. Dahn, *J. Electrochem. Soc.*, 2000, **147**, 1271.
78. A. Darwiche, M. T. Sougrati, B. Fraisse, L. Stievano, and L. Monconduit, *Electrochem. Commun.*, 2013, **32**, 18.

79. A. Ponrouch, E. Marchante, M. Courty, J.-M. Tarascon, and M. R. Palacin, *Energy Environ. Sci.*, 2012, **5**, 8572.
80. N. Imanishi, T. Morikawa, J. Kondo, Y. Takeda, O. Yamamoto, N. Kinugasa, and T. Yamagishi, *J. Power Sources*, 1999, **79**, 215.
81. A. Eftekhari, *J. Power Sources*, 2004, **126**, 221.
82. Y. Lu, L. Wang, J. Cheng, and J. B. Goodenough, *Chem. Commun.*, 2012, **48**, 6544.
83. H. Lee, Y.-I. Kim, J.-K. Park, and J. W. Choi, *Chem. Commun.*, 2012, **48**, 8416.
84. C. D. Wessells, S. V. Peddada, M. T. Mc Dowell, R. A. Huggins, and Y. Cui, *J. Electrochem. Soc.*, 2012, **159**, A98.
85. M. Takachi, T. Matsuda, and Y. Moritomo, *Appl. Phys. Express*, 2013, **6**, 025802.
86. L. Wang, Y. Lu, J. Liu, M. Xu, J. Cheng, D. Zhang, and J. B. Goodenough, *Angew. Chem. Int. Ed.*, 2013, **52**, 1964.
87. C. D. Wessells, S. V. Peddada, R. A. Huggins, and Y. Cui, *Nano Lett.*, 2011, **11**, 5421.
88. C. D. Wessells, M. T. Mc Dowell, S. V. Peddada, M. Pasta, R. A. Huggins, and Y. Cui, *ACS Nano*, 2012, **6**, 1688.
89. A. L. Crumbliss, P. S. Lugg, and N. Morosoff, *Inorg. Chem.*, 1984, **23**, 4701.
90. C.-L. Chen, K.-F. Chiu, H. J. Leu, and C. C. Chen, *J. Electrochem. Soc.*, 2013, **160**, A3126.
91. D. Asakura, C. H. Li, Y. Mizuno, M. Okubo, H. Zhou, and D. R. Talham, *J. Am. Chem. Soc.*, 2013, **135**, 2793.
92. M. Okubo, D. Asakura, Y. Mizuno, T. Kudo, H. Zhou, A. Okazawa, N. Kojima, K. Ikedo, T. Mizokawa, and I. Honma, *Angew. Chem. Int. Ed.*, 2011, **123**, 6393.
93. D. Y. Lee, S. J. Yoon, N. K. Shrestha, S.-H. Lee, H. Ahn, and S.-H. Han, *Microporous Mesoporous Mater.*, 2012, **153**, 163.
94. R. Diaz, M. Gisela Orcajo, J. A. Botas, G. Calleja, and J. Palma, *Mater. Lett.*, 2012, **68**, 126.
95. Y. Wang, H. Zhong, L. Hu, N. Yan, H. Hu, and Q. Chen, *J. Mater. Chem. A*, 2013, **1**, 2621.
96. Y. Gong, T. Wu, P. G. Jiang, J. H. Lin, and Y. X. Yang, *Inorg. Chem.*, 2013, **52**, 777.
97. X. Feng, L. Chen, Y. Dong, and D. Jiang, *Chem. Commun.*, 2011, **47**, 1979.
98. O. K. Farha, A. M. Shultz, A. A. Sarjeant, S. T. Nguyen, and J. T. Hupp, *J. Am. Chem. Soc.*, 2011, **133**, 5652.
99. W. Wei, K. Yu, Z.-H. Su, Y. Yu, B.-B. Zhou, and C.-C. Zhu, *Inorg. Chem. Commun.*, 2012, **17**, 21.
100. B. Smitha, S. Sridhar, and A. A. Khan, *J. Membr. Sci.*, 2005, **259**, 10.
101. Q. Li, J. O. Jensen, R. F. Savinell, and N. J. Bjerrum, *J. Membr. Sci.*, 2009, **34**, 449.
102. J. Rozière and D. J. Jones, *Annu. Rev. Mater. Res.*, 2003, **33**, 503.
103. Y. Nagao, M. Fujishima, R. Ikeda, S. Kanda, and H. Kitagawa, *Synth. Met.*, 2003, **133**, 431.
104. T. Yamada, M. Sadakiyo, and H. Kitagawa, *J. Am. Chem. Soc.*, 2009, **131**, 3144.
105. S. Sen, N. N. Nair, T. Yamada, H. Kitagawa, and P. K. Bharadwaj, *J. Am. Chem. Soc.*, 2012, **134**, 19432.
106. J. M. Taylor, K. W. Dawson, and G. K. H. Shimizu, *J. Am. Chem. Soc.*, 2013, **135**, 1193.
107. S. Kim, K. W. Dawson, B. S. Gelfand, J. M. Taylor, and G. K. H. Shimizu, *J. Am. Chem. Soc.*, 2013, **135**, 963.
108. J. A. Hurd, R. Vaidhyanathan, V. Thangadurai, C. I. Ratcliffe, I. L. Moudrakovski, and G. K. H. Shimizu, *Nat. Chem.*, 2009, **1**, 705.
109. B. Wu, X. Lin, L. Ge, L. Wu, and T. Xu, *Chem. Commun.*, 2013, **49**, 143.
110. S. Bureekaew, S. Horike, M. Higuchi, M. Mizuno, T. Kawamura, D. Tanaka, N. Yanai, and S. Kitagawa, *Nat. Mater.*, 2009, **8**, 831.
111. M. Sadakiyo, T. Yamada, and H. Kitagawa, *J. Am. Chem. Soc.*, 2009, **131**, 9906.
112. C. Dey, T. Kundu, and R. Banerjee, *Chem. Commun.*, 2012, **48**, 266.
113. V. G. Ponomareva, K. A. Kovalenko, A. P. Chupakhin, E. S. Shutova, and V. P. Fedin, *Solid State Ionics*, 2012, **225**, 420.
114. V. G. Ponomareva, K. A. Kovalenko, A. P. Chupakhin, D. N. Dybtsev, E. S. Shutova, and V. P. Fedin, *J. Am. Chem. Soc.*, 2012, **134**, 15640.
115. M. G. Goesten, J. Juan-Alcaniz, E. V. Ramos-Fernandez, K. B. S. S. Gupta, E. Stavitski, H.van Bekkum, J. Gascon, and F. Kapteijn, *J. Catal.*, 2011, **281**, 177.
116. S. W. Li, Z. Zhou, Y. L. Zhang, M. L. Liu, and W. Li, *Chem. Mater.*, 2005, **17**, 5884.
117. J. M. Taylor, R. K. Mah, I. L. Moudrakovski, C. I. Ratcliffe, R. Vaidhyanathan, and G. K. H. Shimizu, *J. Am. Chem. Soc.*, 2010, **132**, 14055.
118. S. J. Yang, T. Kim, J. H. Im, Y. S. Kim, K. Lee, H. Jung, and C. R. Park, *Chem. Mater.*, 2012, **24**, 464.
119. L. Chen, J. Bai, C. Wang, Y. Pan, M. Scheer, and X. You, *Chem. Commun.*, 2008, 1581.
120. W. Chaikittisilp, M. Hu, H. Wang, H.-S. Huang, T. Fujita, K. Wu, L.-C. Chen, Y. Yamauchi, and K. Ariga, *Chem. Commun.*, 2012, **48**, 7259.
121. B. Liu, H. Shioyama, H. Jiang, X. Zhang, and Q. Xu, *Carbon*, 2010, **48**, 456.
122. A. Almasoudi and R. Mokaya, *J. Mater. Chem.*, 2012, **22**, 146.
123. X. W. Lou, D. Deng, J. Y. Lee, and L. A. Archer, *J. Mater. Chem.*, 2008, **18**, 4397.
124. B. Liu, X. Zhang, H. Shioyama, T. Mukai, T. Sakai, and Q. Xu, *J. Power Sources*, 2010, **195**, 857.
125. G. Goenaga, S. Ma, S. Yuan, and D.-J. Liu, *ECS Trans.*, 2010, **33**, 579.

126. W. Chaikittisilp, K. Ariga, and Y. Yamauchi, *J. Mater. Chem. A*, 2013, **1**, 14.

127. H.-K. Youn, J. Kim, and W.-S. Ahn, *Mater. Lett.*, 2011, **65**, 3055.

128. P. Simon and Y. Gogotsi, *Nat. Mater.*, 2008, **7**, 845.

129. F. Zhang, L. Hao, L. Zhang, and X. Zhang, *Int. J. Electrochem. Sci.*, 2011, **6**, 2943.

130. F. M. Courtel, H. Duncan, Y. Abu-Lebdeh, and I. J. Davidson, *J. Mater. Chem.*, 2011, **21**, 10206.

131. J. P. Dodelet, in 'N4-Macrocyclic Metal Complexes', eds J. H. Zagal, F. Bedioui and J. P. Dodelet, Springer, New York, 2006, p. 83.

132. J. Tian, A. Morozan, M. T. Sougrati, M. Lefevre, R. Chenitz, J.-P. Dodelet, D. Jones, and F. Jaouen, *Angew. Chem. Int. Ed.*, 2013, **52**, 6867.

133. H. H. Fei, J. F. Cahill, K. A. Prather, and S. M. Cohen, *Inorg. Chem.*, 2013, **52**, 4011.

134. L. Zhang and Y. H. Hu, *J. Phys. Chem. C*, 2011, **115**, 7967.

135. M. Lefèvre and J.-P. Dodelet, *221st ECS Meeting*, Seattle, Washington, 2012, pp. 35–44.

136. S. Yuan, J.-L. Shui, L. Grabstanowicz, C. Chen, S. Commet, B. Reprogle, T. Xu, L. Yu, and D.-J. Liu, *Angew. Chem. Int. Ed.*, 2013, 52. DOI: 10.1002/anie.201302924.

Applications of Metal-Organic Frameworks to Analytical Chemistry

Na Chang

Tianjin Polytechnic University, Tianjin, PR China

Cheng-Xiong Yang and Xiu-Ping Yan

Nankai University, Tianjin, PR China

1	Introduction	443
2	MOFs for Sample Preparation	443
3	MOFs for Gas Chromatography (GC)	446
4	MOFs as Tandem Molecular Sieves for SPME Coupled with GC	449
5	MOFs for High-Performance Liquid Chromatography (HPLC)	449
6	Conclusions	454
7	Related Articles	454
8	Abbreviations and Acronyms	454
9	References	454

1 INTRODUCTION

Metal-organic frameworks (MOFs) are an emerging class of porous materials constructed from metal ions or clusters and organic ligands. Owing to a number of remarkable properties, such as permanent nanoscale porosity, diverse structures, uniform channels, and cavities, MOFs are now widely explored as advanced materials for diverse applications, including hydrogen storage,[1,2] gas separation,[3–5] catalysis,[6–10] sensing,[11–14] imaging,[15,16] and drug delivery and release.[17–19]

Recently, great progress has been made for the applications of MOFs in analytical chemistry. The possibility of tuning the pore size and geometry, together with the exceptionally high surface area, pore volumes, solvent stability, and the semiorganic frameworks, make MOFs very suitable candidate materials for adsorption and adsorption-based separation applications, including sampling, sample preconcentration, gas chromatographic separation, and liquid chromatographic separation. The results reveal that MOFs are attractive as high-efficient adsorbents and advanced separation media for the targets of environmental, biological, or industrial importance. This chapter focuses on the research of the analytical applications of MOFs and highlights the ability of MOFs in all the important aspects of modern analytical chemistry that are mentioned above (Table 1).

2 MOFs FOR SAMPLE PREPARATION

2.1 MOFs for Sampling and Solid-Phase Extraction (SPE)

Isoreticular MOF (IRMOF)-1 was applied as the sorbent for trapping and preconcentration of standard dimethyl methylphosphonate (DMMP) with high selectivity, adsorption capacity and enrichment factor, and fast adsorption kinetics.[20] The high selective and fast adsorption of DMMP on IRMOF-1 was attributed to the single binding site for DMMP in IRMOF-1 and the strong dipole–dipole interactions between DMMP and the IRMOF-1 frameworks.[20] MOF-5-packed quartz tubes was also reported for in-field sampling and

Metal-Organic Framework Materials. Edited by Leonard R. MacGillivray and Charles M. Lukehart.
© 2014 John Wiley & Sons, Ltd. ISBN 978-1-119-95289-3

Table 1 Applications of MOFs in analytical chemistry

Analytical applications		MOFs	References
Sample preparation	Sampling and solid-phase extraction (SPE)	MOF-5 (IRMOF-1), Copper(II) isonicotinate, $Zn(BTA)_2$, MIL-53, MIL-100, MIL-101, Gd(DPA)(HDPA), $Zn(BDC)(H_2O)_2$, $(La_{0.9}Eu_{0.1})_2(DPA)_3(H_2O)_3$, $Cu_3(BTC)_2$ (MOF-199)	20–31
	Solid-phase microextraction (SPME)	MOF-199, MAF-X8, MIL-53, ZIF-90	32–35
	Micro-solid-phase extraction (μ-SPE)	ZIF-8	36–38
Gas chromatography (GC)	Packed column GC	MOF-508, CUK-1, MIL-47, MIL-53, ZIF-8, IRMOF-1	39–45
	Capillary GC	MIL-101, IRMOF-1, IRMOF-3, MIL-100, ZIF-8, UIO-66, MOF-CJ3, HKUST-1 (MOF-199)	46–53
	Chiral GC	$\{Cu(sala)\}_n$, $Co(D\text{-}Cam)_{1/2}(bdc)_{1/2}(tmdpy)$	54, 55
Sample preparation together with GC	SPME coupled with GC	ZIF-8 coupled with ZIF-8, ZIF-7 coupled with MIL-101	56
High-performance liquid chromatography	Normal-phase high-performance liquid chromatography	MIL-47, MIL-53, MOF-199, MOF-5, MIL-101, Bn-ChirUMCM-1, $[(CH_3)_2NH_2][Cd(bpdc)_{1.5}]$ 2DMA	57–68
	Reverse-phase high-performance liquid chromatography	MIL-53, ZIF-8	69, 70
	Normal- and reverse-phase high-performance liquid chromatography	MIL-100	71
	MOFs composites for high-performance liquid chromatography	$Cu_3(BTC)_2$ (MOF-199), ZIF-8, UIO-66, $Cu_2(BDA)_2$	72–75

preconcentration of atmospheric formaldehyde before thermal desorption gas chromatography–mass spectrography (TD-GC/MS) determination without the need for any chemical derivatization.[21] MOF-5 gave 53 and 73 times better preconcentration factor than Tenax TA and Carbograph 1TD, respectively. The high-efficient preconcentration of formaldehyde on MOF-5 likely resulted from their large surface area and the Zn metal sites. The developed MOF-5-based TD-GC/MS method offered excellent performance with wide linear range, high sensitivity, and good reproducibility in the determination of trace formaldehyde in local indoor and outdoor air samples.

The first example of the utilization of MOFs for solid-phase extraction (SPE) was reported by Yan's group in 2006.[22] Copper(II) isonicotinate $[Cu(4\text{-}C_5H_4N\text{-}COO)_2(H_2O)_4]$ MOF was dry-packed in a precolumn for flow injection SPE on-line coupled with high-performance liquid chromatography (HPLC) for the determination of trace polycyclic aromatic hydrocarbons (PAHs) in coal fly ash and local water samples. Enhancement factors from 200 to 2337 for the studied PAHs ranged were achieved, depending on the shape, size, and hydrophobic property of the PAHs. Recently, $Zn(BTA)_2$ (BTA = benzotriazole)[23] and MOF-5[24] were also explored as novel sorbents for the SPE of trace benzo[α]pyrene in edible oils[23] and PAHs in environmental matrices,[24] respectively.

Mesoporous, well-defined structured MOFs make the adsorption and separation of large biomolecules feasible, such as the efficient enrichment of low-abundance peptides from complex biological samples, which is of great importance in peptidomics research. Gu *et al.*[25] showed the first example of MOF-based enrichment of peptides with simultaneous exclusion of proteins from complex biological samples for subsequent analysis by matrix assisted laser desorption/ionization time of flight mass spectrometry (MALDI-TOF-MS). Cage such as mesoporous Matérial Institut Lavoisier (MIL)-101, MIL-100, and 1D diamond-shaped channel MOFs MIL-53 were used as the sorbents for the extraction of peptides. All of MIL-53, MIL-100, and MIL-101, which have high surface area, large pores, and good chemical stability, gave good reproducibility for the high efficiency and size-selective enrichment of peptides from human plasma and urine samples. These MOFs also showed good ability to exclude proteins (Figure 1).

MOFs were also applied for matrix solid-phase dispersion extraction (MSPDE).[26–28] MSPDE methods based on several MOFs such as Gd(DPA)(HDPA), $Zn(BDC)(H_2O)_2$, and $(La_{0.9}Eu_{0.1})_2(DPA)_3(H_2O)_3$ were developed for the extraction and determination of pesticide residues in medicinal plant and vegetables. The MOFs gave better or similar performance for the pesticides tested than conventional neutral alumina or commercial phase C_{18}-bonded silica.[26–28]

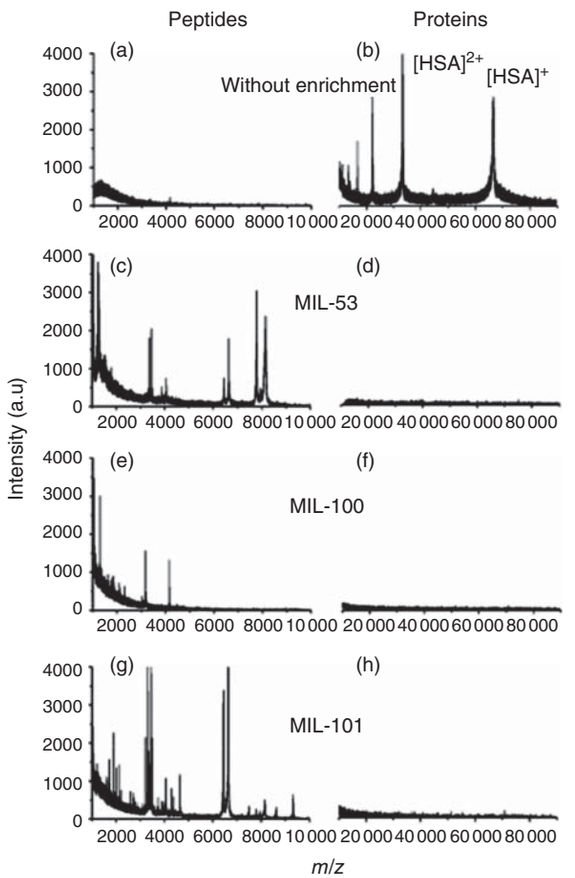


Figure 1 Mass spectra of a human plasma sample obtained by MALDI-TOF-MS before enrichment (a, b) and after enrichment with MIL-53 (c, d), MIL-100 (e, f), and MIL-101 (g, h) in the molecular weight range 1–10 kDa (a, c, e, g) and 10–90 kDa (b, d, f, h). (Reproduced with permission from Ref. 25. © Royal Society of Chemistry, 2011.)

Considering the unique properties of MOFs, subtle coupling of MOFs and magnetic nanoparticles for magnetic solid-phase extraction (MSPE) is interesting and significant for SPE applications. Huo and Yan[29] reported a facile magnetization of MIL-101 using an easy in situ ultrasonic dispersing and mixing method for rapid MSPE of PAHs in environmental water samples. The resulted material, Fe_3O_4@SiO_2-MIL-101, showed large enrichment factor, wide linear range, and good reproducibility toward the extraction and determination of PAHs in water. The effective adsorption of PAHs was attributed to the hydrophobic and π–π interactions between the PAHs and the framework terephthalic acid molecules, and the π-complexation between PAHs and the Lewis acid sites in the pores of MIL-101.[29] Sohrabi *et al*. reported the synthesis and utilization of the magnetic MOF Fe_3O_4–pyridine nanocomposite [(Fe_3O_4–Pyridine)/Cu_3(BTC)$_2$] as a novel adsorbent for fast separation and preconcentration of Pd(II), Cd(II), and Pb(II) ions in various matrixes.[30,31]

2.2 MOFs for Solid-Phase Microextraction (SPME)

The first example that introduced MOFs into solid-phase microextraction (SPME) was reported by Yan's group.[32] A homemade SPME device was prepared from a commercial 5 μL gas chromatography (GC) microsyringe. The SPME fiber was fabricated by in situ hydrothermal growth method with MOF-199 thin films grown homogeneously on etched stainless steel wire. The resulted MOF-199-coated fiber exhibited high affinity, wide linearity, and excellent reproducibility for the SPME of benzene homologues. The in situ hydrothermal growth method was also used by He *et al.*[33] to fabricate MAF-X8-coated SPME fiber for highly sensitive and selective extraction of nonpolar volatile organic compounds, such as benzene, toluene, ethylbenzene, and *o*-xylene.

The above-mentioned in situ hydrothermal growth approach is a simple and facile method to fabricated MOF-based SPME fiber, and the fiber was coated barely by pure MOF materials. However, in some cases, MOFs cannot grow homogeneously on the fiber, or even cannot grow on the fiber, for example, the particle sizes of MOFs were too large to be held on the fiber. For this reason, Chen *et al.*[34] fabricated MIL-53(Al, Cr, Fe)-coated fibers by an adhesive method. The polished stainless steel was firstly inserted into epoxy resin glue, and then inserted into the prepared MIL-53 to make MIL-53 adhered to the SPME fiber. The fabricated MIL-53 fiber was further revealed for the SPME of PAHs in water samples. Among the three MIL-53 coatings, MIL-53(Al) showed the highest extraction efficiency toward PAHs. In addition, Yu and Yan[35] reported a novel covalent bonding approach to fabricate a robust zeolitic imidazolate framework (ZIF)-90 coating for SPME (Figure 2). The ZIF-90-bonded SPME fiber was applied to the enrichment of phenolic endocrine disruptors from water and soil samples. As a result, the ZIF-90-bonded fiber exhibited high enhancement factors, wide linearity, excellent reproducibility, and good lifetime for the extraction of polar endocrine disruptors.

2.3 MOFs for Micro-solid-phase Extraction (μ-SPE)

SPME is a fast, simple, and green sample preparation technique that can easily combine the process of sample preconcentration and GC or HPLC determination. However, in some cases, it still has difficulty in the fabrication of SPME fibers. In 2006, Lee's group reported a novel extraction and preconcentration technique termed micro-solid-phase extraction (μ-SPE), based on the packing of sorbent material in a sealed porous polypropylene membrane envelope.[76] Recently, Lee's group reported

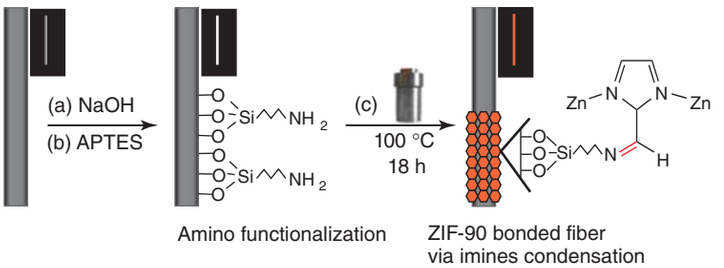


Figure 2 Schematic demonstration for fabricating a ZIF-90-bonded SPME fiber. (Reproduced from Ref. 35 with permission of The Royal Society of Chemistry. DOI: 10.1039/C3CC00123G.)

the utilization of ZIF-8 as novel sorbent for μ-SPE of PAHs in environmental water samples,[36] and sonication-assisted emulsification microextraction combined with vortex-assisted porous-membrane-protected μ-SPE (SAE-VA-μ-SPE) for the extraction and determination of PAHs and acidic drugs from environmental water samples.[37,38]

3 MOFs FOR GAS CHROMATOGRAPHY (GC)

3.1 MOFs for Packed Column GC

The tunable pore size, high thermal stability, and selective adsorption ability make MOFs potentially useful for GC. Chen's[39] group showed the first example of gas chromatographic separation of linear and branched isomers of pentane and hexane, because of their availability and industrial relevance in petroleum refining based on MOF-508-packed column. As the 4.0×4.0 Å cross section of the 1D channels in the guest-filled phase MOF-508 is slightly larger than a methane molecule (3.8×3.8 Å), these isomers were partially separated on MOF-508-packed column, with linear alkanes (*n*-pentane, *n*-hexane) eluted later than their branched isomers. The selective GC separation of alkanes on the MOF-508 column results from their different van der Waals interactions with the microporous MOF-508 walls, which arises from the subtle matching of the size and shape of the alkanes with the MOF-508 micropores.

The above investigation brought a bright future in the application of MOFs in GC separation. Chang and Wood's group investigated the unusual and selective sorption properties of light gases on another MOF material, CUK-1.[40] This MOF material has an intricate structure that made it a good candidate for gas chromatographic separation applications. The dehydrated CUK-1 showed large differences in the adsorption isotherms of several probe gases, such as CO_2 (3.3 Å), O_2 (3.46 Å), N_2 (3.64 Å), Ar (3.40 Å), and CH_4 (3.8 Å), despite only relatively small differences in the kinetic diameters. Specially, CUK-1 was selective for the adsorption of O_2 over N_2 and Ar at 87 K and CO_2 over CH_4 at 298 K, suggesting that the material might behave as a size-selective molecular sieve. The larger molecules, such as Ar, N_2, and CH_4 with revealed very low uptakes at low temperatures, indicated that these gases were barely adsorbed in the pores at low temperature and the adsorption mainly occurred on the external surface. On the basis of the differences in adsorption, a column packed with CUK-1 was fabricated for gas chromatographic separation of light gases, which gave a good separation performance.

Except for gas chromatographic separation, MOFs-based GC-packed columns were also fabricated for the investigation of adsorption characteristics and mechanism. However, the separation performance was usually unsatisfied because the theoretical plate number of the MOF-packed column was always very low.[41–45]

3.2 MOFs for Capillary GC

All of the above pioneer works on the utilization of MOFs as the stationary phase for GC have been performed on packed columns. However, packed columns usually result in low resolution due to peak broadening, and thereby impair the separation efficiency of MOFs. Moreover, gram-scale MOFs are needed for such one packed column, leading to high-cost applications of MOFs as stationary phases in chromatographic separation. In contrast, capillary columns, either the wall-coated open tubular (WCOT) columns or the porous layer open tube (PLOT) columns, permit a thin film of MOFs coated on their inner walls, thus improving the resolving power of MOFs and saving the dosage of MOFs in GC applications.

Yan's group reported the first example of MOF-coated capillary column for high-resolution GC separation.[46] MIL-101 was chosen as the stationary phase, and the MIL-101 crystals were coated on the capillary column by a dynamic coating method. A slurrylike suspension solution of MIL-101 is first filled into the capillary under gas pressure, and then pushed through the capillary at a steady speed, leaving a wet coating layer on the

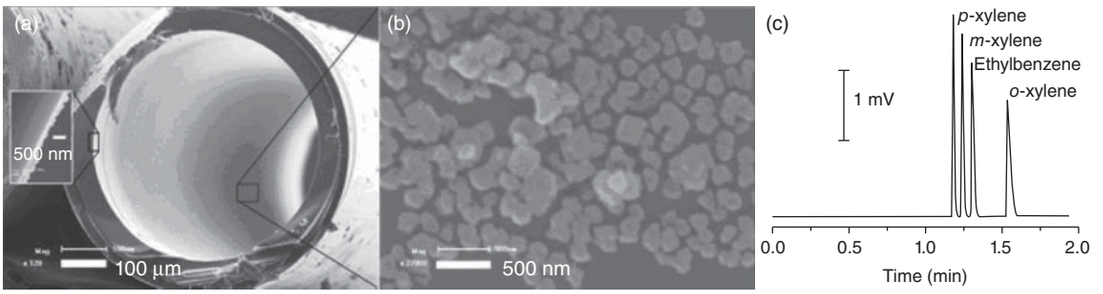


Figure 3 SEM images of (a) the cross section of the MIL-101-coated capillary column, the inset shows the thickness of the MIL-101 coating. (b) The MIL-101 deposited on the inner wall of the capillary column. (c) GC chromatograms on the MIL-101-coated capillary column (15-m long × 0.53-mm i.d.) for the separation of xylene isomers and ethylbenzene at 160 °C under a N_2 flow rate of 3 mL min^{-1}. (Reproduced with permission from Ref. 46. © Wiley-VCH Verlag GmbH & Co. KGaA, Weinheim, 2010.)

inner surface of the capillary to form a homogeneous coating of MOF particles. The fabricated capillary column had an approximate 0.4-μm MIL-101 coating on the inner wall (Figure 3a, b). The MIL-101-coated capillary column showed high resolution and selectivity for the separation of xylene isomers and ethylbenzene in <1.6 min without temperature programming (Figure 3c). The capability of the MIL-101-coated capillary column was further revealed by high-resolution GC separation of other two isomer mixtures of substituted benzene derivatives (*o*-, *m*-, *p*-chlorotoluene and 1,3,5-trimethylbenzene, *n*-proppylbenzene, and isopropylbenzene) and a mixtures *n*-alkanes with a broad range of boiling points. The results show a very promising application of MOFs for high-resolution capillary GC separation.

Yan's group also fabricated a series of MOF-based capillary columns for GC separation.[47,48] Gu *et al.*[47] developed a new method that allowed the synthesis of well-shaped nanosized IRMOFs within 1 min at room temperature without the need for any activation procedure or auxiliary stabilizing agents. The resulting nanosized IRMOFs were used to fabricate the IRMOF-coated capillary columns by dynamic coating method for the high-resolution GC separation of persistent organic pollutants (POPs), including polychlorinated biphenyls (PCBs), PAHs, polybrominated diphenylethers (PBDEs), and hexachlorocyclohexanes (HCHs). The IRMOF-coated capillary columns offered good separation efficiency that is generally comparable to that of a commercial HP-5MS column for POPs (Figure 4). Fan and Yan[48] fabricated MIL-100(Fe)- and MIL-100(Cr)-coated capillary columns for capillary GC separation of alkane isomers. MIL-100(Fe) and MIL-100(Cr) have identical organic linker and Mobil Thirty-Nine zeolitic type, but different metal ions. MIL-100(Fe)-coated capillary column showed great capability and high efficiency for the gas chromatographic separation of alkane isomers without the need of temperature-programming, whereas MIL-100(Cr)-coated capillary column gave poor performance for the separation.[48]

Chang *et al.*[49] fabricated the ZIF-8-coated capillary GC column and observed the molecular sieving effect when separating for alkanes. ZIF-8-coated capillary had the ability for sieving branched alkanes from linear alkanes along with high-resolution GC separation of linear alkanes (Figure 5). The six-membered-ring pore windows of ZIF-8 (about 3.4 Å) which is similar to the critical diameters of linear alkanes are accessible to linear alkanes, but not to the branched alkanes. As a result, linear alkanes are much more strongly retained on the ZIF-8 capillary column than the branched alkanes with the same number of carbon atoms, and are baseline separated from the branched alkanes (Figure 5a, b). Moreover, linear alkanes are also baseline separated on the ZIF-8-coated capillary column (Figure 5d).

The reverse shape selectivity of MOFs was also observed when introducing University of Oslo (UIO)-66 into the GC separation of hydrocarbons.[50] The pore window of the octahedral cavities of UIO-66 is 7 Å, which is accessible to all of the hexane and heptane isomers. However, the elution sequence of hexane isomers is quite different from ZIF-8, MOF-5, and other commercial GC capillary columns.[50] The linear alkanes, hexane, and heptane, eluted first from UIO-66 column, with other branched isomers retained more on UIO-66 column, which performs as reverse shape selectivity. The moderate pore size of UIO-66 (11 Å) makes the adsorbed branched alkanes have a closer distance and stronger Van der Waals interaction with the inside walls, leading to the reverse shape selectivity.

Except for the above work of Yan's group, Fang *et al.*[51] fabricated the MOF-CJ3 capillary via the same dynamic coating procedure with good separation of linear and branched alkanes, as well as aromatic positional isomers.

However, all the above established chromatographic capillaries were coated with micro- or nano-sized

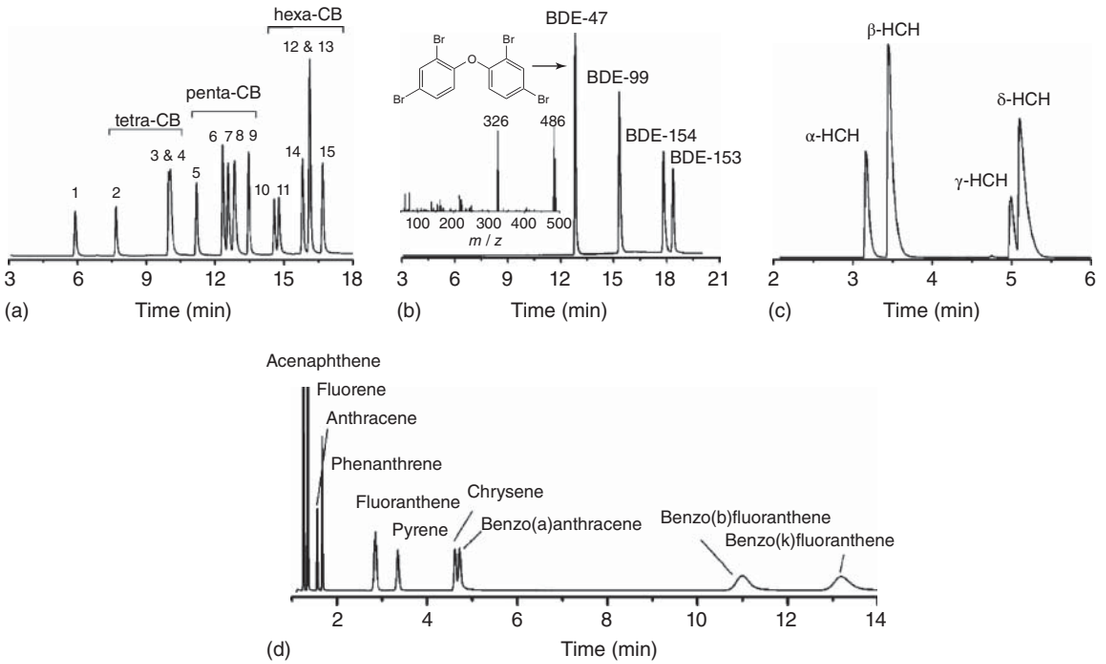


Figure 4 High-resolution GC separation of POPs on an IRMOF-1-coated capillary column (25-m long × 250-μm i.d.). (a) Separation of PCBs using a three-step temperature program: 180 °C for 2 min, then increasing 5 °C min^{-1} to 290 °C, and finally 290 °C for the remainder of the measurement; (b) separation of PBDEs using a three-step temperature program: 180 °C for 2 min, then increasing 5 °C min^{-1} to 310 °C, and finally 310 °C for the remainder of the measurement; (c) separation of HCH isomers using a three-step temperature program: 200 °C for 2 min, then increasing 10 °C min^{-1} to 280 °C, and finally 280 °C for the remainder of the measurement; (d) separation of PAHs at 300 °C. (Reprinted with permission from Ref. 47. Copyright (2011) American Chemical Society.)

MOFs materials. Recently developed MOF surface-coating techniques, the controlled secondary building units approach (CSA) for the generation of MOFs, and the use of self-assembled monolayers (SAMs) have been combined to generate a wall-bonded, cross-linked stationary phase for gas chromatographic capillary columns by Mertens's group.[52,53] The MOF-5-CSA-coated GC-fused silica capillary[52] were equivalent compared to the commercial Al_2O_3-based PLOT column for analytical natural gas separation, with respect to separation time, separation power, and chromatographic resolution. Hong Kong University of Science and Technology (HKUST)-1 that possesses open metal sites was also used to make PLOT column, by the same CSA.[53] The HKUST-1-based column gave excellent performance ability for the separation of small aromatic compounds, including benzene, toluene, ethylbenzene, and *o*-, *m*-, *p*-xylene.

3.3 MOFs for Chiral GC

Chirality is one of the major phenomena in nature, and tremendous research effort has been devoted to the development of chiral recognition technology, including research and development of chiral recognition materials. As a good choice for GC stationary phase, chiral MOFs should made good performance in the separation of racemic compounds. Yuan's group have devoted to the investigation of GC separation of racemic mixture on chiral MOF-based capillary. A chiral MOF, $\{Cu(sala)\}_n$ (H_2sala = *N*-(2-hydroxybenzyl)-L-alanine) capillary column was fabricated by a dynamic coating method for high-resolution GC separation.[54] The most important advantage of this stationary phase in GC is its enantioselective ability. Eleven racemates were rapidly separated on $\{Cu(sala)\}_n$-coated column, including aldehyde, ketone, organic acid, amino acid, and alcohol. Another chiral MOF, $Co(D\text{-}Cam)_{1/2}(bdc)_{1/2}(tmdpy)$ (D-Cam = D-camphoric acid; bdc = 1,4-benzenedicarboxylate; tmdpy = 4,4′-trimethylenedipyridine)-coated capillary column was also fabricated for high-resolution GC separation.[55] As a result, seven tested racemates were separated on $Co(D\text{-}Cam)_{1/2}(bdc)_{1/2}(tmdpy)$-coated capillary, including citronellal, limonene, glutamic acid, proline, 1-phenylenthanol, 1-phenyl-1,2-ethanediol, and 2-amino-1-butanol. Thus, the 3D MOFs with integrated homochiral features have the potential for enhanced chiral recognition and enantioselectivity. The chiral MOF-based stationary phase has excellent chiral recognition ability

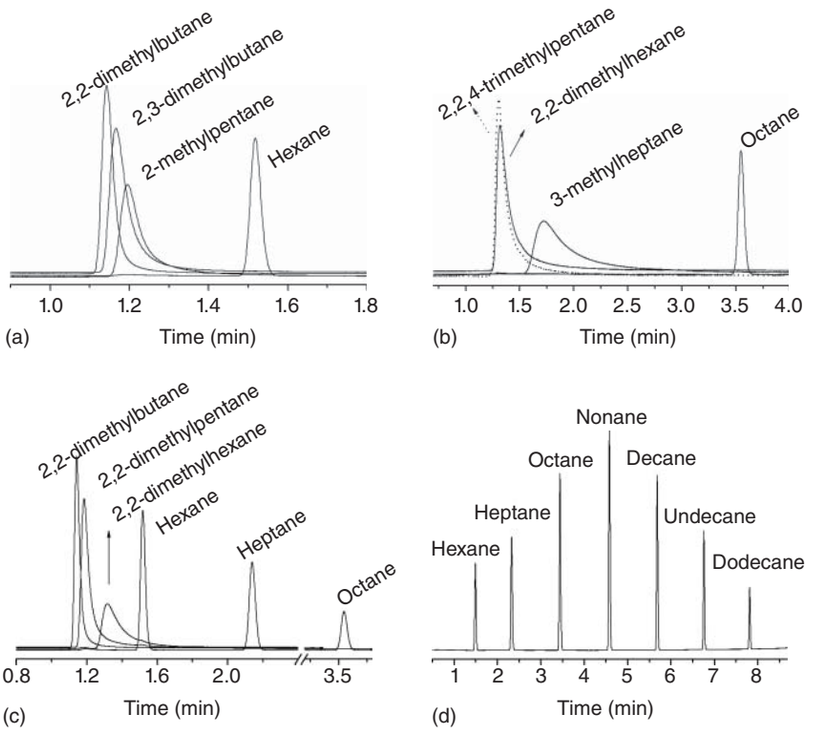


Figure 5 Chromatograms on the ZIF-8-coated capillary (20-m long × 0.25-mm i.d.) for GC separation of (a) hexane and its branched isomers, (b) octane and its branched isomers, (c) 2,2-dimethyl-branched alkanes and linear alkanes at a N_2 flow rate of 1 mL min^{-1} under 170 °C, and (d) linear alkanes at a N_2 flow rate of 1.5 mL min^{-1} using a temperature program: 140 °C for 1 min, then 20 °C min^{-1} to 290 °C for the remainder. (Reproduced with permission from Ref. 49. © 2010 American Chemical Society, 2010.)

toward racemates due to the steric fit of the chiral microenvironment of chiral MOFs with the molecular chirality.

4 MOFs AS TANDEM MOLECULAR SIEVES FOR SPME COUPLED WITH GC

Owing to the well-defined pore structures and small pore apertures, MOFs should have great potential to selectively adsorb and separate specially sized or shaped targets on the basis of the molecular sieve effect of size exclusion mechanism. Combination of various MOFs as tandem molecular sieves for extraction in conjunction with chromatographic separation would be promising for the analysis of complicated samples. Yan's group showed the first example of MOF-based tandem molecular sieves as a dual platform for SPME in combination with capillary GC to achieve both selective extraction and high-resolution GC separation of target analytes in complex matrixes.[56] MOF-coated SPME fibers and stationary phases of GC capillaries were fabricated to separate *n*-alkanes and benzene derivatives. Elegant combination of ZIF-8-coated fiber for SPME with ZIF-8-coated capillary for GC allows selective extraction and separation of *n*-alkanes from complex matrices such as petroleum-based fuel and biological fluids (Figure 6). Optimum results for the extraction and separation of substituted benzene derivatives were observed from a combination of ZIF-7-coated fiber SPME and MIL-101-coated capillary GC.

5 MOFs FOR HIGH-PERFORMANCE LIQUID CHROMATOGRAPHY (HPLC)

The large surface area, semiorganic pore walls, tunable pore size, and unique adsorption selectivity also make MOFs potential as novel stationary phases in HPLC.[77] Since the first example of MOF-based liquid chromatographic separation reported by Nuzhdin *et al.*[78] in 2007, the application of MOFs in HPLC separation has received increasing attention.

5.1 MOFs for Normal-Phase HPLC

The first example of MOFs for normal-phase (NP) HPLC was reported by Alaerts *et al.*[57] in 2007. A 5-cm

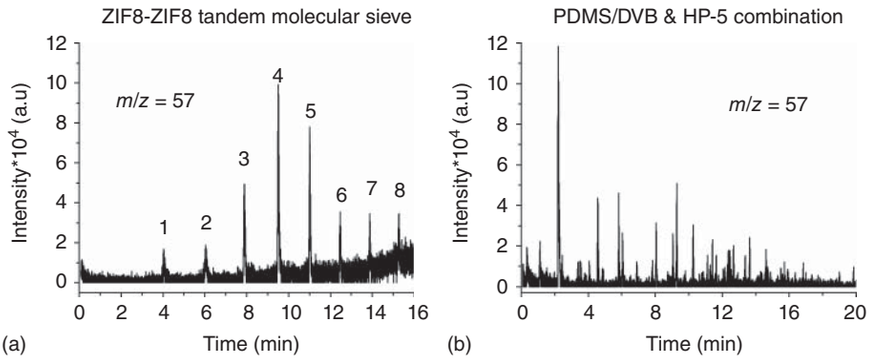


Figure 6 EIC of a human serum sample using: (a) tandem ZIF-8 molecular sieve platform (ZIF-8 based SPME followed by ZIF-8 based GC separation) with MS detection. GC separation was carried out on the ZIF-8-coated capillary column (20 m long × 0.25 mm i.d.) at a He flow rate of 1 mL min^{-1} using temperature programming (80 °C for 1 min, then 10 °C min^{-1} to 290 °C). 1: hexane; 2: heptane; 3: octane; 4: nonane; 5: decane; 6: undecane; 7: dodecane; 8: tridecane; (b) combination of commercial PDMS/DVB SPME fiber with HP-5 capillary (30-m long × 0.25-mm i.d.) with MS detection. GC separation was carried out at a He flow rate of 1 mL min^{-1} using temperature programming (30 °C for 3 min, then 5 °C min^{-1} to 250 °C). (Reprinted with permission from Ref. 56. Copyright (2011) American Chemical Society.)

long column packed with MIL-47 (0.25–2.0 μm) was used for HPLC separation of ethylbenzene and xylene isomers. Baseline separation of ethylbenzene, *m*-xylene, and *p*-xylene was achieved on MIL-47-packed column using hexane as the mobile phase. The interactions between the CH_3 group and the terephthalate ligand, and the molecular packing effects and hydrophobic nature of MIL-47 pores make MIL-47 highly selective for *p*-xylene. The remarkable properties of MIL-47 are favorable for its future application in adsorption and HPLC separation of ethylbenzene and xylene isomers.

Microporous aluminum terephthalate MIL-53 for HPLC separation of xylenes and ethylbenzene, ethyltoluenes, and cymenes was also reported by Alaerts *et al.*[58] in 2008. Compared to the structurally similar MIL-47, the selectivities of alkylaromatics on MIL-53 are different. MIL-53 has the largest adsorption affinity for the ortho-isomer among each group of alkylaromatic compounds. Separations of ortho-compounds from the other isomers were realized on a MIL-53-packed column using hexane as the mobile phase. As evidenced by Rietveld refinements, specific interactions of the xylenes with the pore walls of MIL-53 determine the selectivity. Alaerts *et al.*[59,60] also studied the MIL-47-packed column for selective separation of xylenes and other functionalized aromatics.

Although MIL-47 and MIL-53 have analogous structures, their separation mechanisms are quite different. Maes *et al.*[61] evaluated their HPLC separation mechanisms of ethylbenzene and styrene on the MIL-47 and MIL-53 columns. Despite that, these MOFs are both capable for separating ethylbenzene and styrene, the reason for preferential adsorption of styrene compared to ethylbenzene is quite different. For MIL-47, the separation is of a nonenthalpic nature, whereas for MIL-53, the origin of the preferential adsorption of styrene is related to the enthalpy effect.

The regular and rigid pore structures also make MOFs good shape and size selectivity for HPLC separation. Ahmad *et al.*[62] reported the separation of benzene, naphthalene, anthracene, phenanthrene, pyrene, 1,3,5-triphenylbenzene, and 1,3,5-tris(4-bromophenyl)benzene on MOF-199- and MOF-5-packed columns based on the combination of molecular sieving and adsorption effects. Separation of ethylbenzene and styrene with very similar dimensions was also achieved on MOF-199 column. Unlike shape and size selectivity mechanisms, the separation of ethylbenzene and styrene was ascribed to the π-complexation of styrene with Cu metal site in MOF-199.

All of the above MOFs HPLC separations have been performed on the dry-packed columns and eluted exclusively with single pure solvent, although the composition of the mobile phase can play significant roles in retention, selectivity, and resolution in HPLC. Yang and Yan[63] report the slurry-packed MIL-101(Cr) column for HPLC separation of substituted aromatics. High-resolution separation of ethylbenzene and xylene, dichlorobenzene and chlorotoluene isomers, and ethylbenzene and styrene was achieved on MIL-101(Cr)-packed column using binary solvent as the mobile phase. A column efficiency of 20 000 plates per meter for ethylbenzene was obtained on MIL-101(Cr)-packed column. The MIL-101(Cr) offered high affinity for the ortho-isomer, allowing fast and selective separation of ortho-isomer from other isomers within 3 min. The separation of xylene, dichlorobenzene, and chlorotoluene on MIL-101(Cr) was controlled by entropy change, whereas the separation of ethylbenzene and styrene on MIL-101(Cr) was governed by enthalpy change. Yang *et al.*[64] also studied the HPLC

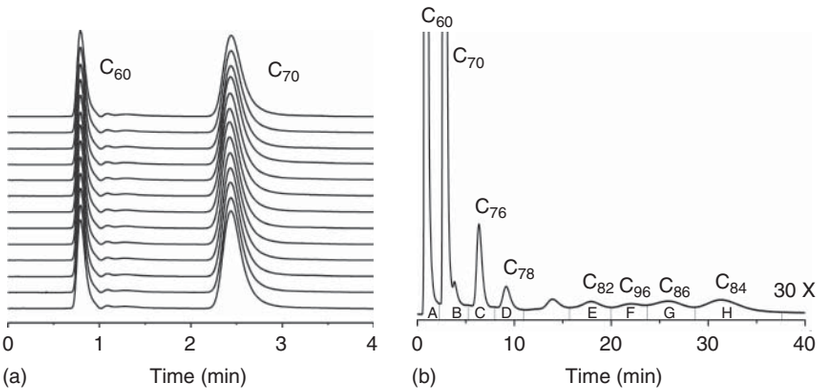


Figure 7 Chromatograms for (a) 13 replicate HPLC separations of C60 and C70 and (b) separation of the fullerenes in the toluene solution of carbon soot (2.63 mg mL^{-1}) on a MIL-101(Cr)-packed column (5-cm long × 4.6-mm i.d.) at room temperature using a dichloromethane/acetonitrile (98:2) as the mobile phase at a flow rate of 1 mL min^{-1} with UV detection at 340 nm. (Reproduced with permission from Ref. 65. © Wiley-VCH Verlag GmbH & Co. KGaA, Weinheim, 2011.)

performance of MIL-53(Al)-packed column for position isomers. Baseline separations of xylene, dichlorobenzene, chlorotoluene, and nitrophenol isomers were also achieved on the slurry-packed MIL-53(Al) column with high resolution and good precision. These results demonstrated MOFs are promising as novel stationary phases for HPLC separation of substituted aromatics and position isomers.

MOFs also showed great potential in fullerene separation. Yang *et al.*[65] reported the utilization of MIL-101(Cr) as the novel stationary phase for HPLC separation of fullerenes with excellent selectivity and high throughput (Figure 7). On the basis of the differences of fullerenes solubility in the mobile phase, adsorption on MIL-101(Cr), and π–π and van de Waals interactions between fullerenes and the frameworks, MIL-101(Cr)-packed column gave high-resolution separation of C60 and C70 at room temperature. Such high-performance separation of C60 and C70 was achieved only within 3 min on a 5-cm long MIL-101(Cr) column. MIL-101(Cr)-packed column also offered a selectivity of α (C70/C60) = 17 and a column efficiency of 13000 plates per meter for C70. High-resolution separation of high fullerenes such as C76 and C78 was also realized on the MIL-101(Cr)-packed column. The potential application of MIL-101(Cr) was further investigated for the separation of fullerenes in carbon soot. The results show that the MIL-101(Cr)-packed column not only gave high-resolution separation for C60, C70, C76, and C78, but also offered baseline separation of the other high fullerenes C82, C84, C86, and C96. This work may bring a bright future for MOFs in the specific adsorption, purification, and separation of carbon nanomaterials.

Most of these pioneering works regarding the utilization of MOFs as the stationary phases in HPLC have focused on nonpolar analytes, although polar compounds have great importance in chemical and pharmaceutical industries. Thus, exploring the potential of MOFs for separating polar compounds is of great significance. MOFs with open metal sites have great potential for enhancing adsorption and separation of polar compounds. However, the elution and separation of polar compounds on open metal-sites-containing MOFs-packed column using nonpolar solvents as the mobile phase in HPLC is difficult because of the strong interaction between polar compounds and the open metal sites of MOFs. To achieve high-performance separation of polar compounds on the MOFs containing open metal sites, Fu *et al.*[66] report the control of the coordination status of the open metal sites in MIL-101(Cr) by adjusting the content of methanol (MeOH) in the mobile phase for fast and high-resolution separation of polar compounds. The interaction between the open metal sites of MIL-101(Cr) and the polar compounds was adjusted by adding an appropriate amount of MeOH to the mobile phase to achieve the effective separation of the polar compounds due to the competition of MeOH with the analytes for the open metal sites. Baseline separation of nitroaniline, aminophenol and naphthol isomers, and sulfadimidine and sulfanilamide was achieved by controlling the content of MeOH in the mobile phase. This approach provides reproducible and high-performance separation of polar compounds on the open metal-sites-containing MOFs.

Recently, Chiral MOFs show high potential as chiral stationary phases (CSP) in chiral separation. Padmanaban *et al.*[67] reported the usage of Bn-Chir University of Michigan Crystalline Material (UMCM)-1 for HPLC separation of chiral compounds. Since the as-synthesized MOF particles are much too large and needle-shaped, they were manually grinded to give a spherical shape of <100 μm and a narrow particle size distribution for HPLC separation of chiral 1-phenylethanol. The selectivity and

the resolution for the separation of 1-phenylethanol was 1.6 and 0.65, respectively, showing the promise of Bn-ChirUMCM-1 as the novel stationary phase for HPLC separation of enantiomers.

Spherical shape and narrow particle size distribution are the two key factors for a good HPLC stationary phase. Very recently, Zhang *et al.*[68] present a chiral MOF with an average particle size of 5 μm for the HPLC separation of alcohol, ketone, flavone, phenol, base, and amide racemates. Ten racemates were well-separated on a 25-cm long MOF column with excellent selectivity. The stereoselectivity likely resulted from the interaction of the analytes with the inner pore space of MOF, which has the most appropriate size and steric fit. Besides, the dispersion, dipole–dipole, and hydrogen-bonding forces which come from the mobile phase may also play significant roles in chiral separation. These results show that chiral MOFs are practicable for HPLC enantioseparation.

5.2 MOFs for Reverse-Phase HPLC

All of the above-mentioned studies on the utilization of MOFs for HPLC have been performed exclusively in NP mode (with nonpolar organic solvent as themobile phase), although reverse-phase (RP) HPLC (with a binary mixture of water and a miscible polar organic solvent as the mobile phase) is the most widely used technique for separation in life and environmental sciences, and biomedical research. Thus, exploring the potential applications of MOFs in reverse-phase high-performance liquid chromatography (RP HPLC) is of imperative necessity and great significance.

Liu *et al.*[69] reported the utilization of MOFs for RP HPLC separation of a wide range of analytes from nonpolar to polar, and acidic to basic solutes with high resolution, good selectivity, stability, and reproducibility (Figure 8). Resulted from the aromatic ring pore walls

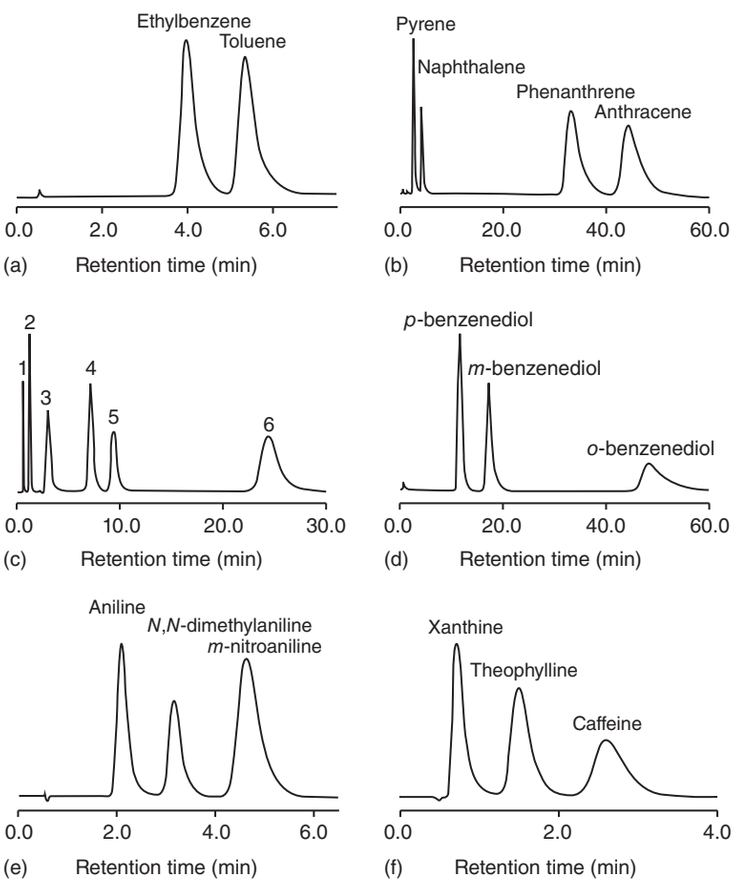


Figure 8 Chromatograms on MIL-53(Al)-packed column (7-cm long × 4.6-mm i.d.) for RP HPLC separation using CH_3CN/H_2O as mobile phase at 1.0 mL min^{-1}: (a) ethylbenzene and toluene; (b) PAHs; (c) thiourea (1), phenol (2), aniline (3), benzaldehyde (4), bromobenzene (5), naphthalene (6); (d) o-benzenediol, m-benzenediol, and p-benzenediol; (e) aniline, N,N-dimethylaniline, and m-nitroaniline; (f) xanthine, theophylline, and caffeine. Mobile phase composition (CH_3CN/H_2O, v/v): (a) 7:3; (b) 10:0; (c) 6:4; (d) 1:9; (e) 9:1; (f) 5:5. UV detection at 210 nm (a, c), 256 nm (b), 70 nm (f), and 280 nm (d, e). (Reproduced from Ref. 69 with permission of The Royal Society of Chemistry. DOI: 10.1039/C2AN15925B.)

and the interaction between the methyl group of toluene and the carboxylate groups of MIL-53(Al), MIL-53(Al)-packed column shows stronger hydrophobic properties than C18 column. The RP separation mechanisms of MIL-53(Al) were further evaluated using thiourea, phenol, aniline, benzaldehyde, bromobenzene, and naphthalene as the probe molecules. A column efficiency of 23705 plates per meter for bromobenzene was obtained on MIL-53(Al)-packed column. The reproducible chromatograms for the separation of the probe molecules after 6 months on the same MIL-53(Al)-packed column show good stability of the MIL-53(Al)-packed column. The unique features of high porosity, shape selectivity, and multiple active sites provide MOF-packed columns greater potential for RP HPLC separation.

The use of MOFs for HPLC separation of products and intermediates in the pharmaceutical industries has received little if any attention, despite the potential advantages of MOFs in adsorption and separation. Centrone *et al.*[70] reported the separation of four small intermediates and byproducts on MOFs columns. Two closely related amines can be well-separated on MOFs columns using methanol as the mobile phase, but not with C18 columns using an optimized mobile phase. The separation of these intermediates on ZIF-8 is the result of the interactions between the thermodynamic driving force for analytes adsorption within the framework pores and the kinetics of analytes diffusion into the ZIF-8 pores, whereas the separation on MIL-100(Fe) is achieved via the specific interactions between the analytes and Fe sites. This work points to the prospects for using MOF materials for the continuous separation and synthesis of pharmaceutical compounds.

5.3 MOFs for Both Normal- and Reverse-Phase HPLC

MOFs can also be used as the stationary phase for both NP- and RP-HPLC. Fu *et al.*[71] explored MIL-100(Fe) as a novel stationary phase for both NP and RP HPLC. Two groups of analytes (benzene, toluene, ethylbenzene, naphthalene, and 1-chloronaphthalene; aniline, acetanilide, 2-nitroaniline, and 1-naphthylamine) were used to test the performance of MIL-100(Fe) in RP mode, whereas chloroaniline and toluidine isomers were employed to evaluate its performance in NP mode. Baseline separation of all the tested analytes was achieved on MIL-100(Fe)-packed column with good precision. The hydrophobic property stemmed from the aromatic ring walls of the pores in MIL-100(Fe) frameworks dominates the selective separation of neutral analytes and basic anilines in RP mode, whereas the interactions between the nitrogen atoms in the analyte and the Fe active sites in MIL-100(Fe) govern the separation of chloroaniline and toluidine isomers in NP mode. The mesoporous cages, accessible windows, excellent chemical and solvent stability, metal active sites, and aromatic pore walls make MIL-100(Fe) a good candidate for both NP and RP HPLC.

5.4 MOFs Composites for HPLC

Although remarkable progress on the MOF-based HPLC columns has been made, the problems of low column efficiency, high column backpressure, and undesirable peak shapes mainly resulting from the direct packing of MOF particles with irregular shapes, submicrometer size, and wide size distribution still exist. Fabrication of uniform spherical MOF composites and monolithic columns are the effective strategies to overcome the above-mentioned problems.

Ameloot *et al.*[72] reported the synthesis of spherical silica-MOF composites via loading $Cu_3(BTC)_2$ inside the pores of the monodisperse silica spheres for HPLC separation of ethylbenzene and styrene. Owing to the broad size distribution of $Cu_3(BTC)_2$ particles (0.5–4 μm), high column backpressure (200 bar) and broad peaks were obtained on $Cu_3(BTC)_2$-packed column. On the other hand, column filled with uniform bare silica spheres demonstrated a lower backpressure of 52 bar and the sharp peaks. However, a mixture of ethylbenzene and styrene could not be separated on bare silica column due to the lack of Cu^{2+} sites. Nevertheless, silica-MOF composite allows the combination of the good column packing properties of the silica and the unique separation ability of $Cu_3(BTC)_2$. Efficient separation of ethylbenzene and styrene mixtures was achieved on silica-MOF composite under the same conditions with a lower column backpressure of 47 bar and the narrow peaks. The results illustrate the synergistic effect of the good packing properties of the monodisperse silica spheres and the selective separation ability of the MOF material.

Although silica-$Cu_3(BTC)_2$ composites provide high-resolution separation of styrene and ethylbenzene, the low mass transfer efficiency between the analytes and $Cu_3(BTC)_2$ inside the silica pores also led to peak broadening. To reduce the separation time and to enhance the column efficiency, Fu *et al.*[73] report the fabrication of monodisperse ZIF-8@SiO_2 core-shell microspheres for fast and efficient HPLC separation of endocrine disrupting chemicals (EDCs) and pesticides. The monodisperse ZIF-8@SiO_2 core-shell microspheres were prepared via the controllable growth of ZIF-8 shells on spherical carboxylate-terminated silica cores. The synergistic effects of the good column packing properties of the silica spheres and the separation ability of ZIF-8 nanocrystals allow the ZIF-8@SiO_2 core-shell microspheres-packed column for fast and high-resolution separation of EDCs and pesticides with low column backpressure. A column efficiency of 23 000 plates per meter for bisphenol A was also obtained on ZIF-8@SiO_2-packed column. This study provides the possibility for the preparation of mutifunctional

MOF-based composites for wide applications of MOFs in HPLC separation.

Monolithic materials with a porous "single particle" structure have advantages in HPLC separation. The marriage of unique properties of MOFs and the excellent features of polymer monolith to develop novel MOF-polymer monoliths should be promising for HPLC. Fu *et al.*[74] report the incorporation of UiO-66 into poly methylarylic acid-co-ethylene dimetharylate (MAA-co-EDMA) to fabricate the UiO-66-incorporated monoliths for enhanced HPLC separation of small molecules. The retention of the small molecules and their resolutions increased with the amount of the UiO-66 incorporated, showing the enhanced separation of small molecules on UiO-66-incorporated monoliths. UiO-66-incorporated monoliths also provide good permeability, high column efficiency (28800 plates per meter for 2,6-dimethylphenol), and excellent reproducibility. The intrinsic characteristics of MOFs such as large surface area, aromatic walls, and active metal sites make the MOFs-incorporated monolithic columns attractive for HPLC separation.

MOFs composites also show great potential for chiral separation. Tanaka *et al.*[75] reported a new homochiral MOF-silica composite for HPLC separation of chiral sulfoxides. (R)-MOF-silica composite was synthesized from a mixture of MOF precursors and monodisperse spherical silica gel under solvothermal conditions. The obtained (R)-MOF-silica composite was slurry-packed into a 15-cm long stainless steel column for HPLC separation of chiral sulfoxides. Eleven sulfoxides were completely separated with excellent selectivity using hexane-EtOH and hexane-i-PrOH as the mobile phase. The (S)-isomer of the sulfoxides elutes first, followed by the (R)-isomer in all cases, suggesting the inclusion of the (R)-enantiomer in the cavity of (R)-MOF, which is likely facilitated by intermolecular hydrogen bonding interactions between the phenolic OH group of (R)-MOF and the O=S group of the sulfoxide. The results may bring a bright future for chiral MOF composites in the enantioselective separation and sorption of various chiral compounds.

6 CONCLUSIONS

In the past few years, great progress has been made for the applications of MOFs in analytical chemistry. Although some kinds of MOFs that are water instable have limited applications in analytical chemistry, MOFs that have good thermostability and water stability (such as ZIF and MIL MOFs) can be available in almost all the important aspects of modern analytical chemistry. With well-defined pore structures, MOFs have great potential in adsorption and adsorption-based separation. Also, MOFs have been engineered to specific forms such as columns, fibers, and films to meet various analytical challenges and to improve analytical sensitivity and selectivity. In the near future, great efforts should be made to explore more practical analytical utilizations of MOFs, to make full use of currently available MOFs to solve analytical problems, and to design specific MOFs for special analytical challenges.

7 RELATED ARTICLES

Mesoporous Metal-Organic Frameworks; Metal-Organic Frameworks for Removal of Harmful Gases; Gas Storage in Metal-Organic Frameworks; Adsorption of Hydrocarbons and Alcohols in Metal-Organic Framework Materials.

8 ABBREVIATIONS AND ACRONYMS

CSA = controlled secondary building units approach; CSP = chiral stationary phases; DMMP = dimethyl methylphosphonate; EDC = endocrine disrupting chemical; GC = gas chromatography; HCH = hexachlorocyclohexane; HKUST = Hong Kong University of Science and Technology; HPLC = high-performance liquid chromatography; IRMOF = Isoreticular MOF; MAA-co-EDMA = methylarylic acid-co-ethylene dimetharylate; MALDI-TOF-MS = matrix assisted laser desorption/ionization time of flight mass spectrometry; MIL = Matérial Institut Lavoisier; MOF = Metal-organic framework; MSPDE = matrix solid-phase dispersion extraction; MSPE = magnetic solid-phase extraction; NP = normal-phase; PAH = polycyclic aromatic hydrocarbon; PBDE = polybrominated diphenylether; PCB = polychlorinated biphenyl; PLOT = porous layer open tube; POP = persistent organic pollutant; RP = reverse-phase; RP HPLC = reverse-phase high-performance liquid chromatography; SAE-VA-μ-SPE = sonication-assisted emulsification microextraction combined with vortex-assisted porous-membrane-protected μ-SPE; SAM = self-assembled monolayer; SPE = solid-phase extraction; SPME = solid-phase microextraction; TD-GC/MS = thermal desorption gas chromatography–mass spectrography; UIO = University of Oslo; UMCM = University of Michigan Crystalline Material; WCOT = wall-coated open tubular; ZIF = zeolitic imidazolate framework; μ-SPE = micro-solid-phase extraction.

9 REFERENCES

1. L. J. Murray, M. Dinca, and J. R. Long, *Chem. Soc. Rev.*, 2009, **38**, 1294.

2. M. P. Suh, H. J. Park, T. K. Prasad, and D.-W. Lim, *Chem. Rev.*, 2011, **112**, 782.
3. J. Y. Lee, D. H. Olson, L. Pan, T. J. Emge, and J. Li, *Adv. Funct. Mater.*, 2007, **17**, 1255.
4. J.-R. Li, R. J. Kuppler, and H.-C. Zhou, *Chem. Soc. Rev.*, 2009, **38**, 1477.
5. J.-R. Li, J. Sculley, and H.-C. Zhou, *Chem. Rev.*, 2011, **112**, 869.
6. J. Lee, O. K. Farha, J. Roberts, K. A. Scheidt, S. T. Nguyen, and J. T. Hupp, *Chem. Soc. Rev.*, 2009, **38**, 1450.
7. L. Ma, C. Abney, and W. Lin, *Chem. Soc. Rev.*, 2009, **38**, 1248.
8. K. K. Tanabe and S. M. Cohen, *Angew. Chem. Int. Ed.*, 2009, **48**, 7424.
9. A. Corma, H. García, and F. X. Llabrés i Xamena, *Chem. Rev.*, 2010, **110**, 4606.
10. M. Yoon, R. Srirambalaji, and K. Kim, *Chem. Rev.*, 2011, **112**, 1196.
11. M. D. Allendorf, C. A. Bauer, R. K. Bhakta, and R. J. T. Houk, *Chem. Soc. Rev.*, 2009, **38**, 1330.
12. Y. Cui, Y. Yue, G. Qian, and B. Chen, *Chem. Rev.*, 2011, **112**, 1126.
13. L. E. Kreno, K. Leong, O. K. Farha, M. Allendorf, R. P. Van Duyne, and J. T. Hupp, *Chem. Rev.*, 2011, **112**, 1105.
14. J. Rocha, L. D. Carlos, F. A. A. Paz, and D. Ananias, *Chem. Soc. Rev.*, 2011, **40**, 926.
15. K. M. L. Taylor, A. Jin, and W. B. Lin, *Angew. Chem. Int. Ed.*, 2008, **47**, 7722.
16. K. M. L. Taylor, W. J. Rieter, and W. Lin, *J. Am. Chem. Soc.*, 2008, **130**, 14358.
17. K. M. L. Taylor-Pashow, J. Della Rocca, Z. Xie, S. Tran, and W. Lin, *J. Am. Chem. Soc.*, 2009, **131**, 14261.
18. P. Horcajada, T. Chalati, C. Serre, B. Gillet, C. Sebrie, T. Baati, J. F. Eubank, D. Heurtaux, P. Clayette, C. Kreuz, J.-S. Chang, Y. K. Hwang, V. Marsaud, P.-N. Bories, L. Cynober, S. Gil, G. Férey, P. Couvreur, and R. Gref, *Nat. Mater.*, 2010, **9**, 172.
19. J. Della Rocca, D. Liu, and W. Lin, *Acc. Chem. Res.*, 2011, **44**, 957.
20. Z. Ni, J. P. Jerrell, K. R. Cadwallader, and R. I. Masel, *Anal. Chem.*, 2007, **79**, 1290.
21. Z.-Y. Gu, G. Wang, and X.-P. Yan, *Anal. Chem.*, 2010, **82**, 1365.
22. Y.-Y. Zhou, X.-P. Yan, K.-N. Kim, S.-W. Wang, and M.-G. Liu, *J. Chromatogr. A*, 2006, **1116**, 172.
23. G.-H. Wang, Y.-Q. Lei, and H.-C. Song, *Anal. Methods*, 2012, **4**, 647.
24. S. Yang, C. Chen, Z. Yan, Q. Cai, and S. Yao, *J. Sep. Sci.*, 2013, **36**, 1283.
25. Z.-Y. Gu, Y.-J. Chen, J.-Q. Jiang, and X.-P. Yan, *Chem. Commun.*, 2011, **47**, 4787.
26. P. H. Viana de Carvalho, A. Santos Barreto, M. O. Rodrigues, V. de Menezes Prata, P. Barreto Alves, M. E. de Mesquita, S. Alves Júnior, and S. Navickiene, *J. Sep. Sci.*, 2009, **32**, 2132.
27. A. Aquino, K. A. Wanderley, C. D. O. Paiva-Santos, G. F. de Sá, M. D. R. Alexandre, S. A. Júnior, and S. Navickiene, *Talanta*, 2010, **83**, 631.
28. A. S. Barreto, R. L. da Silva, S. C. G. dos Santos Silva, M. O. Rodrigues, C. A. de Simone, G. F. de Sá, S. A. Júnior, S. Navickiene, and M. E. de Mesquita, *J. Sep. Sci.*, 2010, **33**, 3811.
29. S.-H. Huo and X.-P. Yan, *Analyst*, 2012, **137**, 3445.
30. A. Bagheri, M. Taghizadeh, M. Behbahani, A. Akbar Asgharinezhad, M. Salarian, A. Dehghani, H. Ebrahimzadeh, and M. M. Amini, *Talanta*, 2012, **99**, 132.
31. M. Sohrabi, Z. Matbouie, A. Asgharinezhad, and A. Dehghani, *Microchim. Acta*, 2013, **180**, 589.
32. X.-Y. Cui, Z.-Y. Gu, D.-Q. Jiang, Y. Li, H.-F. Wang, and X.-P. Yan, *Anal. Chem.*, 2009, **81**, 9771.
33. C.-T. He, J.-Y. Tian, S.-Y. Liu, G. Ouyang, J.-P. Zhang, and X.-M. Chen, *Chem. Sci.*, 2013, **4**, 351.
34. X.-F. Chen, H. Zang, X. Wang, J.-G. Cheng, R.-S. Zhao, C.-G. Cheng, and X.-Q. Lu, *Analyst*, 2012, **137**, 5411.
35. L.-Q. Yu and X.-P. Yan, *Chem. Commun.*, 2013, **49**, 2142.
36. D. Ge and H. K. Lee, *J. Chromatogr. A*, 2011, **1218**, 8490.
37. D. Ge and H. K. Lee, *J. Chromatogr. A*, 2012, **1263**, 1.
38. D. Ge and H. K. Lee, *J. Chromatogr. A*, 2012, **1257**, 19.
39. B. L. Chen, C. D. Liang, J. Yang, D. S. Contreras, Y. L. Clancy, E. B. Lobkovsky, O. M. Yaghi, and S. Dai, *Angew. Chem. Int. Ed.*, 2006, **45**, 1390.
40. J. W. Yoon, S. H. Jhung, Y. K. Hwang, S. M. Humphrey, P. T. Wood, and J. S. Chang, *Adv. Mater.*, 2007, **19**, 1830.
41. V. Finsy, H. Verelst, L. Alaerts, D. De Vos, P. A. Jacobs, G. V. Baron, and J. F. M. Denayer, *J. Am. Chem. Soc.*, 2008, **130**, 7110.
42. V. Finsy, S. Calero, E. Garcia-Perez, P. J. Merkling, G. Vedts, D. E. De Vos, G. V. Baron, and J. F. M. Denayer, *Phys. Chem. Chem. Phys.*, 2009, **11**, 3515.
43. S. Couck, T. Remy, G. V. Baron, J. Gascon, F. Kapteijn, and J. F. M. Denayer, *Phys. Chem. Chem. Phys.*, 2010, **12**, 9413.
44. M. T. Luebbers, T. Wu, L. Shen, and R. I. Masel, *Langmuir*, 2010, **26**, 15625.
45. M. T. Luebbers, T. Wu, L. Shen, and R. I. Masel, *Langmuir*, 2010, **26**, 11319.
46. Z.-Y. Gu and X.-P. Yan, *Angew. Chem. Int. Ed.*, 2010, **49**, 1477.
47. Z.-Y. Gu, J.-Q. Jiang, and X.-P. Yan, *Anal. Chem.*, 2011, **83**, 5093.
48. L. Fan and X.-P. Yan, *Talanta*, 2012, **99**, 944.
49. N. Chang, Z.-Y. Gu, and X.-P. Yan, *J. Am. Chem. Soc.*, 2010, **132**, 13645.
50. N. Chang and X.-P. Yan, *J. Chromatogr. A*, 2012, **1257**, 116.

51. Z.-L. Fang, S.-R. Zheng, J.-B. Tan, S.-L. Cai, J. Fan, X. Yan, and W.-G. Zhang, *J. Chromatogr. A*, 2013, **1285**, 132.
52. A. S. Münch, J. Seidel, A. Obst, E. Weber, and F. O. R. L. Mertens, *Chem. Eur. J.*, 2011, **17**, 10958.
53. A. S. Münch and F. O. R. L. Mertens, *J. Mater. Chem.*, 2012, **22**, 10228.
54. S.-M. Xie, Z.-J. Zhang, Z.-Y. Wang, and L.-M. Yuan, *J. Am. Chem. Soc.*, 2011, **133**, 11892.
55. S.-M. Xie, X.-H. Zhang, Z.-J. Zhang, M. Zhang, J. Jia, and L.-M. Yuan, *Anal. Bioanal. Chem.*, 2013, **405**, 3407.
56. N. Chang, Z.-Y. Gu, H.-F. Wang, and X.-P. Yan, *Anal. Chem.*, 2011, **83**, 7094.
57. L. Alaerts, C. E. A. Kirschhock, M. Maes, M. A. van der Veen, V. Finsy, A. Depla, J. A. Martens, G. V. Baron, P. A. Jacobs, J. E. M. Denayer, and D. E. De Vos, *Angew. Chem. Int. Ed.*, 2007, **46**, 4293.
58. L. Alaerts, M. Maes, L. Giebeler, P. A. Jacobs, J. A. Martens, J. F. M. Denayer, C. E. A. Kirschhock, and D. E. De Vos, *J. Am. Chem. Soc.*, 2008, **130**, 14170.
59. L. Alaerts, M. Maes, P. A. Jacobs, J. F. M. Denayer, and D. E. De Vos, *Phys. Chem. Chem. Phys.*, 2008, **10**, 2979.
60. L. Alaerts, M. Maes, M. A. van der Veen, P. A. Jacobs, and D. E. De Vos, *Phys. Chem. Chem. Phys.*, 2009, **11**, 2903.
61. M. Maes, F. Vermoortele, L. Alaerts, S. Couck, C. E. A. Kirschhock, J. F. M. Denayer, and D. E. De Vos, *J. Am. Chem. Soc.*, 2010, **132**, 15277.
62. R. Ahmad, A. G. Wong-Foy, and A. J. Matzger, *Langmuir*, 2009, **25**, 11977.
63. C.-X. Yang and X.-P. Yan, *Anal. Chem.*, 2011, **83**, 7144.
64. C.-X. Yang, S.-S. Liu, H.-F. Wang, S.-W. Wang, and X.-P. Yan, *Analyst*, 2012, **137**, 133.
65. C.-X. Yang, Y.-J. Chen, H.-F. Wang, and X.-P. Yan, *Chem.—Eur. J.*, 2011, **17**, 11734.
66. Y.-Y. Fu, C.-X. Yang, and X.-P. Yan, *Langmuir*, 2012, **28**, 6794.
67. M. Padmanaban, P. Müller, C. Lieder, K. Gedrich, R. Grünker, V. Bon, I. Senkovska, S. Baumgärtner, S. Opelt, S. Paasch, E. Brunner, F. Glorius, E. Klemm, and S. Kaskel, *Chem. Commun.*, 2011, **47**, 12089.
68. M. Zhang, Z. J. Pu, X. L. Chen, X. L. Gong, A. X. Zhu, and L. M. Yuan, *Chem. Commun.*, 2013, **49**, 5201.
69. S.-S. Liu, C.-X. Yang, S.-W. Wang, and X.-P. Yan, *Analyst*, 2012, **137**, 816.
70. A. Centrone, E. E. Santiso, and T. A. Hatton, *Small*, 2011, **7**, 2356.
71. Y.-Y. Fu, C.-X. Yang, and X.-P. Yan, *J. Chromatogr. A*, 2013, **1274**, 137.
72. R. Ameloot, A. Liekens, L. Alaerts, M. Maes, A. Galarneau, B. Coq, G. Desmet, B. F. Sels, J. F. M. Denayer, and D. E. De Vos, *Eur. J. Inorg. Chem.*, 2010, 3735.
73. Y.-Y. Fu, C.-X. Yang, and X.-P. Yan, *Chem.—Eur. J.*, 2013, **19**, 13484.
74. Y.-Y. Fu, C.-X. Yang, and X.-P. Yan, *Chem. Commun.*, 2013, **49**, 7162.
75. K. Tanaka, T. Muraoka, D. Hirayama, and A. Ohnish, *Chem. Commun.*, 2012, **48**, 8577.
76. C. Basheer, A. A. Alnedhary, B. S. M. Rao, S. Valliyaveettil, and H. K. Lee, *Anal. Chem.*, 2006, **78**, 2853.
77. K. A. Cychosz, R. Ahmad, and A. J. Matzger, *Chem. Sci.*, 2010, **1**, 293.
78. A. L. Nuzhdin, D. N. Dybtsev, K. P. Bryliakov, E. P. Talsi, and V. P. Fedin, *J. Am. Chem. Soc.*, 2007, **129**, 12958.

Recent Solid-State NMR Studies of Quadrupolar Nuclei in Metal-Organic Frameworks

Yining Huang, Jun Xu, Farhana Gul-E-Noor and Peng He

The University of Western Ontario, London, ON, Canada

1	Introduction	457
2	NMR Background	458
3	Direct Characterization of Metal Center Environment in MOFs	460
4	Identifying Spectral Signatures of Various Oxygen Species by ^{17}O SSNMR Spectroscopy	465
5	Summary	468
6	Acknowledgments	468
7	Related Articles	468
8	Abbreviations and Acronyms	468
9	References	469

1 INTRODUCTION

Metal-organic frameworks (MOFs) belong to a novel class of organic–inorganic hybrid porous material. Their diverse topologies, unique properties, and current and potential applications have been discussed in other chapters of this volume. The present chapter focuses on the characterization of MOF-based materials by solid-state nuclear magnetic resonance (SSNMR) spectroscopy. Although the structures of many MOFs have been determined by single crystal X-ray diffraction, a significant number of MOF structures have to be refined from more limited powder X-ray diffraction (XRD) data owing to the lack of suitable single crystals. Further, activation processes such as dehydration and desolvation tend to reduce the crystallinity and, sometimes, lead to the fragmentation of single crystals. In such cases, an unambiguous structure solution requires additional information from complementary techniques, and SSNMR spectroscopy is one of such techniques. SSNMR spectroscopy is sensitive to short-range ordering and local structure, whereas XRD probes long-range ordering and periodicity. When taken together, both techniques provide a more complete picture on overall MOF structure. In addition to the knowledge regarding structure, NMR spectroscopy has a unique ability of providing dynamic information. The beauty and the power of NMR spectroscopy lie in the fact that it furnishes the information which is nuclide-specific. Therefore, one can obtain specific information by performing specific NMR experiments on specific nuclei located at specific positions. For example, ^{13}C, ^{1}H, ^{19}F, ^{31}P, and ^{15}N SSNMR spectroscopy can confirm MOF formation, identify the functional groups upon modification of the linkers, and monitor the adsorption of guest species.[1–9] SSNMR spectroscopy of metal centers themselves can provide direct information on chemical and geometrical environments around metal ions.[9–17] Deuterium NMR is highly suitable for monitoring the dynamics of the guest molecules and the local motion of the organic linkers.[18–21] ^{129}Xe NMR can be utilized to probe pore size and shape.[22–24] Two detailed reviews of MOF characterization by SSNMR spectroscopy up to the middle of 2012 have been presented by us and others.[25,26] Rather than aim for another comprehensive review, this chapter describes several very recent SSNMR studies of some key framework elements whose NMR-active isotopes are quadrupolar ($I > 1/2$) nuclei (where I is the nuclear spin-quantum number) at very high magnetic fields. For many metal centers in MOFs, their NMR-accessible nuclides are quadrupolar, therefore, complicating spectral

Metal-Organic Framework Materials. Edited by Leonard R. MacGillivray and Charles M. Lukehart.
© 2014 John Wiley & Sons, Ltd. ISBN 978-1-119-95289-3

acquisition and interpretation. The examples of such nuclei include ^{27}Al ($I = 5/2$), ^{71}Ga ($I = 3/2$), ^{45}Sc ($I = 7/2$), ^{67}Zn ($I = 5/2$), ^{25}Mg ($I = 5/2$), ^{91}Zr ($I = 5/2$), and ^{43}Ca ($I = 7/2$). As discussed in the next section, SSNMR spectroscopy of quadrupolar nuclei can be very difficult because more often than not, their spectra are severely broadened by the quadrupolar interaction. The above-mentioned nuclei can be divided into two groups. For nuclei such as ^{27}Al, ^{71}Ga, and ^{45}Sc, although quadrupolar, they are very sensitive, that is, they have large gyromagnetic ratios (γ) and high natural abundances, leading to inherently high sensitivity. For ^{67}Zn, ^{25}Mg, ^{91}Zr, $^{47/49}$Ti, and ^{43}Ca, they, on the other hand, have small γ values and low natural abundances. Consequently, they are very unreceptive, resulting in that their SSNMR spectroscopy is much more challenging.

2 NMR BACKGROUND

For a quadrupolar nucleus, the important nuclear spin interactions in solids are the Zeeman interaction, the chemical shielding (CS) interaction, the dipolar interaction, and the quadrupolar interaction. The Zeeman interaction occurs between the magnetic moment of the nucleus and the applied magnetic field $\boldsymbol{B}_0$, resulting in $2I + 1$ energy levels. This interaction dominates NMR Hamiltonian and all other interactions can be treated as the perturbations to it. The CS interaction originates from the magnetic shielding of a nucleus by surrounding electron clouds. This interaction is anisotropic and field-dependent. The direct dipolar interaction arises from the through-space interaction between two magnetic moments of two nuclei in close proximity. It is also anisotropic, but field-independent. For nuclei with a spin-quantum number I greater than $1/2$, their positive nuclear charge distribution is nonspherical, resulting in a nonzero nuclear electric quadrupole moment (Q). The SSNMR spectra of quadrupolar nuclei are often dominated by the quadrupolar interaction, which is the interaction between the electric quadrupole moment and the electric field gradient (EFG) at the nucleus resulting from an asymmetric distribution of electron density. The EFG is described by a second-rank tensor that can be diagonalized in a principal axis system (PAS). In the PAS, the EFG is described by three components that are ordered in such that $|V_{XX}| \leq |V_{YY}| \leq |V_{ZZ}|$, and they satisfy $V_{XX} + V_{YY} + V_{ZZ} = 0$. The quadrupolar interaction is characterized by two parameters: one is quadrupolar coupling constant (C_Q):

$$C_Q = \frac{eQV_{ZZ}}{h} = \frac{eQ\ eq_{ZZ}}{h} \tag{1}$$

where $eq_{ZZ} = V_{ZZ}$ is the largest component of the EFG tensor. C_Q determines the magnitude of the quadrupolar interaction and, therefore, influences the spectral breadth. The other parameter is the asymmetry parameter (η_Q):

$$\eta_Q = \frac{V_{XX} - V_{YY}}{V_{ZZ}} \tag{2}$$

η_Q describes the symmetry of the EFG tensor and affects the observed line-shape. It ranges from $0 \leq \eta_Q \leq 1$. For an axially symmetric EFG tensor, $V_{XX} = V_{YY}$, leading to $\eta_Q = 0$.

When the magnitude of the quadrupolar interaction is rather small compared to the Zeeman interaction, it can be treated by first-order perturbation theory. The effect of first-order quadrupolar interaction is to lift the degeneracy of the NMR transitions, which is illustrated in Figure 1a using a nucleus with $I = 3/2$ as an example. Figure 1b shows the static powder pattern (i.e., the static spectrum of a powdered sample) subject to the first-order interaction, which is a supposition of the powder patterns of three allowed transitions. The sharp peak in the middle is corresponding to the central transition, CT (for $m_I = 1/2 \leftrightarrow m_I = -1/2$). The sharpness of the CT is due to the fact that this transition is not affected by the first-order interaction and therefore remains at the Larmor frequency. The two other transitions termed satellite transitions (STs) are subject to the first-order interaction. Their frequencies depend on C_Q and the orientation of the quadrupolar PAS with respect to the external magnetic field ($\boldsymbol{B}_0$). For half-integer quadrupolar nuclei, usually only CT is observable. STs are often severely broadened by the first-order quadrupolar interaction to such an extent that they are very difficult to observe if not impossible.

Very often the quadrupolar interaction is so strong that the observed spectrum cannot be adequately described by the first-order approximation. Consequently, the second-order perturbation theory must be applied to accurately characterize the spectrum. In such a case, all the transitions are affected by the second-order quadrupolar interaction (Figure 1a), and their frequencies are dependent on C_Q and the orientation of PAS in $\boldsymbol{B}_0$. Although the second-order quadrupolar interaction is much smaller than the first-order interaction, it does have a profound effect on the CT. In a powdered sample, the center of mass of the CT is shifted from the isotropic shift position. The CT is no longer a sharp line owing to the anisotropic second-order broadening (Figure 1b). The spectral width of the powder pattern of the CT is proportional to C_Q^2/ν_0 (where ν_0 = Larmor frequency), which indicates that the second-order line broadening can be minimized by working at very high magnetic fields. The line-shape of CT is determined by η_Q (Figure 2).

When C_Q is not too large, magic-angle spinning (MAS) is the most commonly used method to improve resolution. MAS involves rapidly spinning a powdered sample around an axis that makes an angle of 54.74° with

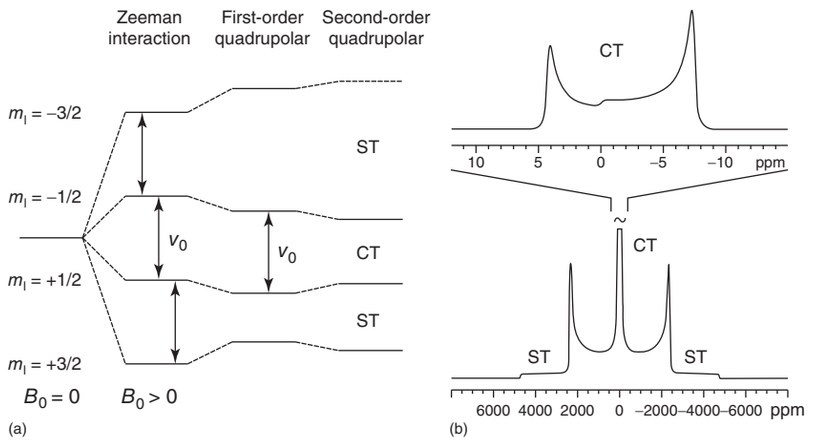


Figure 1 (a) Energy level diagram of a spin-3/2 nucleus, showing the perturbation of the Zeeman levels by the first- and second-order quadrupolar interactions. (b) Simulations of the static powder pattern of spin $I = 3/2$ with parameters $C_Q = 1$ MHz, $\eta_Q = 0$, $\delta_{iso} = 0$ ppm, $\nu_0 = 105.8$ MHz, $B_0 = 9.4$ T

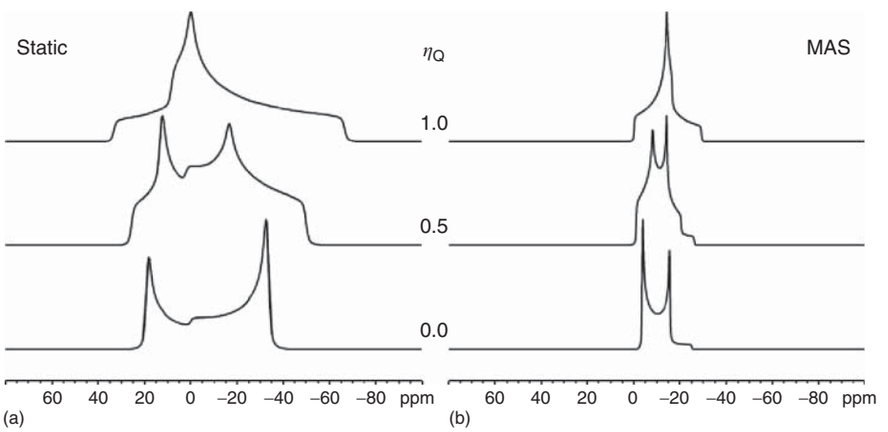


Figure 2 Simulations of the static (a) and MAS (b) powder patterns of spin $I = 3/2$ with different η_Q. Other simulation parameters $C_Q = 2$ MHz, $\delta_{iso} = 0$ ppm, $\nu_0 = 105.8$ MHz, $B_0 = 9.4$ T

respect to $\boldsymbol{B}_0$. It is well known that for *spin*-1/2 nuclei such as ^{13}C, ^{29}Si, and ^{31}P, MAS can produce solution-like high-resolution spectra because MAS can average the chemical shift anisotropy (CSA) to its isotropic value (δ_{iso}). The underlying reasoning is that the CS interaction has an angular dependence of $(3\cos^2\theta - 1)$ where θ is the angle between $\boldsymbol{B}_0$ and principle axes along which the shielding tensor components are defined. However, for the half-integer quadrupolar nuclei, although spinning sample at MAS can reduce the spectral breadth broadened by the quadrupolar coupling by a factor of 3–4, it cannot completely eliminate the second-order quadrupolar interaction owing to a more complex angular dependence. Figure 2b shows the effect of MAS on a powdered sample. As the CSA is averaged out under MAS conditions, the residual line-shape and its position are only determined by the C_Q, η_Q, and δ_{iso}. These parameters contain structural information and can be extracted from the MAS spectrum via spectral simulation using several available software packages.[27–31] The MAS spectrum of quadrupolar nuclei can only provide limited resolution because of the residual second-order quadrupolar broadening. When several chemically and/or crystallographically nonequivalent species coexist, their NMR signals often overlap in the MAS spectrum. An NMR technique that is capable of completely eliminating the line-broadening due to the fact that the second-order quadrupolar interaction is multiple quantum magic-angle spinning (MQMAS).[32] MQMAS is a two-dimensional technique, yielding a truly high-resolution (or "isotropic") spectrum free of both first- and

second-order quadrupolar interactions in the indirect ($F1$) dimension. The direct ($F2$) dimension displays the MAS spectrum with residual second-order broadening.

When the spectral width of the CT is too large to apply spinning-based techniques, the Hahn-echo[33] or quadrupolar-echo[34] sequence can be used to acquire the static spectrum to minimize the distortion of the line-shape owing to the probe ringing. The stationary spectra also contain information about the CSA. If the quadrupolar and the CS interactions both contribute to the line-shape, both the EFG and the CS tensors may be determined.

In the past decade, the ultrahigh-field magnets (with field strength of 18.8 T or higher) have become increasingly accessible. The availability of ultrahigh magnetic field strength has tremendously increased the feasibility of using SSNMR spectroscopy of quadrupolar nuclei for materials characterization. The benefit of acquiring SSNMR spectra of half-integer quadrupolar nuclei on ultrahigh-field NMR instruments is twofold. First, as the second-order quadrupolar broadening is inversely scaled with $\boldsymbol{B}_0$, acquiring spectrum at very high magnetic fields can significantly reduce the line-broadening of the CT because of the second-order quadrupolar interaction. Figure 3 illustrates the effect of magnetic field strength on both stationary and MAS spectra of a quadrupolar nucleus. Secondly, the population difference (thus signal intensity) of the CT increases with increasing the magnetic field strength, which is particularly beneficial to unreceptive quadrupolar nuclei. Thus, SSNMR experiments of half-integer quadrupolar nuclei should be performed at the highest possible magnetic field.

3 DIRECT CHARACTERIZATION OF METAL CENTER ENVIRONMENT IN MOFs

The topology of MOFs depends on metal coordination. The bonding modes involving metal ions influence the MOF properties. The local metal environment in a MOF is often affected by activation (such as dehydration/desolvation) and adsorption of guest species. Therefore, the local structure of metal center needs to be characterized.

As mentioned earlier, ^{27}Al, ^{71}Ga, and ^{45}Sc are highly receptive, and therefore sensitivity is not an issue. As a result, the local environments of these nuclei in several important MOFs have been directly probed by their respective SSNMR spectroscopy.[9–14,25] However, many metal ions in MOFs such as ^{67}Zn, ^{91}Zr, ^{25}Mg, $^{47/49}$Ti, and ^{43}Ca are not only quadrupolar but also unreceptive owing to their unfavorable NMR characteristics such as low gyromagnetic ratios, low natural abundances, and often relatively large nuclear quadrupole moments, resulting in low-sensitivity and broad resonances, making it very difficult to obtain their SSNMR spectra, especially at natural abundance. As a result, SSNMR spectroscopy of these nuclei has rarely been used for characterization. Very recently, several SSNMR studies on directly probing low-γ, unreceptive nuclei such as ^{67}Zn and ^{25}Mg in MOFs at very high magnetic fields have emerged in the literature.[15–17]

The metal centers in many important MOFs are zinc(II) with the IRMOFs (isoreticular metal-organic frameworks)[35] and ZIFs (zeolitic imidazolate frameworks)[36] being the two most important series. ^{67}Zn ($I = 5/2$) is the only stable NMR-active isotope of zinc. Unfortunately, it has a small gyromagnetic ratio

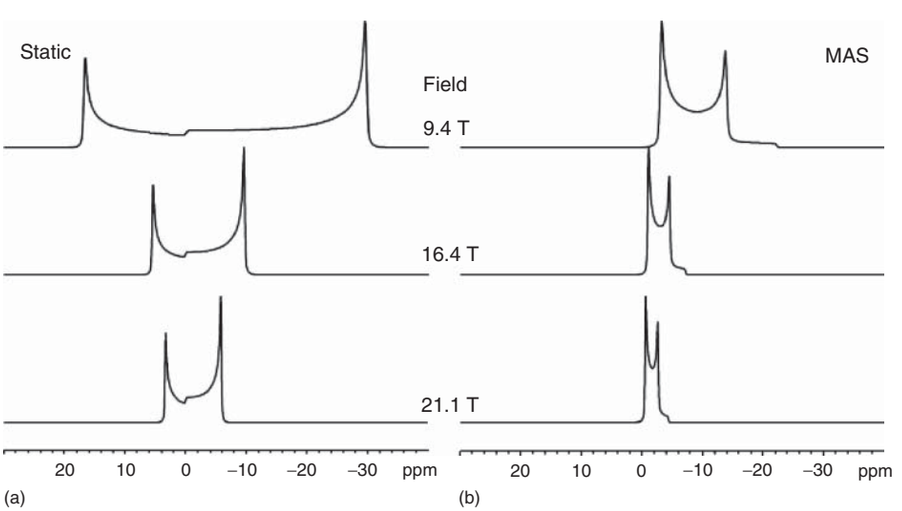


Figure 3 Simulations of the static (a) and MAS (b) powder patterns of spin $I = 3/2$ at different fields. Other simulation parameters $C_Q = 2$ MHz, $\eta_Q = 0$, $\delta_{iso} = 0$ ppm

($\gamma = -2.4975 \times 10^7$ rad T^{-1} s^{-1}). Its resonance frequency at a magnetic field strength of 21.1 T is only about 56 MHz (whereas the resonance frequency of proton is 900 MHz). The natural abundance of ^{67}Zn is only 4.11%. It also has a moderately sized nuclear quadrupole moment, resulting in broad patterns of the CTs that are difficult to be detected specially at natural abundance. Besides the inherently low-sensitivity, a problem specific to the MOF systems is the extremely low ^{67}Zn concentrations owing to their low densities. At natural abundance, the number of ^{67}Zn atoms per nm^3 in most MOFs ranges from 0.10 to 0.15. For comparison, this number for dense ZnO is 1.7 ^{67}Zn atoms/nm^3.

Sutrisno *et al.*[15] recently demonstrated that at 21.1 T, good ^{67}Zn MAS and static NMR spectra of several representative ZIFs including ZIF-8, ZIF-4, ZIF-14, and ZIF-7 can be obtained at natural abundance. The ^{67}Zn MAS spectrum of as-made ZIF-8 (Figure 4) is very sharp and symmetric. This is due to the fact that the ZnN_4 tetrahedron is almost perfect, resulting in a very small EFG and consequently a small $C_Q = 1.1$ MHz. The ^{67}Zn MAS spectrum of as-made ZIF-14 is also fairly narrow, but it is broader than that of ZIF-8 and has a typical second-order quadrupolar line-shape. The $C_Q(^{67}\text{Zn})$ value of ZIF-14 (2.8 MHz) is larger than that in ZIF-8, which results from a slightly more distorted ZnN_4 tetrahedral unit, as reflected by the larger distributions of the Zn–N bond distances and the N–Zn–N bond angles. The distinct line-shape corresponding to an $\eta_Q = 0.85$ indicates that the EFG tensor at the Zn site is not axially symmetric, consistent with its low (twofold) site symmetry. The ^{67}Zn MAS spectrum of ZIF-4 can only be simulated with two Zn sites (Figure 4), which is in agreement with the crystal structure indicting two crystallographically nonequivalent zinc sites. The crystal

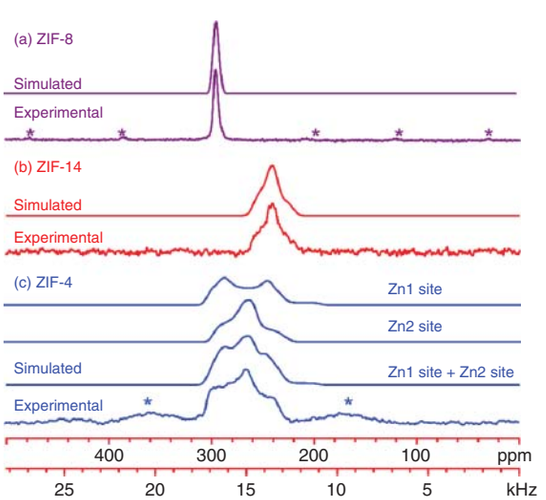


Figure 4 ^{67}Zn MAS NMR spectra of (a) ZIF-8, (b) ZIF-14, and (c) ZIF-4 at 21.1 T. (Reprinted with permission from Ref. 15. © 2012, Wiley-VCH Verlag GmbH & Co. KGaA, 2007.)

structure shows that the dispersions of the Zn–N bond lengths and the N–Zn–N bond angles are larger for Zn1 than those for Zn2. Thus, the ^{67}Zn signal with a larger C_Q value is assigned to the Zn1 site. The assignments are further confirmed by the theoretical calculations. A combination of ^{67}Zn NMR data and molecular dynamics (MD) simulation revealed the distribution and the dynamics of the guest species in the framework. Figure 5 shows the ^{67}Zn MAS spectra of fully desolvated ZIF-8, ZIF-8 loaded with water, and ZIF-8 with benzene trapped inside the cages. The spectrum of the fully desolvated ZIF-8, although is very narrow, does exhibit a typical residual quadrupolar line-shape. ^{67}Zn MAS spectrum of the ZIF-8 containing captured benzene in the cage is very sharp and symmetrical, implying that the small residual quadrupolar interaction detected in the MAS spectrum of the desolvated ZIF-8 vanishes. The proton-decoupled ^{67}Zn MAS spectrum of the ZIF-8 loaded with water is broader than the spectra of both desolvated and benzene-containing ZIF-8. The line-shape suggests that the observed signal likely results from a distribution of chemical shift and/or quadrupolar coupling constant. The MD simulation results presented in Figure 5 show that the water molecules tend to form aggregates within the cages, resulting in some pores completely filled with water and some completely empty. Therefore, the zinc centers have slightly different environments. Benzene trapped in the cages, on the other hand, is evenly distributed in the pores and undergoes a rapid jumping motion within the cage, resulting in that all the Zn sites in the framework experience the same averaged environment. Using ^{67}Zn SSNMR and computational modeling, the authors also examined the effect of desolvation on the local Zn environment in IRMOF-5 (better known as MOF-5). The results suggest that desolvation induces a distortion in ZnO_4 tetrahedron upon removal of the solvent molecules, which occurs through a reduction in the O–C–O angle of the carboxylate group. The degree of the change in O–C–O angle depends on how much solvent is removed from the pore.

In recent years, incorporating Mg^{2+} into MOFs has drawn much attention because magnesium is inexpensive, nontoxic, and especially has low atomic weight.[37] Characterization of local Mg environment is important for understanding the properties of Mg-containing MOFs. Unfortunately, although it has been demonstrated that ^{25}Mg ($I = 5/2$) SSNMR spectroscopy is an effective tool to characterize Mg-containing minerals, organometallics, and biomolecules,[38,39] directly probing the local Mg structure in MOF-based materials by natural abundance ^{25}Mg SSNMR spectroscopy has been very rare because of several reasons: the low intrinsic sensitivity arising from a small gyromagnetic ratio (γ) of -1.639×10^7 rad s^{-1} T^{-1}, a low natural abundance of 10.0%, a relatively large quadrupole moment, and very low ^{25}Mg concentration in MOFs. Despite these problems, two very recent papers reported

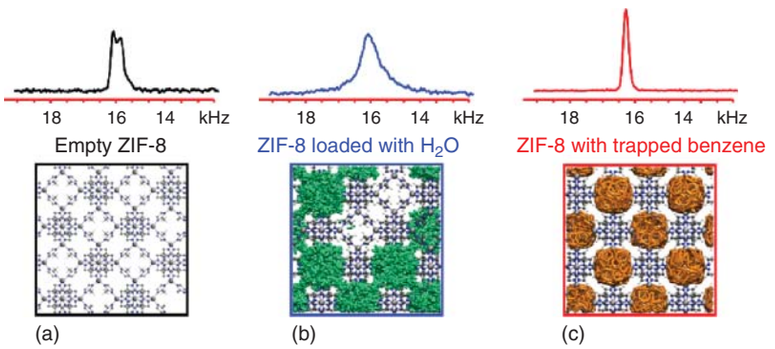


Figure 5 ^{67}Zn MAS spectra of (a) fully desolvated ZIF-8, (b) ZIF-8-H_2O, and (c) ZIF-8-benzene at 21.1 T. (Reprinted with permission from Ref. 15. © 2012, Wiley-VCH Verlag GmbH & Co. KGaA, 2007.)

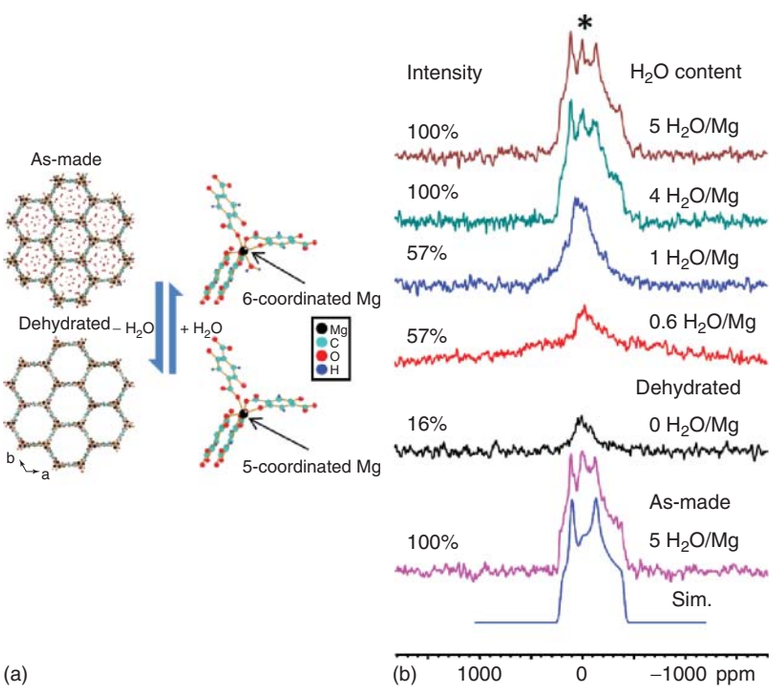


Figure 6 (a) The reversible transformation of local Mg environment[40] in CPO-27-Mg. For clarity, the hydrogens of water in the channels are omitted. (b) ^{25}Mg static SSNMR spectra of CPO-27-Mg as a function of rehydration degree. (Reprinted with permission from Ref. 16. Copyright (2013) American Chemical Society.)

natural abundance ^{25}Mg SSNMR spectroscopic studies of two representative Mg-containing MOFs.[16,17]

Xu *et al.* recently studied the effects of dehydration/rehydration and adsorption of organic molecules on Mg environments in an Mg-containing MOF namely CPO-27-Mg[40] or Mg-MOF-74[41,42] by ^{25}Mg SSNMR spectroscopy at 21.1 T.[16] This MOF has exceptional capability of adsorbing carbon dioxide. The framework of as-made CPO-27-Mg consists of the interconnecting helical chains of edge-shared MgO_6 units, forming one-dimensional honeycomb channels along the *c* axis (Figure 6a).[40] In each MgO_6, five of the six oxygen atoms come from four organic linkers (2,5-dioxido-1,4-benzene-dicarboxylate groups). The sixth oxygen is from a water molecule directly bound to the Mg, and this water molecule can be removed by dehydration, resulting in an open metal site that can strongly interact with guest species. Existence of such vacated coordination sites is responsible for several unique properties that this MOF possesses. ^{25}Mg static SSNMR spectra (Figure 6b) indicate that the local Mg environment

in as-made (i.e., fully hydrated phase) is perfectly ordered.[16] Upon removal of the water molecule bound to the metal, about 84% of ^{25}Mg spins are NMR invisible (i.e., they become unobservable) even at 21.1 T owing to their large $C_Q(^{25}Mg)$ values resulting from distorted square-pyramid geometry. The line-shape of the ^{25}Mg resonance suggests that the local Mg environment becomes disordered, although long-range ordering of the framework remains as indicated by the powder XRD pattern. The local Mg environment remains disordered if the sample is only partially rehydrated. The local ordering can be fully resorted only if enough water molecules are available for hydration. The adsorption of simple organic molecules such as acetone and acetonitrile also induces the disordering in local Mg environment. The origin of the disordering was unraveled by computational modeling.

One area that is important to MOF characterization is the utilization of SSNMR spectroscopy to determine the number of nonequivalent metal sites in unit cell. The ability of differentiating different sites is critical because it allows one to directly compare the NMR spectra with the X-ray determined structure. Recently, Xu and coworkers have demonstrated that multiple Mg sites with very similar local Mg environments in microporous α-$Mg_3(HCOO)_6$, a representative Mg-containing MOF, can be differentiated by natural abundance ^{25}Mg SSNMR at 21.1 T.[17] As mentioned earlier, the quadrupolar interaction broadens CT powder pattern and such broadening cannot be completely removed by magic-angle spinning. Indeed, both the static and the MAS spectra of three samples of microporous α-$Mg_3(HCOO)_6$, which are as-made (i.e., containing solvent dimethylformamide (DMF) molecules), activated (empty), and benzene-loaded phases, exhibit overlapping signals (Figure 7a, b) and therefore cannot confirm the XRD results that all three samples belong to the same space group ($P2_1/n$) and each contains four distinct octahedral Mg sites.[43] To achieve higher resolution, the authors used MQMAS method. As mentioned earlier, MQMAS is a 2D

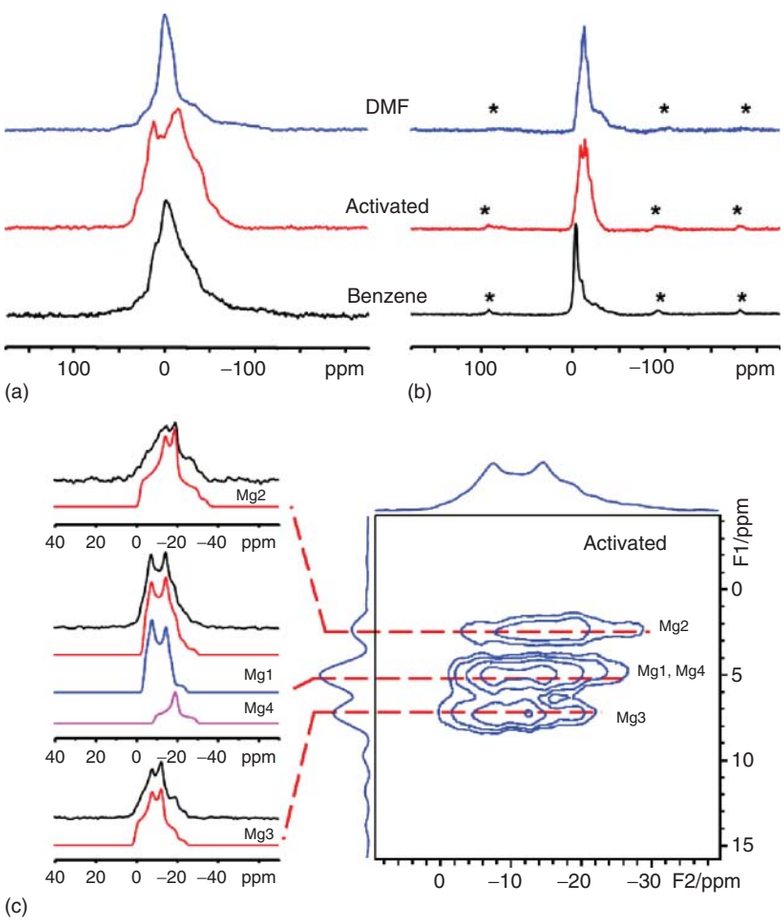


Figure 7 Natural abundance ^{25}Mg static (a), 5 kHz MAS (b) spectra of three microporous α-$Mg_3(HCOO)_6$ phases, and ^{25}Mg SPAM 3QMAS (c) spectrum of the activated sample. *: Spinning sidebands. All the spectra were acquired at 21.1 T. The dashed lines correspond to the slices taken for simulation. (Reprinted with permission from Ref. 17. © 2013, Wiley-VCH Verlag GmbH & Co. KGaA, 2007.)

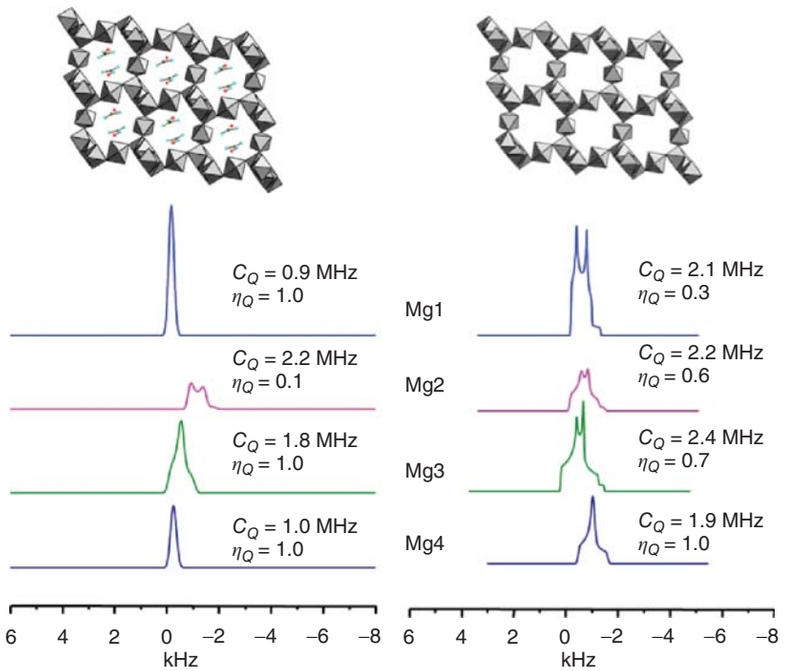


Figure 8 A comparison of the four individual Mg sites in as-made and activated phases obtained from simulating MAS spectra. (Reprinted with permission from Ref. 17. © 2013, Wiley-VCH Verlag GmbH & Co. KGaA, 2007.)

technique that can achieve high-resolution by removing the second-order quadrupolar broadening and separate multiple sites whose signals overlap in 1D spectra. The particular version of MQMAS used is called soft-pulse-added-mixing triple-quantum magic-angle spinning (SPAM-3QMAS),[44] which provides higher sensitivity than the standard triple quantum magic-angle spinning (3QMAS) sequence. The ^{25}Mg SPAM-3QMAS spectrum (Figure 7c) of the *activated* sample clearly exhibits three well-resolved peaks on the high-resolution ($F1$) dimension. The cross sections at the chemical shift positions of the two peaks at high- and low-fields can each be simulated with a single site, whereas the line-shape associated with the slice taken via the middle peak on $F1$ must be fitted by two signals. Thus, four Mg sites were identified by ^{25}Mg 3QMAS experiment. The correct relative intensities of four Mg sites can be obtained via simulation of the ^{25}Mg 1D MAS spectrum, and they are 2:1:2:1 for Mg1:Mg2:Mg3:Mg4, respectively, which is consistent with the occupancies of the four sites indicated by the X-ray structure. The four ^{25}Mg resonances can be further assigned based on the relative intensities in combination with the first principles calculations of ^{25}Mg NMR parameters using gauge including projector augmented wave (GIPAW) approach implemented in the Cambridge Serial Total Energy Package (CASTEP) code.[45,46] Similarly, the multiple Mg sites in the other two phases were also resolved. Figure 8 compares the individual sites before and after activation. It shows clearly that upon removal of DMF (solvent molecule) from the pore, the Mg1 and Mg4 undergo the larger distortion in their local environments compared to the Mg2 and Mg3 as evidenced from the doubling in their C_Q values.

In α-$Mg_3(HCOO)_6$, the line-widths of the Mg signals are quite narrow (the spectra breadths of static spectra are only about 7 kHz). The case of the ^{115}In static spectrum of MIL-68(In) at 21.1 T (Figure 9) (Huang, Peng, Terskikh, unpublished results), on the other hand, provides an example where the powder pattern of a metal ion can be extremely broad, yet the spectral resolution is not low. ^{115}In is a quadrupolar nucleus ($I = 9/2$). It has a high natural abundance (95.72%) and a rather high γ (its resonance frequency at 21.1 T is 197.2 MHz). However, ^{115}In has the largest nuclear quadrupole moment of the main group elements ($Q = 77.0\,\text{fm}^2$).[47] The large Q value leads to proportionally large nuclear quadrupolar coupling constants, often resulting in extremely broad NMR lines that are difficult to measure. For this reason, ^{115}In SSNMR has been very challenging. However, recent work has demonstrated that obtaining ^{115}In NMR spectra of solid samples with $C_Q(^{115}\text{In})$ values as large as 300 MHz is feasible at ultrahigh magnetic field of 21.1 T.[48] In the present case, the CT of ^{115}In in MIL-68(In) is about 4 MHz wide. Such a spectral width is too large to apply spinning-based techniques. As the breadth of the CT spectrum far exceeds

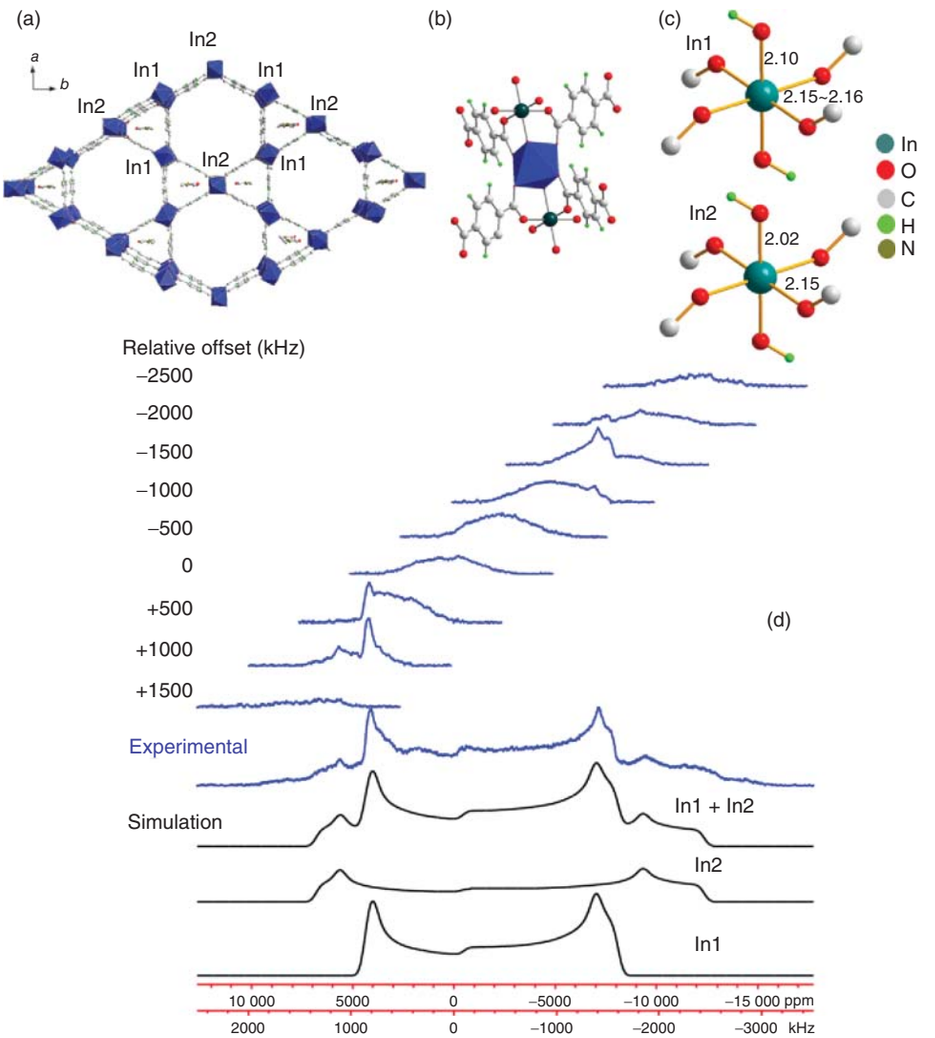


Figure 9 Illustrations of the framework (a), the metal coordination environment (b), two In sites (c), and ^{115}In static NMR spectra of MIL-68(In). (Huang, Peng, Terskikh, unpublished results.)

the radio-frequency (rf) pulse width's excitation profile, the frequency-stepped technique also known as the variable offset cumulative spectroscopy (VOCS) was used for spectral acquisition.[49] Specifically, this approach involves varying the offset of the transmitter frequency in steps to excite different spectral regions. Nine subspectra with different frequency offsets are co-added to give the powder pattern with correct line-shape. As shown in Figure 9, the observed spectrum can be well simulated using two indium sites with $C_Q(^{115}\text{In})$ values being 300 and 248 MHz. The intensity ratio for the broad and narrow components is about 1:2. These results are consistent with the crystal structure reported in the literature, which suggests that there are two crystallographically nonequivalent indium sites (2 In1, 1 In2).[50] On the basis of the intensity ratio, the narrow and broad signals can be assigned to In1 and In2, respectively. The reason why In2 has a larger $C_Q(^{115}\text{In})$ can be rationalized by the fact that the bond lengths (2.02 Å) of two In–OH bonds trans to each other in In(2)O_6 octahedron are noticeably shorter than those (2.10 Å) of In(1)O_6, resulting in the In(2)O_6 octahedron being more compressed along the HO–In–OH direction (Figure 9).

4 IDENTIFYING SPECTRAL SIGNATURES OF VARIOUS OXYGEN SPECIES BY ^{17}O SSNMR SPECTROSCOPY

Oxygen is a key framework element of many MOFs. It exists in various carboxylate ligands that are the

common linkers of many important MOFs. Some organic linkers have phenol groups and the phenol oxygen can bind to a metal ion upon deprotonation. Certain MOFs have terminal (–OH) and bridging hydroxyl (μ_2- and μ_3-OH) species in their frameworks and water molecules directly bound to the metal center. Oxygen anions interacting with multiple metal centers (μ_3-, and μ_4-O^{2-}) can often be found in many representative MOFs. These oxygen species are at the center of desolvation and host–guest interactions. ^{17}O ($I = 5/2$) is the only stable NMR-active isotope of oxygen and is quadrupolar. It has a large chemical shift range and is sensitive to the EFG tensor. It has been shown that ^{17}O SSNMR spectra are very sensitive to the local chemical and geometrical environments of oxygen in solids.[51,52] Thus, ^{17}O NMR spectroscopy should be, in principle, an ideal tool for probing the local environment of various oxygen species in MOF frameworks. However, in reality, ^{17}O SSNMR studies of MOF-based materials have been scarce. There have been only two reports of ^{17}O SSNMR study on MOF systems.[53,54] The rarity is largely due to the fact that ^{17}O has an extremely low natural abundance (0.037%). Consequently, ^{17}O SSNMR study almost always requires ^{17}O enrichment, which can be both financially expensive and synthetically challenging. Müller *et al*.[53] first showed that it is possible to incorporate ^{17}O into specific sites in MOF-5 structure. The ^{17}O signals in carboxylate group and μ_4-$^{17}O^{2-}$ in Zn_4O tetrahedron were observed in the MAS spectra. Further, the ^{17}O resonance due to ZnO nanoparticles impregnated inside MOF-5 via decomposition of Zn-containing organometallic precursors was also observed.

In a very recent paper, He and coworkers discussed several synthetic strategies for preparing different MOFs with ^{17}O-labelling at specific oxygen sites.[54] The approaches described are fairly simple and cost-effective. The authors demonstrate that ^{17}O SSNMR spectroscopy can differentiate chemically and crystallographically nonequivalent oxygen sites. Zr–UiO-66 is a good example that illustrates how several chemically different oxygen species coexisting in the same MOF can be distinguished by ^{17}O SSNMR spectroscopy. The structure of Zr–UiO-66 is built on the polyhedra containing eight coordinated zirconium atoms, which are connected by 1,4-benzenedicarboxylate (1,4-BDC) linkers.[55] The basic building unit of Zr–UiO-66, $Zr_6O_4(OH)_4$, consists of an octahedron formed by six Zr atoms. The eight triangular faces of the octahedron are capped alternatively by four μ_3-O^{2-} anions and four μ_3-OH groups (Figure 10). The ^{17}O SSNMR spectra can easily confirm the existence of three chemically different species (i.e., $-COO^-$, μ_3-O^{2-}, μ_3-OH) in this MOF. The ^{17}O MAS spectrum (Figure 10) exhibits three signals: the broad peak at around 270 ppm can be assigned to the carboxylate oxygen in 1,4-BDC ligands based on its chemical shift value. The resonance appearing at 65 ppm is assigned to the capping μ_3-OH. The identity of this signal is confirmed unambiguously by carrying out $^1H \rightarrow {}^{17}O$ cross polarization (CP) experiments under the MAS conditions. CP is one of the most useful SSNMR techniques often used for signal enhancement. It involves transferring magnetization from abundant sensitive spins (usually proton) to dilute insensitive spins. For instance, $^1H \rightarrow {}^{13}C$ and $^1H \rightarrow {}^{29}Si$ CP MAS have been extensively used for characterization of organic and inorganic materials. CP can also take place between proton and a quadrupolar nucleus (in this case, ^{17}O).[56] CP is mediated by the heteronuclear dipolar interaction between proton and the target spin. As the dipolar interaction strongly depends on the internuclear distance, this method can be used to identify spatially adjacent atomic species. Therefore, it can

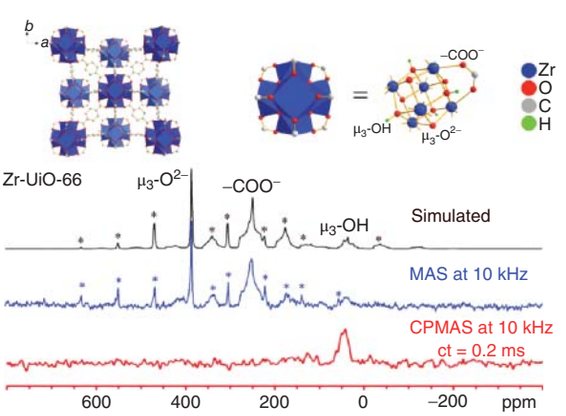


Figure 10 Illustrations of the framework (top left), the metal coordination environment (top right), and ^{17}O MAS and CP-MAS NMR spectra of Zr-UiO-66. *: Spinning sidebands. (Reprinted with permission from Ref. 54. Copyright (2013) American Chemical Society.)

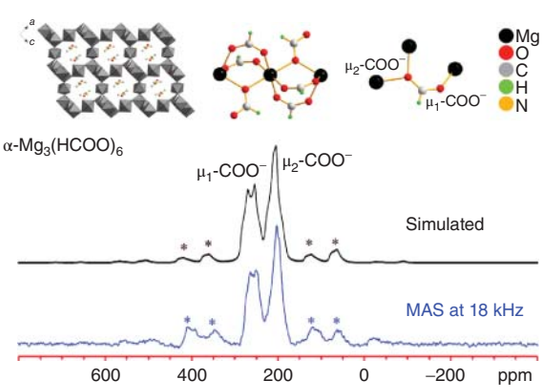


Figure 11 Illustrations of the framework with DMF (solvent) in the pore, Mg, and oxygen coordination environments and ^{17}O MAS NMR spectra of α-$Mg_3(HCOO)_6$. *: Spinning sidebands. (Reprinted with permission from Ref. 54. Copyright (2013) American Chemical Society.)

also be used as a spectral editing technique for spectral assignment. In the present case, when a very short contact time (ct) is used, only the ^{17}O with proton in its close proximity will be observed. Thus, seeing the 65 ppm peak in the CP MAS spectrum (Figure 10) at a short ct of 0.2 ms provides direct evidence that this resonance originates from μ_3-OH species. The third signal is a very sharp line at 386 ppm, which is assigned to the capping μ_3-O^{2-} species based on its chemical shift. It should be pointed out that X-ray diffraction cannot distinguish two different capping species (μ_3-O^{2-} and μ_3-OH), but they can be easily differentiated by ^{17}O SSNMR spectroscopy.

α-Magnesium formate, α-$Mg_3(HCOO)_6$ represents the situation where one of the oxygens in carboxylate group is bonded to one metal center (μ_1-O) and the other oxygen in the same COO^- group bound to two metal ions (μ_2-O).[43] The ^{17}O MAS spectrum of the as-synthesized α-$Mg_3(HCOO)_6$ acquired at 21.1 T (Figure 11) exhibits two separate resonances, indicating the existence of at least two groups of nonequivalent oxygens from the formate ligands. The crystal structure suggests that there are 12 nonequivalent oxygen sites that can be divided into two groups based on their bonding modes. Six independent oxygens adopt μ_2-O bonding mode, whereas the other six crystallographically nonequivalent O sites adopt μ_1-O mode. It appears that the two observed resonances originate from μ_2-O and μ_1-O oxygens. The spectral simulations yield the NMR parameters of the two observed signals. The more shielded resonance: $C_Q = 6.8$ MHz; $\eta_Q = 0.80$, $\delta_{iso} = 230$ ppm, and the more deshielded resonance: $C_Q = 8.0$ MHz; $\eta_Q = 0.45$, $\delta_{iso} = 289$ ppm. The authors further carried out the GIPAW density functional theory (DFT) calculations, and the results indicate that six μ_2-oxygens have very similar EFG parameters and chemical shifts: $C_Q = 5.96–6.82$ MHz; $\eta_Q = 0.74–0.93$, δ_{iso} = 210.3–234.0 ppm, and that the NMR parameters of the six μ_1-oxygens are akin to each other: $C_Q = 7.92–8.07$ MHz; $\eta_Q = 0.19–0.24$, $\delta_{iso} = 275.8–292.0$ ppm. Thus, the signals at 230 and 289 ppm can be assigned to the six μ_2- and the six μ_1-oxygens, respectively.[54]

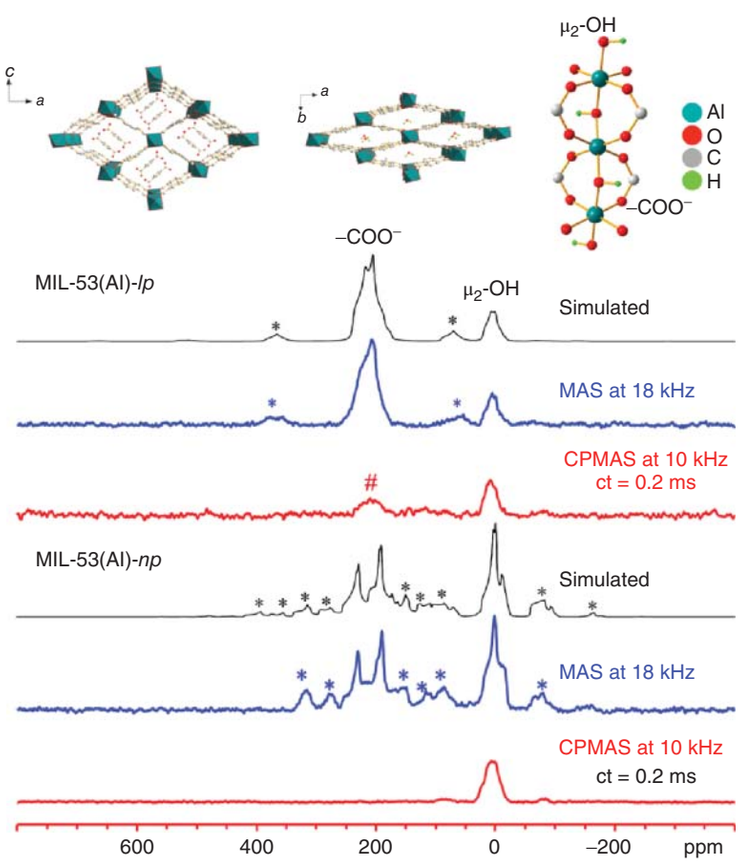


Figure 12 Illustrations of the frameworks of MIL-53(Al)-*lp* (top left) and MIL-53(Al)-*np* (top middle), the metal coordination environment (top right) and ^{17}O MAS NMR spectra of MIL-53(Al). #: Unreacted 1,4-benzenedicarboxylic acid. *: Spinning sidebands. (Reprinted with permission from Ref. 54. Copyright (2013) American Chemical Society.)

Many MOFs exhibit a large degree of framework flexibility. For these MOFs, adsorption/desorption of certain guest molecules can induce a very large change in unit cell volume. Although such change does not usually involve breaking the chemical bonds holding the framework together, the change in unit cell volume is often accompanied by a phase transformation. Using MIL-53(Al), a typical flexible MOF, He and coworkers were able to show that the phase transition can be monitored by ^{17}O SSNMR spectroscopy.[54] As-synthesized MIL-53(Al) crystallizes in an orthorhombic phase (also called the large pore (*lp*) phase).[12] Upon removing the unreacted terephthalic acid from the channels and subsequently adsorption of water, the orthorhombic phase transforms to a monoclinic phase with a much smaller channel dimensions (therefore, it is also referred to as the narrow pore (*np*) phase). The ^{17}O MAS spectrum of the as-synthesized MIL-53(Al) (Figure 12) displays two groups of signals. The strong resonance at about 230 ppm is assigned to the oxygen atoms in the 1,4-BDC linkers. The weaker signal at around 20 ppm is due to the bridging oxygen in the Al–OH–Al group. Significant change occurs in the ^{17}O MAS spectrum upon phase transition from an orthorhombic to a monoclinic phase. Specifically, the single peak due to the framework carboxylate oxygen observed in the *lp* phase now splits into several resonances in the spectrum of the *np* phase owing to the lower symmetry of the unit cell. This example shows that under favorable conditions, the change in the number of crystallographically nonequivalent oxygens due to phase transition can be followed by ^{17}O SSNMR spectroscopy.

5 SUMMARY

As more than 70% of the NMR-active stable isotopes in periodical table are quadrupolar, it is not surprising that vast majority of the metal centers in important MOFs are quadrupolar nuclei. Among the quadrupolar nuclei present in MOFs, many have low gyromagnetic ratios, low natural abundances, and large quadrupole moments, leading to low sensitivity and resolution. Solid-state NMR spectroscopy of quadrupolar nuclei has traditionally been considered very challenging. However, in recent years, significant progresses have been made in developing solid-state NMR spectroscopy of quadrupolar nuclei.[57] The advances in magnet, rf, and probe technologies, the emergence of the new pulse sequences for achieving high resolution and high sensitivity, the progress in NMR theory, and the development of software and computational methods greatly enhance our ability to study quadrupolar nuclei. Several cases were discussed in this chapter, and they illustrate that the SSNMR spectroscopy of quadrupolar nuclei can be used as an effective tool to provide unique structural and dynamic information complementary to that obtained from X-ray diffraction. We hope that this chapter will encourage more researchers to use SSNMR spectroscopy for investigation of MOF properties by interrogating quadrupolar nuclei.

6 ACKNOWLEDGMENTS

Y.H. acknowledges the Natural Sciences and Engineering Research Council of Canada (NSERC) for a Discovery Grant and a Discovery Accelerator Grant. He also thanks Canada Research Chair program for funding. The University of Western Ontario is also acknowledged for a small ADF grant. We thank Dr Victor Terskikh for technical assistance. Access to the 900-MHz NMR spectrometer and the CASTEP software was provided by the Canadian National Ultrahigh-Field NMR Facility for Solids (http://nmr900.ca).

7 RELATED ARTICLES

Edible Metal-Organic Frameworks; Metal-Organic Frameworks for Removal of Harmful Gases; Gas Storage in Metal-Organic Frameworks; Adsorption of Hydrocarbons and Alcohols in Metal-Organic Framework Materials; Open Metal Sites in Metal-Organic-Frameworks.

8 ABBREVIATIONS AND ACRONYMS

CASTEP = Cambridge Serial Total Energy Package; CP = cross polarization; CS = chemical shielding; CSA = chemical shift anisotropy; CT = central transition; ct = contact time; DFT = density functional theory; DMF = dimethylformamide; EFG = electric field gradient; GIPAW = gauge including projector augmented wave; IRMOF = isoreticular metal-organic framework; *lp* = large pore; MAS = magic-angle spinning; MD = molecular dynamics; MOF = Metal-organic framework; MQMAS = multiple quantum magic-angle spinning; *np* = narrow pore; PAS = principal axis system; rf = radio-frequency; SPAM = soft-pulse-added-mixing; SPAM-3QMAS = soft-pulse-added-mixing triple-quantum magic-angle spinning; SSNMR = solid-state nuclear magnetic resonance; ST = satellite transition; VOCS = variable offset cumulative spectroscopy; XRD = X-ray diffraction; ZIF = zeolitic imidazolate framework; 1,4-BDC = 1,4-benzene-dicarboxylate; 3QMAS = triple quantum magic-angle spinning.

9 REFERENCES

1. S. Devautour-Vinot, G. Maurin, C. Serre, P. Horcajada, D. Paula da Cunha, V. Guillerm, E.de Souza Costa, F. Taulelle, and C. Martineau, *Chem. Mater.*, 2012, **24**, 2168.
2. D. M. Dawson, L. E. Jamieson, M. I. H. Mohideen, A. C. McKinlay, I. A. Smellie, R. Cadou, N. S. Keddie, R. E. Morris, and S. E. Ashbrook, *Phys. Chem. Chem. Phys.*, 2013, **15**, 919.
3. L.-C. Lin, J. Kim, X. Kong, E. Scott, T. M. McDonald, J. R. Long, J. A. Reimer, and B. Smit, *Angew. Chem. Int. Ed.*, 2013, **52**, 4410.
4. M. Mazaj, G. Mali, M. Rangus, E. Žunkovič, V. Kaučič, and N. Z. Logar, *J. Phys. Chem. C*, 2013, **117**, 7552.
5. F. Gul-E-Noor, M. Mendt, D. Michel, A. Pöppl, H. Krautscheid, J. Haase, and M. Bertmer, *J. Phys. Chem. C*, 2013, **117**, 7703.
6. X. Kong, H. Deng, F. Yan, J. Kim, J. A. Swisher, B. Smit, O. M. Yaghi, and J. A. Reimer, *Science*, 2013, **341**, 882.
7. T. L. Kinnibrugh, A. A. Ayi, V. I. Bakhmutov, J. Zoń, and A. Clearfield, *Cryst. Growth Des.*, 2013, **13**, 2973.
8. A. J. Rossini, A. Zagdoun, M. Lelli, J. Canivet, S. Aguado, O. Ouari, P. Tordo, M. Rosay, W. E. Maas, C. Copéret, D. Farrusseng, L. Emsley, and A. Lesage, *Angew. Chem. Int. Ed.*, 2012, **51**, 123.
9. A. Cadiau, S. Auguste, F. Taulelle, C. Martineau, and K. Adil, *CrystEngComm*, 2013, **15**, 3430.
10. T. Loiseau, L. Lecroq, C. Volkringer, J. Marrot, G. Férey, M. Haouas, F. Taulelle, S. Bourrelly, P. L. Llewellyn, and M. Latroche, *J. Am. Chem. Soc.*, 2006, **128**, 10223.
11. Y. Jiang, J. Huang, S. Marx, W. Kleist, M. Hunger, and A. Baiker, *J. Phys. Chem. Lett.*, 2010, **1**, 2886.
12. T. Loiseau, C. Serre, C. Huguenard, G. Fink, F. Taulelle, M. Henry, T. Bataille, and G. Férey, *Chem. Eur. J.*, 2004, **10**, 1373.
13. R. Hajjar, C. Volkringer, T. Loiseau, N. Guillou, J. Marrot, G. Férey, I. Margiolaki, G. Fink, C. Morais, and F. Taulelle, *Chem. Mater.*, 2011, **23**, 39.
14. J. P. S. Mowat, S. R. Miller, A. M. Z. Slawin, V. R. Seymour, S. E. Ashbrook, and P. A. Wright, *Microporous Mesoporous Mater.*, 2011, **142**, 322.
15. A. Sutrisno, V. V. Terskikh, Q. Shi, Z. Song, J. Dong, S. Y. Ding, W. Wang, B. R. Provost, T. D. Daff, T. K. Woo, and Y. Huang, *Chem. Eur. J.*, 2012, **18**, 12251.
16. J. Xu, V. V. Terskikh, and Y. Huang, *J. Phys. Chem. Lett.*, 2013, **4**, 7.
17. J. Xu, V. V. Terskikh, and Y. Huang, *Chem. Eur. J.*, 2013, **19**, 4432.
18. T. Uemura, S. Horike, K. Kitagawa, M. Mizuno, K. Endo, S. Bracco, A. Comotti, P. Sozzani, M. Nagaoka, and S. Kitagawa, *J. Am. Chem. Soc.*, 2008, **130**, 6781.
19. N. B. Shustova, T.-C. Ong, A. F. Cozzolino, V. K. Michaelis, R. G. Griffin, and M. Dinca, *J. Am. Chem. Soc.*, 2012, **134**, 15061.
20. V. N. Vukotic, K. J. Harris, K. Zhu, R. W. Schurko, and S. J. Loeb, *Nat. Chem.*, 2012, **4**, 456.
21. S. Rives, H. Jobic, D. I. Kolokolov, A. A. Gabrienko, A. G. Stepanov, Y. Ke, B. Frick, T. Devic, G. Férey, and G. Maurin, *J. Phys. Chem. C*, 2013, **117**, 6293.
22. K. J. Ooms and R. E. Wasylishen, *Microporous Mesoporous Mater.*, 2007, **103**, 341.
23. S. Pawsey, I. Moudrakovski, J. Ripmeester, L.-Q. Wang, G. J. Exarhos, J. L. C. Rowsell, and O. M. Yaghi, *J. Phys. Chem. C*, 2007, **111**, 6060.
24. M.-A. Springuel-Huet, A. Nossov, Z. Adem, F. Guenneau, C. Volkringer, T. Loiseau, G. Férey, and A. Gédéon, *J. Am. Chem. Soc.*, 2010, **132**, 11599.
25. A. Sutrisno and Y. Huang, *Solid State Nucl. Magn. Reson.*, 2013, **49–50**, 1.
26. H. C. Hoffmann, M. Debowski, P. Mueller, S. Paasch, I. Senkovska, S. Kaskel, and E. Brunner, *Materials*, 2012, **5**, 2537.
27. K. Eichele, WSolids1: Solid-State NMR Spectrum Simulation, ver. 1.20.21, Universität Tübingen, 2013.
28. M. Bak, J. T. Rasmussen, and N. C. Nielsen, *J. Magn. Reson.*, 2000, **147**, 296.
29. D. Massiot, F. Fayon, M. Capron, I. King, S. Le Calve, B. Alonso, J.-O. Durand, B. Bujoli, Z. Gan, and G. Hoatson, *Magn. Reson. Chem.*, 2002, **40**, 70.
30. T. F. Kemp and M. E. Smith, *Solid State Nucl. Magn. Reson.*, 2009, **35**, 243.
31. F. A. Perras, C. M. Widdifield, and D. L. Bryce, *Solid State Nucl. Magn. Reson.*, 2012, **45–46**, 36.
32. L. Frydman and J. S. Harwood, *J. Am. Chem. Soc.*, 1995, **117**, 5367.
33. E. L. Hahn, *Phys. Rev.*, 1950, **80**, 580.
34. A. C. Kunwar, G. L. Turner, and E. Oldfield, *J. Magn. Reson.*, 1986, **69**, 124.
35. H. Li, M. Eddaoudi, M. O'Keeffe, and M. Yaghi, *Nature*, 1999, **402**, 276.
36. K. S. Park, Z. Ni, A. P. Côté, J. Y. Choi, R. Huang, F. J. Uribe-Romo, H. K. Chae, M. O'Keeffe, and O. M. Yaghi, *Proc. Natl. Acad. Sci. U. S. A.*, 2006, **103**, 10186.
37. D. Banerjee and J. B. Parise, *Cryst. Growth Des.*, 2011, **11**, 4704.
38. J. C. C. Freitas and M. E. Smith, *Annu. Rep. NMR Spectrosc.*, 2012, **75**, 25.
39. I. L. Moudrakovski, *Annu. Rep. NMR Spectro.*, 2013, **79**, 129.
40. P. D. C. Dietzel, R. Blom, and H. Fjellvåg, *Eur. J. Inorg. Chem.*, 2008, **2008**, 3624.
41. N. L. Rosi, J. Kim, M. Eddaoudi, B. Chen, M. O'Keeffe, and O. M. Yaghi, *J. Am. Chem. Soc.*, 2005, **127**, 1504.

42. T. M. McDonald, W. R. Lee, J. A. Mason, B. M. Wiers, C. S. Hong, and J. R. Long, *J. Am. Chem. Soc.*, 2012, **134**, 7056.
43. J. A. Rood, B. C. Noll, and K. W. Henderson, *Inorg. Chem.*, 2006, **45**, 5521.
44. Z. Gan and H.-T. Kwak, *J. Magn. Reson.*, 2004, **168**, 346.
45. M. D. Segall, P. J. D. Lindan, M. J. Probert, C. J. Pickard, P. J. Hasnip, S. J. Clark, and M. C. Payne, *J. Phys. Condens. Matter*, 2002, **14**, 2717.
46. S. J. Clark, M. D. Segall, C. J. Pickard, P. J. Hasnip, M. J. Probert, K. Refson, and M. C. Payne, *Z. Kristallogr.*, 2005, **220**, 567.
47. P. Pyykkö, *Mol. Phys.*, 2008, **106**, 1965.
48. F. Chen, G. B. Ma, G. M. Bernard, R. G. Cavell, R. McDonald, M. J. Ferguson, and R. E. Wasylishen, *J. Am. Chem. Soc.*, 2010, **132**, 5479.
49. D. Massiot, I. Farnan, N. Gautier, D. Trumeau, A. Trokiner, and J. P. Coutures, *Solid State Nucl. Magn. Reson.*, 1995, **4**, 241.
50. C. Volkringer, M. Meddouri, T. Loiseau, N. Guillou, J. Marrot, G. Férey, M. Haouas, F. Taulelle, N. Audebrand, and M. Latroche, *Inorg. Chem.*, 2008, **47**, 11892.
51. S. E. Ashbrook and M. E. Smith, *Chem. Soc. Rev.*, 2006, **35**, 718.
52. G. Wu, *Prog. Nucl. Magn. Reson. Spectrosc.*, 2008, **52**, 118.
53. M. Müller, S. Hermes, K. Kähler, M. W. E.van den Berg, M. Muhler, and R. A. Fischer, *Chem. Mater.*, 2008, **20**, 4576.
54. P. He, J. Xu, V. V. Terskikh, A. Sutrisno, H.-Y. Nie, and Y. Huang, *J. Phys. Chem. C*, 2013, **117**, 16953.
55. J. Hafizovic Cavka, S. Jakobsen, U. Olsbye, N. Guillou, C. Lamberti, S. Bordiga, and K. P. Lillerud, *J. Am. Chem. Soc.*, 2008, **130**, 13850.
56. T. H. Walter and E. Oldfield, *J. Phys. Chem.*, 1989, **93**, 6744.
57. R. E. Wasylishen, S. E. Ashbrook, and S. Wimperis, 'NMR of Quadrupolar Nuclei in Solid Materials', Wiley, 2012.

PART 4
Nets

Single-Crystal to Single-Crystal Transformations in Metal-Organic Frameworks

Subhadip Neogi, Susan Sen and Parimal K. Bharadwaj

Indian Institute of Technology Kanpur, Uttar Pradesh, India

1	Introduction	473
2	Single-Crystal to Single-Crystal Transformations	474
3	Outlook and Future Perspectives	520
4	Acknowledgment	520
5	Related Articles	520
6	Abbreviations and Acronyms	520
7	References	520

1 INTRODUCTION

Synthesis, characterization, and reactivity of coordination polymers, also called metal-organic frameworks (MOFs), have been an active field of research in recent years. With the explosive growth in the synthesis of these materials, new structural motifs as well as properties are emerging. Compounds with porous frameworks are particularly interesting if the structural integrity is maintained on removal of guest molecules. Such stable porous structures are potentially important in various contemporary applications as functional materials.[1–5] One of the most important findings in porous MOFs is their flexible and dynamic character[6,7] that results from the cooperative action of organic and inorganic moieties. For these materials, changes between solid phases under external stimuli can be interesting, especially when such changes take place without losing crystallinity, allowing direct visualization via X-ray crystallography. Direct observation of guest molecules occupying the voids in a coordination polymer, or change in the framework topologies on heat treatment, will offer ways to modify the coordination space for chemical transformations,[8,9] guest exchange,[10] separation of geometrical isomers,[11] incorporation into a device for substrate-triggered sensor,[12] and so on. Such reactions are known[13] in solids but they are often accompanied by catastrophic failure of crystallinity. On the other hand, the shrinkage and/or expansion of the frameworks correlate well with guest-shape sensitive fitting of the pore, in which a network is transformed into another, in a manner very similar to bioenzymes.

With the ever-increasing tendency of synthesizing more exotic frameworks, a sizable number of systems are available in the literature, which exhibit structural flexibility on removal of guest molecules in the lattice without losing crystallinity. Also, examples are growing[14–18] where metal or ligand exchange takes place in MOFs structures in single-crystal to single-crystal (SC–SC) transformations affording new improved materials with enhanced characteristics. Again, in MOFs, the metal center may coordinate one or more small solvent molecules that can be removed by other organic molecules. These substitution reactions at the metal center are a very important phenomenon[19] and are now beginning to realize their potential in tackling several contemporary problems. All these aspects are also covered here, although literature coverage in the present article is not claimed to be exhaustive. Transformations where two linkers being close to each other undergo photochemical condensation reactions to form a four-membered cyclic product without losing crystallinity is a very interesting postsynthetic modification of MOFs. This aspect is not covered here as an excellent review on this subject[20] is available.

Metal-Organic Framework Materials. Edited by Leonard R. MacGillivray and Charles M. Lukehart.
© 2014 John Wiley & Sons, Ltd. ISBN 978-1-119-95289-3

2 SINGLE-CRYSTAL TO SINGLE-CRYSTAL TRANSFORMATIONS

2.1 Single-Crystal to Single-Crystal Transformations with Lattice Guest Exchanges

Apohost with permanent porosity can be obtained when lattice guest molecules are removed without affecting crystallinity and maintaining the pore sizes and their shapes intact. In these systems, either the same or different types of guest molecules can be reintroduced into the framework. Such systems represent the simplest kind of SC–SC transformation.

A guest-exchange chemistry was observed[21] in the case of a microporous MOF, $[Ni(bpy)_{3/2}(NO_3)_2 \cdot EtOH]$ [**1**] (bpy = 4,4′-bipyridine), where removal and reintroduction of ethanol molecules were observed with a minimum structural change (Figure 1). Although, the ethanol molecules liberate slowly at room temperature, rapid and complete guest desorption occurs only on heating to 100 °C. The channel volume remains almost unchanged on desolvation, allowing analogy of the evacuated framework with zeolites. The minimum structural relaxation observed is owing to a subtle scissorlike action of the bilayers with a slight decrease in the bilayer torsion angle from 65.5° to 63.9°.

Cooperativity can be an integral part of a flexible framework and interesting results may be obtained if the metal sites are involved. Thus, the framework $Fe_2(azpy)_4(NCS)_4 \cdot (EtOH)$ [**2**] (azpy = *trans*-4,4′-azopyridine; EtOH = ethanol), reported by Kepert and coworkers,[22] displays reversible uptake and release of guest molecules. The Fe(II) centers within the framework lattice undergo spin crossover depending on adsorption/desorption of guests. The interpenetrated framework structure displays considerable flexibility with guest uptake and release, causing substantial changes in the local geometry of the Fe(II) centers (Figure 2).

The rodlike linker (Scheme 1) affords two different two-dimensional (2D) coordination polymers with Ni(II),

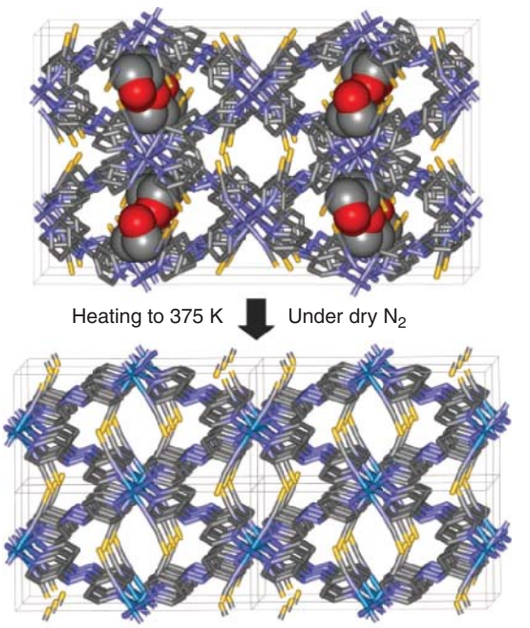
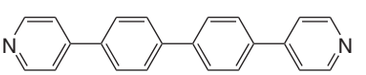


Figure 2 X-ray crystal structures of EtOH sorbed and desorbed compound down the 1D channels (*c*-axis). Framework atoms are represented as sticks and atoms of the ethanol guests as spheres



Scheme 1 Schematic diagram of the long bipyridine ligand, $\mathbf{L_1}$

composed of almost square grids, depending on the reaction conditions.[23] When a solution of $Ni(NO_3)_2$ in MeOH is layered over a solution of the linker in *o*-xylene, single crystals of the polymer, $\{[Ni(\mathbf{L_1})_2(NO_3)_2] \cdot (o\text{-xylene})_4\}_n$ [**3**] is formed in high yields as 2D square-grid structure of dimension $19.9 \times 20.0\ Å^2$. These 2D layers are stacked on each other to create rectangular channels (Figure 3) of dimension, $10.0 \times 20.0\ Å^2$ that are occupied

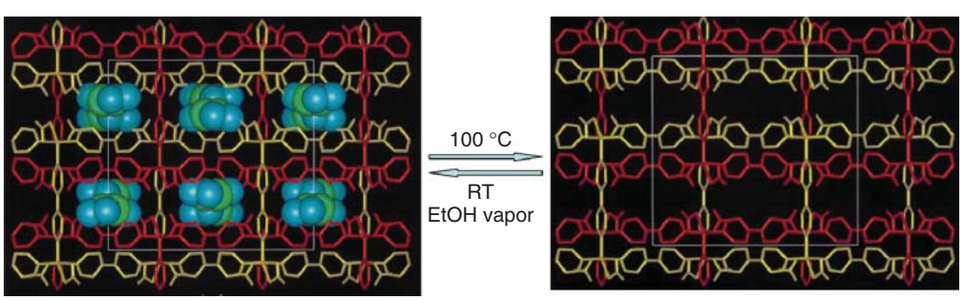


Figure 1 Structural projections down the *a*-axis, drawn to scale, showing the complete removal of ethanol molecules from **A** to form **B**

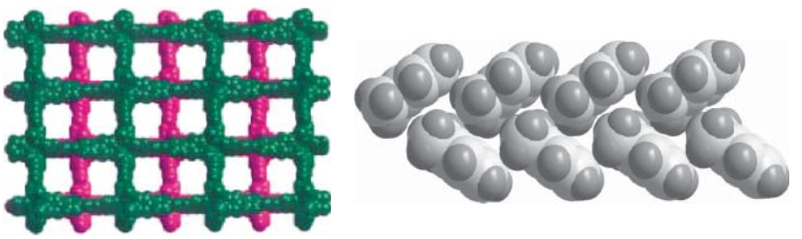
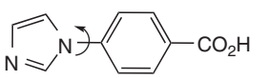


Figure 3 Stacking of 2D layers to form rectangular channels



Scheme 2 Schematic representation of 4-(1H-imidazole-1-yl)benzoic acid (HIBA). (Reproduced with permission from Ref. 24. Copyright 2009 American Chemical Society.)

by 1D arrays of *o*-xylene molecules (Figure 3). These guest molecules can be removed completely by heating the crystals at 150 °C under 100 mm Hg pressure for 3 h with no noticeable change in the cell constants and space group. When benzene is used in place of *o*-xylene, $\{[Ni(\mathbf{L_1})_2(NO_3)_2]\cdot 5(\text{benzene})\cdot 2MeOH\}_n$ [**3′**] is formed which forms a structure similar to that of the one described above. However, in this case, no SC–SC transformation takes place and the crystallinity is lost.

In cases where the linkers have flexible domains such as rotational freedom, guest removal/exchange can be accomplished without losing crystallinity as the system can adjust minor changes. A Cd(II)-containing MOF, $\{[Cd(IBA)_2]\cdot 2DMF\}_n$ [**4**], is built[24] with the linker 4-(1H-imidazole-1-yl)benzoic acid (HIBA), incorporating a rotatable C–N bond (Scheme 2) between imidazole and aromatic carboxylate moieties, and shows interesting guest-exchange properties. In this structure, the imidazole and the benzene moieties are not coplanar but are slightly twisted with respect to each other (torsion angles of 29.7° and 29.1°). This binding mode leads to the formation of large adamantanelike cages (Figure 4). Each cage is delineated by four cyclohexanelike windows in chair conformation. The overall structure (Figure 4) shows a fourfold interpenetration of the diamondoid network. Even with this interpenetration, the framework is highly

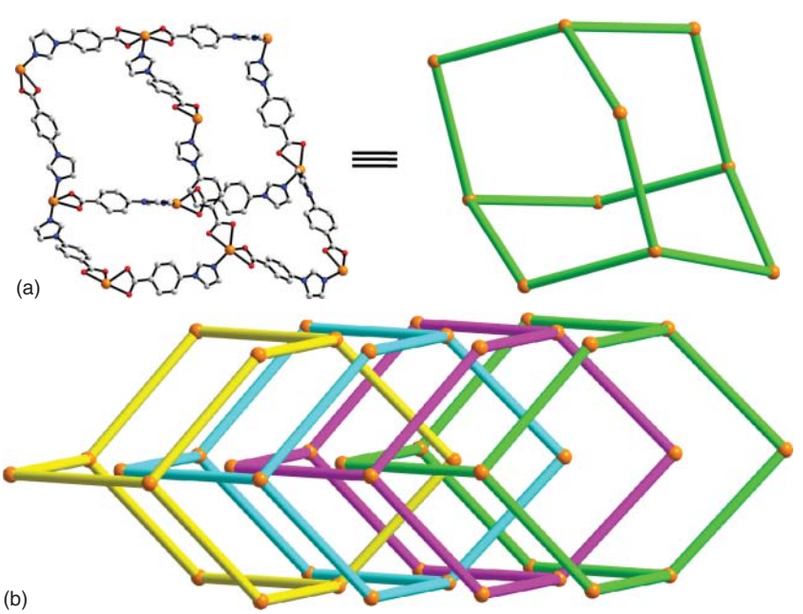


Figure 4 (a) Perspective views of the structure of a single adamantane cage with HIBA connections between cadmium ions. (b) View of the structure of **4**⊃2DMF, showing the fourfold interpenetration of diamondoid networks. (Reprinted with permission from Ref. 24. Copyright (2009) American Chemical Society.)

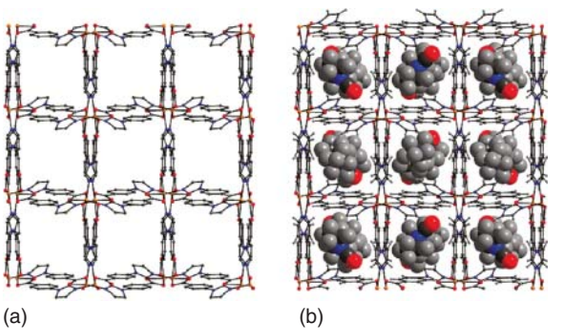


Figure 5 (a) Simplified view of the MOF structure, showing square channels along *b*-axis (hydrogen atoms are omitted for clarity). (b) View showing the inclusion of DEF molecules in the cavity of the framework. (Reprinted with permission from Ref. 24. Copyright (2009) American Chemical Society.)

open containing channels occupied by dimethylformamide (DMF) molecules that are H-bonded to the framework. Heating **4** to 200 °C under 80 mm Hg pressure for 2 h results in $\{[Cd(IBA)_2]\}_n$ [**4′**]. This compound on exposure to DMF vapor for 10 days leads to recovery of the original crystals. Again, crystal **4** on dipping in diethylformamide (DEF) at RT for 4 weeks affords $\{[Cd(IBA)_2]\cdot 3DEF\cdot H_2O\}_n$ [**4″**] in a SC–SC transformation (Figure 5). To accommodate DEF molecules in the voids, the imidazole ring undergoes rotation with respect to the benzene ring. The dihedral angles between the benzene and imidazole rings in **4″** increase from 29.7° and 29.1° (in **4**), to 31.2° and 41.9°. Also, coordination of each metal ion increases from six to seven as one H_2O molecule gets bonded to the metal ion.

Reports on adsorption and separation of organic halocarbons employing MOFs, in SC–SC pathway, are rare. As a notable exception, Liu *et al.*[25] successfully realized the reversible adsorption of volatile chlorocarbon species such as CH_2Cl_2, $CHCl_3$, and CCl_4, (Figure 6) and their complete separation using a Cd(II)-MOF ($[Cd(\mathbf{L_2})_2(ClO_4)_2]\cdot H_2O$ [**5**], $\mathbf{L_2}$ = 4-amino-3,5- bis(4-pyridyl-3-phenyl)-1,2,4-triazole) in the vapor phase. On exposure of crystals of the polymer for 2 days to a mixed vapor containing equimolar amounts of CH_2Cl_2, $CHCl_3$, and CCl_4 in a sealed vial at room temperature, only $CHCl_3$ enters into the pores. The framework shows an overall selectivity sequence: $CHCl_3 > CH_2Cl_2 > CCl_4$.

A novel guest-shape-responsive fitting of porous MOF structure with soft framework has been demonstrated.[26] Using the semirigid octacarboxylic acid [5,5′-(2,2-bis((3,5-dicarboxyphenoxy) methyl)propane-1,3-diyl)bis(oxy)diisophthalic acid] and Zn(II) metal cations, five microporous Zn-MOFs could be isolated using different organic solvents (DMSO/EtOH, DMA, DEA, DMP, and DEP). When the DMSO-solvate crystals [**6**·DMSO] is dipped in another solvent, organic-solvent-substituted single crystals, **10**·DMF, **10**·DMA, and **10**·EtOH are obtained (Figure 7).

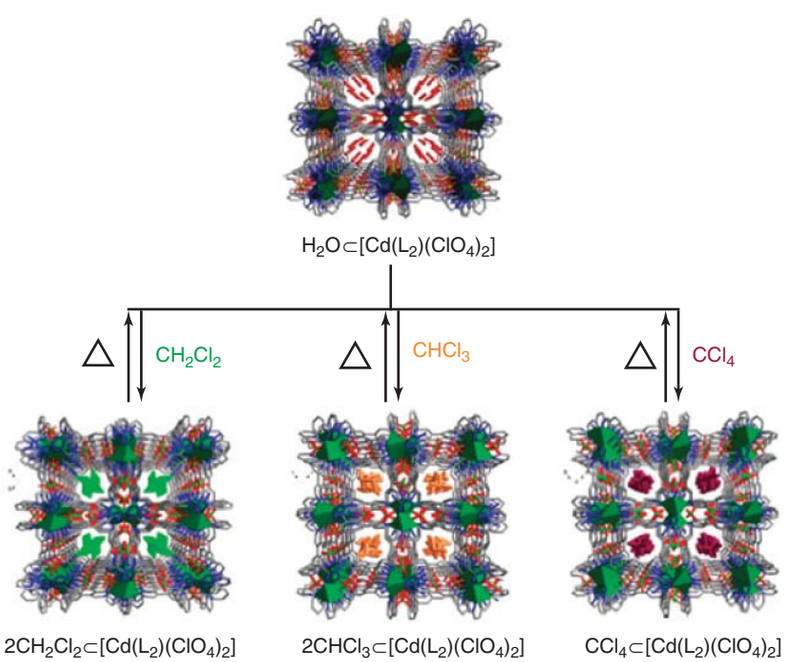


Figure 6 Reversible adsorption of CH_2Cl_2, $CHCl_3$, and CCl_4 based on $H_2OC[Cd(\mathbf{L_2})_2(ClO_4)_2]$ [**5**], and their single-crystal structures. Single-crystal analysis indicates that the encapsulated chlorocarbon species are disordered in the pores, so only major disordered components are shown in the figure. The different chlorocarbon guests are shown in different colors for clarity

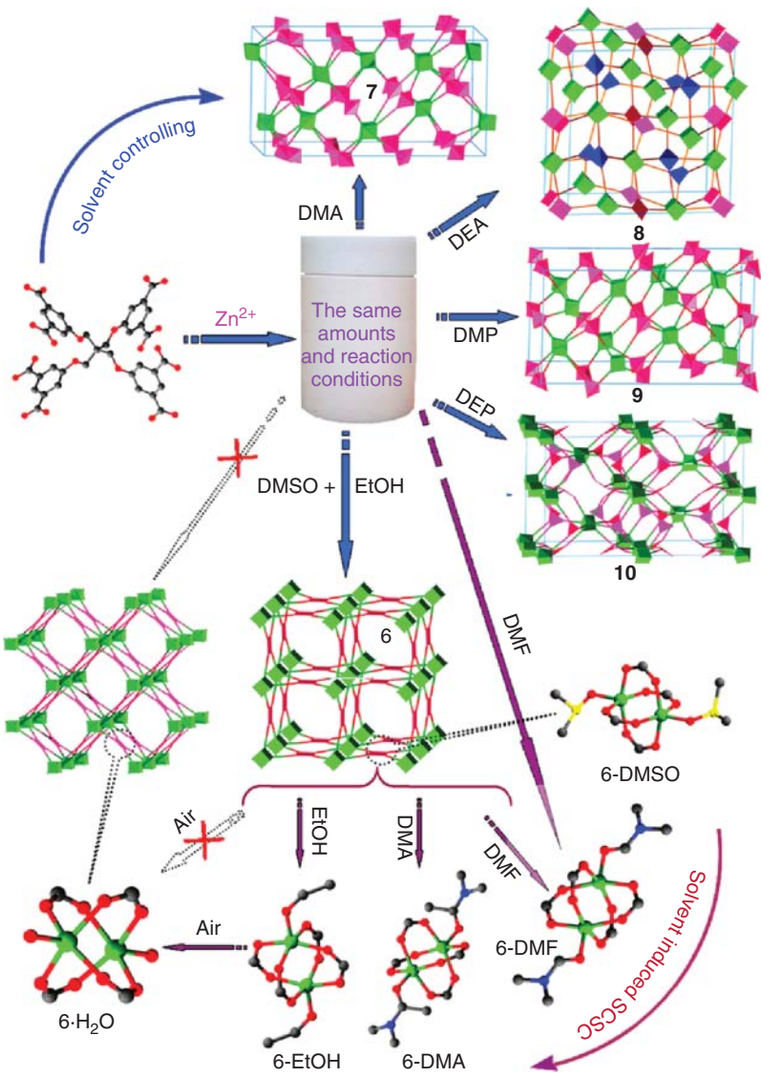


Figure 7 Schematic illustration for the solvent-controlled synthesis of compounds **6–10** (with blue arrows) and solvent-induced SCSC transformation/stepwise synthesis of other MOFs (with purple arrows) from **6**·DMSO. The topological structures are presented in the solvent-controlled synthesis part, and topological structure of **6**·H_2O and only coordination environments of Zn_2 clusters are displayed for the compounds in the SCSC transformation part. (Reprinted with permission from Ref. 26. Copyright (2012) American Chemical Society.)

In an interesting example, a fourfold interpenetrated pseudodiamondoid MOF, $\{[Co(pybz)_2]\cdot 2DMF\}_n$ [**11**] [pybz = 4-(4-pyridyl)benzoate] (Figure 8) has been reported,[27] which contains 1D square channels occupied by DMF molecules. It is a rare example of a stable MOF based on a single octahedral building unit. The structure is stabilized by fourfold interpenetration of the networks (Figure 8). Presence of H-bonding interactions effectively prevents relative motion of each diamondoid net and acts as the main factor for its robustness. The DMF molecules in the channels can be removed by slow warming to ~80 °C in a stream of N_2 to afford a porous framework. This porous framework adsorbs gases such as CO_2, N_2, H_2, and CH_4 to different extents. It also adsorbs vapors of MeOH, EtOH, benzene, and cyclohexane without losing crystallinity. In all of them, the framework is marginally modified and contains a highly distorted and strained octahedral node of Co(II) with two pyridine N and four O from two carboxylate groups bonded to the metal. However, on exposure to air, the crystals readily change colour from claret red to light pink with loss of crystallinity and also loses gas adsorption properties.

In principle, the size and shape of the voids in a framework should allow the possibility of guest

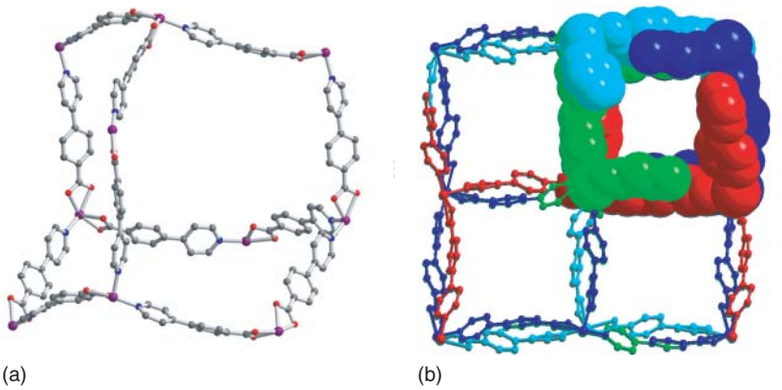


Figure 8 (a) Perspective view of the diamondoid network of a single cobalt node connected by four organic linkers. (b) Perspective views of the 3D open framework with 1D channel. The guest DMF molecules occupying the channels are not shown. (Reprinted with permission from Ref. 27. Copyright (2013) American Chemical Society.)

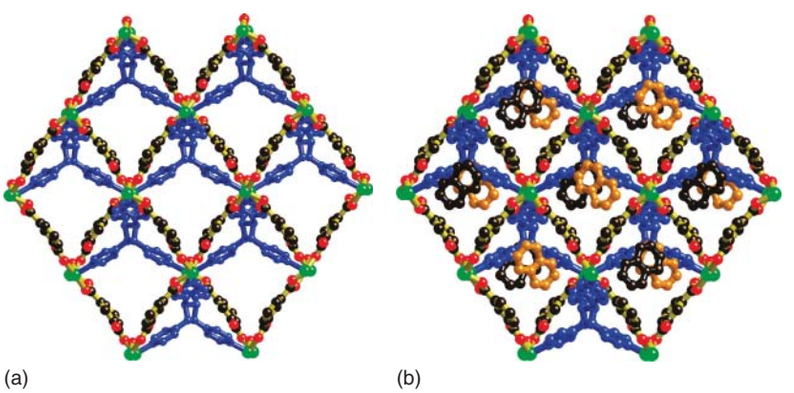


Figure 9 View of the Ni(II)-containing polymer along the *a*-axis without any guest molecules (a) and (b) view of the guest-included structure. (Reprinted with permission from Ref. 28. Copyright (2013) American Chemical Society.)

discrimination based on their size, shape as well as nature. However, examples of such systems through SC–SC modes are very uncommon. In a rare example,[28] the MOF $\{[Ni_2(\mu_2\text{-}OH_2)(1,3\text{-}BDC)_2(tpcb)]\cdot 12H_2O\}_n$ [**12**] (1,3-BDC=1,3-benzenedicarboxylic acid; tpcb=tetrakis(4-pyridyl)cyclobutane) and its porous guest-free form $\{[Ni_2(\mu_2\text{-}OH_2)(1,3\text{-}BDC)_2(tpcb)]\}_n$ [**12′**] have been reported. The structure of the framework reveals infinite and irregular channels with small kite-shaped windows that open up into larger chambers along the channels (Figure 9). Although loss of the lattice water molecules causes a contraction of the cell volume, the framework remains unchanged. The guest-free polymer can separate naphthalene from anthracene in the vapor phase as only the former, having smaller size, is preferentially adsorbed into the pores. The naphthalene, sorbed by the coordination network, can be recovered by soaking in ethanol and the porous guest-free coordination network is regenerated by heating the sample with retention of its crystallinity.

Dynamic guest accommodation of soft porous structures can enable the uniform arrangement and orientation of guest molecules, allowing the possibility to trap even very reactive species that are unstable outside the restricted environment. The ditopic organic linker, $H_2CPMA\cdot$[H_2CPMA = bis(4-carboxyphenyl)-*N*-methylamine], forms a three-dimensional (3D) luminescent MOF,[29] $\{Li_3[Li(DMF)_2](CPMA)_2\}_n$ [**13**]. This compound shows two kinds of rectangular channels, A and B, along the crystallographic *c*-axis (Figure 10). When the as-synthesized compound is immersed in nitrobenzene, the guest enters the channels without losing crystallinity. Color of the crystals change from pale yellow to dark red due to charge-transfer transition between the aromatic rings of the electron-rich $CPMA^{2-}$ and the electron-deficient nitrobenzene, allowing visual detection of explosive nitroaromatics (Figure 11).

A series of porous mixed-MOFs (**M′MOF**s) have been reported[30] by reacting the tridentate preconstructed

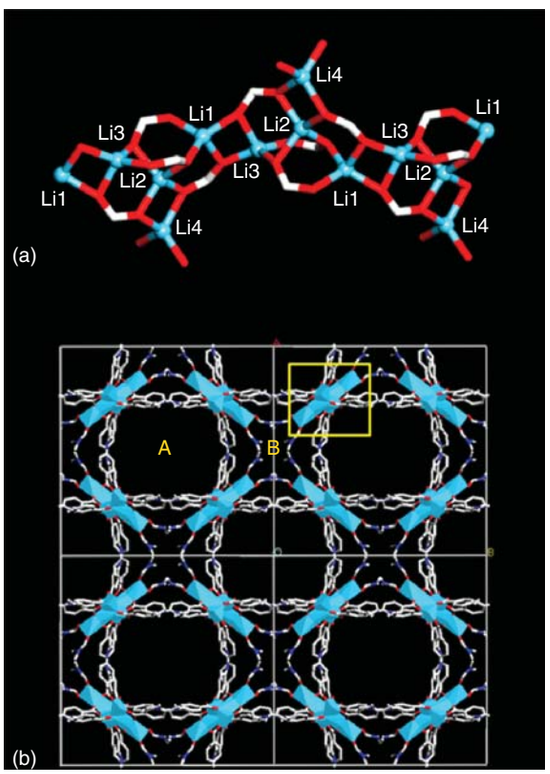


Figure 10 (a, b) Single-crystal X-ray structure of the Li-MOF [**13**] viewed down the *c*-axis. (Reprinted with permission from Ref. 29. Copyright (2013) American Chemical Society.)

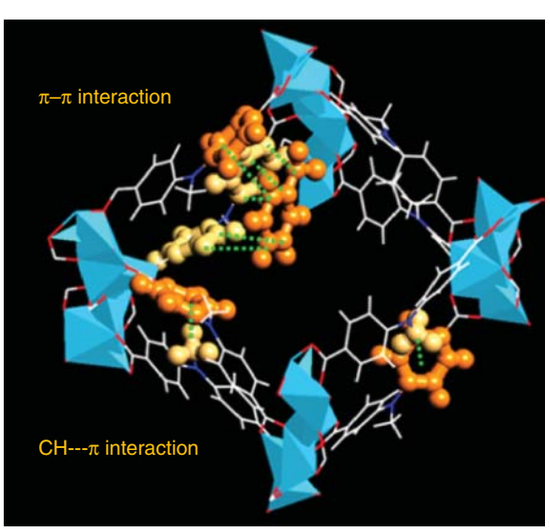


Figure 11 X-ray structure of nitrobenzene-included MOF. (Reprinted with permission from Ref. 29. Copyright (2013) American Chemical Society.)

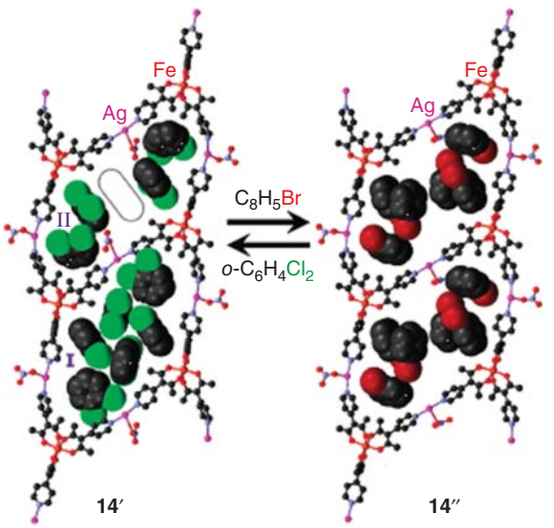


Figure 12 Crystal structures of **M′MOF** [**14′**], $[AgNO_3]_3[Fe(Pyac)_3]_2(1,2\text{-}C_6H_4Cl_2)_{5.5}$, and **M′MOF** [**14″**], $[AgNO_3]_3[Fe(Pyac)_3]_2(C_6H_5Br)_6$, and reactions representing their single-crystal to single-crystal transformation. H atoms and minor components of disordered guest molecules are omitted for clarity. (Reprinted with permission from Ref. 30. Copyright (2008) American Chemical Society.)

building block $Fe(Pyac)_3$ {bis-[3-(4-pyridyl)pentane-2,4-dionato]Iron(II)} with $AgNO_3$. The **M′MOF** [**14**], reinforced by weak Ag … Ag and Ag–nitrate–Ag interactions, is a robust porous 1D ladder structure and exhibits solvent-dependent reversible SC–SC transformations on guest exchange. The authors found that although **M′MOF**s (**14′** and **14″**) contain the same framework (Figure 12), they have slightly different crystal symmetry and their channels have different shapes. This indicates that the framework is not only sufficiently robust to withstand guest exchange but also flexible enough to accommodate guests of slightly different sizes and packing properties.

Structural flexibility in terms of mutual slide of independent frameworks enables a new type of dynamic functionality to occur, the so-called controllable gate-opening property. Aijaz *et al.*[31] reported a Zn(II) coordination polymer having nanotubular threefold entangled (2D→3D) structure (Figure 13) with embedded water molecules in the voids of the framework. The crystals on heating at 100 °C under vacuum for 4 h afford the desolvated compound in a SC–SC transformation, where the overall connectivity remains unchanged. X-ray structural studies reveal relative sliding of the individual motifs, causing expansion of the overall framework. Furthermore, the guest water molecules in the pores are partially exchanged by dipping the as-synthesized crystal in various solvents such as methanol, ethanol, and acetone. This process gives rise to inclusion of EtOH or MeOH, in a reversible SC–SC

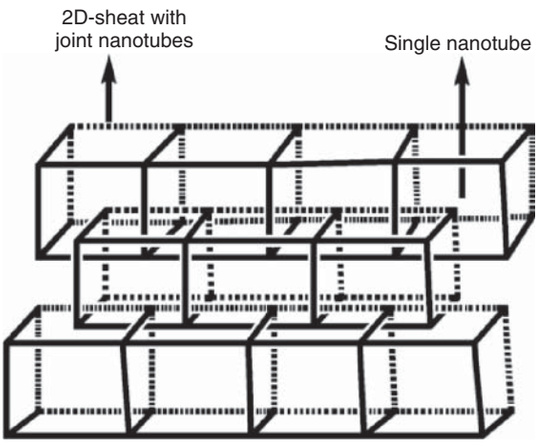


Figure 13 A perspective view of the threefold entangled nanotubular structure

manner and leaves the size of the voids in the framework unaltered. Inclusion of acetone, however, is accompanied by shrinking of the voids in the framework.

A neutral 3D polycatenated framework $[Cu_2I_2(BTTP_4)]\cdot 2CH_3CN$ [**15**] has been reported[32] consisting of two sets of inclined 2D networks that maintain the single crystallinity despite removal of the solvents. The solvent-free framework retains its single crystallinity even after heating in aromatic solvents to include benzene, toluene, or ethylbenzene as guests. The single-crystal X-ray analysis of the guest-inclusion complexes divulges that the coordination frameworks remain unchanged after adsorbing any of these guest molecules. The cell volume, network catenation, and pore size remain nearly constant regardless of guest molecule exchange (Figure 14).

Kyprianidou *et al.*[33] reported a flexible microporous 3D Cd(II) organic framework [**16**], containing the triangular building block $[Cd_3(COO)_6(DMF)_3]$ as the secondary building unit (SBU). The SC–SC solvent-exchange reaction goes smoothly with $CHCl_3$ at 50 °C to replace DMF molecules by those of $CHCl_3$. The solvent exchange is fully reversible and the parent crystals can be regenerated by treating the chloroform-exchanged compound with DMF. The framework is also found to be capable of exchanging its guest molecules by relatively large aromatic molecules such as benzene and toluene without losing crystallinity. Moreover, the framework is able to discriminate toluene from a benzene–toluene mixture. The selective insertion of toluene into the framework cavity is due to the "breathing" of the framework, which is favored by the flexible nature of this MOF (Figure 15).

The MIL-53 (M^{III}) systems, owing to their remarkable framework flexibility coupled with promising gas adsorption properties, have received enormous attention from researchers. Xu *et al.*[10] reported Mn(II)-based structural analogues of MIL-53 and investigated their usage in adsorption and separation of C6–C8 aromatics in SC–SC manner. Using evacuated porous MIL-53(Mn(II)) [**17**] as an absorbent, the authors observed that only C6–C7 molecules can be intercalated from a mixture of benzene, toluene, xylenes, ethylbenzene, and chlorobenzene

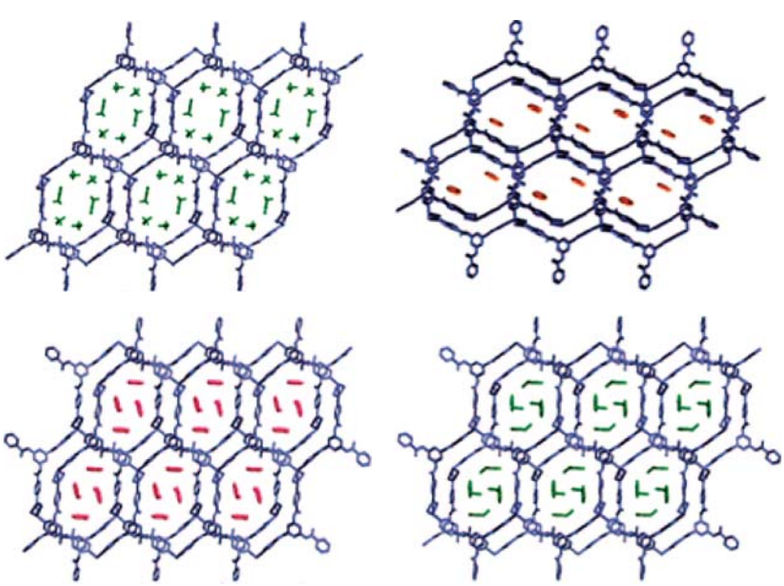


Figure 14 Solvent guest molecule inclusion in the framework. From top to bottom: **15**·$2CH_3CN$, **15**·benzene, **15**·2toluene, and **15**·2ethylbenzene

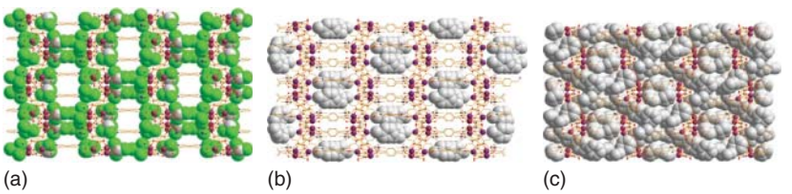


Figure 15 View of the structure of (a) $CHCl_3$, (b) toluene, and (c) benzene inclusion frameworks

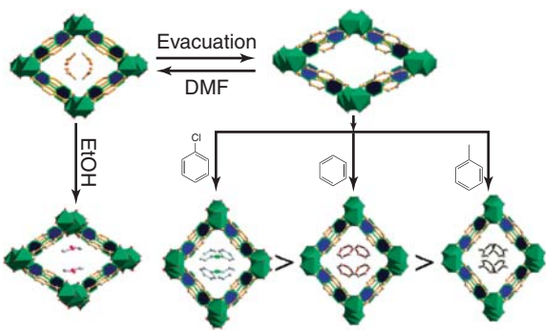


Figure 16 Guest exchange of evacuated MIL-53(Mn(II)) with EtOH and selective absorptions of C6–C8 aromatics in a crystal to crystal transformations. (Reprinted with permission from Ref. 10. Copyright (2010) American Chemical Society.)

(Figure 16). The solvates fill the channels in pairs. For selective adsorption and separation of C6–C8 aromatics, it is proposed that π–π interactions, involving the guest–guest and guest–framework, play pivotal roles. On the basis of the studies, the authors also established the guest selectivity trend: chlorobenzene > benzene > toluene for the adsorbent.

To realize a "shape-responsive fitting" of the voids, a porous framework has to be able to deform its structure using both expansion and shrinkage to accommodate a guest molecule effectively. Medishetty *et al.*[34] successfully described a flexible MOF [**18**], incorporating Zn(II) paddle wheel SBU and studied the structural dynamics through exchanging the guest molecules. The diagonal distances between the centers of paddle wheels in the rhombic channels are 25.301(3) and 18.886(2) Å (*b* and *c* axes of the unit cell). The channels are filled with DMA (*N,N′*-dimethylacetamide) molecules, which can be easily exchanged with ethanol without destroying its single crystallinity. The ethanol-exchanged single crystals can be further replaced by ethylene glycol (EG), triethylene glycol (TEGly), and allyl alcohol (AllylOH) by soaking in the respective guest liquids (Figure 17). Interestingly, a decrease in the cell volume (2681→2522.6 $Å^3$) as well as reduction in the porosity (48.1→44.8%) occurs on exchange with ethanol. This explains the breathing behavior of the framework and shape-responsive dynamic fitting of guest molecules inside the pores. The reduction in pore volume is maximum for TEGly included complex (48.1→37.9%), caused by tight fit for hydrogen-bonded TEGly dimer inside the channel. In all cases, guest molecules can be exchanged with ethanol by soaking in the solvent.

Two fundamental pore deformations, namely, shrinkage and expansion, are prerequisites for the effective accommodation of a guest molecule. While short-range attractive interactions play effective roles in shrinkage, expansion usually occurs when the size of the pore is smaller than the guest molecule and the host framework is able to expand. A diamondoid framework, synthesized by Sharma *et al.*,[35] exhibits intriguing guest-exchange properties in a reversible SC–SC manner. The authors used linear tricarboxylic acid ligand bis{4-[2-(4-pyridyl)ethenyl] benzoic acid (pyebH) in combination with $Zn(NO_3)_2{\cdot}6H_2O$ to obtain $\{[Zn(pyeb)_2]\text{-}(DMF)(H_2O)\}_n$ [**19**] by the solvothermal route. The as-synthesized complex has sevenfold interpenetration with triangular channels that are filled with DMF and water as guest molecules. When a crystal of **19** is kept in acetone at RT for 12 h, all guest molecules are replaced by acetone to afford the daughter product, $\{[Zn(pyeb)_2](acetone)\}_n$ [**19a**]. When crystal **19a** is kept in acetonitrile for 12 h, a new product, $\{[Zn(pyeb)_2](MeCN)\}_n$ [**19b**] is formed without losing crystallinity. Interestingly, when either **19a** or **19b** is kept in dry DMF for 12 h, a new compound, $\{[Zn(pyeb)_2](DMF)\}_n$ [**19c**] is formed. Compound **19** can be regenerated by keeping **19a**, **19c**, or **19c** in aqueous DMF for 12 h at RT (Figure 18). Thus, the framework represents a dynamic porous polymer in true sense, where guest-controlled breathing phenomena is realized.

It is worth noting that even weak interactions between the guest molecules and host framework can induce a chiral→achiral structural change depending on the size of the guest species. Wang *et al.*[36] presented solvent-induced chiral single-crystal to achiral single-crystal structural modification of two isomeric amino-functionalized MOFs (Figure 19). Owing to different sizes between DMA and DMF, the resulting structures have two distinct symmetries. Interestingly, structural modification does not transpire through direct solvent exchange (through dipping crystals of **20** in DMF or **21** in DMA). Conversely, when the single crystals of **20**

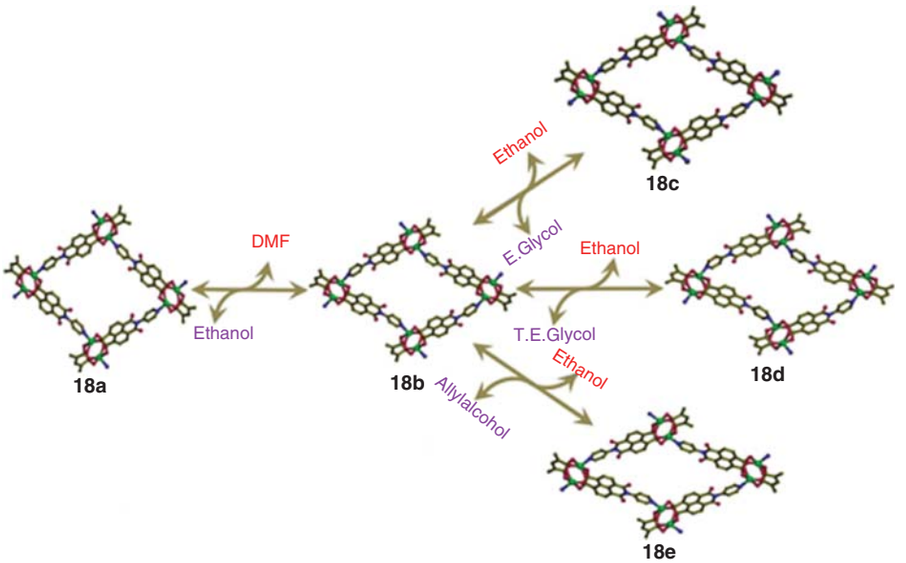


Figure 17 Reversible exchange of guest molecules and the contraction of the pores on exchanging the solvents from **18a** to **18e**. (Reprinted with permission from Ref. 34. Copyright (2013) American Chemical Society.)

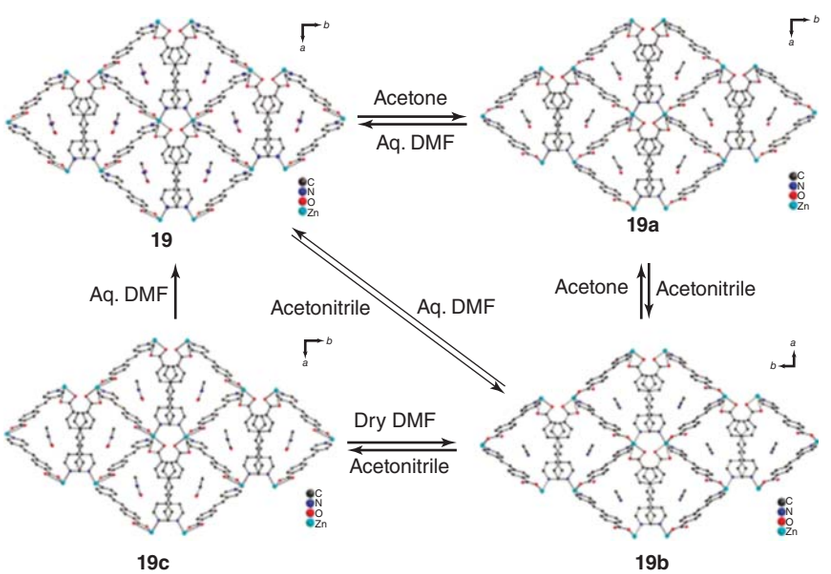


Figure 18 A schematic view of one-dimensional triangular channels showing reversible exchange of guest molecules within the pores of **19**. (Reprinted with permission from Ref. 35. Copyright (2011) American Chemical Society.)

were dipped in methanol for 2 days, its chiral framework changes to achiral framework **21** and a new methanol-exchanged phase $Zn(ain)_2 1/2(CH_3OH)$ [**21′**] (Hain = 2-aminoisonicotinicacid) is obtained. Through close inspection onto the basic tetrahedral units of Zn(II) center for two frameworks, the authors claimed that this unusual SC–SC transformation is accompanied by breaking coordination bonds and forming new ones.

A series of pillared-layer MOFs have been reported[37] by solvothermal synthesis with 5-aminoisophthalic acid, 4,4′-bipyridine and Cd(II) ion. On dipping a crystal in methanol at room temperature, a changeover from chiral to achiral space group (Figure 20) occurs. The transformed crystal exhibits no change in size and morphology. However, single-crystal X-ray diffraction study reveals that the lattice DMA molecules are replaced

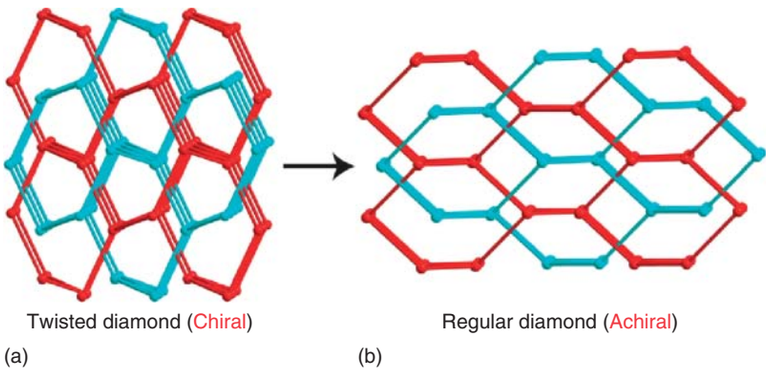


Figure 19 Topological view of the structural transformation from the chiral dia net of **20** (a) to the achiral dia net of **21′** (b)

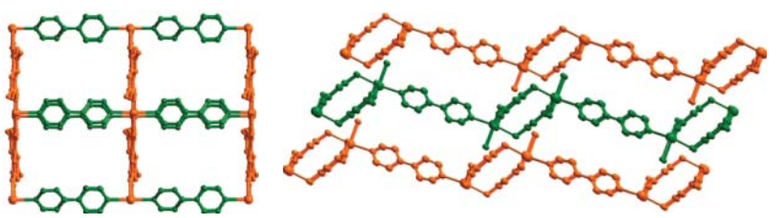


Figure 20 Schematic view of the 3D supramolecular structure having chiral (right) and achiral (left) space group

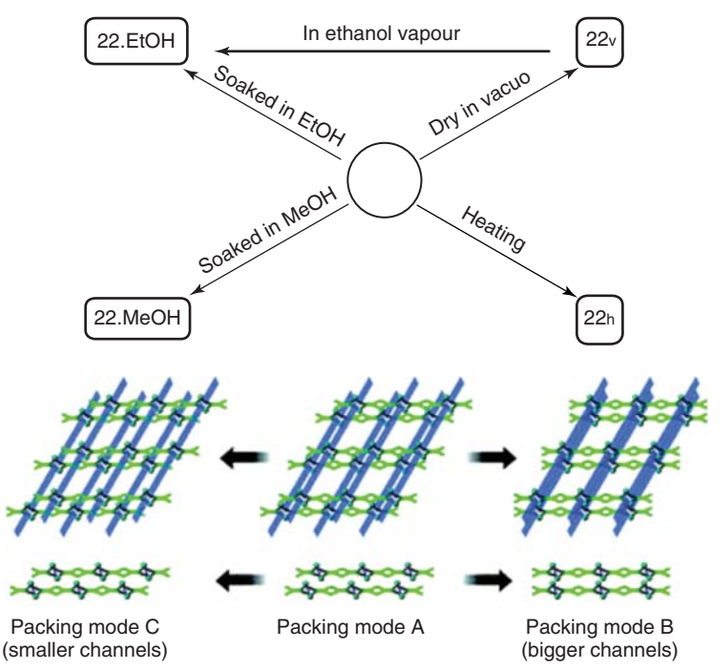


Figure 21 Schematic representation of top and side views of the layers sliding and the contraction and expansion of the channels on the removal or addition of the guest molecules

by methanol. The authors assumed that the change from chiral to achiral space group happens due to the change in the torsion angle of aromatic rings from the bpy ligand, after the DMA molecules are replaced by methanol in the channels.

An opposite effect, that is, shrinkage of the framework on desolvation occurs[38] in a neutral, microporous MOF [**22**] with a double-pillared-layer structure, where offset stacking of the layers generate channels. These channels are occupied by water molecules, which can be exchanged with MeOH or EtOH solvents at room temperature in SC–SC mode. The solvent molecules of the mother crystals can also be removed either by heating or under vacuum to produce the desolvated framework as stable crystals. While the guest-free structure experiences shrinkage, the unit-cell volume of EtOH inclusion framework increases by 2.9%. The anhydrous framework is selective toward ethanol as it preferentially uptakes EtOH from a mixture of DMF-EtOH or EtOH-benzene (Figure 21).

Lama *et al.*[39] reported a La(III) coordination polymer [**23**] where the lattice water molecules are partially replaced at room temperature with different solvent molecules such as ethanol, acetone, and pyridine, leading to three new daughter crystals in SC–SC manner (Figure 22). The structural determination of guest-exchanged crystals revealed insignificant changes in their lattice parameters and the space group remains unchanged, pointing the robustness of the overall framework.

Zhan *et al.*[40] reported unique 3D Ln-TDC (TDC = thiophene-2,5-dicarboxylate) frameworks in

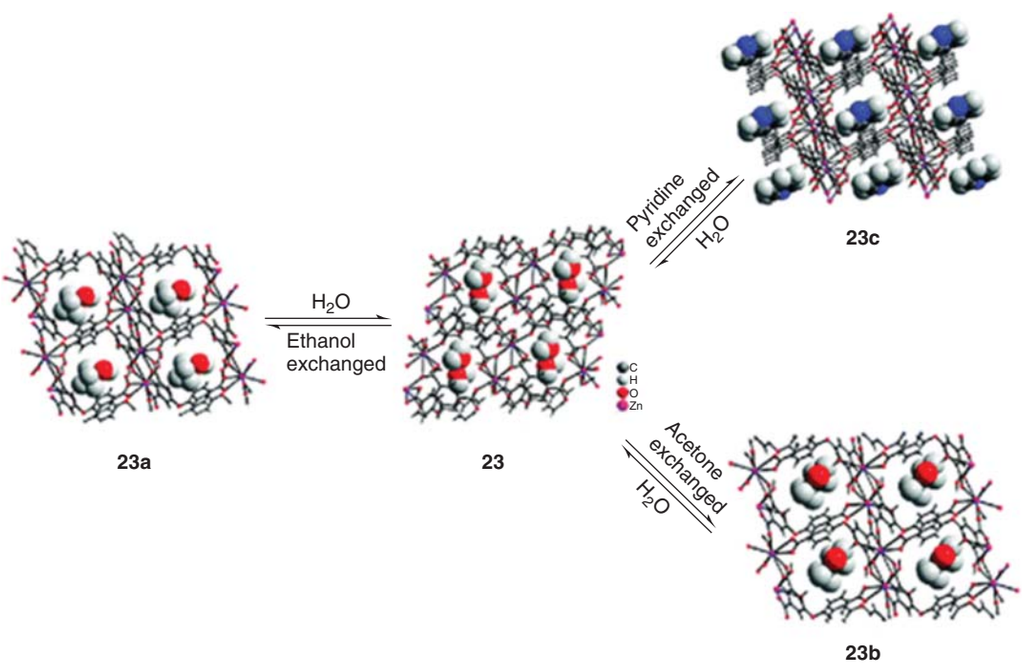


Figure 22 Schematic representation of the reversible exchange of guests within the pores of **23**. (Reprinted with permission from Ref. 39. Copyright (2010) American Chemical Society.)

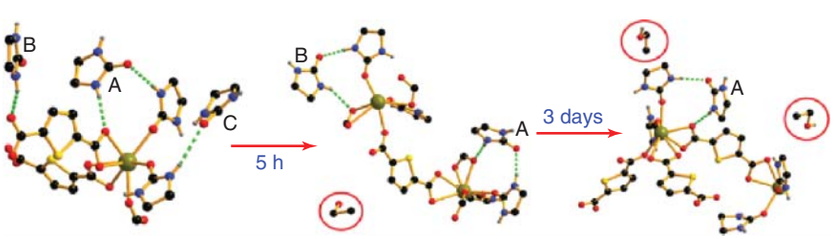


Figure 23 Three kinds of e-ureas in **24** (A, B, and C) (b) e-urea C exchanged by ethanol in **24a** (c) e-urea B and C exchanged by ethanol. (Reprinted with permission from Ref. 40. Copyright (2012) American Chemical Society.)

eutectic solvents. The Nd(III)-containing complex $[Nd_2(TDC)_3(\text{e-urea})_4]\cdot 3(\text{e-urea})$ [**24**] (e-urea = ethyleneurea) features a neutral 6-connected **rob**-type framework with guest e-urea molecules, which can perform SC–SC guest exchange. The ethanol-exchange mechanism is ascribed to the kinetically controlled flexibility (KCF), originating from the momentary rotation/swing motions of the e-urea molecules (Figure 23).

2.2 Single-Crystal to Single-Crystal Transformations through Guest Removal

In contrast to the aforesaid examples, resistivity of the pores to collapsing on guest removal can be achieved with robust MOFs built with carboxylate linkers. From synthetic point of view, SBUs, designed to produce directional polyatomic metal clusters are much advantageous for the rational design of MOFs compared to mononuclear metal centers. Through their pioneering research work, Yaghi and coworkers showed[18] that the as-synthesized structure (MOF-5) is composed of regular Zn_4O tetrahedron, where each edge of Zn tetrahedron is capped by a

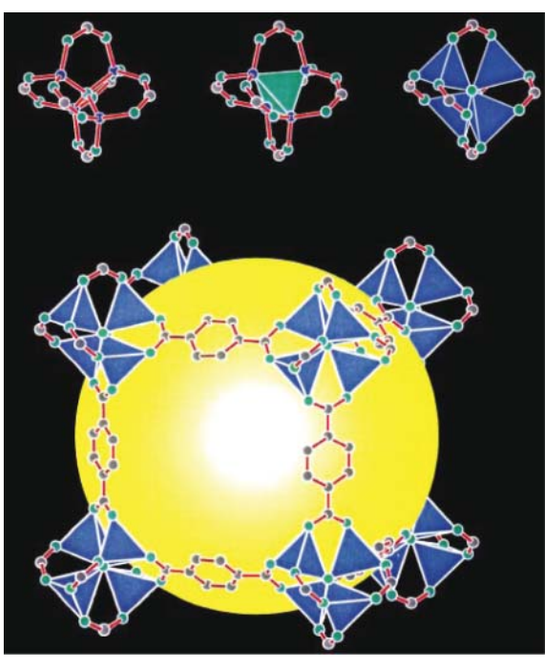


Figure 24 Construction of the MOF-5 framework. Top, the $Zn_4(O)O_{12}C_6$ cluster. Left, as a ball-and-stick model (Zn, blue; O, green; C, gray). Middle, the same with the $Zn_4(O)$ tetrahedron indicated in green. Right, the same but now with the ZnO_4 tetrahedra indicated in blue. Bottom, one of the cavities in the $Zn_4(O)(BDC)_3$, MOF-5, framework. Eight clusters (only seven visible) constitute a unit cell and enclose a large cavity, indicated by a yellow sphere of diameter 18.5AÊ in contact with 72 C atoms (gray)

$-CO_2$ group of a linear aromatic dicarboxylate to form a large porous structure (Figure 24). The pores are occupied by DMF and chlorobenzene guests, which can be removed completely by heating the crystals in air at 300 °C for 24 h without disturbing their morphology or crystallinity. Thus, the rigid and divergent linker allows for the creation of a 3D porous framework with greater surface area and pore volume than most porous crystalline zeolites, as determined from the solvent vapor and gas adsorption isotherms. In a way, the construction of MOF-5[10] proved to be a watershed in fabricating porous MOFs.

Structural retention in SC–SC mode on guest removal can also occur in a framework composed of mixed ligand systems. Employing two different organic connectors: (i) one to generate the rigid pillars and (ii) the other to make the aromatic walls, Zeng *et al.*[41] reported a rigid double-pillared MOF [**25**], containing DMF guests. The presence of pillars and continuous double walls prevent interpenetration of the framework. By soaking the crystals in neat methanol, the latter replaces all the DMF guests in the crystals. The desolvated crystals can be obtained either by heating the as-synthesized DMF-containing crystals under vacuum or by evacuating the methanol-loaded crystals under vacuum. The key features in the desolvated structure are similar to those found for the as-synthesized one, indicating high thermal stability, arising from the strong intra- and inter-rod connections.

Although not in a SC–SC manner, the authors also report that the activated empty phase shows excellent I_2 affinity and it can be controllably delivered to ethanol (Figure 25).

A highly stable 3D Cu(I) coordination polymer [**26**], using 2,3-pyrazinedicarboxylic acid (H_2pyzdc) as a rigid linker,[42] exhibits dehydration/rehydration in a reversible manner without losing crystallinity (Figure 26). No inclusion of N_2 and CO_2 gas molecules into the pores of the dehydrated framework suggests smaller pore size compared to the kinetic diameter of N_2 and CO_2. In contrast, selective hysteretic water adsorption property of the dehydrated framework confirms the presence of coordinatively unsaturated Cu(I) center.

The robust and polymeric coordination chains, $[Ni(\text{cyclam})(\text{bpydc})]\cdot 5H_2O$ [**27**], constructed from the nickel–macrocyclic complex $[Ni(\text{cyclam})](ClO_4)_2\cdot$ (cyclam=1,4,8,11-tetraaza cyclotetradecane) and 2,2′-bipyridyl-5,5′-dicarboxylate ($bpydc^{2-}$) ligand, shows retention of single crystallinity on removal of the water molecules with a visible color change of the crystal (Figure 27) from yellow to orange[43]. Single-crystal X-ray structure determination of the dehydrated crystal [**27′**] indicates that the porous framework is intact. The color change on dehydration is attributed to shortening of the Ni–O(carboxylate) bond, which makes the Ni(II) coordination environment in **27′** closer to the ideal octahedral compared to that in the hydrated solid. The X-ray crystal

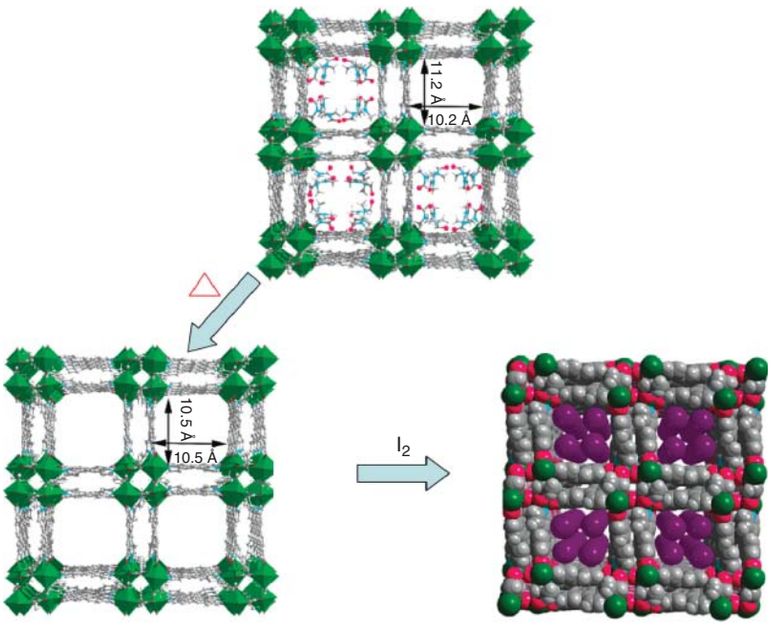


Figure 25 Schematic diagram showing views of the 3D open framework [**25**] with 1D channel in as-synthesized (top), completely desolvated (bottom left), and sketch of I_2 molecules diffusing in the channels of desolvated framework (bottom right). (Reprinted with permission from Ref. 41. Copyright (2010) American Chemical Society.)

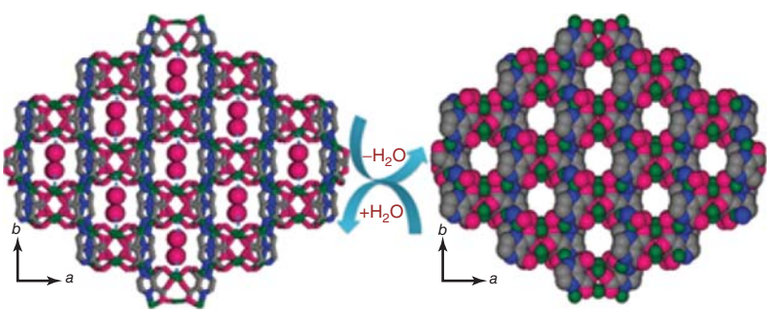


Figure 26 View of the 3D coordination framework [**26**] (left) with channels occupied by the water molecules; right side: CPK diagram of the dehydrated compound, showing 1D channels without water molecules in a SC–SC manner



Figure 27 Photographs of (a) original crystal [**27**] in the mother liquor, (b) after evacuation of **27** at 150 °C and 10^{-5} torr for 2 h [**27′**], and (c) after exposure of **27′** to water vapor for 5 min [**27″**]

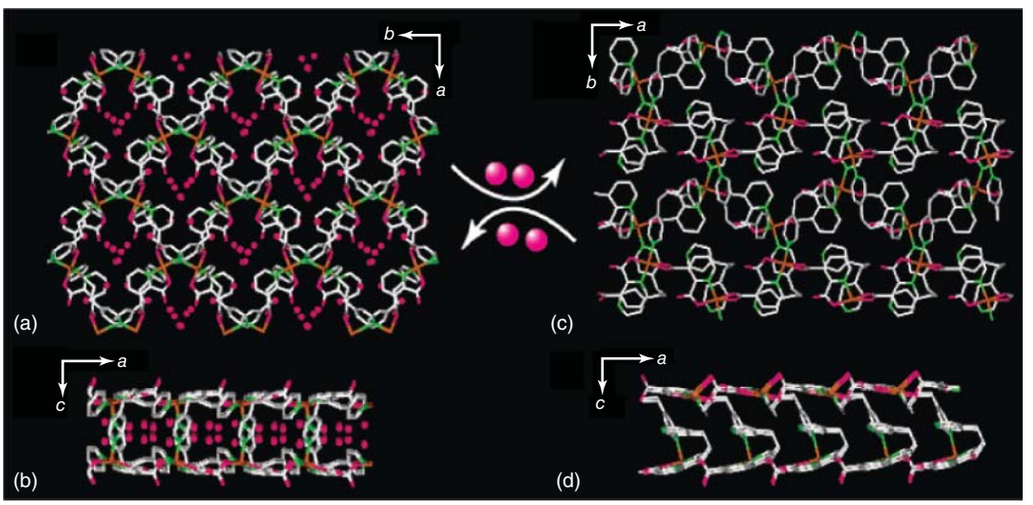


Figure 28 (a) Honeycomblike 2D layers of **28** showing a water-filled channel along the *c*-axis. (b) Pillared-bilayer network of **28** showing the channel along the *b*-axis. (c) Honeycomblike 2D layers of dehydrated framework [**28′**], along the *c*-axis. (d) Pillared-bilayer network along the *b*-axis (the pendent bpp ligand is occupied in the channel). (Reprinted with permission from Ref. 44. Copyright (2005) American Chemical Society.)

structure of the rehydrated crystal [**27″**] was the same as that of **27**. The dehydrated compound exhibits N_2 and H_2 sorption properties without any hysteresis between adsorption and desorption processes.

The elongation and shrinking of pores in a reversible manner with the introduction and removal of guest molecules has been shown[44] in a 2D bilayer open framework structure (Figure 28), $\{[Cu(pyrdc)(bpp)](5H_2O)\}_n$ [**28**] [pyrdc = pyridine-2,3-dicarboxylate; bpp = 1,3-bis(4-pyridyl)-propane]. The long $-CH_2-$ chain of bpp pillar ligand is the only source of conformational flexibility in the framework. In the dehydrated state [**28′**], one of the Cu(II)–N(bpp) pillaring bond breaks and the pendant arm is projected to the groove of the bilayer. The desolvated form is nonporous to O_2 or N_2 gas molecules. The dehydrated single crystals slowly revert back to the original crystal [**28**] in open atmosphere, with an increase in the cell volume. The evacuated host frameworks also interact with CO_2 guest molecules in SC–SC mode. The selective gate-opening phenomenon with CO_2 adsorbate has been credited to hydrogen-bonding interactions. Thus, guests are permitted to pass through the gate at a specific gate-opening pressure that depends on the strength of the intermolecular interactions.

Reversible dehydration and rehydration in SC–SC (Figure 29) manner has also been shown in a 3D porous

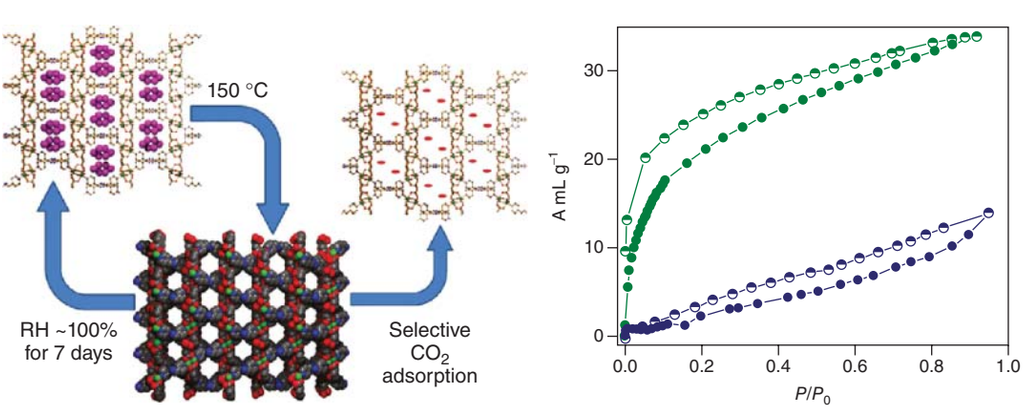


Figure 29 3D honeycomblike structure with and without water molecules (left). Gas adsorption–desorption isotherms for CO_2 (green) at 195 K; N_2 (blue) at 77 K. Adsorption: filled shape, desorption: half filled shape. (Reprinted with permission from Ref. 45. Copyright (2011) American Chemical Society.)

framework [**29**] of Cu(II), where the channel surfaces are decorated with imine linkages.[45] As revealed by X-ray crystallography, the as-synthesized crystals, on heating around 150 °C under reduced pressure for 6 h, changes the color from deep green to light green with the disappearance of the lattice water molecules. The walls of the porous dehydrated framework are decorated with imine linkages and the MOF exhibits selective sorption of CO_2 over N_2. Results of the solvent vapor adsorption studies additionally show the hydrophobic nature of the pore surface.

2.3 Single-Crystal to Single-Crystal Transformations in Dynamic Frameworks

In a dynamic framework, SC–SC transformations lead to substantial structural changes such as pore distortion, spongelike shrinkage/swelling, sliding, swing, bending, and/or rotational motion. In these cases, considerable changes in the framework structures, due to extensive movements of the molecular components, are expected because of extensive cooperation among the components that constitute the framework. Reversible structural changes and associated properties in response to external stimuli are potentially important in several practical applications, for example, in sensors.

A framework that shows shrinkage of pores on guest inclusion and expansion on guest release in a SC–SC manner has been reported.[46] The framework [**30**] is built with 1,4-benzenedicarboxylate (1,4-bdc) and Zn(II) ion under solvothermal condition and can be described as a compressed primitive cubic (α-Po) net with a remarkable bent in the 1,4-bdc ligand. This bending results in severe twisting of the Zn_2 paddle-wheel unit (Figure 30). Interestingly, volume of the evacuated framework expands on complete removal of the lattice DMF molecules and the bent 1,4-bdc linkers are relaxed to a linear topology to afford a perfect 2D square grid. The impact of framework expansion is verified by N_2 and H_2 gas sorption measurements, which show significantly higher gas uptake capacities than those of any zeolites. The same framework, on inclusion of benzene, shows a 2D square to 2D rhombic grid structural changeover, with an overall shrinkage of the pores. This event is confirmed by single-crystal X-ray crystallography.

A different type of the framework distortion, leading to the shrinkage of pores, was observed[47] in

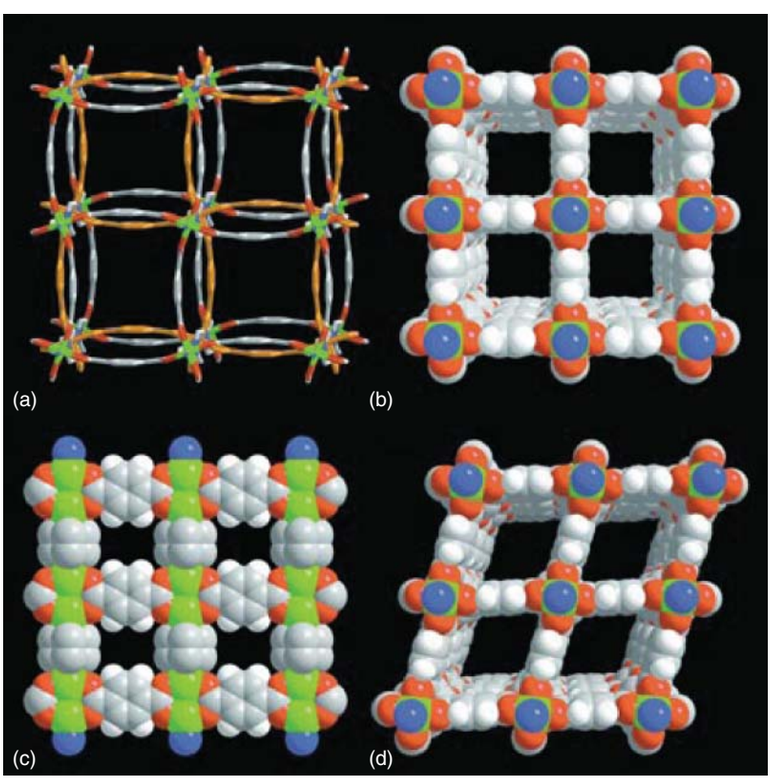


Figure 30 (a) The view along fourfold axis of the metal-organic framework structure, with one $[Zn_2(1,4\text{-bdc})_2]$ [**30**] 2D Layer. (b) Space-filling representation of evacuated framework [**30**], which emphasizes the open square channels view along fourfold axis. (c) Side view of evacuated framework [**30**], showing the windows interconnecting the channels. (d) Space-filing representation of the metal-organic framework structure in **30**·$2C_6H_6$, showing rhombic grid motif of $[Zn_2(1,4\text{-bdc})_2]$ layers

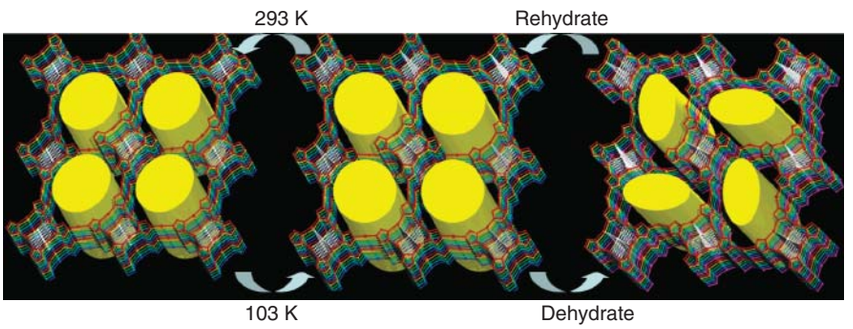
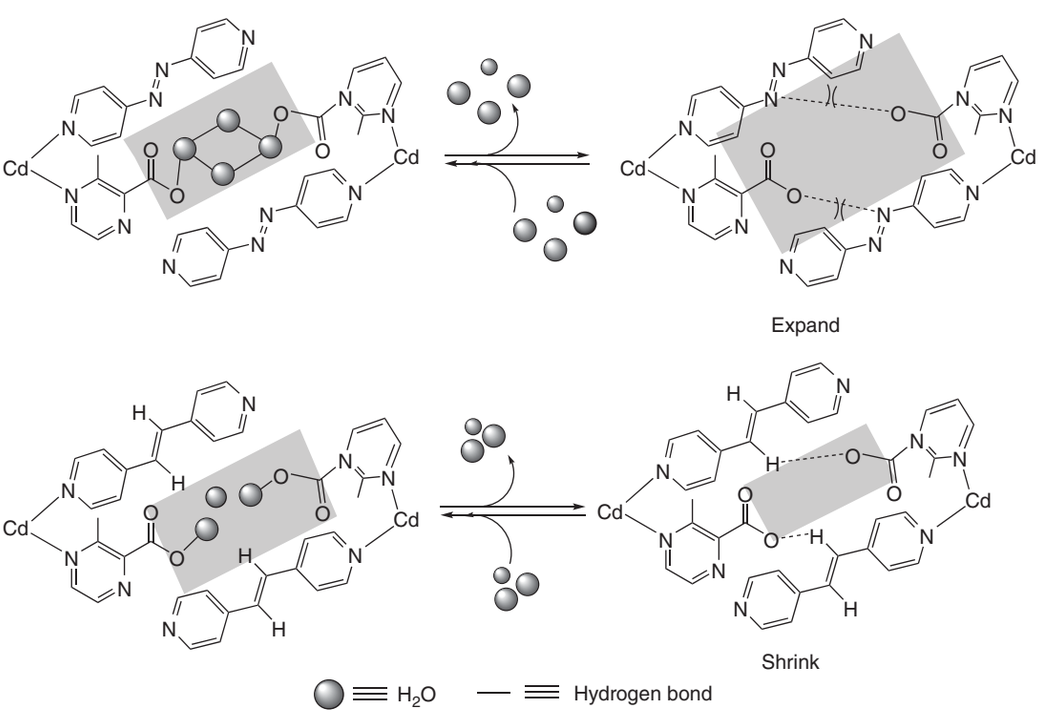


Figure 31 Interconversion of the $[Ag_6Cl(atz)_4]$ host in **31**, **31′**, and **31″** (amino groups and guests are omitted for clarity, 1D channels are highlighted as yellow columns). (Reprinted with permission from Ref. 47. Copyright (2005) American Chemical Society.)

a highly porous open framework metal coordination polymer $[Ag_6Cl(atz)_4]OH{\cdot}6H_2O$ [**31**] (Hatz = 3-amino-1,2,4-triazole). Single-crystal structure analysis at 293 K reveals a tetragonal phase, encompassing both linear and a bent 2-coordinated Ag(I) ions, as well as a μ_3-atz ligand. In spite of parallel fivefold interpenetration along the *c*-axis, the structure still possess large 1D columnar channels, housing disordered HO^- or H_2O guests. At 103 K, the structure transforms to an orthorhombic system [**31′**], where the overall connectivity remains unchanged, but the channels become slightly elliptical (*ca.* 7.8 Å × 9.2 Å). On warming up the crystal from 103 to 293 K, it slowly reverts back to the room temperature structure (Figure 31). Noticeably, a new tetragonal phase of the partially desolvated product $[Ag_6Cl(atz)_4]{\cdot}OH{\cdot}xH_2O$ ($x \leq 2$) [**31″**] evolved at 293 K by placing the same crystals in slow stream of dry air (Figure 31). On desolvation, Ag(I) shows bent coordination with a striking distortion of the host framework and exhibits a sixfold interpenetration of the $Ag_3(atz)_2$ nets. Obviously, such transformation essentially demands not only distortion of the nets but also Ag(I)–ligand bond cleavages and formations. In the



Scheme 3 Schematic diagram of expansion and shrinking of complexes **32** and **33**

present case, both these processes are possible due to the fast adaptability of coordination geometry by Ag(I).

While high framework stability is essential for many practical applications, including gas storage and separation, flexible and dynamic MOFs can undergo various types of structural changes during removal or uptake of guest molecules, and exhibit hysteretic sorption, stepwise guest uptake, and gate-opening adsorption behaviors.

That the occurrence[48] of expansion and contraction on guest removal depends on the nature of linkers is shown in two pillared-layer MOFs, $\{[Cd(pzdc)(azpy)]\cdot 2H_2O\}_n$ [**32**] and $\{[Cd(pzdc)(bpee)]\cdot 1.5H_2O\}_n$ [**33**] (Scheme 3). Here, $\{Cd(pzdc)\}_n$ (pzdc=pyrazine-2,3-dicarboxylate) forms the layer and py-N=N-py (azpy)/py-CH=CH-py (bpee; py is pyridine) acts as pillar linkers. Compound **33** on heating at 130 °C for 30 min forms the guest-free MOF. Structural studies indicate expansion of the framework on desolvation, in which the crystal system and space group remain unaltered but the cell volume increases significantly. In contrast, the interlayer distance of **33**, pillared by bpee linkers, shrinks on the removal of water molecules. A close inspection of the structures of **32** and its solvent-free framework reveals this expansion due to lone pair–lone pair electronic repulsion between the pendant oxygen atom of the carboxylate and nitrogen atom of the azo group.

A bilayer open framework[49] with the formula, $[Ni_2(C_{26}H_{52}N_{10})]_3[BTC]_4\cdot 6C_5H_5N\cdot 36H_2O$ [**34**] known as **BOF-1,** (BTC = benzenetricarboxylate) have been synthesized from dinickel(II) bismacrocyclic complex $[Ni_2(C_{26}H_{52}N_{10})(Cl)_4]\cdot H_2O$ (**A**) (Figure 32) and sodium salt of 1,3,5-benzenetricarboxylate (Na_3BTC) in water. The structure retains its framework integrity and single crystallinity even after removal and exchange of the guest molecules. In open atmosphere, the crystal shows stepwise loss of guest pyridine and water molecules. On heating the crystals, all the guest molecules are removed and the desolvated compound, $[Ni_2(C_{26}H_{52}N_{10})]_3[BTC]_4\cdot 4H_2O$ [**34′**] is formed. The cell parameters and the cell volume change drastically during this transformation. The thickness of the bilayer is reduced remarkably due to significant tilting of the pillars. Thus, the framework exhibits a spongelike behavior through reduction of the interlayer spacing in response to guest removal. The reversibility of the dynamic interconversion from desolvated framework to the parent framework, although not in a SC–SC manner, is proven by the X-ray powder diffraction pattern on exposing the former to water–pyridine vapor.

Using the same framework [**34**], its spongelike dynamic behavior in response to the amount of desolvated guest molecules has been demonstrated.[50] Besides, on keeping the crystals in I_2 solution, a new charged framework formed. The as-synthesized single crystals loose all pyridine and some water guest molecules at room temperature (Figure 33) to produce partially desolvated structure [**34″**].

Using a similar construction protocol, a robust MOF, $[Ni(cyclam)(bpydc)]\cdot 5H_2O$ [**35**] has been constructed in the form of a linear coordination polymeric chains from nickel–macrocyclic complex $[Ni(cyclam)](ClO_4)_2$ (cyclam=1,4,8,11-tetraazacyclotetradecane) and 2,2′-bipyridyl-5,5′-dicarboxylate ($bpydc^{2-}$) ligand.[43] Dehydration by heating, followed by single-crystal X-ray structure determination, indicates that the porous framework structure is intact. A visible color change from pink to yellow is observed when the dehydrated crystal of **35′** is exposed to air or water vapor. The X-ray crystal structure of the rehydrated crystal reveals that it is the same as that of **35**.

Guest exchanges not only induce replacement of lattice or metal-bound solvent molecules in MOF but also might lead to a profound alteration in framework chirality, interpenetration, framework dimension, and so on. Biradha *et al.*[51] reported an unprecedented crystal to crystal dynamic behavior of a doubly interpenetrated 3D network that assembles from 2,4,6-tris(4-pyridyl)triazine (TPT) and ZnI_2. The as-synthesized crystals, containing either nitrobenzene or cyanobenzene guests, changed from

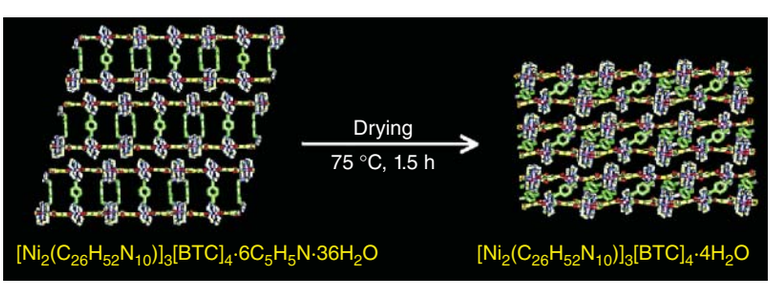


Figure 32 X-ray structures of **34**. (a) Top view of **34**, showing 2D layers of brick-wall motif. (b) Side view of **34**, showing pillared-bilayer structure (thickness of bilayer, 11.91(1) Å). (c) Top view of desolvated crystal **34′**. (d) Side view of **34′** showing tilted pillars (thickness of bilayer, 6.82(2) Å). Ni, pink; O, red; N, blue; C of macrocycle, gray; C of BTC3-, yellow; C of pillars, green. Guest water and pyridine molecules are omitted for clarity. (Reprinted with permission from Ref. 49. Copyright (2002) American Chemical Society.)

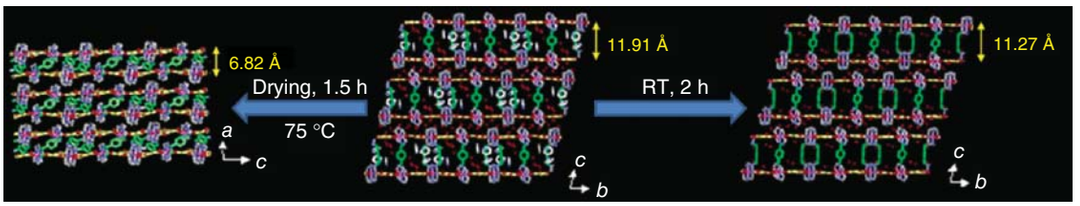
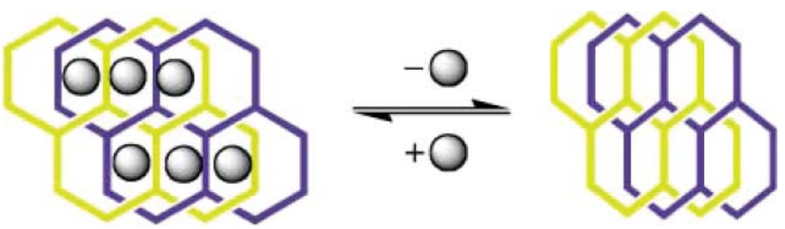


Figure 33 X-ray structures of dried **34**, exhibiting spongelike behavior. (Reprinted with permission from Ref. 50. Copyright (2004) American Chemical Society.)



Scheme 4 Schematic representation of the contraction or expansion of the 3D network on the removal or addition of guest molecules, respectively

colorless to light yellow when left at room temperature for 1 day. Structural analysis of the new crystals indicates the absence of guest molecules inside the pore and significant compression of the network (Scheme 4).

A noteworthy example of dynamic motion and rearrangements of the molecular components in response to guest removal[52] in SC–SC manner is found for the 2D square-grid MOF, $\{[Ni(cyclam)]_2[BPTC]\}_n \cdot 2nH_2O$ [**36**]. This compound on heating loses all the water molecules to yield $\{[Ni(cyclam)]_2[BPTC]\}_n$ [**36′**] (H_4BPTC = 1,1′-biphenyl-2,2′,6,6′-tetracarboxylic acid). Cell parameters and cell volume of the desolvated structure change slightly compared to those of the parent crystal. However, extensive rearrangements of the molecular components involving (i) rotation of the carboxylate and macrocycle, (ii) swing of the biphenyl, and (iii) bending of the macrocyclic coordination plane toward the carboxylate plane occur, which leads to reduction in the interlayer distance (Figure 34).

Breathing behavior of a framework on removal or addition of solvent water molecules was also reported in a copper MOF.[53] The as-synthesized framework [**37**] incorporating semirigid linker di-1,2,4-triazole ($\mathbf{L_3}$),

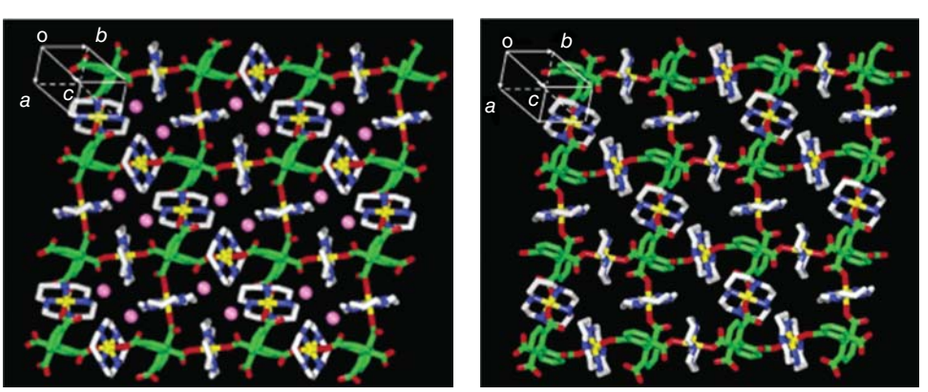
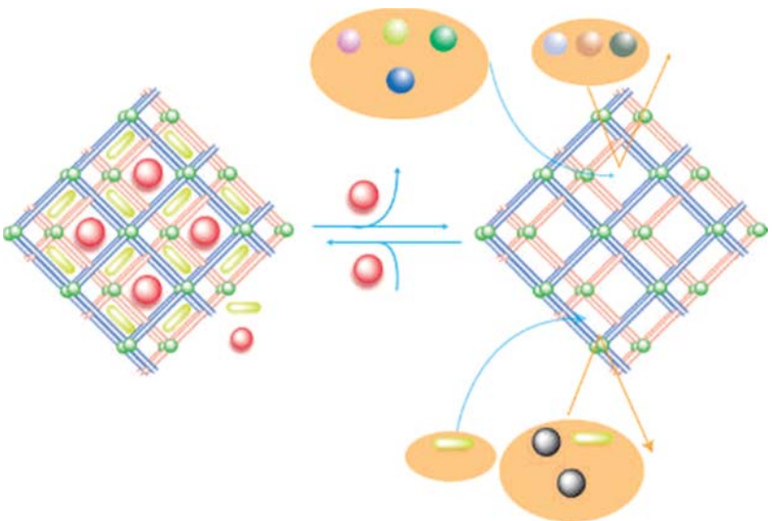


Figure 34 Top view seen on the (110) plane, showing a 2D square grid for the solvated (a) and desolvated (b) framework. (Reprinted with permission from Ref. 52. Copyright (2006) American Chemical Society.)



Scheme 5 Robust α-polonium-type three-dimensional interpenetrating porous framework with multiple functionality

flexes reversibly on removal or addition of water to form semi-hydrated ($[Cu_2(L_3)_2(SO_4)(Br)_2]\cdot 4H_2O$) [**37′**] and dehydrated ($[Cu_2(L_3)_2(SO_4)(Br)_2]$) [**37″**] MOFs in SC–SC mode. Single-crystal characterization shows these structural changes are due to rotation of the 2-butene subunit of the linker and not due to a change in the metal–ligand bond.

Mutual framework sliding on guest exchange is often encountered in structurally flexible interpenetrating frameworks that enable controllable gate-opening function in gas sorption event.[54,55] Kitagawa and coworkers detailed[56] a fascinating example of permanent porosity and high thermal stability in a robust cationic MOF, through SC–SC manner (Scheme 5). The X-ray structure of the original framework is represented as a twofold interpenetrating α-polonium-type topology. Interpenetration provides two different channels in the framework. The rectangular channels incorporate free anions, whereas the hexagonal channels are occupied by water molecules. The X-ray structure of the dehydrated crystal indicates no significant change in the unit-cell parameters and the porous framework is retained. Interestingly, on dehydration, the two closely packed interpenetrating networks undergo stress relaxation due to the expansion of the channel size, which ultimately provide an increased void space. Through CO_2 gas sorption studies, the authors proved the framework can function as a bimodal material. The authors also confirmed that the crystal structure of the rehydrated state is same as that of the parent one.

The work by Husain *et al.*[57] provided structural variation of an interpenetrated framework in SC–SC mode. A different kind of breathing behavior, where the cavity size effectively doubles on going from

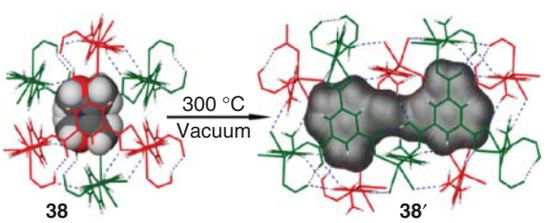
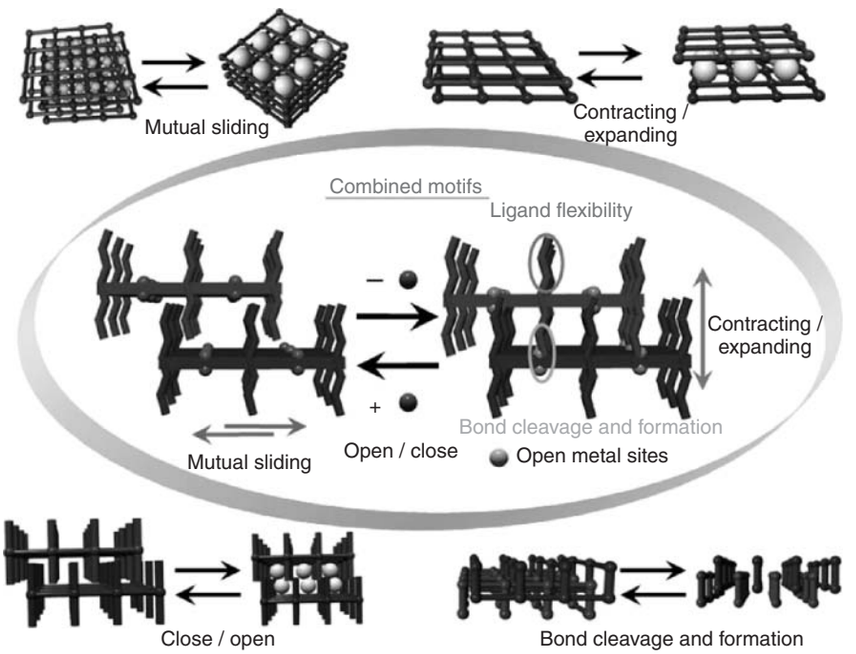


Figure 35 Cavity formed in **38′** by the evacuation of DMF in **38**. Twofold interpenetrated networks (3,5-connected hms topology) are shown in red and green for both **38** and **38′**, and C–H···O and O–H···O interactions between the frameworks are shown for **38′** (also present in **38**). (Reprinted with permission from Ref. 57. Copyright (2013) American Chemical Society.)

solvated to desolvated framework, is observed in a twofold interpenetrated, pillared, cadmium-containing MOF [**38**] (Figure 35). The authors suggested this phenomenon to occur as a result of opening up of two neighboring pyridyl groups, belonging to two independent frameworks. This also allows two neighboring cavities to connect. The SC–SC transformation is also observed when it is immersed in benzene, chloroform, 1,4-dioxane, and tetrahydrofuran. The uptake of different solvent molecules is analyzed, which indicate that desolvated samples selectively adsorb benzene, chloroform, 1,4-dioxane, and THF molecules over other selected polar solvents.

Unlike rigid frameworks, flexible frameworks are very sensitive to the presence of guests and undergo structural variations depending on the amount and nature of the guest molecules inside the framework. Obviously, a low-dimensional (1D or 2D) framework has more



Scheme 6 Schematic representation of fundamental motifs observed for dynamic guest sorption involving 2D coordination frameworks (outside circle) and a model of combined motifs (inside circle)

structural freedom in regards to the metal ions, whereas a 3D framework is sufficiently rigid to prevent recombination of the coordination bonds around the metal ions. If the host framework undergoes SC–SC transformations, crystallographic analysis is a very useful tool for clear understanding of the dynamic behavior and for the correlation of the bistable structures with emergent physical properties.

Along this approach, Kitagawa *et al.*[17] reported a 2D coordination polymer $\{[Cu_2(tci)(OH)(H_2O)_3]1.5H_2O\}_n$ [**39**] (tci=tris(2- carboxyethyl)isocyanurate), consisting of a Cu(II) ion and the flexible ligand (tci) that, on guest removal, transforms into a 3D framework, $\{[Cu_2(tci)(OH)]_2\}_n$ [**39′**]. The transformation is steered by sliding of the 2D sheets on heat treatment through contracting of the spaces between the layers, as indicated by reversible SC–SC transformations (Scheme 6). Importantly, the coordination environment around the metal center is changed from octahedral to square planar Cu(II).

Quite a different scenario is expected for a lanthanide metal ion, where the valence orbitals are buried inside. Thus, a lanthanide ion has less preference for a particular coordination geometry. This can sometime allow ready transformation of coordination geometry around the metal center, leading to drastic changes in the overall structure and making it amorphous. Unlike MOFs built with transition metals, lanthanide MOFs rarely exhibit SC–SC transformation. One example is reported in a thermally stable porous 3D compound $Eu_2(\mu_4\text{-pmdc})_2(OH)_2\cdot 3H_2O$ [**40**] that shows[58] SC–SC transformation without significant structural or coordination changes in the dehydration and rehydration processes (Figure 36).

In another report, Gustafsson *et al.*[59] synthesized and characterized a family of flexible 3D lanthanide MOFs $\{[Ln_2(bpydc)_3(H_2O)_3]\cdot n$DMF [**41**] ($H_2$bpydc =2,2′-bipyridine-5,5′-dicarboxylic acid)} containing 1D rhombic channels. The transformation from as-synthesized to dry MOF was very fast at room temperature and occurred with the retention of single crystallinity, network topology, and metal-coordination although both the unit-cell dimension as well as volume changes significantly (Figure 37). The framework thus shows an unusual breathing behavior.[60]

Neofotistou *et al.*[61] observed a different kind of guest-induced structural change in lanthanide (La, Ce, Pr, and Dy) MOFs using 4,4′-bibenzoic acid-2,2′- sulfone ligand. In the case of Ce and Pr, an unprecedented SC–SC transformation at room temperature is observed on keeping the crystals in fresh DMF. The Ce2 phase [**42**], containing two crystallographically nonequivalent $Ce_2(\mu^2\text{-}CO_2)_4(CO_2)_4$ dimers, transformed into Ce3 phase [**42′**], where the overall connectivity in the framework changes drastically to linear anionic trinuclear cluster with the formula $[Ce_3(CO_2)_{12}]^{3-}$ (Figure 38).

Lanthanide (Ln) metals with high and variable coordination numbers and coordination geometry characteristics should be the ideal candidates for the

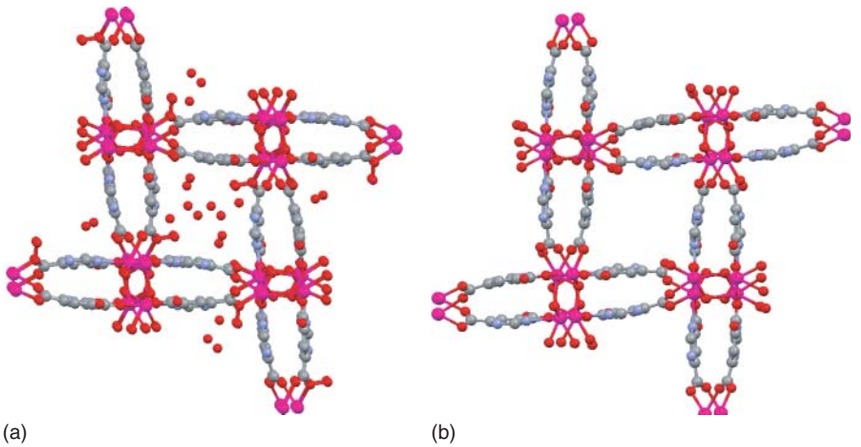


Figure 36 Views of the as-synthesized (a) and dehydrated (b) framework. (Reprinted with permission from Ref. 58. Copyright (2013) American Chemical Society.)

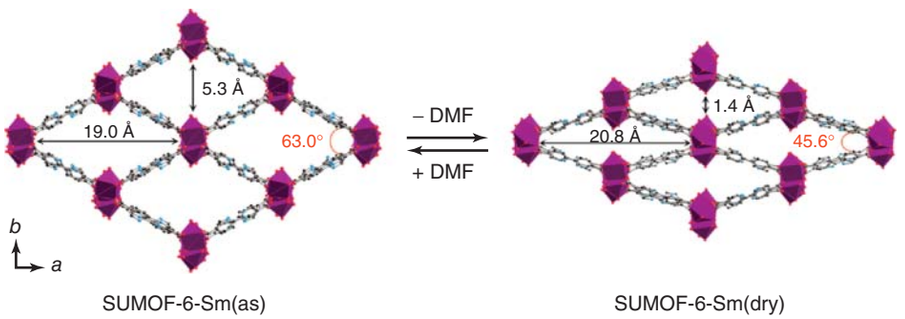


Figure 37 Comparison between the structures of **41** and **41′** viewed along the [001] direction. The shrinkage of the 1D channel on solvent removal caused a large shortening of the *b*-axis and a slight elongation of the *a*-axis. SmO polyhedra are shown in purple; oxygen, carbon, and nitrogen atoms in red, black, and blue, respectively. Hydrogen atoms and guest molecules are omitted for clarity. (Reprinted with permission from Ref. 59. Copyright (2012) American Chemical Society.)

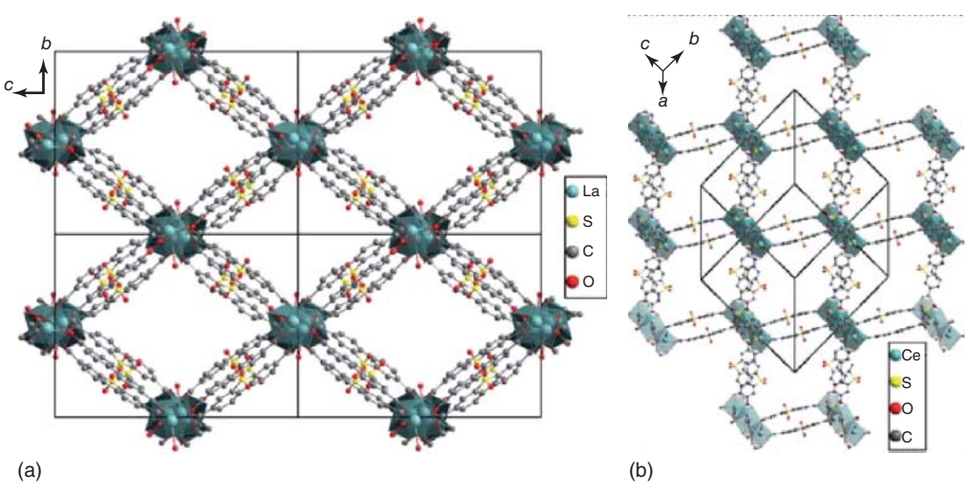


Figure 38 Pseudo-octahedral connectivity to six adjacent SBUs, containing anionic trinuclear $[Ce_3(CO_2)_{12}]_3$ [**42′**] (a) and a representative unit-cell view of transformed SBU (b)

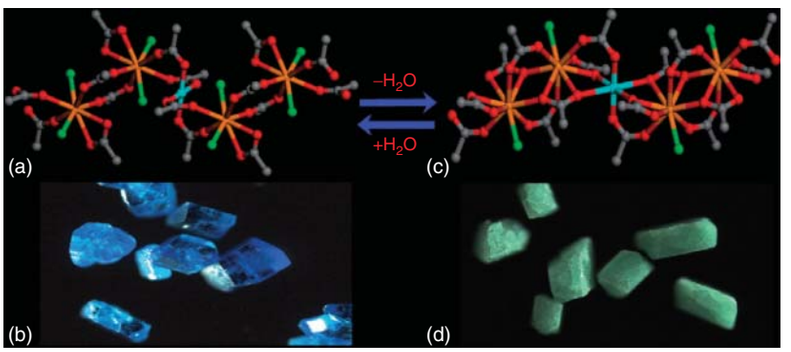


Figure 39 View of the change in the coordination geometry for **43** (a) and **43′** (c). Digital images of the crystals **43** (b) and **43'** (d). Gd: yellow; Cu: pale blue; O for carboxy groups and guest water molecules: red; O for coordinated water molecules: green; C: gray

fabrication of flexible MOFs. Wang *et al.*[15] found that the combination between Ln^{3+} and Cu^{2+} ions promotes the formation of flexible MOFs in which the coordination number and coordination geometry can undergo reversible changes, accompanied by the dehydration and rehydration processes (Figure 39).

The exploration of structural transformations involving 2D and 3D frameworks is most important because it provides not only unique properties and characteristics of 3D frameworks, but also additional external stimulus-responsive properties emerge, based on the 2D–3D transformation. Ghosh *et al.*[62] pioneered the synthesis of a 2D compound via the judicious combination of tetramethylammonium chloride (as a blocking agent to prevent the formation of the 3D structure), a tridentate ligand (having highly flexible arms), and lanthanide metal

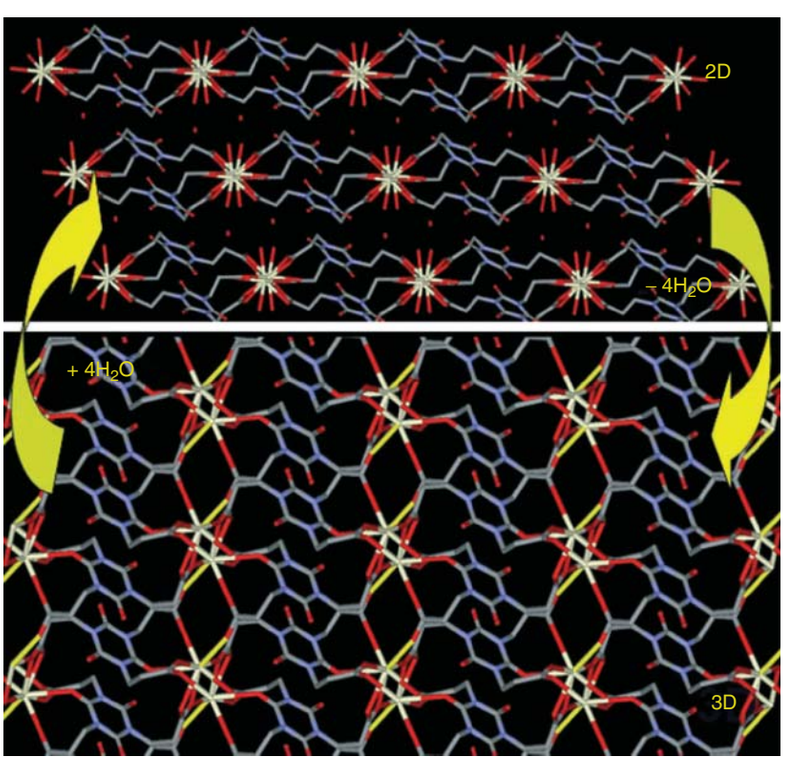


Figure 40 Perspective view of the reversible transformation between the 2D layer structure of **44** (as-synthesized) and the 3D structure of **44′** (dehydrated). New bonds between the sheets are shown in yellow

ions (affording variable and high coordination numbers) to provide enhanced structural freedom toward transformation of a 3D structure. Indeed, dehydration of the 2D framework results in a new structure with a 3D coordination framework, where product **44′** bears close relationship to the as-synthesized compound **44** (with same crystal symmetry) (Figure 40).

The reversibility of the transformation is unambiguously supported by the single-crystal studies. The unusual and previously unreported 2D→3D (and vice versa) interconversion has been credited to the flexible nature of the host framework. Such compounds are also capable of forming bistable phases, whose two states exchange between the component parts; a system could exist in one or two states for the same values of external field parameter.

Bernini[63] reported a novel Yb-MOF [**45**], containing zigzag chains of YbO_8 polyhedra, linked by succinate anions to produce a 3D structure. The framework exhibits reversible temperature-induced polymorphic transformation, between α and β phases without losing or gaining any solvent or guest molecules in SC–SC manner. Variable-temperature single-crystal X-ray studies show a reversible organization of the coordinating atoms by the breaking/formation of Yb–O bonds (Figure 41). During the transformation, the *gauche* ligand coordination of *trans*-succinate ligand changes from $\eta_2\mu_3$–$\eta_2\mu_2$ in the α polymorph to $\eta_2\mu_2$–$\eta_2\mu_2$ in the β polymorph, together with the reduction in the Yb coordination number from YbO_8 to YbO_7 without a change in the stoichiometry of components. The authors further showed that the α polymorph is an active acid and redox heterogeneous catalyst.

2.4 Single-Crystal to Single-Crystal Transformations in the Ligand Component(s)

An interesting protocol in designing flexible MOF structures is the incorporation of a gyratory part in the ligand unit that can respond to the external stimuli to bring about dynamic changes in the overall framework. Particularly demanding are rotational modules as they can act as local molecular gates and if recognized in SC–SC manner, they will have immense importance in the design and control of the MOFs with molecular gates for guest inclusion. To this end, Kitagawa and coworkers[64] successfully reported the design of pore space via introduction of a rotational module on a flexible framework, which features novel locking/unlocking mechanism of the channels depending on the guest inclusion. The 3D coordination pillared-layer structure, $\{[Cd_2(pzdc)_2\mathbf{L_4}(H_2O)_2]\cdot 5(H_2O)\cdot(CH_3CH_2OH)\}_n$ [**46**] (H_2pzdc = 2,3-pyrazinedicarboxylic acid; $\mathbf{L_4}$ = 2,5-bis(2-hydroxyethoxy)-1,4-bis(4-pyridyl)benzene), includes (i) a rotatable pillar bearing ethylene glycol side chains acting as a molecular gate with locking/unlocking interactions

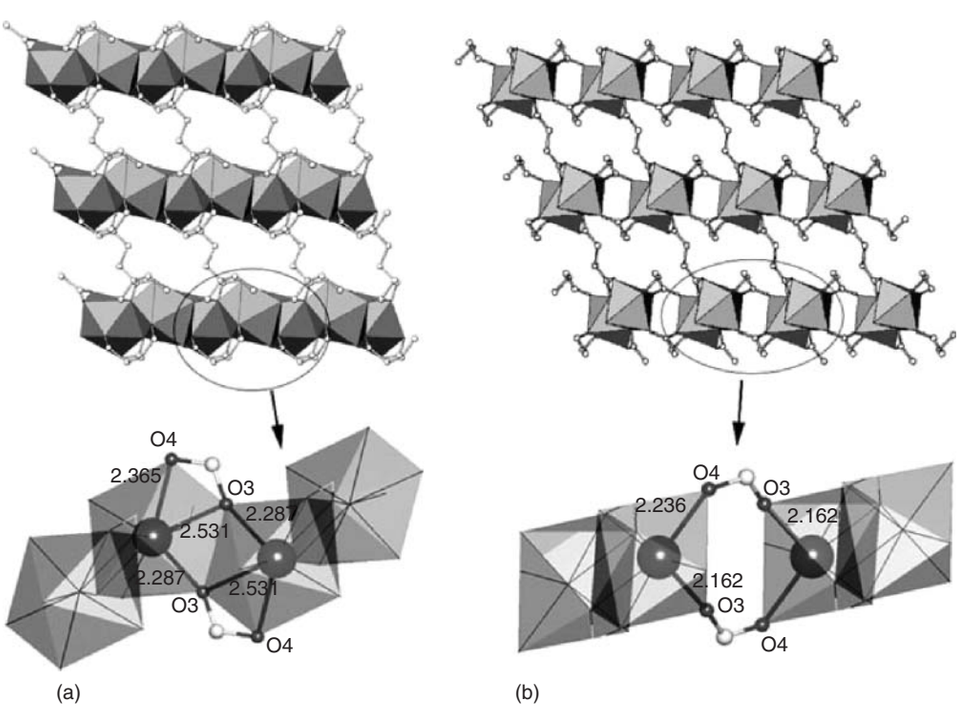
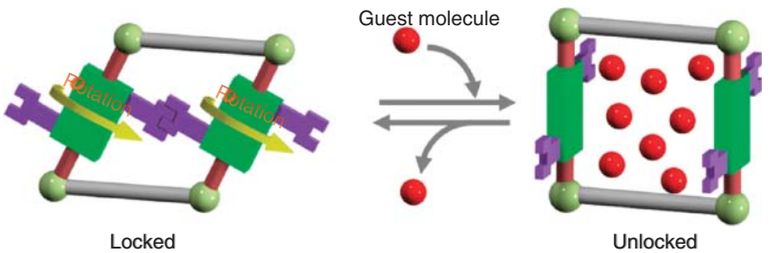


Figure 41 Projection on the ac plane of (a) the α polymorph [**45**] (b) the β polymorph [**45′**]

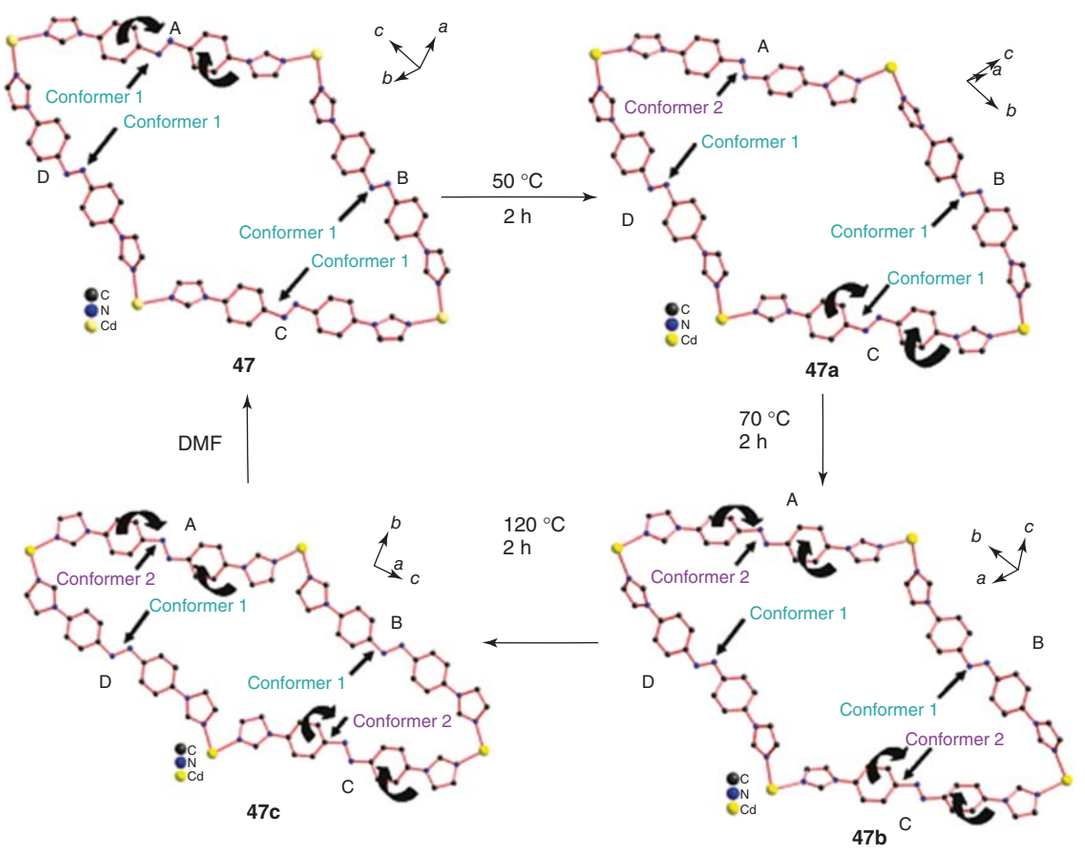


Scheme 7 Design of pore space via the introduction of a rotational module as a molecular gate with locking/unlocking interactions triggered by guest inclusion. (Reprinted with permission from Ref. 64. Copyright (2009) American Chemical Society.)

triggered by guest inclusion (Scheme 7), (ii) framework flexibility with slippage of the layers, and (iii) unsaturated metal centers as guest accessible sites through the removal of the water co-ligand.

The authors also demonstrated for the first time how the SC–SC transformations have direct consequences on the selective, stepwise sorption and gate-opening behavior of the material for various guest molecules.

A sophisticated functional material can manifest its properties because of its high sensitivity to small structural changes, such as the removal, reabsorption, or exchange of guest molecules. Along this line, a noninterpenetrated rhombus 2D grid framework having formula $\{[Cd(azim)_2(DMF)_2]_3(ClO_4)_2{\cdot}2DMF\}_n$ [**47**] is synthesized at room temperature[65] using $Cd(NO_3)_2$ and the ligand, bis(4-imidazol-1-yl-phenyl)diazene (azim) ligand. The



Scheme 8 Schematic representation of reversible SC–SC pedal motion and twisting of phenyl rings in compound [**47**] after guest removal by heating (guest molecules are removed for clarity). (Reprinted with permission from Ref. 65. Copyright (2011) American Chemical Society.)

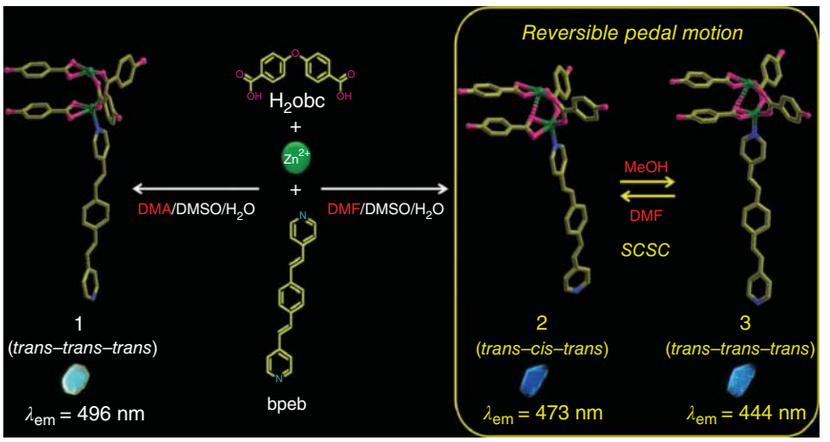


Figure 42 Guest-triggered supramolecular isomerism in a pillared-layer structure [**49**] through reversible pedal-motion-type SCSC transformation. DMA = dimethylacetamide, H_2obc = 4,4′-oxybisbenzoic acid

ligand incorporates an azo moiety at the center and imidazole groups at the terminals. The coordination polymer shows reversible guest-exchange behavior in SC–SC manner. Most interestingly, stepwise heat treatment does not lead to loss of crystallinity, but causes substantial movement or escape of both metal-bound and lattice DMF molecules as well as movement of ClO_4^- anions.

The X-ray structures of as-synthesized and its daughter products reveal step by step reversible bicycle-pedal or crankshaft motion of the azo group (Scheme 8). Similar dynamic pedal motion was also observed[66] in a Zn(II)-based framework [**48**].

Another interesting example of guest-triggered reversible pedal motion in a pillared-layer structure **49**, with unusual isomers of paddle wheel SBUs,[67] was reported by Park *et al*. (Figure 42). The understanding of such molecular motion offers to explain various dynamic aspects of molecules besides being potentially useful in fabricating molecular devices.

The dynamic aspect, arising due to diverse packing arrangements in the solid state, may give rise to anomalous thermal expansion behavior in MOFs, which can find applications in thermomechanical actuator or sensor. Elucidation of the mechanisms of anomalous thermal expansion in MOFs is possible only if the mechanical response occurs in a SC–SC pathway. Barbour *et al.*[68] nicely demonstrated, in a 3D MOF, that structure determinations from single-crystal X-ray diffraction (SCXD) at regular temperature intervals can afford the necessary information to determine the mechanism involved. The as-synthesized MOF [**50**] has 1D channels containing guest molecules that can be removed and/or exchanged for other guest molecules without losing crystallinity. A noticeable effect on the host mechanics, altering the thermal expansion properties of the material, is experienced with the replacement of the original guest molecules by other. The mechanism of the anisotropic expansion involves a substantial increase in the intermolecular host–host interaction distances and deformation of the labile coordination angles around the metal nodes. The macroscopic increase in length of the needle-shaped crystal bears good agreement with the thermal expansion along *c*-axis (α_c) (Figure 43).

The values of thermal expansion coefficients of different inclusion complexes of the host MOF, with systematic alteration of guest size (methanol, ethanol, *n*-propanol, and isopropanol), demonstrate that the PTE (positive thermal expansion) coefficients for the different guests correlate to the size/Van der Waals volume of the guest involved.

2.5 Substitution Reactions at the Metal Center in Single-Crystal to Single-Crystal Manner

Substitution activity at the metal coordination sites can significantly change the electronic and magnetic properties of the metal centers besides activating guest molecules through coordination to the metal for possible applications. Cobalt complexes in the oxidation state +2 exhibit spectra that are not only indicative of their stereochemistry but are sensitive to the donor atoms as well.[69] The effect of donor atoms is evidenced in a coordination polymer built[70] with Co(II) and linear rodlike linker, incorporating ethylene glycol side chains (Scheme 9). The resulting MOF [**51**] forms a square-grid layer structure where the layers are stacked above one another in an offset manner so that every metal center is positioned in the middle of a square grid of another layer (Figure 44a). The ethylene glycol side chains are involved in O–H···O interlayer hydrogen bonding that helps in stabilizing the overall structure. On heating a crystal at 150 °C for 24 h, two apical aqua ligands of Co(II) are lost and substituted by two

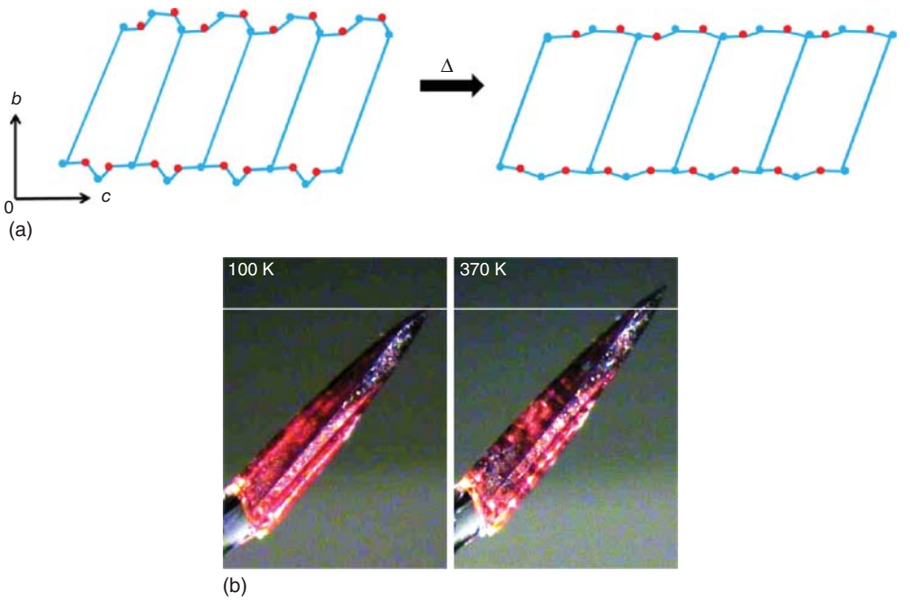
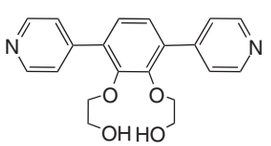


Figure 43 Schematic 2D representation of the framework topology, with the Zn metal centers depicted as blue circles and the hydroxyl bridges as red circles. Photomicrographs of a crystal of **50**·MeOH mounted on a glass fiber, recorded at 100 (a) and 370 K (b). (Reprinted with permission from Ref. 68. Copyright (2013) American Chemical Society.)



Scheme 9 Schematic diagram of the ligand used in the study of apical ligand substitution reaction at Co(II) centers in **51**

lattice nitrate anions (Figure 44b). Compared to the aqua ligand, the nitrate anion is a weaker donor (Co–O(H_2O), 2.095(4) Å; Co–O(NO_3^-), 2.129(8) Å) leading to less splitting of the d-orbitals with concomitant color change from yellow to red. Water being a stronger binder, the original color and structure come back within minutes when the crystal is exposed to air at room temperature, showing reversibility of the exchange process.

In the MOF, $\{[Co_2(bipy)_3(SO_4)_2(H_2O)_2](bipy)(CH_3OH)\}_n$ [**53**] (bipy = 4,4′-bipyridyl) again forms,[71] a 2D square-grid layer that is further linked through the SO_4^{2-}anions into an overall 3D structure. The framework contains both discrete reactive and inert structural motifs that can undergo a reversible substitution reaction, involving the concerted and spatially ordered introduction of bipyridine and methanol molecules at the reactive sites. Structure of the parent compound consists of two distinct layer networks connected by SO_4^{2-} anions to form a 3D hybrid framework. Noncoordinated 4,4′-bipyidine and methanol molecules occupy interlayer spacing. On heating at 95 °C for 1 h, the guest molecules replaces metal-bound aqua ligands, to give a framework composition of $[Co_2(bipy)_4(SO_4)_2(CH_3OH)]$ as [**53′**] (Figure 45). These substitution reactions take place in way such that two MeOH and two bipyridine molecules are bound to alternating metal centers. On exposure to moist air, the original structure can be restored showing the substitution reactions to be reversible. Color of the crystal changes from light purple to dark purple.

For a porous and flexible MOF, the flexibility can be expressed on substitution at the metal center, leading to a new structure with drastic changes. Thus, a porous 1D coordination polymer [**54**] of Zn(II) built with a linear linker with pyridine at either end has been reported.[72] The structure of the material consisting of 1D chain are H-bonded with other such chains to form an overall 3D structure forming 1D channels. When crystals of this polymer are exposed to air at room temperature, two MeOH molecules coordinated at each Zn(II) center are substituted by two H_2O molecules to form a new phase [**54′**] (Figure 46) without losing crystallinity. A close inspection of structural parameters reveal that the M–M–M angles expand from 101.098 (parent) to 106.618° (daughter) due to substitution of relatively bulkier methanol by water. The metal ion does not have any strong coordination preferences and the relatively weak pyridine donors make the polymeric structure soft. Hence, its flexible and dynamic structural behavior results from the cooperative action of organic and

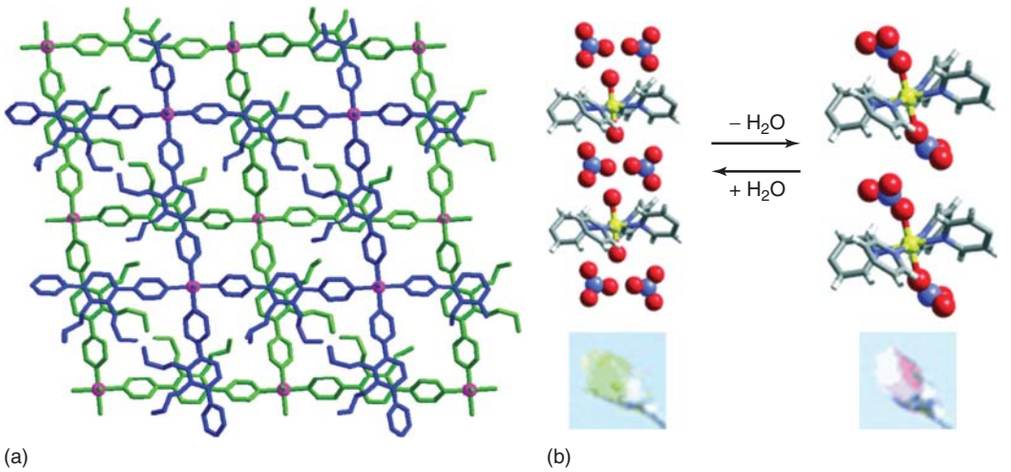


Figure 44 (a) Perspectives view of the square-grid network, showing the two-layer stack in different color. Guest water molecules have been omitted for clarity. Photographs and crystal views around the cobalt ion in as-synthesized crystal ([**52**], a) and after heating at 150 °C for 24 h ([**52′**], b)

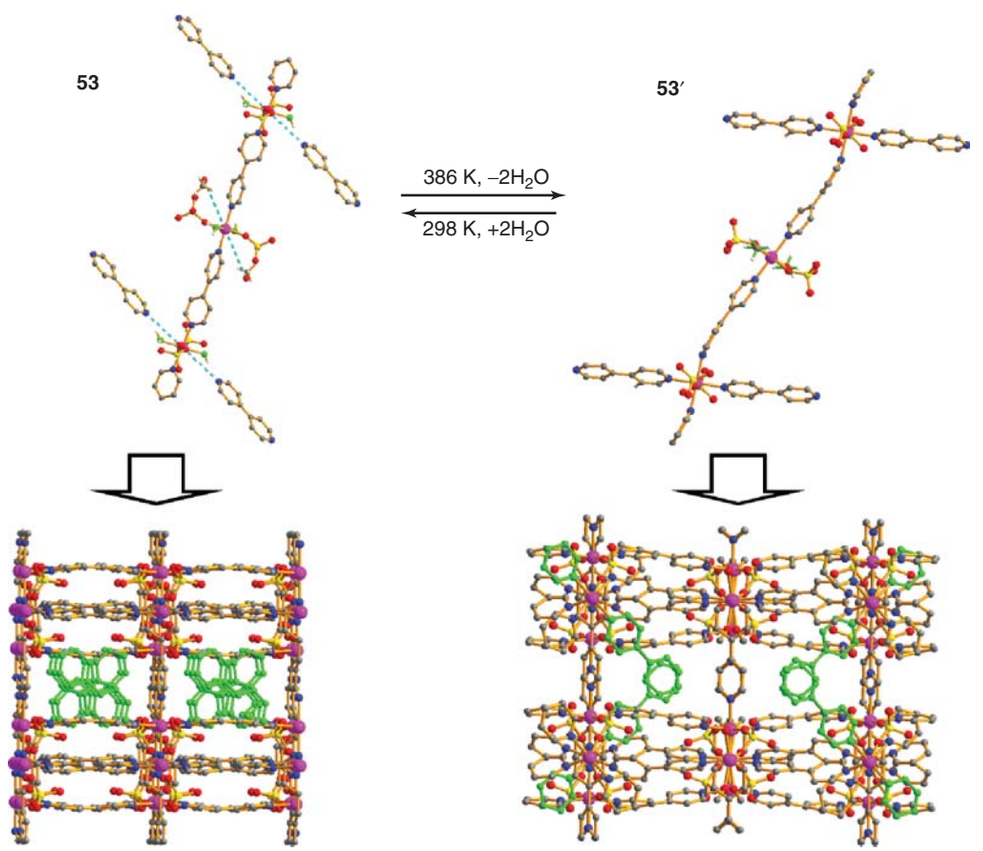


Figure 45 View of the reversible bimolecular substitution reaction in Co(bipy) chains of **53** on heating to 368 K. The bipyridine (green) and CH_3OH guest molecules occupy hydrogen-bonding positions in the channels of **53** (left, bottom). The incoming guest species displace metal-bound water on heating to produce a chain that has bipyridine and CH_3OH bound to alternate metal centers along the chain in **53′**

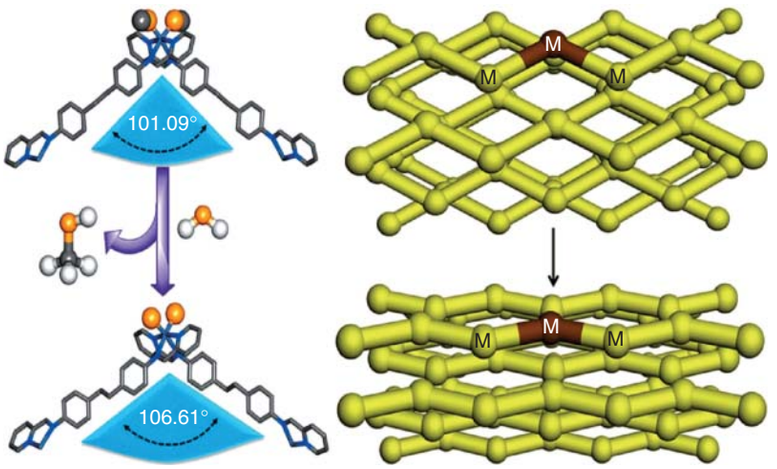


Figure 46 Crystal structures of parent [**54**] (top) and daughter [**54′**] (bottom) compound, showing coordination environment (left) and overall framework (right). Free solvents and anions are omitted for clarity

inorganic moieties. It would be interesting to probe this organic linker with other metal ions such as Pb(II), Cd(II), or lanthanide metal ions for possible structural changes on substitution at the metal center or external stimuli such as heat.

Another interesting example of flexibility of the framework [**55**] has been found[73] in the polymer constructed from Cu(II) and the ligand, 5-sulfoisophthalate. The unique properties of this material can be attributed to the coordination flexibility of the structure, imparted by the use of a linker with the potential for both strong and weak ligand interactions. The two carboxylate donors on the ligand bind relatively strongly to Cu(II) that help maintain the overall structure while chemistry can take place at the weaker sulfonate-metal bonds reversively. The low-temperature structure of the polymer consists of a tetramer of Cu(II) ions as the SBU linked by two three-coordinate hydroxyl groups. The SBUs are linked into layers by the organic linkers. These layers are further connected via coordination of the sulfonate group to a cluster in another layer forming an overall 3D architecture. Only two of the three sulfonate O atoms are involved in coordination while the third points into the space between copper clusters. In addition to metal-bound water, other water molecules occupy the voids defined by the framework. On heating, both lattice and coordinated water are lost. The vacant coordination site on Cu is filled by the third sulfonate O atom. This change in the coordination site of one of the Cu(II) ions leads to drastic changes in the overall structure without losing crystallinity (Figure 47). The structural transition can be reversed completely when the dehydrated crystal is exposed to moisture.

Interestingly, the dehydrated material acts as nonporous and small gas molecules such as H_2, N_2, CO_2, CO,

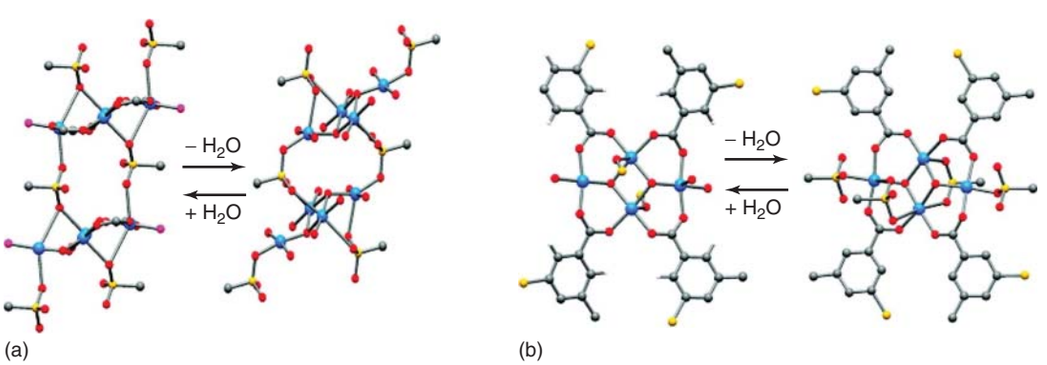


Figure 47 (a) Chains of copper tetramers in the low-temperature structure [**55**] (left) and high-temperature structure [**55′**] (right). (b) Copper tetramers in the low-temperature (left) and high-temperature (right) structures. (Reprinted with permission from Ref. 73. Copyright (2010) American Chemical Society.)

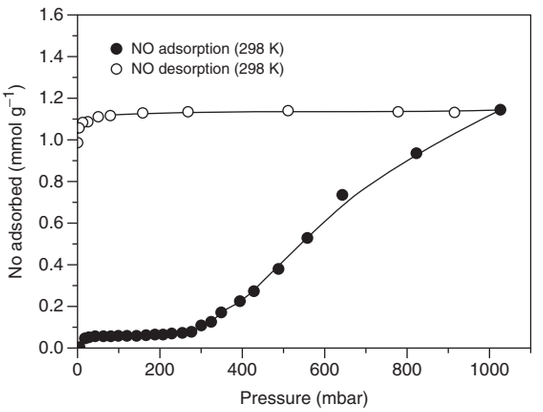


Figure 48 NO adsorption (closed circles) and desorption (open circles) isotherms for the dehydrated framework [**55′**] showing the large hysteresis. (Reprinted with permission from Ref. 73. Copyright (2010) American Chemical Society.)

N_2O, and CH_4 show no uptake up to pressures of 10 bar. However, at 1 bar pressure, it shows uptake of 0.88 NO molecules per formula unit. An important aspect of NO uptake is the significant hysteresis between uptake and removal (Figure 48) pointing to a possible chemisorption interaction with the metal. This is most likely due to weak binding of the sulphonate O atom to the metal and coordination-driven gated adsorption phenomena. The coordinating ability of the NO molecule also comes into play.

In a dynamic flexible framework, guest-induced rearrangement can also happen in a well-concerted SC–SC manner leading to change in the dimensionality of the overall structure. Colorless rod-shaped crystals of $[Zn_2\mathbf{L_5}(DMF)_4]\cdot 2DMF\cdot 4H_2O$ [**56**] ($H_4\mathbf{L_5}$ = methanetetra(biphenyl-*p*-carboxylic acid) were synthesized solvothermally in DMF. Structural studies reveal a 2D hinged layer structure[74] where each metal ion shows distorted octahedral coordination geometry where ligation comes from carboxylates and two DMF molecules (Figure 49). Exposure to CH_2Cl_2 at room temperature causes replacement of two metal-bound DMF by two H_2O molecules. This induces a SC–SC transformation of the 2D network to a 3D one via dimerization of the metal-connecting points (Figure 49a). Replacement of DMF by H_2O allows the two metal ions to come closer to each other and eventually form a chemical bond leading to a 3D structure (Figure 49b). That the process takes place in SC–SC manner is also proven by the inductively coupled plasma-mass spectrometric (ICP-MS) studies.

The coordination polymer of Cd(II) [**47**], synthesized[65] at room temperature with the linker

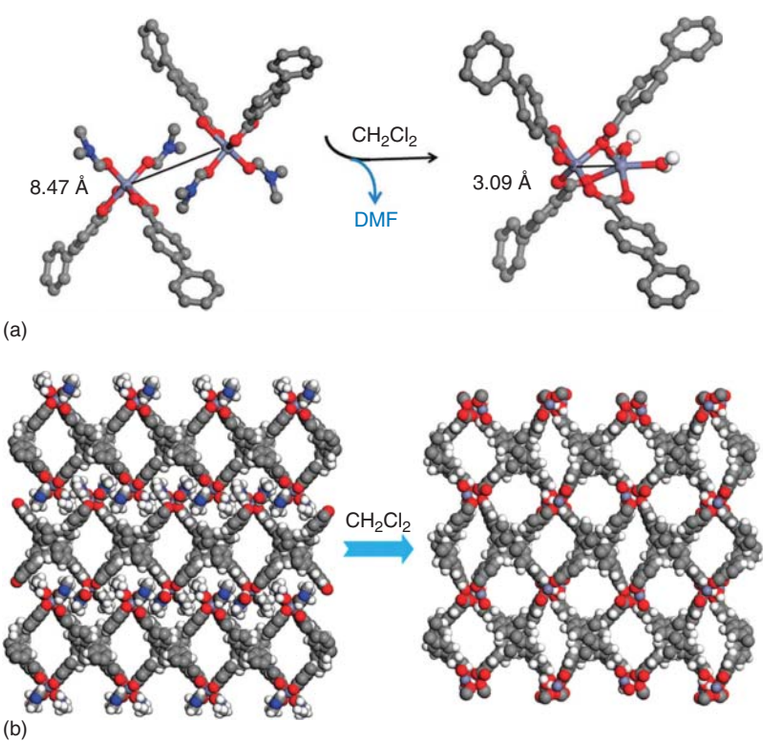


Figure 49 (a) Dimerization of two mononuclear Zn connecting points to a di-zinc SBU. (b) A view of the SC–SC transformation of 2D layers to a 3D structure

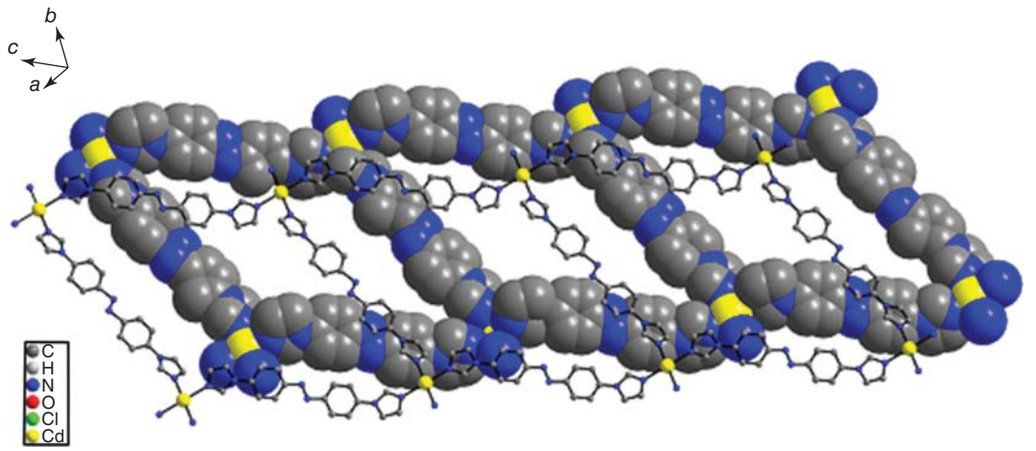


Figure 50 A perspective view of two rhombic grid layers of the coordination polymer **47**. (Reprinted with permission from Ref. 65. Copyright (2011) American Chemical Society.)

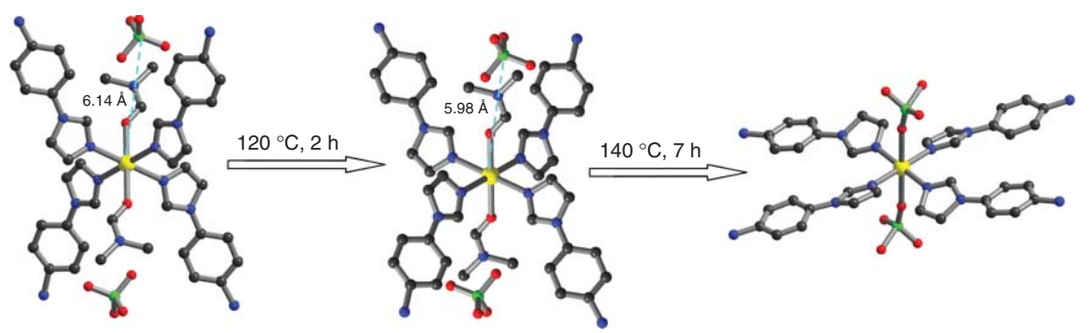


Figure 51 Schematic illustration of the SC–SC transformation, involving DMF→ClO_4 exchange at the Cd(II) center (H atoms are removed for clarity). (Reprinted with permission from Ref. 65. Copyright (2011) American Chemical Society.)

bis(4-imidazol-1-yl-phenyl) diazene (Scheme 8), forms a noninterpenetrated rhombus grid 2D layers that stack on one another in an offset manner (Figure 50). On heating, the axially bound DMF moves away and the ClO_4^- anions move from the void space to the metal (Figure 51). This concerted movement is accompanied by stepwise bicycle-pedal or crankshaft motion of the azo group. In spite of all these movements, crystallinity is maintained and the process can be visualized via X-ray crystallography.

Ultimately, metal-bound DMF molecules are lost along with the lattice ones and the ClO_4^- anions move from lattice to occupy both the axial positions on the metal. Such large movement of a group without losing crystallinity is remarkable. When a single crystal of the original compound is dipped in DEF for 10 h at RT, coordinated DMF molecules are substituted by DEF (Figure 52) with concomitant occurrence of bicycle-pedal motion of the azo moieties.

A multidentate ligand incorporating aromatic carboxylate and pyridine donors separated by a flexible spacer ($\mathbf{L_6}$ = 5-[(Pyridin-4-ylmethyl)-amino]-isophthalic acid) forms the coordination polymer, $Mn(\mathbf{L_6})(H_2O)](H_2O)1.5(DMF)\}_n$ [**57**] in aqueous DMF under solvothermal condition.[75] Each Mn(II) ion shows a distorted octahedral geometry with one water molecule bound to the metal (Figure 53).

The flexible spacer in the ligand makes a relatively fluid cavity within the solid and the metal-bound water molecule can be substituted by various molecules in SC–SC transformations. A series of nitrile compounds as guest molecules including acetonitrile (MeCN), acrylonitrile (ACN), and allylnitrile (AN) is found to substitute the apical aqua ligand in SC–SC manner. The structure of the MeCN-bound framework is shown in Figure 54. All these substitution reactions are reversible in nature and any one product can be reached from another one

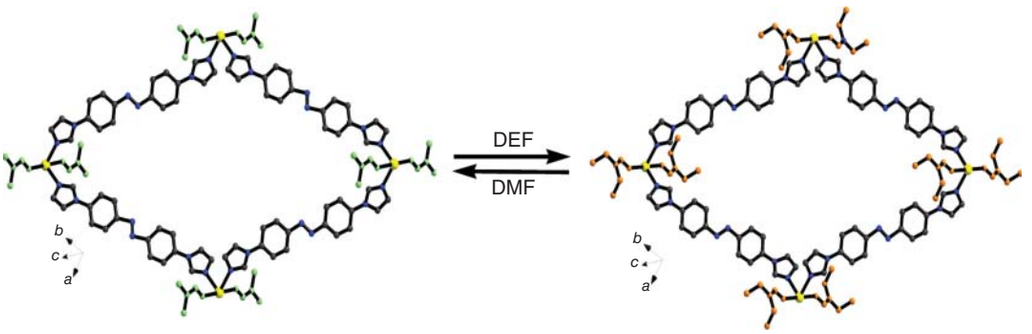


Figure 52 Schematic representation of reversible SC–SC DEF/DMF exchange at the metal center (H atoms are removed for clarity). (Reprinted with permission from Ref. 65. Copyright (2011) American Chemical Society.)

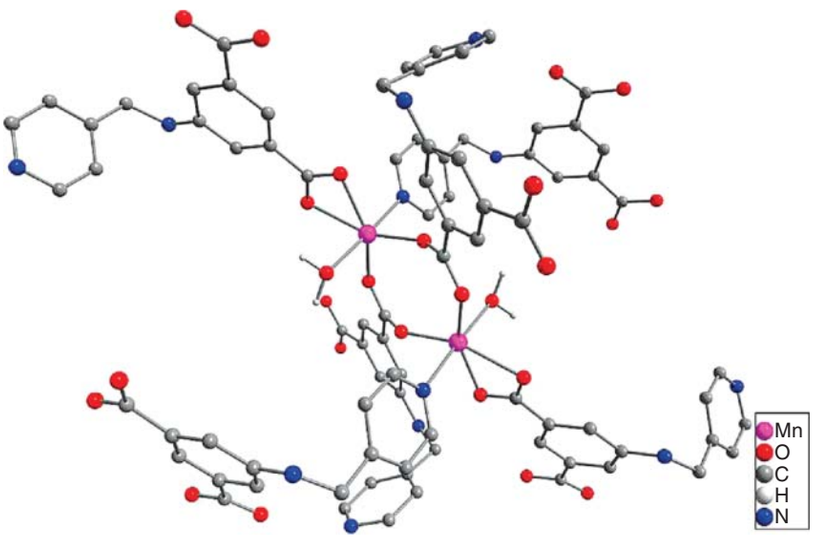


Figure 53 Dimeric unit in the crystal structure of $Mn(\mathbf{L}_6)(H_2O)](H_2O)1.5(DMF)\}_n$ [**57**] (H atoms of the ligand moieties have been omitted for clarity). (Reprinted with permission from Ref. 75. Copyright (2009) American Chemical Society.)

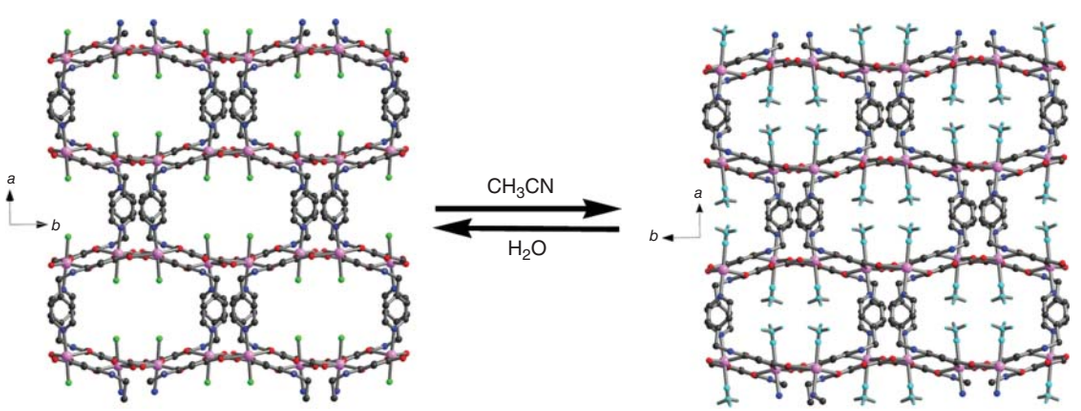
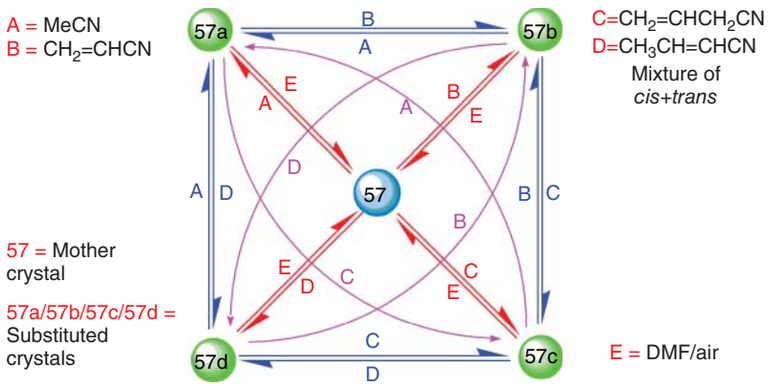


Figure 54 Perspective views of the reversible SC–SC transformation, occurring at the Mn(II) center of the framework **57** at room temperature. (Reprinted with permission from Ref. 75. Copyright (2009) American Chemical Society.)



Scheme 10 A schematic representation for the reversible substitution reactions at Mn(II) center within the pores of **57**. (Reproduced with permission from Ref. 75. Copyright 2009 American Chemical Society.)

Table 1 Preference for nitriles as guests in $[Mn(\mathbf{L_6})(H_2O)](H_2O)\cdot 1.5(DMF)\}_n$ [**57**] with variation of molar ratio

MeCN:ACN:AN	Complex formed
1:1:0	$\{[Mn(L_6)(MeCN)]\cdot 1.5MeCN\}_n$
1:0:1	$\{[Mn(L_6)(MeCN)]\cdot 1.5MeCN\}_n$
1:1:1	$\{[Mn(L_6)(MeCN)]\cdot 1.5MeCN\}_n$
0:1:1	$\{[Mn(L_6)(ACN)]\cdot ACN\}_n$
1:≥5:0	$\{[Mn(L_6)(ACN)]\cdot ACN\}_n$
1:0: ≥15	$\{[Mn(L_6)(AN)]\cdot AN\}_n$
0:1: ≥10	$\{[Mn(L_6)(AN)]\cdot AN\}_n$

Reprinted with permission from Ref. 75. Copyright (2009) American Chemical Society.
MeCN = acetonitrile; ACN = acrylonitrile; AN = allylnitrile.

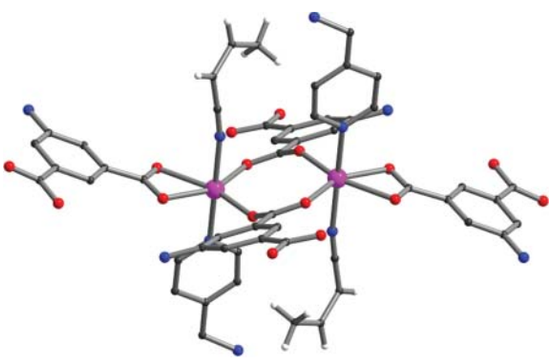


Figure 55 Dimeric unit of *cis*-CTN substituted structure (for clarity, only H atoms of CTN molecules have been shown). Lattice *cis*-CTN molecules are not shown

(Scheme 10). Color of the crystal does not show any perceptible change during these SC–SC transformations. The uptake of a particular nitrile in the presence of others depends on the relative amounts of the nitriles as summarized in Table 1. When a mixture of *cis*- and *trans*-CTN (CTN = crotononitrile) is added to the parent compound, only the cis-isomer replaces the aqua ligand, whereas another cis-isomer occupies the void in the cavity driving out all guest molecules (Figure 55). Methyl protons of the coordinated *cis*-CTN make strong C–H$\cdots\pi$ interactions with the nearby aromatic moiety. For trans-isomer, this would mean unfavorable steric interactions between the methyl protons of trans-CTN and the opposite wall. This size and shape selectivity is further established by the fact that when pure trans-isomer is taken in place of the mixture, it is not incorporated in the cavity.

The parent compound, $[Mn(\mathbf{L_6})(H_2O)](H_2O)\cdot 1.5(DMF)\}_n$ [**57**], also undergoes either partial or complete substitution reactions of the aqua ligand by several N-donor ligands depending on its bulkiness.[76] It involves a new class of substitution reactions within PCPs that involves concerted and spatially controlled introduction of different guest molecules at the reactive Mn(II) sites with the retention of long-range order by cooperative motions to permit molecular transport through a porous solid. If pyridine or 4-picoline is used as a guest, both lattice and coordinated solvent molecules are simultaneously substituted (Figure 56). However, use of a bulky guest such as aniline affects only partial substitution at the metal center and complete substitution at the channels. On the other hand, if the guest is 2-picoline (by varying the position of bulky methyl group with respect to donor N atom), one Mn(II) center is substituted by 2-picoline, whereas the second Mn(II) center is substituted by a DMF molecule that migrates from the channel to the metal center. For the case of other bulky guests such as benzonitrile or 2,6-lutidine, only lattice solvent molecules are replaced, whereas the metal centers are substituted by DMF molecules. A preferential substitution of pyridine over benzonitrile at the metal centers is realized only when the molar ratio of PhCN:Py is 95:5 or less. For the case of an aliphatic dimethylamino acetonitrile guest, the metal

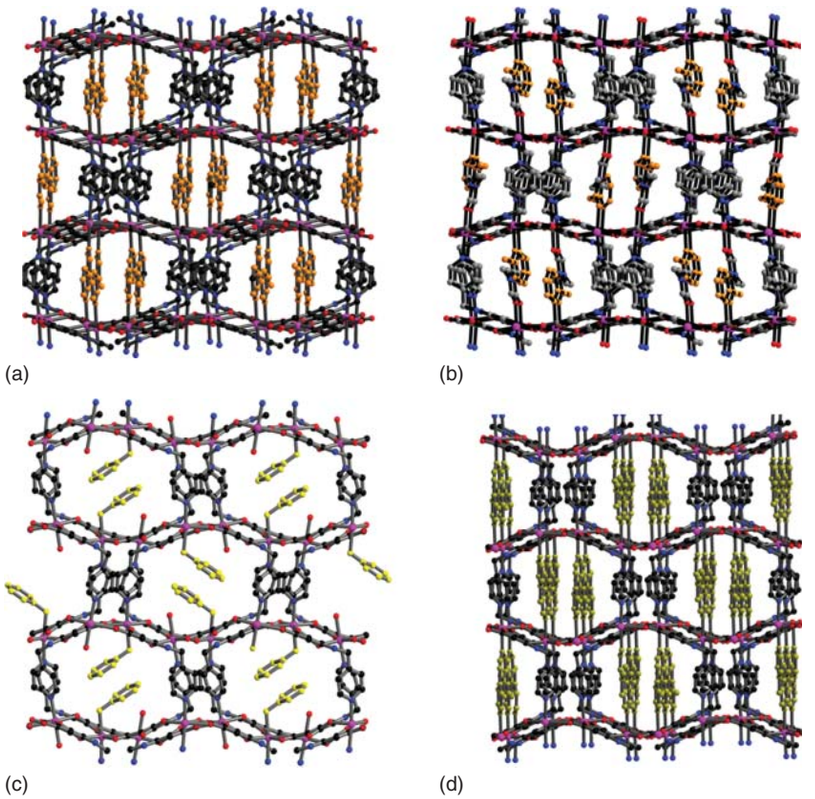


Figure 56 The framework structure showing (a) pyridine-substituted, (b) 2-picoline-substituted (partial), (c) aniline-substituted (partial), and (d) 4-picoline-substituted Mn(II) centers

centers remain unsubstituted. Some of the structures are illustrated in Figure 56.

Removal of coordinating solvent produces MOFs with vacant coordination sites, as efficient candidates to enhance the gas storage capability and catalysis. However, single crystallinities and/or open framework structures are normally destroyed when coordinating solvent molecules are removed from MOFs. Through deliberate design, synthesis, and examination of flexible MOFs, researchers have come to a better understanding that a certain coordination bond could not only sustain a framework but also transform the framework into a new one via reversible making and breaking of coordination bond. As a remarkable example, Suh *et al.*[14] reported porous 3D MOF $[Zn_3\text{-}(ntb)_2(EtOH)_2]_n \cdot 4nEtOH$ [**58**] (ntb = 4′4″4‴-nitrilotrisbenzoic acid) that changes the coordination geometry of Zn(II) ions reversibly from/to trigonal bipyramid to/from tetrahedron on removal and rebinding of coordinating solvent molecules through a reversible crystal dynamics (Figure 57).

Despite the coordination flexibility of metal ions, the host framework as well as the single crystallinity is retained during the desolvation and resolvation processes. The desolvated solid $[Zn_3\text{-}(ntb)_2]_n$ ([**58′**]), without the coordinating EtOH as well as guest EtOH molecules, exhibits permanent porosity and remarkable gas storage capabilities toward N_2, H_2, CO_2, and CH_4.

As an exception to the above category, where metal center experiences a loss in coordination number, Gedrich and coworkers[77] showed an increase in the coordination number of the central metal ion. The 3D chiral MOF [**59**] (MOF: **DUT-7**) was synthesized using enantiopure (S)-2,2′-spirobiindane-5,5′-dicarboxylic acid ligand. The room temperature structure is composed of Zn_4O clusters that are coordinated in rare trigonal prismatic manner. The authors observed reversible SC–SC structural transformation on cooling. The low-temperature single-crystal X-ray diffraction data show that one of the Zn(II) in Zn_4O cluster is transformed from tetrahedral to octahedral geometry by additional solvent coordination, denoted as **DUT-7**(LT) [**59′**] (LT: low temperature) (Figure 58).

Insertion or removal of organic linkers through SC–SC transformation is an unprecedented phenomenon that not only modulates the pore size and shape of a MOF but also influences the physicochemical properties. An unprecedented postsynthetic reversible incorporation of bridging ligands in a PCP through SC–SC transformation has been achieved[78] in case of the coordination polymer,

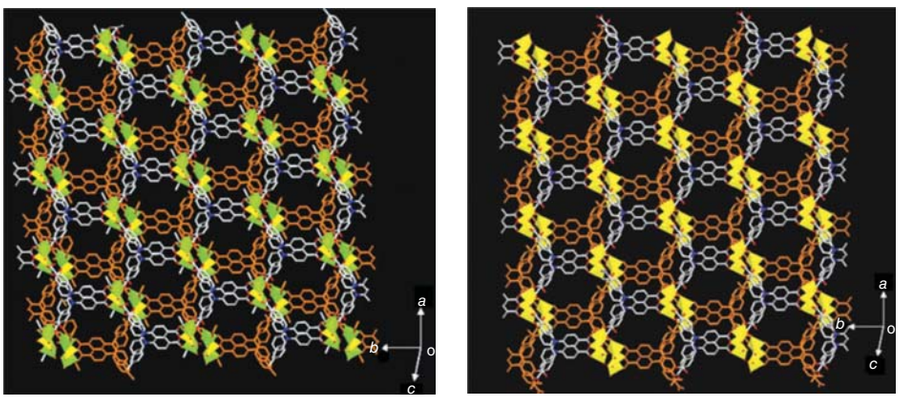


Figure 57 View on the (101) plane, showing the bilayers of honeycomb aperture with Zn_3 pillars in **58** (b) and **58′** (a). Guest EtOH molecules are omitted for clarity. Color scheme: Zn (td), yellow; Zn (tbp), green; N, blue; O, red; O of coordinating EtOH, pink; C of two different bilayers, white and brown

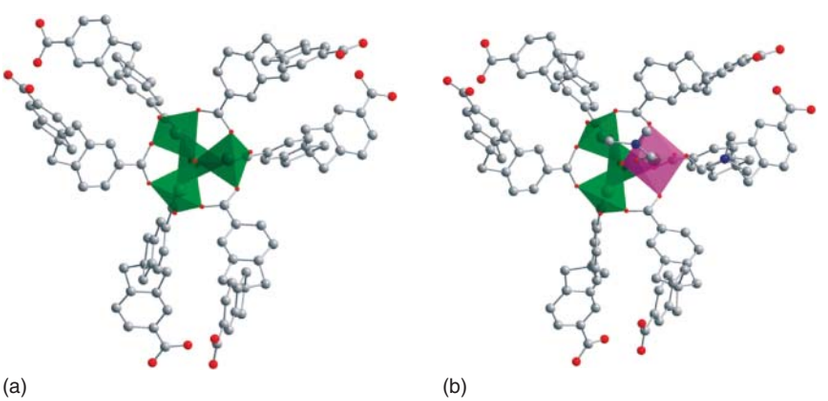
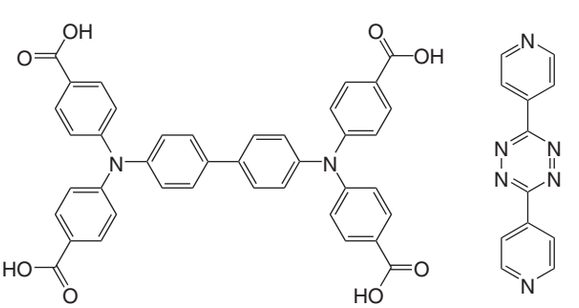


Figure 58 (a) SBUs of **DUT-7**(RT) [**59**] and (b) **DUT-7**(LT) [**59′**], both: view along [001]. (Reprinted with permission from Ref. 77. Copyright (2010) American Chemical Society.)

$\{[Zn_2(TCPBDA)(bpta)]\cdot 20DMF\cdot 4H_2O\}_n$ [**60**], built with a tetracarboxilic acid (Scheme 11) [H_4TCPBDA (*N,N,N′,N′*-tetrakis(4-carboxyphenyl)biphenyl-4,4′-diamine)], a linear co-ligand, 3,6-di(4-pyridyl)-1,2,4,5-tetrazine (bpta), and Zn(II) ion. As the structure reveals, the bpta moiety is significantly bent to fit into the structure (Figure 59). The bent bpta moiety can be removed by water when a crystal of the parent compound is dipped in moist DEF at room temperature for 7 days. Each bpta unit is substituted by two water molecules to afford $\{[Zn_2(TCPBDA)(H_2O)_2]\cdot 23DEF\}_n$ [**60′**] with different pore volume and gas adsorption characteristics.

The relatively weak interactions of coordination bonds are extremely effective to hybridize one MOF with other, in which the ligands participate in the construction of the crystalline framework. Such bond cleavage or ligand exchange reactions, triggered by external incorporation of a second linker, have been shown nicely in pillared porphyrin paddle wheel frameworks (PPFs). In this approach, one of



Scheme 11 Schematic diagram of the ligands used in the post-synthetic ligand exchange reaction of coordination polymer

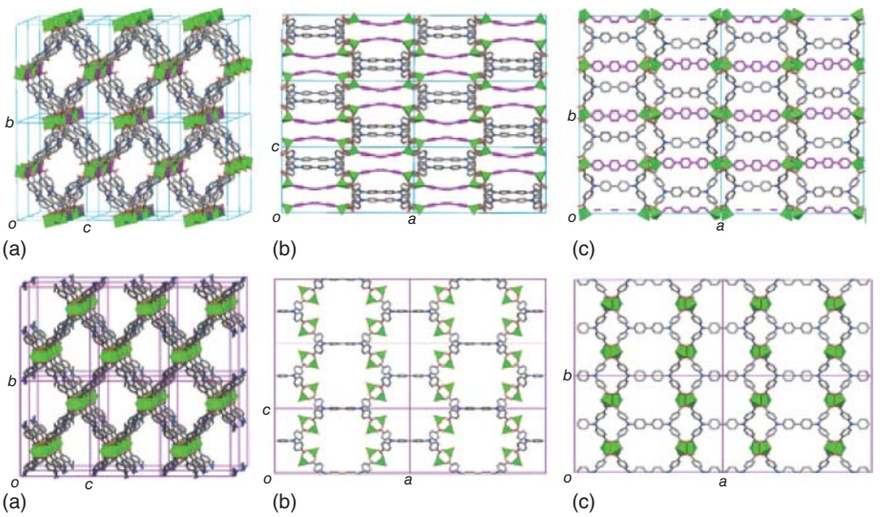
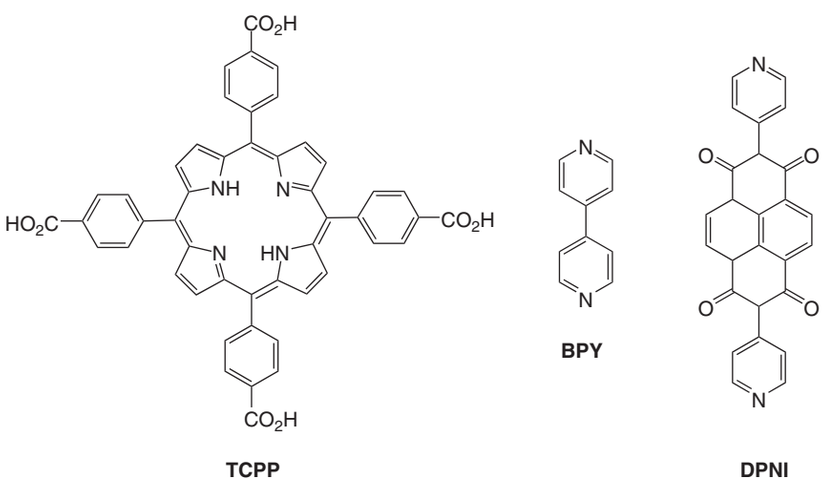


Figure 59 The X-ray crystal structure of the framework **60** before (top) and after (bottom) ligand insertion. Views shown on the (a) *bc*, (b) *ac*, and (c) *ab* planes



Scheme 12 Schematic diagram of the ligands used in the study in linker exchange reaction of pillared porphyrin paddle wheel frameworks. (Reproduced with permission from Ref. 79. Copyright 2011 American Chemical Society.)

the organic linkers (Scheme 12) is replaced by another of different length, altering the shape and size of the voids of the coordination polymer drastically.[79] The stacking patterns of the parent structures are maintained throughout and the old pillar making linkers are substituted by the new ones (Figure 60). Since no lateral movement in the 2D porphyrin paddle wheel layers take place during this pillar linker replacement, crystallinity is maintained. Given the enormous utilities of porous coordination polymers, such replacement reactions can pioneer in manipulating the shape and sizes of these molecules for specific purposes.

Apical ligand substitution at Co(II) center was reported[80] in a 2D pillared bilayer coordination framework [**63**] that exhibits reversible SC–SC transformations on removing and rebinding the coordinated water molecules. The coordination geometry of Co(II) changes from octahedron to square pyramid accompanied by shrinkage/expansion of pore with respect to the subsequent shear motion of bpy pillars and vice versa (Figure 61a). However, substitution of the aqua ligands by MeOH or EtOH (Figure 61b) does not lead to any changes of the network structure.

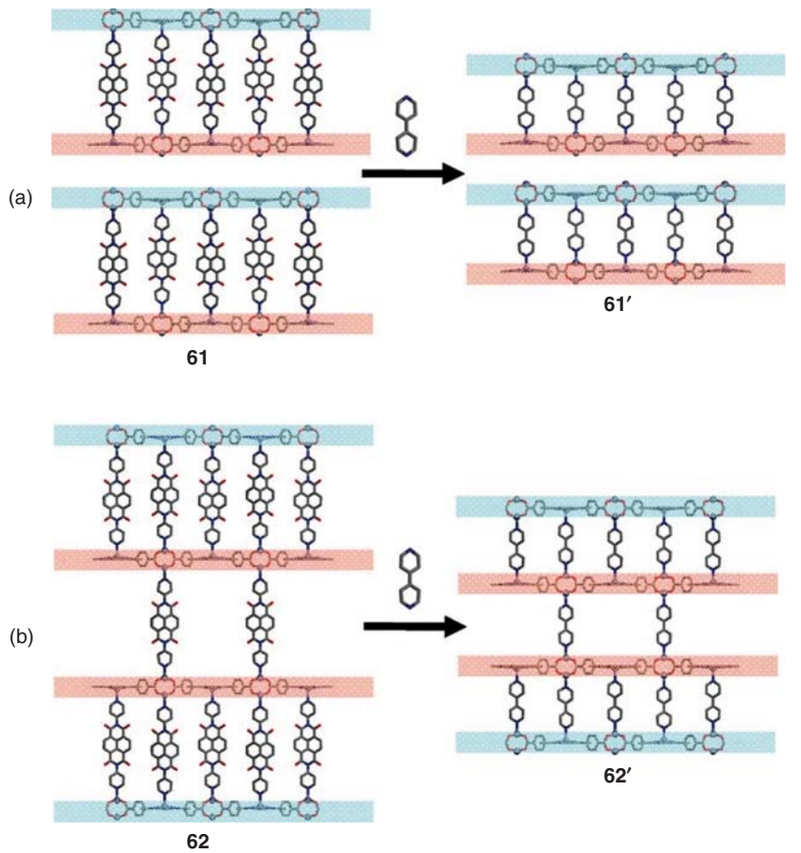


Figure 60 Introduction of the bridging linker BPY to crystals of (a) PPF-18 [**61**] and (b) PPF-20 [**62**], transforming them to PPF-27 [**61′**] and PPF-4 [**62′**], respectively. Blue and pink bands represent "A" and "B" layers, respectively. The AB and ABBA topologies in PPF-18 [**61**] and PPF-20 [**62**] are retained in PPF-27 [**61′**] and PPF-4 [**62′**], respectively, showing a templating effect. (Reprinted with permission from Ref. 79. Copyright (2011) American Chemical Society.)

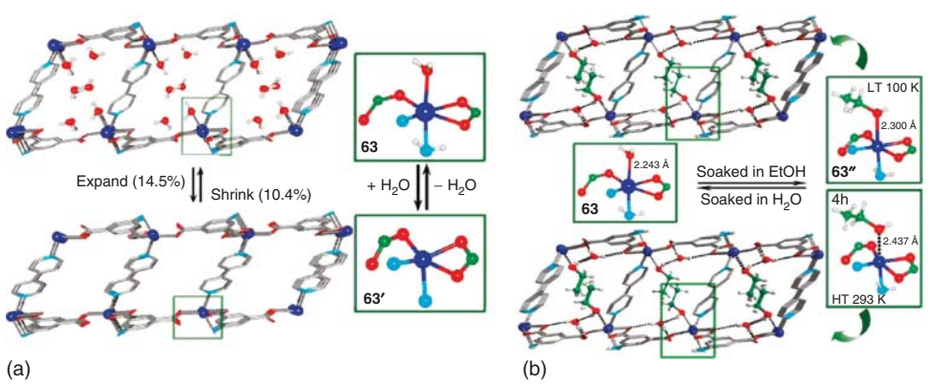


Figure 61 (a) Summary of frameworks, exhibiting reversible SC–SC transformation on removal and rebinding of coordinating water molecules, accompanying a change in the Co(II) coordination environment. (b) View of the framework exhibiting reversible ligand exchange ability in EtOH. Most H atoms are omitted for clarity. (Reprinted with permission from Ref. 80. Copyright (2009) American Chemical Society.)

The kinetics or detailed pathway of the structural change during the assembly processes (mechanisms) in MOF structures is extremely difficult to be experimentally verified due to the fact that the study is generally based only on the crystal structure measurements of the initial and final states. To this end, Wang *et al.* reported[81] an evolutionary pathway for the self-assembly of a flexible pillared-layer MOF [**64**], which includes the identification of two 2D nonpillared and pillared intermediates. The authors conducted a series of parallel sets of experiments during the self-assembly of the pillared-layer MOF at various concentrations of reactant components and were able to isolate the stepwise development of the final product. Moreover, they also reported temperature-induced framework flexibility by SC–SC on cooling and subsequent heating. The pillared-layer MOF reveals a drastic framework distortion on cooling, due to inclination of its pillar ligand. On warming up back, an intermediate phase, with a less slanted orientation of the pillars was captured (Figure 62).

A SC–SC transformation of a 3D framework to 2D framework, due to the replacement of axial ligands by water molecules, has been reported.[82] The precursor 3D framework [**65**] is constructed by using DABCO (1,4-diazabicyclooctane) as a pillaring unit to join the 2D layered framework structure of BDC (benzene-1,4-dicarboxylate)-bridged paddle-wheel $Zn_2(COO)_4$ SBUs. When the framework [**65**] was exposed in air for 3 h, the pillaring unit DABCO gets substituted by the water molecules exhibiting 3D to 2D framework conversion (Figure 63). The reverse process, that is, 3D→2D framework conversion could be established only through PXRD experiment as the crystallinity is lost in this path.

Multiple substitutions at the metal centers with concomitant dynamic changes in SC–SC transformations have been reported[83] recently. This remarkable structural flexibility of the network **66** is a result of structural flexibility of the tripodal ligand, 1,3,5-tri(4-carboxyphenylsulphonyl)benzene (TCPSB), shown in Scheme 13. The metal ion Co(II) takes part in multiple substitution sequences in a SC–SC way (Figure 64). For example, when immersed in CH_3CN, the terminal DMF solvent is replaced by CH_3CN, which in air, readily loses CH_3CN to form terminal aqua-substituted framework. Again, when the aqua-substituted Co(II) was placed in DMF, it reverts back to as-synthesized form in single-crystal form.

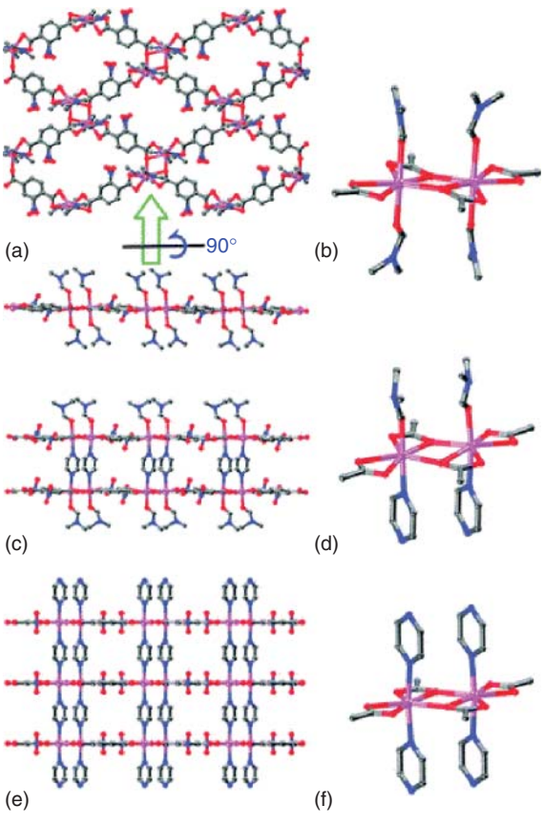


Figure 62 (a–f) Time- and concentration-dependent evolution of the intermediate phases during the formation of a flexible pillared-layer MOF [**64**]

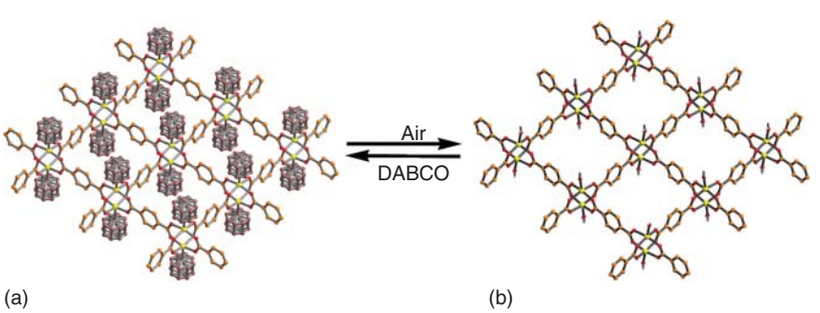
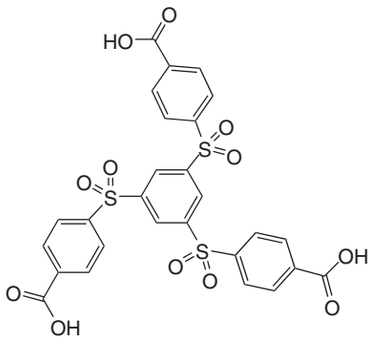


Figure 63 Structures of **65** (a) and **65′** (b), indicating their reversible framework transformation. (Reprinted with permission from Ref. 82. Copyright (2009) American Chemical Society.)



Scheme 13 Flexible tripodal ligand TCPSB, used for studying multiple substitution reactions at the metal centers. (Reproduced with permission from Ref. 83. Copyright 2011 American Chemical Society.)

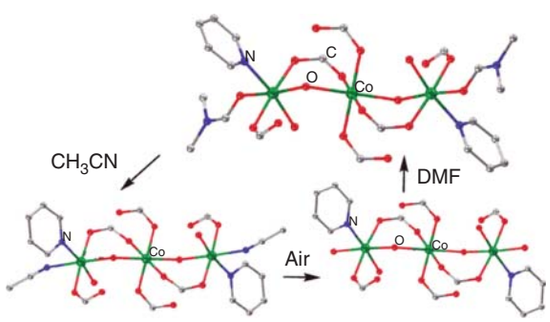


Figure 64 A close view of the Co_3 building unit of the framework **66**, showing apical ligand substitution reaction in a SC–SC manner. (Reprinted with permission from Ref. 83. Copyright (2011) American Chemical Society.)

Xue *et al.*[84] reported a new 3D chiral MOF [**67**], using a flexible dicarboxylate ligand, which exhibits an unprecedented, temperature-induced SC–SC transformation involving release of bridging aqua molecules and helicity conversion of the helical chains in two directions within the MOF (Figure 65).

Although the above examples successfully narrate a SC–SC transformation at the metal center during activation, they hardly enlighten about the mechanisms involved, when substitution transpires at multiple metal centers in the SBUs. This is because no intermediate could be crystallographically characterized during the transformation course. Seo *et al.*[85] elegantly aimed at softening the zinc paddle wheel SBU, using slim and long pyridine ligands in combination with dicarboxylic acid ligand and Zn(II) ion. The as-synthesized crystal **68** shows twofold interpenetrated 3D frameworks, with guest DMF and water molecules inside the framework cavity. The authors envisioned major structural changes, following SC–SC transformation, in the desolvated crystal. The coordination

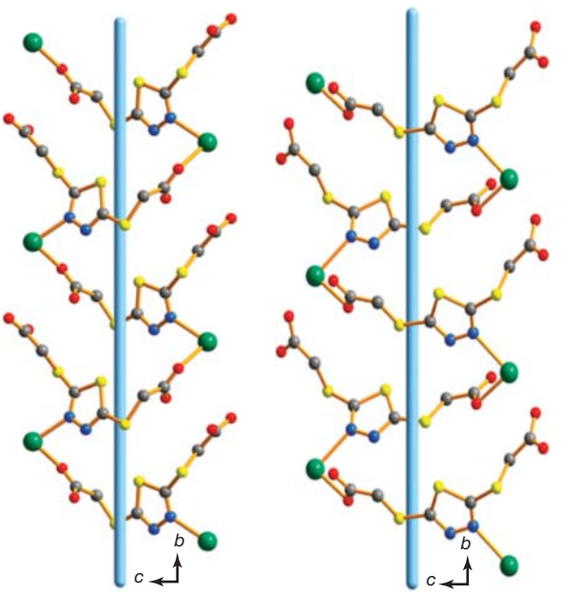


Figure 65 Thermally triggered change in helicity between the as-synthesized [**67**] and the transformed structures [**67′**]

environment about the Zn(II) is changed from square pyramidal to tetrahedral, with one carboxylate out of two being monodentate. Moreover, the paddle-wheel SBU in the original crystal breaks down to "open form" [**68d**] in the desolvated state. The authors were even successful to obtain single-crystal structure of two intermediates, **68b** and **68c**, during the drying process (Figure 66). The framework connectivity and zinc coordination geometry of the intermediates were found nearly identical, indicating that the transition from paddle wheel zinc cores to the "open form" requires complete desolvation. Furthermore, the authors showed the regeneration of the zinc paddle wheel unit from its "open form," although not in a SC–SC manner, is driven by the adsorption of a few gas molecules.

2.6 Anion Exchange in MOF through Single-Crystal to Single-Crystal Transformation

Anion templating can have a profound effect over the final assembly of a MOF structure by virtue of its shape, size, and ability to form hydrogen-bonding interaction with the host framework. Cohen and coworkers[86] reported anion templating through a SC–SC transformation, which permits a control over 2D versus 3D framework structures (Figure 67). The authors used different dipyrrin-based metalloligand systems, with a view to generating materials with strong optical absorptions and illustrate the potential for the synthesis of chiral MOFs. Using either BF_4^-or OTf^- (triflate), a series of heterometallic MOFs are synthesized in the form of doubly interpenetrated networks.

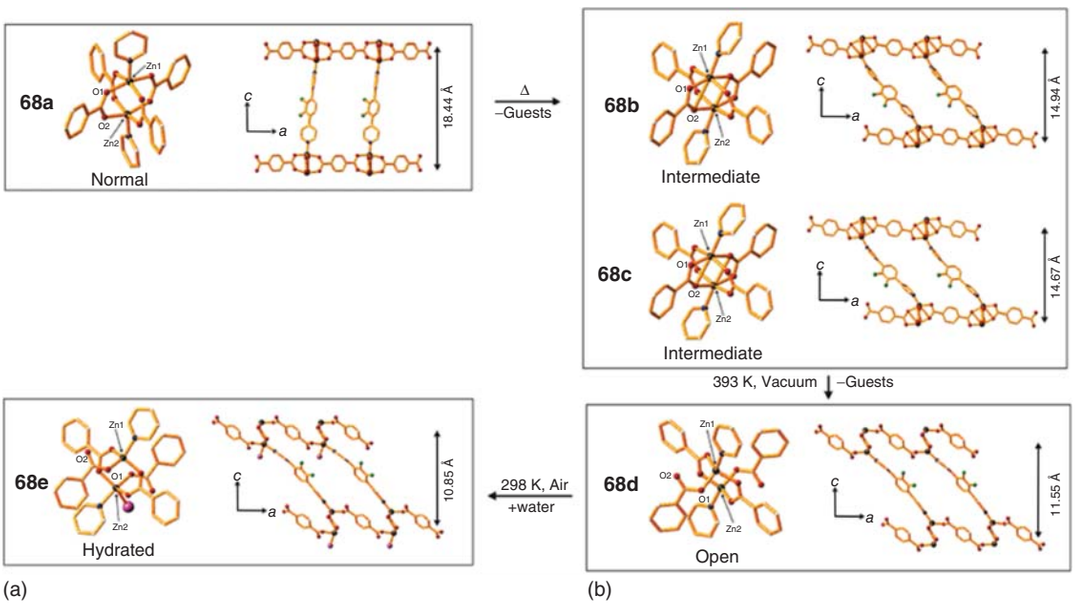


Figure 66 Crystal structure of **68a**, **68b**, **68c**, **68d**, and **68e** showing structural transformations on desolvation and moisture coordination. Ball color: gray, zinc; green, fluorine; blue, nitrogen; red, oxygen; violet in **68e**, coordinated water. Noncoordinated guest molecules and hydrogen atoms are omitted for clarity. Coordination environments of the zinc cluster (a) and views of the single framework along the *b*-axis (b). (Reprinted with permission from Ref. 85. Copyright (2011) American Chemical Society.)

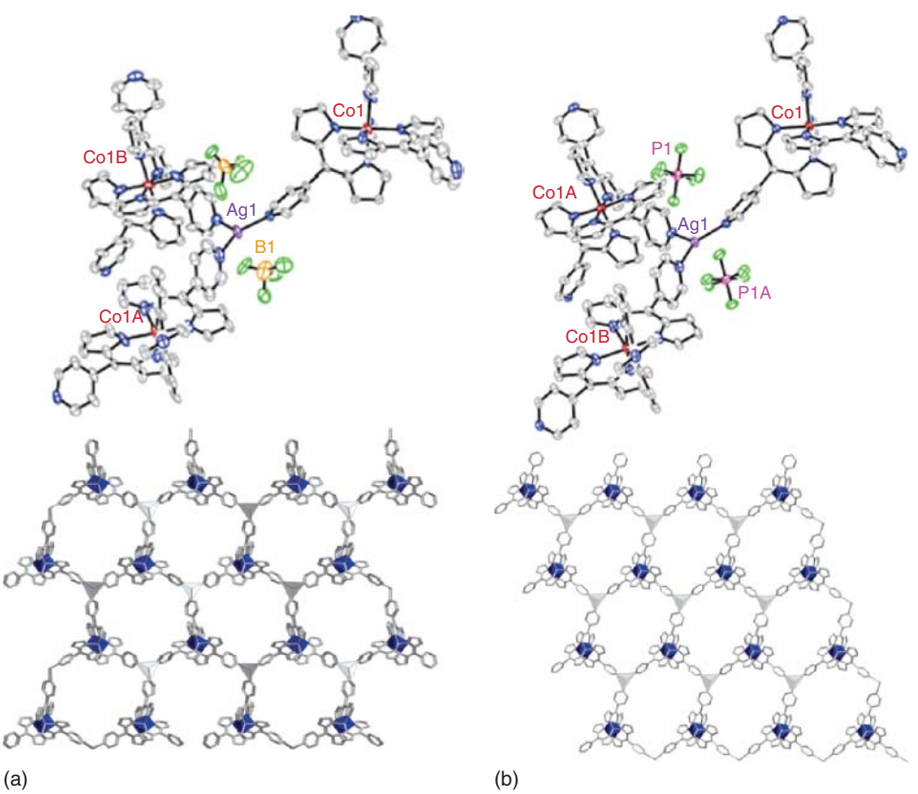


Figure 67 X-ray structures of the (10,3)-d net MOF-Co/$AgBF_4^-$ [**69a**] (a), and (6,3) nets MOF-Co/$AgPF_6^-$ [**69b**] (b), showing asymmetric units (top) and overall packing arrangements (bottom). (Reprinted with permission from Ref. 86. Copyright (2006) American Chemical Society.)

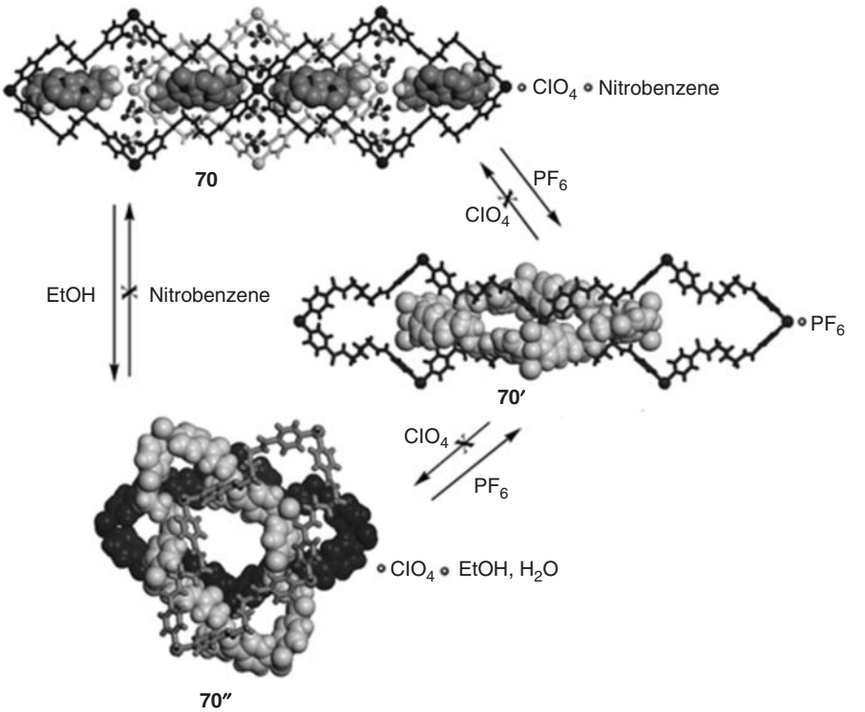


Figure 68 Anion exchange reactions of complexes **70′–70″** in a SC–SC pathway. (Reprinted with permission from Ref. 87. Copyright (2007) American Chemical Society.)

However, the MOF bearing OTf^- anion contains two independent, interpenetrated nets. To explore the effect of anion, the authors even prepared the same MOFs, using either PF_6^- or SbF_6^-. The structures of all new MOFs are determined as 2D honeycomblike network, distinct from the 3D nets found with AgOTf and $AgBF_4$. Overall, the anions exhibit a pronounced templating effect in the synthesis of dipyrrinato-metalloligand-derived MOFs. The authors summarized that the selection of silver(I) salts is crucial for the diverse topological arrangement of metalloligands in the final MOF, where anion templating play a significant role. A series of polymeric 1D chains, 2D grids, and 3D pseudodiamondoid frameworks have been reported[87] using a long flexible bis-pyridine ligand. The role of counter anions as templates for driving the network architecture and structural reorganization (Figure 68) has been studied. One of the frameworks [**70**] containing 1D chain with large rectangular cavities modifies its structure to a new 3D network [**70′**] by exchanging ClO_4^- anions with PF_6^-. A thorough study by the authors revealed the fact that every anion shows dissimilar interactions with the framework and thus offers diverse templating effects that eventually drive the formation of network geometries. For example, there is considerable difference between PF_6^- and ClO_4^- in the templating of the networks because of the added interference of PF_6^- anions in amide-to-amide hydrogen bonding, than that of ClO_4^-.

Anion-exchange-induced structural transformation of a neutral 3D microporous coordination polymer to the ionic 1D polymer has been reported by Michaelides *et al.*[88] in a crystal to crystal manner. The 3D molecular-based microporous material [**71**] was synthesized[89] using flexible multi-dentate adipic acid and lanthanide metal centers, having high coordination numbers. The ligand adopts a "linear" conformation and forms the "walls" of infinite interconnected channels, running in the three directions of space. In an attempt to prepare the same crystals by slow evaporation method, in presence of sodium adipate and very high anion concentration, 3D→1D transformation reaction takes place (Figure 69). The 1D polymeric structure [**71′**] looks like zigzag metal–organic chains, where each metal is nine-coordinated by four carboxylate oxygen atoms and five water molecules. The nitrate or chloride anions and the lattice water molecules are located in the channels. This transformation results due to the departure of one adipate ligand from **71** to **71′** and addition of three water ligands in the coordination sphere of the metal, thus preserving the coordination number of nine. This is a crucial step as the transformation does not take place with La^{3+} or Ce^{3+} (although isostructural to **71**), that

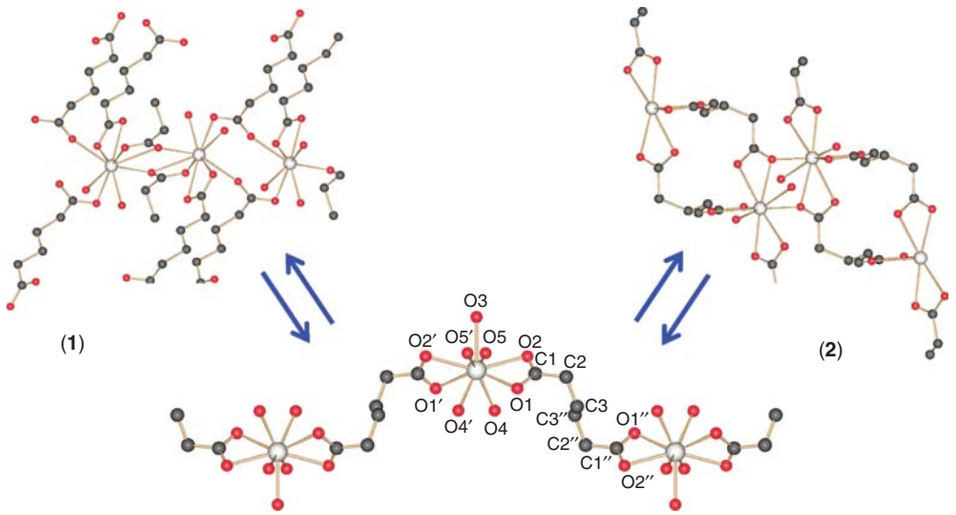


Figure 69 Schematic presentation of 3D lanthanide-adipate polymers [**71**] transforming reversibly into the 1D polymers [**71′**]. (Reprinted with permission from Ref. 88. Copyright (2009) American Chemical Society.)

is, with cations of high crystal radius, thereby lowering metal–water bond strength.

The SC–SC structural transformations caused by anion substitution are hard to achieve in robust MOFs, compared to transformations caused by solvent molecules. This is mainly because the anions often accomplish various functions in the crystal lattice such as complexation with the metal, charge balance, bridging, and so on. It is even harder to maintain single crystallinity during reversible anion exchange, as the charge balance and the size of the appropriate anions are fatal to the structural transformations. As a notable exception, Fu *et al.*[90] reported a 3D framework [**72**] made up of "crab-shaped" hexa-copper units containing NO_3^-, and demonstrated the anion exchange in a SC–SC way. The transformation is accompanied by the formation of weak $Cu^{2+} \ldots I^-$ interactions, and changes in the coordination numbers of Cu(II) (Figure 70). Moreover, the crystals change their color from blue to cyan to dark blue [**72′**], when suspended in aqueous solution of KI or NaI at room temperature. Single-crystal X-ray studies reveal exchange of the occluded NO_3^- anion for I^-, with a change in the coordination environment of the central Cu(II) ion from six to four. Interestingly, the dark blue crystals changed to blue when immersed again into a saturated KNO_3 solution for 5 days. The blue complex [**72′**] reveals the regeneration of original framework with NO_3^- anion, demonstrating anion exchange and subsequent coordination expansion or shrinkage is a reversible process.

On the basis of a C_3 symmetric tripodal pyridine ligand, Tzeng and coworkers[91] reported novel SC–SC anion exchange reactions in a 3D Cd(II) framework [**73**]. Immersion of crystals of the chloride-containing framework[92] in a 0.01 m aqueous solution of $LiClO_4$ or NH_4PF_6 for 12 h leads to complete replacement of Cl^- by ClO_4^- or PF_6^-, respectively. The authors mainly described the structure of the ClO_4^- exchanged framework, which

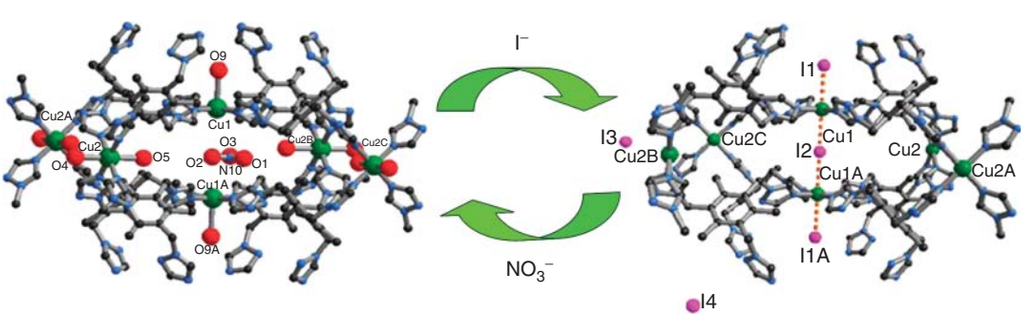


Figure 70 The reversible SC–SC structural transformation from **72** to **72′** in the crab-shaped hexa-copper unit. Hydrogen atoms and water molecules are omitted for clarity. Color code: Cu, green; I, purple; O, red; N, blue; C, black

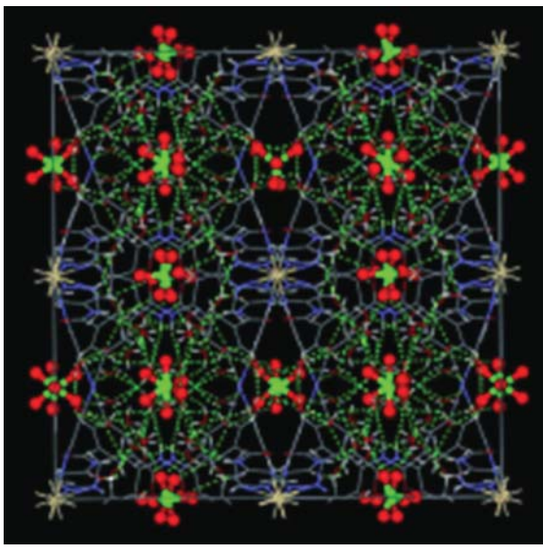


Figure 71 View of the extended network structure, containing ClO_4^- ions

maintains its structural integrity. Each Cd(II) ion is coordinated to six C_3 symmetric tripodal ligand, forming a 3D porous structure. Two such frameworks mutually interpenetrate to give a 3D porous structure with zigzag channels, filled with ClO_4^- anions and a large number of water molecules (Figure 71). The 3D pores contain exposed tripyridylamide moieties as functional units that are particularly attractive for guest uptake and/or ion exchange studies.

A novel 2D rectangular-grid shaped Co(II) coordination polymer [**74**], incorporating neutral rodlike ligand, 3,5-bis(4-imidazol-1-ylphenyl)-[1,2,4]triazol-4-ylamine (**L_7**), and its potential toward anion exchange in SC–SC manner is well-demonstrated by Bharadwaj and coworkers.[93] The authors judiciously incorporated an amino functionality at the center of the ligand with an aim that it might act as a donor in H-bonding interactions with the anion. Single-crystal X-ray analysis reveals the grid structure of the framework where the voids are occupied by BF_4^- anions and DMF guest molecules. The free amino groups in the framework wall are involved in H-bonding, as expected, with the fluorine atoms of the trapped BF_4^- anions. X-ray analysis of the crystals, dipped in aqueous $NaClO_4$ solution over a week, shows complete anion exchange with similar (4,4) net topology as the parent structure (Figure 72). In an identical manner, either NO_3^- or Cl^- can be introduced in the cavity in a SC–SC pathway. Bearing in mind that anion exchange is a size- and shape-based recognition process, the authors also probed the selectivity of the above anions over PF_6^-, BPh_4^-, or larger organic $C_6H_5COO^-$ anions for the given framework.

Three robust coordination polymers $\{[Ni_2(DBIBA)_3]\cdot Cl\cdot 18H_2O\}_n$ [**75**], $\{[Co_2(DBIBA)_3]\cdot Cl\cdot 9H_2O\}_n$ [**76**], and $\{[Mn_2(DBIBA)_3]\cdot Cl\cdot 3H_2O\}_n$ [**77**] (DBIBA = 5-*di*(1H-benzo[d]imidazol-1-yl)benzoate) afford a series of new coordination polymers, $\{[Ni_2(DBIBA)_3]\cdot(BF_4)\cdot 6H_2O\}_n$ (**75a**), $\{[Ni_2(DBIBA)_3]\cdot(ClO_4)\cdot 3H_2O\}_n$ (**75b**), $\{[Ni_2(DBIBA)_3]\cdot(NO_3)\cdot 3H_2O\}_n$ (**75c**), and $\{[Co_2(DBIBA)_3]\cdot(ClO_4)\cdot 3H_2O\}_n$ (**76a**), without losing crystallinity (R. A. Agarwal and P. K. Bharadwaj, unpublished work). Any of the daughter products can be reached from any of the parent frameworks.

2.7 Cation Exchange in MOF through Single-Crystal to Single-Crystal Transformation

While SC–SC exchange of free guest molecules, counterions, removal of solvent molecules, has been frequently experienced in MOFs and detailed in the foregoing sections, the modification or selective replacement of integral parts of the framework, especially the complete metal metathesis from the framework without altering the framework or pore structure is challenging. The first report of complete and reversible exchange of metal ions constituting $[Cd_4O]^{6+}$ SBU in a MOF was reported by Das *et al.*[94] The structure of the original compound [**78**] consists of six $[Cd_4O]^{6+}$ units as an octahedral basic building block (each Cd(II) exhibits distorted square antiprismatic geometry) and eight carboxylate ligand units at the vertices and faces, respectively. The overall cubic framework,

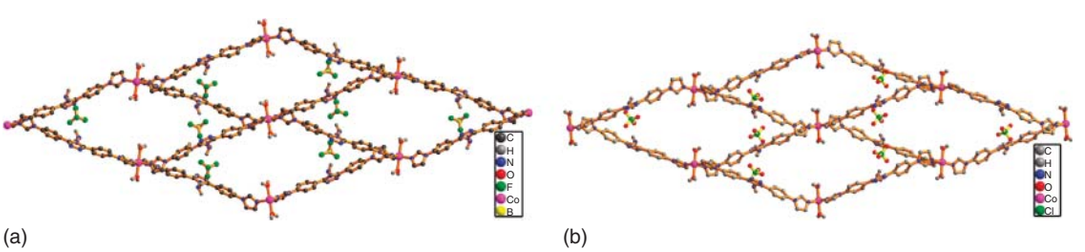


Figure 72 View of the trapped BF_4^- (a) and ClO_4^- (b) anions inside the 2D rectangular-grid structure. (Reprinted with permission from Ref. 93. Copyright (2010) American Chemical Society.)

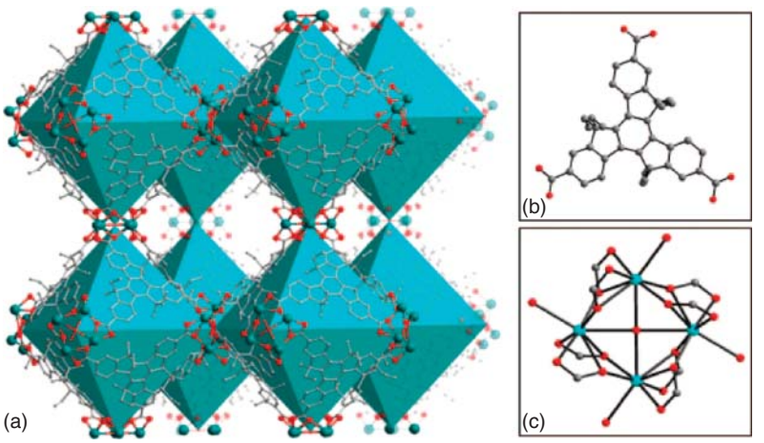


Figure 73 Parts of crystal structure of **78**, (a) a cube of eight octahedral cages sharing $\{Cd_4O\}$ vertices leaving a ~2 nm void space at the center, (b) molecular structure of ligand H_3hett, and (c) a square planar Cd_4O cluster behaving as a SBU. (Reprinted with permission from Ref. 94. Copyright (2009) American Chemical Society.)

comparable to that of sodalite, is generated by sharing the vertices of the octahedron (Figure 73). The exceptional stability and accessibility of the metal ions in the framework provides a platform to possible metal ion exchange. When the crystals of the Cd-framework [**78**] are immersed in aqueous $Pb(NO_3)_2$ solution for a week, complete metal ion replacement takes place. Single-crystal X-ray analysis showed that the Cd-framework changes to Pb-framework [**78′**] with retention of the structural integrity. The reverse process, that is, regeneration of the Cd-framework starting from the Pb-framework in a similar SC–SC manner takes a longer time.

Following the above protocol, Yao *et al.*[95] reported a series of isostructural and mesoporous MOFs (SUMOF-1) through central metal ion exchange in SC–SC transformations. With a view to prepare a

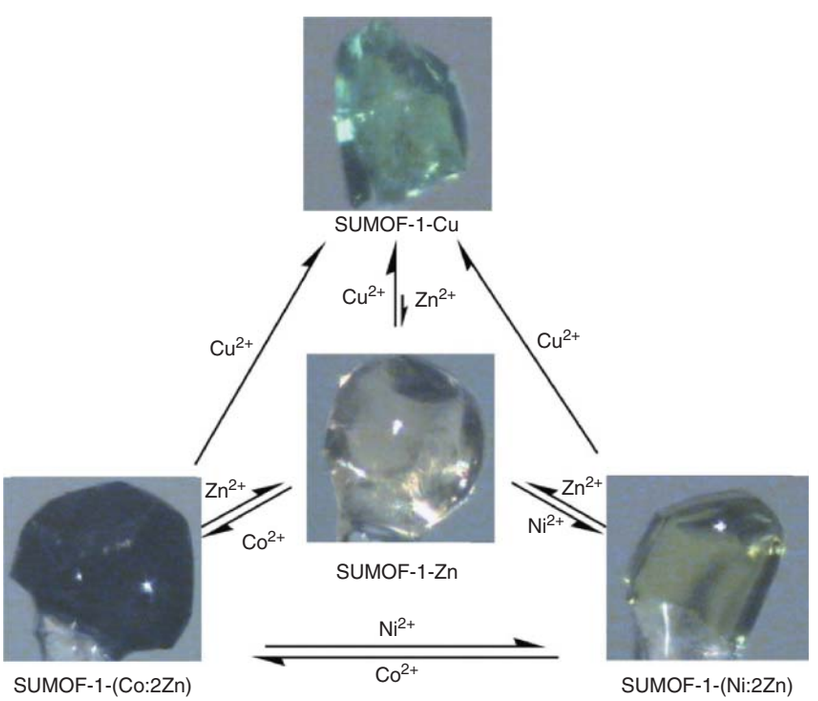
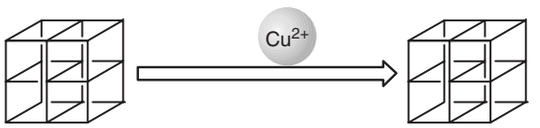


Figure 74 A scheme showing the exchange of framework metal ions at the paddle wheel clusters in **79** (**SUMOF-1**) via single-crystal to single-crystal transformation

noninterpenetrating analogue of MOF-14[96] with extra-large cavities, the authors cross-linked the $[Zn_2(COO)_4]$ paddle wheel clusters with BTB linker and a second 4,4′-bipyridyl linker. From single-crystal X-ray data, the structure of the original framework [**79**] reveals to contain extra-large dodecahedral cavities with (3,4)-connected Pt_3O_4 topology, where the secondary 4,4′-bipyridine linkers suppress the interpenetration. In a postsynthesis approach, the original crystal is immersed in a DMF solution of $Cu(NO_3)_2{\cdot}3H_2O$ (0.04 M) for 3 days, whereupon crystal color changes from faint yellow to cyan (Figure 74), producing copper analogue of **79**. Single-crystal X-ray diffraction analysis clearly reveals that the framework backbone is unaltered but metal ions changed from Zn(II) to Cu(II). The exchange of the framework Zn^{2+} ions in **79** with other 3d transition metal ions are also probed, which leads to partially exchanged Co(II) and Ni(II) framework in SC–SC transformations. The authors deduced the relative stabilities of metal–carboxylate paddle wheel clusters within these frameworks in the order, Co ≈ Ni < Zn < Cu, which is consistent with the Irving–Williams series.[97]

Partial central metal ion exchange in porous MOF, leading to heterobimetallic framework through SC–SC transformation, is reported by Mi *et al.*[98] The authors noticed that the coordinated metal ion exchange is mainly dominated by the coordination ability of metal ions to free functional groups, ionic radii of adsorbed metal ions, steric hindrance, and the solution concentration of adsorbed metal salts (Scheme 14).

In flexible framework structures, SC–SC transformations involving the counterion or guest exchange and



Scheme 14 Single-crystal to single-crystal transformation. (Reproduced with permission from Ref. 98. Copyright 2007 American Chemical Society.)

their mechanisms have already been documented. However, report of the capture of central metal ions by soft MOFs is unknown. Only recently, Thallapally and coworkers[99] reported the cation-promoted renovation of flexible anionic MOFs into neutral heterobimetallic systems through SC–SC transformations. A flexible tetracarboxylic acid ligand, both due to its flexibility and its varying mode of coordination with transition metal ions, is chosen to react with Mn(II) to form stimuli-responsive flexible MOF [**80**]. This MOF displays highly selective uptake of divalent transition metal cations (e.g., Co^{2+} and Ni^{2+}) over alkali-metal cations (Li^+ and Na^+). Single crystals of the precursor MOF undergo a notable color change when immersed in a 0.2 M solution of $M(NO_3)_2$ (M = Co^{2+}, Ni^{2+}) in DMF. The crystal structures show significant differences compared to the precursor MOF, mainly based on ligand-to-metal connectivity, involving the cooperative breakage/formation of metal–carboxylate bonds (Figure 75).

With a quest to MOF-catalyzed heterogeneous asymmetric catalysis via postsynthetic modification of porous backbone with $Ti(OiPr)_4$, Wenbin Lin and coworkers[100] experienced a novel SC–SC cross-linking

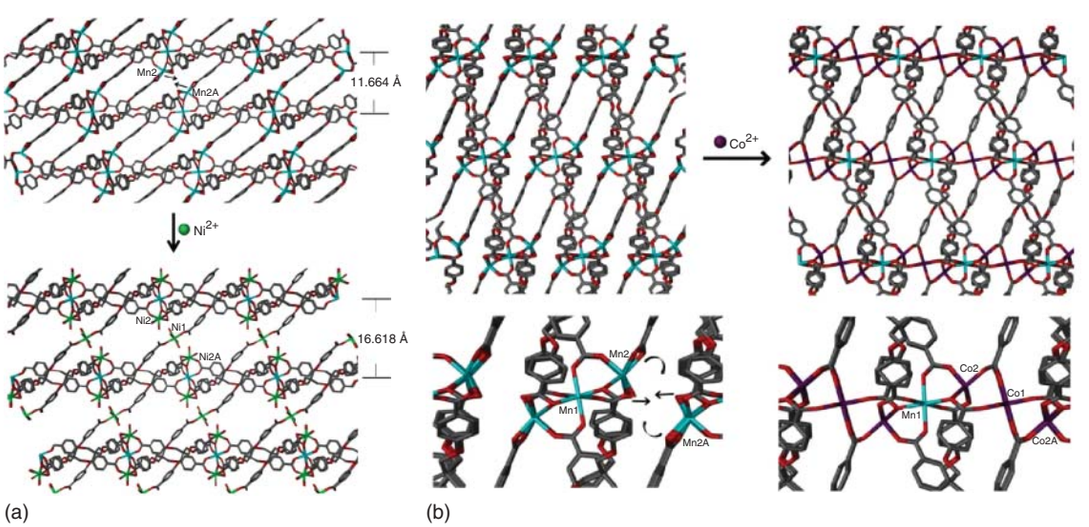


Figure 75 Crystallographic views of (a) **80a** and (b) **80b** along the *b*-axis (C, gray; O, red; Mn, cyan; Co, purple). The arrows propose how the carboxylate groups coordinated to two nearby terminal Mn(II) ions (Mn2 and Mn2A) of the Mn_3 SBUs in **80a** move cooperatively to connect the inserted Co(II) (shown as Co1 on the right-hand side). (Reprinted with permission from Ref. 99. Copyright (2012) American Chemical Society.)

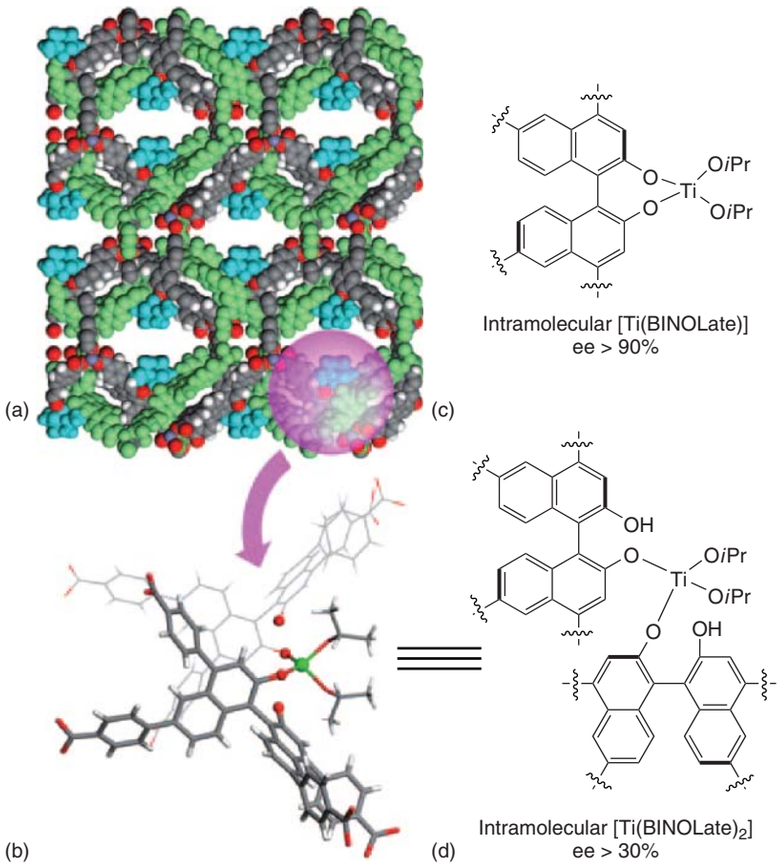


Figure 76 (a) Space-filling model of framework **81′**. $Ti(OiPr)_2$, blue; O, red; C, gray; H, white; all atoms of the other interpenetrating network are shown in green. (b) Stick-and-line model representation showing the X-ray structure of the intermolecular $[(OiPr)_2Ti(BINOLate)_2]$ species formed by cross-linking the two BINOL moieties in the two interpenetrating networks. Partially occupied Ti(OiPr)2 fragments for the Ti1/T1A parts are omitted for clarity. Zn, green; O, red; C, gray; H, white. (c) ChemDraw structure of the intramolecular $[(OiPr)_2Ti(BINOLate)]$ species. (d) ChemDraw structure of the intermolecular $[(OiPr)_2Ti\text{-}(BINOLate)_2]$ species

event in a chiral MOF [**81**]. The authors also study the influence of the modified framework toward enantioselectivity of diethylzinc addition reaction to aromatic aldehydes. The precursor MOF is twofold interpenetrated (Figure 76) and based on a chiral tetracarboxylate bridging ligand and di-zinc SBUs. Interestingly, it offers only very modest enantioselectivity using the $Ti(OiPr)_4$-treated framework. X-ray structure elucidation shows the formation of intermolecular $[Ti(BINOLate)_2]$ species by cross-linking two interpenetrating precursor networks. The authors argued that the intermolecular $[Ti(BINOLate)_2]$ species is less enantioselective in Et_2Zn addition reactions because of the smaller steric demand of the naphthyl rings on the Ti(IV) center.

Through appropriate design and modulation, via postsynthetic cation exchange in the backbone of porous MOF structures, gas storage properties can be improved. Schröder and coworkers[101] reported Li-doped MOF hosts in a SC–SC manner and showed the enhancement of the isosteric heat of adsorption of dihydrogen. The synthetic strategy is based on the formation of anionic 3D network structures with functionalized organic ligands (Figure 77), in which external input of cations of diverse sizes afford a tunable pore environment and provide opportunities for augmented gas separation/storage properties. The study also demonstrates that amine-based organic cations act as too bulky gates to block channels. However, smaller inorganic Li^+ cations can open up the channel and allow rapid gas uptake and release, with an increase in both capacity and heat of adsorption of H_2.

2.8 Selective Recognition and Catalysis through Single-Crystal to Single-Crystal Transformation

When a porous framework is able to expand and shrink its pores without losing crystallinity, the "shape-responsive filling of the pores" can be achieved. To this end, a flexible Gd(III)-based 3D coordination

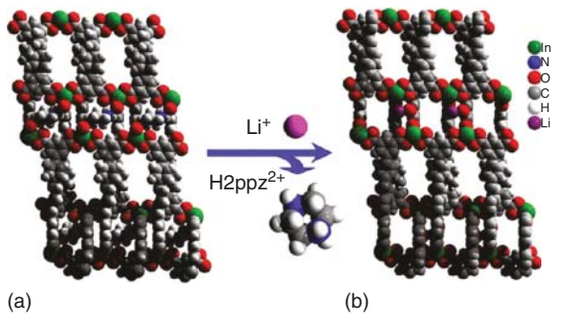


Figure 77 Space-filling views of the framework structures of (a) **82** (NOTT-206) and (b) **82′** (NOTT-207) containing different cations within channels. (Reprinted with permission from Ref. 101. Copyright (2011) American Chemical Society.)

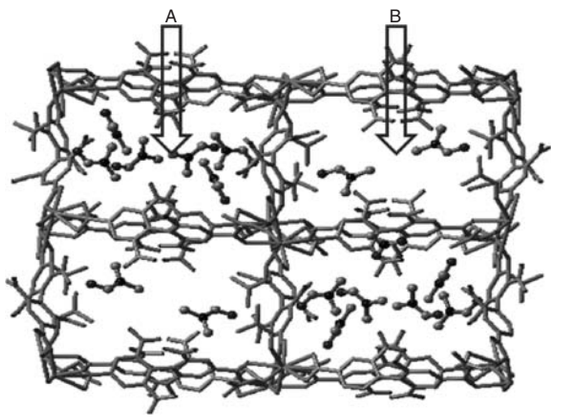


Figure 78 structure of the polymer showing two types of channels containing DMF molecules; hydrogen atoms and water molecules are omitted for clarity

polymer, $\{[Gd_2(\mathbf{L_8})_3(DMF)_4]\cdot 4DMF\cdot 3H_2O\}_n$ [**83**] ($\mathbf{L_8}$= 2,6,2′,6′-tetranitro-biphenyl-4,4′-dicarboxylic acid), has been synthesized[9] solvothermally. The framework possesses two different types of 1D channels (A and B) as a result of two different relative orientations of the phenyl rings in $\mathbf{L_8}$. While channel A is occupied by six water and six DMF molecules, channel B contains two DMF molecules (Figure 78). On exposure of benzaldehyde vapor to a crystal of **83** at RT for 5 days, $\{[Gd_2(\mathbf{L_8})_3(DMF)_4]\cdot 2PhCHO\cdot 4H_2O\}_n$ [**83′**] is formed in SC–SC manner. During the process, the coordination environment around Gd_2 dimeric unit and the overall framework remains unchanged. Interestingly, all lattice guest molecules in channel **A** are replaced by four benzaldehyde molecules, whereas all DMF molecules in channel **B** are replaced by eight water molecules. More importantly, the benzaldehyde guest molecules inside the pores are activated due to noncovalent interactions with the host framework. When a crystal of **83′** is exposed to trimethylsilyl cyanide and malononitrile vapor at RT, these activated benzaldehyde molecules readily undergo cyanosilylation and Knoevenagel condensation reactions, respectively, and the products are trapped inside the pores (Figure 79). The products occupying the cavity can be expunged on exposure to benzaldehyde vapors again in a SC–SC manner. Several other aromatic aldehydes behave similarly albeit at different rates and to different extents.

While metalloenzymes take advantage of their structural flexibility for their superb molecular recognition and catalytic capabilities,[102] a parallelism can be invoked in MOF chemistry where different guest molecules can read out the information encoded in the structure for highly selective recognition, accommodation, and catalysis, due to their "structural dynamism". Provided the entire process takes place in SC–SC manner, it can afford in situ mapping of chemical transformations via X-ray crystallography. A structurally dynamic framework also can allow characterization of unstable intermediates. Thus, reaction between an amine and an aldehyde inside a porous framework has been successful to identify the very short-lived hemi-aminal intermediate, crystallographically (4b). The porous complex, having two dissimilar voids (Pore A and pore B), was prepared by treating 2,4,6-tris(4-pyridyl)-1,3,5-triazine ligand ($\mathbf{L_9}$) and 1-aminotriphenylene

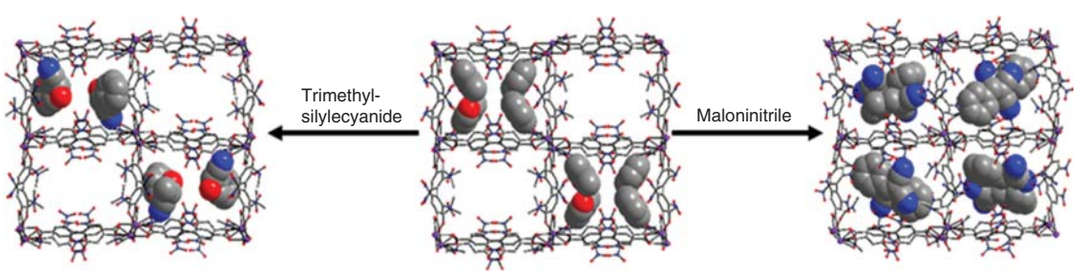


Figure 79 Single-crystal to single-crystal observation of the cyanosilylation (a) and Knoevenagel condensation reactions (b). The framework is shown as a ball-and-stick model; guest molecules are shown as CPK models; hydrogen atoms and water and malononitrile molecules are omitted for clarity

($\mathbf{L_{10}}$) with ZnI_2 in a nitrobenzene–methanol solution, and isolated as single crystals with the formula $\{[(ZnI_2)_3\text{-}(\mathbf{L_9})_2(\mathbf{L_{10}})]\cdot x(C_6H_5NO_2)\cdot y(CH_3OH)\}_n$ [**84**]. The aminotriphenylene guest molecules are trapped inside the network, where the amino groups are directed toward pore **A**. In presence of an aldehyde, the amine is transformed into the transient hemi-aminal intermediate, which is characterized through X-ray analysis. The same framework also catalyzes thermal isomerization of an olefin inside the pore, which is confirmed through SC–SC transformation.

3 OUTLOOK AND FUTURE PERSPECTIVES

Coordination polymers that retain crystallinity on exchange reactions represent a new class of materials and can be regarded as molecular vessels, where guest molecules can be introduced in tandem or at once to facilitate chemical reactivity. Such studies are of enormous importance in heterogeneous catalysis. Although the chemical industry represents a vital part of the economy in many industrialized and developing countries, manufacture of chemical products also leads to large quantities of environmentally harmful waste. The international communities have recognized the importance of cleaner syntheses for environmental protection. In this context, generation of large structures with voids, resembling zeolites for catalysis and adsorption of gas molecules has shown enormous possibilities. Guest or anion exchange, cation exchange, and substitution reactions at the metal center of MOFs, through SC–SC transformation, can be extremely useful in the separation of reactive intermediates, geometrical isomers, and promise to fabricate enhanced systems for gas adsorption or heterogeneous catalysis. Such systems can also be potentially attractive as sensors through change in the coordination environment around the metal centers, whose electronic as well as magnetic properties can be altered.

4 ACKNOWLEDGMENT

Partial support for this work was provided by the DST, New Delhi, to PKB. PKB also wishes to thank all his collaborators and coworkers whose names appear in the references.

5 RELATED ARTICLES

Photoreactive Metal-Organic Frameworks; Post-synthetic Modification of Metal-Organic Frameworks; Metal Uptake in Metal-Organic Frameworks.

6 ABBREVIATIONS AND ACRONYMS

ACN = acrylonitrile; AllylOH = allyl alcohol; AN = allylnitrile; BTC = benzenetricarboxylate; DEF = diethylformamide; DMF = dimethylformamide; DMA = dimethylacetamide; EG = ethylene glycol; HIBA = 4-(1H-imidazole-1-yl)benzoic acid; ICP-MS = inductively coupled plasma-mass spectrometric; KCF = kinetically controlled flexibility; MOF = metal-organic framework; PPF = porphyrin paddle wheel framework; PTE = positive thermal expansion; SBU = secondary building unit; SCXD = single-crystal X-ray diffraction; SC–SC = single-crystal to single-crystal; TCPSB = 1,3,5-tri(4′-carboxyphenylsulphonyl)benzene; TDC = thiophene-2,5-dicarboxylate; TEGly = triethylene glycol; TPT = 2,4,6-tris(4-pyridyl)triazine; 2D = two-dimensional; 3D = three-dimensional.

7 REFERENCES

1. J. Tranchemontagne, J. L. Mendoza-Cortés, M. O'Keeffe, and O. M. Yaghi, *Chem. Soc. Rev.*, 2009, **38**, 1257.
2. B. Moulton and M. Zaworotko, *Chem. Rev.*, 2001, **101**, 1629.
3. L. Ma, C. Abney, and W. Lin, *Chem. Soc. Rev.*, 2009, **38**, 1248.
4. J. Y. Lee, O. K. Farha, J. Roberts, K. A. Scheidt, S. T. Nguyen, and J. T. Hupp, *Chem. Soc. Rev.*, 2009, **38**, 1450.
5. M. D. Allendorf, C. A. Bauer, R. K. Bhakta, and R. J. T. Houk, *Chem. Soc. Rev.*, 2009, **38**, 1330.
6. S. Kitagawa and K. Uemura, *Chem. Soc. Rev.*, 2005, **34**, 109.
7. D. Bradshaw, J. B. Claridge, E. J. Cussen, T. J. Prior, and M. J. Rosseinsky, *Acc. Chem. Res.*, 2005, **38**, 273.
8. Y. Inokuma, S. Yoshioka, J. Ariyoshi, T. Arai, Y. Hitora, K. Takada, S. Matsunaga, K. Rissanen, and M. Fujita, *Nature*, 2013, **495**, 461.
9. R. K. Das, A. Aijaz, M. K. Sharma, P. Lama, and P. K. Bharadwaj, *Chem. Eur. J.*, 2012, **18**, 6866.
10. G. Xu, X. Zhang, P. Guo, C. Pan, H. Zhang, and C. Wang, *J. Am. Chem. Soc.*, 2010, **132**, 3656.
11. M. Maes, L. Alaerts, F. Vermoortele, R. Ameloot, S. Couck, V. Finsy, J. F. M. Denayer, and D. E. De Vos, *J. Am. Chem. Soc.*, 2010, **132**, 2284.
12. G. J. Halder and C. J. Keppert, *J. Am. Chem. Soc.*, 2005, **127**, 7891.
13. K. Hanson, N. Calin, D. Bugaris, M. Scancella, and S. C. Sevov, *J. Am. Chem. Soc.*, 2004, **126**, 10502.
14. M. P. Suh, Y. E. Cheon, and E. Y. Lee, *Chem. Eur. J.*, 2007, **13**, 4208.

15. Y. Ye, Y. Liu, Y. Zhao, X. Mu, P. Zhang, and Y. Wang, *CrystEngComm*, 2008, **10**, 598.
16. J. Demel, P. Kubát, F. Millange, J. Marrot, I. Císařová, and K. Lang, *Inorg. Chem.*, 2013, **52**, 2779.
17. S. K. Ghosh, W. Kaneko, D. Kiriya, M. Ohba, and S. Kitagawa, *Angew. Chem. Int. Ed.*, 2008, **47**, 8843.
18. H. Li, M. Eddaoudi, M. O'Keeffe, and O. M. Yaghi, *Nature*, 1999, **402**, 276.
19. S. Neogi, S. Sen, and P. K. Bharadwaj, *CrystEngComm*, 2013, **15**, 9239.
20. J. J. Vittal, *Cord. Chem. Rev.*, 2007, **251**, 1781.
21. C. J. Kepert and M. J. Rosseinsky, *Chem. Commun.*, 1999, 375.
22. G. J. Halder, C. J. Kepert, B. Moubaraki, K. S. Murray, and J. D. Cashion, *Science*, 2002, **298**, 1762.
23. K. Biradha, Y. Hongo, and M. Fujita, *Angew. Chem. Int. Ed.*, 2000, **39**, 3843.
24. A. Aijaz, E. Barea, and P. K. Bharadwaj, *Cryst. Growth Des.*, 2009, **9**, 4480.
25. Q.-K. Liu, J.-P. Ma, and Y.-B. Dong, *Chem. Commun.*, 2011, **47**, 12343.
26. Y.-Q. Lan, H.-L. Jiang, S.-L. Li, and Q. Xu, *Inorg. Chem.*, 2012, **51**, 7484.
27. M.-H. Zeng, Y.-X. Tan, Y.-P. He, Z. Yin, Q. Chen, and M. Kurmoo, *Inorg. Chem.*, 2013, **52**, 2353.
28. D. Liu, J.-P. Lang, and B. F. Abrahamas, *J. Am. Chem. Soc.*, 2013, **133**, 11042.
29. T. K. Kim, J. H. Lee, D. Moon, and H. R. Moon, *Inorg. Chem.*, 2013, **52**, 589.
30. Y. Zhang, B. Chen, F. R. Fronczek, and A. W. Maverick, *Inorg. Chem.*, 2008, **47**, 4433.
31. A. Aijaz, P. Lama, and P. K. Bharadwaj, *Eur. J. Inorg. Chem.*, 2010, **24**, 3829.
32. R. Yang, L. Li, Y. Xiong, J.-R. Li, H.-C. Zhou, and C.-Y. Su, *Chem. Asian J.*, 2010, **5**, 2358.
33. E. J. Kyprianidou, G. S. Papaefstathiou, M. J. Manos, and A. J. Tasiopoulos, *CrystEngComm*, 2012, **14**, 8368.
34. R. Medishetty, D. Jung, X. Song, D. Kim, S. S. Lee, M. S. Lah, and J. J. Vittal, *Inorg. Chem.*, 2013, **52**, 2951.
35. M. K. Sharma, P. Lama, and P. K. Bharadwaj, *Cryst. Growth Des.*, 2011, **11**, 1411.
36. F. Wang, Y.-X. Tan, H. Yang, Y. Kang, and J. Zhang, *Chem. Commun.*, 2012, **48**, 4842.
37. H.-N. Wang, X. Meng, C. Qin, X.-L. Wang, G.-S. Yang, and Z.-M. Su, *Dalton Trans.*, 2012, **41**, 1047.
38. M.-H. Zeng, X.-L. Feng, and X.-M. Chen, *Dalton Trans.*, 2004, 2217.
39. P. Lama, A. Aijaz, S. Neogi, L. J. Barbour, and P. K. Bharadwaj, *Cryst. Growth Des.*, 2010, **10**, 3410.
40. C.-H. Zhan, F. Wang, Y. Kang, and J. Zhang, *Inorg. Chem.*, 2012, **51**, 523.
41. M.-H. Zeng, Q.-X. Wang, Y.-X. Tan, S. Hu, H.-X. Zhao, L.-S. Long, and M. Kurmoo, *J. Am. Chem. Soc.*, 2010, **131**, 2561.
42. S. Mohapatra, H. Sato, R. Matsuda, S. Kitagawa, and T. K. Maji, *CrystEngComm*, 2012, **4**, 4153.
43. E. Y. Lee and M. P. Suh, *Angew. Chem. Int. Ed.*, 2004, **43**, 2798.
44. T. K. Maji, G. Mostafa, R. Matsuda, and S. Kitagawa, *J. Am. Chem. Soc.*, 2005, **127**, 17152.
45. R. Dey, R. Haldar, T. K. Maji, and D. Ghoshal, *Cryst. Growth Des.*, 2011, **11**, 3905.
46. D. N. Dybtsev, H. Chun, and K. Kim, *Angew. Chem. Int. Ed.*, 2004, **43**, 5033.
47. J.-P. Zhang, Y.-Y. Lin, W.-X. Zhang, and X.-M. Chen, *J. Am. Chem. Soc.*, 2005, **127**, 14162.
48. T. K. Maji, K. Uemura, H.-C. Chang, R. Matsuda, and S. Kitagawa, *Angew. Chem. Int. Ed.*, 2004, **43**, 3269.
49. M. P. Suh, J. W. Ko, and H. J. Choi, *J. Am. Chem. Soc.*, 2002, **124**, 10976.
50. H. J. Choi and M. P. Suh, *J. Am. Chem. Soc.*, 2004, **126**, 15844.
51. K. Biradha and M. Fujita, *Angew. Chem. Int. Ed.*, 2002, **41**, 3392.
52. M. P. Suh, H. R. Moon, E. Y. Lee, and S. Y. Jang, *J. Am. Chem. Soc.*, 2006, **128**, 4710.
53. C. R. Murdock, Z. Lu, and D. M. Jenkins, *Inorg. Chem.*, 2013, **52**, 2182.
54. R. Kitaura, K. Seki, G. Akiyama, and S. Kitagawa, *Angew. Chem. Int. Ed.*, 2003, **42**, 428.
55. K. Seki, *Phys.Chem. Chem. Phys.*, 2002, **4**, 1968.
56. T. K. Maji, R. Matsudaand, and S. Kiatagawa, *Nat. Mater.*, 2007, **6**, 142.
57. A. Husain, M. Ellwart, S. A. Bourne, L. Öhrström, and C. L. Oliver, *Cryst. Growth Des.*, 2013, **13**, 1526.
58. H.-L. Sun, D.-D. Yin, Q. Chen, and Z. Wang, *Inorg. Chem.*, 2013, **52**, 3582.
59. M. Gustafsson, J. Su, H. Yue, Q. Yao, and X. Zou, *Cryst. Growth Des.*, 2012, **12**, 3243.
60. F. Millange, C. Serre, N. Guillou, G. Férey, and R. I. Walton, *Angew. Chem., Int. Ed.*, 2008, **47**, 4100.
61. E. Neofotistou, C. D. Malliakas, and P. N. Trikalitis, *CrystEngComm*, 2010, **12**, 1034.
62. S. K. Ghosh, J.-P. Zhang, and S. Kitagawa, *Angew. Chem. Int. Ed.*, 2007, **46**, 7965.
63. M. C. Bernini, F. Gándara, M. Iglesias, N. Snejko, E. Gutiérrez-Puebla, E. V. Brusau, G. E. Narda, and M. Monge, *Chem. Eur. J.*, 2009, **15**, 4896.
64. J. Seo, R. Matsuda, H. Sakamoto, C. Bonneau, and S. Kitagawa, *J. Am. Chem. Soc.*, 2009, **131**, 12792.
65. M. K. Sharma and P. K. Bharadwaj, *Inorg. Chem.*, 2011, **50**, 1889.

66. R. Singh, M. Ahmed, and P. K. Bharadwaj, *Cryst. Growth. Des.*, 2012, **12**, 5025.
67. I.-H. Park, S. S. Lee, and J. J. Vittal, *Chem. Eur. J.*, 2013, **19**, 2695.
68. I. Grobler, V. J. Smith, P. M. Bhatt, S. A. Herbert, and L. J. Barbour, *J. Am. Chem. Soc.*, 2013, **135**, 6411.
69. S. Banfi, L. Carlucci, E. Caruso, G. Ciani, and D. Proserpio, *J. Chem. Soc. Dalton Trans.*, 2012, 2714.
70. K. Takaoka, M. Kawano, M. Tominaga, and M. Fujita, *Angew. Chem. Int. Ed.*, 2005, **44**, 2151.
71. D. Bradshaw, J. E. Warren, and M. J. Rosseinsky, *Science*, 2007, **315**, 977.
72. B. Manna, A. K. Chaudhari, B. Joarder, A. Karmakar, and S. K. Ghosh, *Angew. Chem. Int. Ed.*, 2013, **52**, 998.
73. P. K. Allan, B. Xiao, S. J. Teat, J. W. Knight, and R. E. Morris, *J. Am. Chem. Soc.*, 2010, **132**, 3605.
74. L. Wen, P. Cheng, and W. Lin, *Chem. Commun.*, 2012, **48**, 2846.
75. M. C. Das and P. K. Bharadwaj, *J. Am. Chem. Soc.*, 2009, **131**, 10942.
76. M. C. Das and P. K. Bharadwaj, *Chem. Eur. J.*, 2010, **16**, 5070.
77. K. Gedrich, I. Senkovska, I. A. Baburin, U. Mueller, O. Trapp, and S. Kaskel, *Inorg. Chem.*, 2010, **49**, 4440.
78. H. J. Park, Y. E. Cheon, and M. P. Suh, *Chem. Eur. J.*, 2010, **16**, 11662.
79. B. J. Burnett, P. M. Barron, C. Hu, and W. Choe, *J. Am. Chem. Soc.*, 2011, **133**, 9984.
80. M.-H. Zeng, S. Hu, Q. Chen, G. Xie, Q. Shuai, S.-L. Gao, and L.-Y. Tang, *Inorg. Chem.*, 2009, **48**, 7070.
81. X.-F. Wang, Y. Wang, Y.-B. Zhang, W. Xue, J.-P. Zhang, and X.-M. Chen, *Chem. Commun.*, 2012, **48**, 133.
82. Z. Chen, S. Xiang, D. Zhao, and B. Chen, *Cryst. Growth Des.*, 2009, **9**, 5293.
83. X.-P. Zhou, Z. Xu, M. Zeller, A. D. Hunter, S. S.-Y. Chui, and C.-M. Che, *Inorg. Chem.*, 2011, **50**, 7142.
84. D.-X. Xue, W.-X. Zhang, X.-M. Chen, and H.-Z. Wang, *Chem. Commun.*, 2008, **44**, 1551.
85. J. Seo, C. Bonneau, R. Matsuda, M. Takata, and S. Kitagawa, *J. Am. Chem. Soc.*, 2011, **133**, 9005.
86. S. R. Halper, L. Do, J. R. Stork, and S. M. Cohen, *J. Am. Chem. Soc.*, 2006, **128**, 15255.
87. M. Sarkar and K. Biradha, *Cryst. Growth Des*, 2007, **7**, 1318.
88. A. Michaelides and S. Skoulika, *Cryst. Growth Des*, 2009, **9**, 2039.
89. V. Kiritsis, A. Michaelides, S. Skoulika, S. Golhen, and L. Ouahab, *Inorg. Chem.*, 1998, **37**, 3407.
90. J. Fu, H. Li, Y. Mu, H. Hou, and Y. Fan, *Chem. Commun.*, 2011, **47**, 5271.
91. B.-C. Tzeng, T.-H. Chiu, B.-S. Chen, and G.-H. Lee, *Chem. Eur. J.*, 2008, **14**, 5237.
92. B.-C. Tzeng, B.-S. Chen, H.-T. Yeh, G.-H. Lee, and S.-M. Peng, *New J. Chem.*, 2006, **30**, 1087.
93. A. Aijaz, P. Lama, and P. K. Bharadwaj, *Inorg. Chem.*, 2010, **49**, 5883.
94. S. Das, H. Kim, and K. Kim, *J. Am. Chem. Soc.*, 2009, **131**, 3814.
95. Q. Yao, J. Sun, K. Li, J. Su, M. V. Peskov, and X. Zou, *Dalton Trans.*, 2012, **41**, 3953.
96. B. Chen, M. Eddaoudi, S. T. Hyde, M. O'Keeffe, and O. M. Yaghi, *Science*, 2001, **291**, 1021.
97. H. Irving and R. J. P. Williams, *J. Chem. Soc.*, 1953, 3192.
98. L. Mi, H. Hou, Z. Song, H. Han, H. Xu, Y. Fan, and S.-W. Ng, *Cryst. Growth Des*, 2007, **7**, 2553.
99. J. Tian, L. V. Saraf, B. Schwenzer, S. M. Taylor, E. K. Brechin, J. Liu, S. J. Dalgarno, and P. K. Thallapally, *J. Am. Chem. Soc.*, 2012, **134**, 9581.
100. L. Ma, C.-D. Wu, M. M. Wanderley, and W. Lin, *Angew. Chem. Int. Ed.*, 2010, **49**, 8244.
101. S. Yang, G. S. B. Martin, J. J. Titman, A. J. Blake, D. R. Allan, N. R. Champness, and M. Schröder, *Inorg. Chem.*, 2011, **50**, 9374.
102. R. Matsuda, R. Kitaura, S. Kitagawa, Y. Kubota, T. C. Kobayashi, S. Horike, and M. Takata, *J. Am. Chem. Soc.*, 2004, **126**, 14063.

Interpenetration and Entanglement in Coordination Polymers

Stuart R. Batten

Monash University, Melbourne, VIC, Australia and King Abdulaziz University, Jeddah, Saudi Arabia

1	Introduction	523
2	Interpenetration	523
3	Self-Penetration	532
4	Other Forms of Entanglement	533
5	Conclusions	536
6	Related Articles	536
7	References	536

1 INTRODUCTION

A crystal is an excellent example of the old adage *nature abhors a vacuum*. In forming a crystal, the constituent molecules will seek to maximize their packing efficiency by whatever means are at their disposal. For crystals composed of infinite networks that leave significant void space, this usually means that the spaces are filled (during crystal formation) with either guest molecules (including ordered or disordered solvent) and (if applicable) counterions or multiple networks that arrange themselves to occupy that space (and sometimes both options). In the case of 1D and 2D networks, the latter option can include interesting entanglements of networks such as polyrotaxanes and interdigitated structures, whereas for 3D nets (and also commonly for 1D and 2D nets), this involves interpenetration of networks.

Interpenetration occurs when two or more networks are entangled such that links would have to be broken in order to separate them. Conversely, if one could, in a purely theoretical, topological sense, "unpick" the entanglement of two or more nets without breaking any of the network bonds, then the nets are not interpenetrating. To give a discrete molecular analogy, the components of a rotaxane are not interpenetrating while those of a catenane are.

Interpenetration is nowadays widespread across the structural landscape of coordination polymers (sometimes also called metal-organic frameworks[1,2]), and the phenomenon has been reviewed extensively before.[3–10] In this chapter, we will look at a few selected examples to illustrate the different ways networks can interpenetrate, as well as other forms of entanglement related to interpenetration.

2 INTERPENETRATION

The use of network topologies is a very important tool in both describing and designing coordination polymers (and other solid-state structures, such as hydrogen bonding networks). But just as networks have a topology, so does the way networks interpenetrate. Thus, to truly understand an interpenetrating structure, it is important to also understand the *topology of interpenetration.*[11] For example, Figure 1 shows pairs of 2D sheets interpenetrating. The topologies of the sheets are the same in each case (i.e., (4,4)), but the way the sheets interpenetrate is topologically different in each of the four cases.

2.1 1D Interpenetration

Interpenetration is less common for 1D nets than it is for 2D or 3D nets, partly due to the fact that many 1D network topologies do not contain rings that can catenate and lead to interpenetration. Conversely, all 2D and 3D nets contain rings and thus interpenetration is more common.

Nonetheless, there are an increasing number of examples of 1D interpenetration, many (but not all) of

Metal-Organic Framework Materials. Edited by Leonard R. MacGillivray and Charles M. Lukehart.
© 2014 John Wiley & Sons, Ltd. ISBN 978-1-119-95289-3

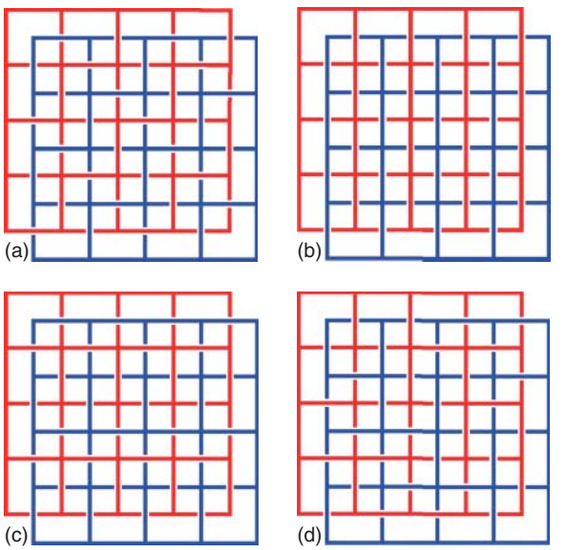


Figure 1 Four different interpenetration topologies for pairs of (4,4) sheets

which have ladderlike topologies. There are also a number of very distinct ways in which 1D (and 2D) nets can interpenetrate, and thus, a notation has been developed to succinctly describe the major features (but not all the features) of the interpenetration topology.[11] It takes the form:

$$\text{mD}/(\text{nD}) \rightarrow \text{pD parallel/inclined}$$

where mD represents the dimensions of the individual net (nD, etc., if there are different types of nets), pD indicates the dimension of the overall entanglement, and parallel or inclined refer to whether the nets are all parallel or are inclined to each other.

Figure 2 shows examples of each of the broad categories possible for 1D nets. For example, in Figure 2(a) is shown 1D→1D parallel interpenetration. This means that the structure contains 1D nets that interpenetrate with other 1D nets, the mean directions of propagation of all the linked nets are parallel (and in this case, likely coincident), and that this interpenetration results in an overall 1D motif.

By contrast, Figure 2(b) shows a situation where parallel 1D nets interpenetrate to give an overall 2D motif (1D→2D parallel interpenetration). This type of interpenetration is shown, for example, by the structures of $[Cu_2L_3(MeCN)_2]X_2 \cdot solv$, L = 1,4-bis(4-pyridyl)butadiene and $X = PF_6^-$, BF_4^-, which contain interpenetrating ladderlike polymers.[12,13] In cases such as this, where the overall dimensionality of the entanglement is larger than that of the individual nets (e.g., 1D nets giving a 2D entanglement), the nets can also be described as being *polycatenated*.[5]

Another example of 1D→2D parallel interpenetration is found in the structure of $[Cd(AlaNDI)(DMF)_2]$, where AlaNDI is a chiral amino-acid-functionalized naphthalenediimide.[14] In this structure, the topology is best described as a chain of loops, where each loop is composed of pairs of AlaNDI ligands bridging pairs of Cd dimers, and the dimers are shared between loops to generate the chain. Crucially, the large aromatic π surfaces of the AlaNDI ligands are separated by *ca.* 7 Å, meaning that there is a significant incentive for the loops to catenate and thereby generate a stack of four ligands in which the large π surfaces are parallel and separated by *ca.* 3.5 Å. The combination of the local incentive to form catenane motifs and the fact that the rings are part of polymeric nets leads to the formation of this unusual interpenetration motif (Figure 3).

This structure also illustrates a wider observation, which is that weaker interactions *between* networks can often be important in the formation of interpenetrating systems, and in determining the way the nets interpenetrate. These include, for coordination polymers, interactions such as hydrogen bonding and π stacking.

1D→3D parallel interpenetration is shown schematically in Figure 2(c). An example of this interpenetration is the structure of $[Cu_3(4,4'\text{-bipy})_3(H_2O)[PMo_{12}O_{40}(VO)_2]].5H_2O$, 4,4′-bipy = 4,4′-bipyridine.[15] In this structure, the individual nets have a 1D ladder topology, but with three legs to the ladder instead of two (a "double ladder"). The mean directions of propagation are all parallel (and hence it is parallel interpenetration), but the mean planes are inclined, which allows the interpenetration (Figure 4).

For inclined 1D nets, there are only two possibilities for the overall entanglement: 2D or 3D. 1D→2D inclined interpenetration (Figure 2d) occurs in a series of ladderlike coordination polymers of 1-(1-imidazolyl)-4-(imidazole-1-ylmethyl)benzene.[16,17] 1D→3D inclined interpenetration (Figure 2e) has also been observed for ladderlike coordination polymers, this time containing the 1,4-bis(4-pyridylmethyl)benzene ligand.[18,19] The structure of $[Co(bib)(hoip)].6H_2O$, bib = 1,4-bis(2-methylimidazol-1-yl)butane, H_2hoip = 5-hydroxy-isophthalic acid also shows 1D→3D inclined interpenetration, but in this case, the individual nets have a ribbonlike topology containing 3-membered rings, rather than a ladder motif.[20]

2.2 2D Interpenetration

Similarly to 1D nets, 2D nets can interpenetrate in either a parallel or inclined manner, leading to overall entanglements that are either 2D or 3D in nature. A classic example of 2D→2D parallel interpenetration is the structure of [Ag(tcm)], tcm = tricyanomethanide ($C(CN)_3^-$).[21–23] This structure contains pairs of interpenetrating (6,3) nets in which the mean planes of each

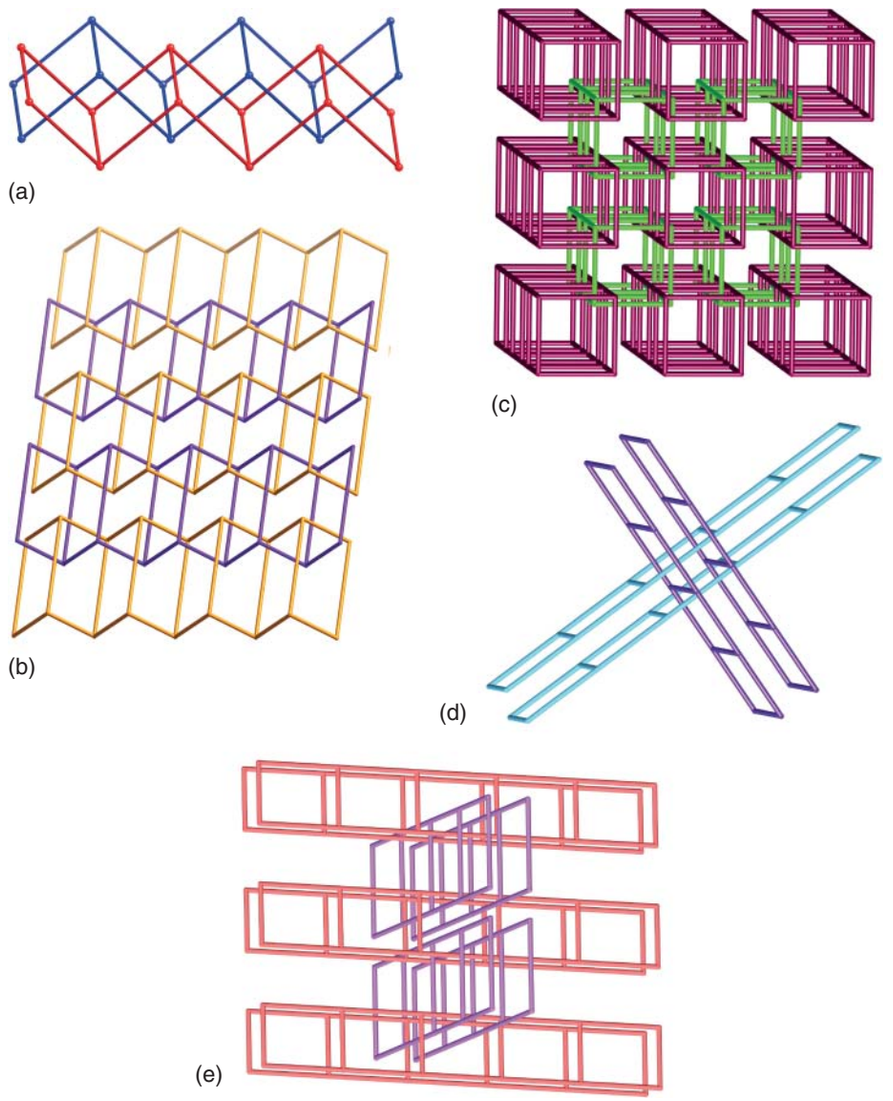


Figure 2 Different topologies of interpenetration for 1D networks: (a) 1D→1D parallel interpenetration; (b) 1D→2D parallel interpenetration; (c) 1D→3D parallel interpenetration; (d) 1D→2D inclined interpenetration; (e) 1D→3D inclined interpenetration

net are parallel (and in this case, coincident). The sheets are corrugated, with the peaks of the corrugation of one sheet lying above the troughs of the other, and the sheets crossing through each other midway between the peaks and the troughs (Figure 5). 2D→2D parallel interpenetration can, of course, occur for more than two nets at a time—the structure of one polymorph of [Ag(TEB)(CF_3SO_3)], TEB = 1,3,5-tris(4-ethynylbenzonitrile)benzene, for example, shows sixfold interpenetration of this type.[24]

2D→2D parallel interpenetration also occurs regularly for the other common type of 2D sheet, the (4,4) net. For example, the structure of [Cu(tcm)(4,4′-bipy)] contains (4,4) sheets showing twofold 2D→2D parallel interpenetration.[25] Again, corrugation of the sheets is important in allowing the interpenetration to occur, although in this case, the troughs of one net are somewhat offset relative to the peaks of the other net. The topology of interpenetration is the same as that shown in Figure 1(c); this figure also shows other possible interpenetration topologies for pairs of (4,4) sheets within this broad class of interpenetration.

More extreme corrugation of sheets can lead to 2D→3D parallel interpenetration. Again, in this mode, the mean planes of the interpenetrating sheets are all parallel, but now they are no longer coincident (as they often are for 2D entanglements). The structure of [Cu(dde)(bpe)].H_2O, dde = 4,4′-dicarboxydiphenyl ether, bpe = 1,2-bis(4-pyridyl)ethene typifies this interpenetration

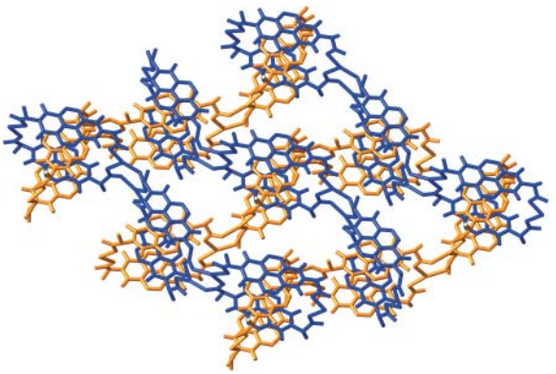


Figure 3 1D→2D inclined interpenetration induced by the formation of catenane interactions featuring four π-stacked naphthalenediimide ligands[14]

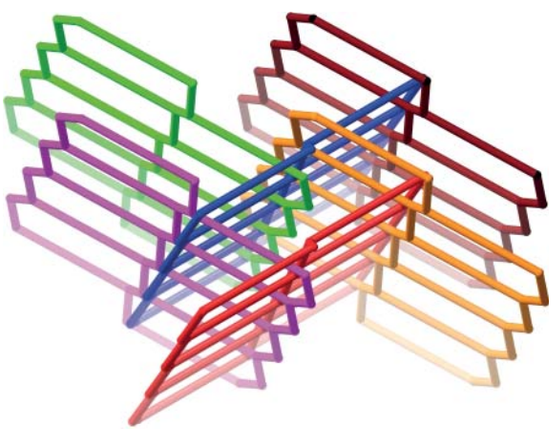


Figure 4 1D→3D parallel interpenetration of double ladders[15]

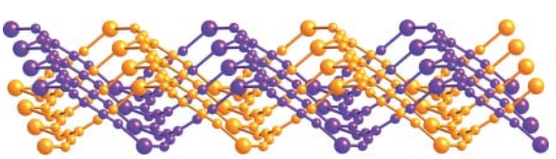


Figure 5 The 2D→2D parallel interpenetration in [Ag(tcm)][21–23]

mode.[26] The structure contains (4,4) sheets that are highly corrugated. Each sheet interpenetrates with a sheet above it, with its peaks entangled with troughs of the adjoining sheet, and another sheet below, with its troughs entangled with peaks of the adjoining sheet. All sheets are equivalent, leading to an overall 3D entanglement (Figure 6).

Another way of generating 3D entanglements from parallel 2D networks is with "thick" 2D networks—nets

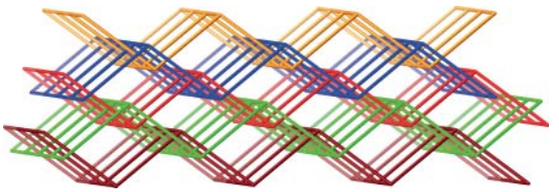


Figure 6 2D→3D parallel interpenetration of corrugated sheets[26]

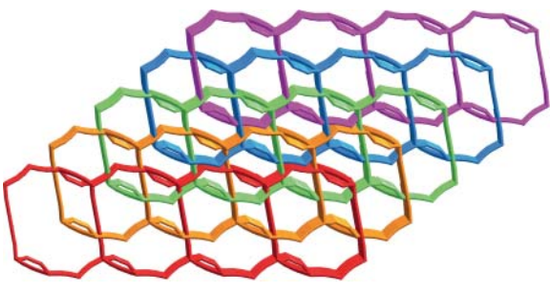


Figure 7 2D→3D parallel interpenetration of "thick" 2D bilayers[27]

with some depth in them, such as bilayers and similar nets. An example of this is the structure of $[Cu_4(dca)_4(4,4'\text{-bipy})_3(MeCN)_2]$, dca = dicyanamide ($N(CN)_2^-$).[27] The structure contains 2D nets composed of pairs of (6,3) sheets linked by 4,4′-bipy bridges to give bilayers. Each bilayer is equivalent and is penetrated by two bilayers above and two bilayers below, leading to an overall 3D entanglement (Figure 7). As for the previous example, the mean planes of the bilayers are parallel but offset.

A particularly fascinating way that parallel sheets can interpenetrate is through "Borromean" interpenetration.[28] The Borromean ring motif refers to three discrete rings entangled in such a way that removal of any one ring leads to the other two no longer being entangled (Figure 8a). Thus, no two rings are catenated, and they only become entangled and inseparable if all three are present. For polymeric networks, the same unusual type of entanglement can also exist. 2D (6,3) sheets showing threefold 2D→2D parallel interpenetration can be defined in the structure of $[Cu(tmeda)_2\{Ag(CN)_2\}_3]ClO_4$, tmeda = *N*,*N*,*N*′,*N*′-tetramethylethylenediamine.[29] Removal of any one of the three interpenetrating nets leads to the two remaining no longer being interpenetrated (Figure 8b). Borromean interpenetration can even occur for 3D entanglements—$[Ag_2L_3]X_2$, L = *N*,*N*′-bis(salicylidene)-1,4-diaminobutane, X = NO_3, ClO_4 shows 2D→3D parallel interpenetration (Figure 8c), but again no two nets are themselves entangled, and only the presence of a third leads to them being inseparable.[30]

The inclined interpenetration of 2D nets must always lead to 3D networks, and thus this can be referred

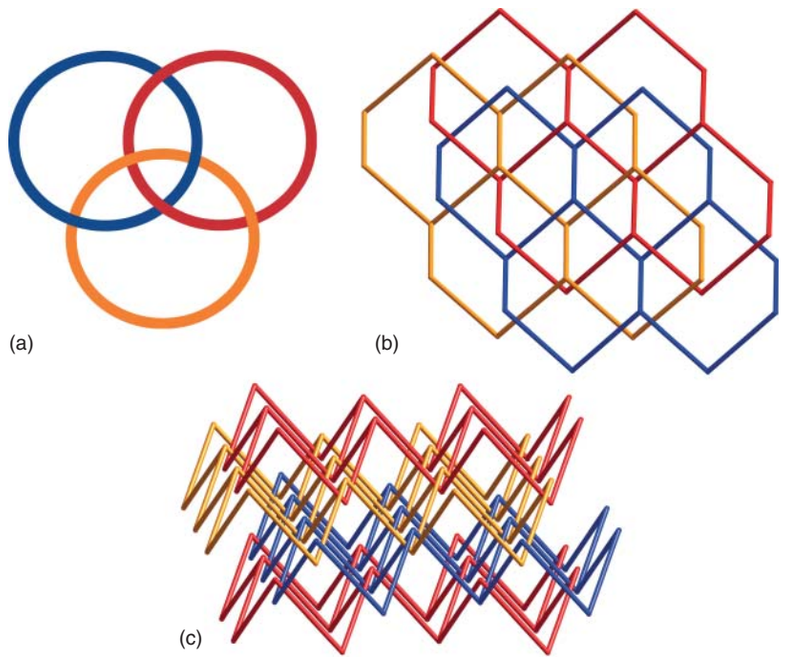


Figure 8 Borromean interpenetration of (a) rings; (b) 2D→2D parallel interpenetrating sheets[29]; (c) 2D→3D parallel interpenetrating sheets[30]

to as simply 2D inclined interpenetration. The structure of $[Co(dca)_2(4,4'\text{-bipy})] \cdot 0.5H_2O \cdot 0.5MeOH$ shows 2D inclined interpenetration of (4,4) sheets; each window of each sheet contains a rod from one other inclined sheet passing through it (Figure 9a).[31] As for parallel interpenetration, there are different interpenetration topologies possible for inclined interpenetration of (4,4) sheets. Thus, the structures of $[M(4,4'\text{-bipy})_2(H_2O)_2]SiF_6$, M = Cu, Zn, Cd, for example, contain inclined interpenetrating (4,4) sheets in which each window hosts a *node* of another inclined net (Figure 9b).[32] More complicated examples are also possible, such as structures with more than one inclined sheet passing through each window, or with sheets inclined at more than two directions relative to each other. A remarkable example of the latter is the structure of $[Co_2(azpy)_3(NO_3)_4] \cdot Me_2CO \cdot 3H_2O$, azpy = *trans*-4,4′-azobis(pyridine), which contains four different stacks of (6,3) sheets interpenetrating each other in an inclined manner (Figure 10).[33]

2.3 3D Interpenetration

Interpenetration is also common for 3D networks, although obviously the parallel/inclined distinction no longer applies. Nonetheless, there are different ways for nets to interpenetrate, even when the topologies of the nets themselves are the same.

One of the simplest examples of 3D interpenetration is the twofold interpenetration of diamond nets (Figure 11a) in the structures of $[M(CN)_2]$, M = Zn, Cd.[34–36] These nets interpenetrate such that the nodes of one net lie in the center of the adamantane cavities of the other, with links from this node penetrating each of the four windows of the adamantane cavity (Figure 11b). Every adamantane cavity is interpenetrated in the same way, and this interpenetration topology is the most common for interpenetrating diamond networks. Even $[Ag(ddn)_2]NO_3$, ddn = 1,12-dodecanedinitrile, which contains 10 interpenetrating networks, shows a similar relationship between the networks (Figure 11c).[37] One reason for this is that the diamond net is a rare example of a *self-dual* net,[38] and thus, this is the most logical way for diamond nets to interpenetrate.

Increasingly, however, structures are being found which have diamond nets that show different interpenetration topologies. One such example is the structure of β-[Cu(dca)(bpe)].[27] This compound contains five interpenetrating diamond nets, with all nets crystallographically equivalent. Although many of the interpenetrating adamantane cavities between pairs of these nets show the same relationship as those shown in Figure 11(b), others have different relationships, such as the one shown in Figure 11(d).

Other interpenetration topologies are also possible for diamond;[6] notably one such unusual interpenetration

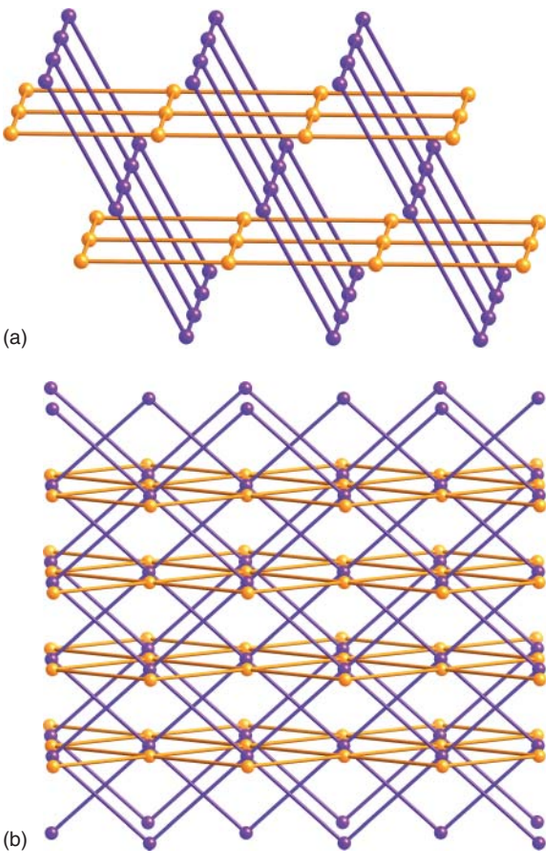


Figure 9 Two different 2D inclined interpenetration topologies for (4,4) sheets: (a) $[Co(dca)_2(4,4'\text{-bipy})].0.5H_2O.0.5MeOH$[31]; (b) $[M(4,4'\text{-bipy})_2(H_2O)_2]SiF_6$, M = Cu, Zn, Cd[32]

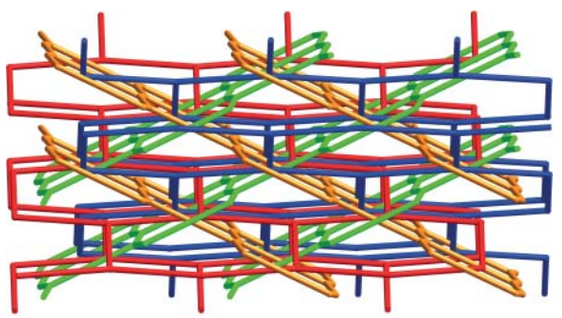


Figure 10 2D inclined interpenetration of four different stacks of sheets[33]

mode is shown by $[CdCu_2(pybz)_4]$, Hpybz = 4-(pyridine-4-yl)benzoic acid, which contains a record 25 interpenetrating networks.[39]

Another 3D net to show differing interpenetration topologies is the α-Po (or **pcu**) net. In, for example, the structures of α-$[M(dca)_2(pyrazine)]$, M = Mn, Fe, Co, Ni, Cu, Zn pairs of α-Po nets interpenetrate such that each boxlike cavity is catenated with eight cavities of the other net (Figure 12a).[40,41] Again, α-Po is a self-dual net, and this is the usual mode of interpenetration observed. In the structure of $[Mn(bpea)(H_2O)_4](ClO_4)_2(bpea)_4$, bpea = 1,4-bis(4-pyridyl)ethane, however, each cube is catenated with *10* others from the interpenetrating net (Figure 12b).[42]

The introduction of chirality into networks leads to another way that nets can interpenetrate in different ways. For example, the (10,3)-a net is inherently chiral, meaning that the interpenetrating nets may be of all the same handedness, of opposite handedness, or a combination of both (in equal or unequal numbers). Interpenetration of two (10,3)-a nets with either the same or the opposite handedness is shown in Figure 13. As examples, $[Ni_3(btc)_2(pyridine)_6(eg)_6].\sim 3eg.\sim 4H_2O$, btc = benzene-1,3,5-tricarboxylate, eg = ethylene glycol contains four interpenetrating nets of the same handedness,[43] $[Ag_2L_3](SbF_6)_2$, L = 2,3-dimethylpyrazine contains two nets of opposite handedness,[44] and $[Zn(tpt)_{2/3}(SiF_6)(H_2O)_2(MeOH)]$, tpt = 2,4,6-tri(4-pyridyl)-1,3,5-triazine contains eight interpenetrating nets, four of each handedness.[45] The most remarkable example of this topology is the structure of $[Ag_3(OH)(H_2O)_2(tipa)_{2.5}][Mo_2O_7].4.5H_2O$, tipa = tri(4-imidazolylphenyl)amine, which contains an incredible 54 interpenetrating nets, 27 of each hand.[46] This is the record for the highest degree of interpenetration in any structure reported to date.

An important aspect of interpenetration is that the geometric arrangement of the nets does not necessarily have to be symmetric with respect to the way one net fills the voids of the other. This can be important for porosity, with large open channels still remaining despite the presence of interpenetrating networks. This can even lead to variable porosity due to networks being able to move relative to each other. An early example of this asymmetric interpenetration is the structure of $[Cu(tcp)CuBF_4].17C_6H_5NO_2$, Cu(tcp) = 5,10,15,20-tetrakis(4-cyanophenyl)-21H,23H-porphine copper(II).[47] This structure contains two interpenetrating networks with PtS topology, but the second network is geometrically closely aligned with the first, rather than occupying the centers of the cavities and channels defined by the other net, leading to larger residual nonframework spaces than would otherwise be expected (Figure 14).

The asymmetric interpenetration in this porphyrin-based material is likely due to favorable interactions between the networks which, as mentioned before, can be important to both the formation of interpenetrating nets, and in the way those nets associate with each other. The structure of $[Cu_3(tpt)_4](ClO_4)_3\cdot solv$ is an excellent illustration of this.[48] The structure contains two interpenetrating 3,4-connected networks with boracite topology that interpenetrate in such a way that pairs of tpt ligands come in close contact and form π-stacked pairs between

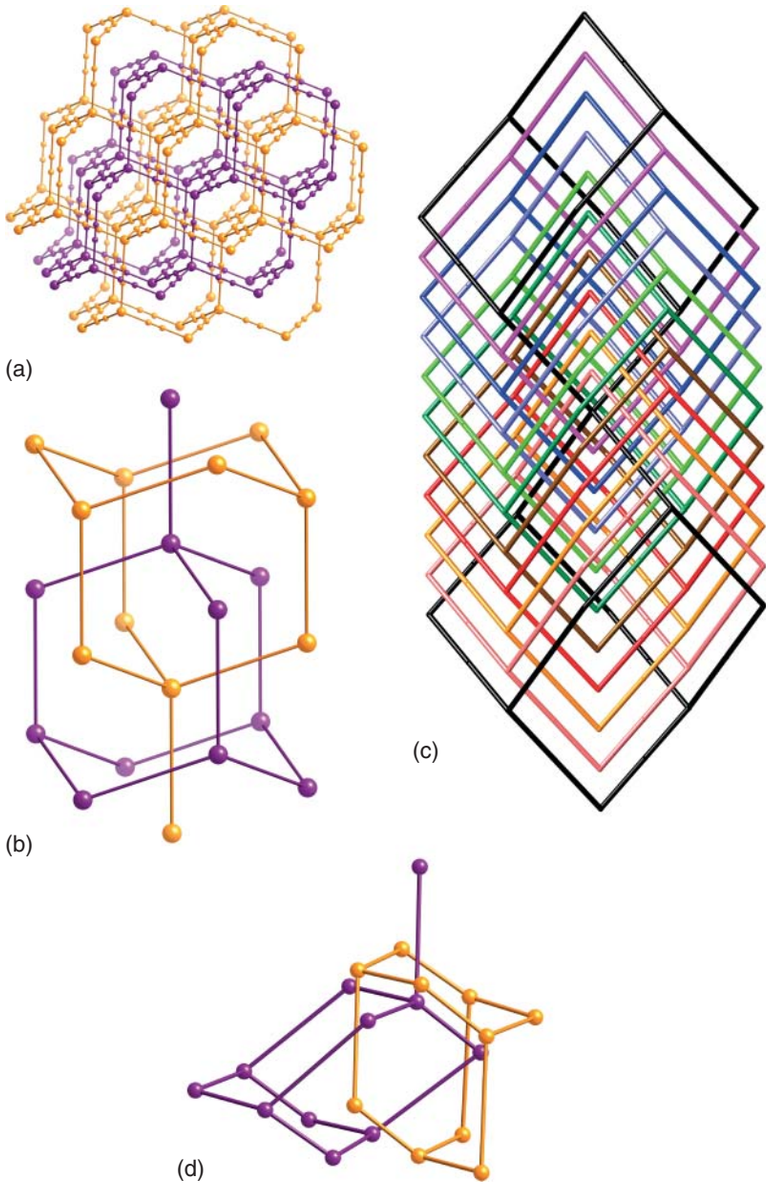


Figure 11 Interpenetration in diamond networks: (a) the two interpenetrating nets in $[M(CN)_2]$, M = Zn, Cd[34–36]; (b) the normal mode of interpenetration of two adamantane cavities; (c) interpenetration of ten diamond nets[37]; (d) unusual interpenetration topology of adamantane cavities in the structure of β-[Cu(dca)(bpe)][27]

the central triazine rings. The mean planes of the triazine rings are as close as 3.29(2) Å (Figure 15).

2.4 Heterointerpenetration

So far, we have considered only situations where the interpenetrating networks are all chemically and topologically identical, and they interpenetrate in only one way in a particular structure. Although this is easily the most common way for structures to interpenetrate, there are a number of illustrative examples where this is not the case.

The structure of $[AgL_2]SbF_6$, L = 3-cyanophenyl-4-cyanobenzoate is one case in point.[49] The 2D (4,4) nets in this structure are all identical but interpenetrate in two different ways. First, they doubly interpenetrate in a parallel manner to give discrete layers. These layers then interpenetrate in an inclined manner, to give overall 2D→2D parallel →3D inclined interpenetration.

Interpenetrating nets can also be chemically different but topologically the same. The structure of $K_2[PdSe_{10}]$ contains two interpenetrating diamond nets.[50] In one net,

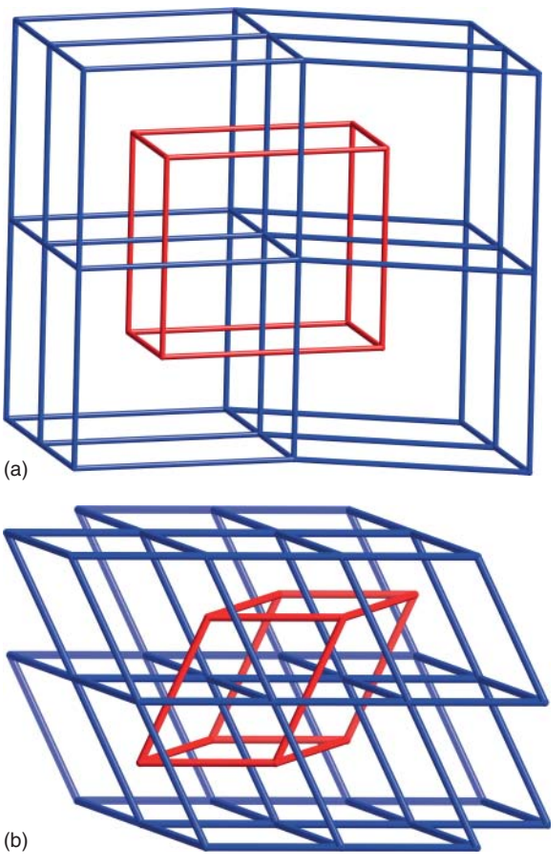


Figure 12 Interpenetration of α-Po networks: (a) the usual mode of interpenetration, where each cubic cavity is catenated with eight others[40,41]; (b) an unusual interpenetration topology where cubic cavities are catenated with *10* cavities of the other net[42]

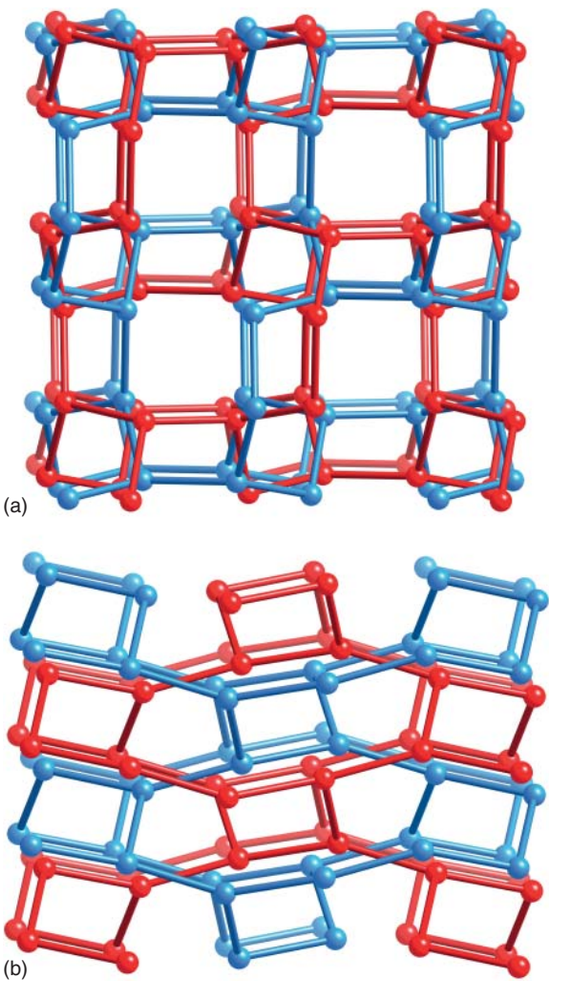


Figure 13 Interpenetration of chiral (10,3)-a nets that are (a) all the same hand and (b) of opposite hands

the Pd ions are connected by Se_4^{2-} anions, whereas in the other net, the bridging ligands are Se_6^{2-} anions (Figure 16). Despite the different numbers of selenium atoms in the two different ligands, the flexibility of the bridging chains leads to them both having the same bridging length between palladium atoms, as they necessarily have to be in order for the two nets to interpenetrate without colliding with each other.

Another example is the structure of $[Zn_7L_3(H_2O)_7][Zn_5L_3(H_2O)_5]$·solv, H_2L = *N*-phenyl-*N*′-phenylbicyclo[2,2,2]oct-7-ene-2,3,5,6-tetracarboxdiimide tetracarboxylic acid.[51] This compound contains two interpenetrating 3D nets, however the nets are not only chemically different (although topologically the same), but also one net acts as the cation (the Zn_7 net of the formula) whereas the other acts as the anion (the Zn_5 net). The cationic net contains $[Zn_2(CO_2)_3]^+$ triangular paddle wheel SBUs, whereas in the anionic net, the equivalent node is missing one of the zinc atoms, giving a $[Zn(CO_2)_3]^-$ motif.

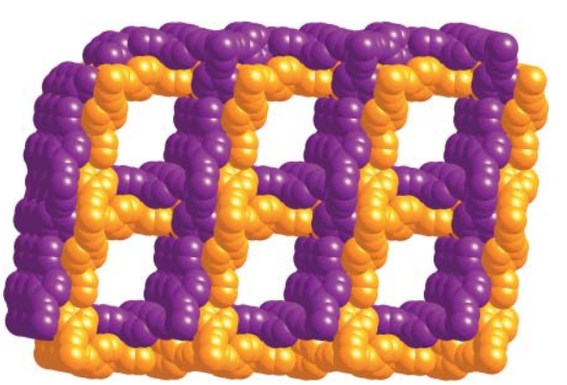


Figure 14 Asymmetric interpenetration of two PtS networks in the structure of $[Cu(tcp)CuBF_4].17C_6H_5NO_2$, Cu(tcp) = 5,10,15,20-tetrakis(4-cyanophenyl)-21H,23H-porphine copper(II)[47]

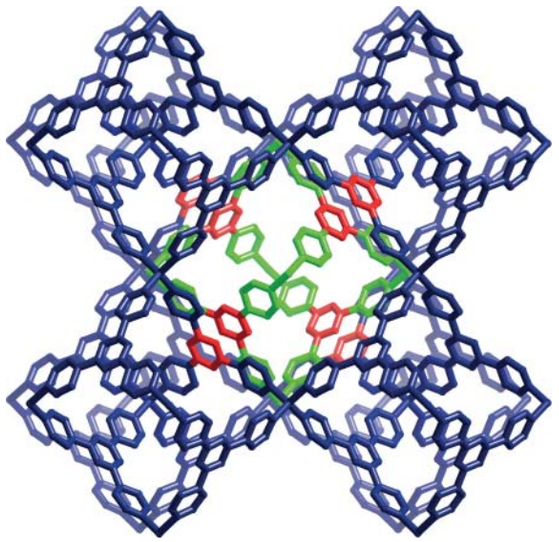


Figure 15 π-stacking interactions (highlighted in red) between two interpenetrating networks in $[Cu_3(tpt)_4](ClO_4)_3 \cdot solv$[48]

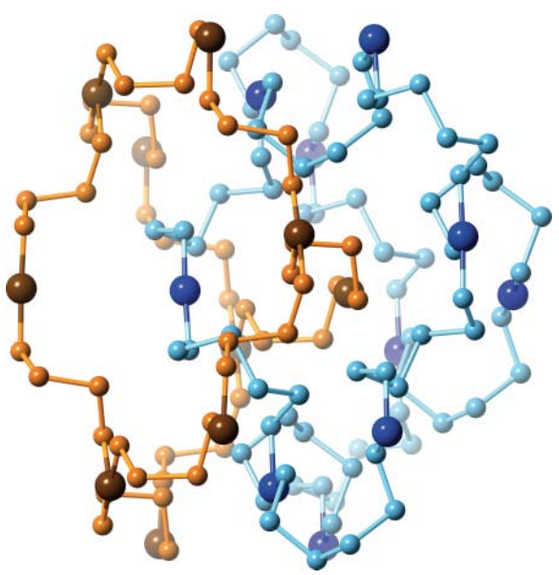


Figure 16 Interpenetration of $[Pd(Se_4)_2]^{2-}$ (orange) and $[Pd(Se_6)_2]^{2-}$ (blue) nets in the structure of $K_2[PdSe_{10}]$[50]

An even more interesting case of heterointerpenetration is the interpenetration of nets with different topologies. In $[Ni(azpy)_2(NO_3)_2]_2[Ni_2(azpy)_3(NO_3)_4].4CH_2Cl_2$, 2D (4,4) and (6,3) sheets interpenetrate at an inclined angle (2D/2D inclined interpenetration).[52] Each window of the (4,4) sheets has one (6,3) sheet passing through it, whereas each (6,3) window has two (4,4) nets passing through it.

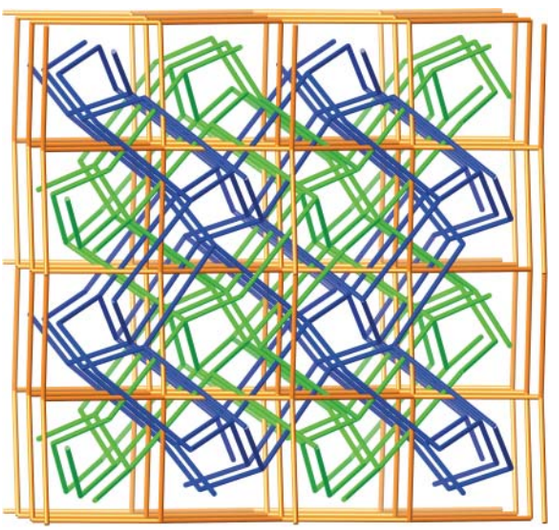


Figure 17 3D/3D interpenetration of one diamond net (orange) and two **mdf** (green, blue) networks[54]

Interpenetration of differing 3D nets is geometrically even harder to achieve. Three 3D nets, one with NbO topology and two with diamond topology, have been delineated in the structure of $Bi_3GaSb_2O_{11}$.[53] Similarly, three interpenetrating 3D nets are found in the structures of $[LnCuL_4][Ln_{0.25}Cu_{0.25}L]$, Ln = Dy, Er, HL = 4-(pyridine-4-yl)benzoic acid, although in this case, one net has diamond topology, and the other two have a new 8^6 **mdf** topology (Figure 17).[54]

The most extreme form of heterointerpenetration is when the interpenetrating nets are not only chemically and topologically different but also of different dimensions. 1D chains and 2D sheets interpenetrate in an inclined manner (1D/2D inclined interpenetration; Figure 18a), giving an overall 3D entanglement in the structure of $[Cu_5(bpp)_8(SO_4)_4(EtOH)(H_2O)_5](SO_4).EtOH.25.5H_2O$, bpp = 1,3-bis(4-pyridyl)propane.[55] $[Co(bix)_2(H_2O)_2](SO_4).7H_2O$, bix = 1,4-bis(imidazole-1-ylmethyl)benzene shows 1D/3D interpenetration (Figure 18b), with the 3D net having **cds** topology.[56] 2D/3D interpenetration of (4,4) sheets and two **cds** nets (Figure 18c) is observed in the structure of $[Co(mppe)_2(NCS)_2][Co(mppe)_2(NCS)_2]_2.5MeOH$, mppe = 1-methyl-1′-(4-pyridyl)-2-(4-pyrimidyl)ethylene.[57]

Finally, the structure of $(Me_2NH_2)_{1.75}[InL]_{1.75}(DMF)_{12}(H_2O)_{10}$, H_4L = biphenyl-3,3′,5,5′-tetra(phenyl-4-carboxylic acid) shows the peculiar property of *partial* interpenetration.[58] The structure is nominally composed of two interpenetrating diamond networks; however, whereas one net is fully occupied, the second net is not only equally disordered over two positions (which is unusual in itself), but the total occupancy of these two positions is only *ca.* 75%.

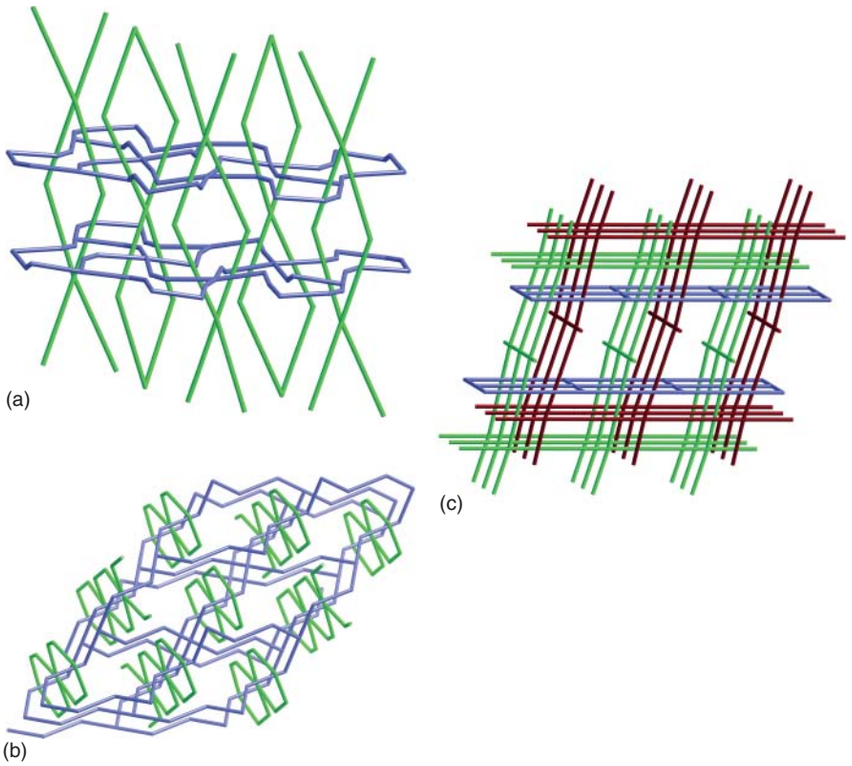


Figure 18 Interpenetration of nets of different dimensions: (a) 1D/2D inclined interpenetration[55]; (b) 1D/3D interpenetration[56]; (c) 2D/3D interpenetration[57]

3 SELF-PENETRATION

There is an obvious relationship between interpenetrating nets formed by polymeric systems and catenanes and rotaxanes formed by discrete molecular systems. But another form of molecular entanglement is the molecular knot, and the polymeric equivalent is a self-penetrating system. These are nets in which rings are catenated like they are in interpenetrating systems, but in this case the interlocked rings are in fact all part of a single network.[59] While this at first seems like a sufficient definition, in reality, catenated rings can be defined in most single networks provided that one makes the rings large enough. Thus, self-penetration is defined to occur only when the catenated rings are topological shortest circuits.

A reasonably simple way to derive a self-penetrating network is to cross-link 2D (4,4) sheets with bridges that lie significantly inclined to the normals of the sheets. The catenated shortest circuits then inevitably include two of the intersheet links in each circuit. For example, in the structure of $[Cd(CN)_2(pyrazine)]$, corrugation of the (4,4) sheets of $Cd(CN)_2$ leads to the bridging pyrazine ligands connecting the sheets at an angle to the normal.[60] This leads to a 6-connected net that has catenated 6-membered rings (Figure 19a) rather than the α-Po topology one might expect for planar (4,4) sheets connected by perpendicular bridges. A similar bridging of (4,4) sheets but with twice the number of intersheet connections leads to 8-connected nets that may also show self-penetration, such as the structure of $[Zn_5(OH)_2(bdc)_4(phen)_2]$, H_2bdc = 1,4-benzenedicarboxylic acid, phen = 1,10-phenanthroline (Figure 19b).[61] This structure can also be derived by cross-linking two interpenetrating α-Po nets; linking of interpenetrating nets into a single net is another effective way to derive a self-penetrating net.

Two other self-penetrating nets are also worthy of discussion here due to their fundamental topologies. The first is the (12,3) net found in the structure of $Ni(tpt)(NO_3)_2 \cdot solv$,[62] and shows catenation of the 12-membered rings as shown in Figure 20(a). The second is a self-penetrating (8,4) (or 8^6) net discovered in 2003 (Figure 20b);[63,64] a number of other self-penetrating nets with different 8^6 topologies have also been reported since.[65] Self-penetrating networks can even themselves interpenetrate—for example, two interpenetrating (12,3)

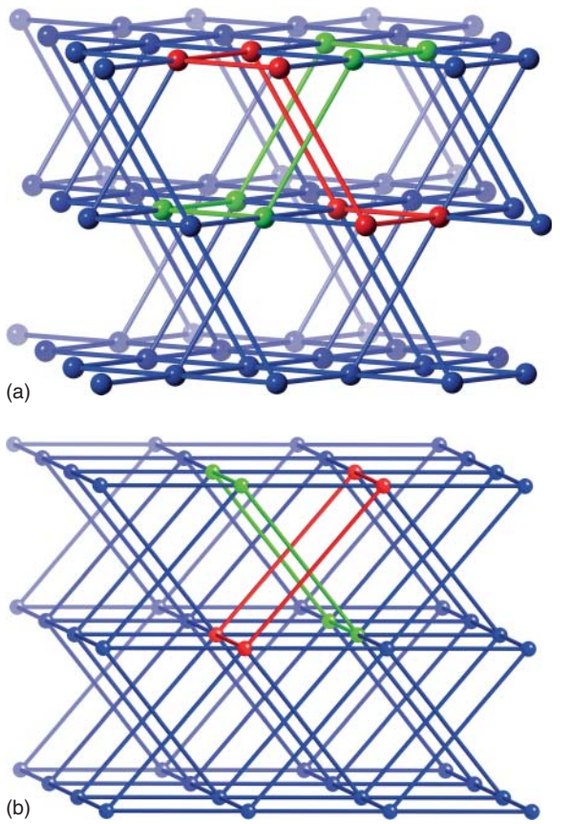


Figure 19 Self-penetrating nets based on cross-linked (4,4) sheets: (a) the 6-connected net of $[Cd(CN)_2(pyrazine)]$[60]; (b) the 8-connected net of $[Zn_5(OH)_2(bdc)_4(phen)_2]$, H_2bdc = 1,4-benzenedicarboxylic acid, phen = 1,10-phenanthroline.[61] Catenated rings are highlighted in red and green in each net

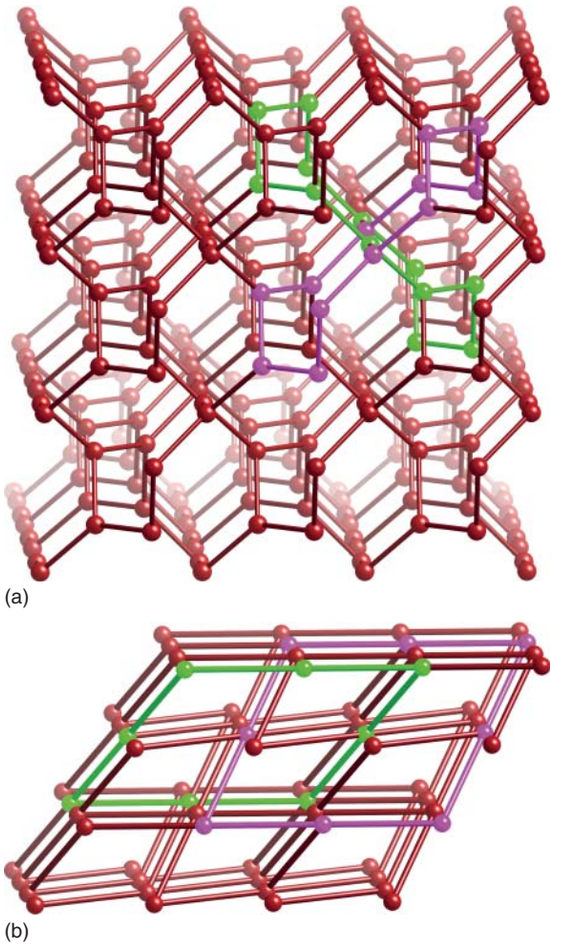


Figure 20 Self-penetrating nets: (a) (12,3) net of $Ni(tpt)(NO_3)_2 \cdot solv$[62]; (b) a self-penetrating (8,4) network.[63,64] Catenated rings are highlighted in green and pink in each net

nets are found in the structure of $[CoL(H_2O)_2]$, H_2L = 2,2′-bipyridine-4,4′-dicarboxylic acid.[66] The rich variety of self-penetrating structures now known has recently been extensively reviewed.[65]

4 OTHER FORMS OF ENTANGLEMENT

There are a number of other forms of entanglement besides interpenetration (and self-penetration), which have received considerable interest in recent times. One such class of materials is the *polyrotaxane* or *polythreaded* structures.[5,67] These entanglements show great variety, partly because there are a number of different types of entanglement which can fall under this banner.

One useful way to categorize these entanglements is to delineate whether all or only some of the components are polymeric. An additional selection rule might then be applied which separates trivial and nontrivial entanglements. A trivial entanglement is one in which the components can be separated without breaking of bonds, such as is the case for molecular rotaxanes and pseudorotaxanes (the differences between the two are not topological but rather are chemical/geometric—i.e., topologically it does not matter whether dethreading of the axle is energetically favorable or not, just that it is possible without breaking links). Nontrivial entanglements are ones in which links must be broken, such as in catenanes or interpenetrating networks.

There have been a considerable number of polyrotaxanes reported in which the rotaxane motifs combine polymeric and discrete components.[68–70] The most common of these involve preformed molecular rotaxanes acting as ligands, with the axle component containing coordinating groups at either end. Reaction of these rotaxane-based ligands with metals then gives polymeric structures. An example of a 1D polymer constructed in

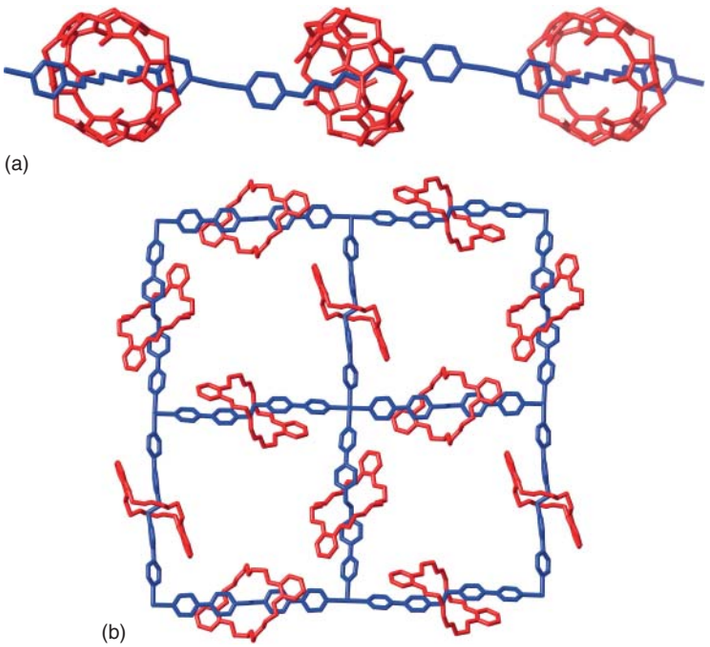


Figure 21 Polyrotaxanes with rotaxane-based ligands: (a) a trivial entanglement[71]; (b) a nontrivial entanglement[72]

this way is shown in Figure 21(a). Silver atoms are linked by long bipyridyl bridging ligands, with the ligands also threading cucurbituril wheels.[71] Topologically, this entanglement is trivial—the wheels could, in theory, be slid off the end of the polymeric axle, just as they could be in a molecular rotaxane.

An example of a nontrivial polyrotaxane formed using a similar synthetic approach is shown in Figure 21(b). In this case, rotaxane ligands bridge cadmium ions into 2D (4,4) sheets,[72] and the wheels (in this case dibenzo-24-crown-8) can no longer be separated from the polymeric network. Indeed, while the previous example contained only rotaxane motifs, in this nontrivial example one can also define catenane-type interactions between the wheels and M_4L_4 rings formed by the coordination polymer.

Similar approaches to using already entangled bridging ligands have also led to a number of other very interesting entanglements. One example is a coordination polymer in which the rotaxane bridging ligand connects the metals via the wheel component instead of the axle, leading to a trivial entanglement where the axles could, in theory, dethread from the wheels (which are now part of the polymeric net).[73] In the same paper, the authors then went a step further by designing a rotaxane-based ligand in which *both* the wheel and the axle act as bridging ligands. This leads to pairs of polymeric nets that interpenetrate via the rotaxane motifs, and even more remarkably, these nets are then interpenetrated by another identical pair of nets. Finally, [2]catenane-based ligands have been used to construct 2D (4,4) sheets; the catenanes bridge through peripheral coordinating groups attached to one of the two rings, whereas the other ring hangs pendant to, but catenated with, the network.[74]

One final notable structure worth mentioning is that of $[Cu^{II}L_2(H_2O)_2][Cu^{I}{}_2L_2]PMO_{12}O_{40}$, L = 4,4′-bis(1,2,4-triazol-1-ylmethyl)biphenyl.[75] This structure contains two interpenetrating diamond networks containing Cu^{II} ions, discrete square rings containing Cu^{I} ions, and large Keggin anions. Remarkably, [3]rotaxane motifs are formed in which each Cu^{I} ring is threaded by a rod from each of the two diamond networks.

The formation of rotaxane motifs between only polymeric networks can, for trivial entanglements, be as simple as the threading of linear or zigzag 1D networks through the windows of 2D or 3D networks (or even other 1D nets, provided they contain windows (e.g., ladders)). Some of the more interesting motifs involve the formation of trivial polyrotaxanes from 1D networks containing both rings and rods, such as the entanglement of 1D chains to give the overall 2D entanglement shown in Figure 22.[76]

With nontrivial entanglements of polymeric networks (which can also be classed as interpenetration), the defining of a polyrotaxane can be more complicated. Any interpenetrating structure contains rotaxanelike motifs—rods going through rings—and thus, the danger is that the term polyrotaxane can become meaningless if applied too liberally. Nonetheless, there are structures where clear rotaxanelike interactions seem to be present,

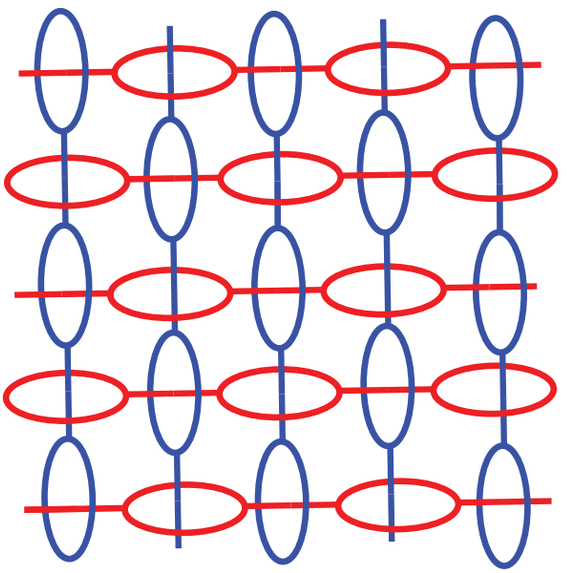


Figure 22 Schematic representation of a 1D→2D trivial polyrotaxane[76]

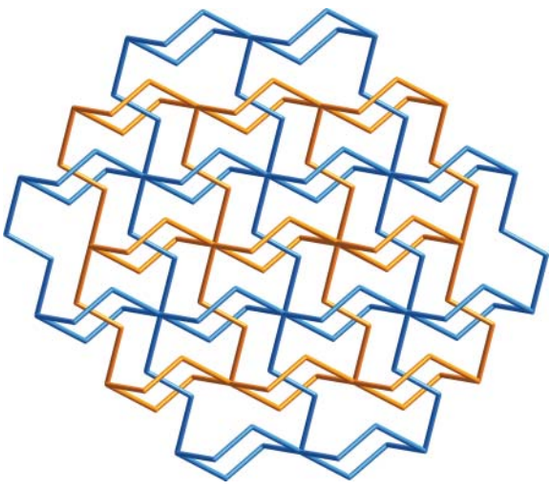


Figure 23 A 2D→2D parallel interpenetration motif that can also be classed as a nontrivial polyrotaxane[77]

and classification of structures as having polyrotaxane features seems reasonable.

A significant feature of these latter entanglements, however, is that the rotaxane motifs involve topological 2-membered rings acting as the wheels of the rotaxane. This is particularly noteworthy as the normal topological analysis of a network reduces the 2-membered rings to single links between nodes. But because the entanglement involves these 2-membered rings, their elimination results in network descriptions that can no longer accommodate a description of the interpenetration. Thus, it has been proposed that a nontrivial polyrotaxane is "any system with at least one polymeric component where the components cannot be separated without the breaking of links, and where the entanglement is such that 2-membered rings of one component are penetrated by rods of another."[67] This therefore provides a useful delineation between interpenetrating systems that can also be described as polyrotaxanes, and those that cannot.

An example of this in practice can be found in the structure of $[Mn(p\text{-XBP4})_3](ClO_4)_2$, *p*-XBP4 = *N*,*N*′-*p*-phenylenedimethylenebis(pyridine-4-one).[77] This structure contains 2D sheets showing 2D→2D parallel interpenetration (Figure 23). Within each sheet, the metal ions are bridged by single ligands in one direction and by pairs of ligands in the other direction. The connections between metals that involve pairs of ligands form a loop motif, and the nets interpenetrate such that the single ligand bridges of one net pass through the double ligand loops of the other net, and vice versa. Notably, if each net is considered in isolation, the net would be described topologically as a 4-connected (4,4) sheet, with the double ligand loops reduced to a single link between the metal nodes. This simplification, however, means that the interpenetration topology then cannot be accurately represented, and thus, a better description of the net would be as a 6-connected network containing 2-membered rings. As a result, this structure can be described as also being a polyrotaxane.

There are a number of other forms of entanglement that, while topologically trivial, are of significant interest. The first of these is the *weave* motif. These are structures that contain 1D chains that are woven together like the warp and woof threads in a cloth. An example of this can be found in the structure of HgI_2L, L = 2,6-bis(4-pyridinylmethyl)-benzo[1,2-*c*:4,5-*c*′]dipyrrole-1,3,5,7(2*H*,6*H*)-tetrone.[78] This contains zigzag chains that run in two different directions and interweave as shown in Figure 24. Even more remarkable is the structure [Zn(phen)L], phen = 1,10-phenanthroline, H_2L = *trans*-stilbene-4,4′-dicarboxylic acid.[79] This contains sheets of interwoven zigzag chains like the previous structure, but the layers of chains then interpenetrate each other in an inclined manner, leading to a structure containing entangled chains that run in four different directions.

The second unusual way to entangle 1D chains is in the form of molecular *braids*.[80] In a molecular braid, three or more chains are entangled to form a 1D ribbon motif. Notably, a three-stranded braid differs (for example) from a triple helix in that removal of any one strand of the braid results in the other two strands no longer being entangled (analogous to the removal of one ring or net from a Borromean entanglement). By contrast, removal of one strand from a triple helix still leaves the remaining two strands wrapped around each other in a double helix.

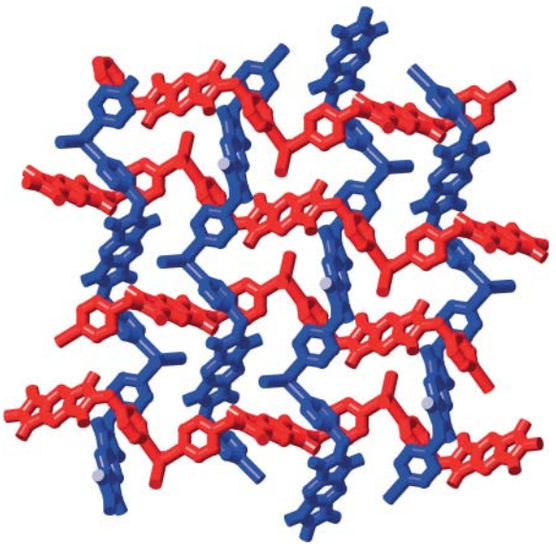


Figure 24 1D chains showing a weave-type entanglement[78]

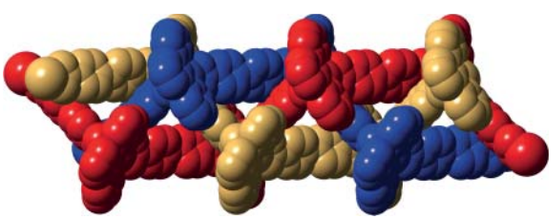


Figure 25 A triple-stranded braid[81]

Braids with up to six strands have been reported;[80] a typical triple-stranded braid is shown in Figure 25.[81]

Finally, it is also possible to generate polymeric entanglements of discrete (0D) components. The structure of $[(ZnCl_2)_{12}(pytpy)_8]\cdot x CHCl_3$, pytpy = 2,4,6-tris(4-pyridyl)pyridine contains discrete cage compounds that catenate to give 1D strands (0D→1D entanglement).[82] Each cage is catenated with two others, on opposite sides. In $\{[Ag_2(trz)_2][Ag_{24}(trz)_{18}]\}[PW_{12}O_{40}]_2$, trz = 1,2,4-triazole, the entanglement is even more complicated.[83] Each $[Ag_{24}(trz)_{18}]^{6+}$ cage is catenated with six others and acts as a 6-connecting node of a 3D α-Po network of interlocked cages. These networks then display twofold interpenetration!

5 CONCLUSIONS

A true understanding of network structures requires analysis of not only network topology but also interpenetration topology. It is clear from the small selection of examples here that there are numerous ways in which polymeric structures can entangle, and the challenge for chemists now is to not only understand this but also to control or direct the entanglement in a designed manner. This is not just an academic exercise; the network entanglement can have a significant effect on the properties of the resultant material, including porosity, framework stability, and magnetic, electronic, and optical properties.

6 RELATED ARTICLES

Polyrotaxane Metal-Organic Frameworks; Nanoscale Metal-Organic Frameworks; Porphyrinic Metal-Organic Frameworks

7 REFERENCES

1. S. R. Batten, N. R. Champness, X.-M. Chen, J. Garcia-Martinez, S. Kitagawa, L. Öhrström, M. O'Keeffe, M. P. Suh, and J. Reedijk, *CrystEngComm*, 2012, **14**, 3001.
2. S. R. Batten, N. R. Champness, X.-M. Chen, J. Garcia-Martinez, S. Kitagawa, L. Öhrström, M. O'Keeffe, M. P. Suh, and J. Reedijk, *Pure Appl. Chem.*, 2013, **85**, 1715.
3. S. R. Batten and R. Robson, *Angew. Chem., Int. Ed. Engl.*, 1998, **37**, 1460.
4. S. R. Batten, S. M. Neville, and D. R. Turner, 'Coordination Polymers: Design, Analysis and Application', Royal Society of Chemistry, Cambridge, 2009.
5. L. Carlucci, G. Ciani, and D. M. Proserpio, *Coord. Chem. Rev.*, 2003, **246**, 247.
6. V. A. Blatov, L. Carlucci, G. Ciani, and D. M. Proserpio, *CrystEngComm*, 2004, **6**, 377.
7. I. A. Baburin, V. A. Blatov, L. Carlucci, G. Ciani, and D. M. Proserpio, *J. Solid State Chem.*, 2005, **178**, 2452.
8. I. A. Baburin, V. A. Blatov, L. Carlucci, G. Ciani, and D. M. Prosperio, *CrystEngComm*, 2008, **10**, 1822.
9. I. A. Baburin, V. A. Blatov, L. Carlucci, G. Ciani, and D. M. Prosperio, *Cryst. Growth Des.*, 2008, **8**, 519.
10. H.-L. Jiang, T. A. Makal, and H.-C. Zhou, *Coord. Chem. Rev.*, 2013, **257**, 2232.
11. S. R. Batten, *CrystEngComm*, 2001, **3**, 67.
12. A. J. Blake, N. R. Champness, A. Khlobystov, D. A. Lemenovskii, W.-S. Li, and M. Schroder, *Chem. Commun.*, 2027, **1997**.
13. M. Maekawa, H. Konaka, Y. Suenaga, T. Kuroda-Sowa, and M. Munakata, *J. Chem. Soc., Dalton Trans.*, 2000, 4160.
14. L. J. McCormick and D. R. Turner, *CrystEngComm*, 2013, **15**, 8234.

15. Z. Shi, X. Gu, J. Peng, X. Yu, and E. Wang, *Eur. J. Inorg. Chem.*, 2006, 385.
16. H.-F. Zhu, W. Zhao, T. Okamura, J. Fan, W.-Y. Sun, and N. Ueyama, *New J. Chem.*, 2004, **28**, 1010.
17. H. F. Zhu, J. Fan, T. Okamura, W.-Y. Sun, and N. Ueyama, *Cryst. Growth Des.*, 2005, **5**, 289.
18. M. Fujita, Y. J. Kwon, O. Sasaki, K. Yamaguchi, and K. Ogura, *J. Am. Chem. Soc.*, 1995, **117**, 7287.
19. M. Fujita, O. Sasaki, K.-Y. Watanabe, K. Ogura, and K. Yamaguchi, *New J. Chem.*, 1998, **22**, 189.
20. Y.-L. Liu, K.-F. Yue, D.-S. Li, Y. Yu, L. Hou, and Y.-Y. Wang, *CrystEngComm*, 2013, **15**, 2791.
21. J. Konnert and D. Britton, *Inorg. Chem.*, 1966, **5**, 1193.
22. S. R. Batten, B. F. Hoskins, and R. Robson, *New J. Chem.*, 1998, **22**, 173.
23. B. F. Abrahams, S. R. Batten, B. F. Hoskins, and R. Robson, *Inorg. Chem.*, 2003, **42**, 2654.
24. D. Venkataraman, S. Lee, J. S. Moore, P. Zhang, K. A. Hirsch, G. B. Gardner, A. C. Covey, and C. L. Prentice, *Chem. Mater.*, 1996, **8**, 2030.
25. S. R. Batten, B. F. Hoskins, and R. Robson, *Chem. Eur. J.*, 2000, **6**, 156.
26. J.-Q. Liu, Y.-Y. Wang, L.-F. Ma, F. Zhong, X.-R. Zeng, W.-P. Wu, and Q.-Z. Shi, *Inorg. Chem. Commun.*, 2007, **10**, 979.
27. S. R. Batten, A. R. Harris, P. Jensen, K. S. Murray, and A. Ziebell, *J. Chem. Soc., Dalton Trans.*, 2000, 3829.
28. L. Carlucci, G. Ciani, and D. M. Proserpio, *CrystEng-Comm*, 2003, **5**, 269.
29. D. B. Leznoff, B.-Y. Xue, R. J. Batchelor, F. W. B. Einstein, and B. O. Patrick, *Inorg. Chem.*, 2001, **40**, 6026.
30. M. L. Tong, X.-M. Chen, B.-H. Ye, and L.-N. Ji, *Angew. Chem. Int. Ed.*, 1999, **38**, 2237.
31. P. Jensen, S. R. Batten, B. Moubaraki, and K. S. Murray, *J. Chem. Soc., Dalton Trans.*, 2002, 3715.
32. R. W. Gable, B. F. Hoskins, and R. Robson, *J. Chem. Soc., Chem. Commun.*, 1990, 1677.
33. M. Kondo, M. Shimamura, S. Noro, S. Minakoshi, A. Asami, K. Seki, and S. Kitagawa, *Chem. Mater.*, 2000, **12**, 1288.
34. B. F. Hoskins and R. Robson, *J. Am. Chem. Soc.*, 1990, **112**, 1546.
35. H. S. Zhdanov, *C.R. Acad. Sci. URSS*, 1941, **31**, 352.
36. E. Shugam and H. S. Zhdanov, *Acta Physiochim. URSS*, 1945, **20**, 247.
37. L. Carlucci, G. Ciani, D. M. Proserpio, and S. Rizzato, *Chem. Eur. J.*, 2002, **8**, 1520.
38. O. Delgado-Friedrichs, M. D. Foster, M. O'Keeffe, D. M. Proserpio, M. M. J. Treacy, and O. M. Yaghi, *J. Solid State Chem.*, 2005, **178**, 2533.
39. J.-P. He, Y.-X. Tan, and J. Zhang, *CrystEngComm*, 2012, **14**, 6359.
40. P. Jensen, S. R. Batten, G. D. Fallon, D. C. R. Hockless, B. Moubaraki, K. S. Murray, and R. Robson, *J. Solid State Chem.*, 1999, **145**, 387.
41. P. Jensen, S. R. Batten, B. Moubaraki, and K. S. Murray, *J. Solid State Chem.*, 2001, **159**, 352.
42. C. S. Hong, S.-K. Son, Y. S. Lee, M.-J. Jun, and Y. Do, *Inorg. Chem.*, 1999, **38**, 5602.
43. C. J. Kepert and M. J. Rosseinsky, *Chem. Commun.*, 1998, 31.
44. L. Carlucci, G. Ciani, D. M. Proserpio, and A. Sironi, *Chem. Commun.*, 1996, 1393.
45. B. F. Abrahams, S. R. Batten, H. Hamit, B. F. Hoskins, and R. Robson, *Chem. Commun.*, 1996, 1313.
46. H. Wu, J. Yang, Z.-M. Su, S. R. Batten, and J.-F. Ma, *J. Am. Chem. Soc.*, 2011, **133**, 11406.
47. B. F. Abrahams, B. F. Hoskins, D. M. Michail, and R. Robson, *Nature*, 1994, **369**, 727.
48. B. F. Abrahams, S. R. Batten, H. Hamit, B. F. Hoskins, and R. Robson, *Angew. Chem., Int. Ed. Engl.*, 1996, **35**, 1690.
49. N. Moliner, C. Munoz, S. Letard, X. Solans, N. Menendez, A. Goujon, F. Varret, and J. A. Real, *Inorg. Chem.*, 2000, **39**, 5390.
50. K. W. Kim and M. G. Kanatzidis, *J. Am. Chem. Soc.*, 1992, **114**, 4878.
51. Z.-J. Zhang, W. Shi, Z. Niu, H.-H. Li, B. Zhao, P. Cheng, D.-L. Liao, and S.-P. Yan, *Chem. Commun.*, 2011, **47**, 6425.
52. L. Carlucci, G. Ciani, and D. M. Proserpio, *New J. Chem.*, 1998, **22**, 1319.
53. A. W. Sleight and R. J. Bouchard, *Inorg. Chem.*, 1973, **12**, 2314.
54. Z.-L. Wang, W.-H. Fang, and G.-Y. Yang, *Chem. Commun.*, 2010, **46**, 8216.
55. L. Carlucci, G. Ciani, M. Moret, D. M. Proserpio, and S. Rizzato, *Angew. Chem. Int. Ed.*, 2000, **39**, 1506.
56. L. Carlucci, G. Ciani, and D. M. Proserpio, *Chem. Commun.*, 2004, 380.
57. D. M. Shin, I. S. Lee, Y. K. Chung, and M. S. Lah, *Chem. Commun.*, 2003, 1036.
58. S. Yang, X. Lin, W. Lewis, M. Suyetin, E. Bichoutskaia, J. E. Parker, C. C. Tang, D. R. Allan, P. J. Rizkallah, P. Hubberstey, N. R. Champness, K. M. Thomas, A. J. Blake, and M. Schröder, *Nat. Mater.*, 2012, **11**, 710.
59. S. R. Batten and R. Robson, in 'Molecular Catenanes, Rotaxanes and Knots, A Journey Through the World of Molecular Topology', eds J.-P. Sauvage and C. Dietrich-Buchecker, Wiley-VCH, Weinheim, 1999, p.77.
60. B. F. Abrahams, M. J. Hardie, B. F. Hoskins, R. Robson, and E. E. Sutherland, *J. Chem. Soc., Chem. Commun.*, 1994, 1049.
61. X.-L. Wang, C. Qin, E.-B. Wang, Z.-M. Su, L. Xu, and S. R. Batten, *Chem. Commun.*, 2005, 4789.

62. B. F. Abrahams, S. R. Batten, M. J. Grannas, H. Hamit, B. F. Hoskins, and R. Robson, *Angew. Chem. Int. Ed.*, 1999, **38**, 1475.

63. M.-L. Tong, X.-M. Chen, and S. R. Batten, *J. Am. Chem. Soc.*, 2003, **125**, 16170.

64. J.-F. Ma, J. Yang, G.-L. Zheng, L. Li, and J.-F. Liu, *Inorg. Chem.*, 2003, **42**, 7531.

65. X.-J. Ke, D.-S. Li, and M. Du, *Inorg. Chem. Commun.*, 2011, **14**, 788.

66. T. Schareina, C. Schick, B. F. Abrahams, and R. Kempe, *Z. Anorg. Allg. Chem.*, 2001, **627**, 1711.

67. J. Yang, J.-F. Ma, and S. R. Batten, *Chem. Commun.*, 2012, **48**, 7899.

68. S. J. Loeb, *Chem. Soc. Rev.*, 2007, **36**, 226.

69. V. N. Vukotic and S. J. Loeb, *Chem. Soc. Rev.*, 2012, **41**, 5896.

70. K. Kim, *Chem. Soc. Rev.*, 2002, **31**, 96.

71. D. Whang and K. Kim, *J. Am. Chem. Soc.*, 1997, **119**, 451.

72. G. J. E. Davidson and S. J. Loeb, *Angew. Chem. Int. Ed.*, 2003, **42**, 74.

73. N. C. Frank, D. J. Mercer, and S. J. Loeb, *Chem. Eur. J.*, 2013, **19**, 14076.

74. D. Cao, M. Juricek, Z. J. Brown, A. C.-H. Sue, Z. Liu, J. Lei, A. K. Blackburn, S. Grunder, A. A. Sarjeant, A. Coskun, C. Wang, O. K. Farha, J. T. Hupp, and J. F. Stoddart, *Chem. Eur. J.*, 2013, **19**, 8457.

75. X.-L. Wang, C. Qin, E.-B. Wang, and Z.-M. Su, *Chem. Commun.*, 2007, 4245.

76. B. F. Hoskins, R. Robson, and D. A. Slizys, *J. Am. Chem. Soc.*, 1997, **119**, 2952.

77. D. M. L. Goodgame, S. Menzer, A. M. Smith, and D. J. Williams, *Angew. Chem., Int. Ed. Engl.*, 1995, **34**, 574.

78. Y.-H. Li, C.-Y. Su, A. M. Goforth, K. D. Shimizu, K. D. Gray, M. D. Smith, and H.-C. zur Loye, *Chem. Commun.*, 2003, 1630.

79. A.-L. Cheng, N. Liu, Y.-F. Yue, Y.-W. Jiang, E.-Q. Gao, C.-H. Yan, and M.-Y. He, *Chem. Commun.*, 2007, 407.

80. G.-P. Yang, L. Hou, X.-J. Luan, B. Wu, and Y.-Y. Wang, *Chem. Soc. Rev.*, 2012, **41**, 6992.

81. X.-J. Luan, X.-H. Cai, Y.-Y. Wang, D.-S. Li, C.-J. Wang, P. Liu, H.-M. Hu, Q.-Z. Shi, and S.-M. Peng, *Chem. Eur. J.*, 2006, **12**, 6281.

82. J. Heine, J. S. auf der Gunne, and S. Dehnen, *J. Am. Chem. Soc.*, 2011, **133**, 10018.

83. X. Kuang, X. Wu, R. Yu, J. P. Donahue, J. Huang, and C.-Z. Lu, *Nat. Chem.*, 2010, **2**, 461.

Index

0D nanoscale metal–organic frameworks, 20–22
1D coordination polymers
  formation by [2+2] cycloaddition, 136–137
    Ag…C interactions, 136, 137
    dinuclear Zn(II) complex, 136–137
    from photoreactive hydrogen-bonded zwitter ionic metal complexes, 137, 138
  forming 2D structures, 143–144
  forming 3D structures, 145
  heterointerpenetration with 2D/3D nets, 531, 532
  interpenetration, 523–524
  nanoscale metal–organic frameworks, 20, 22
  photoreactive ladder polymers, 137–143
  photoreactivity, 143–145
  structural transformation to ladders, 140–143
1D hexagonal channels, mesoporous metal–organic frameworks, 42–43, 63
[2+2] cycloaddition reactions, photoreactive coordination polymers, 135–143, 150–151
2D→3D structural change
  guest removal/exchange, single-crystal to single-crystal transformations, 493, 495–496, 502
  interpenetration3–4
  ligand substitution, single-crystal to single-crystal transformations, 510
  photoreactive transformation, 149
2D coordination polymers
  formation of 3D metal–organic frameworks, 149
  formation from photoreactive 1D structures, 143–144
  heterointerpenetration with 1D/3D nets, 530, 531, 532
  heterointerpenetration, 529, 530, 531
  interpenetration, 524–527, 528
  MOFs from single-molecule magnets, 247–252
  nanoscale metal–organic frameworks, 22–23
  photoconversion
    3D coordination polymers, 148–149
    interpenetrated sheet structures, 145–146
  photodimerization, 145
  photoreactivity, 145–150
    formation of 3D metal–organic frameworks, 149
    PSM to control sorption behavior, 149–150
    structural transformations, 147–148
  self penetration, 532, 533
  thermal cyclo-reversion of photoreacted polymers, 146–147
3D coordination polymers
  formation from photoreactive 1D coordination polymers, 145
  formation from photoreactive 2D coordination polymers, 148–149
  heterointerpenetration, 530, 531, 532
  interpenetration, 527–531
  MOFs from single-molecule magnets, 253–255
  photoreactive metal–organic frameworks, 150–153

abundances of quadrupolar nuclei, sensitivity to solid-state NMR, 458, 460
accessible metal sites *see* open metal sites
acetone sensing, open metal sites, 273–274
acetylene adsorption
  commensurate adsorption, 324
  separation/purification, open metal sites, 272–273
  storage, open metal sites, 267–269
adamantane-like structures
  see also diamondoid MOFs
  interpenetration, 527
  single-crystal to single-crystal transformations, 475–476
adenine
  see also bio-MOF series
  edible metal–organic frameworks, 166–167
adsorption isotherms
  characterization, 323
  gas storage, 284, 286, 291, 292, 294, 298
  mesoporous metal–organic frameworks, 39, 40, 47, 50, 51
  nanoMOFs, 28
  single component isotherms, gas selection prediction, 290, 307
  surface area calculation, 284, 378
  types, 264
adsorption mechanisms, 321–341
  alcohols, 333, 335–337
  commensurate adsorption, 324–326
  hydrocarbons, 326–333, 334
  incommensurate adsorption, 326
  MOFs, 323–326
  physisorption, 321–323
aerosol time-of-flight mass spectrometry (ATOF-MS), linker exchange, inorganic postsynthetic modification, 212
AFE *see* antiferroelectricity
AFM *see* atomic force microscope
Ag *see* silver centers
air pollution
  see also carbon dioxide; environmental issues
  harmful gas removal, 303–320
  inorganic toxic gases, 309–310, 315–316
  luminescent sensing MOFs, 364–365
  radioactive gases, 313–315, 316
  volatile organic compounds, 310–311, 316
alcohols
  adsorption and separation, 333, 335–337
  guest-shape-responsive fitting, deforming Zn-MOFs, single-crystal to single-crystal transformations, 481

alcohols (*continued*)
reversible adsorption, single-crystal to single-crystal transformations, 474
solvents for edible metal–organic frameworks, 160, 161, 170
alkali metal ions ternary metal formate frameworks incorporation, functional magnetic materials, 224
alkaline fuel cells, 437–438
alkanes (paraffins), adsorption and separation, 326, 327–330
alkenes (olefins)
see also olefin bonds
adsorption and separation, 326, 327–330
Al-MOF-53, characteristics, 99–100
α-magnesium formate (α-$Mg_3(HCOO)_6$), solid-state NMR studies of quadrupolar nuclei, 463, 464, 466, 467
α-Po networks
see also pcu topology
entanglement, 536
interpenetration, 528, 530
aluminum-based metal–organic frameworks, 99–114
^{27}Al quadrupolar nuclei, sensitivity to solid-state NMR, 458, 460
structures, 108–110
synthesis, 100, 103–108
types, 100, 101–103
AMFFs *see* ammonium metal formate frameworks
amino acids, edible metal–organic frameworks, 163–165
ammonia adsorption, 91, 309–310
ammonium cations, incorporation in magnetic metal formate frameworks, 224–225
ammonium metal formate frameworks (AMFFs), 224–231
magnetic ferroelectric combination, 229–231
magnetic properties, 227–229
multiferroic materials, 227, 230, 231
structures, 225–227
analytical chemistry applications, 443–456
gas chromatography, 446–449
high-performance liquid chromatography, 449–454
sample preparation by solid-phase extraction, 443–446
animal testing, edible metal–organic frameworks, 159, 161
anion exchanges in MOFs, single-crystal to single-crystal transformations, 511–515
anionic MOFs
cation exchange, 352, 354
chemical modification to induce cation uptake, 355–356
anionic part of SBU, inorganic postsynthetic modification, 209–210
anion-induced fluorination, fluorinated metal–organic frameworks, 86–88
anion templating for MOF assembly, single-crystal to single-crystal transformations, 511, 512, 513
annealing of ground/milled material, mechanosynthesis of coordination bonds, 175, 181, 182
antiferroelectricity (AFE), magnetic metal formate frameworks, 227, 228, 229, 231
ant topology, 3D MOFs from single-molecule magnets, 253
apical ligand substitution, single-crystal to single-crystal transformations, 508, 509
applications
analytical chemistry, 443–456
gas chromatography, 446–449
high-performance liquid chromatography, 449–454
sample preparation by solid-phase extraction, 443–446
aqueous stability
see also hydrothermal stability of MOFs
fluorinated metal–organic frameworks, 85, 87, 88, 95
arene rings, direct metallation, 350
aromatic hydrocarbons
see also polycyclic aromatic hydrocarbons
adsorption and separation, 326
HKUST-1, 448
MIL-47(V) benzene adsorption, 311–312
MIL-53 (Mn(II)) systems, 312, 480–481
aspartate ligands, edible metal–organic frameworks, 163–164
assemblies, preformed porous coordination polymer crystals, 11–16
asymmetric interpenetration, 528–529, 530
atmospheric carbon dioxide, 269, 304–305, 306
ATOF-MS *see* aerosol time-of-flight mass spectrometry
atomic force microscope (AFM)
MOF patterning, 388, 392
nanoscale MOFs, 23
automobile fuel carriers, gas storage MOFs, 296
axles, polyrotaxane frameworks, 116, 119, 120, 123–125, 128–130

ball milling, mechanosynthesis of metal–organic structures, 177, 178
batteries *see* rechargeable batteries
bdc *see* 1,4-benzenedicarboxylate
bending, framework dynamics on guest removal exchange, 491
benzene, MIL-47(V) adsorption, 311–312
1,4-benzenedicarboxylate (bdc), 10^{2-} axles, Texas-Sized Molecular Box, polyrotaxane frameworks, 126
1,4-benzenedicarboxylate (bdc)-based MOFs, postsynthetic modification, 196
benzene-1,4-dicarboxylic acid (H_2bdc) ligands
see also MOF-5
pendant thiols/thioether groups for metal grafting, 344, 347
1,4-benzenedicarboxylic acid (terephthalic acid), edible metal–organic frameworks, 161
benzene-1,3,5-tricarboxylate (btc) *see* copper-btc structures
BET surface area *see* Brunauer-Emmett-Teller surface area
bioactive dicarboxylates, photoreactive ladder coordination polymers, 140
biocatalysts, mesoporous metal–organic frameworks, 54–58
biological/medical applications
see also drug delivery
nitrous oxide delivery, 309
biomimetic activity
catalysts, porphyrinic metal–organic frameworks, 76, 80
photosynthesis-like light harvesting, porphyrinic metal–organic frameworks, 77–78
bio-MOF 1, edible metal–organic frameworks, 167, 168, 169
bio-MOF 11, edible metal–organic frameworks, 167
bio-MOF-14, selective carbon dioxide adsorption, 308
bio-MOF 100, edible metal–organic frameworks, 168, 169

bio-MOF series
edible metal–organic frameworks, 166–169
structures, 40, 46
synthesis, 47
biomolecules, solid-phase extraction with MOFs, 444, 445
2,2′-bipyridine (bpy) ligands, metal grafting onto MOF framework, 348
4,4′-bipyridine (bpy) ligands, porphyrinic metal–organic frameworks, 72, 73
4,4′-bipyridyl ethene (bpe)
photoreactive 1D coordination polymers, 137
photoreactive ladder coordination polymers, 137–139
5,15-bis(3,5-dicarboxyphenyl)porphine (DDCPP) ligands, porphyrinic metal–organic frameworks, 68, 69
bis(pyridinium)ethane axles, dibenzo[24]crown-8 wheels, polyrotaxane frameworks, 119, 120, 123–125
trans-1,2-bis(4-pyridyl)ethene *see* 4,4′-bipyridyl ethene
bis(triphenylphosphino)silver(I) hydrogencarbonate, carbon dioxide binding during mechanosynthesis, 187
Borromean interpenetration, 526
bottom-up approach, MOF patterning, 388, 397
bpe *see* 4,4′-bipyridyl ethene
bpy *see* 2,2′-bipyridine; 4,4′-bipyridine
braid entanglement, 535–536
"breathing" behavior
ammonium metal formate frameworks, 226
hydration–dehydration cycle, MIL-53, 333
selective gas adsorption, 87, 92, 310, 312
single-crystal to single-crystal transformations, 480, 481, 491–492, 493
Brunauer-Emmett-Teller (BET) surface area
CO_2 relationship in modified bio-MOFs, 167–168
mechanochemical MOF synthesis, 185
mesoporous MOFs, 50
porosity and gas adsorption, 284, 287–288, 295
semiconducting MOFs, 378
simulated versus experimental, 295
BTC series MOFs
see also copper-btc structures
sensors, 273–274
BTT series MOFs, hydrogen adsorption/storage, 262–263, 285, 286, 287
bulky secondary building units, mesoporous metal–organic frameworks, 46, 47
butane adsorption and separation, 326, 330

C_1 hydrocarbons *see* methane
C_2-C_3 hydrocarbons, separation, 327–330
C_4 hydrocarbons, separation, 330
C_6 hydrocarbons, separation, 330–332, 480–481
C_8 hydrocarbons
separation, 332–333
MIL-53 systems, 312, 480–481
C_Q *see* quadrupolar coupling constant
caged mesoporous metal–organic frameworks, 40, 43–46
solid supports for biocatalysts, 56
cage effects
commensurate adsorption, 324–325
incommensurate adsorption, 325
cage-like pores, mesoporous metal–organic frameworks, 39, 40
cages, entanglement of discrete components, 536
capillary gas chromatography
MOF applications, 446–448, 449
nanoMOFs, 28–29, 30
volatile organic compounds, 312
capping agents, particle growth control for nanoscale metal–organic frameworks, 21
carbohydrates, edible metal–organic frameworks, 169–170
carbon capture and sequestration (CCS), 269–271, 287, 290, 306–307, 315
carbon dioxide
in atmosphere, 269, 304–305, 306
binding during mechanosynthesis of bis(triphenylphosphino)silver(I) hydrogencarbonate, 187
electrochemical conversion, electrocatalytic MOFs, 434
separation from mixtures, mixed-matrix membranes, 407, 410–414
carbon dioxide adsorption and selection
adsorbent/MOF comparisons, 306
fluorinated metal–organic frameworks, 87, 88, 91–94
from flue gases, 77, 269, 287, 290, 305–309, 315, 323
high pressure uptake by MOFs, 287–288
photoresponsive metal–organic frameworks, 153, 154
physisorption mechanisms, 322–323
removal from natural gas, polymer membranes, 403, 405–406
selection over nitrogen, 307
selection over water vapor, 307–308
with sulfur dioxide, 309
carbon dioxide storage, 287–290, 291, 305–309
economic viability of MOFs, 315, 316
mesoporous metal–organic frameworks, 50–51
need for removal, 304–305, 306
open metal sites, 269–271
porphyrinic metal–organic frameworks, 76–77
postcombustion capture, 269–271
carbon nanoparticles, sacrificial MOF precursors, 436–437
carboxylate bridges, photoreactive ladder coordination polymers, 137–139
carboxylate linkers, single-crystal to single-crystal transformations, 474, 485–488
carboxylates, *see also* metal formate frameworks
carboxyl groups, thiol group combination, semiconducting MOFs, 377–378
carboxylic acids, edible metal–organic frameworks, 162
catalysts
biocatalysts, 54–58
biomimetic activity, 76, 80
electrocatalysis, 419–420, 432–434
mesoporous metal–organic frameworks, 51–58
nanoscale metal–organic frameworks, 31–32
open metal sites, 274–277
porphyrinic metal–organic frameworks, 76, 80
single-crystal to single-crystal transformations, 518–520
catalytic amounts of liquid phase mechanosynthesis of metal–organic structures, 174, 176, 185

catalytic amounts of salts, ion- and liquid-assisted grinding, mechanosynthesis of metal–organic structures 177, 178, 184
catecholate moieties in MOFs, protection and photochemical cleavage of protecting group, 365–366
catenanes, entanglement, 523, 524, 526, 532, 533, 534
cation exchange
  see also metal ion exchange
  metal uptake into pores, 352, 354–355
  single-crystal to single-crystal transformations, 515–518
cation metathesis *see* metal ion exchange
cation uptake induction, chemical modification of MOF, 355–356
CB[6] *see* cucurbit[6]uril
CCS *see* carbon capture and sequestration
CD *see* cylodextrin
CE *see* conventional electric
CFT *see* copper formate tetrahydrate
chalcogenide subdomains in solid matrix, semiconducting MOFs, 379
channeled nanoporous metal–organic frameworks, hydrocarbon sorption, 95
channel-like pores, mesoporous metal–organic frameworks, 39, 40–43, 63
channel locking/unlocking, rotational modules, single-crystal to single-crystal transformations, 496–497
charge storage applications *see* rechargeable batteries
chemical etching, nanoscale metal–organic frameworks, 22
chemical sensing *see* sensors
chemical shielding (CS) interactions, quadrupolar nuclei, 458, 459, 460
chemical shift anisotropy (CSA), quadrupolar nuclei, 459, 460
chemical vapor deposition (CVD), metallation, 350, 356, 357
chemisorption, 321
  CO_2, 169
  H_2, 356
  NO, 502
  O_2, 297
chemistry of organized matter, porous coordination polymers, 3
chiral catalysts
  mesoporous metal–organic frameworks, 53, 54
  open metal sites, 276
chiral MOFs
  anion exchange, 511
  cation exchange, 517–518
  edible metal–organic frameworks, 163–165
  magnetic metal formate frameworks, 223, 224, 225–226, 227, 232
chiral networks, interpenetration, 528, 530
chiral separation
  gas chromatography, 448–449
  high-performance liquid chromatography, 451–452, 454
chiral–achiral structural changes, guest exchange properties, 481–484
chlorocarbons, reversible adsorption, 476
chromium
  MIL-100/MIL-101, 87–88, 208, 269, 352, 426
  redox-active MOFs, 426–428
cinnamic acids, photochemistry, 135–136
cis corner-sharing polyhedra motifs, aluminum-based metal–organic frameworks, 108, 109
climate change, 269, 305
cobalt centers, polyrotaxane frameworks, 117, 119–120
cobalt clusters
  2D MOFs from single-molecule magnets, 252
  3D MOFs from single-molecule magnets, 253
cobalt/lanthanide cores, 2D MOFs from single-molecule magnets, 251
co-ligands
  edible metal–organic frameworks, 165, 167–168, 169
  fluorinated MOFs, 89
  magnetic metal formate frameworks, 222, 223, 228, 234–237
colloidal MOF solutions, films, 396–397
colloidosomes, porous coordination polymer assemblies, 11,12
color changes
  coordination environment of metal sites, 262
  metal uptake/sensing by MOFs, 347, 352
  photoreactive MOFs, 140
  pH-sensitive CO_2 sensor, 169, 170
  polyrotaxane MOFs, 125–126
  single-crystal to single-crystal transformations
    anion substitution, 514
    cation substitution, 516, 517
    dehydration/rehydration of robust frameworks, 485–486, 488, 490–491
    explosive nitroaromatic detection, 478, 479
    ligand substitution at the metal center, 498–499
commensurate adsorption, 322, 324–326
Co-MOF-74, light hydrocarbon separation, 271, 272
composites
  high-performance liquid chromatography, 453–454
  porous coordination polymers, 13, 16
  redox-active materials, 422, 428–430
contrast agents in medical imaging/computed tomography, nanoscale metal–organic frameworks, 30–31
controllable gate-opening, framework sliding, single-crystal to single-crystal transformations, 479–480, 492
controlled nucleation, MOF patterning by promoting agent, 388, 389–390
controlled secondary building units approach (CSA), MOF synthesis, 448
controlled thin film growth, MOF patterning by promoting agents, 388–389
conventional electric (CE) heating, aluminum-based metal–organic framework synthesis, 104, 107
coordination bonds
  mechanosynthesis methods, 174–178
  single-crystal to single-crystal transformations, 506
coordination modulation approach, crystal size/morphology determination, 7–8, 21
coordination modulation combined with microwave-assisted synthesis, crystal size/morphology determination, 8–9
coordination modulators, nanoscale metal–organic frameworks, 21
coordination polymers

see also 1D/2D/3D coordination polymers; porous coordination polymers
mechanosynthesis
acid–base reactions, 180–181, 182
from metal oxides and carbonates, 181, 183
ligand addition, 179–180
ligand exchange, 180, 181
photo-polymerization, 154–155
coordinatively unsaturated metals (CUS) *see* open metal sites
copolymerization with two ligands, defective MOF analogs for metal grafting, 352
copper
see also dicopper paddlewheel SBUs
Cu^1 templated [2]pseudorotaxane, polyrotaxane frameworks, 127–128
[Cu(hfipbb)(H2hfipbb)0.5] MOF, 322, 325–326, 330
Cu-TDPAT, carbon dioxide adsorption, 270
redox-active MOFs, 426
copper-bpy structures, Cu-BPY-HFS, mixed-matrix membranes, 407, 408, 409
copper-btc structures
see also HKUST-1
mixed-matrix membranes, 407, 408, 409
MOF composites, high-performance liquid chromatography, 453
copper centers
polyrotaxane frameworks
copper templated pseudorotaxane, 127–128
cucurbit[6]uril wheels, 117
dibenzo[24]crown-8 wheels, 119–120, 123, 124
rotational dynamics, 130, 131–132
copper formate tetrahydrate (CFT), magnetic metal formate frameworks, 223
copper-tetracarboxylate MOFs, hydrogen storage, 261–262
core-shell spherical composites, nanoscale metal–organic frameworks, 26
corner-sharing polyhedra motifs, aluminum-based metal–organic frameworks, 108, 109, 110
costs
carbon dioxide storage methods, 287, 290
catalysts, 51, 55
chemical separation methods, 403, 405
harmful gas removal, 315–317
hydrocarbon separation methods, 94–95, 271, 298, 327
hydrogen storage methods, 261, 285
lithium for batteries, 430
MOF production
mechanosynthesis, 174
nanoMOFs, 29, 33
patterning methods, 393
coupled ion/electron transfer, 420
covalent postsynthetic modification, 195, 196, 197–204, 206
electrochemical reactions, 206
photochemical reactions, 204, 206
reagent addition, 197–203
thermal reactions, 203–204
CP *see* cross polarization
CP MAS *see* cross polarization magic angle spinning
CPO-27 series MOFs *see* M-MOF-74 series
C_Q *see* quadrupolar coupling constant
crankshaft/pedal motion of ligand groups, reversible guest exchange/removal behavior, 497–498
cross polarization (CP), solid-state NMR studies of quadrupolar nuclei, 466–467
cross polarization magic angle spinning (CP MAS), solid-state NMR studies of quadrupolar nuclei, 466–467
crystal growth control, nanoscale metal–organic frameworks, 20–21
crystalline structure
0D-3D MOFs, 304
aluminum-based metal–organic frameworks, 108–110
mesoporous metal–organic frameworks, 39
semiconducting MOFs, 373, 374–375, 376, 380–381
verification after postsynthetic modification, 196–197
crystallization followed by functionalization, two-step construction of semiconducting MOFs, 374, 378–380
crystallization site positioning, porous coordination polymer crystal assembly, 12–16
crystallization studies, aluminum-based metal–organic frameworks, 99, 106–107
crystal packing effects, single-molecule magnets, 246, 256
crystal size and morphology
property dependence, 3, 10–11
synthesis strategies, 4–10
crystal suspensions casted on solid platforms, porous coordination polymer assemblies, 11
CS *see* chemical shielding
CSA *see* chemical shift anisotropy; controlled secondary building units approach
Cu^1 templated [2]pseudorotaxane, polyrotaxane frameworks, 127–128
Cu-BPY-HFS, mixed-matrix membranes, 407, 408, 409
Cu-BTC *see* copper-btc structures
[Cu(hfipbb)(H2hfipbb)0.5] MOF
commensurate adsorption, 325–326
hydrocarbon separation, 330
structure, 322
cucurbit[6]uril (CB[6]), polyrotaxane frameworks, 115–119
CUS (coordinatively unsaturated metals) *see* open metal sites
Cu-TDPAT, carbon dioxide adsorption, 270
CVD *see* chemical vapor deposition
cyanosilylation, MOF catalysis, 274–275, 394, 519
[2+2] cycloaddition reactions, photoreactive coordination polymers, 135–143, 150–151
cyclo-reversion, thermal, photoreacted 2D coordination polymers, 146–147
CYCU-3 (MIL-68 analog), structure/synthesis, 43
cylodextrin (CD), edible metal–organic frameworks, 169–170
cytochrome c, translocation into Tb-mesoMOF, 58, 59, 60

D_2 *see* deuterium
dative postsynthetic modification, 195, 196, 205, 206–208
DB24C8 *see* dibenzo[24]crown-8
DDCPP *see* 5,15-bis(3,5-dicarboxyphenyl)porphine
DEF *see* diethylformamide
degree of conversion, postsynthetic modification characterization, 197, 201, 202

dehydration
amino acid MOFs, 164
MOF mechanosynthesis, 183–184
dehydration/rehydration
"breathing" behavior, 333
single-crystal to single-crystal transformations, 485–491
dehydrohalogenation, mechanosynthesis, 181, 182
delamination method, nanosheet synthesis from bulk MOF crystals, 22–23
dendritic ligands, stability of MOFs with extended ligands, 295
dense binary metal formate frameworks, functional magnetic materials, 224
deuterium (D_2) adsorption
HKUST-1 open metal sites, 261
Mn-btt MOF binding sites, 285, 286, 287
device fabrication, MOF patterning, 387–401
diaminoalkane-based axles, cucurbit[6]uril wheels in polyrotaxane frameworks, 116
diamondoid MOFs
gas/alcohol adsorption, 477, 478
guest removal/exchange, 475–476, 481, 483
heterointerpenetration with mdf nets, 531
interpenetration, 527–528, 529–530
porous metal formate frameworks, 231–234
single-crystal to single-crystal transformations, 475–476, 477, 478, 481, 483
dibenzo[24]crown-8 (DB24C8), polyrotaxane frameworks, 119–126
dicarboxylate MOFs, postsynthetic modification, 196
dicopper paddlewheel SBUs
gas storage MOFs, 284, 287, 289, 290, 292, 294–296
open metal sites, 259–260, 261
dielectric anomalies
ammonium magnetic metal formate frameworks, 227, 229
porous diamondoid metal formate frameworks, 234
diethylformamide (DEF), reversible adsorption, 476, 478
diffusion effect study, photoactive groups in MOFs, 368–369
digital microfluidics, MOF patterning, 393–394, 395
2,5-dimercaptobenzene dicarboxylic acid (DMBD) building blocks, semiconducting MOFs, 376, 377–378
dimethylammonium (DMA), edible metal–organic frameworks, 167
dimethylbipyridine (DMBPY) ligands, porphyrinic metal–organic frameworks, 72, 73
2,3-dimethyl-2,3-dinitrobutane (DMNB), photoreactive explosive detectors, 365
dimethylether (DME), adsorption, 335–336
dimethylformamide (DMF)
crankshaft/pedal molecular motion, 503, 504
diethylformamide substitution, 503, 504
guest exchange properties, 476–478, 480, 481–482, 484
guest removal, 485
solvent in open metal site MOFs, 263, 273–274
dimethyl methylphosphonate (DMMP), solid-phase extraction with IRMOF-1, 443
2,4-dinitrotoluene (DNT), photoreactive explosive detectors, 365
dipolar interactions, solid-state NMR studies of quadrupolar nuclei, 458, 466
direct characterization of metal center environments, solid-state NMR, 460–465
direct deposition, nanoscale metal–organic frameworks on surfaces, 23–24
direct nucleation growth process, porous coordination polymer crystal assembly, 12–13
disorder–order transitions
copper formate tetrahydrate, 223
magnetic metal formate frameworks, 225, 226, 227
distortions of frameworks, single-crystal to single-crystal transformations, 488–514
dithioalloxy-1,4-benzenedicarboxylate (dtabc), 347, 349
DMA *see* dimethylammonium
DMBD *see* 2,5-dimercaptobenzene dicarboxylic acid
DMBPY *see* dimethylbipyridine
DME *see* dimethylether
DMF *see* dimethylformamide
DMMP *see* dimethyl methylphosphonate
DMNB *see* 2,3-dimethyl-2,3-dinitrobutane
DNT *see* 2,4-dinitrotoluene
DOBDC series MOFs *see* M-MOF-74 series
donor groups, macrocycle linkage, polyrotaxane frameworks, 128
doping *see* pore loading
double [2+2] cycloaddition reactions, photoreactive ladder coordination polymers, 139, 140
double-pillared metal–organic frameworks, photoreactivity, 150–151
drug delivery
edible metal–organic frameworks, 159–171
magnetic metal–organic frameworks, 394–395
mesoporous metal–organic frameworks, 58–62
nanoscale metal–organic frameworks, 30
nitrous oxide delivery, 309
dtabc *see* dithioalloxy-1,4-benzenedicarboxylate
dynamic frameworks, single-crystal to single-crystal transformations, 488–496
dynamic motion, polyrotaxane frameworks, 130–132
dynamic photo-switching of spacer ligands, 153
dysprosium clusters, 2D MOFs from single-molecule magnets, 251–252

economic issues *see* costs
edge-sharing polyhedra motifs, aluminum-based metal–organic frameworks, 108, 109, 110
edible metal–organic frameworks, 159–171
amino acids, 163–165
carbohydrates, 169–170
choice of metal ions, 161
choice of solvents, 160, 161
choice of struts/organic linkers, 161–170
endogenous ligands, 162–163
exogenous ligands, 161–162
nucleobases, 166–169
peptides, 165–166
synthetic considerations, 159–161
EDLCs *see* electrochemical double layer capacitors
EDXRD *see* energy dispersive X-ray diffraction
electroactive materials, *see also* semiconducting MOFs

electrocatalysis, 374, 419–420, 428, 432–434, 438
electrochemical applications
  pristine MOFs, 430–436
    electrocataysts, 432–434
    ORRs, 432–434
    proton-conductive membranes in fuel cells, 434–436
    rechargeable batteries/superconductors, 420, 430–432
  rechargeable batteries, 210, 355, 430–432, 437
  sacrificial MOFs, 436–438
    oxygen reduction reaction, 437–438
    rechargeable batteries/superconsuctors, 437
  superconductors, 419, 430–432, 437
electrochemical approaches
  covalent postsynthetic modification, 206
  MOF patterning, 390–391
electrochemical double layer capacitors (EDLCs), microporous carbon or metal/metal oxide nanoparticles, 437
electrochemical MOF responses, 420–430
  ion-size effects, 420–422
  reversible redox responses, 420, 422–430
electrochemical reduction of nitrates/nitrites, electrocatalytic MOFs, 434
electrodeposition-based lithographic techniques, MOF patterning, 390
electrodics, potential for MOF use, 420, 430–432
electromagnetic fields, preformed porous coordination polymer crystal assembly, 12
electrooxidation of liquid fuels, electrocatalytic MOFs, 434
electrowetting-on-dielectric (EWOD), MOF patterning, 393
EMCs *see* entactic metal centers
emulsion-based synthesis method, nanoscale metal–organic frameworks, 21–22
endogenous ligands, edible metal–organic frameworks, 162–163
energy dispersive X-ray diffraction (EDXRD), aluminum-based metal–organic frameworks, 106, 107
energy storage and conversion *see* fuel cells; rechargeable batteries; supercapacitors
energy transfer, porphyrinic metal–organic frameworks, 77–78
entactic metal centers (EMCs), hydrogen storage, 263–264
entanglement, 523–538
  braids, 535–536
  interpenetration, 523–532
  nanotubes, controllable gate-opening, 479–480
  other forms, 533–536
  polyrotaxanes, 523, 533–535
  self-penetration, 532–533
  weaves, 535, 536
environmental issues
  see also carbon dioxide storage
  aluminum-based metal–organic frameworks, 99
  biocatalysts, 54
  carbon capture and sequestration, 269–271, 287, 290, 306–307
  climate change, 269, 305
  harmful gas adsorption, 303–320
    inorganic toxic gas removal, 309–310, 315–316
    radioactive gas immobilization, 313–315
    volatile organic compound removal, 310–313
  mechanosynthesis, 174, 185
  MOF importance, 304–305
enzymes, solid supports for biocatalysts, 54–58
equilibrium processes, physisorption, 322
ethanol, edible metal–organic frameworks, 161, 170
ethoxysuccinato-cisplatin prodrug, 61, 203
Eu(BTC), sensors, 273
EuTMBD–AgCl framework, semiconducting MOFs, 379
evaporation-induced growth, MOF patterning, 391–393
EWOD *see* electrowetting-on-dielectric
exogenous ligands, edible metal–organic frameworks, 161–162
explosives detection, 32, 365, 478, 479
exposed metal sites *see* open metal sites
ex-situ crystallization studies, aluminum-based metal–organic frameworks, 106, 107
extended ligands
  mesoporous metal–organic framework synthesis, 46, 47
  stability of MOFs, mesopores and branching, 295
external control
  MOF patterning, 390–397
    digital microfluidics, 393–394, 395
    dynamic relocation of magnetic framework composites, 394–396
    electrochemical approach, 390–391
    electromagnetic fields, 12
    films from colloidal MOF solutions, 396–397
    microcontact printing and evaporation-induced growth, 391–393, 394
    positioning preformed MOFs, 394–397

Fc *see* ferrocene
FCs *see* framework composites
$Fe_2(BDP)_3$ MOF, volatile organic compound adsorption, 312, 313
FE *see* ferroelectric; ferroelectricity
Fe-MIL-100 *see* MIL-100(Fe)
Fe-MOF-74
  hydrocarbon separation, 271, 272, 298–299
  oxygen storage, 297–298
ferrocene (Fc), redox-active MOFs, 423, 425
ferroelectric (FE) transitions
  ammonium magnetic metal formate frameworks, 225, 227, 228, 229, 230
  porous diamondoid metal formate frameworks, 234
ferroelectricity (FE), metal formate frameworks, 222
FESEM *see* field emission scanning electron microscopy
fibers for solid-phase microextraction, MOFs on stainless steel wire, 445
field emission scanning electron microscopy (FESEM), mechanosynthesis of MOFs, 190
films *see* nanofilms; thin films
flexibility of MOFs, 374, 419
  see also rigidity of MOFs; single-crystal to single-crystal transformations; structural dynamics
  crystal size, 10–11
  edible MOFs, 160, 162–163, 166
  helical polyrotaxane frameworks, 117

flexibility of MOFs (*continued*)
hydrocarbon selection, 327, 329
intraframework interactions/synthesis method and temperature, 108–109
lanthanide MOFs, 494, 495–496
metal ion effects, 108, 211
organic linkers, 109, 374, 475
reversible uptake and release of guests, 162–163, 166, 474, 475, 479–481
SSNMR studies, 468
flexible frameworks *see* flexibility of MOFs; rigidity of MOFs
flue gases
carbon dioxide capture, 77, 269, 287, 290, 305–309, 315, 323
sulfur dioxide removal, 309
fluorescence *see* luminescence
fluorinated metal–organic frameworks (FMOFs), 85–98
anion-induced fluorination, 86–88
applications, 85, 91–96
fluorinated ligands, 88–90
hydrophobicity, carbon dioxide adsorption from water vapor, 308
noble gas selection, 314
structure, 74
fluorine, incorporation into porous materials, 85
FMOFs *see* fluorinated metal–organic frameworks
food-grade ingredients, edible metal–organic frameworks, 170
formaldehyde adsorption, 312
formate
see also metal formate frameworks
advantages in MOFs, 221, 223
coordination modes, 221, 222
framework composites (FCs), MOF patterning, 394
framework density, fluorinated MOFs, gas sorption, 93–94
framework shrinkage and expansion, single-crystal to single-crystal transformations, 481, 483, 484, 487, 488–489
framework sliding, single-crystal to single-crystal transformations, 479–480, 483, 492
framework structural changes, *see also* single-crystal to single-crystal transformations
framework superstructures, nanoscale metal–organic framework self-assembly, 27, 28
fuel carriers, automobiles, 296
fuel cells
alkaline, 437–438
polymer electrolyte membranes, 434–436, 437–438
proton-conductive membranes, 434–436
guest loaded MOFs, 434, 436
postsynthetically functionalized MOFs, 436
pristine MOFs, 434–436
sacrificial MOF precursors, 437–438
fuel electrooxidation, electrocatalytic MOFs, 434
fumaric acid *see* iron(III)fumarate
functional composites, hybrid MOF nanocomposites, 26, 29, 31
functionalized metal–organic frameworks
see also postsynthetic modification
functionalized linkers, 195
gas storage, 283, 284–285, 288–290, 299
metal uptake, 343
functional magnetic materials
see also magnetic metal formate frameworks
ammonium metal formate frameworks, 224–231
dense binary metal formate frameworks, 224
historical comments, 222–224
metal formate frameworks, 221–243
metal formate frameworks with co-ligands, 234–237
porous diamondoid metal formate frameworks, 231–234
ternary metal formate frameworks incorporating alkali metal ions, 224
functional MOF materials, crankshaft/pedal motion of ligand groups, 497–498
^{71}Ga, quadrupolar nuclei, sensitivity to solid-state NMR, 458, 460

gadolinium Gd(III) ions, contrast agents in medical imaging, 30
γ *see* gyromagnetic ratios
γ-cylodextrin (γ-CD), edible metal–organic frameworks, 169–170
gas adsorption
see also carbon dioxide adsorption and selection; hydrogen adsorption and storage
advantages of MOFs, 304, 316
costs of MOFs, 315–317
environmental applications, 303–320
fluorinated metal–organic frameworks, 85–86, 91–94
framework density/steric hindrance effects, 93–94
mesoporous metal–organic frameworks, 49–51
nanoscale metal–organic frameworks, 28–30
photoreactive 2D coordination polymers, 147
photoresponsive metal–organic frameworks, *trans–cis* isomerization influence, 153, 154
porous diamondoid metal formate frameworks, 231–232
surface area and pore size increase, 304
gas chromatography (GC)
alcohol adsorption, 335
coupled with solid-phase microextraction, tandem molecular sieves, 449, 450
hydrocarbon adsorption, 323
MOF applications, 446–449
nanoscale metal–organic frameworks, 28–29
gas separation
see also carbon dioxide adsorption and selection
hydrocarbons, 298–299
membranes, 404–405
mesoporous metal–organic frameworks, 51
mixed-matrix membranes, 406
mixed-matrix membranes with MOFs, 407–414
nanoscale metal–organic frameworks, 28–30
open metal sites, 269–273
porphyrinic metal–organic frameworks, 76–77
gas storage, 283–301
see also carbon dioxide storage; hydrogen adsorption and storage
mesoporous metal–organic frameworks, 49–51
methane, 50, 265–267, 290, 292–297

open metal sites, 261–269
other hydrocarbons, 298–299
oxygen, 297–298
physisorption mechanisms, 322–323
porphyrinic metal–organic frameworks, 76–77
structural characteristics of metal–organic frameworks, 283–284
gates *see* controllable gate-opening; molecular gates
GC *see* gas chromatography
GCMC *see* Grand Canonical Monte Carlo simulations
ginding–annealing, mechanosynthesis of coordination bonds, 175, 181, 182
glassy polymers, membranes, 405
global warming, 269, 305
glycouril units, cucurbit[6]uril wheels, 115–116
gold nanorods (GNRs), photoresponsive metal–organic frameworks, 154
grafting additional metals onto MOF framework, 343–344, 347–352
Grand Canonical Monte Carlo (GCMC) simulations
benzene/thiophene adsorption, 312
CO_2/N_2 selectivity, 307
hydrocarbon separation, 332, 333
methane adsorption, 294
noble gas separation, 314, 315
graphine-like materials, 2D nanoscale metal–organic frameworks, 22
green chemistry
aluminum MOFs, 99
mechanosynthesis, 185
greenhouse gases, 50, 287, 304–305
see also carbon dioxide
grinding *see* liquid-assisted grinding; neat grinding
guest detection, photoreactive MOFs, 364–365
guest exchange, single-crystal to single-crystal transformations, 474–485
guest exchanges, single-crystal to single-crystal transformations, 474–485
guest inclusions, porous diamondoid metal formate frameworks, 231–232
guest-modulated magnetism, porous diamondoid metal formate frameworks, 233–234
guest removal, single-crystal to single-crystal transformations, 474, 485–488
guest-shape-responsive fitting
deforming Zn-MOFs, 476, 481
selective recognition and catalysis, 518–519
gyratory ligand units, dynamic framework changes, 496–498
gyromagnetic ratios (γ), quadrupolar nuclei, sensitivity to solid-state NMR, 458, 460

H_2bdc *see* benzene-1,4-dicarboxylic acid
halocarbons, reversible adsorption, single-crystal to single-crystal transformations, 476
hard-and-soft principle, two-step strategy for semiconducting MOFs, 377, 378–380
hard–soft coordination chemistry, grafting additional metals onto MOF framework, 343, 344, 347–348
harmful gases
see also carbon dioxide; inorganic toxic gases; radioactive gas immobilization; volatile organic compounds
examples, 304
removal, 303–320
hcb topology, 2D MOFs from single-molecule magnets, 249
heat, *see also* hydrothermal stability; temperature…; thermal…
heterogeneous catalysis
intrinsic catalytic activity of MOF, 275–276
mesoporous metal–organic frameworks, 51–58
biocatalysts, 54–58
solid supports, 53–54
open metal sites, 274–277
organometallic catalysts incorporated into framework, 276
porphyrinic metal–organic frameworks, 78–81
heterogeneous crystallization, porous coordination polymers, 12–14
heterogeneous nucleation, porous coordination polymer crystals, 12–14
heterogeneous structures, porous coordination polymers, 13
heterointerpenetration, 529–532
hexane adsorption, $Fe_2(BDP)_3$ MOF, 312, 313
hexane isomers, separation, 330–332
hexanuclear manganese clusters, 2D MOFs from single-molecule magnets, 247–249
hexanuclear metal–organic bowl, mechanochemical construction by neat grinding, 174, 175
HIBA *see* 4-(1H-imidazole-1-yl)benzoic acid
hierarchical mesoporous metal–organic frameworks
template-directed synthesis, 46, 47–48, 49
template-free synthesis, 46, 48
high-performance liquid chromatography (HPLC), MOF applications, 449–454
high pressure carbon dioxide uptake, MOF-177, 287–288
high-throughput (HT) methods, aluminum-based metal–organic framework synthesis, 104–105
4-(1H-imidazole-1-yl)benzoic acid (HIBA) linker, rotational C–N bond, 475
historical comments
magnetic metal formate frameworks, 222–224
solid-state [2+2] cycloaddition reaction, 135–136
HKUST-1 (MOF-199/Cu^{II}-btc)
acetylene adsorption, 267–268
aromatic hydrocarbon adsorption and separation, 448
benzene/thiophene separation, 312
carbon dioxide adsorption, 269, 308
CO_2/N_2 separation, 307
D_2 adsorption, 261
heterogeneous catalysis, 275
krypton/xenon adsorption, 314
light hydrocarbon separation, 271
magnetic, drug delivery, 394–395
methane storage, 294
NO_2 adsorption, 309
reversible redox reactions, 426
structure, 44, 45
synthesis, patterning control, 390–391, 392, 398

homochiral MOFs, amino acids, 163–165
HPLC *see* high-performance liquid chromatography
HT *see* high-throughput
human consumption *see* edible metal–organic frameworks
hybrid metal–organic framework nanocomposites, 25–27
  catalysts, 31
  gas chromatography, 29
hydration–dehydration cycle
  "breathing behavior", MIL-53, 333
  single-crystal to single-crystal transformations, 485–491
hydrocarbon adsorption and separation, 298–299, 326–333
  see also methane
  advantages of MOFs, 324
  fluorinated metal–organic frameworks, 85, 94–96
  gas chromatography, 323
  guest-free Ni-MOF, single-crystal to single-crystal transformations, 478
  nanoscale metal–organic frameworks, 29–30
  open metal sites, light hydrocarbons-acetone/DMF, 271–272
  physisorption mechanisms, 321–323
  small molecule separation, 271–272, 326–330
  volatile organic compounds, 311–313, 316
hydrocarbons
  physical properties, 332
  saturated/unsaturated, 327, 328, 329–330
  types and classification, 326
hydrogen adsorption and storage, 285–287
  fluorinated metal–organic frameworks, 85, 86, 88, 91–94
  interaction energy, 261
  ligand functionalization effect studies, 262
  mesoporous metal–organic frameworks, 49–50
  open metal site effect studies, 262
  open metal sites, 261–265
  pore size effect studies, 262
  porphyrinic metal–organic frameworks, 76, 77
hydrogen-bonding acceptors, formate, 221–222
hydrogen sulfide
  adsorption from natural gas, 309
  environmental concern, 305, 309
hydrophobosity
  fluorinated metal–organic frameworks, 85
    carbon dioxide adsorption from water vapor, 308
    hydrocarbon adsorption/separation, 95–96
    stabilization, 91, 95
hydrothermal stability of MOFs, harmful gas adsorption, 308, 311, 316
hydrothermal synthesis, porphyrinic metal–organic frameworks, 73
hydroxyl groups, pendant ligand metal-binding sites, 348–349
hysteresis loops
  adsorption isotherms, mesoporous metal–organic frameworks, 39, 40
  magnetic MOFs, 229, 230
  magnetic nanomaterials, 32
  NO uptake/removal, 502
  single-molecule magnets, 246, 247, 251, 253, 255
IAST *see* ideal adsorption solution theory
ibuprofen delivery
  magnetic MOFs, 394–395
  mesoporous metal–organic frameworks, 60
  MIL-53(Fe), 160
ideal adsorption solution theory (IAST), gas selection prediction, 270, 272, 307, 315, 337
ILAG *see* ion- and liquid-assisted grinding
immobilization methods, open metal sites, 259–260
imprinting, MOF patterning, 397
inclined interpenetration, 524, 526–527
incommensurate adsorption, 326
incomplete conversion, postsynthetic modification, 197, 201, 202
inorganic building units
  see also metal centers; metal clusters; secondary building units
  aluminum-based metal–organic frameworks, 100, 101–103, 106, 108
inorganic membranes, 405
inorganic-nanoparticle@MOF nanocomposites, 25–26
inorganic nanoparticles, synthesized inside metal–organic framework pores, 25, 26
inorganic postsynthetic modification, 196, 208–213
  labile terminal ligand substitution, 208–209
  linker ligand substitution, 212–213
  metal center oxidation/reduction, 210–211
  metal center substitution, 210, 211–212
  reaction at the anionic part of SBU, 209–210
inorganic toxic gases
  adsorption, 309–310
  environmental harm, 304, 305, 309
  MOF costs, 315–316
in-situ crystallization
  aluminum-based metal–organic framework synthesis, 99, 106, 107
  nanoscale metal–organic frameworks on surfaces, 23–24
in situ/real-time X-ray diffraction studies, mechanosynthesis of MOFs, 188–189
interaction energy, hydrogen adsorption, 261
interlocking molecules
  see also mechanically interlocked molecules
  polyrotaxane frameworks, 115–133
interpenetration, 523–532
  1D networks, 523–524, 532
  2D networks, 524–527, 528, 532
  3D networks, 527–532
  control/blocking, 43, 47, 89, 231, 485
  electrochemical properties, 422, 428
  heterointerpenetration, 529–532
  magnetic MOFs, 254–255
  open metal site MOFs, 261, 272–273, 276, 277
  photoreactive MOFs, 136, 145–149, 365
  polyrotaxane frameworks, 115–133
  porphyrinic MOFs, 72–73
  post synthetic modification, 206, 213
  single-crystal to single-crystal transformations, 474, 475–476, 477, 489, 490–491, 492, 518
  topology, 523, 524

intraframework energy transfer, photochemical processes in MOFs, 367–368
in vivo testing, edible metal–organic frameworks, 159, 161
iodine adsorption, radioisotope removal, 313–314
ionics, potential for MOF use, 420
ion- and liquid-assisted grinding (ILAG), mechanosynthesis, 174, 177–178, 184–185
ion pairs
  grafting of additional metals onto MOF framework, 352, 354
  pore loading of metal complexes, 356
ion-size effects, electrochemical properties of MOFs, 420–422
IRMOF-1
  krypton/xenon adsorption, 314, 315
  solid-phase extraction, 443
  volatile organic compound adsorption, 311, 312
IRMOF-3, grafting metals onto framework, 350–352
IRMOF-16, structure, 40–41
IRMOF-74-I to XI, structure, 42, 43, 47
IRMOF series
  carbon dioxide adsorption, 306
  CO_2/N_2 selectivity, 307
  postsynthetic modification, 196
iron
  see also ferrocene; ferroelectricity
  redox-active MOFs, 425–426
iron(III)carboxylate nanoscale metal–organic frameworks, drug delivery, 60–61
iron(III)fumarate, MIL-88A, edible metal–organic frameworks, 160–161, 162–163
iron(III) ions, contrast agents in medical imaging, nanoscale metal–organic frameworks, 30
iron MOFs
  drug delivery, 159, 160
  edible metal–organic frameworks, 161
  $Fe_2(BDP)_3$ MOF, volatile organic compound adsorption, 312, 313
  Fe-MIL-101-NH_2, proton conductivity, 435–436
  Fe-MOF-74
    hydrocarbon separation, 271, 272, 298–299
    oxygen storage, 297–298
  MIL-100
    high-performance liquid chromatography, 453
    light hydrocarbon separation, 271
  rechargeable batteries, 430, 432
isoreticular MOFs *see* IRMOF…
isostructural coordination polymers, mechanosynthesis of solid solutions, 186–187
IUPAC classification, adsorption isotherms, 39, 40

JUC-48/Rh6G, temperature-sensing fluorescent devices, 63

Keggin type polyoxometalates, 107, 312, 428–429
kinetic and pathway studies, stepwise self-assembly, 510
kneading
  see also liquid-assisted grinding
  mechanosynthesis of coordination bonds, 175–177
Knoevenagel condensation, MOF catalysis, 52, 53, 519
krypton adsorption, radioisotopes, 314–315, 316

labile terminal ligand substitution, inorganic postsynthetic modification, 208–209
LAG *see* liquid-assisted grinding
Langmuir surface area
  mesoporous MOFs, 40
  porosity and gas adsorption, 284, 295
Langmuir–Blodgett (LB) film synthesis
  MOF patterning, 389
  nanoMOFs, 24, 25
  PCP assembly, 4
  porphyrinic MOFs, 77
lanthanide MOFs
  2D MOFs from single-molecule magnets, 251
  ammonium magnetic metal formate frameworks, 227
  edible metal–organic frameworks, 168
  luminescence, mesoporous metal–organic frameworks, 63
  photoreactive metal–organic frameworks, 152–153
  polyrotaxane frameworks, 117–118, 123, 127
  single-crystal to single-crystal transformations, 494, 495–496
layer-by-layer (LbL) synthetic approach, nanoscale metal–organic frameworks, 22, 24, 25
LB *see* Langmuir–Blodgett
LbL *see* layer-by-layer
LCW *see* lithographically controlled wetting
Lewis acid catalysts, porphyrinic metal–organic frameworks, 79
Lewis bases, functionalized MOFs for carbon dioxide storage, 288–289
ligand addition, mechanosynthesis of coordination polymers, 179–180
ligand components
  see also linkers
  single-crystal to single-crystal transformations 496–498
ligand defect approach, grafting additional metals onto MOF framework, 352
ligand deprotonating agents, crystal size/morphology determination, porous coordination polymer synthesis, 4–5
ligand substitution
  aluminum-based metal–organic frameworks, 105
  at the metal coordination center, single-crystal to single-crystal transformations, 499–511
  inorganic postsynthetic modification, 196, 212–213
    labile terminal ligands, 208–209
    linker ligands, 196, 212–213
  mechanosynthesis of coordination polymers, 180, 181
light, *see also* photo…
light harvesting, porphyrinic metal–organic frameworks, 77–78
light hydrocarbons *see* methane; small hydrocarbons
light-induced release of molecules, photoresponsive metal–organic frameworks, 154

linkers
see also ligands
aluminum-based metal–organic frameworks, 100, 101–103, 109
edible metal–organic frameworks, 161–170
insertion/removal, single-crystal to single-crystal transformations, 506–508
mesoporous MOFs, 45
MOF structure, 159
rotational freedoms, guest removal/exchange, 475
rotaxane, 115–132
linker substitution
at metal centers, single-crystal to single-crystal transformations, 499–511
inorganic postsynthetic modification, 196, 212–213
solvent-assisted linker exchange, 213
liquid adsorption, physisorption mechanisms, 323
liquid–air interface, porous coordination polymer crystal assembly, 11–12
liquid-assisted grinding (LAG)
mechanosynthesis, 174, 175–177
coordination polymer synthesis by ligand addition, 179
ion- and liquid-assisted grinding, 174, 177–178, 184–185
MOF synthesis by mechanochemical dehydration, 183–184
porous MOF synthesis, 184–185
liquid–liquid interface, porous coordination polymer crystal assembly, 12, 14, 15
liquid-phase epitaxy (LPE), nanoscale metal–organic frameworks on surfaces, 25
lithium ion (Li-ion) batteries, MOF applications, 210, 355, 430–432
lithium-modified MOFs
theoretical, CO_2/N_2 selective adsorption, 307
volatile organic compound adsorption, 312
lithographically controlled wetting (LCW), MOF patterning, 391
lithographic methods
MOF patterning, 388, 389–390, 391–392, 396, 397
nanoscale metal–organic frameworks, 33
porous coordination polymer synthesis, 14
LPE *see* liquid-phase epitaxy
luminescence
photoluminescence quenching by metals, 347–348
temperature-sensing fluorescent devices, 63
VOCs/tropospheric air pollutant sensing, 364–365

macrocycles
cucurbit[6]uril wheels, polyrotaxane frameworks, 115–119
dibenzo[24]crown-8 wheels, polyrotaxane frameworks, 119–126
rotational dynamics, polyrotaxane frameworks, 130–132
wheels with donor groups, polyrotaxane frameworks, 128–130
macrostructures
porous coordination polymers, 3
crystal assembly, 11–16
magic angle spinning (MAS), solid-state NMR studies of quadrupolar nuclei, 458–460, 464, 466–467
α-magnesium formate (α-$Mg_3(HCOO)_6$), solid-state NMR studies of quadrupolar nuclei, 463, 464, 466, 467
magnesium MOFs
see also Mg-MOF-74
^{25}Mg quadrupolar nuclei, solid-state NMR studies, 460, 461–463
magnetic framework composites (MFCs), MOF patterning, 394–396
magnetic metal formate frameworks
ammonium cations, 224–231
magnetism and multiferroics, 227–231
structures, 225–227
co-ligands, 234–237
large ditopic/polytopic co-ligands, 236–237
MFL, 222, 223, 228
small/short co-ligands, 234–235
dense binary frameworks, 224
functional magnetic materials, 221–243
historical comments, 222–224
porous diamondoids, 231–234
magnetism and multifunctionalities, 233–234
structures and physical properties, 231–233
ternary frameworks incorporating alkali metal ions, 224
magnetic particles, dynamic relocation of framework composites, MOF patterning, 394–396
magnetic quantum tunneling (MQT), single-molecule magnets, 246
magnetic resonance imaging (MRI), contrast agents, nanoscale metal–organic frameworks, 30–31
magnetic solid-phase extraction (MSPE), MOFs with magnetic nanoparticles, 445
magnetism
see also functional magnetic materials; magnetic metal formate frameworks
ammonium metal formate frameworks, 227–229
apohost porous diamondoid metal formate frameworks, 233
guest dependent, porous diamondoid metal formate frameworks, 233–234
nanoscale metal–organic frameworks, 32
magnets
MOFs from single-molecule magnets, 245–258
polynuclear metal complexes/metal clusters, 246
manganese clusters
2D MOFs from single-molecule magnets, 247–251
3D MOFs from single-molecule magnets, 252–255
manganese Mn(III) ions, contrast agents in medical imaging, nanoscale metal–organic frameworks, 30
manganese MOFs
Mn-btt MOF, 285, 286, 287
Mn-MOF-74, 272
MAS *see* magic angle spinning
Matérial Institut Lavoisier (MIL) *see* MIL-47; MIL-53; MIL-100; MIL-101; MIL series
Matrimid® membrane, mixed-matrix membranes with MOFs, 407–411, 414
matrix solid-phase dispersion extraction (MSPDE), MOF applications, 444

Mb *see* myoglobin
M-BTC series, sensors, 273–274
M-BTT series, hydrogen storage, 262–263, 285, 286, 287
mdf networks, heterointerpenetration with diamond nets, 531
mechanically interlocked molecules (MIMs)
  see also interpenetration
  polyrotaxane frameworks, 115–133
mechanochemical approach to synthesis *see* mechanosynthesis
mechanochemical dehydration, liquid-assisted grinding, metal–organic framework synthesis, 183–184
mechanosynthesis, 173–191
  advantages, 174
  carbon dioxide binding, 187
  coordination bonds
    ginding–annealing, 175, 181, 182
    ion- and liquid-assisted grinding, 177–178
    liquid-assisted grinding and kneading, 174, 175–177
    methods, 174–178
    neat grinding, 174–175
    product characterization, 178–179
  extended metal–organic structures, 179–184
    acid–base reactions, 180–181, 182
    emergent properties, 185–187
    ligand addition, 179–180
    ligand exchange, 180
    mechanochemical dehydration, 183–184
    porous MOFs, 184–185
  MOFs
    mechanistic studies, 187–190
    porous, 184–185
    scanning electron microscope studies, 189–190
    in situ/real-time X-ray diffraction studies, 188–189
    stepwise analysis, 187–188
  solid solutions, 186–187
  solvent-based synthesis comparison, 174
  structural dynamics, interconversion of different MOF forms, 185–186
  thermal dehydrohalogenation, 181, 182
membranes
  mixed-matrix membranes, 403–417
  nanoscale metal–organic frameworks on surfaces, 23
  polymer membranes, 403, 405–406, 407, 412
  pure MOF, 414
  separation theory, 403–405
mercury
  detection by photoluminescence quenching, 347
  grafting onto MOF framework pendant thiols/thioether groups, 344, 347
mesoporous metal–organic frameworks (MesoMOFs), 39–65
  adsorption isotherms, 39, 40, 47, 50, 51
  applications, 39, 49–63
  definition, 39
  design and synthesis, 46–49
  drug delivery, 58–62
  gas storage and separation, 39, 49–51
  heterogeneous catalysts, 51–58
  sensors, 62–63
  solid-phase extraction, 444
  solid supports for biocatalysts, 54–58
  solid supports for heterogeneous catalysts, 53–54
  structures, 40–46
mesoporous nanospheres, nanoscale metal–organic frameworks, 22
metal addition
  dative postsynthetic modification at metal center, 195, 196, 207
  examples, 345–346
  grafting onto MOF framework, 343–344, 347–352
    hard–soft coordination chemistry, 344, 347–348
    ion pair grafting, 352, 354
    ligand defect approach, 352
    organometallics, 350–351
    pendant alcohols and carbenes, 348–349
    PSM creation of pendant ligand sites, 351–352
  in pores/as guests, 352–357
    cation exchange, 352, 354–355
    cation uptake after chemical modification of MOF, 355–356
    pore loading of metal complexes, 356–357
metal carbonates, mechanosynthesis, 174, 181, 183
metal cation metathesis *see* metal ion exchange
metal centers
  see also metal ion exchange
  direct characterization of environments, solid-state NMR, 460–465
  oxidation/reduction, inorganic postsynthetic modification, 210–211
  substitutions of ligands/linkers, 499–511
metal clusters (polynuclear metal complexes), 245, 246, 255
  see also inorganic building units
metal complexes, pore loading, 356–357
metal coordination sphere modification, inorganic postsynthetic modification, 208–213
metal detection, grafting onto MOF framework, 347–348
metal formate with co-ligands (MFL), 222, 223, 228
metal formate dihydrate (MFD), 222–223, 228
metal formate frameworks (MFFs)
  see also ammonium metal formate frameworks
  commensurate adsorption, 324–325
  magnetic metal formate frameworks, 222–223, 228
  porous diamondoid metal formate frameworks, 231–234
metal ion choice, edible metal–organic frameworks, 161
metal ion exchange
  aluminum-based metal–organic frameworks, 105
  inorganic postsynthetic modification, 196, 208, 210, 211–212
  single-crystal to single-crystal transformations, 515–518
  transmetallation, 343, 352, 354, 355, 357–358
metal ions
  see also open metal sites
  hydrogen gas interaction, 285
metalloligand approach
  open metal sites, 260
    hydrogen storage, 264
metalloporphyrin complex incorporation, heterogeneous catalytic MOFs, 277
metallosalen complex incorporation, heterogeneous catalytic MOFs, 276–277

metal–metalloporphyrin frameworks (MMPFs)
gas sorption, 76
MOF-545 analog, 41–42
synthesis strategies, 68–69
metal/metal oxide nanoparticles, sacrificial MOF precursors, 436–437
metal metathesis *see* metal ion exchange
metal nanoparticles, synthesized inside metal–organic framework pores, 25
metaloporphyrins, oxygen reduction catalyst precursors, 438
metal–organic rotaxane frameworks (MORFs) *see* polyrotaxane frameworks
metal oxides, mechanosynthesis of extended metal–organic structures, 174, 181, 183
metal sensing, photoluminescence quenching, 347–348
metal–sulfur networks, semiconducting MOFs, 375–378
metal templated photoreactive ladder coordination polymers, 139
metal–tetracarboxylate porphyrin (M-TCPP) ligands, porphyrinic metal–organic frameworks, 70, 71, 72, 73, 74
metal–thiolate subdomains, semiconducting MOFs, 379–380
metal uptake, 343–361
see also metal addition; metal ion exchange
methane adsorption/storage, 290, 292–297, 327
mesoporous metal–organic frameworks, 50
open metal sites, 265–267
MFC *see* magnetic framework composites
MFD *see* metal formate dihydrate
MFFs *see* metal formate frameworks
MFL *see* metal formate with co-ligands
α-$Mg_3(HCOO)_6$ (α-magnesium formate), solid-state NMR studies of quadrupolar nuclei, 463, 464, 466, 467
^{25}Mg, quadrupolar nuclei, sensitivity to solid-state NMR, 458, 460, 461–463
Mg-MOF-74 (Mg/DOBDC)
carbon dioxide adsorption/storage, 269–270, 288, 306, 307, 308
heterogeneous catalysis, 275
light hydrocarbon separation, 271
structure, 284, 288
microcontact printing (μCP), MOF patterning, 388, 389, 391–393, 394
microfluidic pens, MOF patterning, 392
microfluidics
digital, MOF patterning, 392, 393–394, 395, 396
nanoscale metal–organic framework synthesis, 22, 33
micromolding in capillaries (MIMIC), MOF patterning, 392
microperoxidase-11 (MP-11), mesoporous metal–organic framework encapsulation, 56, 57
microporous carbon or metal/metal oxide nanoparticles, sacrificial MOF precursors, 436–437
microporous metal–organic frameworks (MMOFs)
adsorption mechanisms, 321, 323–326
alcohol adsorption and separation, 333, 335–337
commensurate adsorption, 322, 324–326
hydrocarbon adsorption and separation, 326–333, 334
incommensurate adsorption, 326
mesoporous comparison, 39
structures, 322, 325, 331, 336
micro-solid-phase extraction (μ-SPE), MOF applications, 445–446
microwave-assisted synthesis
aluminum-based metal–organic frameworks, 99, 104, 107
mesoporous metal–organic frameworks, 46
nanoscale metal–organic frameworks, 21
porous coordination polymers, 4, 8–10
MIL (Matérial Institut Lavoisier) series, xylene separation, 332–333
MIL-47
high-performance liquid chromatography, 450
volatile organic compound adsorption, 311–312
xylene adsorption, 312
MIL-47(V)
benzene adsorption, 311–312
H_2S adsorption, 309
xylene separation, 332–333
MIL-53
high-performance liquid chromatography, 450
hydration–dehydration cycle, 333
solid-phase extraction, 444, 445
xylene separation, 333
MIL-53(Al)
H_2S adsorption, 309
high-performance liquid chromatography, 451, 452–453
membranes and variants, gas separation, 411
volatile organic compound adsorption, 312
MIL-53 (Mn(II)) systems, aromatic hydrocarbon separation, single-crystal to single-crystal transformations, 480–481
MIL-88A
as-synthesized/dried/hydrated forms, 162
edible metal–organic frameworks, 160–161, 162–163
synthesis, 160–161
MIL-100
ibuprofen loading, 60
solid-phase extraction, 444, 445
structure, 44, 45
MIL-100(Fe)
high-performance liquid chromatography, 453
light hydrocarbon separation, 271
MIL-101
H_2S adsorption, 309
magnetization, magnetic solid-phase extraction, 445
mixed-matrix membranes, 411–412, 413
polyoxometalate encapsulation, 429
reversible redox reactions, 426–427, 429
solid-phase extraction, 444, 445
volatile organic compound adsorption, 312
MIL-101(Cr), high-performance liquid chromatography, 450, 451
MIL-101 family
carbon dioxide storage, 50–51
catalytic activity, 53, 55
ibuprofen loading, 60
polyethyleneimine incorporation, 50–51
proton conductivity, 435–436
as solid supports for heterogeneous catalysts, 53–54, 55
structure, 44, 45
MIL-101(Fe), MIL-101-NH_2, proton conductivity, 435–436

milling *see* ball milling; liquid-assisted grinding; mechanosynthesis; neat grinding
MIMIC *see* micromolding in capillaries
MIMs *see* mechanically interlocked molecules
mineralizing agents, fluorine, 85, 86
mixed-linker/ligand MOFs *see* mixed metal–organic frameworks
mixed-matrix membranes (MMMs), 403–417
  MOFs, 407–414
  types, 405, 406
mixed metal–organic frameworks (MIXMOFs/M'MOFs)
  acetylene separation/purification, 272
  construction, 260, 265
  guest exchange transformations, 478–479
  postsynthetic modification, 202–203
  structural retention on guest removal, 485
mixing synthetic method, semiconducting MOFs, 382
MIXMOFs *see* mixed metal–organic frameworks
MMMs *see* mixed-matrix membranes
M-MOF-74 series (M/DOBDC CPO-27 series)
  see also Fe-MOF-74; Mg-MOF-74; Ni-MOF-74; Zn-MOF-74
  analog structures, 42–43
  carbon dioxide adsorption, 306
    CO_2/H_2O selectivity, 308
    CO_2/N_2 selectivity, 307
    postcombustion capture, 269–270
  hydrocarbon separation, 271–272, 327
  methane storage, 266, 294
  nitrogen dioxide adsorption, 309
  noble gas (radioactive) adsorption, 314
  structure, 307
MMOFs *see* microporous metal–organic frameworks
M'MOFs *see* mixed metal–organic frameworks
MMPF-1
  gas sorption, 76
  synthesis, 68–69
MMPF-222, MOF-545 analog, 41–42
MMPFs *see* metal–metalloporphyrin frameworks
Mn-btt MOF, deuterium adsorption, 285, 286, 287
Mn-MOF-74, light hydrocarbon separation, 272
MNMs *see* molecular nanomagnets
modular synthesis, definition of MOFs, 374–375
MOF-5
  ammonia adsorption, 310
  direct metallation of arene ring, 350
  edible metal–organic frameworks, 161, 162
  hydrogen storage, 285
  mixed-matrix membranes, 408, 409
  patterning, 398
    magnetic nanocomposites, 395, 396
    promoting agents, 388, 389–390
    surface patterning, 393, 394
  pore loading by metal complexes, 356, 357
  solid-phase extraction, 443–444
  stability, 316
  structural retention on guest removal, 485
  structure, 284
  volatile organic compound adsorption, 311, 312
MOF-5 analogs
  see also IRMOF-3; IRMOF-16; $Zn_4O(dtabc)_3$
  metal grafting, 344, 352
  photoluminescence quenching by metals, 347
  structure, 40–41
MOF-53(Al), characteristics, 99–100
MOF-53(Fe)
  drug delivery, 160
  edible metal–organic frameworks, 161, 162
MOF-177
  ammonia adsorption, 310
  carbon dioxide adsorption, 306
MOF-199, coated fibers, solid-phase microextraction, 445
MOF-505
  acetylene storage, 267
  hydrogen storage, 261–262
MOF-505 analogs, acetylene storage, 268
MOF-545 analogs, structure, 41–42
molds and stamps, MOF patterning, 391, 392, 393
molecular bowls, mechanochemical construction by neat grinding, 174, 175
molecular gates
  rotational modules, 496–497
  single-crystal to single-crystal transformations, 479–480, 487, 492, 496–497, 502
molecular nanomagnets (MNMs), 246
  see also single-molecule magnets
molecular recognition, single-crystal to single-crystal transformations, 518–520
molecular rotors *see* solid-state rotational dynamics
molecular sieves, solid-phase microextraction coupled with gas chromatography, 449
molecular simulations, gas adsorption, 311, 312, 315, 316
molecular squares, mechanochemical construction by neat grinding, 174, 175
molecular switches
  light-induced molecular release systems, 16
  polyrotaxane frameworks, 119, 128, 130, 132
molybdenum (Mo), polyoxometalate-metal–organic frameworks, 428
Monte Carlo simulations
  see also Grand Canonical Monte Carlo simulations
  modulators in crystal growth, 10
MORFs (metal–organic rotaxane frameworks) *see* polyrotaxane frameworks
MP-11 *see* microperoxidase-11
MQMAS *see* multiple quantum magic angle spinning
MQT *see* magnetic quantum tunneling
MRI *see* magnetic resonance imaging
MSPDE *see* matrix solid-phase dispersion extraction
MSPE *see* magnetic solid-phase extraction
M-TCPP *see* metal–tetracarboxylate porphyrin
Mukaiyama aldol reaction, MOF catalysis, 275
multiferroic materials, metal formate frameworks, 224, 227, 229–231, 234, 237
multifunctional materials
  metal formate frameworks, 222, 227, 233–234
  MOFs from single-molecule magnets, 246
multiple quantum magic angle spinning (MQMAS)
  solid-state NMR studies of quadrupolar nuclei, 459–460, 464

multiple substitutions at the metal center single-crystal to single-crystal transformations, 510
multivariate MOFs *see* mixed metal–organic frameworks
μCP *see* microcontact printing
μ-SPE *see* micro-solid-phase extraction
myoglobin (Mb), Tb-mesoMOF hierarchical nanoscopic cage encapsulation, size selective biocatalysis, 57, 58

nanocages, mesoporous metal–organic framework, 44, 54, 56
nanocomposites, metal–organic framework hybrids, 25–27, 29, 31–32
nanofibers, nanoscale metal–organic frameworks, 22
nanofilms, layering porphyrinic metal–organic framework sheets, 77
nanolithography, 33
nanomagnets, 246
  see also single-molecule magnets
nanoMOFs *see* nanoscale metal–organic frameworks
nanoparticles
  generation, photochemical processes in MOFs, 369
  pore loading of metal complexes, 53–54, 56, 356–357
  porous coordination polymers, 3
    nanocrystal synthesis and morphology, 4–11
  sacrificial MOF precursors, 436–437
nanoparticle templates, nanoscale metal–organic framework synthesis, 25–26
nanorods
  gold, photoresponsive metal–organic frameworks, 154
  synthesis, nanoscale metal–organic frameworks, 22
nanoscale metal–organic frameworks (nanoMOFs/NMOFs), 19–37
  0D particles, 20–22
  1D fibers and tubes, 22
  2D sheets, 22–23
  applications, 27–32
  drug delivery, 58, 60–61
  hybrid composites, 25–27, 29, 31–32
  superstructures, 27
  surface integration, 23–25
  synthesis, 20–27, 33
nanosheets, 2D nanoscale metal–organic frameworks, 22–23
nanospheres, nanoscale metal–organic frameworks, 21–22, 26
nanotherapeutic formulations, mesoporous metal–organic framework, 58, 60–61
nanotubes
  nanoscale metal–organic frameworks, 22
  threefold entangled structures, controllable gate-opening, 479–480
2,6-naphthalene-dicarboxylate, 9^{2-} axles, Texas-Sized Molecular Box, 126
naphthalene diimide (NDI), photoactive ligands for guest detection, 364–365
natural gas treatment, polymer membranes, 403, 405–406
NDI *see* naphthalene diimide
N-donor groups, pendant ligand binding sites for metal grafting, 344, 347, 348
neat grinding
  mechanosynthesis of coordination bonds, 174–175
  mechanosynthesis of extended structures by ligand addition, 179
neutral MOFs, anionic chemical modification to induce cation uptake, 355–356
neutron powder diffraction (NPD) studies, hydrogen adsorption at open metal sites, 261
niccolites, ammonium magnetic metal formate frameworks, 226–227
nickel aspartates, edible metal–organic frameworks, 163–164
Ni-MOF-74 (Ni/DOBDC)
  carbon dioxide adsorption/storage, 269–270, 288, 306, 307, 308
  methane storage, 266, 267, 294
  nitrogen dioxide adsorption, 309
  noble gas (radioactive) adsorption, 314
  structure, 288
nitroaromatic explosive detection, single-crystal to single-crystal transformations, 478, 479
nitrogen dioxide adsorption, 309
nitrogen oxides, environmental concern, 305, 309
nitrous oxide (NO)
  delivery to biological tissues, 309
  storage, 309
NMOFs *see* nanoscale metal–organic frameworks
NMR *see* nuclear magnetic resonance; solid-state nuclear magnetic resonance
NO *see* nitrous oxide
noble gas adsorption
  radioactive xenon and krypton removal, 314–315, 316
  xenon/krypton and xenon/argon selection, 314–315
nontrivial versus trivial entanglement, polyrotaxanes, 533, 534, 535
normal-phase high-performance liquid chromatography (NP HPLC), MOF applications, 449–452, 453
NOTT-7, methane storage, 266
NOTT-107, methane storage, 294–295
NOTT-112a, carbon dioxide adsorption, 270
NOTT-300, sulfur dioxide removal, 309
NOTT series (NOTT-100 to 108), hydrogen storage, 262
NPD *see* neutron powder diffraction
NP HPLC *see* normal-phase high-performance liquid chromatography
NU-125, methane storage, 296
NU-1000, MOF-545 analog, 41, 42
nuclear magnetic resonance (NMR)
  see also solid-state nuclear magnetic resonance
  photoreactive MOFs, 137–138, 140–145, 147, 150–153
  postsynthetic modification, 197
nucleation
  MOF patterning by promoting agents, 389–390
  nanoscale metal–organic frameworks, 20–21
nucleobases, edible metal–organic frameworks, 166–169

OCPP *see* tetrakis(3,5-dicarboxyphenyl)porphine
oil spill cleanup, fluorinated metal–organic frameworks, 85, 96

olefin bonds
photoreactive ladder coordination polymers, 140, 141
photoreactive molecules, 135–136
olefins (alkenes), adsorption and separation, 326, 327–330
olefin–paraffin separation, 298
OMSs *see* open metal sites
open frameworks, mechanochemical MOF synthesis, 173–191
open metal sites (OMSs/UMCs/CUS), 259–281
acetylene separation/purification, 272–273
acetylene storage, 267–269
alcohol adsorption, 335
alignment, hydrogen adsorption, 262
carbon dioxide adsorption, 269–270, 288, 306
electrochemical properties, 419–420
gas storage, 261–269, 284, 285
heterogeneous catalysis, 274–277
hydrocarbon separation and storage, 271–272, 298
hydrogen storage, 261–265, 285, 286, 287
methane storage, 265–267, 294
MIL-101 family catalysis, 53
nitrous oxide adsorption, 309
oxygen storage, 297
postcombustion carbon dioxide capture, 269–270
selective gas separation, 269–273
sensing small molecules, 273–274
order–disorder transitions
copper formate tetrahydrate, 223
magnetic metal formate frameworks, 225, 226, 227
organic additives, crystal size/morphology determination, 7
organic linkers *see* linkers
organic-polymer@MOF nanocomposites, 25, 26
organic solvents
see also solvents; volatile organic compounds
aluminum-based metal–organic frameworks, 103–104, 108
biocatalysts stability, 54, 56
edible MOFs, 160, 161
HPLC, 452
undesirability in MOF synthesis, 160, 174
organic-solvent-substituted single crystals, guest-shape-responsive fitting, 476
organic transformation, reagent addition, covalent postsynthetic modification, 197–203
organometallic complexes
direct metallation of arene ring ligands, 350
grafting onto pendant functional groups, 350–351
pore loading, 356–357
ORR *see* oxygen reduction reaction
oxidation catalysts, porphyrinic metal–organic frameworks, 79–81
oxidation/reduction reactions, framework metal centers, inorganic postsynthetic modification, 210–211
oxide@MOF nanocomposites, 25, 27
oxygen reduction reaction (ORR)
electrocatalytic MOFs, 432–434
sacrificial MOF catalyst precursors, 437–438
oxygen species, spectral signatures, ^{17}O solid-state NMR, 465–468
oxygen storage, 297–298
packed column gas chromatography, MOF applications, 335, 446
PAHs *see* polycyclic aromatic hydrocarbons
paraelectricity (PE)
transition to antiferro-electric, magnetic metal formate frameworks, 228, 231
transition to ferro-electric, magnetic metal formate frameworks, 225, 228, 230, 234
paraffins (alkanes), adsorption and separation, 326, 327–330
paraffin–olefin separation, 298
parallel interpenetration, 524–525
paramagnetic metal ions
contrast agents, 30–31
metal clusters, 246
particle growth control, capping agents, nanoMOFs, 21
patterning techniques, 387–401
controlled thin film growth, 388–389
digital microfluidics, 393–394, 395
electrochemical approach, 390–391
evaporation-induced growth, 391–393
external control of fabrication, 390–397
films from colloidal MOF solutions, 396–397
magnetic particles, 394–396
microcontact printing, 388, 389, 391–393, 394
preformed MOFs, 394–397
promoting agents, 388–390
seeding method, 389–390
PB *see* Prussian blue
PBAs *see* Prussian blue analogs
PCN-6X series (PCX-61/66/68), methane storage, 295–296
PCN-11, methane storage, 293–294
PCN-14
adip^{4-}11 ligand structure, 293
methane storage, 266, 292
PCN-100/PCN-101, Knoevenagel condensation catalysis, 52, 53
PCN-222, MOF-545 analog, 41–42
PCPs *see* porous coordination polymers
pcu topology
3D MOFs from single-molecule magnets, 254
entanglement, 536
interpenetration, 528, 530
PDMS *see* polydimethylsiloxane
P-donor groups, pendant ligand binding sites for metal grafting, 348
PE *see* paraelectricity
pedal motion of ligand groups, reversible guest exchange/removal behavior, 497–498
PEI *see* polyethylene imine
PEMs *see* polymer electrolyte membranes
pendant ligand metal-binding sites
grafting additional metals onto MOF framework, 343–344, 347–352
alcohols and carbenes, 348–349
hard–soft coordination chemistry, 344, 347–348
N and P donor atoms, 348
pendant thiols/thioether groups, 344, 347–348
post synthetic pendant site creation, 351–352
organometallics, 350–351
pentane, separation, 330

pentane, separation (*continued*)
peptides, edible metal–organic frameworks, 165–166
permanent inner porosity, metal–organic frameworks for gas storage, 283–284
permanently interlocked [2]rotaxane linkers, polyrotaxane frameworks, 128–130, 131
permeabilities, membranes, 404–405
permeability/selectivity trade off, membranes, 405–406, 407
perovskites, ammonium magnetic metal formate frameworks, 226
persistent organic pollutants (POPs), GC separation, 447–448
phase transitions, magnetic metal formate frameworks, 222, 226–232, 234, 237
photoactivation, protecting group cleavage in MOFs, 365–366
photoactive groups, 363–371
  guest detection, 364–365
  isomerization product studies, 366–367
  MOF modified reactions, 365–367
  photochemical modification of MOFs, 365–367
photocatalysts, porphyrinic metal–organic frameworks, 81
photochemical processes
  dimerization reactions, historical background, 135–136
  light harvesting, porphyrinic metal–organic frameworks, 77–78
  modification by MOF structure, 367–370
  postsynthetic modification of MOFs, 204, 206, 365–367
photo-cycloaddition, metal–organic framework formation, 145
photogenerated reactive species, 365
photo-isomerization
  photoactive groups in MOFs, 366–367
  photoresponsive MOFs, 154, 155
photolithography, preformed MOF crystals, MOF patterning, 397
photolithography assisted fabrication, MOF patterning, 388, 390, 397
photoluminescence quenching, heavy metal grafted MOFs, 347
photo-polymerization, coordination polymers, 154–155
photoreactive 1D coordination polymers, creating 2D structures, 143–144
photoreactive 2D coordination polymers, control of pore size and gas uptake properties, 147
photoreactive 3D coordination polymers, 150–153
photoreactive coordination polymers, 135
  formation from metal complexes by [2+2] cycloaddition, 136–137
  photo-polymerization, 154
photoreactive ladder coordination polymers, 137–143
  bpe pairs occupying rungs, 139
  carboxylate bridged, 137–139
  containing bioactive dicarboxylates, 140
  double [2+2] cycloaddition reactions, 140
  metal templated, 139
  step-wise double [2+2] cycloaddition in structures, 139–140
photoreactive metal–organic frameworks, 135–157
  double-pillared
    conjugated C=C bond containing ligands, 151
    PSM by [2+2] cycloaddition, 150–151
  formation from photoreactive 2D interdigitated coordination polymers, 149
  lanthanides, 152–153
photoreactive properties in MOFs, 363–371
  guest detection, 364–365
  modification of processes within MOFs, 367–370
  postsynthetic modification of MOFs, 365–367
photoreactivity
  1D coordination polymers
    forming 2D structures, 143–144
    forming 3D structures, 145
    triple stranded polymers, 144
photoreactivity-induced structural transformations, 2D coordination polymers, 147–148
photoresponsive metal–organic frameworks, 153–154
  carbon dioxide adsorption, 153
  dynamic photo-switching of spacer ligands, 153
  gas adsorption, 153, 154
  light-induced release of molecules, 154
photo-switching
  dynamic switching of spacer ligands, 153
  light-induced molecular release systems, 16
photosynthesis-like light harvesting, porphyrinic metal–organic frameworks, 77–78
physisorption mechanisms, 321–323
  carbon dioxide, 305–306
  MOFs, 323–326
pillared-layer metal–organic frameworks
  host–guest photoreactions, 151–152
  self-assembly, 510
pillared structures, porphyrinic metal–organic frameworks, 72–73
π-stacking, interpenetrated networks, 528–529, 531
plasma-enhanced chemical vapor deposition, fluorinated metal–organic frameworks, 90–91
pollution *see* air pollution; environmental issues; persistent organic pollutants
polycarboxylic linker molecules, aluminum-based metal–organic frameworks, 99, 103, 106, 109
polycatenation, 524
polycyclic aromatic hydrocarbons (PAHs), solid-phase extraction with MOFs, 444, 445, 446
polydimethylsiloxane (PDMS), molds and stamps, MOF patterning, 391, 392, 393
polyethylene imine (PEI)
  crystal size/morphology determination, 4–5, 6
  MIL-101 loading, carbon dioxide storage, 50–51
polymer amount, particle growth control, nanoscale metal–organic frameworks, 21
polymer electrolyte membranes (PEMs), fuel cell, 434–436, 437–438
polymer membranes
  see also mixed-matrix membranes
  additives, 406
  modification options, 405–406
  MOF addition advantages, 403, 407
  plasticization, 406
  repeat units, 412

polymer monoliths, MOF composites, high-performance liquid chromatography, 454
polymer–surfactant combination, particle growth control, nanoscale metal–organic frameworks, 21
polynuclear metal complexes (metal clusters), 245, 246, 255
see also inorganic building units
polyoxometalate-metal–organic frameworks (POMOFs)
electrocatalysts, 432, 434
electrochemical properties, 419–420, 428–430
polyoxometalates (POMs)
Keggin type, 107, 312, 428–429
porphyrinic metal–organic frameworks, 73
PSM functionalization, VOC adsorption, 312
Wells–Dawson type, redox-active MOF composites, 429–430
polyrotaxane frameworks (PRFs), 115–133
cucurbit[6]uril wheels, 115–119
dibenzo[24]crown-8 wheels, 119–126
entanglement, 523, 533–535
[2]pseudorotaxane linkers, 116–128
rotational dynamics, 130–132
[2]rotaxane linkers, 128–132
Texas-Sized Molecular Box, 126–127
trivial versus nontrivial entanglement, 533, 534, 535
wheels with donor groups, 128–130
polysulfone membrane, mixed-matrix membranes with MOFs, 406, 407, 410, 411, 412, 414
POMOFs *see* polyoxometalate-metal–organic frameworks
POMs *see* polyoxometalates
POPs *see* persistent organic pollutants
pore characteristics
alcohol adsorption, 335–336
functional group incorporation from linkers, 195
mesoporous metal–organic frameworks, 39, 40
pore loading, metal complexes/nanoparticles, 356–357
pore shape change
see also guest-shape-responsive fitting
framework distortion with temperature and dehydration, 489–490
pore shrinkage and expansion
dynamic frameworks, single-crystal to single-crystal transformations, 488–489
guest-shape-responsive fitting, single-crystal to single-crystal transformations, 481
reversible guest removal properties, single-crystal to single-crystal transformations, 487
pore size
gas adsorption effects, 304
hydrogen sulfide reversible adsorption, 309
ion-size effects, 420
IUPAC definitions, 39
porosity
see also permanent inner porosity; van der Waals potential pockets
diamondoid metal formate frameworks, 231–232
metal–organic frameworks for gas storage, 283–284
porous coordination polymers (PCPs)
crystal assembly into macrostructures, 11–16
crystal synthesis and morphology, 4–11
introduction, 3–18
porous diamondoid metal formate frameworks, 231–234
magnetism and multifunctionalities, 233–234
structures and physical characteristics, 231–233
porous materials, commensurate adsorption, 324–326
porphyrinic metal–organic frameworks, 67–83
applications, 76–81
gas storage and separation, 76–77
heterogeneous catalysts, 78–81
light harvesting and energy transfer, 77–78
nanofilms, 77
photochemical processes, 369–370
selective sorption, 77
synthesis strategies, 67–76
porphyrin ligands, structures, 68
positioning MOFs
see also patterning techniques
methods, 388–397
postcombustion carbon dioxide capture *see* carbon capture and sequestration; flue gases
postsynthetic exchange (PSE) *see* inorganic postsynthetic modification; ligand substitution; metal ion exchange
postsynthetic modification (PSM), 195–218
see also ligand substitution; metal ion exchange
aluminum-based metal–organic frameworks, 100, 105–106, 107, 109
characterization, 196–197
covalent, 195, 196, 197–204, 206
dative, 195, 196, 205, 206–208
edible metal–organic frameworks, 167
electrochemical reactions, 206
functionalized MOFs, volatile organic compound adsorption, 312
grafting additional metals onto framework, 343–344, 347–352
heterogeneous catalysts, 52, 54, 56
inorganic, 196, 208–213
ligand substitution, 196, 208–209, 212–213
metal center modification, 196, 208, 210–212
metal ion insertion, carbon dioxide adsorption, 270
metal–thiolate links, semiconducting MOFs, 378
open metal sites, hydrogen storage, 264
photochemical processes, 204, 206, 365–367
prodrugs, 61, 203
reagent addition, 197–203
secondary building units, 196, 208–213
single-crystal to single-crystal transformations, 473–522
thermal reactions, 203–204
transmetallation, 357–358
types, 195–196
potassium benzoate, edible metal–organic frameworks, 170
powder X-ray diffraction (PXRD)
crystallization studies, aluminum-based metal–organic frameworks, 99, 106, 108
peptide-based edible MOFs, 166
postsynthetic modification characterization, 196–197
power stations *see* flue gases
preformed MOF crystals, photolithography, MOF patterning, 397
PRFs *see* polyrotaxane frameworks
prodrugs, 61, 203

promoting agents
MOF patterning, 388–390
controlled thin film growth, 388–389
seeding method, 389–390
propane
adsorption, 325–326, 327, 328
separation, 329–330
propene, separation, 329–330
proteins
edible metal–organic frameworks, 165–166
mesoporous metal–organic frameworks encapsulation, 58, 59, 60
solid-phase extraction with MOFs, 444
solid supports for biocatalysts, 54–58
protonated amine cations *see* ammonium cations
proton-conductive membranes, fuel cells, 434–436
proton transfer, mechanosynthesis of metal–organic structures, 180–181
Prussian blue/Prussian blue analogs (PB/PBAs), rechargeable batteries, 431, 432
PSE (postsynthetic exchange) *see* inorganic postsynthetic modification; ligand substitution; metal ion exchange
pseudomorphic replacement, porous coordination polymer crystal assembly, 14–16
[2]pseudorotaxane linkers, polyrotaxane frameworks, 116–128
PSM *see* postsynthetic modification
purification of gases
acetylene adsorption, open metal sites, 272–273
inorganic toxic gas removal, 309–310, 315–316
PXRD *see* powder X-ray diffraction
pyrazine MOFs
commensurate adsorption, 324, 325
mechanosynthesis, 179, 209
metal formate frameworks, 235
self-penetrating networks, 532
pyridine-based ligands, fluorinated metal–organic frameworks, 86
pyridinium-based axles, dibenzo[24]crown-8 wheels, polyrotaxane frameworks, 119, 120, 123–125
pyrimidine (pym) ligands, metal formate frameworks, 235

QDs *see* quantum dots
QENS *see* quasielastic neutron scattering
quadrupolar coupling constant (C_Q), 458, 459
quadrupolar interactions, solid-state NMR, 458, 459, 460
quadrupolar nuclei, 457–470
quantum dots (QDs), light harvesting by porphyrinic metal–organic frameworks, 78
quasielastic neutron scattering (QENS), benzene adsorption, 311

radioactive gas immobilization, 304, 305, 313–315
RCPs (rotaxane coordination polymers) *see* polyrotaxane frameworks
reactive species
photogenerated within MOFs, 365
trapping, dynamic guest accommodation, 478
reagent addition, covalent postsynthetic modification, 197–203
receptivity (sensitivity) of quadrupolar nuclei, solid-state NMR, 458, 460
rechargeable batteries, MOF applications, 210, 355, 420, 430–432, 437
redox-active MOFs
chromium, 426–428
copper, 426
electrochemical properties, 420, 422–430
ferrocene, 423, 425
iron, 425–426
polyoxometalate-metal–organic frameworks, 428–430
standard hydrogen electrode comparison, 427–428, 429
reduction/oxidation reactions at metal centers, inorganic postsynthetic modification, 210–211
reverse microemulsion (water-in-oil or reverse micelles), crystal size/morphology determination, 5–7
reverse-phase high-performance liquid chromatography (RP HPLC), MOF applications, 452–453
reversible photochemical reactions, thermal cyclo-reversion, 146–147
reversible redox responses, electrochemical properties of MOFs, 420, 422–430
reversible uptake and release of guests
see also guest exchange; guest removal
single-crystal to single-crystal transformations, 474
rhomicuboctaheral cages, porphyrinic metal–organic frameworks, 68–69
rht net, mesoporous metal–organic frameworks, 43–44
rigidity of MOFs, 373–374
see also flexibility of MOFs
metal clusters, 246
metal ion effects, 108, 211
organic linkers, 109, 283–284, 373–374
semiconductors, 374, 381
robust MOF structures, guest removal, single-crystal to single-crystal transformations, 485–488
rotational dynamics
pedal motion of ligand groups, 497–498
polyrotaxane frameworks, 130–132
reversible guest removal/exchange, 491, 492, 497–498
rotational freedom in linkers, guest removal/exchange, 475
rotational modules, dynamic framework changes, 496–498
rotaxane coordination polymers (RCPs) *see* polyrotaxane frameworks
rotaxane linkers, polyrotaxane frameworks, 128–132, 533–534
RP HPLC *see* reverse-phase high-performance liquid chromatography
rtct *see* regio trans-cis-trans
rubbery polymers, membranes, 405
rubeanato-Cu(II) systems, semiconducting MOFs, 375–376

sacrificial MOFs
electrochemical applications, 436–438
nanoparticle precursors, 436–437
oxygen reduction reaction catalysts, 437–438

rechargeable batteries, 437
supercapacitors, 437
SALE *see* solvent-assisted linker exchange
salt catalysts, mechanosynthesis of metal–organic structures, 177, 178, 184
sample preparation for solid-phase extraction, MOF applications, 443–446
SAMs *see* self-assembled monolayers
saturated versus unsaturated hydrocarbons
adsorption mechanisms, 327, 328
separation, 329–330
SAXS *see* small-angle X-ray scattering
SBB *see* supermolecular building block
SBUs *see* secondary building units
^{45}Sc, quadrupolar nuclei, sensitivity to solid-state NMR, 458, 460
scanning electron microscopy (SEM), mechanosynthesis of MOFs, 189–190
SC–SC *see* single-crystal to single-crystal transformations
S-donor groups, pendant ligand binding sites for metal grafting, 344, 347
secondary building units (SBUs)
anionic part, inorganic postsynthetic modification, 209–210
inorganic postsynthetic modification, 196, 208–213
mesoporous metal–organic frameworks, 42, 43, 46, 47
single-crystal to single-crystal transformations, 485–488
secondary growth process, crystallization site positioning, 12
seeding method, MOF patterning by promoting agents, 389–390
selective adsorption of guest molecules, porphyrinic metal–organic frameworks, 77
selective gas adsorption
carbon dioxide over nitrogen, 307
carbon dioxide over water vapor, 308
xenon/krypton, 314–315, 316
selective recognition and catalysis, single-crystal to single-crystal transformations, 518–520
selectivity
see also separation
membranes, 404–405
selectivity/permeability trade off, membranes, 405–406, 407
self-assembled monolayers (SAMs)
crystallization site positioning, 13–14
gas chromatographic capillary columns, 392
MOF patterning, 388–389, 392
nanoscale metal–organic frameworks on surfaces, 24–25
self-assembly
kinetic and pathway studies, 510
nanoscale metal–organic framework superstructures, 27, 28, 33
pillared-layer metal–organic frameworks, 510
self-penetration, 532–533
SEM *see* scanning electron microscopy
semiconducting MOFs, 373–384
one-pot strategy for less-ordered metal–thiolate frameworks, 380–382
sulfur groups, 375–378
two-step strategy, 378–380
sensitivity, quadrupolar nuclei, solid-state NMR, 458, 460
sensors
explosives detection, 32, 365, 478, 479
luminescent VOCs/tropospheric air pollutant sensing, 364–365
mesoporous metal–organic frameworks, 62–63
metal detection, photoluminescence quenching, 347–348
nanoscale metal–organic frameworks, 32
open metal sites, 273–274
photoreactive properties, 364–365
temperature-sensing fluorescent devices, 63
separation mechanisms
see also selective adsorption; selectivity
physisorption, 322
separation theory, membranes, 403–405
severing synthetic method, semiconducting MOFs, 382
shape-dependent properties, porous coordination polymers, 3
shape-response filling of pores
see also guest-shape-responsive fitting
selective recognition and catalysis, 518–519
SHE *see* standard hydrogen electrode
ship-in-a-bottle configuration, porphyrinic metal–organic frameworks, 74–75
silica/MOF composites, high-performance liquid chromatography, 453–454
silver centers
Ag(I) porous coordination polymer, distortion with temperature and dehydration, 489–490
polyrotaxane frameworks, 116, 117, 118, 126, 129–130
simulations
CO_2/N_2 selectivity, 307
comparison with experimental Brunauer-Emmett-Teller surface area, 295
gas adsorption, 311, 312, 315, 316
hydrocarbon separation, 332, 333
krypton/xenon separation, 314–315
methane adsorption, 294
modulators in crystal growth, 10
volatile organic compound adsorption, 311, 312, 316
single component isotherms, gas selection prediction, 290, 307
single-crystal to single-crystal (SC–SC) transformations, 473–522
anion exchanges in MOFs, 511–515
cation exchanges in MOFs, 515–518
dynamic frameworks, 488–496
guest removal, 485–488
lattice guest exchanges, 474–485
ligand components, 496–498
metal uptake
anion–cation exchange, 354
grafting onto framework, 348, 352
transmetallation, 357, 358
selective recognition and catalysis, 518–520
substitutions at the metal center, 498–511
single crystal X-ray crystallography, postsynthetic modification characterization, 197
single molecular traps (SMTs), carbon dioxide storage, 288, 289–290, 291
single-molecule magnets (SMMs), 245–258
2D MOFs, 247–252
3D MOFs, 253–255

single-molecule magnets (SMMs) (*continued*)
cobalt clusters, 251, 252, 253
crystal packing effects, 246, 256
lanthanide clusters, 251
manganese clusters, 247–251, 252–255
MOF formation, 246–247
terminology, 246
size-dependent properties, porous coordination polymers, 3, 10–11
size exclusion separation, membranes, 403
size selective biocatalysis, mesoporous MOFs, myoglobin encapsulation, 57, 58
small-angle X-ray scattering (SAXS), crystallization studies, aluminum-based metal–organic frameworks, 106, 107
small hydrocarbons
see also methane
separation, 271–272, 326–330
small molecule sensing, open metal sites, 273–274
SMMs *see* single-molecule magnets
SMTs *see* single molecular traps
sodium ion batteries, MOF applications, 431
soft-pulse-added-mixing triple-quantum magic-angle spinning (SPAM-3QMAS), solid-state NMR studies of quadrupolar nuclei, 464
solid–liquid interface, porous coordination polymer crystal assembly, 12–14
solid-phase extraction (SPE), MOF applications, 443–445
solid-phase microextraction (SPME)
coupled with gas chromatography, tandem molecular sieves, 449, 450
MOF applications, 445
solid solutions, mechanosynthesis, 186–187
solid-state [2+2] cycloaddition reactions, historical background of photochemistry, 135–136
solid-state chemistry, mechanosynthesis, 173–191
solid-state nuclear magnetic resonance (SSNMR)
benzene adsorption, 311
crystallization studies, aluminum-based metal–organic frameworks, 99, 106–108
direct characterization of metal center environments, 460–465
edible MOFs, 166, 170
mechanosynthesis, 178
photoreactive MOFs, 137–138, 140–145, 147, 150–153
polyrotaxane frameworks, rotational dynamics, 131, 132
postsynthetic modification characterization, 197
quadrupolar nuclei in MOFs, 457–470
spectral signatures of oxygen species, 465–468
theory, 458–460
solid-state rotational dynamics, polyrotaxane frameworks, 130–132
solution-diffusion separation, membranes, 403–404, 405
solvent-assisted grinding/solvent-drop grinding *see* liquid-assisted grinding
solvent-assisted linker exchange (SALE), inorganic postsynthetic modification, 213
solvent choice, edible metal–organic frameworks, 160, 161
solvent effect removal, photoactive groups in MOFs, 366
"solvent-free" synthesis, mechanochemical approaches, 173–191
solvent removal
edible metal–organic frameworks, 162, 165, 166, 168, 170
open metal sites, 260
solvents
aluminum-based metal–organic frameworks, 100, 101–104
catalytic amounts of liquid phase, mechanosynthesis of metal–organic structures, 174, 176, 185
sensor effects, open metal site MOFs, 263, 273–274
solubility problems, mechanosynthesis solutions, 174
solvothermal synthesis
see also hydrothermal synthesis
aluminum-based metal–organic frameworks, 100, 104
mesoporous metal–organic frameworks, 46
porphyrinic metal–organic frameworks, 67, 68, 79
typical procedure, 303–304
sonochemistry synthesis, nanoscale metal–organic frameworks, 21
SPAM-3QMAS *see* soft-pulse-added-mixing triple-quantum magic-angle spinning
SPE *see* solid-phase extraction
spectral signatures of oxygen species, ^{17}O solid-state NMR, 465–468
spectroscopic studies
see also nuclear magnetic resonance; solid-state nuclear magnetic resonance
postsynthetic modification characterization, 197
spin-crossover nanoscale metal–organic frameworks, magnetism, 32
SPME *see* solid-phase microextraction
spongelike behavior, dynamic frameworks, 490, 491
spray-drying, nanoscale metal–organic framework synthesis, 33
sql topology, 2D MOFs from single-molecule magnets, 250, 251, 252
srs topology, 3D MOFs from single-molecule magnets, 255
SSNMR *see* solid-state nuclear magnetic resonance
stability of MOFs
against agglomeration, nanoMOFs, 21
Al-based MOFs, 99, 105, 110
mesoporous MOFs, 56, 60
semiconducting MOFs, 381
stabilization of reactive species
dynamic guest accommodation, 478
light transformed MOFs with photoactive groups, 365
stabilizing agents, capping particle growth, nanoscale metal–organic frameworks, 21
stacking models, porphyrin rings, metal effects, 70
stainless steel wire, MOF coatings, fibers for solid-phase microextraction, 445
stamps and molds, MOF patterning, 391, 392, 393
standard hydrogen electrode (SHE), redox-active MOF comparison, 427–428, 429
stepwise mechanisms, mechanosynthesis, 184, 187–188, 189
stepwise self-assembly, kinetic and pathway studies, 510
steric hindrance effects, fluorinated metal–organic frameworks, 94
structural dynamics
mechanosynthesis of MOFs, 185–186
single-crystal to single-crystal transformations, 473–522
struts *see* linkers

4-styrylpyridine ligands, photoreactive coordination polymers, 143–144
subsidiary net construction, semiconducting MOFs, 379–380
substrate surface reactive groups, crystallization site positioning, 13–14
sulfur
  rubeanic acid moieties, semiconducting MOFs, 375–376
  thiol units, semiconducting MOFs, 376–380
sulfur–carboxyl group combination, semiconducting MOFs, 377–378
sulfur dioxide
  adsorption, 309
  environmental concern, 305, 309
sulfur–metal interactions, semiconducting MOFs, 376
supercapacitors, 419, 430–432, 437
supermolecular building block (SBB) strategy, porphyrinic metal–organic framework synthesis, 67–69
superstructures
  nanoscale metal–organic framework self-assembly, 27, 28, 33
  porous coordination polymer crystal assembly, 11–16
supramolecular chemistry
  MOFs from single-molecule magnets, 245–258
  polyrotaxane frameworks, 115–133
surface area of MOFs *see* Brunauer-Emmett-Teller surface area; Langmuir surface area
surface metal–organic frameworks (SURMOFs)
  nanolithography, 33
  nanoscale metal–organic frameworks on surfaces, 23–25
    gas separation, 28
    magnetism, 32
    sensors, 32
surfactants, particle growth control for nanoscale MOFs, 21
SURMOFs *see* surface metal–organic frameworks
swing motion, framework dynamics on guest removal/exchange, 485, 491
synthesis of MOFs *see* Langmuir–Blodgett film synthesis; mechanosynthesis; microwave-assisted synthesis; patterning techniques; self-assembly; solvothermal synthesis; ultrasonication-assisted synthesis

tags, reactive group on linker for postsynthetic modification, 196
tandem molecular sieves, solid-phase microextraction coupled with gas chromatography, 449, 450
tandem postsynthetic modifications, 196, 201, 202, 207
TATB *see* 4,4′,4″-*s*-triazine-2,4,6-triyltribenzoate
Tb(BTC), sensors, 274
Tb-mesoMOF
  biocatalyst encapsulation, 56–58, 59, 60
  structure, 44
tbo net, mesoporous metal–organic frameworks, 44
TCPP *see* tetracarboxylate porphyrin
TEA *see* triethylamine
Teflon like channeled nanoporous MOFs, hydrocarbon sorption, 95
temperature-dependent structural changes
  aluminum-based metal–organic frameworks, 108–109
  framework distortion and pore shape, 489–490
temperature-sensing fluorescent devices, JUC-48/Rh6G, 63
tempering synthetic method, semiconducting MOFs, 376, 377, 382
template-based synthesis
  Cu-templated pseudorotaxane frameworks, 127
  hierarchical mesoporous metal–organic frameworks, 46, 47–48, 49
  MOF nanocomposites with nanoparticles, 25, 26
  nanoscale metal–organic frameworks, 22
  PCP crystallization, 13, 16
  photoreactive ladder coordination polymers, 139
  superstructures from nanoMOFs, 27
template-free synthesis, hierarchical mesoporous metal–organic frameworks, 46, 48
terbium
  mesoporous MOFs, 44, 56–58, 59, 60
  polyrotaxane frameworks, 117–118
  Tb(BTC) sensors, 274
terephthalic acid, edible metal–organic frameworks, 161
terminal ligand substitution, inorganic postsynthetic modification, 208–209
ternary metal formate frameworks incorporating alkali metal ions, functional magnetic materials, 224
tetracarboxylate porphyrin (TCPP) ligands, porphyrinic metal–organic frameworks, 68, 70
5,10,15,20-tetrakis(4-sulfonatophenyl)porphyrin (TPPS), porphyrinic metal–organic frameworks, 68, 70, 71
tetrakis(3,5-dicarboxyphenyl)porphine (OCPP), porphyrinic metal–organic frameworks, 68, 69
tetrakis(methylthio)benzenedicarboxylic acid (TMBD) building blocks, semiconducting MOFs, 379
tetranuclear manganese clusters, MOFs from single-molecule magnets, 249–250, 253–254
tetranuclear metal–organic square, mechanochemical construction by neat grinding, 174, 175
Texas-Sized Molecular Box (TSMB), polyrotaxane frameworks, 126–127
thermal annealing, ground material, mechanosynthesis of coordination bonds, 175, 181, 182
thermal cyclo-reversion, photoreacted 2D coordination polymers, 146–147
thermal dehydrohalogenation, mechanosynthesis, 181, 182
thermally driven rotation, macrocycles, polyrotaxane frameworks, 132
thermal modification
  aluminum-based metal–organic frameworks, 109
  covalent postsynthetic modification, 203–204
thermal stability
  see also hydrothermal stability
  mesoporous MOFs, 43, 46
  porous diamondoid metal formate frameworks, 232–233
thin films
  2D nanoscale metal–organic frameworks, 23
  3D nanoscale metal–organic frameworks on surfaces, 25
  controlled growth, MOF patterning by promoting agents, 388–389
  from colloidal MOF solutions, MOF patterning 396–397
thiols/thioethers, grafting additional metals onto MOF framework, 344, 347–348

thiol units, semiconducting MOFs, 376–380
thiophene adsorption, 312
time-resolved crystallization studies, aluminum-based metal–organic frameworks, 106, 107
titanium, Ti-MOF-74, carbon dioxide adsorption, 270
TMBD *see* tetrakis(methylthio)benzenedicarboxylic acid
top-down approach, MOF patterning, 388, 397
topology of MOFs
  interpenetration, 523, 524
  metal center characterization by solid-state NMR, 460
toxic gases *see* inorganic toxic gases; radioactive gas immobilization; volatile organic compounds
toxicity, edible metal–organic frameworks, 161
TPPS *see* 5,10,15,20-tetrakis(4-sulfonatophenyl)porphyrin
trans corner-sharing polyhedra motifs, aluminum-based metal–organic frameworks, 108, 109, 110
transition metal centers, unsaturated, electrochemical properties, 419–420
transmetallation (metal cation metathesis), 343, 352, 354, 355, 357–358, 515–518
  see also metal ion exchange
trans–cis isomerization influence, gas adsorption by photoresponsive metal–organic frameworks, 263, 264
4,4′,4″-*s*-triazine-2,4,6-triyltribenzoate (TATB) ligands, mesoporous metal–organic frameworks, 44
triethylamine (TEA), crystal size/morphology determination, porous coordination polymer synthesis, 5
trinuclear manganese clusters, 2D MOFs from single-molecule magnets, 247–249
triple stranded photoreactive 1D coordination polymers, 144
trivial versus nontrivial entanglement, polyrotaxanes, 533, 534, 535
tropospheric air pollutants, luminescent sensing MOFs, 364–365
trypsin protease, mesoporous metal–organic framework bioreactor, 57–58, 59
TSMB *see* Texas-Sized Molecular Box
tungsten (W), polyoxometalate-metal–organic frameworks, 428, 429–430
twofold interpenetration, diamond networks, 527, 529
two-step strategy, semiconducting MOFs, 378–380

UiO-66
  hydrothermal stability, 308, 316
  nitrogen dioxide adsorption, 309
  post synthetic modifications, 308–309
  selective carbon dioxide adsorption, 308–309
  structure, 308
UiO-67, nitrogen dioxide adsorption, 309
ultrasonication-assisted synthesis
  nanoscale metal–organic frameworks, 21
  porous coordination polymers, 4
UMCM (University of Michigan Crystalline Materials)
  UMCM-1
    HPLC applications, 451
    postsynthetic modification, 201, 204, 207
    structure and synthesis, 46, 47
  UMCM-1-NH_2, 201, 425
UMCs (unsaturated metal centers) *see* open metal sites
University of Michigan Crystalline Materials *see* UMCM
University of Texas San Antonio *see* USTA
unsaturated bonds *see* olefin bonds
unsaturated metal centers (UMCs) *see* open metal sites
unsaturated versus saturated hydrocarbons
  adsorption mechanisms, 327, 328
  separation, 329–330
USTA (University of Texas San Antonio)
  USTA-20, methane storage, 266–267, 295
  USTA-50a, acetylene separation/purification, 273

vanadium, V-MOF-74, carbon dioxide adsorption, 270
van der Waals potential pockets, methane storage, 292, 295
variable offset cumulative spectroscopy (VOCS), solid-state NMR studies of quadrupolar nuclei, 465
V-MOF-74, carbon dioxide adsorption, 270
VOCs *see* volatile organic compounds
VOCS *see* variable offset cumulative spectroscopy
volatile organic compounds (VOCs), 304, 305, 310–313
  luminescent sensing MOFs, photoactive NDI ligands, 364–365

W *see* tungsten
water
  see also dehydration; hydration; hydrothermal stability
  carbon dioxide adsorption effects, 307–308
  content control, edible metal–organic frameworks, 162
  dehydrohalogenation, mechanosynthesis, 181, 182
  hydrated compounds/moisture, mechanosynthesis of metal–organic structures, 174, 179, 180, 181, 187–188
  liquid assisted grinding, mechanosynthesis of metal–organic structures, 176, 183
  synthesis solvent
    aluminum-based metal–organic frameworks, 100, 104
    edible metal–organic frameworks, 160–161
water-in-oil microemulsion (reverse micelles), crystal size/morphology determination, 5–7
water removal from framework, open metal sites, 260
water stable MOFs, mixed-matrix membranes, 411, 414
WAXS *see* wide-angle X-ray scattering
weave entanglement, 535, 536
Wells–Dawson type polyoxometalates, redox-active MOF composites, 429–430
wetting, MOF patterning, 391, 393
wheel structures *see* macrocycles
wide-angle X-ray scattering (WAXS), crystallization studies, aluminum-based metal–organic frameworks, 106, 107

xenon adsorption, radioisotopes, 314–315, 316
X-ray crystallography, postsynthetic modification characterization, 197
X-ray diffraction (XRD)
  see also powder X-ray diffraction
  crystallization studies, aluminum-based metal–organic frameworks, 106–107
  mechanosynthesis of MOFs, 188–189

MOF structure study limitations, 457
X-ray scattering, crystallization studies, aluminum-based metal–organic frameworks, 106, 107
X-ray structure determination, aluminum-based metal–organic frameworks, 101–103, 106–107
XRD *see* X-ray diffraction
xylene
guest exchange for structural transformation, 474–475
isomer separation, 29, 312, 326, 332–333, 447, 450
toxicity, 311

Zeeman interactions, solid-state NMR studies of quadrupolar nuclei, 458, 459
zeolite-like-mesoporous metal–organic frameworks, 43–44
zeolites
commensurate adsorption, MOF comparison, 324
hydrocarbon separation, 95
incommensurate adsorption, 325
mixed-matrix membranes, 406, 407
zeolitic imidazolate frameworks (ZIFs)
mechanosynthesis, 174, 178, 184–185, 187, 188–189, 190
mesoporous metal–organic frameworks, 44
gas separation, 51
synthesis, patterning, 389, 396, 397
volatile organic compound adsorption, 311–312
ZIF-8
hydrothermal stability, 316
mixed-matrix membranes, 410–411
oxygen reduction catalyst precursors, 438
volatile organic compound adsorption, 311, 312
ZIF-20, mixed-matrix membranes, 410, 411
ZIF-90
coated fibers, solid-phase microextraction, 445, 446
mixed-matrix membranes, 410, 411
solid-state NMR studies, 460–461
zinc adeninates
edible metal–organic frameworks, 167, 168, 169
mesoporous metal–organic frameworks, 46, 47
zinc aspartates, edible metal–organic frameworks, 164
zinc centers
^{67}Zn quadrupolar nuclei, sensitivity to solid-state NMR, 458, 460–461
polyrotaxane frameworks, 120, 124–125, 126, 127–128
zinc dipeptides, edible metal–organic frameworks, 165–166
zinc MOFs
edible metal–organic frameworks, 161
$Zn_4O(dtabc)_3$, metal grafting onto framework, 347, 349, 352
Zn-MOF-74
acetylene separation/purification, 272
carbon dioxide adsorption, 269
ZJN-18/ZJN-19/ZJN-20
catalytic activity, 80, 277
structures, 69–70, 277
ZJU-5, acetylene storage, 268–269
$Zn_4O(dtabc)_3$ (isoreticular to MOF-5), metal grafting onto framework, 347, 349, 352
Zn-MOF-74, 80, 269, 277

Abbrevations and Acronyms used in this Volume

AAS	atomic absorption spectroscopy
abdc	5-amino-benzene-1,3-dicarboxylate
ABTS	2,2′-azinodi(3-ethylbenzothiazoline)-6-sulfonate
acac	acetylacetonate
ACN	acrylonitrile
adip	5,5′-(9,10-anthracediyl)diisophthalate
AFM	atomic force microscope
AMFF	ammonium metal formate framework
AOT	Aerosol-OT
asp	aspartic acid
ATOF-MS	aerosol time-of-flight mass spectrometry
AzDC	4,4′-azobenzene dicarboxylate
BBC	4,4′,4′-(benzene-1,3,5-triyl-tris (benzene-4,1-diyl)) tribenzoate
1,4-BDC	1,4-benzene-dicarboxylate
bdc	1,4-benzenedicarboxylate
bdp	1,4-benzenedipyrazolate
BET	Brunauer-Emmett-Teller
bfbpdc	2,2′-bistrifluoromethyl-biphenyl-4,4′-dicarboxylate
2-bim	2-bromoimidazole
bimb	1,4-bis(1-imidazolyl)benzene
bipy	4,4′-bipyridine (also bpy)
bispybpy	*N*,*N*′-bis(pyridin-4-yl)-2,2′-bipyridine-5,5′-dicarboxamide
bpdc	1,1′-biphenyl-4,4′-dicarboxylate
bpdc	1,3,5-benzenetricarboxylate
BPDC	biphenyl-4,4′-dicarboxylate
bpe	1,2-bis(2-pyridyl)ethane
bpe	1,2-bis(4-pyridyl)ethane
Bpe	*trans*-1,2-bis(4-pyridyl)ethene or 4,4′-bipyridyl ethene
Bpeb	1,4-bis[2-(4-pyridyl)ethenyl]benzene
bpee	1,2-bis(2-pyridyl)ethylene)
BPT	biphenyl-3,4′,5-tricarboxylate
2,2′-bpy	2,2′-bipyridine
Bpy	4,4′-bipyridine
bpydc	2,2′-bipyridine-5,5′-dicarboxylate
BSA	bovine serum albumin
btapa	1,3,5-benzenetricarboxyate tris[*N*-(4-pyridyl)amide]
btb	1,3,5-benzenetribenzoate
btb	4,4′,4′-benzene-1,3,5-triylbenzoate
BTB	4,4′,4′-Benzene-1,3,5-triyltribenzoate
btb	benzene-1,3,5-tris(benzene-4-carboxylate)
btc	1,3,5-benzenetricarboxylate
1,2,4-BTC	benzene-1,2,4-tricarboxylate
BTC	1,3,5-benzenetricarboxylic acid
btp	biphenyl-3,4′,5-tricarboxylate
btt	1,3,5-benzenetristetrazolate
Calcd	calculated
CASTEP	Cambridge Serial Total Energy Package
CAU	Christian-Albrechts Universität
CBMC	configurational-bias Monte Carlo
cca	4-carboxycinnamate
CCS	carbon capture and sequestration
CCS	CO_2 capture and sequestration
CDO	chelidonic acid
cds	cadmium sulphide framework topology
CFT	copper formate tetrahydrate
chdc	*trans*-1,2-cyclohexanedicarboxylate
CIF	Crystallographic Information File
2-cim	2-chloroimidazole
CMON	covalent metal–organic networks
CN	coordination number
CNG	compressed natural gas
cnge	cyanoguanidine
CNT	carbon nanotube
CP	coordination polymer
CP	cross polarization
CP-MAS	cross polarization magic angle spinning
CSA	chemical shift anisotropy
CSA	controlled secondary building units approach
CSD	Cambridge Structural Database
CSP	chiral stationary phases
CT	Computed tomography
ct	contact time
CTAB	cetyltrimethylammonium bromide
CTF	covalent triazine-based framework
CUS	coordinatively unsaturated metal sites
CV	cyclic voltammogram
CVD	chemical vapor deposition
cyc	3,10-dimethyl-hexaazacyclotetradecane
Cyt c	cytochrome c
0D	zero dimension
1-D	one-dimensional
2-D	two-dimensional
3-D	three-dimensional
dace	1,4-diaminocyclohexane
dabco	1,4-diazabicyclo[2.2.2]octane
dcbinol	(*S*)-2,2′-dihydroxy-6,6′-dimethyl(1,1′-biphenyl)-4,4′-dicarboxylate
DCQNI	*N*,*N*′-dicyanoquinodiimine
DEF	*N*,*N*-diethylformamide
dhbd	2,5-dihydroxybenzene-1,4-dicarboxylate
diPyNI	*N*,*N*′-di-(4-pyridyl)-1,4,5,8-naphthalenetetracarboxydiimide
dipyni	*N*,*N*′-di-(4-pyridyl)-1,4,5,8-napthalenetetracarboxydiimide
DMA	*N*,*N*-dimethylacetamide
22-DMB	2,2-dimethylbutane
23-DMB	2,3-dimethylbutane
dmbd	2,5-dimercapto-1,4-benzenedicarboxylate
DME	dimethylether
DMF	*N*,*N*-dimethylformamide
dmf	*N*,*N*′-dimethyl-formamide
DMMP	dimethyl methylphosphonate
DMNB	2,3-dimethyl-2,3-dinitrobutane
DMS	2,3-dimethylsuccinate
DMSO	dimethyl sulfoxide
DNT	2,4-dinitrotoluene
DOBDC	2,5-dioxido-1,4-benzenedicarboxylate
DOE	Department of Energy
dpdiol	diphenyl-2,2′-dihydroxy-4,4′-dicarboxylate
dped	1,2-di-4-pyridyl-1,2-ethanediol
DPNI	*N*,*N*′-di-(4-pyridyl)-1,4,5,8-naphthalenetetracarboxydiimide
dpq	dipyrido[3,2-d:2′,3′-f]quinoxaline
DPT	3,6-di-4-pyridyl-1,2,4,5-tetrazine
dpyg	1,2-di(4-pyridyl)-glycol
DSC	differential scanning calorimetry
dtabc	2,5-dithioalloxy-1,4-benzenedicarboxylate
DUT	Dresden University of Technology
DXRL	deep X-ray lithography
EBTC	1,1′-ethynebenzene-3,3′,5,5′-tetracarboxylate
EDC	endocrine disrupting chemical
EDLC	electrochemical double layer capacitor
EDTA	ethylenediaminetetraacetic acid
EDX	energy-dispersive X-ray spectroscopy
EDXRD	energy dispersive X-ray diffraction
EFG	electric field gradient
EG	ethylene glycol
EMC	entatic metal center
ESCP	ethoxysuccinato-cisplatin
ESI-MS	electrospray ionisation mass spectrometry
ESR	electron spin resonance
Et	ethyl
etz	3,5-diethyl-1,2,4-triazole
EWOD	electrowetting-on-dielectric
EXAFS	extended X-ray absorption fine structure
Fc	ferrocenyl
FC	field-cooled
FC	framework composite
fma	fumarate
FMOF	fluorinated metal-organic framework
FMOF-1	first perfluorinated metal-organic framework
FP-TRMC	flash-photolysis time-resolved microwave conductivity
FTIR	Fourier transform infrared
H_2fum	fumaric acid
FWHM	full-width-at-half-maximum
GC	gas chromatography
GCMC	Grand Canonical Monte Carlo
GIPAW	gauge including projector augmented wave
gla	*R*-2-methylglutarate
GO	Graphite oxide

GPU	gas permeation unit
h	hour
H_2bdc	1,4-benzenedicarboxylic acid
H_2BDC	benzene-1,4-dicarboxylic acid
H_2CDC	cyclohexane-1,4-dicarboxylic acid
H_2hfipbb	4,4′-(hexafluoroisopropylidene)bis(benzoic acid)
H_2ip	(isophthalic acid or 1,3-benzenedicarboxylic acid)
H_2muco	*trans*,*trans*-muconic acid
H_2ndc	naphthalene dicarboxylic acid
H_2TMPyPs	5,10,15,20-tetrakis(1-methyl-4-pyridinio)porphyrins
H_3BPT	biphenyl-3,4′,5-tricarboxylic acid
H_3btc	1,3,5-benzene tricarboxylic acid
H_3BTT	1,3,5-benzenetristetrazolate
H_3TATAB	4,4′,4′-s-triazine-1,3,5-triyltrip-aminobenzenecarboxylic acid
H_3TPO	tris-(4-carboxylphenyl)phosphine oxide
H_4bptc	3,3′,5,5′-biphenyltetracarboxylic acid
H_4mdip	5,5′-methylene-diisophthalate
H_4PDDI	5,5′-(pyridine-2,5-diyl)diisophthalic acid
H_4salphdc	*N*,*N*′-phenylenebis(salicylideneimine)dicarboxylic acid
H_4T(*p*-CO_2)PP	meso-tetrakis(4-carboxyphenyl)porphine
H_6bhb	H_6bhb = 3,3′,3′,5,5′5′-benzene-1,3,5-triyl-hexabenzoic acid
hbd	2-hydroxy-benzene-1,4-dicarboxylate
HCF	hexacyanoferrate
HCH	hexachlorocyclohexane
HCNacac	3-cyanoacetylacetone
HDT	1-hexadecanethiol
HER	hydrogen evolution reaction
HH	head to head
HHT	2,3,6,7,10,11-hexahydroxytriphenylene
HIBA	4-(1H-imidazole-1-yl)benzoic acid
Him	imidazole
Hina	isonicotinic acid
HKURST-1	$[Cu_3(btc)_2(H_2O)_2]$
HKUST	Hong Kong University of Science and Technology
HPLC	high-performance liquid chromatography
HT	head to tail
HT/RT/LT	high/room/low temperature
HTB	4,4′,4′-(1,3,4,6,7,9,9b-heptaazaphenalene-2,5,8-triyl)tribenzoate
HTFA	trifluoroacetic acid
Htrz	1,2,4-1*H*-triazole
IAST	Ideal adsorbed solution theory
ICP-AES	inductively coupled plasma atomic emission spectroscopy
ICP-MS	inductively coupled plasma mass spectrometry
IL	ionic liquid
ILAG	ion- and liquid-assisted grinding
imc	1*H*-imidazolium,3,3′-methylenebis[1-(4-carboxyphenyl)]
INS	inelastic neutron scattering
IR	infra red
IRMOF	isoreticular metal-organic framework
IRMOF-3	$[Zn_4O(NH_2bdc)_3]$
iso	isophthalate (benzene-1, 3-dicarboxylate)
J	magnetic coupling
KCF	kinetically controlled flexibility
L3	1,5-bis(1,2,4-triazol-1-yl)pentane
LAG	liquid-assisted grinding
LB	Langmuir–Blodgett
LbL	layer-by-layer
LBS	Lewis basic sites
LCD	Largest cavity diameter
LCW	lithographically controlled wetting
Ln	lanthanide
LNG	liquefied natural gas
lp	large pore
LPE	liquid-phase epitaxy
LRMO	long-range magnetic order
LRO	long-range ordering
M	metal
M'MOF	mixed metal–organic framework
M–CAT	metal–catecholate
MAA-co-EDMA	methylarylic acid-co-ethylene dimetharylate
MAF	metal azide framework
MALDI-TOF-MS	matrix assisted laser desorption/ionization time of flight mass spectrometry
MAS	magic-angle spinning
Mb	myoglobin
MBB	molecular building block
MCM-41	mesoporous organosilica
MD	molecular dynamics
mdip	5,5′-methylene-di-isophthalate
ME	magnetoelectric
Me	methyl
MeCN	acetonitrile
Meim	imidazolate-2-methyl
MEM	maximum entropy method
mesoMOF	mesoporous metal–organic framework
metbd	2,5-bis-(2-(methylthio)ethylthio)-1,4-benzenedicarboxylate
MFC	magnetic framework composite
MFF	metal formate framework
μCP	microcontact printing
μ-SPE	micro-solid-phase extraction
MIL	Matèrial Institut Lavoisier
MIL	Matèriaux de l'Institut Lavoisier
MIL	Materials from Institut Lavoisier
MIL	Materials of "Institut Lavoisier"
MIL-100(M)	$[M_3F(H_2O)O(btc)_2]$, M
MIL-101(Cr)	$[Cr_3F(H_2O)O(bdc)_2]$
MIL-53(Al)	[Al(OH)(bdc)]
2-mim	2-methylimidazole
MIM	mechanically interlocked molecule
MIMIC	micromolding in capillaries
mipt	5-methylisophthalate
mmen	*N*,*N*′-dimethylethylenediamine
MMM	mixed-matrix membrane
MMOF	microporous metal-organic framework
MMPF	metal–metalloporphyrin framework
MNM	molecular nanomagnet
MOF	Metal-organic framework
MOF-5	$[Zn_4O(bdc)_3]$
MOFs	Metal–organic frameworks
moip	5-methoxy-isophthalic acid
MOP	metal-organic polyhedra
MORF	metal-organic rotaxane framework
2-MP	2-methylpentane
3-MP	3-methylpentane
mp	melting point
MPF	metalloporphyrinic framework
MQMAS	multiple quantum magic-angle spinning
MQT	magnetic quantum tunneling
MRI	magnetic resonance imaging
MSPDE	matrix solid-phase dispersion extraction
MSPE	magnetic solid-phase extraction
MTBS	methyltributylammonium methyl sulfate
MTN	montmorillonite
*m*X	*meta*-xylene
N-EtFOSA	N-ethyl perfluorooctylsulfonamide
NAFS-1	MOFs nanofilm on a solid surface
NAI	*N*-acetylimidazole
nanoMOF	nanoscale metal organic framework
NASA	National Aeronautics and Space Administration
1,4-ndc	1,4-naphthalenedicarboxylate
2,6-ndc	2,6-naphthalenedicarboxylate
NDC	2,6-naphthalenedicarboxylate
NGV	natural gas vehicle
NH_2bdc	2-amino-benzene-1,4-dicarboxylate
nHEX	normal hexane
NIR	Near infrared
NMOF	nanoscale metal–organic framework
NMR	nuclear magnetic resonance
NOVA	NO void analysis
np	narrow pore
NP	normal-phase
NPD	neutron powder diffraction
o/w	oil-in-water
OAc	acetate
ODA	4,4-oxydianiline
OMS	open metal site
ORR	oxygen reduction reaction
ox	oxalate
*o*X	*ortho*-xylene
PAA	poly(acrylic acid)
PAH	polycyclic aromatic hydrocarbon
PAS	principal axis system
PBA	Prussian blue analogs
PBDE	polybrominated diphenylether
PCB	polychlorinated biphenyl
PcF16	perfluorophthalocyanine
pci	pyridine-4-carboxylic ion

PCN	porous coordination network
PCP	porous coordination polymer
1,3-H_2pda	1,3-phenylenediacetic acid
3,5-PDC	3,5-pyridinedicarboxylate
pdc	pyridine-1,3-dicarboxylate
PDI	polydispersity index
PDMS	polydimethylsiloxane
pdt	pyrazine-2,3-dithiolate
PE/AFE/FE	para-/antiferro-/ferroelectric/electricity
PEI	polyethyleneimine
PEM	polymer electrolyte membrane
PEMFC	polymer electrolyte membrane fuel cell
PET	polyethylene terephthalate
PFG	pulsed field gradient
pfmbc	*p*-perfluoromethylbenzenecarboxylate
PhTES	phenyltriethoxysilane
PIZA	porphyrinic Illinois zeolite analog
PL	photoluminescence
PLD	Pore limiting diameter
PLO	porous layered oxide
PLOT	porous layer open tube
PMDA	pyromellitic dianhydride
pn	1,3-bis(4-pyridyl)propane
POM	Polyoxometalate
POMOF	polyoxometalate-metal–organic framework
POMs	Polyoxometalates
POP	persistent organic pollutant
porph	tetra(*N*-methyl-4-pyridyl)porphine
ppb	Parts per billion
PPEES	poly-(1,4-phenylene ether-ether-sulfone)
PPF	porphyrin paddle wheel framework
PPh_3	triphenylphosphine
ppm	Parts per million
ppz	piperazine
Pr	propyl
PRF	polyrotaxane framework
PSD	postsynthetic deprotection
PSE	post-synthetic exchange
PSM	post-synthetic modification
ptcda	perylene-3,4,9,10-tetracarboxylic dianhydride
PTE	positive thermal expansion
pvba	*trans*-2-(4′-pyridyl)vinylbenzoic acid
PVP	polyvinylpyrrolidone
*p*X	*para*-xylene
PXRD	Powder X-ray diffraction
py	pyridine
pybinol	(*R*)-6,6′-dichloro-2,2′-dihydroxy-1,1′-binaphthyl-4,4′-bipyridine
pyz	pyrazine
pz	pyrazine
pzdc	pyrazine-2,3-dicarboxylate
3QMAS	triple quantum magic-angle spinning
*Q*st	isotectic heats of adsorption
QD	quantum dot
QENS	Quasielastic neutron scattering
RCP	rotaxane coordination polymer
rtct-tpcb	regio *trans*, *cis*, trans-tetrakis(4-pyridyl)cyclobutane
rctt-tpcb	regio *cis*, *trans*, trans-tetrakis(4-pyridyl)cyclobutane
rf	radio-frequency
RH	relative humidity
RON	Research Octane Number
RP	reverse-phase
RP HPLC	reverse-phase high-performance liquid chromatography
RPM	robust porphyrinic material
RPM	Rutgers Recyclable Porous Materials
RT	room temperature
SAE-VA-μ-SPE	sonication-assisted emulsification microextraction combined with vortex-assisted porous-membrane-protected μ-SPE
SALE	solvent-assisted linker exchange
SAM	self-assembled monolayer
SAM	self-assembled organic monolayer
SAXS	small-angle X-ray scattering
SBB	supermolecular building block
SBU	secondary building unit
SC–SC	single-crystal to single-crystal
$SCCO_2$	supercritical CO_2
SCSC	single crystal-to-single crystal
SCXD	single-crystal X-ray diffraction
SDC	4,4′-stilbenedicarboxylic acid
SEM	scanning electron microscopy
SG	space group
SHE	scanning electron microscope
SIM	single ion magnet
5-H_3sipa	5-sulfoisophthalic acid
SMM	single molecule magnet
SMT	single molecular trap
SPAM	soft-pulse-added-mixing
SPAM-3QMAS	soft-pulse-added-mixing triple-quantum magic-angle spinning
SPE	solid-phase extraction
SPME	solid-phase microextraction
SPPO	sulfonated poly (2,6-dimethyl-1,4-phenylene oxide)
4-spy	4-styrylpyridine
SSNMR	solid-state nuclear magnetic resonance
ST	satellite transition
STM	scanning tunneling microscope
SURMOF	surface metal organic framework
TATB	4,4′,4′-*s*-triazine-2,4,6-triyltribenzoate
TBA	tetra-*n*-butylammonium
tba	tetrabutylammonium
TBAPy	1,3,6,8-tetrakis(*p*-benzoate)pyrene
tbdc	tetra bromodicarboxylic acid
TBHP	tertbutylhydroperoxide
tbip	5-tert-butylisophthalate
*T*C	critical temperature and phase transition temperature
tci	tris(2-carboxyethyl) isocyanurate
TCNQ	tetracyanoquinodimethane
tcpb	1,2,4,5-tetrakis(4-carboxyphenyl)benzene
TCPB	tetracarboxylate acid ligand
TCPP	5,10,15,20-tetrakis(4-carboxyphenyl)porphyrin
TCPP	*tetra*(4-carboxy)-phenyl-porphyrin
TCPP	tetrakis(4-carboxyphenyl) porphyrin
tcpp-H_2	tetra(carboxyphenyl)porphyrin
TCPSB	1,3,5-tri(4′-carboxyphenylsulphonyl)benzene
TD-GC/MS	thermal desorption gas chromatography–mass spectrography
TDC	thiophene-2,5-dicarboxylate
tdcpp	tetrakis(3,5-dicarboxyphenyl)porphine
TDPAT	2,4,6-tris(3,5-dicarboxyphenylamino)-1,3,5-triazine
TDS	Thermal desorption spectroscopy
TEA	tetraethylammonium
TEA	triethylamine
ted	triethylenediamine
TEGly	triethylene glycol
TEM	transmission electron microscopy
TFA	trifluoroacetate
tfbda	2,3,5,6-tetrafluoro-1,4-benzenedicarboxylic acid
TGA	thermogravimetric analysis
THF	tetrahydrofuran
TLS	time-resolved static light scattering
TM	transition metal
TMA	tetramethylammonium
tmbd	tetrakis(methylthio-)-1,4-benzenedicarboxylate
*T*N	Nèel temperature
TNT	2,4,6-trinitrotoluene
TOF	time-of-flight
TPDC	triphenyl-4,4′-dicarboxylate
TPT	2,4,6-tris(4-pyridyl)triazine
TPTZ	2,4,6-tris-(2-pyridyl)-*s*-triazine
TRIR	time-resolved IR
TTF	tetrathiafulvalene
UiO-66	$[Zr_6O_4(OH)_4(bdc)_6]$
UMC	unsaturated metal center
UMCM	University of Michigan Crystalline Material
UMCs	Unsaturated metal centers
USTA	University of Texas San Antonio
UV	Ultraviolet
VOC	volatile organic compound
VOCS	variable offset cumulative spectroscopy
VOCs	Volatile organic compounds
VT	variable temperature
WAXS	small-angle X-ray scattering
WCOT	wall-coated open tubular
XRD	X-ray diffraction
XRPD	X-ray powder diffraction
ZFC	zero-field-cooled
ZIF	Zeolitic imidazolate framework
ZIF-8	$[Zn(Meim)_2]$

WILEY END USER LICENSE AGREEMENT

Go to www.wiley.com/go/eula to access Wiley's ebook EULA.